S-N/99205--076

STOLLER-NAVARRO

Groundwater Flow Model of Corrective Action Units 101 and 102: Central and Western Pahute Mesa, Nevada Test Site, Nye County, Nevada

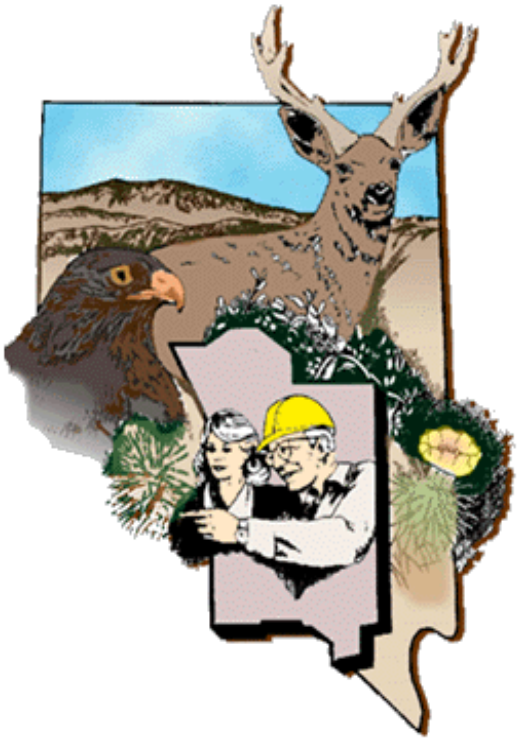

Revision No.: 0

June 2006

Prepared for U.S. Department of Energy under Contract No. DE-AC52-03NA99205.

Available for public sale, in paper, from:

U.S. Department of Commerce
National Technical Information Service
5285 Port Royal Road
Springfield, VA 22161
Phone: 800.553.6847
Fax: 703.605.6900
Email: *orders@ntis.gov*
Online ordering: *http://www.ntis.gov/ordering.htm*

Available electronically at *http://www.osti.gov/bridge*

Available for a processing fee to U.S. Department of Energy and its contractors, in paper, from:

U.S. Department of Energy
Office of Scientific and Technical Information
P.O. Box 62
Oak Ridge, TN 37831-0062
Phone: 865.576.8401
Fax: 865.576.5728
Email: *reports@adonis.osti.gov*

S-N/99205--076

GROUNDWATER FLOW MODEL OF CORRECTIVE ACTION UNITS 101 AND 102: CENTRAL AND WESTERN PAHUTE MESA, NEVADA TEST SITE, NYE COUNTY, NEVADA

Contributors:

Stoller-Navarro Joint Venture
Greg Ruskauff
John Ewing
Eric Bhark
Srikanta Mishra
Neil Deeds
Tad Beard
Richard Rondeau
John McCord
Alaa Aly

Los Alamos National Laboratory
Andrew Wolfsberg
Wendy Soll
Zora Dash
Carl Gable

Revision No.: 0

June 2006

Stoller-Navarro Joint Venture
7710 W. Cheyenne, Building 3
Las Vegas, NV 89129

Prepared for U.S. Department of Energy under Contract No. DE-AC52-03NA99205.

GROUNDWATER FLOW MODEL OF CORRECTIVE ACTION UNITS 101 AND 102: CENTRAL AND WESTERN PAHUTE MESA, NEVADA TEST SITE, NYE COUNTY, NEVADA

Approved by: Approved signature Date: 6-2-06

John McCord, UGTA Project Manager
Stoller-Navarro Joint Venture

TABLE OF CONTENTS

TABLE OF CONTENTS (CONTINUED)

TABLE OF CONTENTS (CONTINUED)

TABLE OF CONTENTS (CONTINUED)

TABLE OF CONTENTS (CONTINUED)

TABLE OF CONTENTS (CONTINUED)

TABLE OF CONTENTS (CONTINUED)

TABLE OF CONTENTS (CONTINUED)

TABLE OF CONTENTS (CONTINUED)

Appendix C - Development of a Steady-State Thermal Field and Evaluation of the Potential Use of Temperature Data To Constrain Pahute Mesa CAU Groundwater Flow Models

TABLE OF CONTENTS (CONTINUED)

LIST OF FIGURES

LIST OF FIGURES (CONTINUED)

LIST OF FIGURES (CONTINUED)

LIST OF FIGURES (CONTINUED)

LIST OF FIGURES (CONTINUED)

LIST OF FIGURES (CONTINUED)

LIST OF FIGURES (CONTINUED)

LIST OF FIGURES (CONTINUED)

LIST OF FIGURES (CONTINUED)

LIST OF FIGURES (CONTINUED)

LIST OF FIGURES (CONTINUED)

LIST OF FIGURES (CONTINUED)

LIST OF FIGURES (CONTINUED)

LIST OF FIGURES (CONTINUED)

LIST OF FIGURES (CONTINUED)

LIST OF FIGURES (CONTINUED)

LIST OF FIGURES (CONTINUED)

LIST OF FIGURES (CONTINUED)

LIST OF FIGURES (CONTINUED)

LIST OF FIGURES (CONTINUED)

LIST OF FIGURES (CONTINUED)

LIST OF FIGURES (CONTINUED)

LIST OF FIGURES (CONTINUED)

LIST OF FIGURES (CONTINUED)

LIST OF FIGURES (CONTINUED)

LIST OF FIGURES (CONTINUED)

LIST OF TABLES

LIST OF TABLES (CONTINUED)

LIST OF TABLES (CONTINUED)

LIST OF TABLES (CONTINUED)

LIST OF TABLES (CONTINUED)

LIST OF TABLES (CONTINUED)

LIST OF TABLES (CONTINUED)

LIST OF PLATES

NUMBER **TITLE**

LIST OF ACRONYMS AND ABBREVIATIONS

ac-ft	Acre-foot
ac-ft/yr	Acre-feet per year
Am	Americium
amsl	Above mean sea level
ASTM	American Society for Testing and Materials
bmsl	Below mean sea level
BN	Bechtel Nevada
°C	Degrees Celsius
CADD	Corrective Action Decision Document
CAI	Corrective Action Investigation
CAIP	Corrective Action Investigation Plan
CAP	Corrective Action Plan
CAS	Corrective Action Site
CAU	Corrective Action Unit
Cl^-	Chloride
cm	Centimeter
cm/yr	Centimeters per year
CP	Control Point
CR	Closure Report
CRWMS M&O	Civilian Radioactive Waste Management System Management and Operating Contractor
DOE	U.S. Department of Energy
DRI	Desert Research Institute
ERP	Environmental Restoration Program
ET	Evapotranspiration
EV	EarthVision®
°F	Degrees Fahrenheit
FEHM	Finite element heat-mass
FFACO	*Federal Facility Agreement and Consent Order*
FGE	Forced-Gradient Experiment
ft	Foot
ft/d	Feet per day
GB	Gigabyte

LIST OF ACRONYMS AND ABBREVIATIONS (CONTINUED)

GHz	Gigahertz
HST	Hydrologic Source Term
HTH	Hydrologic Test Hole
in.	Inch
in./yr	Inches per year
IT	IT Corporation
°/km	Degrees per kilometer
K	Hydraulic conductivity
k	Intrinsic permeability
k_0	Reference permeability
K_d	Distribution coefficient
kg/s	Kilograms per second
km	Kilometer
km^2	Square kilometer
LaGriT	Los Alamos Grid Toolbox
LANL	Los Alamos National Laboratory
LLNL	Lawrence Livermore National Laboratory
m	Meter
m/d	Meters per day
m^2	Square meter
m^3	Cubic meter
m^3/d	Cubic meters per day
m^3/yr	Cubic meters per year
ME	Mean error
mg/L	Milligrams per liter
mi	Mile
mi^2	Square mile
moles/kg	Moles per kilogram
moles/L	Moles per liter
mW/m^2	Milliwatts per square meter
N/A	Not applicable
NAD	North American Datum
NDEP	Nevada Division of Environmental Protection

LIST OF ACRONYMS AND ABBREVIATIONS (CONTINUED)

NNSA/NSO	U.S. Department of Energy, National Nuclear Security Administration Nevada Site Office
NTS	Nevada Test Site
OMR	Ochtree mesh refinement
PC	Personal computer
PEST	Parameter Estimation Software
PM/OV	Pahute Mesa/Oasis Valley
PTRK	Residence time transfer function particle-tracking method
Pu	Plutonium
QA	Quality Assurance
RAM	Random access memory
S	Storativity
SD	Standard deviation of error
SDWA	*Safe Drinking Water Act*
s/kg	Seconds per kilogram
SNJV	Stoller-Navarro Joint Venture
SO_4^{2-}	Sulfate
SPTR	Streamline-particle-tracking method
Sr	Strontium
SWIFT	Sandia Waste Isolation Fractured Transport
SWIP	Survey Waste Injection Program
T	Transmissivity
TTR	Tonopah Test Range
TW	Test Well
TWG	Technical Working Group
UGTA	Underground Test Area
USGS	U.S. Geological Survey
UTM	Universal Transverse Mercator
WW	Water Well
YMP	Yucca Mountain Project
3-D	Three-dimensional
δD	Delta deuterium
$\delta^{13}C$	Delta carbon-13
$\delta^{18}O$	Delta oxygen-18

LIST OF GEOLOGICAL ABBREVIATIONS AND SYMBOLS

AA	Alluvial Aquifer
ADA	All HSU Depth Decay and Anisotropy
ATICU	Ammonia Tanks Intrusive Confining Unit
BA	Benham Aquifer
BAQ	Basal Aquifer
BCU	Basal Confining Unit
BFCU	Bullfrog Confining Unit
BMICU	Black Mountain Intrusive Confining Unit
BRA	Belted Range Aquifer
CA	Carbonate Aquifer
CCICU	Claim Canyon Intrusive Confining Unit
CCU	Clastic Confining Unit
CFCM	Crater Flat Composite Unit
CFCU	Crater Flat Confining Unit
CHCU	Calico Hills Confining Unit
CHICU	Calico Hills Intrusive Confining Unit
CHVCM	Calico Hills Vitric Composite Unit
CHVTA	Calico Hills Vitric-Tuff Aquifer
CHZCM	Calico Hills Zeolitic Composite Unit
DRIA	Desert Research Institute Chloride Mass-Balance Alluvial and No Elevation Screen Recharge Model
DRIAE	Desert Research Institute Chloride Mass-Balance Alluvial and Elevation Screen Recharge Model
DRT	Deeply Rooted Belted Range Thrust Fault
DVA	Detached Volcanic Aquifer
DVCM	Detached Volcanic Composite Unit
DVRFM	Death Valley Regional Flow Model
DVRFS	Death Valley Regional Flow System
FCA	Fortymile Canyon Aquifer
FCCM	Fortymile Canyon Composite Unit
FCCU	Fluorspar Canyon Confining Unit
HFM	Hydrostratigraphic Framework Model
HGU	Hydrologic Unit
HST	Hydrologic Source Term

LIST OF GEOLOGICAL ABBREVIATIONS AND SYMBOLS (CONTINUED)

HSU	Hydrostratigraphic Unit
I	Intrusives
IA	Inlet Aquifer
ICU	Intrusive Confining Unit
KA	Kearsarge Aquifer
LCA	Lower Carbonate Aquifer
LCA1	Lower Carbonate Aquifer-Thrust Plate
LCA3	Lower Carbonate Aquifer-Thrust Plate
LCCU	Lower Clastic Confining Unit
LCCU1	Lower Clastic Confining Unit-Thrust Plate
LFA	Lava-Flow Aquifer
LPCU	Lower Paintbrush Confining Unit
MGCU	Mesozoic Granite Confining Unit
MME	Modified Maxey-Eakin Recharge Model
PBRCM	Pre-Belted Range Composite Unit
PCM	Paintbrush Composite Unit
PLFA	Paintbrush Lava-Flow Aquifer
PM/OV	Pahute Mesa/Oasis Valley
PVTA	Paintbrush Vitric-Tuff Aquifer
PreT	Pre-Tertiary
PZUP	Raised Pre-Tertiary Surface
RIDGE	Basement Ridge Model
RMICU	Rainier Mesa Intrusive Confining Unit
SCCC	Silent Canyon Caldera Complex
SCICU	Silent Canyon Intrusive Confining Unit
SCVCU	Subcaldera Volcanic Confining Unit
SDA	Selected HSU Depth Decay and Anisotropy
SEPZ	Contiguous Imbricate Thrust Sheet
SWNVF	Southwestern Nevada Volcanic Field
TC	Tuff Cone
TCA	Tiva Canyon Aquifer
TCL	Thirsty Canyon Lineament
TCU	Tuff Confining Unit

LIST OF GEOLOGICAL ABBREVIATIONS AND SYMBOLS (CONTINUED)

TCVA	Thirsty Canyon Volcanic Aquifer
THCM	Tannenbaum Hill Composite Unit
THLFA	Tannenbaum Hill Lava-Flow Aquifer
TM	Timber Mountain
TMA	Timber Mountain Aquifer
TMCM	Timber Mountain Composite Unit
TSA	Topopah Spring Aquifer
UCCU	Upper Clastic Confining Unit
UPCU	Upper Paintbrush Confining Unit
USGSD	U.S. Geological Survey Redistribution Recharge Model
USGSND	U.S. Geological Survey No Redistribution Recharge Model
VA	Volcanic Aquifer
VCU	Volcanic Confining Unit
VTA	Vitric-Tuff Aquifer
VU	Volcanics Undifferentiated
WTA	Welded-Tuff Aquifer
WWA	Windy Wash Aquifer
YMCFCM	Yucca Mountain Crater Flat Composite Unit
YVCM	Younger Volcanic Composite Unit

ACKNOWLEDGEMENTS

The Pahute Mesa CAU flow model report is a very large and complicated document, and many people in addition to the authors aided in its production. In particular, the project team acknowledges the efforts of Janice Rose, Barbara Deshler, Yvonne Lewis, Ellen Cook, Shirley Murray, Afief Fadil, Caroline Gilbert, and John Flinn. We also thank the following individuals for their contributions and review of this report: John McCord, Bill Fryer, John Pickens, and Van Kelley.

We also gratefully acknowledge the advice of Sig Drellack and Lance Protho, the supporting analyses from Edward Kwicklis, and the code enhancement of Sharad Kelkar.

EXECUTIVE SUMMARY

This Executive Summary is a synopsis of the report entitled *Groundwater Flow Models of CAUs 101 and 102: Central and Western Pahute Mesa, Nye County, Nevada*, prepared for the U.S. Department of Energy (DOE). A steady-state groundwater flow model of the Pahute Mesa Corrective Action Unit (CAU) has been constructed using a suite of hydrostratigraphic frameworks, recharge distributions, and hydraulic parameter assignment conceptualizations. Model calibration and sensitivity analyses, and geochemical verification were conducted and documented.

INTRODUCTION

The DOE, National Nuclear Security Administration Nevada Site Office (NNSA/NSO) initiated the Underground Test Area (UGTA) Project to assess and evaluate the effects of the underground nuclear weapons tests on groundwater on the Nevada Test Site (NTS) and vicinity through the *Federal Facility Agreement and Consent Order* (FFACO) (1996). The processes that will be used to complete UGTA corrective actions are described in the "Corrective Action Strategy" in the FFACO Appendix VI, Rev. 1 (December 7, 2000). The objective of the strategy is to analyze and evaluate each UGTA CAU through a combination of data and information collection and evaluation, and modeling groundwater flow and contaminant transport, including uncertainty. The FFACO corrective action process for the Central and Western Pahute Mesa CAUs was initiated with the Corrective Action Investigation Plan (CAIP) (DOE/NV, 1999). This CAIP identified a three-step model development process to evaluate the impact of testing on groundwater and simulate a contaminant boundary. The first step is the compilation and evaluation of existing and new data for use in the flow model and is documented in a series of data compilation and analysis reports, including *Hydrologic Data for Groundwater Flow and Contaminant Transport Model of Corrective Action Units 101 and 102: Central and Western Pahute Mesa, Nye County, Nevada* (SNJV, 2004a). The second step is the development of the groundwater flow model, documented in this report. The third step is the development of the transport model to assess the migration of radionuclides away from underground nuclear test cavities on Pahute Mesa.

Underground nuclear tests conducted at Pahute Mesa that are of interest to the UGTA Project are those detonated in deep vertical shafts, or drilled into volcanic rock near or below the water table.

A total of 82 such underground nuclear tests were conducted in Pahute Mesa. Sixty-four of these tests were detonated on Central Pahute Mesa (CAU 101), and 18 tests were detonated in Western Pahute Mesa (CAU 102) (DOE/NV, 2000). Transport in groundwater is the primary mechanism of migration for the subsurface contamination away from Pahute Mesa underground nuclear tests.

Pahute Mesa is located in the northwestern part of the NTS. Pahute Mesa is an elevated plateau of about 500 square kilometers (km^2) (200 square miles [mi^2]). The area of interest for the Pahute Mesa flow model is defined by the potentially affected portion of the regional groundwater flow system, which includes a region stretching from the northern side of Pahute Mesa south and southwestward to Oasis Valley. Pahute Mesa geology is dominated by the deposition of rock units from volcanic eruptions from nested calderas of the Southwestern Nevada Volcanic Field. The Silent Canyon Caldera is the oldest series of calderas and consists of at least two nested calderas, the Area 20 Caldera and the older Grouse Canyon Caldera. Both calderas were formed, and subsequently filled, by voluminous eruptions of tuff and lava of generally rhyolitic composition. The youngest caldera complex of hydrologic significance is the Timber Mountain Caldera. This caldera collapse and its filling with volcanic materials affect the southern portion of the Pahute Mesa CAU.

Groundwater beneath Pahute Mesa generally flows in a southwest direction, primarily through fractures in the lava-flow and tuff aquifers. Zeolitized bedded and nonwelded tuffs act as confining units that inhibit the flow of groundwater. The spatial distribution of permeable aquifers relative to the confining units is not well understood. Thickness variations of aquifers and confining units and their connectivity across faults or caldera boundaries are important hydrostratigraphic relationships that are also not well understood. A number of wells provide water-level information in the areas of Pahute Mesa and Oasis Valley, but water levels in the area between Pahute Mesa and Oasis Valley are less well defined. However, what data are available suggest that groundwater elevations generally gently mimic the topography. Some groundwater discharges to the surface within the Oasis Valley discharge area in the form of springs. Groundwater recharge occurs locally from precipitation and by underflow from areas located to the north of Pahute Mesa. Groundwater then flows south southwestward to the Oasis Valley and Death Valley to the southwest.

Specific objectives of the Central and Western Pahute Mesa (referred to hereafter as simply Pahute Mesa) groundwater flow model are to:

- Develop a three-dimensional (3-D), numerical flow model that incorporates the important physical features of the flow system and honors CAU-specific data and information.
- Simulate the groundwater flow system to determine the direction and magnitude of groundwater fluxes based on calibration to Pahute Mesa hydrogeologic data and boundary flux data determined from the UGTA regional flow model.
- Quantify the uncertainty in the direction and magnitude of groundwater flow due to uncertainty in parameter values and alternative component conceptual models (e.g., hydrostratigraphic framework, boundary flux, and recharge).

FRAMEWORK FOR GROUNDWATER FLOW MODELING OF CENTRAL AND WESTERN PAHUTE MESA - DATA, INFORMATION, AND CONCEPTUAL MODELS

The data, information, and conceptual models used to develop the Pahute Mesa flow model represent a large body of work and are described in detail in the integrating report *Hydrologic Data for the Groundwater Flow and Contaminant Transport Model of Corrective Action Units 101 and 102: Central and Western Pahute Mesa, Nye County, Nevada* (SNJV 2004a). The regional and site-specific elements that are integrated into the Pahute Mesa flow model include:

- Regional data and information that provide the hydrogeologic context for the CAU-specific flow model.
- CAU-specific geologic data and information that establish the local hydrostratigraphic framework (BN, 2002).
- Alternative CAU-specific data that address uncertainty in hydrostratigraphy, lateral boundary flux and heads, and recharge (BN, 2002).
- CAU-specific hydrologic parameters, including their uncertainty.

An overview of the data, information, and conceptual models is presented below.

Hydrostratigraphic Framework Models (HFMs)

HFM Development. The Pahute Mesa area HFMs were constructed using EarthVision®, a 3-D geologic model building and visualization software package. Input data included drill-hole data, digital elevation model data, and outcrop and fault data from surface geologic maps. The 3-D HFM area encompasses over 2,700 km^2 (1,042 mi^2). The HFM has a north-south length of 53.4 kilometers (km) (33.2 miles [mi]) and an east-west length of 50.8 km (31.6 mi), and includes geologic units as deep as 7 km (4.3 mi) below mean sea level (bmsl).

All rocks of the NTS and vicinity can be classified as one of eight hydrogeologic units (HGUs), which include the alluvial aquifer (AA), four volcanic HGUs, an intrusive HGU, and two HGUs that represent the pre-Tertiary sedimentary and metasedimentary rocks. Hydrostratigraphic units (HSUs) are groupings of contiguous stratigraphic units that have a particular hydrogeologic character, such as an aquifer or a confining unit. An HSU may contain several HGUs but is defined so that a single general type of HGU dominates (for example, mostly welded-tuff and vitric-tuff aquifers, or mostly tuff confining units).

Following the completion of the preliminary base HFM, a number of alternative HFM conceptual models were considered. The main criterion for selecting alternative HFMs for full grid development was the potential impact of the alternative interpretation on groundwater flow and the transport of contaminants in groundwater. The results using the above criterion showed that only the Silent Canyon Caldera Complex (SCCC) alternative produced results that were clearly different from those produced by the base HFM (SNJV, 2004a). Therefore, only distinct meshes were developed for the base HFM and the SCCC alternative. An additional five HFM alternatives are evaluated by varying the hydraulic parameters within the base HFM mesh.

Base HFM. The base HFM includes a total of 47 structural elements that are either faults or calderas. Only faults that were considered to be significant were included in the model. These include the larger ones and the ones that seem to form significant structural boundaries. Six calderas have been identified in the Pahute Mesa model area, two of which are buried. The base HFM for the area also includes 20 faults and structural zones in addition to the caldera-forming faults. Thirteen of these 20 structural features are basin-and-range type faults mapped at the surface that are extended to the bottom of the model. There are a total of 46 HSUs included in the base HFM.

SCCC HFM Alternative. The alternative SCCC model is based on the same HGUs as the base HFM. Differences between the two models relate to the structural model used and the categorizing of HGUs into HSUs. The alternative structural model of the SCCC is more simplified than the base HFM, as is the hydrostratigraphy. The SCCC HFM includes an elliptical ring-fracture fault system elongated to the north-northeast. Major structural differences with the base HFM include the margins of this caldera complex, locations of caldera-forming faults, and the number and depth of the faults considered. The SCCC HFM includes the single caldera ring-fracture system, and only 11 of the basin-and-range faults mapped at the surface. Another key difference is that the faults in the SCCC HFM end at shallower depths than in the base HFM.

Hydrostratigraphic differences between the two HFMs of the Pahute Mesa area are the number of HSUs, their definition, and their distribution. In the base HFM, the Pahute Mesa area includes 25 HSUs; only 12 are included in the SCCC alternative model. Six post-Paintbrush HSUs are lumped together in the SCCC alternative model. Significant differences also exist in the configuration of the HSU surfaces. The surfaces of the HSUs are less rugged in the SCCC HFM than in the base HFM. The upper surfaces of HSUs in the SCCC HFM are generally bowl-shaped and dip more gently than those in the base HFM. Upper surfaces of HSUs in the SCCC HFM are also higher along the down-thrown sides of faults, and lower along the up-thrown sides. The differences in the locations of caldera margins and in structure result in differences in HSU thicknesses. Generally, the thicknesses of HSUs located within the Pahute Mesa area vary to a greater degree in the base HFM. In comparison, in the SCCC HFM, the HSUs are generally lens-shaped. These lenses are thick in the middle and thin out towards the margins of the SCCC. The hydrogeologic importance of the Calico Hills Formation in the SCCC area is recognized in both the base and SCCC HFMs. It is, however, handled differently in the two models. In the base HFM, the Calico Hills Formation is subdivided into four HSUs based on differences in lithologic composition and alteration effects, whereas it is treated as a single composite unit in the SCCC HFM.

Groundwater Flow System Characteristics

Lateral Boundary Fluxes. A set of boundary fluxes to be used with the CAU flow model was developed based on results generated for eight alternate regional-scale flow models using the UGTA regional model. The eight models represent combinations of different flow system conceptual

models (HFMs described above) and recharge models. The recharge models represent different methods of approximating recharge for the NTS area. The alternate flux boundary conditions can be used to help evaluate the uncertainty in the CAU flow model associated with the choice of flow system conceptual model (and associated HFM) and recharge model. The approach used to calculate these fluxes does not specify the locations on the boundary where the flux occurs, just quantifies bounds on the total amount of flow through the CAU-model lateral edges.

Recharge. Three basic approaches have been used to develop alternative recharge models for the NTS area. These are: Maxey-Eakin empirical approach, net-infiltration recharge model from watershed distributed parameter modeling by the U.S. Geological Survey (USGS), and chloride mass-balance modeling by the Desert Research Institute (DRI).

Natural Discharge. Within the Pahute Mesa area and vicinity, most groundwater discharge to the surface occurs naturally in the form of evapotranspiration (ET) and springs at the Oasis Valley discharge area. The area of interest to this activity includes the Pahute Mesa area and all of the Oasis Valley hydrographic area because the discharge area extends outside of the Pahute Mesa CAU area boundary. The majority of the groundwater discharged by springs is effectively lost from the groundwater system through ET within the discharge area. The net natural groundwater discharge to the surface is best approximated by an estimate of ET.

Well Discharge. Wells of interest include nine NTS water supply wells, one Beatty water supply well, and two mine wells. The well discharge volume represents only 15 percent of the ET estimate. Transient well-related effects are very localized and likely not representative of conditions over a majority of the model area. Thus, discharge from pumping wells is not included in the model.

Hydraulic Heads. Observed hydraulic heads are derived from depth-to-water measurements and well information. Hydraulic heads may also be approximated by the land surface elevations of regional springs. The results of the water-level data analysis were used to identify hydraulic head values that are most representative of steady state, predevelopment conditions at specific boreholes and well locations. Each temporal subset of measurements that represents steady-state conditions was reduced statistically to a mean, standard deviation, and variance of the mean. The hydraulic head data derived from the water-level data were supplemented with land surface elevations of the selected regional springs.

Hydraulic Conductivity Data. Analysis of hydraulic conductivity data included evaluations of measurement scale (laboratory-scale, slug-test-scale, and constant-rate-scale data), scaling and spatial variability, vertical anisotropy, and the alteration of hydraulic conductivity in test cavities. Approximately 300 hydraulic conductivity values were obtained from analyses of constant-rate test data from the NTS area. These tests sample a larger volume of the tested formation than either laboratory or slug-scale tests. For the purposes of the Pahute Mesa CAU flow model, the constant-rate-scale data are the most appropriate. No HSU-specific hydraulic conductivity data are available for 21 of the 46 HSUs. For these HSUs, mean and standard deviation of hydraulic conductivity is determined from units with similar lithology for which data are available.

Groundwater Chemistry. Groundwater geochemistry data are considered during the evaluation of the groundwater flow system because they provide a means for determining the origin, pathway, and timescale of groundwater flow that is independent of estimates based on conventional hydraulic data. Groundwater geochemistry evaluations were performed for the Central and Western Pahute Mesa CAUs that address groundwater flow path, water budget, and travel-time evaluations. These geochemical evaluations were performed on representative Pahute Mesa data in order to identify and assess viable flow paths and groundwater mixing models. The comparison of flow model results and geochemical evaluations was performed as a verification step after model calibration using hydraulic information (heads and fluxes) only.

COMPUTER CODE SELECTION

The Pahute Mesa CAIP (DOE/NV, 1999) identified a process for the identification and selection of the numerical code for use in Pahute Mesa flow and transport modeling. The process identified three objectives for the numerical code used in the CAU model. The first objective requires the CAU model to have the ability to represent the important physical and chemical features of the CAU groundwater flow system. The features include faulting, stratigraphy, sources and sinks of water, the distribution of contaminants and their rates of introduction into the groundwater flow system, and other physical or chemical features unique to the CAU. The second objective requires the CAU model to simulate the movement of a variety of contaminants for which their distribution and abundance serve to define the contaminant boundary. The third objective requires flexibility in the CAU model to allow grid changes, placement of additional wells, and boundary condition variations.

The Pahute Mesa CAIP (DOE/NV, 1999) identified 14 numerical codes as possible candidates for Pahute Mesa CAU modeling. Three codes were evaluated further. The features of the test problem used to evaluate the three candidates codes were chosen to represent conditions expected in the Pahute Mesa model area. The features included in the test problem were: complex caldera geology, such as lithologic and structural features; temperature-dependent flow; radionuclide migration from a cavity; and matrix diffusion. Code testing criteria were used to represent the CAU hydrogeology, portability, quality assurance evaluation, ease of use, and speed of simulation. The code testing and evaluation of relative rankings of the tested codes was completed in 1999, and the finite element heat-mass (FEHM) code was selected as the flow and transport simulator for the Pahute Mesa CAU model.

GROUNDWATER FLOW MODEL CONSTRUCTION

The overall goal of the approach for construction of the Pahute Mesa flow model is the transformation of the conceptual model into a mathematical model for simulating groundwater flow in and around Pahute Mesa. Development and implementation of the CAU flow model involves the following activities:

- Defining the CAU numerical model boundaries
- Mesh generation
- Establishing boundary and initial conditions

CAU Numerical Model Boundaries. The numerical model boundaries were chosen such that they coincide with perceived geologic and hydrologic domains to the extent possible, contain the contaminant source areas and discharge points with some buffer, and are within practical constraints. The CAU model lies within the geologic model domain with lower-left plan coordinates of 519,125 and 4,085,000 meters (m) Universal Transverse Mercator (UTM) (UTM Zone 11 North American Datum 27) and upper-right plan coordinates of 569,000 and 4,138,000 m. The model is aligned north-south, with no rotation. The numerical model extends from the estimated water table to a depth of -3,500 m bmsl. The hydrologic model area encompasses more than 2,700 km^2 (1,042 mi^2). This area incorporates both the Pahute Mesa CAUs, including Timber Mountain; the eastern edge of Oasis Valley; the northern part of Fortymile Canyon; and the northern portion of Yucca Mountain. The area has a north-south length of 53.4 km (33.2 mi) and an east-west length of 50.8 km (31.6 mi).

Contained within these boundaries are the well data within the Pahute Mesa area, and the springs and regional discharge area at Oasis Valley.

Mesh Generation. The model construction involved building finite-element meshes for use with the FEHM code to capture the complex HSU geometries, faults, and test chimneys for the two primary HFMs: the base and SCCC cases. In general, the criteria for grid generation are as follows (DOE/NV, 1999):

- The external boundary of the CAU model will correspond to appropriate cell boundaries within the UGTA regional groundwater flow model. Because the regional model is rotated with respect to the coordinate system and the CAU model is not, interpolation procedures were developed to account for the non-coincidence of CAU and regional model nodes.
- Nodes will be placed as close as practical at each underground test location and at specific well locations.
- Nodes will be placed along faults that are identified as being important to the distribution of HSUs.
- The node density will be greatest in the vicinity of the underground tests and at other points of interest, and will decrease in density towards the CAU-model boundaries.
- Nodes will be preferentially placed along HSU contacts to more precisely incorporate the geologic model structure in the simulations. The nodes will form a pattern representative of the CAU-scale geology.
- The node spacing will vary from small in the vicinity of test cavities and wells to nearly as large as the regional groundwater flow model grid at the CAU boundary.

The mesh node spacing ranged from 67.5 m to 1 km, with refinement in thinner HSUs and faults, around tests, and estimated flow paths from Areas 19 and 20 to Oasis Valley. Two FEHM computational meshes were produced. One represents the base HFM; the other, the SCCC alternative HFM. The base HFM has 45 HSU surfaces (the Windy Wash Aquifer was omitted due to nearly negligible saturated extent) and 37 faults. The SCCC HFM model has 40 HSU surfaces and 25 faults. The list of HSUs is identical with the exception of the Calico Hills HSUs, which are lumped into a single HSU in the SCCC HFM. This resulted in two meshes with approximately 1.4 million and 1.3 million nodes for the base and SCCC HFMs, respectively.

Boundary Conditions. The solution of the groundwater flow equations requires specification of head and/or flow at the edges of the numerical model. The Pahute Mesa CAU model must account for regional inflow and outflow across all four lateral edges, internal flow from precipitation recharge, and internal discharge from springs and ET at Oasis Valley.

There are three categories of recharge estimates for consideration in the CAU model: Maxey-Eakin elevation-based approach as described in the UGTA regional model evaluation and modified to reflect an updated base precipitation map (case MME), USGS distributed-parameter watershed model, and DRI chloride mass-balance estimate. Two subsets of the USGS and DRI recharge maps were also considered. For the USGS map, the recharge with (case USGSD) and without runoff or run-on (redistribution) (case USGSND) was used. For the DRI map, the recharge with (case DRIAE) and without an elevation (case DRIA) mask at 1,237 m was also used. Recharge is implemented in the CAU model as a specified flux condition. Recharge flux is considered to be constant over time but varies over the domain. The MME recharge distribution is chosen as the base recharge model for use in groundwater flow modeling because, in general, the method yields recharge volumes that are within the ranges of the other models. The other alternative recharge models are incorporated into the Pahute Mesa flow model to evaluate uncertainty associated with recharge.

The only internal discharge represented in the Pahute Mesa CAU model is Oasis Valley springs and ET outflow. Discharge from pumping wells is not included in the model. Spring and ET discharge are represented in a similar manner with FEHM as with the regional flow model with "drain" boundary conditions.

The FEHM simulations utilize a confined aquifer approximation in which the water table defines the top of the model domain location and is estimated as a potentiometric surface in the simulations. An estimate of the water table, approximated by contouring observed heads from wells with relatively shallow sampling intervals, provides a guide for setting the upper confining surface in the grid. The approach does not include an unsaturated zone or moving water table and, therefore, solves a simplified and computationally more efficient numerical model.

Boundary heads interpolated from the UGTA regional model analysis were initially assigned to the edge nodes of the FEHM CAU model as boundary conditions. These heads represent a mass conservative calibrated solution to the groundwater flow equation from the UGTA regional model

(DOE/NV, 1997). During the calibration process, these heads were reviewed, and in spots, revised based on further examination of measured heads and heads determined from the UGTA regional model.

Part of the CAU flow modeling strategy is to use the UGTA regional model as a mass conservative integrating model that allows evaluation of water-balance uncertainty around the lateral edges of the CAU model. In this analysis, the flows are not directly specified on all edges; heads are specified, and FEHM computes and reports the lateral boundary flows, which are used as calibration targets.

Initial Conditions. Initial conditions are those applied at the start of a simulation. Theoretically, for steady-state flow, the initial conditions are not important. Practically, the iterative solvers employed in large numerical models gain efficiency if the starting conditions are as consistent as possible with the properties and boundary conditions used in calibration. The initial conditions were determined from interpolation of the UGTA regional model results onto the FEHM nodes in the CAU domain. However, once converged CAU steady-state model results were obtained, they became the new initial conditions for the continuation of model calibration.

Within the model domain, temperature varies enough that it should be considered in the calculation of flow. A 3-D steady-state heat-conduction model was developed for the model domain in order to provide a 3-D temperature distribution for the steady-state flow model calibration. The calibrated thermal fields from the heat-conduction model were used to specify the temperature distribution as a fixed condition; that is, thermal transport was not simulated, but the effect of the variable temperature field was included.

FLOW MODEL CALIBRATION

The purpose of the CAU flow model calibration is to use observed head data, discharge estimates from Oasis Valley, boundary flow estimates from the UGTA regional model, and estimated hydraulic properties for HSUs to develop a numerical model representation of the groundwater flow system in the Pahute Mesa CAU area. The Pahute Mesa CAU flow model considered seven HFMs and five recharge models. The following naming convention was used to identify the various flow models that were calibrated. The first part of the name is the HFM and the second is the water-balance condition. An additional naming modification is applied to denote the permeability parameterization approach: denoted SDA and ADA, for selected HSU depth decay and anisotropy, and for all HSU depth decay and anisotropy, respectively. In addition to the base and SCCC alternative HFMs, there are five other HFMs that were investigated using the base HFM grid: PZUP - Raised pre-Tertiary Surface, DRT - Deeply Rooted Belted Range Thrust Fault, RIDGE - Basement Ridge Model, TCL - Thirsty Canyon Lineament, and SEPZ - Contiguous Imbricate Thrust Sheet.

Calibration Approach. Flow model calibration followed a generally accepted protocol in which model parameter sensitivities to calibration were evaluated and interpreted in light of the conceptual model of the system. An automated approach for groundwater flow model calibration was adopted where the model response to parameter changes is systematically evaluated and the more important parameters that improve calibration identified. The parameter-estimation (PEST) code was used for this purpose (Watermark, 2004). The PEST code also includes a variety of statistical analyses that help develop understanding of the model. These features include sensitivity and correlation coefficients, parameter confidence limits, and eigenvalue and eigenvector analysis. The sensitivity and correlation coefficients describe how much the model calibration changes relative to a parameter's change, and how parameters may influence one another. This is useful in testing the conceptual model as to what parameters are believed to control model behavior, and what parameters may act similarly on model results. In addition, parameters that may be important to model calibration can be quantitatively identified and considered in more detail. The confidence limits and eigenvalue and eigenvector analysis are useful in understanding how well the observation data support the model parameters and how many parameters should be considered for calibration.

Several approaches for evaluating the agreement between a flow model and modeled system were utilized. These procedures were used in calibrating the Pahute Mesa flow model, and include qualitative and quantitative comparisons between model results and the following: measured heads at wells and springs, water-balance information (Oasis Valley discharge flux and model boundary flows), flow-direction information, and estimated values of HFM hydraulic parameters from characterization data.

The goal of model calibration is to make the model agree with reality by adjusting, within their ranges of variation, model parameters and boundary conditions. Achieving the best calibration is not the sole objective of model calibration. The reasonableness of the flow directions was also assessed qualitatively during the calibration phase via streamline particle tracking and quantitatively via geochemical analysis (as a verification step subsequent to head and flux calibration). Finally, it is important to recognize that no matter the procedure, the goal of model calibration is a set of model parameters that best (or at least reasonably) represents the hydrogeologic system. A further constraint was the desire to honor, within the range of uncertainty, the estimated hydraulic properties for the HSUs.

Calibration Data. Considering different types of data, especially flows, enhances the goodness of the flow model. In particular, matching both head and flow in Oasis Valley increases confidence that the model behavior is correct in this area. Four data types, or targets, were used for calibration of the Pahute Mesa flow model as follows:

- Hydraulic head from wells
- Estimated spring head in and near Oasis Valley
- Oasis Valley discharge
- Lateral boundary flows on CAU model estimated from regional flow model

Because an automated procedure was used to aid calibration, multiplicative weight factors were developed and assigned to data with different levels of accuracy and measurement units. The standard deviations of reference point uncertainty, head value uncertainty, and heterogeneity were summed and the initial weights for PEST computed. However, an alternate empirical approach was also adopted in which the weights are assigned by considering accuracy along with judgment to give the desired contribution to the calibration for selected data types. Mathematically, Oasis Valley

discharge is important to constraining the flow model because it is well known that a steady-state model with constant head boundaries calibrated only to head is not unique.

Boundary Head Adjustments. The starting point for the CAU model specified-head boundary conditions was the UGTA regional model results interpolated onto the mesh edges. Changes were made during calibration to address inconsistencies to measured heads in the following areas: western part of the northern boundary, the north-central model edge near UE-20p and PM-2, southern edge of the model east of Oasis Valley, and eastern boundary near TW-1. Also, the northwest corner of the model (both north and west faces) was converted to a no-flow in conjunction with correction of heads north of PM-2 and UE-20p.

Base HFM Flow Model Calibration. A variety of permeability parameterization approaches have been used to simulate groundwater flow in the NTS area (e.g., the UGTA regional model [DOE/NV, 1997], the USGS flow model of D'Agnese et al. [1997], and the Yucca Mountain Project [YMP] saturated-zone model [DOE/ORD, 2004]). For the base HFM, the viability of four different parameterization approaches was tested:

- No anisotropy and no depth decay of HSU permeability
- Depth decay applied to selected HSUs
- Anisotropy and depth decay applied to selected HSUs
- Anisotropy and depth decay applied to all HSUs

The same calibration data and model structure was used in each case; only the approach to assigning parameters was changed. The first approach is a limiting case of simplicity; the second and third approaches reflect parts of the 1997 USGS regional model (D'Agnese et al., 1997), the Death Valley regional flow model (DVRFM) (Belcher et al., 2004), and the YMP saturated zone models (DOE/ORD, 2004); and the fourth approach reflects the same approach used in the UGTA regional model (DOE/NV, 1997).

Flow model calibration was conducted with the four approaches above. The no-anisotropy and no-depth-decay case was rejected as a reasonable approach because flow paths from Pahute Mesa tended to dive deep below Oasis Valley, reflecting the poor match to Oasis Valley discharge data. It also required systematically low permeabilities relative to the expected values and ranges as described in the Pahute Mesa hydrologic data document (SNJV, 2004a). The selected HSU depth

decay with no anisotropy was investigated briefly, but completely neglecting anisotropy was deemed unreasonable, and it was discarded. The application of anisotropy and depth decay to selected HSUs and to all HSUs cases was carried to final calibrations. Both models could represent the flow system reasonably well, as defined by matching the head and flow calibration targets.

The selected HSU depth-decay and anisotropy parameterization approach began by assessing the effect of permeability depth decay only, and its effects were found to be quite pronounced in terms of not requiring consistently low permeabilities as in the case described in the no-depth-decay, no-anisotropy case. Depth decay applied to regionally contiguous units existing at a wide variety of depths along with horizontal-to-vertical anisotropy of 10:1 in selected units provided reasonable results.

SCCC HFM Flow Model Calibration. This model has fewer HSUs than the base HFM, and does not have as deep or extensive of a fault system. In particular, the Calico Hills formation is reduced from four separate HSUs to one that is several hundred meters thick. The calibration of the SCCC alternative began with the calibrated parameters from the selected HSU depth decay and anisotropy base HFM for both HSUs (where still present) and faults (where still present). However, because of the lumped nature of the Calico Hills unit, its anisotropy was increased to 50:1 because many dissimilar types of units were combined. In addition, the Benham Aquifer (BA) also incorporates the Lower Paintbrush Confining Unit in the SCCC HFM. The BA was assigned anisotropy of 20:1. The units selected to have permeability depth decay and anisotropy are the same as presented for base HFM selected depth decay and anisotropy. The SCCC HFM did not calibrate as well as the SDA and ADA models using the base HFM.

Calibration Summary. Three calibrations for the base and SCCC HFMs were carried to completion: base HFM with selected HSU depth decay and anisotropy with MME recharge, base HFM with all HSU depth decay and anisotropy with MME recharge, and SCCC HFM with selected HSU depth decay and anisotropy with MME recharge. Key behaviors and observations of the model calibrations are summarized below:

1. **Purse Fault Behavior**. A striking difference between the base and SCCC HFMs is the area along the Purse Fault. An area of "hydraulic discontinuity" exists coincident with the Purse Fault that shows about 100-m head difference (west to east) across the fault with flow directed sub-parallel to the fault (e.g., the fault may act as an approximate no-flow barrier). In order to

match the head in Wells PM-3, PM-2, UE-20p, UE-20j, and U-20m in the base HFM on the western side of the Purse Fault and wells in southwestern Area 20, the Purse Fault permeability had to be reduced by a factor of 10,000 relative to the surrounding HSUs in order to maintain the 100 m or so difference between the two areas. In contrast, the SCCC HFM does not have a Purse Fault geometry that allowed fault continuity along its length or goes as deep (the base HFM has faults projected to the bottom of the model). Thus, simulated head at PM-3 was too low and head in southwestern Area 20 too high because the fault did not separate the two areas sufficiently. The SCCC does incorporate juxtaposition across the caldera margins, so HSU juxtaposition alone seems insufficient to replicate the observed behavior. Whether or not the Purse Fault alone is the source of the observed discontinuity is unclear, but its configuration in the base HFM does allow the observed head to be reproduced, whereas HSU juxtaposition alone does not.

2. **Comparison of Model and Estimated HSU Permeabilities**. Estimates of mean hydraulic properties and their uncertainty were made before beginning model calibration. These estimates were used as a guideline during calibration. The model-calibrated permeabilities were compared to the estimated values for all HSUs. The comparisons suggest that the flow model has been reasonably parameterized for the three calibrated models with respect to the expected values of HSU permeability.

3. **Water-Balance Summary**. An additional check on the CAU water balance is the comparison of flow along the northern edge of the Yucca Mountain saturated zone model, which lies entirely within the Pahute Mesa CAU flow model. The YMP saturated zone model (DOE/ORD, 2004) gives a value of 196 kilograms per second (kg/s) inflow. The calibrated base HFM with MME recharge and selected and all depth decay of 250 and 300 kg/s for the SCCC with MME recharge. The DVRFM (Belcher et al., 2004) boundary flows were also estimated for the Pahute Mesa CAU flow model boundaries, and found to be in reasonable agreement with estimates developed from the UGTA regional model (DOE/NV, 1997). Thus, the Pahute Mesa CAU model is in reasonable agreement with other independent water-balance analyses in the area.

4. **Data Components of Calibration**. Four categories of data, representing two types (head and flow), were used to calibrate the Pahute Mesa CAU flow model: observation well head, spring head, Oasis Valley ET discharge, and net model boundary flow. An evaluation of the contribution of each data type to the model goodness of fit shows that observation well heads comprised the bulk (between about 50 to 60 percent) of the objective function, followed by Oasis Valley discharge (about 25 percent), estimated regional boundary flow (about 15 percent), and spring head (5 to 10 percent). Clearly, observation well data must be given strong consideration in model calibration because they define the direction and magnitude of the hydraulic gradient, which is directly related to the velocity field that will be used to simulate radionuclide transport. Oasis Valley discharge is the only internal flow constraint for the model, and as such is a major control on the effective permeability. Oasis Valley is also the nearest access point for radionuclides that might leave Pahute Mesa, and matching its discharge ensures that the potential for such migration is properly captured in the flow model. In addition, matching the spring data also helps ensure that the heads in Oasis

Valley are reasonably matched, and that the combination of head and flow that results is plausible.

5. **HFM Assessment**. Two HFMs, the base and SCCC alternative, were considered during model calibration. The SCCC does not perform as well in matching observed heads along the Purse Fault, and, in general, does not calibrate as well as the base HFM. The parameter set or model that reduces the value of the objective function is considered superior to those that give higher values because it improves the model fit according to the criterion embedded in the objective function itself. Thus, from purely the standpoint of flow model calibration goodness, the SCCC HFM is not as likely as the base HFM.

6. **Model Limitations**. The Pahute Mesa CAU flow model covers a plan area of approximately 2,000 km^2 and has a saturated thickness of nearly 5 km, for a total volume of about 10,000 cubic kilometers. A total of 191 calibration targets of head and flow were used in calibration. The overall density of the data versus the size of the model suggests that the calibration data are somewhat sparse. Not all of the uncertainty is likely to be important; for instance, it is almost certain that flow in the intrusive confining units is very slow, if not nil, which has no effect on the shallower part of the flow system. However, many types of analysis such as head mapping and geochemistry tend to give a similar broad picture of flow from Pahute Mesa southwest to Oasis Valley, and while there may be further refinements in understanding if more data are collected, the key point of migration to Oasis Valley is unlikely to change.

The CAU flow model was calibrated to estimated steady-state conditions and is not currently configured for transient flow analysis. The flow model also assumes regional steady state in the CAU area, and any future change in hydrologic conditions could affect this assumption.

FLOW MODEL SENSITIVITY AND UNCERTAINTY ANALYSIS

Approach. The Pahute Mesa CAU flow model has a large number of parameters that can be changed in order to calibrate the model to observations of hydraulic heads, spring heads, lateral boundary flows, and ET flows. It is necessary to identify those parameters to which the model outputs are most sensitive, and how they relate to the conceptual model. The results of sensitivity analyses are presented for three models: base HFM with selected HSU depth decay and anisotropy with MME recharge, base HFM with all HSU depth decay and anisotropy with MME recharge, and SCCC HFM with selected HSU depth decay and anisotropy with MME recharge. While sensitivity analyses are formally presented below, such analyses were also carried out as an integral part of the calibration process. In addition, alternative HFMs and alternative recharge models and boundary flows have been considered in the CAU flow model sensitivity and uncertainty analysis.

Additional sensitivity and uncertainty analyses were conducted after model calibration. The sensitivity analysis used local techniques (all parameters are perturbed slightly or one at a time over their range of uncertainty) and global techniques (considered effects of joint parameter uncertainty over full range of uncertainty) to identify and evaluate key parameters in the Pahute Mesa CAU groundwater model. The local sensitivity analysis techniques include PEST sensitivity analysis and perturbation analysis. The PEST code calculates a sensitivity coefficient for each parameter with respect to all weighted observations.

This analysis is termed "local" because only slight changes are made that investigate parameter values near the base value. The second local approach involves perturbing each of the parameters, one at a time, from a reference value and computing the corresponding change in the model output.

The global sensitivity analysis techniques include classification tree analysis and entropy analysis. Global sensitivity analysis techniques are used for investigating input-output sensitivities that are valid over the entire range of possible parameter variations and not just at or near the reference point.

To address HFM and water-balance uncertainty seven HFMs, five recharge models, and five sets of lateral boundary flows were considered. If all combinations were considered, this would result in 175 calibrated flow models. However, it is neither necessary nor reasonable to investigate all combinations. The approach taken was to use a given recharge model in the Pahute Mesa CAU flow model with the regional model boundary flows derived from the same recharge model in the regional model. The strategy is to combine HFMs with recharge models and corresponding lateral boundary flows in order to at least bound uncertainty associated with each model component.

Summary of Parameter Sensitivity Analyses. Parameter sensitivity analysis was performed on the two major HFMs in the Pahute Mesa CAU-scale groundwater model using a complementary suite of techniques.

The local approach used PEST to identify sensitive model parameters and parameter correlations. This analysis led to the following findings:

- The Paintbrush Composite Unit (PCU), Lower Clastic Confining Unit-Thrust Plate (LCCU1), Yucca Mountain Crater Flat Composite Unit (YMCFCM), Detached Volcanic Composite

Unit (DVCM), and Claim Canyon Caldera Structural Margin fault were sensitive in controlling heads in the base and SCCC HFMs.

- Reference permeability and depth decay have a nearly perfect correlation, which considering the formulation of depth decay is expected.

- Over their range of uncertainty, the reference permeability of HSUs with depth decay was more sensitive than the depth-decay parameter itself. It is important to note that this was recognized during calibration, and depth-decay coefficients as estimated for each type of HSU (e.g., volcanics and carbonates) were fixed and reference permeability calibrated.

The perturbation analysis varied properties of HSUs and faults over their range of uncertainty, providing a comprehensive picture of model behavior (although without considering compensating effects). Major faults often showed a one-sided sensitivity behavior, where fault permeability multiplier ceased to have a noticeable effect below a certain value.

Global sensitivity analysis was conducted by generating 1,000 uncorrelated parameter samples using Latin Hypercube sampling, computing flow models for these samples, and recording the model results for the two calibrated versions of the base HFM (all and selected HSU depth decay and anisotropy) and SCCC HFM. This approach was taken to attempt to identify whether there were parameter combinations that were as good as or better in calibrating the model than the chosen sets over the range of parameter uncertainty, and whether there were systematic effects of some model parameters. The results were analyzed using Spearman rank correlations, classification and regression trees, and entropy statistics. Similar sets of sensitive variables were identified as in the local and perturbation analyses.

The local and global sensitivity analyses confirmed what was observed during flow model calibration: that the major controls on the groundwater flow system are not necessarily all the HSUs on Pahute Mesa. For instance, while it appears that the Pre-Belted Range Composite Unit, and to a lesser extent the Belted Range Aquifer, have a noticeable role in calibration, the fact that the DVCM, PCM, YMCFCM, and LCCU1 dominate calibration (and that the Timber Mountain Confining Unit had any role at all) was unexpected. The underground nuclear tests were all conducted in Areas 19 and 20; hence, the observation well data tend to be clustered there, and the base HFM is also relatively complex in this area.

The Pahute Mesa HFMs, base and SCCC, incorporate a number of faults and other structural features. The Purse and Boxcar Fault systems have been previously identified as having sealing properties. Many others though, are unknown. The sensitivity analysis revealed the Claim Canyon Caldera Structural Margin as a consistently sensitive feature due to its location on the southern edge of the model. Perturbation analysis showed the Hogback and the Rainier Mesa Caldera Structural Margin have a strong effect at a permeability multiplier of 100 (the response between 10 and 100 appears very nonlinear and shows little effect at 10). The Ribbon Cliff Structural Zone that runs east-west between Black Mountain and the Purse Fault is strongly sensitive at low values because it can restrict flow through the area; the North Timber Mountain Moat Structural Zone (Moat Fault), Rainier Mesa Caldera Structural Margin, and Ammonia Tanks Caldera Structural Margin are sensitive for the same reason. Fault sensitivity tends to be one-sided; only lower values have any impact. Conceptually, this is sensible because a low- (or high-) permeability feature located in line with a flow path would have little obvious effect; the faults noted above all tend to lay across groundwater flow paths.

HFM Uncertainty Analysis. The complexity of the geology in the area, and the resulting uncertainty in geologic interpretation, was addressed in the development of the geologic models by including five additional alternatives beyond the base and SCCC HFMs. The additional HFM alternatives were addressed using the mesh developed for the base HFM. The selected HSU depth-decay and anisotropy approach was used in parameterizing the models beginning with the calibrated parameters. The flow model was calibrated with each of these alternative HFMs utilizing the MME recharge and boundary flow targets. Thus, the uncertainty in geologic structure was further addressed.

Calibrations were performed for all five alternative HFMs. Of the five alternatives, three required no additional effort over the base HFM to recalibrate, although the calibrations and simulated flow paths did show some differences. In the case of TCL, RIDGE, and SEPZ alternatives, parameters are identical to those used for the base HFM with selected HSU depth decay and anisotropy because the effects of the HSU changes required minimal parameter adjustment. Two alternatives (DRT and PZUP), both involving raising or otherwise increasing the amount of low-permeability rocks in the domain, required extensive effort to recalibrate. The calibration process resulted in metrics similar to the base HFM calibration, with some modest changes in simulated flow paths.

A summary understanding can be developed of the relative HFM performance by considering the goodness of the respective calibrations. The objective function of each alternative HFM, normalized by the results presented for base HFM with MME recharge and selected depth decay and anisotropy was compared. The alternative SEPZ HFM actually performed slightly better than the base HFM, with all of the improvement coming from a better agreement to the observation well data. The TCL alternative was nearly identical to the base HFM. The RIDGE case was mildly worse than the base HFM, primarily from increased misfit with the wells, although Oasis Valley flow was also noticeably undersimulated. The RIDGE alternative truncated the extent of volcanic aquifers (Benham Aquifer, Tiva Canyon Aquifer, and Topopah Spring Aquifer) in southern Area 20 with older, lower permeability units. This results in more scatter in the model agreement with the observation well data, as shown by the increased error standard deviation. The PZUP and DRT alternatives give the most different results in comparison to the base HFM calibration, which relative to the degree of HFM changes is not unreasonable. The DRT alternative has significant misfit on the boundary flows because the large section of low-permeability LCCU1 extending westward and northward into the model greatly reduces transmissivity along the northern boundary.

Water-Balance Uncertainty Analysis. Recalibrating the base and SCCC HFMs to a suite of recharge models and boundary flows addresses the water-balance component of flow model uncertainty. A total of eight combinations of recharge model, boundary flow, and HFM were considered. The boundary flows developed from the UGTA regional model analysis for the corresponding recharge models were used in conjunction with each respective recharge model. The base HFM with anisotropy and depth decay applied to selected HSUs was recalibrated using the two USGS and two DRI recharge models. The results were very similar between the pairs of models (e.g., USGS with and without runoff). The USGS recharge model with run-on and runoff (USGSD) is conceptually more reasonable, so it was retained for further analysis for the SCCC HFM. Likewise, the DRI recharge model with alluvial screen (DRIA) was retained because it has the highest flux rates and should bound the upper end of flow through the system. Thus, the SCCC HFM was tested with the DRIA and USGSD recharge models only. The USGSD recharge model provided some of the best calibrations, with the DRIA recharge giving results similar to or worse than the MME recharge model. The most noticeable effect was that flow paths in the SCCC HFM changed with the different recharge models such that more paths were directed down Fortymile Canyon.

In general, all the combinations of HFMs, recharge models, and boundary flows could be as well calibrated as with the MME recharge and boundary flow. This recalibration, however, can result in a few marginal parameter values. In general, reducing recharge via the USGS recharge model had the effect of dropping permeability, with the converse resulting from the DRI recharge model. This is expected behavior in a steady-state model. Some of the downward changes, notably the Inlet Aquifer for the USGS recharge model cases, are to the lower limit of estimated parameter uncertainty range. The poorest-performing HFM considered under all recharge models was the SCCC alternative. The lack of deep faults, particularly along the Purse Fault, limits the key degrees of freedom necessary to give a reasonable calibration. The SCCC HFM also showed the greatest sensitivity of simulated flow paths to recharge model, with significantly more flow paths down Fortymile Canyon for the DRIA and the USGSD recharges than for the MME recharge, as compared to any other HFM and recharge combination. The particle paths, with the notable exception of the SCCC HFM, tend to behave similarly across all recharge alternatives, suggesting that HFM uncertainty plays a greater role than recharge uncertainty.

Combining HFM and Water-Balance Uncertainty. Another type of uncertainty analysis was to combine HFM and water-balance uncertainty. Two of the alternative HFMs that are most distinctly different than the base HFM (i.e., the DRT and PZUP cases) were combined with the DRIA and USGSD recharge models to further bound flow system uncertainty. Both the DRT and PZUP HFMs have increased volumes of low permeability rock, although as a consequence of the different conceptual models. Not surprisingly, both these alternatives do not perform well in matching boundary flows with the high volume (relative to the USGS and MME recharge models) DRIA recharge model simply because they do not have sufficient system transmissivity to move enough water across the boundaries. The simulated Oasis Valley flows tend to be on the high side, but not unreasonably so, and the heads are matched with a slight oversimulation bias. With respect to the boundary flows, these HFMs do perform reasonably with the USGSD recharge model, which is a direct consequence of the larger amount of lower permeability rocks in each HFM. However, there is a bias, modest for DRT and severe for PZUP, to undersimulate observation well head.

The PZUP HFM with the USGSD recharge model has a bias on the order of 20 m to undersimulate head on Pahute Mesa, but qualitatively the flow paths still appear reasonable. This is because the bias is ubiquitous; thus, the flow direction is maintained. The DRT HFM, in all cases, simulates a focused

flow path that seems counterintuitive to the conceptual model of flow from Pahute Mesa to Oasis Valley, but still can match Oasis Valley discharge. With changing recharge models the main simulated flow paths do not change in the DRT HFM, but at the highest recharge (DRIA) distinctly more paths exit in Oasis Valley than with the lowest recharge (USGSD). Thus, the large changes in flow paths from the DRT HFM are generated by the HFM itself, not the variation in recharge models. Conversely, the goodness of the calibrations varies in the PZUP case, but the flow paths show relatively minor variations. In both cases it appears that the HFM uncertainty dominates over the recharge model uncertainty.

Other Sensitivity Analyses. A set of discrete sensitivity analyses was also considered including the following: testing the effects of permeability enhancement of test chimneys, evaluating two additional rooting depths for Oasis Valley discharge, assessing the effect of the reduced LCCU1 permeability alternative (suggested by the sensitivity analysis), and testing the consequences of trying to enhance flow down Fortymile Canyon. The effects of test chimneys was found to be negligible, the extinction depth is not a greatly sensitive parameter, the model could still be calibrated well with lower LCCU1 permeability alternative, and enhancing flow down Fortymile Canyon does not look feasible.

GEOCHEMICAL VERIFICATION

Geochemical signatures of various groundwaters in the area were used to generate mixing targets at key points in the model domain for model verification purposes as described in the Pahute Mesa CAIP (DOE/NV, 1999). Nineteen of the calibrated flow models are evaluated with respect to independently developed groundwater mixing targets determined from geochemical analyses. The purpose of these comparisons is to determine whether the sources of groundwater at eight target wells within the domain, as modeled, are consistent with the geochemical interpretation. In the comparisons, the sources of groundwater in the models are determined with reverse-particle simulations. The top of the model has been discretized into nine separate recharge zones and the side boundaries have been discretized into seven separate inflow zones for a total of 16 unique source zones associated with specific groundwater chemical signatures. With this method, the fraction of water from each of the recharge and boundary inflow zones that is present in the groundwater at the

mixing target wells is computed. These fractions are compared with the mixing ratios estimated by interpreting geochemical compositions.

Comparison of calibrated flow models, via reverse-particle tracking, with geochemistry mixing targets was performed as a blind evaluation. The mixing targets were developed independently of the flow model calibration and were only considered after calibration was complete. However, absolute acceptance or rejection of flow models cannot be determined based upon the geochemistry comparisons alone. If flow models are to be either weighted or rejected for subsequent use in transport modeling, then such evaluation would have to be conducted with simultaneous consideration of the following: (a) the quality of the calibration, (b) the likelihood and/or reasonableness of the alternative stratigraphic model, (c) the specific water-balance condition considered, and (d) the results of the geochemistry comparison. Many of the discrepancies between calibrated flow models and geochemistry-mixing targets are local in nature and due to small-scale processes, forcing flow paths slightly away from intended targets. A primary source of such discrepancies is related to the independently developed recharge maps used in the models. A large component of local recharge serves to force flow paths from upgradient sources away, but only slightly for certain target wells. Other large-scale issues involve the magnitude of flow into the model from side boundaries. The impacts of such model differences can be seen tens of kilometers away from the source. The target wells at the higher parts of the flow system were more difficult to match because there is less distance for mixing to occur, and very complex flow paths (at ER-EC-6, for instance) produce poor comparisons because of narrow flow-path deviations. Thus, the various discrepancies identified should not be weighted equally in quantitative evaluation of the calibrated flow models advanced in this study. In general, the trends are captured.

Cluster analysis of the geochemical verification results was used to group the combinations of calibrated HFM and recharge models. The best cluster of models with respect to the geochemical verification included DRT-MME-SDA, DRT-DRIA-SDA, PZUP-MME-SDA, SCCC-MME-SDA, BN-MME-SDA with reduced LCCU1 permeability, and BN-USGSD-SDA with reduced LCCU1 permeability.

THERMAL SENSITIVITY AND VERIFICATION

Thermal analysis identified specific locations where pure vertical conduction of heat did not adequately explain thermal anomalies observed in borehole temperature profiles. Such locations were identified during the development of the calibrated steady-state heat-conduction model. Several of these locations qualitatively suggested areas where flow of cooler water downward could explain the temperature anomalies.

Four locations within the CAU model, identified as being affected by downward-groundwater flow, were investigated. Following these identifications, reverse-particle-tracking simulations (with the particles released in deeper zones) were conducted to investigate whether shallow groundwater sources were feasible at the depths indicated in the heat-conduction study. The BN-MME-SDA reduced LCCU1 permeability alternative is evaluated with respect to vertical flow indicated by analysis of temperature data. For two locations within the Silent Canyon Caldera, one within the Timber Mountain Caldera and one to the west of the Timber Mountain Caldera, the results were positive with the simulations verifying that the flow model could qualitatively capture the convective components identified.

The sensitivity of the calibrated base HFM with MME recharge and selected depth decay and anisotropy was evaluated with respect to changes in the prescribed steady-state temperature profiles. Starting with the calibrated parameters for the BN-MME-SDA flow model, the temperature distribution is changed to reflect the low and high linear geothermal gradients. The flow model is not recalibrated, and forward simulations are compared with the base-case model. Here, as part of an assessment of model sensitivity to temperature, two different temperature distributions based on linear thermal gradients and extrapolation from a high-quality measurement are considered. It is not surprising that the model objective function increases with the two sensitivity runs, because these fields are different than that determined from the calibrated conduction model. Increased temperature at depth results in larger hydraulic conductivities for the same permeability developed in the calibrated base model. Thus, it is likely that the objective function could be reduced through recalibration. It is possible that reasonable calibrated permeability fields could be achieved with the linear thermal gradients. To offset the higher viscosities, lower rock permeabilities would be needed.

However, it is unlikely that linear thermal gradients would lead to as good or better results than those achieved with the calibrated thermal field, which captures non-linear distributions of rock properties

The pathlines and reverse-particle-tracking simulations are nearly identical for the base model and the two thermal sensitivity runs. This is likely due to the fact that the models are most similar at the shallower depths where the forward particles are introduced. Recharge also enters the model at the shallower depths and is the same for each of the model runs. Thus, the reverse particles are likely to exit at the locations where recharge occurs.

1.0 INTRODUCTION

The U.S. Department of Energy (DOE), National Nuclear Security Administration Nevada Site Office (NNSA/NSO) initiated the Underground Test Area (UGTA) Project to assess and evaluate the effects of the underground nuclear weapons tests on groundwater on the Nevada Test Site (NTS) and vicinity. The framework for this evaluation is provided in Appendix VI, Revision No. 1 (December 7, 2000) of the *Federal Facility Agreement and Consent Order* (FFACO) (1996). Appendix VI of the FFACO, "Corrective Action Strategy," describes the processes that will be used to complete corrective actions, including those in the UGTA Project. The objective of the strategy is to analyze and evaluate each UGTA corrective action unit (CAU) (Figure 1-1) through a combination of data and information collection and evaluation, and modeling groundwater flow and contaminant transport. Section 1.3 of this report provides a summary of the FFACO corrective action process and the UGTA corrective action strategy.

The FFACO corrective action process for Central and Western Pahute Mesa was initiated with the Corrective Action Investigation Plan (CAIP) (DOE/NV, 1999). This Pahute Mesa CAIP identified a three-step model development process to evaluate the impact of underground nuclear testing on groundwater and simulate a contaminant boundary (DOE/NV, 1999, Section 5.1.1). The first step is the data analysis task to compile and evaluate existing and new data for use in the model. The second step is the development of the groundwater flow model. The third step is the development of the transport model.

The first step has been completed and is documented in a series of data compilation and analysis reports, including the *Hydrologic Data for Groundwater Flow and Contaminant Transport Model of Corrective Action Units 101 and 102: Central and Western Pahute Mesa, Nye County, Nevada* (SNJV, 2004a). A listing and summary of these supporting reports is provided in Section 1.5.

This report completes the second step and documents the development of the groundwater flow model to assess the migration of radionuclides away from underground nuclear test cavities on Pahute

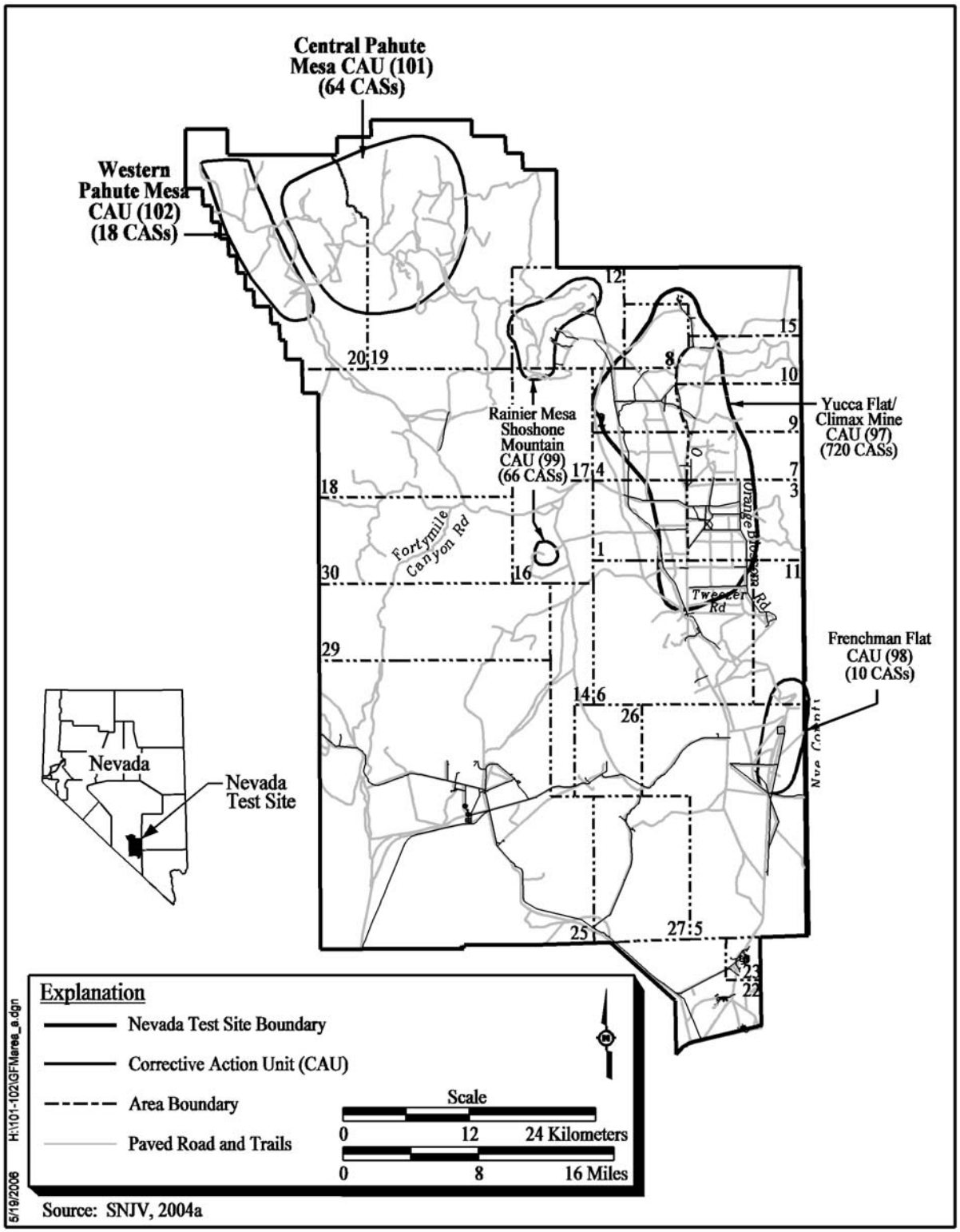

Figure 1-1
Location of the Pahute Mesa Corrective Action Units

Mesa. The third step, the development of the contaminant transport model, will be documented in a future report.

1.1 Purpose and Scope

The Pahute Mesa groundwater flow model supports the FFACO UGTA corrective action strategy objective of providing an estimate of the vertical and horizontal extent of contaminant migration for each CAU in order to predict contaminant boundaries. A contaminant boundary is the model-predicted perimeter that defines the extent of radionuclide-contaminated groundwater from underground nuclear testing above background conditions exceeding *Safe Drinking Water Act* (SDWA) standards. The contaminant boundary will be composed of both a perimeter boundary and a lower hydrostratigraphic unit (HSU) boundary. Additional results showing contaminant concentrations and the location of the contaminant boundary at selected times will also be presented. These times may include the verification period, the end of the five-year proof-of-concept period, as well as other times that are of specific interest.

The FFACO (1996) requires that the contaminant transport model predict the contaminant boundary at 1,000 years and "at a 95% level of confidence." The Pahute Mesa Phase I flow model described in this report provides, through the flow fields derived from alternative hydrostratigraphic framework models (HFMs) and recharge models, one part of the data required to compute the contaminant boundary. Other components include the simplified source term model, which incorporates uncertainty and variability in the factors that control radionuclide release from an underground nuclear test (SNJV, 2004a), and the transport model with the concomitant parameter uncertainty as described in Shaw (2003). The uncertainty in all the above model components will be evaluated to produce the final contaminant boundary.

This report documents the development of the groundwater flow model for the Central and Western Pahute Mesa CAUs.

Specific objectives of the Central and Western Pahute Mesa flow model are to:

- Develop a three-dimensional (3-D), mathematical flow model that incorporates the important physical features of the flow system and honors CAU-specific data and information.

- Simulate the groundwater flow system to determine the direction and magnitude of groundwater fluxes based on calibration to Pahute Mesa hydrogeologic data.
- Quantify the uncertainty in the direction and magnitude of groundwater flow due to uncertainty in parameter values and alternative component conceptual models (e.g., geology, boundary flux, and recharge).

Figure 1-2 shows the hydrologic model area that encompasses the Pahute Mesa CAUs, including Timber Mountain, the eastern edge of Oasis Valley, the northern part of Fortymile Canyon, and the northern portion of Yucca Mountain (DOE/NV, 1999). This area was selected to better define the regional groundwater flow system of the Lower Carbonate Aquifer (LCA) in the vicinity of Pahute Mesa.

1.2 Project Participants

The UGTA Project is a component of the NNSA/NSO Environmental Restoration Program (ERP). The UGTA Project Corrective Action Investigations (CAIs) are managed by the NNSA/NSO UGTA Project Manager. A Technical Working Group (TWG) has been established to assist the NNSA/NSO UGTA Project Manager with technical management issues. Tasks assigned to the TWG include providing expert technical support to plan, guide, and monitor UGTA technical work and serve as internal peer reviewers of UGTA products. The TWG consists of representatives from the participating organizations, which are: Bechtel Nevada (BN), Desert Research Institute (DRI), Lawrence Livermore National Laboratory (LLNL), Los Alamos National Laboratory (LANL), Stoller-Navarro Joint Venture (SNJV), and the U.S. Geological Survey (USGS).

1.3 Summary of the Federal Facility Agreement and Consent Order

Since 1996, the Nevada Division of Environmental Protection (NDEP) has regulated the NNSA/NSO corrective actions through the FFACO (1996). The individual locations covered by the agreement are known as corrective action sites (CASs), and they are grouped into CAUs. The UGTA CAUs are Frenchman Flat, Central and Western Pahute Mesa, Yucca Flat, and Rainier Mesa/Shoshone Mountain (Figure 1-1). Central Pahute Mesa (CAU 101) and Western Pahute Mesa (CAU 102) are addressed together due to their adjacent locations and common groundwater regime as well as similarities in testing practices, geology, and hydrology (SNJV, 2004a).

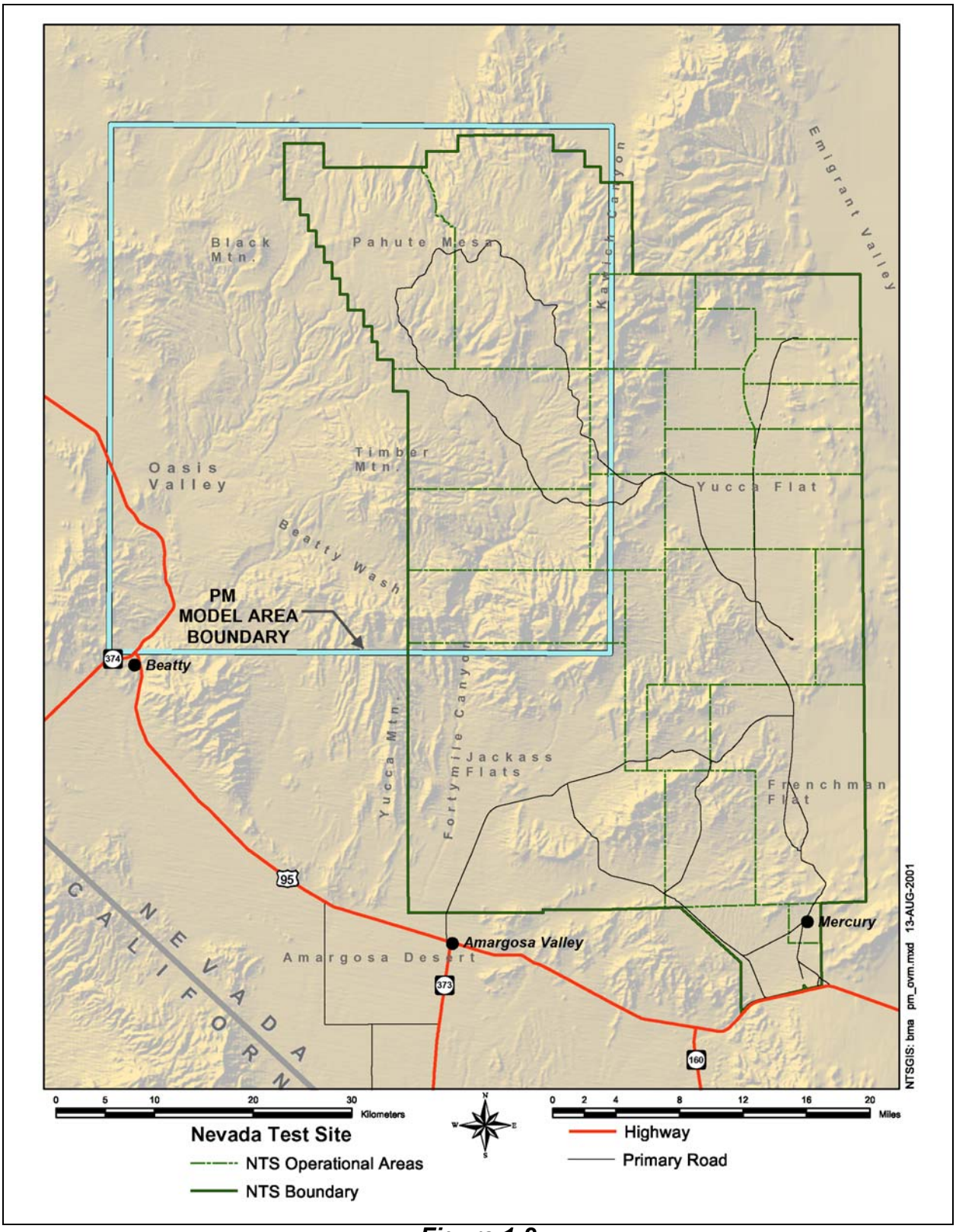

Figure 1-2
Map Showing Location of the Pahute Mesa Model Area
(Modified from BN, 2002)

Appendix VI, Revision No. 1 (December 7, 2000) of the FFACO (1996), "Corrective Action Strategy," describes the processes that will be used to complete corrective actions, including those in the UGTA Project. The UGTA corrective action strategy, described in Section 3.0 of the FFACO, provides the current regulatory guidance on the UGTA corrective action strategy and is incorporated into this document. All references to the FFACO or its appendices in this document will refer to the FFACO as a whole (i.e., FFACO, 1996) because it is the official document that incorporates the Appendix VI, December 2000 revision.

The CAU-specific corrective action process includes six major components: CAIP, CAI, Corrective Action Decision Document (CADD), Corrective Action Plan (CAP), Closure Report (CR), and long-term monitoring. The purpose or contents of these documents are summarized as follows:

- The CAI planning is documented in the CAIP, an FFACO-required document that provides or references all specific information for planning investigation activities associated with CAUs or sites.
- The CAI includes the collection of new data, the evaluation of new and existing data, and the development and use of CAU-specific groundwater flow and transport model(s).
- The CADD is an FFACO-required report that documents the CAI. It describes the results of the CAI, the corrective action alternatives considered, the results of their comparative evaluation, the selected corrective action, and the rationale for its selection.
- The CAP is an FFACO-required document describing how the selected remedial alternative is to be implemented. The CAP will contain the engineering design and all necessary specifications to implement the selected remedial alternative.
- The UGTA strategy has provisions for CAU closure only if the long-term-monitoring alternative is selected. Closure activities include the preparation of a CR, a review of the CR by NDEP, and long-term closure monitoring by NNSA/NSO.
- The long-term, post-closure monitoring is designed to ensure the compliance boundary is not violated (SNJV, 2004a).

Figure 1-3 presents the decision process used to achieve the strategy for the Pahute Mesa CAU groundwater flow model. The shaded portion of the diagram illustrates the portion of the process that has been completed as part of the Pahute Mesa CAI.

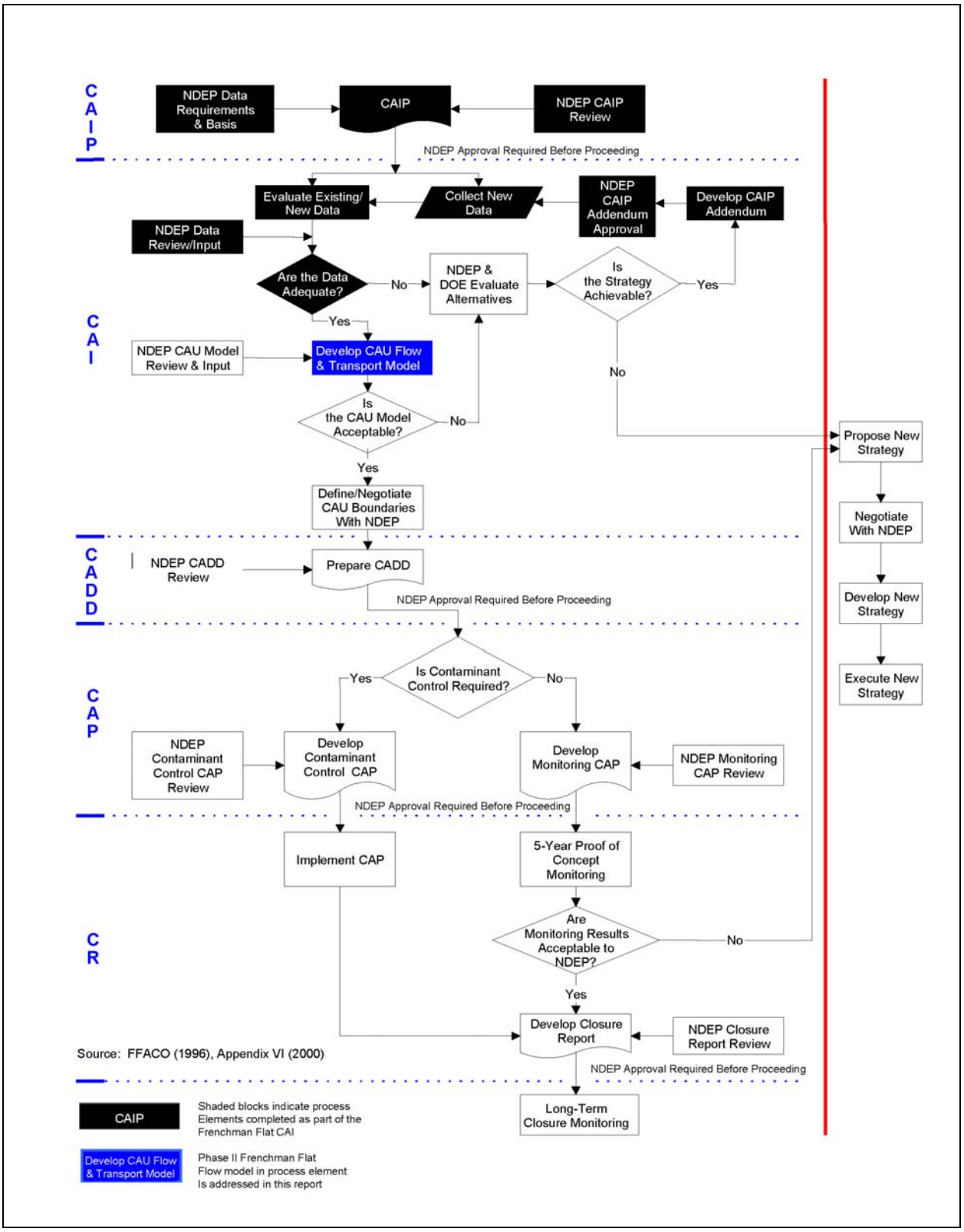

Figure 1-3
Process Flow Diagram for the Underground Test Area Corrective Action Units

1.3.1 Summary of the FFACO UGTA Corrective Action Strategy

The UGTA corrective action strategy consists of two major phases: development of a regional flow model for use in evaluation and coordination for all the UGTA CAUs, and a corrective action process for each of the CAUs. A model of regional flow encompassing the NTS and the groundwater flow systems extending to downgradient discharge has been completed and is documented in *Regional Groundwater Flow and Tritium Transport Modeling and Risk Assessment of the Underground Test Area, Nevada Test Site, Nevada* (DOE/NV, 1997). Regional modeling is a cross-cutting activity, supporting the entire UGTA Project, which provides the initial basis for assessing flow paths from CAUs, determining potential receptors, evaluating isolation or interaction of CAUs, and creating a consistent hydrogeologic framework across all the CAUs. Regional transport modeling provided the initial basis for determining the magnitude of risk from the source to potential receptors and for scaling individual CAU work (FFACO, 1996).

The second phase of the CAI process focuses on developing CAU-specific models that include CAU-specific data. The CAU-specific modeling objectives are to determine boundaries that encompass the extent of contamination, as defined in the FFACO (1996). Thus, this second phase is the basis for the analysis of relevant hydrologic data, and the development of the Pahute Mesa groundwater flow and transport model. The development of the groundwater flow model is presented in this report.

1.4 Pahute Mesa Background

Pahute Mesa is located in the northwestern part of the NTS. It includes NTS Areas 19 and 20 (Figure 1-1). Pahute Mesa is an elevated plateau of about 500 square kilometers (km^2) (200 square miles [mi^2]) at an altitude that ranges from 1,676 meters (m) (5,500 feet [ft]) on the western edge to over 2,134 m (7,000 ft) above mean sea level (amsl) throughout the eastern range (Blankennagel and Weir, 1973). The area of interest for the Pahute Mesa CAU is defined by the potentially affected portion of the regional groundwater flow system, which includes a region stretching from the northern side of Pahute Mesa south and southwestward to Oasis Valley (Figure 1-2).

Pahute Mesa geology is dominated by deposition of rock units from volcanic eruptions from nested calderas of the Southwestern Nevada Volcanic Field (SWNVF) (Figure 1-4). All rocks known to

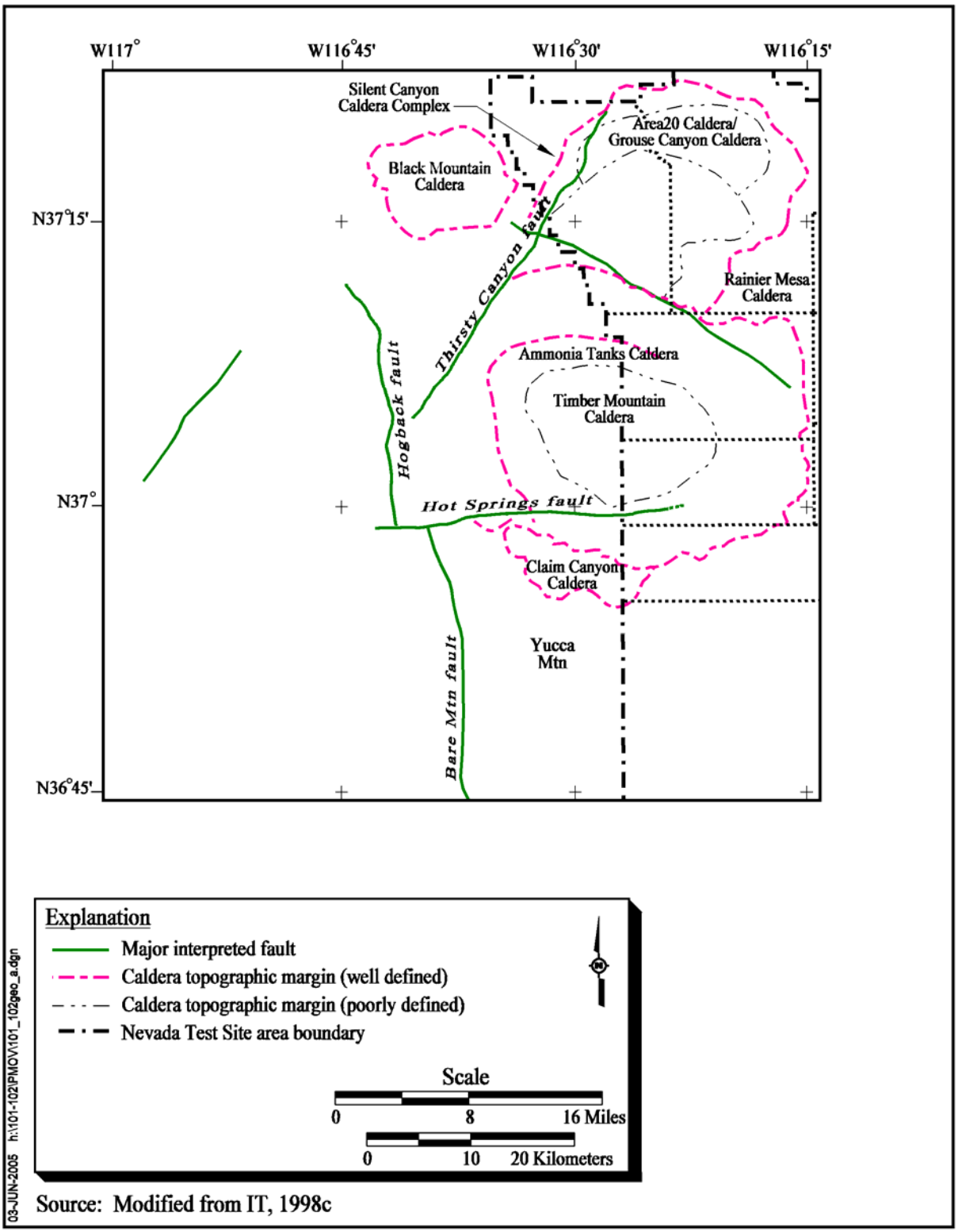

Figure 1-4
Geophysically Inferred Geologic Features of the Pahute Mesa Area

underlie Pahute Mesa are volcanic. The younger caldera complex of hydrologic significance is the Timber Mountain Caldera. This caldera collapse and its filling with volcanic materials affect the southern portion of the Western Pahute Mesa CAU. The Timber Mountain Caldera erupted volcanic ash flows that covered much of Pahute Mesa to the north.

On Pahute Mesa, the rocks from Timber Mountain Caldera cover an older series of calderas that make up the Silent Canyon Caldera Complex (SCCC). This caldera complex consists of at least two nested calderas, the Area 20 Caldera and the older Grouse Canyon Caldera (Sawyer and Sargent, 1989). Both calderas were formed and subsequently filled by voluminous eruptions of tuff and lava of generally rhyolitic composition. Total thickness of volcanic rocks beneath Pahute Mesa approaches 5 kilometers (km) (Ferguson et al., 1994).

The volcanic rocks that control groundwater flow beneath Pahute Mesa can be grouped into four volcanic hydrogeologic units (HGUs) based mainly on lithology and secondary alteration. These units are lava-flow aquifers (LFAs), welded-tuff aquifers (WTAs), vitric-tuff aquifers (VTAs), and tuff confining units (TCUs).

Groundwater beneath Pahute Mesa generally flows in a southwest direction, primarily through fractures in the lava-flow and tuff aquifers. Zeolitized bedded and nonwelded tuffs act as confining units that inhibit the flow of groundwater. The spatial distribution of permeable aquifers relative to the confining units is not well understood. Thickness variations of aquifers and confining units and their connectivity across faults or caldera boundaries are important hydrostratigraphic relationships that are also not well understood outside Pahute Mesa.

Groundwater-elevation data in the area of interest are sparse. A number of wells provide water-level information in the area of Pahute Mesa and Oasis Valley, but water levels in the area between Pahute Mesa and Oasis Valley are less well defined. However, what data are available suggest that groundwater elevations generally mimic the topography. Groundwater elevations are highest beneath northern Pahute Mesa, ranging in elevation from approximately 1,280 to nearly 1,500 m (4,200 to 4,900 ft). Groundwater elevations drop off gradually to the south and west, ranging from 1,100 to 1,250 m (3,600 to 4,100 ft) in Oasis Valley. Some groundwater discharges to the surface within the Oasis Valley discharge area in the form of springs. Figure 1-4 shows the regional topography, and

Figure 1-5 shows the generalized groundwater flow directions for the regional groundwater flow system.

Groundwater recharge occurs locally from precipitation and by underflow from areas located to the north of Pahute Mesa. Groundwater then flows south-southwestward to the Oasis Valley and Death Valley to the southwest. Several factors are believed to account for the flow around Timber Mountain. Due to its elevation, Timber Mountain receives excess precipitation compared to surrounding areas of lower elevation, which leads to additional groundwater recharge beneath Timber Mountain. In addition, extensive zeolitization and clay alteration of the tuffs within the Timber Mountain Caldera causes these volcanic units to behave more like confining units than aquifers. Both of these factors are expected to lead to a mounding of the groundwater levels beneath the mountain, which affects groundwater flow path from Pahute Mesa such that they go around both sides of Timber Mountain.

The bulk of the groundwater flow from Pahute Mesa to Oasis Valley occurs around the northwest side of Timber Mountain. However, a significant portion flows south along the east side of Timber Mountain and makes an abrupt turn to the west to converge with the remaining flow at Oasis Valley (Figure 1-5). This westerly turn appears to be caused by a structural high of the Lower Clastic Confining Unit (LCCU) associated with the Belted Range thrust system, which forces the groundwater to turn west at this point and flow towards the discharge areas. Pathlines from underground nuclear tests on Pahute Mesa generally move downgradient in volcanic aquifers above the LCA before discharging in Oasis Valley.

The east-west striking boundary of the Timber Mountain and Claim Canyon Calderas may line up with a geophysically inferred east-west structure (Hot Springs Fault) (Grauch et al., 1997) (Figure 1-4). The combination of these structures may inhibit southerly flow of groundwater in the vicinity, and impart an east-west gradient to groundwater flow south of Timber Mountain (IT, 1998c).

1.4.1 Underground Nuclear Testing on Pahute Mesa

Pahute Mesa was used as an underground nuclear testing area of the NTS for 27 years. Underground nuclear testing on Pahute Mesa began with Operation Whetstone in 1965 and ended with Operation Julin in 1992 (DOE/NV, 2000). Underground nuclear tests conducted at Pahute Mesa that are of

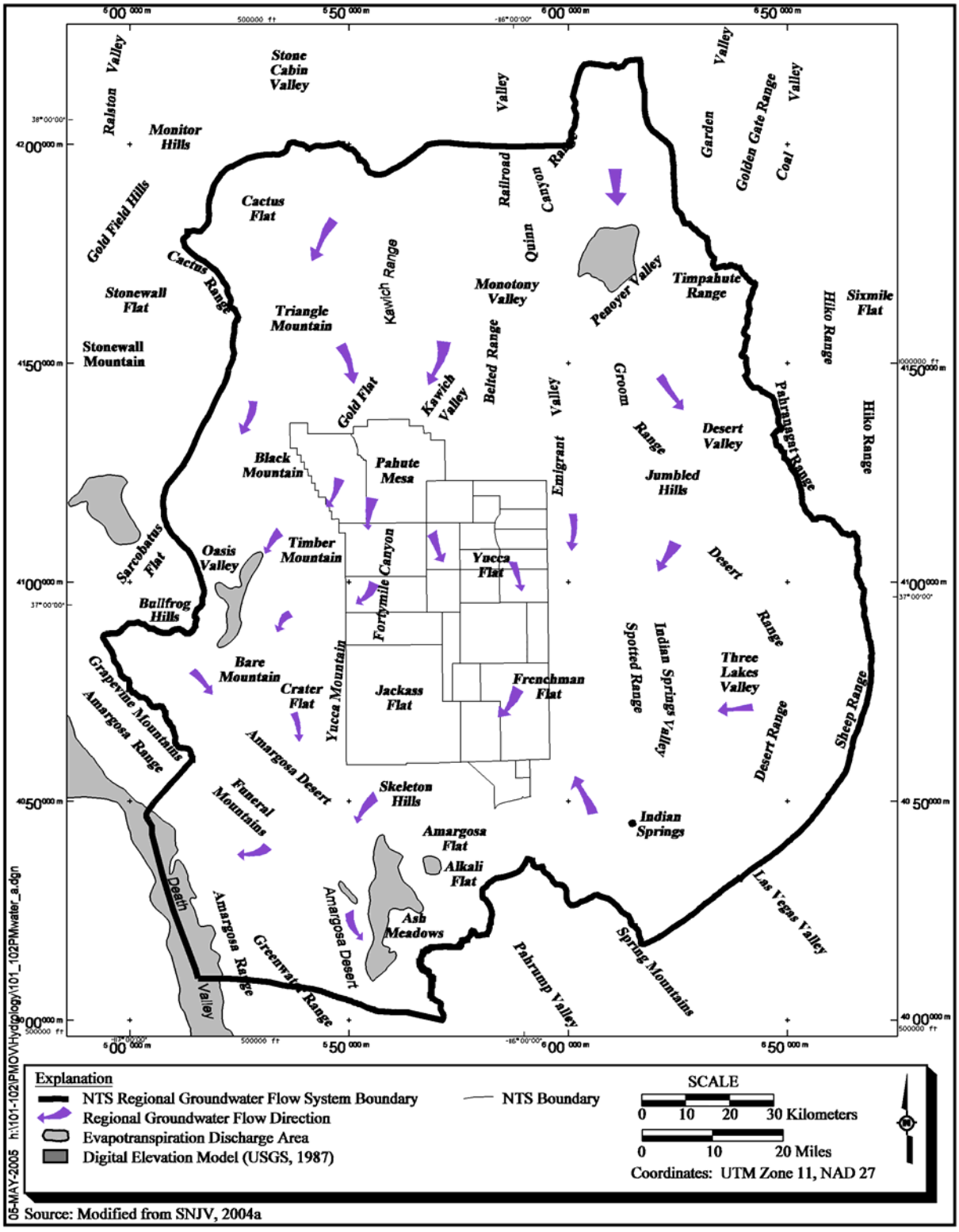

Figure 1-5
Features of the Nevada Test Site Regional Groundwater Flow System

interest to the UGTA Project are those detonated in deep vertical shafts, drilled into volcanic rock near or below the water table. A total of 82 such underground nuclear tests were conducted in Pahute Mesa. Sixty-four of these tests were detonated on Central Pahute Mesa (CAU 101), and 18 tests were detonated in Western Pahute Mesa (CAU 102) (DOE/NV, 1999). Media contaminated by the underground nuclear tests on Pahute Mesa are geologic formations within the unsaturated and saturated zones. Transport in groundwater is the primary mechanism of migration for the subsurface contamination away from the Pahute Mesa underground nuclear tests.

1.5 Major Supporting Reports Documenting CAU-Specific Data Analysis and Evaluation

The Pahute Mesa CAUs 101 and 102 groundwater flow model is supported by a number of major reports that describe a series of data analysis and modeling tasks. Table 1-1 summarizes these reports and identifies their contribution to the development of the Pahute Mesa flow model.

1.6 Report Organization

This report is organized into the following sections:

Section 1.0 presents an introduction to the document.

Section 2.0 presents the stratigraphic framework and alternative conceptual models of the geologic framework and groundwater flow that represent the information base for the CAU flow system; the numerical models of groundwater flow are constructed to replicate these conceptual geologic and flow system models.

Section 3.0 presents the computer code selection and code description.

Section 4.0 is the groundwater flow model construction that explains and demonstrates how the model was converted into its numerical representation.

Section 5.0 presents the flow model calibration and describes the purpose of calibration, the calibration protocol, use of parameter estimation (PEST), and how parameter sensitivities and constraint of flow paths were utilized.

Table 1-1
Major Supporting Documents
(Page 1 of 3)

Report	Report Synopsis	Contribution to Flow Model
Summary of Hydrogeologic Controls on Ground-Water Flow at the Nevada Test Site, Nye County, Nevada (Laczniak et al., 1996)	This report summarizes what is known and inferred about groundwater flow throughout the NTS region. As such, major controls on groundwater flow are identified, some uncertainties about groundwater flow are highlighted, and technical needs are prioritized and identified relative to the ERP.	• Conceptual model
Regional Groundwater Flow and Tritium Transport Modeling and Risk Assessment of the Underground Test Area, Nevada Test Site, Nevada (DOE/NV, 1997)	This report provided the initial rationale to determine the magnitude of risk from various underground nuclear tests on the NTS to potential downgradient receptors, such as the public and the environment from possible groundwater contamination. The regional evaluation consisted of data analysis, model development, and model predictions. Results of the regional evaluation of groundwater flow, tritium migration, and risk assessment performed for the underground test areas are presented in this report. As such, the regional evaluation was used during the planning of the Pahute Mesa CAI and is the basis for the development of the CAU conceptual model.	• Conceptual model • Regional model framework • Boundary fluxes
Corrective Action Investigation Plan for Corrective Action Units 101 and 102: Central and Western Pahute Mesa, Nevada Test Site, Nevada (DOE/NV, 1999)	This report is a requirement of the FFACO (1996) that summarizes the site-specific historic data for the Pahute Mesa CAUs and describes the characterization activities implemented to evaluate the extent of contamination in groundwater due to the underground nuclear testing, and the development of a groundwater flow model to predict the contaminant boundary.	• Summary of historic data • Background information • CAU model approach
Quality Assurance and Analysis of Water Levels in Wells on Pahute Mesa and Vicinity, Nevada Test Site, Nye County, Nevada (Fenelon, 2000)	This report states that accurate water-level measurements are essential to determine groundwater flow paths that may contain contaminants from underground nuclear tests conducted on Pahute Mesa. As such, quality-assured data can be utilized to construct flow maps, calibrate steady-state and transient groundwater flow models, locate sites for future remedial monitoring, and identify existing trends that can be used as a means to understand the factors that influence the groundwater flow system.	• Supplement water-level targets for flow model calibration
A Hydrostratigraphic Model and Alternatives for the Groundwater Flow and Contaminant Transport Model of Corrective Action Units 101 and 102: Central and Western Pahute Mesa, Nye County, Nevada (BN, 2002)	This report presents the evaluation of geologic data and the resulting 3-D HFM. The framework was built utilizing a collection of stratigraphic, lithologic, and alteration data; a structural model; and results of geophysical, geological, and hydrological studies to formulate the hydrostratigraphic system.	• HFM • Alternative HFMs • HSU definition and description

Table 1-1
Major Supporting Documents
(Page 2 of 3)

Report	Report Synopsis	Contribution to Flow Model
Evaluation of the Hydrologic Source Term from Underground Nuclear Tests on Pahute Mesa at the Nevada Test Site: The CHESHIRE Test (Pawloski et al., 2001)	This report develops, summarizes, and interprets a series of detailed, unclassified simulations to forecast the nature and extent of radionuclide release and near-field migration in groundwater away from the CHESHIRE test over 1,000 years. The results are referred to as the CHESHIRE Hydrologic Source Term (HST).	• Background • Input into conceptual flow model
Geochemical and Isotopic Interpretations of Groundwater Flow in the Oasis Valley Flow System, Southern Nevada (Thomas et al., 2002)	This report summarizes the findings of a geochemical investigation of the Pahute Mesa/Oasis Valley (PM/OV) groundwater flow system in support of the flow and contaminant transport modeling for the Western Pahute Mesa CAU.	• Flow paths derived from geochemical analysis used to qualitatively assess flow model
Ground-Water Discharge Determined from Measurements of Evapotranspiration, Other Available Hydrologic Components, and Shallow Water-Level Changes, Oasis Valley, Nye County, Nevada (Reiner et al., 2002)	This report describes the natural groundwater discharge in the Oasis Valley, an area within the groundwater flow system of the Death Valley region and California. An estimate of groundwater discharge from the Oasis Valley was examined in numerous studies. As a result of these studies, this report refined the estimated groundwater discharge from Oasis Valley by quantifying evapotranspiration (ET), compiling groundwater withdrawal data, and estimating subsurface outflow.	• Flow system discharge from ET used as calibration data
TYBO/BENHAM: Model Analysis of Groundwater Flow and Radionuclide Migration from Underground Nuclear Tests in Southwestern Pahute Mesa, Nevada (Wolfsberg et al., 2002)	This report provides a description of an integrated modeling approach used to simulate groundwater flow, radionuclide release, and radionuclide transport near the TYBO and BENHAM underground nuclear test sites.	• Test case for finite element heat-mass (FEHM) transfer code model • Results used to help parameterize CAU model
Reconnaissance Estimates of Recharge Based on an Elevation-Dependent Chloride Mass-Balance Approach (Russell and Minor, 2002)	This study describes the DRI evaluation of net infiltration and determination of recharge via the development of recharge models for data gathered from 17 springs located in the Sheep Range, Spring Mountains, and on the NTS. The objective was to improve an existing aquifer-response method based on the chloride mass-balance approach. Results of the recharge estimates are reported.	• Recharge models
Simulation of Net Infiltration and Potential and Potential Recharge Using a Distributed Parameter Watershed Model for the Death Valley Region, Nevada and California (Hevesi et al., 2003)	This study reports the development and application of a distributed parameter watershed model to estimate the temporal and spatial distribution of net infiltration for the Death Valley region. As stated, because of uncertainty relative to the input parameters, “averaging results from multiple realizations is more likely to provide a more robust estimate of current climate potential recharge.”	• Recharge models

Table 1-1
Major Supporting Documents
(Page 3 of 3)

Report	Report Synopsis	Contribution to Flow Model
Evaluation of Groundwater Flow in the Pahute Mesa - Oasis Valley Flow System Using Groundwater Chemical and Isotopic Data (Kwicklis et al., 2005)	This report documents the utilization of groundwater geochemical and isotopic data from the vicinity of the PM/OV flow system to interpret groundwater flow patterns as well as to independently evaluate the groundwater flow model that is currently being developed. A combination of graphical methods and inverse geochemical models form the basis for the PM/OV model area.	• Flow paths derived from geochemical analysis • Geochemical verification dataset
Hydrologic Data for the Groundwater Flow and Contaminant Transport Model of Corrective Action Units 101 and 102: Central and Western Pahute Mesa, Nye County, Nevada (SNJV, 2004a)	This report describes an assessment of hydrologic data and information in support of the CAU groundwater flow model. Relevant information, existing data, and newly-acquired data were analyzed for the hydrologic components of the groundwater flow system of Pahute Mesa and vicinity.	• Hydraulic head data for calibration • Hydraulic properties data • Discharge due to pumping • Boundary fluxes • Recharge models • Flow paths derived from geochemical analysis
Modeling Approach/Strategy for Corrective Action Units 101 and 102, Central and Western Pahute Mesa (SNJV, 2004b)	This report summarizes the data and information that are the technical basis for the groundwater flow model. Two approaches are described that propose developing the models to forecast how the hydrogeologic system, which includes the underground nuclear test cavities, will behave over time. One approach is the development of numerical process models to represent the processes that influence flow and transport. The other approach shows how simplified representations of the process models are utilized to assess the interactions between model and parameter uncertainty.	• Numerical code selection • Overall approach

Section 6.0 is the flow model sensitivity and uncertainty analysis.

Section 7.0 presents the geochemical verification.

Section 8.0 presents the thermal verification.

Section 9.0 is the summary and conclusions.

Section 10.0 contains the reference list.

Appendix A provides the 1999 letter report documenting the evaluation of flow and transport codes for application to the Pahute Mesa CAUs.

Appendix B is the LANL fault study.

Appendix C is the LANL thermal field analysis.

Appendix D presents the perturbation sensitivity analysis plots.

Appendix E presents permeabilities on cross sections A through J of the geologic model for several HFMs.

Appendix F presents the well and spring head calibration data.

2.0 FRAMEWORK FOR GROUNDWATER FLOW MODELING OF CENTRAL AND WESTERN PAHUTE MESA - DATA, INFORMATION, AND CONCEPTUAL MODELS

The development of a CAU-scale groundwater flow model for Central and Western Mesa Pahute Mesa is a key element of the FFACO corrective action strategy. The framework for this flow model incorporates data and information related to multiple component models of the Pahute Mesa hydrogeologic system. Each of these component models is characterized by uncertainties in both the data and information that characterize the processes described by the component model, and in the conceptual models that incorporate the data and information.

Figure 2-1 summarizes the regional and site-specific elements that are integrated into the Pahute Mesa flow model. These elements include:

- Regional data and information that provide the hydrogeologic context for the CAU-specific flow model.
- CAU-specific geologic data and information that establish the local hydrostratigraphic framework within which groundwater flows.
- Component models that integrate the regional hydrogeology into the CAU-specific hydrogeology.
- Alternative CAU-specific models to address uncertainty in hydrostratigraphy, lateral boundary flux and heads, and recharge.
- CAU-specific hydrologic parameters (including their uncertainty).

This section provides an overview of the data, information, and conceptual models that are incorporated into the Pahute Mesa flow model. The data, information, and conceptual models presented in this overview represent a large body of work (Table 1-1) and are described in more detail in the integrating report *Hydrologic Data for the Groundwater Flow and Contaminant Transport*

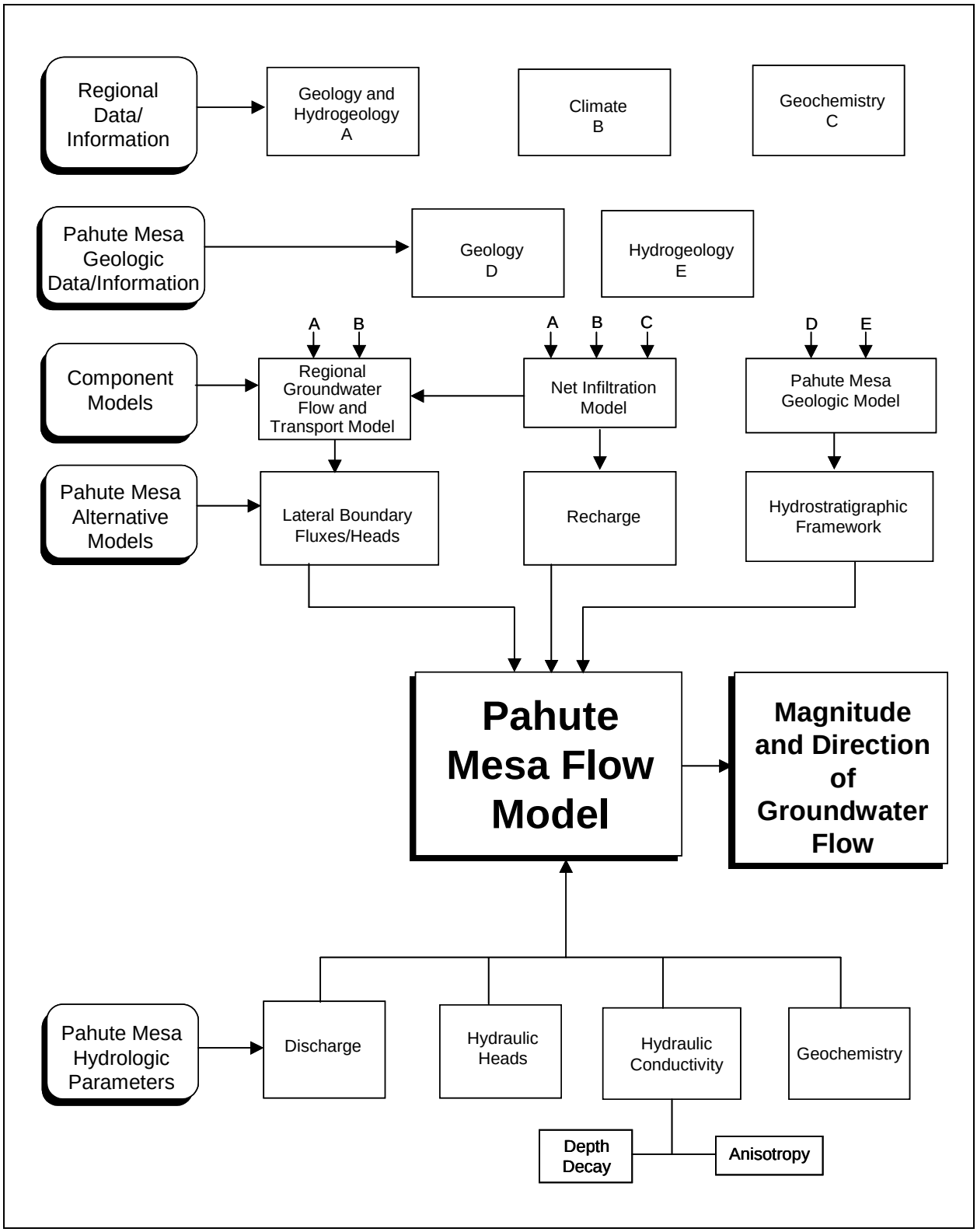

Figure 2-1
Information Flow into the Pahute Mesa Groundwater Flow Model

Model of Corrective Action Units 101 and 102: Central and Western Pahute Mesa, Nye County, Nevada (SNJV 2004a).

2.1 Summary of the UGTA Regional Model

A model of the regional groundwater flow through the NTS extending to downgradient discharge areas was developed during the regional evaluation (DOE/NV, 1997). The Pahute Mesa flow system model area is part of the NTS regional flow system model area (Figure 1-2), which is part of the Death Valley regional flow system (DVRFS) (Faunt et al., 2004; Hevesi et al., 2003). The following sections provide an overview of this regional model.

Belcher et al. (2004) published a revised regional model, the Death Valley regional flow model (DVRFM), in early 2005, after the Pahute Mesa flow model analysis was largely complete. It is DOE policy not to use work products that are unpublished. Thus, it was not possible to include the newer results in any comprehensive way.

2.1.1 UGTA Regional Model Hydrostratigraphic Framework

The hydrogeologic framework used in the UGTA regional groundwater flow model is based on the conceptual hydrologic system established for the NTS area by Winograd and Thordarson (1975) and Blankennagel and Weir (1973). This early work was summarized and updated by Laczniak et al. (1996) and was further developed by UGTA (IT, 1996d).

All rocks of the NTS and vicinity can be classified as one of eight HGUs, which include the alluvial aquifer (AA), four volcanic HGUs, an intrusive HGU, and two HGUs that represent the pre-Tertiary sedimentary and metasedimentary rocks. Table 2-1 summarizes the HGUs of the UGTA regional model.

Hydrostratigraphic units are groupings of contiguous stratigraphic units that have a particular hydrogeologic character, such as aquifer (unit through which water moves readily) or confining unit (unit that generally impedes water movement). An HSU may contain several HGUs but is defined so that a single general type of HGU dominates (for example, mostly WTAs and VTAs, or mostly TCUs). Twenty HSUs were defined in the UGTA regional HFM (IT, 1996d).

Table 2-1
Hydrogeologic Units of the UGTA Regional Model

Hydrogeologic Unit	Typical Lithologies	Hydrologic Significance
Alluvial Aquifer (AA) (AA is also an HSU in hydrogeologic models.)	Unconsolidated to partially consolidated gravelly sand, aeolian sand, and colluvium; thin, basalt flows of limited extent	Has characteristics of a highly conductive aquifer, but less so where lenses of clay-rich paleocolluvium or playa deposits are present.
Welded-Tuff Aquifer (WTA)	Welded ash-flow tuff; vitric to devitrified	Degree of welding greatly affects interstitial porosity (less porosity as degree of welding increases) and permeability (greater fracture permeability as degree of welding increases).
Vitric-Tuff Aquifer (VTA)	Bedded tuff; ash-fall and reworked tuff; vitric	Constitutes a volumetrically minor HGU; generally does not extend far below the static water level due to tendency of tuffs to become zeolitic (which drastically reduces permeability) under saturated conditions; significant interstitial porosity (20 to 40 percent); generally insignificant fracture permeability.
Lava-Flow Aquifer (LFA)	Rhyolite lava flows; includes flow breccias (commonly at base) and pumiceous zones (commonly at top)	Generally a caldera-filling unit; hydrologically complex, wide range of transmissivities, fracture density and interstitial porosity differ with lithologic variations.
Tuff Confining Unit (TCU)	Zeolitic bedded tuff with interbedded, but less significant, zeolitic, nonwelded to partially welded ash-flow tuff	May be saturated but measured transmissivities are very low; may cause accumulation of perched and/or semi-perched water in overlying units.
Intrusive Confining Unit (ICU)	Granodiorite, quartz monzonite	Relatively impermeable; forms local bulbous stocks, north of Rainier Mesa, Yucca Flat, and scattered elsewhere in the UGTA regional model area; may contain perched water.
Clastic Confining Unit (CCU)	Argillite, siltstone, quartzite	Clay-rich rocks are relatively impermeable; more siliceous rocks are fractured, but with fracture porosity generally sealed due to secondary mineralization.
Carbonate Aquifer (CA)	Dolomite, limestone	Transmissivity values vary greatly and are directly dependent on fracture frequency.

Source: Modified from SNJV, 2004a

In the Pahute Mesa-Timber Mountain caldera complex area, the rocks were divided into six Tertiary volcanic HSUs, one intrusive HSU, and five pre-Tertiary HSUs. The volcanic rocks west of the Timber Mountain-Oasis Valley caldera complex were not subdivided and are represented by a single HSU, volcanics undifferentiated (VU). The HSUs defined for the UGTA regional HFM that are within the Pahute Mesa model area are listed in Table 2-2. These units are listed in approximate order from surface to basement, although some are laterally rather than vertically contiguous, and not all units are present in all parts of the model area.

Table 2-2
Hydrostratigraphic Units of the Pahute Mesa Area Included in the UGTA Regional HFM
(Page 1 of 2)

Model HSU Number[a]	Hydrostratigraphic Unit (Symbol)	Dominant Hydrogeologic Unit(s)[b]	Stratigraphic Unit Map Symbols[c]	General Description
20	Alluvial Aquifer (AA) (this term is also used to designate a hydrogeologic unit)	AA	Qay, QTc, Qs, Qam, QTa, QTu, Qb, Tgy, Tgc, Tgm, Tgyx, Tt	Consists mainly of alluvium that fills extensional basins such as Crater Flat. Also includes generally older Tertiary gravels, tuffaceous sediments, and nonwelded tuffs (where thin) that partially fill other basins such as Oasis Valley and the moat of the Timber Mountain caldera complex.
19	Timber Mountain Aquifer (TMA)	Mostly WTA, minor VTA; TCU within the Tm caldera complex	Tt, Tf, Tm	"The uppermost welded tuffs" in the Pahute Mesa model area. Consists mainly of extra-caldera welded ash-flow tuffs (aquifer-like lithologies). However, the altered intra-caldera equivalent rocks within the Timber Mountain caldera are modeled as confining units.
18	Tuff Cone (TC)	LFA, TCU	Tp, Th (formerly Ta), Tc	Complex three-dimensional distribution of rhyolite lava and zeolitic nonwelded tuff of the Paintbrush Group, Calico Hills Formation or Crater Flat Group. Present in the northern portion of the Pahute Mesa model area beneath most of eastern and central Area 20.
17	Bullfrog Confining Unit (BFCU)	TCU	Tcb	Major confining unit differentiated within the NTS caldera complex area. Unit consists of thick intra-caldera, zeolitic, mostly nonwelded tuff of the Bullfrog Formation.
16	Belted Range Aquifer (BRA)	LFA and WTA, with lesser TCU	Tub, Tcbs, Tr	Consists of welded ash-flow tuff and lava of the Belted Range Group (Tb) above the Grouse Canyon Tuff (Tbg), but may also include the lava-flow lithofacies of the commendite of Split Ridge (Tbgs) and the commendite of Quartet Dome (Tbq) where present. Differentiated within the NTS caldera complex area.
15	Basal Confining Unit (BCU)	TCU	Tn, Tub, To, Tr, Tq	Mostly zeolitized nonwelded tuffs differentiated in the NTS caldera complex area.
14	Basal Aquifer (BAQ)	WTA	To, Tlt, Tqm	Mostly aquifer-like older volcanic rocks. Differentiated within the NTS caldera complex area.
11	Volcanics Undifferentiated (VU)	WTA, TCU, lesser LFA	Potentially includes all Tertiary volcanic units	All Quaternary and Tertiary volcanic units outside the NTS proper and the proximal NTS caldera complex.
8	Upper Clastic Confining Unit (UCCU)	CCU	MDc, MDe	Late Devonian through Mississippian siliciclastic rocks. Present in the eastern third of the Pahute Mesa model area.
7	Lower Carbonate Aquifer (LCA)	CA	Dg through Cc	Cambrian through Devonian mostly limestone and dolomite. Widespread throughout the Pahute Mesa area.

Table 2-2
Hydrostratigraphic Units of the Pahute Mesa Area Included in the UGTA Regional HFM
(Page 2 of 2)

Model HSU Number[a]	Hydrostratigraphic Unit (Symbol)	Dominant Hydrogeologic Unit(s)[b]	Stratigraphic Unit Map Symbols[c]	General Description
6	Lower Clastic Confining Unit (LCCU)	CCU	Cc, Cz, Czw, Zs, Zj	Late Proterozoic through Early Cambrian siliciclastic rocks. Widespread throughout the Pahute Mesa area.
5	Lower Carbonate Aquifer - Thrust Plate (LCA1)	CA	Dg through Cc	Cambrian through Devonian, mostly limestone and dolomite, rocks that occur in the hanging wall of the Belted Range thrust fault.
4	Lower Clastic Confining Unit - Thrust Plate (LCCU1)	CCU	Cc, Cz, Czw, Zs	Late Proterozoic to Early Cambrian siliciclastic rocks that occur within the hanging wall of the Belted Range thrust fault.
1	Intrusives (I)	ICU	Ti, Kg	Consists of granitic rocks that comprise the Gold Meadows stock along the northeastern margin of the Pahute Mesa area and intrusives greater than 2 km in size elsewhere in the UGTA regional HFM.

[a]UGTA regional model (IT, 1996d; DOE/NV, 1997)
[b]See Table 2-1 for definitions of HGUs.
[c]Refer to Slate et al. (1999) and Ferguson et al. (1994) for definitions of stratigraphic unit map symbols.

Source: Modified from SNJV, 2004a

Based on data used in the UGTA regional model (IT, 1996b; DOE/NV, 1997), hydraulic conductivity ranges for the main aquifers are as summarized in Table 2-3. The mean hydraulic conductivity of the AA is smaller than that of carbonate aquifers (CAs), but higher than that of the volcanic aquifers (VAs). The ranges extend over orders of magnitude. For example, within the LCA, the range of hydraulic conductivity is estimated to be between 0.0008 and 1,570 meters per day (m/d) (0.003 and 5,150 feet per day [ft/d]), representing interstitial and fracture porosity, respectively. This large range suggests that at the local scale, large variability in hydraulic conductivity can be expected. At the larger scales, the degree of fracturing controls the heterogeneity. It was also found that a linear trend exists, showing a decrease in hydraulic conductivity with increased depth. The data, however, displayed a significant level of scatter (SNJV, 2004a).

Table 2-3
Range of Hydraulic Parameters for Major Aquifers

Aquifer	Hydraulic Conductivity	
	Mean (m/d)	**Range** (m/d)
Alluvial Aquifer	8.44	0.00005-83
Volcanic Aquifers	1.18	0.0003-12
Carbonate Aquifer	31.71	0.0008-1,570

Source: Modified from DOE/NV, 1997

2.1.2 Groundwater Occurrence and Movement

Within the NTS region, groundwater occurs in alluvial, volcanic, and carbonate materials. Saturated alluvial materials are present in central and southern Yucca Flat, Frenchman Flat, and Jackass Flats on the NTS and in the basins located throughout the flow system. Saturated Tertiary volcanics are present in the western section of the region. The distribution and thickness of alluvial and volcanic aquifers are highly variable throughout the region and are not interpreted to be continuous. In most instances, an AA is confined to a basin by surrounding mountain ranges. In some basins, AAs are discontinuous due to structural controls elevating the bottom of the alluvium above the water table. In general, alluvial and volcanic aquifers are considered depositional elements overlying the regional flow system and only influence regional flow in localized areas. The underlying LCA is the principal aquifer of the UGTA regional flow system. The LCA forms a nearly continuous aquifer across the

region except where interrupted by calderas, truncated by structural controls, or penetrated by intrusive rocks.

Based on the water-level dataset compiled during the regional evaluation (IT, 1996c; DOE/NV, 1997), depths to groundwater beneath the NTS and surrounding region vary greatly. Groundwater depths in the southern NTS range from about 23 m (75 ft) beneath upper Fortymile Wash to over 213 m (700 ft) beneath Frenchman Flat, compared to more than 610 m (2,000 ft) beneath Pahute Mesa in the northern NTS (IT, 1996c; DOE/NV, 1997). Perched groundwater is found locally throughout the NTS and occurs within the TCUs and, to some extent, overlying units. In the highlands, springs emerge from perched groundwater lenses. Spring discharge rates are low and this water is used only by wildlife.

The general direction of groundwater flow in the regional flow system is from north to south and east to southwest (Figure 1-5). The direction of groundwater flow is locally influenced in areas where structural and geologic conditions have controlled the distribution and thickness of the LCA. In some areas of the regional flow system, groundwater encounters structural and geologic conditions, such as structural highs of the LCCU, that promote an upward flow component. The upward flow component brings water to discharge at the surface in the form of a wet playa or springs. Groundwater flow between basins occurs in the form of subsurface inflow and outflow.

Horizontal hydraulic gradients are very low to the east and west of the NTS (see Figure 2-16). In other areas, the prevailing flow direction and hydraulic gradients may locally be influenced by the structural position of geologic units with significantly lower transmissivity than that of the LCA. If the low transmissive units are structurally oriented so that they are perpendicular to flow, flow might be significantly altered, causing large hydraulic gradients. If their structural orientation is parallel to the prevailing flow direction, their effect may be insignificant. Structural uplifts of the LCCU and the distribution of the UCCU have caused several of the observed steep gradients within the flow system. Low-permeability sediments along the Funeral Mountains, such as the Tertiary Death Valley section sediments, also cause a steep hydraulic gradient between Amargosa Desert and Death Valley.

Groundwater recharge results from precipitation at higher elevations, and infiltration along stream courses and in playas. Recharge rates and distribution may be estimated. The estimates are, however,

uncertain. The recharge model used in the regional flow model was based on a modification of the Maxey-Eakin method (Maxey and Eakin, 1949; IT, 1996a).

Groundwater discharges to the surface in the form of springs, seeps, and ET in several areas. Major areas of natural groundwater discharge include Oasis Valley, Ash Meadows, Alkali Flat, Death Valley, and Penoyer Valley. Estimates of ET have recently been updated by the USGS for the first four areas listed above (Laczniak et al., 2001). Within the NTS region, artificial discharge occurs as groundwater pumpage from drinking water supply wells (public and domestic), agricultural wells, and industrial wells. Public, domestic, and industrial water supply wells for the NTS produce water from the carbonate, volcanic, and valley-fill aquifers. South of the NTS, private and public water supply wells are completed in the valley-fill aquifer.

An estimate of the regional, steady-state, groundwater budget is provided in Table 2-4.

Table 2-4
Estimated Steady-State Groundwater Budget
for the Regional Groundwater Flow System

Recharge	
Recharge from precipitation	177,484 - 289,410 m^3/d
Subsurface inflow	5,405 - 70,100 m^3/d
Total Natural Recharge	**182,889 - 359,510 m^3/d**
Discharge	
Surface discharge (ET)	135,340 - 300,700 m^3/d
Subsurface outflow	850 - 5,100 m^3/d
Total Natural Discharge	**136,190 - 305,800 m^3/d**

Source: SNJV, 2004a

m^3/d = Cubic meters per day

2.2 Pahute Mesa Flow System Hydrostratigraphic Framework Models

The Pahute Mesa area HFMs were constructed using EarthVision® (EV) (Version 5.1, by Dynamic Graphics [2002]), a 3-D geologic model building and visualization software package. Input data included drill-hole data, digital elevation model data, and outcrop and fault data from surface geologic maps. Where deemed necessary, the data were supplemented with interpretations in the form of "pseudo drill holes," cross sections, and structure-contour maps. A "pseudo drill hole" is an

assumed data point used to facilitate the automated contouring of data. The data for the pseudo drill hole are obtained from surficial geology maps and/or geologist's interpretations.

The 3-D HFM area encompasses more than 2,700 km^2 (1,678 mi^2) of southern Nye County, Nevada (Figure 1-2). The model has a north-south length of 53.4 km (33.2 miles [mi]) and an east-west length of 50.8 km (31.6 mi), and includes geologic units as deep as 7 km (4.3 mi) below mean sea level (bmsl) (BN, 2002).

The processes of HFM development and screening are summarized in this section along with the geologic models retained for use in the CAU groundwater flow and transport model. The details may be found in the HFM report (BN, 2002).

2.2.1 Hydrostratigraphic Framework Model Development

A preliminary base HFM was constructed based on the conceptual model of the UGTA hydrologic system described by Winograd and Thordarson (1975). Further developments made by Laczniak et al. (1996), IT Corporation (IT) (1996a, b, and c), and Drellack and Prothro (1997) were also used to develop the Pahute Mesa CAU base HFM. A revised structural block model for the SWNVF (Warren et al., 2003) and an alternative 3-D model of the SCCC (McKee et al., 1999 and 2001) were incorporated into the information used for development of the base HFM. The hydrologic and geologic information developed for the USGS Death Valley region groundwater flow model was also included (D'Agnese et al., 1997; Faunt, 1997). Finally, information from the Yucca Mountain Project (YMP) hydrogeologic and flow model was incorporated in assessments of the southern part of the Western Pahute Mesa CAU.

Following the completion of the preliminary base HFM, a number of alternative HSU conceptual models were considered. These alternatives were screened for impact on groundwater flow and then evaluated and organized into four groups as follows:

- Group A - Alternatives of this group were developed using EV to improve the base HFM.
- Group B - Alternative HFMs were further developed in EV.
- Group C - These alternatives could be addressed by varying hydrologic parameters during the analysis and evaluation of the Pahute Mesa flow model.

- Group D - These alternatives were identified as low priority or not necessary to model.

The main criterion for selecting alternative HFMs for full development was the potential impact of the alternative interpretation on groundwater flow and the transport of contaminants in groundwater. Following this evaluation of the alternative HFMs, the base HFM was updated using the Group A alternatives, and the alternatives placed under Group B were further developed into EV models. Table 2-5 summarizes the Group B alternative HSUs.

For details on the base HFM and the alternative HSUs models, see *A Hydrostratigraphic Model for the Groundwater Flow and Contaminant Transport Model of Corrective Action Units 101 and 102: Central and Western Pahute Mesa, Nye County, Nevada* (BN, 2002).

After the development of all alternative HFMs, screening groundwater flow models were used to evaluate the impact of each alternative on contaminant transport (SNJV, 2004a). These models were developed using the Finite Element Heat-Mass (FEHM) Transfer Computer Code (Zyvoloski et al., 1997a and b) (see Section 3.0). The "particle-tracking" capability of FEHM was used to approximate the transport of radionuclides in groundwater using the base HFM and the six alternatives. None of these flow models were calibrated.

Except for the SCCC alternative, the results of the "particle-tracking" analyses for the other five alternatives were statistically similar to those of the base HFM. The results of the SCCC alternative produced results that were clearly different from those produced by the base HFM. Based on the screening results, only the base HFM and the SCCC alternative are used to develop alternative CAU flow models. The other five HFM alternatives are evaluated by varying the hydrologic parameters of the base HFM.

2.2.2 Base HFM

The structural features, HGUs, and HSUs of the base HFM developed for the Pahute Mesa area are summarized in this section. A 3-D view of this model is shown in Figure 2-2. A west-east cross section along C-C' (as shown in Figure 2-3) is shown in Figure 2-4 (BN 2002).

Table 2-5
Summary of Alternative HFMs Considered in the Pahute Mesa Flow Model
(Page 1 of 2)

Alternative HFM	Key Difference(s) Compared to Base HFM	Potential Impacts on Flow Model
Silent Canyon Caldera Complex (SCCC)	The SCCC alternative is stratigraphically and structurally less complex than the base HFM in the vicinity of the Silent Canyon caldera. The SCCC has a reduced number of HSUs, faults, and structural zones. In addition, the eastern and western margins of the SCCC area are different.	• Simplifications may impact flow directions and magnitudes in this area of the flow model. Comparisons between flow model results for this HFM and the base HFM will support an evaluation of the impact of faults on groundwater flow.
Basement Ridge Model (RIDGE)	The RIDGE alternative focuses on the bench area between the Timber Mountain caldera and SCCC. For this alternative, the southward distribution of important aquifer units (BA, TCA, TSA, and CFCM) pinch out or truncate against older, less conductive units that, for this HFM, are assumed to form the gravity-high ridge.	• Alternate HSU geometries may impact flow through the bench area between the Timber Mountain caldera and SCCC.
Thirsty Canyon Lineament (TCL)	The TCL alternative treats the north-northeast trending linear feature extending from just west of Well ER-EC-8 northeastward beneath western Pahute Mesa east of the Black Mountain caldera to the southern edge of Gold Flat as a continuous structural feature. The base HFM treats this feature as a continuous zone of en echelon faults 2 to 3 km wide.	• Treating the TCL as a continuous feature (interpreted in this HFM as a normal fault, down to the east) will help explore whether this feature on the west side of the ridge between the Timber Mountain caldera and SCCC acts as a potential hydraulic connection or barrier to groundwater flow.
Raised Pre-Tertiary Surface (PZUP)	The PZUP alternative raises the pre-Tertiary basement surface to its highest geologically permissible elevation (or least possible depth) and raises the basement inside the calderas. Paleozoic rock tops were raised over the entire domain. Under parts of Area 19 and 20 the SCICU was raised 750 m.	• This alternative examines the impact on groundwater flow from the reduction of the thickness of the transmissive units that results from maximizing the elevation of the basement.
Contiguous Imbricate Thrust Sheet (SEPZ)	The SEPZ alternative models the isolated surface exposure of Paleozoic carbonate rocks that are mapped in the southeast corner of the model area, east of the Belted Range thrust fault, as part of a more extensive imbricate fault. The base HFM considers this outcrop as a small erosional remnant of the hanging wall of an imbricate fault.	• This alternative tests the impact of the Paleozoic carbonate rock on the direction of groundwater flow around the east side of Timber Mountain.

Table 2-5
Summary of Alternative HFMs Considered in the Pahute Mesa Flow Model
(Page 2 of 2)

Alternative HFM	Key Difference(s) Compared to Base HFM	Potential Impacts on Flow Model
Deeply Rooted Belted Range Thrust Fault (DRT)	The DRT alternative considers the Belted Range thrust fault to be more deeply rooted than the base HFM resulting in a very thick thrust sheet over most of the model area.	• This alternative results in the LCA not being a continuous, coherent sheet across the model area. The uppermost pre-Tertiary rock immediately downgradient of Pahute Mesa is the nonconductive LCCU1 rather than the conductive LCA.

BA = Benham Aquifer
CFCM = Crater Flat Composite Unit
LCA = Lower Carbonate Aquifer
LCCU1 = Lower Clastic Confining Unit-Thrust Plate
SCICU = Silent Canyon Intrusive Confining Unit
TCA = Tiva Canyon Aquifer
TSA = Topopah Spring Aquifer

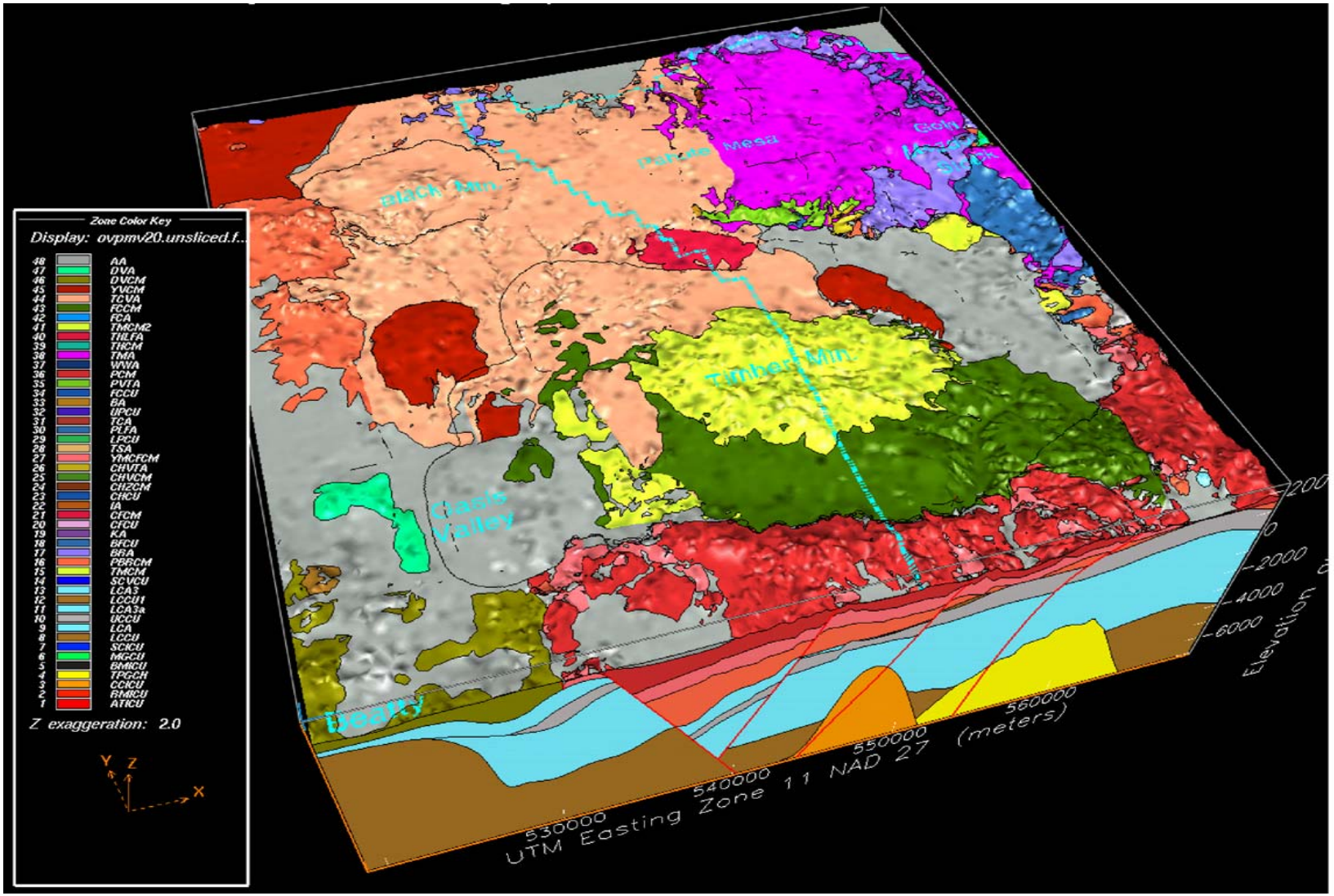

Source: Adapted from SNJV, 2004a

Figure 2-2
Three-Dimensional View of the Base Hydrostratigraphic Model of the Pahute Mesa Area, Top at Land Surface (BN, 2002)

2.2.2.1 Structural Features

The base HFM includes a total of 47 structural elements that are either faults or calderas. Only faults that were considered to be significant were included in the model. These include the larger ones and the ones that seem to form significant structural boundaries. Thus, only faults with significant displacement were included in the model. Six calderas have been identified in the Pahute Mesa model area, two of which are buried. Of particular interest is the SCCC. As stated previously, an alternative scenario was developed to evaluate the effect of caldera shape (see following subsection).

In the base HFM, the SCCC includes two calderas: the Grouse Canyon and Area 20 calderas. The base HFM for the SCCC area also includes 20 faults and structural zones in addition to the caldera-forming faults. Thirteen of these 20 structural features are basin-and-range type faults mapped at the surface.

2.2.2.2 Stratigraphy

As described in Section 2.1.1, the rocks of the NTS have been classified for hydrologic modeling using a two-level classification scheme in which HGUs are grouped to form HSUs (IT, 1996d). New units and additional detail have been added to the basic framework definition, but the systems developed by these early workers remain the best way to understand the groundwater of the NTS region.

Table 2-6 shows the correlation of Pahute Mesa HSUs with HSUs from earlier hydrostratigraphic models for this region. They are listed in approximate order from surface to basement, although some are laterally rather than vertically contiguous, and not all units are present in all parts of the model area.

As can be seen from the information presented in this section, the Pahute Mesa HFM (BN, 2002) includes considerable structural detail and stratigraphic enhancement over the UGTA regional HFM (IT, 1996d). The total number of HSUs increased from 20 to 46; most of the increase affected the Tertiary volcanic section. The six Tertiary volcanic HSUs in the Pahute Mesa and Timber Mountain caldera complex and the single volcanics undifferentiated outside the caldera complex (of the UGTA regional HFM) were subdivided into 40 HSUs for the Pahute Mesa model. Except for geometry details, the five pre-Tertiary HSUs remain as initially defined.

Table 2-6
Correlation of Hydrostratigraphic Units of the Pahute Mesa Base HFM and Earlier Models[a]
(Page 1 of 3)

HSU Layer No.[b]	Hydrostratigraphic Unit	Symbol This Report[b]	Correlation with PM-300 Model[c]	Correlation with UGTA Phase I[d]	Correlation with YMP[e] (Lithostratigraphic Units)
46	Alluvial Aquifer	AA	TMA	AA	QAL, TPAL, TLIM
45	Younger Volcanic Composite Unit	YVCM	NP[f]	VU	B
44	Thirsty Canyon Volcanic Aquifer	TCVA	TMA	TMA, VU	NP
43	Detached Volcanic Aquifer	DVA	NP	VU	
42	Detached Volcanic Composite Unit	DVCM			NR[g]
41	Fortymile Canyon Composite Unit	FCCM	TMA	TMA, VA	NP
40	Fortymile Canyon Aquifer	FCA	NP	VU	
39	Timber Mountain Composite Unit	TMCM	TMCU	TMA	
38	Tannenbaum Hill Lava-Flow Aquifer	THLFA	TMA		
37	Tannenbaum Hill Composite Unit	THCM			
36	Timber Mountain Aquifer	TMA		TMA, VA	UVA
35	Subcaldera Volcanic Confining Unit	SCVCU	Pre-T	BCU	NR
34	Fluorspar Canyon Confining Unit	FCCU	TMA	TMA, VA	NP
33	Windy Wash Aquifer	WWA	WWA	TMA	
32	Paintbrush Composite Unit	PCM	NP	TMA, VA, TC	UVA
31	Paintbrush Vitric-Tuff Aquifer	PVTA	PVTA	TMA, TC, VA	
30	Benham Aquifer	BA	BA	TC	NP
29	Upper Paintbrush Confining Unit	UPCU	UPCU		NR
28	Tiva Canyon Aquifer	TCA	TCA	TMA, TC, VA	UVA
27	Paintbrush Lava-Flow Aquifer	PLFA	PLFA	TC	NP
26	Lower Paintbrush Confining Unit	LPCU	LPCU	TC	NR
25	Topopah Spring Aquifer	TSA	TSA	TC, VA	UVA

Table 2-6
Correlation of Hydrostratigraphic Units of the Pahute Mesa Base HFM and Earlier Models[a]
(Page 2 of 3)

HSU Layer No.[b]	Hydrostratigraphic Unit	Symbol This Report[b]	Correlation with PM-300 Model[c]	Correlation with UGTA Phase I[d]	Correlation with YMP[e] (Lithostratigraphic Units)
24	Yucca Mountain Crater Flat Composite Unit	YMCFCM	NP	VA, VU	UVCU, MVA
23	Calico Hills Vitric-Tuff Aquifer	CHVTA	CHVTA	TC	MVA
22	Calico Hills Vitric Composite Unit	CHVCM	CHVCM		
21	Calico Hills Zeolitic Composite Unit	CHZCM	CHZCM		
20	Calico Hills Confining Unit	CHCU	CHCU	TC	NR
19	Inlet Aquifer	IA	IA	TC, VA	NP
18	Crater Flat Composite Unit	CFCM	CFCM	TC, VU	MVA
17	Crater Flat Confining Unit	CFCU	CFCU		NR
16	Kearsarge Aquifer	KA	KA	TC	NP
15	Bullfrog Confining Unit	BFCU	BFCU	TCB	
14	Belted Range Aquifer	BRA	BRA	TBA	NR
13	Pre-Belted Range Composite Unit	PBRCM	PBRCM	BAQ, BCU	MVCU, LVA, LVCU, LCU
12	Black Mountain Intrusive Confining Unit	BMICU	NP	VU	NP
11	Ammonia Tanks Intrusive Confining Unit	ATICU	TMCM	TMA	
10	Rainier Mesa Intrusive Confining Unit	RMICU			
9	Claim Canyon Intrusive Confining Unit	CCICU	NP	VA	NR
8	Calico Hills Intrusive Confining Unit	CHICU		I	NP
7	Silent Canyon Intrusive Confining Unit	SCICU	PreT	LCCU	
6	Mesozoic Granite Confining Unit	MGCU		I	
5	Lower Carbonate Aquifer-Thrust Plate	LCA3	NP	LCA3	NR
4	Lower Clastic Confining Unit-Thrust Plate	LCCU1	PreT	LCCU1	
3	Upper Clastic Confining Unit	UCCU	NP	UCCU	ECU

Table 2-6
Correlation of Hydrostratigraphic Units of the Pahute Mesa Base HFM and Earlier Models[a]
(Page 3 of 3)

HSU Layer No.[b]	Hydrostratigraphic Unit	Symbol This Report[b]	Correlation with PM-300 Model[c]	Correlation with UGTA Phase I[d]	Correlation with YMP[e] (Lithostratigraphic Units)
2	Lower Carbonate Aquifer	LCA	PreT	LCA	LCA
1	Lower Clastic Confining Unit	LCCU		LCCU	QCU

Source: Modified from SNJV, 2004a

[a]If correlative to more than one HSU, all HSUs are listed.
[b]See BN (2002) and SNJV (2004a) model HSU nomenclature.
[c]See Drellack and Prothro (1997) for explanation of PM-300 HSU nomenclature.
[d]See IT (1996d) for explanation of the UGTA Phase I HSU nomenclature.
[e]See CRWMS M&O (1997 and 2000) for explanation of the YMP lithostratigraphic unit nomenclature.
[f]Not present.
[g]Not recognized as a separate HSU.

2.2.3 Silent Canyon Caldera Complex HFM Alternative

The alternative SCCC model is based on the same HGUs as the base HFM. Despite the considerable differences in basic concepts such as style of caldera formation and number and activity of faults, as well as in scale and level of detail, both models honor the available drill-hole and outcrop data. Differences between the two models relate to the structural model used and the categorizing of HGUs into HSUs. Descriptions of these features are summarized from the HFM report (BN, 2002).

2.2.3.1 Structural Features

The alternative structural model of the SCCC is more simplified than the base HFM. Figure 2-3 shows a comparison of structural features and caldera margins for the base HFM model and the SCCC alternative. This structural model is based on previous models of calderas of the Pahute Mesa region developed by Noble et al. (1968) and Orkild et al. (1969), and analogies with other calderas of the world.

The SCCC HFM includes an elliptical ring-fracture fault system elongated to the north-northeast (Figure 2-3). Major structural differences with the base HFM include the margins of this caldera complex, locations of caldera-forming faults, and the number and depth of the faults considered.

The number of faults is different. The SCCC HFM includes the single caldera ring-fracture system, and only 11 of the basin-and-range faults mapped at the surface. Another difference is that the faults in the SCCC HFM end at shallower depths than in the base HFM.

2.2.3.2 Stratigraphy

Hydrostratigraphic differences between the two models of the SCCC area are the number of HSUs, their definition, and their distribution (BN, 2002).

Whereas in the base HFM, the SCCC area includes 25 HSUs, it includes only 12 in the SCCC alternative model (Table 2-7). Six post-Paintbrush HSUs are lumped together in the alternative model. This simplification may not be important because these units are mostly unsaturated, but other simplifications such as the lumping of the four Calico Hills HSUs may be important (BN, 2002).

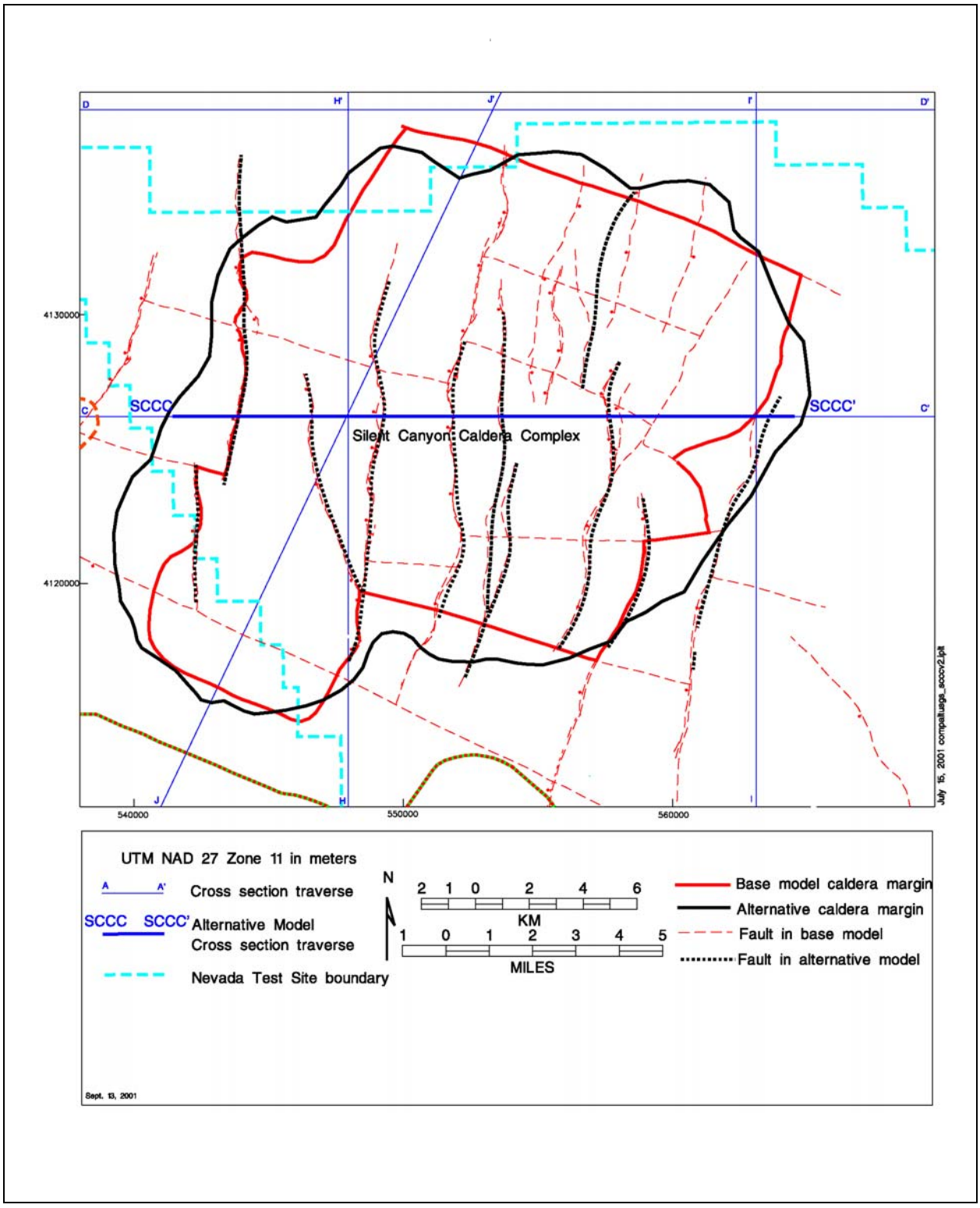

Figure 2-3
Comparison of Silent Canyon Caldera Margins:
Base HFM Model and SCCC Alternative (Modified from BN, 2002)

Table 2-7
Correlation of Hydrostratigraphic Units Between the Silent Canyon Caldera Complex HFM and the Base HFM

UGTA Base Model HSUs	Alternative SCCC Model HSUs
Thirsty Canyon Volcanic Aquifer	Silent Canyon Timber Mountain Composite Unit
Tannenbaum Hill Lava-Flow Aquifer	
Tannenbaum Hill Composite Unit	
Timber Mountain Aquifer	
Fluorspar Canyon Confining Unit	
Windy Wash Aquifer	
Paintbrush Vitric-Tuff Aquifer	
Benham Aquifer	Silent Canyon Benham Aquifer
Upper Paintbrush Confining Unit	
Tiva Canyon Aquifer	Silent Canyon Tiva Canyon Aquifer
Paintbrush Lava-Flow Aquifer	Silent Canyon Lower Paintbrush Confining Unit
Lower Paintbrush Confining Unit	
Topopah Spring Aquifer	Silent Canyon Topopah Spring Aquifer
Calico Hills Vitric-Tuff Aquifer	Silent Canyon Calico Hills Composite Unit
Calico Hills Vitric Composite Unit	
Calico Hills Zeolitic Composite Unit	
Calico Hills Confining Unit	
Inlet Aquifer	Silent Canyon Inlet Aquifer
Crater Flat Composite Unit	Silent Canyon Crater Flat Composite Unit
Crater Flat Confining Unit	
Kearsarge Aquifer	
Bullfrog Confining Unit	Silent Canyon Bullfrog Confining Unit
Belted Range Aquifer	Silent Canyon Belted Range Aquifer
Pre-Belted Range Composite Unit	Silent Canyon Pre-Belted Range Composite Unit
Silent Canyon Intrusive Confining Unit	Silent Canyon Intrusive Confining Unit

Source: Modified from SNJV, 2004a

Note: The HSU names used in the alternative model were modified by adding the prefix "Silent Canyon" for differentiation purposes.

Significant differences also exist in the configuration of the HSU surfaces. The surfaces of the HSUs are less rugged in the SCCC model than in the base HFM. Within the SCCC area, the upper surfaces of HSUs in the SCCC HFM (Figure 2-4) are generally bowl-shaped, and dip more gently than those in the base HFM (Figure 2-5). Upper surfaces of HSUs in the SCCC HFM are also higher along the down-thrown sides of faults, and lower along the up-thrown sides (BN [2002] and McKee et al. [1999 and 2001] show the same section line through the BN HFM).

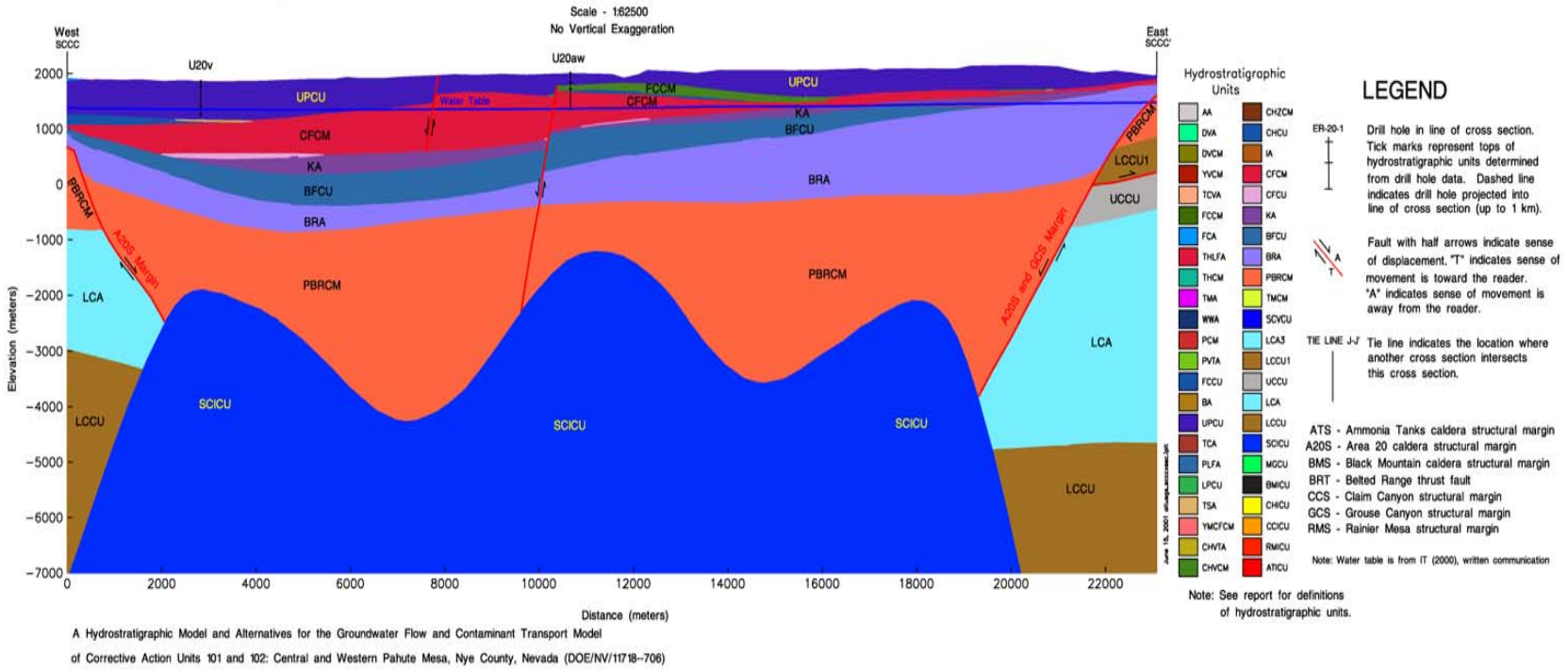

Figure 2-4
Typical West-East Cross Section through the Silent Canyon Caldera for the SCCC Model (BN, 2002)
Cross-section location shown in Figure 2-2.

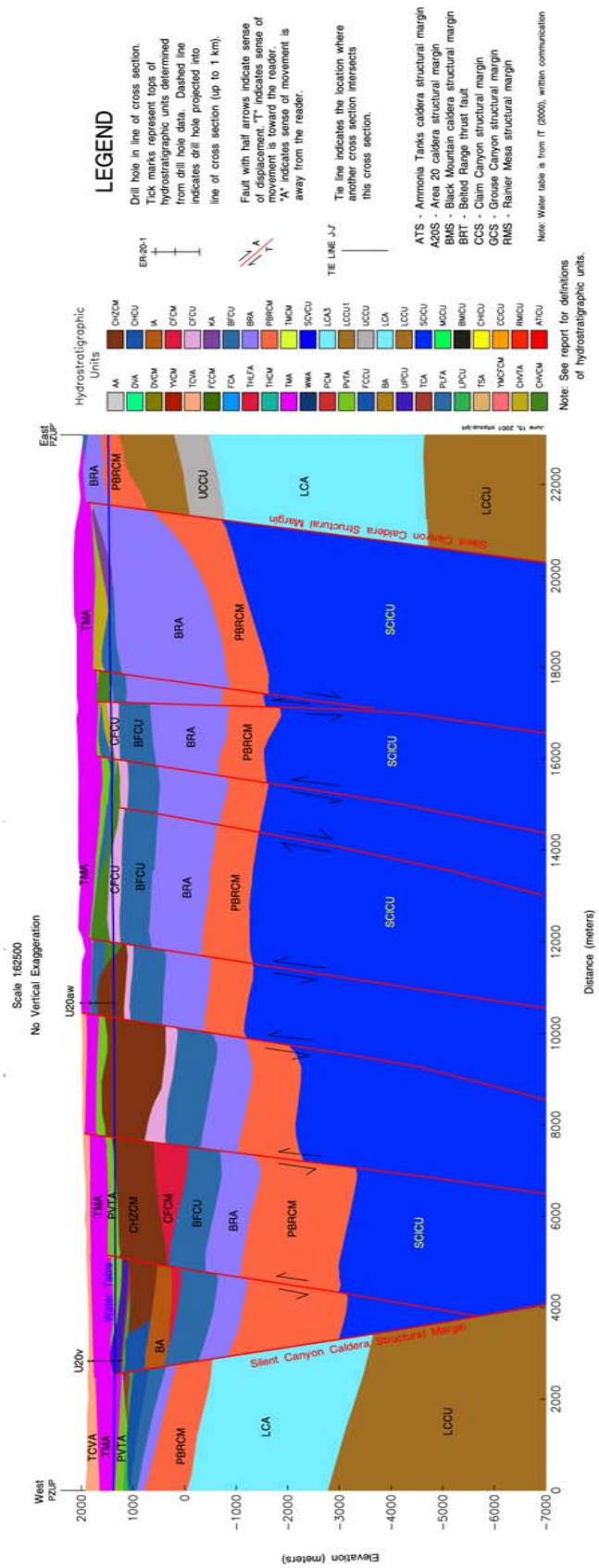

Figure 2-5
Typical West-East Cross Section through the Silent Canyon Caldera for the BN Model (BN, 2002)
Cross-section location shown in Figure 2-2.

The differences in the locations of caldera margins and in structure result in differences in HSU thicknesses. Generally, the thicknesses of HSUs located within the SCCC vary to a greater degree in the base HFM. In comparison, in the SCCC HFM, the HSUs are generally lens-shaped. These lenses are thick in the middle and thin out towards the margins of the SCCC (BN, 2002).

The hydrogeologic importance of the Calico Hills Formation in the SCCC area is recognized in both the base and SCCC HFMs. It is, however, handled differently in the two models. In the base HFM, the Calico Hills Formation is subdivided into four HSUs based on differences in lithologic composition and alteration effects, whereas it is treated as a single composite unit in the SCCC HFM (Table 2-7). A more detailed discussion of the SCCC HFM may be found in the HFM report (BN, 2002).

2.3 Groundwater Characteristics

This section summarizes data, information, and alternative component models that characterize the groundwater budget and general flow directions in the Pahute Mesa flow domain.

2.3.1 Inflow and Outflow (Lateral Boundary Fluxes)

A set of boundary fluxes to be used with the CAU flow model have been developed based on results generated for eight alternate regional-scale flow models using the UGTA regional model (DOE/NV, 1997). The eight models represent combinations of different flow system conceptual models and recharge models. Hydrostratigraphic models reflecting the different conceptual models were chosen from a larger set of conceptual models based on the difference in the flow field (and associated radionuclide transport) they generate. The recharge models represent different methods of approximating recharge for the NTS area (see Section 2.3.2). The alternate flux boundary conditions can be used to help evaluate the uncertainty in the CAU flow model associated with the choice of a flow system conceptual model (and associated HFM) and recharge model. A more detailed discussion of the development of boundary fluxes is provided in SNJV (2004a, Section 9.0). The range in net boundary flux across each of the CAU model boundaries is summarized in Table 2-8. These fluxes are rounded to the nearest 100 m^3/d for presentation. The approach used to calculate these fluxes does not specify the location or locations on the boundary where the flux occurs, just

Table 2-8
Summary of Net Boundary Flux Ranges (m^3/d)

Model Boundary	Range in Net Inflow	Range in Net Outflow
Northern	14,000 to 28,000	100 to 6,700
Southern	200 to 3,500	26,000 to 54,000
Eastern	5,600 to 17,000	300 to 5,000
Western	1,700 to 17,000	2,400 to 17,000

Source: SNJV, 2004a

bounds on the total amount of flow. More specific ranges were developed for the CAU model using the interpolation approach and tools developed by LANL (Gable and Cherry, 2001) (see Section 5.2).

2.3.2 Precipitation and Recharge

The groundwater flow system of the Pahute Mesa area is replenished by areal recharge from precipitation and inflow into the Pahute Mesa area. Inflow is summarized in Section 2.3.1.

In the arid environment of the NTS region, quantification of precipitation recharge is an important aspect of the groundwater flow system. This section provides a summary of precipitation distribution for the NTS area and recharge estimates from this precipitation for six alternative recharge models.

2.3.2.1 Precipitation Distribution

The distribution of mean annual precipitation is shown on Figure 2-6. Figure 2-6 was generated from the precipitation station data only. Table 2-9 summarizes the precipitation stations used in this evaluation. As indicated by Figure 2-6, the precipitation depth increases with increasing land surface elevation and follows the general topography. On the NTS, precipitation ranges from a high of approximately 32.4 centimeters per year (cm/yr) (12.76 inches per year [in./yr]) at the Area 12 Mesa Station to a low of 12.7 cm/yr (5.0 in./yr) at the Well 5B Station.

Table 2-10 compares precipitation totals calculated for hydrographic areas. The total precipitation calculated from the precipitation distribution (column 3) only includes the precipitation within the UGTA groundwater flow system boundary. Any precipitation outside the groundwater flow system boundary is not included in the total for the hydrographic area. Total precipitation from Scott et al.

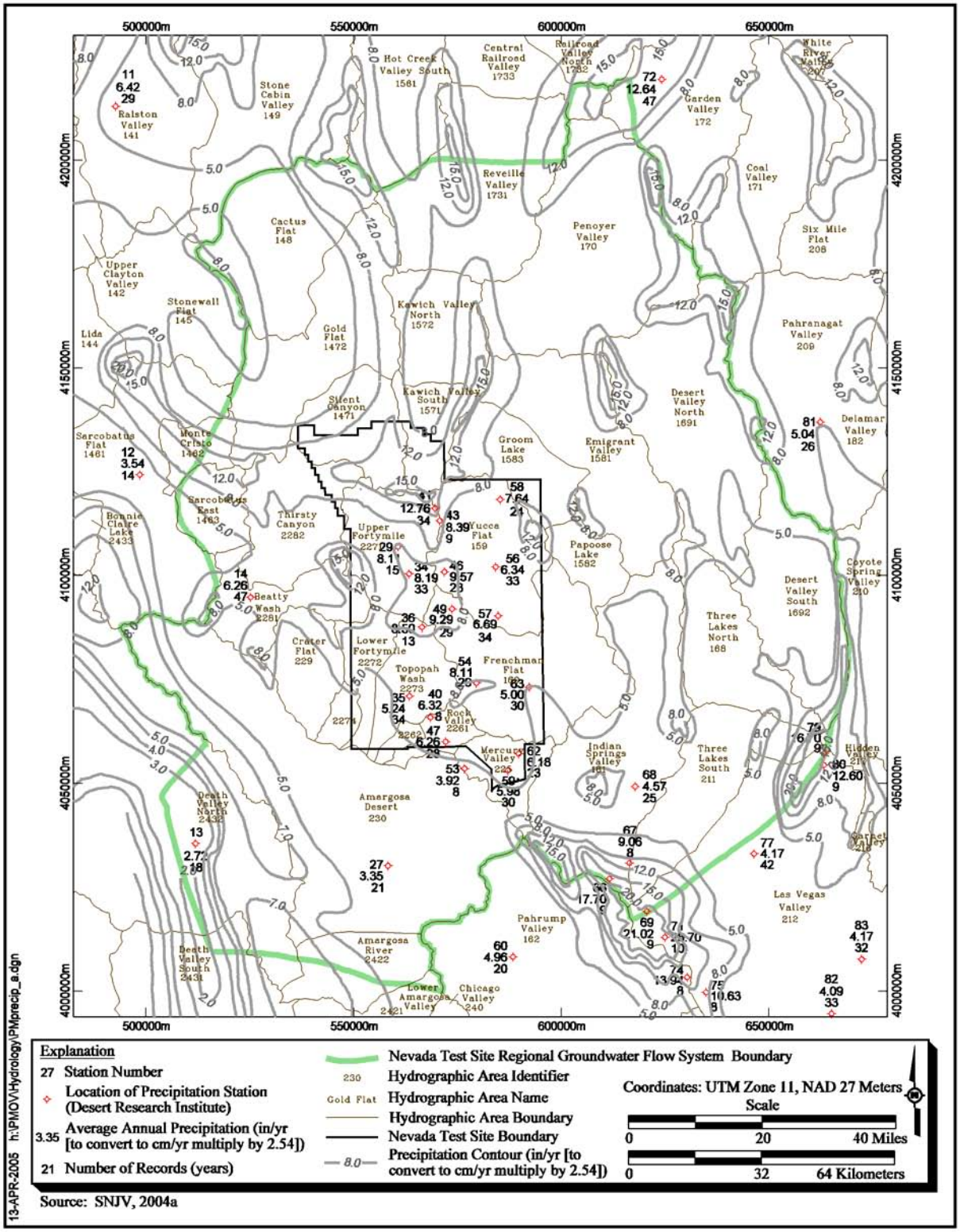

Figure 2-6
Precipitation Map for the Nevada Test Site Region

Table 2-9
Precipitation Station Data
(Page 1 of 2)

Station Number	Station Name	UTM Zone 11, NAD 27		Land Surface Elevation (m)	Average Annual Precipitation	
		Easting (m)	Northing (m)		Depth cm/yr (in./yr)	Years Record
11	Tonopah Airport	492,689	4,213,009	1,655	16.3 (6.42)	29
12	Sarcobatus	498,522	4,124,251	1,225	9.0 (3.54)	14
13	Death Valley	511,946	4,035,517	-52	6.9 (2.72)	18
14	Beatty	525,210	4,094,706	1,082	15.9 (6.26)	47
27	Lathrop Wells	558,275	4,030,159	664	8.5 (3.35)	21
29	Little Feller 2	560,698	4,106,882	1,573	20.6 (8.11)	15
34	40 MN	563,341	4,100,364	1,469	20.8 (8.19)	33
35	4JA	563,445	4,071,032	1,043	13.3 (5.24)	34
36	Shoshone Basin	566,464	4,087,547	1,725	21.6 (8.50)	13
40	Skull Mountain Pass	568,500	4,065,887	1,186	16.1 (6.32)	8
41	Area 12 Mesa	569,624	4,116,171	2,283	32.4 (12.76)	34
43	Stockade Pass	570,759	4,113,178	2,053	21.3 (8.39)	9
46	Tippipah Spring 2	571,887	4,100,851	1,518	24.3 (9.57)	28
47	RV-1	572,151	4,060,050	1,036	15.9 (6.26)	28
49	Mid Valley	573,701	4,091,914	1,420	23.6 (9.29)	29
53	RV-Wash	576,721	4,053,568	866	10.0 (3.92)	8
54	Cane Springs	579,583	4,074,185	1,219	20.6 (8.11)	29
56	BJY	584,209	4,102,022	1,241	16.1 (6.34)	33
57	Yucca	584,791	4,090,231	1,195	17.0 (6.69)	34
58	PHS Farm	585,301	4,118,280	1,391	19.4 (7.64)	24
59	Desert Rock	587,122	4,053,108	1,005	15.2 (5.98)	30
60	Pahrump	588,385	4,008,227	823	12.6 (4.96)	20
62	Mercury	589,740	4,057,169	1,149	15.7 (6.18)	23
63	Well 5B	592,263	4,073,193	939	12.7 (5.00)	30
66	Trough Spring	610,107	4,026,349	2,512	45.0 (17.70)	9
67	Cold Creek	613,563	4,030,708	1,862	23.0 (9.06)	8
68	Indian Springs	617,793	4,049,256	951	11.6 (4.57)	25
69	Lee Canyon	619,087	4,018,516	2,594	53.4 (21.02)	9
71	Kyle Canyon	623,466	4,012,260	2,365	67.8 (26.70)	10
72	Adaven	624,188	4,219,501	1,905	32.1 (12.64)	47
74	Roberts Ranch	627,418	4,003,163	1,862	35.4 (13.94)	8
75	Red Rock Summit	631,972	3,999,532	1,984	27.0 (10.63)	8
79	Hayford Peak	660,932	4,058,248	2,999	42.4 (16.70)	9

Table 2-9
Precipitation Station Data
(Page 2 of 2)

Station Number	Station Name	UTM Zone 11, NAD 27		Land Surface Elevation (m)	Average Annual Precipitation	
		Easting (m)	Northing (m)		Depth cm/yr (in./yr)	Years Record
80	Hidden Forest	660,934	4,055,504	2,304	32.0 (12.60)	9
81	Alamo	662,347	4,136,921	1,049	12.8 (5.04)	26
82	Las Vegas Airport	665,072	3,994,546	661	10.4 (4.09)	33
83	Sunrise Manor	672,321	4,007,633	555	10.6 (4.17)	32

Source: SNJV, 2004a

(1971) is included in the table for comparison (columns 4 and 5). The footnoted totals in column 4 were prorated based on the area within the flow system boundary using the following equation: (published precipitation total) x ([area within flow system boundary] ÷ [total area of hydrographic area]).

In general, the comparison between the calculated precipitation and published precipitation is reasonably good; the difference between the two totals is 118,343 m^3/d. For each, the maximum precipitation is found in the Tikaboo and Emigrant Valley hydrographic areas. The precipitation totals for those hydrographic areas including testing areas (Gold Flat, Yucca Flat, and Frenchman Flat) are similar to the published data. The hydrographic areas with the largest discrepancy between totals are the Las Vegas Valley and Amargosa Desert. These hydrographic areas lend very little, if any, recharge to the UGTA groundwater flow system and should not affect the modeling results.

2.3.2.2 Alternative Recharge Models

Three basic approaches have been used to develop alternative recharge models for the NTS area (including the Pahute Mesa flow model area). These are:

- Maxey-Eakin estimation techniques
- Net infiltration-recharge distributed parameter modeling
- Chloride mass-balance modeling

Table 2-10
Comparison of Calculated Precipitation Volumes to Published Values by Hydrographic Area
(Page 1 of 2)

Hydrographic Area		Total Precipitation Calculated from Distribution (m^3/d)	Published Precipitation Data (Scott et al., 1971)	
Hydrographic Area No.	Hydrographic Area Name		Total Precipitation within Flow System (m^3/d)	Total Precipitation in Hydrographic Area (m^3/d)
145	Stonewall Flat	2,546	4,878	371,737
146	Sarcobatus Flat	202,290	311,556	642,091
147	Gold Flat	889,195	844,856	844,856
148	Cactus Flat	491,956	439,325	439,325
149	Stone Cabin Valley	1,471	2,402	1,182,799
156	Hot Creek Valley	1,846	2,544	1,317,976
157	Kawich Valley	622,296	506,914	506,914
158	Emigrant Valley	1,164,236	959,757	959,757
159	Yucca Flat	461,941	337,942	337,942
160	Frenchman Flat	511,223	506,914	506,914
161	Indian Springs Valley	728,691	912,445	912,445
162	Pahrump Valley	1,531	5,397	1,419,358
168	Three Lakes Valley North	276,120	371,737	371,737
169	Tikaboo Valley	1,260,641	1,284,181	1,284,181
170	Penoyer Valley	1,127,129	912,445	912,445
171	Coal Valley	835	1,249	574,502
172	Garden Valley	68,283	115,092	777,268
173	Railroad Valley South	681,245	844,856	844,856
209	Pahranagat Valley	1,446	3,564	912,445
210	Coyote Spring Valley	13,005	18,106	743,473
211	Three Lakes Valley South	359,289	439,325	439,325
212	Las Vegas Valley	248,265	613,223	2,230,420
225	Mercury Valley	104,576	128,418	128,418
226	Rock Valley	85,759	87,865	87,865
227	Fortymile Canyon	715,443	669,126	669,126
228	Oasis Valley	660,013	506,914	506,914
229	Crater Flat	153,895	206,145	206,145
230	Amargosa Desert	1,131,415	811,062	811,062

Table 2-10
Comparison of Calculated Precipitation Volumes to Published Values by Hydrographic Area
(Page 2 of 2)

Hydrographic Area		Total Precipitation Calculated from Distribution (m^3/d)	Published Precipitation Data (Scott et al., 1971)	
Hydrographic Area No.	Hydrographic Area Name		Total Precipitation within Flow System (m^3/d)	Total Precipitation in Hydrographic Area (m^3/d)
242	Amargosa River	117,067	117,067[a]	--
243	Death Valley	398,318	398,318[a]	--
	Total Precipitation:	**12,481,966**	**12,363,623**	--

Source: SNJV, 2004a

[a]Calculated hydrographic area total is included in published precipitation total. Published data for this hydrographic area are not available at time of printing.

The Maxey-Eakin approach is an empirically-derived method relating recharge to precipitation zones from a base precipitation map. Several modified versions of this approach are analyzed, including a model from the UGTA regional groundwater flow modeling results and a revised Maxey-Eakin model using a revised base precipitation map.

Maxey and Eakin (1949) first described a method of estimating recharge to groundwater from precipitation in a report on groundwater in White River Valley, Nevada. In this method recharge is estimated from precipitation by assuming that a set percentage of precipitation recharge occurs for specific ranges of precipitation. The initial percentages (Maxey-Eakin coefficients) were: 0 percent recharge for precipitation less than 20.3 centimeters (cm); 3 percent recharge when precipitation ranges between 20.3 to 30.5 cm; 7 percent recharge when precipitation ranges between 30.5 to 38 cm; 15 percent recharge when precipitation ranges between 38 to 50.8 cm; and 25 percent recharge when precipitation is greater than 50.8 cm. These Maxey-Eakin coefficients were determined by trial and error by balancing of recharge with estimates of groundwater discharge for 13 valleys in east-central Nevada (Maxey and Eakin, 1949).

The recharge distribution used in the UGTA regional groundwater flow model (DOE/NV, 1997) was constructed using a modification of the Maxey-Eakin method (1949). This modification incorporated:

- An updated precipitation map using new and existing data
- The calculation of recharge using modified Maxey-Eakin coefficients
- The calculation of total recharge volumes for individual hydrographic areas
- The redistribution of a percentage of the total recharge within selected subareas to stream channels

Figure 2-7 shows the Maxey-Eakin recharge distribution for the UGTA Regional Model. This recharge distribution model is designated as the UGTA Regional Model recharge alternative (SNJV, 2004a).

Subsequent to the development of the UGTA regional flow model (DOE/NV, 1997) a revised recharge distribution was generated for the NTS area by updating the original UGTA recharge model. The update included the redigitization and recontouring of the precipitation map, and the redigitization of the hydrographic areas using larger-scale maps. Following the update, a comparison to other recharge models was conducted. This updated recharge distribution model is designated as the UGTA Revised Maxey-Eakin recharge alternative. Figure 2-8 shows the UGTA Revised Maxey-Eakin recharge distribution in the NTS area.

Two alternative recharge models are taken from the USGS net infiltration/recharge model (Hevesi et al., 2003). The USGS net infiltration/recharge model is a distributed parameter watershed model to estimate temporal and spacial distribution of net infiltration for the Death Valley region. The major components of this model include infiltration of rain, snowmelt, or surface water into the soil or bedrock, with subsequent bare-soil evaporation and transpiration from the root zone. All water percolating past the root zone is considered net infiltration. The two alternative USGS recharge models include the recharge model that includes a runoff/run-on component (USGSD) and the recharge model that does not include the runoff/run-on component (USGSND). Figures 2-9 and 2-10 show the recharge distribution for these two alternative models.

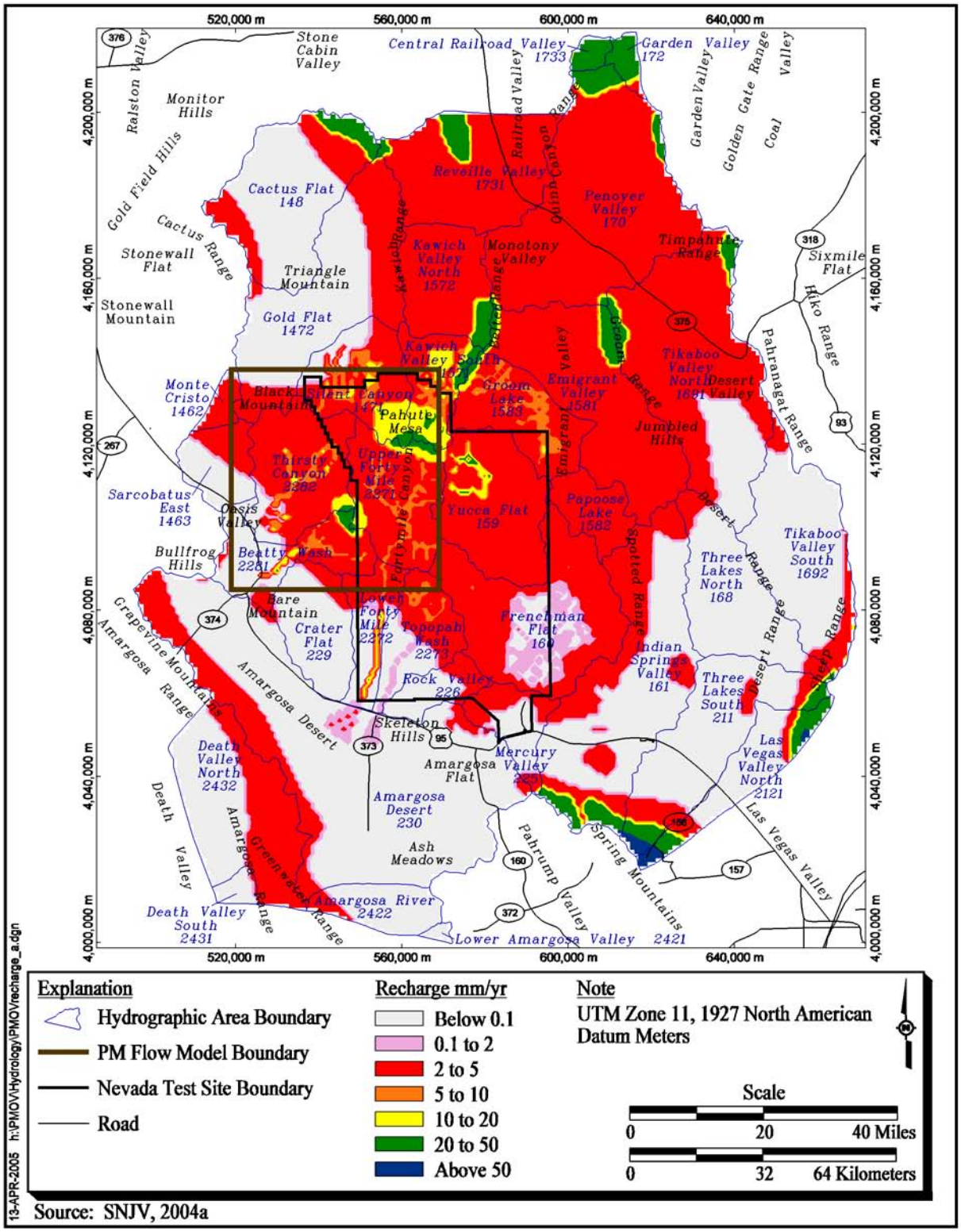

Figure 2-7
UGTA Regional Model Recharge Distribution

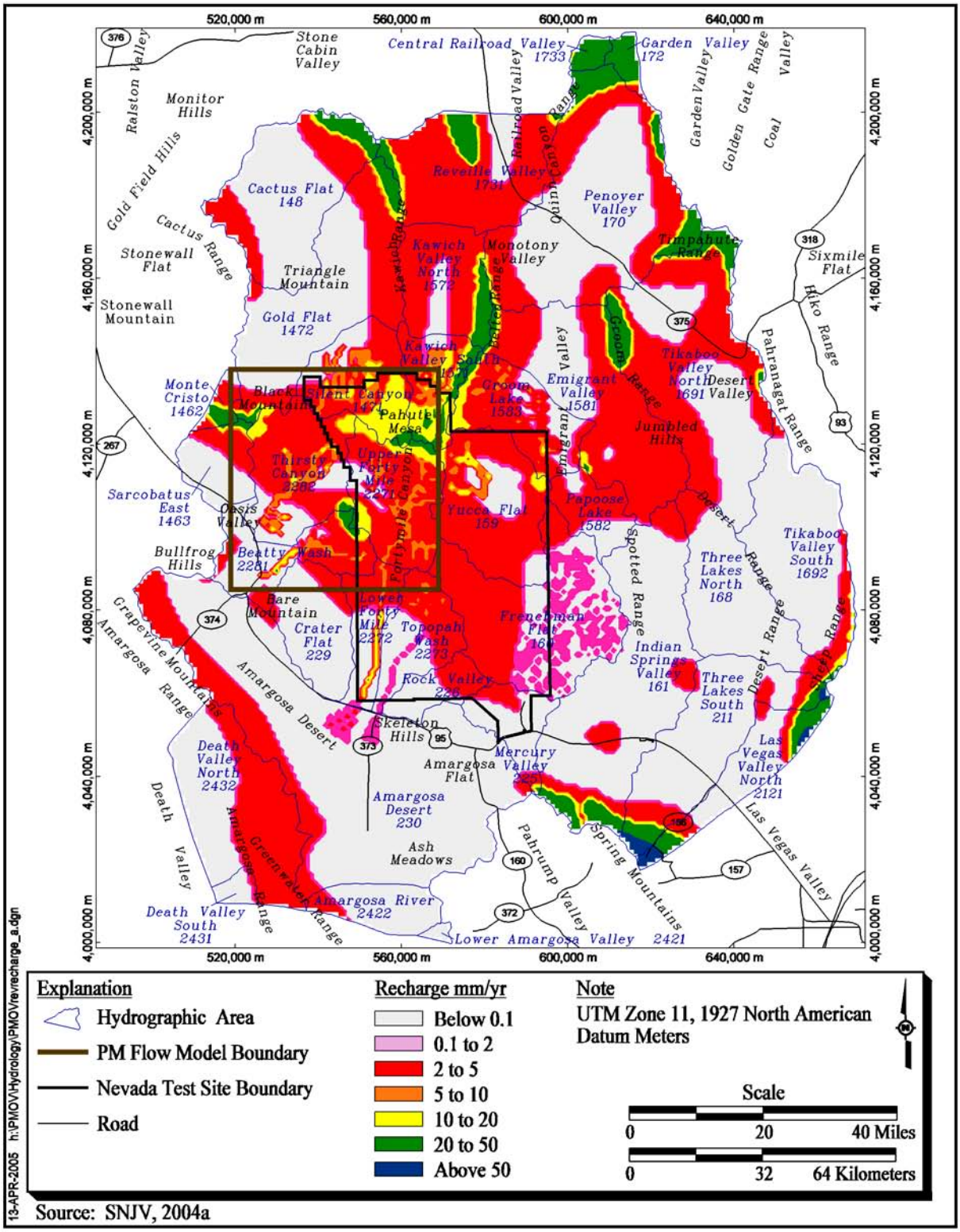

Figure 2-8
UGTA Revised Maxey-Eakin Recharge Distribution in the NTS Region

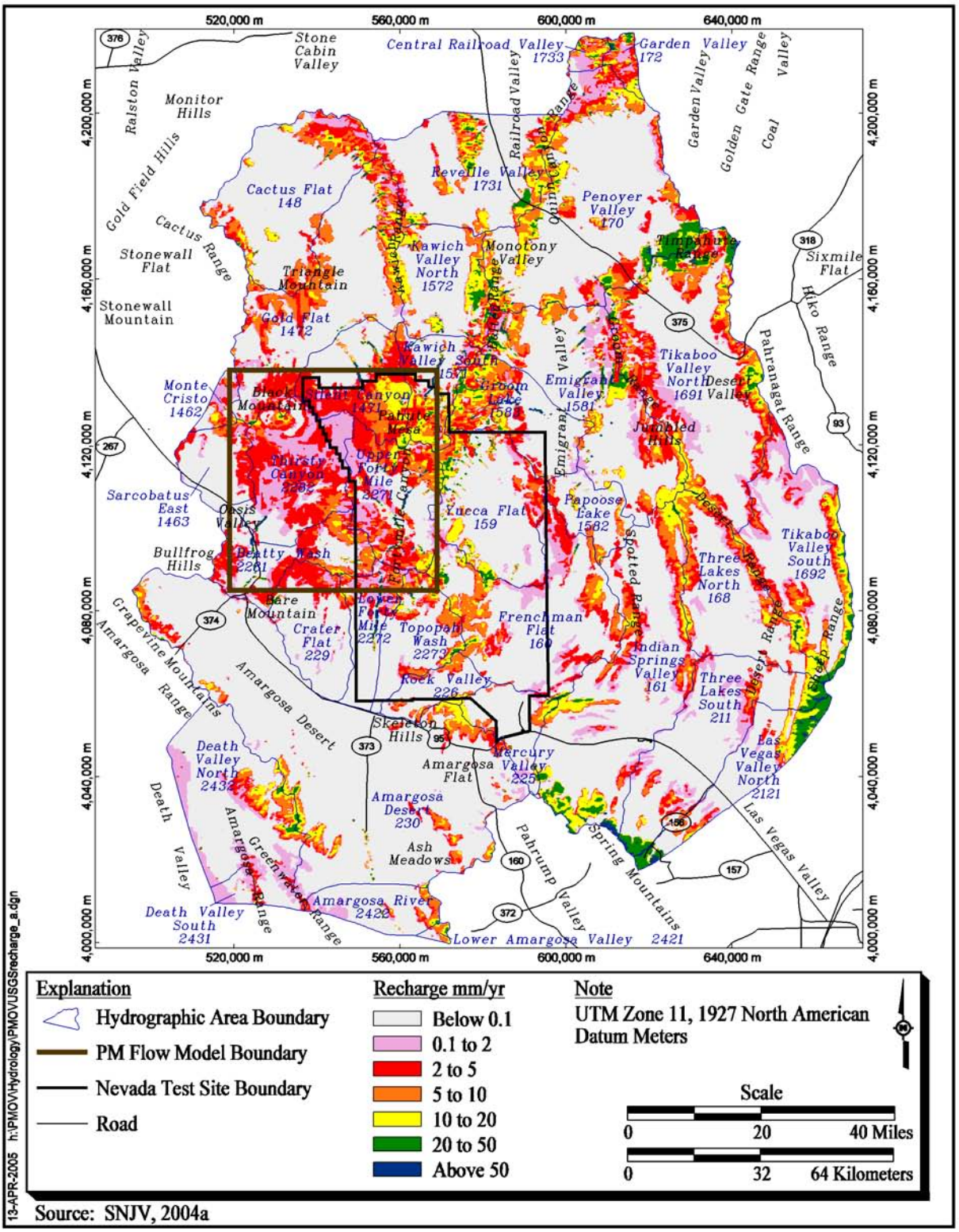

Figure 2-9
USGS Recharge Distribution Model (USGSD), Overland Flow Component Included

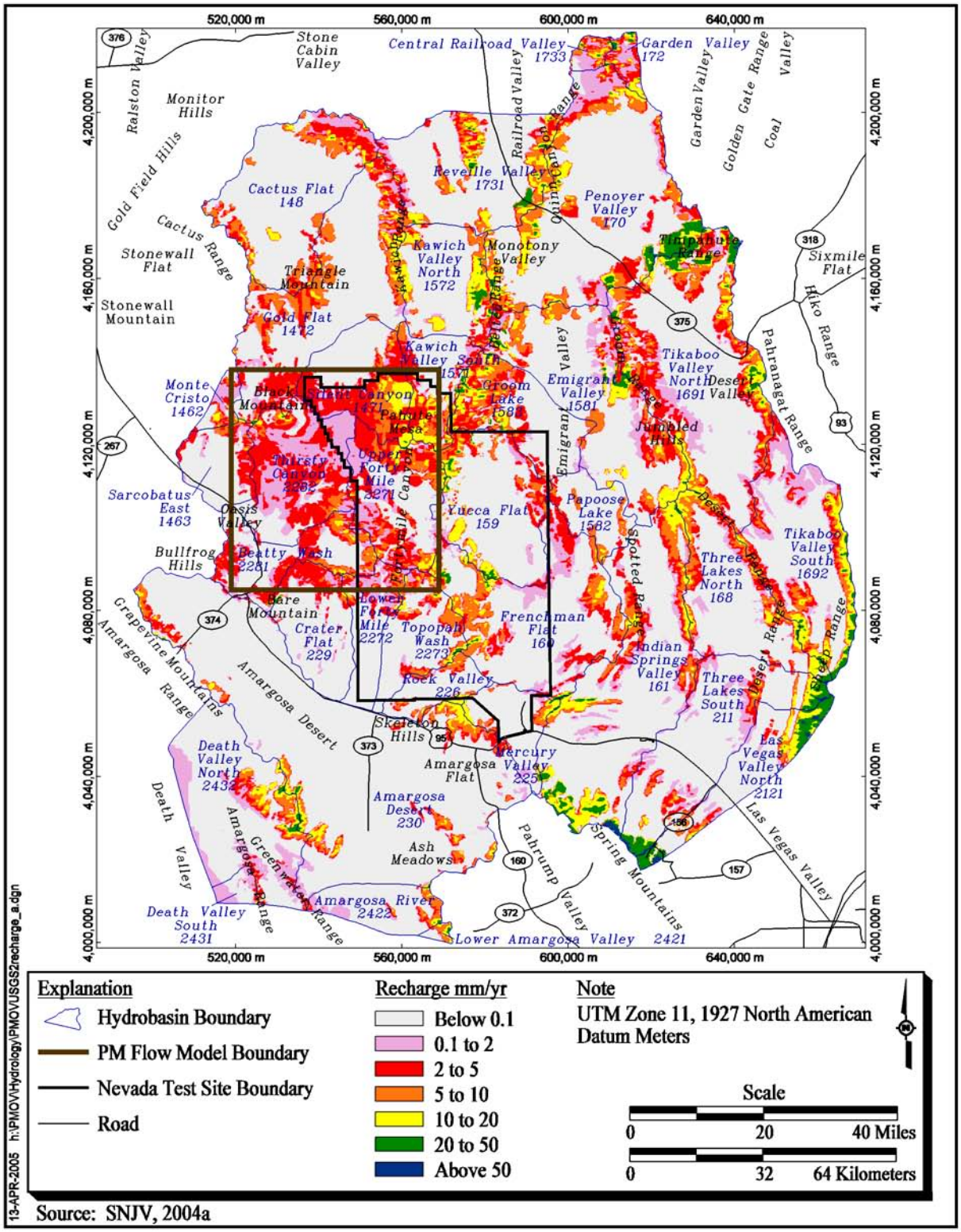

Figure 2-10
USGS Recharge Distribution Model (USGSND), No Overland Flow Component

Two alternative recharge models have been developed by DRI for the NTS area using an elevation-dependent chloride mass-balance approach (Russell and Minor, 2002). The DRI chloride mass-balance approach estimates recharge by analyzing the chloride ratios of precipitation and groundwater. Higher chloride concentrations in groundwater discharged from springs result from ET of precipitation that contains low amounts of conservative atmospheric chloride ion, thus providing a relative gauge of recharge. This information, in conjunction with soil chloride profiles in differing recharge locales (wash versus non-wash), allowed DRI to estimate recharge and associated confidence intervals. The alternative recharge models included one model for no recharge in the alluvial areas (DRI alluvial mask alternative) and one model for no recharge in the alluvial areas and no recharge below an elevation of 1,237 m (DRI alluvial and elevation mask alternative). The data for each model were compiled in a geographic information system and used in a Monte Carlo analysis to determine recharge in the study area. Results of the analysis yielded estimates of the mean and standard deviation of recharge. The resultant recharge distributions for the entire UGTA regional model area for the alluvial mask alternative 50th percentile is shown in Figure 2-11. The recharge distribution for the alluvial and elevation mask, alternative 50th percentile distribution is shown in Figure 2-12 (SNJV, 2004a).

Comparison of recharge volumes in the NTS area for all alternative recharge models are summarized in Table 2-11. The recharge volumes for both UGTA-based recharge distributions differ from the original values found in the UGTA regional flow model report (DOE/NV, 1997) because of the changes to the definitions of the hydrographic areas. The UGTA Revised Maxey-Eakin recharge distribution model was chosen as the base recharge model for use in groundwater flow modeling because, in general, the method yields recharge volumes that are within the ranges of the other models. The other alternative recharge models are incorporated into the Pahute Mesa flow model to evaluate uncertainty associated with recharge.

2.4 Surface Groundwater Discharge

Within the Pahute Mesa area and vicinity, most groundwater discharge to the surface occurs naturally in the form of ET and springs at the Oasis Valley discharge area. Some groundwater is also withdrawn from the flow system by wells. The area of interest to this activity includes the Pahute Mesa area and all of the Oasis Valley hydrographic area because the discharge area extends outside of

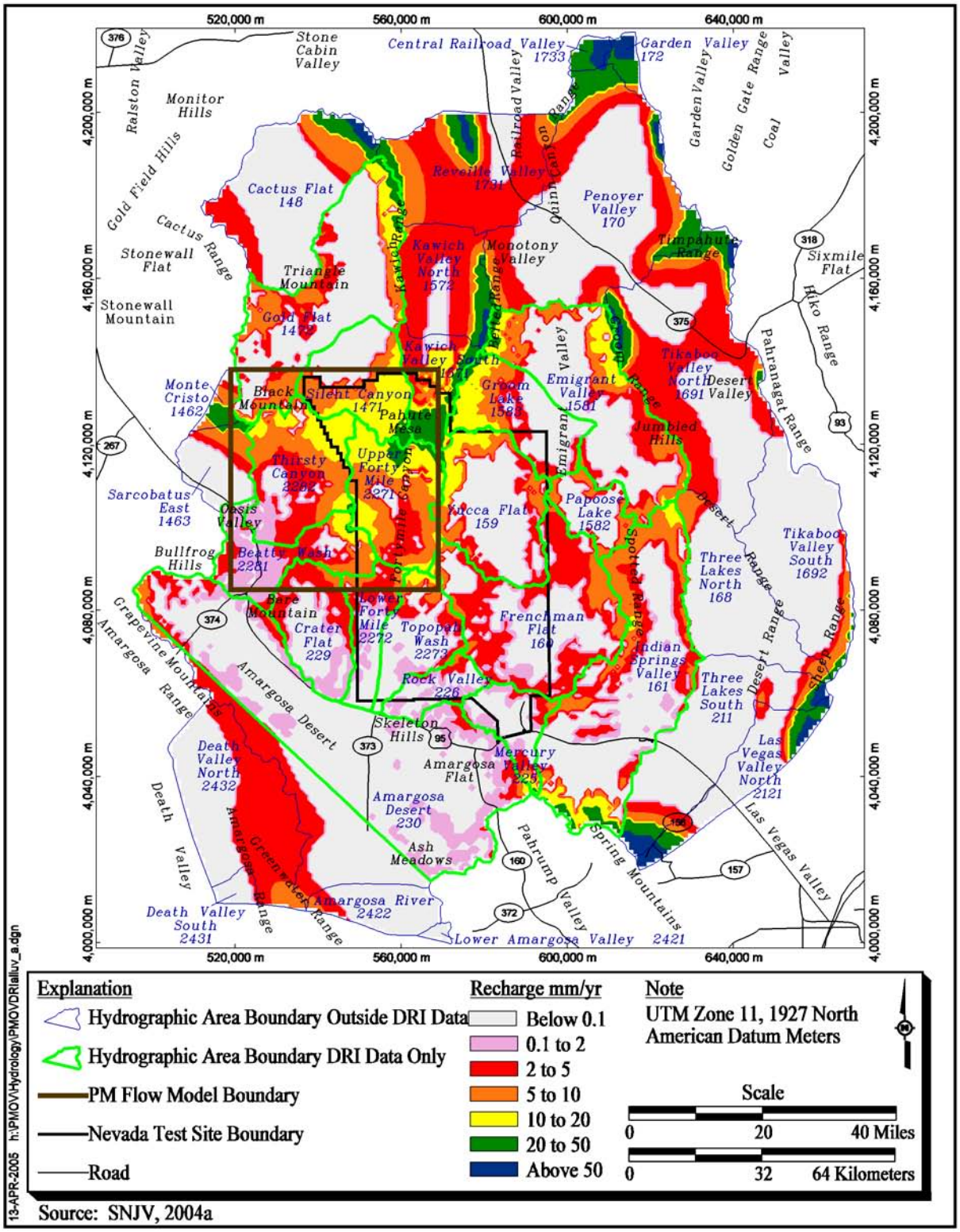

Figure 2-11
DRI Recharge Distribution with Alluvial Mask
(Russell and Minor, 2002)

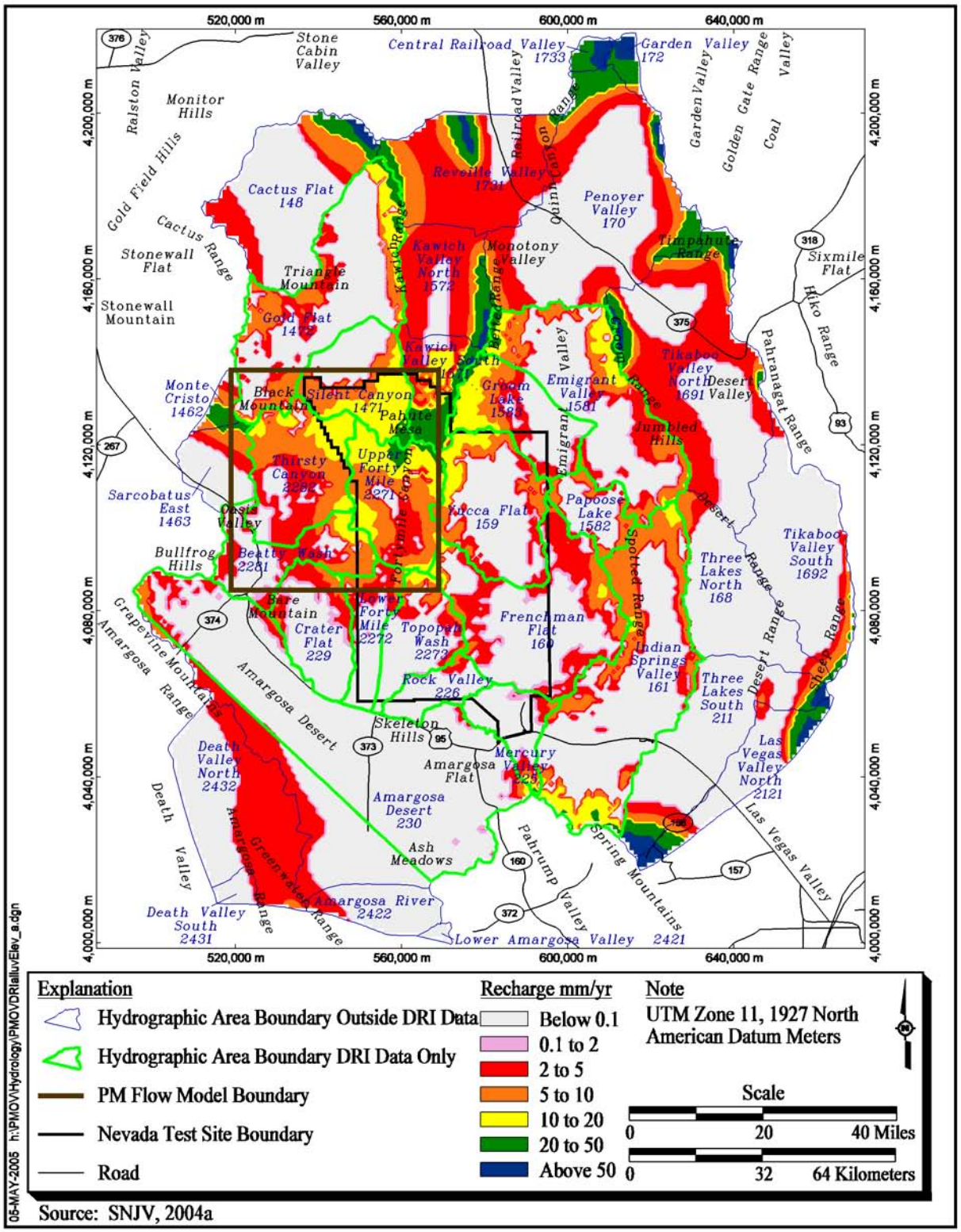

Figure 2-12
DRI Recharge Distribution with Alluvial and Elevation Mask (Russell and Minor, 2002)

Table 2-11
Recharge Volumes for Hydrographic Areas for all Recharge Models
(Page 1 of 2)

Subarea Number	Area Name	Secondary Name	UGTA	UGTA	USGS	USGS	DRI-Alluvial Mask Only			DRI-Alluvial and Elevation Mask		
			Regional Model Phase I (m^3/yr)	Revised Maxey-Eakin Based (m^3/yr)	Model 1 (m^3/yr)	Model 2 (m^3/yr)	5% (m^3/yr)	50% (m^3/yr)	95% (m^3/yr)	5% (m^3/yr)	50% (m^3/yr)	95% (m^3/yr)
1462	Sarcobatus Flat-2	Monte Cristo	324,700	794,500	162,400	153,300		1,277,000			1,196,000	
1463	Sarcobatus Flat-3	Sarcobatus East	420,300	568,900	297,400	280,800		922,300			861,700	
1471	Gold Flat-1 & 2	Silent Canyon	4,739,000	6,389,000	5,269,000	4,052,000	3,889,000	8,350,000	12,810,000	3,889,000	8,350,000	12,810,000
148	Cactus Flat		3,147,000	3,304,000	1,653,000	1,326,000		4,814,000			4,643,000	
1571	Kawich Valley-1 & 2	Kawich Valley South	6,952,000	7,456,000	4,372,000	2,923,000	2,063,000	5,176,000	8,289,000	2,063,000	5,176,000	8,289,000
1582	Emigrant Valley-2	Papoose Lake	887,800	466,900	412,600	305,300	352,800	552,800	752,700	352,800	552,800	752,700
1581	Emigrant Valley-1 & 3[a]	Emigrant Valley	7,891,000	5,982,000	6,897,000	4,510,000	3,805,000	7,375,000	10,950,000	3,805,000	7,375,000	10,950,000
159	Yucca Flat		2,589,000	2,040,000	1,950,000	1,508,000	1,467,000	2,465,000	3,463,000	1,459,000	2,456,000	3,453,000
160	Frenchman Flat		2,542,000	1,466,000	2,340,000	2,183,000	1,560,000	2,506,000	3,452,000	1,404,000	2,224,000	3,044,000
161	Indian Springs Valley		4,741,000	3,655,000	4,376,000	4,210,000	2,842,000	5,013,000	7,184,000	2,610,000	4,772,000	6,934,000
168	Three Lakes Valley North		300,600	319,000	1,824,000	1,819,000		521,900			486,400	
1691	Tikaboo Valley-1	Tikaboo Valley North	5,997,000	6,452,000	4,595,000	4,241,000		8,182,000			8,254,000	
1692	Tikaboo Valley-2	Tikaboo Valley South	606,700	760,400	2,401,000	2,402,000		1,224,000			1,146,000	
170	Penoyer Valley		8,382,000	6,487,000	6,289,000	5,175,000		8,213,000			8,291,000	
172	Garden Valley		1,859,000	2,476,000	587,500	478,600		3,731,000			3,562,000	
1731	Railroad Valley South-1	Reveille Valley	5,416,000	5,464,000	2,696,000	2,266,000		7,253,000			7,207,000	
1733	Railroad Valley South-3	Central Railroad Valley	1,914,000	1,920,000	373,500	290,000		2,957,000			2,805,000	

Table 2-11
Recharge Volumes for Hydrographic Areas for all Recharge Models
(Page 2 of 2)

Subarea Number	Area Name	Secondary Name	UGTA	UGTA	USGS	USGS	DRI-Alluvial Mask Only			DRI-Alluvial and Elevation Mask		
			Regional Model Phase I (m^3/yr)	Revised Maxey-Eakin Based (m^3/yr)	Model 1 (m^3/yr)	Model 2 (m^3/yr)	5% (m^3/yr)	50% (m^3/yr)	95% (m^3/yr)	5% (m^3/yr)	50% (m^3/yr)	95% (m^3/yr)
211	Three Lakes Valley South		4,221,000	4,220,000	2,143,000	2,117,000		5,916,000			5,775,000	
2121	Las Vegas Valley-1		5,063,000	5,083,000	2,412,000	2,382,000		6,863,000			6,781,000	
225	Mercury Valley		424,800	229,300	475,000	446,400	307,600	480,600	653,700	236,500	370,700	504,900
226	Rock Valley		176,700	239,200	385,200	374,600	103,300	193,200	283,000	58,500	94,940	131,400
2271	Fortymile Canyon-1	Upper Fortymile	3,477,000	3,679,000	2,545,000	1,709,000	3,241,000	5,951,000	8,662,000	3,241,000	5,951,000	8,662,000
2272	Fortymile Canyon-2 & 3	Lower Fortymile	1,129,300	1,018,800	1,932,900	1,146,300	916,000	1,426,000	1,936,000	832,700	1,303,000	1,772,000
2281	Oasis Valley-1 & 2	Beatty Wash	4,022,000	4,138,000	3,041,000	2,380,800	3,866,000	6,149,000	8,432,000	3,642,000	5,860,000	8,078,000
229	Crater Flat		179,800	187,800	347,500	327,500	395,500	661,400	927,300	335,400	540,300	745,200
230	Amargosa Desert		1,457,000	1,456,000	1,893,000	1,730,000		2,548,000			1,958,000	
2421	Amargosa River-1	Lower Amargosa Valley	0	0	17,920	17,600		0			0	
2422	Amargosa River-2	Amargosa River	105,000	103,700	279,900	257,300		171,000			159,000	
2431	Death Valley Central-1	Death Valley South	15,870	23,980	41,670	37,180		39,670			36,850	
2432	Death Valley Central-2	Death Valley North	1,348,000	1,559,000	1,216,000	1,195,000		2,435,000			2,300,000	

Source: SNJV, 2004a

[a]The reported recharge volume is only for the Emigrant Valley-3 basin.

m^3/yr = Cubic meters per year

the Pahute Mesa CAU area boundary. A more detailed discussion of the evaluation of surface groundwater discharge is provided in SNJV (2004a, Section 7.0).

2.4.1 Natural Discharge

Natural discharge to the surface from the Pahute Mesa area and vicinity occurs in the form of springs and ET in the Oasis Valley discharge area. However, because of the processes involved, these two forms of discharge are not independent. In Oasis Valley, most groundwater discharged from springs does not leave the valley by surface flow. Surface water flow out of the valley occurs mostly through the Amargosa River on an intermittent basis. Spring water either re-infiltrates into the flow system or evaporates. Thus, the majority of the groundwater discharged by springs is effectively lost from the groundwater system through ET within the discharge area. In addition, ET estimates include water that moves up from the underlying regional flow system into the shallow flow system. Total spring discharge could provide a lower bound for ET estimates; however, spring flow rates are difficult to measure at the numerous seeps and at spring locations that are inaccessible. The net natural groundwater discharge to the surface is, therefore, best approximated by an estimate of ET.

2.4.2 Evapotranspiration Summary

Figure 2-13 and Table 2-12 summarize the locations and descriptions of Oasis Valley springs. Two reports provide the basis for estimates of natural discharge to the surface in the Pahute Mesa flow model area. Reiner et al. (2002) documents a comprehensive study on groundwater discharge in Oasis Valley. This study estimated groundwater discharge by quantifying ET, estimating subsurface outflow, and compiling groundwater withdrawal data. Laczniak et al. (2001) documents estimates of annual ET from discharge areas located within the Death Valley flow system, including Oasis Valley. The estimates of mean annual Oasis Valley ET from these two studies are slightly different due to differences in data interpretation. These studies are discussed in detail in SNJV (2004a, Section 7.5) and summarized below.

Evapotranspiration rates and volumes as derived by Reiner et al. (2002) and Laczniak et al. (2001) were determined for 10 different ET units in the Oasis Valley discharge area. Table 2-13 identifies these ET units. Table 2-14 compares the estimated mean annual ET for these Oasis Valley ET units from these two studies.

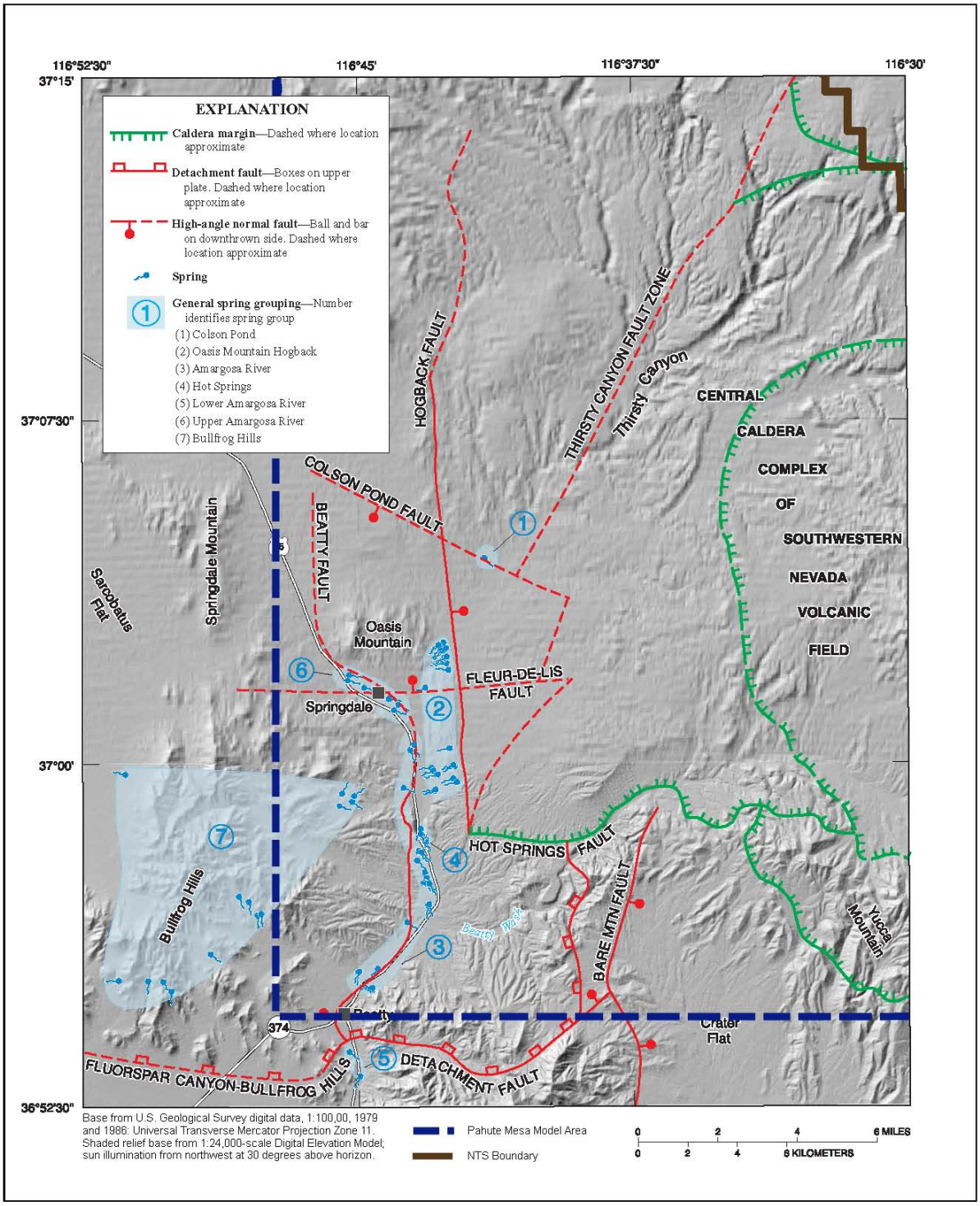

Figure 2-13
General Spring Locations and Major Structural Features Controlling Spring Discharge in Oasis Valley, NV (Modified from Reiner et al., 2002)

Table 2-12
Description of Springs Occurring in Oasis Valley

Group Number	Group Name	Probable Cause	Source
1	Colson Pond Group	Transmissivity change across the Colson Pond Fault	Likely fed by groundwater flowing from the north and northeast
2	Oasis Mountain Hogback Group	Abrupt westward thinning of the welded-tuff aquifer across the Hogback Fault	Likely fed by groundwater flowing from Pahute Mesa
3	Amargosa River Group	Transmissivity change and disruption in aquifer continuity across the Beatty Fault	Likely fed by a mixture of the groundwater flowing into Oasis Valley from the east, west, and north
4	Hot Springs Group	Upward flow along the fault (elevated water temperatures [about 105°F])	Likely fed by groundwater flow from the east and north, possibly Timber Mountain and/or Pahute Mesa
5	Lower Amargosa River Group	--	Probably fed primarily by groundwater flowing from the north through Oasis Valley
6	Upper Amargosa River Group	Transmissivity change and disruption in aquifer continuity across the Beatty Fault	Likely fed by groundwater inflow from the north and northwest (White, 1979)
7	Bullfrog Hills Group	Permeability changes within the welded-tuff aquifer caused by hydrothermal alteration	Likely fed by local recharge to nearby highlands and therefore perched

Source: SNJV, 2004a

See Figure 2-13 for locations.

In addition to mean annual ET, Laczniak et al. (2001) assessed uncertainty in annual ET using Monte Carlo simulations. Table 2-15 provides the summary statistics from this uncertainty analysis. Section 5.2 documents how these data were used in the Pahute Mesa flow model calibration.

2.4.3 Well Discharge

Wells of interest to this activity are only those that were pumped or have been pumping for longer than a year. Discharge data collected during short-term pumping such as during well testing were not included. The locations of pumping wells located within the Pahute Mesa modeling area and vicinity are shown in Figure 2-14. These include nine NTS water supply wells, one Beatty water supply well, and two mine wells (Gexa Well 4 and nearby PW-2). Well PW-2 is located within 500 m of Gexa Well 4 and was used as a substitute pumping well for Gexa Well 4 during 1997 and 1998.

Table 2-13
ET Units Determined from Spectral Analysis of Satellite Imagery Data (June 13, 1992), Oasis Valley Discharge Area, Nevada
(Page 1 of 2)

Laczniak et al. (2001)			Reiner et al. (2002)		
ET-Unit Number	**ET-Unit Area (m^2)**	**General Description of ET Unit**	**ET-Unit Identifier**	**ET-Unit Area (m^2)**	**General Description of ET Unit**
0	0	Area of no significant ET from groundwater source (unclassified); water table typically greater than 50 ft below land surface	UCL	0	Area of no substantial ET from ground-water source (unclassified); water table typically greater than 20 ft below land surface; soil very dry
1	4,047	Area of open water, primarily reservoir or large spring pool	OWB	4,047	Area of open water, primarily spring pool or pond
2	20,234	Area of submerged aquatic vegetation; includes sparse emergent vegetation and shallow part of open water areas; perennially loaded; water at surface	SAV	16,187	Area of submerged and sparse emergent aquatic vegetation; includes primarily shallow part of open water areas; perennially flooded; water at surface
3	161,874	Area dominated by dense wetland vegetation, primarily tall reedy and rushy marsh plants, typically tule, cattail, or giant reed; perennially flooded; water at surface	DWV	161,874	Area dominated by dense wetland vegetation, primarily tall reedy and rushy marsh plants, typically tule, cattail, or giant reed; perennially flooded; water at surface
4	3,767,627	Area dominated by dense meadow and forested vegetation, primarily trees, meadow grasses, or mixed trees, shrubs, and grasses; trees include saltcedar, mesquite, or desert willow; water table typically ranges from a few feet to about 20 ft below land surface; soil moist to dry	DMV	3,366,988	Area dominated by dense meadow and woodland vegetation, primarily trees, meadow and marsh grasses, or mixed trees, shrubs, and grasses; trees include desert ash and cottonwood, with some desert willow and mesquite; water table typically ranges from above land surface to about 20 ft below land surface; soil wet to dry
5	2,610,225	Area dominated by dense to moderately dense grassland vegetation, primarily saltgrass, and/or short rushes with an occasional tree or shrub; intermittently flooded; water table typically less than 5 ft below land surface; soil wet to moist	DGV	1,375,932	Area dominated by moderately dense to dense grassland vegetation, primarily saltgrass, and/or short rushes with an occasional tree or shrub; intermittently flooded; water table typically less than 10 ft below land surface; soil wet to moist

Table 2-13
ET Units Determined from Spectral Analysis of Satellite Imagery Data (June 13, 1992), Oasis Valley Discharge Area, Nevada
(Page 2 of 2)

Laczniak et al. (2001)			Reiner et al. (2002)		
ET-Unit Number	**ET-Unit Area (m^2)**	**General Description of ET Unit**	**ET-Unit Identifier**	**ET-Unit Area (m^2)**	**General Description of ET Unit**
6	3,893,079	Area dominated by sparse grassland vegetation, primarily salt and bunch grasses but also includes areas of very low density shrubs (mesquite); water table typically ranges from a few feet to about 12 ft below land surface; soil dry	SGV	4,916,935	Area dominated by sparse to moderately dense grassland vegetation, primarily salt and bunch grasses with occasional tree or shrub; water table typically ranges from a few feet below land surface to about 10 ft below land surface; soil damp to dry
7	327,796	Area dominated by moist bare soil; vegetation very sparse, primarily grasses; intermittently flooded, water table typically near land surface throughout most of the year but in some areas declines to a maximum depth of about 5 ft below land surface during late summer and early fall; soil typically moist	MBS	412,780	Area dominated by moist bare soil; vegetation very sparse, primarily grasses; intermittently flooded, water table typically near land surface throughout most of the year but in some areas declines to a maximum depth of about 5 ft below land surface during late summer and early fall; soil wet to moist
8	3,265,816	Area dominated by sparse to moderately dense shrub land vegetation, primarily greasewood, rabbitbrush, wolfberry, and seepweed; water table typically ranges from about 5 ft to about 20 ft below land surface; soil dry	SSV	3,609,799	Area dominated by sparse to moderately dense shrubland vegetation, primarily greasewood, rabbitbrush, and wolfberry; water table typically ranges from about 5 ft below land surface to about 20 ft below land surface; soil damp to dry
9	N/A	Area dominated by sparse woodland vegetation, primarily mesquite; water table typically ranges from about 10 to 40 ft below land surface; soil dry	N/A	N/A	N/A
10	4,047	Area dominated by open playa, primarily bare soil, often encrusted with salts; water table ranges from about 5 to 40 ft below land surface; soil typically dry but can be moist for short periods after intermittent flooding	N/A	N/A	N/A

Source: Modified from SNJV, 2004a

m^2 = Square meter N/A = Not applicable

Table 2-14
Estimated Mean Annual ET and Groundwater ET by ET Unit from Oasis Valley Discharge Area, Nevada

Laczniak et al., 2001						Reiner et al., 2002					
ET-Unit Identification	Area (m^2)	ET Rate (m/d)	Annual ET (m^3)	Mean ET Rate (m/d)[a]	Mean Annual ET (m^3)	ET-Unit Identification	Area (m^2)	ET Rate (m/d)	Annual ET (m^3)	Mean ET Rate (m/d)[a]	Mean Annual ET (m^3)
1	4,047	7.182×10^{-3}	11,101	6.764×10^{-3}	9,868	OWB	4,047	7.182×10^{-3}	10,608	6.764×10^{-3}	9,991
2	20,234	7.098×10^{-3}	51,806	6.681×10^{-3}	49,339	SAV	16,187	7.182×10^{-3}	41,938	6.764×10^{-3}	39,471
3	161,874	3.507×10^{-3}	209,692	3.090×10^{-3}	185,022	DWV	161,874	3.257×10^{-3}	197,357	2.839×10^{-3}	172,687
4	3,767,627	2.589×10^{-3}	3,577,092	2.171×10^{-3}	2,960,352	DMV	3,366,988	2.756×10^{-3}	3,330,396	2.338×10^{-3}	2,837,004
5	2,610,225	2.589×10^{-3}	2,466,960	2.171×10^{-3}	2,096,916	DGV	1,375,932	2.672×10^{-3}	1,356,828	2.255×10^{-3}	1,134,802
6	3,893,079	1.002×10^{-3}	1,480,176	5.845×10^{-4}	826,432	SGV	4,916,935	1.670×10^{-3}	2,960,352	1.253×10^{-3}	2,220,264
7	327,796	2.255×10^{-3}	271,366	1.837×10^{-3}	222,026	MBS	412,780	2.171×10^{-3}	333,040	1.754×10^{-3}	259,031
8	3,265,816	1.587×10^{-3}	1,850,220	1.169×10^{-3}	1,356,828	SSV	3,609,799	1.002×10^{-3}	1,356,828	5.845×10^{-4}	764,758
9	--	--	--	--	--	--	--	--	--	--	--
10	4,047	4.175×10^{-4}	1,233	8.351×10^{-6}	--	--	--	--	--	--	--
Total	14,054,745	1.921×10^{-3}	9,867,840	1.503×10^{-3}	7,647,576	--	13,864,542	1.921×10^{-3}	9,621,144	1.420×10^{-3}	7,400,880

Source: Modified from SNJV, 2004a

[a]Subtract precipitation rate from ET rate (Precipitation rate = 4.175×10^{-4} m/d)

Table 2-15
Summary Statistics of Simulated Annual ET from 1,000 Monte Carlo Realizations for the Oasis Valley Discharge Area

Statistic	Value	Unit
Mean	7,754,889	m^3
Median	7,758,589	m^3
Minimum	5,142,378	m^3
Maximum	11,005,109	m^3
Standard Deviation	953,480	m^3
5% Confidence Bound	6,185,950	m^3
95% Confidence Bound	9,325,180	m^3
Coefficient of Variability	0.12	unitless

Source: SNJV, 2004a

Note: Added 95% confidence range as mean minus 2 standard deviations and mean plus 2 standard deviations.

The total yearly water withdrawals for wells located within the boundaries of the Pahute Mesa area are shown in Figure 2-15. Only NTS water supply wells that contributed to the total pumpage from 1963 to 1993 are included in this figure. In 1995 and 1996, the totals include contributions from Beatty Well No. 1. For the remainder of the years, the totals also include the mine wells. The total yearly volumes are based on available data only and are, therefore, an underestimation of the actual volumes pumped. Records for NTS water supply wells are not available from 1972 to 1982. For the area of interest, the gap in the dataset is from 1968 to 1982, as shown on the graph (Figure 2-15). The graph shows a general increase in pumping from 1983 to 1989. The peak annual production of 1,154,700 cubic meters (m^3) occurred in 1989. All water was pumped from U-20 WW (cased), UE-19c WW, and WW-8 at that time. A decreasing trend started in 1990 and ended in 1993. A marked drop in pumping occurred from 1992 to 1993. This drop coincides with the end of underground nuclear testing in 1992.

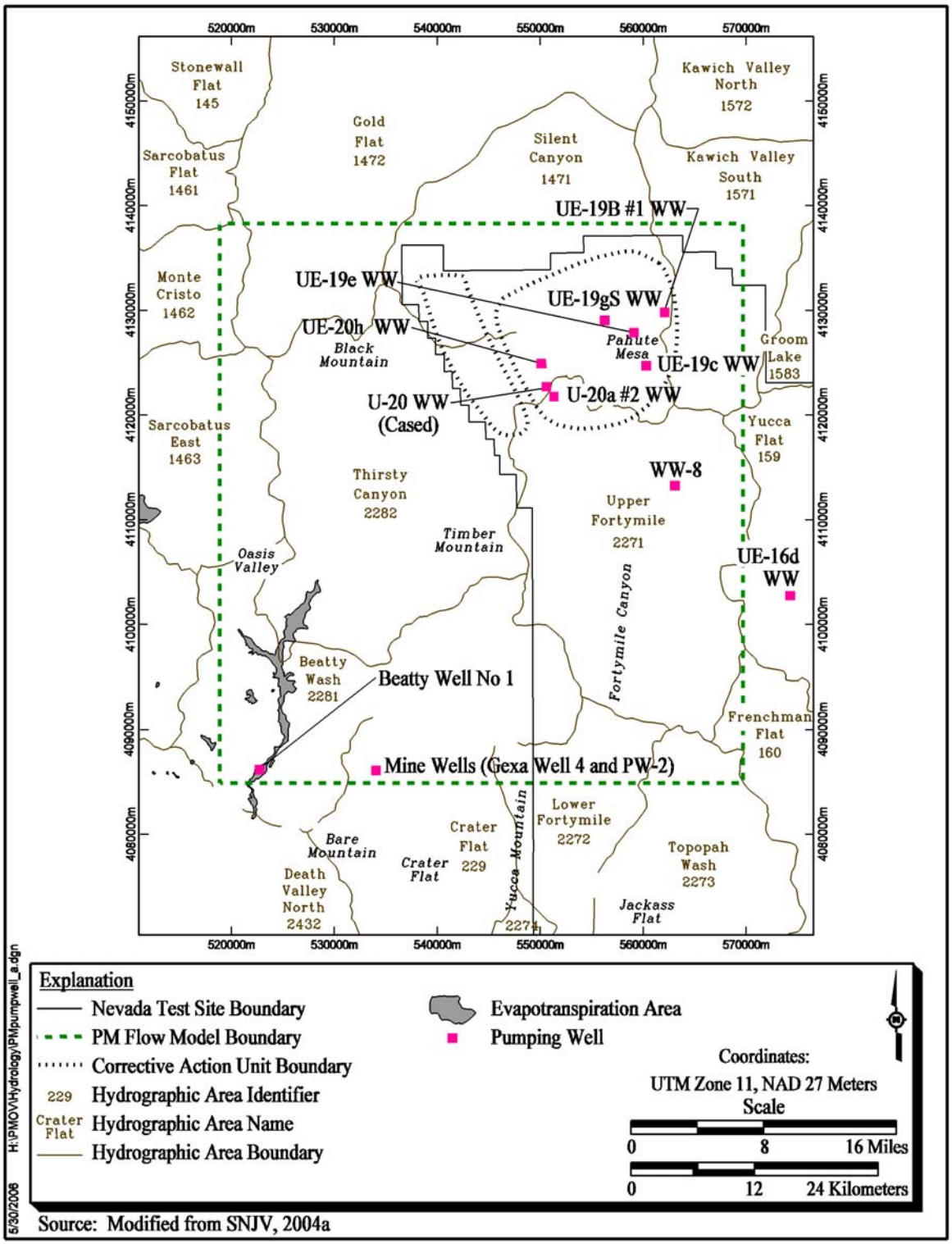

Figure 2-14
Locations of Pumping Wells in the Pahute Mesa Area Used in the Well Discharge Analysis

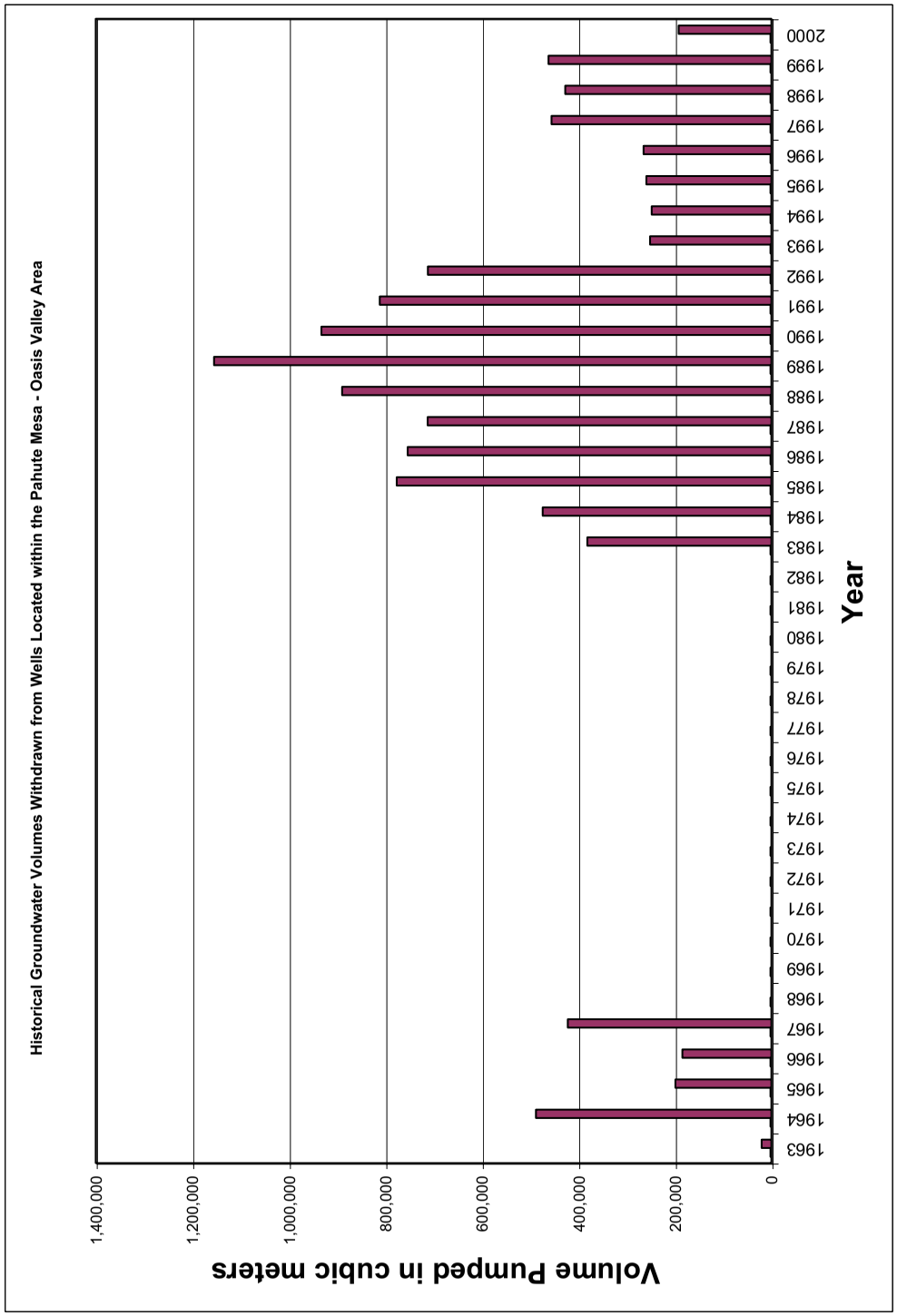

Figure 2-15
Total Withdrawals from Pumping Wells Located within the Pahute Mesa Area (No Data Available between 1968 and 1982)
Source: Modified from SNJV, 2004a

2.5 Hydraulic Heads

Observed hydraulic heads are derived from depth-to-water measurements and well information. Hydraulic heads may also be approximated by the land surface elevations of regional springs. This section provides a summary of the evaluation of hydraulic head data in the Pahute Mesa area. A more detailed description of this evaluation is provided in SNJV (2004a, Section 8.0).

The results of the water-level data analysis were used to identify hydraulic head values that are most representative of steady-state, predevelopment conditions at specific boreholes and well locations. Each temporal subset of measurements that represents steady-state conditions was reduced statistically to a mean, standard deviation, and variance of the mean. The hydraulic head data derived from the water-level data were supplemented with land surface elevations of the selected regional springs.

The uncertainty associated with each of the hydraulic head values was estimated in several different ways depending on the case. The uncertainty associated with hydraulic heads derived from multiple water-level measurements is represented by the total variance. In this case, a given steady-state hydraulic head variance was calculated as the sum of the variance of the mean hydraulic head and the variance of the land surface elevation derived from the accuracy estimates provided in SNJV (2004a). The uncertainty associated with hydraulic heads derived from land surface elevations at spring locations was equated to the variance of the land surface elevation derived from the accuracy estimates also provided in SNJV (2004a). It was not possible to quantify the measurement variance for many of the wells due to a lack of information. No estimates of uncertainty have been made for these cases. As part of the modeling analysis, weights will be derived and assigned to the hydraulic heads as described in Section 5.2.

A potentiometric contour map was prepared using composite water-level data to provide a general understanding of the hydraulic gradient and direction of groundwater flow. Figure 2-16 shows the potentiometric surface and the HSUs at the water table. The wells and hydraulic heads used in the calibration of the Pahute Mesa flow model are summarized in Table 5-2.

Vertical flow analysis was performed with the aid of the EV software program (Version 5.1 by Dynamic Graphics, 2002) to produce an isocontour model. The amount of information available on

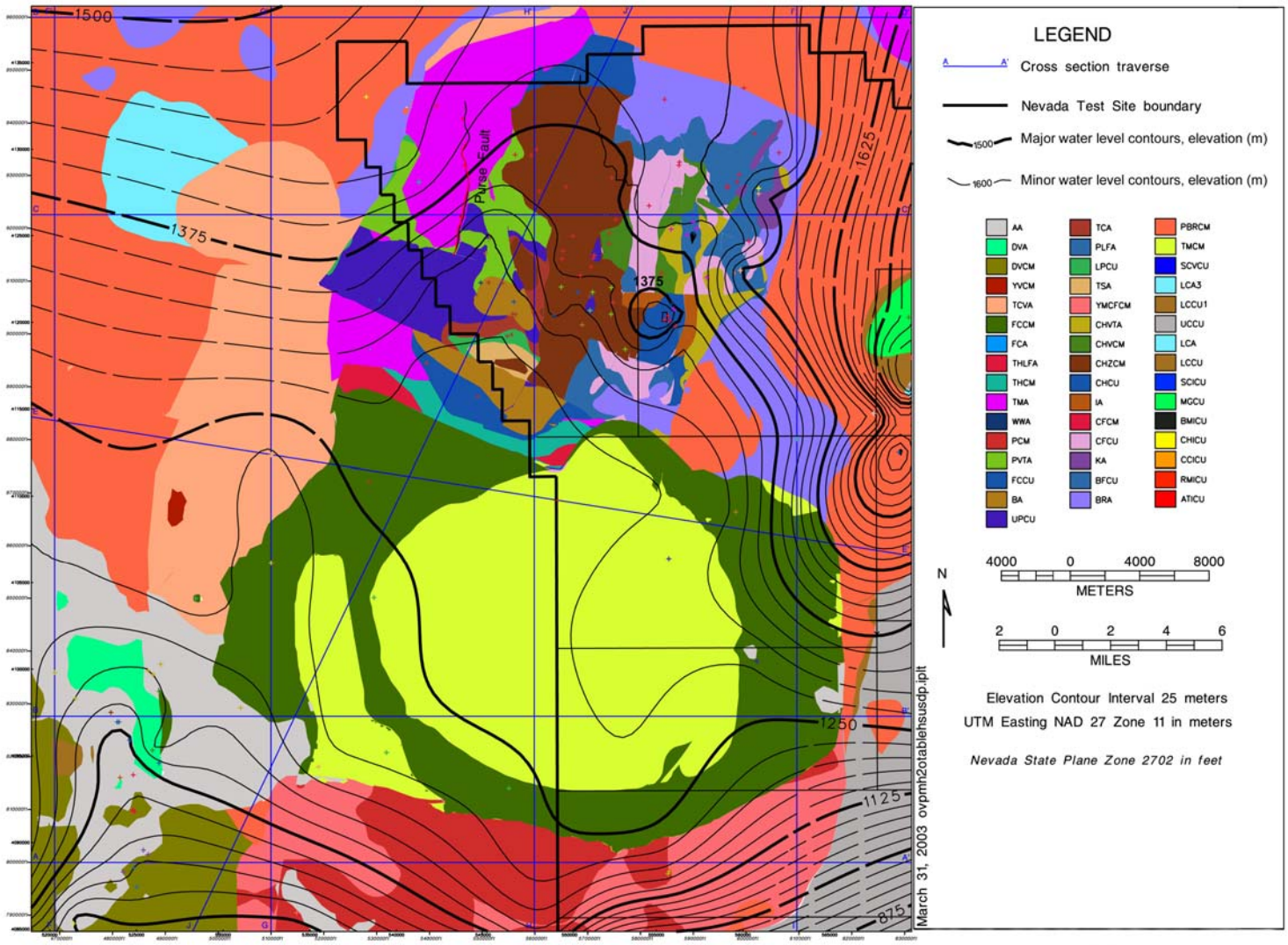

Figure 2-16
Map Showing Composite Potentiometric Surface with Elevated Heads in the Northwest and HSUs at the Water Table
Source: SNJV, 2004a

the vertical distribution of hydraulic heads in the region is sparse. The EV model was, therefore, only used to evaluate regions with sufficient data. In wells with multiple screened intervals, the vertical gradient was calculated as the difference in hydraulic heads divided by the difference in vertical distance between open intervals. The vertical gradient was then applied to the midpoint between effective open intervals.

An analysis of vertical flows indicated:

- A strong downward vertical gradient occurs near the water table in the Rainier Mesa region with a slight upward gradient at depth.
- A moderate downward gradient occurs in the area of Beatty Wash.
- There is a slight upward gradient at intermediate depths throughout the central portions of NTS Area 19 and Area 20.
- The Oasis Valley region contains a mixture of vertical gradients. Near the surface, there is a very weak upward gradient as well as areas of localized downward gradients.

As described in Section 2.4, 10 pumping wells have been historically used to withdraw groundwater from the Pahute Mesa area; eight of them are NTS water supply wells located in Pahute Mesa. The two other wells are Beatty Well No. 1 and Gexa Well 4, located outside of the NTS. In 1989, the maximum volume of 1,154,700 m^3 was pumped. This volume represents only 15 percent of the ET estimate. The three largest producing wells are WW 8, UE-19c WW, and U-20 WW. The effects of pumping at U-20 WW were observed as drawdown at several wells located up to 5.9 km away (Fenelon, 2000). As reported by Fenelon (2000), the correlation of monthly withdrawal rates and drawdown is hindered because of relatively long periods of no pumping interspersed with periods of pumping. In conclusion, transient well-related effects are very localized and likely not representative of conditions over a majority of the model area.

2.6 Hydraulic Parameters

Hydraulic parameters are required to simulate groundwater movement. The following sections summarize the assessment of hydraulic parameter data presented in SNJV (2004a.)

2.6.1 Hydraulic Conductivity Data

Analysis of hydraulic conductivity data included evaluations of measurement scale (laboratory-scale data, slug-test-scale data, constant-rate-scale data), scaling and spatial variability, vertical anisotropy, and the alteration of hydraulic conductivity in test cavities (SNJV 2004a). Hydraulic conductivity parameters for each HSU are presented at the end of this section. All hydraulic conductivities are in m/d. Figure 2-17 shows the locations where the hydraulic conductivity data were obtained.

Approximately 1,200 laboratory-scale data measurements are available for 44 locations, nearly all of which are outside the Pahute Mesa model boundary. Laboratory data have been subdivided on the basis of the regional model HSUs including the AA, LCA, LCCU, VCU, VA, and VU. Table 2-16 provides the statistics of laboratory-scale hydraulic conductivity data.

More than 200 hydraulic conductivity values were obtained by methods that have been lumped into the general category of slug tests. The types of tests in this category include bailing recovery, drill-stem test, falling-head slug test, packer-injection test, pressure-injection test, slug-injection test, slug-withdrawal test, and swabbing-recovery test. Each of these test types are of relatively short duration, involving the movement of smaller volumes of water through the formation than would be typical for a constant-rate test. Therefore, hydraulic conductivity values derived from slug tests represent a smaller volume of the tested formation than either single-well or multi-well constant-rate aquifer tests. Table 2-17 provides the statistics of the slug-test-scale hydraulic conductivity data. Plots of slug-test hydraulic conductivity versus depth from SNJV (2004a, Section 5.5.4, Figures 5-9 and 5-10) suggest that there is a trend of decreasing hydraulic conductivity with increasing depth.

Approximately 300 hydraulic conductivity values were obtained from analyses of constant-rate test data. The data classified as constant-rate-scale represent tests in which water was injected or withdrawn at a constant rate for several hours to several days. As a result, these tests sampled a larger volume of the tested formation than either laboratory-scale or slug-scale tests. This group of data contains results from both single- and multi-well aquifer tests. Table 2-18 summarizes the statistics for these analyses.

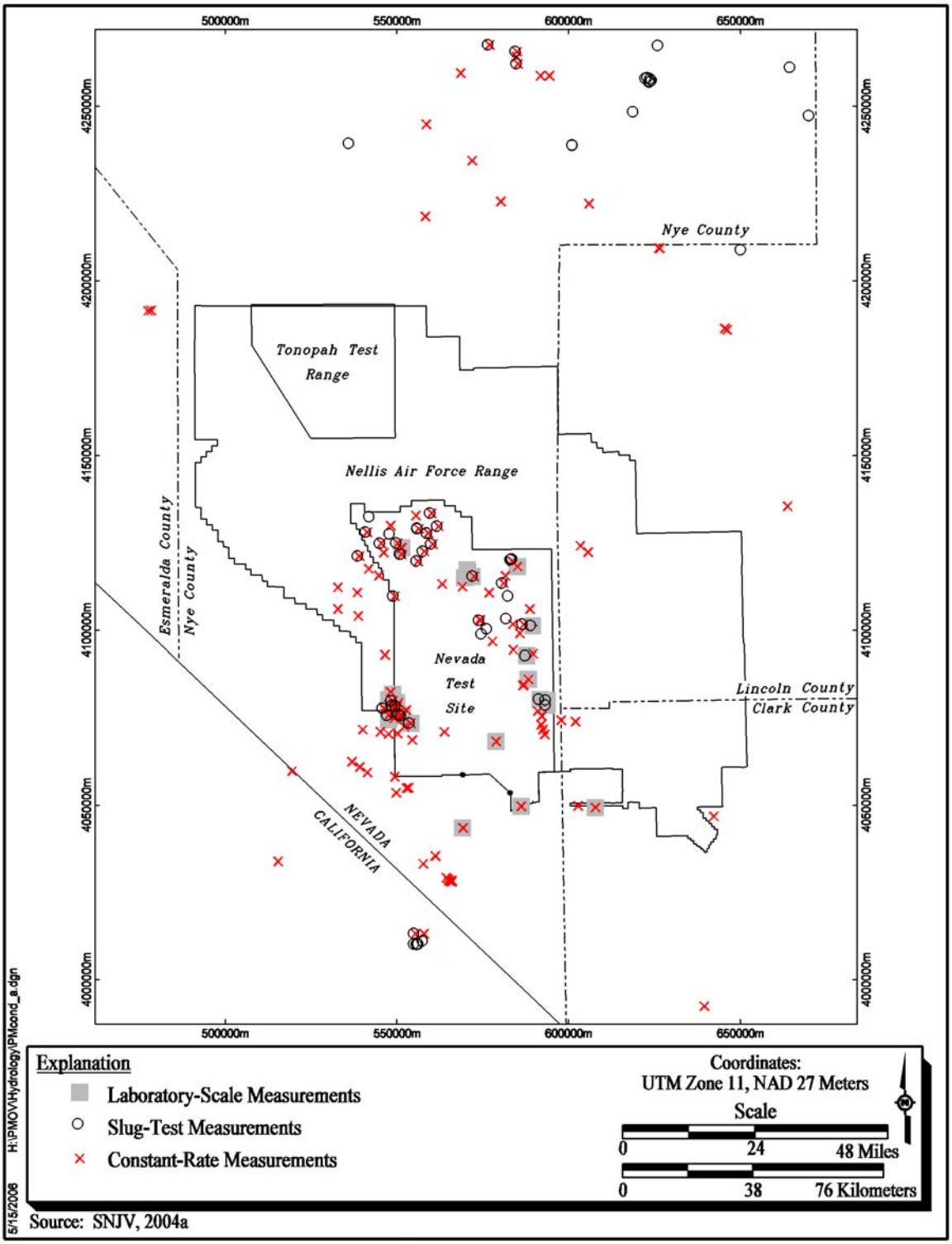

Figure 2-17
Map of the Locations of Hydraulic Conductivity Data

Table 2-16
Statistics of Laboratory-Scale Hydraulic Conductivity[a] Data

Hydrostratigraphic Unit[b]	Number of Data Points	Log 10 Mean of Hydraulic Conductivity	Log 10 Standard Deviation of Hydraulic Conductivity	Accept Log Normality at the 5% Level
Alluvial Aquifer (AA)	66	-0.4	0.8	Yes
Lower Carbonate Aquifer (LCA)	33	-4.2	1.6	Yes
Lower Clastic Confining Unit (LCCU)	30	-6.6	0.7	Yes
Volcanic Aquifer (VA)	400	-3.8	2.2	No
Volcanic Confining Unit (VCU)	639	-4.4	1.5	No
Volcanic Aquifer (VA)	19	-3.0	2.0	Yes

Source: SNJV, 2004a

[a]Hydraulic conductivity is in m/d.
[b]See Table 2-6 for HSU descriptions.

Plots of constant-rate-test hydraulic conductivity versus depth from SNJV (2004a, Section 5.5.5, Figure 5-22) show a strong trend of decreasing hydraulic conductivity with increasing depth. The treatment of hydraulic conductivity depth decay is described in SNJV (2004a, Section 5.5.6).

For the purposes of the Pahute Mesa CAU flow model, the constant-rate-scale data are the most appropriate. Slug tests are judged less reliable because they are strongly affected by near-well mechanical disturbance (Butler, 1997).

In the general case, hydraulic conductivity is not a scalar value, but a second rank tensor, where hydraulic conductivity at a point in space is a function of direction. The measurement of horizontal anisotropy requires multiple observation wells during aquifer testing. Anisotropy in the vertical direction can be determined from oriented core, or observation wells set at depths that differ from the pumped well. Data to define anisotropy are limited. Laboratory data are not appropriate for large-scale model parameters such as those needed for the Pahute Mesa CAU model. Careful testing at the C-well complex at Yucca Mountain yielded a range of anisotropy values (defined as vertical/horizontal hydraulic conductivity) from 0.025 to as large as 2.0. Because the dataset is limited, it is not possible to provide anisotropy values for each HSU. Vertical anisotropy is treated in the Pahute Mesa flow model (see SNJV, 2004a, Section 5.5.8). Horizontal anisotropy is not considered.

Table 2-17
Statistics of Slug-Test-Scale Hydraulic Conductivity[a] Data

Hydrostratigraphic Unit[b]	Number of Data Points	Log 10 Mean Hydraulic Conductivity	Log 10 Standard Deviation of Hydraulic Conductivity	Accept Log Normality at the 5% Level
Alluvial Aquifer (AA)	15	-1.0	1.4	Yes
Lower Carbonate Aquifer (LCA)	32	-1.2	1.0	Yes
Bullfrog Confining Unit (BFCU)	19	-3.3	0.6	Yes
Belted Range Aquifer (BRA)	76	-2.9	0.9	Yes
Crater Flat Composite Unit (CFCM)	5	-3.1	0.3	Yes
Crater Flat Confining Unit (CFCU)	2	-2.6	1.3	N/A
Calico Hills Confining Unit (CHCU)	2	-2.8	0.6	N/A
Calico Hills Zeolitic Composite Unit (CHZCM)	29	-2.7	0.8	Yes
Inlet Aquifer (IA)	8	-2.4	0.9	Yes
Pre-Belted Range Composite Unit (PBRCM)	16	-3.7	1.1	Yes
Timber Mountain Composite Unit (TMCM)	16	-2.5	1.1	Yes
Upper Paintbrush Confining Unit (UPCU)	3	-3.2	0.3	N/A

Source: SNJV, 2004a

[a]Hydraulic conductivity is in m/d.
[b]See Table 2-6 for HSU descriptions.

The detonation of underground nuclear tests creates underground cavities and collapsed chimneys (Pawloski et al., 2001). The melt glass that forms at the bottom of the cavity is generally accepted to be of very low permeability, as is the crushed zone beneath the cavity. However, the chimney region, because of its rubblized nature, may be more permeable than the surrounding host rock. In their study of flow and transport from an underground nuclear test cavity, Pawloski et al. (2001) used chimney hydraulic conductivity values that were at least 70 times larger than in the native rock. As Pawloski et al. (2001) note, these values were estimated using the scant data available from underground nuclear tests, insights gained from calibration of flow and transport models, and understanding of the phenomenology of underground nuclear tests. The scale of these effects should be small with respect to the size of the Pahute Mesa flow model domain. However, this assumption on increased chimney

Table 2-18
Statistics of Constant-Rate-Scale Hydraulic Conductivity[a] Data as Compared to Statistics of Slug-Test-Scale and Laboratory-Scale Data

Hydrostratigraphic Unit[b]	Number of Data Points	Log 10 Mean of Hydraulic Conductivity	Log 10 Standard Deviation of Hydraulic Conductivity	Accept Log Normality at the 5% Level	Slug-Test-Scale Log 10 Mean of Hydraulic Conductivity	Slug-Test-Scale Log 10 Standard Deviation of Hydraulic Conductivity	Laboratory-Scale Log 10 Mean of Hydraulic Conductivity	Laboratory-Scale Log 10 Standard Deviation of Hydraulic Conductivity
Alluvial Aquifer (AA)	38	0.7	0.7	Yes	-1.0	1.4	-0.4	0.8
Lower Carbonate Aquifer (LCA)	49	-0.3	1.2	Yes	-1.2	1.0	-4.2	1.6
Intrusives (I)	1	-2.5	N/A	N/A				
Upper Clastic Confining Unit (UCCU)	2	-2.2	1.3	N/A				
Lower Clastic Confining Unit (LCCU)	3	-0.5	1.5	N/A			-6.6	0.7
Volcanic Confining Unit (VCU)	101	-1.0	1.4	Yes			-4.4	1.5
Volcanic Aquifer (VA)	35	0.1	0.9	Yes			-3.8	2.2
Volcanics Undifferentiated (VU)	7	-1.3	1.2	Yes			-3.0	2.0
Benham Aquifer (BA)	6	0.6	0.8	N/A				
Belted Range Aquifer (BRA)	15	-0.1	0.9	Yes	-2.9	1.0		
Bullfrog Confining Unit (BFCU)	1	-0.3	N/A	N/A	-2.3	1.0		
Inlet Aquifer (IA)	3	-1.0	1.6	N/A	-2.0	0.9		
Calico Hills Zeolitic Composite Unit (CHZCM)	6	-0.2	0.5	N/A	-1.9	0.9		
Fortymile Canyon Composite Unit (FCCM)	11	-0.1	1.1	Yes				
Pre-Belted Range Composite Unit (PBRCM)	2	-0.7	0	N/A	-2.8	1.5		
Thirsty Canyon Volcanic Aquifer (TCVA)	4	1.8	0.4	N/A				
Timber Mountain Composite Unit (TMCM)	13	0.4	1.1	Yes	-2.1	1.0		
Upper Paintbrush Confining Unit (UPCU)	3	-0.9	0.9	N/A				

Source: SNJV, 2004a

[a]Hydraulic conductivity is in m/d.
[b]See Table 2-6 for HSU descriptions.

hydraulic conductivity was addressed in the sensitivity analysis of the Pahute Mesa flow model (see Section 6.2).

Table 2-19 summarizes the hydraulic conductivity parameters determined for each HSU. The table contains the HSU number and identifier, the log 10 mean and standard deviation, and a description of where the chosen mean and standard deviation were obtained. The given distributions were applied to the model at the start of calibration (see Section 5.2).

Table 2-19
Hydraulic Conductivity[a] Distributions of Hydrostratigraphic Units of the Pahute Mesa Hydrostratigraphic Framework Model
(Page 1 of 5)

HFM Layer Number[a]	Hydrostratigraphic Unit (Symbol)	Dominant Hydrogeologic Unit(s)[b]	Mean Hydraulic Conductivity Log 10 (m/d)	Mean Intrinsic Permeability (m^2)	Log 10 Hydraulic Conductivity Standard Deviation	Source of the Parameters
45	Alluvial Aquifer (AA) (this term is also used to designate a hydrogeologic unit)	AA	0.7	5.9×10^{-12}	0.7	Values obtained from the constant-rate-scale data in Table 2-18.
44	Younger Volcanic Composite Unit (YVCM)	LFA, WTA, VTA	1.8	7.4×10^{-11}	0.4	No data were available for this unit. Used values from the TCVA in Table 2-18 because of lithologic similarity. This minor unsaturated unit is not expected to influence the flow model.
43	Thirsty Canyon Volcanic Aquifer (TCVA)	WTA, LFA, lesser VTA	1.8	7.4×10^{-11}	0.4	Values obtained from the constant-rate-scale data in Table 2-18.
42	Detached Volcanics Composite Unit (DVCM)	WTA, LFA, TCU	-1.0	1.2×10^{-13}	1.4	No data were available for this unit. Used value from the VCU in Table 2-18 because it provides a distribution that spans nearly the full range of observed values. It is expected that composite units have a larger range of values because of the varied lithologies.
41	Detached Volcanics Aquifer (DVA)	WTA, LFA	0.1	1.5×10^{-12}	0.9	No data were available for this unit. Used value from the VA in Table 2-18 because it provides a distribution that spans nearly the full range of observed values for an aquifer lithology.
40	Fortymile Canyon Composite Unit (FCCM)	LFA, TCU, lesser WTA	-0.1	9.4×10^{-13}	1.1	Values obtained from the constant-rate-scale data in Table 2-18.
39	Fortymile Canyon Aquifer (FCA)	WTA, LFA	0.1	1.5×10^{-12}	0.9	No data were available for this unit. Used value from the VA in Table 2-18 because it provides a distribution that spans nearly the full range of observed values for an aquifer lithology.

Table 2-19
Hydraulic Conductivity[a] Distributions of Hydrostratigraphic Units of the Pahute Mesa Hydrostratigraphic Framework Model
(Page 2 of 5)

HFM Layer Number[a]	Hydrostratigraphic Unit (Symbol)	Dominant Hydrogeologic Unit(s)[b]	Mean Hydraulic Conductivity Log 10 (m/d)	Mean Intrinsic Permeability (m^2)	Log 10 Hydraulic Conductivity Standard Deviation	Source of the Parameters
38	Timber Mountain Composite Unit (TMCM)	TCU (altered tuffs, lavas) and unaltered WTA and lesser LFA	0.4	3.0×10^{-12}	1.1	Values obtained from the constant-rate-scale data in Table 2-18.
37	Tannenbaum Hill Lava-Flow Aquifer (THLFA)	LFA	0.1	1.5×10^{-12}	0.9	No data were available for this unit. Used value from the VA in Table 2-18 because it provides a distribution that spans nearly the full range of observed values for an aquifer lithology.
36	Tannenbaum Hill Composite Unit (THCM)	Mostly TCU, lesser WTA	-1.0	1.2×10^{-13}	1.4	No data were available for this unit. Used value from the VCU in Table 2-18 because it provides a distribution that spans nearly the full range of observed values. It is expected that composite units have a larger range of values because of the varied lithologies.
35	Timber Mountain Aquifer (TMA)	Mostly WTA, minor VTA	0.1	1.5×10^{-13}	0.9	No data were available for this unit. Used value from the VA in Table 2-18 because it provides a distribution that spans nearly the full range of observed values for an aquifer lithology.
34	Subcaldera Volcanic Confining Unit (SCVCU)	TCU	-4.4	4.7×10^{-17}	1.5	No data were available for this unit. Used value from the VCU in Table 2-18 because it is expected that this unit will be of low permeability.
33	Fluorspar Canyon Confining Unit (FCCU)	TCU	-1.0	1.2×10^{-13}	1.4	No data were available for this unit. Used value from the VCU in Table 2-18 because it provides a distribution that spans nearly the full range of observed values.
32	Paintbrush Composite Unit (PCM)	WTA, LFA, TCU	-1.0	1.2×10^{-13}	1.4	No data were available for this unit. Used value from the VCU in Table 2-18 because it provides a distribution that spans nearly the full range of observed values. It is expected that composite units have a larger range of values because of the varied lithologies.
31	Paintbrush Vitric-Tuff Aquifer (PVTA)	VTA	0.1	1.5×10^{-12}	0.9	No data were available for this unit. Used value from the VA in Table 2-18 because it provides a distribution that spans nearly the full range of observed values for an aquifer lithology.
30	Benham Aquifer (BA)	LFA	0.6	4.7×10^{-12}	0.8	Values obtained from the constant-rate-scale data in Table 2-18.
29	Upper Paintbrush Confining Unit (UPCU)	TCU	-0.9	1.5×10^{-13}	0.9	Values obtained from the constant-rate-scale data in Table 2-18.

Table 2-19
Hydraulic Conductivity[a] Distributions of Hydrostratigraphic Units of the Pahute Mesa Hydrostratigraphic Framework Model
(Page 3 of 5)

HFM Layer Number[a]	Hydrostratigraphic Unit (Symbol)	Dominant Hydrogeologic Unit(s)[b]	Mean Hydraulic Conductivity Log 10 (m/d)	Mean Intrinsic Permeability (m^2)	Log 10 Hydraulic Conductivity Standard Deviation	Source of the Parameters
28	Tiva Canyon Aquifer (TCA)	WTA	0.1	1.5×10^{-12}	0.9	No data were available for this unit. Used value from the VA in Table 2-18 because it provides a distribution that spans nearly the full range of observed values for an aquifer lithology.
27	Paintbrush Lava-Flow Aquifer (PLFA)	LFA	0.1	1.5×10^{-12}	0.9	No data were available for this unit. Used value from the VA in Table 2-18 because it provides a distribution that spans nearly the full range of observed values for an aquifer lithology.
26	Lower Paintbrush Confining Unit (LPCU)	TCU	-0.9	1.5×10^{-13}	0.9	No data were available for this unit. Used values from the UPCU in Table 2-18 because of lithologic similarity.
25	Topopah Spring Aquifer (TSA)	WTA	0.1	1.5×10^{-12}	0.9	No data were available for this unit. Used value from the VA in Table 2-18 because it provides a distribution that spans nearly the full range of observed values for an aquifer lithology.
24	Yucca Mountain Crater Flat Composite Unit (YMCFCM)	LFA, WTA, TCU	-1.0	1.2×10^{-13}	1.4	No data were available for this unit. Used value from the VCU in Table 2-18 because it provides a distribution that spans nearly the full range of observed values. It is expected that composite units have a larger range of values because of the varied lithologies.
23	Calico Hills Vitric-Tuff Aquifer (CHVTA)	VTA	0.1	1.5×10^{-12}	0.9	No data were available for this unit. Used value from the VA in Table 2-18 because it provides a distribution that spans nearly the full range of observed values for an aquifer lithology.
22	Calico Hills Vitric Composite Unit (CHVCM)	VTA, LFA	-1.0	1.2×10^{-13}	1.4	No data were available for this unit. Used value from the VCU in Table 2-18 because it provides a distribution that spans nearly the full range of observed values. It is expected that composite units have a larger range of values because of the varied lithologies.
21	Calico Hills Zeolitic Composite Unit (CHZCM)	LFA, TCU	-0.2	7.4×10^{-13}	0.5	Values obtained from the constant-rate-scale data in Table 2-18.
20	Calico Hills Confining Unit (CHCU)	Mostly TCU, minor LFA	-0.9	1.5×10^{-13}	0.9	No data were available for this unit. Used values from the UPCU in Table 2-18 because of lithologic similarity.
19	Inlet Aquifer (IA)	LFA	-1.0	1.2×10^{-13}	1.6	Values obtained from the constant-rate-scale data in Table 2-18.

Table 2-19
Hydraulic Conductivity[a] Distributions of Hydrostratigraphic Units of the Pahute Mesa Hydrostratigraphic Framework Model
(Page 4 of 5)

HFM Layer Number[a]	Hydrostratigraphic Unit (Symbol)	Dominant Hydrogeologic Unit(s)[b]	Mean Hydraulic Conductivity Log 10 (m/d)	Mean Intrinsic Permeability (m^2)	Log 10 Hydraulic Conductivity Standard Deviation	Source of the Parameters
18	Crater Flat Composite Unit (CFCM)	Mostly LFA, intercalated with TCU	-1.4	4.7×10^{-14}	0.9	Values obtained from the slug-scale data in Table 2-18. The magnitude of the mean was increased one order of magnitude to account for observed differences between the slug and constant-rate-scale.
17	Crater Flat Confining Unit (CFCU)	TCU	-0.9	1.5×10^{-13}	0.9	No data were available for this unit. Used values from the UPCU in Table 2-18 because of lithologic similarity.
16	Kearsarge Aquifer (KA)	LFA	0.1	1.5×10^{-12}	0.9	No data were available for this unit. Used value from the VA in Table 2-18 because it provides a distribution that spans nearly the full range of observed values for an aquifer lithology.
15	Bullfrog Confining Unit (BFCU)	TCU	-1.3	5.9×10^{-14}	1.0	Values obtained from the slug-scale data in Table 2-18. The magnitude of the mean was increased one order of magnitude to account for observed differences between the slug and constant-rate-scale.
14	Belted Range Aquifer (BRA)	LFA and WTA, with lesser TCU	-0.1	9.4×10^{-13}	0.9	Values obtained from the constant-rate-scale data in Table 2-18.
13	Pre-Belted Range Composite Unit (PBRCM)	TCU, WTA, LFA	-0.7	2.4×10^{-13}	1.5	Mean Value obtained from the constant-rate-scale data in Table 2-18. The standard deviation was taken from the slug-scale data in Table 2-17.
12	Black Mountain Intrusive Confining Unit (BMICU)	IICU	-2.5	3.7×10^{-15}		Mean Value obtained from the Intrusive (I) in the constant-rate-scale data in Table 2-18. No standard deviation was calculated.
11	Ammonia Tanks Intrusive Confining Unit (ATICU)	IICU	-2.5	3.7×10^{-15}		
10	Rainier Mesa Intrusive Confining Unit (RMICU)	IICU	-2.5	3.7×10^{-15}		
9	Claim Canyon Intrusive Confining Unit (CCICU)	IICU	-2.5	3.7×10^{-15}		
8	Calico Hills Intrusive Confining Unit (CHICU)	IICU	-2.5	3.7×10^{-15}		

Table 2-19
Hydraulic Conductivity[a] Distributions of Hydrostratigraphic Units of the Pahute Mesa Hydrostratigraphic Framework Model
(Page 5 of 5)

HFM Layer Number[a]	Hydrostratigraphic Unit (Symbol)	Dominant Hydrogeologic Unit(s)[b]	Mean Hydraulic Conductivity Log 10 (m/d)	Mean Intrinsic Permeability (m^2)	Log 10 Hydraulic Conductivity Standard Deviation	Source of the Parameters
7	Silent Canyon Intrusive Confining Unit (SCICU)	IICU	-2.5	3.7×10^{-15}		Mean Value obtained from the Intrusive (I) in the constant-rate-scale data in Table 2-18. No standard deviation was calculated.
6	Mesozoic Granite Confining Unit (MGCU)	GCU	-2.5	3.7×10^{-15}		Mean Value obtained from the Intrusive (I) in the constant-rate-scale data in Table 2-18. No standard deviation was calculated.
5	Lower Carbonate Aquifer - Thrust Plate (LCA3)	CA	-0.3	5.9×10^{-13}	1.2	Values obtained from the constant-rate-scale data in Table 2-18 for the LCA.
4	Lower Clastic Confining Unit - Thrust Plate (LCCU1)	CCU	-0.5	3.7×10^{-13}	1.5	Values obtained from the constant-rate-scale data in Table 2-18. This unit may be broken up and have a larger permeability than when at depth.
3	Upper Clastic Confining Unit (UCCU)	CCU	-2.2	7.4×10^{-15}	1.3	Values obtained from the constant-rate-scale data in Table 2-18.
2	Lower Carbonate Aquifer (LCA)	CA	-0.3	5.9×10^{-13}	1.2	Values obtained from the constant-rate-scale data in Table 2-18 for the LCA.
1	Lower Clastic Confining Unit (LCCU)	CCU	-6.6	3.0×10^{-19}	0.7	Values taken from the laboratory-scale data in Table 2-16 because this unit is expected to be very impermeable.

Source: Modified from SNJV, 2004a

[a]PM 3-D Hydrostratigraphic Framework model (BN, 2002)
[b]See Table 2-1 for HGU descriptions.

2.7 Groundwater Chemistry

Groundwater geochemistry data are considered during the evaluation of the groundwater flow system because they provide a means for determining the origin, pathway, and timescale of groundwater flow that is independent of estimates based on conventional hydraulic data. Geochemical and hydraulic data reflect distinct but complimentary aspects of a groundwater flow system, and must be considered in unison in order to develop a consistent, comprehensive, and defensible flow system assessment. For example, geochemical data may identify flow paths and source areas that would otherwise not be recognized on the basis of hydraulic information alone; however, these flow paths must be consistent with potentiometric data in order to be valid.

A detailed discussion of groundwater geochemistry is provided in SNJV (2004a, Section 10.0). This section provides a summary of groundwater geochemistry evaluations for the Central and Western Pahute Mesa CAUs that address groundwater flow path, water budget, and travel time evaluations. These geochemical evaluations were performed on representative Pahute Mesa-CAU data in order to identify and assess viable flow paths and groundwater mixing models and included the evaluation of both conservative tracers and of non-conservative tracers. In addition, the NETPATH computer program (Plummer et al., 1994) was used as part of the evaluation process to calculate the net geochemical mass-balance reactions, groundwater mixing ratios, and apparent groundwater travel times along viable flow paths (SNJV, 2004a).

More than 1,200 sampling events, conducted before 1992, generated data from 220 individual locations for more than 280 different parameters within the area of interest (oldest recorded sample date within the area of interest is February 22, 1956). Note that only 95 of the total number of individual parameters measured before 1992 were analyzed 10 or more times. Since 1992 (and the initiation of the ERP), more than 600 sample events have generated data from 138 individual well, spring, and seep locations within the same area of interest for more than 500 different parameters. Note that only 307 of the total number of individual parameters measured since 1992 were analyzed 10 or more times. There are 54 locations that have been sampled both before and since 1992.

2.7.1 Conservative Tracers

Conservative tracers are geochemical species that move with groundwater, exhibiting little or no change in concentration caused by reactive processes. Conservative tracers can be used to support the identification of groundwater flow paths, mixing ratios, and timescales of environmental processes (Cook and Bohlke, 2000). The chloride (Cl^-) and often sulfate (SO_4^{2-}) ions, and the stable isotopes of hydrogen and oxygen are considered conservative tracers. These parameters provide the fundamental basis for the flow path identification and mixing model estimates reported in SNJV (2004a).

2.7.1.1 Conservative Tracer Data

Figures 2-18 and 2-19 illustrate the geographic variations in groundwater delta deuterium (δD) values and Cl^- concentrations, respectively, in the Pahute Mesa flow system. Deuterium is a heavy stable isotope of hydrogen that can substitute for hydrogen in water (hence "heavy water"); the

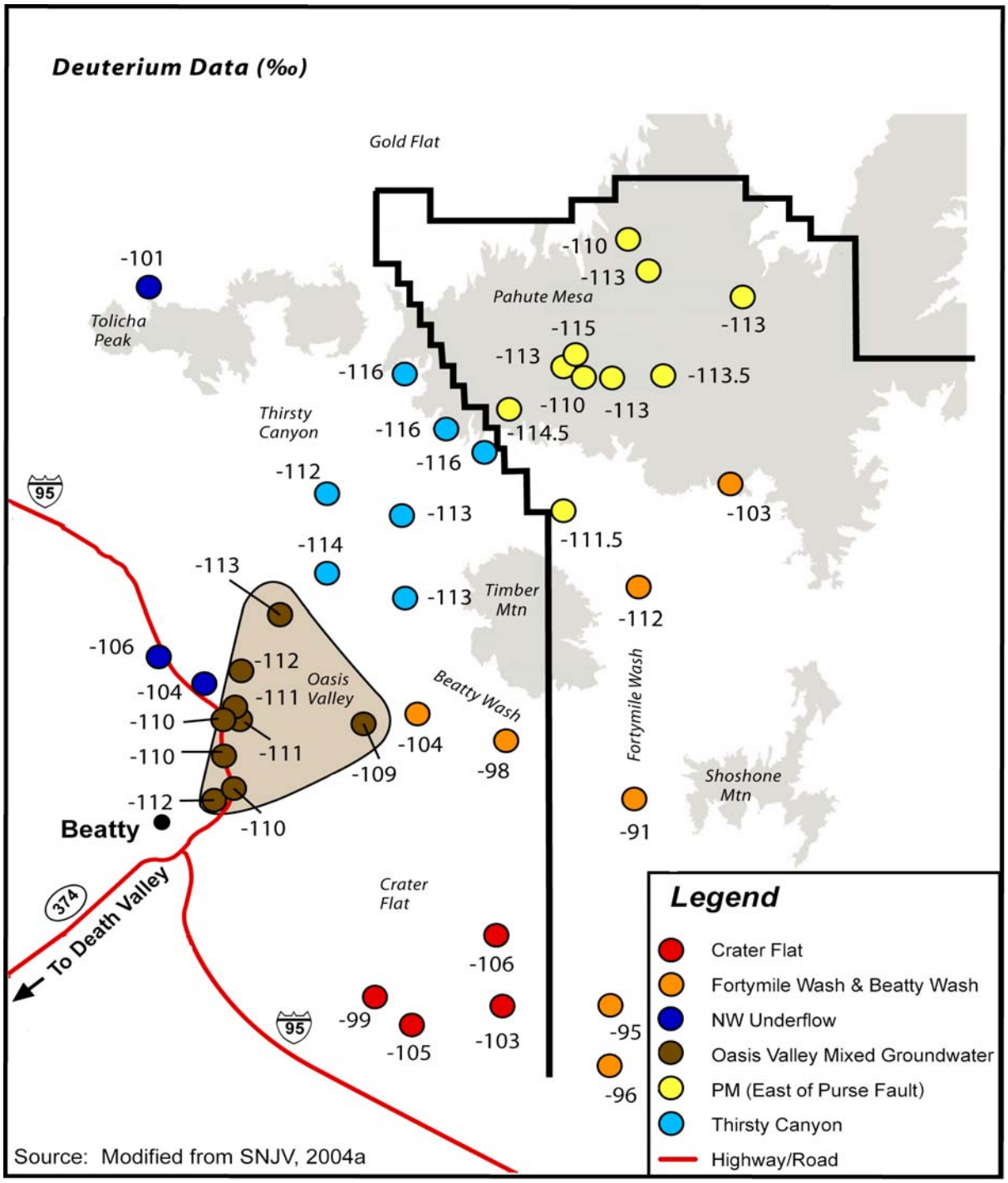

Figure 2-18
Geographic Distribution of δD Values for Wells and Springs in the Study Area

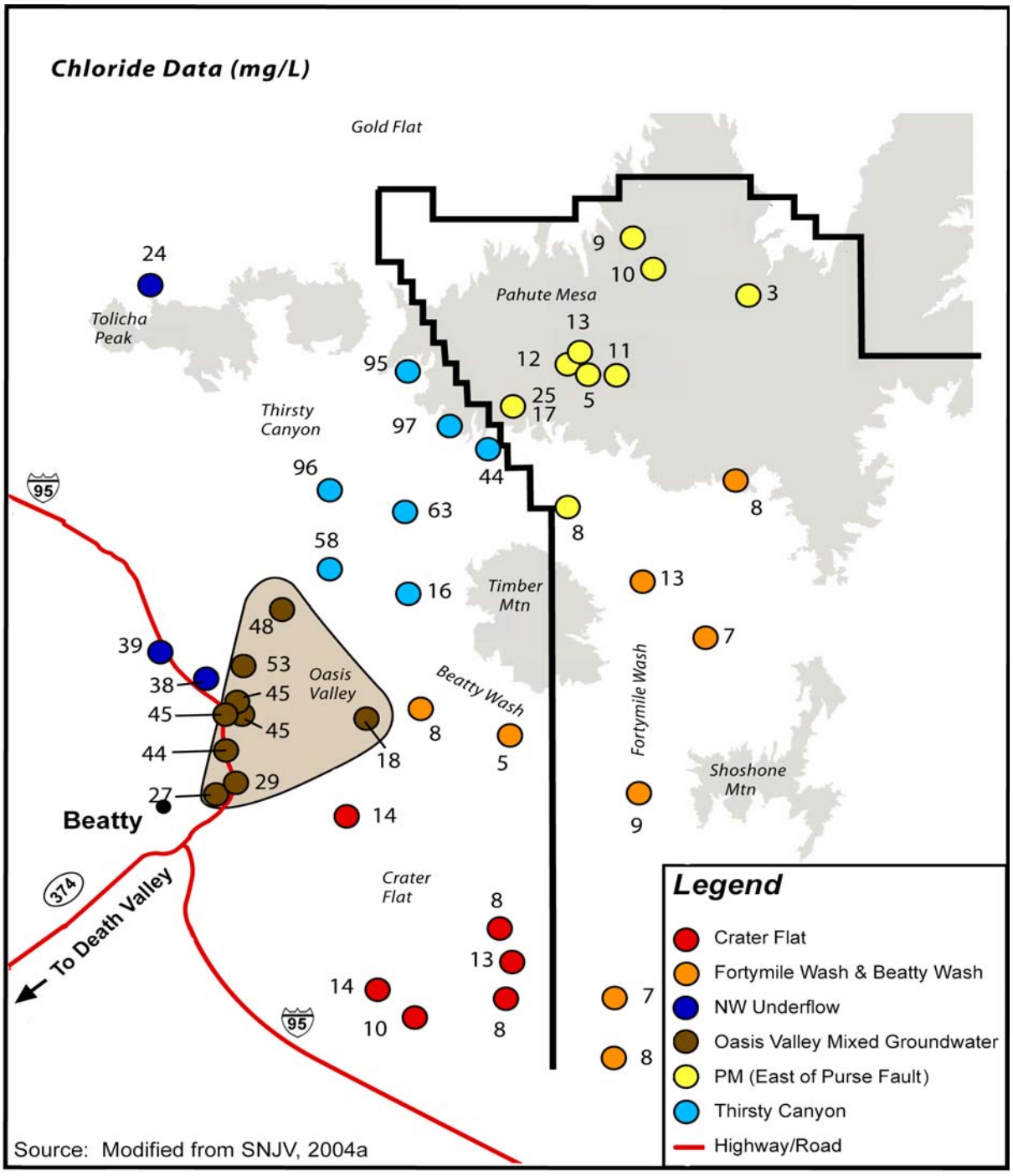

Figure 2-19
Geographic Distribution of Dissolved Cl^- Concentrations for Wells and Springs in the Study Area

concentration of deuterium is expressed as a change, or "delta," from a global standard. Reactions occur more slowly with heavy water. Thus, precipitation condensed at higher altitudes and lower temperatures is lighter, or depleted with respect to deuterium. This information allows inferences about recharge areas and groundwater flow paths. These figures illustrate that groundwater in upper Thirsty Canyon, west of the Purse Fault, has relatively light δD values (as light as -116 per mil) and high Cl^- concentrations (up to 97 milligrams per liter [mg/L]) that are distinct from Pahute Mesa groundwater immediately to the east. In the Pahute Mesa area east of the Purse Fault, the δD values ranged from -110 to -115 per mil and the Cl^- values ranged from 5 to 25 mg/L. The Purse Fault is spatially associated with a major discontinuity in regional water levels, in the western part of Area 20 (O'Hagan and Laczniak, 1996; Laczniak et al., 1996). According to SNJV (2004a), the difference in the conservative tracer compositions of groundwater on either side of the Purse Fault indicates that two distinct water masses are present in that area. Downgradient from this water level discontinuity, changes in δD and Cl^- values indicate that mixing of these two water masses occurs in the area downgradient from ER-EC-1 and PM-3 toward the Oasis Valley discharge area (SNJV, 2004a).

2.7.1.2 Conservative Tracer Data Evaluation

Representative well sites were selected for the conservative tracer modeling effort. The following section describes the criteria reported by SNJV (2004a) in the selection process to define representative data for use in the conservative tracer modeling. Conservative tracer data for a number of well locations within the Pahute Mesa flow system are summarized in Table 2-20. The range in reported values is indicated for those sites that have been sampled on more than one occasion. The "n" value after each record indicates the number of independent analyses. The data in Table 2-20 have been subdivided into three categories (Pahute Mesa - West of Purse Fault, Pahute Mesa - East of Purse Fault, and "Local" Recharge) to represent the end-member mixing components that are present in the flow system. These components are inferred to mix within the flow system and contribute to groundwater discharge in central Oasis Valley. Conservative tracer data are also presented for the Oasis Valley groundwater discharge area.

Stoller-Navarro Joint Venture (2004a) used various combinations of the conservative tracer data to identify six plausible paths for groundwater flow from Pahute Mesa. These flow paths, and the wells/source areas considered as contributory sources, are described in Table 2-21. The location of

Table 2-20
Statistical Summary of Representative Conservative Tracer Data
(Page 1 of 2)

Site ID	δ D	n	δ ^{18}O	n	Cl^- (mg/L)	n	SO_4^{2-} (mg/L)	n
Pahute Mesa - West of Purse Fault								
ER-EC-1	-116	2	-14.8	2	92 - 97	4	120 - 145	4
ER-EC-2A	-113 / -116	2	-14.9	2	59 - 63	3	87 - 99	3
ER-EC-4	-112 / -115	2	-14.6	2	78 - 95.7	5	110 - 130	5
ER-EC-6	-116	2	-15.0	2	44 - 52	4	56 - 79	4
Pahute Mesa #3 (PM-3)	-116	1	-14.8	1	84.2 - 95.2	2	92.3 - 114	2
Range	-112 / -116	9	-14.6 / -15.0	9	44 - 97	18	56 - 145	18
Mean	-115.2	5	-14.82	5	76.1	5	102.7	5
Median	-116	5	-14.8	5	85.5	5	103.2	5
Pahute Mesa - East of Purse Fault								
ER-20-5 #3 (TYBO)	-114	3	-15.0 / -15.1	4	17.0 - 18.9	4	33.3 - 35.3	4
ER-20-6 #3 (BULLION)	-114 / -115	3	-15.0 / -15.1	4	11.9 - 15.3	4	30.5 - 34.0	4
U-19ba #1	---	---	---	---	40.9	1	10.2	1
U-19q PS#1d (CAMEMBERT)	-113	1	-14.6	1	10.4	1	29.7	1
U-20 Water Well	-113	1	-14.7	1	11 - 12.1	2	31 - 31.5	2
U-20a #2 Water Well	-114	1	-14.75	1	9.5 - 11.2	3	28 - 38.4	3
U-20al (EGMONT)	---	---	---	---	30.5 - 32.8	2	68 - 77.6	2
U-20n PS #1 DDH (CHESHIRE)	-113	3	-14.6 / -15.0	9	11.1 - 14.1	7	26.5 - 35.3	7
UE-18r	-110 / -112	2	-14.6 / -14.7	2	6.3 - 12	4	18 - 24	3
UE-19c Water Well	---	---	-15.0	1	2.4	2	5.8 - 6.2	2
UE-19gs	-113.5	1	-14.5	1	9.9	1	75 - 100	2
UE-19h	-110 / -112	2	-14.4 / -14.8	2	8.5 - 9.7	2	38.2	1
UE-20bh #1	-109 / -112	3	-14.7 / -14.8	3	3.5 - 4.7	3	8.3 - 14	2
Range	-109 / -115	20	-14.4 / -15.1	29	2.4 - 40.9	36	8.3 - 100	34
Mean	-112.8	10	-14.77	11	14.0	13	33.6	13
Median	-113	10	-14.73	11	10.4	13	31.3	13
"Local" Recharge								
NTS Springs	-88 / -101	5	-11.0 / -12.7	5	4.7 - 11	4	7.7 - 33.2	4
Rainier Mesa Tunnel Seeps	-90 / -101	80	-11.9 / -14.2	80	6 - 12	17	7.9 - 28.8	17
NTS Surface Runoff	-82.3 / -88.1	2	-11.3 / -12.4	2	3.2 - 4.3	2	8.3 - 9.0	2
UE-29a Wells	-91	2	-12.6	2	7.7 to 9.0	6	15 - 16.5	6

Table 2-20
Statistical Summary of Representative Conservative Tracer Data
(Page 2 of 2)

Site ID	δ D	n	δ ^{18}O	n	Cl^- (mg/L)	n	SO_4^{2-} (mg/L)	n
Range	-82.3 / -101	89	-11.0 / -14.2	89	3.2 - 12	29	7.7 - 33.2	29
Mean	-91.3	4	-12.39	4	7.1	4	14.8	4
Median	-92	4	-12.28	4	7.7	4	16.1	4
Central Oasis Valley Discharge								
Bailey's Hot Spring	-108 / -110	2	-14.6	2	39.5 - 43.5	7	111 - 119	7
ER-OV-02	-112	1	-14.7	1	49.2 - 53.1	2	86 - 90.2	2
ER-OV-03a	-111	1	-14.7	1	41.6 - 44.6	2	76 - 76.1	2
ER-OV-04a	-109	1	-14.8	1	27.6 - 28.8	3	58.7 - 61	3
Goss Spring	-110 / -112	2	-14.7	2	41.9 - 44.8	3	76 - 77	3
Mullen Spring	-111	1	-14.7	1	42.5 - 45.1	2	76 - 76.7	2
Range	-108 / -112	8	-14.6 / -14.8	8	27.6 - 53.1	19	58.7 - 119	19
Mean	-110.3	6	-14.7	6	41.8	6	82.1	6
Median	-110.5	6	-14.7	6	43.1	6	76.6	6

Source: SNJV, 2004a

Cl^- = Chloride
mg/L = Milligrams per liter
n = Number of independent analyses
SO_4^{2-} = Sulfate
δD = Delta deuterium
$\delta^{18}O$ = Delta oxygen-18

these flow paths are shown in Figure 2-20. Relatively abundant data from the well characterized flow path directly between Pahute Mesa and Oasis Valley (Flow Path 1) suggest that central Oasis Valley discharge consists of 29 to 47 percent groundwater from west of the Purse Fault, 45 to 57 percent groundwater from east of the Purse Fault, with 0 to 16 percent local recharge. Several other potential flow paths for groundwater movement away from Pahute Mesa are also identified by SNJV (2004a) using conservative tracers. While these other flow paths are plausible based on existing data, they exhibit greater uncertainties with respect to contributory water sources because of data limitations (scarcity of wells or lack of diagnostic parameters in key areas).

Table 2-21
Description of Plausible Groundwater Flow Paths in the Pahute Mesa Flow System (SNJV, 2004a)
(Page 1 of 2)

Groundwater and/or recharge source end-member groups (with list of individual well and/or spring locations used in flow-path modeling																							
	Pahute Mesa Groundwater from East of the Purse Fault			**Pahute Mesa Groundwater from West of the Purse Fault**					**Gold Flat/Tonopah Test Range (TTR)**				**NW Groundwater Inflow**	**Timber Mountain Area**		**Local Recharge**	**Oasis Valley**					**Amargosa Valley**	**Crater Flat**
Flow path designation and description	U-20 WW	UE-19h	WW-8	ER-EC-1	ER-EC-2a	ER-EC-4	ER-EC-6	ER-EC-8	Cedar Pass	Sandia #6	Roller Coaster	Rose Spring	Tolicha Peak	ER-EC-7	Coffers Windmill	UE-29a#2	ER-OV-01	ER-OV-03a	ER-OV-04a	ER-OV-05	Springdale	J-12	USW-VH-1
Flow Path 1[a]	Pahute Mesa groundwater + local recharge → Oasis Valley groundwater																						
	M1	M1	M1	M1	M1	M1	M1	M1								R	T	T	T	T	T		
Flow Path 2[b]	Pahute Mesa groundwater + Gold Flat/TTR groundwater + local recharge → Oasis Valley groundwater																						
	M1	M1	M1	M1	M1	M1	M1	M1	M2	M2	M2	M2				R	T	T	T	T	T		
Flow Path 3[c]	Tolicha Peak +/- Pahute Mesa groundwater +/- Gold Flat/TTR groundwater +/- local recharge → Oasis Valley groundwater																						
	M1	M1	M1	M1	M1	M1	M1	M1	M2	M2	M2	M2	M3			R	T	T	T	T	T		
Flow Path 4[d]	Pahute Mesa groundwater + local recharge (in Timber Mountain area) → Beatty Wash to Oasis Valley discharge area																						
	M1	M1	M1	M1	M1	M1	M1	M1						R	R		T	T	T	T	T		
Flow Path 5[e]	Pahute Mesa groundwater + local recharge → flow down Fortymile Wash toward the Amargosa Valley																						
	M1	M1	M1	M1	M1	M1	M1	M1								R						T	
Flow Path 6[f]	Pahute Mesa groundwater + local recharge → Crater Flat																						
	M1	M1	M1	M1	M1	M1	M1	M1						R	R	R							T

Table 2-21
Description of Plausible Groundwater Flow Paths in the Pahute Mesa Flow System (SNJV, 2004a)
(Page 2 of 2)

Table Footnotes:

Source: Modified from SNJV, 2004a

Groundwater mixing components	M1- Pahute Mesa Groundwater, M2- Gold Flat/TTR Groundwater, M3- NW Groundwater Inflow
Recharge components	R- Timber Mountain Area or Local Recharge
Mixing target	T- Mixing target in Oasis Valley, Amargosa Valley, or Crater Flat

[a]This flow path considers mixing of Pahute Mesa groundwater with local recharge to yield central Oasis Valley discharge. Reasonable models for this flow path can be derived using three end-member compositions: (1) Pahute Mesa groundwater from wells east of the Purse Fault, (2) Thirsty Canyon groundwater from wells west of the Purse Fault, and (3) local recharge.
[b]Flow Path 2 represents groundwater from north of Pahute Mesa (Cactus Flat area) mixing with Pahute Mesa groundwater and local recharge and then flowing to Oasis Valley.
[c]Flow Path 3 represents groundwater flow from north of Oasis Valley into Northwest Oasis Valley. Potential mixing sources of inflow to northwest Oasis Valley include groundwater from the Tolicha Peak area, groundwater from the Cactus Flat area north of Oasis Valley, and groundwater from Pahute Mesa. Groundwater in wells ER-OV-05 and Springdale Upper have deuterium values that are significantly different than wells and springs in the rest of the Oasis Valley area, therefore justifying an attempt to identify potential sources for that water.
[d]Flow Path 4 represents groundwater flow from Pahute Mesa to southern Oasis Valley through the Timber Mountain-Beatty Wash area. Local recharge along this flow path may include Timber Mountain recharge (represented by ER-EC-7) and/or recharge from surface water flow in Beatty Wash (represented by UE-29a #1). Well ER-OV-04a is used to represent southern Oasis Valley groundwater because it has the lowest carbon-14 value of the three samples in this area and does not appear to have interacted with shallow local groundwater or been subjected to exchange with soil-zone gases (Thomas et al., 2002).
[e]Flow Path 5 represents groundwater flow from Pahute Mesa down Fortymile Wash toward Amargosa Valley combining with local recharge. Thomas et al. (2002) developed models for groundwater from Wells WW-8 and UE-29a#1 mixing to produce the water chemistry observed at Well J-13.
[f]Flow Path 6 represents groundwater from Pahute Mesa mixing with local recharge and flowing south toward Crater Flat.

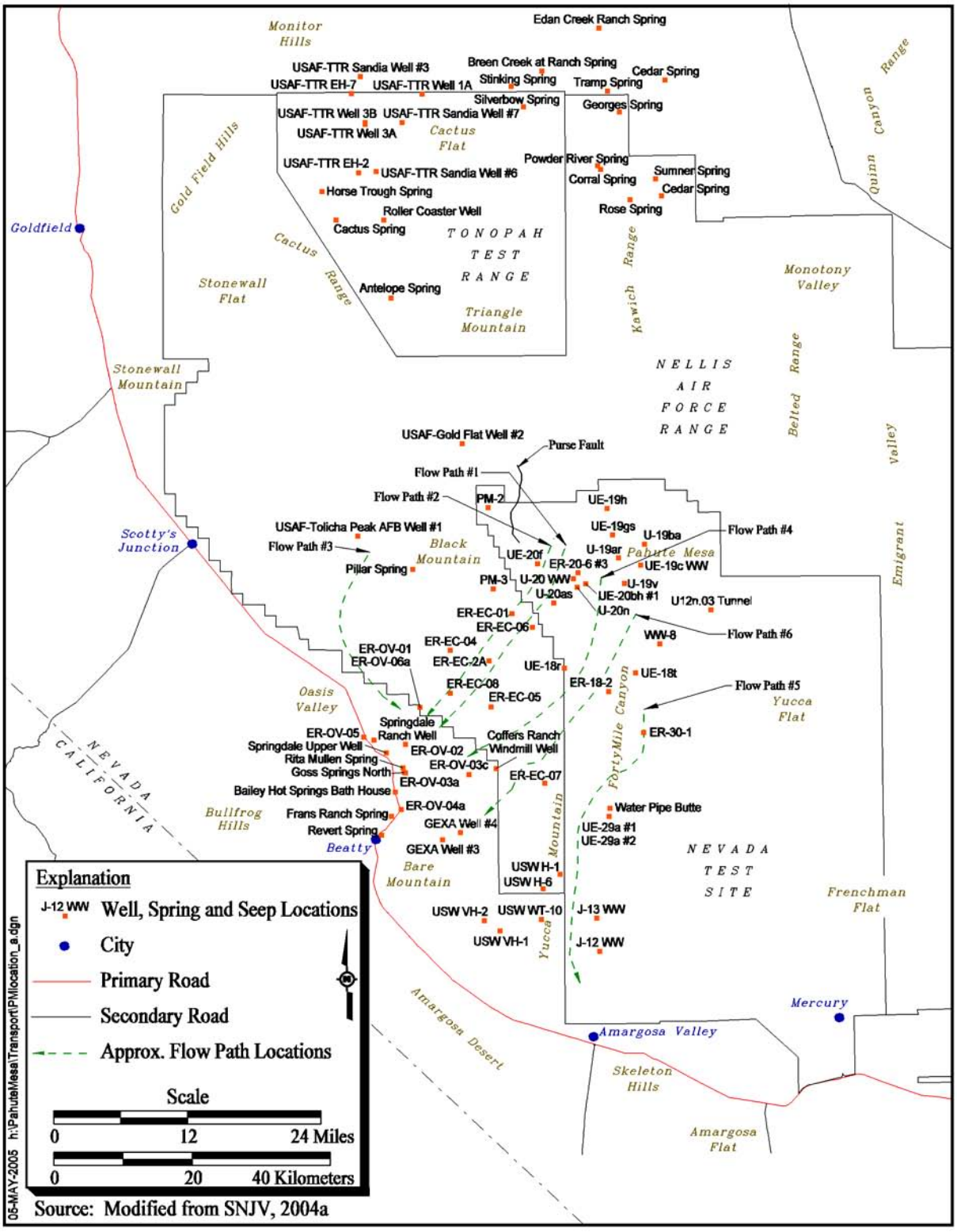

Figure 2-20
Approximate Flow Paths Determined from Conservative Tracer Analyses

2.7.2 Geochemical Modeling

Flow paths defined by SNJV (2004a) based on conservative mixing models were further evaluated using the NETPATH geochemical computer code (Plummer et al., 1994). The NETPATH modeling performed by SNJV (2004a) incorporates data for the ER-EC wells and builds on previous NETPATH modeling done in the Pahute Mesa flow system by Thomas et al. (2002). The geochemical calculations performed using NETPATH were conducted in accordance with procedures described in Plummer et al. (1994) and summarized in SNJV (2004a) and Thomas et al. (2002).

The results of NETPATH geochemical models for the six conceptual flow paths identified by SNJV (2004a), and described in Table 2-21, are summarized (along with the results from the conservative tracer modeling) in Table 2-22. These flow paths are illustrated in Figure 2-20.

The NETPATH program calculates the changes in major ion chemistry that occur along a flow path and determines groundwater-mixing ratios on the basis of chemical mass-balance relationships. The models generated by SNJV (2004a), incorporating new data from the ER-EC wells, provide generally consistent results using both NETPATH and the conservative tracer models presented in Section 2.7.1.2. The variation between results generated by these two methodologies is considered (SNJV, 2004a) to reflect differences in the approach of the two modeling techniques. This variation is also consistent with the natural variability in water chemistry within the system. Whereas the wells used as mixing "end-members" in the respective models are specific in composition, the groundwater compositions within each end-member sub-region or source area of the flow system are more variable, and cannot be completely described using specific individual wells.

Five of six potential groundwater flow paths identified by SNJV (2004a) using conservative tracers also had valid NETPATH models. Valid NETPATH models were not obtained for Flow Path 6, which considered southerly groundwater flow from Pahute Mesa to the Crater Flat area. It was concluded in SNJV (2004a) that insufficient data are available at this time to adequately determine the viability of this flow path. Groundwater travel time estimates generated using delta carbon-13 ($\delta^{13}C$) mass-balance calculations in NETPATH for Flow Paths 1 through 5 range from modern (fewer than 1,000 years) to 3,900 years.

Additional geochemical modeling addressing the evaluation of potential geochemical flow paths is provided in Section 7.0 of this report.

Table 2-22
Summary of Geochemical Flow Path Model Results for the Pahute Mesa Flow System (SNJV, 2004a)
(Page 1 of 2)

Flow Path Designation and Description	Groundwater and/or recharge source and contributory fraction (with flow-path target)								Apparent Travel Time (yrs)
	Pahute Mesa Groundwater from East of the Purse Fault	Pahute Mesa Groundwater from West of the Purse Fault	Gold Flat/Tonopah Test Range (TTR)/Tolicha Peak	Timber Mountain Area	Local Recharge	Oasis Valley	Amargosa Valley	Crater Flat	
Flow Path 1 Pahute Mesa groundwater + local recharge = Oasis Valley groundwater									
Conservative Tracers	0.45 - 0.56	0.39 - 0.42			0.02 - 0.16	Target			
NETPATH	0.39 - 0.57	0.29 - 0.56			0.05 - 0.14	Target			modern (> 1,000) to 3,900
Flow Path 2 Pahute Mesa groundwater + Gold Flat/TTR groundwater + local recharge = Oasis Valley groundwater									
Conservative Tracers	0.09 - 0.12	0.24 - 0.50	0.34 - 0.60		0.33 - 0.42	Target			
NETPATH	0.10 - 0.83	0.10 - 0.40	0.17 - 0.72			Target			modern (> 1,000) to 2,300
Flow Path 3 Tolicha Peak +/- Pahute Mesa groundwater +/- Gold Flat/TTR groundwater +/- local recharge = Oasis Valley groundwater									
Conservative Tracers		0.23 - 0.27	0.73 - 0.77			Target			
NETPATH			1			Target			modern (<1,000) to 1,500
Flow Path 4 Pahute Mesa groundwater + local recharge (in Timber Mountain area) = Beatty Wash to Oasis Valley discharge area									
Conservative Tracers	0.47 - 0.53	0.22 - 0.23		0.24 - 0.31		Target			
NETPATH	0.00 - 0.76			0.24 - 1.0		Target			modern (> 1,000) to 1,600

Table 2-22
Summary of Geochemical Flow Path Model Results for the Pahute Mesa Flow System (SNJV, 2004a)
(Page 2 of 2)

Flow Path Designation and Description	Groundwater and/or recharge source and contributory fraction (with flow-path target)								Apparent Travel Time (yrs)
	Pahute Mesa Groundwater from East of the Purse Fault	Pahute Mesa Groundwater from West of the Purse Fault	Gold Flat/Tonopah Test Range (TTR)/Tolicha Peak	Timber Mountain Area	Local Recharge	Oasis Valley	Amargosa Valley	Crater Flat	
Flow Path 5 Pahute Mesa groundwater + local recharge = flow down Fortymile Wash toward the Amargosa Valley									
Conservative Tracers	0.13 - 0.39			0.05 - 0.29	0.56 - 0.57		Target		
NETPATH	0.08 - 0.37			0.32 - 0.65	0.14 - 0.54		Target		1,000 to 3,800
Flow Path 6 Pahute Mesa groundwater + local recharge = Crater Flat[a]									
Conservative Tracers	0.44 - 0.57	0.00 - 0.02		0.20 - 0.54	0.00 - 0.22			Target	
NETPATH								Target	no valid model

Source: Modified from SNJV, 2004a

[a]No valid NETPATH models were obtained for Flow Path 6; for discussion, see SNJV, 2004a.

3.0 COMPUTER CODE SELECTION

The *Corrective Action Investigation Plan for Corrective Action Units 101 and 102: Central and Western Pahute Mesa, Nevada Test Site Nevada* (DOE/NV, 1999) identified a process for the identification and selection of a numerical code for use in Pahute Mesa flow and transport modeling. This process was completed in 1999, and the FEHM code (Zyvoloski et al., 1997b) was selected as the flow and transport simulator for the Pahute Mesa CAU model. This section provides an overview of the code selection process that supported the selection of the FEHM code. Appendix A provides the 1999 Letter Report that documents the evaluation of flow and transport codes for application to the Pahute Mesa CAUs.

3.1 Code Selection Process

The code selection process was identified in the Pahute Mesa CAIP (DOE/NV, 1999, Section 5.1.2). This process included:

- Identifying a set of desired code attributes.
- Developing a preliminary list of potentially viable codes.
- Evaluating a short list of codes that incorporate key code attributes using a test problem.

The ultimate objective of this code-selection process was to provide a recommendation for the numerical code to use for Pahute Mesa CAU modeling.

3.2 Code Attributes

The Pahute Mesa CAIP (DOE/NV, 1999) identified three objectives for the numerical code used in the CAU model. The first objective requires the CAU model to have the ability to represent the important physical and chemical features of the CAU groundwater flow system. The features include faulting, stratigraphy, sources and sinks of water, the distribution of contaminants and their rates of introduction into the groundwater flow system, and other physical or chemical features unique to the CAU. The second objective requires the CAU model to simulate the movement of a variety of

contaminants for which their distribution and abundance serve to define the contaminant boundary. The third objective requires flexibility in the CAU model to allow grid changes, placement of additional wells, and boundary condition variations.

The required code attributes that were defined to meet these modeling objectives were categorized under "general," "flow model," and "transport model." Table 3-1 summarizes these attributes.

Table 3-1
Required Hydrologic Code Attributes[a]

General Attributes	Flow Model Attributes	Transport Model Attributes
Fully three-dimensional	Saturated groundwater flow	Advection, dispersion, sorption, and matrix diffusion
Large number of nodes (500,000 or more) capability	Heterogeneous and anisotropic hydraulic conductivity	Radioactive decay
Transient capability	Point and distributed sources and sinks of water	Transport of colloids
Multiple boundary condition options	Temperature dependence	
Efficient solver	Simulate complex geology	
Acceptable numerical accuracy		
Minimal numerical dispersion		
Acceptable verification and validation		
Access to source code		

Source: Modified from DOE/NV, 1999

[a]Order of attributes does not indicate order of importance.

In addition, other desirable code attributes were identified including:

- Finite element formulation
- Steady-state capability
- Double-porosity/double-permeability formulation
- Multiple solutes
- Daughter products
- Established pre- and post-processors

The following discussion provides a brief description of these attributes.

General Attributes

The general attributes are defined with the goal of using a code that can closely represent a large modeling domain, in addition to being flexible, user-friendly and efficient.

Fully Three-Dimensional

The groundwater flow system is controlled by the distribution of geologic units as well as the location of sources and sinks of water. Additionally, transport properties including source location and strength, porosity, and diffusion may vary in space. The 3-D nature of the groundwater flow system requires that the CAU model will need to be 3-D to adequately simulate migration of the potential contaminants within the CAU-model area.

Large Numbers of Nodes Capability

For a given formulation, the greater the number of nodes in the CAU model, the greater the detail that can be included. Given the large geographic area of the Pahute Mesa CAU model, the ability of the CAU model to simulate many nodes will control the amount of detail that can be included. In general, each of the selected codes will only be limited by the capacity of the hardware, not by the software used.

Transient Capability

The flow simulations for the CAU model will be steady state. The contaminant transport simulations will all be performed under transient concentration conditions.

Multiple Boundary Condition Options

Options for specified pressure and specified flux boundary conditions for fluids, as well as specified temperature or specified heat flow, may be required in implementing the CAU model.

Efficient Solver

To simulate in sufficient detail, the CAU model will require a large number of nodes as mentioned above. To make a large model practical, the codes must run efficiently. Generally, a code has a selection of solvers available. The solvers must be efficient enough to allow for reasonable simulation times.

Acceptable Numerical Accuracy

The numerical solution of the transport equation is typically more difficult than the solution of the flow equation. This attribute requires the results of the code for a given test problem to have been checked against analytical solutions and also against the results of other numerical codes for the same problem. Documentation of this quality assurance (QA) checking must be available.

Minimal Numerical Dispersion

Under certain circumstances, the error in the numerical approximation of concentration can become as large as the value itself. When this occurs, the numerical solution combines an exclusively numerical dispersion with the real hydrodynamic dispersion, producing an overestimate of the actual dispersion. Solution techniques that minimize numerical dispersion are required.

Acceptable Verification and Validation

The degree of computer code verification and validation varies widely depending on the code being considered. The extent to which this process has been documented for a particular code varies even more. Thoroughly documented testing is required to ensure that the code satisfies requirements specified for its options and features.

Access to Source Code

Computer codes are initially written in a high-level language, such as FORTRAN, and then translated into machine language for execution on the computer. The high-level version of the code is called the "source code," and can be read and modified. The machine-language version is called the "executable code," and can be deciphered only by the computer. Many distributors of computer codes provide only the executable version of the code to the user. During the course of the development or application of the CAU model, it may be necessary to examine or modify the step-by-step procedure implemented in the computer code. To accomplish this, access to the source code will be required.

Groundwater Flow Model Attributes

The attributes for the groundwater flow model are defined with the goal of simulating the flow paths and fluxes.

Saturated Groundwater Flow

The codes must be able to simulate saturated groundwater flow.

Heterogeneous and Anisotropic Hydraulic Conductivity

Aquifer heterogeneity reflects the natural variability in the subsurface. The CAU model must be capable of simulating flow through aquifers in which the hydraulic conductivity may vary from location to location. Anisotropy is a directional dependence of the hydraulic conductivity. In fractured aquifers, it is common for hydraulic conductivity to be larger in a direction parallel to fracturing and smaller perpendicular to fracturing.

Point and Distributed Sources and Sinks of Water

Recharge may occur over a large spatial area due to precipitation or may be concentrated into washes or craters. Discharge may occur at wells or individual springs, or may occur over larger areas such as playas. The CAU model should have the capability to simulate these various cases.

Temperature Dependence

The flow of groundwater may be influenced by water temperature variations. Warm water is more buoyant than colder water and tends to rise. Additionally, warm water is less viscous and tends to move more easily than cold water. These processes may be important in some portions of the CAU where naturally occurring sources of heat have caused elevated groundwater temperatures. An additional source of warm water may be the underground test cavities. It may be important to account for these temperature effects in the simulations.

Simulate Complex Geology

The geology of the Pahute Mesa area is complex. It consists of multiple stratigraphic units, some of which are truncated by faults and other structural features. Even within units, changes in facies result in spatial variations in material properties. The flow of groundwater (amount and direction) is governed, in large part, by the distribution of geologic units. The code must be able to include important features of the geology such as lateral and vertical changes in material properties. Much of this attribute is similar to earlier general attributes related to the number of grid nodes and simulation

speed. The greater the number of nodes, the more detail that can be incorporated into the CAU model.

Transport Model Attributes

The contaminant transport model portion defines the attributes that will be necessary to simulate the migration of potential contaminants including radionuclides and lead.

Advection, Dispersion, Sorption, and Matrix Diffusion

The primary processes of interest in Pahute Mesa that are expected to influence the concentration of radioncludes in groundwater are listed here. The regional contaminant transport model (IT, 1996e) simulations and the Value of Information Analysis (IT, 1998b) showed that advection (via the groundwater flux) and matrix diffusion were the primary factors influencing tritium transport. It is expected that sorption will also be important for reactive contaminants, but this may not be the dominant contributor to the location of contaminant boundary. Dispersion was not shown to be of primary importance in the regional simulations, but is included here because it may be more important at smaller scales.

Radioactive Decay

Most, but not all, of the potential contaminants of interest are radionuclides. The activity per volume of radionuclides decreases via the process of radioactive decay.

Transport of Colloids

The movement of colloids may enhance the movement of otherwise immobile contaminants. Colloids are submicron size particles to which radionuclides or other solutes sorb. The colloids are then transported via the groundwater flow, and the sorbed solutes move with the colloids. Currently, no known contaminant transport codes explicitly simulate the transport of colloids. Thus, this attribute will only be considered if codes that simulate colloid transport are available at the time of the code selection.

Desirable Attributes

Other attributes that were identified during the code selection process address both technical capabilities and code characteristics.

Finite Element Formulation

A finite element formulation allows much more flexibility in representing the geology being modeled. Grids can be developed to represent complex structures such as faults, pinchouts and layer truncations. In addition, grid refinement allows the grid to be modified to provide more resolution in the area of interest.

Steady-State Capability

Some of the codes do not include a steady flow option, but rather reach steady-state by leaving parameters fixed in time and performing transient simulations over large periods of time until steady state is reached. This approach is adequate, but somewhat slower than if a true steady-state option were available.

Double-Porosity/Double-Permeability Formulation

The double-porosity/double-permeability method is similar to the dual-porosity method in that it allows for communication between fractures and matrix material. This feature allows for the modeling of matrix diffusion. The double-porosity/double-permeability method differs in that it allows matrix cells that communicate with fractures to also communicate with other matrix cells. While this method provides a more realistic simulation, its use is more important for unsaturated flow problems.

Multiple Solutes

Many codes are designed to provide a simulation of the migration of a single solute in a given run. Using a code with the ability to model transport for multiple solutes in a single run may be more efficient.

Daughter Products

A radionuclide may decay into another radionuclide (called a daughter product) or into a stable isotope. More accurate estimates of dose can be obtained if the code is capable of simulating the ingrowth and transport of a radionuclide and daughter product(s).

Established Pre- and Post-Processors

The task of creating the input datasets for any model is simplified by having pre-processors take data and put them into a form that is required by the model. Post-processors take model output and typically create graphic images of some simulated parameter such as water level or solute concentration. Pre- and post-processors generally speed up the modeling task. If the processors are not available, then the appropriate processors would be developed.

3.3 Code Testing Criteria

The criteria used to assess the codes were defined in the CAIP for Pahute Mesa (DOE/NV, 1999). These criteria range from a somewhat subjective assessment of ease of use to more quantifiable assessments such as the run time for a sample problem. The testing criteria are as follows:

Ability To Represent the CAU Hydrogeology

The primary geologic features that control flow need to be represented in the CAU model. These features include the hydrostratigraphy, physical boundaries, and structural features such as faults. In addition, the ability to model physical processes of concern (e.g., advection, dispersion, matrix diffusion, adsorption, and radioactive decay) is also important. The criteria also include an assessment of the ability of the model to include sufficient detail and stay within the memory limitations of the computer platform chosen for simulation.

Portability

The CAU model may be sent to independent reviewers as well as the State of Nevada. Each of these stakeholders may want to run the code themselves. This requires that the code, when complete, should require minimal special equipment or software in order to make it usable. Additionally, the CAU model will likely need to be run on a classified computer at the NNSA/NSO or another approved secure location to produce a final estimate of the contaminant boundary (results based on

classified data will be reported in a classified report). The code and associated pre- and post-processors must be portable to the selected secure location to allow for efficient classified simulations.

Quality Assurance Evaluation

The chosen code must have been appropriately verified to ensure the output is accurate. The QA evaluation refers to the level of documentation and testing for a code. The ability of the code to simulate the processes of interest is a function of the formulation of the equations and the quality of the programming. A code meets the QA requirements if its results have been verified against those of other codes as well as compared with analytical solutions. These comparisons must be documented before a code will be used for the Pahute Mesa model.

Ease of Use

The ease of use is a subjective judgment that assesses the modeler's degree of difficulty in getting the model running. This is, by necessity, a value judgment of the modeler and reflects the modeler's experience and background. A great deal of work will be spent calibrating the CAU model and setting up sensitivity and uncertainty analyses. A code that is difficult to use makes the job of calibration more difficult and reduces the code's portability. Ease of use includes factors such as the structure of the input datasets used in the model and the flexibility of pre- and post-processors.

Speed of Simulation

The time required for a solution is also of importance to the evaluation of the codes. The faster the code, the shorter the time to complete each model run. As calibration normally requires many (often greater than 500) model runs, the simulation time becomes a problem if it is too long. To enhance calibration performance, simulation times should be as short as possible. In addition, the ability to carry out model runs in parallel by distributing them across a network can greatly enhance calibration efficiency.

3.4 Initial Screening of Candidate Codes

The Pahute Mesa CAIP (DOE/NV, 1999) identified 14 numerical codes as possible candidates for Pahute Mesa CAU modeling. These codes were:

- AQUA3D (Vatnaskil Consulting Engineers, 1988)
- BIOF&T-3D (Katyal, 1995)
- CFEST (Gupta, 1996)
- FEHM (Zyvoloski et al., 1996)
- FRAC3DVS (Waterloo Hydrogeologic Inc., 1998)
- HST3D (Kipp, 1986)
- MODFLOWT (Duffield et al., 1996)
- MT3D96 (Scientific Software Group, 1998)
- NUFT (Nitao, 1998)
- PARFLOW (Ashby, et al., 1996)
- PORMC (Westinghouse Hanford Co., 1991)
- SWIFT-98 (HSI GeoTrans, 1998). Note this version of SWIFT was identified as a newer version than SWIFT III (HSI GeoTrans, 1990)
- TOUGH2 (Pruess, 1991)
- 3DFEMFAT (Scientific Software Group, 1998)

An initial screening of the codes was performed with respect to the attributes. The results of the comparison are presented in Table 3-2.

Table 3-2
Comparison of Candidate Codes by Attribute
(Page 1 of 2)

Code Attribute	AQUA3D	BIOF&T-3D	CFEST	FEHM	FRAC3DVS	HST3D	MODFLOWT	MT3D96	NUFT	PARFLOW	PORMC	SWIFT-98	TOUGH2	3DFEMFAT
GENERAL														
Fully three-dimensional	Y[a]	Y	Y	Y	Y	Y	Y	Y	Y	Y	Y	Y	Y	Y
Large number (500,000) of nodes	?[b]	Y	Y	Y	Y	?	Y	Y	Y	Y	Y	Y	Y	Y
Transient capability	Y	Y	Y	Y	Y	Y	Y	Y	Y	Y	Y	Y	Y	Y
Multiple boundary condition options	Y	Y	Y	Y	Y	Y	Y	Y	Y	Y	Y	Y	Y	Y
Efficient solver	Y	Y	Y	Y	Y	?	Y	Y	Y	Y	Y	Y	Y	Y
Acceptable numerical accuracy	Y	Y	Y	Y	Y	?	Y	Y	Y	Y	Y	Y	Y	Y
Minimal numerical dispersion	Y	Y	Y	Y	Y	?	Y	Y	Y	Y	Y	Y	Y	Y
Acceptable verification and validation	Y	Y	Y	Y	Y	?	Y	Y	Y	Y	N	Y	Y	Y
Access to source code	N[c]	N	N	Y	Y	Y	Y	Y	N	Y	Y	Y	Y	N
FLOW MODEL														
Saturated groundwater flow	Y	Y	Y	Y	Y	Y	Y	N	Y	Y	Y	Y	Y	Y
Heterogeneous hydraulic conductivity	Y	Y	Y	Y	Y	?	Y	N	Y	Y	Y	Y	Y	Y
Anisotropic hydraulic conductivity	Y	Y	Y	Y	Y	?	Y	N	Y	Y	Y	Y	Y	Y
Point/distributed sources/sinks of water	Y	Y	Y	Y	Y	Y	Y	N	Y	Y	Y	Y	Y	Y
Temperature dependence	Y	N	Y	Y	N	Y	N	N	Y	N	Y	Y	Y	N
Ability to simulate complex geology	Y	Y	Y	Y	Y	?	Y	Y	Y	Y	Y	Y	Y	Y
TRANSPORT MODEL[d]														
Advection	Y	Y	Y	Y	Y	Y	Y	Y	Y	N	Y	Y	Y	Y
Dispersion	Y	Y	Y	Y	Y	Y	Y	Y	N	N	Y	Y	N	Y
Sorption	Y	Y	Y	Y	Y	Y	Y	Y	Y	N	Y	Y	N	Y
Matrix diffusion	Y	Y	N	Y	Y	N	Y	N	Y	N	N	Y	N	N
Radioactive decay	Y	Y	Y	Y	Y	Y	Y	Y	Y	N	Y	Y	Y	Y

Table 3-2
Comparison of Candidate Codes by Attribute
(Page 2 of 2)

Code Attribute	AQUA3D	BIOF&T-3D	CFEST	FEHM	FRAC3DVS	HST3D	MODFLOWT	MT3D96	NUFT	PARFLOW	PORMC	SWIFT-98	TOUGH2	3DFEMFAT
OTHER DESIRABLE ATTRIBUTES														
Finite element formulation	Y	Y	Y	Y	Y	N	N	N	N	N	N	N	N	Y
Steady-state capability	N	N	N	Y	Y	?	Y	Y	N	N	Y	Y	N	N
Double-porosity/double-permeability	N	N	N	Y	N	N	N	N	Y	N	N	N	Y	N
Multiple solutes	N	Y	?	Y	Y	N	N	N	Y	N	N	N	N	N
Daughter products	N	Y	N	Y	Y	N	Y	Y	Y	N	N	Y	N	N
Established pre- and post-processors	Y	Y	Y	Y	Y	?	Y	Y	Y	Y	Y	Y	Y	Y

Source: Modified from DOE/NV, 1999

[a]Y = Yes
[b]? = No data
[c]N = No
[d]The transport of colloids was not considered during the code selection process.

Of this list, 10 codes were eliminated from further consideration. Seven codes (CFEST, HST3D, MT3D96, PARFLOW, PORMC, TOUGH2, and 3DFEMFAT) were eliminated because they do not have the ability to simulate matrix diffusion explicitly. The BIOF&T-3D and AQUA3D codes were eliminated because access to the source codes was not available. The NUFT code was eliminated because current documentation (Nitao, 1998) indicated that hydrodynamic dispersion was not implemented in the code.

Of the remaining four codes, only FEHM and SWIFT-98 have all of the required attributes. The FRAC3DVS and MODFLOWT codes lacked only the ability to simulate thermal effects. The FRAC3DVS code was ranked above MODFLOWT and retained for testing because its finite element formulation would allow a more accurate representation of the complex geology. Therefore, the three codes that were retained for further evaluation are FEHM, FRAC3DVS, and SWIFT-98.

3.5 Description of Selected Candidate Codes

Features of the three codes identified as possible candidates for use in the Pahute Mesa CAU model are described below.

FEHM

The FEHM code (Zyvoloski et al., 1997b) was developed by LANL. The FEHM code simulates 3-D, time-dependent, multiphase, nonisothermal flow, and multicomponent reactive groundwater transport through porous and fractured media. The FEHM finite-element formulation allows for representation of complex 3-D geologic media and structures and their effects on subsurface flow and transport. The hydrologic source term, recharge, lateral boundary conditions, and parameter values are inputs to FEHM. The FEHM output consists of spatial distribution of head and concentration at specified times and concentration with time through specified boundaries and planes. The transport processes of interest include advection, dispersion, sorption, matrix diffusion, radioactive decay, colloid-facilitated transport, and daughter product ingrowth. Specific capabilities include:

- Three-dimensional
- Flow of gas, water, oil, and heat
- Flow of air, water, and heat
- Multiple chemically reactive and sorbing tracers
- Colloid transport

- Finite element/finite volume formulation
- Coupled stress module
- Saturated and unsaturated media
- Preconditioned conjugate gradient solution of coupled nonlinear equations
- Double-porosity and double-porosity/double-permeability capabilities
- Complex geometries with unstructured grids

A number of documents supporting the FEHM code are readily available from LANL. In addition to the user's manual (Zyvoloski, et al., 1997a), these documents include a description of the mathematical models and numerical methods used by FEHM (Zyvoloski, et al., 1997b); documentation of the functional and performance requirements for FEHM; description of the FEHM software, the verification and validation plan; and description of the verification and validation activities (Dash et al., 1997; Dash, 2000 and 2001).

FRAC3DVS

FRAC3DVS (Waterloo Hydrologic, Inc., 1998) is a 3-D, finite element code for simulating steady-state or transient, variably-saturated groundwater flow, and advective-dispersive solute transport in porous or discretely-fractured porous media. The code was developed by E.A. Sudicky at the Waterloo Centre for Groundwater Research and R. Thierren at Laval University. Specific capabilities of this code include:

- Three-dimensional
- Flow of water
- Multi-species transport of either straight or branching decay chains
- Sorption according to a linear or Freundlich isotherm
- Control-volume finite element, Galerkin finite element, or finite difference formulation
- Saturated and unsaturated media
- Conjugate-gradient-like solver
- Dual-porosity and discrete fracture capabilities
- Irregular, layered grids composed of blocks or prisms

SWIFT

The Sandia Waste Isolation Flow and Transport (SWIFT) computer code (Reeves et al., 1986; Ward et al., 1984; HSI GeoTrans, 1990) is a 3-D groundwater flow and transport model that simulates the movement of solutes, including radionuclides, in groundwater. The code is finite-difference and includes fluid flow, heat transfer, and brine transport in saturated porous media.

The SWIFT code evolved from the USGS Survey Waste Injection Program (SWIP) Code (Intercomp, 1976) and has undergone several modifications since its inception. The version of the SWIFT code used in this code comparison is SWIFT-98 (HSI GeoTrans, 1998). Specific capabilities include:

- Simulation of advective-dispersive transport with adsorption and decay
- Simulation of transport in fractured media via a dual-porosity/dual-permeability conceptualization
- Simulation of brine and heat transport in porous or fractured formations
- Inclusion of variable fluid density and variable fluid viscosity
- Accounts for leaching of waste
- Includes a wellbore submodel that simulates energy losses in and surrounding a borehole
- Simulation of planar or spherical matrix block geometry
- Specification of longitudinal, transverse, and vertical dispersivities
- Variable decay rates, retardation factors, and porosities available for transport simulations
- Radioactive decay and simultaneous simulation of up to three daughter products
- Transient and steady-state flow and transport options available
- Can choose time-stepping either as centered in time or backward in time
- A direct or two-line successive, over-relaxation method of solving the governing equation

3.6 Test Problem Used To Evaluate Candidate Codes

The features of the test problem used to evaluate the three candidates codes were chosen to represent conditions expected in the Pahute Mesa model area. The features included in the test problem were: complex caldera geology such as lithologic and structural features, temperature-dependent flow, radionuclide migration from a cavity, and matrix diffusion.

The test problem was designed to represent the expected level of complexity anticipated for Pahute Mesa. The Pahute Mesa hydrostratigraphic model (Drellack and Prothro, 1997) provided the definition and distribution of HSUs for the test problem. A portion of the model area was selected for

the test problem as representative of the complex geology of the Pahute Mesa CAU. The test problem model area was approximately 21 km (13.1 mi) by 19.5 km (12.1 mi) by 5,500 m (18,045 ft) in depth. The locations of the test problem boundaries are shown in Figure 3-1. The 3-D hydrostratigraphic model is shown in Figure 3-2 as viewed from the southwest corner of the test problem area. A cross-section of the test area (Figure 3-3) shows the complexity of the hydrostratigraphic layering and the occurrence of non-vertical faults.

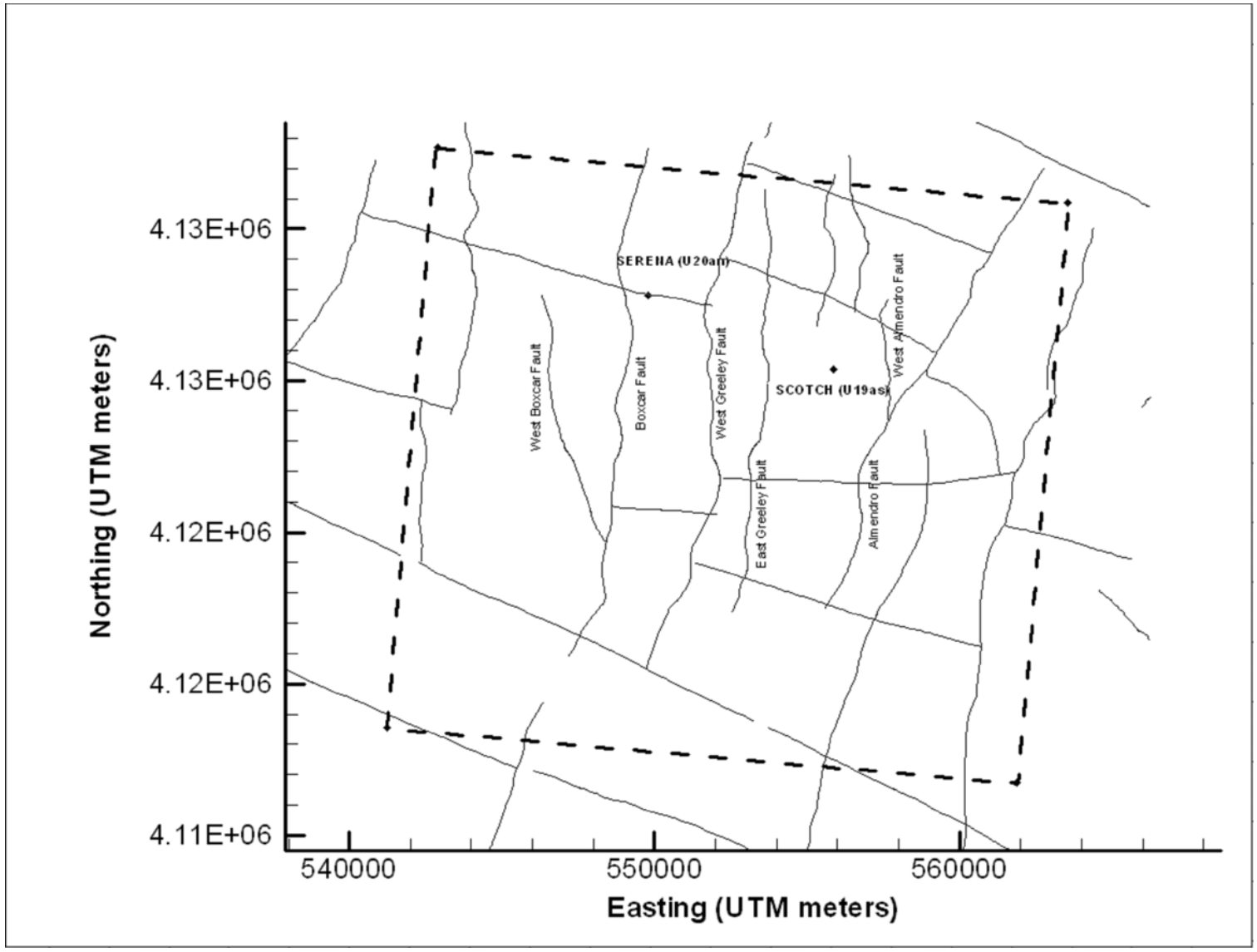

Figure 3-1
Code Evaluation Test Problem Boundaries, Selected Faults, and Locations of SERENA (U20an) and SCOTCH (U19as) Tests

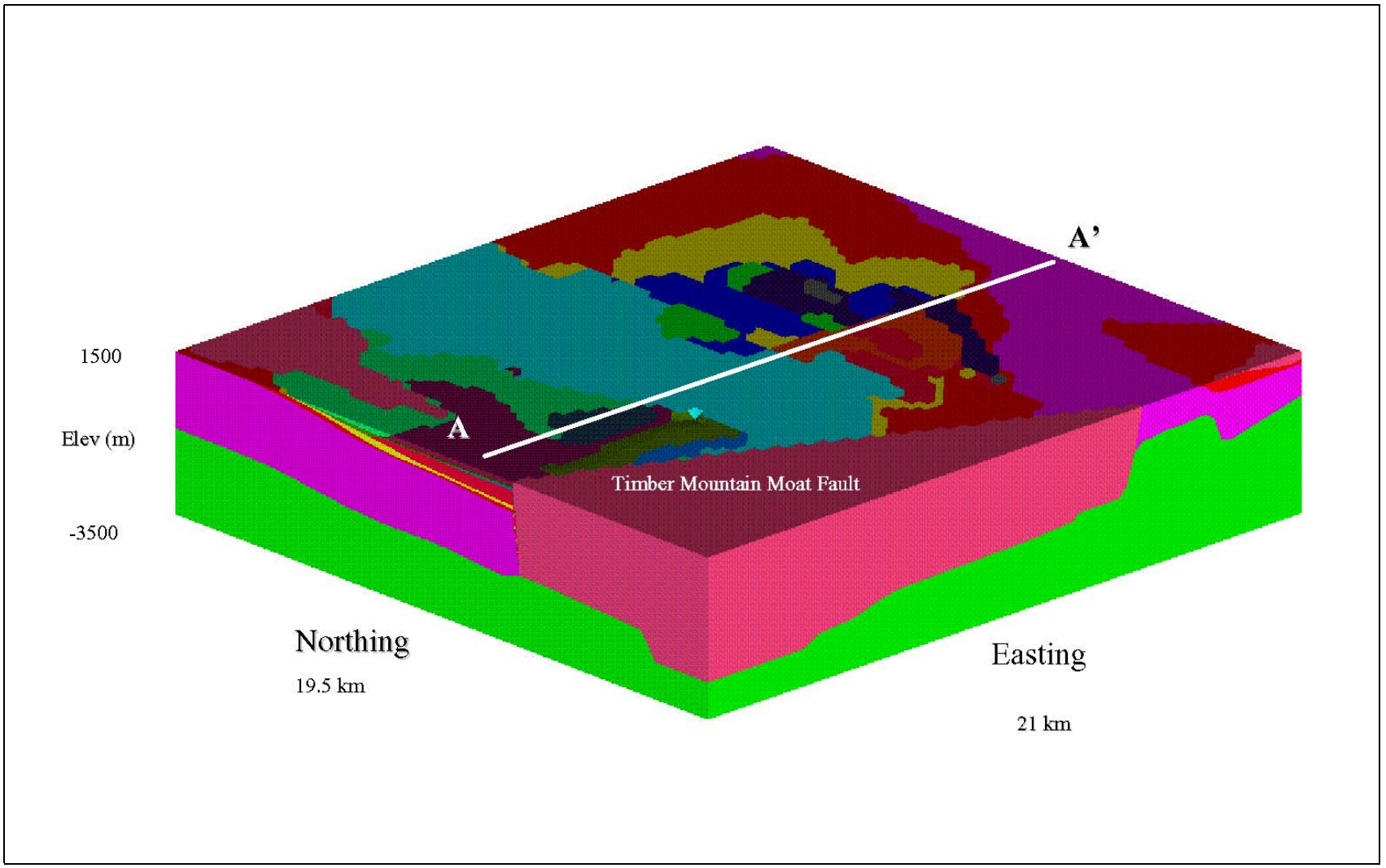

Figure 3-2
3-D Hydrostratigraphic Model Used for the Code Evaluation Test Problem
View is from the southwest.

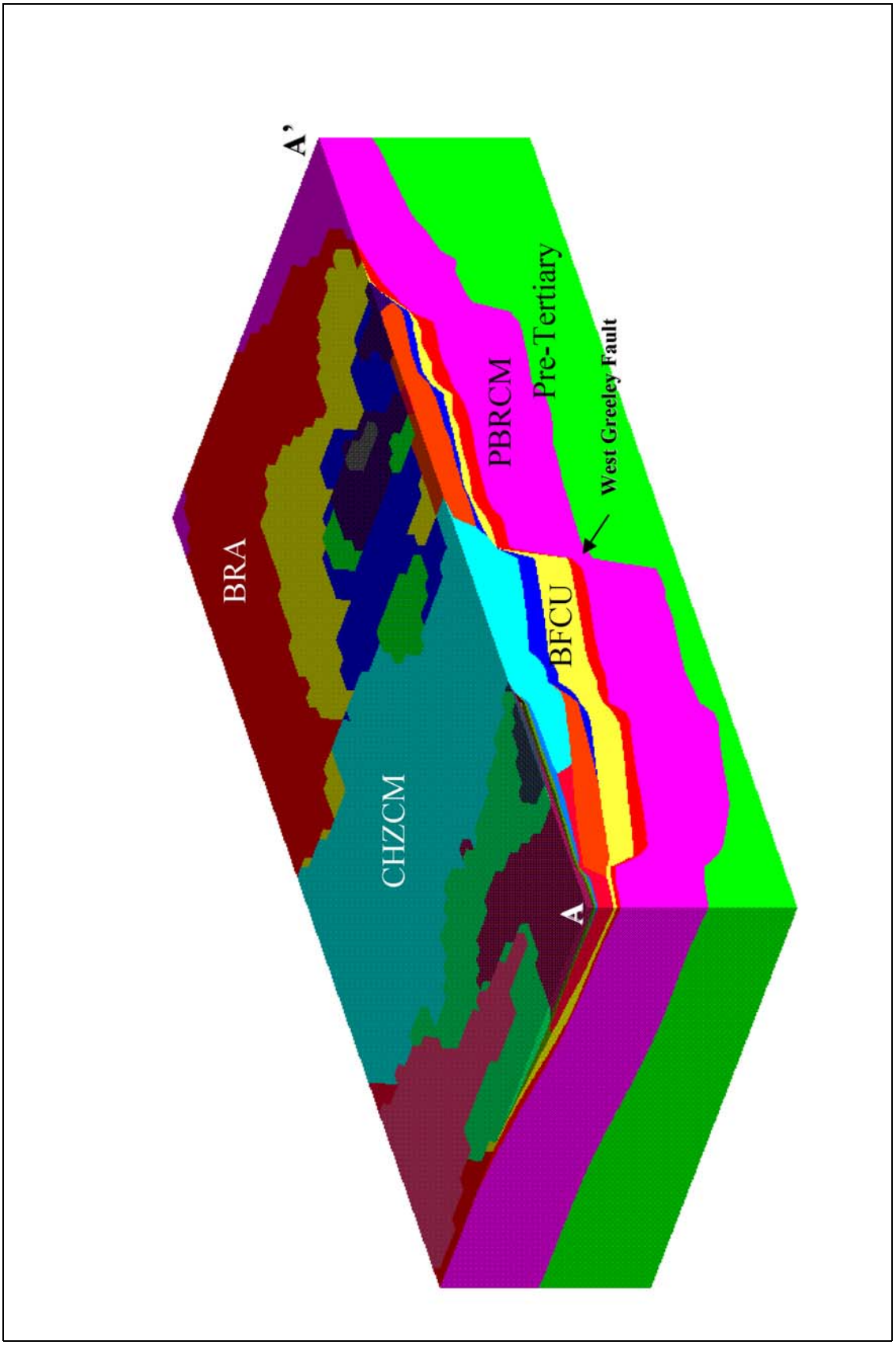

Figure 3-3
Schematic Representation of a Cross Section Through Test Problem Domain as Viewed from the Southwest
Units identified are BFCU, BRA, CHZCM, PBRCM, and Pre-Tertiary rocks.

The hydrogeologic model for the test problem included many of the hydrostratigraphic layers and faults in the Pahute Mesa hydrogeologic model. When using finite-element codes, the grid flexibility is used to attempt to reproduce the stratigraphic contacts and fault contacts. Finite-difference codes do not offer this flexibility; several identical horizontal and uniform grids must be stacked vertically to represent the model layers. As a result of this limitation, faults must be represented as vertical. The present Pahute Mesa geologic model explicitly accounts for dipping faults. As such, the location of a fault shifts, in plan view, for various layers. Thus, to use the finite-difference grid in the test problem, the faults will be approximated as vertical.

Each of the HSUs was assigned a hydraulic conductivity, porosity, and fracture volume fraction consistent with current best estimates of these properties. Parameter values used for the test problem are shown in Table 3-3.

Boundary conditions for the test problem were obtained from the UGTA regional flow model (DOE/NV, 1997). The process used was to average the properties of the Pahute Mesa hydrogeologic model to the same resolution as the regional model. The HSUs from the Pahute Mesa hydrogeologic model were then added to the regional model. A visualization application, EV, was used to examine the correspondence between the CAU-scale model and the regional model. All layers were checked for inversions of layers and that a constant elevation of at least 1 m vertically was maintained in the hydrogeologic model layering. Using this modified regional hydrogeologic model, the UGTA regional flow model (DOE/NV, 1997) was run, without recalibration, to obtain the heads along the boundaries of the test problem. Figure 3-4 shows the head distribution for the northern boundary of the test problem.

Two underground nuclear tests were chosen for consideration as sources in the test problem, SERENA (U20an) and SCOTCH (U19as). The locations of these tests are shown in Figure 3-1. SERENA was chosen because of its location on a fault, and SCOTCH was chosen because of the depth of the working point and the absence of faults in the immediate vicinity in the Pahute Mesa hydrogeologic model. Because the location of SCOTCH is within the BFCU, very little transport was expected. To provide a better test for the codes, additional simulations considered the source to be translated vertically upward to the location of the CHVTA.

Table 3-3
Summary of HSU/Fault Parameter Values Used in the Test Model

HSU or Fault	HSU[a]	Permeability Range (m/d)[a]	Permeability (m/d) (PM Test Problem)	Fracture Volume Fraction	Matrix Porosity
Timber Mountain Aquifer	TMA	1.0-30	1.000	0.001	0.1
Timber Mountain Composite Unit	TMCM	0.001-0.5	0.014	0.01	0.1
Windy Wash Aquifer	WWA	1.0-20	1.000	0.01	0.1
Paintbrush Vitric-Tuff Aquifer	PVTA	0.1-1	0.100	0.01	0.3
Benham Aquifer	BA	1.0-20	1.000	0.01	0.1
Upper Paintbrush Confining Unit	UPCU	0.001-0.5	0.007	0.01	0.3
Tiva Canyon Aquifer	TCA	0.5-0.1	0.500	0.001	0.1
Paintbrush Lava-Flow Aquifer	PLFA	1.0-20	1.000	0.01	0.1
Lower-Paintbrush Confining Unit	LPCU	0.001-0.5	0.011	0.01	0.3
Topopah Spring Aquifer	TSA	5.0-30	30.000	0.001	0.1
Calico Hills Vitric-Tuff Aquifer	CHVTA	0.1-1	0.100	0.01	0.3
Calico Hills Vitric Composite Unit	CHVCM	0.1-20	0.100	0.005	0.2
Calico Hills Zeolitized Composite Unit	CHZCM	0.001-15	0.003	0.01	0.3
Calico Hills Confining Unit	CHCU	0.001-0.5	0.001	0.01	0.3
Inlet Aquifer	IA	0.1-5	2.010	0.01	0.1
Crater Flat Composite Unit	CFCM	0.001-5	5.000	0.01	0.2
Crater Flat Confining Unit	CFCU	0.001-0.5	0.001	0.01	0.3
Kearsarge Aquifer	KA	0.1-5	2.000	0.01	0.1
Bullfrog Confining Unit	BFCU	0.001-0.5	0.001	0.01	0.3
Belted Range Aquifer	BRA	0.5-15	0.500	0.005	0.1
Pre-Belted Range Composite Unit	PBRCM	0.001-0.01	0.001	0.005	0.2
Pre-Tertiary	PreT	-	0.000085	-	-
Moat Fault	N/A	0.0000075-75	75		
South Boxcar Fault	N/A	0.0000075-75	75		
West Boxcar Fault	N/A	0.0000075-75	75		
East Boxcar Fault	N/A	0.0000075-75	75		

[a]Drellack and Prothro, 1997

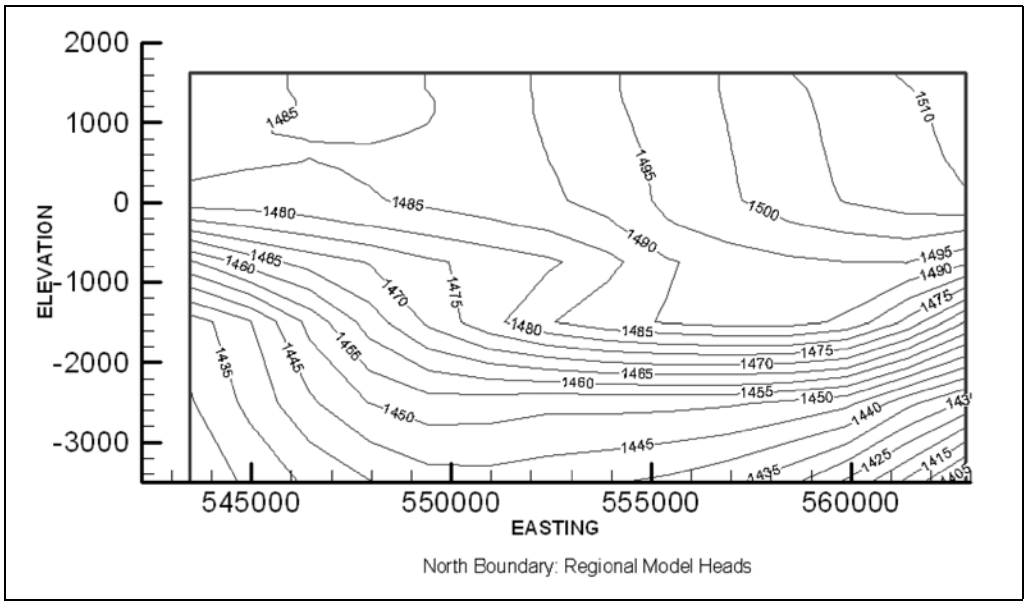

Figure 3-4
Head Distribution for the North Boundary of the Test Problem Domain from the UGTA Regional Model

The unclassified hydrologic source term used for these sources in the test problem was developed by Tompson et al. (1999) for CAMBRIC. Four radionuclides were considered: tritium, strontium (Sr)-90, plutonium (Pu)-239, and americium (Am)-241. A total of 2.04 moles of tritium were introduced instantaneously as a pulse. The other radionuclides entered the flow system as a time-varying flux as determined by Tompson et al. (1999). Tritium and Sr-90 were treated as non-sorbing. Plutonium-239 and Am-241 were assigned distribution coefficient (K_d) values of 50 and 100 liters and kilograms, respectively. These values are consistent with the Frenchman Flat CAU model (IT, 1999, Table 9-1). Analysis of the BULLION Forced-Gradient Experiment (FGE) (IT, 1998a) suggested values of dispersivities of 10, 3, and 2 m for longitudinal, transverse, and vertical directions, respectively. Because this experiment involved transport on the scale of 100 m, dispersivities were increased to 50 and 5 m for longitudinal and transverse directions for the Frenchman Flat CAU model. Consistent with the Frenchman Flat CAU model, dispersivities used for the Pahute Mesa test problem were 50 and 5 m.

The local geothermal gradient was included in the test problem for the two codes that account for temperature dependence. The value of the selected geothermal gradient was 0.0257 degrees Centigrade per meter.

The test problem was simulated without calibration, in some cases using extreme values of properties and hydrologic source terms in order to test the capability of the codes. With this in mind, it is important to note that the results of test problem simulations should not in any way be interpreted as accurately representing the magnitudes of flow and transport processes associated with the Pahute Mesa CAU.

3.7 Results of Code Evaluation

Flow and transport models of the defined test problem were developed and implemented using FRAC3DVS, SWIFT-98, and FEHM. The experience gained in developing these models and the assessment of output from each model provided the information that was used in the code evaluation process. This evaluation process included:

- Evaluation of the capabilities of each code to successfully model the test problem.
- Comparison of SWIFT-98 and FEHM models relative to the testing criteria detailed in Section 3.3.
- Identification of the recommended code for use in Pahute Mesa CAU flow and transport modeling.

3.7.1 Evaluation of Code Capabilities

During the evaluation of the FRAC3DVS transport model output, problems were identified in the simulation of non-decaying, non-sorbing tracers. The model output was characterized by alternating bands of positive and negative concentrations, and solute mass-balance errors as high as 10 percent when the sources were modeled at their working points. When the source was translated upward to the aquifer unit, mass-balance errors were as large as 100 percent due to the model simulating movement of the tracer into the unsaturated zone. In addition, the tested version of FRAC3DVS did not support specification of solute flux at nodes in the interior of the model domain and could not simulate thermal effects. Based on these issues, FRAC3DVS was eliminated from further consideration.

The evaluation of the flow and transport model output results for SWIFT-98 and FEHM simulations were satisfactory and demonstrated the required code capabilities.

3.7.2 Comparison of SWIFT-98 and FEHM Relative to the Testing Criteria

Ability To Represent CAU Hydrogeology

A major difference between FEHM and SWIFT-98 was how the hydrogeologic model was represented by the computational grid. The SWIFT-98 code is a finite-difference program and, as such, is not as flexible as a finite-element model at capturing the geometric shape of the individual HSUs. The FEHM code is a finite-element code that can more accurately represent complex hydrostratigraphy.

The rectangular prism-type blocks used for the SWIFT-98 grid can be defined by rows, columns, and horizontal layers, or in a stair-step fashion by rows and columns with the top elevation of the uppermost block. The latter method allows for flexibility in defining the layering of a system, but not the discretization in the plan view. In plan view, all blocks along a column or a row must have the same width. In the SWIFT-98 test simulations, a simpler horizontal layering scheme was utilized. The change of hydrologic properties with depth as defined by HSUs was implicitly considered in block properties by averaging all of the different HSU properties contained in each finite difference block. When a block contained material from more than one HSU a composite property was generated using a pre-processor. The pre-processor also considers the influence of faults and fault zones by combining fault properties with the porous media properties generated from the hydrogeologic model. Fault properties are combined in parallel to porous-media block properties in the direction of the faults and in series perpendicular to the fault. The trace of all faults is assumed to follow a path from block center to block center parallel (or perpendicular to the block faces). The block structure of the grid does not allow for non-vertical faults.

The grid generation tools interfaced with the FEHM code allowed for the accurate representation of the complexities of the hydrogeologic model for Pahute Mesa. The hydrostratigraphic structure as provided by the hydrogeologic model was captured in the finite-element grid. This included units of variable thickness and units that pinch out. Faults were included through a method that creates fault planes from surface maps of faults. With this method the specific offset across a fault was only as accurate as the resolution of the geologic model. While faults for the test problem were vertical, faults may be specified as non-vertical. Higher resolution of the grid was provided in source and

down gradient regions. The exact specification of HSUs eliminates the need to use composite properties in the model.

For this testing criteria element, FEHM was ranked above SWIFT-98 because it more accurately represented the CAU hydrostratigraphy.

Portability

The SWIFT-98 code was designed to run on personal computer (PC)-based Pentium processors and was specifically designed for use in conjunction with the Lahey LF90 Fortran compiler. The associated pre- and post- processors are also designed to run on Pentium processors. The only restriction on these codes involves GEO2MOD, which generates a binary input file for SWIFT-98 and required the Lahey LF90 Fortran compiler for compatibility if recompilation was necessary. All the other pre- and post-processors could be compiled with any Fortran compiler. Results of the simulations were saved in ASCII map files which could be converted to a format that could be used in any standard contouring package. For the test problem, EXCEL® macro programs were used to plot the results of simulations.

Computational mesh generation tools used with FEHM included the Los Alamos Grid Toolbox (LaGriT) (George, 1997) suite of grid meshing tools. LaGriT is a library of user callable tools that provide mesh generation, mesh optimization and dynamic mesh maintenance in 3-D for a variety of applications. LaGriT and associated applications required a UNIX-based platform. The software, user's manuals, and examples were available at no cost from LANL. However, considerable training is required to use these tools effectively. The FEHM code was available for a number of platforms, including PC. However, the application of FEHM to the test problem was conducted on a workstation computer with twin 400 megahertz Pentium II Xeon processors and 1 gigabyte of physical memory. A post-processor that runs on a PC was available to convert FEHM output files into a format readable by visualization software such as TECPLOT®.

For this testing criteria element, SWIFT-98 was ranked above FEHM because it required less specialized hardware and software.

Quality Assurance Evaluation

The SWIFT genre of codes had undergone verification and field comparison (validation) testing during their development and maintenance by Sandia National Laboratories (Ward et. al., 1984). The SWIFT-98 code, which was maintained by HSI GeoTrans, Inc., had also undergone the same testing procedure as described in Ward et al. (1984). Additionally, all changes made to the code have been tested. The testing was concluded March 1998. All test problems were included on the compact disc release of the code.

The FEHM code was subjected to an extensive verification and validation effort and is maintained in a formal software configuration management system. The verification and validation plan were provided in detail by Dash et al. (1997). The objective of the verification was to test the options and features of the code. This was accomplished by comparing the results of simulations with published analytical solutions and results from other codes. Every time a modification is made to the code, it is tested with a suite of verification problems to ensure no errors were introduced or capabilities eliminated. The tests considered in the verification effort were described in detail by Dash et al. (1997), and test results were discussed. A number of additional documents supporting FEHM were readily available from LANL. These documents included the user's manual (Zyvoloski, et al., 1997a), and a description of the mathematical models and numerical methods used by FEHM (Zyvoloski, et al., 1997b).

For this testing criteria element, FEHM was ranked above SWIFT-98 because it was maintained under a formal LANL software configuration management system.

Ease of Use

The SWIFT-98 code was judged as a difficult code to use, relative to standard groundwater flow and solute transport codes such as MODFLOW/MODFLOWT. The major difficulties were associated with the rigorous nature of the code, which allowed the user to couple density-dependent heat and brine transport with the groundwater flow model. In addition, the user's manual was sometimes unclear as to input needed, but the documented sample problems helped (Ward, et al., 1984). Still, for a fully coupled model, the code was considered average in difficulty of usage.

Because the FEHM test was conducted by an evaluator with only limited previous exposure to FEHM, the model development was completed with technical support from LANL by telephone. With the availability of LANL technical support, all the test model simulations were completed in seven weeks. The user's manual for FEHM was clearly written describing in detail all the data files, input data, and output files, and included examples for many of the macro control statements. Combining the available documentation with some training and telephone access to an experienced user, FEHM was easy to use.

For this testing criteria element, FEHM was ranked above SWIFT-98 primarily because its documentation was more comprehensive.

Speed of Simulation

The time required for simulation of a steady-state flow field with the presence of faults, FEHM required 15 minutes and SWIFT-98, 23 minutes. Transport simulations were consistently faster for SWIFT-98 than for FEHM. The time required to simulate 200 years of tritium transport with faults for sources located at the working points of SCOTCH and SERENA was 64 minutes for SWIFT-98 and 77 minutes for FEHM. When the source was moved up to the CHVTA, SWIFT-98 required 58 minutes and FEHM, 103 minutes. For the simulations with time-varying fluxes the times for simulation of individual radionuclides required by SWIFT-98 must be added for comparison to the multi-species FEHM simulations. Total times required to simulate 1,000 years of transport for Am-241, Pu-239, and Sr-90 with faults for sources located at the working points were 106 minutes for SWIFT-98 and 142 minutes for FEHM. When the source was moved up to the CHVTA, simulation times were 120 minutes for SWIFT-98 and 153 minutes for FEHM.

While the transport simulation times for SWIFT-98 were somewhat faster than for FEHM, an additional characteristic of the SWIFT-98 code must be considered when evaluating the speed of simulation for the CAU modeling effort. The SWIFT-98 code requires that most of the solute transport parameters required for radionuclide transport in a steady-state flow field be input into the steady-state flow simulation dataset. As a result, if a change is desired in the transport parameters, the flow field must be simulated again. This makes it difficult to perform multiple transport simulations based on a single steady-state flow simulation. The FEHM code does not have this limitation.

For this testing criteria element, FEHM was ranked above SWIFT-98 based on the SWIFT-98 requirement to re-simulate the steady-state flow field whenever the transport parameter input files were updated.

3.7.3 Recommended Code for Use in the Pahute Mesa CAU Flow and Transport Model

Based on the relative rankings of SWIFT-98 and FEHM for the five measures discussed in Section 3.7.2, FEHM was the code recommended for the Pahute Mesa CAU flow and transport model.

3.8 TYBO-BENHAM Case Study

Subsequent to completing the code selection process, a sub-CAU-scale model and a site-scale model were developed using FEHM. This summary of the TYBO-BENHAM case study (Wolfsberg et al., 2002) documents the successful application of the FEHM code in UGTA flow and transport models.

The TYBO-BENHAM FEHM models were developed as part of an integrated field, laboratory, and modeling analysis and evaluation of radionuclide transport in the Pahute Mesa groundwater (Wolfsberg et al., 2002). This study was motivated by the discovery of plutonium and other radionuclides in two groundwater observation wells 1.3 km from the BENHAM site located in Area 20 of the NTS on Pahute Mesa (Kersting et al., 1999).

The sub-CAU-scale flow model that was developed used FEHM to model flow with depth-dependent thermal properties. The model domain, approximately 10 km on a side, was discretized using an unstructured finite-element grid that represented the 22 distinct deterministic HSUs in the area. Faults were included as discrete features. The HSU permeabilities were calibrated and the model was used to provide boundary conditions for a site-scale flow model located within the domain of the sub-CAU-scale model.

The site-scale flow model developed using FEHM provided steady-state flow in the BENHAM and TYBO vicinity. This model was developed using a structured high-resolution grid and represented a domain 3.2 by 2.6 km. Boundary conditions were provided by the sub-CAU-scale flow model. The

site-scale flow model was run using the CAU deterministic hydrostratigraphy and 30 geostatistical attribute fields.

A 3-D source model was developed for this study using FEHM. The processes modeled included coupled nonisothermal transient flow, glass dissolution, and particle transport in the BENHAM cavity/chimney system. This model provided mass flux of sorbing and nonsorbing radionuclides into the local aquifers. Linear sorption of radionuclides in the chimney is included in the model. The modeling also considered multiple chimney material properties and thermal conditions in a sensitivity analysis. This model did not include aqueous speciation, rock-water reactions, or pH variations.

Two site-scale transport models were developed using FEHM, a particle transport model and a reactive transport model. Reactive, dual-porosity transport in steady-state, 3-D flow fields were modeled using the particle-tracking approach. This model was very computationally efficient, allowing multiple realizations to be run for sensitivity of source term, flow field, and transport parameters. In addition, the CAU deterministic hydrostratigraphy and 30 heterogeneous realizations were run.

The site-scale reactive transport model included more detailed chemical processes. As this model was significantly more complex, only a single heterogeneous realization was run. Processes modeled were reactive, dual-porosity, solute, and colloid-facilitated plutonium transport along steady-state streamtubes in a 3-D flow field.

These component models were combined with others in a system of models to: (1) simulate complex flow in layered, faulted, and fractured volcanic tuff; (2) investigate temperature-dependent processes associated with radionuclide release from melt glass and cavity-chimney systems; and (3) simulate radionuclide transport in fractured media, addressing fracture properties, diffusion, groundwater chemistry, colloids, fracture mineral exposure, and heterogeneity.

The observed features of the TYBO-BENHAM sub-CAU-scale flow system captured by the calibrated model included steep gradients across faults, downward vertical gradients in the shallow units, and upward vertical gradients in the deep units (Wolfsberg et al., 2002). With respect to the TYBO-BENHAM study, Wolfsberg et al. (2002) concluded:

"With these results, we are confident that we have generally captured the complex processes of source release and site scale migration."

4.0 GROUNDWATER FLOW MODEL CONSTRUCTION

This section describes the approach and results of construction of the Pahute Mesa flow model. The overall goal of this process is the transformation of the conceptual model described in Section 2.0 into a mathematical model for simulating groundwater flow in and around the Pahute Mesa CAUs. For more general information on this subject, refer to American Society for Testing and Materials (ASTM) Standard Guide D 5447-93 (ASTM, 1993a), which summarizes various aspects of this process, including spatial dimensionality and discretization, boundary and initial condition specification, and initial assignment of properties. In addition, ASTM Standard Guides D 5609-94 (ASTM, 1994a) and D 5610-94 (ASTM, 1994b) describe in more detail the process of defining initial and boundary conditions, respectively. Specific elements in the model construction are described in the following subsections.

4.1 General Approach

The Pahute Mesa modeling approach/strategy report (SNJV, 2004b) reviewed the conceptual model of flow and transport, and defined the following needs in implementing the CAU process model relevant to this section:

- Defining the geologic model boundaries
- Defining the CAU numerical model boundary
- Defining multiple alternative conceptual models
- Grid generation
- Establishing boundary conditions and initial condition

The geologic model boundaries are defined in BN (2002) and were chosen such that they coincide with perceived geologic and hydrologic domains to the extent possible, contain the contaminant source areas and discharge points with some buffer, and are within practical constraints. The CAU numerical model lies within the geologic model domain with lower-left plan coordinates of 519,125 and 4,085,000 m Universal Transverse Mercator (UTM) (UTM Zone 11) and upper-right plan coordinates of 569,000 and 4,138,000 m. The model is aligned north-south, with no rotation. The

numerical model extends from the estimated water table to a depth of -3,500 m bmsl. The hydrologic model area encompasses more than 2,700 km^2 (1,042 mi^2) of southern Nye County, Nevada (Figure 1-2). This area incorporates the Pahute Mesa CAUs, including Timber Mountain, the eastern edge of Oasis Valley, the northern part of Fortymile Canyon, and the northern portion of Yucca Mountain. The area has a north-south length of 53.4 km (33.2 mi) and an east-west length of 50.8 km (31.6 mi). The numerical model boundary is approximately the same as the study area boundary shown in Figure 5-2 in the modeling approach/strategy (SNJV, 2004b). Contained within these boundaries are the well data within the Pahute Mesa area, and the springs and regional discharge area at Oasis Valley. The horizontal boundaries of the numerical model do not, because of the great extent of the flow system, coincide with natural hydrologic and geologic boundaries. Thus, the boundaries are, to some degree, arbitrary and must be determined from well data and other regional information. Development of boundary conditions is discussed in Section 4.3.

The UGTA modeling strategy (SNJV, 2004b) includes development of multiple models based on HFMs, each of which must be represented on the model mesh. The alternative HFMs were developed and documented by BN (2002). More detail is provided in Section 4.2 on grid generation and the multiple HFMs. In general, the criteria for grid generation are as follows (DOE/NV, 1999; SNJV, 2004b):

- The external boundary of the CAU model will correspond to appropriate cell boundaries within the regional groundwater flow model. However, the regional model is rotated with respect to the coordinate system, and the CAU model is not. Therefore, interpolation procedures were developed to account for the non-coincidence of CAU and regional model nodes, and are described in Section 5.2.

- Nodes will be placed as close as practical to each underground nuclear test location as well as at specific well locations.

- Nodes will be placed along faults that are identified as being important to the distribution of HSUs.

- The node density will be greatest in the vicinity of the underground nuclear tests and at other points of interest such as discharge wells, and will decrease in density towards the CAU model boundaries.

- Nodes will be preferentially placed along HSU contacts to more precisely incorporate the geologic model structure in the simulations. The nodes will not be layered in the finite-difference sense, but rather will form a pattern representative of the CAU-scale geology.

- The node spacing will vary from small in the vicinity of test cavities and wells to nearly as large as the regional groundwater flow model grid at the CAU boundary.

4.2 Mesh Generation

A set of criteria, outlined below, were developed that produce a mesh that is suitable for flow and transport calculations using FEHM. The resultant mesh should have sufficient resolution to represent features such as hydrostratigraphy, faults, contaminant source zone, wells and the water table, yet not be too large to make computations impractical. In general, it is easy to define criteria that lead to increased refinement in certain volumes of the mesh. The more difficult process is designing criteria that limit the refined volume so that the mesh size (number of nodes) does not grow beyond practical limits. The process of developing these criteria is iterative. During the iterative process, mesh-refinement criteria are defined; control files for the LaGriT (George, 1997) mesh-generation package are written to implement the criteria; mesh-generation calculations are performed; checking is done to ensure the implementation is correct; and the resulting mesh is analyzed to determine whether goals have been met. As stated in the Pahute Mesa modeling strategy (SNJV, 2004b) contaminant boundary calculations will be done with a particle-based method that is not susceptible to numerical dispersion, and grid refinement for transport may yet be undertaken.

4.2.1 Base-Case and SCCC HFMs

Two FEHM computational meshes were produced. One represents the base (or BN) HFM; the other, the SCCC alternative HFM. The EV representation of each geologic model has the same format, a set of surfaces, z(x,y) on uniformly spaced 50-m intervals, defining HSU interfaces, and another set of surfaces defining faults. However, the details of the models are different. The initial base HFM has 45 HSU surfaces and 37 faults. Table 4-1 shows the base HSU abbreviations and names. The SCCC HFM model has 40 HSU surfaces and 25 faults. The list of HSUs is identical with the exception of the Calico Hills HSUs, which are lumped into a single HSU in the SCCC HFM. In both cases, similar criteria are used to decide upon the strategy and logic used to control mesh construction algorithms. Building of the base HFM mesh was done first, so the process involved more iterations. The SCCC

Table 4-1
Hydrostratigraphic Unit Abbreviations and Names
(Page 1 of 2)

HSU Abbreviation	Name
LCCU	Lower Clastic Confining Unit
LCA	Lower Carbonate Aquifer
UCCU	Upper Clastic Confining Unit
LCCU1	Lower Clastic Confining Unit 1 – thrusted LCCU
LCA3	Lower Carbonate Aquifer 3 – thrusted LCA
MGCU	Mesozoic Granite Confining Unit (aka Gold Meadows Stock)
SCICU	Silent Canyon Intrusive Confining Unit
CHICU	Calico Hills Intrusive Confining Unit
CCICU	Claim Canyon Intrusive Confining Unit
RMICU	Rainier Mesa Intrusive Confining Unit
ATICU	Ammonia Tanks Intrusive Confining Unit
BMICU	Black Mountain Intrusive Confining Unit
PBRCM	Pre-Belted Range Composite
BRA	Belted Range Aquifer
BFCU	Bullfrog Confining Unit
KA	Kearsarge Aquifer
CFCU	Crater Flats Confining Unit
CFCM	Crater Flats Composite Unit
IA	Inlet Aquifer
CHCU	Calico Hills Confining Unit
CHZCM	Calico Hills Zeolitized Composite Unit
CHVCM	Calico Hills Vitric Composite Unit
CHVTA	Calico Hills Vitric-Tuff Aquifer
YMCFCM	Yucca Mountain Crater Flat Composite unit
TSA	Topopah Springs Aquifer
LPCU	Lower Paintbrush Confining Unit
PLFA	Paintbrush Lava-Flow Aquifer
TCA	Tiva Canyon Aquifer
UPCU	Upper Paintbrush Confining Unit
BA	Benham Aquifer
PVTA	Paintbrush Vitric-Tuff Aquifer
PCM	Paintbrush Composite Unit
LCA3A	Lower Carbonate Aquifer 3 – thrusted LCA subdivision under Oasis Valley
FCCU	Fluorspar Canyon Confining Unit
SCVCU	Subcaldera Volcanic Confining Unit
TMA	Timber Mountain Aquifer
THCM	Tannenbaum Hill Composite Unit
THLFA	Tannenbaum Hill Lava-Flow Aquifer
TMCM	Timber Mountain Composite Unit
FCA	Fortymile Canyon Aquifer
FCCM	Fortymile Canyon Composite Unit

Table 4-1
Hydrostratigraphic Unit Abbreviations and Names
(Page 2 of 2)

HSU Abbreviation	Name
DVA	Detached Volcanic Aquifer
DVCM	Detached Volcanic Composite Unit
TCVA	Thirsty Canyon Volcanic Aquifer
YVCM	Younger Volcanics Composite Unit
AA	Alluvial Aquifer
LCAr1	Lower Carbonate Aquifer – subdivision from UGTA regional model LCA Zone 1
TCVAr6	Thirsty Canyon Volcanic Aquifer - subdivision from UGTA regional model TCVA Zone 6
TMAr6	Timber Mountain Aquifer - subdivision from UGTA regional model TMA Zone 6
PBRCM Zone 80	Pre-Belted Range Composite – material 80 (see Figure 5-5)
PBRCM Zone 81	Pre-Belted Range Composite – material 81 (see Figure 5-5)
PBRCM Zone 82	Pre-Belted Range Composite – material 82 (see Figure 5-5)
PBRCM Zone 83	Pre-Belted Range Composite – material 83 (see Figure 5-5)
PBRCM Zone 84	Pre-Belted Range Composite – material 84 (see Figure 5-5)
PBRCM Zone 87	Pre-Belted Range Composite – material 87 (see Figure 5-5)
TMCM-ERM	Timber Mountain Composite – East Rainier Mesa sub domain (see Figure 5-6)
TMCM-ATCW	Timber Mountain Composite – Ammonia Tanks sub domain west of 560,000 m (see Figure 5-6)
TMCM-ATCE	Timber Mountain Composite – East Rainier Mesa sub domain east of 560,000 m (see Figure 5-6)
TMCM-THS	Timber Mountain Composite – Tannenbaum Hill sub domain (see Figure 5-6)
TMCM-OV	Timber Mountain Composite – Oasis Valley sub domain (see Figure 5-6)
TMCM-TMD	Timber Mountain Composite – Timber Mountain Dome sub domain (see Figure 5-6)
TMCM-NTMW	Timber Mountain Composite – Northern Timber Mountain sub domain west of 560,000 m (see Figure 5-6)
TMCM-NTME	Timber Mountain Composite – Northern Timber Mountain sub domain east of 560,000 m (see Figure 5-6)

alternative HFM mesh construction also required iteration, but the overall process was more direct because experience from building the base HFM mesh was utilized.

The method of octree mesh refinement (OMR) is used to generate finite element meshes to represent HSUs, structural features such as faults, and engineered features such as wells with spatially variable resolution so as to provide high resolution where needed and allow coarse resolution where it is sufficient. The OMR method helps to achieve the two conflicting goals of providing high resolution and minimizing the number of nodes in the model.

Figure 4-1 shows a simple example of the OMR technique. Octree mesh refinement is used to provide increased resolution in limited volumes of the model volume while maintaining coarse

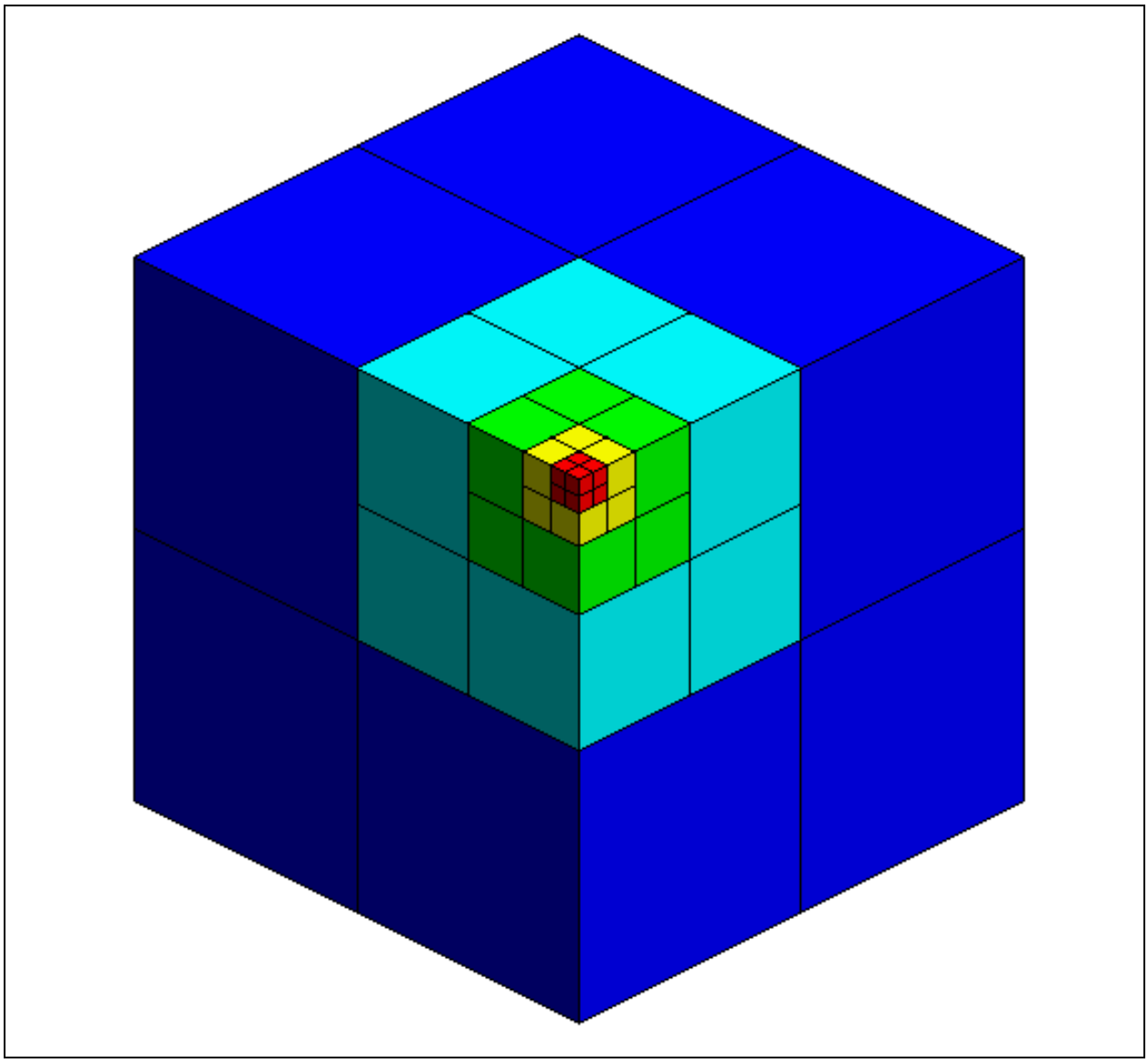

Figure 4-1
Octree Mesh Refinement Example

resolution in other volumes. The process of building an octree mesh begins with an orthogonal uniform mesh. Then the mesh is progressively refined until features of interest are adequately resolved (Figure 4-1). For both the base HFM and SCCC alternative HFM, the coarsest elements are uniform in the X and Y directions with 1,000-m spacing between nodes. The vertical spacing is variable with nodes at -3,500 m, -2,500 m, -1,500 m, -750 m, 0 m, 750 m and 1,500 m. Each time a hexahedral element is refined, eight new elements are formed with the space between nodes cut in

half in each of the coordinate directions. The horizontal spacing of the mesh at different levels of refinement is 1,000 m, 500 m, 250 m, and 125 m, and the highest level of refinement used is 67.5 m.

Octree mesh refinement creates a balanced mesh. This means neighbors to any element are either of the same refinement level or at most one level higher or lower. As a result, progressive refinement of one element may result in the propagation of some refinement of neighboring elements.

The criteria used to determine which elements are refined and to what level they are refined involves tradeoffs. Even using the octree method, if all elements intersecting faults are refined to 67.5 m, the size of the mesh is too large for practical flow and transport calculations. Therefore, criteria are developed to prioritize where mesh refinement occurs and allow the mesh to remain coarse wherever possible.

To represent HSU geometry, criteria are developed to refine thin or steeply dipping portions of an HSU to higher levels and represent thick portions of an HSU with coarser elements. Figure 4-2 illustrates the variable grid resolution that results as HSUs change thickness.

To represent faults, criteria are developed to refine cells that are intersected by fault surfaces. The level of refinement is a function of depth. Elements intersecting fault surfaces at elevations higher than 0 m are refined to 125 m, between 0 m and -1,000 m to 250 m, and below -1,000 to 500 m. In addition, only a subset of the faults is refined to 125 m. As a result, the representation of faults is broader at depth and narrower near the top of the model (Figure 4-3). In all cases, continuity of fault surfaces is maintained and the FEHM computational mesh, which uses node based properties, has a region at least two nodes wide labeled as fault (Figure 4-4). Figures 4-5 through 4-8 show the faults in the base HFM. Table 4-2 shows the fault IDs and associated names for the base HFM. Figures 4-9 and 4-10 show the fault IDs in the SCCC alternative HFM. Figure 4-11 shows the mesh detail near the test chimney. Table 4-3 shows the SCCC fault IDs and names for the SCCC alternative HFM.

Particle paths originating at the Pahute Mesa tests (as shown in the Pahute Mesa hydrologic data document [SNJV, 2004a]) for both BN and SCCC HFMs are used to define 3-D polyhedra for additional refinement for transport paths. If elements are outside that polyhedra, refinement is limited to 125 m; however, inside that polyhedra, thin HSUs may be refined to 67.5 m.

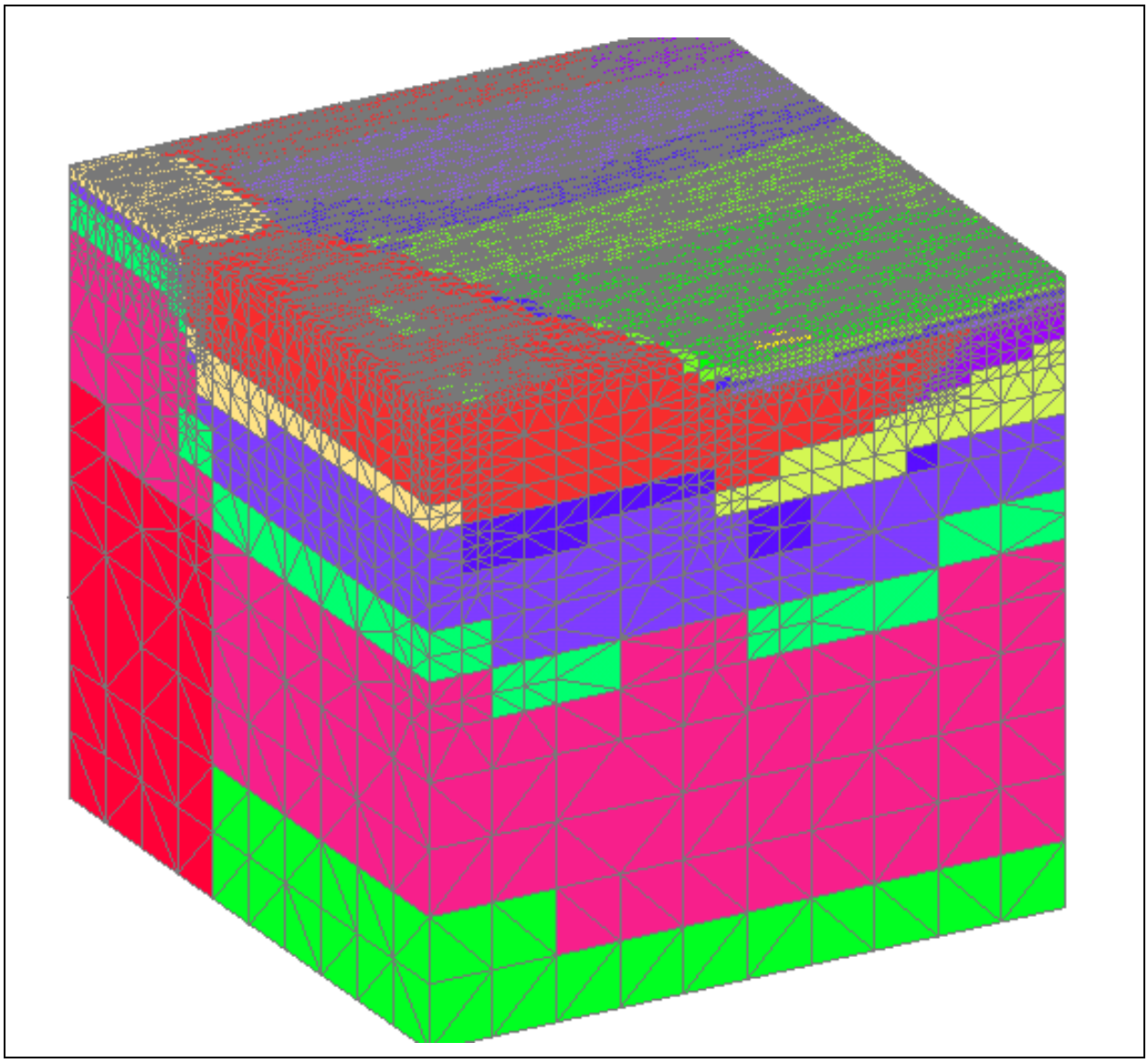

Figure 4-2
Example Mesh Refinement in HSUs

To represent volumes where potential source locations exist, vertical columns of elements are refined to 67.5 m starting just below the coordinate where each are defined. The refined elements continue up to the surface of the model. In addition, all elements that are adjacent to the vertical column are refined to 67.5 m. This ensures that the FEHM control volumes in potential contaminant source locations are uniform. Figure 4-11 shows an example of such refinement.

Vertical columns of elements are refined to 67.5 m if the open interval of one of the 152 wells intersects the mesh. As with the source terms, this ensures that the FEHM control volumes

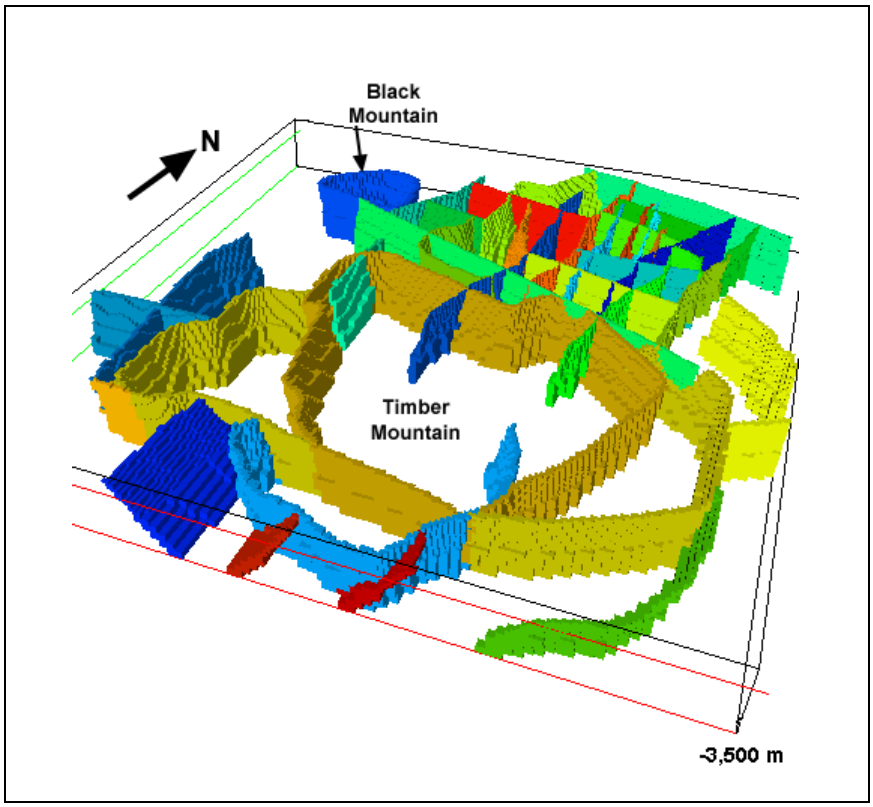

Figure 4-3
3-D View Showing Fault Thickness with Depth

surrounding a well interval are uniform. Table 4-4 summarizes the mesh statistics for the base and SCCC HFMs.

4.2.2 Truncation of Top Surface of Mesh To Represent Water Table

The FEHM simulations utilize a confined aquifer approximation. The estimated water table defines the top of the model domain. The approach does not include an unsaturated zone or moving water table and, therefore, solves a simplified but computationally more efficient numerical model. An estimate of the water table, approximated by contouring observed heads in wells with relatively shallow sampling intervals, provides a guide for setting the upper confining surface in the grid. However, it is impossible to represent continuously the contoured surface without utilizing an impractically large number of grid nodes discretized very finely. Therefore, the contoured surface is approximated with a method that specifies discrete elevations that are consistent with the OMR vertical coordinates. The highest elevation of the contoured water table is 1,500 m, which defines the highest nodal elevation in the grid. Discretization steps of either 125 m or 250 m are used down to

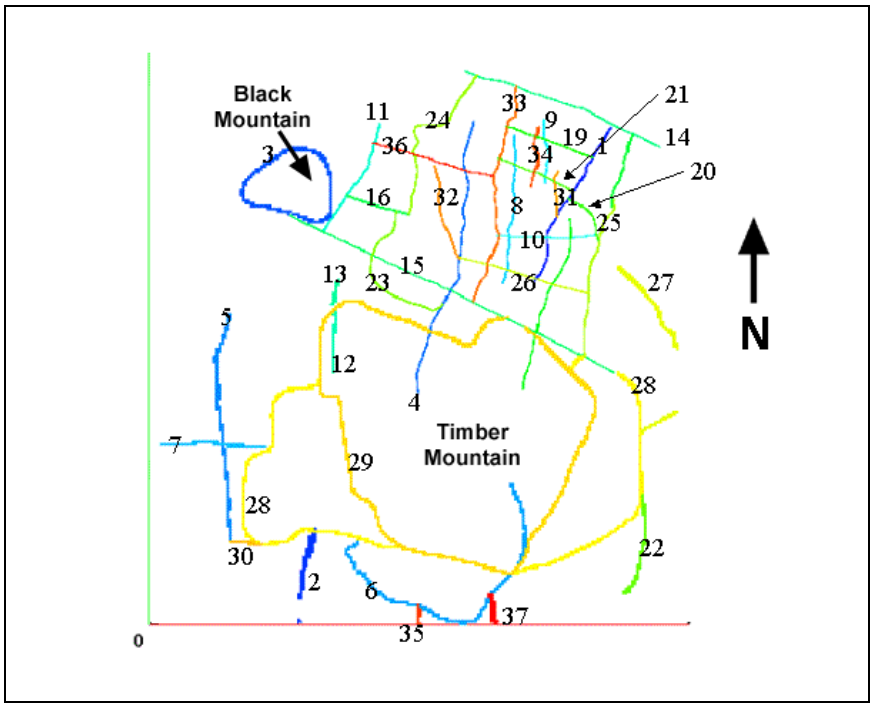

Figure 4-4
Fault Numbering Key - Base HFM

the lowest contoured water-table elevation. The differences are minimized along the primary flow pathway, with errors incurred in the northwest and southeast.

In the numerical model, the top surface has boundary conditions of applied recharge flux. Because none of the fluid or rock properties depend on head, no changes to the true solution occur other than forcing the bookkeeping in FEHM to assume fully saturated conditions. The potential negative side of this approach is that the top surface of the numerical model corresponds to the estimated water-table surface and may be inconsistent with the model-derived water-table surface. This discrepancy could affect the flux through the model. The error is small because the flowing cross-sectional area is proportional to the thickness of the model in the north-south direction, and the average error between the calibrated and field data is small compared to a model thickness of approximately 5,000 m.

4.3 Boundary Conditions

The solution of the groundwater flow equations requires specification of head and/or flow at the edges and at internal discharge points (e.g., springs in Oasis Valley) of the numerical model. This is

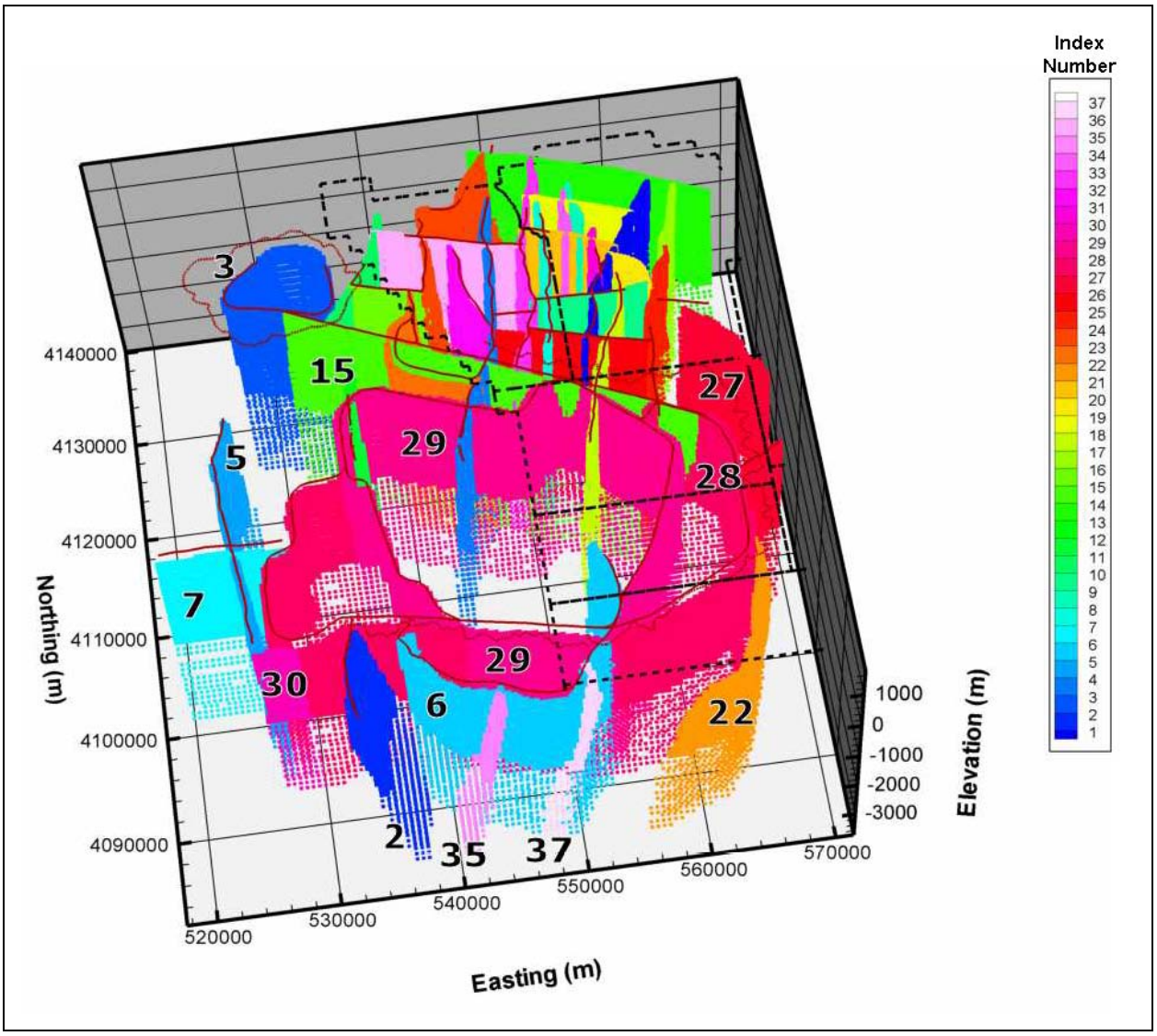

Figure 4-5
Base HFM Fault Structure Viewed from the Southwest

particularly important for the Pahute Mesa CAU model because the model boundaries do not coincide with natural hydrologic boundaries. The Pahute Mesa CAU model must account for regional inflow and outflow across all four lateral edges, internal flow from precipitation recharge, and internal discharge at Oasis Valley. The following sections describe the implementation of these conditions in the Pahute Mesa CAU flow model.

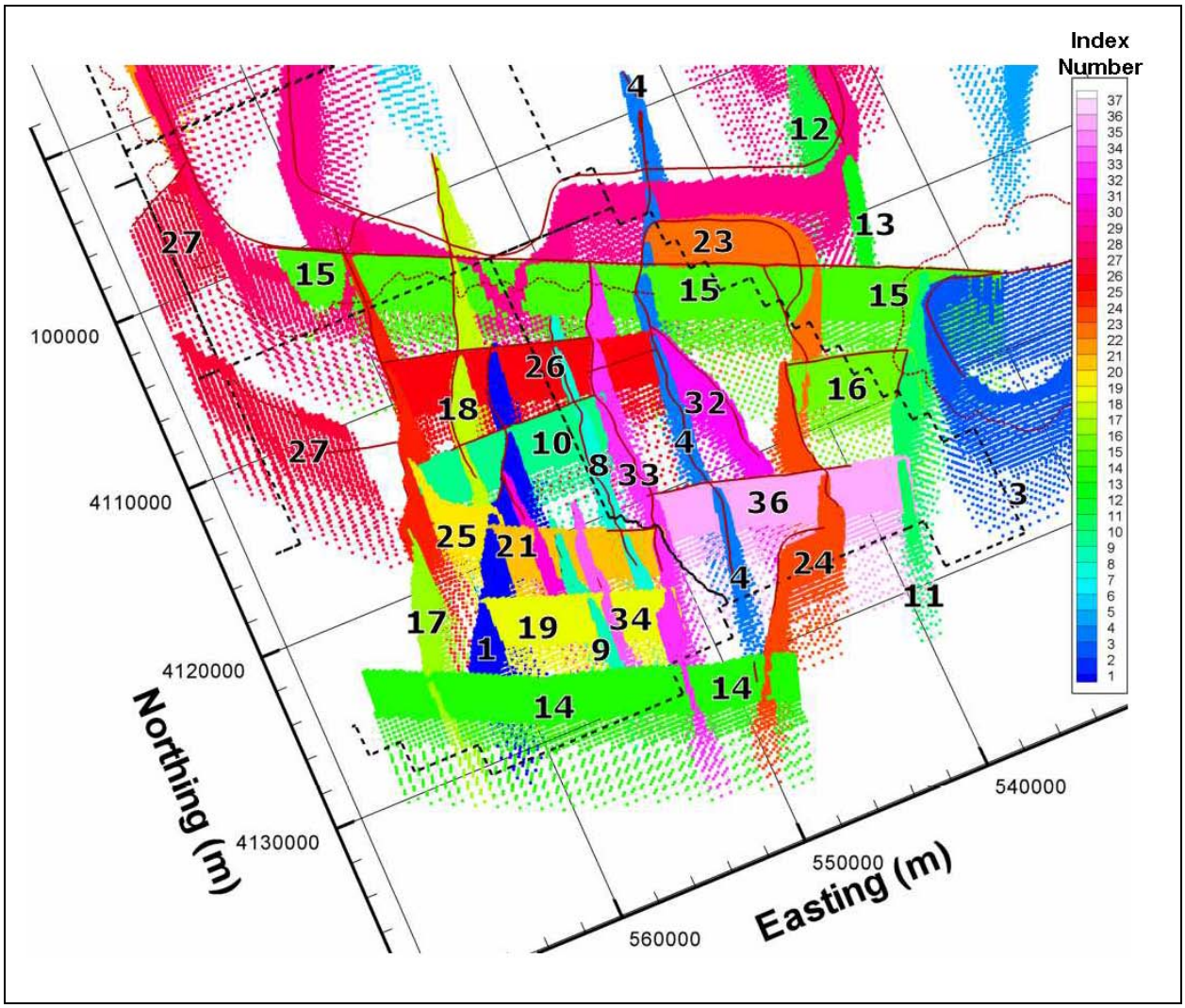

Figure 4-6
Base HFM Fault Structure Viewed from the Northeast

4.3.1 Recharge

As discussed in the conceptual model (Section 2.3.2.2), there are three categories of recharge estimates for consideration in the CAU model as follows: the USGS distributed-parameter watershed model of Hevesi et al. (2003); a Maxey-Eakin elevation-based approach as described in the UGTA regional model evaluation (DOE/NV, 1997; IT, 1996a) and modified to reflect an updated base precipitation map; and the DRI chloride mass-balance estimate of Russell and Minor (2002). Two subsets of the USGS and DRI recharge maps were also considered. For the USGS map, the recharge with (case USGSD) and without runoff or run on (redistribution) (case USGSND) was used. For the

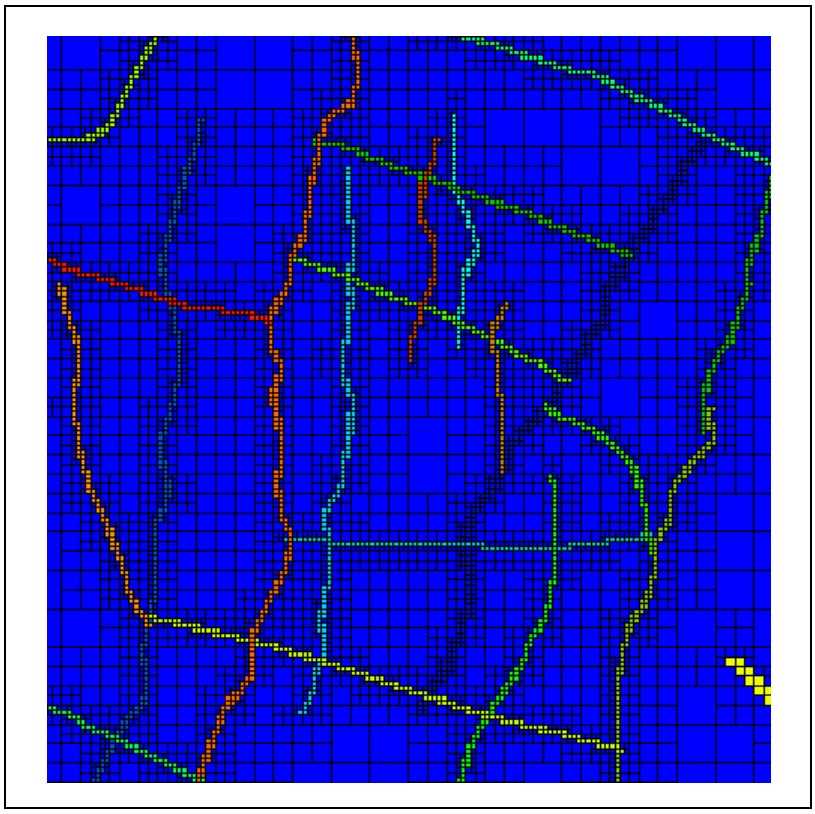

Figure 4-7
Closeup View of Faults in Area 19

DRI map, the recharge with (case DRIAE) and without an elevation (case DRIA) mask at 1,237 m was also used. Section 2.3.2.2 provides more discussion on these alternative recharge models.

Recharge is implemented in the CAU model as a specified flux condition, where a given volume (mass) of water is applied based on the above recharge models. Recharge flux is considered to be constant over time, but varies over the domain as a function of altitude, soil and vegetation types, etc. The recharge flows for FEHM were calculated by averaging a fine grid (30 m) over the contributing area of each node at the top of the FEHM model to obtain the required input in mass per time. Figures 4-12 through 4-16 show the recharge for the USGSD, USGSND, modified Maxey-Eakin (MME), DRIA and DRIAE cases, respectively, as implemented for FEHM input. Table 4-5 summarizes the total mass flows over the numerical model area for each recharge model considered.

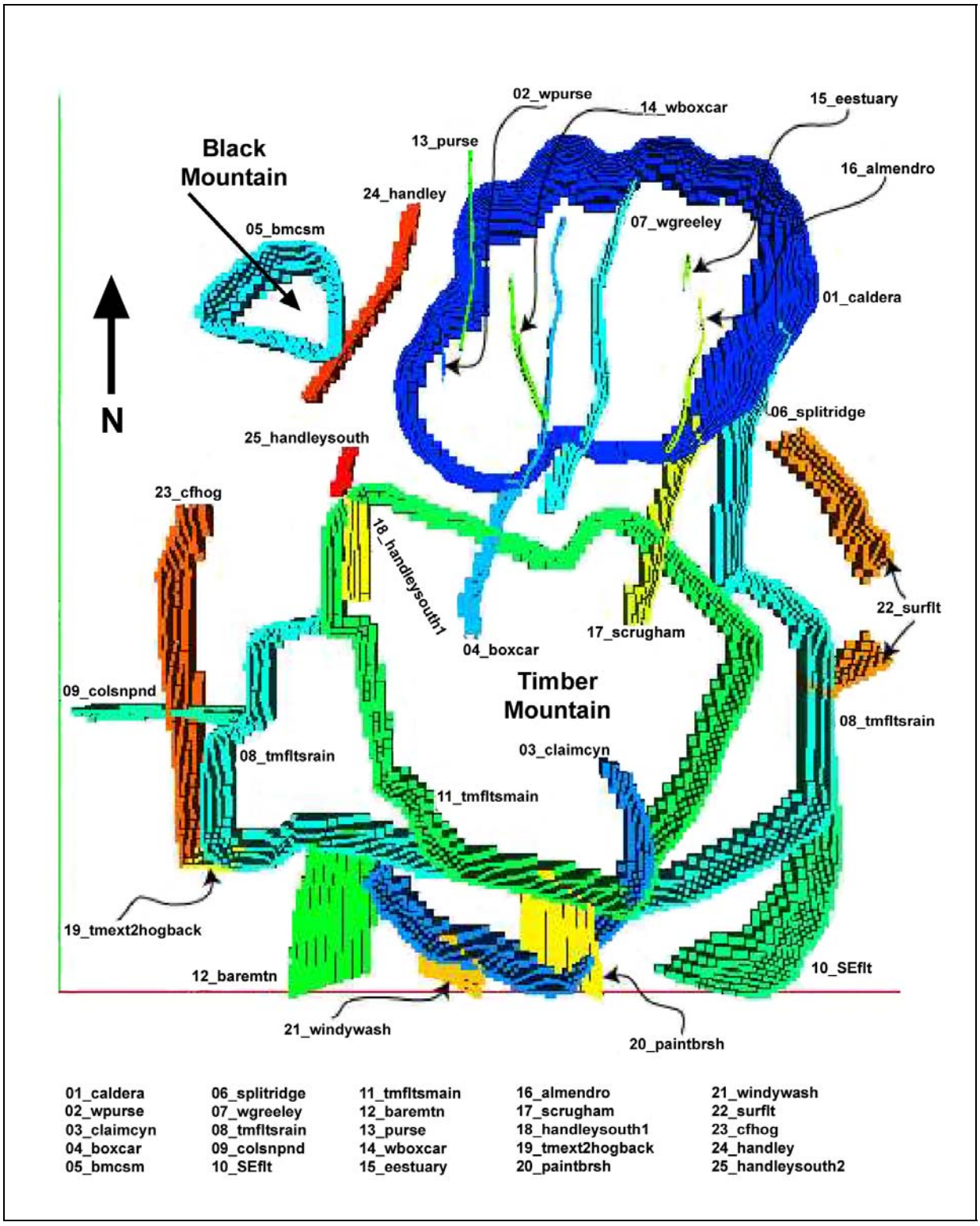

Figure 4-8
Fault Numbering Key - SCCC HFM

Table 4-2
Base HFM Fault Indices and Names

Fault ID	Name
01	Almendro
02	Bare Mountain
03	Black Mountain Caldera Structural Margin
04	Boxcar
05	Hogback
06	Claim Canyon Caldera Structural Margin
07	Colson Pond
08	East Greeley
09	East Estuary
10	East Thirsty Canyon Structural Zone
11	Handley
12	Handley South
13	Handley North
14	Moor Hen Meadow Structural Zone
15	North Timber Mountain Moat Structural Zone
16	Ribbon Cliff Structural Zone
17	Richey
18	Scrugham Peak
19	Silent Canyon Northern Structural Zone
20	Silent Canyon Structural Zone East
21	Silent Canyon Structural Zone West
22	YMP inferred/CP Thrust
23	Silent Canyon/West Purse
24	Purse North
25	Split Ridge
26	Southern Pahute Mesa Structural Zone
27	Gold Meadows Structural Zone/Big Burn Valley
28	Rainier Mesa Caldera Structural Margin
29	Ammonia Tanks Caldera Structural Margin
30	Hot Springs Lineament extension of Rainier Mesa Caldera Structural Margin
31	West Almendro
32	West Boxcar
33	West Greeley
34	West Estuary
35	Windy Wash/Claim Canyon 1
36	West Silent Canyon Structural Zone
37	Paintbrush Canyon
38	Fault 23 south of North Timber Mountain Moat Structural Zone
39	Fault 16 between faults 23 and 24
40	Extension of Purse Fault to northern edge of model
41	Purse Fault repair where fault 36 crosses

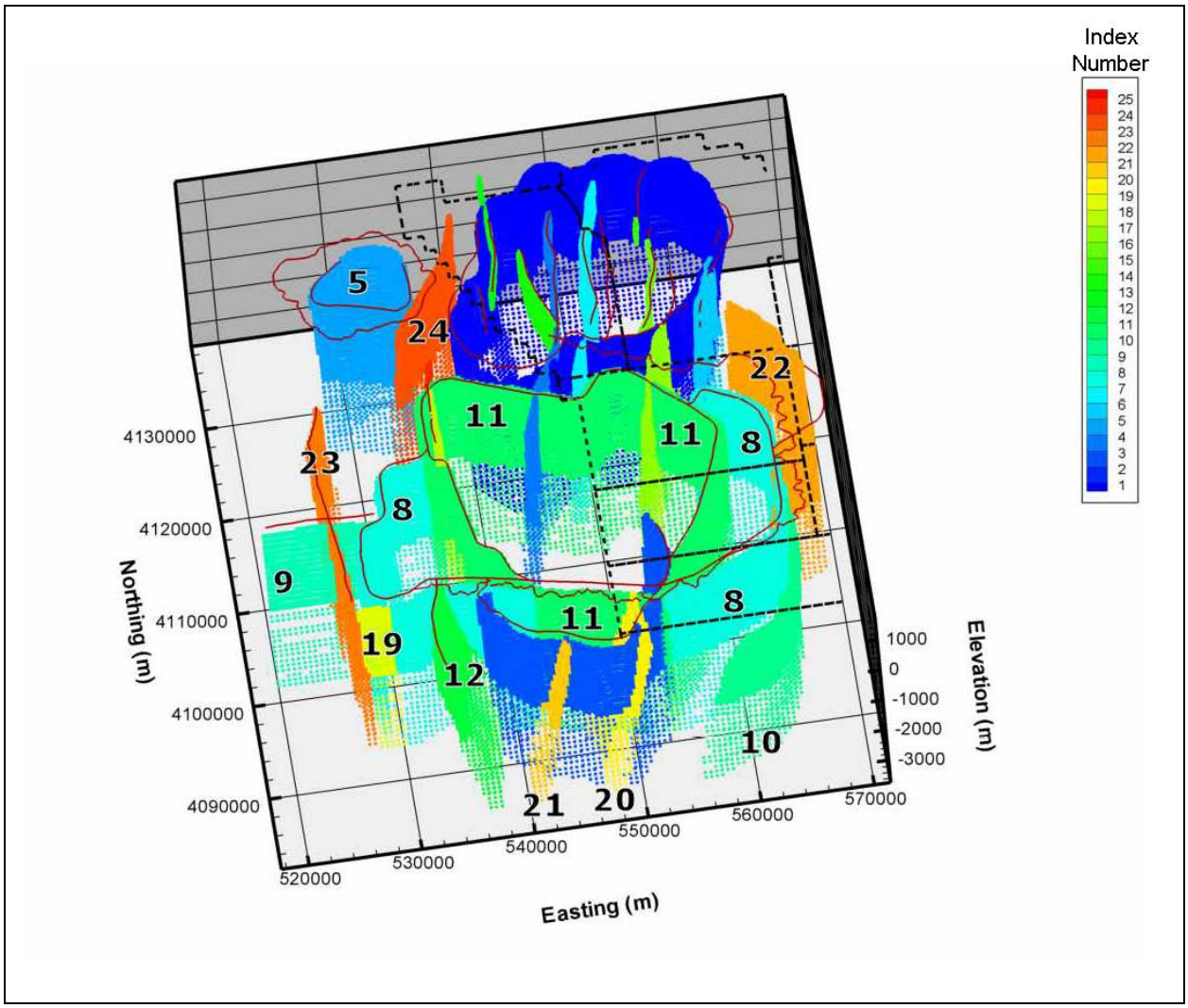

Figure 4-9
SCCC HFM Fault Structure Viewed from the Southwest

4.3.2 Discharge

The only internal discharge represented in the Pahute Mesa CAU model is Oasis Valley springs and ET outflow. Discharge from pumping wells is not included in the model. Spring and ET discharge are represented in a similar manner with FEHM as with the regional model with "drain" boundary conditions. In this condition, a head is set at the elevation of the point of discharge. If the model head at the node is above the specified elevation outflow representing spring or ET, spring discharge or ET loss flows occur. If head is below the set head, no flow of any kind occurs. This is different than a constant-head boundary condition, which will allow in or outflow; the boundary condition used to represent Oasis Valley only allows outflow. Nodes at the top of the model within the areas where

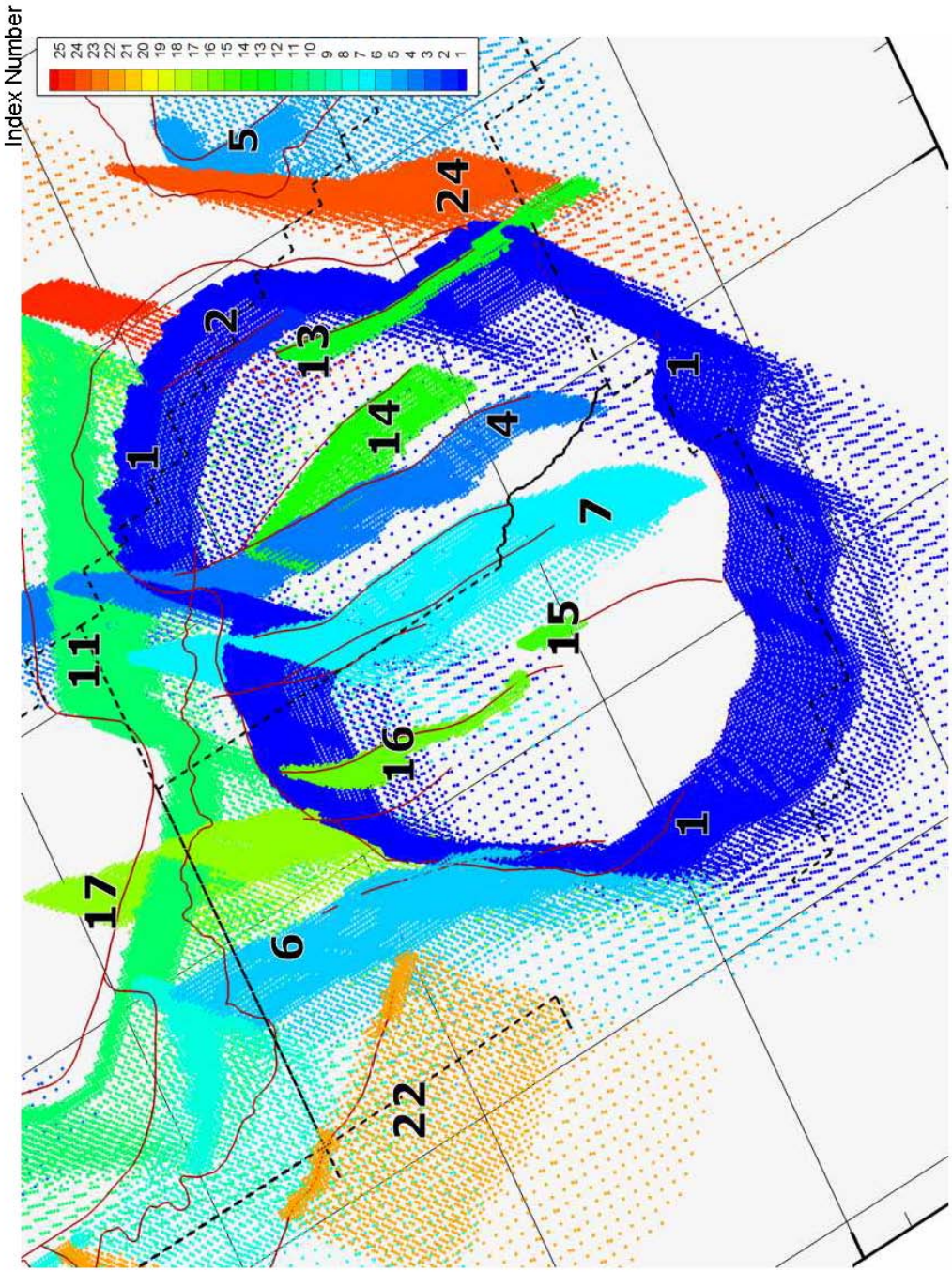

Figure 4-10
SCCC HFM Fault Structure Viewed from the Northeast

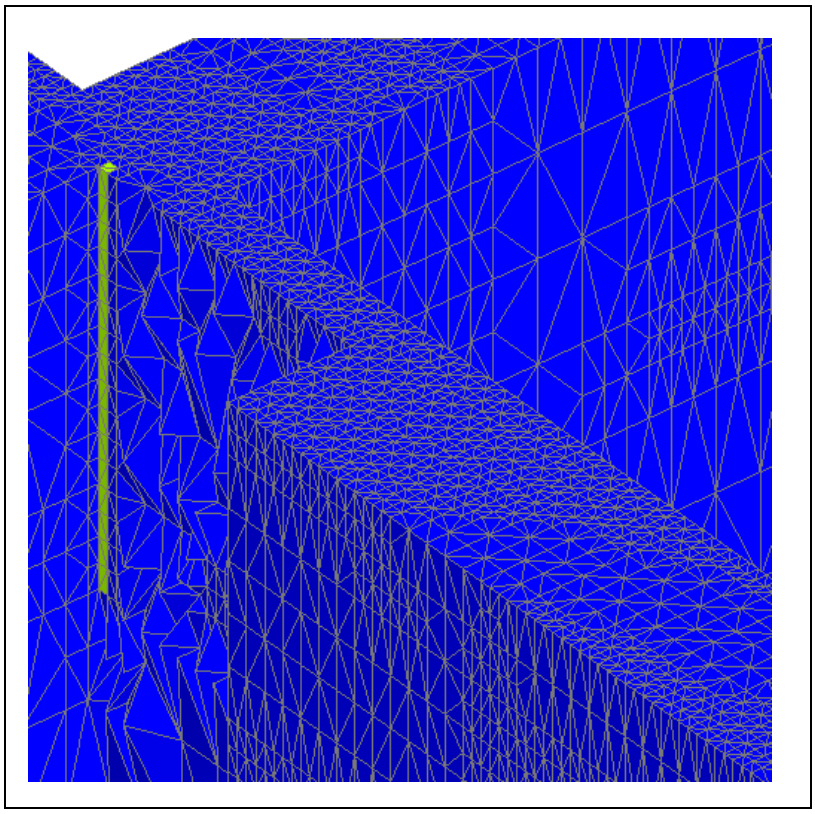

Figure 4-11
Mesh Detail Near Test Chimney

Table 4-3
SCCC HFM Fault Indices and Names
(Page 1 of 2)

Fault ID	Fault Name
01	Silent Canyon Caldera Margin
02	West Purse
03	Claim Canyon Caldera Structural Margin
04	Boxcar
05	Black Mountain Caldera Structural Margin
06	Split Ridge
07	West Greeley
08	Rainier Mesa Caldera Structural Margin
09	Colson Pond
10	YMP inferred/CP Thrust

Table 4-3
SCCC HFM Fault Indices and Names
(Page 2 of 2)

Fault ID	Fault Name
11	Ammonia Tanks Caldera Structural Margin
12	Bare Mountain
13	Purse
14	West Boxcar
15	East Estuary
16	Almendro
17	Scrugham Peak
18	Handley South
19	Hot Springs Lineament extension over to Hogback
20	Paintbrush Canyon
21	Windy Wash
22	Gold Meadows Structural Zone/Big Burn Valley
23	Hogback
24	Handley
25	Handley South

Laczniak et al. (2001) mapped ET were identified and drains assigned. In the case of springs, head was assigned at the estimated spring elevation. To represent ET, head equal to land surface elevation less 3 m was used to represent the maximum root depth from which plants could draw water (the effects of extinction depth are examined more in Section 6.2.4.1). Laczniak et al. (2001) estimated that 30 percent of Oasis Valley plant coverage was dense wetland vegetation (e.g., tall reedy and rushy marsh plants) where water was perennially at or very near land surface, 24 percent of plant coverage was dense meadow and forest with the water table from a few up to 20 ft (~1 to 6 m) below ground surface, and 14 percent dense to moderately dense grassland vegetation with the water table up to 5 ft (1.5 m) below ground surface; these 3 categories account for about 2/3 of the Oasis Valley discharge area. The water table in Oasis Valley is known to vary seasonally from ET (Reiner et al., 2002); thus, the depth of water table given above is a first approximation of the rooting depth, which ranges from 0 to 6 m. The UGTA regional model (DOE/NV, 1997) and USGS Death Valley regional flow model (DVRFM) (Faunt et al., 2004) both used values of 10 m. Figure 4-17 shows the discharge areas of Oasis Valley considered in the CAU model.

Table 4-4
Base and SCCC Mesh Statistics

	Base HFM	SCCC Alternative HFM
Number of Nodes	1,449,785	1,301,168
Number of Tetrahedral Elements	7,961,005	6,996,374
Number of Connections uncompressed matrix compressed matrix	 N/A 11,882,601	 18,315,432 10,706,526
Model Extents (UTM meters) xmin (West) xmax (East) xmax - xmin ymin (South) ymax (North) ymax - ymin zmin (Bottom) zmax (Top) zmax - zmin	 519,000 569,000 50,000 4,085,000 4,138,000 53,000 -3,500 1,500 5,000	 519,000 569,000 50,000 4,085,000 4,138,000 53,000 -3,500 1,500 5,000
Number of Hydrostratigraphic Units	45	40
Number of Faults	37	25
Number of Tests (Area 19)	36	36
Number of Tests (Area 20)	46	46
Number of Tests Inside Model	36	36
Number of Well Intervals	152	152

4.3.3 Boundary Heads

Initially, boundary heads from the UGTA regional model analysis described in SNJV (2004a) were interpolated onto the edge nodes of the FEHM CAU model. These heads represent a mass conservative calibrated solution to the groundwater flow equation from the UGTA regional model. During the calibration process these heads were reviewed, and in spots, revised based on further examination of measured heads and heads determined from the regional model. An additional factor that may cause slight adjustment is that the edge heads and head immediately inside the model may be different from different model resolution or properties. The beginning boundary head configuration is shown in Figure 4-18.

4.3.4 Lateral-Boundary Fluxes

Part of the CAU flow modeling strategy is to use the UGTA regional flow model (DOE/NV, 1997) as a mass conservative integrating model that allows evaluation of water-balance uncertainty around the

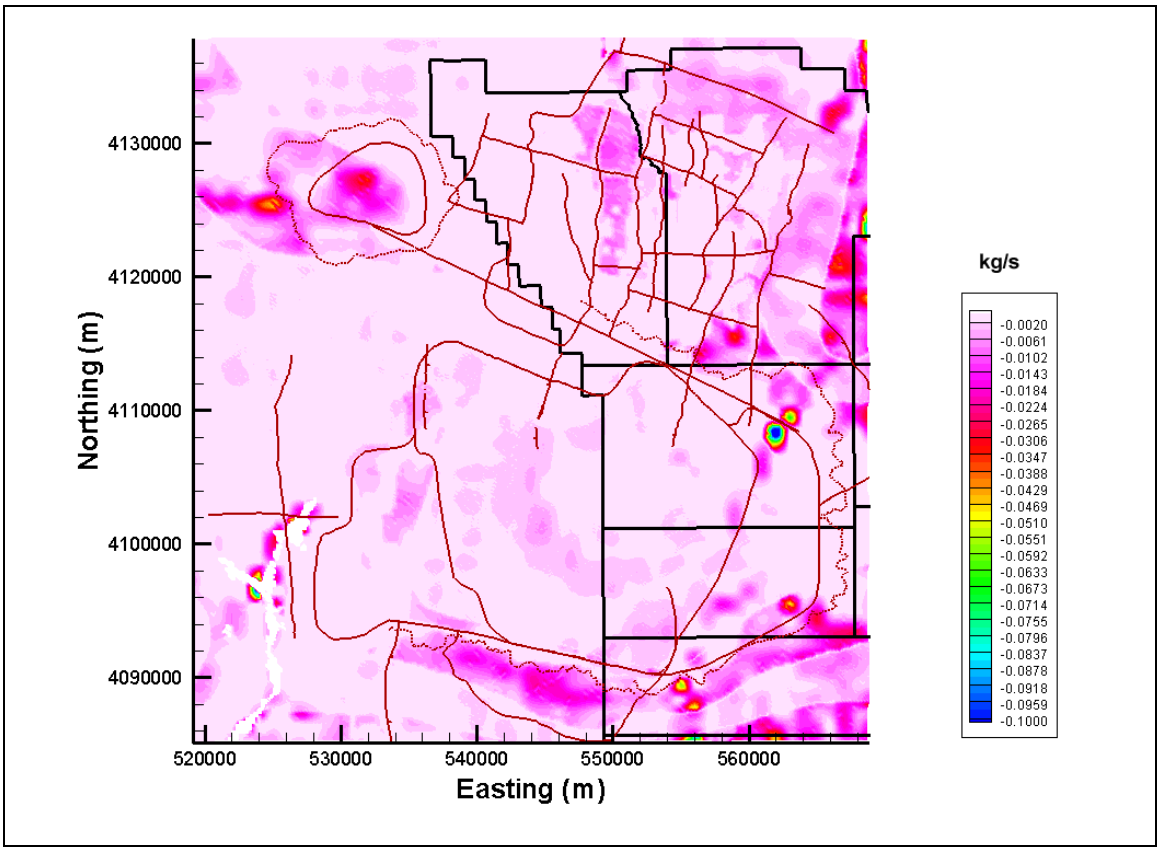

Figure 4-12
USGS Recharge Model (Hevesi et al., 2003), Redistribution Included

edges of the CAU model. In this analysis, the flows are not directly specified on all edges (to do so creates a numerically unstable problem, see Anderson and Woessner [1992]); head is specified and FEHM computes and reports the flows, which are used as calibration targets. Wolfsberg et al. (2002) used the same approach. Section 5.2 discusses these data in more detail.

4.4 Initial Conditions

Initial conditions are those applied at the start of a simulation. Theoretically, for steady-state flow, the initial conditions are not important. Practically, the iterative solvers employed in large numerical models gain efficiency if the starting conditions are consistent as possible with the properties and boundary conditions used in calibration. As described in the Pahute Mesa CAIP (DOE/NV, 1999), the initial conditions were determined from interpolation of the regional model results in the CAU domain onto the FEHM nodes. However, once converged steady-state model results were obtained, they became the new initial conditions for the continuation of model calibration.

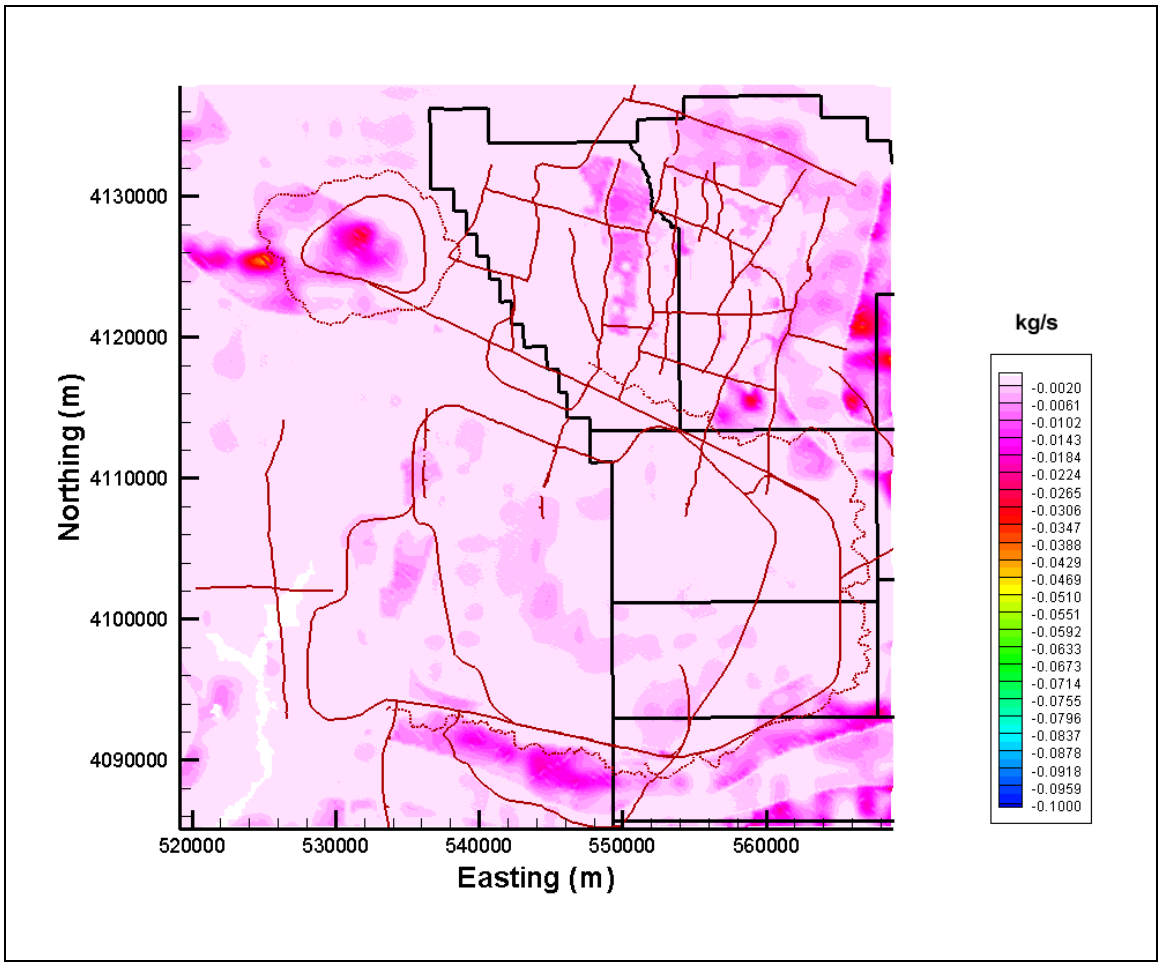

Figure 4-13
USGS Recharge Model (Hevesi et al., 2003), Redistribution Not Included

Los Alamos National Laboratory analyzed thermal data from the Pahute Mesa area and calibrated a thermal conduction model described in Appendix C of this report. Within the model domain, temperature varies enough that it should be considered in flow calculation. The FEHM code has the capability to allow specification of a thermal field without the need to simulate thermal transport. This feature was used in the CAU model to specify a fixed temperature distribution over the CAU model domain. Figure 4-19 shows a fence diagram of the calibrated temperature field.

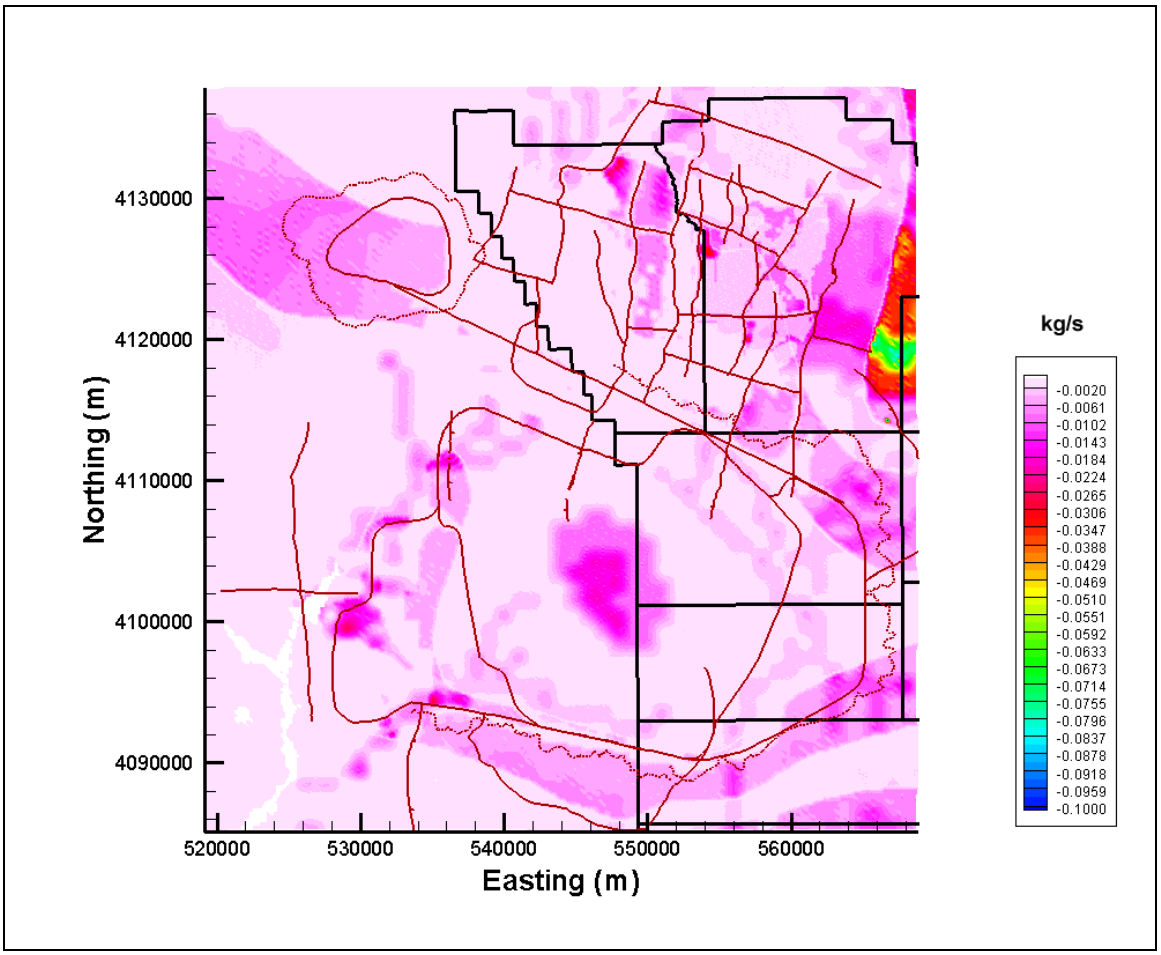

Figure 4-14
MME Recharge

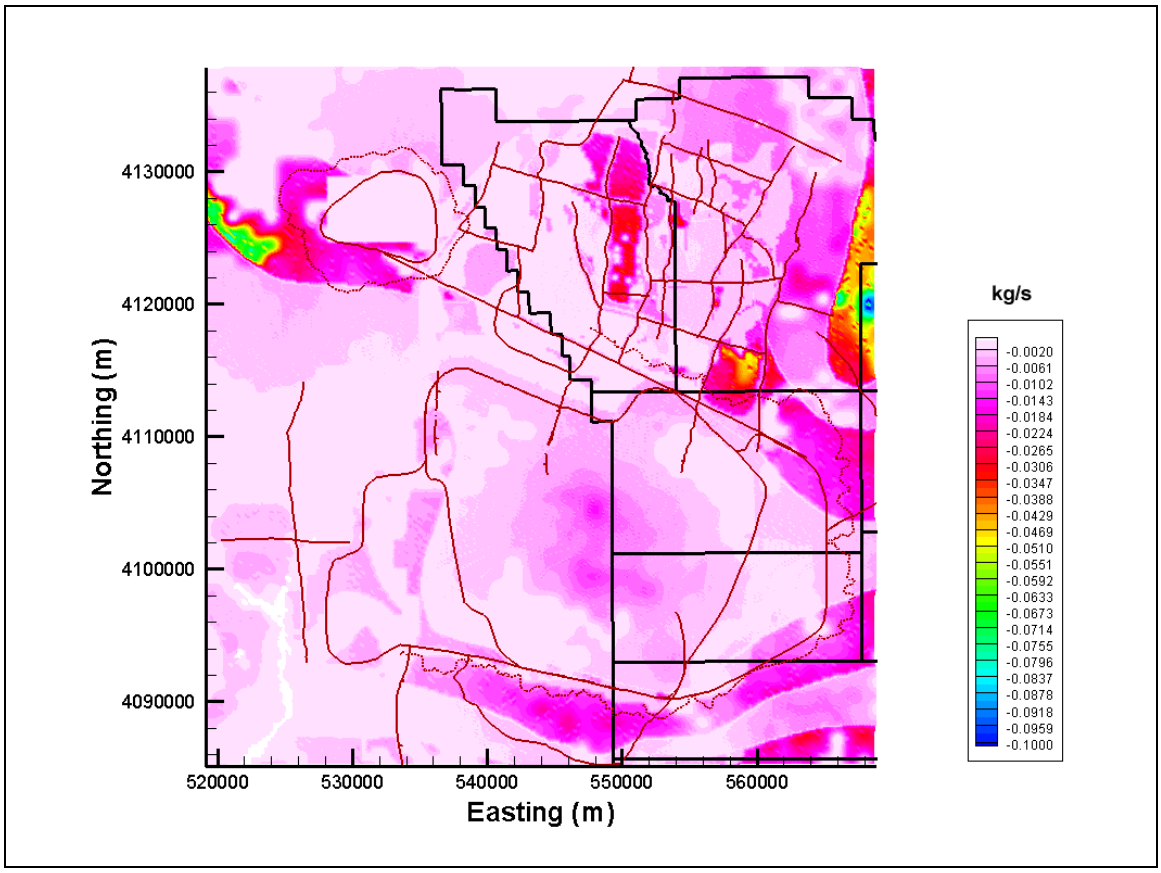

Figure 4-15
DRI Chloride Mass-Balance Recharge (Russell and Minor, 2002) with Alluvial Mask

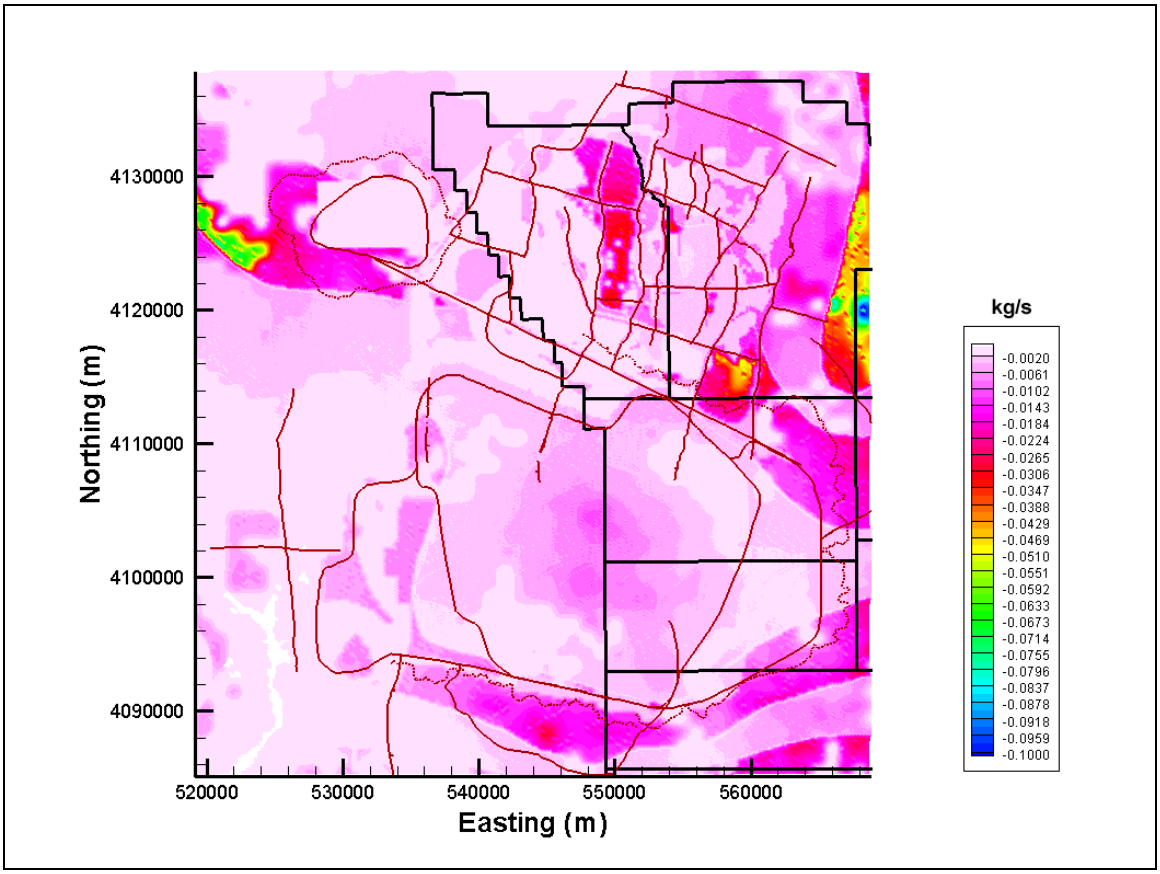

Figure 4-16
DRI Chloride Mass-Balance Recharge (Russell and Minor, 2002) with Alluvial Mask and Elevation Screen

Table 4-5
Mass Flows for USGS, MME, and DRI Recharge Maps

Recharge Model	Total Recharge Mass Rate (kg/s)
USGS - redistribution (USGSD)	318
USGS - no redistribution (USGSND)	233
Modified Maxey-Eakin (MME)	393
DRI - alluvial and no elevation screen (DRIA)	633
DRI - alluvial and elevation screen (DRIAE)	624

kg/s = Kilograms per second

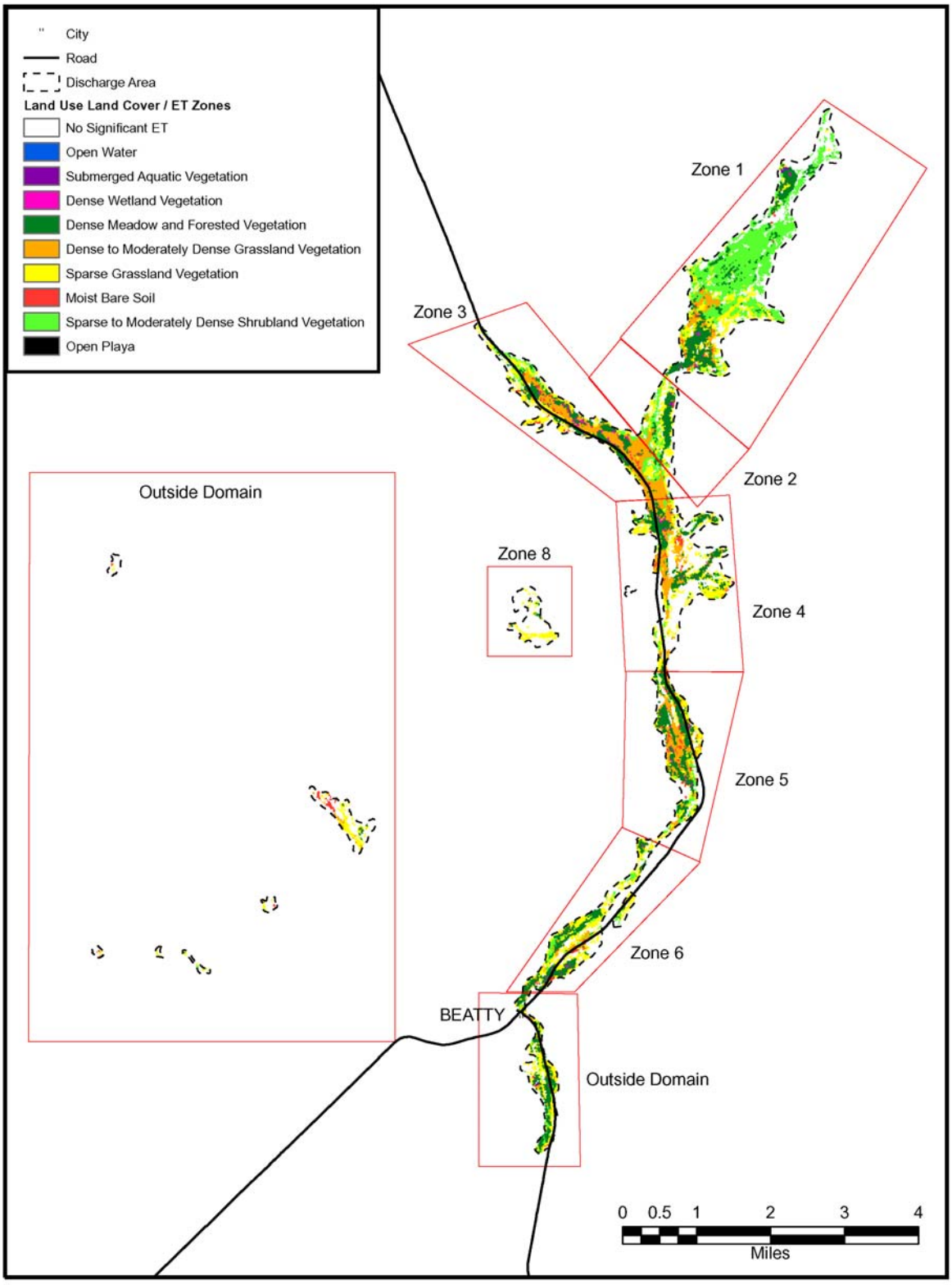

Figure 4-17
Oasis Valley Discharge Zones
(Source: Adapted from Laczniak et al., 2001)

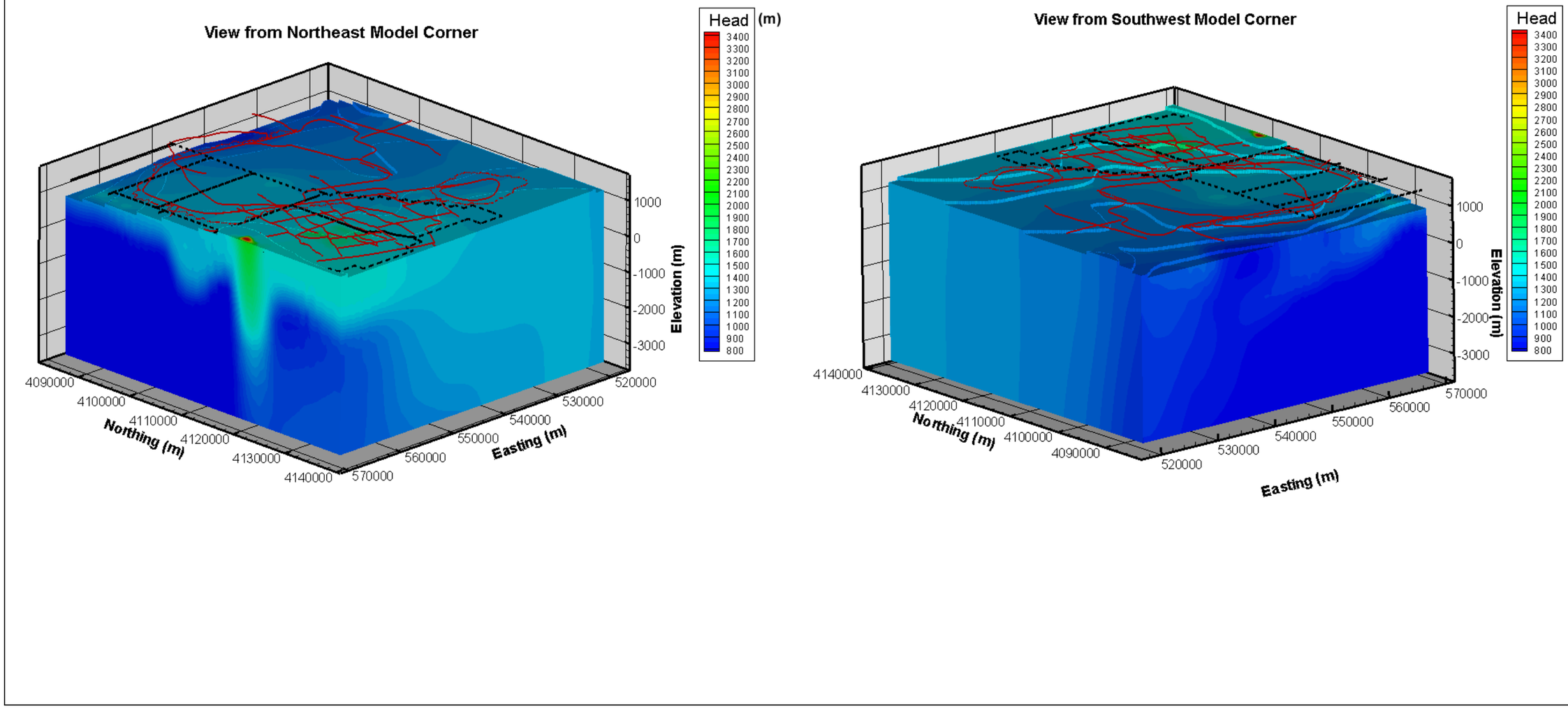

Figure 4-18
CAU Model Boundary Heads Modified from the UGTA Regional Model (SNJV, 2004a)

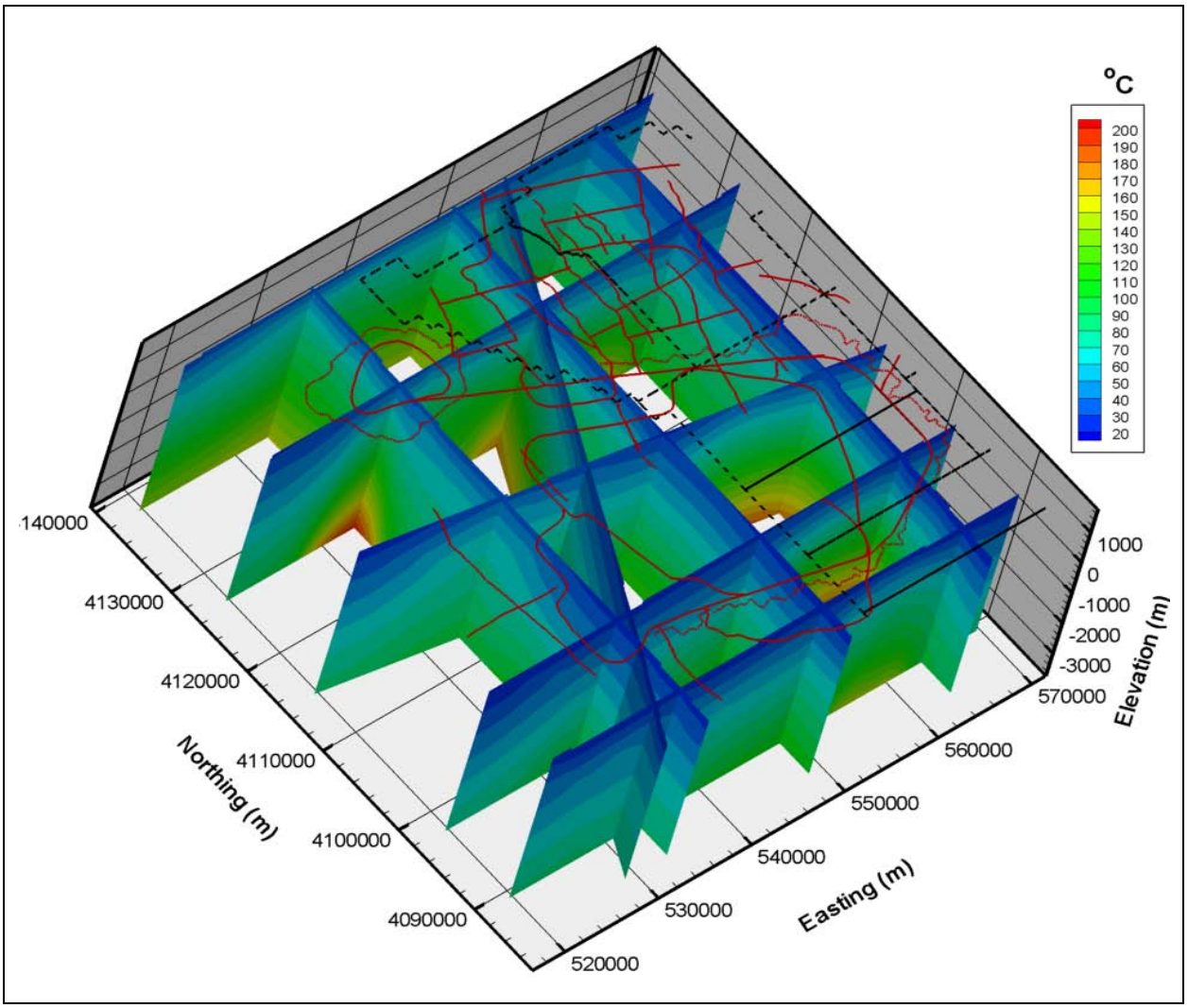

Figure 4-19
Calibrated Temperature Field

5.0 FLOW MODEL CALIBRATION

The Pahute Mesa CAIP (DOE/NV, 1999) and modeling approach/strategy (SNJV, 2004b) indicate that model calibration will be conducted after flow model construction. These documents describe model calibration as "the process of matching historical data" and "calibration consists of determining model parameter values such that simulated heads and fluxes are consistent with observed or target values." In addition, ASTM Standard Guide D 5490-93 (ASTM, 1993b) defines calibration as, "… the process of refining the model representation of the hydrogeologic framework, hydraulic properties, and boundary conditions to achieve a desired degree of correspondence between the model simulations and observations of the groundwater flow system." The purpose of the Pahute Mesa CAU-model calibration is to use observed head data, discharge estimates from Oasis Valley, boundary flow estimates from the regional model, and estimated hydraulic properties for HSUs to develop a numerical model representation of the groundwater flow system in the Pahute Mesa CAU area. This will be used to assess underground-test related radionuclide migration.

This section describes the flow model calibration approach, and the calibration results for the base HFM and the major alternative HFM, the SCCC. These HFMs, presented in Section 2.2.1, are described in detail by BN (2002). Other HFMs are considered in Section 6.3. In addition, the calibrations described in this section are with the MME recharge model; other recharge models are investigated in Section 6.4.

The flow model sensitivity and uncertainty analysis are presented in Section 6.0. Geochemical verification is presented in Section 7.0, and thermal sensitivity and verification is shown in Section 8.0.

The Pahute Mesa CAU flow model considered seven HFMs and five recharge models. In the interest of brevity, the following shorthand is used. The first part of the name is the HFM and the second is the water-balance condition. Two other modifications are applied only to the base model: SDA for selected HSU depth decay and anisotropy, and ADA for all HSU depth decay and anisotropy.

Examples of the naming conventions are as follows:

- BN-MME - Bechtel Nevada (or base) HFM with the MME recharge model and boundary flows.
- BN-DRIA - Bechtel Nevada (or base) HFM with the DRI alluvial recharge model and boundary flows.
- BN-USGSD - Bechtel Nevada (or base) HFM with the USGS redistribution recharge model and boundary flows.
- BN-USGSD - Bechtel Nevada (or base) HFM with the USGS no redistribution recharge model and boundary flows.

The other HFMs are:

- SCCC - Silent Canyon Caldera Complex
- PZUP - Raised Pre-Tertiary/Surface
- DRT - Deeply Rooted Belted Range Thrust Fault
- RIDGE - Basement Ridge
- TCL - Thirsty Canyon Lineament
- SEPZ - Contiguous Imbricate Thrust Sheet

Thus, SEPZ-MME is the contiguous southeast LCA HFM with the MME recharge model and boundary flows.

The five recharge models are:

- MME - Modified Maxey-Eakin
- USGSD - USGS recharge with redistribution
- USGSND - USGS recharge without redistribution
- DRIA - DRI recharge with alluvial mask
- DRIAE - DRI recharge with alluvial and elevation mask

5.1 Calibration Approach

The ASTM Standard Guide D 5981-96 (ASTM, 1996) (also Anderson and Woessner, 1992) describes a general protocol for model calibration. In this protocol, each cycle of parameter adjustment should begin with sensitivity and error analysis (Figure 5-1). The sensitive parameters to be adjusted should be considered in light of the data certainty. Conceptually, the process is not much different than if an automated parameter estimation technique is used (Poeter and Hill, 1997). The general protocol, as

used for the Pahute Mesa flow model, is shown in Figure 5-1. Notice that it is a process that iterates through model sensitivity and parameter adjustment. The Pahute Mesa CAIP (DOE/NV, 1999) states that the model calibration will be conducted by the trial-and-error method. The modeling approach/strategy (SNJV, 2004b) indicates that PEST (Watermark, 2004) parameter estimation software will be used. Both techniques have their strengths and weaknesses, and were used in calibrating the Pahute Mesa flow model.

Hill (1998) also presents a general model calibration procedure that has several components; the most relevant and how they were addressed in the Pahute Mesa flow model are shown in Table 5-1. In the trial-and-error approach the model is run, errors analyzed, adjustments made, and the cycle repeated. When this is improperly done, a shotgun type of approach results. Changes are made in an *ad hoc* manner without insight into the root cause of the model misfit. The trial-and-error method allows for more interpretive information to be considered, but can also be very tedious in that model datasets must be prepared and run by hand for analysis. Discrete sensitivity simulations to test model behavior are also often performed in a manual fashion. With a proper protocol (Figure 5-1), a trial-and-error calibration can yield reasonable and reliable results.

An alternative to trial-and-error calibration is to use an automated approach where the model response to parameter changes is systematically evaluated and the more important parameters that improve calibration identified. The PEST (Watermark, 2004) code was used for this purpose. The PEST code begins by changing each parameter to be considered by a certain amount and recording how the model calibration changes. The Levenberg-Marquardt procedure is used to compute parameters that improve the model agreement with the target data. The basic algorithm used by PEST has a long history of successful use in solving groundwater problems, and is also available in such codes as MODFLOW-2000 and UCODE. For more detail, refer to the PEST manual (Watermark, 2004).

Use of a parameter estimation code has several benefits, including using analyst time more effectively because less manual preparation and manipulation of datasets are required. In addition, a parameter estimation tool provides a framework that helps focus attention on analyzing model errors and their cause, and in the case of complicated models such as the Pahute Mesa CAU flow model, can greatly speed calibration. The PEST code also includes a variety of statistical analyses that help develop

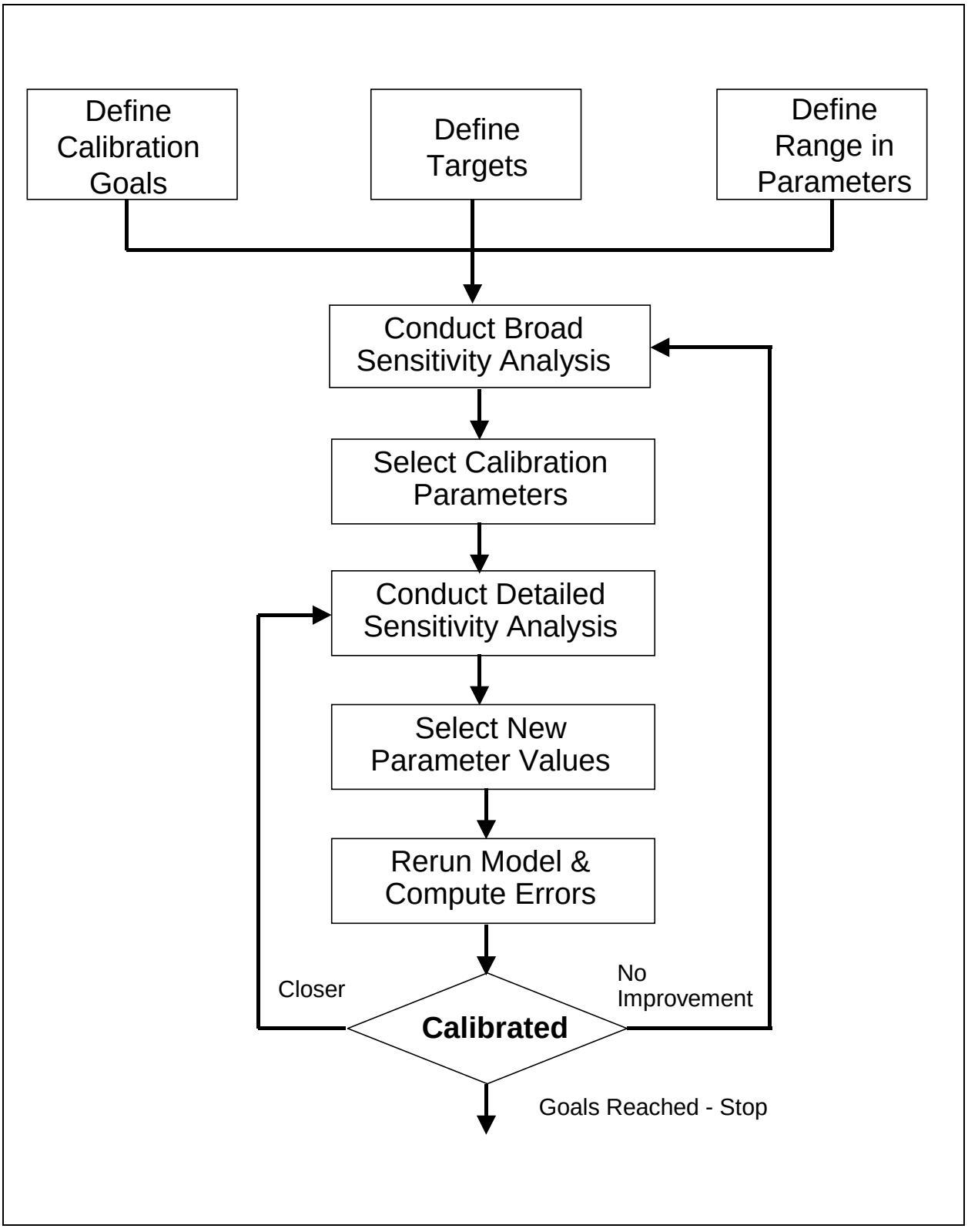

Figure 5-1
General Calibration Protocol

Table 5-1
Calibration Components and Implementation

Calibration Component[a]	Implementation in the Pahute Mesa CAU Flow Model
Apply the principle of parsimony	Hydrostratigraphic units or other geologic properties were not subdivided unless persistent model errors suggested it was necessary for model improvement, with some geologic rationale considered.
Include many kinds of data as observations	Well and spring head, regional water-balance considerations at the model edges, and Oasis Valley discharge were considered.
Assign weights that reflect measurement errors	Weights were developed from uncertainty estimates published in the Pahute Mesa hydrologic data document (SNJV, 2004a).
Evaluate model fit	Model fit was continually evaluated with residual post plots and other tools.
Evaluate optimized parameter values	The reasonableness of PEST revised model parameters was compared to estimated values. Review parameter correlations and fix selected correlated parameters.
Evaluate the potential for additional estimated parameters	Sensitivity analysis and post plots were used to identify locations where additional parameter adjustment was necessary.

[a]Hill, 1998

understanding of the model. These features include sensitivity and correlation coefficients, parameter confidence limits, and eigenvalue and eigenvector analysis. The sensitivity and correlation coefficients describe how much the model calibration changes relative to parameter change, and how parameters may influence one another. This is useful in testing the conceptual model as to what parameters are believed to control model behavior, and what parameters may act similarly on objective function. In addition, parameters that may be important to model calibration can be quantitatively identified and considered in more detail. The confidence limits and eigenvalue and eigenvector analysis are useful in understanding how well the observation data support the model parameters, and how many parameters should be considered for calibration. All these tools were used in calibrating the Pahute Mesa flow model.

The ASTM Standard Guide D 5490-93 (ASTM, 1993b) describes several approaches for evaluating the agreement between a flow model and modeled system. These procedures were used in calibrating

the Pahute Mesa flow model, and include qualitative and quantitative comparisons between model results and the following:

- Measured heads at wells and springs
- Water-balance information (recharge and discharge fluxes)
- Flow-direction information
- Estimated values of HFM hydraulic parameters from characterization data

The ASTM Standard Guide D 5490-93 recommends the use of quantitative measures for the agreement of hydraulic head and suggests quantitative measures for water-balance information if possible (ASTM, 1993b). For the Pahute Mesa CAU flow model, quantitative measures of the fit with head (wells and springs) data, Oasis Valley discharge, and lateral water balance were considered.

A variety of numeric and graphical tools are used to investigate flow model calibration. These include summary statistical measures such as the mean error (or residual) (ME), largest and smallest errors, standard deviation of the errors (SD), and sum of weighted squared errors. Error, or residual, is defined as follows:

$$r_i = H_i - h_i \tag{5-1}$$

where h_i is the computed head at the location where H_i was measured. Mean error, ME, is defined as follows:

$$ME = \Sigma w_i r_i / n w_i \tag{5-2}$$

The SD is defined as follows:

$$SD = \frac{\Sigma (r_i w_i)^2}{n} \tag{5-3}$$

Sum of weighted squared errors (also called phi after the Greek alphabet symbol used to denote it, as well as "goodness of fit") is defined as (Watermark, 2004):

$$\Phi = \sum_{i=1}^{m} (w_i r_i)^2 \tag{5-4}$$

where Φ is the objective function (phi, or goodness of fit), *w* is the observation weight, *r* is the residual or difference between the simulated and measured values, and *n* is the number of observations of non-zero weight. If the weights assigned to calibration data change, all these measures will change even if the model results are the same. Thus, it is important to compare results using a consistent weighting scheme (see Section 5.2).

During calibration, it is desired to reduce the ME to zero; that is, there should be no bias in the ME. This will give a model that has no systematic (at least in the univariate statistical sense) bias. However, errors of –1 and +1 give the same ME as –50 and +50, but it is obvious a model with 50 ft of error is not as good as one with 1 ft. Consequently, the standard deviation is used to describe spread of the errors. The ME may be low, but if the spread is large, the model may be inadequate.

Statistical measures are useful for summarizing model behavior but do not readily give a sense for the spatial distribution of errors. To address this issue, the following graphical analyses are also used (see ASTM Standard Guide D 5490-93 [ASTM, 1993b] for more information):

- The *scattergram*, or cross plot, shows the observed data versus computed results plotted against each other, and is useful for identifying overall goodness and bias.
- Post plots of head residuals in plan view show the distribution of errors in the model. Recalling the ME example from above, it would be possible to have an ME of 0, with all the errors on one side of the domain at a +50 error and on the other with a –50 error, which is a vastly different result than if the errors are scattered randomly in space (the ideal case).
- Flow residuals are also examined using bar charts, although they can also be visualized with a scattergram.

The goal of model calibration (also called "parameter estimation," "solving the inverse problem," and "inversion") is to make the model agree with reality by adjusting, within their ranges of variation, model parameters. How this is approached can be critical. Freyberg (1988) presented a study in which students were given a model to calibrate. They had to calibrate the model and then make a prediction. The best-calibrated model actually made the worst predictions. This is because the best-calibrated model was fitted by tweaking hydraulic conductivity on a block-by-block basis, but the best predictive model chose to zone the hydraulic conductivity into a few homogenous regions. Minimizing the ME, standard deviation, and goodness of fit is not the sole objective of model calibration.

The reasonableness of the flow directions was also assessed qualitatively during the calibration phase via streamline particle tracking and quantitatively via geochemical analysis in Section 7.0. Finally, it is important to recognize that no matter the procedure, the goal of model calibration is a set of model parameters that best (or at least reasonably) represents the hydrogeologic system.

5.2 Calibration Data

Four types of information, or targets, were used for calibration of the Pahute Mesa flow model as follows:

- Hydraulic head from wells (see Appendix F)
- Estimated spring head in and near Oasis Valley (see Appendix F)
- Oasis Valley discharge derived from Laczniak et al. (2001)
- Edge flows estimated from regional model analysis presented in the Pahute Mesa hydrologic data document (SNJV, 2004a)

Because an automated procedure was used to aid calibration, multiplicative weighting factors were developed and assigned to data with different levels of accuracy and measurement units. The factors that PEST needs are the inverses of the measurement error standard deviations (Watermark, 2004). Thus, measurements with a larger standard deviation receive a smaller weight. The weights, which have reciprocal units of the target data, also transform the objective function contribution from different data types into dimensionless values that can be compared regardless of measurement units. However, an alternate empirical approach is also commonly used (e.g., Wolfsberg et al., 2002; DOE/ORD, 2004) in which the weights are assigned by considering accuracy along with judgment to give the desired contribution to the calibration for selected data.

The head calibration dataset was presented in Appendix E of the Pahute Mesa hydrologic data document (SNJV, 2004a) (see Plate 1). Along the east-central edge of the model, Wells Hagestad 1 (which may be perched), TW-1 (the upper two intervals may be perched), UE-12n #15A (which may be perched), and U-12s (which may be perched) were either outside the model boundary or just inside it (as well as perched), thus making them unsuitable for calibration because they were so close to the specified-head conditions at the edge of the model. Along the southern edge, Well Gexa 4 (also

suspected perched by the YMP [DOE/ORD, 2004]) was just inside the model boundary. These wells were used to check the model boundary head in these areas for reasonableness and were included in the calibration with a very low weight so the results could still be evaluated without unduly influencing the calibration.

As part of the hydraulic head dataset, the reference point elevation accuracy and the measurement uncertainty (as a standard deviation) were presented. Hill (1998) shows how to convert an estimated land surface error into a standard deviation. When the land surface elevation is estimated from USGS topographic maps, the formula is (contour interval/[2*1.65]). Reference point elevation accuracy of 6.096 m corresponds to locations estimated from USGS topographic maps with 40-ft (12-m) contour intervals.

The natural variability of rock permeability, which is not represented other than in a broad way in the Pahute Mesa flow model, creates variability in water levels. Gelhar (1986) shows how to use a solution by Naff (1978) to estimate the magnitude of this error. Appendix G of Wolfsberg et al. (2002) estimated correlation scales for the various types of volcanic rocks found on Pahute Mesa. These scales range from several tens of meters to a few hundred meters in the horizontal, to a few tens of meters in the vertical direction. Depending on the various assumptions required in the calculation, the standard deviation in head from heterogeneity could be as high as 2 m.

Simulated heads were not interpolated to the actual well location within an element, which gives up to 1 m of error when the gradient of Blankennagel and Weir (1973) and the smallest element size of 67.5 m is used. A value of 1 m was used to account for heterogeneity and interpolation error. Finally, all the standard deviations of reference point uncertainty, head value uncertainty, and heterogeneity were summed and the weight for PEST computed. Table 5-2 shows the weights used in model calibration for well and spring heads. Figure 5-2 shows a histogram of the weights used in model calibration for well and spring heads. The weights between 0 and 0.1 (none of which were actually zero) are mainly associated with wells and springs that had reference point elevation accuracy estimate from topographic maps with 6 or 3 m accuracy (40- or 20-ft contour interval) that result in low weights. Twelve of the lowest weights are from the wells described above that were located outside the model or just on its edge.

Table 5-2
Head and Spring Calibration Weights
(Page 1 of 6)

ID No.	Site Name	Weight	Comment
1	Beatty Wash Terrace Well	0.2	
2	Beatty Well No. 1	1.00×10^{-3}	Downweighted, just inside edge of mesh
3	Boiling Pot Road Well	0.2	ET Cycles but good
4	Coffer Dune Well	0.34	ET Cycles but good
5	Coffer Lower ET Well	0.32	ET Cycles but good
6	Coffer Middle ET Well	0.31	ET Cycles but good
7	Coffer Windmill Well	0.35	
8	ER-18-2	0.84	May still be rising
9	ER-19-1 #1 (deep)	1.00×10^{-3}	Downweighted, just inside edge of mesh; Fenelon (2000) suggests depressed below regional
10	ER-19-1 #2 (middle)	1.00×10^{-3}	Downweighted, just inside edge of mesh; large uncertainty from hydrograph
11	ER-19-1 #3 (shallow)	1.00×10^{-3}	Downweighted, just inside edge of mesh; Fenelon (2000) suggests elevated (perched?) above regional
12	ER-20-1	0.89	
13	ER-20-2-1	0.2	
14	ER-20-5 #1 (3-in. string)	0.72	
15	ER-20-6 #1 (3-in. string)	0.92	
16	ER-20-6 #2 (3-in. string)	0.95	
17	ER-20-6 #3 (3-in. string)	0.91	
18	ER-30-1	0.94	
19	ER-EC-1	0.83	
20	ER-EC-2A (498.3-681.5 m)	0.82	
21	ER-EC-2A (498.35-1,515.8 m)	0.78	
22	ER-EC-4 (290.2-1,062.8 m)	0.83	
23	ER-EC-4 (290.2-699.5 m)	0.83	
24	ER-EC-4 (Lower Interval)	0.84	
25	ER-EC-5	0.81	
26	ER-EC-6 (481.9-1,164.3 m)	0.83	
27	ER-EC-6 (481.9-1,524 m)	0.84	
28	ER-EC-7	0.78	
29	ER-EC-8	0.81	
30	ER-OV-01	0.83	
31	ER-OV-02	0.81	
32	ER-OV-03a	0.76	Declining trend (very small)
33	ER-OV-03a2	0.78	

Table 5-2
Head and Spring Calibration Weights
(Page 2 of 6)

ID No.	Site Name	Weight	Comment
34	ER-OV-03a3	0.76	Declining trend (very small)
35	ER-OV-03b	0.8	
36	ER-OV-03c	0.82	
37	ER-OV-03c2	0.82	
38	ER-OV-04a	0.77	ET Cycles but good
39	ER-OV-05	1.00×10^{-3}	Downweighted, just inside edge of mesh
40	ER-OV-06a	0.82	
41	ER-OV-06a2	0.82	
42	Gexa Well 4	1.00×10^{-3}	Downweighted, just inside edge of mesh; YMP also weighted low
43	Hagestad 1	2.00×10^{-3}	Downweighted, outside mesh; may be perched
44	Matheny Well	0.21	
45	Middle Oasis Valley ET Well	0.31	ET Cycles but good
46	Pioneer Road Seep Well	0.2	ET Cycles but good
47	PM-1 (2,356.408 m)	0.66	Hot water, so true water level may be lower
48	PM-2	0.67	
49	PM-3 (Upper Borehole)	0.67	Hydrograph declining
50	PM-3 (Lower Borehole)	0.67	
51	PM-3-1 (Piezometer 1)	0.67	Hydrograph still rising
52	PM-3-2 (Piezometer 2)	0.67	Hydrograph still rising
53	Springdale ET Deep Well	0.32	ET Cycles but good
54	Springdale ET Shallow Well	0.31	ET Cycles but good
55	Springdale Lower Well	0.18	ET Cycles but good
56	Springdale Upper Well	0.34	ET Cycles but good
57	Springdale Windmill Well	0.34	ET Cycles but good
58	TW-1 (1,125 m)	1.00×10^{-3}	Downweighted, edge of mesh
59	TW-1 (1,127-1,137 m)	1.00×10^{-3}	Downweighted, edge of mesh
60	TW-1 (170 m)	2.00×10^{-3}	Downweighted, edge of mesh; may be perched
61	TW-1 (492 m)	2.00×10^{-3}	Downweighted, edge of mesh; may be perched
62	TW-1 (560 m)	1.00×10^{-3}	Downweighted, edge of mesh
63	TW-1 (826 m)	1.00×10^{-3}	Downweighted, edge of mesh
64	TW-1 (839 m)	1.00×10^{-3}	Downweighted, edge of mesh
65	TW-1 (839-1,279 m)	1.00×10^{-3}	Downweighted, edge of mesh
66	U-12s (451.1 m)	2.00×10^{-3}	Downweighted, outside mesh; may be perched; fluctuating
67	U-19ab	2.00×10^{-3}	Fenelon (2000) indicates possibly perched
68	U-19ab 2	2.00×10^{-3}	Fenelon (2000) indicates possibly perched

Table 5-2
Head and Spring Calibration Weights
(Page 3 of 6)

ID No.	Site Name	Weight	Comment
69	U-19ad	0.98	Large uncertainty from hydrograph
70	U-19ae	0.69	
71	U-19ai	0.68	
72	U-19aj	0.52	
73	U-19aq	2.00×10^{-3}	Fenelon (2000) indicates possibly perched
74	U-19ar	0.18	
75	U-19aS (857 m)	0.98	
76	U-19au	0.86	
77	U-19au #1	0.68	
78	U-19ay	0.94	
79	U-19az	2.00×10^{-3}	Fenelon (2000) indicates possibly perched
80	U-19ba	2.00×10^{-3}	Fenelon (2000) indicates possibly perched
81	U-19bg #1	0.86	
82	U-19bh	2.00×10^{-3}	Fenelon (2000) indicates possibly perched
83	U-19bj	0.002	Declining trend may be perched
84	U-19bk	2.00×10^{-3}	Fenelon (2000) indicates possibly perched
85	U-19d #2	0.98	
86	U-19e	0.98	
87	U-19g	0.5	
88	U-19x	0.98	
89	U-20 WW (Open)	0.9	
90	U-20a	0.003	
91	U-20a #2 WW	0.84	
92	U-20ah	0.49	
93	U-20ai	0.59	
94	U-20ak	0.64	
95	U-20am	0.69	
96	U-20an	0.79	
97	U-20ao	2.00×10^{-3}	Perched
98	U-20ar #1	0.6	
99	U-20as	0.95	
100	U-20at #1	0.76	
101	U-20av	0.58	
102	U-20aw	0.89	Only about 4 m worth of saturated zone here
103	U-20ax	2.00×10^{-3}	Fenelon (2000) indicates possibly perched

Table 5-2
Head and Spring Calibration Weights
(Page 4 of 6)

ID No.	Site Name	Weight	Comment
104	U-20ay	0.003	
105	U-20az	0.98	
106	U-20bb (579.12 m)	0.003	
107	U-20bb (676.66 m)	0.52	
108	U-20bb #1	0.33	
109	U-20bc	0.003	Elevated compared to regional
110	U-20bd (689.15 m)	0.94	
111	U-20bd #1	0.86	
112	U-20bd #2	0.7	
113	U-20be	0.5	
114	U-20bf	0.5	
115	U-20bg	0.98	
116	U-20c	0.98	
117	U-20e	0.98	
118	U-20g	0.98	
119	U-20i	0.98	
120	U-20m	0.67	
121	U-20n PS #1DD-H (922 m)	0.98	Fenelon (2000) indicates impacted by pumping at U-20 WW
122	U-20y	0.56	
123	UE-12n #15A	2.00×10^{-3}	Downweighted, outside mesh; may be perched
124	UE-18r	0.61	
125	UE-18t	0.71	
126	UE-19b #1 WW	0.82	
127	UE-19c WW	0.67	
128	UE-19e WW	0.39	
129	UE-19fs	0.98	
130	UE-19gS	0.98	
131	UE-19gS WW	0.84	
132	UE-19h	0.89	
133	UE-19i	0.98	
134	UE-19z	0.2	
135	UE-20ab	0.52	
136	UE-20av	0.84	
137	UE-20bh #1	0.64	Fenelon (2000) indicates impacted by pumping at U-20 WW
138	UE-20c	0.003	

Table 5-2
Head and Spring Calibration Weights
(Page 5 of 6)

ID No.	Site Name	Weight	Comment
139	UE-20d	0.54	
140	UE-20e #1	0.98	
141	UE-20f (1,384.7 m)	0.93	
142	UE-20f (4,171 m)	0.45	
143	UE-20h WW	0.59	
144	UE-20j WW	1.67	
145	UE-20n #1 (1,005.84 m)	0.98	
146	UE-20n #1 (863.8 m)	0.98	Fenelon (2000) indicates impacted by pumping at U-20 WW
147	UE-20p	0.67	
148	UE-29a #1 HTH	2.00×10^{-3}	May be perched or local flow system
149	UE-29a #2 HTH	2.00×10^{-3}	May be perched or local flow system; YMP also weighted low
150	USW UZ-N91	0.44	Recharge seen in hydrograph
151	Ute Springs Drainage Well	0.19	ET Cycles but good
152	WW-8	0.98	Declining hydrograph trend
153	Spring	1	
154	Crystal Springs Area	2.00×10^{-3}	Downweighted; source water may be local or perched according to HDD
155	Revert Springs Channel	1.00×10^{-3}	Downweighted, just inside edge of mesh
156	Revert Springs Area	1.00×10^{-3}	Downweighted, just inside edge of mesh
157	Revert Springs Area	1.00×10^{-3}	Downweighted, just inside edge of mesh
158	Spring (Report R10)	1	
159	Spring	1	
160	Springdale Culvert	1	
161	Torrance Spring	1	
162	Ute Springs Area	1	
163	Spring	1	
164	Oasis Valley Upper Culvert Spring	1	
165	Hot Springs Area	1	
166	Hot Springs Pump House	1	
167	Hot Springs Bath House 1	1	
168	Hot Springs Bath House 2	1	
169	Hot Springs below Culvert 1	1	
170	Hot Springs Culvert 2	1	
171	Hot Springs above Culvert 2	1	
172	Ute Springs Area	1	

Table 5-2
Head and Spring Calibration Weights
(Page 6 of 6)

ID No.	Site Name	Weight	Comment
173	Spring	1	
174	Ute Springs Culvert	1	
175	Ute Springs	1	
176	Oleo Road Spring	0.004	Spring located in area of very high topographic gradient
177	Goss Spring - North	0.006	Locations uncertain
178	Goss Spring	0.006	Locations uncertain
179	Spring	0.006	Locations uncertain
180	Spring	1	

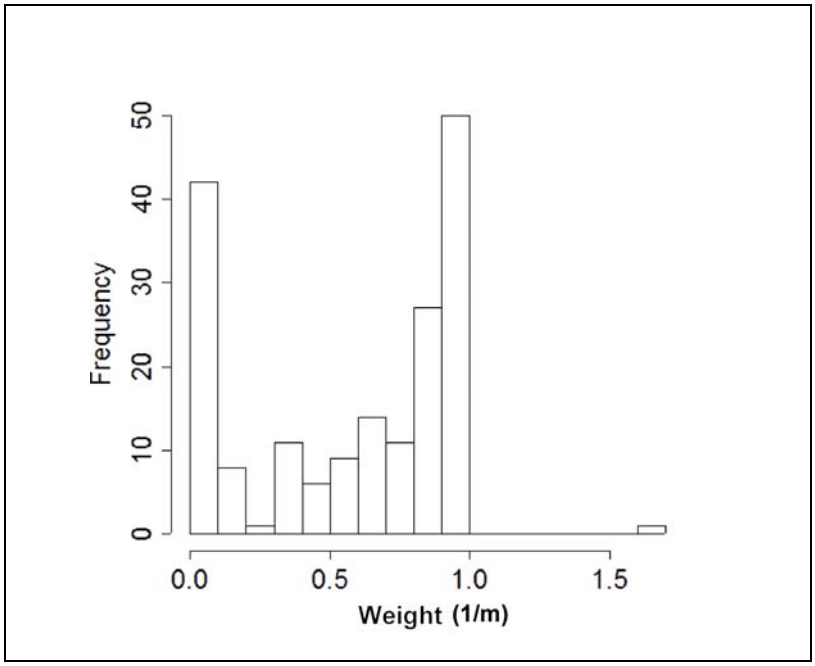

Figure 5-2
Histogram of Head Calibration Weights

The estimated spring head in the Oasis Valley area was also presented in the Pahute Mesa hydrologic data document (SNJV, 2004a). These data were assigned a unit weight in order to help emphasize Oasis Valley discharge, and in a few cases lower weights were assigned based on proximity to model edge and other factors (e.g., Oleo Road Spring was assigned a low weight because it lies in an area of high topographic gradient that made the model unable to match it). The location of three springs –

Goss Spring, Goss Spring-North, and Spring id 179 – had incorrect locations reported in the Pahute Mesa hydrologic data document (SNJV, 2004a). They were relocated as shown in Table 5-3.

Table 5-3
Corrected Spring Locations

Spring	Easting (UTM Zone 11, NAD 27) (m)	Northing (UTM Zone 11, NAD 27) (m)	Elevation (m)
Goss Spring	525419.43	4094275.13	1,139.34
Goss Spring-North	525289.20	4094402.54	1,139.34
Spring id 179	525460.21	4094286.46	1,139.35

Source: Watrus, 2004

NAD = North American Datum

Oasis Valley has long been known to be a groundwater discharge area. The UGTA regional model (DOE/NV, 1997) summarized the range in estimated discharge in this area. More recently, Laczniak et al. (2001) conducted an extensive field study to further refine the discharge estimate. Figure 4-17 shows the Laczniak et al. (2001) digital data overlaid on the southwestern part of the model domain, with seven zones (numbered 1-6, and 8) overlaid to define individual discharge segments. The CAU model does not completely encompass the discharge area studied by Laczniak et al. (2001). Table 5-4 summarizes the flow rates for each segment shown on Figure 4-17; the total is 227 kg/s. By comparison, the total mean Oasis Valley discharge estimated by Laczniak et al. (2001) is 242 kg/s.

Table 5-4
Oasis Valley Zone Discharge

Discharge Zone	Discharge (kg/s)
1	70.7
2	13.0
3	47.7
4	38.0
5	33.9
6	22.2
8	1.50

Oasis Valley discharge uncertainty was assessed by Laczniak et al. (2001). Using the reciprocal of the published Oasis Valley discharge standard deviation gives a weight of 0.0013 in measurement

units of acre-feet (ac-ft), or 0.034 in seconds per kilogram (s/kg) (the units used in FEHM). Laczniak et al. (2001) estimate the total mean discharge in Oasis Valley at 6,200 acre-feet per year (ac-ft/yr) (242 kg/s). With a weight of 0.034, a 50 percent error (3,100 ac-ft/yr or 121 kg/s) would result in a weighted error of only 16. This would be an equivalent well head error of only 4 m with a unit weight. Mathematically, Oasis Valley discharge is key to constraining the flow model because it is well known that a model with constant head boundaries calibrated only to head is not unique. To address a similar problem, Wolfsberg et al. (2002) used the flow estimated by Blankennagel and Weir (1973) (80 kg/s) to constrain their TYBO/BENHAM sub-CAU model, and assigned it a unit weight. This resulted in a strong contribution from flow to their model goodness of fit relative to the 22 wells used for head calibration, which were generally matched within a few meters. During calibration, a weight value of 2 s/kg was found to give good results in matching Oasis Valley discharge.

The UGTA regional model boundary flow analysis is summarized in Appendix F of the Pahute Mesa hydrologic data document (SNJV, 2004a). However, the CAU mesh is not aligned precisely with the UGTA regional model (DOE/NV, 1997); thus, some interpolation of the edge flows is necessary. Gable and Cherry (2001) developed a general procedure for interpolating MODFLOW (McDonald and Harbaugh, 1988) cell flows onto a piecewise linear surface. In the case of the Pahute Mesa CAU model, the surfaces are the planes that define the north, west, south, and east edge for which the UGTA regional model flow into or out of the CAU model is to be interpolated. The approach transforms the flows into an approximate Darcy velocity at each face of the MODFLOW cell. The velocity is interpolated onto the linear control surface, and flow is completed by integration of the velocity normal to the control surface. The interpolated edge flows are shown in Table 5-5. These flows were used as calibration targets that the CAU model was required to reasonably honor.

Model boundary flow uncertainty was derived in a discrete manner from the regional model by combining different combinations of HFM and recharge. An initial weighting procedure was attempted by considering the base HFM and MME recharge boundary flow as the mean, with results of the base HFM and DRI and USGS recharge defining the upper and lower 95 percent confidence limits. This gives approximately (considering only the northern edge for example) a weight of 0.027. With this weight, an error of 100 kg/s would give a squared weighted error of about 9 ([100*0.027]^2); as with the weights for Oasis Valley discharge, this seems an unreasonably small

Table 5-5
Interpolated Regional Model Boundary Flows

Case[a]	North[b] (kg/s)	South[c] (kg/s)	East[c] (kg/s)	West[a] (kg/s)	HFM	Recharge Model
g1ar1a	263.2	-324.6	-32.4	23.6	BN[d]	MME[e]
g1ar1b	291.6	-415.9	-40.9	56.5	BN	ME[f]
g1ar2	156.2	-296.0	-38.4	39.2	BN	USGSND[g]
g1ar3a	335.4	-547.4	-81.6	75.0	BN	DRIA[h]
g1ar3b	289.1	-524.7	-49.7	57.8	BN	DRIAE[i]
g1br1a	280.3	-418.6	-38.0	59.8	BN	MME
g2ar1a	305.1	-536.6	-66.4	64.0	SCCC[j]	MME
g2br1a	328.3	-547.5	-73.1	64.1	SCCC	MME
dvrfs[k]	350	-350	-8	50	-	-

[a]As defined in the Pahute Mesa hydrologic data document SNJV (2004a)
[b](-) = is into model
[c](+) = is out of model
[d]BN = Bechtel Nevada base model
[e]MME = Modified Maxey-Eakin
[f]ME = Maxey-Eakin
[g]USGSND = USGS no redistribution
[h]DRIA = DRI alluvial mask
[i]DRIAE = Alluvial and elevation masks
[j]SCCC = Silent Canyon Caldera Complex
[k]dvrfs = Not interpolated

contribution and was adjusted during calibration to a value of 0.5 for all boundaries. The contribution of each type of data is presented in Sections 5.6 and 5.7 and discussed in Section 5.8.

5.3 Boundary Head Adjustments

The starting point for the CAU-model specified-head boundary conditions was the UGTA regional model (DOE/NV, 1997) results interpolated onto the mesh edges as described in Section 4.3.3. Changes were made during calibration based on the following considerations:

- When the UGTA regional model (DOE/NV, 1997) was developed, the exact nature of the western boundary (just west of Oasis Valley) was unknown but was assumed to be a no flow, or streamline. More recent work by SNJV (2004a) and the USGS (Faunt et al., 2004) suggests that there is flow east from Sarcobatus Flat into Oasis Valley. For the CAU model, the boundary head west of Oasis Valley and south of northing 4,098,000 m, the boundary head was raised to create flow into Oasis Valley (Figure 5-3). The head along the northern edge west of about easting 550,000 m was adjusted to better approximate the head on the northern edge of the model.

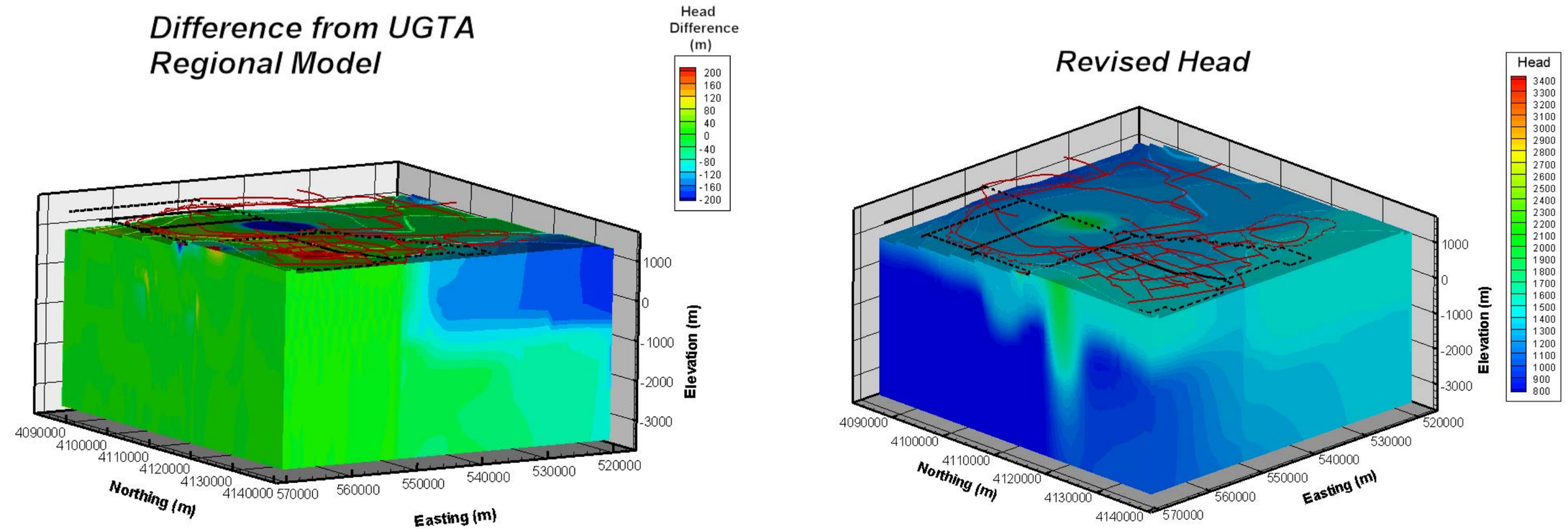

Note: Head difference is defined as initial minus adjusted.

Figure 5-3
Calibrated CAU-Model Boundary Heads and Difference from UGTA Regional Model Viewed from the Northeast

- The UGTA regional model (DOE/NV, 1997) (and the recent DVRFM [Faunt et al., 2004]) has a persistent misfit at the Gold Flat 2 well just outside the north-central edge of the CAU-model domain of over 100 m with simulated head about 1,320 m. Just south of Gold Flat inside the CAU model are Wells UE-20p and PM-2, both of which have mean water levels of over 1,400 m. Thus, if the boundary head in the part of the model is used directly from the UGTA regional model (or DVRFM), there will be an immediate 100-m error that should not be corrected by parameter adjustment because the error is entirely a consequence of an inaccurate boundary condition assignment. Figure 5-3 shows the view of the head field used to calibrate the model and its change from the starting interpolated UGTA regional model head.

- The southern edge of the model east of Oasis Valley is coincident with an area of high-hydraulic gradient that is poorly understood. Zyvoloski et al. (2003) investigated several conceptual models of this area, and in general found that some type of low-permeability feature (possibly from hydrothermal alteration) was required to replicate this feature. The UGTA regional model (DOE/NV, 1997) performed only fairly in this area. Gexa 4, USW UZ-Na91, and UE-29a #1 and UE-29a #2 Hydrologic Test Holes (HTHs) are the only wells in this area selected for calibration, and it is unclear whether UE-29a taps an aquifer system or a local and possibly perched flow system. The water level at Gexa 4 was combined with regional model data and interpolated onto the southern CAU-model edge. The effects of the change can be seen in Figure 5-4 near easting of 535,000 m and at an elevation above 0 m.

- Well TW-1, excluding the upper two intervals, was used to revise the eastern boundary heads, which otherwise remained relatively unchanged from the UGTA regional model (DOE/NV, 1997) results seen in Figure 5-4.

- The interpolated and corrected heads on the northwest corner (both north and west faces) of the model created a local flow cell, where flow entered on the far west northern edge and then immediately departed on the far northwestern edge. This created an erroneous boundary flow estimate that was not in the UGTA regional model (DOE/NV, 1997), which had a no-flow boundary along its western edge. Thus, this flow was entirely an artifact of the constant-head specification on the western edge. Water-level maps were reviewed, and the western edge north of 4,103,000 m was specified as a no-flow boundary along what is reasonably believed to be a regional flow divide. The conversion of this boundary to no-flow and the effects of correcting the heads on the northwestern edge to better match PM-2 and UE-20p cause the changes seen in Figure 5-4. Also see Figure 3-4 in Section 3.0 for a water-level map that supports this interpretation.

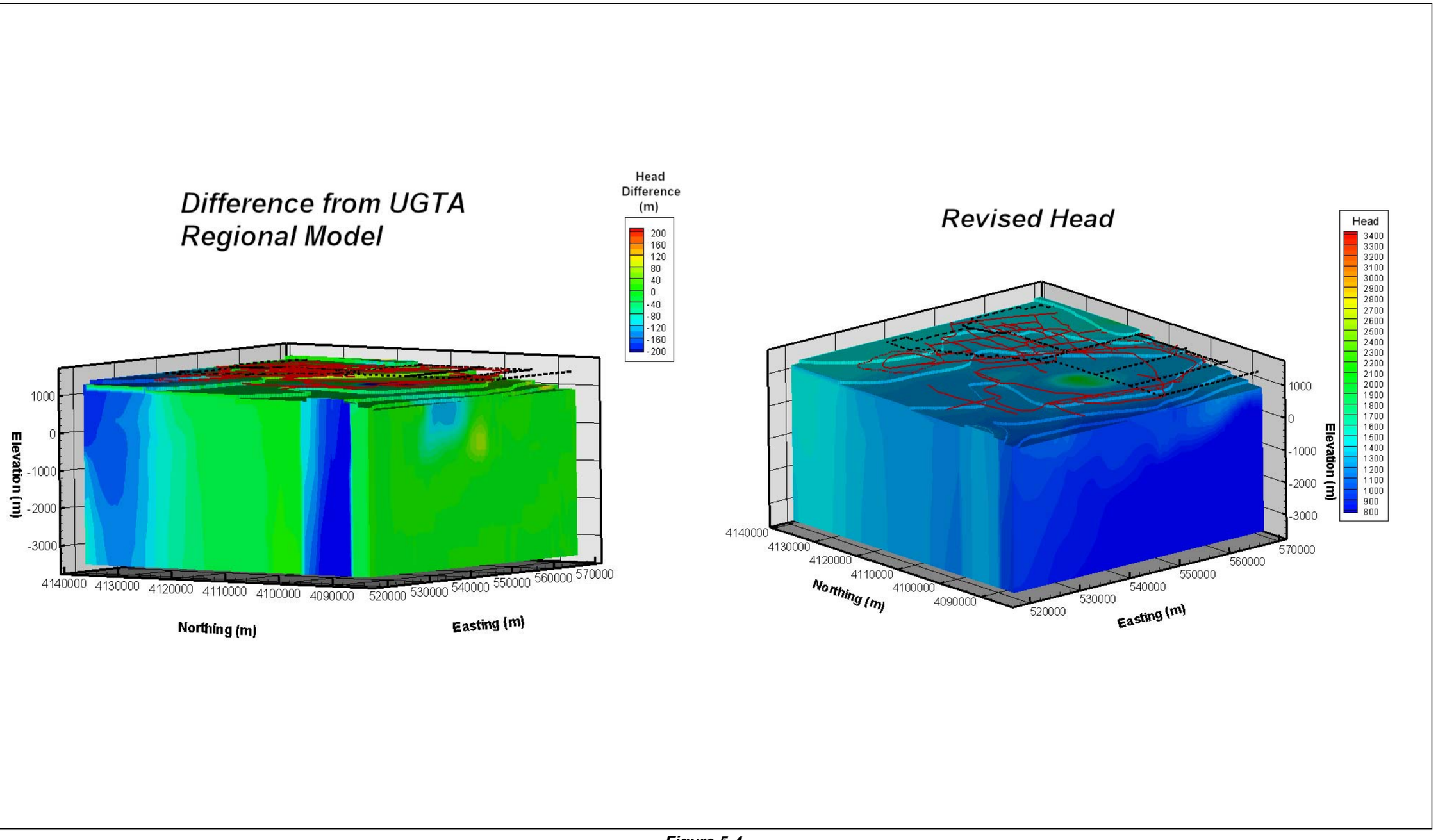

Figure 5-4
Calibrated CAU-Model Boundary Heads and Difference from UGTA Regional Model Viewed from the Southwest

5.4 Geologic Model Subdivision

During the calibration process, it was discovered that the flow model was particularly sensitive to the properties of two regionally extensive HSUs: the PBRCM and the TMCM. Both of these units exist over large areas of the model. In order to better address the geologic heterogeneity that almost certainly exists in these two large units, they were subdivided areally. In the case of the PBRCM, it was divided outside of Areas 19 and 20 as defined by the Silent Canyon Caldera bounding faults in the base model as shown in Figure 5-5. Figure 5-5 also shows faults and structure contours. Bechtel Nevada (2002) suggested subdivision of the TMCM into several hydrogeologic domains (Figure 5-6) that were adopted with the further subdivision of the Northern Timber Mountain and Ammonia Tanks subdomains into east and west sections at easting 560,000 m.

In addition, the UGTA regional model further subdivided the LCA, TCVA, and TMA (see Volume VI, DOE/NV, 1997). These divisions were propagated into the CAU model, as they were originally made for hydrogeologic reasons. Figure 5-7 shows the nodes as solid blue rectangles from the subdivision of the LCA along the southeastern corner of the model domain as derived from the UTGA regional model (DOE/NV, 1997). This fragment of LCA belongs to the larger subdivision that extended to the east and encompassed the eastern part of the NTS and low hydraulic gradient area in the UGTA regional model. Figure 5-8 shows the nodes from the subdivision of the TMA. Note that the node spacing is so dense that the nodes appear as a solid fill. Also note that the nodes are entirely at the top of the model domain. The UGTA regional model subdivided the TMA to allow for potential alteration effects within the Timber and Black Mountain calderas. Zone, or material, 36 is the TMA in the CAU model (top panel), which was further divided by Zone 6, which represents the area near Black Mountain, from the UGTA regional model (DOE/NV, 1997). Thus, Zones 6 and 36 give the entire extent of the TMA. The TMCM HSU replaced the other TMA zones and the division suggested in Figure 5-6. Figure 5-9 shows the nodes from the subdivision of the TCVA. The TCVA, like the TMA, also was divided to allow for alteration effects. Zone 44 is the TCVA in the CAU model (top panel), which was further subdivided by Zone 6, again representing the area near Black Mountain. Zones 6 and 44 give the extent of the TCVA in the CAU model.

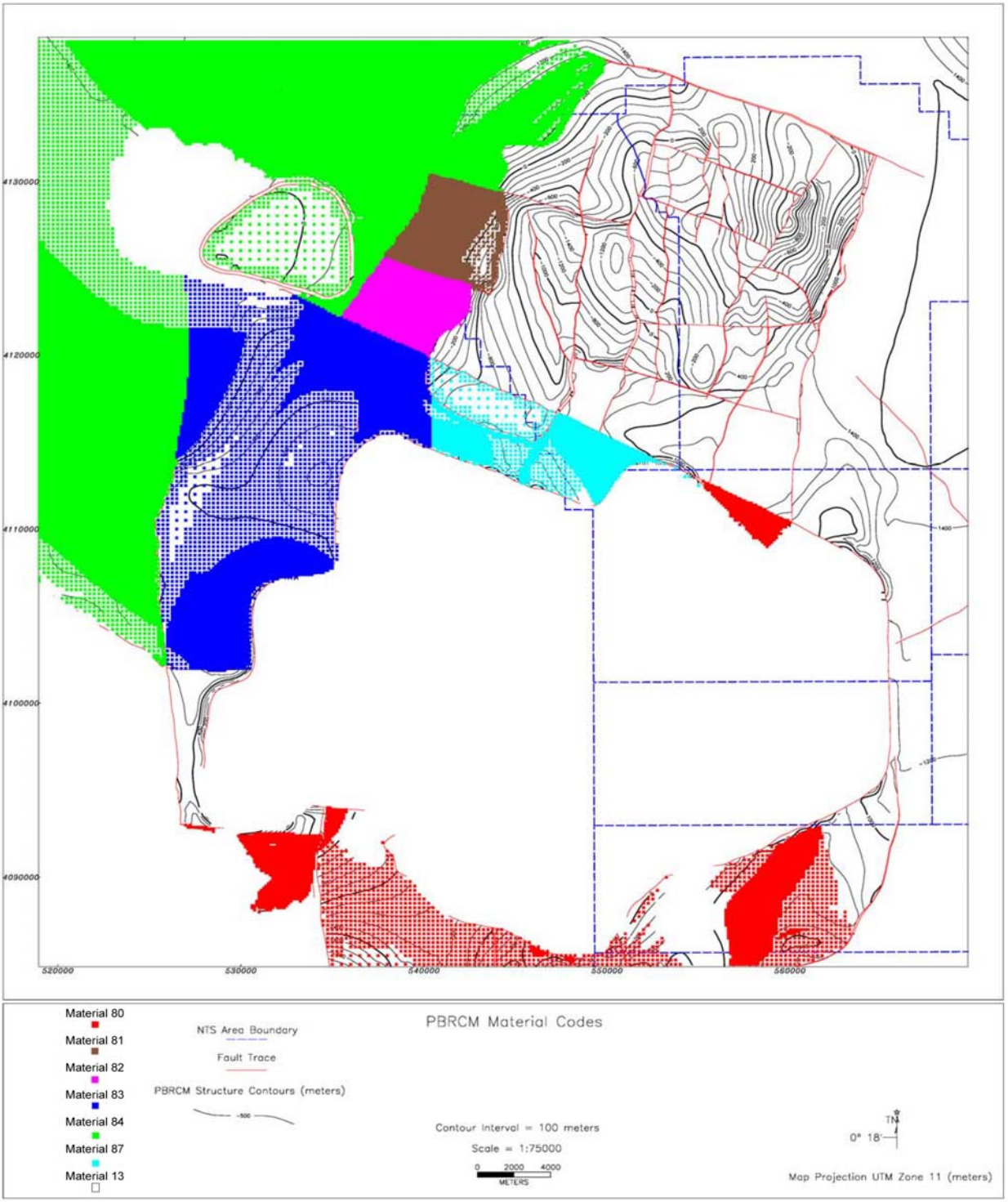

Figure 5-5
CAU-Model Pre-Belted Range Composite (PBRCM) Material Zones

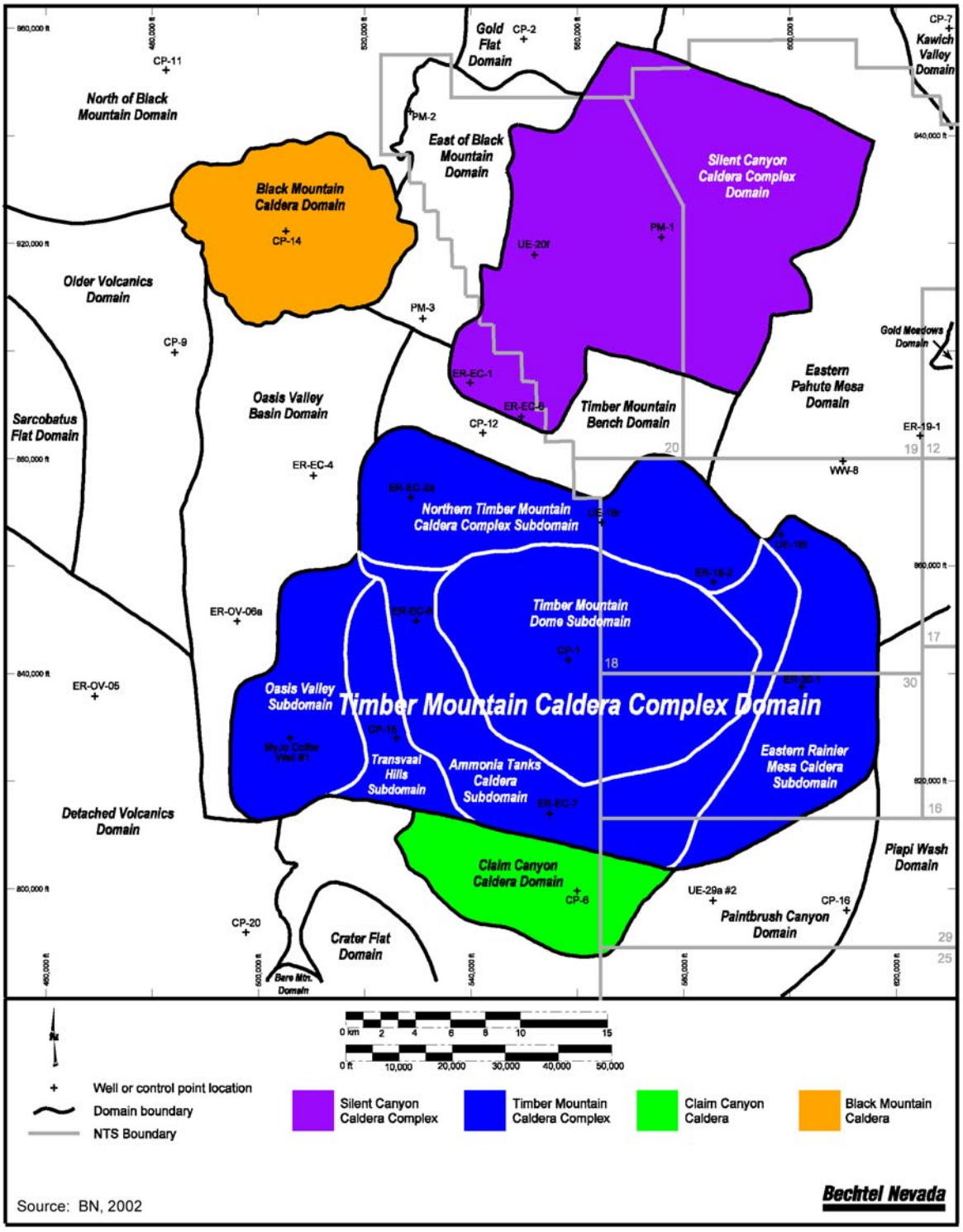

Figure 5-6
Map Showing Hydrogeologic Domains in the Pahute Mesa/Oasis Valley Model Area

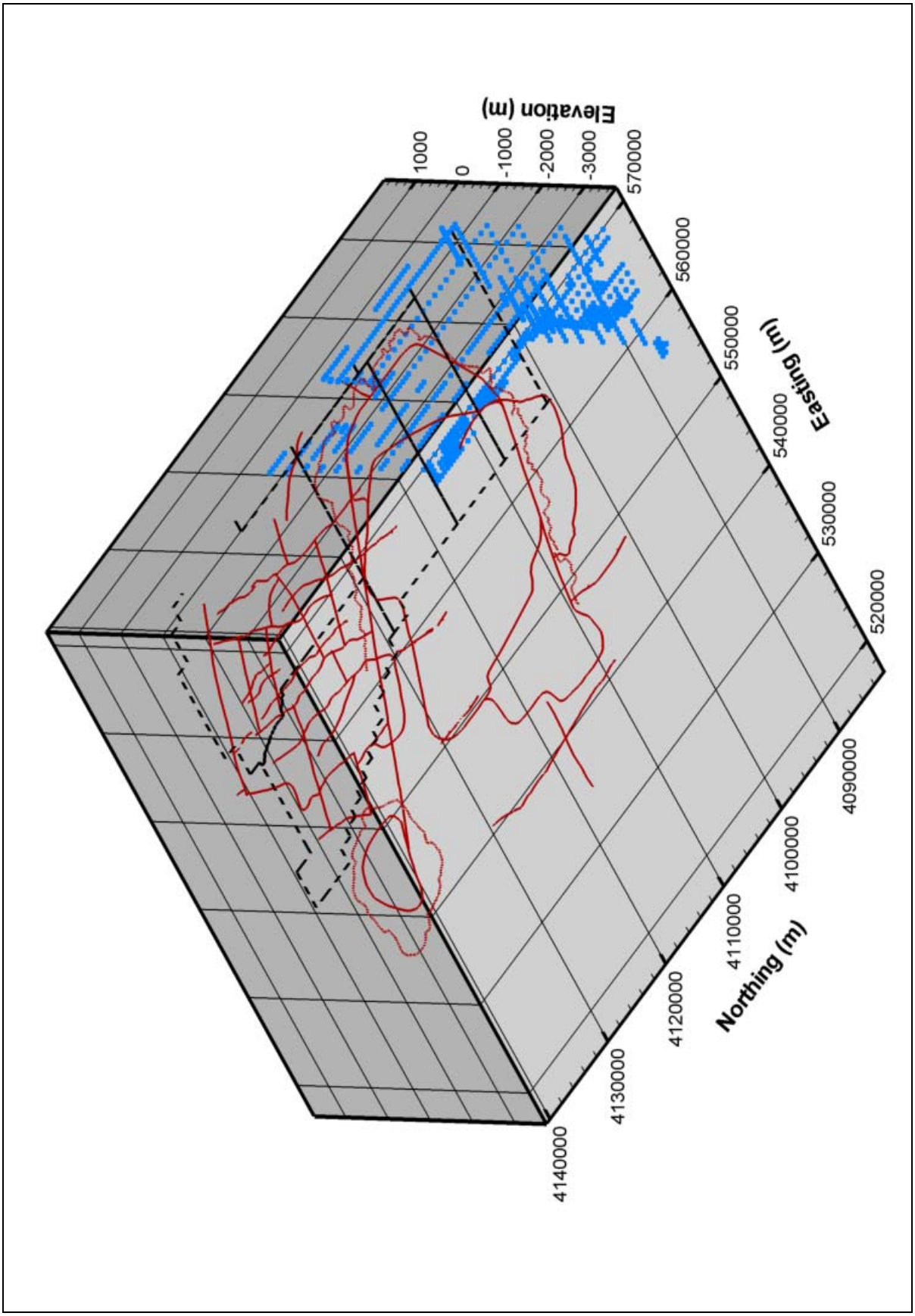

Figure 5-7
Map Showing LCA Nodes from UGTA Regional Model Zone 1

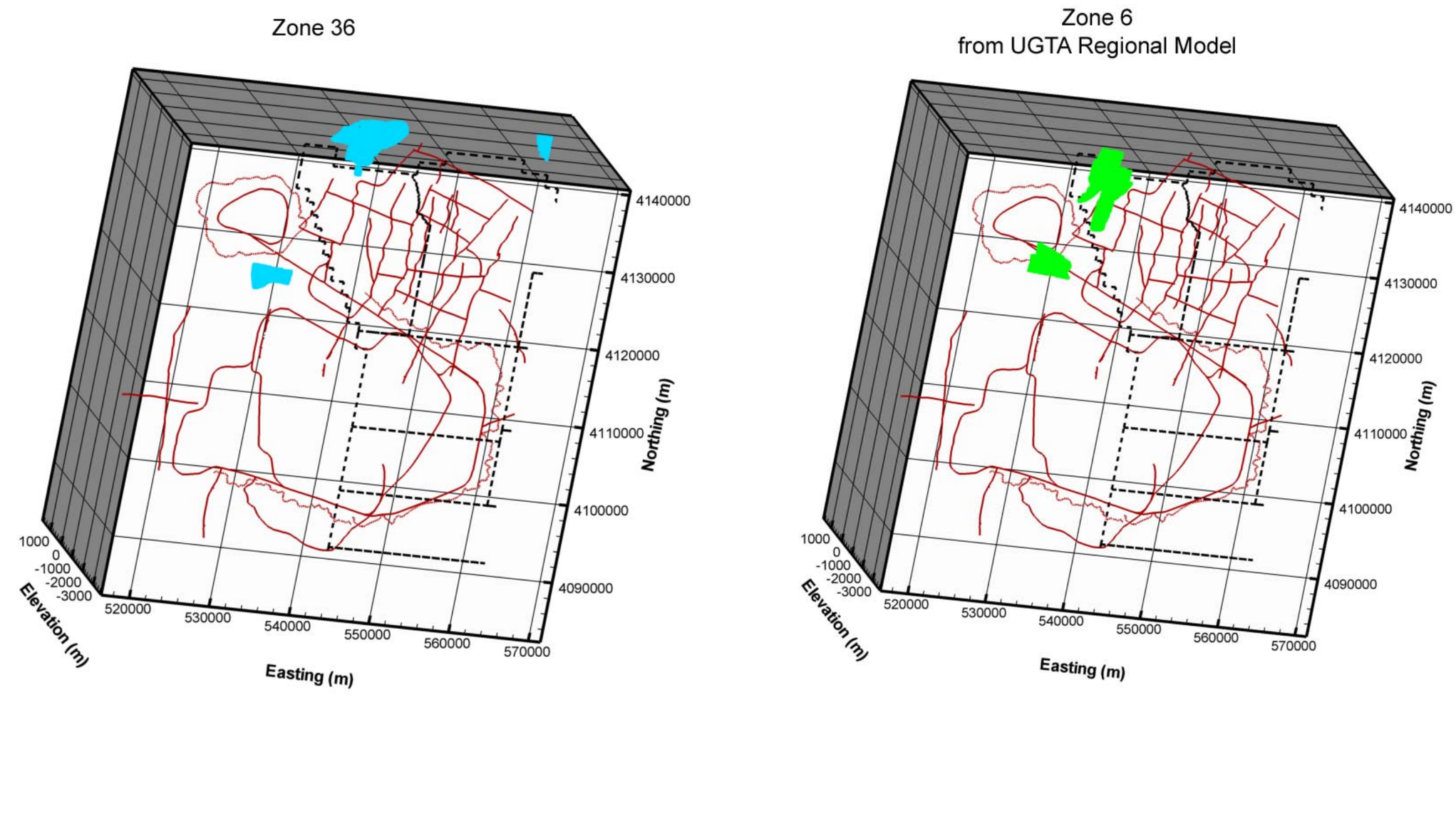

Figure 5-8
Map Showing TMA Nodes Following UGTA Regional Model TMA Subdivision

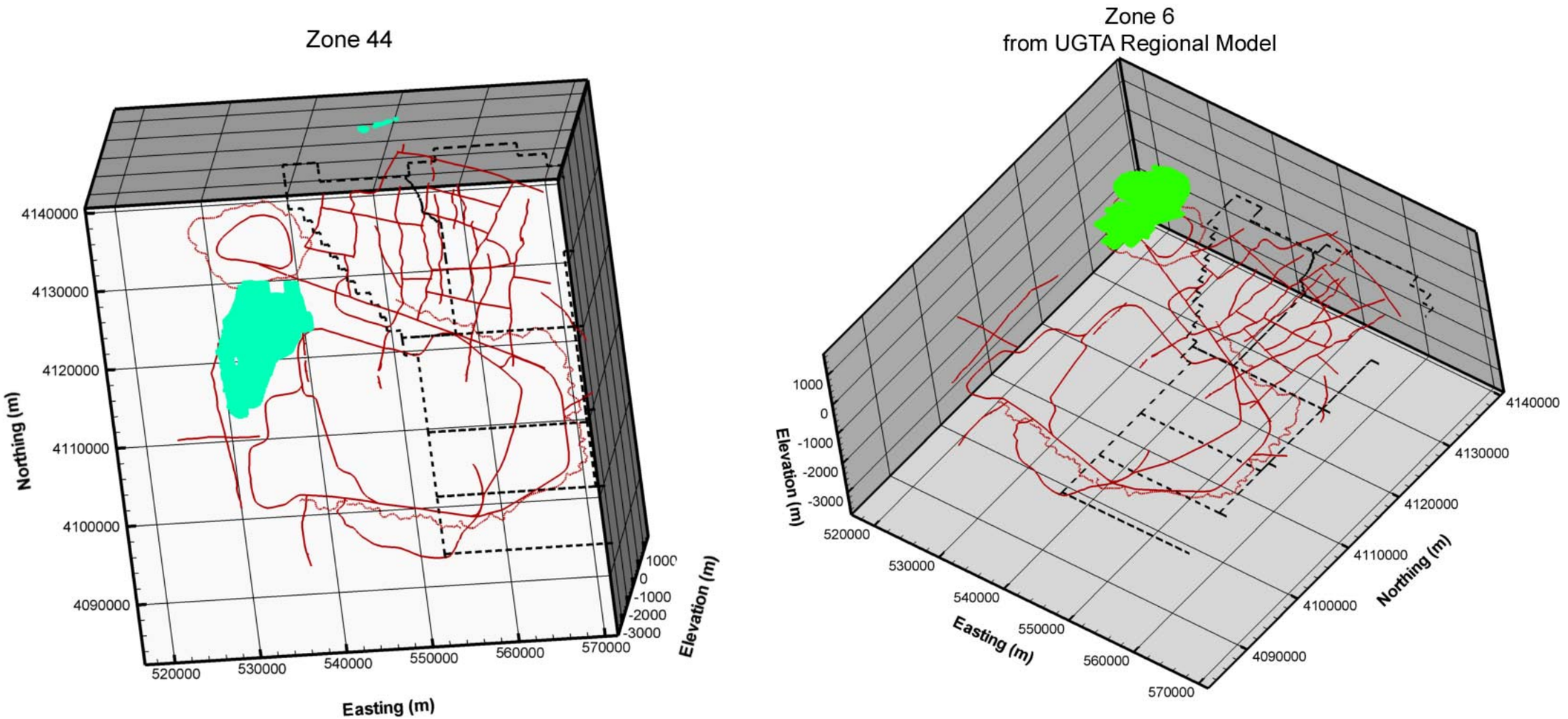

Figure 5-9
Map Showing TCA Subdivision from UGTA Regional Model Zone 52

5.5 Parameter Assignment

Each node in the FEHM mesh has an associated material property index that is used to assign hydraulic properties. Faults are also specified by material zones, and are specified after the HSUs are defined. However, the material properties associated with the HSU nodes remain assigned to the fault nodes pending another property assignment. The approach in parameterizing the faults was to assign a permeability factor that multiplies the existing fault node properties (still derived from an HSU). Thus, the difficulty that could be encountered in directly assigning a fault permeability that is reconciled with each HSU that it crosses is avoided. For instance, if a vertical fault crosses both aquifers and confining units (which most do), and a uniform fault permeability of 10^{-16} m^2 is assigned, the aquifer (with a permeability of 10^{-12} m^2) would see the fault as a barrier, but a confining unit with a permeability of 10^{-16} m^2 would see the fault as neutral. This approach tacitly assumes that a fault acts the same in each HSU that it encounters. Depth decay was computed in the depth-integrated manner described in the UGTA regional model (DOE/NV, 1997). Because FEHM determines its control volumes from node locations (unlike the block-centered code used in the regional model), which also may not necessarily be rectangles or squares, the bounding control volume coordinates were used in the depth-decay calculation. In the case of non-rectangular control volumes, the computed depth decay is approximate because the height of the control volume may not be constant. This was deemed a reasonable approximation in light of the overall uncertainty surrounding the depth-decay process.

5.6 Base Hydrostratigraphic Framework Model Flow Model Calibration

Bechtel Nevada (2002) presents a best estimate, or what will be referred to hereafter as the "base," HFM of Pahute Mesa and the surrounding area, as well as several alternative interpretations. The following sections document the evaluation of four different approaches (two in Section 5.6.2) to assigning model parameters in the base model. The same calibration data and model structure were used in each case; only the approach to assigning parameters was changed. These approaches include:

- No depth decay, no anisotropy
- Selected HSU depth decay
- Selected HSU depth decay and anisotropy
- All HSU depth decay and anisotropy

5.6.1 No-Depth-Decay, No-Anisotropy Case

The Pahute Mesa CAU model discretizes each HSU with multiple nodes in the horizontal and vertical dimensions. It was thought that this level of discretization might not require horizontal-to-vertical anisotropy because the arrangement of the HSUs would naturally produce the stratification of flow, and the approach described in this section was designed to test this hypothesis. In addition, the necessity of permeability depth decay was also tested by using a single permeability for each HSU estimated from characterization data as described in the Pahute Mesa hydrologic data document (SNJV, 2004a).

This case was not as extensively examined as the others described in Section 5.6 for reasons that are explained in the following text. It also was set aside before other changes were made to the model, but this section describes the process and results used in developing the Pahute Mesa CAU flow model.

Figures 5-10 through 5-13 show the observed (or estimated in the case of boundary flows) and unweighted simulated values for the calibration wells, springs, Oasis Valley discharge, and boundary flows, respectively. On Figures 5-10 and 5-11, the line of perfect agreement is shown, and ideally the data would plot exactly onto this line. Figure 5-13 compares the regional and CAU-model boundary flows. The scatter around the line of perfect agreement is generally random in Figure 5-10, although there are some large errors at around 1,450 m and a bias toward undersimulation above 1,300 m. Figure 5-14 shows a histogram of weighted observation well residuals. The bulk of the weighted errors are less than 20 m. The errors are approximately symmetrically distributed around zero, with a single large undersimulated (positive sign) PM-2, and single large oversimulated UE-19b #1 WW.

The Oasis Valley discharge and boundary flow components provide the water-balance constraint on the model. The total estimated Oasis Valley discharge, divided among seven zones numbered 1-6 and 8, is 227 kg/s. The simulated discharge, shown in Figure 5-12, is 128 kg/s. The model captures the northernmost two discharge zones well, but performs poorly for the rest of Oasis Valley. This suggests that the head in the southern part of Oasis Valley needs to rise in order to produce the observed discharge. The boundary flows, estimated from regional model analysis, do not trend the same way on the western edge, although the north, south, and east flows reasonably agree with the regional model.

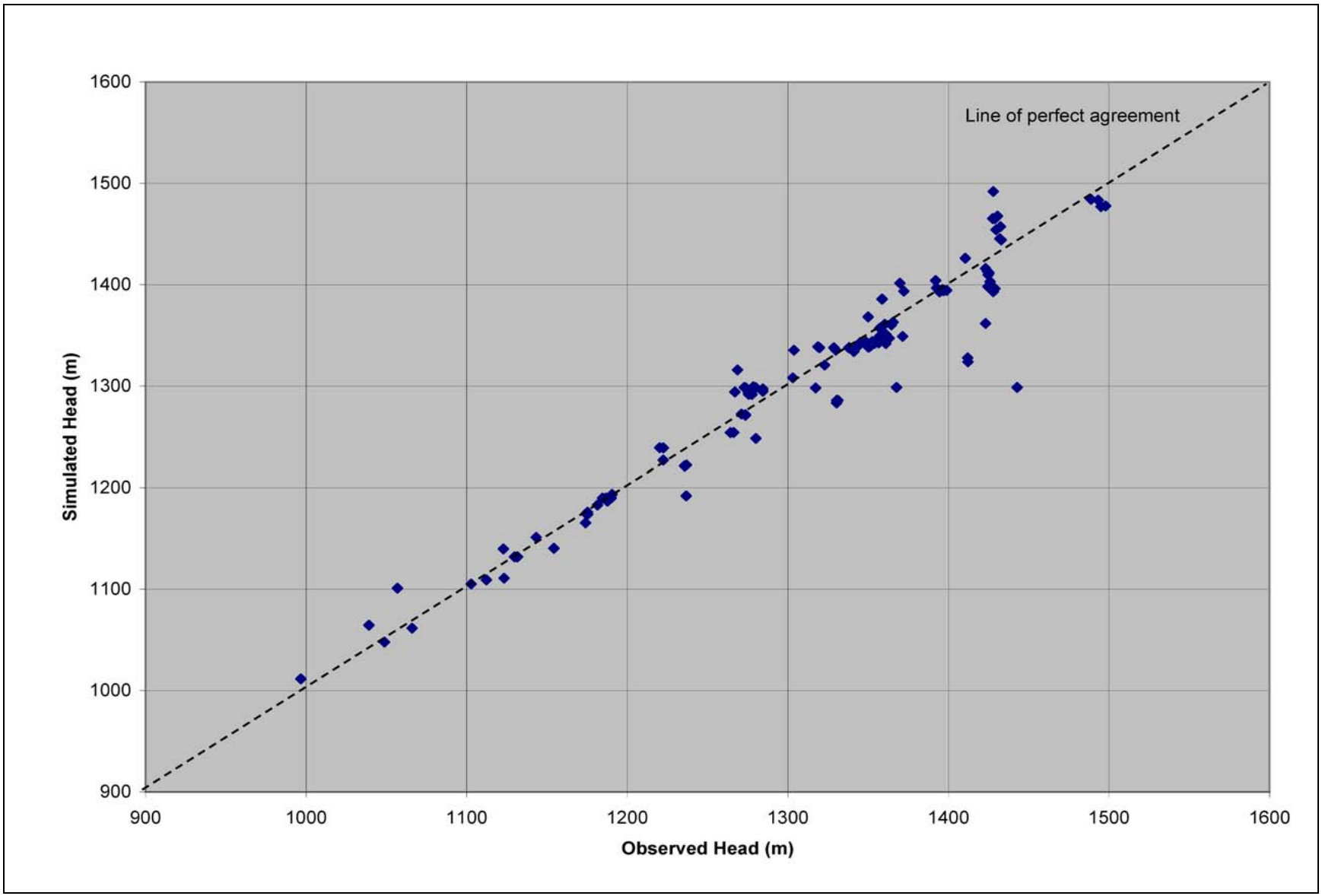

Figure 5-10
Observed Versus Simulated Well Head - Base HFM, No Depth Decay, No Anisotropy

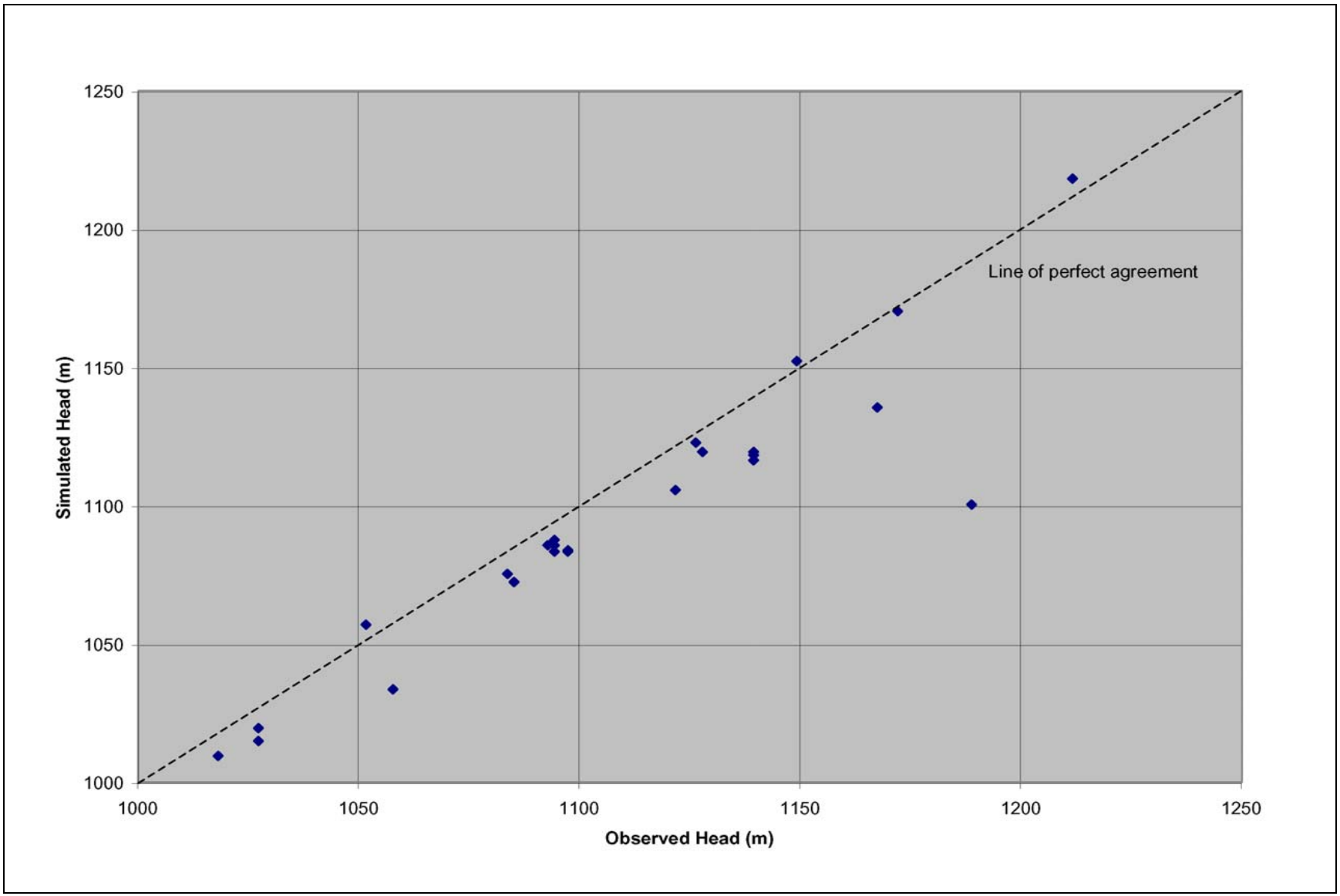

Figure 5-11
Observed Versus Simulated Spring Head - Base HFM, No Depth Decay, No Anisotropy

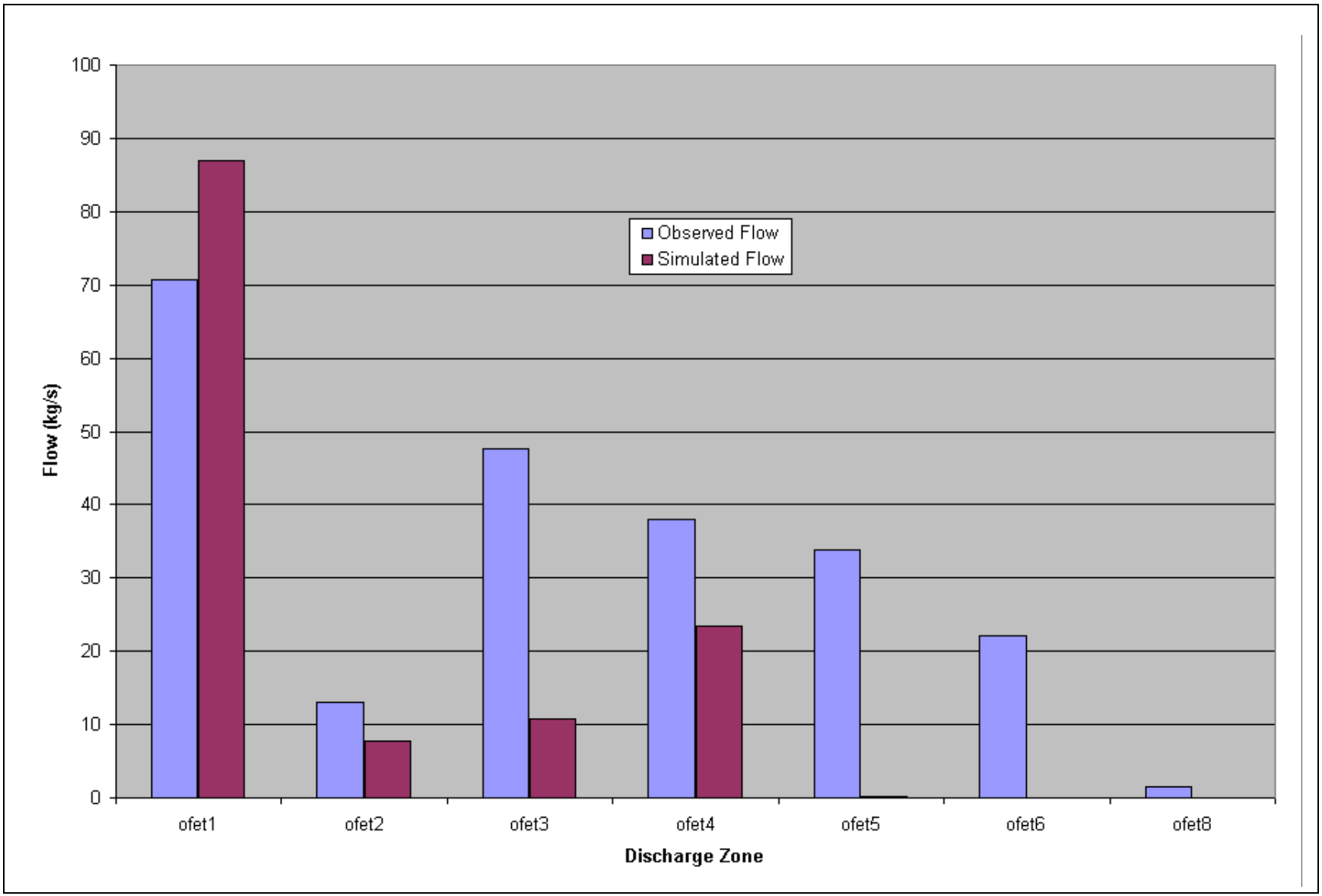

Figure 5-12
Observed Versus Simulated Oasis Valley Discharge - Base HFM, No Depth Decay, No Anisotropy

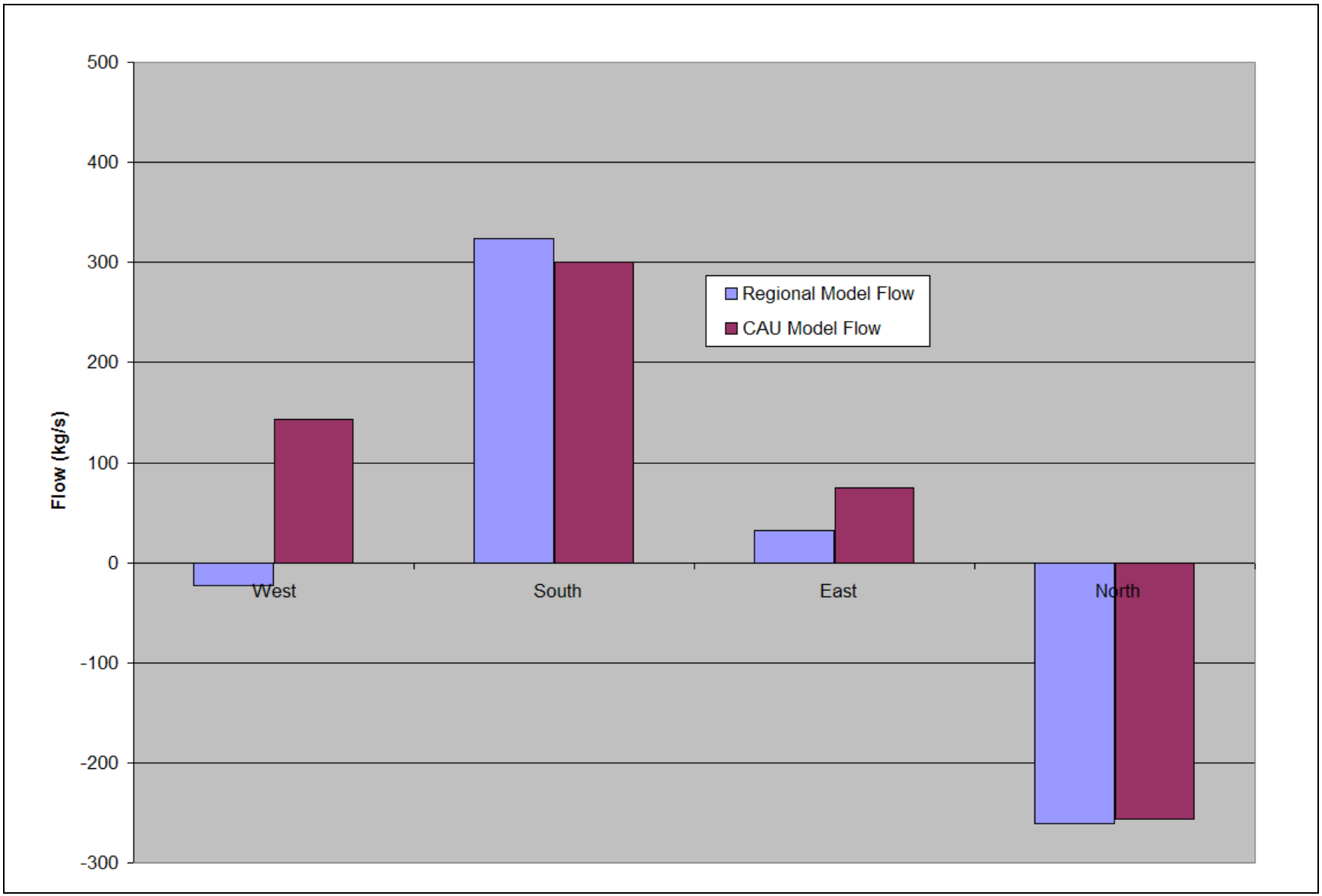

Figure 5-13
Estimated and Simulated Boundary Flows - Base HFM, No Depth Decay, No Anisotropy

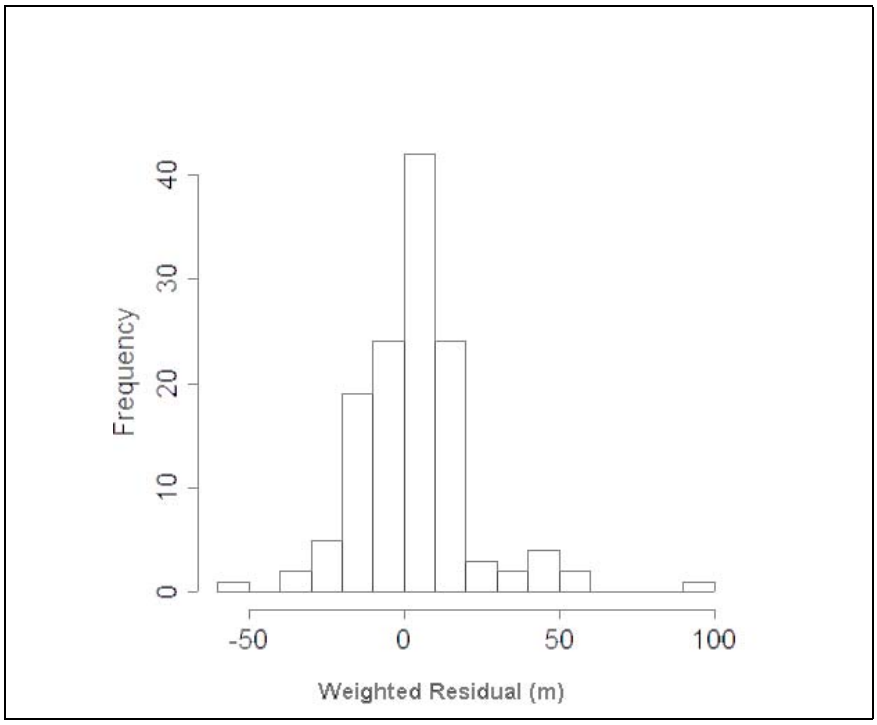

Figure 5-14
Histogram of Weighted Head Residuals - Base HFM, No Depth Decay, No Anisotropy

The weighted head and spring errors (or residuals), defined as observed minus simulated heads, are shown on Figure 5-15, color-coded by value and sign. Only locations with weights greater than 0.01 (m^{-1}) are shown in order not to bias the display (low weight observations will give an erroneously favorable impression because almost any error times the low weight will be low). There is a pattern of undersimulated wells west of the Purse Fault and in Oasis Valley. The low simulated water levels in Oasis Valley result in the undersimulation of observed discharge in the valley. There is an area of high bias in northeastern Area 19.

The quantitative measures of the model calibration are given by summary statistics shown in Table 5-6. There is a noticeable low bias in the spring heads, resulting in the undersimulation of Oasis Valley discharge. The standard deviation is wider than the other cases described in Section 5.6, reflecting the overall poorer fit of this case. Table 5-7 shows the contribution to model goodness of fit from each data type.

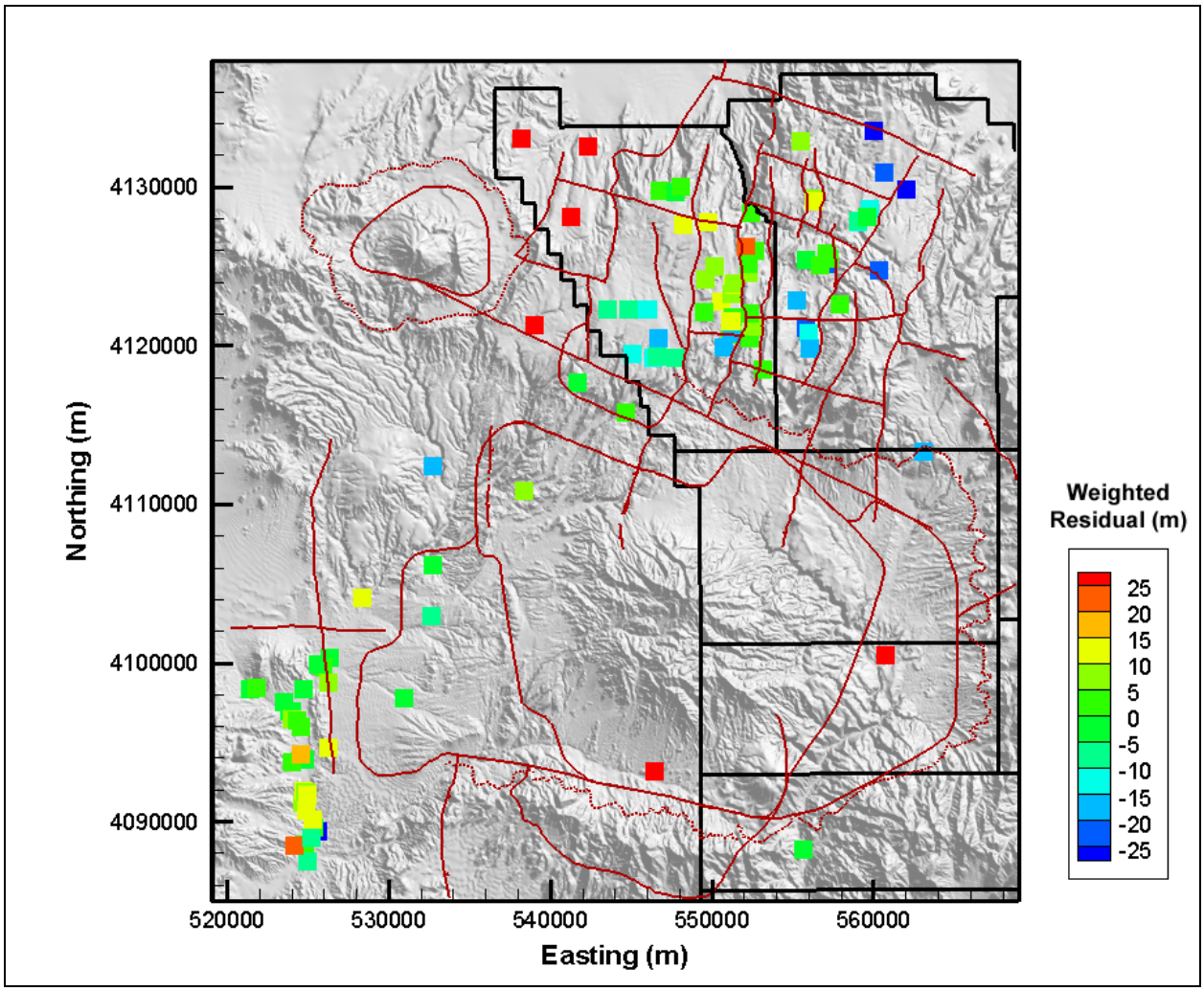

Figure 5-15
Post Plot of Weighted Well and Spring Head Residuals - Base HFM, No Depth Decay, No Anisotropy

Figure 5-16 shows the simulated water table for this model case. In the western part of Area 20, the influence of the Purse Fault is absent except along the northern part of the fault. Head in southern Area 20 is very similar to that on the other side of the Purse Fault, which is the incorrect representation and results in the low heads at PM-2, PM-3, UE-20j WW, U-20m, and UE-20p (the area of low bias in Figure 5-15). The misfit at PM-2 is particularly large and, as described in Section 5.3, is directly caused by regional model misfit just north of the CAU-model boundary. This result led to the revision of boundary head (also described in Section 5.3) on the northern CAU-model edge. A mound is not simulated under Timber Mountain; this interpretive feature was added after this case was no longer being investigated. If implemented, it may raise head and discharge in Oasis

Table 5-6
Calibration Summary Statistics - Base HFM, No Depth Decay, No Anisotropy

Calibration Data	Number of Data	Mean Weighted Error (m or kg/s)[a]	Maximum Weighted Residual	Minimum Weighted Residual	Error Standard Deviation (m or kg/s)
Well Head	152	1.6	96 (PM-2)	-52 (UE-19b #1 WW)	16
Spring Head	28	5.8	24 (Spring id 159)	-6.5 (Spring id 180)	9.2
Oasis Valley Discharge	7	28	74 (Zone 3)	-33 (Zone 1)	45
Boundary Flow	4	-15	50 (North)	-91 (West)	53

[a]Positive is undersimulation of target data, negative is oversimulation.

Table 5-7
Contribution to Model Goodness of Fit by Data Type for Base HFM Selected HSU Depth Decay and Anisotropy

Data Type	Value (-)	% of Total
Well Head	42,531	61
Spring Head	2,387	3
Oasis Valley Discharge	14,029	20
Boundary Flow	11,156	16
Total	70,103	100

Valley by diverting water to the west. Oasis Valley discharge is apparent, but not as pronounced as in other cases because it only is about half of the observed flow (the other cases capture the flow much better).

Particle tracking (Figure 5-17) from each of the NTS wells used in model calibration shows generally the same noted flow paths as shown by SNJV (2004a) and as shown in Appendix A of the Pahute Mesa hydrologic data document (SNJV, 2004a). However, very few of the particles discharge in Oasis Valley, and as previously noted, this model greatly undersimulates Oasis Valley discharge. The broad flow path through the Timber Mountain area is not known to exist. However, data do not exist to rule it out. The flow paths shown are consistent with the boundary conditions applied to the model. However, as a matter of first principles, an area of higher elevation and commensurate recharge should have higher hydraulic head underlying it. Thus, the flat potentiometric surface and associated flow paths through Timber Mountain shown in Figure 5-17 are not thought to be realistic. In southern Area 20, the flow paths look reasonable, but the heads are not correct along the Purse Fault. Finally,

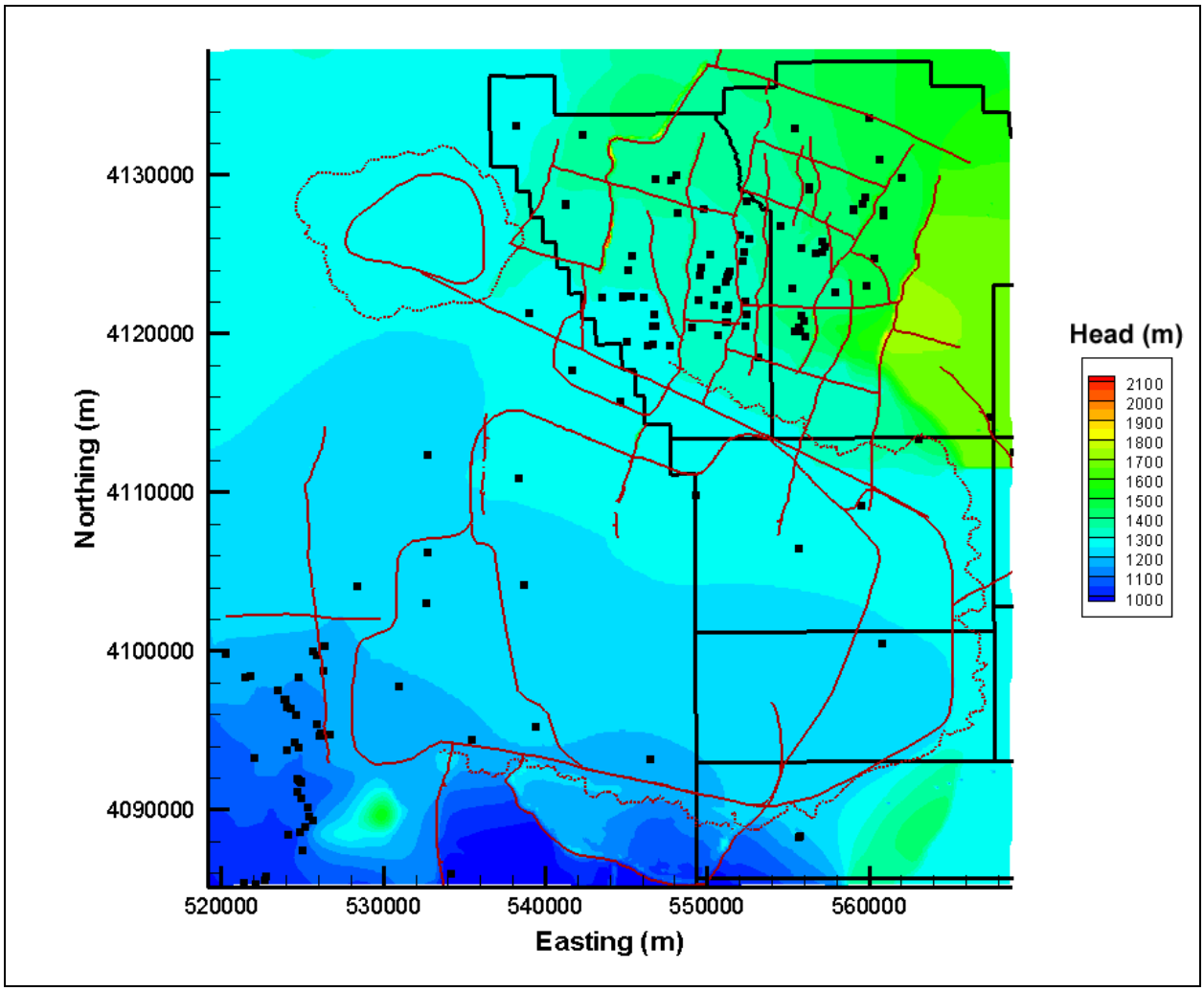

Figure 5-16
Simulated Water Table - Base HFM, No Depth Decay, No Anisotropy

a large number of flow paths exit the model deep (elevation of –1,000 m or more) in the LCA underlying Oasis Valley, which is unsupported by the analysis of SNJV (2004a). This was one of the key observations that lead to this parameterization of the base HFM not being investigated further.

This parameterization approach, no depth decay and no anisotropy, produced flow paths that were judged unrealistically deep and represented Oasis Valley discharge poorly. It also required systematically low permeabilities relative to the expected values and ranges as described in the Pahute Mesa hydrologic data document (SNJV, 2004a). Figure 5-18 shows the estimated versus calibrated permeabilities; the estimated standard deviation is published in SNJV (2004a), but for practical purposes can be considered to be one order of magnitude. Nearly all the values are multiple

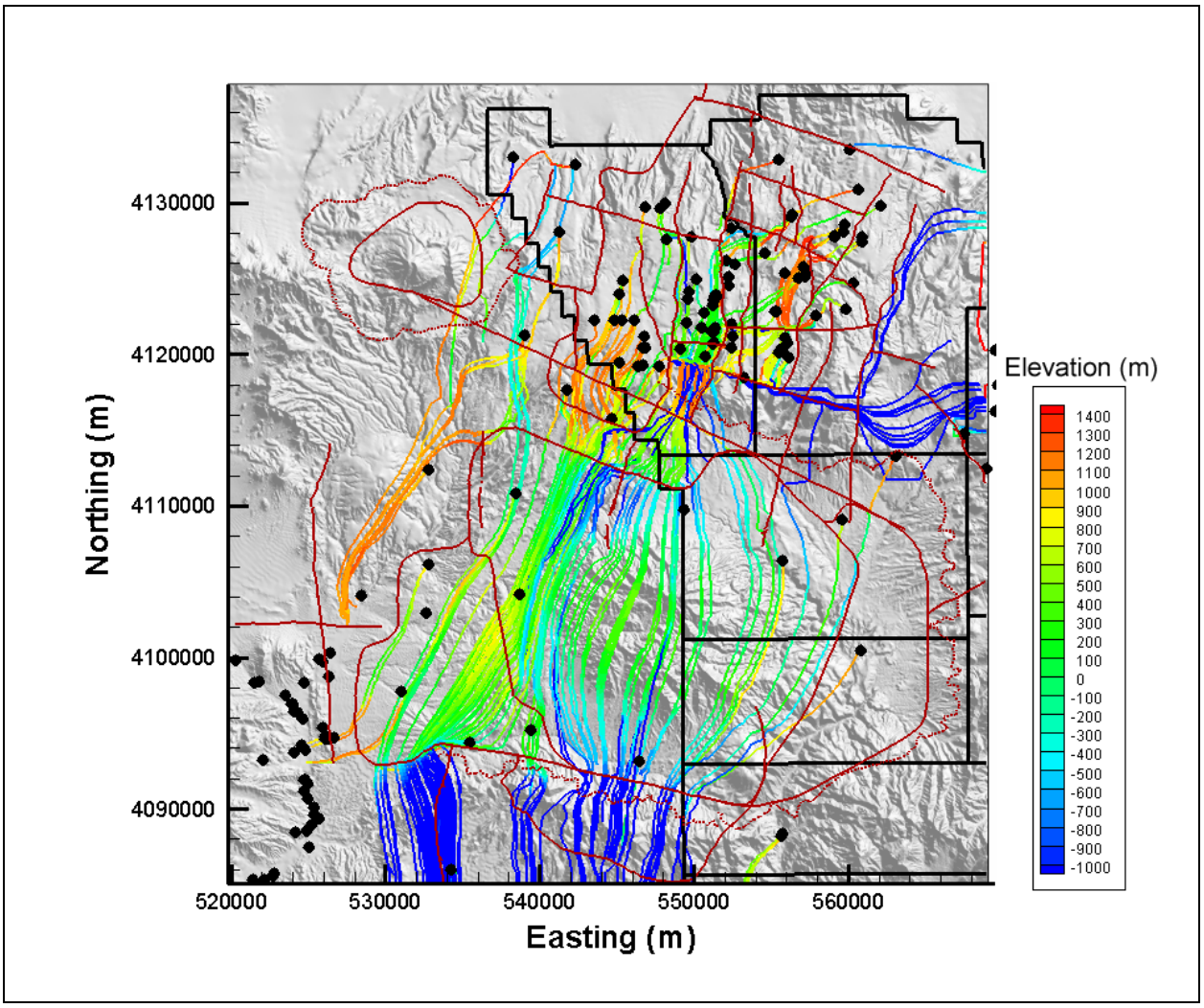

Figure 5-17
Particle Tracks - Base HFM, No Depth Decay, No Anisotropy

orders of magnitude lower than the estimated. However, not all these low values are significant. For instance, a single hydraulic test was used to assign permeability for all the ICUs. Because they are brittle, the intrusive units tend to be fractured at shallow depths, and it is probably sampling bias that gives the relatively high single value. Concepts of caldera formation of the ICUs is poorly understood, and their presence is inferred from first principles and gravity measurements (BN, 2002). Bechtel Nevada (2002) conceptualizes the ICUs as igneous intrusive masses, postulates that they behave as confining units, and indicates that at depth fractures are probably filled with secondary minerals from circulation of hot, mineral-rich waters associated with deep magma bodies. Thus, the low permeabilities of the ICUs are less important. However, model performance could only be

enhanced with systematically lower values of permeability throughout the model. Anisotropy could be introduced to constrain vertical flow, but in units where fracture flow predominates, the concept of horizontal-to-vertical anisotropy was judged to be inappropriate because, in general, overburden loading will tend to close low-angle fractures. Anisotropy could be applied to the more bedded units, but given the poor performance of this case, excessively low values were likely to be required and were not investigated.

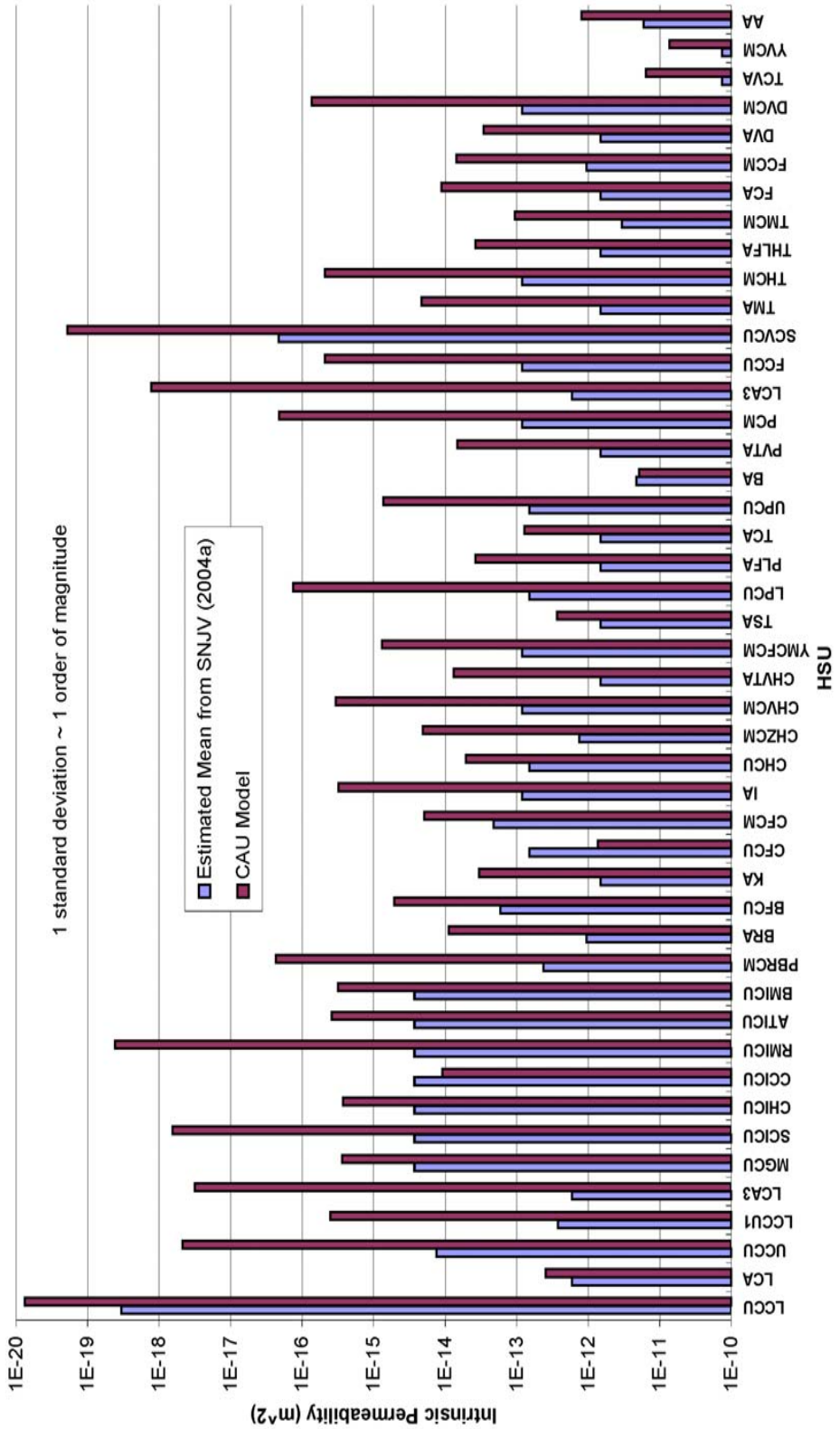

Figure 5-18
Hydrostratigraphic Unit Parameters - No Depth Decay, No Anisotropy
See Table 2-6 for HSU descriptions.

5.6.2 Selected HSU Depth Decay and Anisotropy (SDA)

The SDA parameterization approach began by assessing the effect of permeability depth decay only, and its effects were found to be quite pronounced in terms of not requiring consistently low permeabilities as in the case described in Section 5.6.1. The depth-decay-only case was used to establish the insight into the need for permeability depth decay and was not extensively investigated.

In the UGTA regional model (DOE/NV, 1997), depth decay and horizontal-to-vertical anisotropy were assigned to every HSU. An alternate parameterization of the base HFM was designed to test whether depth decay applied to regionally contiguous units existing at a wide variety of depths along with anisotropy in selected units could give a reasonable result. Table 5-8 shows the units selected for depth decay and anisotropy. The rationale for selectively applying depth decay is that units that are contiguous over the CAU and that exist over a great range of depths (such as the LCA and PBRCM) would have large variation in permeability, which is conceptually best addressed via depth decay rather than, for instance, subdividing HSUs by burial depth and assigning individual permeabilities based on depth. The depth-decay coefficients are the mean values presented in the UGTA regional model report (DOE/NV, 1997). The vertical-to-horizontal anisotropy value is derived from the YMP site-scale saturated zone model (DOE/ORD, 2004).

Horizontal-to-vertical anisotropy, typically associated with granular media, may not be a meaningful concept in fractured rock. Pawloski et al. (2001) did not use horizontal-to-vertical anisotropy in the analysis of the CHESHIRE HST. They showed that it was reasonable to have permeability along the main flow direction be the same through the vertical extent of fractured HSUs. The composite units in the CAU HFM model are, by definition, an amalgamation of HGUs that could not be extensively mapped. Thus, internally a layer-cake arrangement of massive fractured units with bedded tuffs, for example, would tend to impart horizontal-to-vertical anisotropy over the scale of a CAU-model element. If the geologic description were detailed enough, and if the computational mesh could accommodate such detail, such anisotropy would result naturally. However, as described in Section 5.6.1 it appears that the HFM model and FEHM mesh are not fine enough for this to occur.

Figures 5-19 through 5-22 show the observed (or otherwise estimated) and unweighted simulated values for wells, springs, Oasis Valley discharge, and boundary flows, respectively. On Figures 5-19 and 5-20, the line of perfect agreement is shown, and ideally the data would plot exactly onto this

Table 5-8
Hydrostratigraphic Units with Depth Decay and Anisotropy

HSU	Depth Decay λ	Anisotropy
TMCM	0.0026	0.1
YMCFCM	0.0026	N/A
LCA	0.001	N/A
PBRCM	0.0026	0.1
BRA	0.0026	N/A
PCM	0.0026	N/A
TCVA	0.0026	N/A
TMA	0.0026	N/A
CFCM	N/A	0.1
CHZCM, CHVCM, CHVTA	N/A	0.1
FCCM	N/A	0.1
YVCM	N/A	0.1
AA	N/A	0.1

See Table 2-6 for HSU descriptions.

line. However, in practice, there is always some model misfit. The scatter around the line of perfect agreement is generally random in Figure 5-19, until an observed head of 1,450 m is exceeded. At the very highest-observed observation well water levels, the model has a tendency towards undersimulation. The largest error is associated with the ER-19-1 deep completion. The remaining errors above 1,450 m are all in far eastern Area 19, where data become very sparse and uncertainty increases. Figure 5-23 shows a histogram of weighted observation well residuals. The bulk of the weighted errors (95 percent) are less than ±10 m. The errors are not symmetrically distributed around zero, with larger oversimulated (negative sign) wells. Total number of errors above +10 m and below –10 m appear to be about the same.

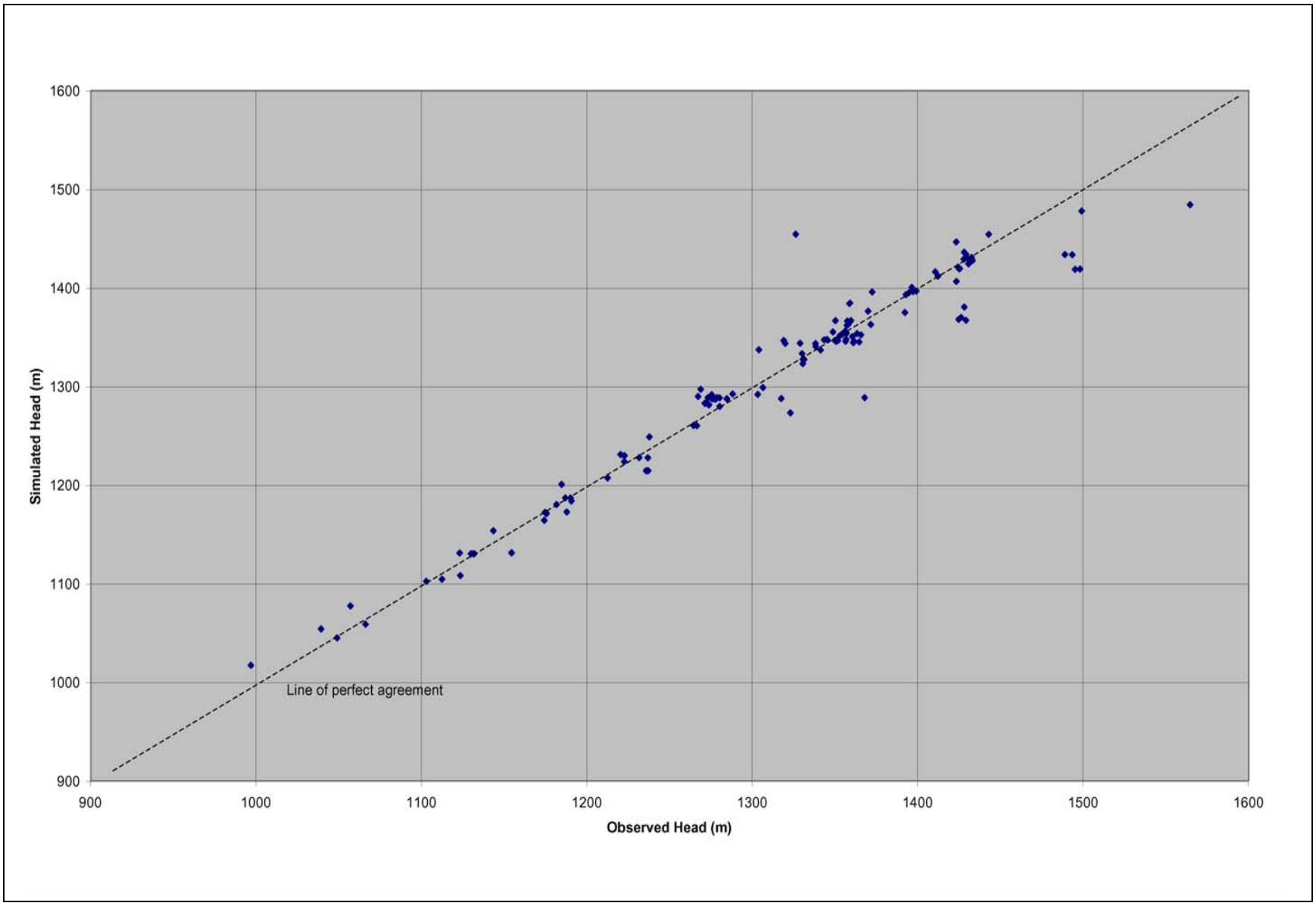

Figure 5-19
Observed Versus Simulated Well Head for BN-MME-SDA

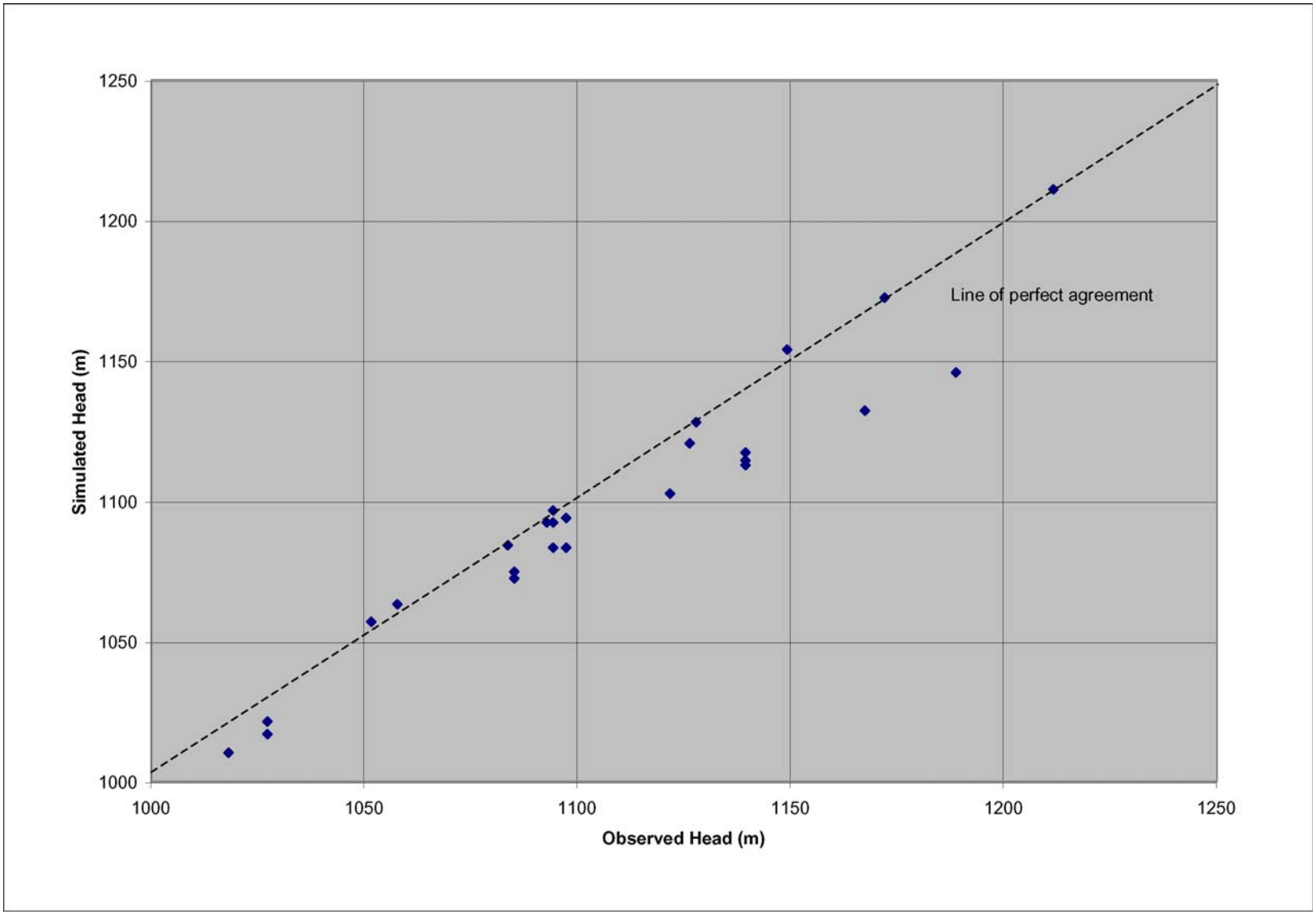

Figure 5-20
Observed Versus Simulated Spring Head for BN-MME-SDA

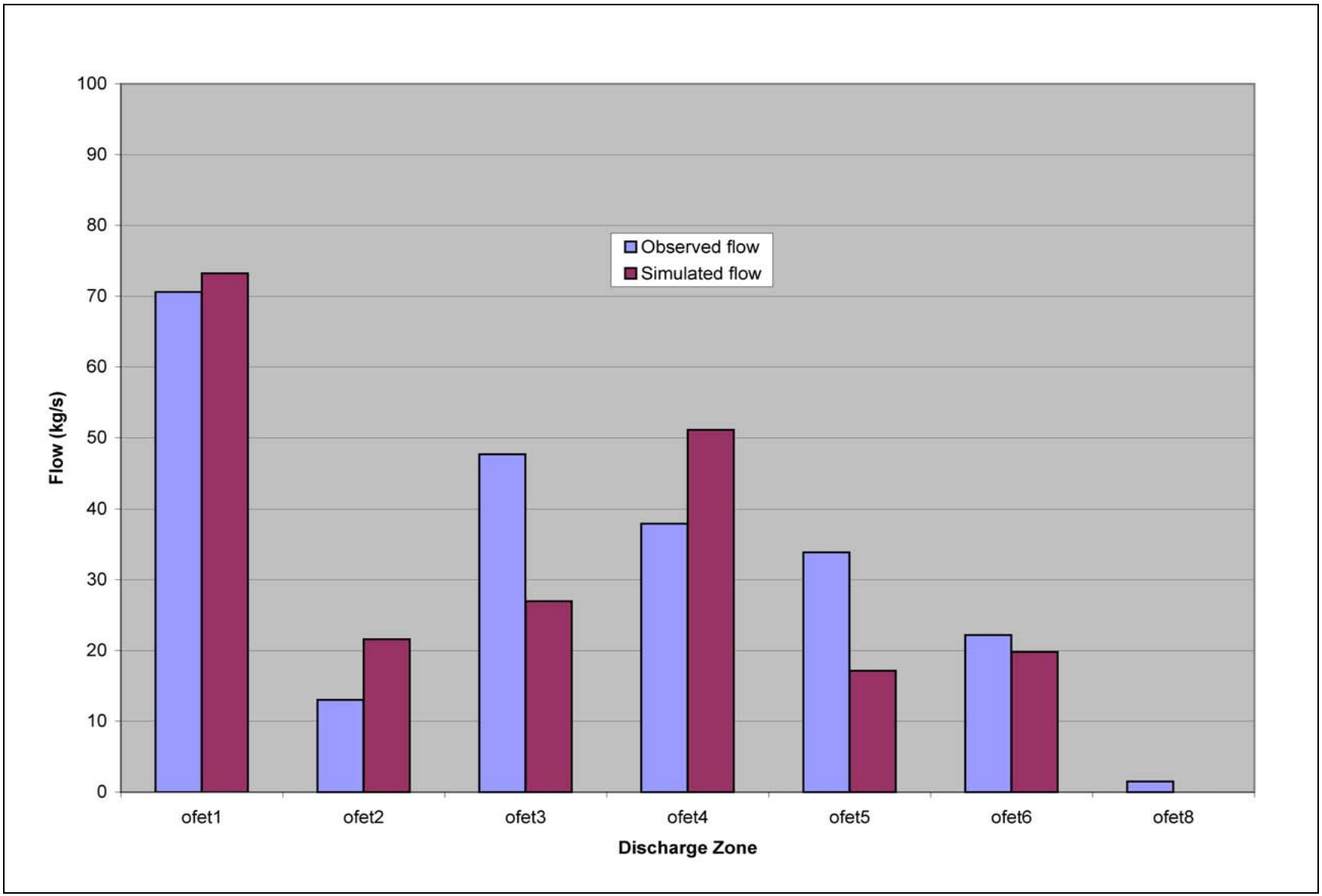

Figure 5-21
Observed Versus Simulated Oasis Valley Discharge for BN-MME-SDA

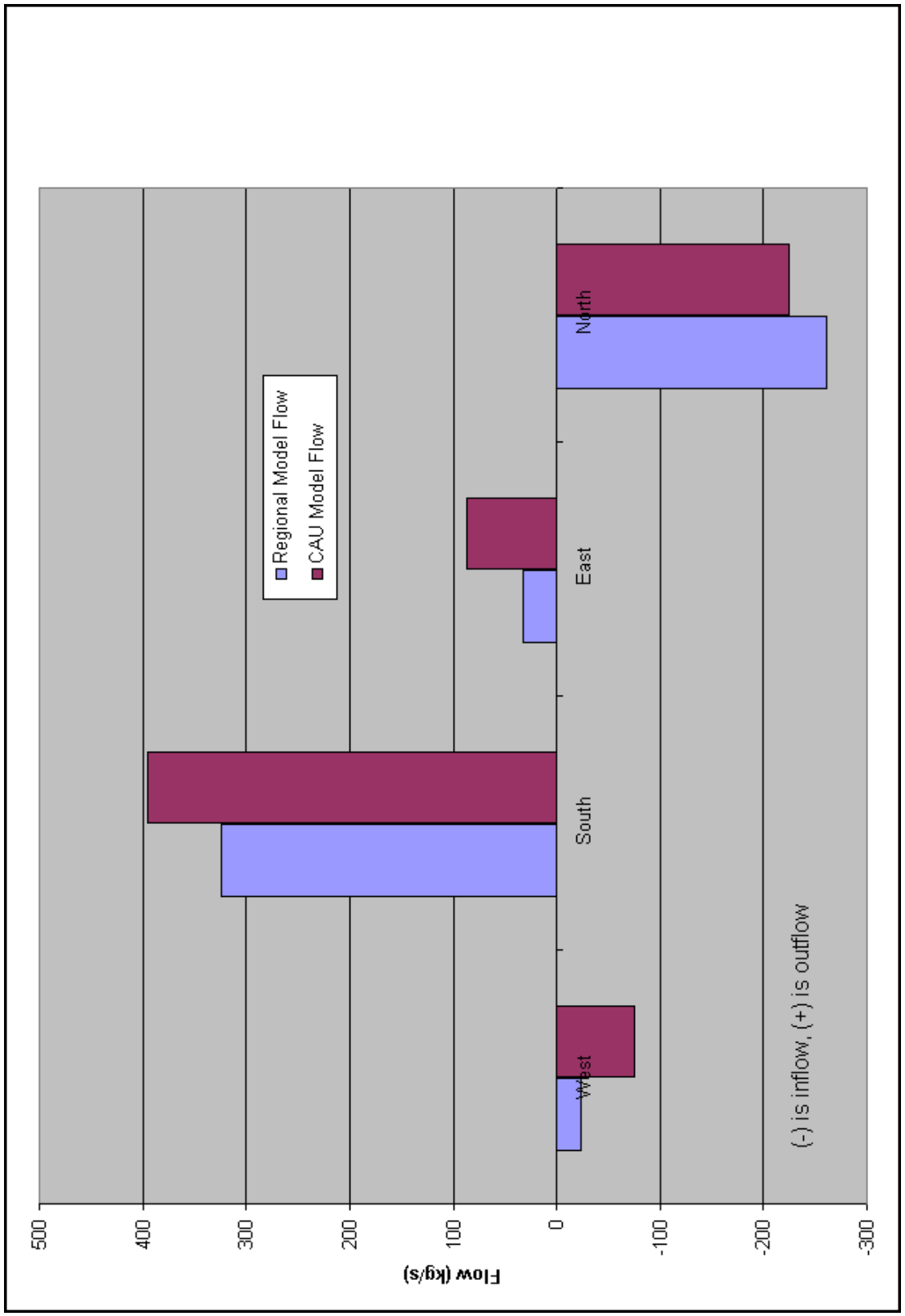

Figure 5-22
Estimated and Simulated Boundary Flow for BN-MME-SDA

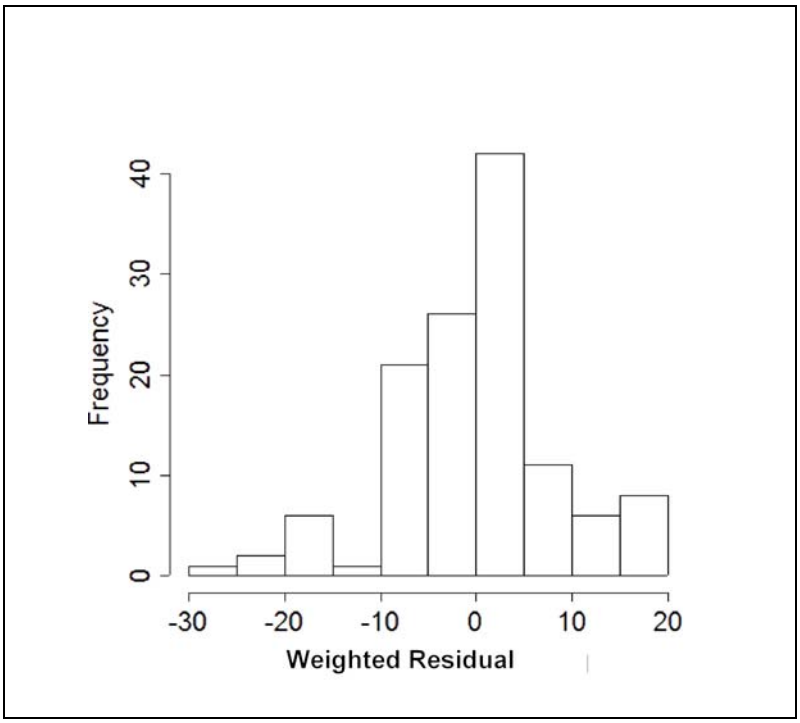

Figure 5-23
Histogram of Weighted Head Residuals for BN-MME-SDA

The weighted head and spring errors are shown on Figure 5-24, color coded by value and sign. The two lowest, or undersimulated, wells were ER-OV-06a and ER-OV-01. The single highest well was UE-20a #1 in northern Area 19. In general, the errors are randomly distributed, although there is a slight low bias in northern Area 20 at easting and northing of about 547,500 and 4,130,000 m, which includes wells U-20i, UE-20e #1, U-20e, and U-20ar #1.

The two springs with the largest errors are Goss Spring, which has an uncertain location, and Oleo Road Spring in an area of very high topographic gradient that the model is unlikely to represent in sufficient detail. Goss Spring was incorrectly located in the Pahute Mesa hydrologic data document (SNJV, 2004a), and locations were re-estimated based on USGS 1:24,000 maps. These two springs were assigned low weights because of their questionable representativeness. However, springs at similar and higher elevations were matched well, and this misfit appears to be a local issue.

The Oasis Valley discharge and UGTA regional model (DOE/NV, 1997) boundary flows provide the water-balance constraint on the model. The total estimated Oasis Valley discharge is 227 kg/s. The simulated discharge, shown in Figure 5-21, is 209 kg/s. The total error is within one standard

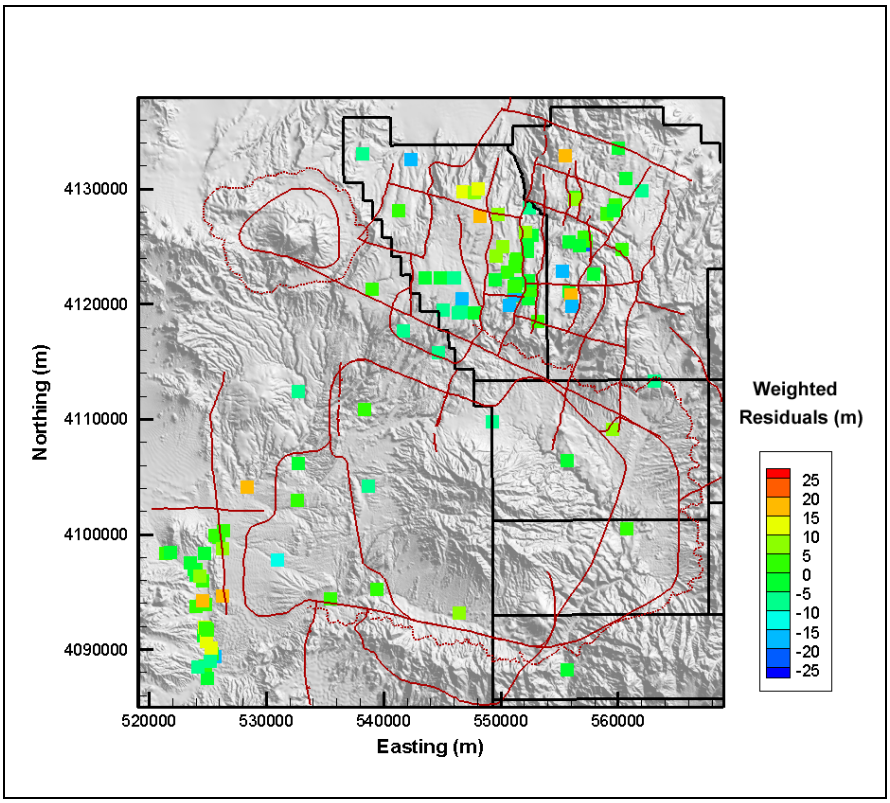

Figure 5-24
Post Plot of Weighted Well and Spring Head Residuals for BN-MME-SDA

deviation (30 kg/s) as reported by Laczniak et al. (2001). The model trends the same as the data with some scatter, showing that the general representation of Oasis Valley is correct. The northernmost (and closest to the NTS) zone is matched well. The boundary flows (Figure 5-22), estimated from regional model analysis, all trend the correct way (e.g., have the proper sign), with the largest relative misfit on the western edge.

The quantitative measures of the model calibration are given by summary statistics shown in Table 5-9. These statistics alone are not used to judge model calibration; they are used in conjunction with the graphical approaches shown previously. There is a slight dry bias in the spring heads, with a slight overprediction bias for the flows. The total model objective function was 16,651. Table 5-10 shows the contribution of each data type to the total model goodness of fit. The strongest contributors are observation well heads and Oasis Valley flow, which are also the two key pieces of calibration data.

Table 5-9
Calibration Summary Statistics for BN-MME-SDA

Calibration Data	Number of Data	Mean Weighted Error (m or kg/s)[a]	Maximum Weighted Residuals	Minimum Weighted Residual	Error Standard Deviation (m or kg/s)
Well Head	152	-0.46	18 (ER-OV-06a)	-27 (UE-20n #1)	7.4
Spring Head	28	2.7	19 (Torrance Spring)	-5.5 (Spring id 159)	6.7
Oasis Valley Discharge	7	4.8	41 (Zone 3)	-26 (Zone 4)	23
Boundary Flow	4	-13	26 (West)	-35 (South)	27

[a]Positive is undersimulation of target data, negative is oversimulation.

Table 5-10
Contribution to Model Goodness of Fit by Data Type for BN-MME-SDA

Data Type	Value (-)	% of Total
Well Head	8,487	51
Spring Head	1,283	8
Oasis Valley Discharge	3,883	23
Boundary Flow	2,997	18
Total	16,651	100

Figure 5-25 shows the simulated water table for this model case. In the western part of Area 20, the influence of the Purse Fault (Figure 4-7) is evident by nearly 100 m offset in water levels across it, with more subdued effects also present at West Boxcar Fault. Water flows from Areas 19 and 20 towards the southwest and Oasis Valley. A mound is simulated under Timber Mountain. It is unknown whether such a feature exists, but from first principles, a higher elevation area where recharge occurs should have a higher groundwater potential. This assumption tends to focus flow between the northern part of the Timber Mountain Caldera and the southern Silent Canyon Caldera. Ubiquitous discharge in Oasis Valley, including flow from Sarcobatus Flat to the west, is also evident by the simulated low trough-shaped potentiometric surface. Finally, flow occurs out across the southern boundary towards Yucca Mountain and Crater Flat.

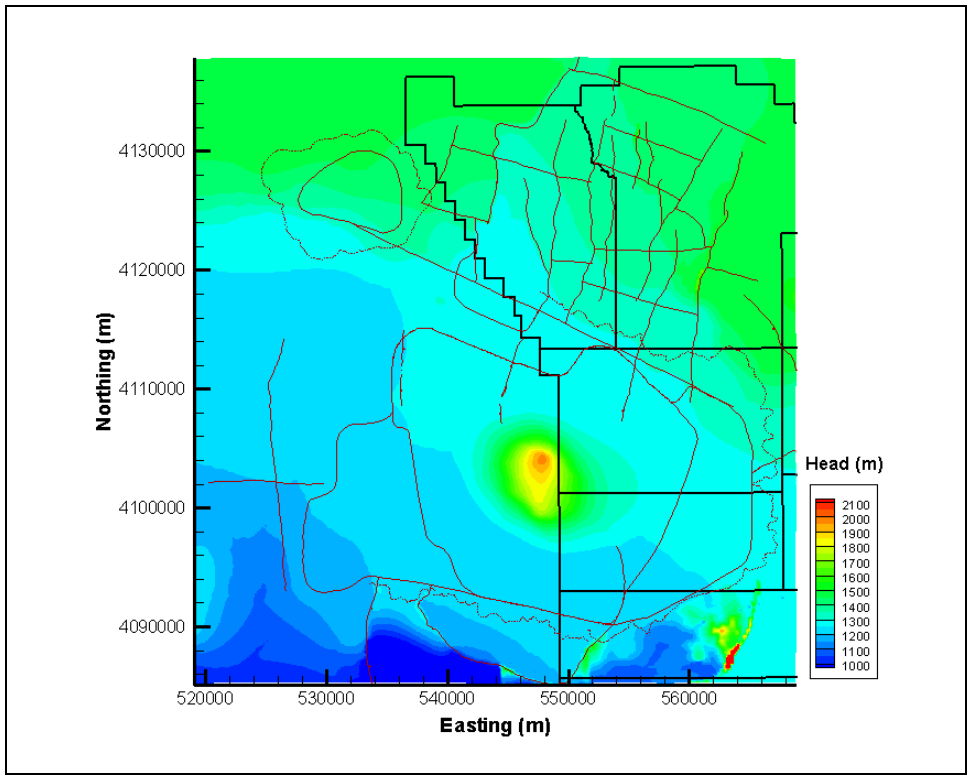

Figure 5-25
Simulated Water Table for BN-MME-SDA

Particle tracking from each of the NTS calibration wells was run until all particles discharged from the model or ceased to move (Figure 5-26). Because the flow field is steady state, porosity does not change the trajectories, and an arbitrary value of effective porosity can be used. In southern Area 20, where the influence of the Purse Fault on the calibration was pronounced, flow is west-southwest but quickly changes at the end of the Purse Fault to southeasterly and then hugs the western flank of Timber Mountain to the southwest because of the influence of the simulated recharge mound under Timber Mountain. Note that some of the wells shown do not have tracks leaving them; this is because the motion of the particle was so minor that it does not show a legible trace. This occurred at PM-2 and UE-20p in northern Area 20. The particle release points in PM-2 are nearly 1 km bmsl. The flow velocities are apparently simulated as being very low in this area of the model. There is only minor flow from Area 18, southern Area 19, and the Rainier Mesa area south down Fortymile Canyon. Particles that go to the west of Timber Mountain are all in the TMCM, and then move into the FCA in the lower part of Oasis Valley. Flow paths rise in elevation as flow converges into Oasis Valley. Moreover, they also rise near Bare Mountain due to the complex arrangement of rocks caused by the Bare Mountain Fault and the UCCU.

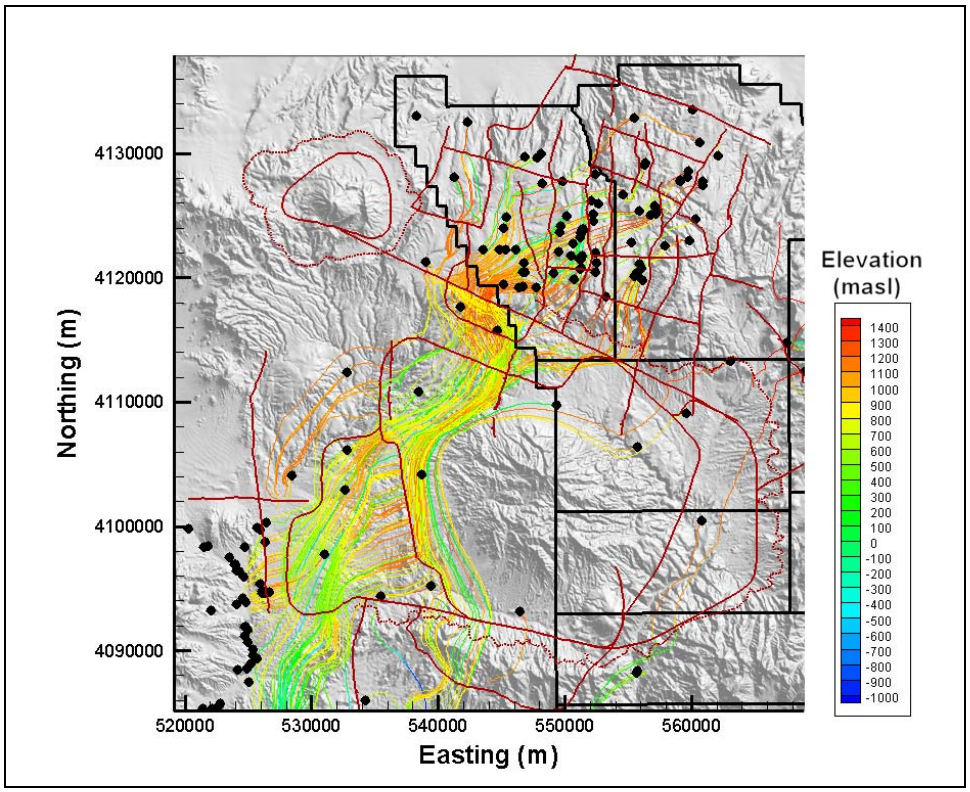

Figure 5-26
Particle Tracks for BN-MME-SDA

The properties used to parameterize this model are shown in Tables 5-11 and 5-12 for HSU and faults, respectively. The HSUs with depth decay are bolded in Table 5-11. The key to the fault locations is presented in Section 4.2.1

Table 5-11
Hydrostratigraphic Unit Parameters for BN-MME-SDA
(Page 1 of 3)

HSU	Log (k or k_0) (m^2)	Notes
LCCU	-18	k
LCA	**-14.20**	**k_0**
UCCU	-16.78	k
LCCU1	-12.43	k
LCA3	**-13.38**	**k_0**
MGCU	-18.38	k
SCICU	-18.38	k
CHICU	-18.38	k
CCICU	-18.38	k
RMICU	-18.38	k

Table 5-11
Hydrostratigraphic Unit Parameters for BN-MME-SDA
(Page 2 of 3)

HSU	Log (k or k_0) (m^2)	Notes
ATICU	-18.38	k
BMICU	-18.38	k
PBRCM	**-11.91**	**k_0**
BRA	**-11.51**	**k_0**
BCU	-13.67	k
KA	-11.78	k
CFCU	-12.60	k
CFCM	-15.07	k
IA	-13.56	k
CHCU	-14.61	k
CHZCM	-13.49	k
CHVCM	-13.39	k
CHVTA	-11.81	k
YMCFCM	**-14.54**	**k_0**
TSA	-10.09	k
LPCU	-13.04	k
PLFA	-11.78	k
TCA	-11.48	k
UPCU	-15.33	k
BA	-11.34	k
PVTA	-12.33	k
PCM	**-10.82**	**k_0**
LCA3a	**-14.03**	**k_0**
FCCU	-12.98	k
SCVCU	-16.28	k
TMA	**-14.55**	**k_0**
THCM	-12.88	k
THLFA	-11.78	k
TMCM	**-11.04**	**k_0**
FCA	-11.50	k
FCCM	-13.04	k
DVA	-12.71	k
DVCM	-13.23	k
TCVA	**-10.65**	**k_0**
YVCM	-10.08	k
AA	-13.50	k
LCA Zone 1	**-14.37**	**k_0**
TCVA Zone 6[a]	**-12.52**	**k_0**
TMA Zone 6[b]	**-12.18**	**k_0**

Table 5-11
Hydrostratigraphic Unit Parameters for BN-MME-SDA
(Page 3 of 3)

HSU	Log (k or k_0) (m^2)	Notes
PBRCM Zone 80[c]	**-10.42**	**k_0**
PBRCM Zone 81[c]	**-8.84**	**k_0**
PBRCM Zone 82[c]	**-11.30**	**k_0**
PBRCM Zone 83[c]	**-14**	**k_0**
PBRCM Zone 84[c]	**-11.49**	**k_0**
PBRCM Zone 87[c]	**-10.452**	**k_0**
TMCM-ERM[d]	**-11.26**	**k_0**
TMCM-ATCW[d]	**-10.05**	**k_0**
TMCM-ATCE[d]	**-11.05**	**k_0**
TMCM-THS[d]	**-11.94**	**k_0**
TMCM-OV[d]	**-10.76**	**k_0**
TMCM-TMD[d]	**-12.5**	**k_0**
TMCM-NTMW[d]	**-9.40**	**k_0**
TMCM-NTME[d]	**-10.19**	**k_0**
LPCU West of Purse Fault	-15.95	k
UPCU West of Purse Fault	-14.09	k
BRA West of Purse Fault	**-10.80**	**k_0**

See Table 2-6 for HSU descriptions.

k = Intrinsic permeability
k_0 = Reference permeability

[a]See Figure 5-8 for TCVA subdivisions.
[b]See Figure 5-9 for TMA subdivisions.
[c]See Figure 5-5 for PBRCM subdivisions.
[d]See Figure 5-8 for TMCM subdivisions.

Table 5-12
Fault Permeability Multiplier for BN-MME-SDA
(Page 1 of 2)

Fault ID	Name	Fault Permeability Multiplier
01	Almendro	0.32
02	Bare Mountain	0.1
03	Black Mountain Caldera Structural Margin	1
04	Boxcar	1.13
05	Hogback	1
06	Claim Canyon Caldera Structural Margin	0.1
07	Colson Pond	1
08	East Greeley	3.44
09	East Estuary	0.24
10	East Thirsty Canyon Structural Zone	1.28
11	Handley	1.34

Table 5-12
Fault Permeability Multiplier for BN-MME-SDA
(Page 2 of 2)

Fault ID	Name	Fault Permeability Multiplier
12	Handley South	9.32×10^{-2}
13	Handley North	0.1
14	Moor Hen Meadow Structural Zone	1
15	North Timber Mountain Moat Structural Zone	0.29
16	Ribbon Cliff Structural Zone	1.04
17	Richey	0.92
18	Scrugham Peak	0.26
19	Silent Canyon Northern Structural Zone	1
20	Silent Canyon Structural Zone East	1
21	Silent Canyon Structural Zone West	1
22	YMP inferred/CP Thrust	0.1
23	Silent Canyon/ West Purse	1.00×10^{-6}
24	Purse North	1.00×10^{-6}
25	Split Ridge	0.1
26	Southern Pahute Mesa Structural Zone	2.42
27	Gold Meadows Structural Zone/Big Burn Valley	0.86
28	Rainier Mesa Caldera Structural Margin	1
29	Ammonia Tanks Caldera Structural Margin	1
30	Hot Springs Lineament extension of Rainier Mesa Caldera Structural Margin	1
31	West Almendro	7.25×10^{-2}
32	West Boxcar	4.40×10^{-2}
33	West Greeley	2.31756
34	West Estuary	8.43×10^{-3}
35	Windy Wash/Claim Canyon 1	0.1
36	West Silent Canyon Structural Zone	2.558146
37	Paintbrush Canyon	0.1
38	Fault 23 south of North Timber Mountain Moat Structural Zone	1
39	Fault 16 between faults 23 and 24	1.00×10^{-6}
40	Extension of fault 24 to northern model edge	1.00×10^{-5}
41	Repair of fault 24 where crossed by fault 36	1.00×10^{-6}

5.6.3 All HSU Depth Decay and Anisotropy (ADA)

In the UGTA regional model (DOE/NV, 1997), depth decay and horizontal-to-vertical anisotropy were assigned to every HSU. Parameterization of the base HFM described in this section was designed to examine whether this approach would result in a reasonable calibration. Corrective action unit model calibration began with parameters developed from the regional model analysis performed to evaluate CAU-model boundary flows as presented in the Pahute Mesa hydrologic data document (SNJV, 2004a).

Figures 5-27 through 5-30 show the observed (or otherwise estimated) and unweighted simulated values for the calibration wells, springs, Oasis Valley discharge, and boundary flows, respectively. On Figures 5-27 and 5-28, the line of perfect agreement is shown, and ideally the data would plot exactly onto this line. However, in practice there is always some model misfit. The scatter around the line of perfect agreement is generally random in Figure 5-27, until an observed head of 1,450 m is exceeded. At the very highest-observed observation well water levels, the model has a tendency towards undersimulation. However, the highest water level (and the largest error) shown is associated with the ER-19-1 shallow completion, which may be perched (Fenelon, 2000). The remaining errors above 1,450 m are all in far eastern Area 19, where data became very sparse and uncertainty increases. Figure 5-31 shows a histogram of weighted observation well errors. There is a strong central tendency, with a few undersimulated wells (positive values) with errors greater than 20 m (WW-8 and ER-EC-7). The behavior of this parameterization with respect to WW-8 is investigated further in Section 6.2.

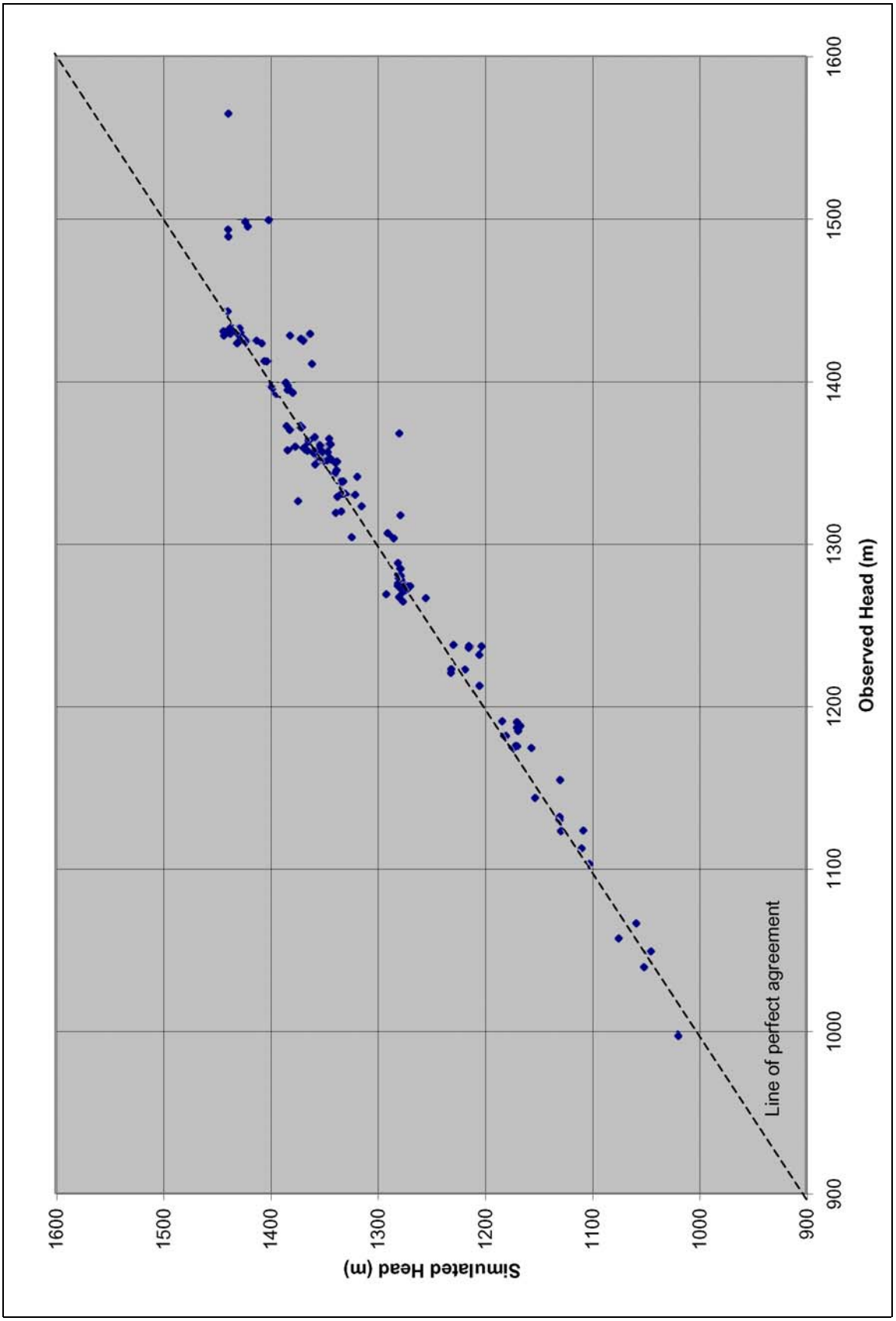

Figure 5-27
Observed Versus Simulated Well Head for BN-MME-ADA

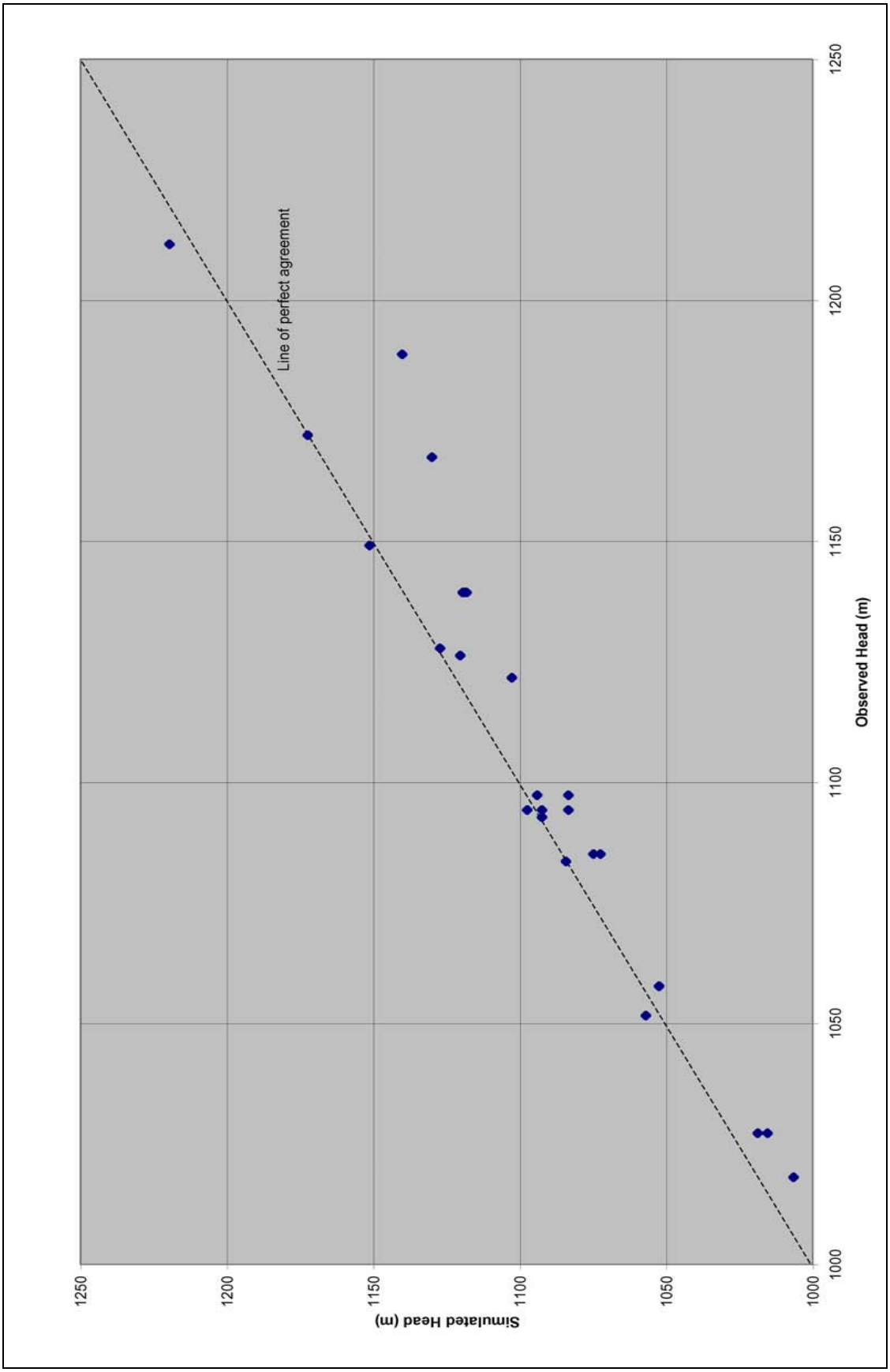

Figure 5-28
Observed Versus Simulated Spring Head for BN-MME-ADA

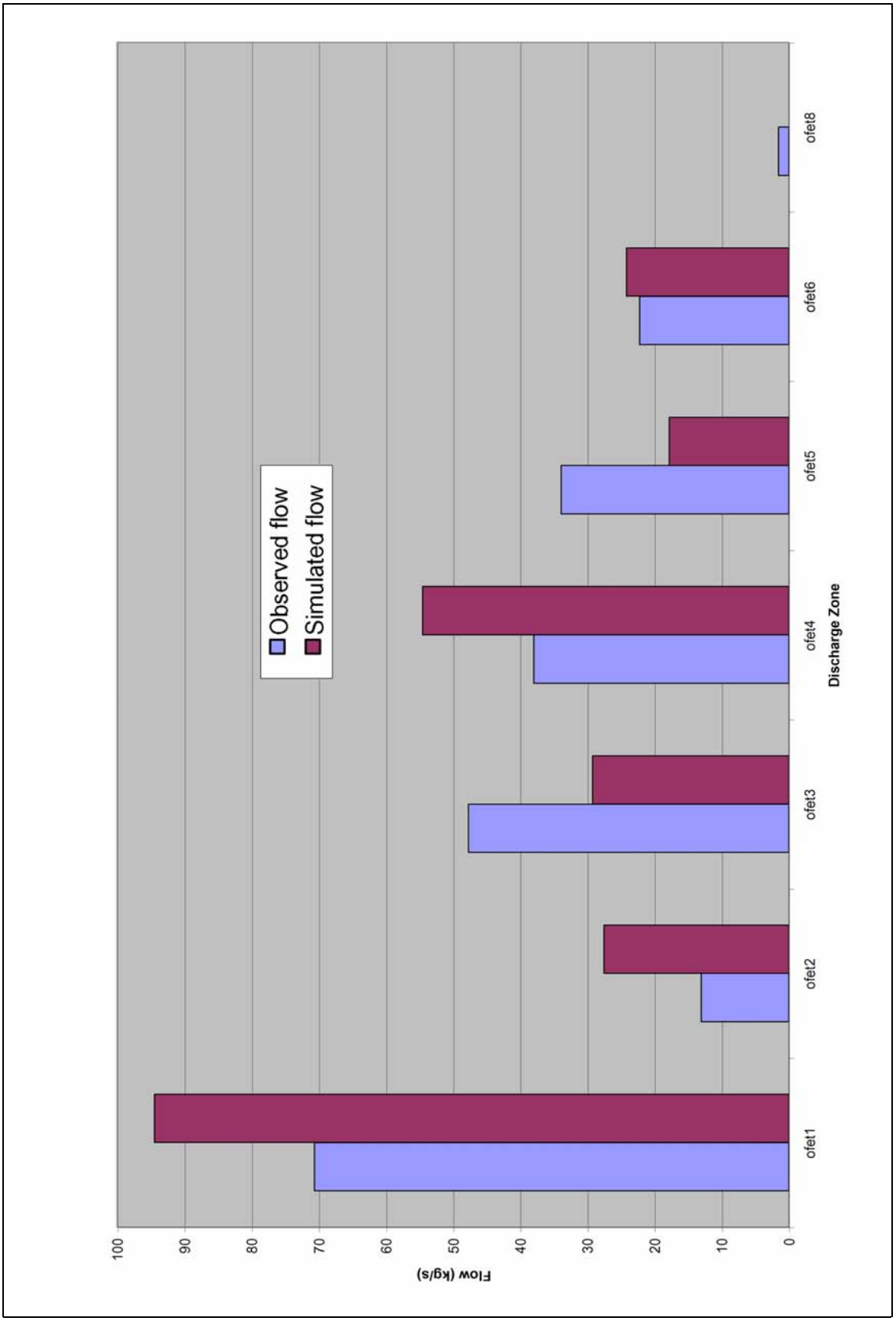

Figure 5-29
Observed and Simulated Oasis Valley Discharge for BN-MME-ADA

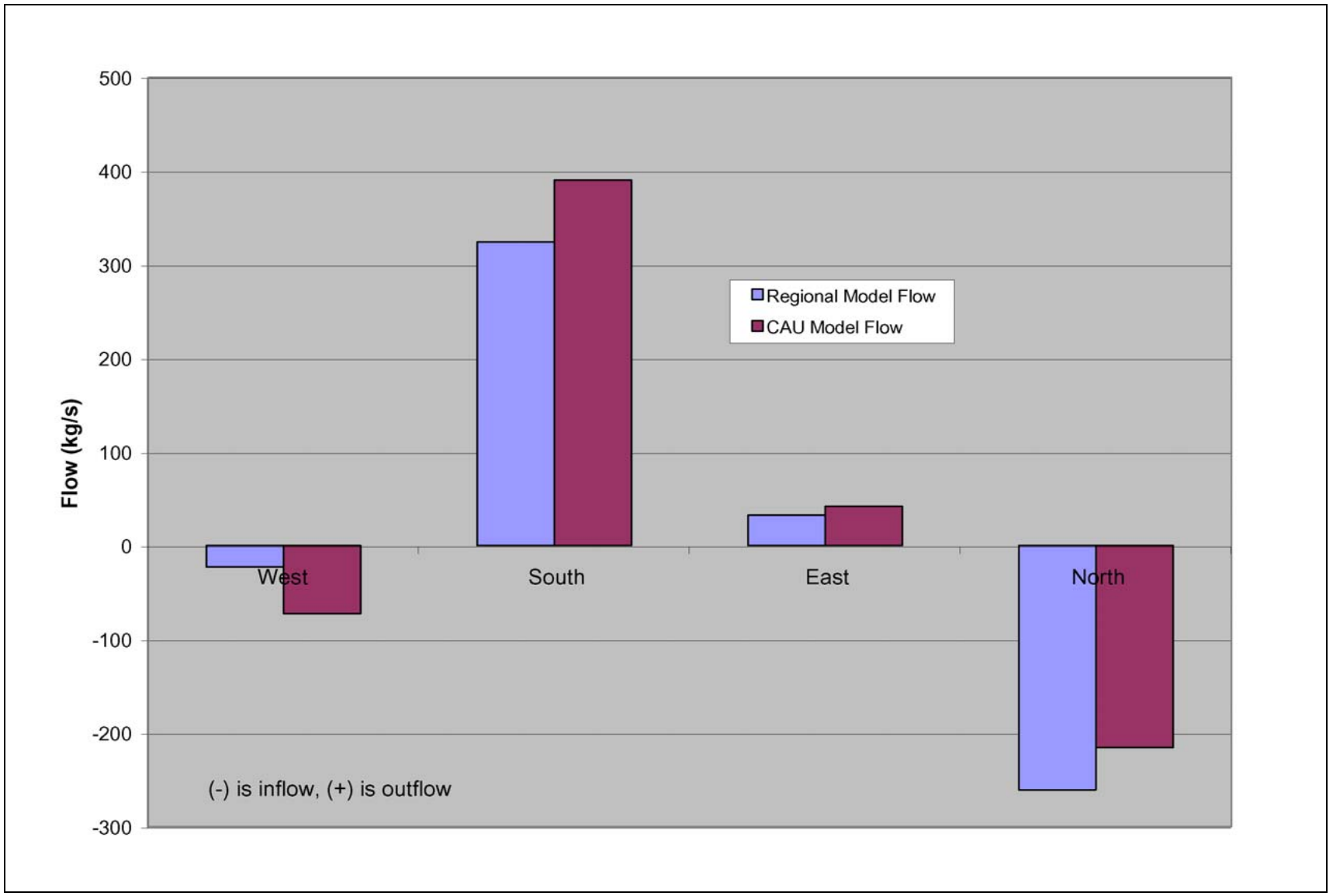

Figure 5-30
Estimated and Simulated Boundary Flows for BN-MME-ADA

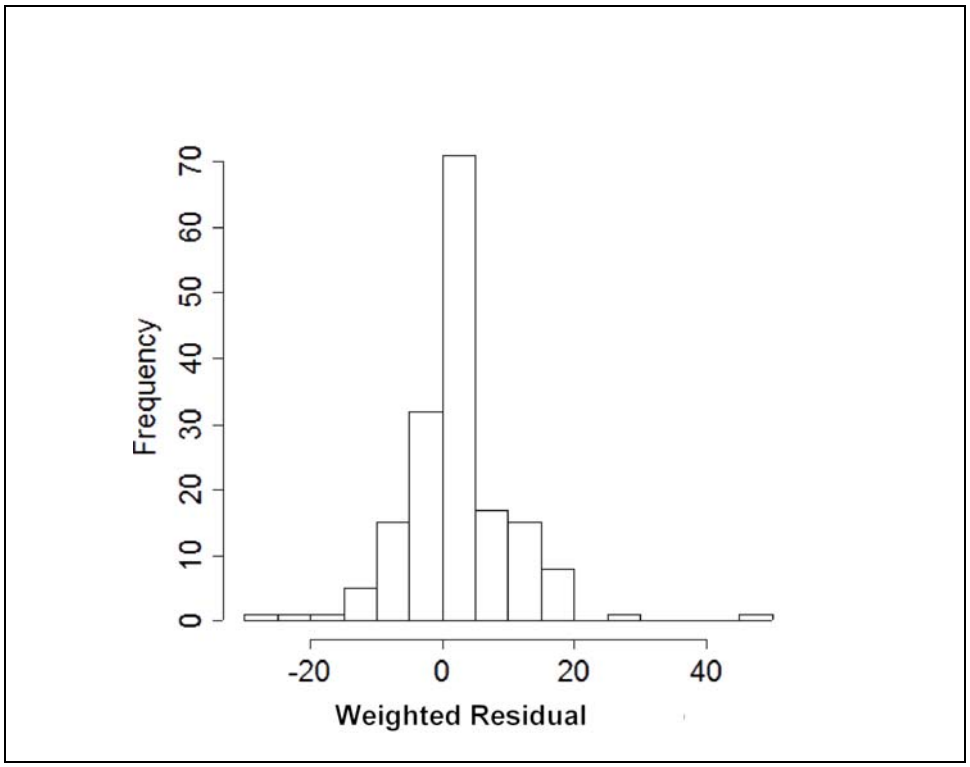

Figure 5-31
Histogram of Weighted Head Residuals for BN-MME-ADA

The weighted head and spring errors are shown on Figure 5-32, color coded by value and sign. The two lowest, or undersimulated, wells were WW-8 and ER-EC-7. The most oversimulated water level was U-20g in northern Area 19. Well U-20g has a target head of 1,357.27 m, while Well U-20aw approximately 2,100 m nearly due south has a target head of 1,371.43 m. Well U-20g is primarily in the BFCU, and thus its connection to the flow system may be marginal. In general, the errors are randomly distributed, although there is a slight low bias in northern Area 20.

The two springs with the largest errors are Goss Spring, which has an uncertain location, and Oleo Road Spring in an area of very high topographic gradient that the model is unlikely to represent in sufficient detail. Thus, these two springs were assigned low weights because of their questionable representativeness. However, springs at similar and higher elevations were matched well, and this misfit appears to be a local issue.

The total estimated Oasis Valley discharge is 227 kg/s. The simulated discharge, shown in Figure 5-29, is 247 kg/s. The total error is within one standard deviation (30 kg/s) as reported by Laczniak et al. (2001). With the exception of Zone 4, the model trends the same as the data with

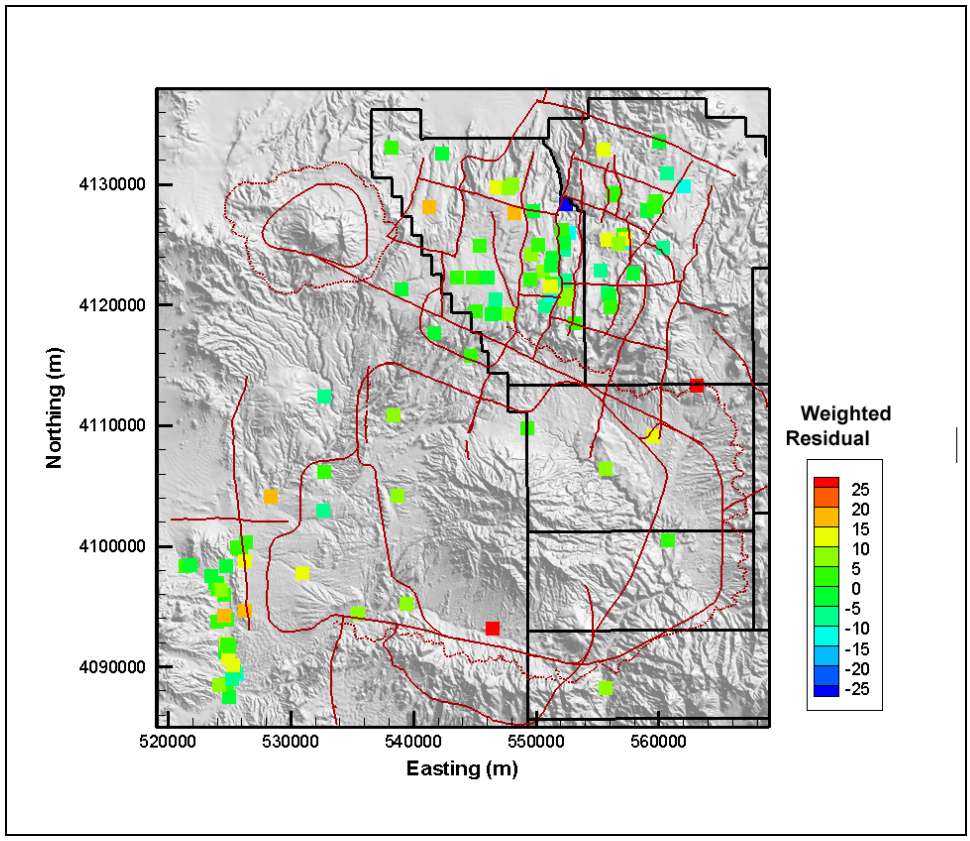

Figure 5-32
Post Plot of Weighted Well and Spring Head Residuals for BN-MME-ADA

some scatter, showing that the general representation of the area is correct. The northernmost zone accounts for 38 percent of the discharge versus 30 percent observed, which is important because this area is closest to the NTS. The boundary flows (Figure 5-30), estimated from regional model analysis, all trend the correct way (e.g., have the proper sign), with the largest relative misfit on the western edge.

The quantitative measures of the model calibration are given by the summary statistics shown in Table 5-13. These statistics alone are not used to judge model calibration; they are used in conjunction with the graphical approaches described previously. There is a slight low bias in the spring heads, with a slight overprediction bias for the flows. The total model objective function was 21,292. Table 5-14 shows the contribution of each data type to the total model goodness of fit. The strongest contributors are observation well heads and Oasis Valley flow, which are also the two key components of calibration data.

Table 5-13
Calibration Summary Statistics for BN-MME-ADA

Calibration Data	Number of Data	Mean Weighted Error (m or kg/s)[a]	Maximum Weighted Residual	Minimum Weighted Residual	Error Standard Deviation (m or kg/s)
Well Head	152	1.5	48 (WW-8)	-25 (U-20g)	8.5
Spring Head	28	2.9	19 (Torrance Spring)	-7.9 (Spring id 180)	6.9
Oasis Valley Discharge	7	-5.9	37 (Zone 3)	-47 (Zone 1)	30
Boundary Flow	4	-8.9	25 (West)	-33 (South)	23

[a]Positive is undersimulation of target data, negative is oversimulation.

Table 5-14
Contribution to Model Goodness of Fit by Data Type for BN-MME-ADA

Data Type	Value (-)	% of total
Well Head	11,060	52
Spring Head	1,331	6
Oasis Valley Discharge	6,638	31
Boundary Flow	2,263	11
Total	21,292	100

Flow paths were qualitatively assessed during calibration by inspecting the simulated water table configuration and tracking particles forward from NTS calibration well locations. Figures 5-33 and 5-34 show the simulated water table and travel paths for this model case. The water table shows higher heads on the eastern edge at a northing of about 4,120,000 m, which is coincident with Gold Meadows stock and the western edge of Rainier Mesa. In the western part of Area 20, the influence of the Purse Fault is evident by nearly 100 m offset in water levels across it, with more subdued effects also present at West Boxcar Fault. Water flows from Areas 19 and 20 towards the southwest and Oasis Valley. Ubiquitous discharge in Oasis Valley, including flow from Sarcobatus Flat to the

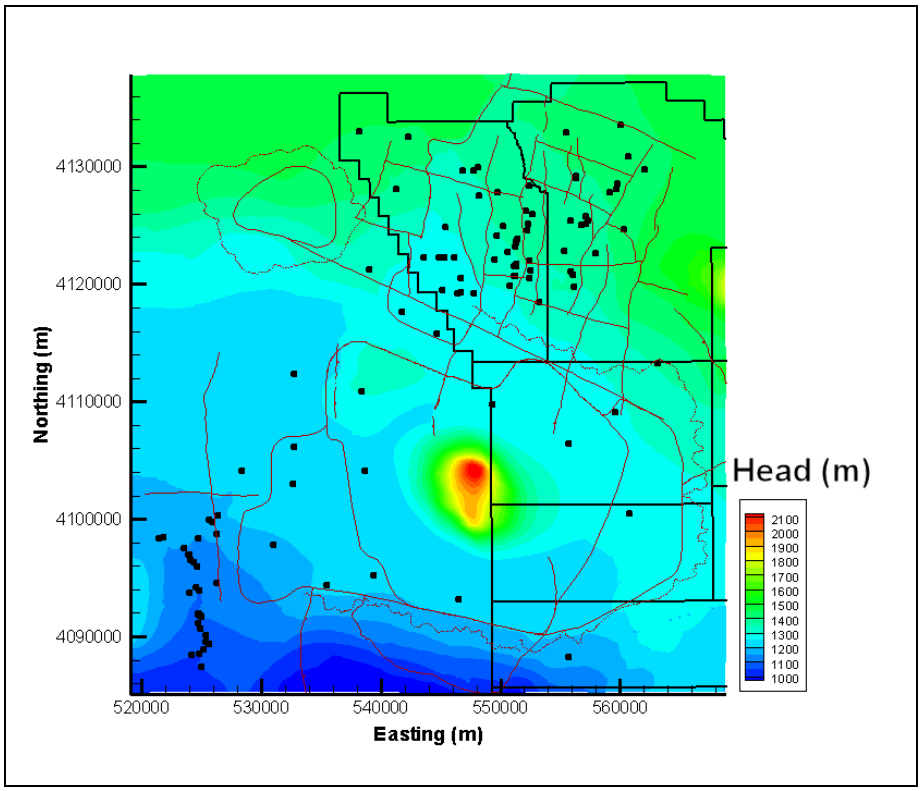

Figure 5-33
Simulated Water Table for BN-MME-ADA

west is also evident. The particle trajectories along the western side of Timber Mountain are influenced by either the contact between the TMCM and TMA, or the fault that defines the contact, and lie mainly within the TMCM.

Particle tracking shows the same generally noted flow paths as SNJV (2004a) with flow noticeably skirting the Purse Fault on the west from flow originating in northwestern Area 20. Like the selected HSU depth decay and anisotropy case, the flow paths become very complicated where the Purse Fault has been assumed to end near the Moat Fault. This case also shows flow along the western flank of Timber Mountain down into Oasis Valley and out to the south. Unlike the selected HSU depth-decay and anisotropy case, particles move from northwestern Area 20 down the western side of Purse Fault. Thus, this parameterization of the base HFM simulates a higher velocity in this area than the selected HSU depth-decay and anisotropy case. This model also has poorer agreement on the edge flows in the direction of oversimulation; thus, it is possible that in order to improve the agreement with the edge flows that permeability must decrease, and the effects are seen in the change in flow velocity in northern Area 20.

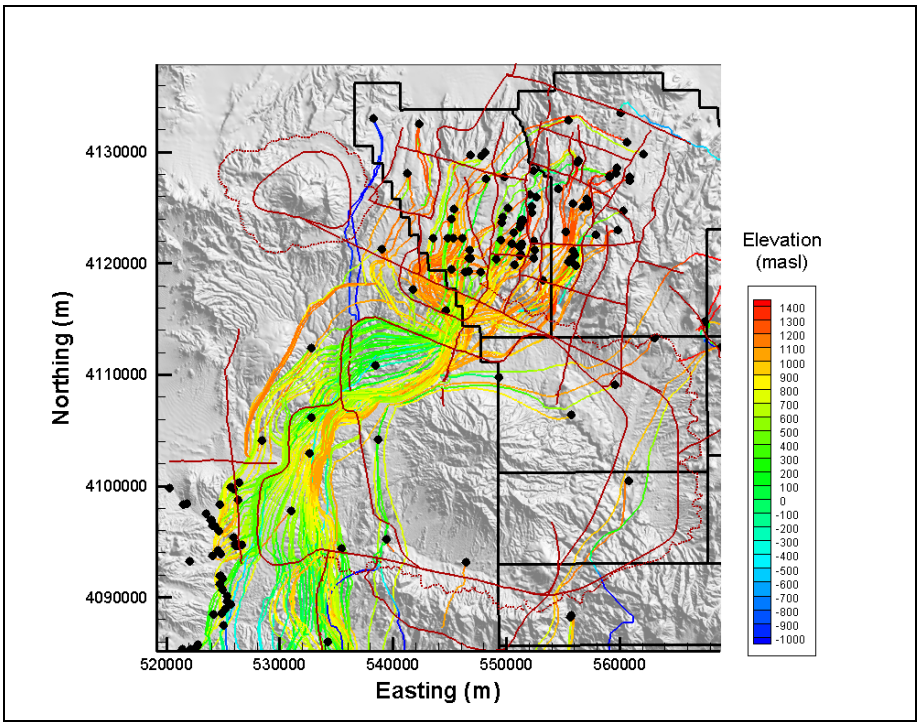

Figure 5-34
Particle Tracks for BN-MME-ADA

The properties used to parameterize this model are shown in Tables 5-15 and 5-16 for HSUs and faults, respectively.

Table 5-15
Hydrostratigraphic Unit Parameters for BN-MME-ADA
(Page 1 of 2)

HSU	Log (k or k_0) (m^2)	Horizontal/Vertical Permeability	Depth Decay λ	Notes
LCCU	-15	0.15	1.20×10^{-3}	
LCA	-13	1.50×10^{-2}	1.00×10^{-3}	
UCCU	-13.93	2.00×10^{-2}	1.50×10^{-3}	
LCCU1	-12.72	2.00×10^{-2}	2.60×10^{-3}	
LCA3	-11	2.00×10^{-2}	1.00×10^{-3}	
MGCU	-12.93	0.5	1.50×10^{-3}	
SCICU	-9.81	0.5	1.50×10^{-3}	
CHICU	-9.81	0.5	1.50×10^{-3}	
CCICU	-11.81	0.5	1.50×10^{-3}	
RMICU	-12.81	0.5	1.50×10^{-3}	
ATICU	-11.81	0.5	1.50×10^{-3}	
BMICU	-10.81	0.5	1.50×10^{-3}	
PBRCM	-11.73	2.0×10^{-2}	2.60×10^{-3}	
BRA	-10.47	8.00×10^{-2}	2.60×10^{-3}	
BCU	-13.81	2.00×10^{-2}	2.60×10^{-3}	
KA	-10.71	8.00×10^{-2}	2.60×10^{-3}	
CFCU	-9.73	2.00×10^{-2}	2.60×10^{-3}	
CFCM	-10.03	2.00×10^{-2}	2.60×10^{-3}	
IA	-10.06	8.00×10^{-2}	2.60×10^{-3}	
CHCU	-12.71	2.00×10^{-2}	2.60×10^{-3}	
CHZCM	-11.49	2.00×10^{-2}	2.60×10^{-3}	Depth decay all parameters
CHVCM	-11.14	2.00×10^{-2}	2.60×10^{-3}	
CHVTA	-12	8.00×10^{-2}	2.60×10^{-3}	
YMCFCM	-11.90	8.00×10^{-2}	2.60×10^{-3}	
TSA	-9.21	8.00×10^{-2}	2.60×10^{-3}	
LPCU	-12.93	2.00×10^{-2}	2.60×10^{-3}	
PLFA	-10.84	8.00×10^{-2}	2.60×10^{-3}	
TCA	-8.49	8.00×10^{-2}	2.60×10^{-3}	
UPCU	-11.99	2.00×10^{-2}	2.60×10^{-3}	
BA	-9.89	8.00×10^{-2}	2.60×10^{-3}	
PVTA	-10.41	8.00×10^{-2}	2.60×10^{-3}	
PCM	-11.35	2.00×10^{-2}	2.60×10^{-3}	
LCA3a	-12.06	2.00×10^{-2}	1.00×10^{-3}	
FCCU	-12.71	2.00×10^{-2}	2.60×10^{-3}	
SCVCU	-12.71	2.00×10^{-2}	2.60×10^{-3}	
TMA	-10.86	8.00×10^{-2}	2.60×10^{-3}	
THCM	-12.71	2.00×10^{-2}	2.60×10^{-3}	
THLFA	-10.71	8.00×10^{-2}	2.60×10^{-3}	
TMCM	-9.41	2.00×10^{-2}	2.60×10^{-3}	
FCA	-9	8.00×10^{-2}	2.60×10^{-3}	
FCCM	-13.37	2.00×10^{-2}	2.60×10^{-3}	
DVA	-11.75	2.00×10^{-2}	2.60×10^{-3}	

Table 5-15
Hydrostratigraphic Unit Parameters for BN-MME-ADA
(Page 2 of 2)

HSU	Log (k or k_0) (m^2)	Horizontal/Vertical Permeability	Depth Decay λ	Notes
DVCM	-12.40	2.00×10^{-2}	2.60×10^{-3}	Depth decay all parameters
TCVA	-10.52	8.00×10^{-2}	2.60×10^{-3}	
YVCM	-11.36	2.00×10^{-2}	2.60×10^{-3}	
AA	-12	0.22	3.70×10^{-3}	
LCA Zone 1	-9.89	1.50×10^{-2}	1.00×10^{-3}	
TCVA Zone 6[a]	-12.33	8.00×10^{-2}	2.60×10^{-3}	
TMAR Zone 6[b]	-12.80	8.00×10^{-2}	2.60×10^{-3}	
TMCM-ERM[c]	-11	2.00×10^{-2}	2.60×10^{-3}	
TMCM-ATC	-10.5	2.00×10^{-2}	2.60×10^{-3}	
TMCM-TH	-11.21	2.00×10^{-2}	2.60×10^{-3}	
TMCM-OV	-9.89	2.00×10^{-2}	2.60×10^{-3}	
TMCM-TM	-12.5	2.00×10^{-2}	2.60×10^{-3}	
TMCM-NTM	-9	2.00×10^{-2}	2.60×10^{-3}	
TMCM-ATCE	-10.80	2.00×10^{-2}	2.60×10^{-3}	
TMCM-NTME	-10.18	2.00×10^{-2}	2.60×10^{-3}	
UPCU West of Purse Fault	-11.36	2.00×10^{-2}	2.60×10^{-3}	
LPCU West of Purse Fault	-11.90	2.00×10^{-2}	2.60×10^{-3}	
BRA West of Purse Fault	-9	8.00×10^{-2}	2.60×10^{-3}	

See Table 2-6 for HSU descriptions.

[a]See Figure 5-8 for TCVA subdivisions.
[b]See Figure 5-9 for TMA subdivisions.
[c]See Figure 5-8 for TMCM subdivisions.

Table 5-16
Fault Permeability Multiplier for BN-MME-ADA

Fault ID	Fault Name	Fault Permeability Multiplier
01	Almendro	10
02	Bare Mountain	1
03	Black Mountain Caldera Structural Margin	1
04	Boxcar	7.00×10^{-2}
05	Hogback	1
06	Claim Canyon Caldera Structural Margin	1
07	Colson Pond	1
08	East Greeley	1
09	East Estuary	0.1
10	East Thirsty Canyon Structural Zone	1
11	Handley	5
12	Handley South	1
13	Handley North	1
14	Moor Hen Meadow Structural Zone	1
15	North Timber Mountain Moat Structural Zone	1
16	Ribbon Cliff Structural Zone	5
17	Richey	1
18	Scrugham Peak	1
19	Silent Canyon Northern Structural Zone	1
20	Silent Canyon Structural Zone East	1
21	Silent Canyon Structural Zone West	1
22	YMP inferred/CP Thrust	1
23	Silent Canyon/ West Purse	1.00×10^{-4}
24	Purse North	1.00×10^{-4}
25	Split Ridge	1
26	Southern Pahute Mesa Structural Zone	1
27	Gold Meadows Structural Zone/Big Burn Valley	1
28	Rainier Mesa Caldera Structural Margin	1
29	Ammonia Tanks Caldera Structural Margin	1
30	Hot Springs Lineament extension of Rainier Mesa Caldera Structural Margin	1
31	West Almendro	10
32	West Boxcar	7.00×10^{-2}
33	West Greeley	1
34	West Estuary	1.00×10^{-2}
35	Windy Wash/Claim Canyon 1	1
36	West Silent Canyon Structural Zone	5
37	Paintbrush Canyon	1
38	Fault 23 south of North Timber Mountain Moat Structural Zone	1
39	Fault 16 between faults 23 and 24	1.00×10^{-4}
40	Extension of Purse Fault to northern edge of model	1.00×10^{-5}
41	Purse Fault repair where fault 36 crosses	1.00×10^{-5}

5.7 Silent Canyon Caldera Complex Hydrostratigraphic Framework Model Flow Model Calibration

The major alternative model presented by BN (2002) is the SCCC. This model has fewer HSUs than the base HFM, and does not have as deep or extensive of a fault system. In particular, the Calico Hills formation is reduced from five separate HSUs to one that is several hundred meters thick. More details are given in BN (2002).

The calibration of the SCCC alternative began with the calibrated parameters from the selected HSU depth decay and anisotropy base HFM for both the HSUs (where still present) and faults (where still present). However, because of the lumped nature of the Calico Hills unit its anisotropy was increased to 50:1 because many dissimilar types of units were combined. In addition, the BA also incorporates the LPCU in the SCCC HFM. The BA was assigned anistropy of 20:1. The units selected to have permeability depth decay and anisotropy are the same as presented in Table 5-8 in Section 5.6.2. Figures 5-35 through 5-38 show the observed and unweighted simulated values for the calibration wells, springs, Oasis Valley discharge, and boundary flows, respectively. The scatter around the line of perfect agreement is generally random in Figure 5-35, although a large error occurs at 1,326 m associated with Well ER-19-1 (deep completion). Above an observed head of 1,450 m, there is a bias towards underprediction. However, the highest water level (and the largest error) shown is associated with the Well ER-19-1 shallow completion, which may be perched (Fenelon, 2000). Figure 5-39 shows a histogram of weighted observation well water levels. There is a strong central tendency with relatively even tails. Unlike the calibration cases for the base HFM, there are more large errors at both ends of the distribution, which qualitatively suggests that this calibration (and underlying model structure) is not as good as the others.

The weighted head and spring errors are shown on Figure 5-40, color coded by value and sign. The two lowest, or undersimulated, wells were WW-8 in the east-central part of the model and PM-3 (at coordinates of about 540,000 and 4,120,000 m). After these two wells, UE-18t was the next largest undersimulation to the southwest of WW-8.

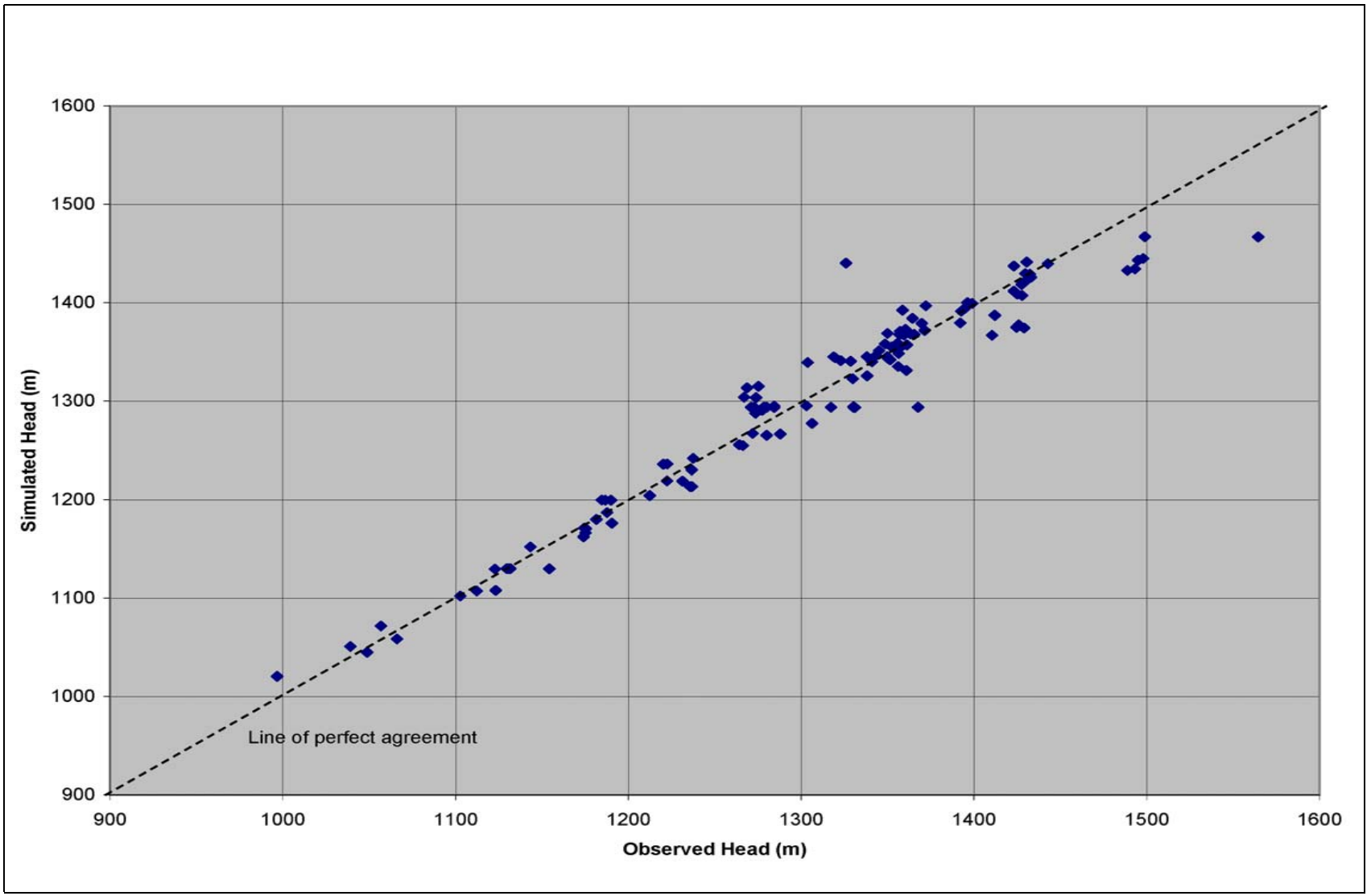

Figure 5-35
Observed Versus Simulated Well Head for SCCC-MME-SDA

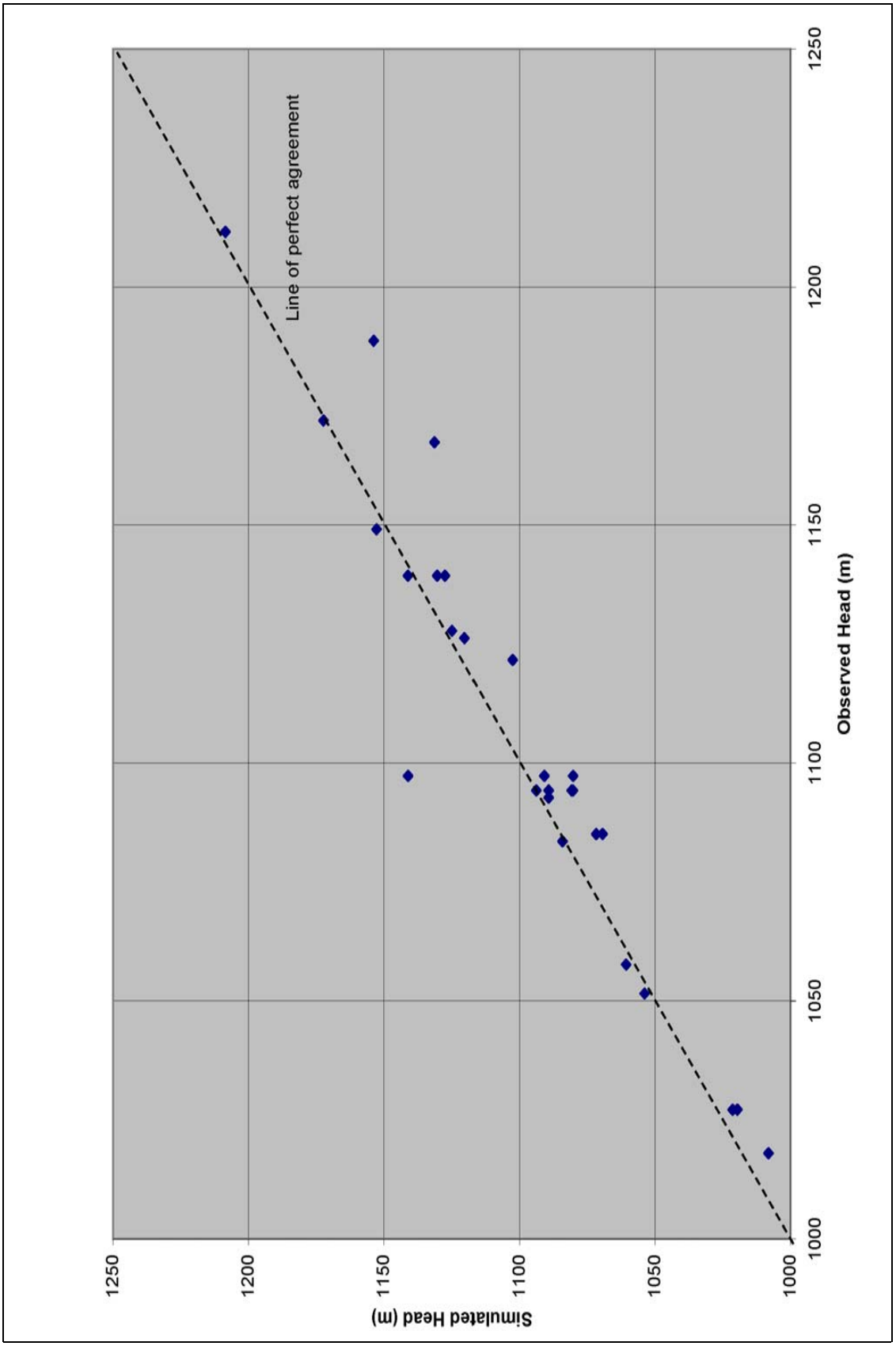

Figure 5-36
Observed Versus Simulated Spring Head for SCCC-MME-SDA

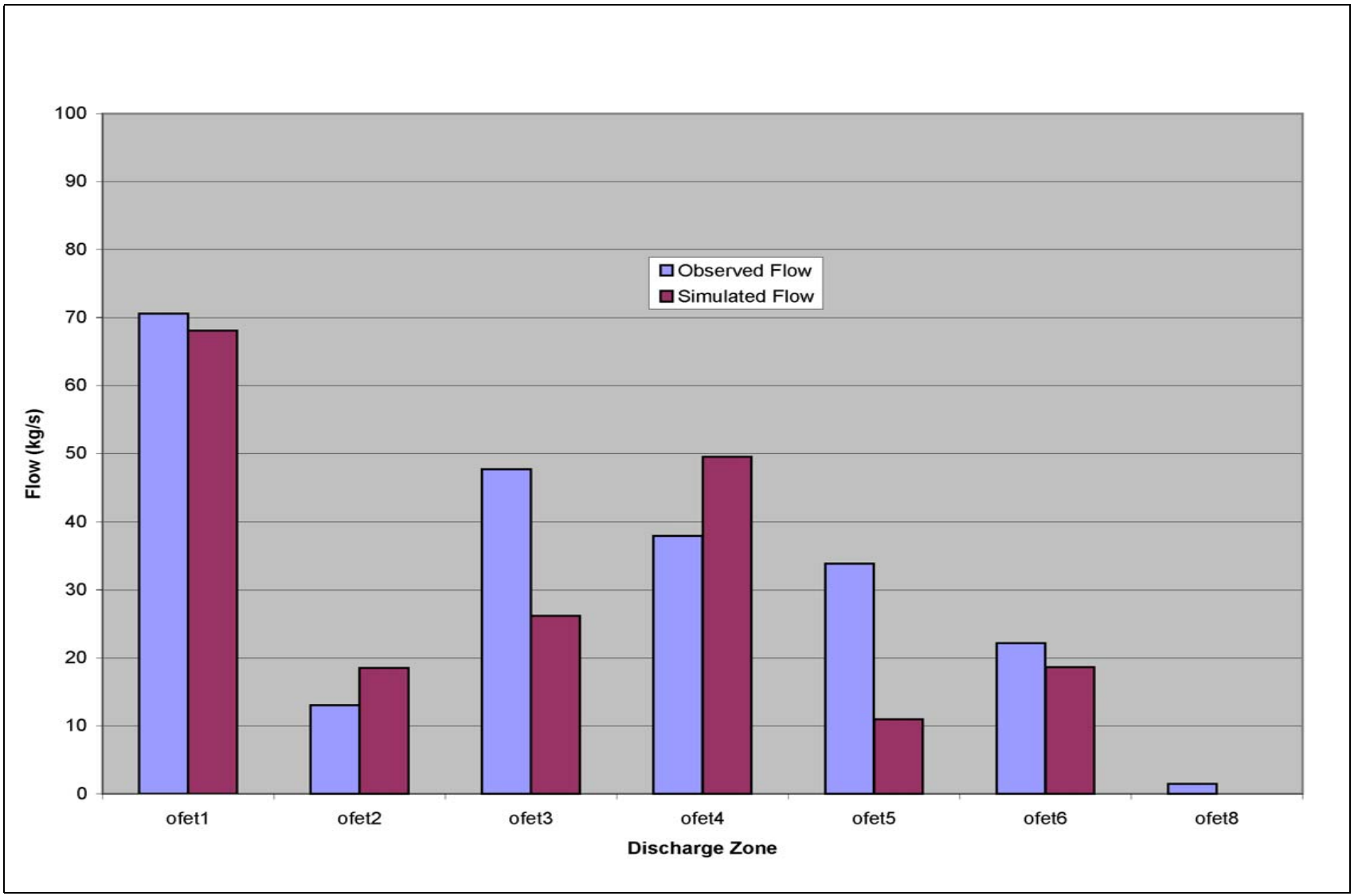

Figure 5-37
Observed Versus Simulated Oasis Valley Discharge for SCCC-MME-SDA

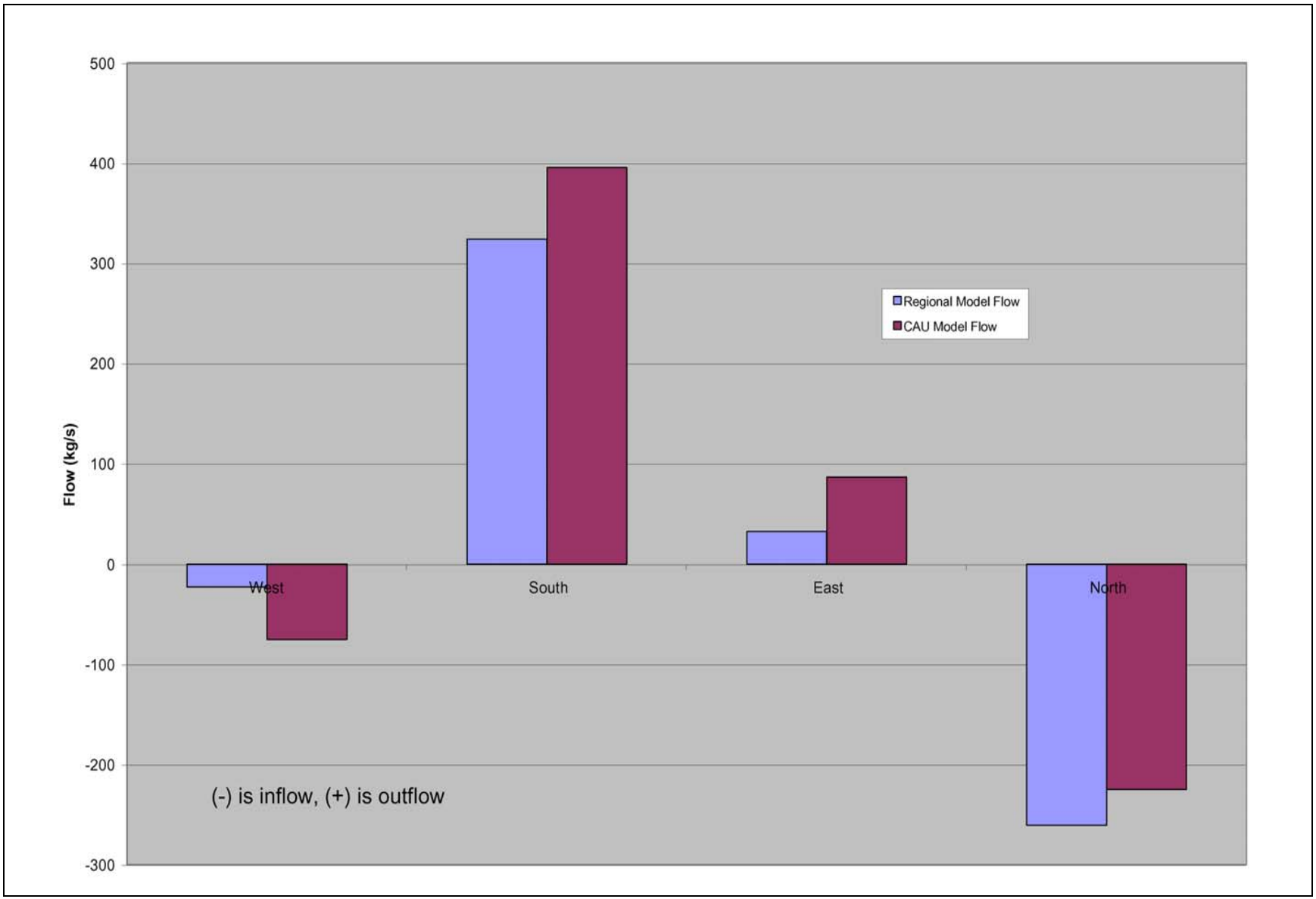

Figure 5-38
Estimated Versus Simulated Boundary Flows for SCCC-MME-SDA

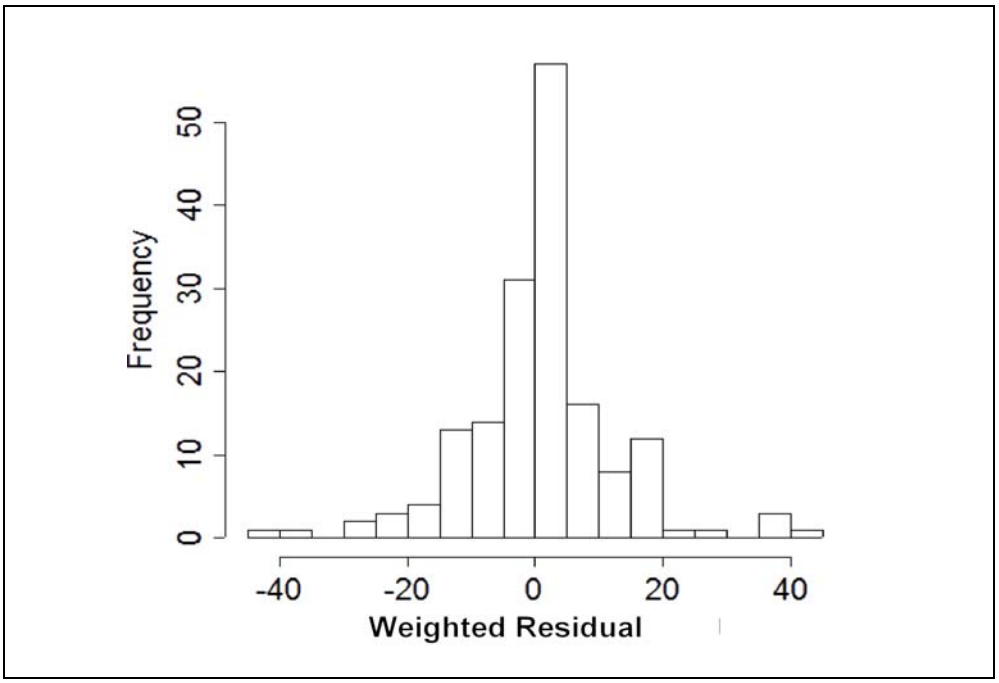

Figure 5-39
Histogram of Weighted Head Residuals for SCCC-MME-SDA

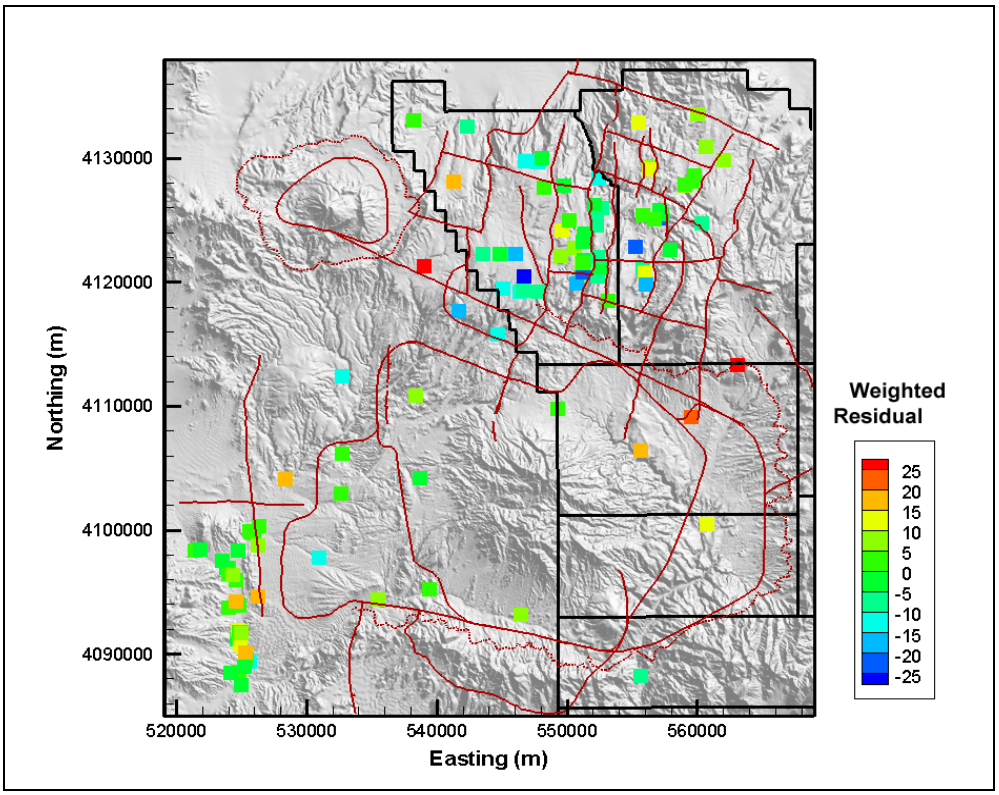

Figure 5-40
Post Plot of Weighted Well and Spring Head Residuals for SCCC-MME-SDA

The total estimated Oasis Valley discharge is 227 kg/s. The simulated discharge, shown in Figure 5-37, is 192 kg/s. The total error is nearly within one standard deviation (30 kg/s) as reported by Laczniak et al. (2001). As with the other flow models, with the exception of Zone 4 (Figure 4-17), the model trends the same as the data with some scatter, showing that the general representation of Oasis Valley is correct. The northernmost zone is in nearly perfect agreement with the data. The boundary flows (Figure 5-38), estimated from regional model analysis, all trend the correct way (e.g., have the proper sign), with the largest relative misfit on the eastern and western edges.

The quantitative measures of the model calibration are given by summary statistics shown in Table 5-17. Note that the ME for the well heads is better than some of the previous models for the base HFM, but that the standard deviation is nearly 50 percent larger than for depth decay and anisotropy applied to all HSUs case in Section 5.6.3. The low ME is a reflection of the even scatter of larger residuals towards both under and overprediction seen earlier in the weighted residual histogram. The total model goodness-of-fit statistic is 31,869, which is nearly double that of the selected depth-decay and anisotropy case in Section 5.6.2 and 150 percent of the all depth-decay and anisotropy case in Section 5.6.3. Table 5-18 shows the contribution of each data type to the total model goodness of fit.

Table 5-17
Calibration Summary Statistics for SCCC-MME-SDA

Calibration Data	Number of Data	Mean Weighted Error (m or kg/s)[a]	Maximum Weighted Residual	Minimum Weighted Residual	Error Standard Deviation (m or kg/s)
Well Head	152	0.34	43 (WW-8)	-39 (U-20c)	11
Spring Head	28	2.5	19 (Torrance Spring)	-43 (Spring id 163)	11
Oasis Valley Discharge	7	9.9	45 (Zone 5)	-23 (Zone 4)	25
Boundary Flow	4	-16	20 (West)	-43 (North)	30

[a]Positive is undersimulation of target data, negative is oversimulation.

Table 5-18
Contribution to Model Goodness of Fit by Data Type for SCCC-MME-SDA

Data Type	Value (-)	% of Total
Well Head	19,998	63
Spring Head	3,538	11
Oasis Valley Discharge	4,681	15
Boundary Flow	3,632	11
Total	31,849	100

Flow paths were qualitatively assessed during calibration by inspecting the simulated water table configuration and tracking particles forward from calibration well locations. Figures 5-41 and 5-42 show the simulated water table and travel paths, respectively, for this model case. As shown on these figures, water flows from Areas 19 and 20 towards the southwest and Oasis Valley as suggested by observed regional groundwater potentials and geochemical analysis. The effects of the West Boxcar Fault can be seen clearly. Observed heads at PM-3 are more than 100 m higher than those in southern Area 20, and it is the relatively shallow and disconnected Purse Fault in this alternative that allows groundwater from PM-3 and the eastern side of Black Mountain to spill into Area 20. This causes misfit at both PM-3 and the wells throughout southern Area 20. A slight mound is simulated under Timber Mountain. Discharge in Oasis Valley, including flow from Sarcobatus Flat to the west, is also evident. Unlike the other HFMs discussed in this section, the SCCC has more particle tracks going down Fortymile Canyon. The flow paths in southern Area 20 are nearly due south, in contrast to the base HFM models and the observed water-table surface. While the goodness of fit and qualitative assessment of the residuals suggest that this HFM does not perform as well as the base HFM, the broad characteristics of the flow system are still correct. This may be at least a partial consequence of specifying head around the edges of the CAU model.

The properties used to parameterize this model are shown in Tables 5-19 and 5-20 for HSU and faults, respectively.

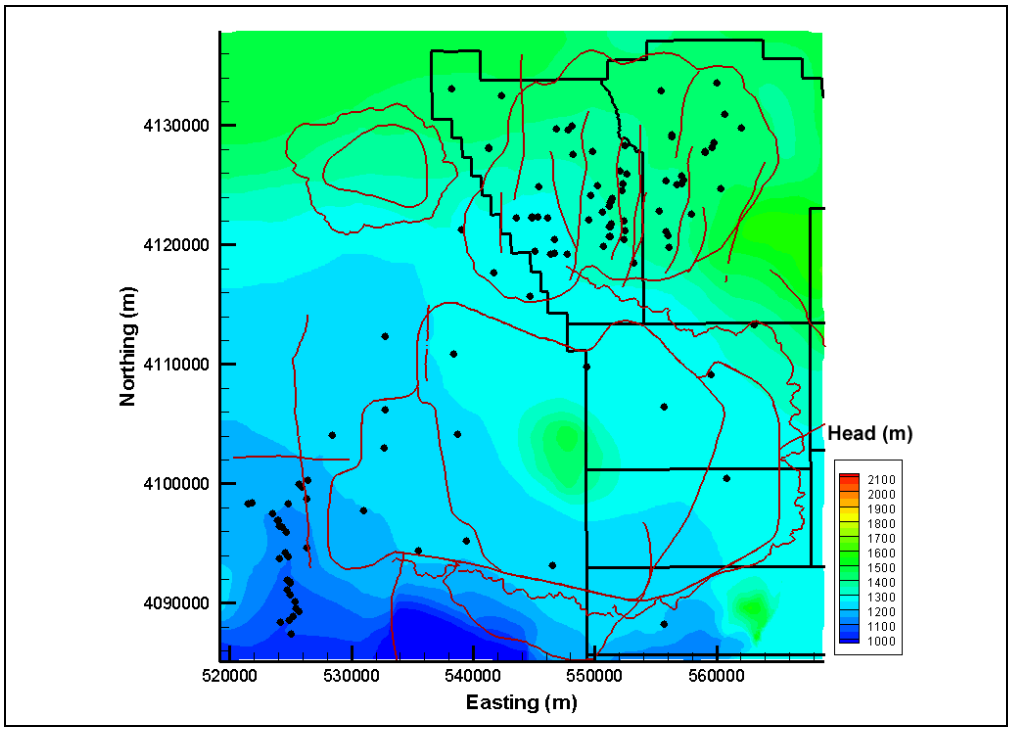

Figure 5-41
Simulated Water Table for SCCC-MME-SDA

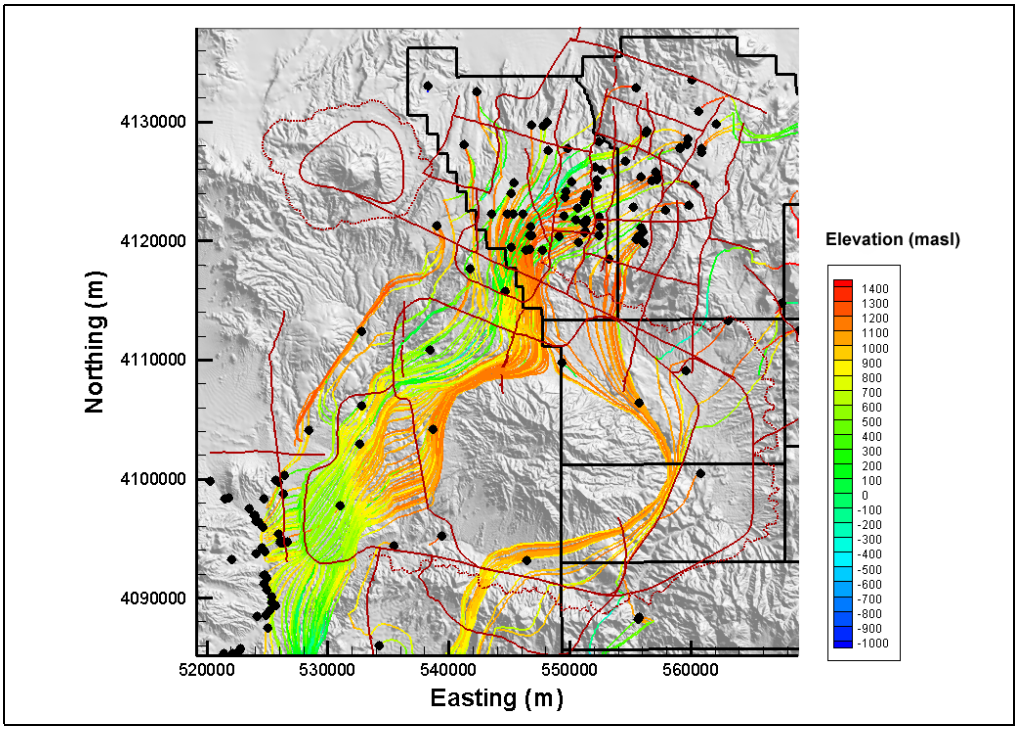

Figure 5-42
Particle Tracks for SCCC-MME-SDA

Table 5-19
Hydrostratigraphic Unit Parameters for SCCC-MME-SDA
(Page 1 of 2)

HSU	Log (k or k_0) (m^2)	Notes
LCCU	-18	k
LCA	**-13.78**	**k_0**
UCCU	-16.78	k
LCCU1	-12.99	k
LCA3a	**-13.04**	**k_0**
MGCU	-18.38	k
SCICU	-18.38	k
CHICU	-18.38	k
CCICU	-18.38	k
RMICU	-18.38	k
ATICU	-18.38	k
BMICU	-18.38	k
PBRCM	**-11.91**	**k_0**
BRA	**-11.51**	**k_0**
BCU	-13.67	k
KA	-11.78	k
CFCU	-12.73	k
IA	-13.56	k
CHCU	-13.83	k
YMCFCM	**-14.54**	**k_0**
TSA	-13.84	k
LPCU	-13.04	k
PLFA	-11.78	k
TCA	-11.48	k
UPCU	-15.33	k
BA	-12.57	k
PVTA	-12.90	k
PCM	**-11.08**	**k_0**
LCA	**-14.28**	**k_0**
FCCU	-12.98	k
SCVCU	-16.28	k
TMA	**-12.04**	**k_0**
THCM	-12.88	k
THLFA	-11.78	k
TMCM	**-11.04**	**k_0**
FCA	-11.50	k
FCCM	-13.48	k
DVA	-12.71	k
DVCM	-13.27	k

Table 5-19
Hydrostratigraphic Unit Parameters for SCCC-MME-SDA
(Page 2 of 2)

HSU	Log (k or k_0) (m^2)	Notes
TCVA	**-10.76**	**k_0**
YVCM	-10.08	k
AA	-13.50	k
LCA Zone 1	**-14.43**	**k_0**
TCVA[a] Zone 6	**-11.45**	**k_0**
TMA[b] Zone 6	**-15.16**	**k_0**
TMCM-ERM[b]	**-11.65**	**k_0**
TMCM-ATCW	**-9.74**	**k_0**
TMCM-ATCE	**-10.79**	**k_0**
TMCM-THS	**-11.93**	**k_0**
TMCM-OV	**-10.72**	**k_0**
TMCM-TMD	**-12.01**	**k_0**
TMCM-NTMW	**-9.31**	**k_0**
TMCM-NTME	**-9.93**	**k_0**
LPCU West of Purse Fault	-14.55	k
UPCU West of Purse Fault	-13.09	k
BRA West of Purse Fault	**-10.80**	**k_0**

See Table 2-6 for HSU descriptions.

[a]See Figure 5-7 for TCVA subdivisions.
[b]See Figure 5-8 for TMA and TMCM subdivision.

Table 5-20
Fault Permeability Multipliers for SCCC-MME-SDA
(Page 1 of 2)

Fault ID	Fault Name	Fault Permeability Multiplier
01	Silent Canyon Caldera Margin	1.3
02	West Purse	1.00×10^{-4}
03	Claim Canyon Caldera Structural Margin	1.1
04	Boxcar	1.07
05	Black Mountain Caldera Structural Margin	1
06	Split Ridge	1.1
07	West Greeley	2.32
08	Rainier Mesa Caldera Structural Margin	1
09	Colson Pond	1
10	YMP inferred/CP Thrust	0.1
11	Ammonia Tanks Caldera Structural Margin	1
12	Bare Mountain	0.1
13	Purse	1.00×10^{-5}

Table 5-20
Fault Permeability Multipliers for SCCC-MME-SDA
(Page 2 of 2)

Fault ID	Fault Name	Fault Permeability Multiplier
14	West Boxcar	3.69×10^{-2}
15	East Estuary	0.24
16	Almendro	0.32
17	Scrugham Peak	0.26
18	Handley South	1
19	Hot Springs Lineament extension over to Hogback	1
20	Paintbrush Canyon	0.1
21	Windy Wash	0.1
22	Gold Meadows Structural Zone/Big Burn Valley	0.86
23	Hogback	1
24	Handley	1.34
25	Handley South	1.1

CP = Control Point

5.8 Calibration Summary

During the Pahute Mesa CAU flow model calibration analysis, the base HFM was parameterized with four different strategies in order to test the impact of the concepts of permeability depth decay and anisotropy. In addition, an alternative HFM, the SCCC, was also calibrated. In all, a total of five calibration analyses with the MME recharge model were performed on two HFMs. Key behaviors and observations are summarized in this section.

The Pahute Mesa CAIP (DOE/NV, 1999) states that many ("often greater than 100") flow model simulations are necessary during the model calibration analysis. Flow model calibration, sensitivity, and uncertainty analysis was conducted jointly by SNJV and LANL on two separate computer systems. Los Alamos National Laboratory used its LAMBDA computer cluster comprised of 164 nodes each with two Intel Pentium processors (1 to 1.4 gigahertz [GHz] clock speed) and 4 gigabytes (GB) of random access memory (RAM). Stoller-Navarro Joint Venture began with six Intel Pentium 2 GHz workstations and finished the project with 28 computers, of which 20 were rack-mounted 3.4 GHz Xeon processors with 4 GB of RAM each. It is estimated that about 5,000 simulations were performed during the calibration phase of the Pahute Mesa CAU flow model. This level of computing power was necessary in order to calibrate the models to the state presented in this report;

the classic computing model of a single fast computer, even a workstation, would not have allowed the timely completion of the project.

5.8.1 Purse Fault Behavior

A striking difference between the base and SCCC HFMs is the area along the Purse Fault. Figure 5-43 (taken from Fenelon, 2000) shows groundwater levels in western Area 19, Area 20, and west of Area 20 along with a view of the BN-MME-SDA (Figure 5-44) and SCCC-MME-SDA results in the area (Figure 5-45). An area of "hydraulic discontinuity" exists coincident with the Purse Fault that shows about 100-m head difference across the fault with flow directed sub-parallel to the fault (e.g., the fault may act as an approximate no-flow barrier). In order to match the head in Wells PM-3, PM-2, UE-20p, UE-20j, and U-20m in the base HFM on the western side of the Purse Fault and wells in southwestern Area 20, the Purse Fault permeability had to be reduced by a factor (10,000) relative to the surrounding HSUs in order to maintain the 100 m or so difference between the two areas. The sensitivity of this is tested further in Section 6.2.

It is important to note that not just the single segment of the Purse Fault in the base HFM actually designated as the Purse Fault had to be adjusted. All of fault 24, part of fault 16 where it connected fault 24 and fault 23, fault 23 north of the Moat Fault (fault 15), and where fault 36 crossed fault 24 all had to be assigned a low permeability multiplier in order to reproduce the observed data. In contrast, the SCCC HFM does not have a Purse Fault geometry that allowed connection or goes as deep (the base HFM has faults projected to the bottom of the model). Thus, as described in Section 5.7, simulated head at Well PM-3 was too low and head in southwestern Area 20 too high because the fault did not separate the two areas sufficiently. The geology along the caldera margins is quite complex, and it is possible that with further geologic review the SCCC HFM could be modified to give a better calibration, although considerable effort was expended to calibrate this HFM. However, the SCCC does incorporate juxtaposition across the caldera margins and the low permeability nodes of the Black Mountain ICU, so the explanation would have to be an amplification of what has already been done. Whether or not the Purse Fault alone is the source of the observed discontinuity is unclear, but its configuration in the base HFM does allow the observed head to be reproduced, which juxtaposition alone does not. The UGTA regional model used lower permeability from between alteration between Black Mountain and the Purse Fault to try to generate the observed

differences. Hydraulic testing of PM-3 (DOE/NV, 1996) showed relatively low permeabilities in this area, but little other information is available.

The effects of the Boxcar Fault can also be seen in Figures 5-44 and 5-45, and both the BN-MME-SDA and SCCC-MME-SDA calibrations improved as its permeability multiplier decreased. Wolfsberg et al. (2002) also noted similar model performance as the West Boxcar and southern part of the main Boxcar Fault permeability decreased. Heads to the east of the fault are higher than those to the west and require some portion of the Boxcar faults to have a lower permeability. Thus, these results are consistent with the data and previous analysis.

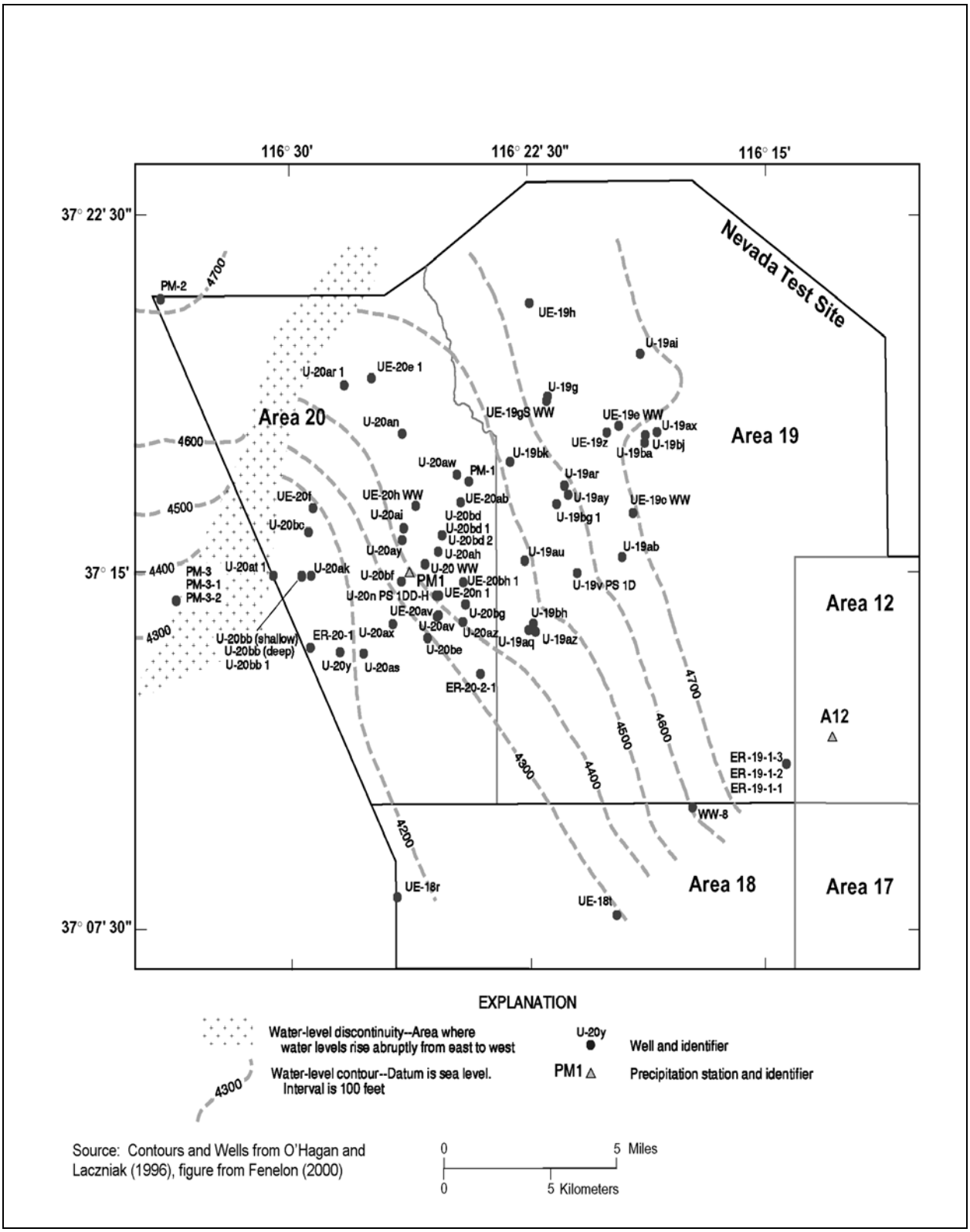

Figure 5-43
Groundwater Levels on Pahute Mesa and Vicinity

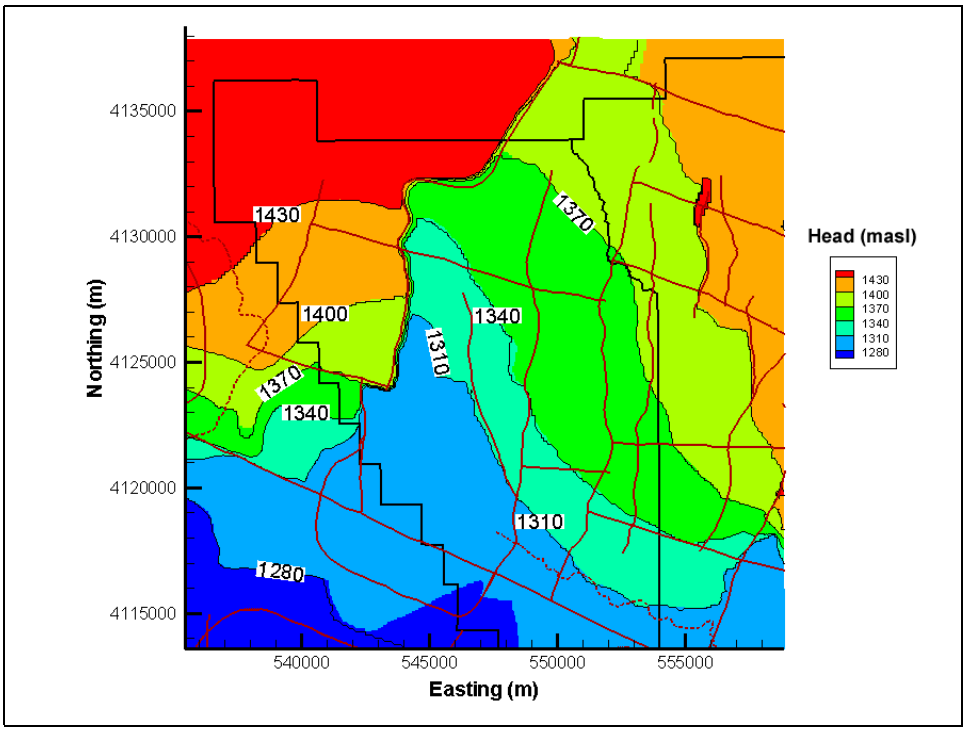

Figure 5-44
Simulated Heads Near the Purse Fault for BN-MME-SDA

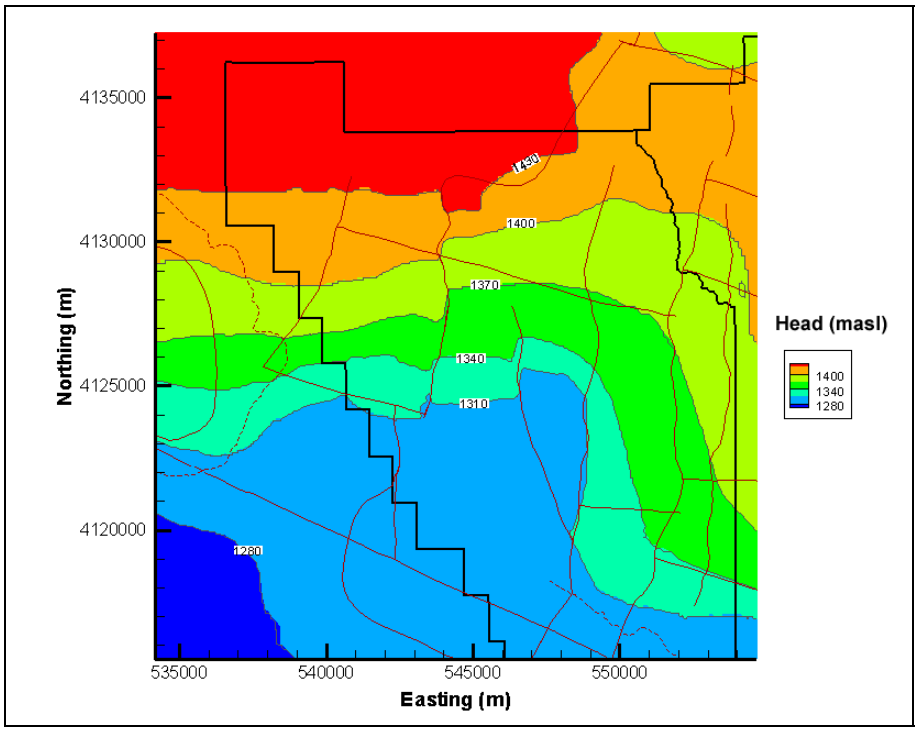

Figure 5-45
Simulated Heads Near the Purse Fault for SCCC-MME-SDA

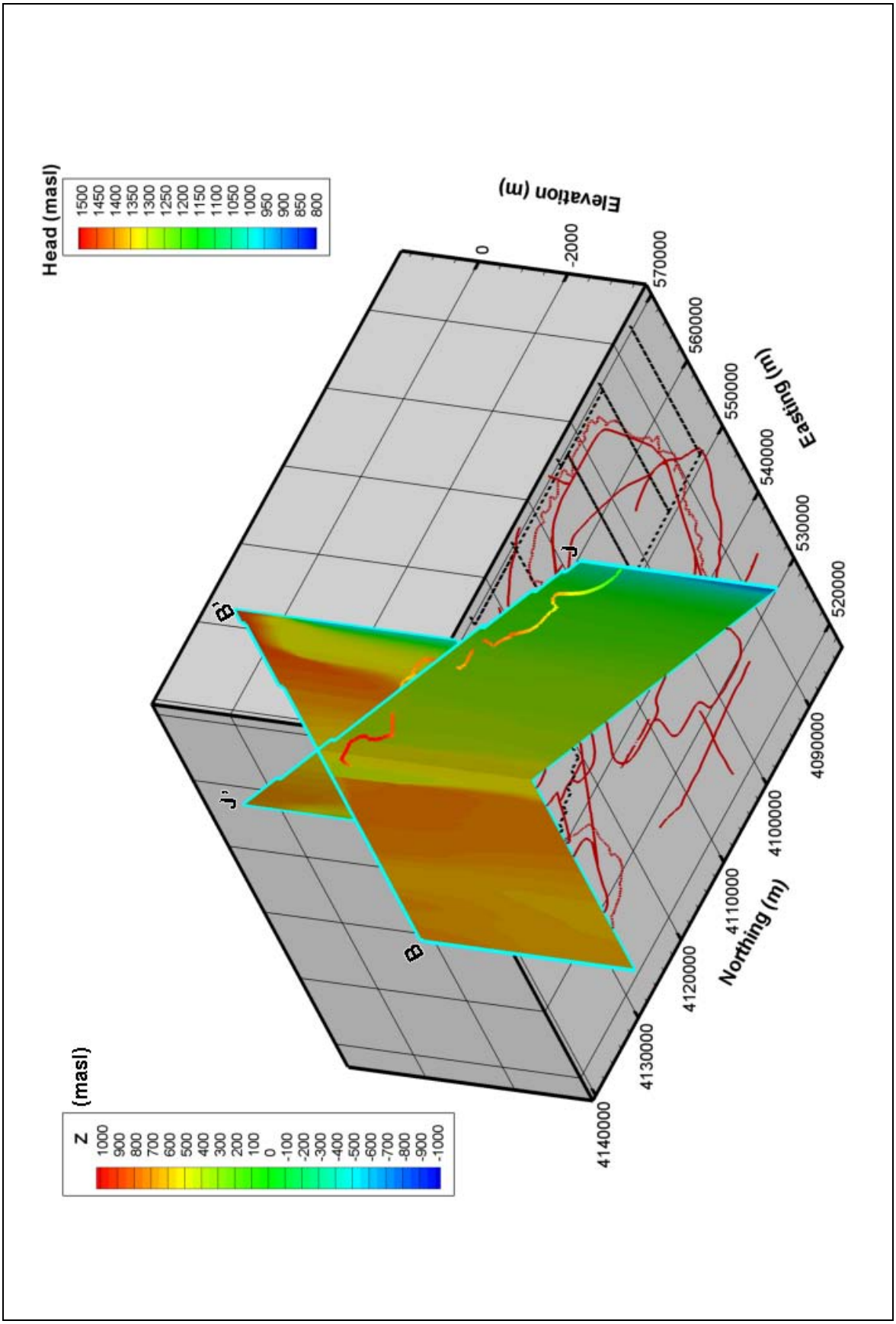

Figure 5-46
Simulated Head Along B-B' and J-J' with Simulated Flow Path for SCCC-MME-SDA

5.8.2 Head and Flow Path Comparison Along B-B' and J-J'

Figures 5-46 through 5-48 show head along geologic model cross-section planes B-B' and J-J', along the trajectory of a particle of water released in central Area 20, BN-MME-SDA, BN-MME-ADA, and SCCC-MME-SDA models. Figures 5-49 and 5-50 also show the permeability along B-B' and J-J' for the same cases. Along the eastern boundary, a lower head is specified in all cases, but its effects are quite different near the edge among the alternatives because of the variation in MGCU (Gold Meadows Stock) permeability. However, the effect dies out in similar locations in each alternative. Another striking difference along B-B' is the sharp gradient just west of where J-J' crosses B-B'. This feature is from the Purse Fault and is clear in base HFMs, but it is imperceptible in the SCCC HFM. The vertical gradient in the western part of B-B' is less for the selected HSU depth decay and anisotropy than the all HSU depth decay and anisotropy. This is a consequence of ubiquitously applying depth decay and anisotropy, which tends to continuously reduce permeability with depth and stratify flow.

Simulated head along J-J' is (Figures 5-46 through 5-48) broadly similar for all HFMs, with flow down to Oasis Valley with gentle horizontal and vertical gradients. At the southern end of the section, the head in the all HSU depth decay case is lower, reflecting the persistence of the specified head boundary condition caused by a higher LCA permeability.

Flow paths from central Area 20 for the three calibrated models have the same basic trajectory with discharge in the Oasis Valley area, but the detailed behavior of the trajectories are quite different (Figures 5-46 through 5-48). For instance, initially the particle rises in the selected HSU depth-decay case, but flows more horizontally in the all HSU depth-decay case. All the particles show a hook behind the plane of J-J' and then returning to the front of the J-J' plane from the influence of Timber Mountain. Thus, while the general model characteristics are similar in terms of calibration and boundary flows, the variability in flow paths resulting from alternative parameterization approaches and the major HFMs are noticeable, although not in disagreement with the data that show flow from Pahute Mesa to the south-southwest into Oasis Valley (SNJV, 2004a). Quantitative measures of flow-path goodness are discussed in Section 7.0.

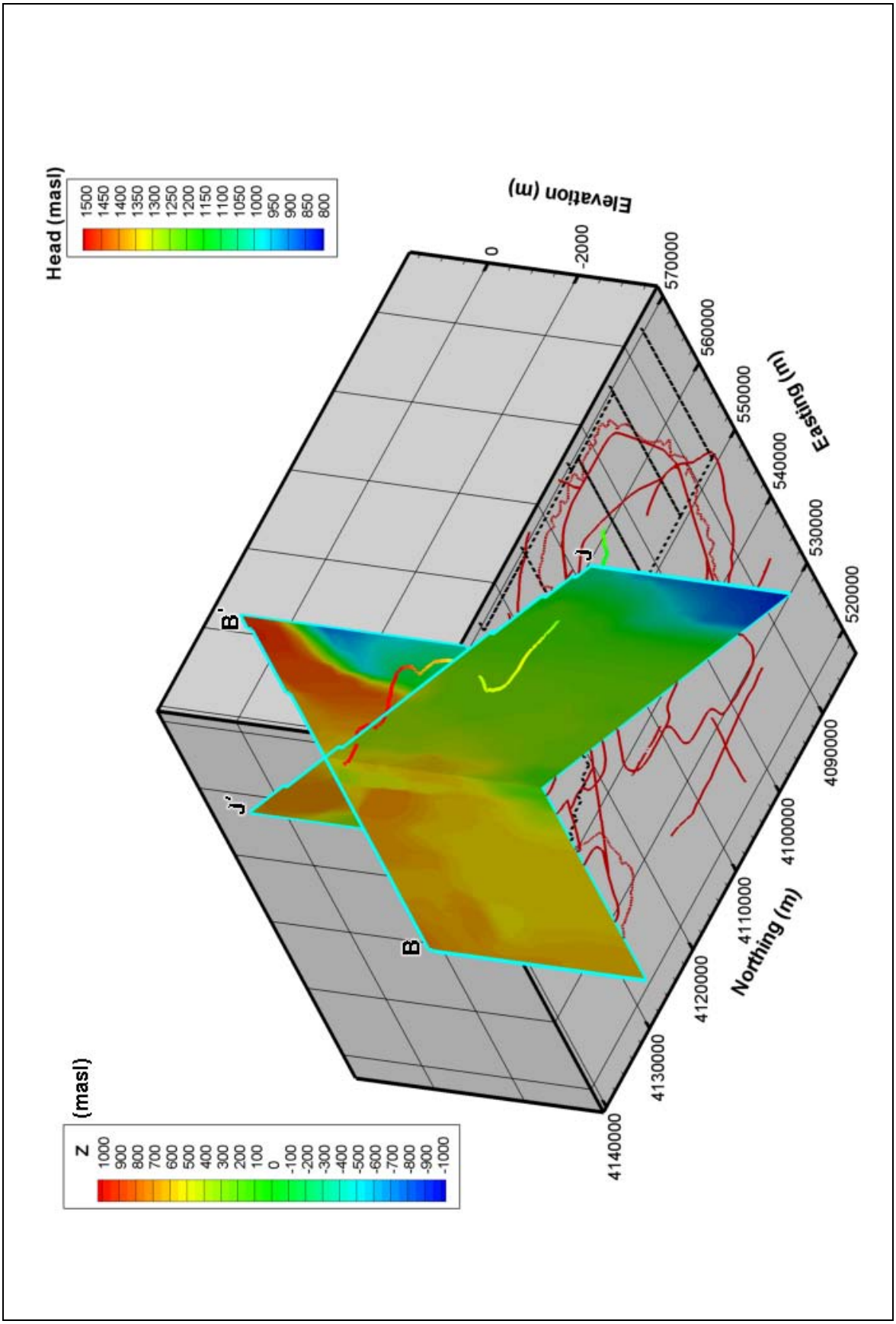

Figure 5-47
Simulated Head Along B-B' and J-J' with Simulated Flow Path for BN-MME-SDA

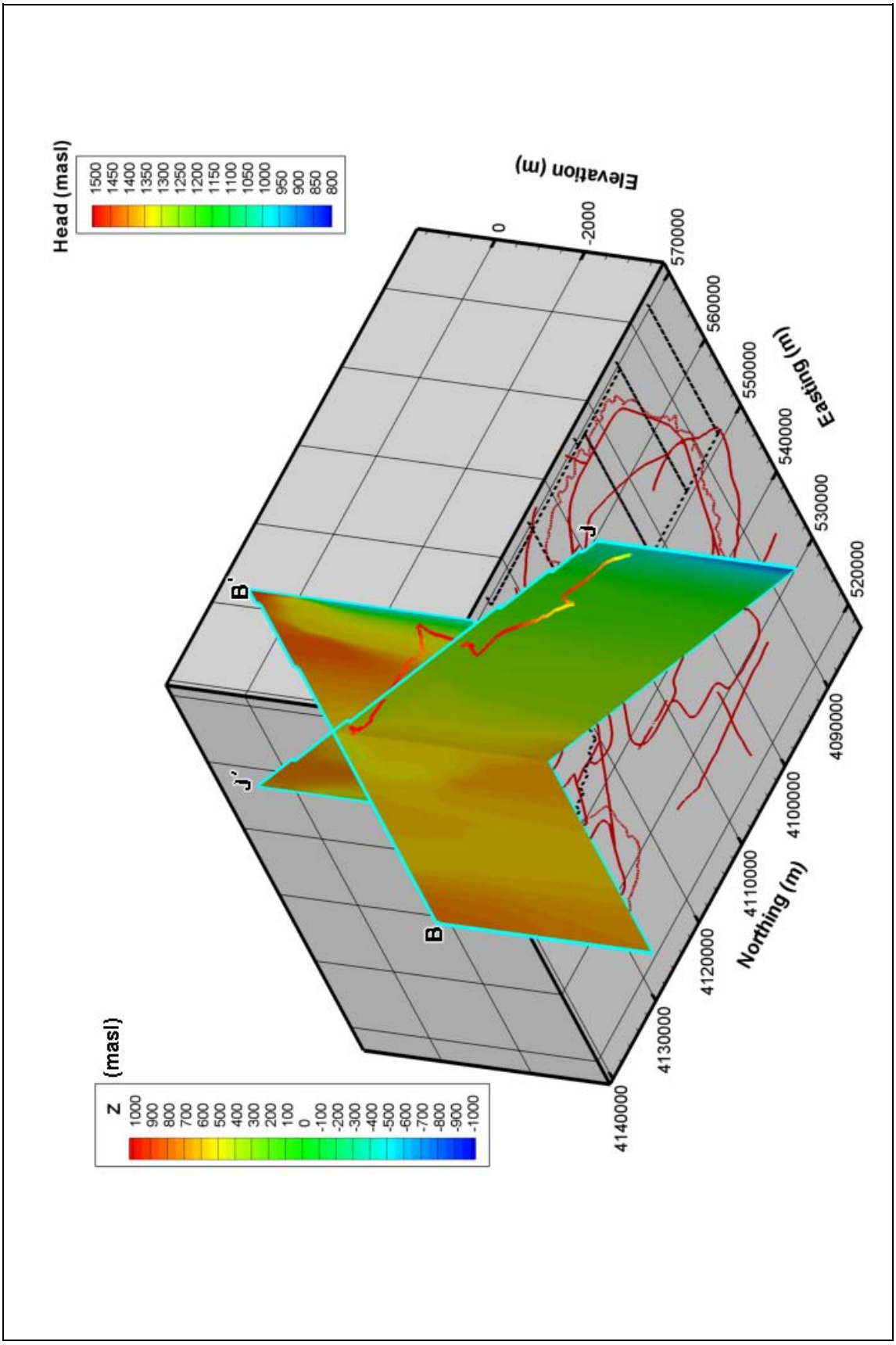

Figure 5-48
Simulated Head Along B-B' and J-J' with Simulated Flow Path for BN-MME-ADA

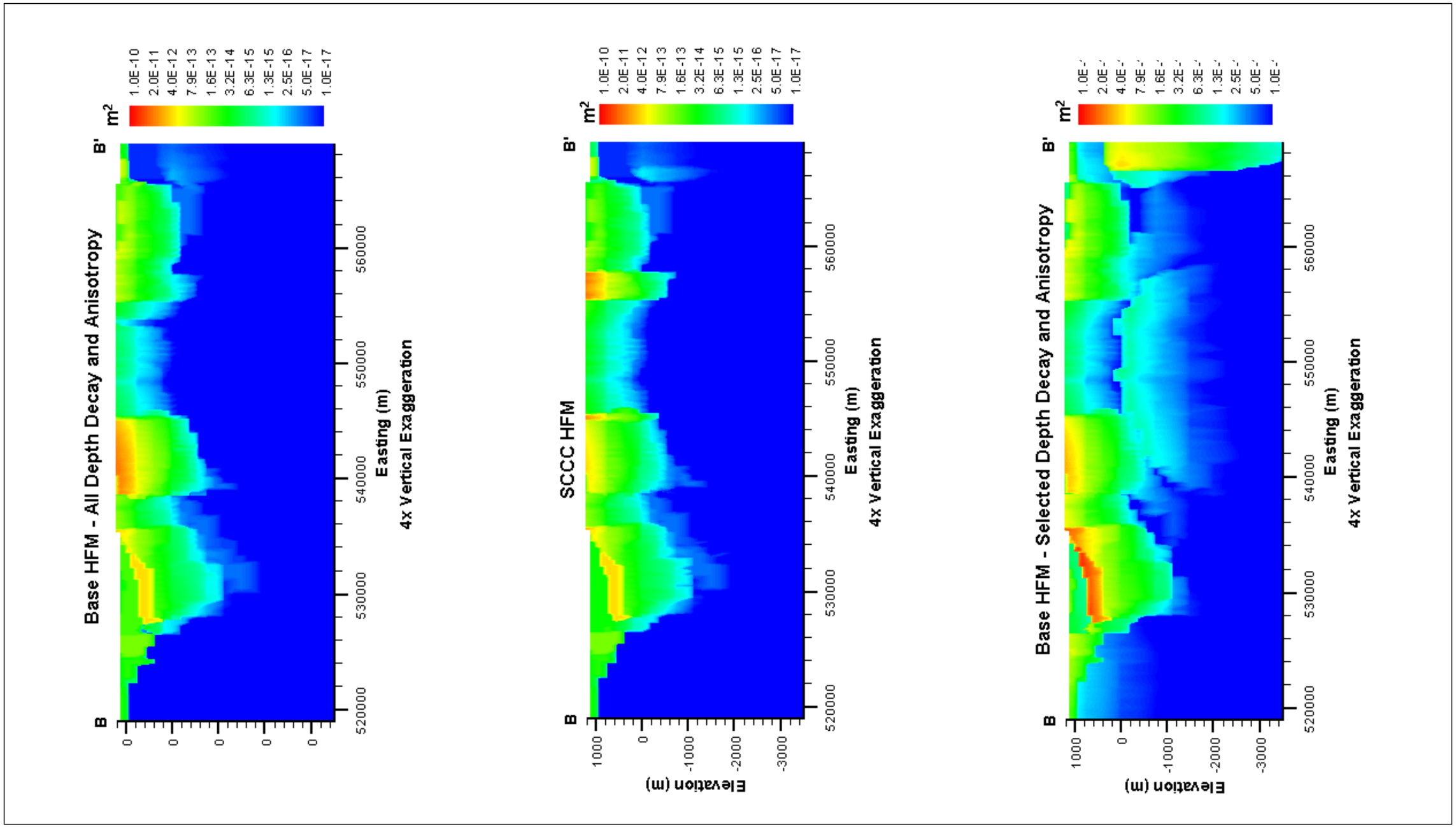

Figure 5-49
Permeability Along Section B-B'

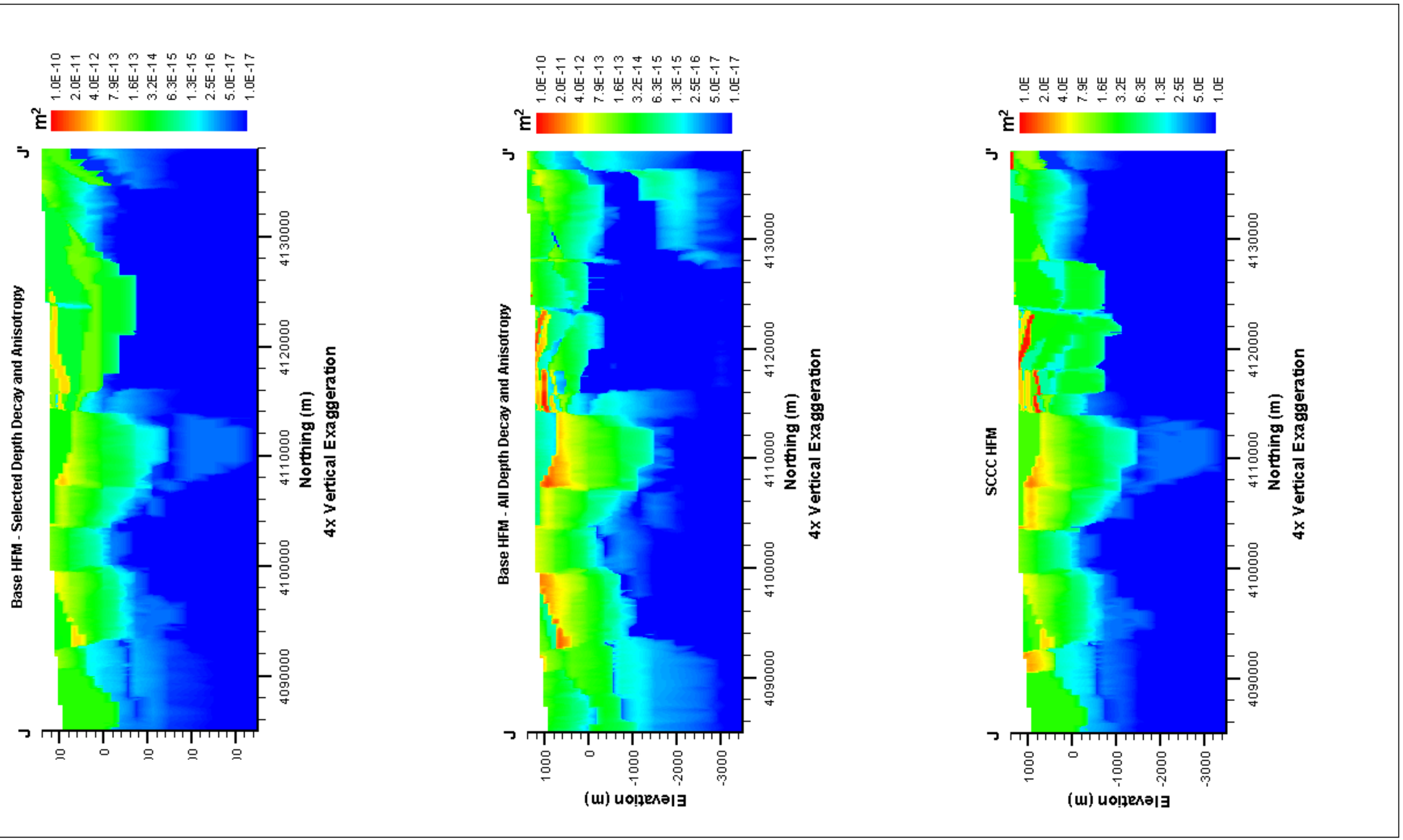

Figure 5-50
Permeability Along Section J-J'

5.8.3 Comparison of Model and Single-Well Test Permeabilities

The estimates of HSU permeability used to guide the calibration were developed from the interpretation of hydraulic tests. As a qualitative model check, permeability from the CAU-model nodes associated with each well test interval were extracted and arithmetically averaged in the case of a test zone with more than one associated node, and are shown in Figures 5-51 and 5-52 with the model-calibrated values. Also shown is the mean permeability estimated for the test HSU as given by SNJV (2004a). Wells ER-EC-1, ER-EC-4, UE-19e, UE-19h, UE-20f, and UE-20h had noisy test data, and the estimated permeability should be considered very uncertain. The model-calibrated permeabilities at the two observation wells from the BULLION FGE (IT, 1998a) (ER-20-6 #1 and ER-20-6 #2) are about an order of magnitude and a half lower than the test values and lower than the value estimated (1.13×10^{-13} m^2) from the model calibration by Wolfsberg et al. (2002) for the CHZCM. The CHZCM HSU has multiple rock types in it. Protho and Warren (2001) characterized an LFA embedded in it that is not accounted for in the model. The CHZCM, a zeolitized composite unit, would be considered to have low permeability and sparse fracturing. In the BULLION FGE (IT, 1998a) the geologic section clearly shows that the pumping test tested the embedded LFA. Thus, because this feature was not included in the CHZCM, which in the model is undifferentiated, it is not surprising that the model-calibrated value is lower. The model agreement with UE-19h has the largest scatter among the HFMs, but the test value is fairly uncertain. There is some observed scatter that appears to be related to the HFMs. For instance, at ER-EC-7, the SCCC HFM has a permeability an order of magnitude less than the base HFMs, which themselves are half an order of magnitude less than the estimated test value, but in good agreement with the estimated mean value. Similar results are also seen at Wells ER-EC-1 and ER-EC-6, and at ER-18-2 where the SCCC HFM is actually quite a bit lower than the other data. However, no general conclusions can be drawn from the permeability comparison about the goodness of the HFMs because at ER-EC-8, ER-EC-4, UE-19c, and UE-19gS, the BN-SDA and SCCC-SDA cases compare better to each other than the BN-ADA case (two different HFMs that were parameterized the same way).

It appears that some of the difference in model permeabilities is from the HFM; some is from the parameterization approach and some is also probably from the goodness of each calibration, which while similar are not identical. In general, because tested zones in fractured rock are those that typically have higher permeabilities while the model incorporates the entire thickness of rock, the

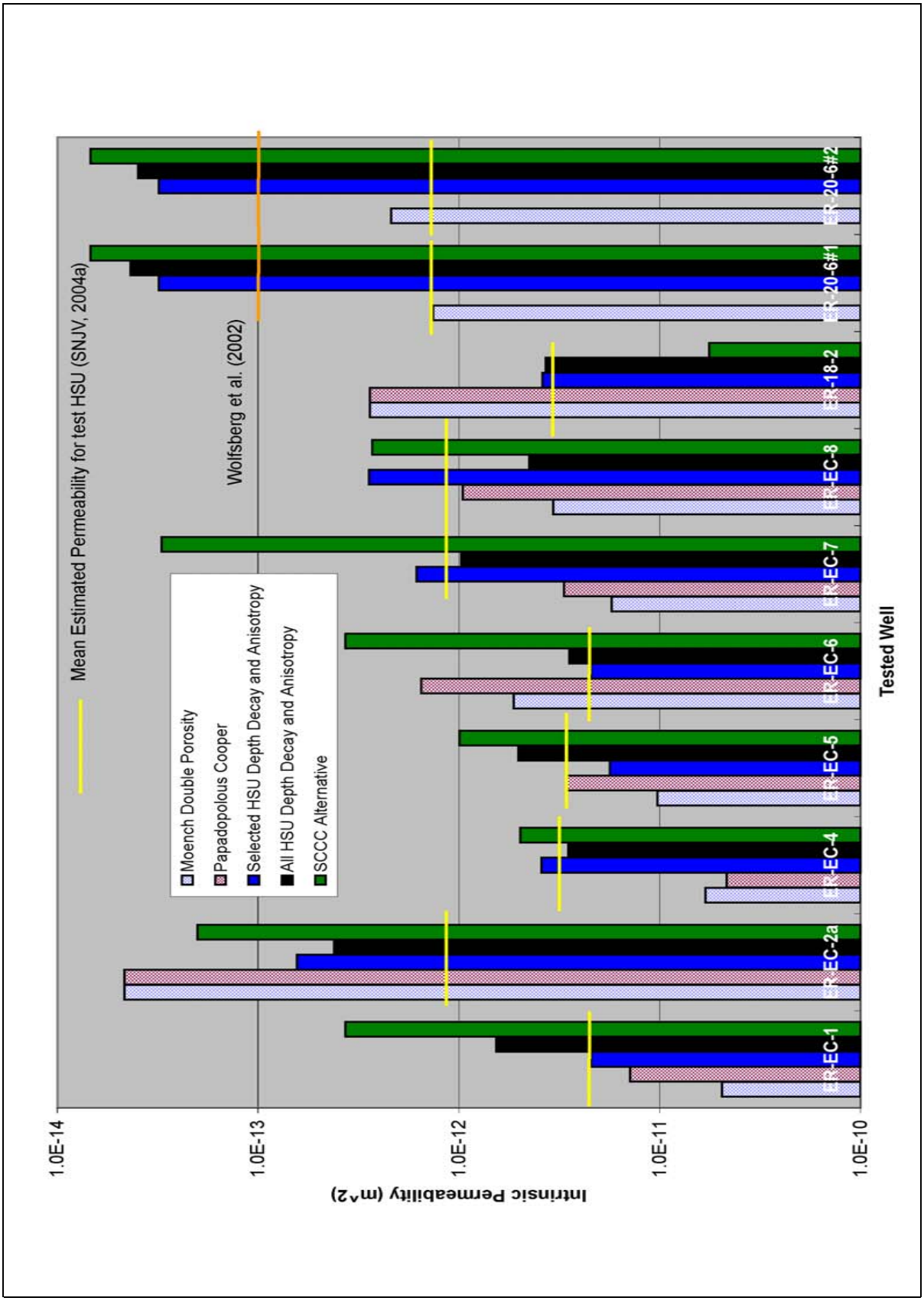

Figure 5-51
Comparison of Hydraulic Test and Model Permeability - Newer Well Data

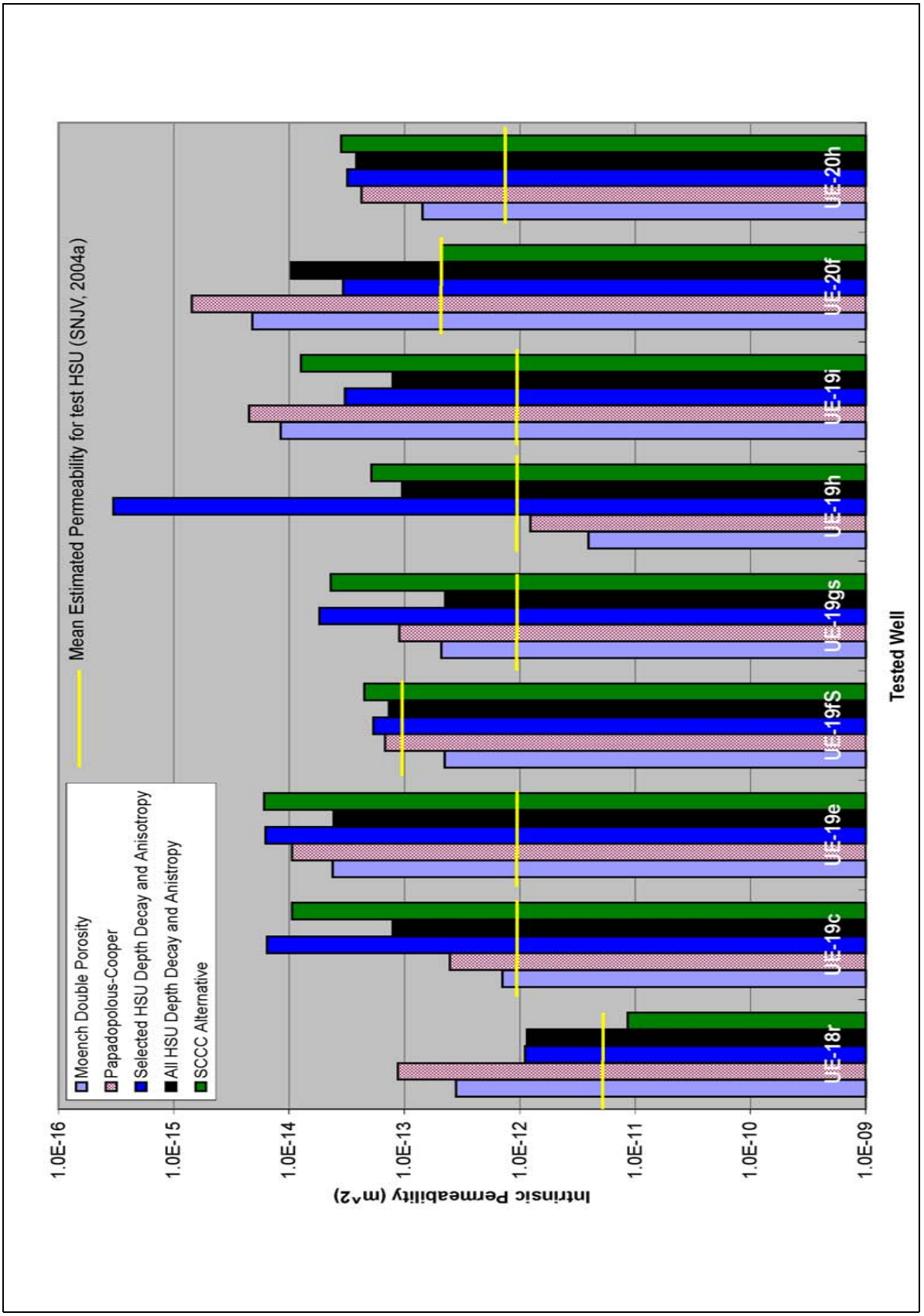

Figure 5-52
Comparison of Hydraulic Test and Model Permeability - Older Well Data

comparison could reasonably be expected to show the model biased low, which it is. In addition, it has been shown that effective properties of a porous medium, especially permeability, decrease with the scale of analysis (Neuman, 1990); the so-called "scale effect." With the exception of ER-20-6 #1 and ER-20-6 #2, all the tests were single- well, which would tend to have a relatively small sampling radius. Slug tests were not considered in this comparison because they are strongly affected by near-well mechanical disturbance (e.g., drilling) (Butler, 1997) and have an even smaller sample volume than single-well tests. Finally, the approach taken (and described in the Pahute Mesa CAIP [DOE/NV, 1999]) in parameterizing HSUs for the HFMs was to avoid specifying many small patches of different properties, but rather to use broad zones of constant parameters that were developed from characterization data. Any individual test describes only a small volume of the zone in which it lies; thus, some misfit must be tolerated because the data density does not allow anything but a broad description of HSU properties.

5.8.4 Comparison of Model and Estimated Permeabilities

As part of the modeling protocol described in Section 5.1, estimates of mean hydraulic properties and their uncertainty were made in the Pahute Mesa hydrologic data document (SNJV, 2004a) before beginning model calibration. These estimates were used as a guideline during calibration for determining whether a permeability adjustment was plausible. This section compares the model-calibrated permeabilities to estimated values for all HSUs. In the case of HSUs with depth decay, a single value has no meaning; thus, the evaluation is based on the range of permeabilities computed over the depth of the HSU versus the estimated range of uncertainty.

Figures 5-53 through 5-55 show the TMCM, TMA, PBRCM, YMCFCM, PCM, and LCA permeability ranges from depth decay versus the mean and estimated uncertainty at 95 percent (approximately two standard deviations) for the BN-MME-SDA, BN-MME-ADA, and SCCC-MME-SDA calibrated models. Reference permeability is shown at the top of each depth range; it does not exactly lie at the top (and is not expected to, because it would require all units at land surface), but at the scale used the slight offsets cannot be seen. For the TMCM, the model range spans the estimated uncertainty and more because no floor was used to limit depth decay; at greater depths, the TMCM permeability is unknown, but because permeability is related to fracture intensity (which tends to diminish with increasing overburden pressure), continued decline seems reasonable.

Recall that the ICUs underlay the calderas, and this rock is expected to be essentially impermeable. The TMA, which does not extend to as great a depth as TMCM, shows a lower limit on permeability due to the limit of its depth. The magnitude of the range is comparable to the range of uncertainty, with a shift to extend slightly outside the lower uncertainty limit for the BN-MME-SDA case. The PBRCM, which exists over most of the model at a wide variety of depths, has a permeability range that spans the uncertainty and goes to even lower values at great depths. Like the TMCM, the PBRCM is not well characterized over its full depth, and no floor on permeability was applied. The YMCFCM, which is not characterized at all, has similar ranges of uncertainty, although biased to the low side. The PCM, which occurs over a limited depth, shows a range of variability similar to the range of uncertainty.

Figures 5-56 through 5-58 mainly show the comparison of model and estimated permeabilities for the non-depth decayed HSUs, although for the case of the BN-MME-ADA, reference permeability was reported. The reference permeability cannot be directly compared to the permeability, but because of depth decay, the reference permeability should be higher than the mean permeability, and this qualitative assessment can be made from these figures. In Figure 5-56, KA, CHVTA, CHVCM, CFCU, and BFCU model-calibrated values are very similar to the estimated mean. The IA is about an order of magnitude lower than expected. In contrast, CHZCM, CFCM, and CHCU are toward the lower end of uncertainty (close to two orders of magnitude lower than the mean). Composite units are a mixture of HGUs, and because homogeneous parameters were used for these HSUs, it may be the heterogeneity of the HSU causing this variance. In Figure 5-57, THLFA, THCM, LPCU, TCA, PLFA, and FCCU all are close (less than half an order of magnitude variation) to the expected mean. The BA is close to the mean for BN-MME-SDA but an order of magnitude lower for SCCC-MME-SDA because it also includes the UPCU. The TSA has the greatest fluctuation among HFMs. The UPCU for BN-MME-SDA is about two orders of magnitude lower than the mean. In Figure 5-58, FCA, YVCM, DVCM, LCCU1, and PVTA are close (within a half an order of magnitude), while FCCM and DVA are about an order of magnitude lower than expected. The AA and UCCU are lower than even the lower limit by 2 and 1.5 orders of magnitude, respectively. The estimated mean permeability for the UCCU of 3.7×10^{-13} m^2 seems somewhat high, and is based on two data points (see Figure 5-22 in SNJV, 2004a). The two constant-rate tests used to estimate the mean UCCU permeability show a pronounced reduction in permeability with depth, which while not

particularly convincing with two data points do establish that considerable uncertainty exists in UCCC permeability.

The preceding comparisons suggest that the flow model has been reasonably parameterized with respect to the expected values of HSU permeability.

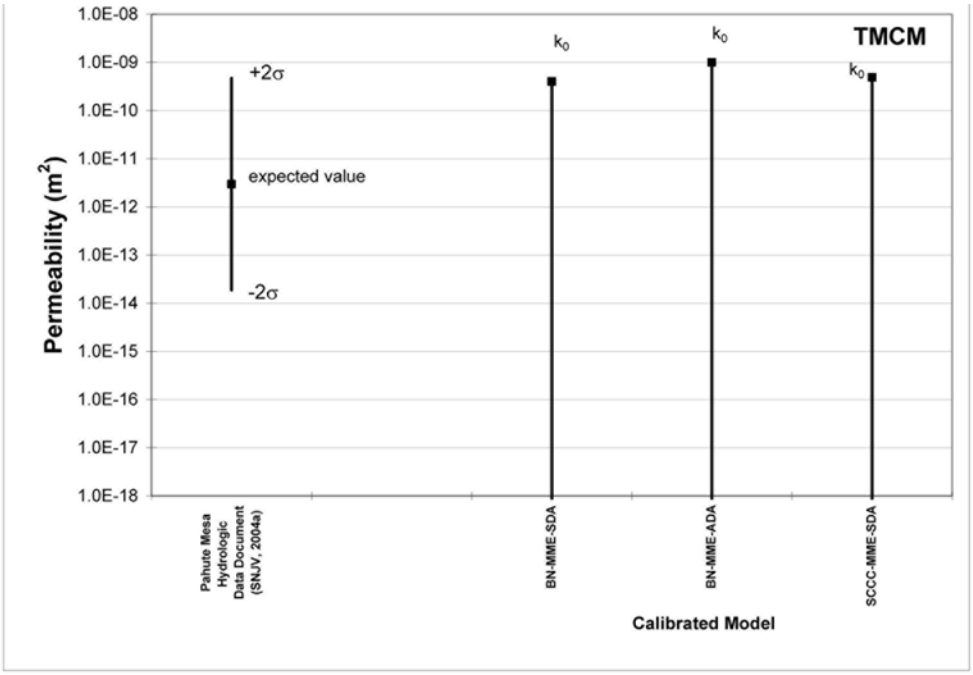

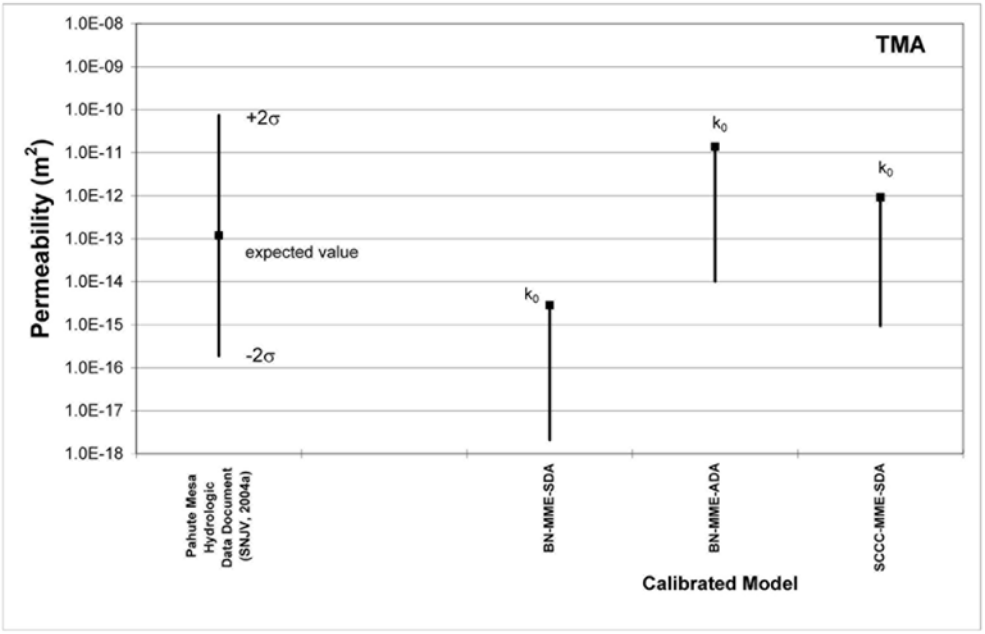

Figure 5-53
Comparison of Model and Permeabilities for TMCM and TMA

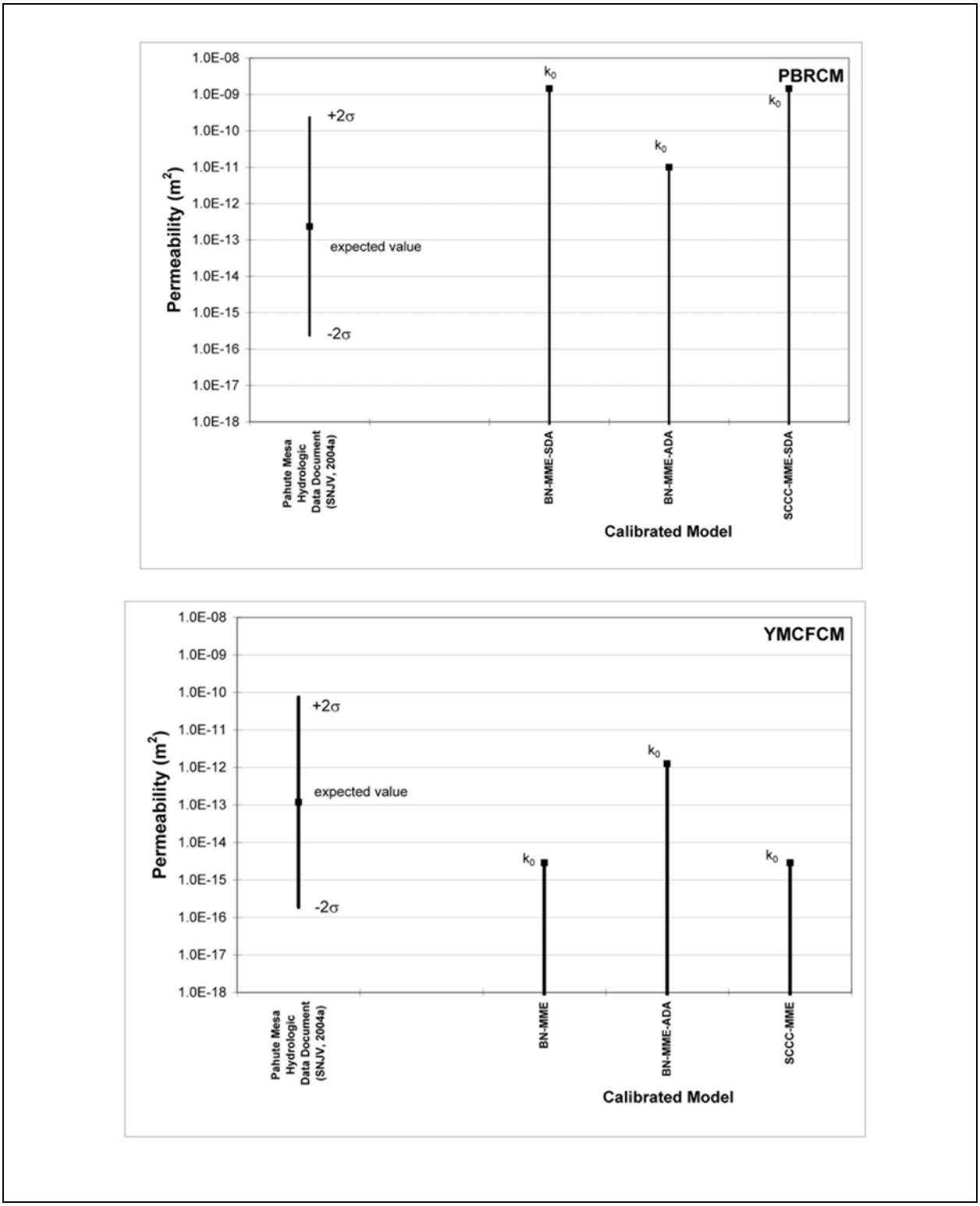

Figure 5-54
Comparison of Model and Estimated Permeabilities for PBRCM and YMCFCM

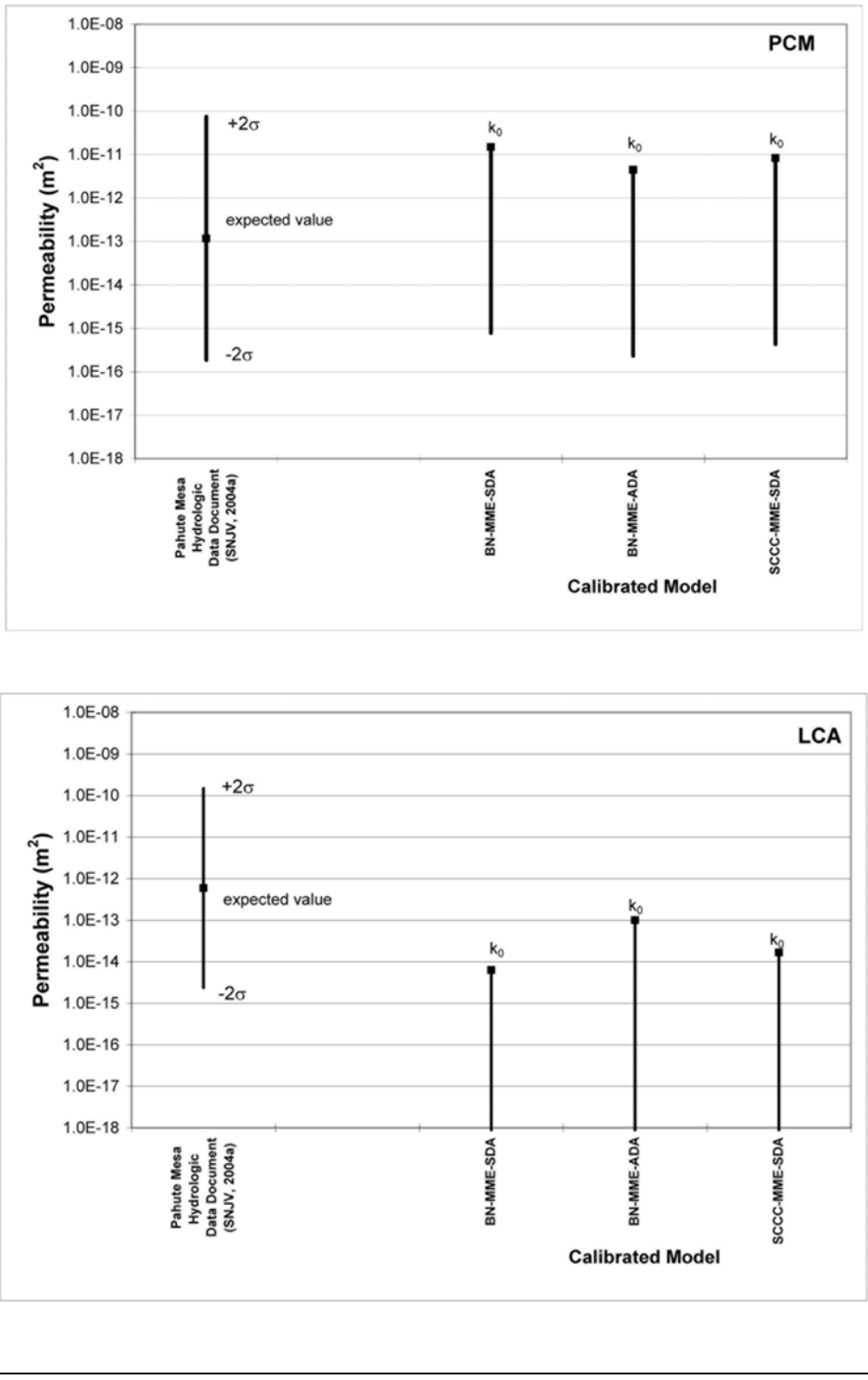

Figure 5-55
Comparison of Model and Estimated Permeabilities for PCM and LCA

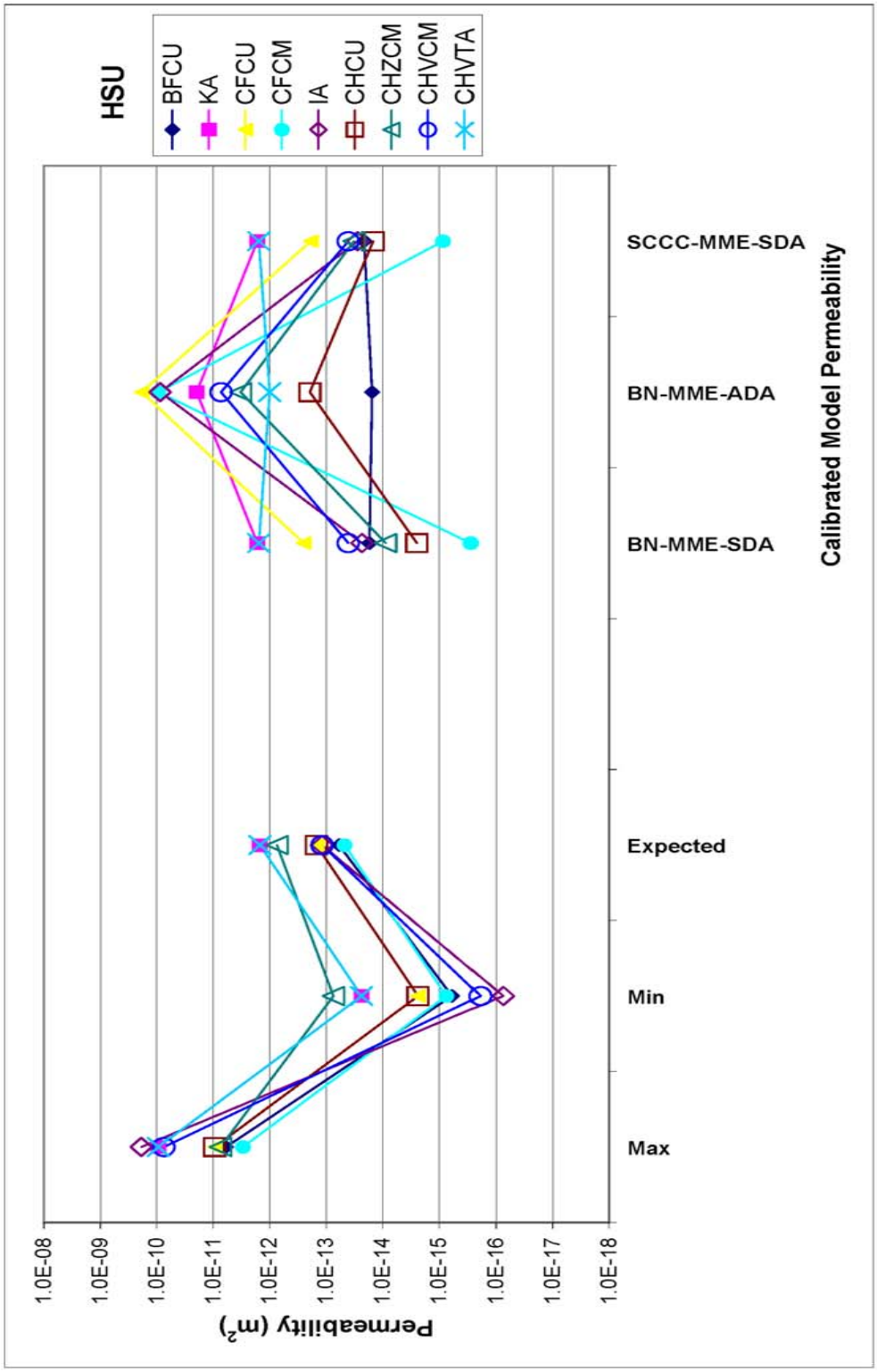

Figure 5-56
Comparison of Model and Estimated Permeabilities for BFCU, KA, CFCU, CFCM, IA, CHCU, CHZCM, CHVCM, and CHVTA

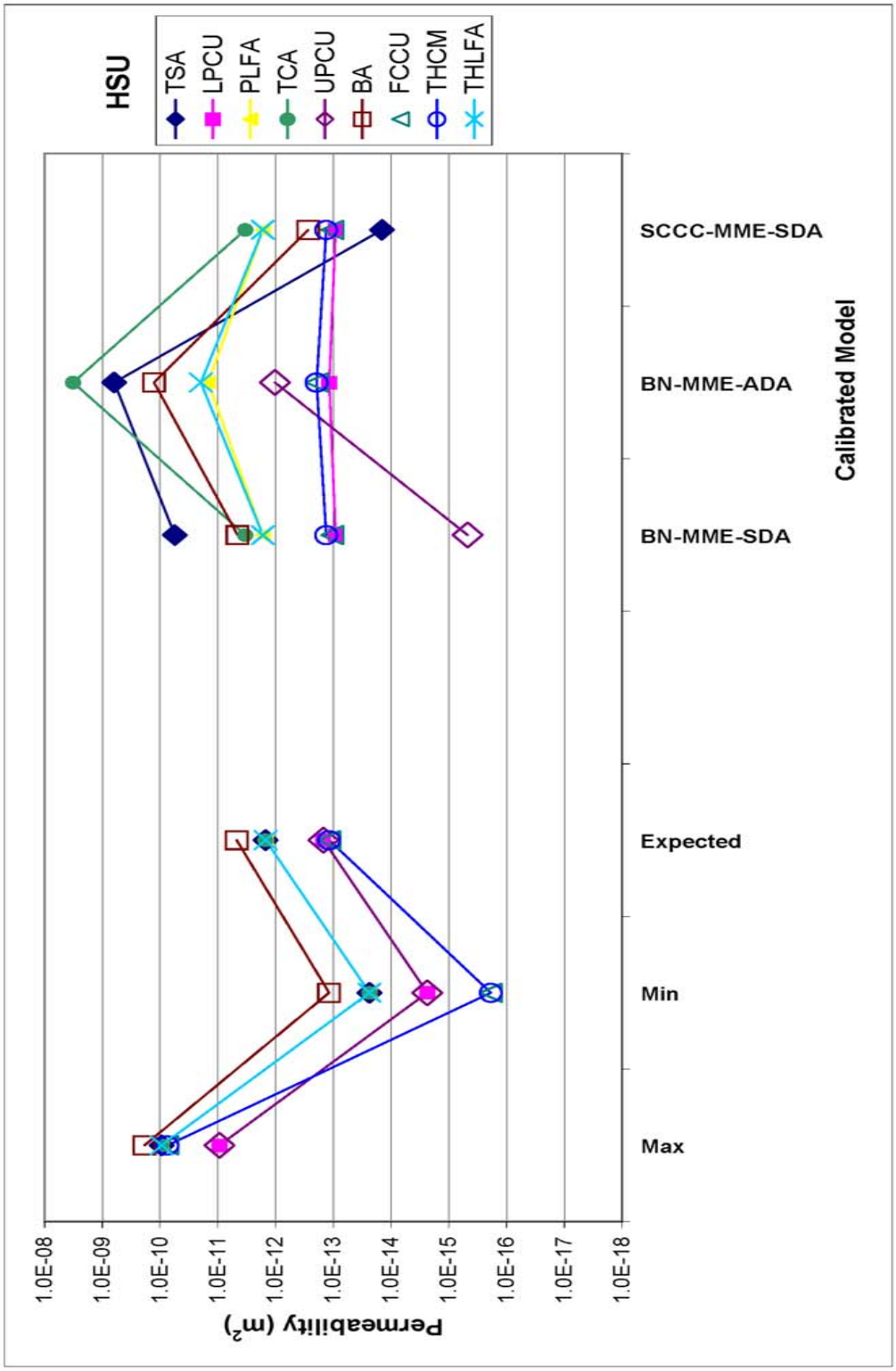

Figure 5-57
Comparison of Model and Estimated Permeabilities for TSA, LPCU, PLFA, TCA, UPCU, BA, FCCU, THCM, and THLFA

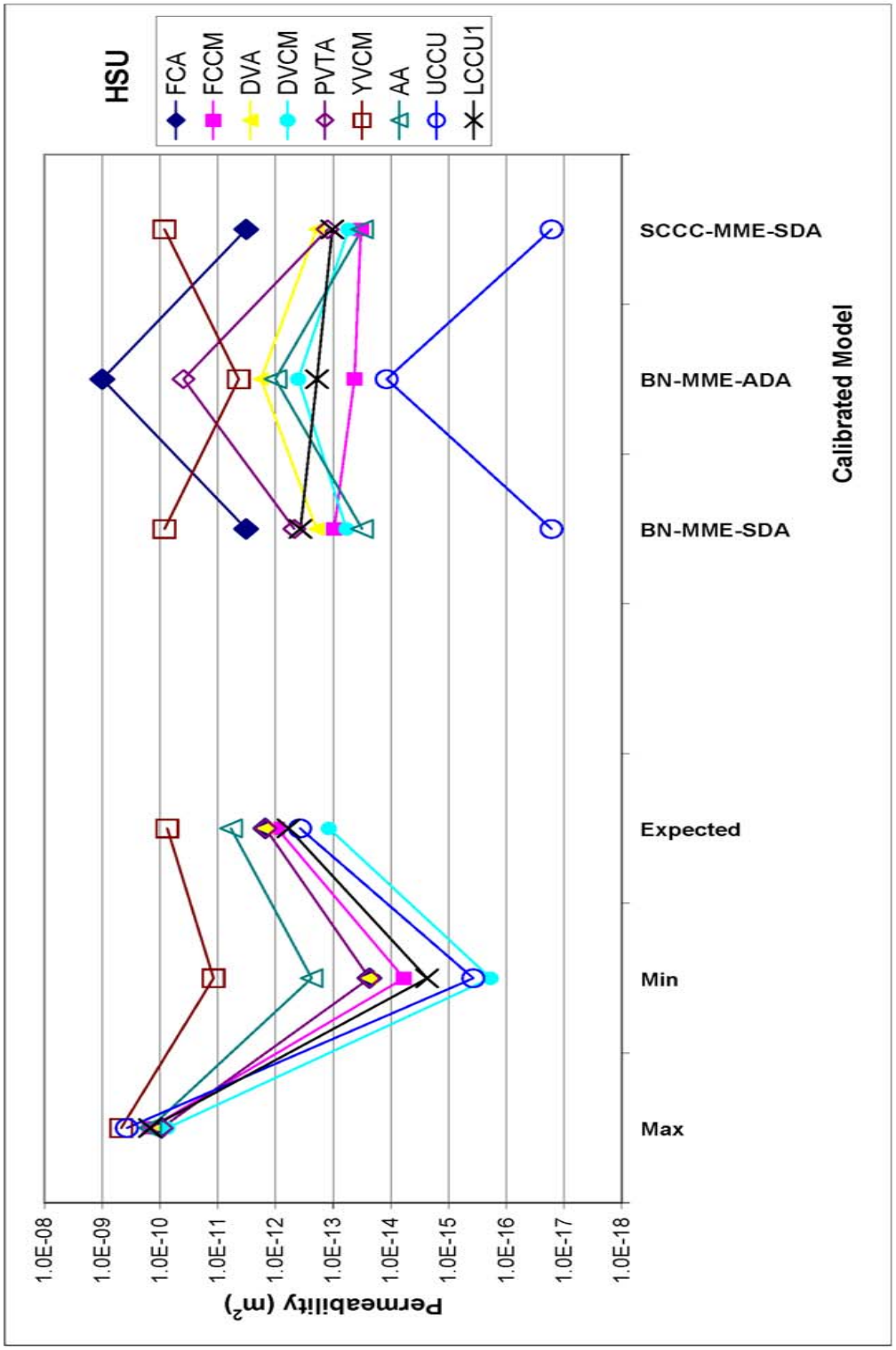

Figure 5-58
Comparison of Model and Estimated Permeabilities for FCA, FCCM, DVA, DVCM, PVTA, YVCM, AA, UCCU, and LCCU1

5.8.5 Water-Balance Summary

The water balance of the models is shown in Table 5-21. There is about a 0.4 percent discrepancy between the inflow and outflow relative to the inflow (e.g. -3/[-393+-75+-225]) for the first case in Table 5-1). This difference is from deactivating recharge along the low permeability faults at the top of the model to prevent the ridge-like features noted in Wolfsberg et al. (2002). Flow along the north, south, and eastern boundaries fluctuated more than that along the west because, as discussed previously, most of the western boundary was changed to no-flow based on the interpretation that it lays on a streamline.

Table 5-21
Water-Balance Components (kg/s)

Case	North[a]	South[b]	East	West	Oasis Valley	Recharge	Sum (kg/s)
Base HFM - Selected HSU depth decay and anisotropy	-225	395	86	-75	209	-393	-3
Base HFM - All HSU depth decay and anisotropy	-216	390	42	-73	246	-393	-3
SCCC HFM - Selected HSU depth decay and anisotropy	-174	334	104	-64	192	-393	-1

[a] (-) = is into model
[b] (+) = is out of model

An additional check on the CAU water balance is the comparison of flow along the northern edge of the Yucca Mountain saturated zone model, which lies entirely within the Pahute Mesa CAU flow model. The YMP saturated zone model (DOE/ORD, 2004) gives a value of 196 kg/s inflow. The calibrated models give values of 250, 300, and 218 kg/s for the BN-MME-SDA, BN-MME-ADA, and SCCC-MME-SDA cases, respectively. The DVRFM (Faunt et al., 2004) boundary flows were also estimated (see Table 5-5) for the Pahute Mesa CAU flow model boundaries and were found to be in reasonable agreement with estimates developed from the UGTA regional model (DOE/NV, 1997). Thus, the Pahute Mesa CAU model is in reasonable agreement with other independent water-balance analyses in the area.

5.8.6 Evaluation of Low-Weight Head Data

It is suspected that some of the wells in the calibration dataset for Pahute Mesa may be perched, or otherwise of questionable representativeness (Fenelon, 2000; SNJV, 2004a; DOE/ORD, 2004). As described in Section 5.2, weights were assigned to calibration data that generally reflected data accuracy using an approach suggested by Hill (1998). Because successful calibration hinges on the use of representative data, questionable data were assigned low (less than 0.01) weights as shown in Table 5-2. However, it is also important to check the consistency of model results with the suspect data. Figure 5-59 compares the estimated data and simulated results for all the head data (wells and springs) assigned low weights for the BN-MME-SDA, BN-MME-ADA, and SCCC-MME-SDA models. In general, the model and data trend from low to high properly.

The models agree quite well with the suspect values in Oasis Valley, probably because the overall constraint of wells, springs, and discharge has a very strong influence on all the results in the area. Gexa 4, whose companion Gexa 3 is perched, is located in an area of high hydraulic gradient from an unknown source and is also reasonably captured. The UE-29a #1 and UE-29a #2 HTHs were also quite consistent with the calibrated results, probably because Well USW UZ-N91 is located nearby and was reasonably matched. Well ER-19-1 deep was simulated 50 to 125 m too high, but was better represented by the all HSU depth-decay and anisotropy case because it has higher permeability for the Gold Meadows Stock, which allows the high head boundary to propagate further into the model. Well ER-19-1 shallow is thought to be perched (Fenelon, 2000), and is undersimulated by the model (which is a consistent representation). However, data in that area are sparse, and this cannot be proven conclusively. The TW-1 (492 m) may also be perched, and the model correctly represents such a condition, as it also does for UE-12n #15A. Hagestad 1 may also be perched and is outside the model boundary (it was projected to the nearest edge node for this comparison). There is a larger spread in and around the line of best fit in Figure 5-59 relative to the other calibration results, although some of this effect may simply be because the data in Figure 5-59 did not strongly participate in the calibration, although they were considered qualitatively. The qualitative behavior of high head in the east-central part of the model (near Rainier Mesa and Gold Meadows) is properly captured, and the fact that the water balance on the eastern boundary was reasonably matched (see Sections 5.3 and 5.4) suggests the model representation is acceptable in this area.

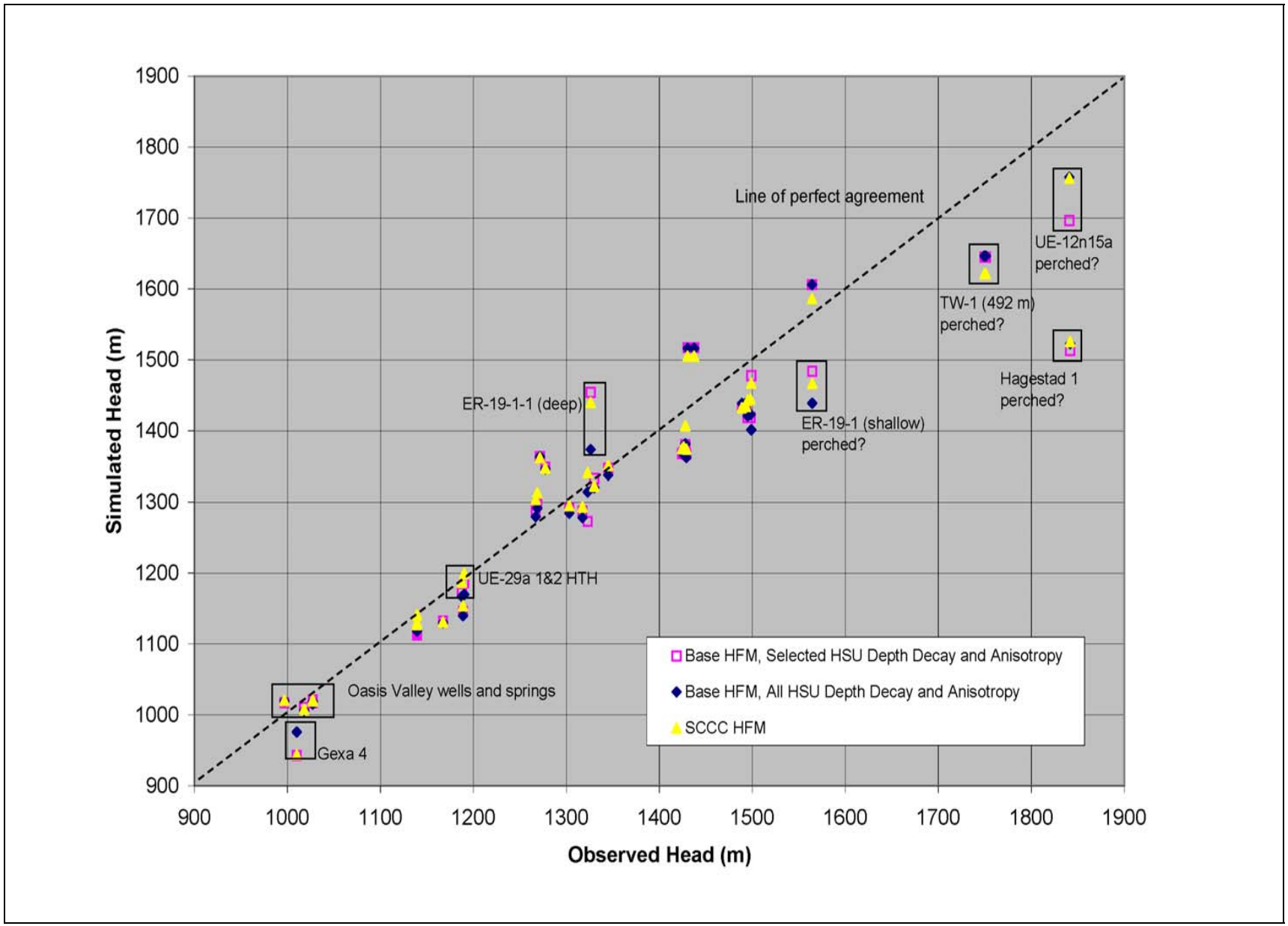

Figure 5-59
Observed Versus Simulated Low-Weight Head Data

5.8.7 Data Components of Calibration

Four categories of data, representing two types (head and flow), were used to calibrate the Pahute Mesa CAU flow model: observation well head, spring head, Oasis Valley ET discharge, and net model boundary flow. Weights, as discussed in Section 5.2, were developed from data accuracy and other qualitative considerations. Tables 5-7, 5-10, 5-14, and 5-18 show the contribution of each data type to the model goodness of fit. In all cases, observation well heads comprised the bulk (between about 50 to 60 percent) of the objective function, followed by Oasis Valley discharge (about 25 percent), estimated regional boundary flow (about 15 percent), and spring head (5 to 10 percent). Clearly, observation well data must be given strong consideration in model calibration because they define the direction and magnitude of the hydraulic gradient, which is directly related to the velocity field that will be used to simulate radionuclide transport. Oasis Valley discharge is the only internal flow constraint for the model, and as such is a major control on the effective permeability. Oasis Valley is also the nearest access point for radionuclides that might leave Pahute Mesa, and matching its discharge ensures that the potential for such migration is properly captured in the flow model. In addition, matching the spring data also helps ensure that the heads in Oasis Valley are reasonably matched, and that the combination of head and flow that results is plausible. All the calibrated models showed similar patterns of error in fitting Oasis Valley flow, and it may be possible to improve the discharge by more explicitly accounting for the rooting depths of the different plant communities in the discharge area. Finally, the regional model water balance is considered via the boundary flow targets, which clearly play some role in calibration.

There is no general rule as to what the share of the model objective function different data types should have, but it should be considered that the simulated Oasis Valley discharge is generally within one standard deviation of the mean value, which suggests that its weight was assigned appropriately. Faunt et al. (2004) presents a similar analysis for the DVRFM, and shows for that regional model the contribution from steady-state heads is 95 percent of the objective function, with the balance coming from flow targets. If well and spring head are considered together, head comprises about 70 percent of the objective function, a value comparable to that shown by Faunt et al. (2004).

5.8.8 Hydrostratigraphic Framework Model Assessment

Two HFMs, the base and SCCC alternative, were considered during model calibration. As noted in Section 5.8.1 the SCCC does not perform as well in matching observed heads along the Purse Fault, and, in general, does not calibrate as well as the base HFM as can be seen from comparing Tables 5-9 and 5-17.

The least weighted fitting squares (as embodied in PEST) is a special case of maximum likelihood estimation arising from the assumption that the errors are normally distributed (see Appendix A of Hill, 1998). The parameter set or model that reduces the value of the objective function is considered superior to those that give higher values because it improves the model fit according to the criterion embedded in the objective function itself. Thus, from purely the standpoint of flow model calibration goodness, the SCCC HFM is not as likely as the base BN HFM.

5.8.9 Model Limitations

The Pahute Mesa CAU flow model covers a plan area of approximately 2,000 km^2 and has a saturated thickness of nearly 5 km, for a total volume of about 10,000 km^3. A total of 191 calibration targets of head and flow were used in calibration. The overall density of the data versus the size of the model suggests that the calibration data are somewhat sparse. Not all of the uncertainty is likely to be important; for instance, it is almost certain that flow in the ICUs is very slow, if not nil, which has no effect on the shallower part of the flow system. However, many types of analysis such as head mapping and geochemistry tend to give a similar broad picture of flow from Pahute Mesa southwest to Oasis Valley, and while there may be further refinements in understanding if more data are collected the key point of migration to Oasis Valley is unlikely to change.

The CAU flow model was calibrated to estimated steady-state condition, and is not currently set up for transient flow analysis. The flow model also assumes regional steady state in the CAU area, and any future change in hydrologic conditions could affect this assumption.

6.0 FLOW MODEL SENSITIVITY AND UNCERTAINTY ANALYSIS

The Pahute Mesa CAIP (DOE/NV, 1999) requires and general modeling protocol (ASTM *Standard Guide for Conducting a Sensitivity Analysis for a Ground-Water Flow Model Application* [ASTM, 1994c]) recommends analysis of parameter sensitivity and conceptual model uncertainty. This section presents these analyses.

The Pahute Mesa CAU flow model has a large number of parameters that can be changed in order to calibrate the model to observations of hydraulic heads, spring heads, lateral boundary flows, and ET flows. Not all of these parameters have the same influence on the performance of the model. Therefore, it is necessary to identify those parameters to which the model outputs are most sensitive, and how they relate to the conceptual model. The results of sensitivity analyses are presented for three models described in Sections 5.6 and 5.7. These models are:

- Base HFM - selected HSU depth decay and anisotropy with MME recharge (BN-MME-SDA)
- Base HFM - all HSU depth decay and anisotropy with MME recharge (BN-MME-ADA)
- SCCC HFM - selected HSU depth decay and anisotropy with MME recharge (SCCC-MME-SDA)

While sensitivity analyses are formally presented in Section 6.2, such analyses were also carried out as an integral part of the calibration process.

In addition, alternative HFMs, recharge models, and boundary flows have been considered in the CAU flow model. Sections 6.3 through 6.5 describe the approach and results of the uncertainty analysis associated with these model alternatives.

6.1 Approach

6.1.1 Parameter Sensitivity Analysis

Both local and global sensitivity analysis techniques are used to identify and evaluate key parameters in the Pahute Mesa CAU groundwater model. The local sensitivity analysis techniques include PEST sensitivity analysis and perturbation analysis. The global sensitivity analysis techniques include classification tree analysis and entropy analysis.

6.1.1.1 Local Sensitivity Analysis

Two approaches to local parameter sensitivity analysis were implemented for the Pahute Mesa flow model. In the first approach, parameter sensitivity and correlations were evaluated using PEST (Watermark, 2004). The PEST code calculates a sensitivity coefficient for each parameter with respect to all weighted observations. This analysis is termed "local" because only slight changes are made that investigate parameter values near the base value. The second approach involves perturbing each of the parameters, one at a time, from a reference value and computing the corresponding change in the model output (Anderson and Woessner, 1990).

PEST Sensitivity Analysis

Sensitivity coefficients, computed as the change in output divided by the change in input, reflect the slope of the input-output relationship at a reference point. These sensitivities can be obtained quantitatively from the outputs of PEST (Watermark, 2004), a non-linear parameter estimation code. In the process of optimizing a nonlinear model, PEST calculates the Jacobian matrix. The Jacobian matrix relates the model-calculated observations to the model input parameters where any element of the Jacobian matrix, J_{ij}, describes the derivative of the *i*'th observation with respect to the *j*'th parameter. Based on the Jacobian matrix, PEST calculates the composite sensitivity of each parameter with respect to all weighted observations. The composite sensitivity of parameter *i* (s_i) is defined as:

$$s_i = \frac{\sqrt{(J^t Q J)_{ii}}}{m} \quad (6\text{-}1)$$

where J is the Jacobian matrix; J^t is the transpose of J; Q is the "cofactor matrix," an m-dimensional, square, diagonal matrix comprised of the squared observation weights; and m is the number of observations of non-zero weight (Watermark, 2004). In other words, the sensitivity coefficient for a given parameter is the weighted average of the derivatives of all the observations with respect to that parameter.

These composite sensitivity coefficients reflect the weighted slope of the input-output relationship at a reference point. In the case of the sensitivity analysis presented here, the reference point refers to the parameter values at calibration and the derivative is approximated by a forward finite-difference method with a 3 percent parameter increment. These sensitivity coefficients are therefore indicative of the parameter sensitivity in the vicinity of the calibration point and apply only to the parameter range over which the input-output relationship is linear.

The Jacobian matrix is also manipulated to derive the covariance matrix, which in turn can be used to estimate parameter correlations and confidence limits. The correlations and confidence limits are, themselves, subject to the same linearity assumption as sensitivity coefficients but still provide a useful semi-quantitative tool for understanding how model parameters interact and how the data support the model (Poeter and Hill, 1997).

To provide some estimate of the sensitivity of observations to all the adjustable parameters, PEST also calculates composite observation sensitivity. The composite observation sensitivity of observation j (s_i) is defined as:

$$s_j = \frac{\sqrt{Q(JJ^t)_{jj}}}{n} \tag{6-2}$$

where J and Q are the Jacobian and cofactor matrices, respectively, and n is the number of adjustable parameters (Watermark, 2004). While the observation sensitivities do not generally provide as much useful information in guiding model calibration as the parameter sensitivities, they may provide some insight into which observations are sensitive to many parameters.

To describe the degree to which parameters are correlated to one another, PEST computes the correlation coefficient matrix. The correlation coefficient matrix is a symmetric, n-dimensional,

square matrix, ρ_{ij}, where *n* is the number of adjustable parameters. Each element of the matrix ρ_{ij} represents the correlation between parameter *i* and parameter *j*. The diagonal elements of the correlation coefficient matrix are always equal to 1 because a parameter is perfectly correlated with itself. The off-diagonal elements range between -1 and 1 and, the closer the absolute value is to 1, the more highly (either directly or inversely) correlated the parameters are. Again, these values are subject to the assumption of linear model input-output response near the reference point.

Perturbation Analysis

In a perturbation analysis, individual model input parameters are systematically increased and decreased from reference values (in this case, calibrated values) while all other parameter values are held constant. The model is then run for each "perturbed" parameter case, and some summarized metric of the model output is calculated. This exercise provides information about the sensitivity of model outputs to changes in individual parameter values over the parameter range.

In contrast to the sensitivity coefficients, a perturbation analysis can provide information about the input-output relationship away from the reference point, and nonlinear input-output relationships can be identified. By varying input parameters over their range of uncertainty (i.e., multiple standard deviations away from the reference point), some insight into the corresponding uncertainty in model output can also be gained. However, because parameters are perturbed individually, synergistic effects between multiple input parameters on the model output are neglected.

Perturbation analysis corresponds to computing a cross section of the objective function (model goodness of fit) along the dimension of the variable under consideration. For instance, Figure 6-1 shows a sample objective function surface (from Hill, 1998) that involves transmissivity (T) and storativity (S).

If a profile of the objective function in Figure 6-1 is visualized at a fixed T of 0.12 with S varying, it would be relatively flat between S values of 0.00025 and 0.00075, rising gently to higher and lower S values. If a profile at fixed S (say 0.0050) is considered, it has a steep slope and narrow valley bottom at the calibration point. Perturbation analysis describes these types of responses for the Pahute Mesa CAU flow model.

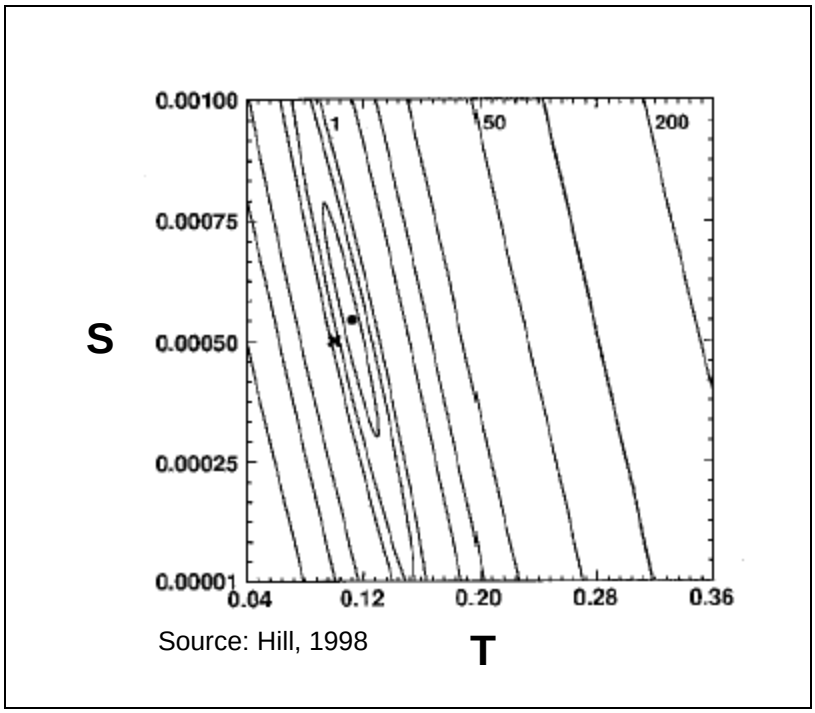

Figure 6-1
Sample Objective Function for Perturbation Analysis

If the calibration data weights or the number or type of calibration data are changed, then the results from the perturbation analysis that follows will only generally still be applicable.

6.1.1.2 Global Sensitivity Analysis

Unless the functional relationship between the output and the input of interest is linear over the entire range of input values, local analyses only provide information regarding the relative sensitivities of input parameters valid in the vicinity of the reference point. As a result, global sensitivity analysis techniques are used for investigating input-output sensitivities that are valid over the entire range of possible parameter variations and not just at or near the reference point (Saltelli et al., 2000).

The starting point for global sensitivity analysis is the selection of a strategy for exploring the entire parameter space over which model calculations will be performed. The approach adopted is a Monte Carlo simulation based uncertainty analysis methodology using Latin Hypercube sampling (McKay et al., 1979). The values resulting from calibration are taken as the mean, and the log normal distribution and associated standard deviation from SNJV (2004a) are used with the code of Iman et al. (1980) to generate 1,000 uncorrelated samples, which are then run through FEHM. For fault

permeability multipliers, a log-uniform distribution was sampled that went about two orders of magnitude above and below the calibrated values. Classification tree and mutual information (entropy) analysis are used to analyze the sampling results.

Although several methods are available for global sensitivity analysis (e.g., Saltelli et al., 2000), analyzing input-output relationships for a non-monotonic output (i.e., quadratic objective function) requires special consideration. As shown by Mishra and Knowlton (2003), entropy (mutual information) analysis is particularly useful for determining the strength of input-output association for any general non-linear non-monotonic relationship, whereas commonly used sensitivity analysis techniques such as stepwise rank regression are known to fail under such conditions. A second issue is the determination of decision rules that identify which variables or combinations of variables lead to low values of the objective function (i.e., good fit) versus high values (i.e., bad fits). Classification tree analysis has been shown to be a useful tool for analyzing such categorical problems (Mishra et al., 2003).

For the global sensitivity analysis of the Pahute Mesa flow model, the goodness-of-fit criteria are evaluated for several types of calibration targets (also discussed in Section 5.2). These are as follow:

- WELL – groundwater elevation in observation wells
- SPRING – groundwater elevation in springs
- FLUX - boundary flow
- ETF – Oasis Valley ET flux
- PHI - total of above

These are the same components used to calibrate the flow model, including data values and weights.

Classification Tree Analysis

Classification tree analysis can provide useful insights into what variable or variables are most important in determining whether outputs fall in one particular category. Categories are generally based on meeting some acceptable threshold (e.g., pass versus fail, fit versus misfit). Traditional applications of classification trees have primarily been in medical decision making and data mining for social sciences. Mishra et al. (2003) describe an application of the methodology to a Monte Carlo simulation-based model for predicting performance of a potential nuclear waste repository.

The setting up of the Monte Carlo simulations is described in Section 6.2.3. The number of uncertain parameters is the same as that used in the perturbation analysis, and can be found in the first paragraph of Sections 6.2.2.1, 6.2.2.2 and 6.2.2.3. The code of Iman and Conover (1979) is used to ensure that no spurious correlation exists between any two arbitrary parameters during the Latin Hypercube Sampling process. The composition of the RMS objective function, used as the performance measure of interest for the sensitivity analyses, is also described in Section 6.2.3.

A binary decision tree is at the heart of classification tree analysis. The decision tree is generated by recursively finding the variable splits that best separate the output into groups where a single category dominates. The degree by which a single category dominates is called the split "purity." For each successive fork of the binary decision tree, the algorithm searches through the variables one by one to find the purest split within each variable. The splits are then compared among all the variables to find the best split for that fork. The process is repeated until all groups contain a single category, or a specified level of purity is reached for all groups. In general, the variables that are chosen by the algorithm for the first several splits are most important, with less important variables involved in the splitting near the terminal nodes of the tree.

The tree-building methodology used here is based on a probability model approach. Classifiers at each node are selected based on an overall maximum reduction in impurity, for all possible binary splits over all the input variables. The impurity at a given node A (I_A) is based on the Gini index (Breiman et al., 1984), which for the two class case reduces to:

$$I_A = 2\rho_{1A}\rho_{2A} \tag{6-3}$$

where ρ_{1A} and ρ_{2A} are the estimated probabilities of classes 1 and 2, respectively, at node A. The probabilities are estimated from the proportion where n is the number of observations in a class at a node by:

$$\rho_{1A} = \frac{n_{1A}}{n_A} \tag{6-4}$$

where ^{n}A is the total number of observations at node A, and $^{n}1A$ is the proportion belonging to class 1.

The decrease in impurity for a given split of node A into nodes L and R (left and right) is:

$$\Delta I = I_A - \rho_L I_L - \rho_R I_R \quad (6\text{-}5)$$

where ρ_L and ρ_R are the proportions of the cases that go to L and R, respectively.

The classification tree is built by successively taking the maximum reduction in purity over all the allowed splits of the branch to determine the next split. Termination occurs when the number of cases at a node drops below a set minimum, or when the maximum possible reduction in purity for splitting a particular node drops below a set minimum.

As an example, Figure 6-34 in Section 6.2.3.1 shows the results of a classification tree analysis to determine the decision rules separating the smallest and largest 10 percent values for the dependent variable PHI. Here, the category "low" refers to the smallest 10 percent PHI values and the category "high" refers to the largest 10 percent PHI values. In Figure 6-34, each node of the classification tree is labeled with the numbers of each category that have been assigned to that node, with the number of high values comprising the first and the number of low values comprising the second. For example, "68/0" indicates that 68 from the high category have cascaded to the node. Note that the "83 low" and "68 high" observations can be perfectly categorized with just two splits. Also, some judgment of the importance of the variables can be made from the structure of the tree itself. Here, variable LCCU thrust sheet (LCCU1) is the most important because it was chosen for the first split, followed by Detached Volcanics Composite (DVCM).

Tree-based models are attractive because: (a) they are adept at capturing non-additive behavior, (b) they can handle more general interactions between predictor variables, and (c) they are invariant to monotonic transformations of the input variables. These attributes make classification trees more suitable for input-output modeling as compared to regression analysis, which is restricted to a linear (or linearized) input-output relationship and where the functional form of the relationship has to be specified *a priori*.

Entropy Analysis

The information-theoretic concept of entropy is a useful metric for the characterization of uncertainty (or information) in the univariate case, and redundancy (or mutual information) in the multivariate case (Press et al., 1992). The concept of mutual information has been utilized to select key input variables in neural network based input-output modeling (Bonnlander and Weigand, 1994). Because mutual information is a natural measure of input variable relevance, it is also being used as an indicator of variable importance in many areas of science (Moddmeijer, 1989).

The following theoretical discussion is based on Press et al. (1992). Let the input variable x have I possible states (labeled by i), and the output variable y have J possible states (labeled by j). This information can be compactly organized in terms of a contingency table – a table whose rows are labeled by the values of the independent variable, x, and whose columns are labeled by the values of the dependent variable, y. The entries of the contingency table are non-negative integers giving the number of observed events for each combination of row and column.

The contingency table can also be visualized using a "bubble plot," where the entries of the contingency table are shown as bubbles of varying sizes. Here, the contingency table is organized such that the quintiles of the independent variable (input) increase from left to right, and that of the dependent variable (output) increase from top to bottom. The size of the bubble indicates how many observations fall in each quintile-quintile box. Bubble plots generated for this report are presented beginning in Section 6.2.3.1.

The probability of outcomes corresponding to both states x_i and y_j is $\rho_{ij} = N_{ij}/N$, where N_{ij} denote the number of events occurring when x takes its i-th value and y takes its j-th value. Let $N_{i.}$ denote the number of events for which x takes its i-th value regardless of the value of y; similarly, let $N_{.j}$ denote the number of events with the j-th value of y regardless of x. The probability of outcomes corresponding to state x_i alone is: $\rho_{i.} = N_i/N$, and the probability of outcomes corresponding to state y_j alone is: $\rho_{.j} = N_{.j}/N$. Then, the entropies of x and y are defined as:

$$H(x) = -\sum_i \rho_{i.} \ln \rho_{i.}; \; H(y) = -\sum_j \rho_{.j} \ln \rho_{.j} \tag{6-6}$$

and denote the average information in observing x (or y). Similarly, the joint entropy of x and y, denoting the average information in observing both x and y, is defined as:

$$H(x, y) = -\sum_i \rho_{ij} \mathrm{In} \rho_{ij} \tag{6-7}$$

The mutual information between x and y, which measures the reduction in uncertainty of y due to knowledge of x (or vice versa), is defined as:

$$I(x, y) = H(x) + H(y) - H(x, y) = -\sum_i \sum_j \rho_{ij} \mathrm{In}\left(\frac{\rho_{ij}}{\rho_{i.} \rho_{.j}}\right) \tag{6-8}$$

If x and y are completely independent, then $H(x,y) = H(x) + H(y)$, so $I(x,y) = 0$. On the other hand, if x and y are completely dependent, then $H(x,y) = 0.5[H(x) + H(y)]$, so $I(x,y) = 0.5[H(x) + H(y)]$.

The R-statistic has been proposed as a measure of association based on the concept of entropy or mutual information as follows (Granger and Lin, 1994):

$$R[x, y] = [1 - \exp\{-2I(x, y)\}]^{1/2} \tag{6-9}$$

R takes values in the range [0,1], with values increasing with I. R is zero if x and y are independent, and is unity if there is an exact non-linear relationship between x and y. It can also be shown that if x and y have a bivariate normal distribution with correlation ρ, then $R = |\rho|$ (Cover and Thomas, 1991).

The entropy-based measure R-statistic can thus be recognized as a very general tool for quantifying the strength of an association. It is applicable to both linear/non-linear and monotonic/non-monotonic relationships, whereas commonly used regression-based measures are restricted to linear and monotonic associations only.

6.1.2 Conceptual Model Uncertainty Analysis

There are seven HFMs for the Pahute Mesa CAU flow model, five recharge models, and five sets of lateral boundary flows. If all combinations were considered, this would result in 175 calibrated flow

models. However, as discussed further in Section 6.4.2, it is neither necessary nor reasonable to investigate all combinations. The approach taken was to use a given recharge model in the Pahute Mesa CAU flow model with the UGTA regional model (DOE/NV, 1997) boundary flows derived from the same recharge model in the UGTA regional model. Table 6-1 summarizes the combinations of HFM, recharge, and boundary flow uncertainties that were investigated.

Table 6-1
Recharge, Boundary, and HFM Uncertainty Matrix

Geology/Boundary	DRIA/ DRIA	DRIAE/ DRIAE	MME/ MME	USGSND/ USGSND	USGSD/ USGSND
BN[a]	X	X	X	X	X
SCCC	X		X		X
DRT	X		X		X
PZUP	X		X		X
TCL			X		
SEPZ			X		
RIDGE			X		

Note: Row header is recharge model/boundary flow, and column header is HFM.

[a]Only for selected HSU depth decay and anisotropy.

In general, the strategy is to discretely combine HFMs, recharge models, and lateral boundary flows in order to at least bound uncertainty associated with each model component. Thus, for the PZUP alternative HFM for the DRIA water balance, the DRIA recharge map is used as input, and the boundary flows estimated from the UGTA regional model (DOE/NV, 1997) with the DRIA recharge map were used as calibration constraints. In this way, the effects of the recharge model on regional-scale results are indirectly captured in the CAU-scale flow model.

6.2 Parameter Sensitivity Analysis

6.2.1 Local Parameter Sensitivity and Correlations

After the calibration of the Pahute Mesa flow model, local parameter sensitivity and correlations were evaluated using a PEST control file that was updated to reflect the calibrated parameter values. The PEST code was then run, calculating statistics and sensitivity coefficients for the calibrated parameter set. Sensitivity coefficients were ranked in descending order, and the 15 largest were plotted.

In PEST, the objective function, or PHI, is the sum of the squares of the weighted residuals:

$$\Phi = \sum_{i=1}^{m} (w_i r_i)^2 \quad (6\text{-}10)$$

where Φ is the objective function, *w* is the observation weight, *r* is the residual or difference between the simulated and measured values, and *m* is the number of observations of non-zero weight. For the Pahute Mesa flow model, PHI can be divided into four components representing different types of calibration target data. Head measurements at wells are described by the WELL component. The FLUX component represents lateral boundary flow estimates from the regional model. The heads and flows at discharge locations are represented by the SPRING and ETF components, respectively. It is important to note, this sensitivity analysis only addresses the model response with respect to the flow model calibration data; direct references cannot be drawn about transport prediction sensitivity.

The sensitivity of HSUs that are connected to the model boundaries is somewhat distorted by the arbitrary model boundaries required by the scale of the problem. For instance, if an HSU permeability increased the head remains unchanged at the model edge but the flow would increase. However, if the full regional context was maintained, the head could conceivably change rather than the flow.

For the objective function and the individual portions contributing to it, a simple difference (*D*) was used:

$$D = \Phi_{sens} - \Phi_{cal} \quad (6\text{-}11)$$

where Φ_{sens} is the sensitivity simulation objective function and Φ_{cal} is the calibrated simulation objective function.

6.2.1.1 Base HFM - Selected HSU Depth-Decay and Anisotropy (BN-MME-SDA) Model Parameter Sensitivity and Correlations

For this model, permeability, reference permeability (k_0), and fault permeability multiplier parameters were varied individually by HSU or fault, as appropriate. A single vertical anisotropy parameter was

used for HSUs for which anisotropy was assigned (see Table 5-7). A single depth-decay coefficient for the volcanic HSUs and another for carbonate HSUs was also used. This latter approach mimics in a broad way how these parameters were assigned during calibration. This resulted in approximately 100 parameters for which sensitivity coefficients (to all calibration data, hence "composite") were calculated.

The 15 largest sensitivity coefficients calculated by PEST are shown in Figure 6-2. This figure shows that the two depth-decay parameters have much greater sensitivity coefficients than any of the other parameters (note the log-scale used for the y-axis). This is not surprising because permeability in the model is an exponential function of the depth-decay coefficient. After depth decay, the next three most sensitive parameters are the permeability of the LCCU1, k_0 of the PCM, and the permeability of the DVCM. The permeability of the LCCU1 is completely unknown, and is estimated to be relatively high based on enhanced fracturing from being overthrust (SNJV, 2004a). The PCM lies along the southern edge of the model, and its sensitivity is derived from controlling head in the domain by throttling the sharp drop in head imposed along the southern boundary, and outflow along the southern boundary. The DVCM lies on the western edge of Oasis Valley and controls inflow from Sarcobatus Flat to the west; it is also located proximal to a large number of calibration targets in Oasis Valley. The DVA is nearly as sensitive as the DVCM, and it also lies in a critical location to control head and flow in central and southern Oasis Valley. The only fault to show much sensitivity is the Claim Canyon Caldera Structural Margin (fault 06; see Figure 4-5 for fault locations). Considering its location (see Figure 4-5), this is because it controls flow and head in much the same manner as the PCM by acting as a check on the southern outflow and controlling the influence of the southern boundary. The PBRCM permeability Zones 84 and 13 are the areas on the western side of the domain, and under Areas 19 and 20, respectively. The PBRCM Zone 84 is shown in Section 6.2.3.1 to control flow into northern Oasis Valley, and Zone 13 is interpreted as having sensitivity because of its large extent, presence in an area that includes a large part of the calibration data, and connection with the northern edge of the model, which very few HSUs have. The FCCM rings Timber Mountain and is another HSU with large areal extent. The CHZCM has 23 calibration targets in it exclusively, hence its sensitivity. Vertical anisotropy is relatively far down on the list of sensitive parameters. The TMCM-ERM subdivision (see Figure 5-6) and TCVA, two areally extensive HSUs, have mild sensitivity, finally followed by the BFCU.

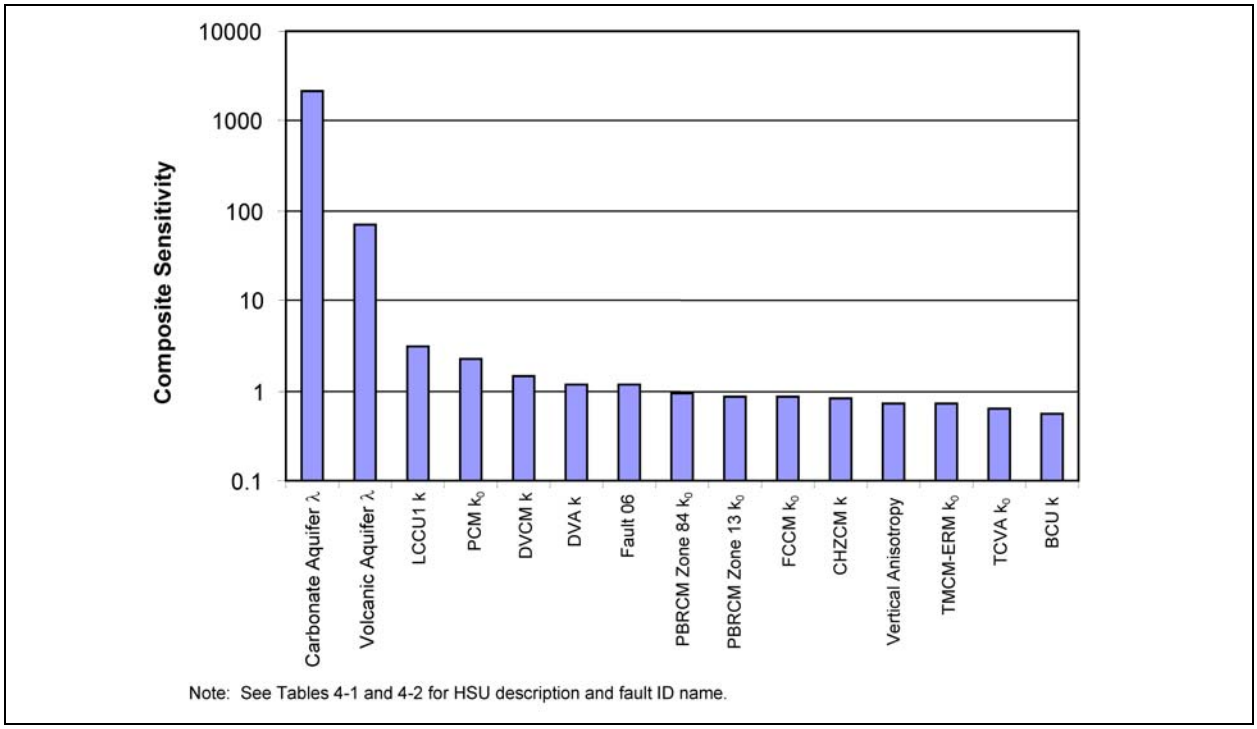

Figure 6-2
Largest Sensitivity Coefficients from PEST for BN-MME-SDA

Recall that the sensitivity coefficient relates to the weighted slope of the input-output relationship at the calibration point and, unlike perturbation or global sensitivity analyses, is independent of the range in uncertainty of a parameter. Because the depth-decay coefficients have a small range in uncertainty with respect to other parameters, they were perturbed over a smaller range and were not observed to have such pronounced sensitivity in the perturbation analysis or the global sensitivity analysis.

The 15 most sensitive observation targets to all the calibration data (hence "composite") calculated using PEST are depicted in Figure 6-3. This figure shows that the lateral boundary flux targets for the eastern and southern model boundaries are the most sensitive observations. This may indicate that many parameters impact the flow through the eastern and southern boundaries. Another interpretation is that relatively few, but broadly defined, HSUs influence flow on the east and south model edges. Considering the parameter sensitivities noted above the latter interpretation seems more likely, particularly with regard to the PCM and Claim Canyon Caldera Structural Margin. Following these two boundary fluxes, head observations in selected wells have very comparable observation sensitivity coefficients that are less than half the magnitude of those for the boundary

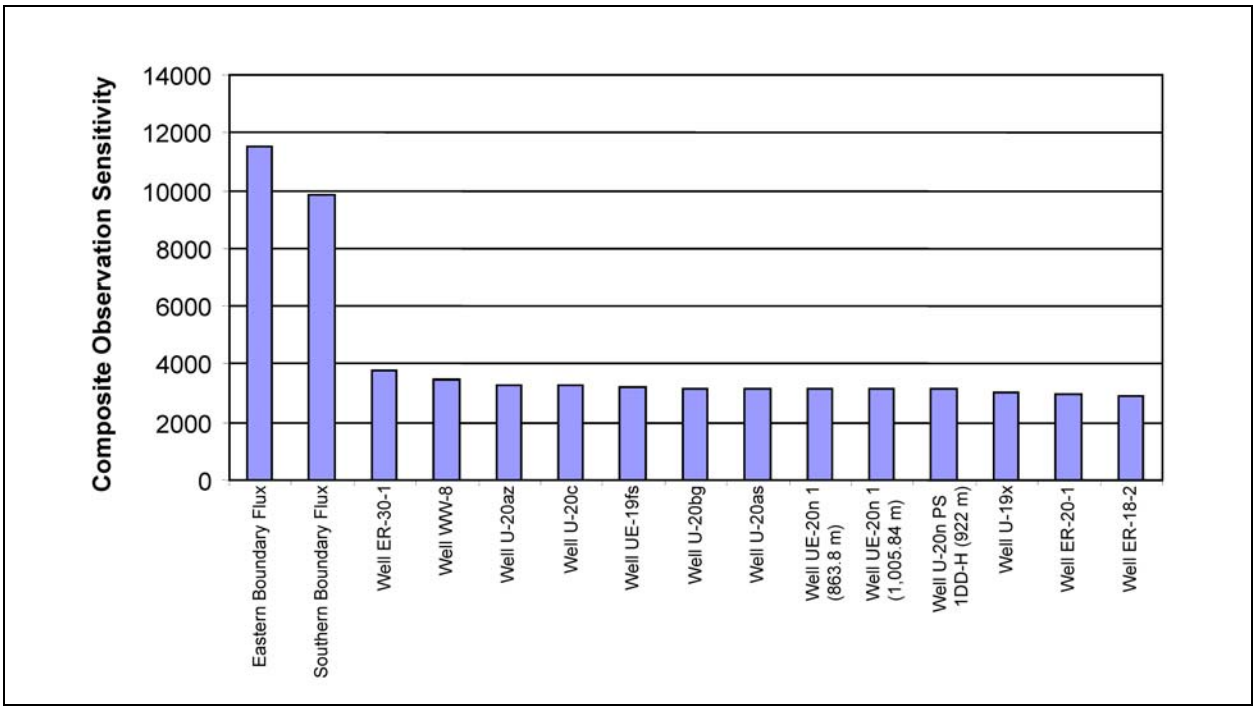

Figure 6-3
Composite Observation Sensitivity from PEST for BN-MME-SDA

fluxes. Well ER-30-1 is one of the few wells on eastern Timber Mountain, and WW-8 is located to the east of it. Both wells are located in a sparsely populated area of the model, with respect to calibration data, and are concluded to provide a great deal of useful calibration information in this area of the model. Most of the other sensitive observations are located throughout Areas 19 and 20, and do not appear to have any special significance other than they tend to have the high weights.

The 15 most highly correlated pairs of parameters (from the PEST correlation coefficient matrix) are shown in Figure 6-4. For context, Hill (1998) suggests a significant level of correlation is 0.90. This figure shows that the fault permeability multiplier for the Claim Canyon Caldera Structural Margin and the k_0 parameter for PCM are almost perfectly inversely correlated. The Claim Canyon Caldera Structural Margin also has strong correlation with carbonate depth decay. This supports the observation made previously in this section that the Claim Canyon Caldera Structural Margin acts to control the flow domain along the southern edge of the model. Its nearly perfect inverse correlation shows that the effect of decreasing the fault permeability multiplier can be offset, at least over the range of perturbation, by increasing PCM permeability. The control of the Claim Canyon Caldera Structural Margin on the southern boundary is also expressed by the correlation with LCA depth

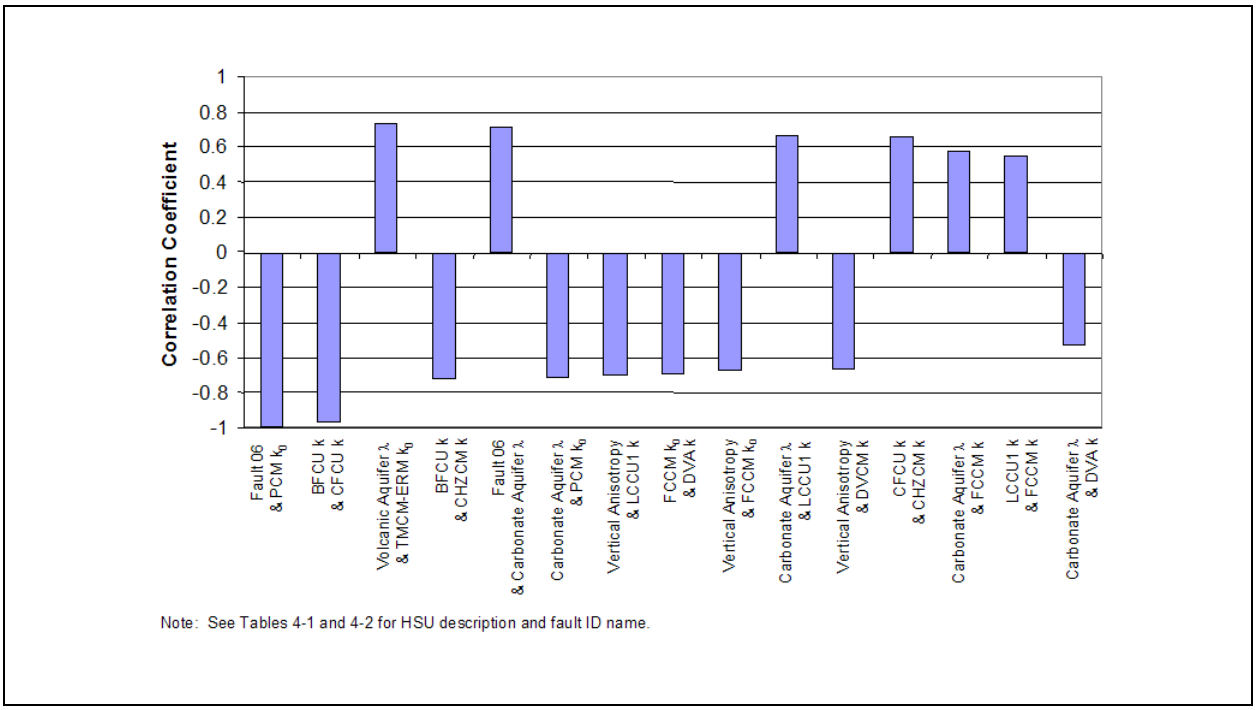

Figure 6-4
Correlation Coefficients from PEST for BN-MME-SDA

decay, only in the reverse sense of the correlation with PCM, the fault and LCA depth decay act similarly to control flow (recall that southern boundary flow was one of the most sensitive observations); the inverse correlation of PCM permeability and LCA depth decay further demonstrates this effect. The permeability of the BFCU and CFCU are also show a high inverse correlation, which, considering their location and role as major confining units in Areas 19 and 20, is a reasonable outcome.

6.2.1.2 Base HFM - All HSU Depth-Decay and Anisotropy (BN-MME-ADA) Model Parameter Sensitivity and Correlations

For this model, k_0, fault permeability multiplier, vertical anisotropy, and depth-decay coefficient parameters were varied individually by HSU or fault. This replicates the more detailed approach inherited from the UGTA regional model (DOE/NV, 1997) where depth decay and anisotropy were ubiquitously used. This resulted in a total of approximately 200 parameters for which sensitivity coefficients were calculated.

The 15 largest sensitivity coefficients calculated for this model using PEST are shown in Figure 6-5 and are all depth-decay parameters. The LCA3a is the LCA3 under Oasis Valley; the LCA Zone 1 (LCAr1) is the LCA along the southeastern edge of the model inherited from the UGTA regional model (DOE/NV, 1997) (see Figure 5-7). The PCM depth-decay parameter (λ) is also a sensitive parameter in this model and acts, as noted in the selected HSU depth-decay and anisotropy case, to control outflow on the south and the influence of the southern boundary. The PBRCM is one of the most extensive units in the Pahute Mesa CAU model and exists at a large range of depths, and it is the λ for the portion that lies under the Silent Canyon Caldera (and Areas 19 and 20) that is the fourth most sensitive parameter. The PBRCM λ is also sensitive in the selected HSU depth-decay and anisotropy case described in Section 6.2.1.1, but not to the same degree. The YMCFCM, like the PCM, lies along the southern boundary and is in position to control the effects of the southern boundary. The BRA, North Timber Mountain subdivision of the TMCM, and TCA are all extensive permeable units in the model. The IA and CHZCM are not so extensive, but CHZCM has 23 calibration wells in it. The DVA λ, as described in Section 6.2.1.1, is also a sensitive parameter. Clearly, with this parameterization approach, the volcanic units' depth decay is a dominant parameter as is depth decay in general.

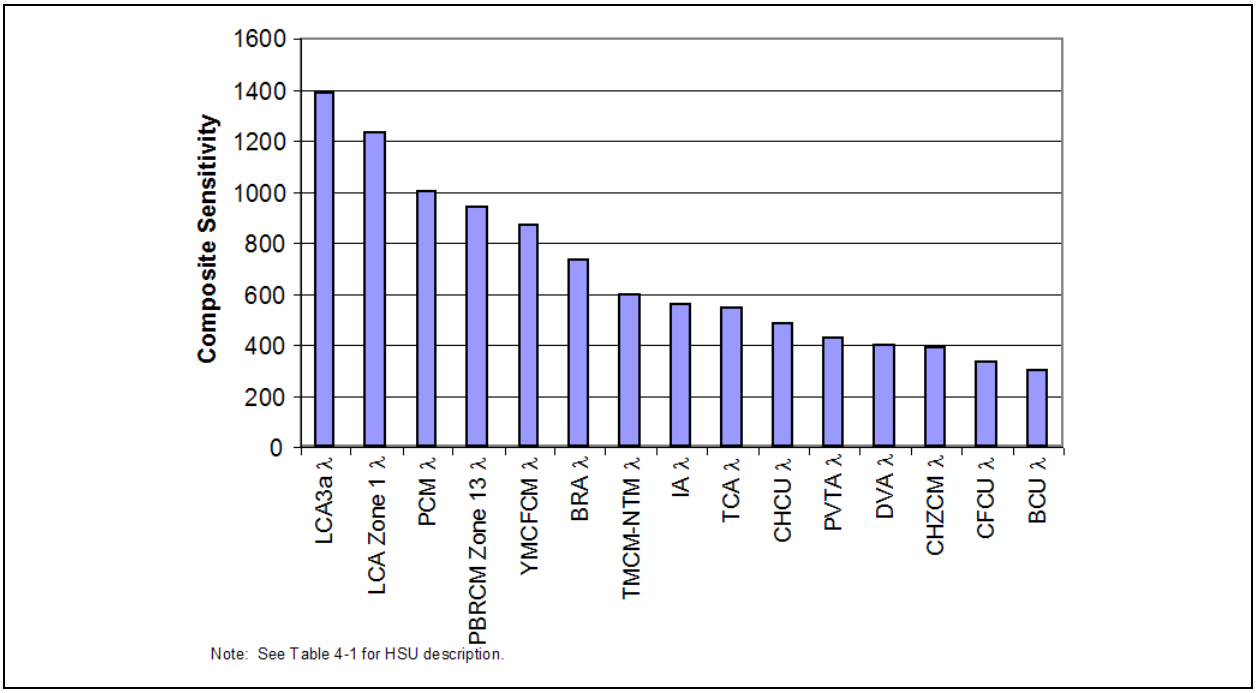

Figure 6-5
Largest Sensitivity Coefficients from PEST for BN-MME-ADA

The 15 most sensitive targets calculated using PEST are depicted in Figure 6-6. This figure shows that Oasis Valley discharge Zone 1, the northernmost target, is the most sensitive observation (unlike the selected HSU depth-decay and anisotropy case) followed by the lateral boundary flux targets for the southern and eastern model boundaries (like the selected HSU depth-decay and anisotropy case). Following these three observations, the observation sensitivity coefficients tend to drop off quickly.

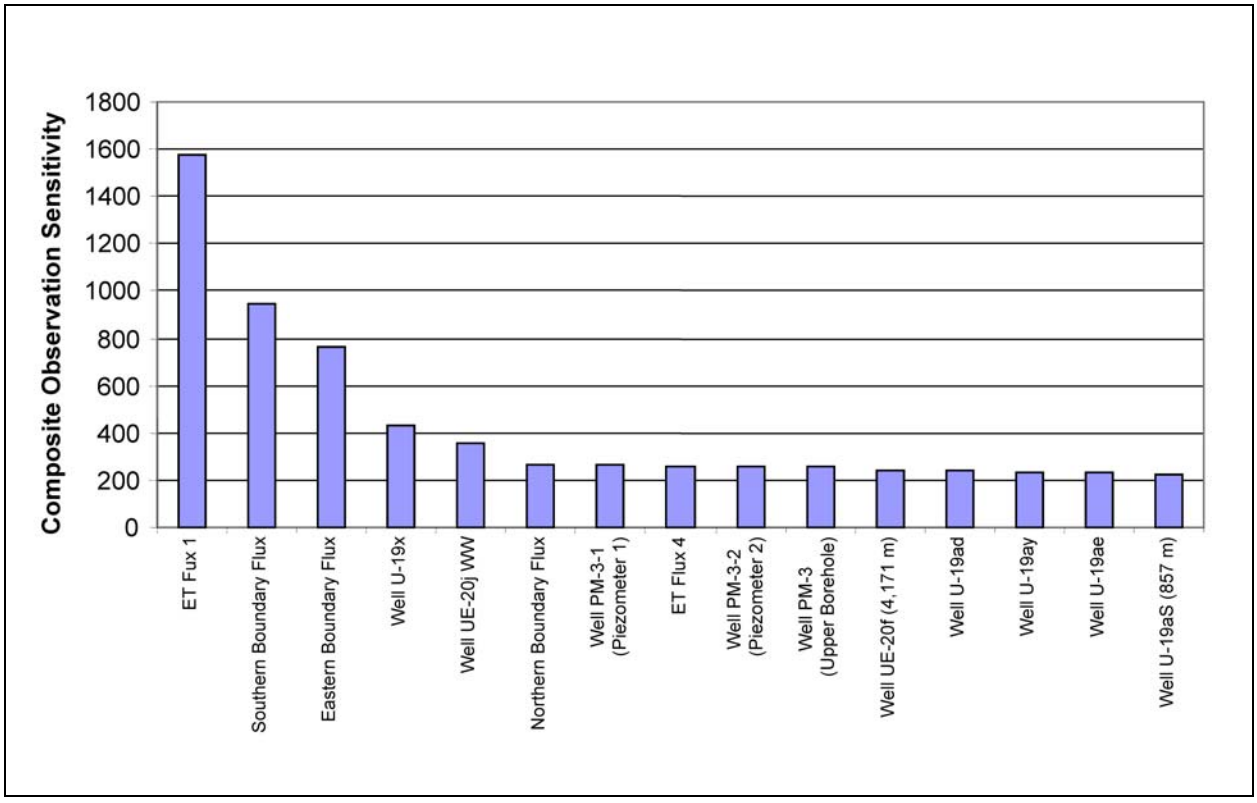

Figure 6-6
Composite Observation Sensitivity from PEST for BN-MME-ADA

The effect of consolidating the depth decay and anisotropy to affect all volcanic aquifers at once was also considered to investigate the representation of the shallower volcanic rocks as a package (the ICUs were not considered in this grouping). The 15 most highly correlated pairs of parameters from the PEST correlation coefficient matrix are shown in Figure 6-7. This figure shows that many parameters appear to be highly correlated (correlation coefficients greater than 0.90 [Hill, 1998]). The first relationship on Figure 6-7 shows that the reference permeability and depth-decay parameter for the UCCU are nearly perfectly (0.99) correlated (the LCCU also shows this behavior, as does the volcanic units to the grouped volcanic depth-decay parameter). Review of the formulation of depth

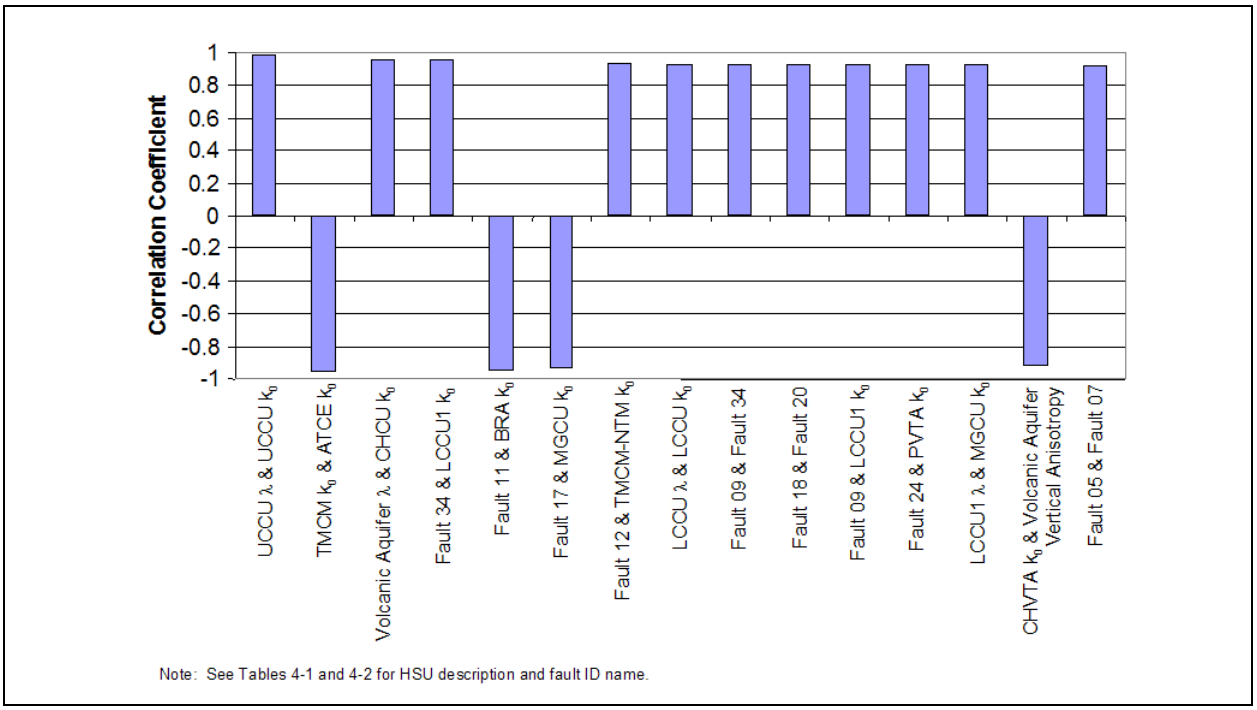

Figure 6-7
Correlation Coefficients from PEST for BN-MME-ADA

decay $k(z) = k_0[10^{(-\lambda d)}]$ shows that as λ gets larger (i.e., depth decay increases), k(z) can be maintained by increasing k_0 proportionally. Oddly, the MGCU k_0 appears as a parameter correlated with LCCU1 k_0. This is interpreted as arising from both units connection along the central-eastern boundary to high regional heads; permeability can be raised in concert to achieve the same effect. The effects of the MGCU in the ADA case were also noted in Section 5.8.2.

Of the faults shown in Figure 6-7, fault 09 is the only one that appears with any consistency (only twice at that). Fault 09 is East Estuary, which is indicated as being correlated with West Estuary and LCCU1 k_0. Like the Boxcar Faults, the Estuary Faults (which have reduced fault permeability in the BN-ADA case) may act in concert, but the reason why East Estuary Fault would be correlated with the LCCU1 permeability is unknown. Hill (1998) states that nonlinear and slight precision effects can make correlation coefficients unreliable. Section 6.2.2.2 shows that the model response to parameter changes is noticeably nonlinear; thus, these results (as all results from local analysis) should be considered approximate and are valid inasmuch as the conceptual model can be used to understand the cause and effect implied by the statistical analysis. Overall, this parameterization approach shows many more extremely correlated parameters than the selected HSU depth-decay and

anisotropy approach described in Section 6.2.1.1. This should not be entirely surprising considering that more than 200 adjustable parameters exist in this model with only 191 observations.

6.2.1.3 SCCC HFM - Selected Depth-Decay and Anisotropy (SCCC-MME-SDA) Model Parameter Sensitivity and Correlations

For this model, permeability, k_0, and fault permeability multiplier parameters were varied individually by HSU or fault, as appropriate. Two HSUs (Calico Hills and BA) were assigned individual vertical anisotropy parameters, and the others were grouped into a single parameter. A single depth-decay coefficient for the volcanic HSUs and another for carbonate HSUs were used. This resulted in approximately 100 parameters for which sensitivity coefficients were calculated using PEST.

The 15 largest sensitivity coefficients calculated for this model using PEST are shown in Figure 6-8. This figure shows that, like the selected HSU depth-decay and anisotropy parameterization of the base HFM, the two depth-decay parameters have much greater sensitivity coefficients than any of the other parameters (note the log-scale used for the y-axis). Other HSUs shown in Figure 6-8 include the FCA, YVCM (a patchy unit near the northern end of Oasis Valley), and THLFA. None of these appear, at least in a similar rank, in the base HFM model sensitivities shown in previous sections. The sensitivity of the Calico Hills anisotropy (recall that the five Calico Hills HSUs in the base HFM were grouped into one for the SCCC HFM, and that about 23 calibration wells exist in it) is attributed to the greater influence that the lumped unit exercises, although vertical anisotropy (as applied to selected volcanic HSUs) still ranks similarly in sensitivity to the base HFM. Unlike the BN-MME-SDA case the model has many sensitive faults. Indeed, seven of the 15 largest sensitivity coefficients belong to permeability multipliers for faults that are scattered throughout the model domain. The three most sensitive are the Timber Mountain Structural Margin (fault 11), the Gold Meadows Structural Zone/Big Burn Valley (fault 22), and the Hot Springs extension to the Timber Mountain Structural Margin (fault 19). Faults 11 and 22 are located such that they can control flow out of Timber Mountain and along the eastern edge of the model, and their sensitivity is easily interpreted as consistent with the conceptual model. It seems odd that the relatively short fault 19 has much impact, but it is located in Oasis Valley where there are discharge, spring, and head data.

The 15 most sensitive targets calculated using PEST are depicted in Figure 6-9. This figure shows that the northernmost Oasis Valley discharge target (Zone 1) is the most sensitive observation,

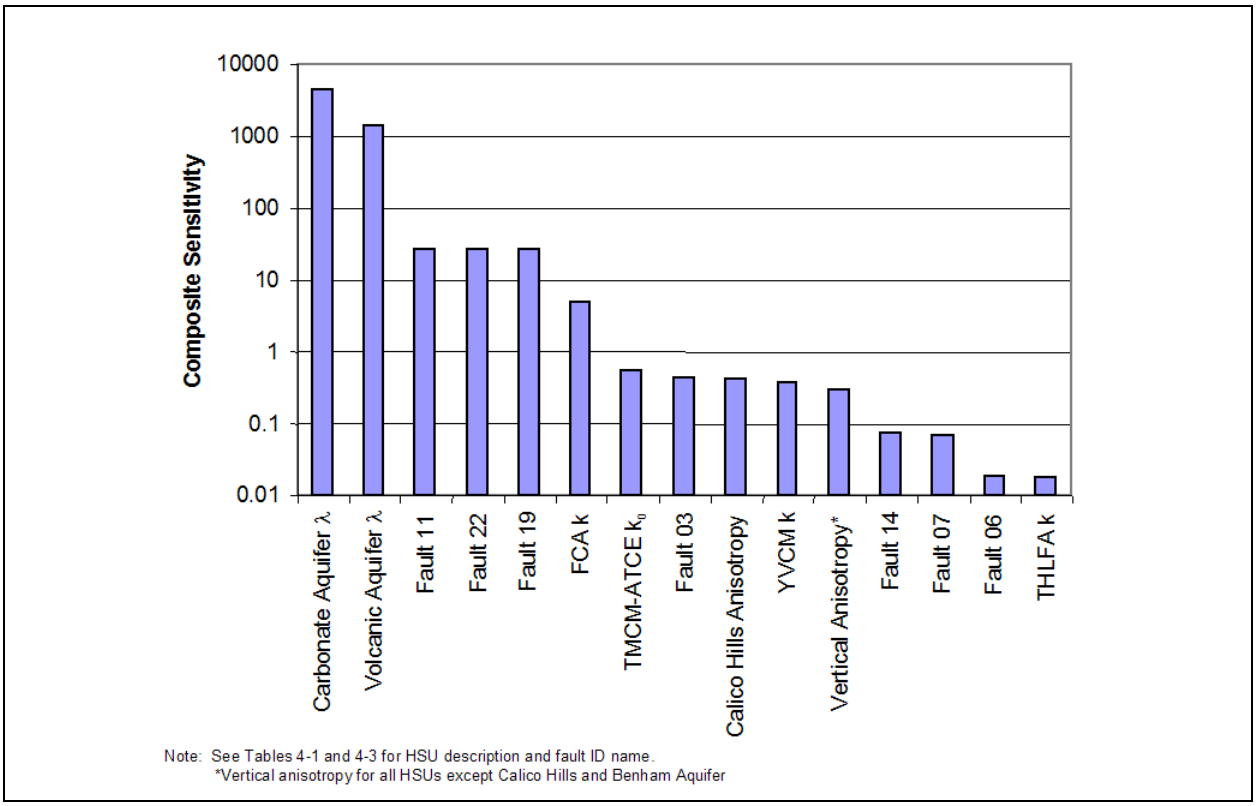

Figure 6-8
Largest Sensitivity Coefficients from PEST for SCCC-MME-SDA

followed by UE-19i, and the southern boundary flux. This may indicate that many parameters impact the flow out ET Zone 1. Following this observation, a series of head observations in wells and the southern boundary flux have very comparable observation sensitivity coefficients but less than half the magnitude of that for discharge Zone 1.

The 15 most highly correlated pairs of parameters (from the correlation coefficient matrix) are shown in Figure 6-10. This figure shows that the carbonate depth-decay coefficient and the permeability of the YVCM are almost perfectly (-0.994) inversely correlated. That the YVCM displays much sensitivity at all is surprising considering its patchy nature, but it lies near ER-EC-4 and ER-18-2. There is no obvious reason as to why the permeability of the YVCM and carbonate depth decay should be so highly correlated. This may be an instance of less-reliable correlation coefficients as noted by Hill (1998). Taken as a group, the depth decay applied to the selected volcanic HSUs is inversely correlated to carbonate depth decay; as depth decay, increases in one group of units it can be counterbalanced by a reduction in depth decay in the other. Considering that the southern boundary

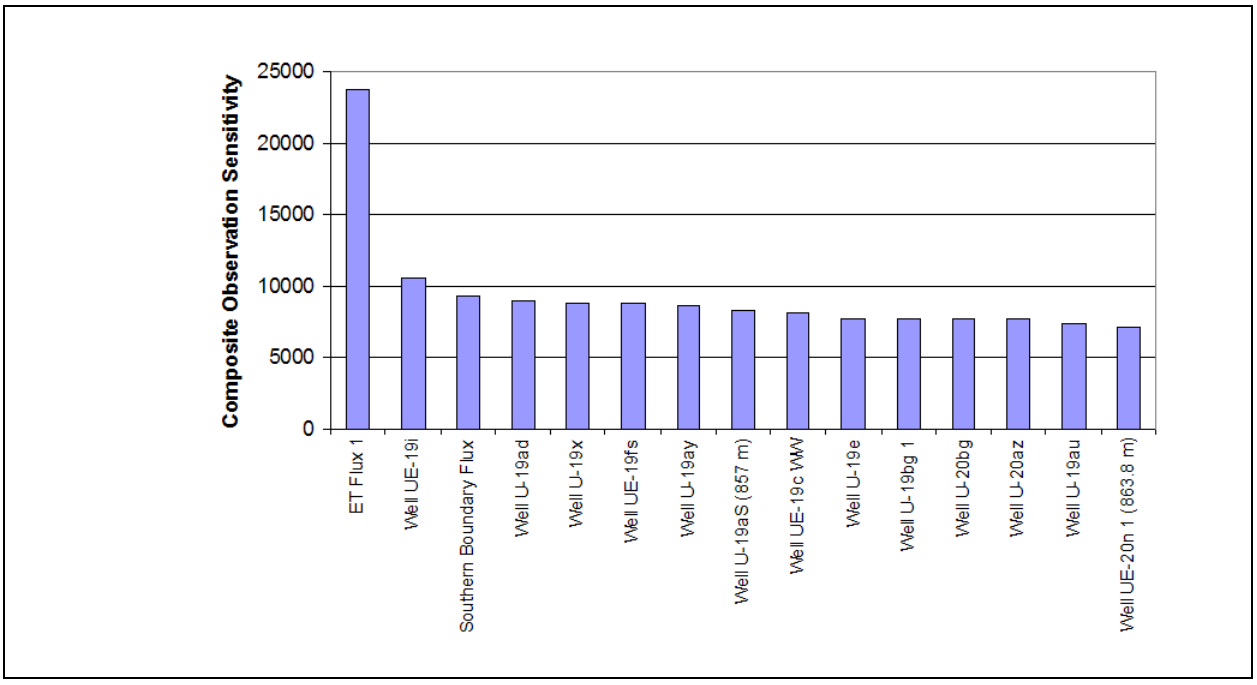

Figure 6-9
Composite Observation Sensitivity from PEST for SCCC-MME-SDA

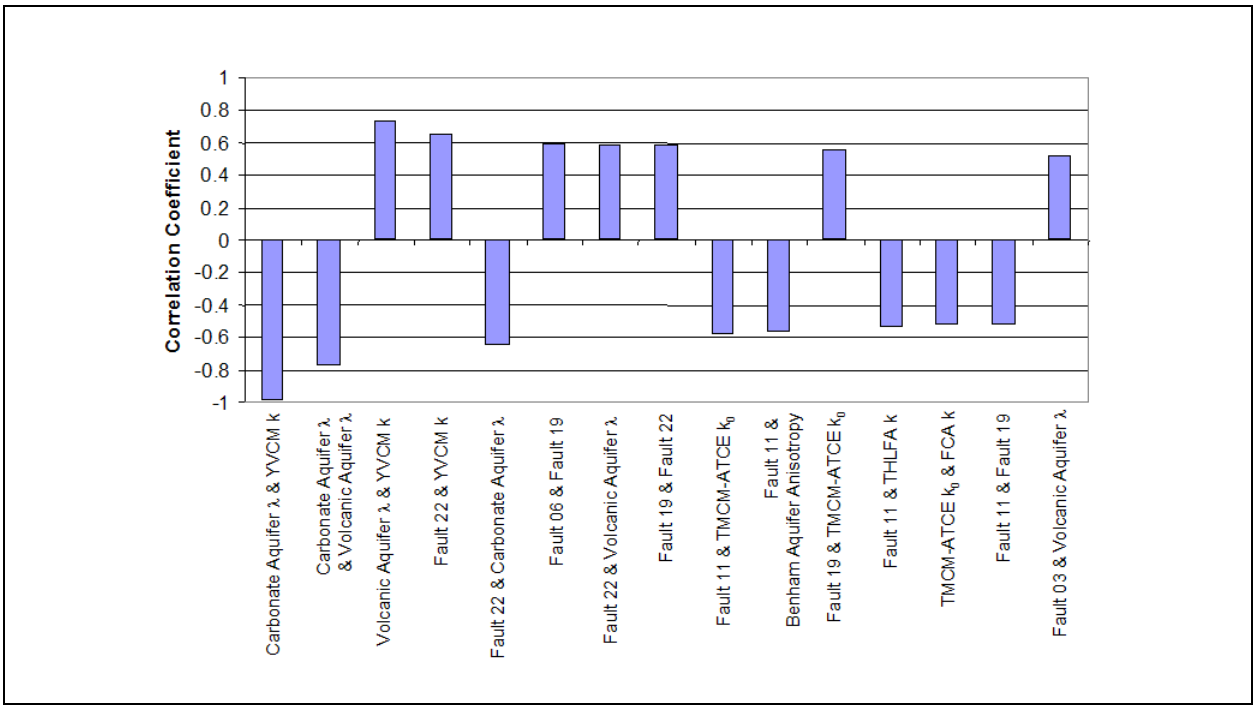

Figure 6-10
Correlation Coefficients from PEST for SCCC-MME-SDA

flow is a strongly sensitive observation and there are no head observations in the LCA, this effect must arise from trying to match boundary flows. In this case, it makes sense that as T in one type (e.g., LCA) of HSU drops from increased depth decay, it can be compensated for by lessening the effect of depth decay in the other type of HSU (e.g., volcanics with depth decay). This relationship is not noticed in the BN-MME-ADA or BN-MME-SDA cases. A number of other parameter pairs exhibit moderately high correlation, more like the selected HSU depth decay and anisotropy parameterization of the base HFM than the all HSU depth-decay and anisotropy case.

6.2.2 Parameter Perturbation Analysis

In the perturbation analysis, input parameters were systematically increased and decreased while changes in the objective function, heads, and various fluxes were recorded. Estimated standard deviations in HSU permeability (SNJV, 2004a; Section 2.0 of this report) and depth decay were available (IT, 1996a through f; IT, 1997a and b; Section 5.0 of this report). It was assumed that these standard deviations were applicable in describing the uncertainty in the calibrated values of these parameters. For each HSU permeability and depth decay, six simulations were completed where the input value was perturbed up and down one-half, one, and two standard deviations from the calibrated value. Vertical anisotropy and fault permeability multipliers were assumed to have log-uniform distributions and were perturbed over several orders of magnitude with ranges depending on assumptions about the uncertainty in the individual parameters.

The same components of the objective function that were used for calibration were also computed for perturbation analysis. An additional metric for the output heads was also computed; the mean difference (*MD*) between the sensitivity simulated output and the calibrated simulated output heads at each of the target wells was calculated as:

$$MD = \frac{1}{n}\sum_{i=1}^{n}(h_{sens,\,i} - h_{cal,\,i}) \qquad (6\text{-}12)$$

where $h_{sens,i}$ is the perturbation simulation head at well i, $h_{cal,i}$ is the calibrated simulation head at well i, and n is the number of wells. This metric describes more than the objective function components;

the direction of the head change can also be assessed. A positive value indicates that the sensitivity simulation has overall higher heads and a negative value has overall lower heads.

6.2.2.1 Base HFM - Selected HSU Depth-Decay and Anisotropy (BN-MME-SDA) Model Parameter Perturbation Analysis

For perturbation analysis, each HSU's permeability (including k_0), depth decay (if assigned,), and anisotropy (if assigned) were varied. Thus, the detailed effects of each parameter with each HSU were investigated. This resulted in 61 permeability and k_0 parameters, 11 vertical anisotropy parameters, 15 depth-decay parameters, and 11 fault permeability multiplier parameters being varied. In addition, vertical anisotropy was varied as single grouped parameter, the fault permeability multiplier for the Purse Fault was varied as a group, and depth decay was varied as two groups – one for the carbonates and one for the volcanics (the list of HSUs with depth decay and anisotropy is shown in Section 5.6.2) as well as for each HSU. This resulted in approximately 100 parameters that were varied. Approximately 600 simulations were conducted during the analysis shown in this section.

Plots of mean difference in heads, change in the objective function and its constituents, and change in boundary flows were generated for perturbation of each of the approximately 100 parameters in the BN-MME-SDA perturbation analysis. While all of these plots are shown in Appendix D, Figures 6-11 through 6-18 demonstrate selected sensitivity relationships.

Figures 6-11 through 6-14 show plots of the mean difference in heads at the target locations. Figures 6-11 through 6-13 indicate that the permeability (including k_0) and depth-decay parameters exhibit a classical, albeit nonlinear in some cases, sensitivity relationship where an increase in a parameter value is accompanied by a consistent trend of either an increase or decrease in the simulated head. It is also interesting that increases in the permeability (i.e., higher k_0 or lower depth-decay coefficient) for some HSUs result in higher heads while the opposite is true for other HSUs, and that permeability (including k_0) has a larger effect than the depth-decay parameter itself. This may simply be because the range of uncertainty for k_0 is smaller than that for λ (which spans multiple orders of magnitude). The TMCM is by far the most sensitive of all the HSUs with depth decay, followed by the PBRCM under Pahute Mesa. The TMCM has a very large areal coverage, and its properties affect flow in a large part of the domain, hence its sensitivity. The PBRCM under

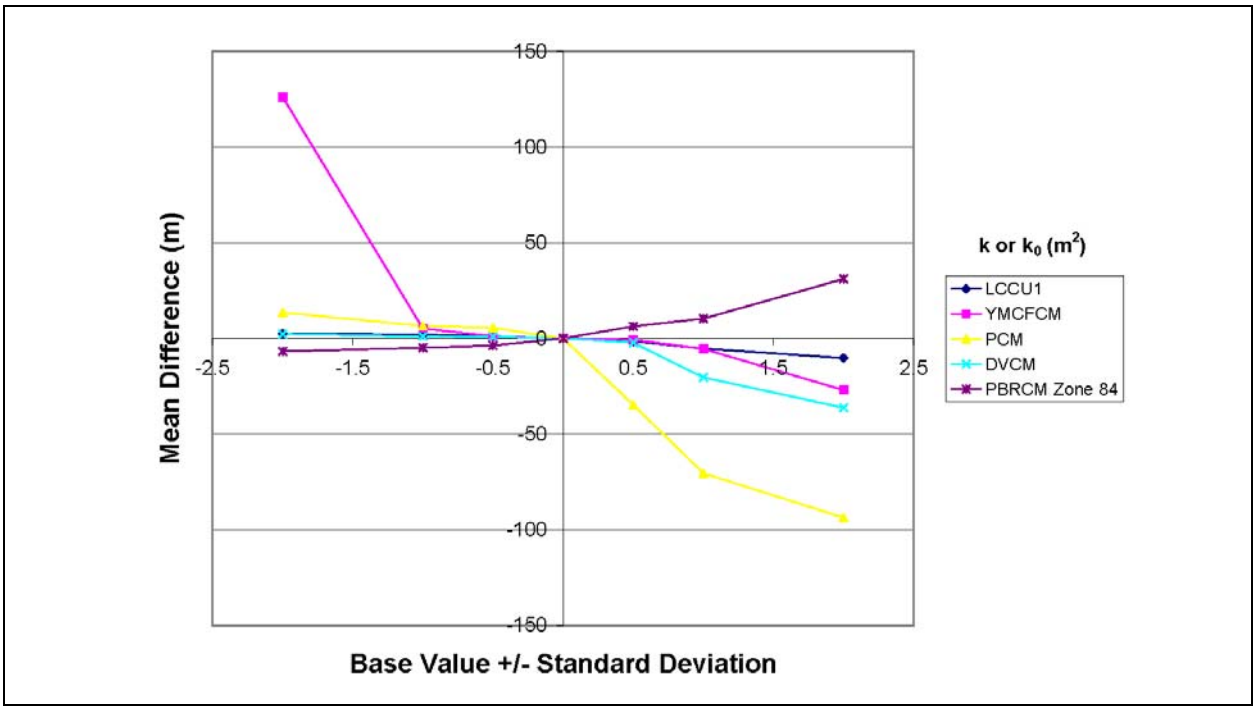

Figure 6-11
Mean Head Difference for BN-MME-SDA

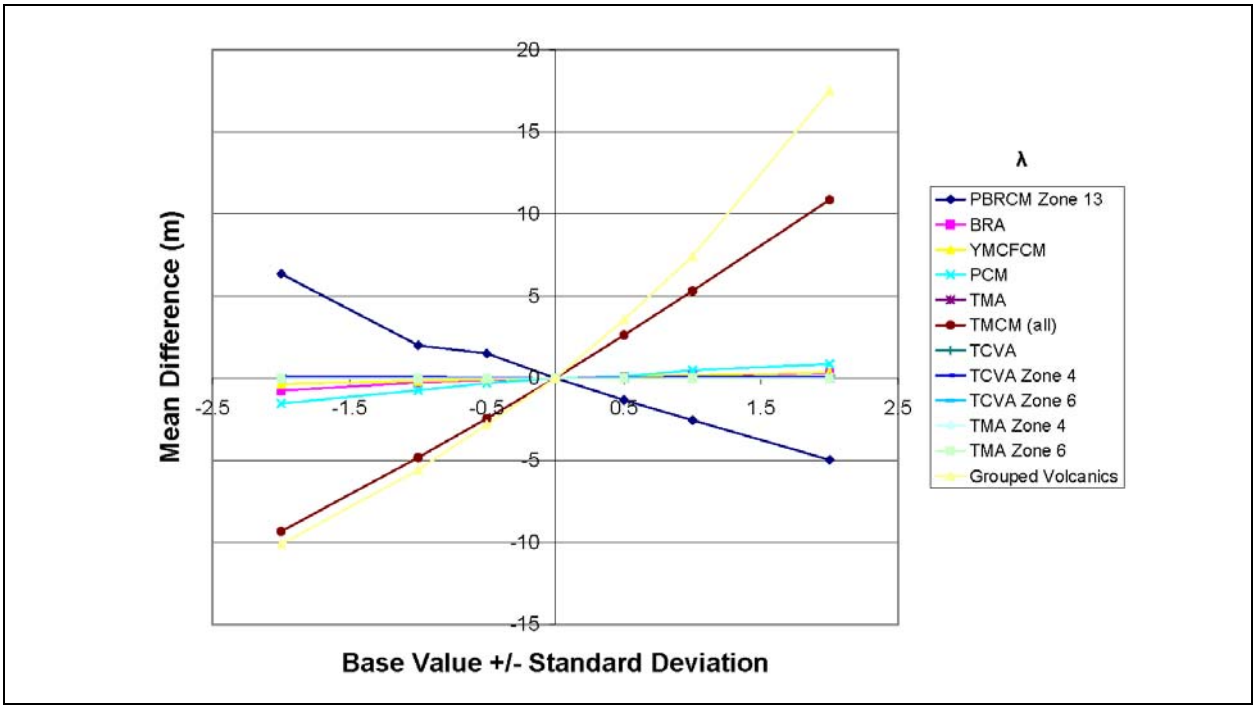

Figure 6-12
Mean Head Difference for Volcanic HSU Depth Decay for BN-MME-SDA

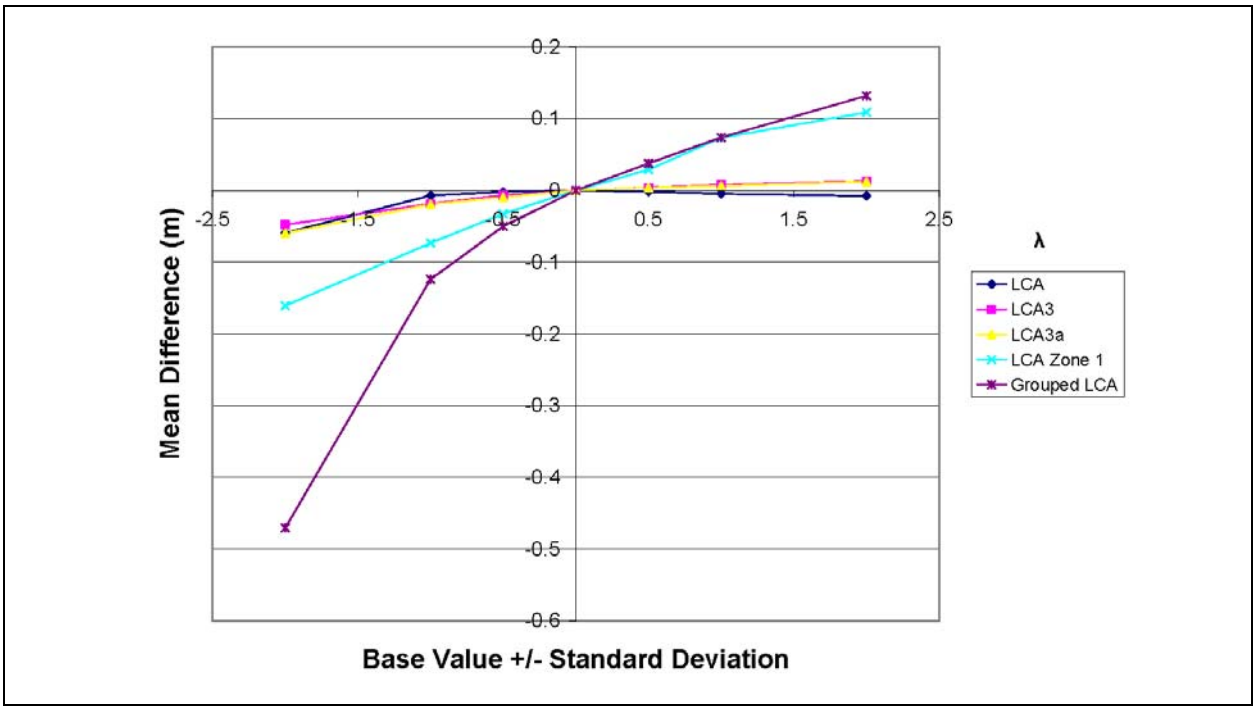

Figure 6-13
Mean Head Difference for Carbonate HSU Depth Decay for BN-MME-SDA

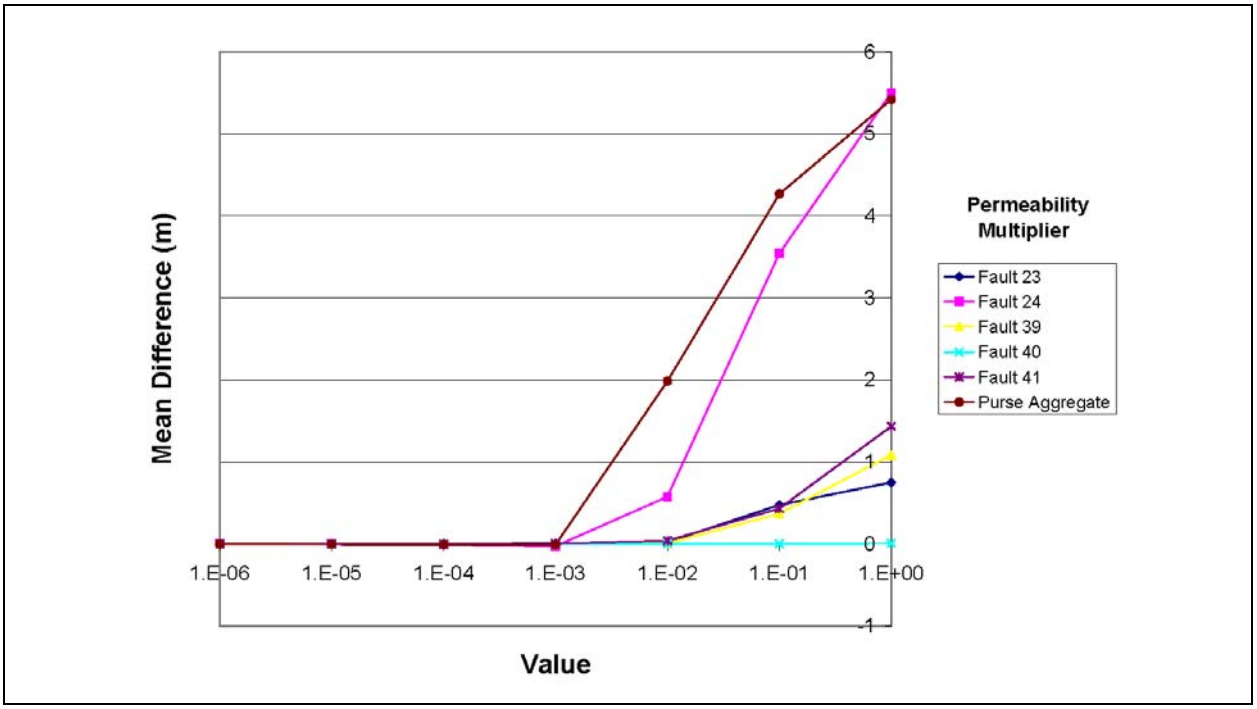

Figure 6-14
Mean Head Difference for Purse Fault Permeability Multipliers for BN-MME-SDA

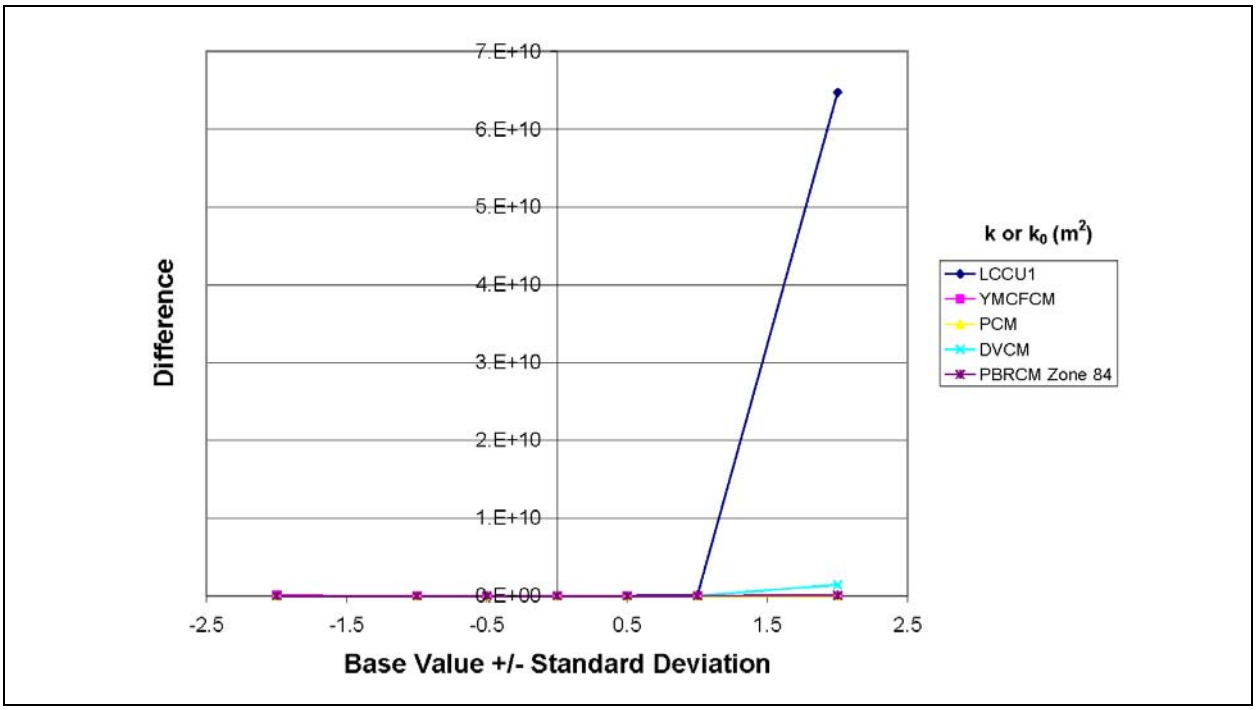

Figure 6-15
PHI Perturbation Plot for BN-MME-SDA

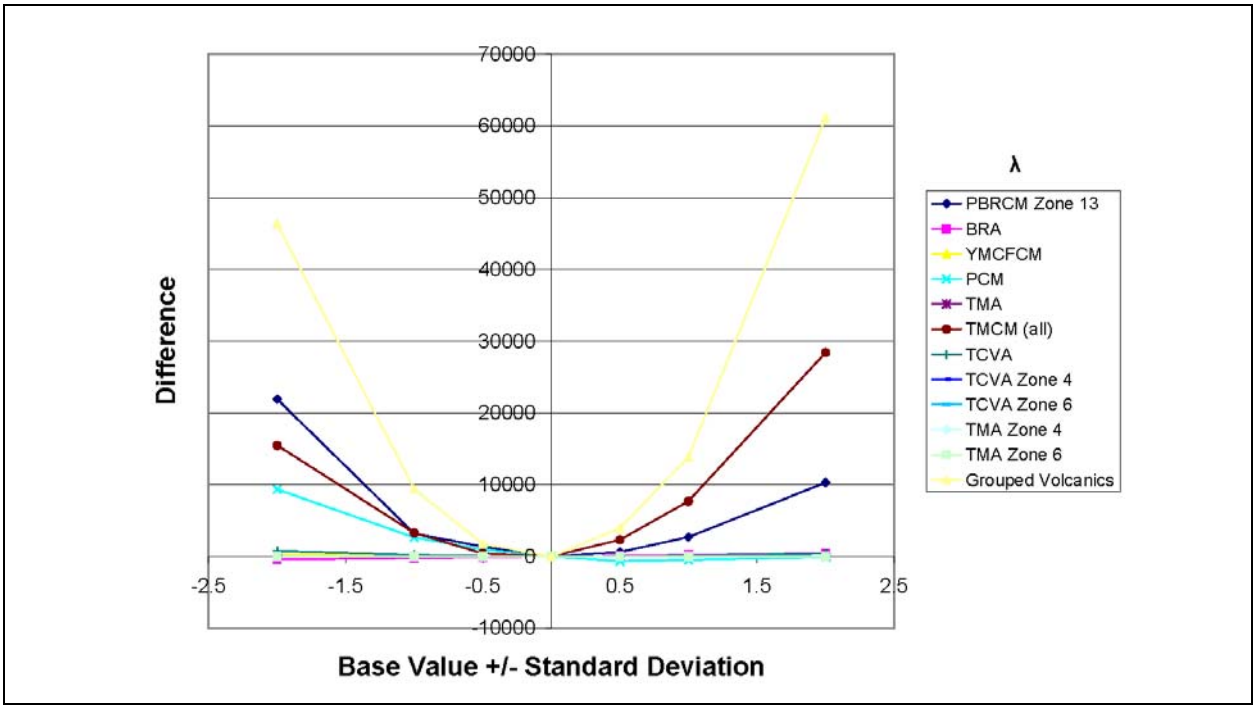

Figure 6-16
PHI Perturbation Plot for Volcanic HSU Depth Decay for BN-MME-SDA

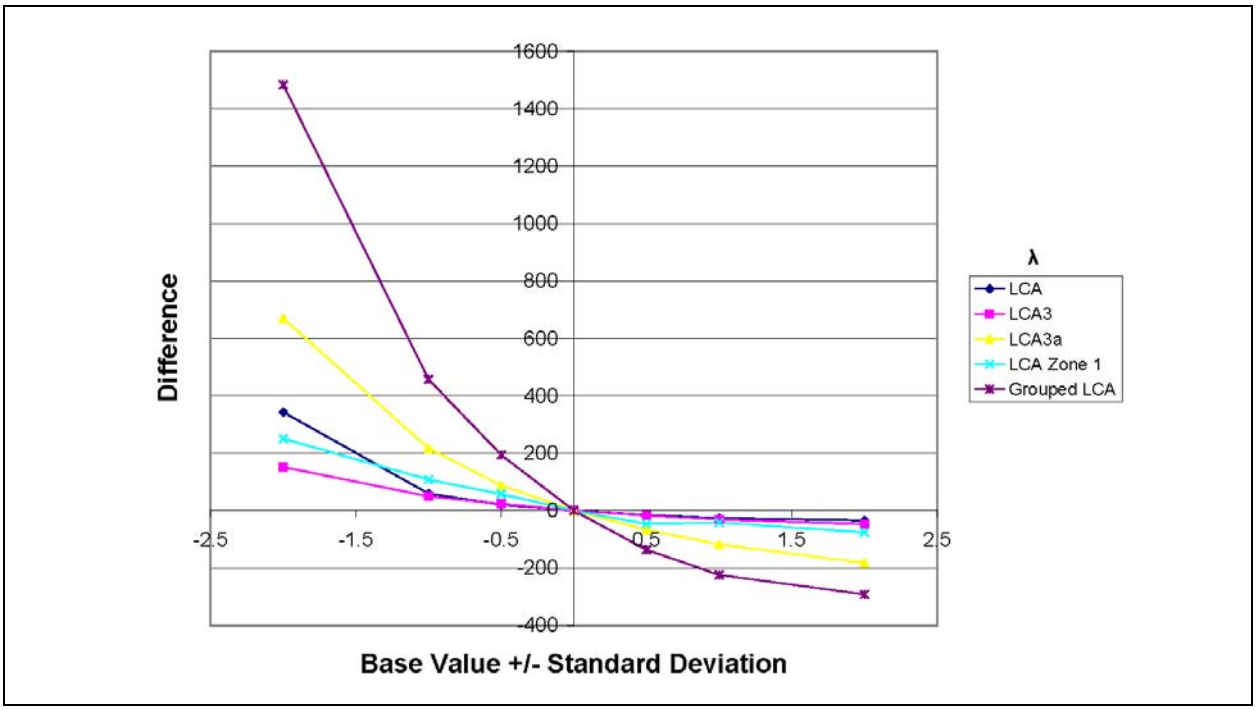

Figure 6-17
PHI Perturbation Plot for Carbonate HSU Depth Decay for BN-MME-SDA

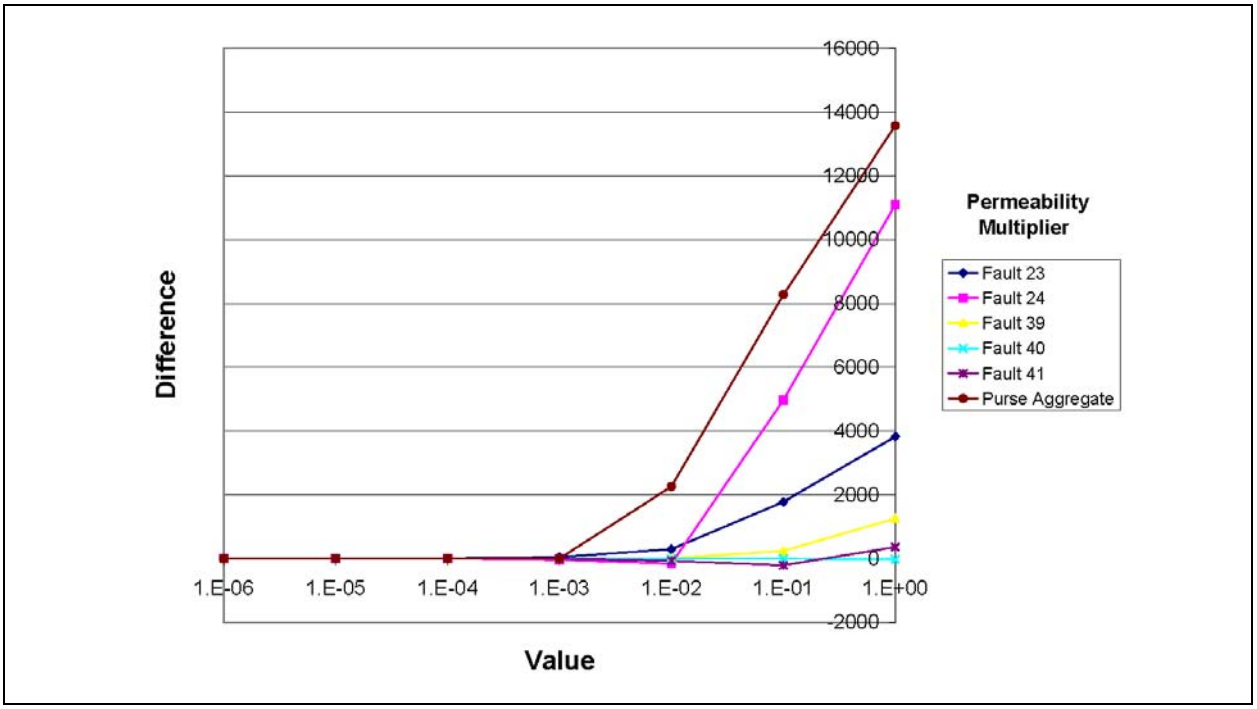

Figure 6-18
PHI Perturbation Plot for Purse Fault Permeability Multipliers for BN-MME-SDA

Pahute Mesa is located where a large part of the calibration data exists, and is connected, like the BRA, to the northern boundary of the model. The PBRCM is also distributed over most of the domain. The BRA is also areally extensive under Pahute Mesa, but is not present much outside Pahute Mesa. Thus, it is concluded that it is this larger connection to the flow system that accounts for the different behavior of the PBRCM and BRA. The TMA and TCVA only had minor influence. The carbonate aquifer (LCA, LCA3, LCA3a, and LCA Zone 1) λ has almost no effect on mean head (Figure 6-13); its primary function seems to be to control the overall water balance with respect to the estimated regional flows.

In contrast, Figure 6-14 shows that the fault permeability multipliers of the Purse Fault system and its individual components exhibit a threshold sensitivity relationship where heads increase with an increase in the fault permeability above a multiplier of 0.001 but heads do not decrease for lower fault permeabilities. As previously discussed, the Purse Fault is comprised of segments of other faults as well as the main fault. Figure 6-14 shows that it is the main part of the fault (fault 24) that has the largest influence on model results, which is reasonable because it comprises most of the length of the fault.

Figure 6-11 indicates that YMCFCM and PCM have the greatest effect on the simulated heads. The PCM and YMCFCM, by the virtue of their location along the southern edge of the model, can affect mean heads in the model by tens of meters. It is probably not depth decay *per se* that drives these sensitivities, but the HSU positions on the southern edge; if they did not have depth decay, their permeability would still be expected to be a sensitive parameter. The DVCM, because of its role in controlling what water is allowed to discharge in Oasis Valley from the west, also has a noticeable, and one-sided, control on lowering heads as its permeability is raised. The western portion of the PBRCM has some control on raising heads, presumably via its connection to the northern edge of the model (and higher) heads down to northern Oasis Valley.

Figures 6-15 through 6-18 show select perturbation plots for the objective function (PHI). Note that these include the same parameters shown in Figures 6-11 through 6-14. Because the PEST sensitivity coefficients and the global sensitivity analysis both focus primarily on the objective function as the model output metric, these plots are most pertinent in comparing the perturbation results to those of the other analysis types. It is immediately apparent that most of the parameters shown in Figures 6-15

through 6-18 exhibit highly nonlinear sensitivity relationships over the range through which they were perturbed. This indicates that the sensitivity coefficients calculated by PEST are, in most cases, valid only locally in the vicinity of the calibration point.

Several other observations can also be made with respect to the perturbation plots of the objective function. Figure 6-15 shows that high values of permeability for LCCU1 have a very large effect on PHI, the permeability of which is unknown, and other diagnostic results such as parameter correlations. Figure 6-16 indicates that the minimum PHI with respect to the volcanic depth-decay parameters is generally centered on the calibration point; it would be difficult to further improve calibration by adjusting k_0 in the volcanic HSUs with depth decay. Depth decay has the largest influence in TMCM and PBRCM (as also noted in the composite head in Figure 6-13), two HSUs that have a large areal extent. In contrast, the minimum PHI with respect to the carbonate depth-decay parameter occurs at values higher than the calibrated value as seen in Figure 6-17, although the change in the objective function is minor. Figure 6-18 indicates that the fault permeability multipliers for the Purse Fault system and its individual components exhibit a threshold sensitivity with low PHI values occurring for multipliers below approximately 0.001, consistent with the threshold value noticed in the mean head difference metric.

There are clearly differences in the sensitivity relationships for mean heads and for the objective function, particularly with respect to the parameters with the highest sensitivity. This is because the large differences in the objective function are dominated by the contribution from the lateral boundary fluxes rather than from the head-based targets. This is also demonstrated in the global sensitivity analysis (see Section 6.2.3), where parameters governing the highest 10 percent of PHI typically coincide with parameters driving the highest 10 percent of boundary flux.

6.2.2.2 Base HFM - All HSU Depth-Decay and Anisotropy (BN-MME-ADA) Model Parameter Perturbation Analysis

For the base HFM - all HSU depth-decay and anisotropy model (BN-MME-ADA), 57 k_0 parameters, 64 vertical anisotropy parameters, 64 depth-decay parameters, and 41 fault parameters were varied. In addition, the fault permeability multiplier for the Purse Fault was varied as a group and for each fault segment, and both vertical anisotropy and depth decay were varied as three groups – one for each of the carbonates, the volcanic units, and the intrusive confining units as well as by HSU. This

resulted in approximately 200 parameters that were varied. Generating results for this perturbation analysis required approximately 1,400 simulations.

Plots of mean difference in heads, difference in the objective function and its constituents, and difference in boundary fluxes were generated for each of the approximately 200 parameters in the base HFM - all HSU depth-decay and anisotropy model perturbation analysis. While all of these plots are shown in Appendix D, Figures 6-19 though 6-24 describe selected sensitivity relationships.

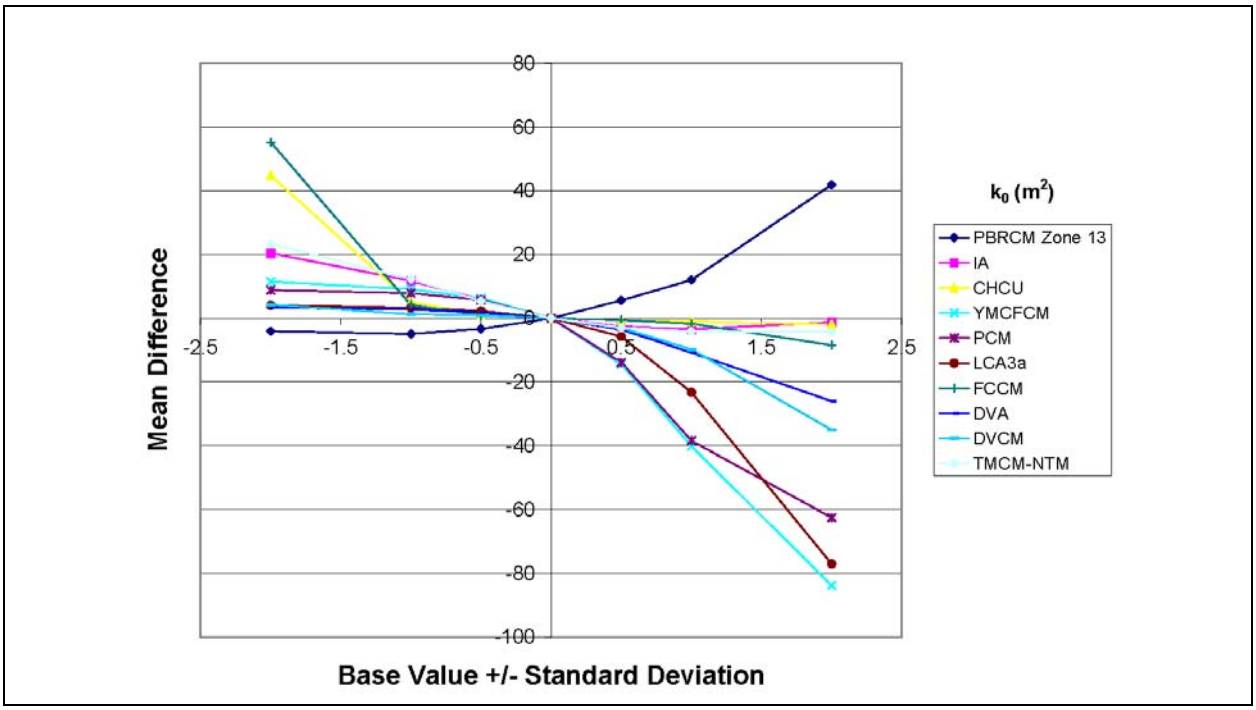

Figure 6-19
Mean Head Difference for BN-MME-ADA

Figures 6-19 through 6-21 depict select perturbation plots for the mean difference in heads at target locations. Figures 6-19 and 6-20 show that the k_0 and depth-decay parameters exhibit a nonlinear sensitivity relationship. It is also interesting that increases in the permeability for some HSUs results in higher heads while the opposite is true for other HSUs. Figure 6-19 indicates that the reference permeability of YMCFCM, LCA3a, and PCM have the greatest effect on simulated heads, although the DVCM, DVA, and PBRCM under Pahute Mesa also have noticeable influence. The YMCFCM and PCM are likely sensitive because (as discussed in the previous section) they lie along the southern edge of the model and can control both flow and head in the model. The PBRCM under

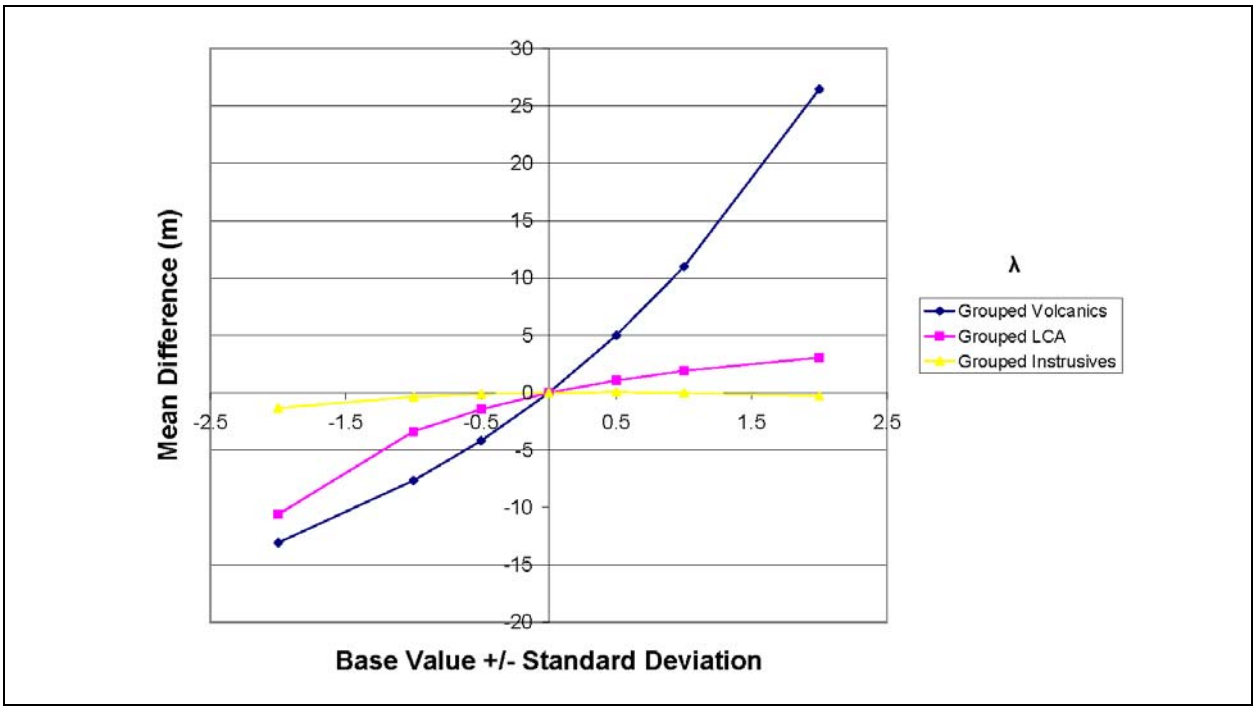

Figure 6-20
Mean Head Difference for Depth-Decay Parameters for BN-MME-ADA

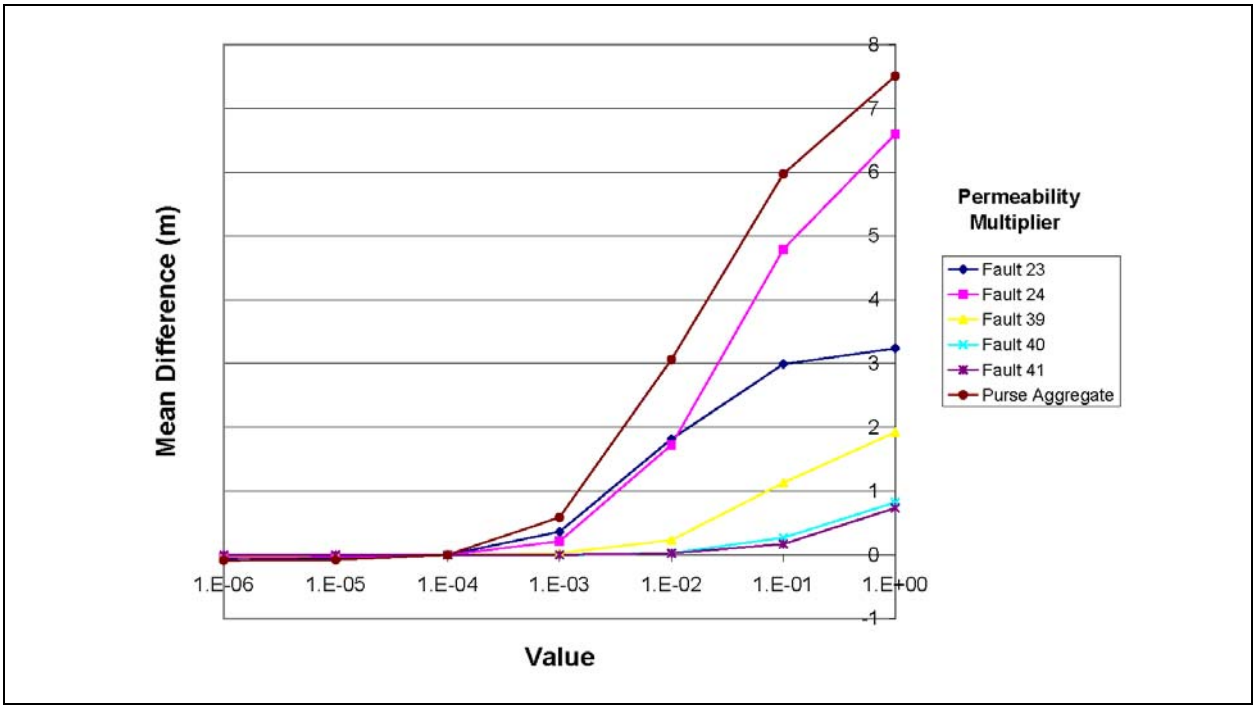

Figure 6-21
Mean Head Difference for Purse Fault Permeability Multipliers for BN-MME-ADA

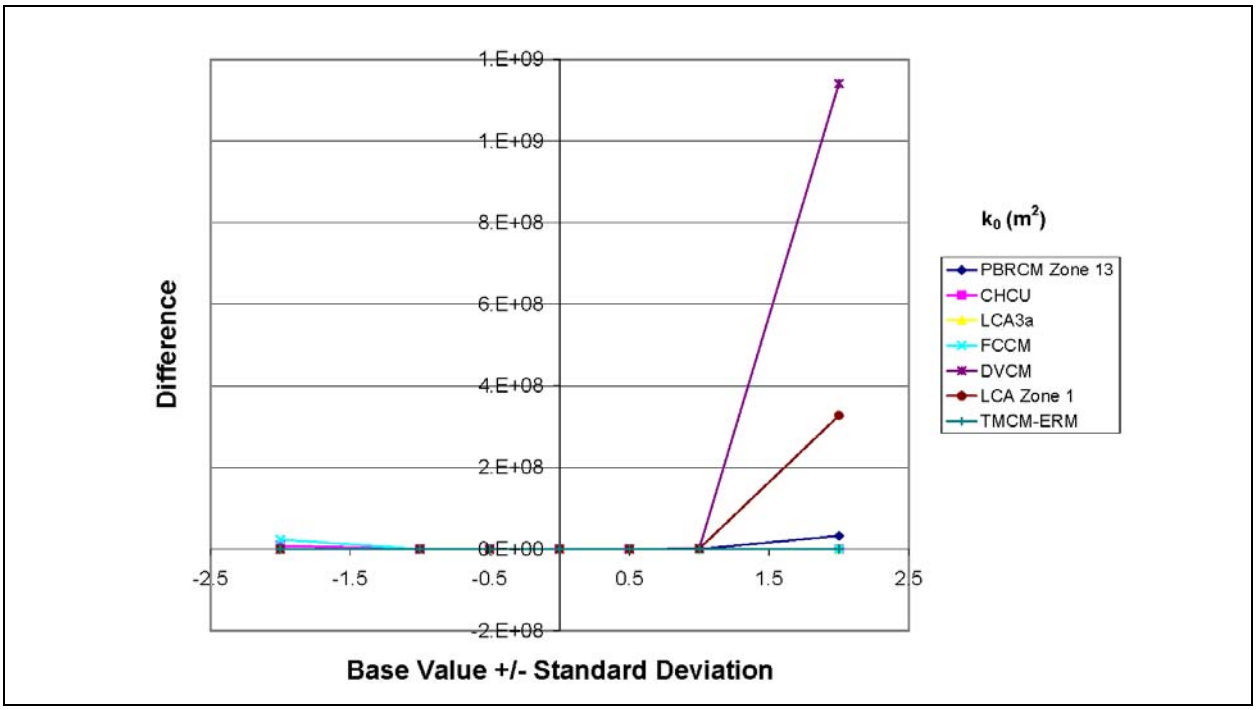

Figure 6-22
PHI Perturbation Plot for BN-MME-ADA

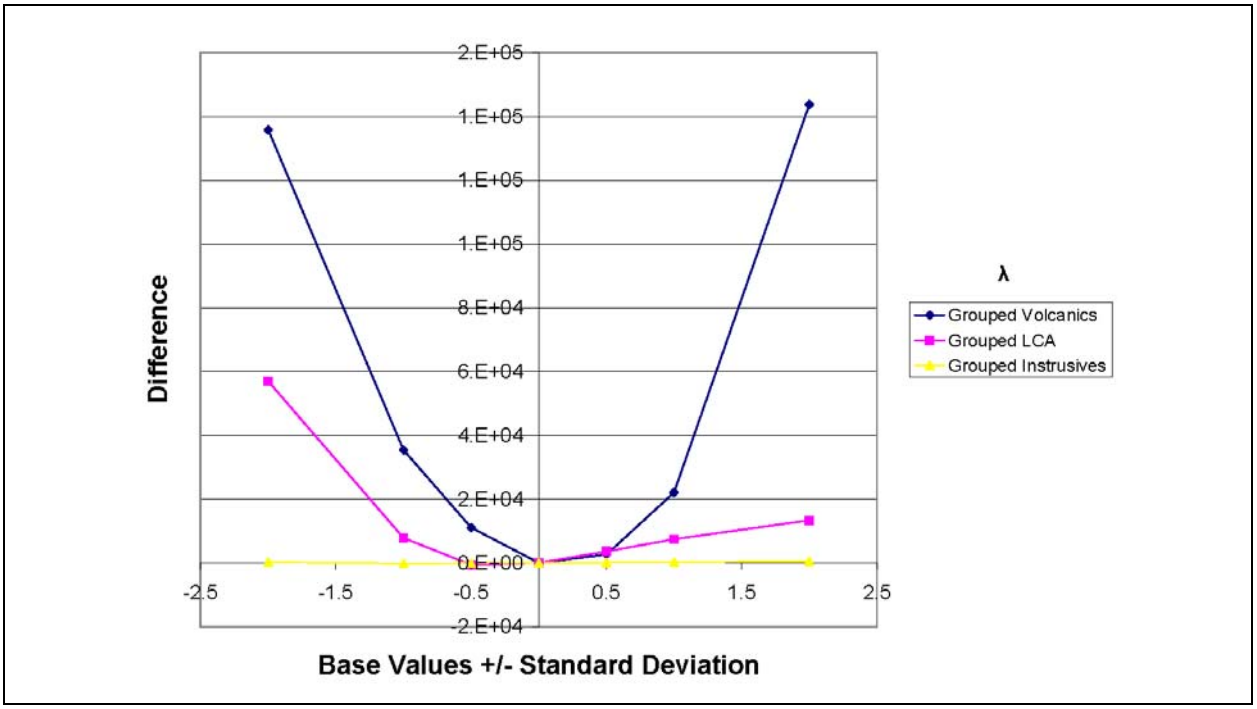

Figure 6-23
PHI Perturbation Plot for Depth Decay for BN-MME-ADA

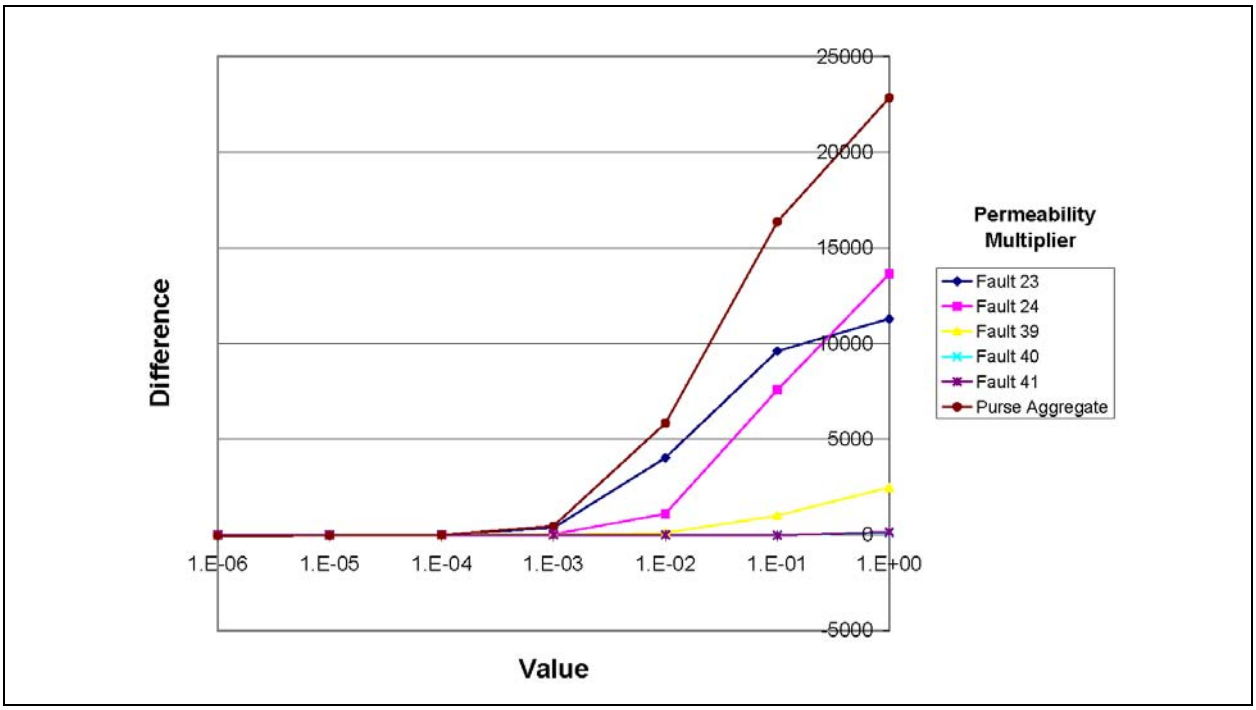

Figure 6-24
PHI Perturbation Plot for Purse Fault Permeability Multipliers for BN-MME-ADA

Pahute Mesa maintains its sensitivity in this model, although the BRA (sensitive in the selected HSU case) drops out. Thus, it seems that the interpretation of the cause of PBRCM sensitivity (presence throughout the CAU model, connection to northern boundary, and presence proximal to a large amount of calibration data) is valid. The sensitivity of the DVCM also suggests that it has a role that is independent of depth decay. In contrast, the IA k_0 appears as a mild influence on mean head, which is not like the selected HSU case.

The impact of the depth-decay parameter (Figure 6-20) of the volcanic HSUs dominates in comparison to the impact for those assigned to the LCA and the ICU; although the overall effect is not as strong as for the reference permeability, it is not negligible. This suggests that uncertainty in the depth-decay parameter (λ) is not, by itself, as critical as the reference permeability and the ICU properties matter very little (at least over the range investigated). Figure 6-21 shows that the fault permeability multipliers of the Purse Fault system and its individual components exhibit a threshold sensitivity relationship where heads increase with an increase in the fault permeability above a multiplier of 0.0001 but heads do not decrease for lower fault permeabilities. The Purse Fault permeability multiplier threshold is 10 times less than that observed for the base HFM - selected HSU

depth-decay and anisotropy parameterization. This may be because in order to maintain the same transmissivity with depth decay as without the permeability, the shallower parts of the HSU must be higher than the average value applied uniformly over the HSU thickness. Thus, a stronger fault to HSU contrast is required to achieve the same sealing effect. The main segment of the fault controls average head the most (it is also the longest individual segment of the Purse Fault system).

Figures 6-22 through 6-24 depict the perturbation plots for the objective function (PHI). Because the PEST sensitivity coefficients and the global sensitivity analysis both focus primarily on the objective function as the model output metric, these plots are most pertinent in comparing the results to those of the other analysis types. It is immediately apparent that most of the parameters shown in Figures 6-22 through 6-24 exhibit highly nonlinear sensitivity relationships over the range through which they were perturbed. This indicates that the sensitivity coefficients calculated by PEST are, in most cases, valid only locally (within a one-half standard deviation of parameter uncertainty or less).

Several other observations can also be made with respect to the perturbation plots of the objective function. Figure 6-22 shows that high values of k_0 for DVCM and LCA Zone 1 (zone along the southeastern edge from the UGTA regional model [DOE/NV, 1997]) have a very large effect on PHI while the large values distort the scale, within about ±1 standard deviation the effects of these parameters are minimal. In contrast, the depth-decay and fault permeability multiplier parameters have a significantly lower impact on PHI at the ends of the range of uncertainty. Figure 6-23 indicates that the minimum PHI with respect to the depth-decay parameters is generally centered (implying that it would be hard to improve the calibration by adjusting k_0) on the calibration point. The largest impact on PHI is coming from the volcanic HSU depth decay and the lowest impact from the depth decay of ICUs. The effects of carbonate HSU depth decay is more similar to ICUs than volcanic HSUs, but non-negligible. Figure 6-24 indicates that the fault permeability multipliers for the Purse Fault and its individual components exhibit a threshold sensitivity with low PHI values occurring for multipliers below approximately 0.0001 (consistent with the mean head behavior). Also, while the main segment of the Purse Fault (fault 24) has the greatest control on mean heads, it is the combined effects of the North Purse Fault (fault 24) and West Purse Fault (fault 23) that contribute to model calibration.

The most sensitive parameters with respect to the objective function are different than for the selected HSU depth-decay and anisotropy parameterization approach. Notably, the IA k_0 has some control on mean heads. Some parameters are sensitive in both this parameterization approach and in the BN-MME-SDA case (see Section 6.2.2.1), including the PCM, YMCFCM, and DVCM. The PCM and YMCFCM have depth decay in the all HSU and selected HSU decay cases, but DVCM does not, and yet it is still sensitive. On the other hand, the LCCU1 permeability was very sensitive without depth decay, but much less so with depth decay (this is explored further in Section 6.2.4.2).

6.2.2.3 SCCC HFM - Selected Depth-Decay and Anisotropy (SCCC-MME-SDA) Model Parameter Perturbation Analysis

For the SCCC HFM – selected depth-decay and anisotropy model (SCCC-MME-SDA), 45 permeability (including k_0) parameters, 10 vertical anisotropy parameters, 15 depth-decay parameters, and 29 fault permeability multiplier parameters were varied. In addition, vertical anisotropy was varied as a single grouped parameter and depth decay was varied as two groups – one for the carbonates and one for the volcanics as well as by HSU. This resulted in approximately 100 parameters that were varied. To generate results for each perturbation case required approximately 600 model runs.

Plots of mean difference in heads, difference in the objective function and its constituents, and difference in boundary fluxes were generated for each of the approximately 100 parameters in the SCCC-MME-SDA model perturbation analysis. All of these plots are shown in Appendix D, but Figures 6-25 through 6-28 describe selected sensitivity relationships.

Figures 6-25 through 6-28 show selected perturbation plots for the mean difference in heads at target locations. These figures indicate that the permeability, k_0, depth decay, and fault permeability multiplier parameters generally exhibit the same type of sensitivity relationships as observed in the base HFM where an increase in a parameter value is accompanied by a consistent trend of either an increase or decrease in the simulated head. In particular, PCM k_0 and DVCM permeability have the same one-sided behavior for all three models analyzed, where average head drops with increasing value; PCM much less so for this HFM. This is reasonable because outside the Silent Canyon Caldera all the HFMs are the same. The PBRCM k_0 also affects heads in the same one-sided fashion in all three models with head rising at higher values. The CHCU permeability, which in the SCCC

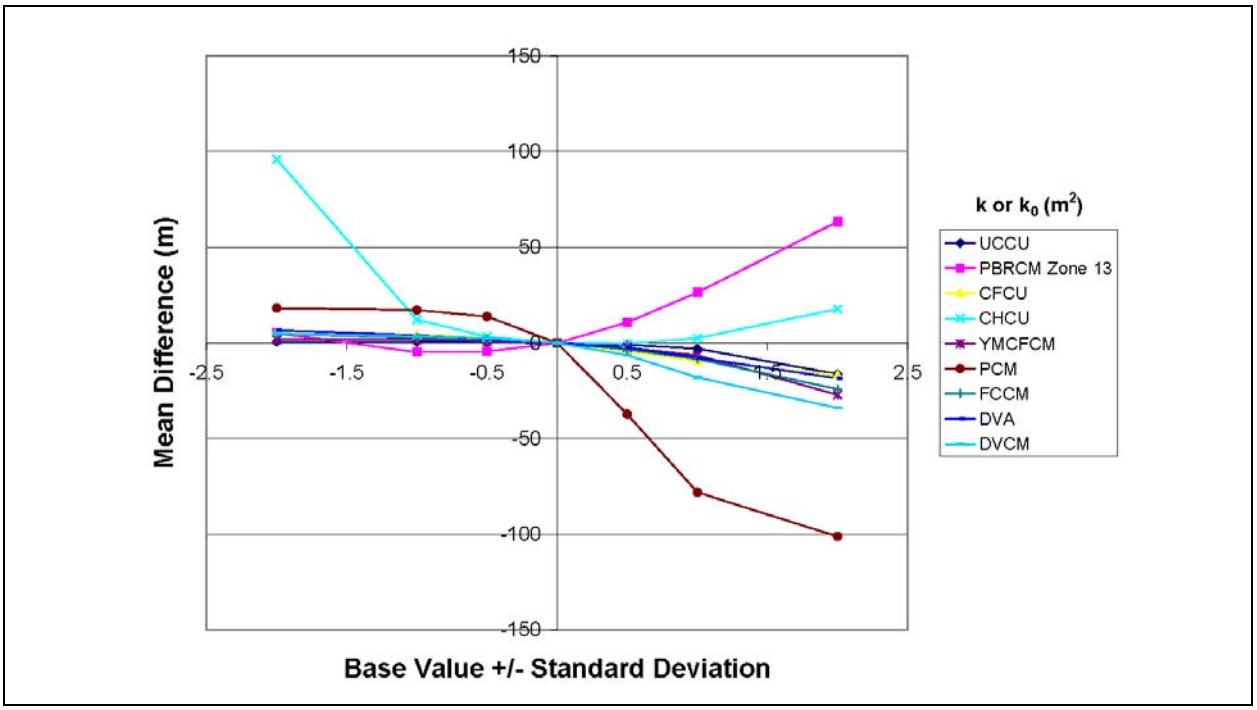

Figure 6-25
Mean Head Difference for SCCC-MME-SDA

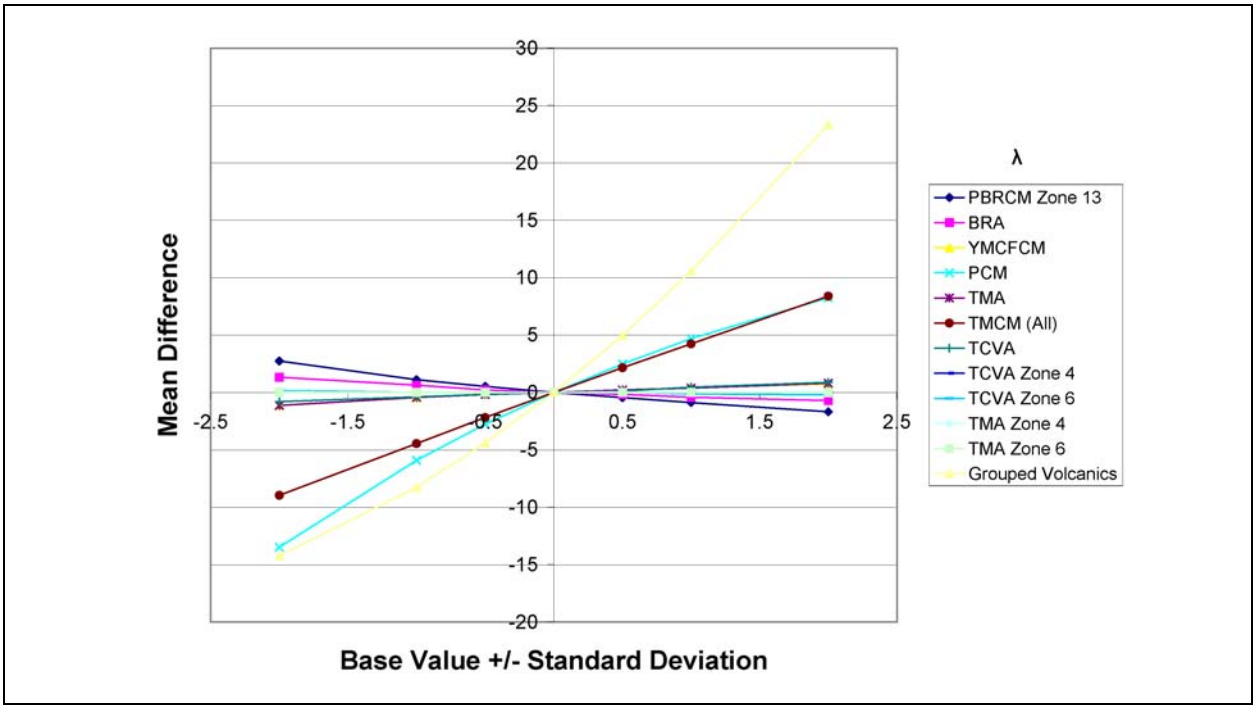

Figure 6-26
Mean Head Difference for Volcanic HSU Depth Decay for SCCC-MME-SDA

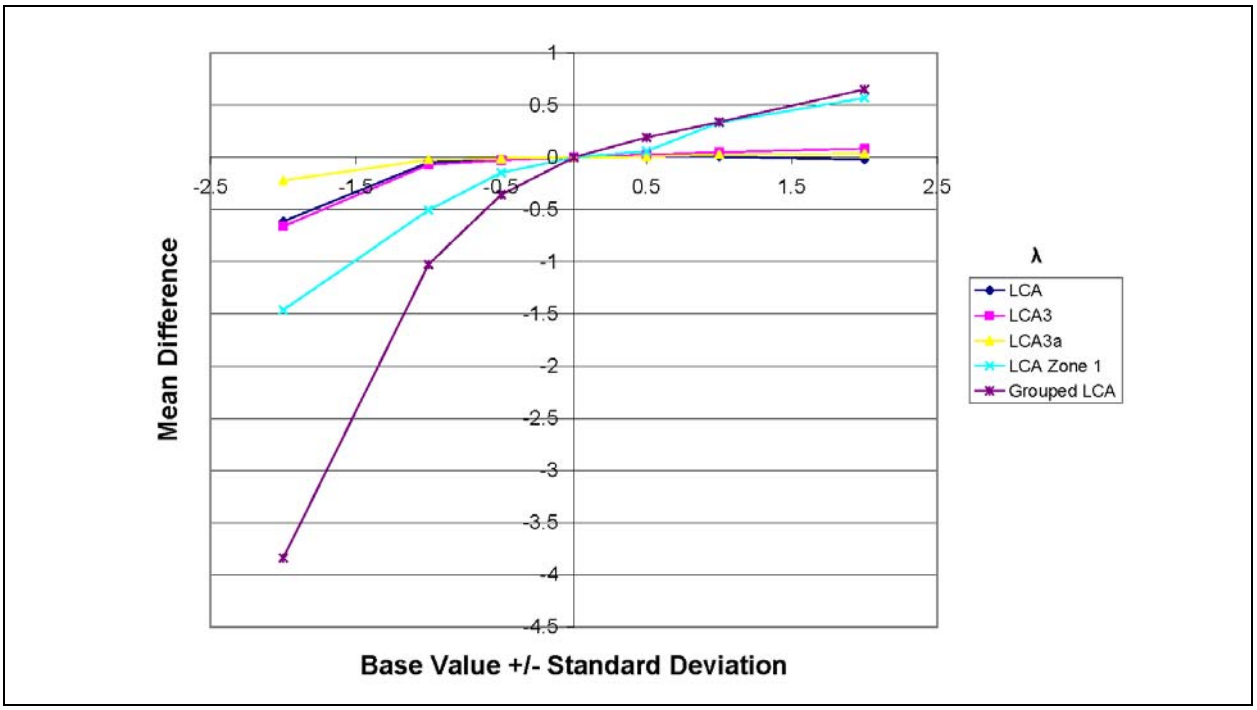

Figure 6-27
Mean Head Difference for Carbonate HSU Depth Decay for SCCC-MME-SDA

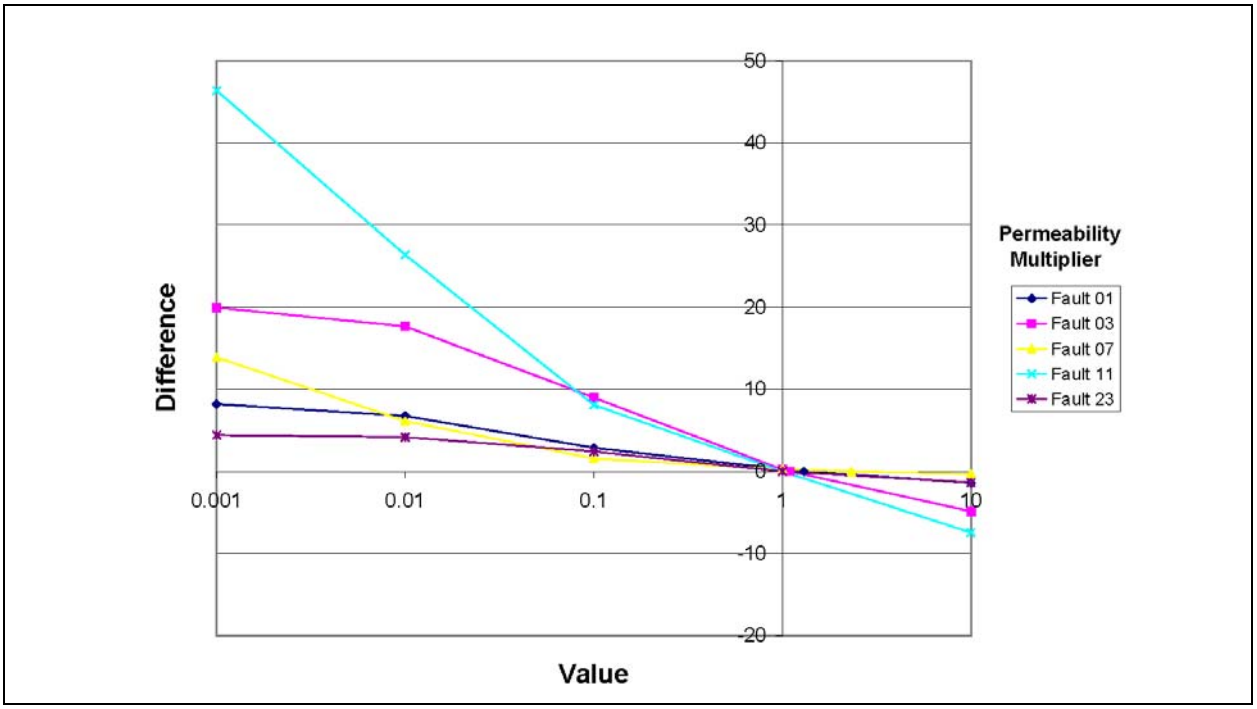

Figure 6-28
Mean Head Difference for Sensitive Fault Permeability Multipliers for SCCC-MME-SDA

HFM represents all the Calico Hills units (represented as five HSUs in the base HFM) affects mean heads the same (always higher) at either the lowest or highest values, and appears as a sensitive parameter because its lumping makes it a relatively large unit with many calibration targets. Physically, the interpretation of the effect of the YMCFCM and PCM to lower heads at increased permeability is to allow water to exit out of and head to drop lower on the southern boundary. The PBRCM effect at higher permeabilities is to increase the influence of areas of higher head to the northeast and east.

The effect of depth decay (Figures 6-26 and 6-27) is larger for the volcanic HSUs than the LCA, most likely because all the head calibration data exist in the volcanic HSUs, with the LCA deriving its sensitivity from the boundary flows. Figure 6-26 shows that it is cumulative effect of depth decay, rather than depth decay of any single unit, that gives depth decay control on mean head, although the PCM (followed closely by the TMCM) is the single most important HSU.

The effects of the faults, shown in Figure 6-28, is similar to the base HFM in that an approximate one-sided behavior is noticed. The faults shown in Figure 6-28, in order of influence on mean head difference, are the Ammonia Tanks Caldera Structural Margin (fault 11), the Claim Canyon Caldera Structural Margin (fault 03), West Greeley (fault 07), Silent Canyon Caldera Margin (fault 01), and the Hogback (fault 23) (see Figure 4-9 for locations). Fault 11 rings Timber Mountain, and as its permeability multiplier is dropped, recharge that occurs there due to orographic effects accumulates and increases heads. The Claim Canyon Caldera Structural Margin is interesting because it was identified in the BN-MME-SDA sensitivity coefficient analysis (see Section 6.2.1.1) as a sensitive feature. The West Greeley Fault, as shown in Figure 4-10, is one of the deepest and most continuous faults in the SCCC HFM, hence its sensitivity. Fault 01 rings most of Areas 19 and 20, and while it is sensitive conceptually, it would be thought that it would have a stronger influence. Finally, the Hogback Fault runs north-south through Oasis Valley, and is thought to exercise some kind of control on heads and flows in that region.

Figures 6-29 through 6-32 present the perturbation plots for the objective function (PHI). Because the PEST sensitivity coefficients and the global sensitivity analysis both focus primarily on the objective function as the model output metric, these plots are most pertinent in comparing the results to those of the other analysis types. It is immediately apparent that most of the parameters shown in

Figures 6-29 through 6-32 exhibit highly nonlinear sensitivity relationships over the range through which they were perturbed. This indicates that the sensitivity coefficients and other statistical diagnostics calculated by PEST are, in most cases, valid only locally in the vicinity of the calibration point.

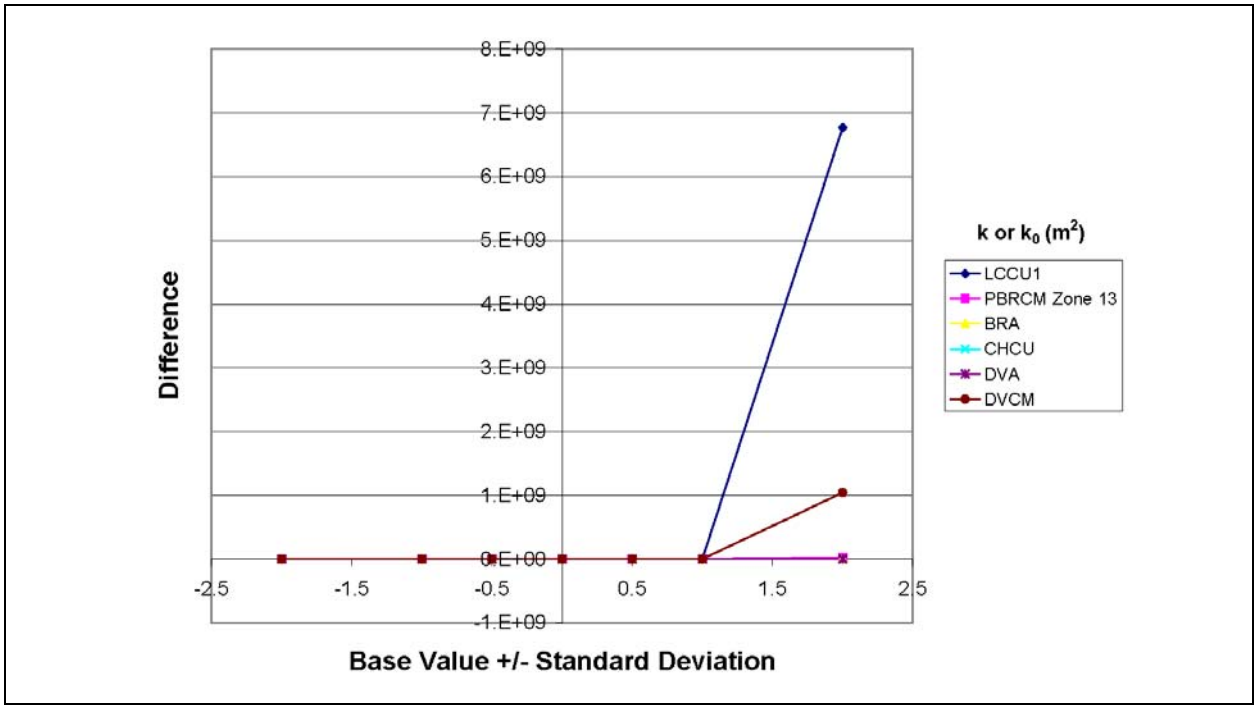

Figure 6-29
PHI Perturbation Plot for SCCC-MME-SDA

Several other observations can also be made with respect to the perturbation plots of the objective function. Like the selected HSU depth-decay and anisotropy base HFM, Figure 6-29 shows that higher permeability for LCCU1 and DVCM have a very large effect on PHI. The role of the LCCU1 in the base HFM selected HSU depth decay and anisotropy is the same as in the SCCC HFM, and it is concluded that adding depth decay to the LCCU1 causes a fundamental change in how the unit acts in the model. It was noted in Section 5.6.3 that WW-8 had the largest misfit in the all HSU depth-decay case, but is reasonably fit in the selected HSU approach even with two different HFMs (although outside the Silent Canyon Caldera the HFMs are the same). The depth-decay and fault permeability multiplier parameters have a significantly lower impact on PHI, although relative to the calibration, the PCM depth decay almost completely dominates the volcanic HSU depth-decay parameter sensitivity on PHI. Figure 6-30 indicates that the minimum PHI with respect to the volcanic

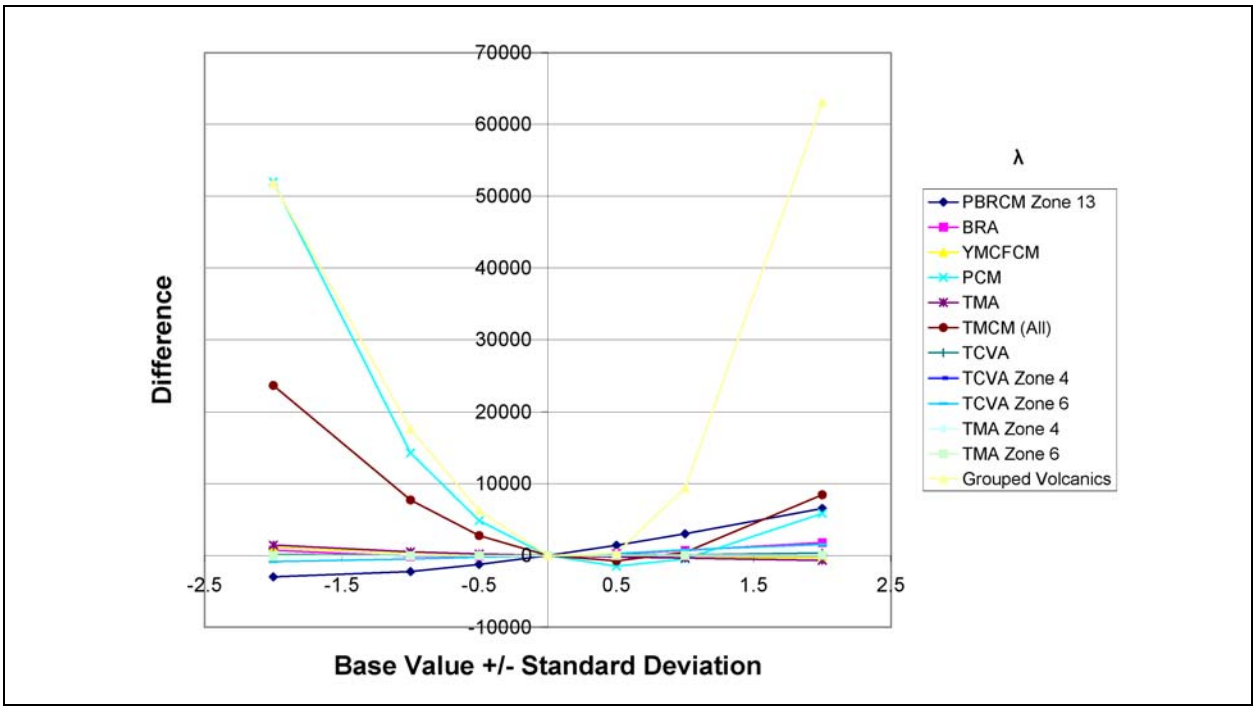

Figure 6-30
PHI Perturbation Plot for Volcanic HSU Depth Decay for SCCC-MME-SDA

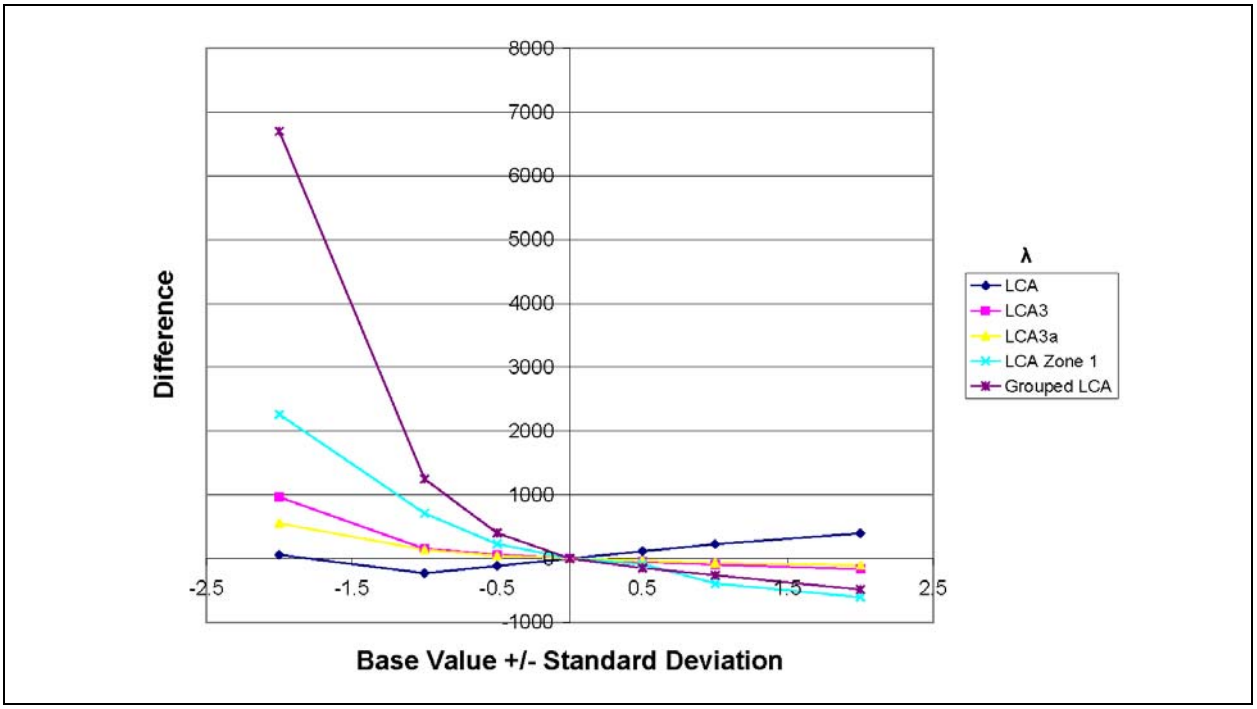

Figure 6-31
PHI Perturbation Plot for Carbonate HSU Depth Decay for SCCC-MME-SDA

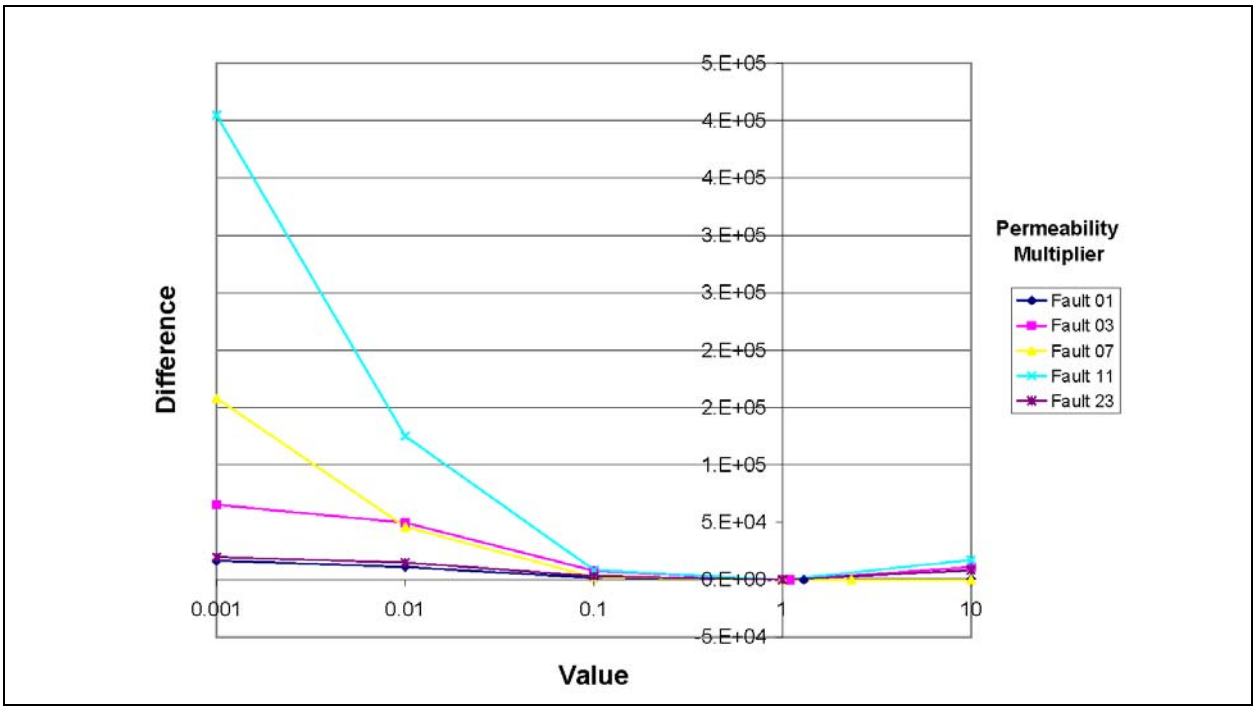

Figure 6-32
PHI Perturbation Plot for Sensitive Fault Permeability Multipliers for SCCC-MME-SDA

depth-decay parameters is generally centered on the calibration point. In contrast, the minimum PHI with respect to the carbonate depth-decay parameter occurs at values higher than the calibrated value as seen in Figure 6-31, although the effect is minor. Figure 6-32 shows the perturbation plots for the most sensitive faults in the SCCC HFM - selected depth-decay and anisotropy model. Dropping the fault permeability multiplier for the Silent Canyon Caldera Margin causes degradation in model fit, while enhancing the fault causes no improvement. Again, there is little sensitivity to the Purse and Boxcar Faults because their limited depth does not give a strong model response. The most sensitive fault is the Ammonia Tanks Caldera Structural Margin (fault 11) ringing Timber Mountain. The West Greeley Fault (fault 07) is also sensitive in controlling calibration on Pahute Mesa, at least in part because it extends to a greater depth on Pahute Mesa than most other faults in the SCCC HFM (see Figure 4-11).

6.2.3 Global Parameter Sensitivity

The motivation for this analysis is described in Section 6.1.1.2. The work flow for the global sensitivity analysis was as follows:

1. Identify adjustable parameters and their ranges.
2. Determine form and components of objective function used for model calibration.
3. Create an experimental design that uniformly samples parameter space.
4. Run forward model for each design point and compute the objective function.
5. Analyze variable importance with respect to objective function.

The adjustable model parameters can be broadly divided into three categories: (a) permeability (including k_0) of the HSUs and the faults (permeability multiplier), (b) anisotropy ratios for a limited number of HSUs, and (c) depth-decay parameters for HSU groups. The parameters were assigned log-normal/normal or log-uniform/uniform distributions to capture the expected range over which they are realistically expected to vary. The central tendency value for each distribution was taken to be the best estimate from the calibrated models.

The objective function is the standard weighted sum-of-squares form, and has four components including: (1) measured heads at observation wells, (2) estimated model boundary flows, (3) spring heads, and (4) Oasis Valley flow. Each observation was assigned a unique weight as described in Section 5.2. Weights were chosen to reflect measurement error and/or reliability of the individual measurement, as well as judgment of the relative importance of different kinds of measurements.

Sampling of the adjustable parameters over the assigned range was carried out using Latin Hypercube sampling, an efficient modification of Monte Carlo random sampling. In order to ensure that this stratified sampling approach does not produce any spurious correlation between any two arbitrary parameters, the restricted pairing technique (Iman and Conover, 1979) was used to force zero correlation between all variable pairs. This strategy produces a "space-filling" design such that all regions of an input-input scatter plot would appear to be equally filled by the sampling scheme. A sample size of 1,000 was chosen as a compromise between sampling density and computational overhead. Forward simulations were carried out for each of the 1,000 sample sets of parameters, and the components of the objective function computed.

After eliminating the non-convergent realizations, classification tree analyses were completed using the lowest 10 percent and the highest 10 percent values of each metric. The rationale for using the 10 percent cutoff is to generate a subset with about 100 realizations so that statistical sensitivity analysis techniques can be applied to produce results with a reasonable degree of reliability. The R-statistical software (Gentleman and Ihaka, 2005) was used for the classification tree analysis. Entropy analyses were completed on the entire dataset for each metric. Model-specific details are given in the results section for each model.

In interpreting classification tree results, it is important to remember that the category "low" refers to the smallest 10 percent PHI values and the category "high" refers to the largest 10 percent PHI values. Each node of a classification tree is labeled with the number of each category that has cascaded to that node, with the number of "high" values comprising the first and the number of "low" values comprising the second. For example, "68/0" indicates that 68 from the "high" category have cascaded to the node. A perfect categorization can be obtained with just two splits. Also, some judgment of the importance of the variables can be made from the structure of the tree itself.

6.2.3.1 Base HFM - Selected HSU Depth-Decay and Anisotropy (BN-MME-SDA) Model

Of the 1,000 Monte Carlo realizations performed to identify key parameters for the base HFM - selected HSU depth-decay and anisotropy (BN-MME-SDA) model, approximately 17 percent did not converge. Global sensitivity analyses of the 83 percent remaining simulations are presented below.

Figure 6-33 shows a line plot of the best 100 percent simulations ranked in terms of PHI. Also shown are the components of PHI based on head measurements (WELL), boundary fluxes (FLUX), spring elevations (SPRING) and Oasis Valley discharge (ETF). It is clear that the primary contributors to PHI are WELL and FLUX, with lesser contributions from ETF and SPRING. Another interesting observation is that simulations where WELL is the dominant contributor to PHI are distinct from simulations where FLUX is the dominant contributor. This suggests that these two components of the objective function are controlled by different groups of model parameters.

Table 6-2 shows the Spearman rank correlation matrix for PHI, WELL, SPRING, FLUX and ETF for the simulations with the lowest 10 percent PHI values (the data shown in Figure 6-34). The strong correlation between PHI and WELL and PHI and FLUX noticed in Figure 6-34 can be clearly

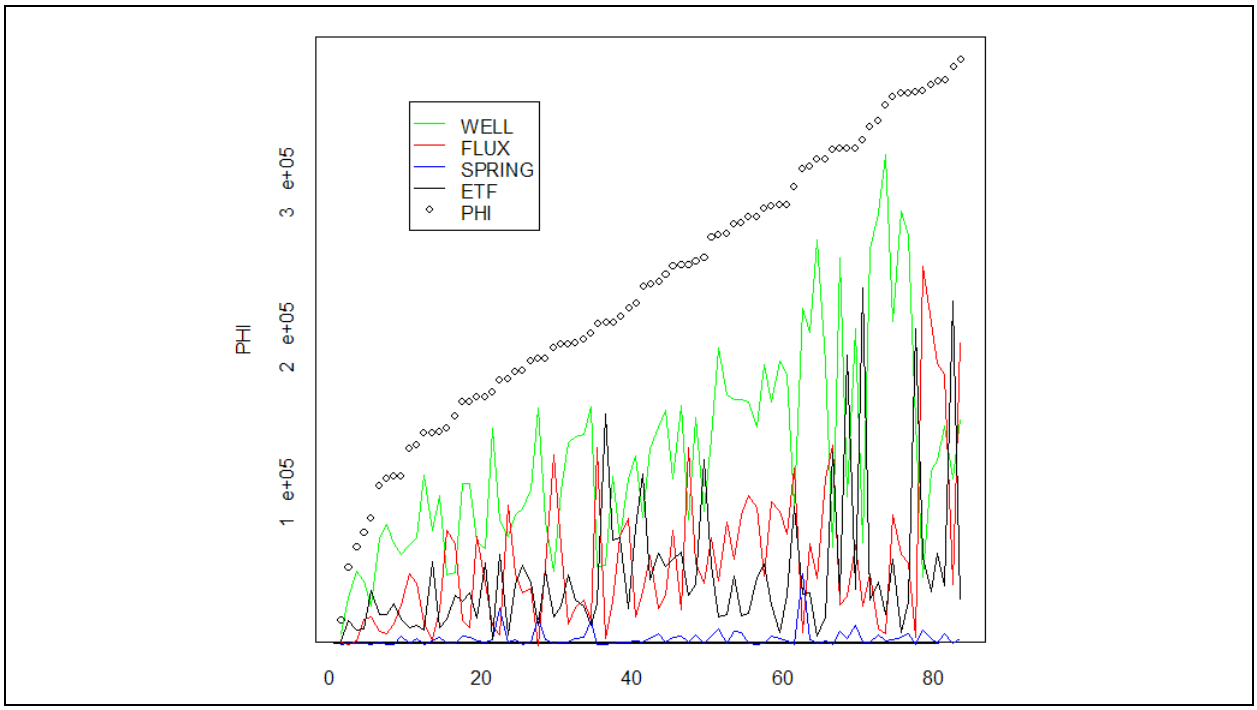

Figure 6-33
100 Best Simulations Ranked by PHI for BN-MME-SDA

Table 6-2
Spearman Rank Correlation Matrix for BN-MME-SDA

	PHI	WELL	SPRING	FLUX	ETF
PHI	1	0.66	0.26	0.49	0.39
WELL	0.66	1	0.46	0.11	-0.03
SPRING	0.26	0.46	1	0.03	-0.04
FLUX	0.49	0.11	0.03	1	0.05
ETF	0.39	-0.03	-0.04	0.05	1

discerned in this table. Also note the strong correlation between WELL and SPRING, suggesting a common set of controlling parameters for these two components of the objective function.

In the following classification tree analyses, the logarithm of permeability will be presented; all other variables will be untransformed. This results in negative numbers because permeability units are m^2, which nearly always has a negative exponent.

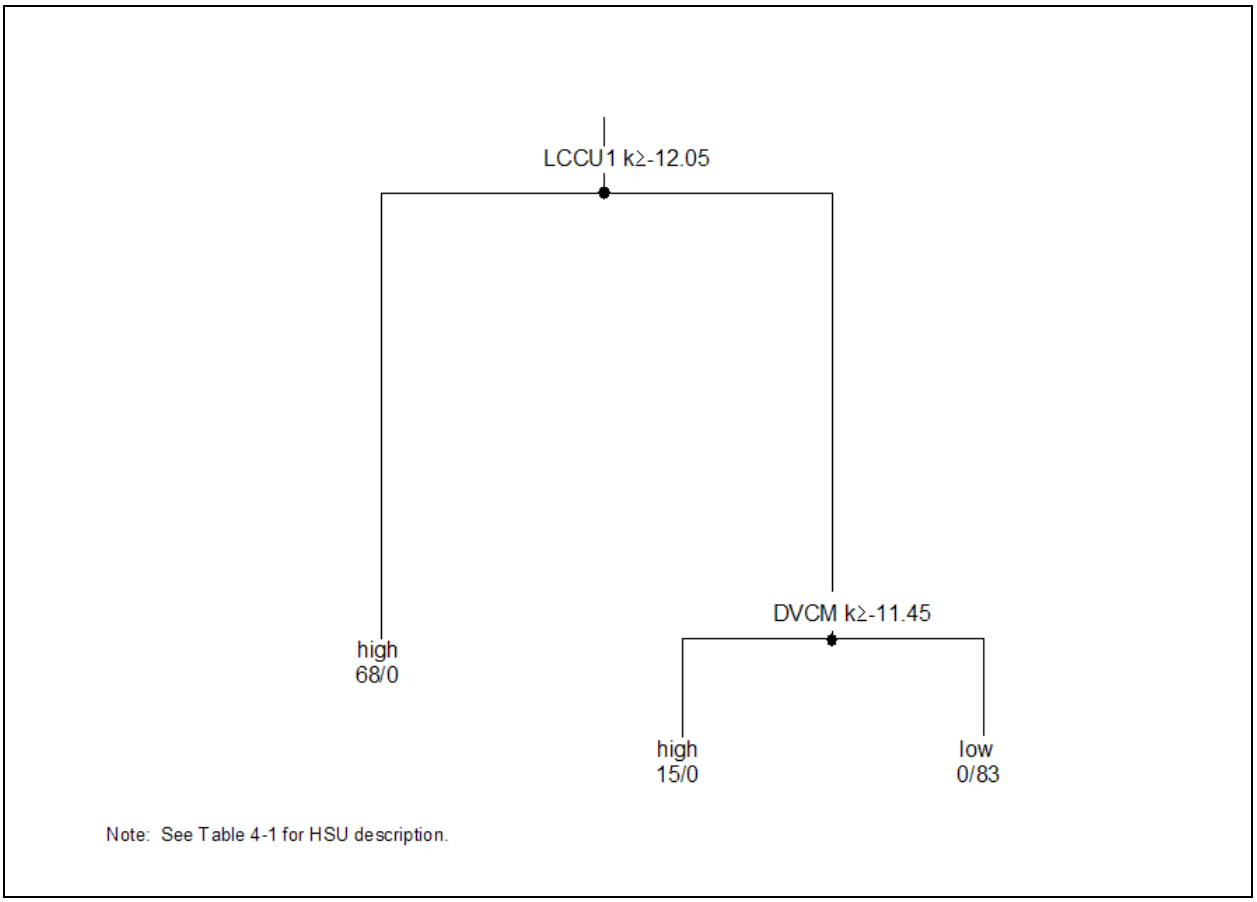

Figure 6-34
Classification Tree on PHI for BN-MME-SDA

A classification tree analysis to determine the decision rules separating the smallest and largest 10 percent of PHI values in Figure 6-33 is shown in Figure 6-34. Here, LCCU1 permeability is the most important because it was chosen for the first split, followed by DVCM permeability. Recall that these parameters were also identified in the sensitivity coefficient and parameter perturbation analyses. The fact that they are identified in the global sensitivity analysis means that their sensitivity is not just a local effect, and that they exercise control on PHI over the full range of possible model outcomes and parameter uncertainty.

The next set of analyses deal with the individual components of PHI. Figure 6-35 shows a classification tree analysis for WELL. Note that the important variables for this case, YMCFCM and PCM reference permeability, are different from those identified earlier for the total objective function (PHI). Also note that the two-variable classification does not produce two pure groups, because the

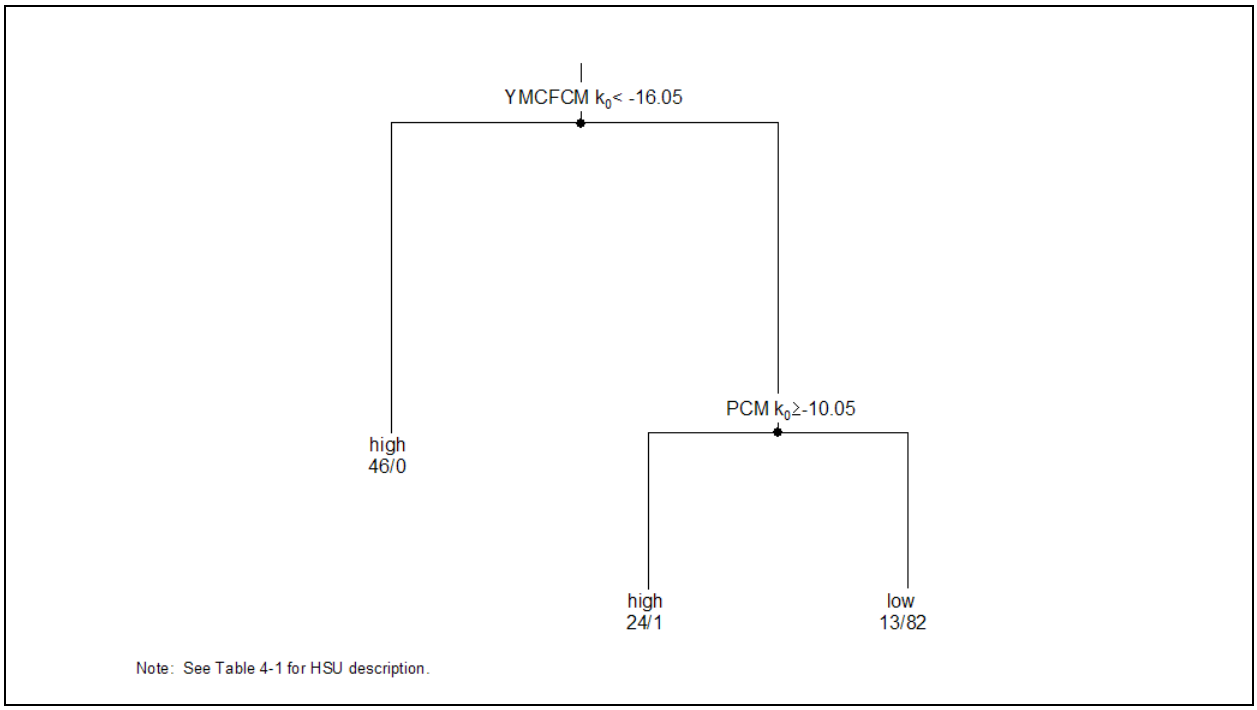

Figure 6-35
Classification Tree on WELL for BN-MME-SDA

node at the far right-hand side of the tree contains 13 high and 82 low values. Thus, the isolation of the group corresponding to the smallest 10 percent of WELL values is not as straightforward as in the case of PHI. Again, the reference permeabilities of YMCFCM and PCM have been previously identified as having an important role in controlling mean head in the model domain and the goodness-of-model calibration.

A similar situation can be seen in the classification tree analysis for SPRING. Figure 6-36 shows the classification tree for SPRING. The lowest 10 percent SPRING values cannot be perfectly explained using two or three variables. Also, the key variables controlling the "low" SPRING values (i.e., PCM k_0 and YMCFCM k_0) are the same as those controlling the lowest 10 percent WELL values (hence the correlation in model output shown in Table 6-2).

Figure 6-37 presents the classification tree separating the subset of FLUX values. The main parameter that influences this model output, almost exclusively by the purity of the split, is LCCU1 permeability. These are very similar to those presented earlier for the total objective function PHI, and primarily reflect the strong correlation between high PHI and high FLUX values. The conclusion

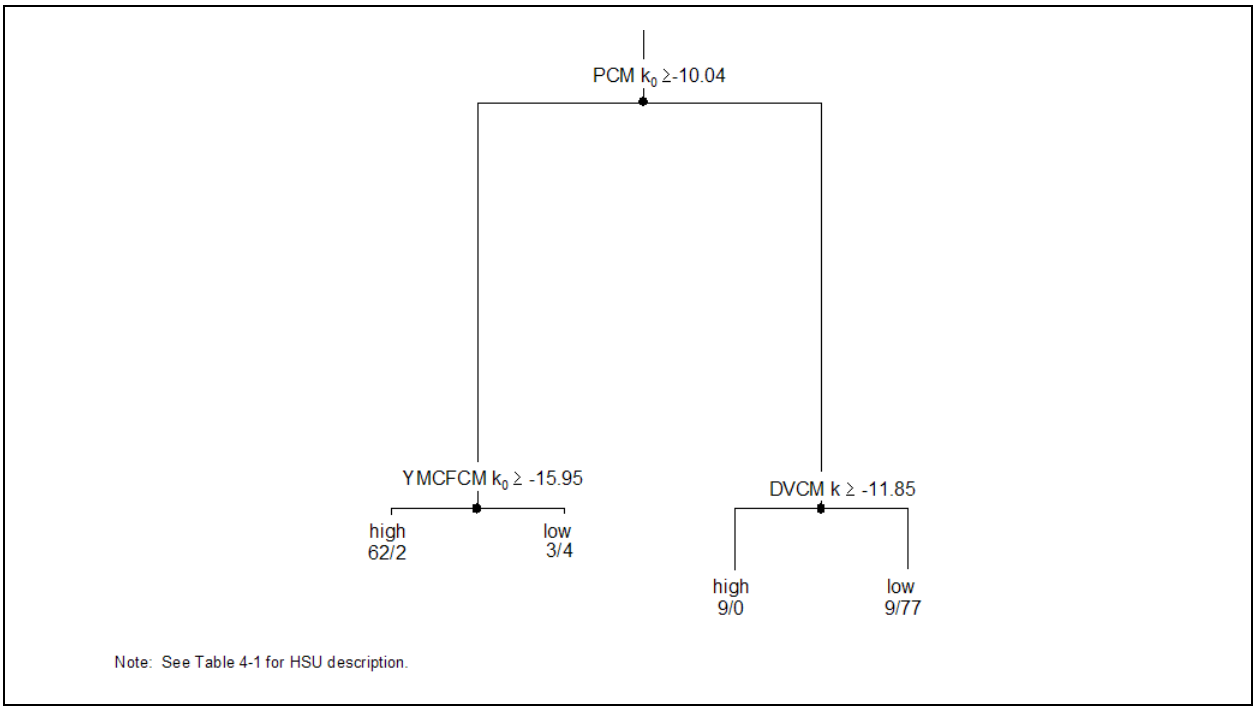

Figure 6-36
Classification Tree on SPRING for BN-MME-SDA

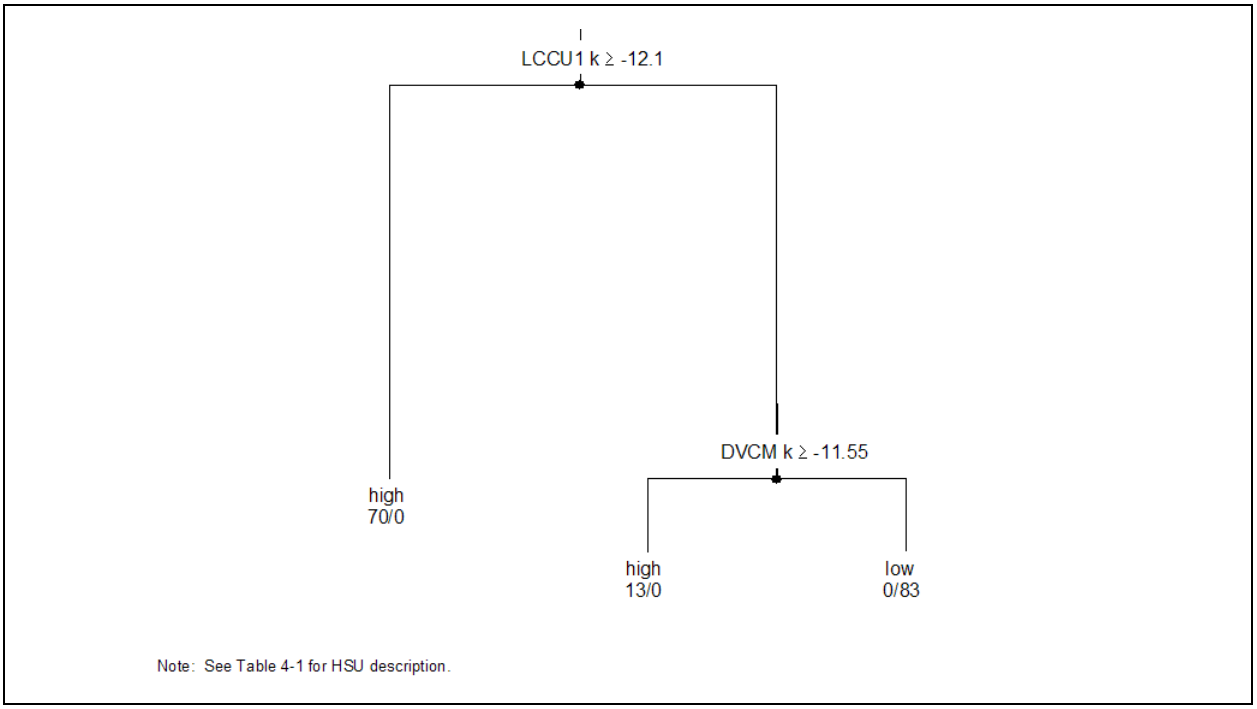

Figure 6-37
Classification Tree on FLUX for BN-MME-SDA

to be drawn from this observation is that combinations of parameter values that produce high FLUX (e.g., high LCCU1 permeability) values are incompatible with low PHI values.

Finally, the classification tree for Oasis Valley discharge is presented in Figure 6-38. Here, a two-variable split is almost perfectly capable of separating the ETF values. Also of interest is the fact that one of the important variables (DVCM permeability) was also identified as important in isolating low values for FLUX and SPRING.

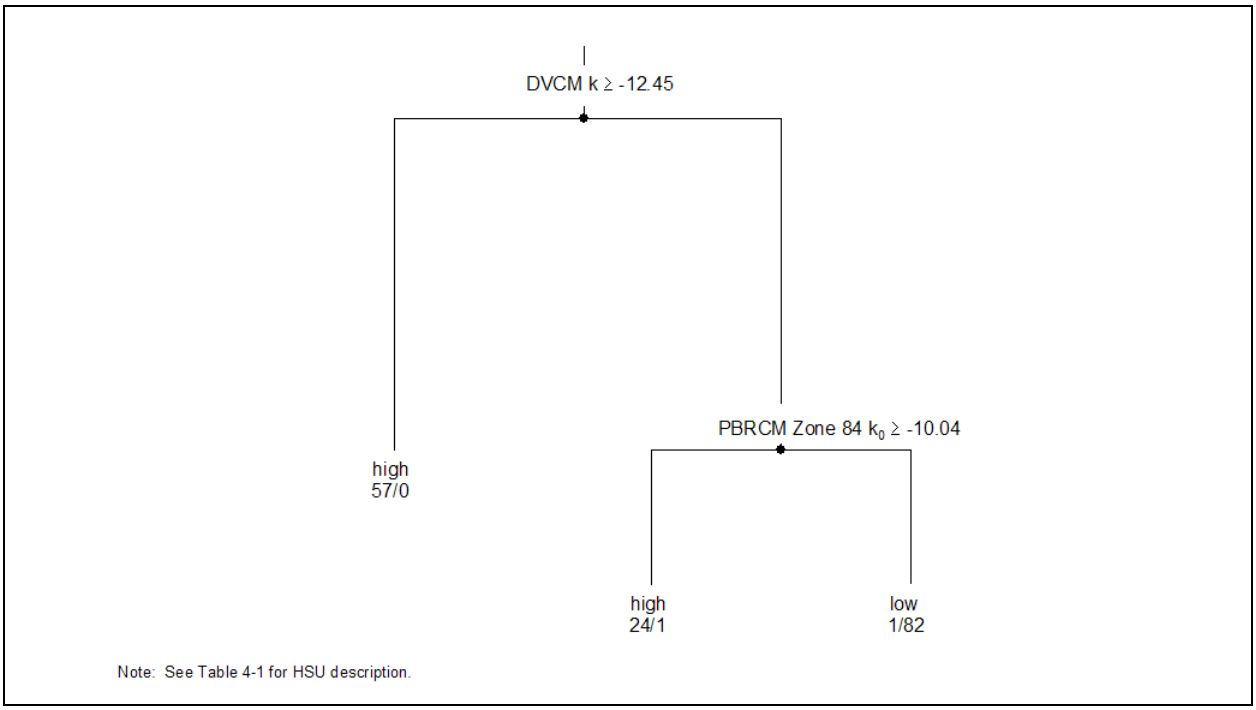

Figure 6-38
Classification Tree on ETF for BN-MME-SDA

The entropy analysis for PHI is shown in Table 6-3. Based on the R-statistic, the top two variables have distinct patterns of association with PHI, and also happen to be the same in order of importance as the top two variables identified from classification tree analysis in Figure 6-34. The other variables appear to have less definitive association.

Figure 6-39 shows bubble plots for the top four variables, where the entries of the contingency table are shown as bubbles of varying sizes. Here, the contingency table is organized such that the quintiles (0-20 percentile, 20-40 percentile, 40-60 percentile, 60-80 percentile, 80-100 percentile) of the

Table 6-3
Results of Entropy Analysis on PHI for BN-MME-SDA

Rank	Variable	R-Statistic
1	LCCU1 k	0.68
2	DVCM k	0.46
3	PBRCM Zone 84 k_0	0.30
4	PCM k_0	0.22
5	TCVA λ	0.19

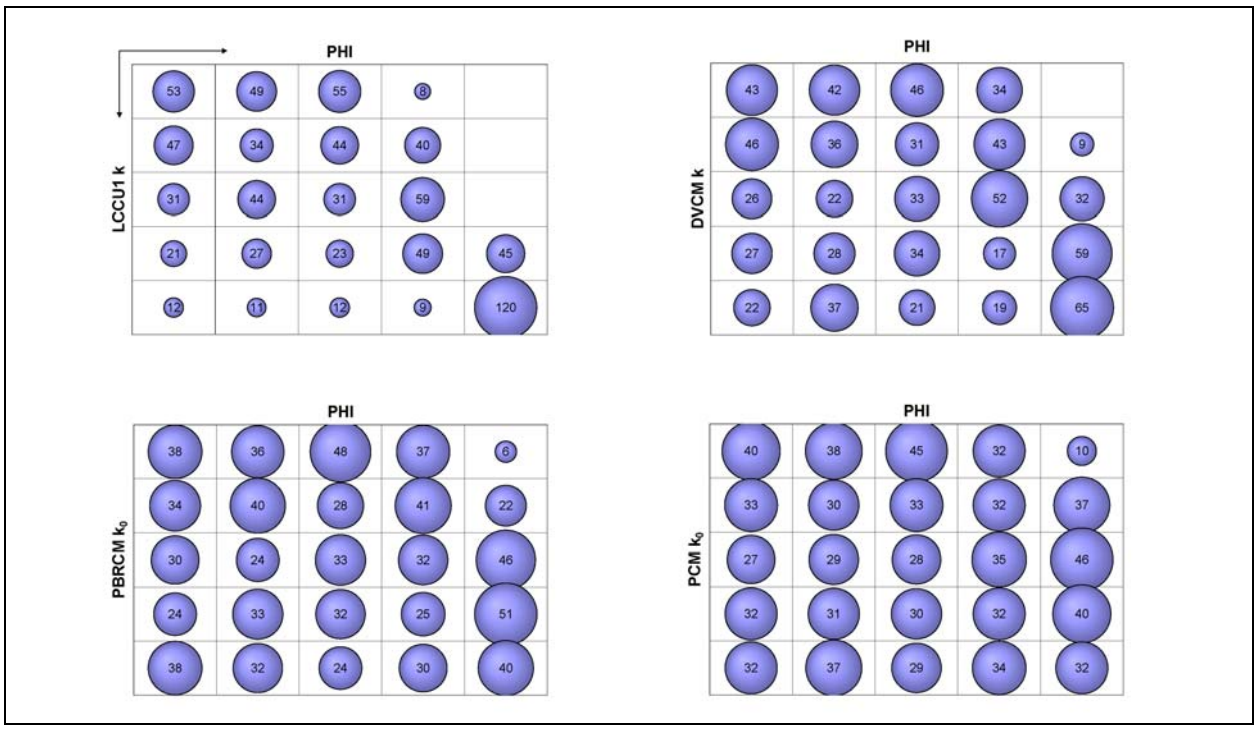

Figure 6-39
Bubble Plots from Entropy Analysis on PHI for BN-MME-SDA

independent variable (input) increase from left to right, and that of the dependent variable (output) increase from top to bottom. The size of the bubble indicates how many observations fall in each quintile-quintile box. The relative importance of the top two variables, LCCU1 and DVCM, is clearly seen through the distinctive patterns in the upper panels. On the other hand, the near-uniform size of the bubbles in the bottom charts indicates the marginal relevance of the other two top-ranked variables.

Results for the entropy analysis of WELL are shown in Table 6-4. Based on the R-statistic, the top two variables are not as dominant or as distinctive as those corresponding to PHI. Also, the order of importance is reversed as compared to the importance ranking from classification tree analysis shown in Figure 6-35. The effects of PCM k_0 and YMCFM k_0 are also opposite; many good results are associated with high values of YMCFCM k_0 and many good results are associated with lower PCM k_0. This effect was also noticed in the perturbation analysis. Because the perturbation analysis sampled for the same distribution types and parameters, the results are similar. However, the global analysis would allow any compensating effects to manifest themselves, and either there are not any or the sample set is too small. The absence of distinctive input-output patterns can also be seen in the bubble plots presented in Figure 6-40, where even the top two variables (top panel) do not appear to be significantly different from the next two variables (bottom panel) in terms of exhibiting distinctive trends.

Results for the entropy analysis for FLUX are given in Table 6-5, with the corresponding bubble plots presented in Figure 6-41. The top two variables (LCCU1 and DVCM permeability) are the same as those identified by the classification tree analysis for FLUX in Figure 6-37 and were noted as sensitive in the sensitivity coefficient and perturbation analyses. As noted earlier, the top-ranked variables for PHI and FLUX are identical, suggesting that a strong correlation between high PHI and high FLUX values may be influencing these results. As mentioned previously, the thrusted LCCU (LCCU1) permeability is unknown, and it seems odd conceptually that it should have an important role in the flow model. It is possible to generate reasonable results at lower LCCU permeability as shown in Figure 6-41, but poor results are strongly associated with the highest values. Thus, while a great deal of uncertainty exists in LCCU1 permeability, at least the upper limit is implausible, and lower values may be more appropriate. Section 6.2.4.2 and Section 7.0 explore this further.

Table 6-4
Results of Entropy Analysis on WELL for BN-MME-SDA

Rank	Variable	R-Statistic
1	PCM k_0	0.34
2	YMCFCM k_0	0.32
3	PBRCM Zone 84 k_0	0.22
4	CFCU k	0.20
5	DVCM k	0.20

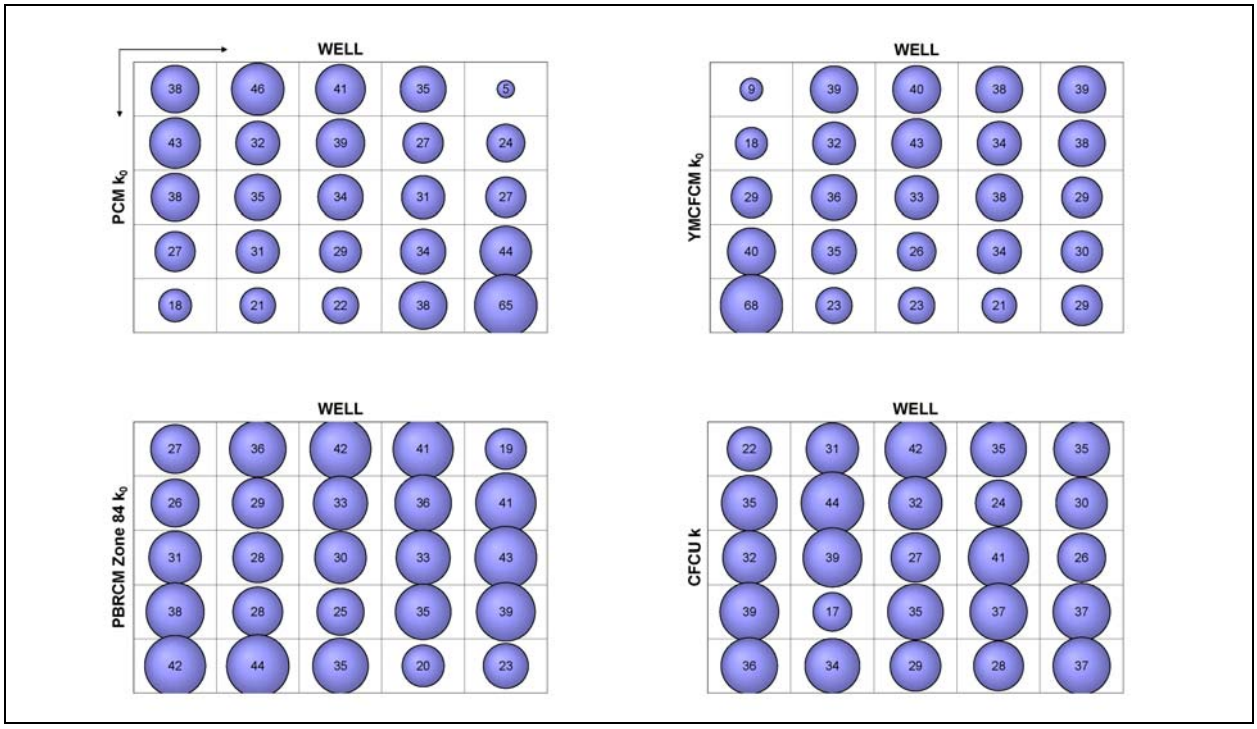

Figure 6-40
Bubble Plots from Entropy Analysis on WELL for BN-MME-SDA

Table 6-5
Results of Entropy Analysis for FLUX for BN-MME-SDA

Rank	Variable	R-Statistic
1	LCCU1 k	0.72
2	DVCM k	0.53
3	PBRCM k_0	0.24
4	PCM k_0	0.24
5	PBRCM k_0	0.23

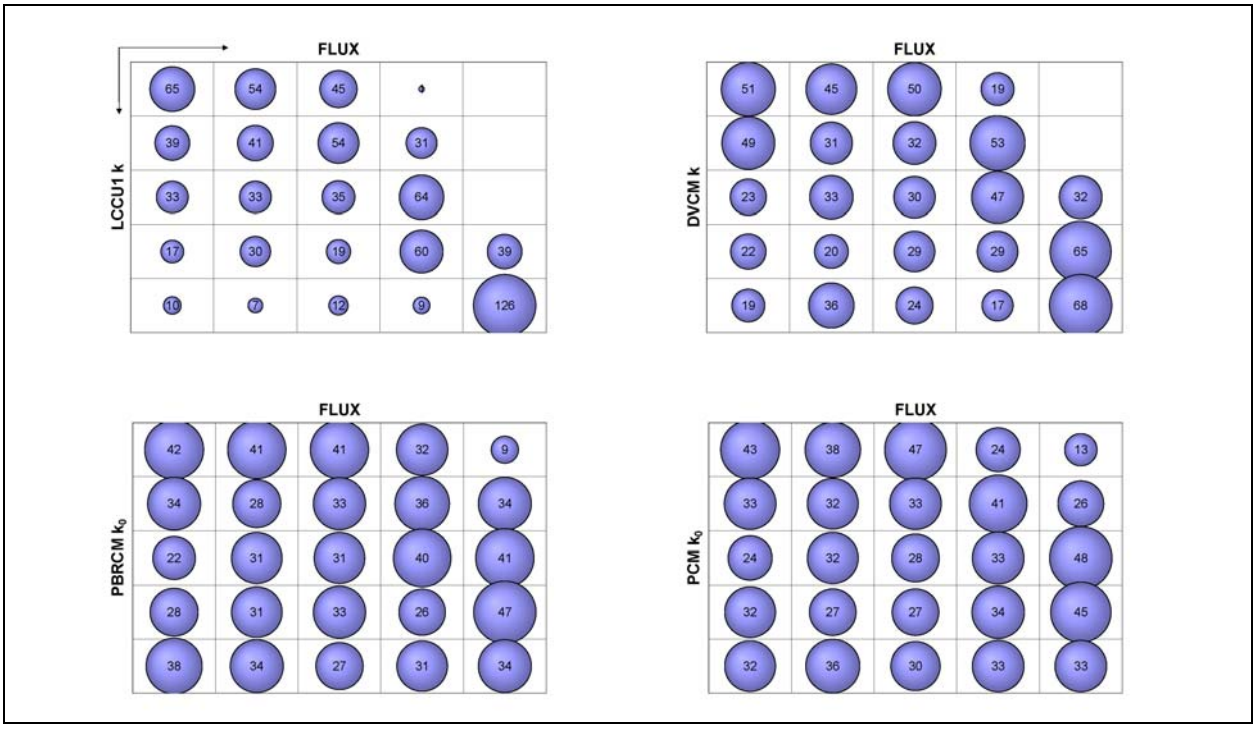

Figure 6-41
Bubble Plots from Entropy Analysis on FLUX for BN-MME-SDA

6.2.3.2 Base HFM - All HSU Depth-Decay and Anisotropy (BN-MME-ADA)

Global sensitivity analysis using Monte Carlo simulation to identify key parameters for the base HFM - all HSU depth-decay and anisotropy case required about 200 parameters to be varied over the 1,000 realizations generated. Approximately 29 percent of the simulations did not converge. Figure 6-42 shows a line plot of the best 10 percent of simulations ranked in terms of PHI, along with its various components. The most consistent and largest contributor to PHI is WELL, with some intermittent contribution by FLUX and ETF and a marginal contribution from SPRING. This is by design through the choice of calibration target weights as described in Section 5.2. This figure also shows that when FLUX and ETF have a significant contribution, WELL does not. This suggests that these two components of the objective function are controlled by different groups of input parameters. This behavior is also noticed in the selected HSU depth-decay and anisotropy parameterization of the base HFM; thus, the effect of parameterization approach does not broadly change model performance.

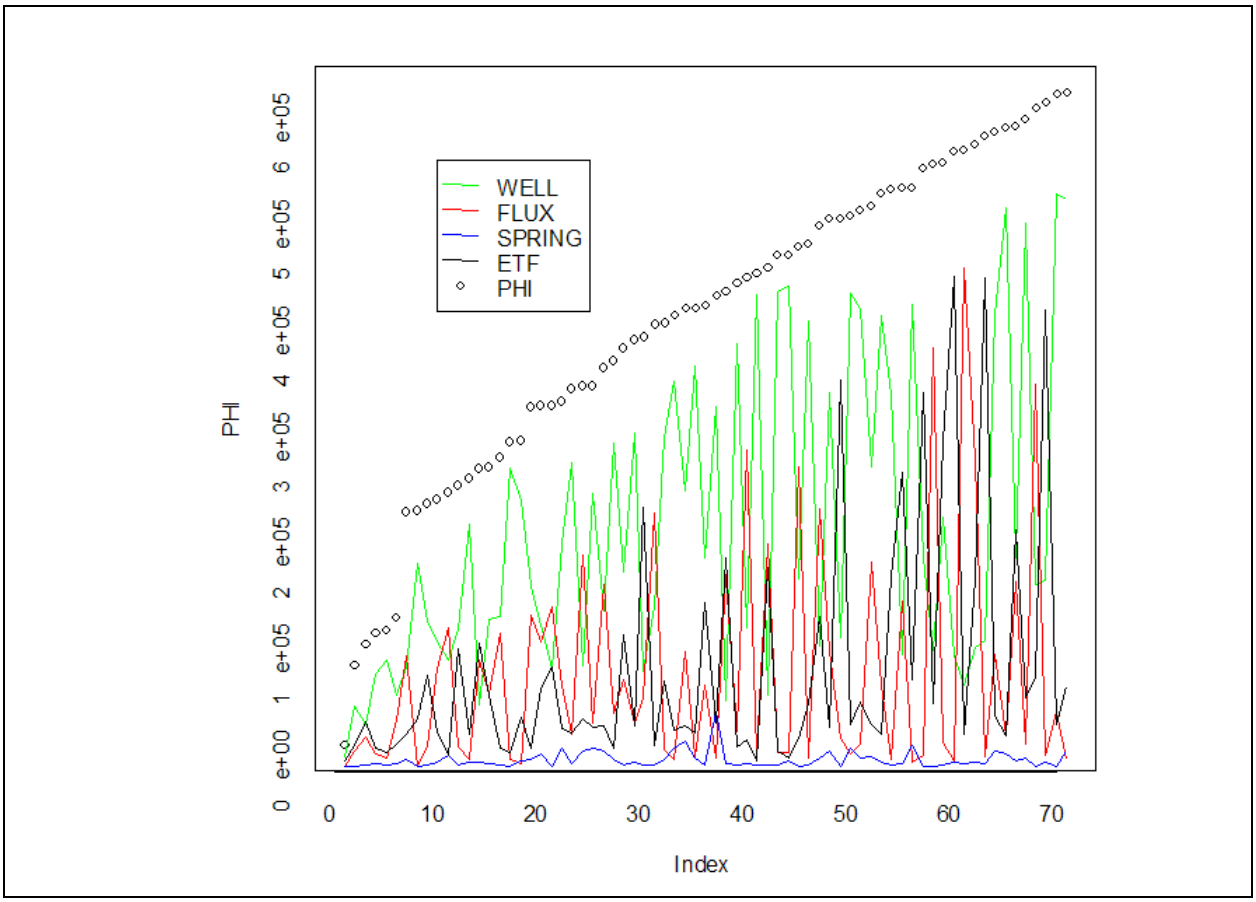

Figure 6-42
100 Best Simulations Ranked by PHI for BN-MME-ADA

Table 6-6 shows the Spearman rank correlation matrix for the best 10 percent of simulations ranked by objective function. WELL has the highest correlation with PHI at 0.47. ETF and PHI also have a relatively high correlation at 0.44. Also note the relatively high correlation between WELL and SPRING at 0.37, and the negative correlation (-0.35) between WELL and FLUX. The correlation of PHI and WELL is also noticed in the selected HSU depth-decay and anisotropy case, as is the correlation between WELL and SPRING. However, the correlation between FLUX and WELL is positive in the aforementioned case, but is negative in Table 6-6. The parameter dominating FLUX in the selected HSU case is the LCCU1 permeability. Thus, as noted in the sensitivity coefficient and perturbation analysis for this parameterization, there is something distinctly different about the behavior of LCCU1 in the selected HSU depth-decay and anisotropy case.

Table 6-6
Spearman Rank Correlation Matrix for BN-MME-ADA

	PHI	WELL	SPRING	FLUX	ETF
PHI	1	0.47	0.14	0.13	0.44
WELL	0.47	1	0.37	-0.35	-0.15
SPRING	0.14	0.37	1	0.02	-0.05
FLUX	0.13	-0.35	0.02	1	0.05
ETF	0.44	-0.15	-0.05	0.05	1

In the following classification tree analyses, the logarithm of permeability will be presented; all other variables will be untransformed.

Figure 6-43 shows a classification tree plot for PHI. The tree has a misclassification rate of only 6 percent [(1+7)/(44+21+77)] after two splits. Based on the order of the splits, variable LCA Zone 1 (the subdivision of the LCA along the southeastern edge of the CAU model propagated from UGTA regional model [DOE/NV, 1997] Zone 1) is the most important followed by DVCM. This also is different from the results shown in Section 6.2.3.1 for base HFM - selected HSU depth decay and anisotropy, although the DVCM is still the second best explanatory variable for both parameterization approaches.

Figure 6-44 shows a classification tree analysis for WELL. Note that the important variables for this case, FCCM and CHCU permeability, are different from those identified earlier for the total objective function (PHI). This classification tree has a misclassification rate of 9 percent after two splits.

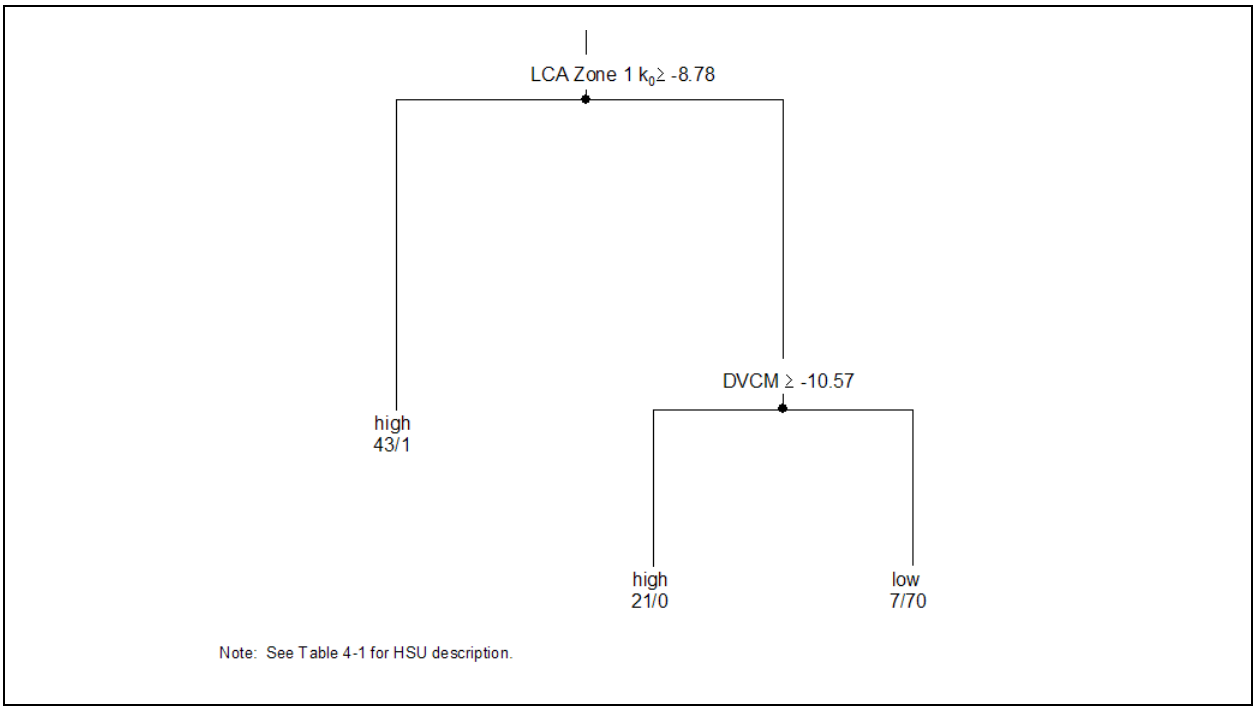

Figure 6-43
Classification Tree on PHI for BN-MME-ADA

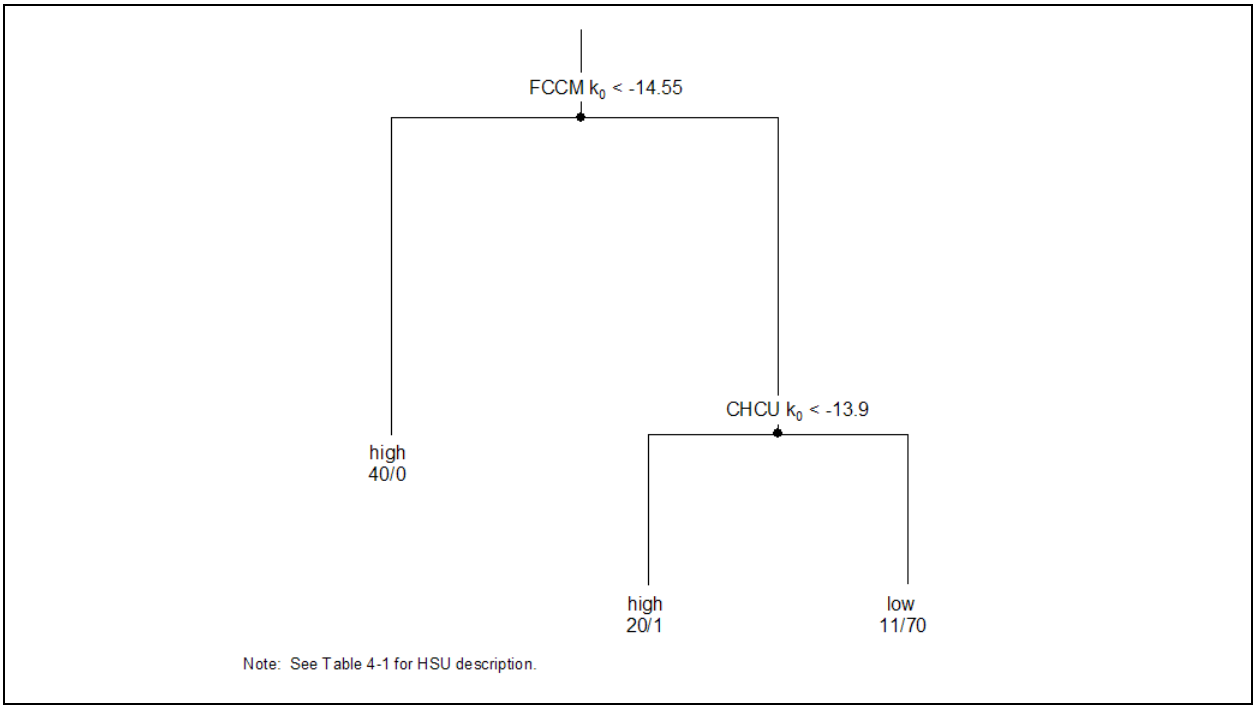

Figure 6-44
Classification Tree on WELL for BN-MME-ADA

When CHCU is less than 1.2 x 10^{-14} m^2, the model results are poorer than when it is larger. Stoller-Navarro Joint Venture (2004a) estimated the mean permeability of the CHCU at about 1 x 10^{-13} m^2 with a standard deviation of about one order of magnitude (see Table 2-19). Thus, the estimated value and its uncertainty appear reasonable in light of model performance.

Figure 6-45 shows the classification tree for SPRING. The lowest 10 percent SPRING values cannot be perfectly explained using three variables, with a misclassification rate of 16 percent. Note that one of the key variables, FCCM k_0, is shared with the set of key variables for WELL. The thrusted LCA (LCA3a) k_0 under Oasis Valley is the primary explanatory variable, most probably because it can drain water under the valley. A depth-decay parameter, that of the East Rainier Mesa subdivision of the TMCM, is also important in explaining misfit for less obvious reasons, although it may be that at lower depth decay more water drains down Fortymile Canyon than is needed to maintain spring heads. Both SNJV (2004a) and Kwicklis et al. (2005) show that some flow from north of the TMCM-ERM area occurs to Oasis Valley, so while peculiar, this explanation is possible.

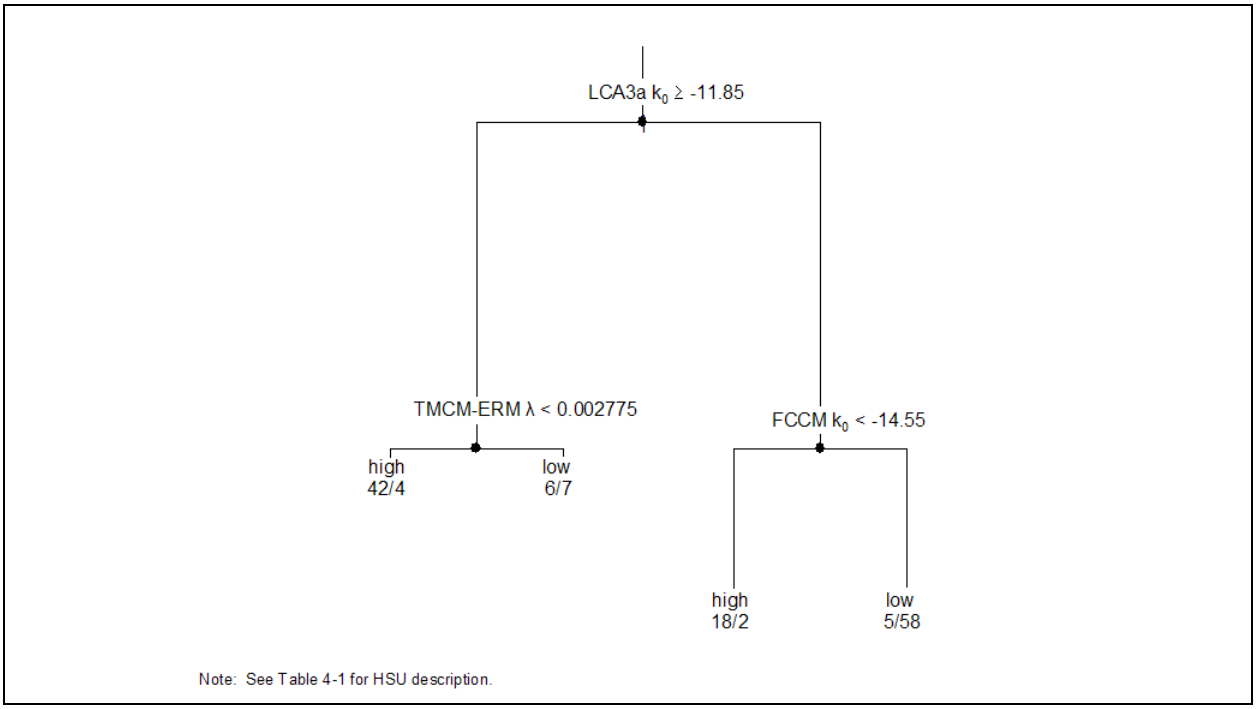

Figure 6-45
Classification Tree on SPRING for BN-MME-ADA

Figure 6-46 presents the classification tree for FLUX. These results appear to be very similar to those presented earlier for the total objective function PHI, and primarily reflect the strong correlation between high PHI and high FLUX values. LCA Zone 1 replaces LCCU1 as the major controlling factor in this parameterization of the base HFM. The LCA Zone 1 was also noted as sensitive in previous all HSU depth-decay and anisotropy case analyses (see Sections 6.2.1.2 and 6.2.2.2), and here is identified explicitly as being associated with southern boundary flow.

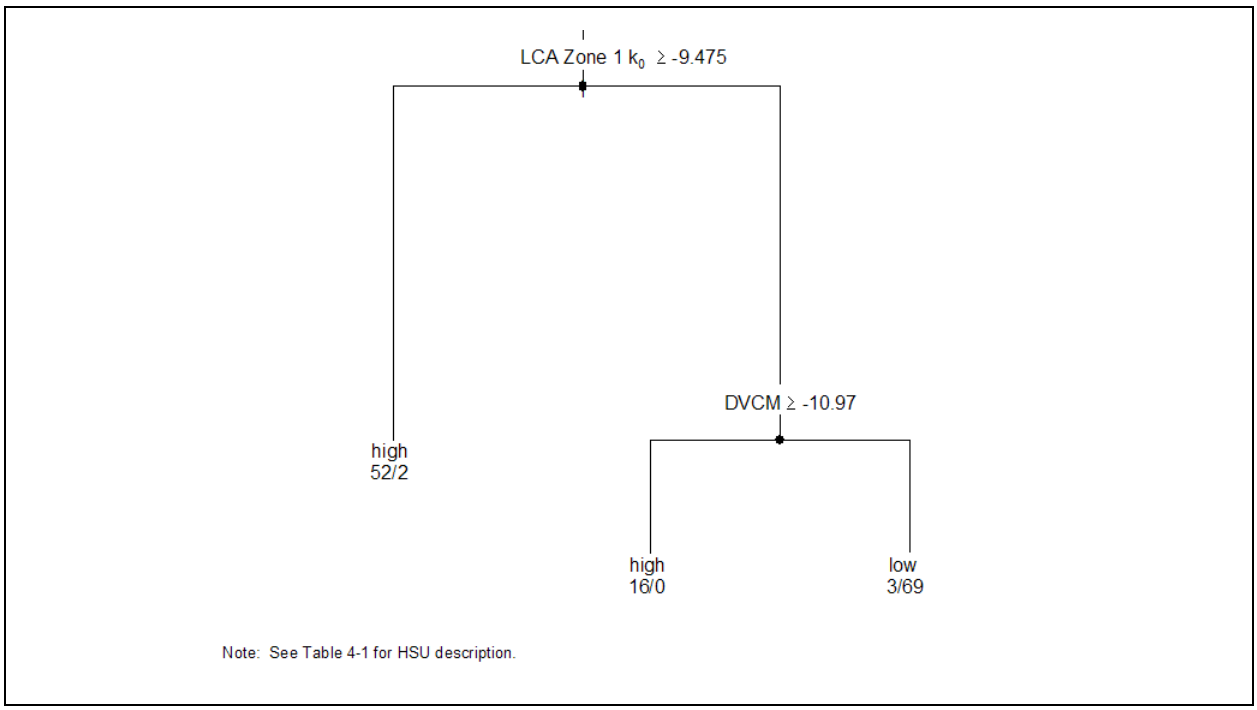

Figure 6-46
Classification Tree on FLUX for BN-MME-ADA

Finally, the classification tree for Oasis Valley discharge is presented in Figure 6-47. Here, a two-variable split perfectly separates the lowest 10 percent of ETF values from the highest 10 percent. Also of interest is the fact that one of the important variables (DVCM) was also identified as important in isolating low values for WELL and SPRING. Both with and without depth decay, the DVCM is important in controlling Oasis Valley discharge. The PBRCM is key in both the selected and all HSU depth-decay cases, but in Section 6.2.3.1, the western zone of the PBRCM versus the PBRCM under Pahute Mesa/Silent Canyon is identified as being an important control.

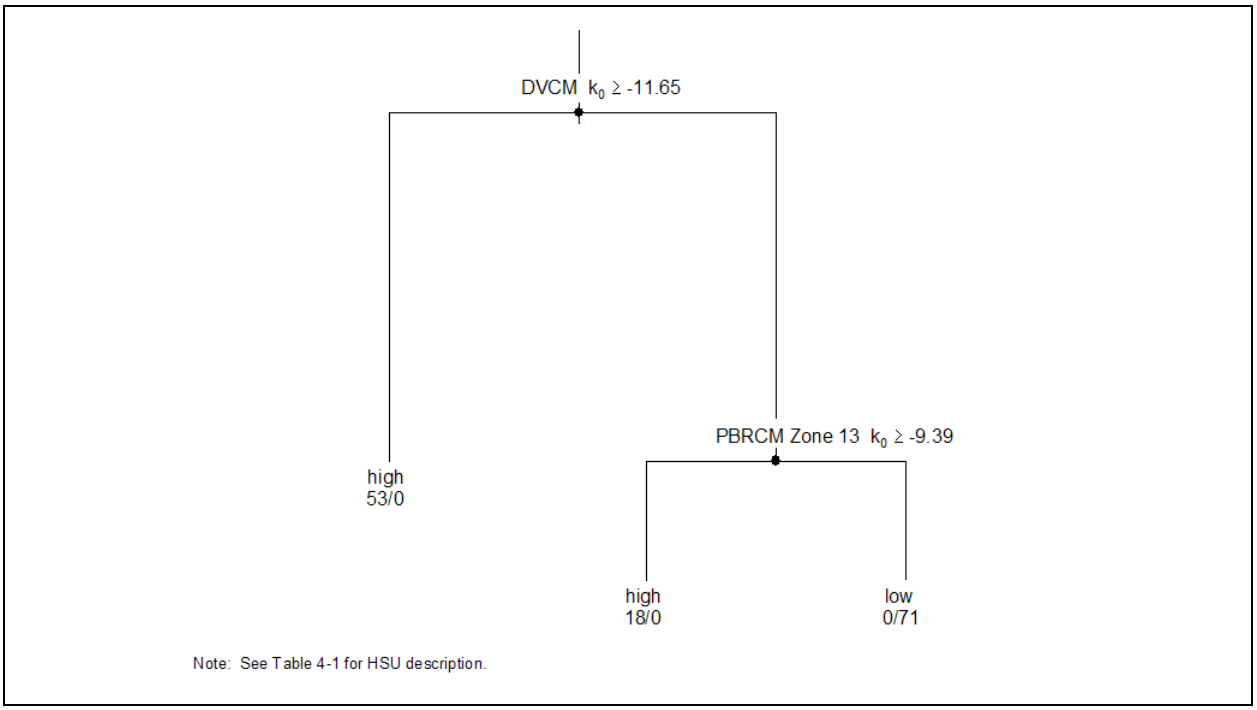

Figure 6-47
Classification Tree on ETF for BN-MME-ADA

Entropy analysis for PHI is shown Table 6-7. Based on the R-statistic, the top two variables have distinct patterns of association with PHI and also happen to be the same in order of importance as the top two variables identified from classification tree analysis in Figure 6-43. The other variables appear to have less definitive association. The second most important variable, DVCM k_0, was also identified in Section 6.2.3.1 for selected depth decay and anisotropy. Figure 6-48 shows bubble plots for the top four variables for PHI, where the entries of the contingency table are shown as bubbles of varying sizes. The relative importance of the top two variables, LCA Zone 1 and DVCM, is clearly seen through the distinctive patterns in the upper panels. On the other hand, the near-uniform size of the bubbles in the bottom panels indicates the marginal relevance of the other two top-ranked variables.

Results for the entropy analysis of WELL are shown in Table 6-8. Based on the R-statistic, the top two variables are not as dominant or as distinctive as those corresponding to PHI. The order of importance is the same as the importance ranking from classification tree analysis shown in Figure 6-44. The absence of distinctive input-output patterns can also be seen in the bubble plots

Table 6-7
Results of Entropy Analysis on PHI for BN-MME-ADA

Rank	Variable	R-Statistic
1	LCA Zone 1 k_0	0.45
2	DVCM k_0	0.43
3	PBRCM Zone 13 k_0	0.26
4	LCA Zone 1 Vertical Anisotropy	0.22
5	CHZCM k_0	0.21

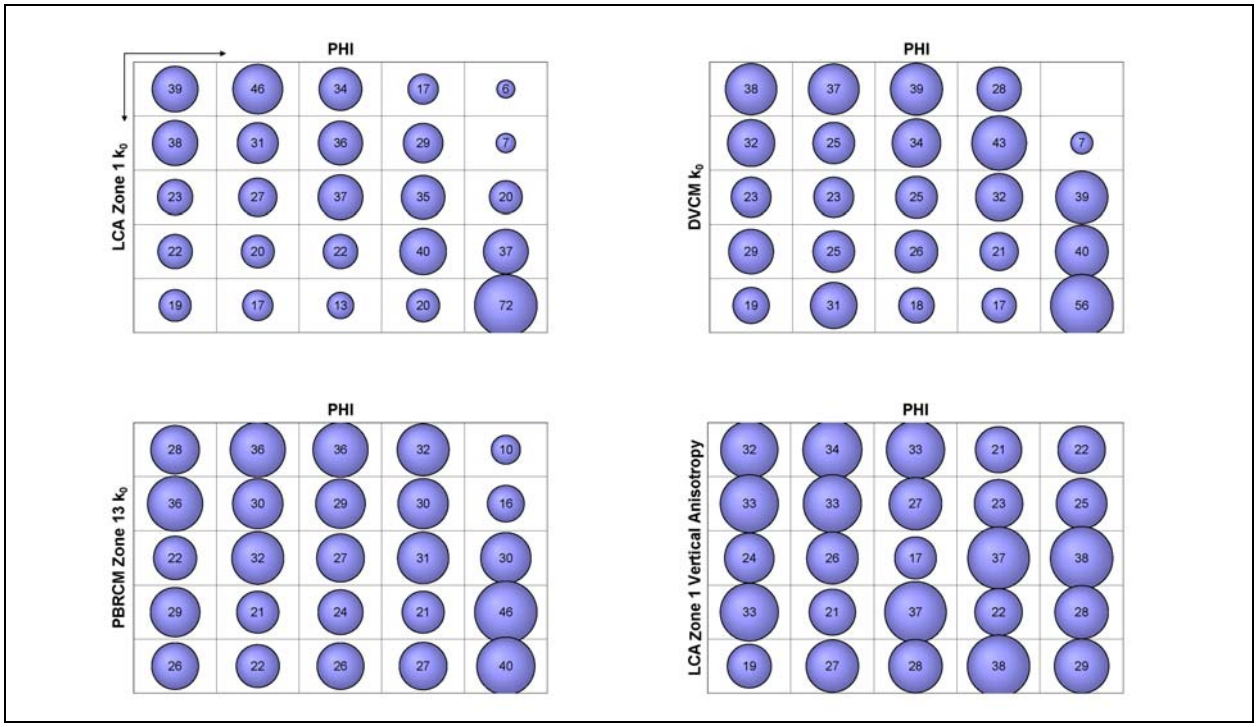

Figure 6-48
Bubble Plots from Entropy Analysis on PHI for BN-MME-ADA

presented in Figure 6-49, where even the top two variables (top panels) do not appear to significantly different from the next two variables (bottom panels) in terms of exhibiting distinctive trends.

Interestingly, this is the first occasion where a fault (West Greeley, in this case) and a volcanic aquifer (IA) on Pahute Mesa are identified as a potentially important factor, although PEST sensitivity and perturbation analyses suggested these variables were important (see Sections 6.2.1.2 and 6.2.2.2).

Table 6-8
Results of Entropy Analysis on WELL for BN-MME-ADA

Rank	Variable	R-Statistic
1	FCCM k_0	0.36
2	CHCU k_0	0.28
3	IA k_0	0.24
4	West Greeley Fault	0.23
5	PBRCM Zone 13 k_0	0.22

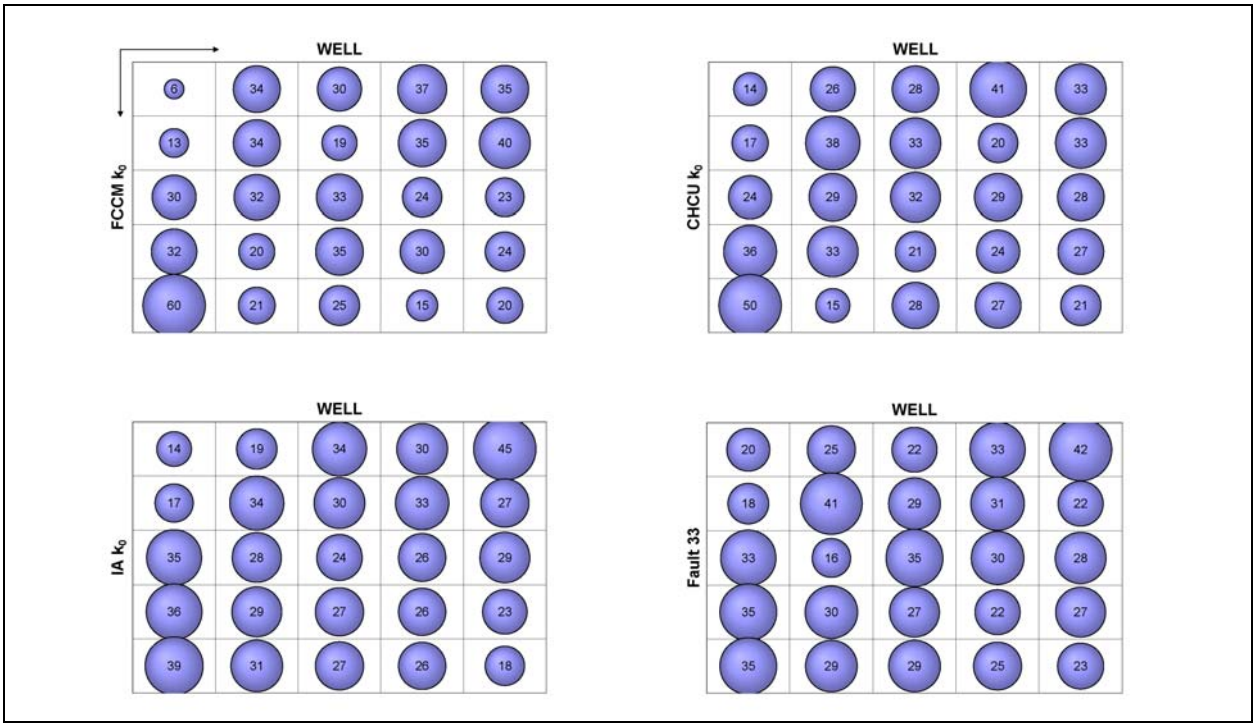

Figure 6-49
Bubble Plots from Entropy Analysis on WELL for BN-MME-ADA

Results for the entropy analysis for FLUX are given in Table 6-9, and the corresponding bubble plots are presented in Figure 6-50. The top two variables are the same as those identified by the classification tree analysis for FLUX. As noted earlier, the top-ranked variables for PHI and FLUX are identical, suggesting that a strong correlation between high PHI and high FLUX values may be influencing these results.

Table 6-9
Results of Entropy Analysis on FLUX for BN-MME-ADA

Rank	Variable	R-Statistic
1	LCA Zone 1 k_0	0.53
2	DVCM k_0	0.50
3	PBRCM k_0	0.30
4	TMCM-ATCE Vertical Anisotropy	0.22
5	UPCU West of Purse Fault k_0	0.22

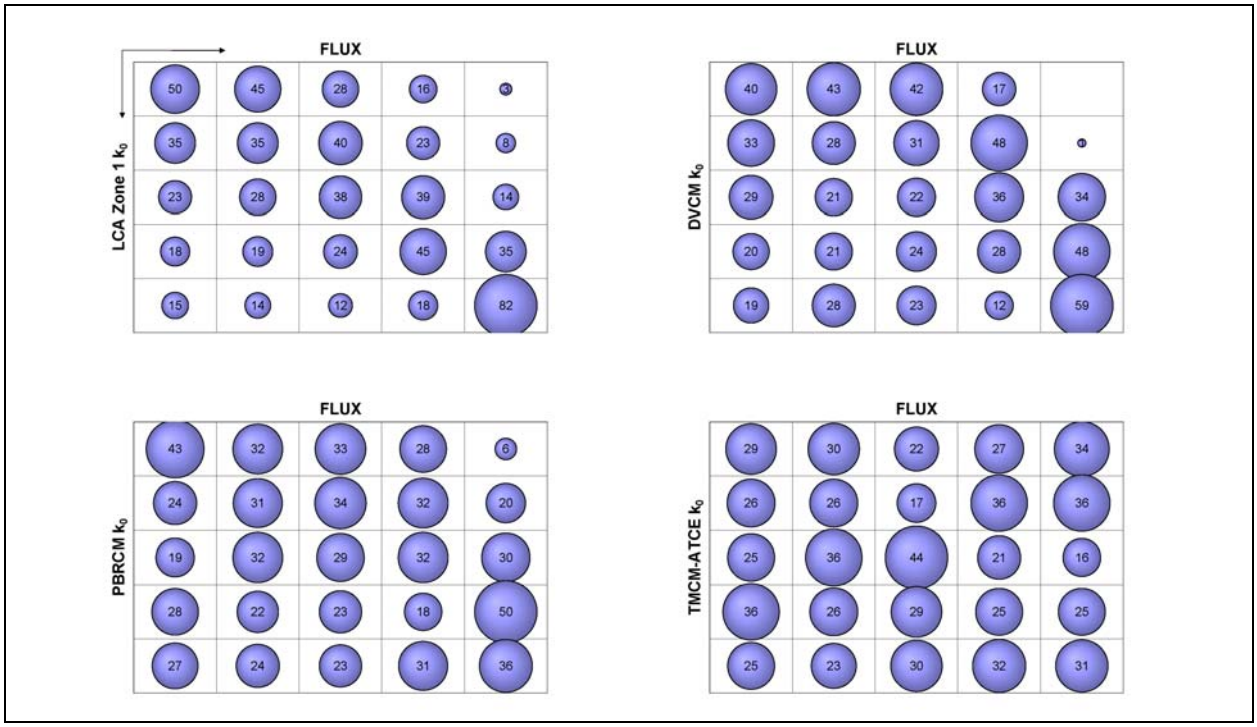

Figure 6-50
Bubble Plots from Entropy Analysis on FLUX for BN-MME-ADA

6.2.3.3 SCCC HFM - Selected HSU Depth Decay and Anisotropy (SCCC-MME-SDA)

Approximately 100 parameters were varied to investigate the global sensitivity using Monte Carlo simulation for the SCCC HFM. Approximately 26 percent of the simulations did not converge.

Figure 6-51 shows a line plot of the best 10 percent of simulations ranked in terms of PHI, along with its various components. The most consistent contributor to PHI is WELL, with some contribution by FLUX, occasional contribution by ETF and a marginal contribution from SPRING. This figure also

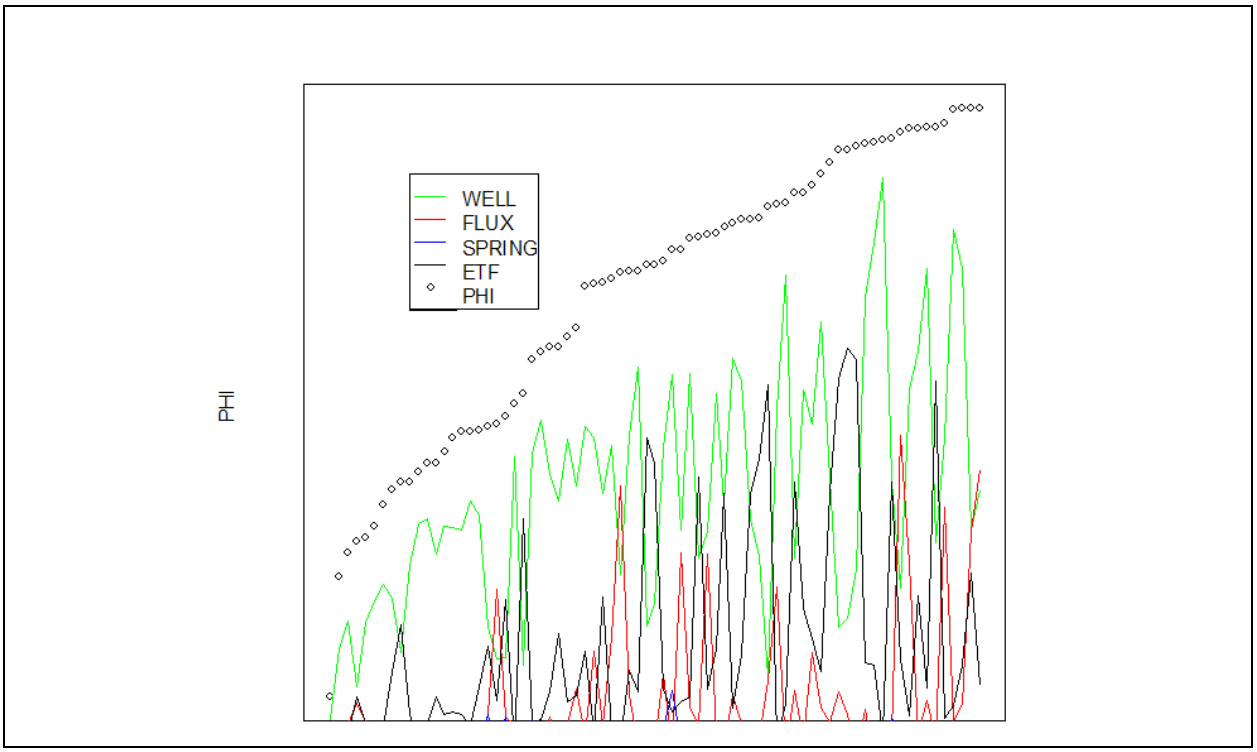

Figure 6-51
100 Best Simulations Ranked by PHI for SCCC-MME-SDA

shows that when FLUX and ETF have a significant contribution, WELL does not. This suggests that these two components of the objective function are controlled by different groups of input parameters.

Table 6-10 shows the Spearman rank correlation matrix for the best 10 percent of simulations ranked by objective function. WELL has the highest correlation with PHI at 0.53. ETF and PHI also have a relatively high correlation at 0.47. Unlike the base HFM - selected HSU depth-decay and anisotropy flow model and the base HFM - all HSU depth-decay and anisotropy case, which both showed correlation between WELL and SPRING, there is little evidence of inter-component metric correlation. Thus, the SCCC HFM is distinctly different than the base HFM in this regard, even though the HFM is the same outside Silent Canyon.

Classification tree analysis to determine the decision rules separating the smallest and largest 10 percent of PHI values is shown in Figure 6-52. The tree has a misclassification rate of less than 1 percent after two splits. Based on the order of the splits, LCCU1 permeability (all permeabilities in log space) is the most important followed by DVCM. While the SCCC HFM shows some differences

Table 6-10
Spearman Rank Correlation Matrix for SCCC-MME-SDA

	PHI	WELL	SPRING	FLUX	ETF
PHI	1	0.53	0.11	0.26	0.47
WELL	0.53	1	-0.06	-0.01	-0.16
SPRING	0.11	-0.06	1	0.19	0.11
FLUX	0.26	-0.01	0.19	1	-0.02
ETF	0.47	-0.16	0.11	-0.02	1

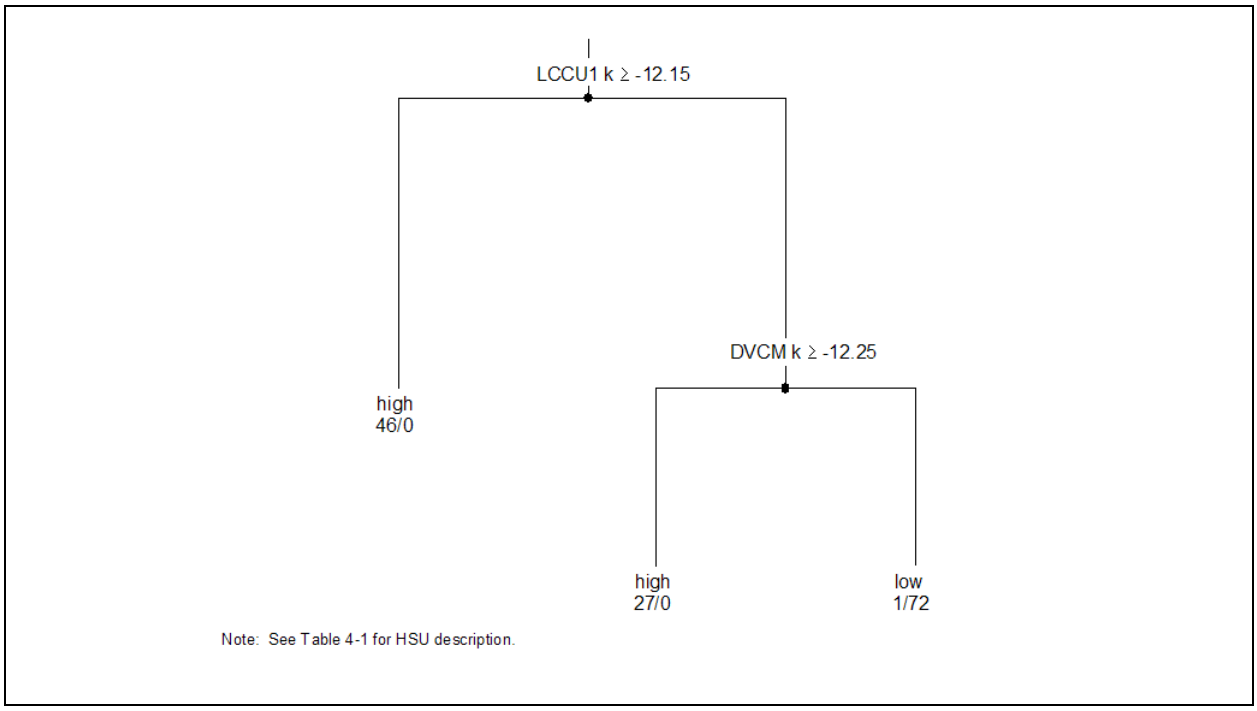

Figure 6-52
Classification Tree on PHI for SCCC-MME-SDA

from the base HFM, the classification tree clearly shows the same parameters as identified in Section 6.2.3.1 for BN-MME-SDA having control on PHI. Thus, because the only difference in how the LCCU1 is handled between the base HFM/SCCC HFM combination and the base HFM - all HSU depth decay and anisotropy is the assignment of depth decay, it is concluded that it is the permeability of the LCCU1, not the HFM, that causes its different roles in model calibration. This is investigated further in Section 6.2.4.2 and Section 7.0.

The next set of analyses deals with the individual components of PHI. Figure 6-53 shows a classification tree analysis for WELL. Note that the important variables for this case, BRA and PBRCM permeability, are different from those identified earlier for the total objective function (PHI). Recall that all Calico Hills HSUs in the base HFM are grouped in the SCCC HFM into the CHCU. This classification tree has a misclassification rate of 16 percent after three splits. The CHCU was also a sensitive parameter for BN-MME-SDA (see Sections 6.2.1.3 and 6.2.2.3).

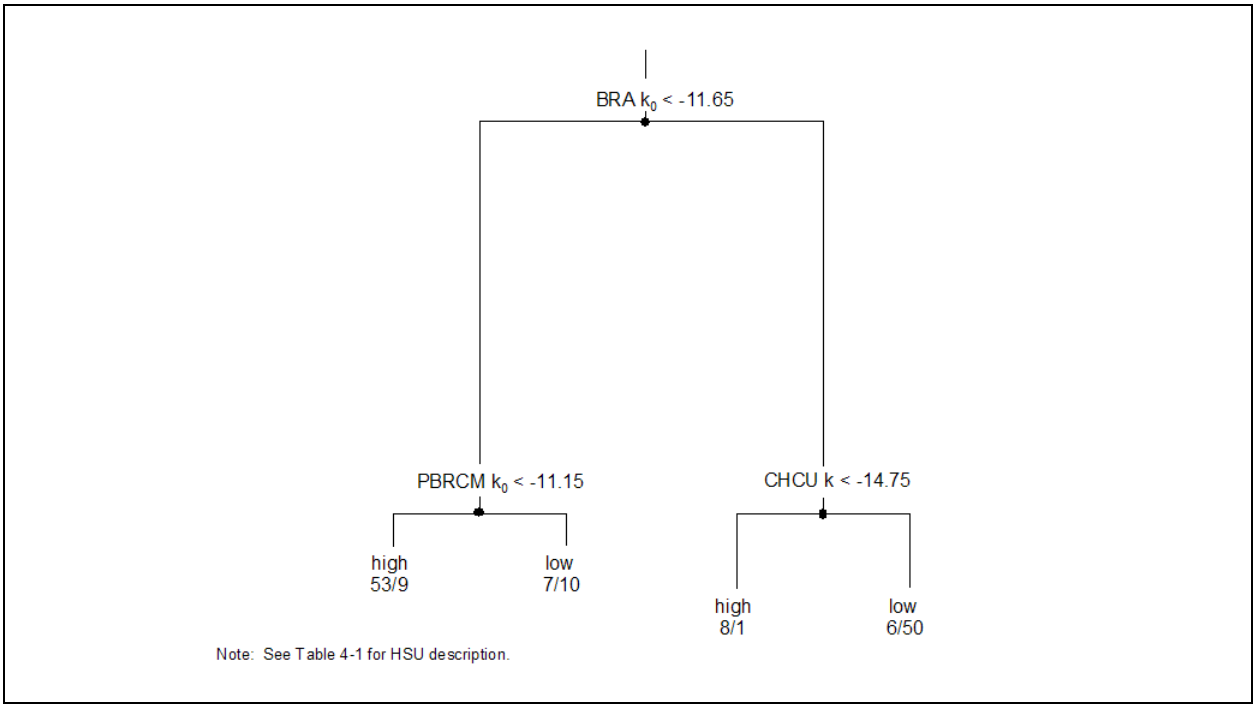

Figure 6-53
Classification Tree on WELL for SCCC-MME-SDA

Figure 6-54 shows the classification tree for SPRING. The lowest 10 percent SPRING values cannot be perfectly explained using two variables, with a misclassification rate of 16 percent. In contrast to the base HFM - selected HSU depth-decay and anisotropy flow model and the base HFM - all HSU depth-decay and anisotropy flow model, no key variables are shared with key variables for WELL. This is expected given the lack of correlation between SPRING and any of the other component variables. This is also the only case where a fault, the Hogback Fault, influences springs. This is not unreasonable, because the Hogback Fault runs north-south through Oasis Valley, and could physically be expected to exert some control on springs, although the other HFMs do not show the Hogback Fault to be especially sensitive. Moreover, the split to low values requires a fault permeability

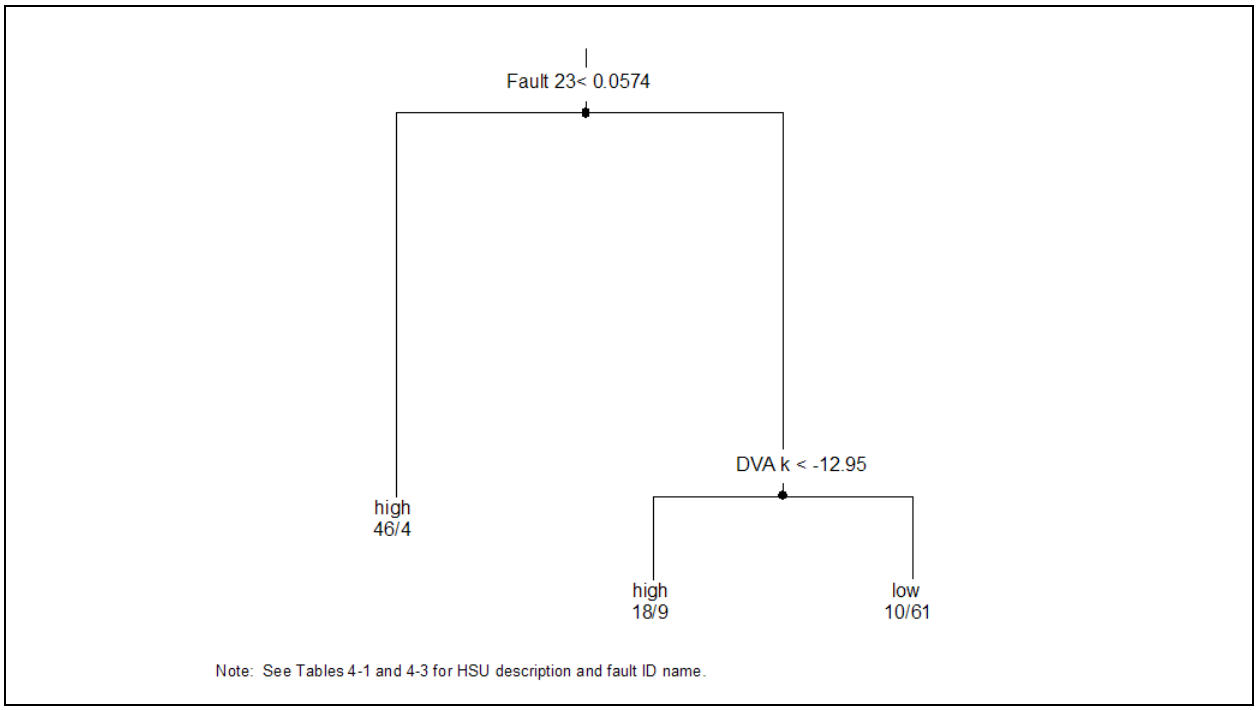

Figure 6-54
Classification Tree on SPRING for SCCC-MME-SDA

multiplier to be greater than about 0.05. Thus, this fault in the SCCC HFM cannot be greatly sealing (as the Purse Fault is in the base HFM).

Figure 6-55 presents the classification tree for FLUX. These results appear to be very similar to those presented earlier for the total objective function PHI, and primarily reflect the strong correlation between high PHI and high FLUX values. These results are also similar to those in Section 6.2.3.1, which is the base HFM parameterized the same way (selected HSU depth decay and anisotropy), but dissimilar to those in Section 6.2.3.2 (the base HFM with all HSU depth decay and anisotropy). Thus, it appears that the difference in how permeability is assigned to the LCCU1 is an important factor.

Finally, the classification tree plot for ETF is presented in Figure 6-56. Here, a two-variable split perfectly separates the ETF values. Also of interest is the fact that one of the important variables, DVCM permeability, was also identified as important in isolating low values for PHI and FLUX, while PBRCM is also identified as key to isolating low values for WELL.

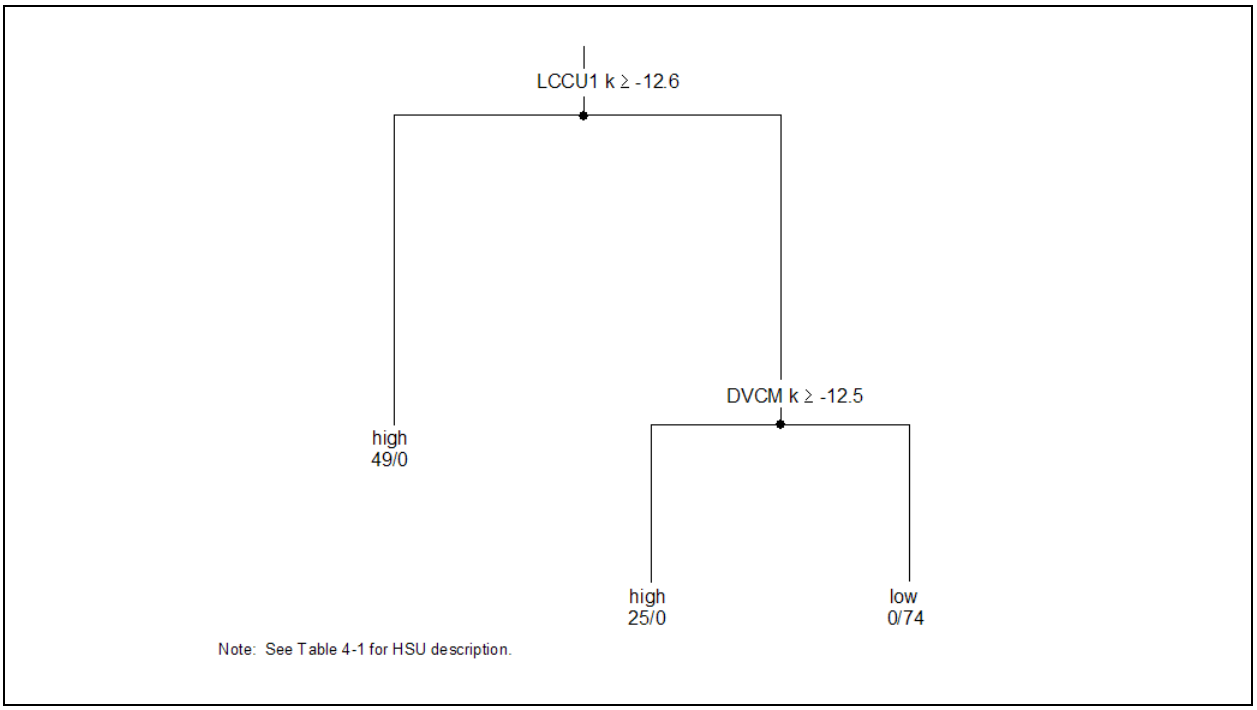

Figure 6-55
Classification Tree on FLUX for SCCC-MME-SDA

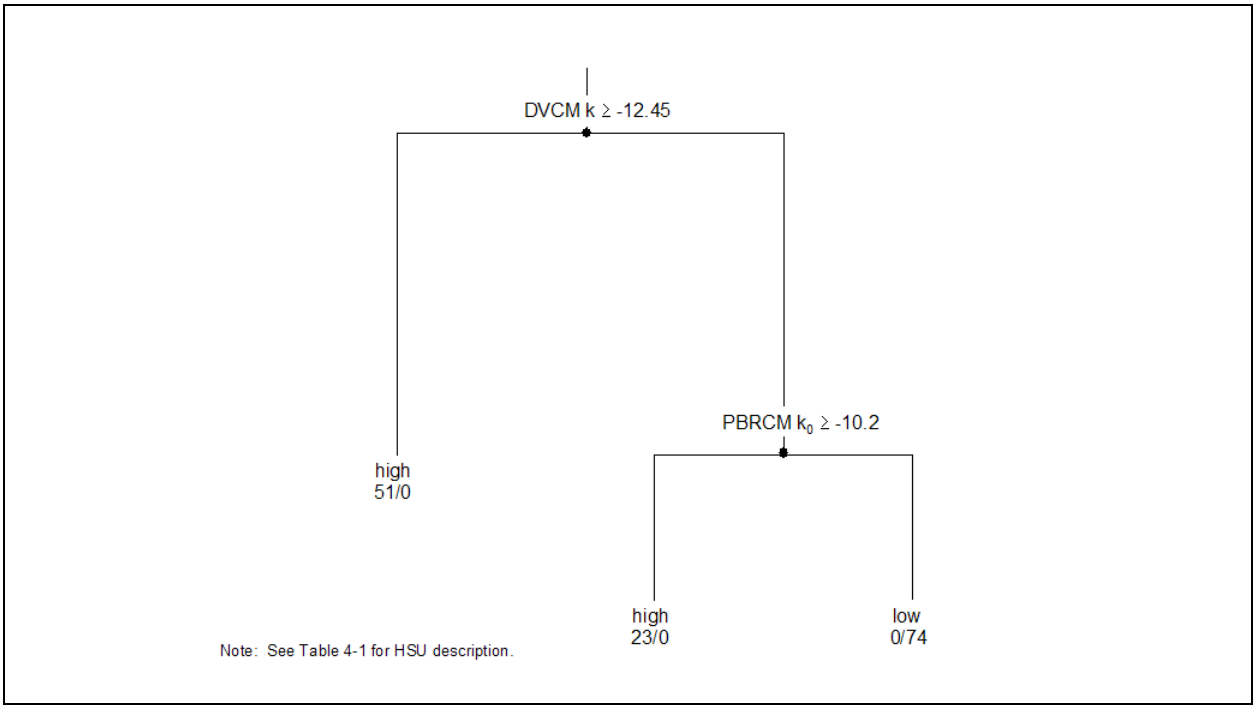

Figure 6-56
Classification Tree on ETF for SCCC-MME-SDA

Entropy analysis for PHI is shown in Table 6-11. Based on the R-statistic, the top two variables have distinct patterns of association with PHI, and also happen to be the same in order of importance as the top two variables identified from classification tree analysis in Figure 6-52. The other variables appear to have less definitive association. The top two variables are the same as found in Section 6.2.3.1 for BN-MME-SDA, and all the models found DVCM permeability as the second most important variable.

Figure 6-57 shows bubble plots for the top four variables, where the entries of the contingency table are shown as bubbles of varying sizes. The relative importance of the top two variables, LCCU1 and DVCM, is clearly seen through the distinctive patterns in the upper panels. On the other hand, the near-uniform size of the bubbles in the bottom panels indicates the marginal relevance of the other two top-ranked variables.

Results for the entropy analysis of WELL are shown in Table 6-12. Based on the R-statistic, the top two variables are not as dominant or as distinctive as those corresponding to PHI. Also, the order of importance is reversed for the first two parameters, compared to the classification tree shown in Figure 6-53. The absence of distinctive input parameter correlation to model performance patterns can also be seen in the bubble plots presented in Figure 6-58, where even the top two variables (top panels) do not appear to be significantly different from the next two variables (bottom panels).

Results for the entropy analysis for FLUX are given in Table 6-13, with the corresponding bubble plots presented in Figure 6-59. The top two variables are the same as those identified by the classification tree analysis for FLUX in Figure 6-55. As noted earlier, the top-ranked variables for PHI and FLUX are identical, suggesting that a strong correlation between high PHI and high FLUX values may be influencing these results.

Table 6-11
Results of Entropy Analysis on PHI for SCCC-MME-SDA

Rank	Variable	R-Statistic
1	LCCU1 k	0.55
2	DVCM k	0.49
3	PBRCM k_0	0.31
4	Fault 05	0.21
5	LCA3 k_0	0.20

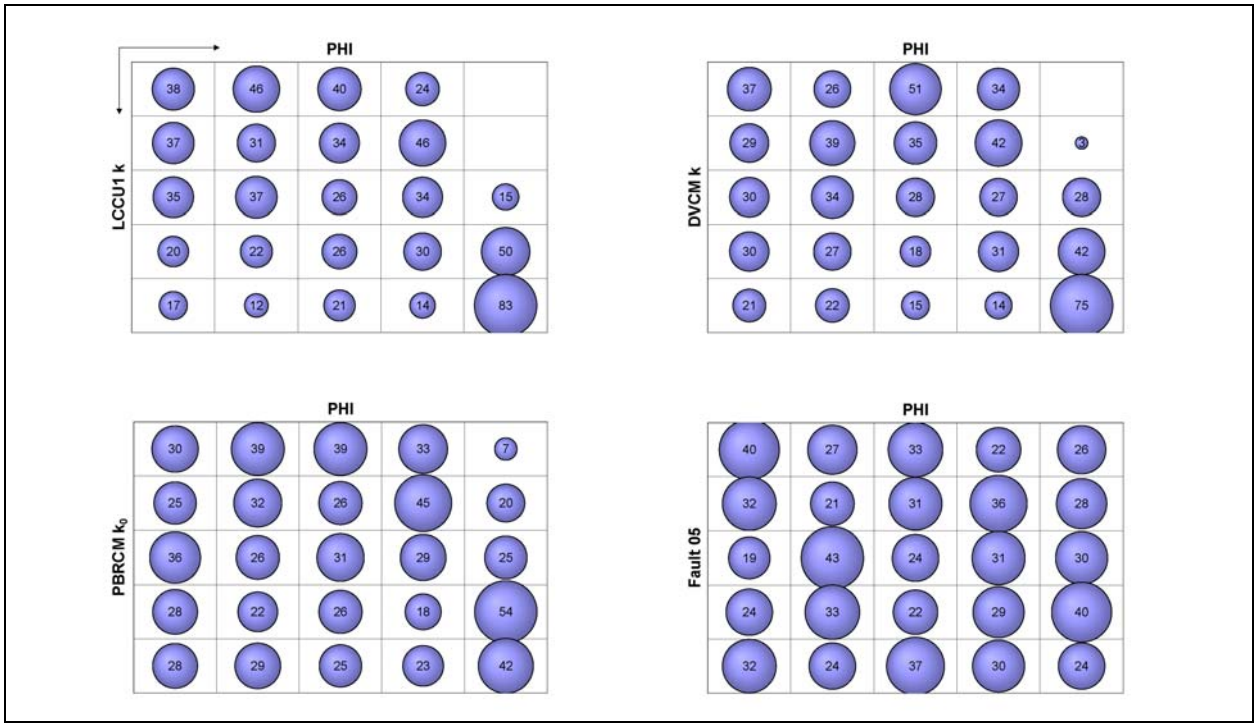

Figure 6-57
Bubble Plots from Entropy Analysis on PHI for SCCC-MME-SDA

Table 6-12
Results of Entropy Analysis on WELL for SCCC-MME-SDA

Rank	Variable	R-Statistic
1	PBRCM k_0	0.31
2	BRA k_0	0.31
3	CHCU k	0.28
4	Fault 11	0.26
5	LCA3 k_0	0.22

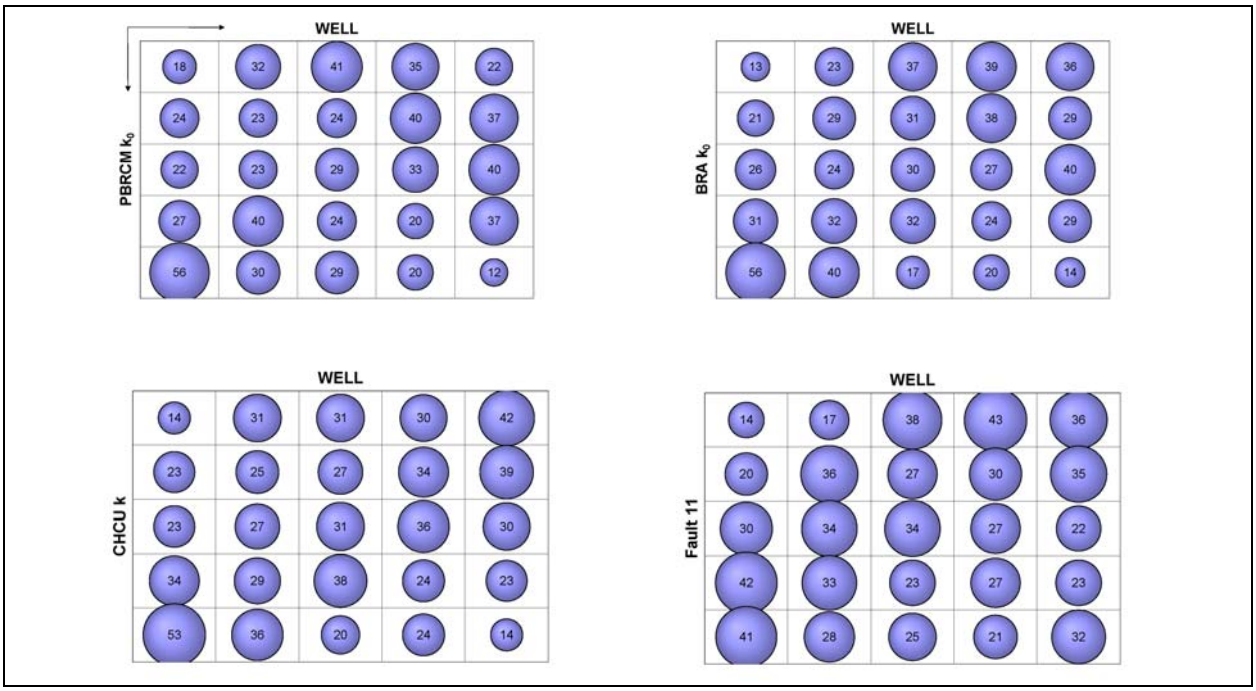

Figure 6-58
Bubble Plots from Entropy Analysis on WELL for SCCC-MME-SDA

Table 6-13
Results of Entropy Analysis on FLUX for SCCC-MME-SDA

Rank	Variable	R-Statistic
1	LCCU1 k	0.70
2	DVCM k	0.61
3	PBRCM k_0	0.26
4	LCA3 k_0	0.21
5	PCM k_0	0.20

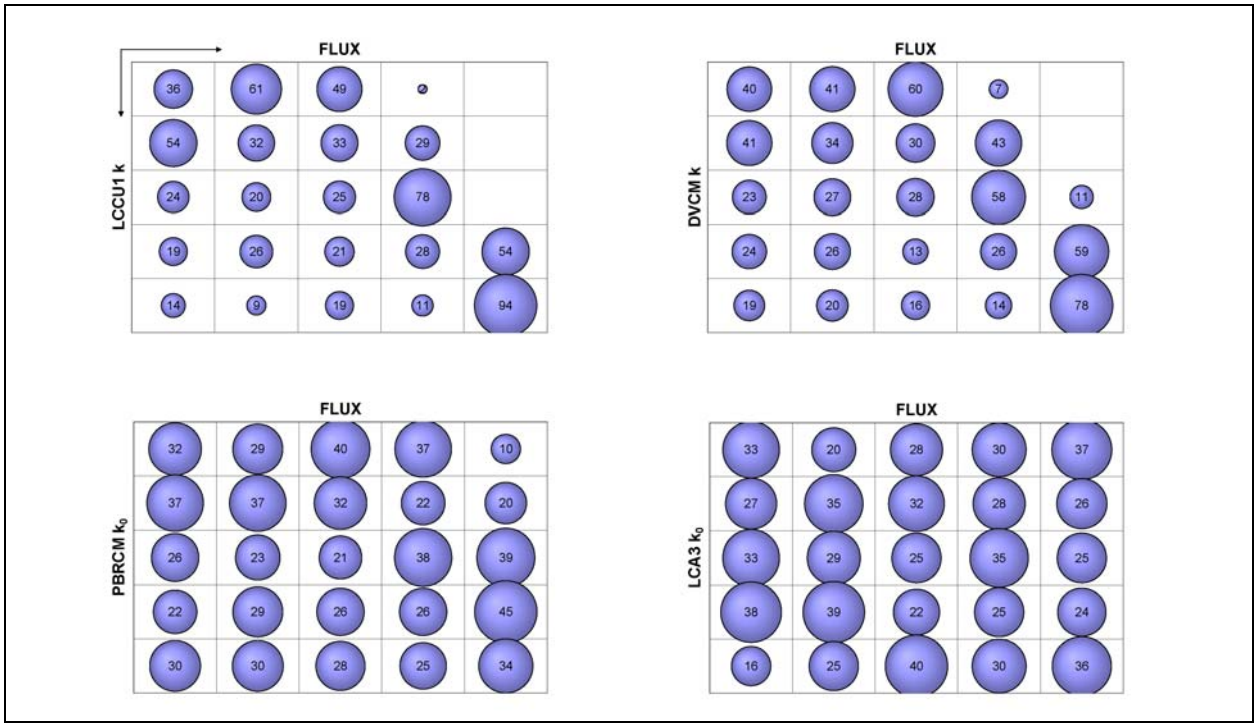

Figure 6-59
Bubble Plots from Entropy Analysis on FLUX for SCCC-MME-SDA

6.2.3.4 Boundary Flux Sensitivity

The CAU model water-balance uncertainty must be considered in the flow model analysis (IT, 1997a). It has been presumed in the Pahute Mesa CAIP (DOE/NV, 1999) that recharge and other high-level uncertainties are the major issue with respect to water-balance uncertainty. However, the global sensitivity analysis suggested that there may be strong variations in water balance from parametric uncertainty, and the following analysis explores this further.

As a subset of the global sensitivity analysis, a classification tree analysis was completed on the base HFM selected HSU depth-decay and anisotropy case to determine the important variables governing the model boundary fluxes. For each of the four model boundaries, there is a specified range of fluxes derived from regional model results. The stochastic simulations completed for the global sensitivity analysis resulted in a distribution of fluxes that spanned beyond these specified ranges. The goal of the classification tree analysis was to attempt to determine what variables were important in determining whether the boundary flux stayed within the specified range.

As an example, Figure 6-60 shows a histogram of the fluxes from the northern boundary, along with the flux range estimated from UGTA regional model analysis (SNJV, 2004a). The x-axis is a log scale, where flux (χ) values have been transformed by:

$$\begin{Bmatrix} \chi < 0, -\log 10\ (-\chi) \\ \chi > 0, \log 10\ (\chi) \\ \chi = 0 \qquad 0 \end{Bmatrix} \tag{6-13}$$

The bimodal look of the transformed distribution is expected, because the tail of the untransformed distribution crosses from negative to positive (from inflow to outflow), and the transformation has the effect of creating two log-normal distributions. Note that a large percentage of the resulting fluxes fall outside the prescribed range just as a consequence of parameter uncertainty.

Classification tree analysis requires binning the data into two classes. In this case, "pass" and "fail" classes were created, where the "pass" class consists of those realizations that fall within flux range and the "fail" class consists of those realizations that fall outside flux range. The histogram in

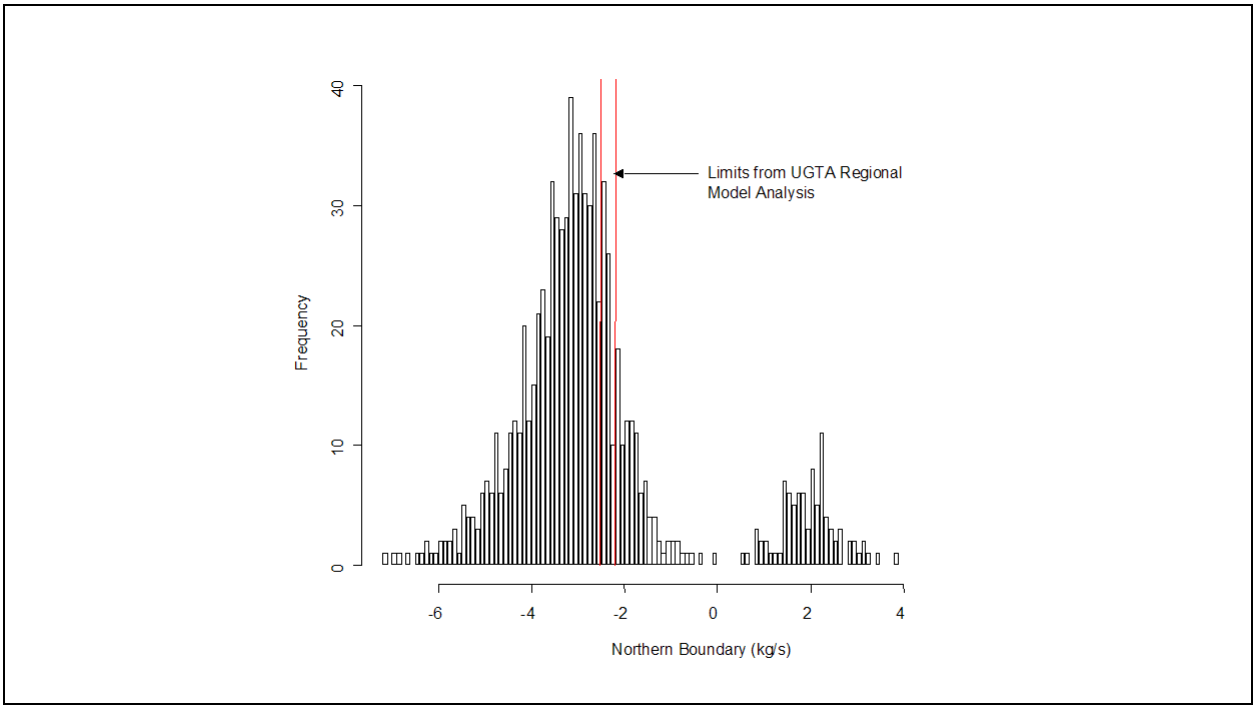

Figure 6-60
Histogram of Log-Transformed Northern Boundary Flux for BN-MME-SDA

Figure 6-60 shows that the classes are highly unbalanced (i.e., there are only 83 passing realizations compared to some 751 failing realizations). The classification tree analysis will be ineffective unless the classes are more balanced. So we will randomly sample twice the number of "pass" realizations from the "fail" class to compare against the passing realizations. For the northern boundary, this means there will be 166 samples in the "fail" class.

Figure 6-61 shows the histogram from the above sampling procedure for the northern boundary flux. Figure 6-62 shows the resulting classification tree. Note that the misclassification rate for this tree is quite high, at about 26 percent. However, the first split (LCCU1 permeability greater than or equal to -12.25) does produce a pure "fail" (i.e., flux outside the UGTA regional model [DOE/NV, 1997] analysis) node, and the second split (LPCU west of Purse Fault 58 less than -16.85) also produces a nearly pure "fail" node. So although the analysis cannot separate the "fail" realizations where the flux falls very near the specified range, a large number (about 92 of the 183) of the "fail" realizations can be separated with just two splits. The physical reasons for the classification tree results is that the LCCU1, which is connected to the highest boundary heads along the northeastern quadrant of the model, moves excessive water at higher permeabilities. The parameter LPCU west of Purse Fault is

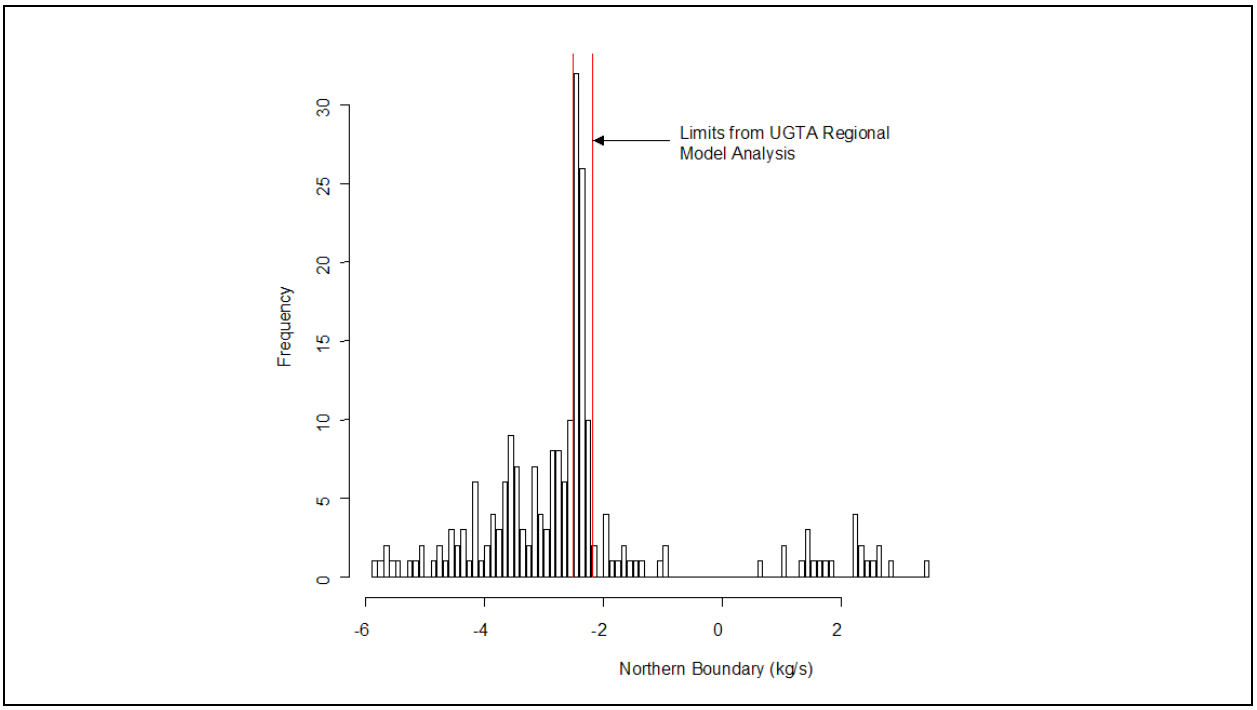

Figure 6-61
Histogram of Log-Transformed Resampled Northern Boundary Flux for BN-MME-SDA

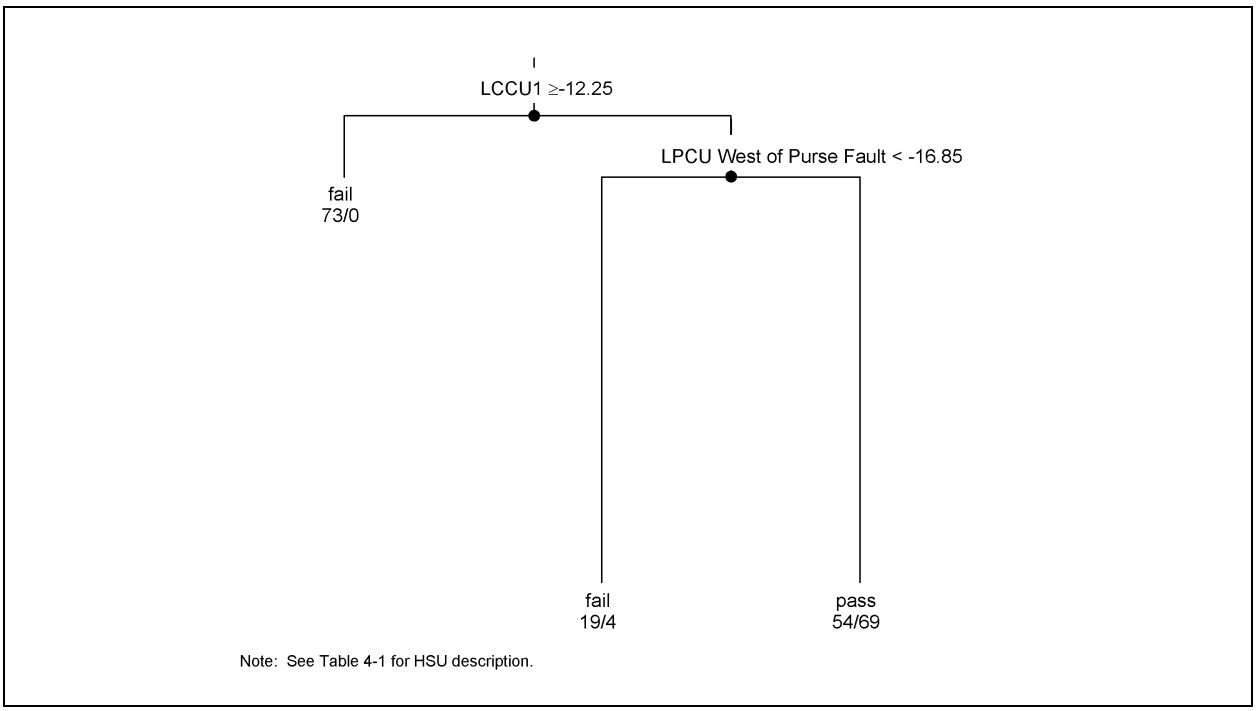

Figure 6-62
Classification Tree for Northern Boundary Flux for BN-MME-SDA

only the portion in the "throat" between Black Mountain and the Purse Fault where PM-3 lies, and acts to check flow through the area, which can be high given the upstream boundary condition was raised over 100 m (see Section 5.3).

Figure 6-63 shows the histogram result for the southern boundary flux. Because all of these fluxes are positive, the transformation process does not produce the bimodal distribution. Also, even in log space, the distribution tails toward the values that are larger in magnitude. Figure 6-64 shows the classification tree for the southern boundary flux. Again, the overall misclassification rate for this tree is high, at about 31 percent. The first split (DVCM permeability greater than or equal to -12.75) does produce a nearly pure "fail" node. The second split, PBRCM anisotropy, is less successful, with both classes rather well represented in the nodes. In this case, only the first parameter in the tree, DVCM, would be considered important for separating the "fail" realizations. Physically, the importance of these two parameters is interpreted as follows: the DVCM permeability controls inflow from Sarcobatus Flat from the west into Oasis Valley that is a relatively short and direct flow path. If the DVCM permeability is too high, flow from the west easily satisfies Oasis Valley discharge, thus increasing flow out of the model across the southern boundary and model misfit with respect to this flow. The PBRCM permeability moves water all across the domain, although substantial faulting breaks its continuity. The PBRCM has previously been shown to be a very sensitive parameter in controlling Oasis Valley discharge because it exists near the water table over much of the western domain (BN, 2002). High horizontal-to-vertical permeability contrast results in a more horizontal character of groundwater flow. The classification tree analysis shows that at vertical-to-horizontal permeability ratios of greater than 0.03, the southern boundary flow "passes" (i.e., falls within the estimated range). Thus, excessive horizontal-to-vertical permeability contrast tends to hold head up and move water to the south with more continuity than more reasonable values. This analysis qualitatively suggests that with the current HFM structure and parameterization, PBRCM vertical-to-horizontal permeability ratio should be greater than 0.03.

Figure 6-65 shows the histogram result for the eastern boundary flux. Figure 6-66 shows the classification tree for the eastern boundary flux. The misclassification rate is lower than the previously discussed flux analyses, at about 18 percent. The first split (PBRCM permeability greater than or equal to -13.15) does a good job of separating the "fail" realizations from the "pass" realizations. The second level splits are less consequential. In this case, the first parameter in the

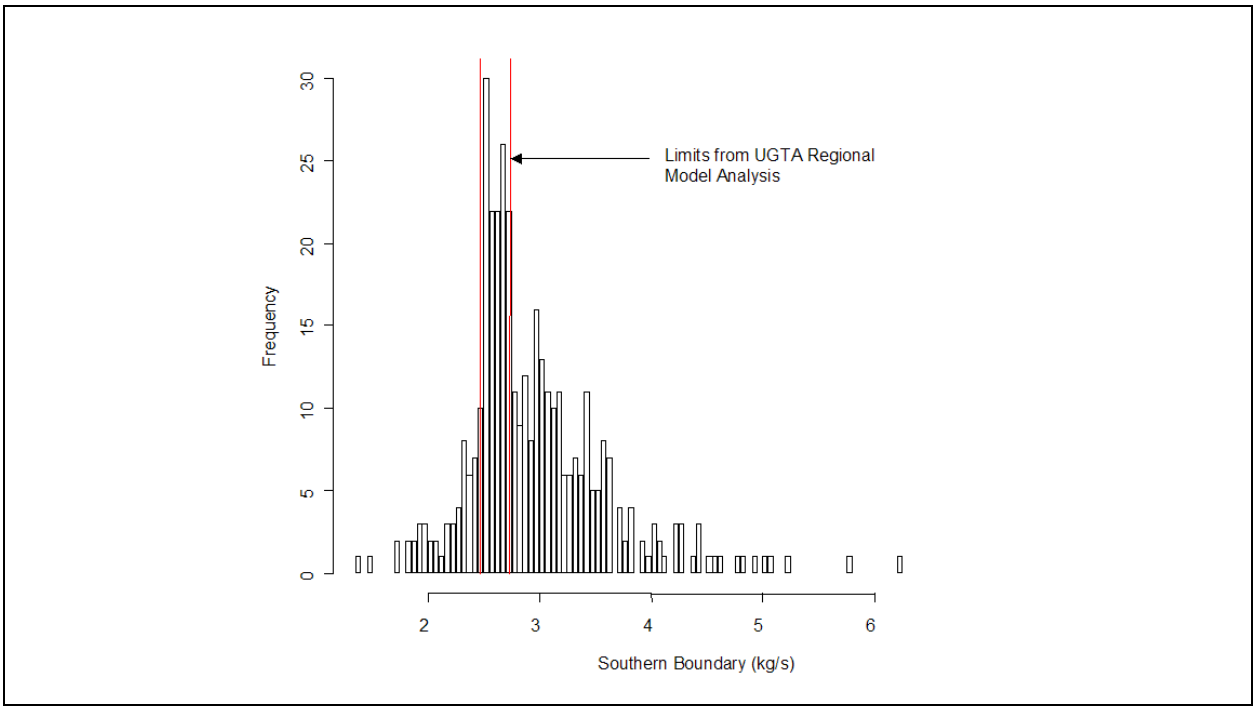

Figure 6-63
Histogram of Log-Transformed Resampled Southern Boundary Flux for BN-MME-SDA

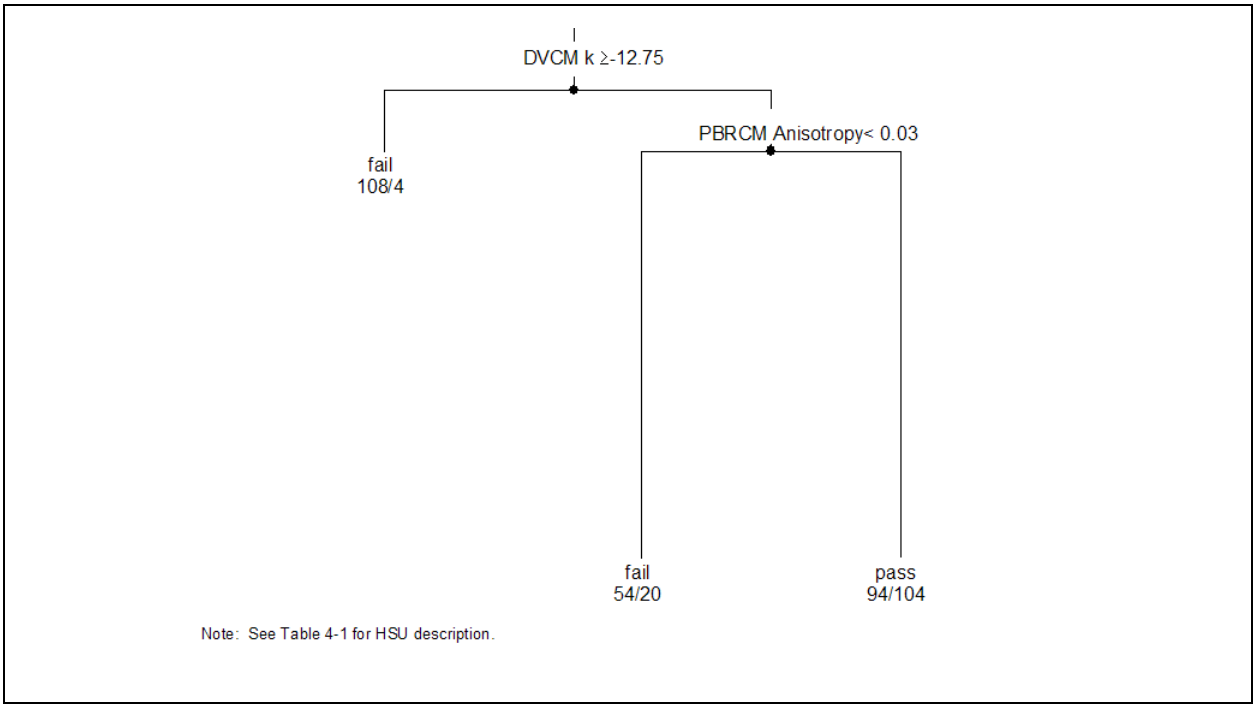

Figure 6-64
Classification Tree for Southern Boundary Flux for BN-MME-SDA

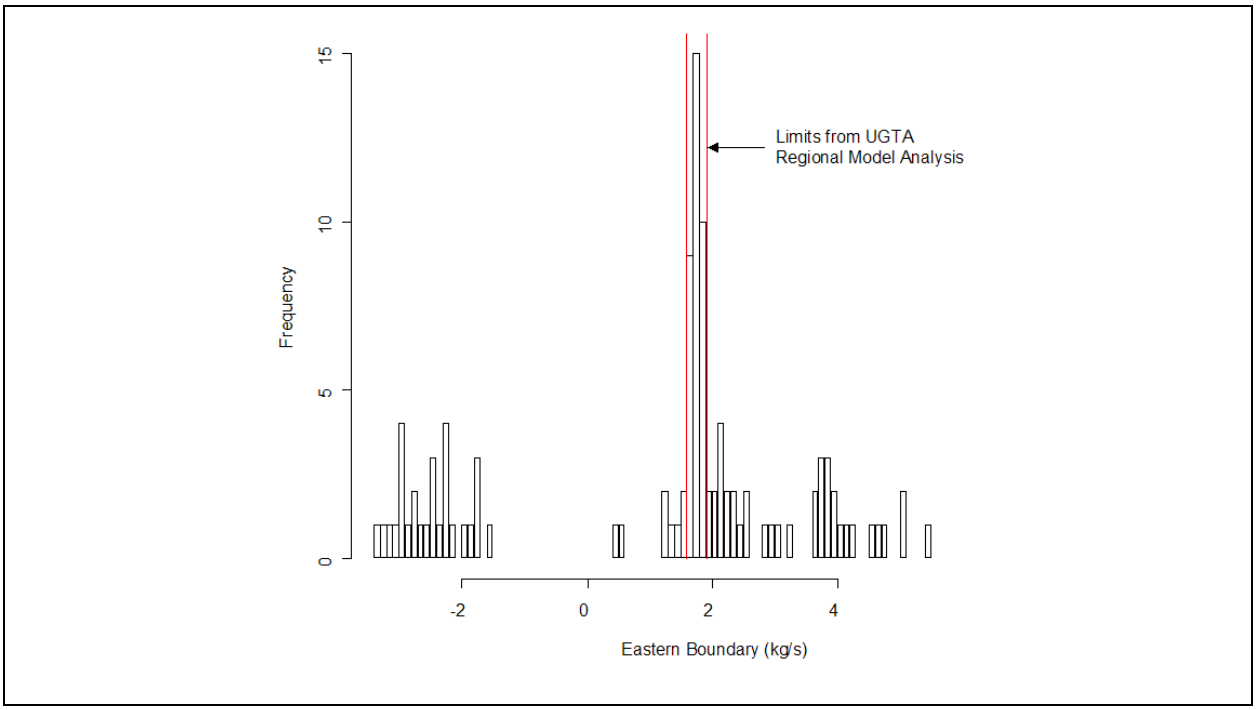

Figure 6-65
Histogram of Log-Transformed Resampled Eastern Boundary Flux for BN-MME-SDA

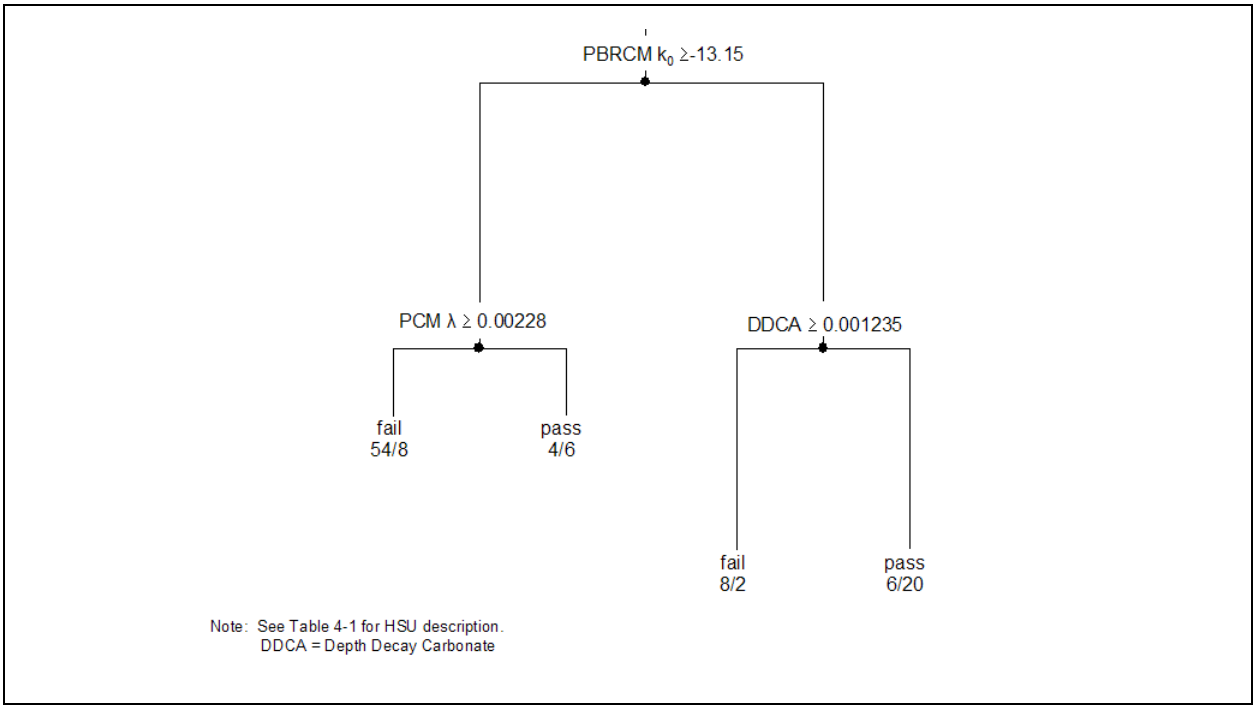

Figure 6-66
Classification Tree for Eastern Boundary Flux for BN-MME-SDA

tree, PBRCM, would be considered most important for separating the "fail" realizations, with a lesser emphasis on PCM depth decay and carbonate aquifer depth decay. The PBRCM is connected to the high hydraulic head near Gold Meadows, which allows it to control eastern boundary flow. The PCM and LCA both lie along (and are the major permeable units) the southern part of the eastern edge, and depth decay in these units helps control flow along this boundary.

Figure 6-67 shows the histogram result for the western boundary flux. The histogram shows a symmetrical lognormal distribution. Figure 6-68 shows the classification tree for the western boundary flux. This classification tree is different from the others in that the first two splits involve the same variable, DVCM. Also, the first two splits are of roughly equal importance, in that they both do a good job of separating "fail" from "pass." Log permeability is between -13.15 and -13.75. This single parameter is controlling the simulated western boundary flux result, and DVCM permeability must lie within the range between 1.7×10^{-14} and 7.1×10^{-14} m^2 in order to give a satisfactory western boundary flux. This is an illustration of the constraint that the strategy of using regional-model water-balance estimates provides and is also a consequence of having a no-flow boundary along much of the western model edge.

It is clear from this analysis that parameter uncertainty can have a large impact on CAU water-balance uncertainty, and that some sort of flow constraint is needed.

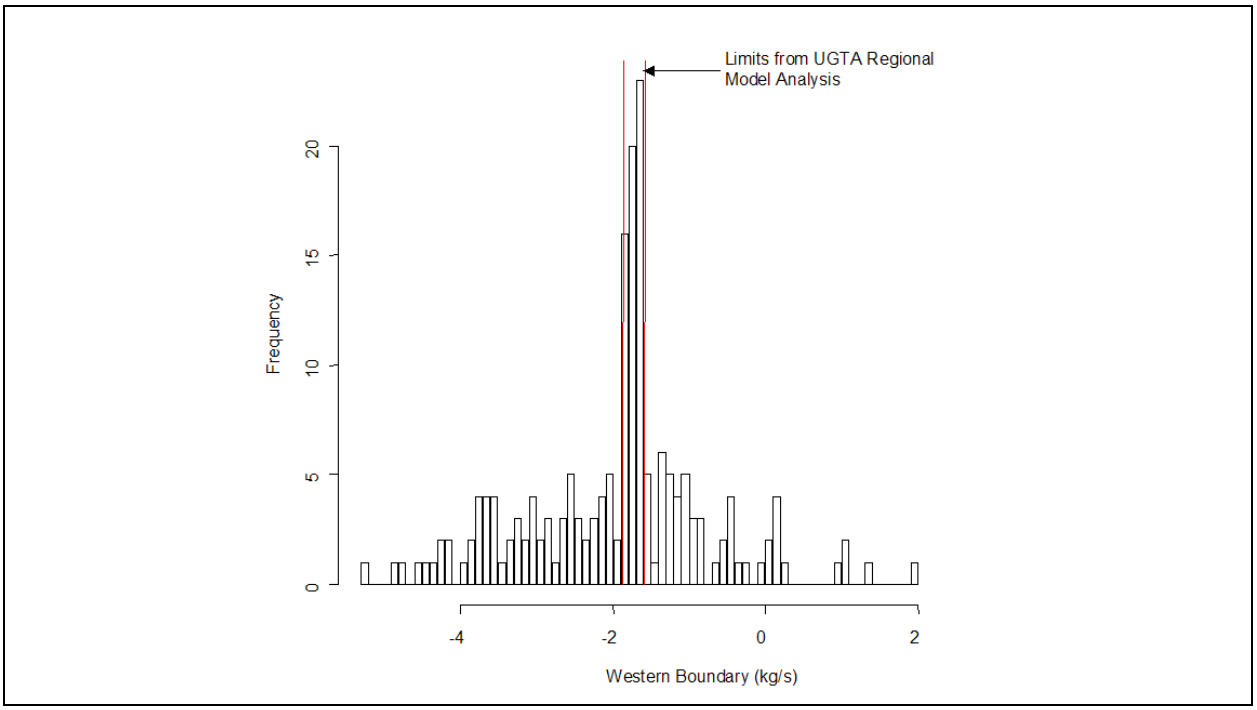

Figure 6-67
Histogram of Log-Transformed Resampled Western Boundary Flux for BN-MME-SDA

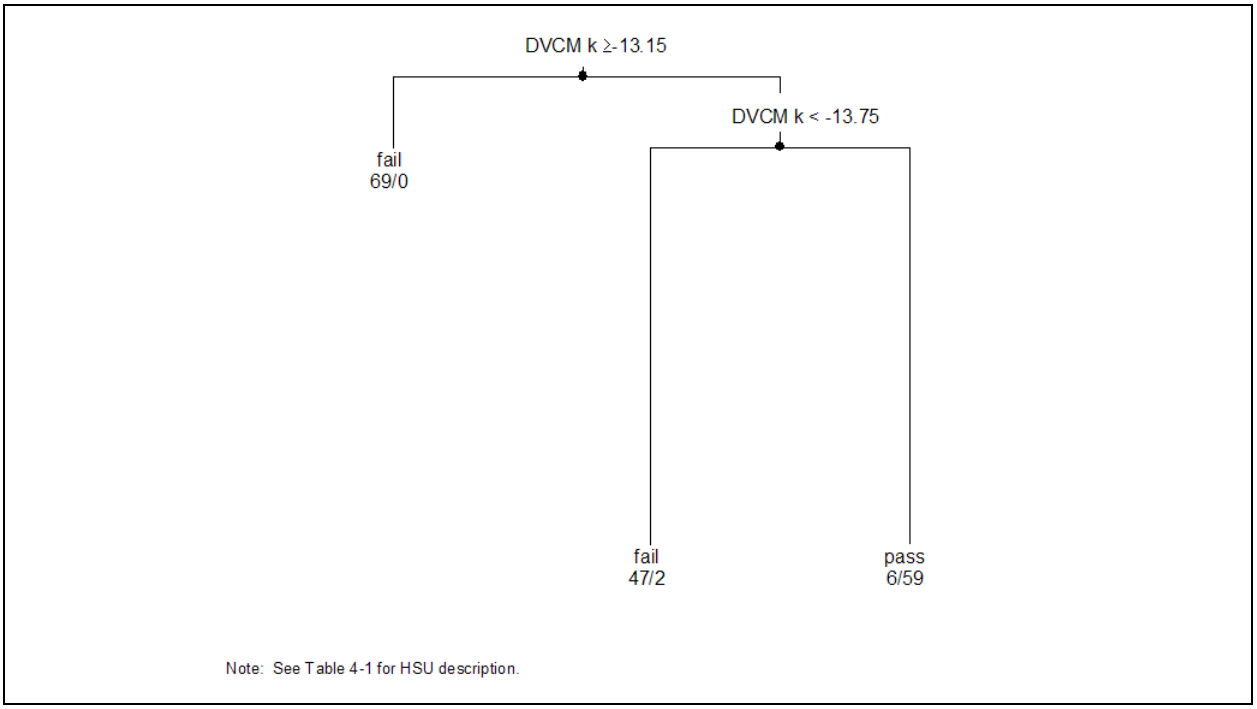

Figure 6-68
Classification Tree for Western Boundary Flux for BN-MME-SDA

6.2.4 Other Model Sensitivities

6.2.4.1 Sensitivity to Evapotranspiration Extinction Depth in Oasis Valley

The DVRFS model (Faunt et al., 2004), the UGTA regional model (DOE/NV, 1997, IT, 1996a through f; IT, 1997a and b), and the CAU flow model all treat ET discharge in Oasis Valley with a third-type boundary condition, where head is set at a value below ground surface representative of the maximum depth that plants can draw water from the water table (the extinction depth). When the simulated head drops below this value, discharge no longer occurs. In the UGTA regional flow model (DOE/NV, 1997), this head was determined by locating the lowest land surface elevation in the cell that encompassed all or part of the Oasis Valley discharge area and assigning a head 10 m below that point. A similar approach was used in the DVRFS. Both these regional models had grid blocks up to 1.5 km on a side in the Oasis Valley region. The Pahute Mesa CAU model has much smaller elements (down to 67.5 m) in Oasis Valley. The land surface elevation at the node was estimated from a digital elevation model, and then a head 3 m below that was assigned from depth to water considerations described in Section 4.3.2.

The sensitivity of the flow model to assumed extinction depth was tested by changing the head at nodes where Oasis Valley ET was simulated for 5 and 10 m less than land surface, the latter value being consistent with the regional models. Increasing the extinction depth to 5 m only increased the model goodness of fit by 0.6 percent, changing the simulated Oasis Valley discharge from 209 to 215 kg/s. Increasing the extinction depth to 10 m increased the objective function by 8 percent (to 18,032) and discharge to 228 kg/s. Thus, it is concluded that over the range deemed reasonable extinction depth is not a greatly sensitive parameter.

6.2.4.2 Reduced LCCU1 Permeability Alternative

The PEST sensitivity, perturbation, and global analyses all ranked the LCCU1 for both the base and SCCC HFM as sensitive. This result is unexpected, because the unthrusted LCCU has such low permeability that it can be considered the bottom of the UGTA regional flow system. The mean permeability estimated for the LCCU1 is relatively high (3×10^{-13} thrusted versus 3×10^{-19} m^2 unthrusted) based on assumed fracturing from thrusting, but is unknown. This discrete sensitivity analysis investigates how the model behaves when the LCCU1 permeability is decreased from

3.7×10^{-13} to 2.9×10^{-14} m^2 and recalibrated. This analysis was done only on the base HFM - selected HSU depth-decay and anisotropy case (BN-MME-SDA).

Figures 6-69 through 6-72 show the observed and unweighted simulated values for the calibration wells, springs, Oasis Valley discharge, and boundary flows. On Figures 6-69 and 6-70, the line of perfect agreement is shown [LCCU1 wells and LCCU1 springs], and ideally the data would plot exactly onto this line. At the very highest observed observation well heads, the model has a tendency toward undersimulation. These plots are not significantly different than those shown in Section 5.6.2.

Calibration summary statistics are shown in Table 6-14, and again are not appreciably different from those in Section 5.6.2. WW-8 is the well with the highest undersimulation in this case, which is a change from the base HFM. It is concluded that the LCCU1 was acting to support heads in the far east-central part of the model domain. It is not known whether this is reasonable, but there are geochemical consequences as further shown in Section 7.0. The objective function for these results is 16,623, which is nearly identical to the value of 16,651 shown in Section 5.6.2.

Figure 6-73 shows the simulated water table, and Figure 6-74 shows the particle tracks from NTS wells. The overall sense of the water table and flow paths do not change appreciably from Section 5.6.2. Some tracks on the eastern part of the domain go much deeper than before, presumably because less flow is routed into the LCCU1 to drive particles horizontally.

Compensating changes in permeability to maintain model calibration resulted in an increase of almost four orders of magnitude in the LCA3 (the thrusted eastern portion of the LCA) reference permeability. Lesser changes were noted in the CHZCM (about an order of magnitude drop), and an order of magnitude drop in the PRBCM Zone 87 (the wedge that separates the SCCC and Timber Mountain).

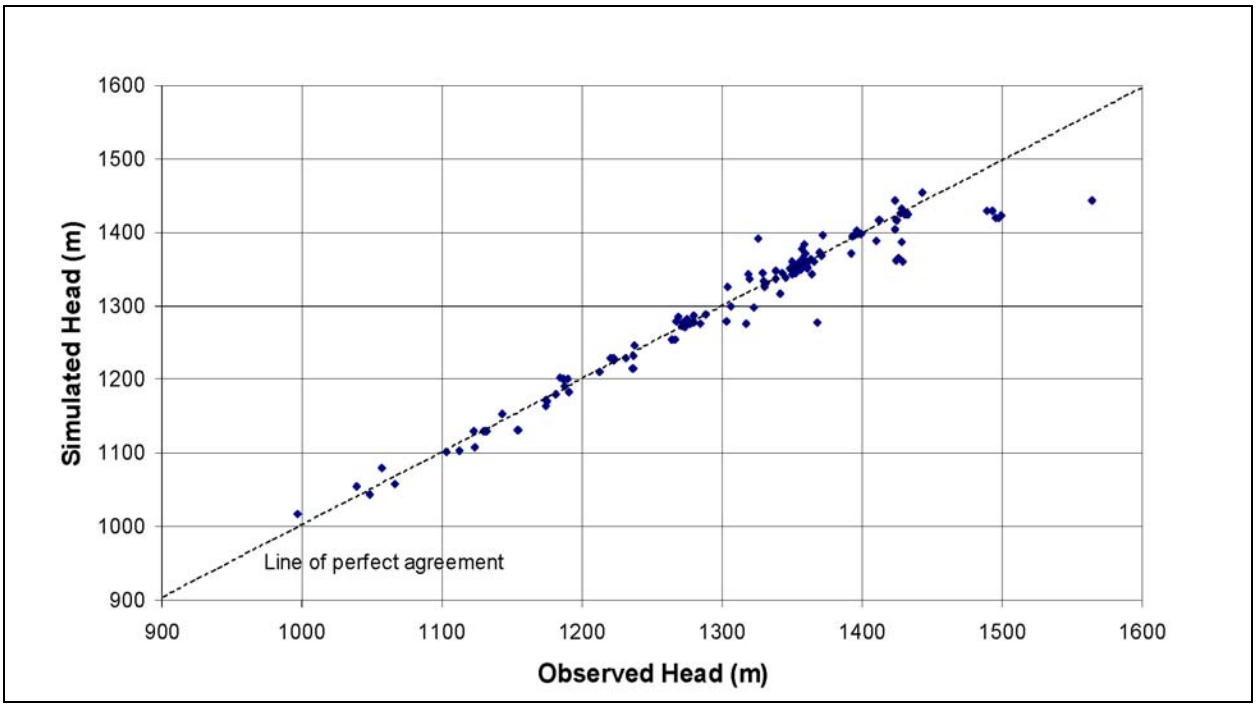

Figure 6-69
Observed Versus Simulated Observation Well Head for BN-MME-SDA Reduced LCCU1 Permeability Alternative

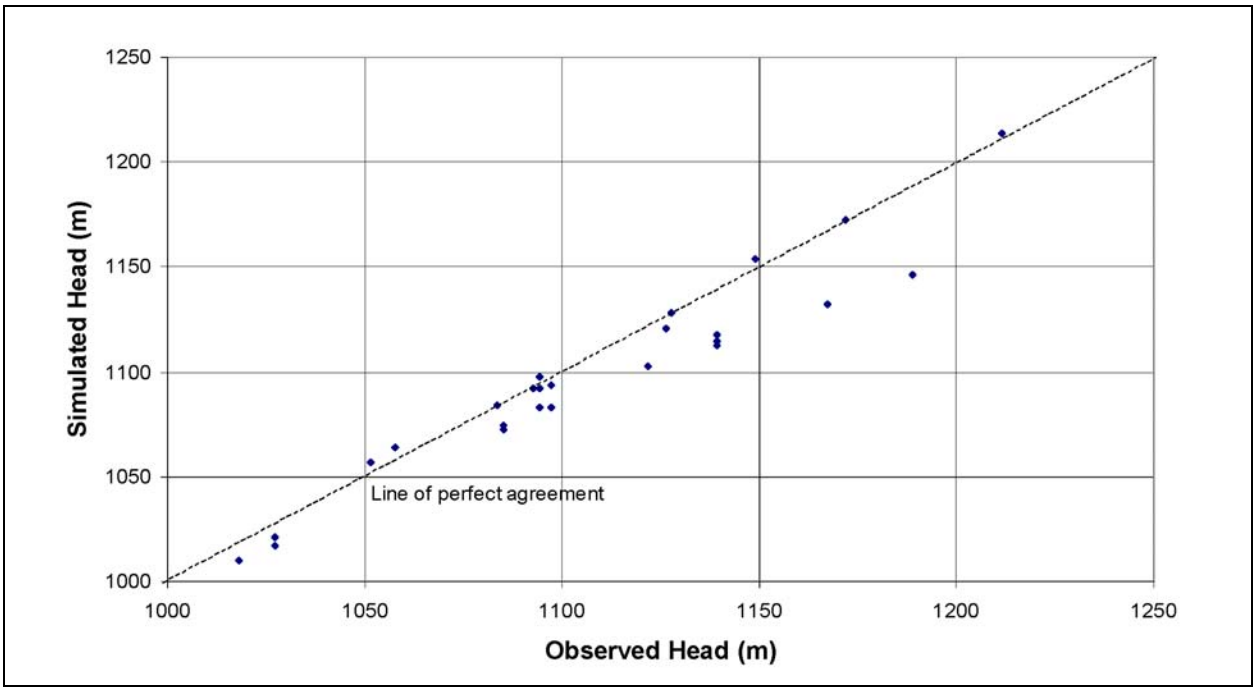

Figure 6-70
Observed Versus Simulated Spring Head for BN-MME-SDA Reduced LCCU1 Permeability Alternative

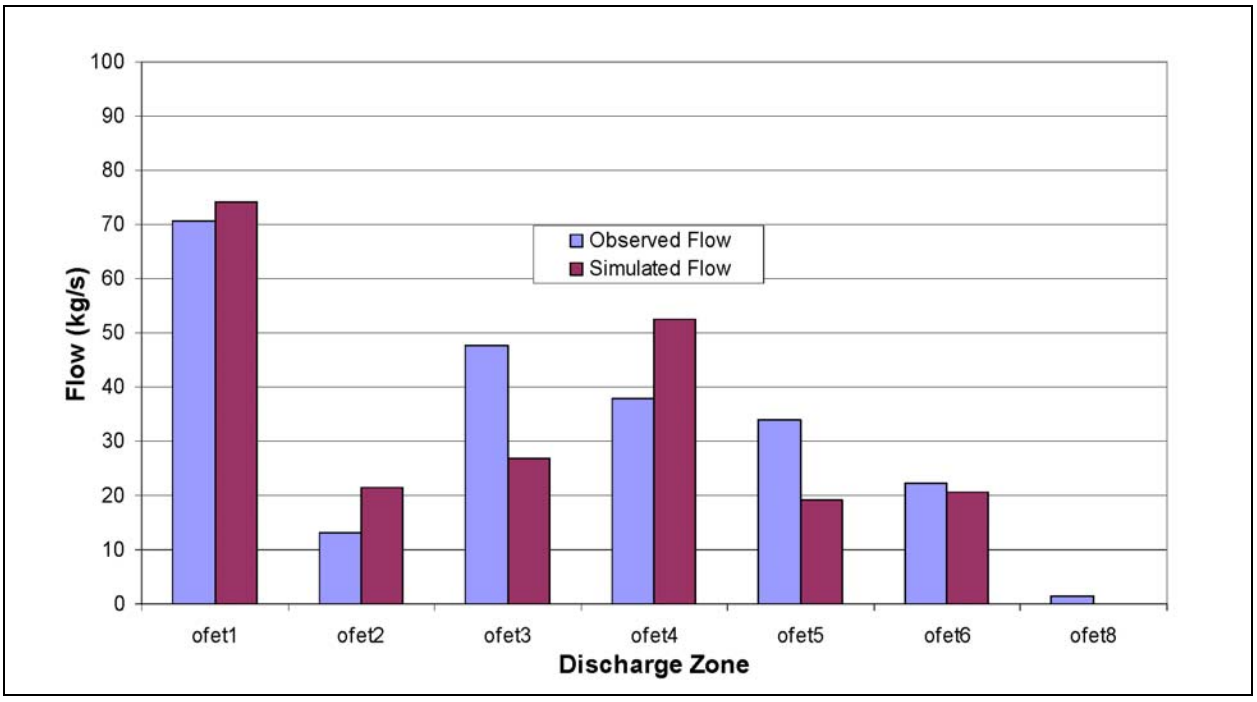

Figure 6-71
Observed and Simulated Oasis Valley Discharge for BN-MME-SDA Reduced LCCU1 Permeability Alternative

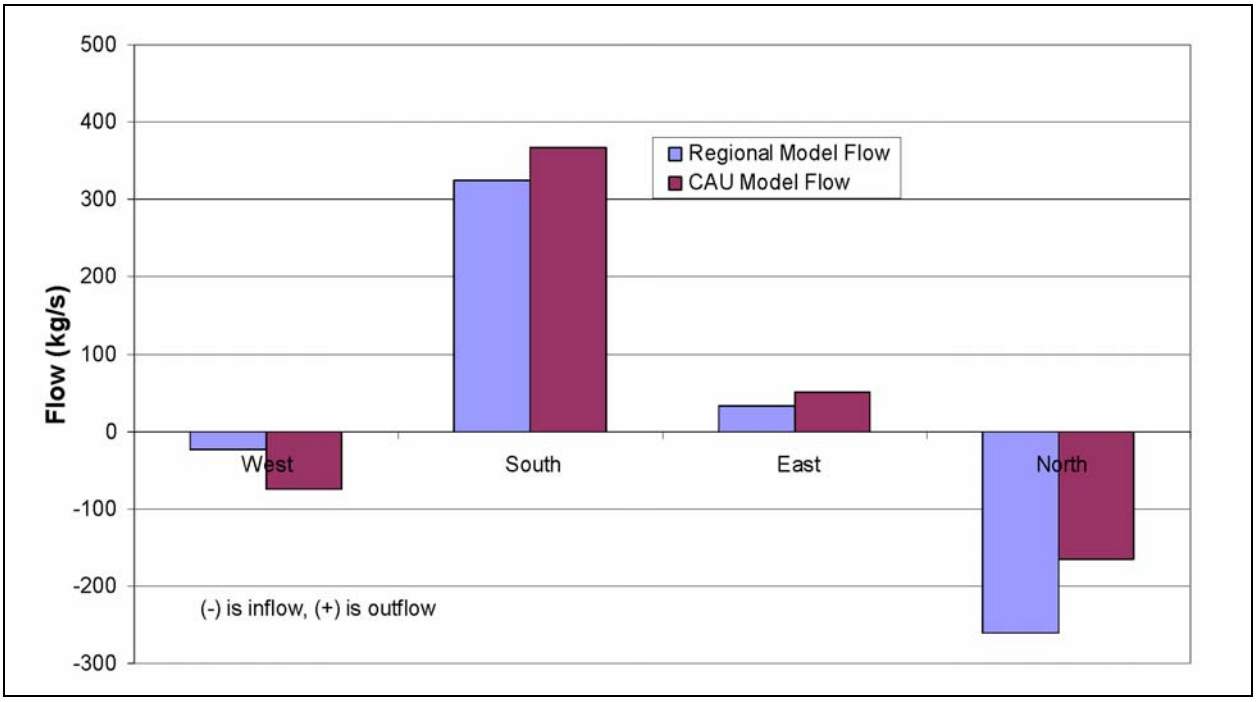

Figure 6-72
Observed and Simulated Boundary Flows for BN-MME-SDA Reduced LCCU1 Permeability Alternative

Table 6-14
Calibration Summary Statistics for BN-MME-SDA Reduced LCCU1 Permeability Alternative

Calibration Data	Number of Data	Mean Weighted Error (m or kg/s)[a]	Maximum Weighted Residual	Minimum Weighted Residual	Error Standard Deviation (m or kg/s)
Well Head	152	-0.056	21 (WW-8)	-24 (U-19ad)	7.3
Spring Head	28	2.6	19 (Torrance Spring)	-6.3 (Spring id 159)	6.8
Oasis Valley Discharge	7	3.4	41 (Zone 3)	-29 (Zone 4)	23
Boundary Flow	4	-13	26 (West)	-47 (North)	29

[a]Positive sign is simulated less than target, negative is larger.

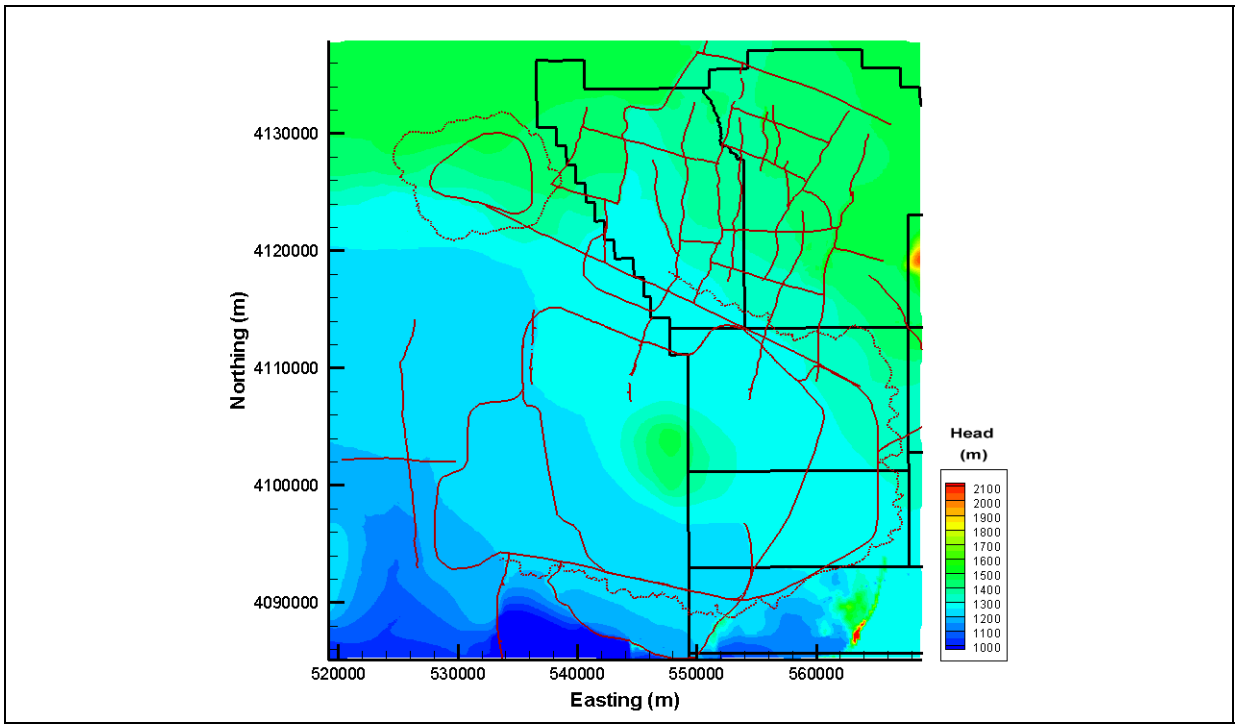

Figure 6-73
Simulated Water Table for BN-MME-SDA Reduced LCCU1 Permeability Alternative

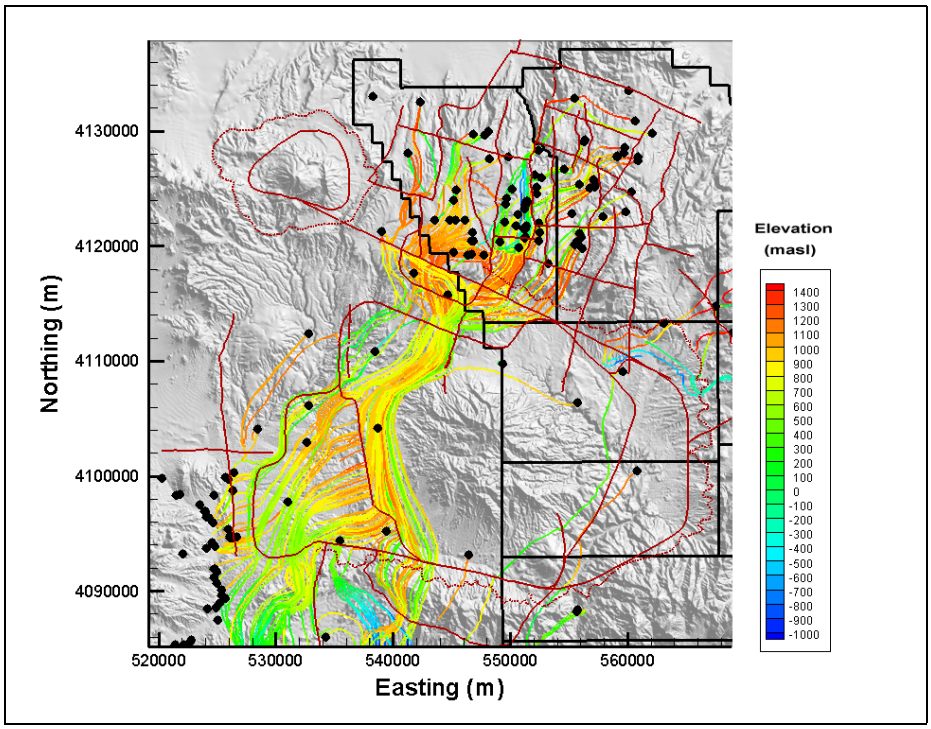

Figure 6-74
Particle Tracks for BN-MME-SDA
Reduced LCCU1 Permeability Alternative

6.2.4.3 Chimney Permeability Enhancement

Pawloski et al. (2001) used chimney permeability values that were at least 70 times higher than the native rock to simulate groundwater flow near CHESHIRE. The chimneys were incorporated in the CAU flow model mesh where the tests were below the water table, and their effect on the flow model was investigated by applying a permeability multiplier of 70 for the chimney nodes. Table 6-15 summarizes the calibration statistics. The objective function changed slightly to 16,609 from 16,651 in the base HFM. Figure 6-75 shows the simulated flow paths, which are very similar to the base HFM - selected HSU depth-decay and anisotropy results. It is concluded that there is very little flow model sensitivity to chimney permeability alteration.

Conceptually this is correct, because the overall scale of alteration is relatively small and any observation well close enough to a test to detect the chimney permeability alteration would be so affected by the test that it would be difficult to use in the calibration.

Table 6-15
Calibration Summary Statistics for
Chimney Permeability Enhancement

Calibration Data	Number of Data	Mean Weighted Error (m or kg/s)[a]	Maximum Weighted Residual	Minimum Weighted Residual	Error Standard Deviation (m or kg/s)
Well Head	152	-0.4	19 (ER-OV-06a)	-27 (UE-20n #1 1,005.84 m)	7.5
Spring Head	28	2.8	19 (Torrance Spring)	-5.5 (Ute Springs Culvert)	6.7
Oasis Valley Discharge	7	4.9	41 (Zone 3)	-26 (Zone 4)	24
Boundary Flow	4	-14	26 (West)	-36 (South)	27

[a]Positive sign is simulated less than target, negative is larger.

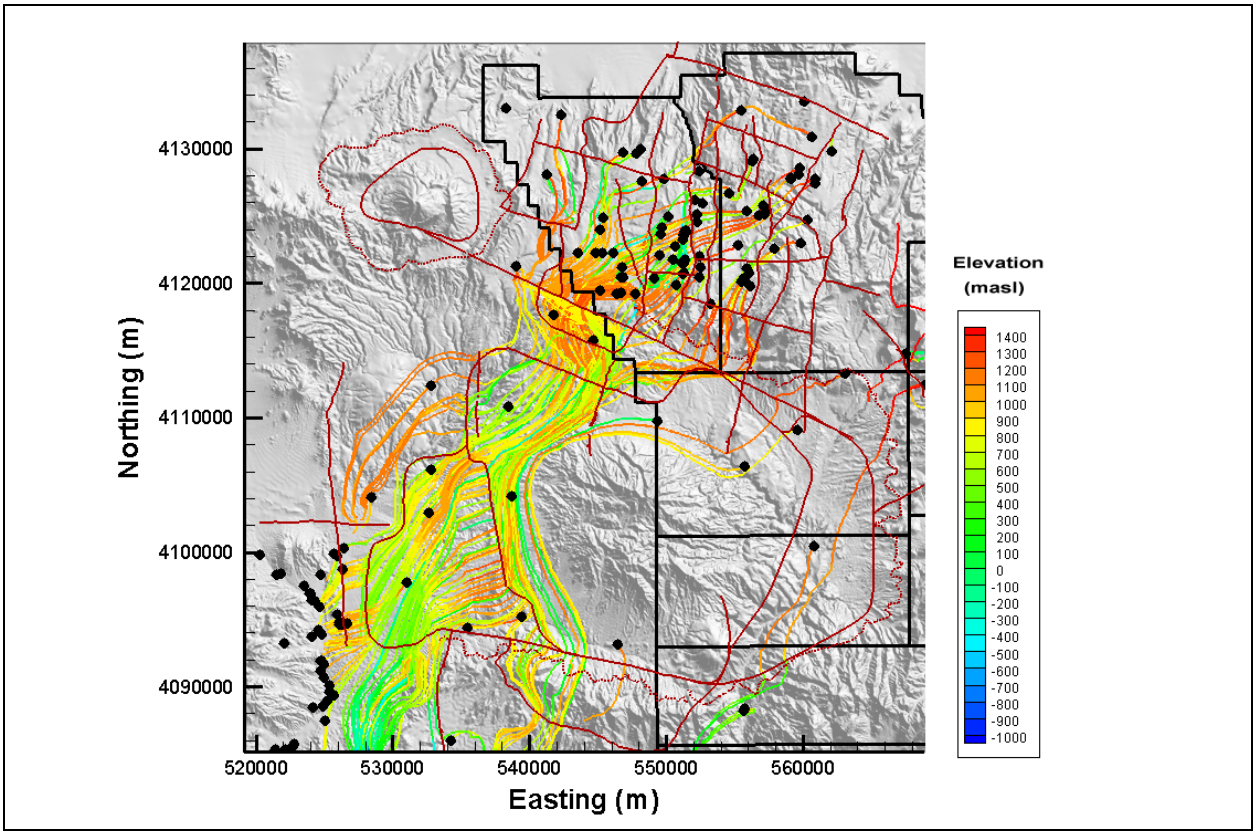

Figure 6-75
Particle Tracks for Chimney Permeability Enhancement

6.2.4.4 Fortymile Canyon Alternative

This variation was designed to test the model sensitivity to flow down Fortymile Canyon. The TMCM Northern Timber Mountain eastern subdivision, Timber Mountain Dome, and Ammonia Tanks eastern subdivision permeabilities were all raised an order of magnitude to try to direct more flow down Fortymile Canyon. The LCCU1 permeability was dropped an order of magnitude to remove its influence and test the ability of recharge in the canyon to support the flow field. This analysis was done only on the base HFM selected HSU depth-decay and anisotropy parameterization, with the USGSD recharge model (which generally tends to give the best calibration results).

Calibration summary statistics are shown in Table 6-16, with simulated Oasis Valley (179 simulated versus 227 kg/s observed) discharge is noticeably lower as the mean observation well error with respect to Table 5-9 in Section 5.6.2. The simulated Oasis Valley discharge is about two standard deviations (about 30 kg/s) away from the estimated value; thus, this model has a lower plausibility than others that agree better with Oasis Valley discharge data. WW-8 is the well with the highest undersimulation in this case, which is consistent with the effects of dropping the LCCU1 permeability. The objective simulation for these results is 19,588, which is slightly worse than the value of 16,651 shown in Section 5.6.2, but still better than the SCCC-MME-SDA and BN-MME-ADA cases.

Table 6-16
Calibration Summary Statistics for BN-MME-SDA Fortymile Canyon Alternative

Calibration Data	Number of Data	Mean Weighted Error (m or kg/s)	Maximum Weighted Residual	Minimum Weighted Residual	Error Standard Deviation (m or kg/s)
Well Head	152	1.3	52 (WW-8)	-23 (U-19ad)	8.7
Spring Head	28	3.1	19 (Torrance Spring)	-5.3 (Spring id 159)	6.8
Oasis Valley Discharge	7	14	47 (Zone 2)	-11 (Zone 3)	26
Boundary Flow	4	2.8	30 (East)	-32 (North)	24

[a]Positive sign is simulated less than target, negative is larger.

Figure 6-76 shows weighted residuals, and Figure 6-77 shows the particle tracks. There is clearly a bias in Fortymile Canyon from the changes that is not easily compensated for with other parameters. This is interpreted as arising from the draining off of water along the canyon from the higher permeabilities. Many more particle tracks exit Areas 19 and 20 and flow down Fortymile Canyon than in the BN-MME-SDA case, which is consistent with the bias to undersimulate Oasis Valley discharge noted in Table 6-16.

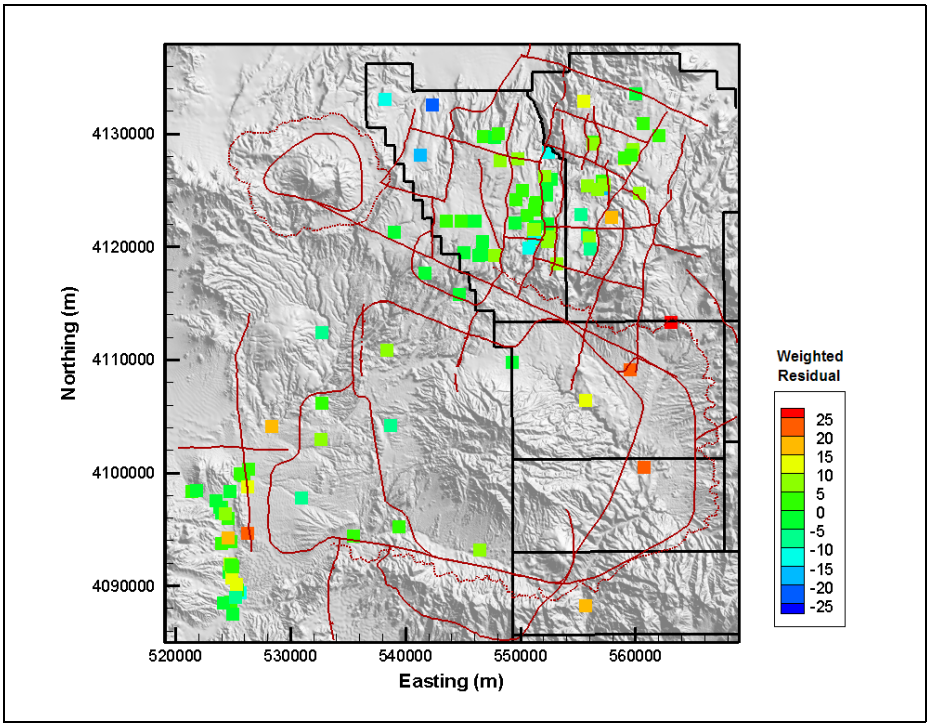

Figure 6-76
Post Plot of Weighted Well and Spring Head Residuals for BN-MME-SDA Fortymile Canyon Alternative

6.2.4.5 Selected Hydrostratigraphic Horizontal Anisotropy

Anisotropy, or directional dependency, in permeability is a characteristic property of fractured rocks (NRC, 1996). Hydraulic anisotropy is commonly determined from multiwell hydraulic test analysis, such as that performed during the BULLION FGE in Area 20 (IT, 1998a) that estimated an average major-to-minor direction permeability ratio of 8 striking about N30°E. These are the only data available for Pahute Mesa. However, fracture analysis as observed in borehole logs can be used as a qualitative tool to assess possible anisotropy. Analysis of composite data for fractures identified in

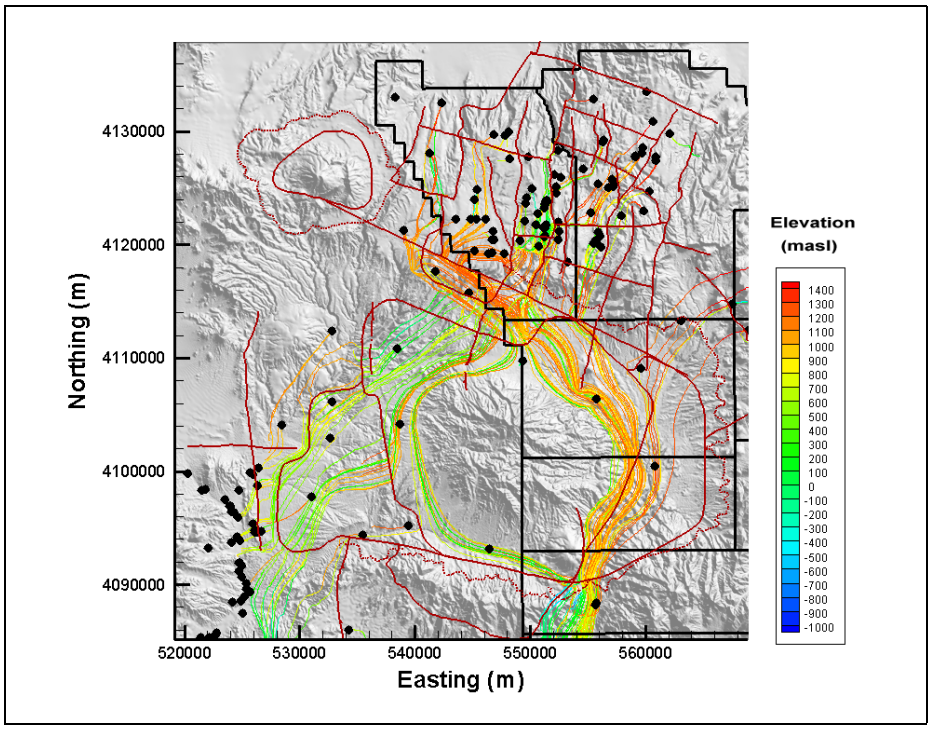

Figure 6-77
Particle Tracks for BN-MME-SDA Fortymile Canyon Alternative

Pahute Mesa and Oasis Valley wells completed in volcanic rocks (LFA, WTA, VTA, and TCU HGUs) reveals four mean fracture populations (IT, 2001). The two predominant populations trend roughly north, and dip west and east. The two secondary populations trend roughly northeast and northwest, and dip northwest and northeast, respectively. The difficulty in utilizing fracture data is illustrated by comparing the BULLION FGE results to the fracture analysis; the hydraulic test is within the range of directions, but the range in direction is very wide (essentially 90°). Horizontal anisotropy was not used in the model because the sparseness of the data were felt to be prohibitive. In addition, the computational demands of using an arbitrary permeability tensor with FEHM make it computationally infeasible. However, the FEHM mesh for the Pahute Mesa flow model is aligned north-south, which allows testing of anisotropy aligned with the strike of the mesh.

Increasing the permeability by a factor of 5 in the y, or north-south, direction for the reduced LCCU1 permeability case (see Section 6.2.4.2) for selected HSUs and recalibrating the model investigated the effects of horizontal anisotropy. Pawloski et al. (2001) used the same value of horizontal anisotropy in their analysis of the CHESHIRE test. Conceptually not all HSUs should have anisotropy, and the ones that were included were lavas and units that had welded tuff present. Thus, all the composite

HSUs were changed, as well as lava-flow aquifers. The changed HSUs are as follows: PBRCM, DVCM, YMCFCM, PCM, TMA, KA, BA, PLFA, CHZCM, TSA, TCA, TMCM, THLFA, THCM, FCA, FCCM, DVA, and TCVA.

Figures 6-78 through 6-81 show the observed and unweighted simulated values for the calibration wells, springs, Oasis Valley discharge, and boundary flows. The Oasis Valley discharge is much too high for Zone 4, which results in the downstream flows being too low. The spring heads also show a bias toward undersimulation that is related to the discharge imbalance. The FCCM and, to a lesser degree, TMCM control shallow flow in that area, and thus the effects on discharge are attributed to the impact anisotropy has on these units.

Table 6-17 summarizes the calibration statistics. The objective function is 32,011. Relative to the LCCU1-MME-SDA calibration, this calibration is distinctly worse and is one of the poorest models evaluated. The degradation in model calibration primarily occurred because of Oasis Valley discharge misfit, although the bias to underpredict spring heads is also increased relative to LCCU1-MME-SDA.

Figure 6-82 shows the posted weighted residuals; there is a slight bias to undersimulate water levels in Oasis Valley that is also suggested by the spring head mean error. There is a pattern of oversimulation through the Thirsty Canyon area down to Oasis Valley that probably causes the oversimulation of discharge in the northern part of the valley. Simulated Oasis Valley discharge is 244 kg/s, which is within 10 percent of the estimated only because of the averaging of errors. Figure 6-83 shows the simulated water table, and Figure 6-84 shows the simulated flow paths. The water table and flow paths have the same general character seen in all the simulation. Thus, including horizontal anisotropy does not create completely implausible results, although the oversimulation of Oasis Valley discharge is probably related to horizontal anisotropy because it is harder to move water east-west into Oasis Valley and it is ringed with composite units that, for this test, had horizontal anisotropy. This effect may also be related to the north-south orientation dictated by the mesh, conceptually if a more easterly strike is used the concentration of flow into northern Oasis Valley might not be so severe. A spatially variable anisotropy would also offset the north-south effects, but no data exist to define such patterns.

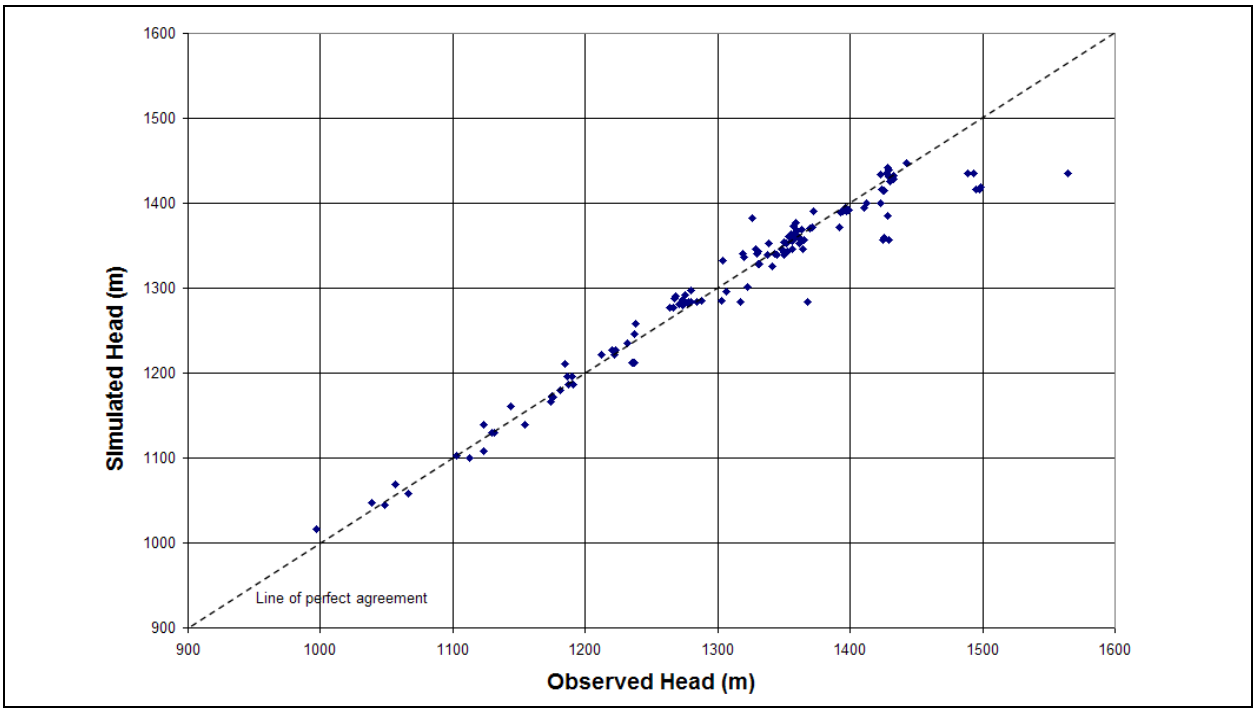

Figure 6-78
Observed Versus Simulated Observation Well Head for BN-MME-SDA Reduced LCCU1 Permeability Alternative with 5:1 North-South Anisotropy

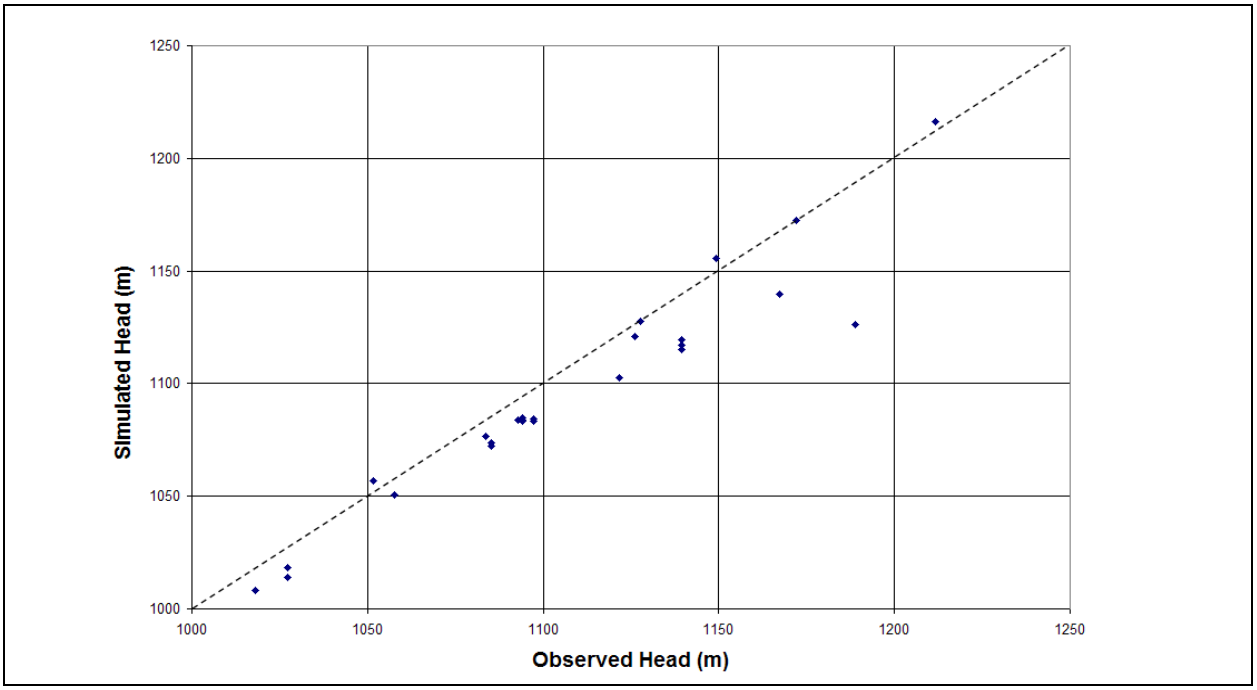

Figure 6-79
Observed Versus Simulated Spring Head for BN-MME-SDA Reduced LCCU1 Permeability Alternative with 5:1 North-South Anisotropy

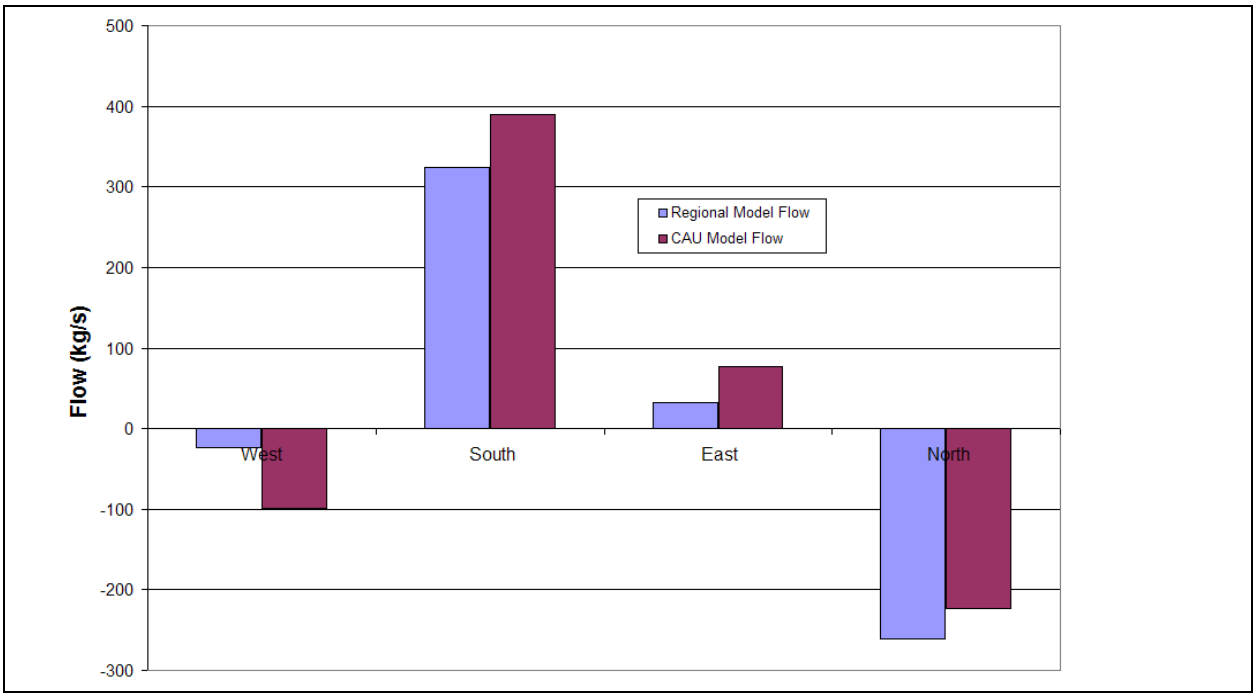

Figure 6-80
Observed and Simulated Oasis Valley Discharge for BN-MME-SDA Reduced LCCU1 Permeability Alternative with 5:1 North-South Anisotropy

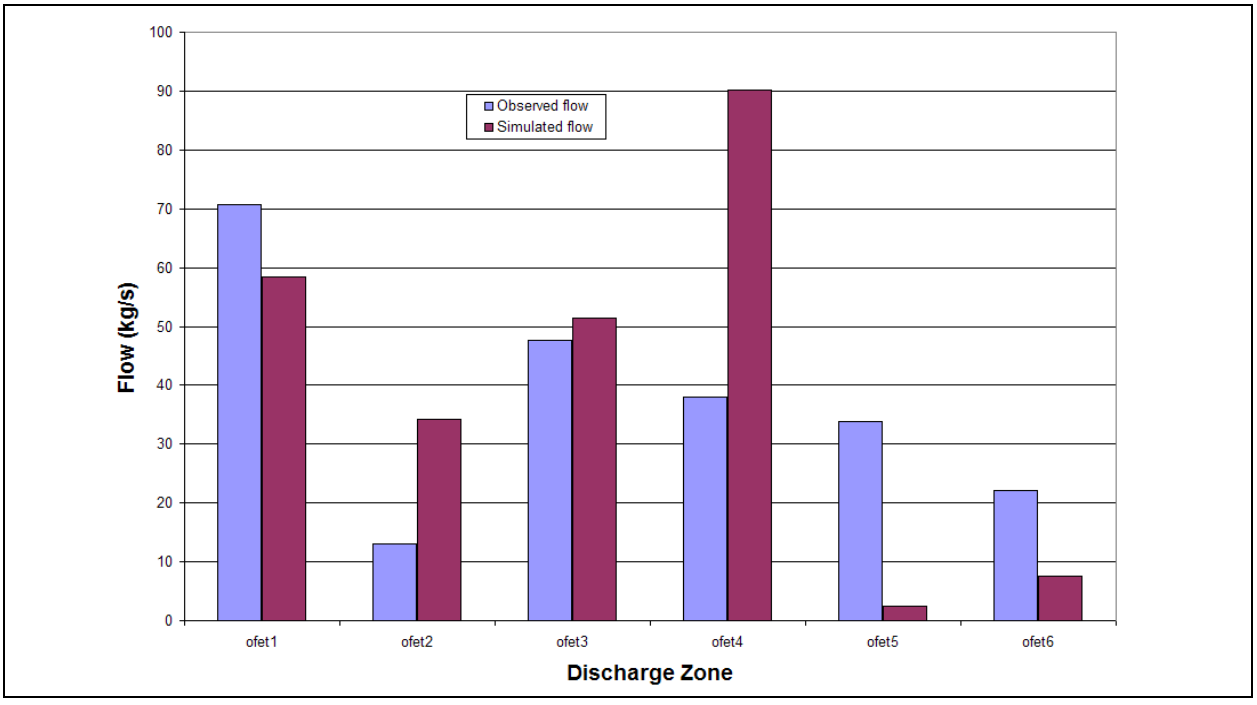

Figure 6-81
Observed and Simulated Boundary Flows for BN-MME-SDA Reduced LCCU1 Permeability Alternative with 5:1 North-South Anisotropy

Table 6-17
Calibration Summary Statistics for LCCU1-MME-SDA with Selected HSU Horizontal Anisotropy of 5:1

Calibration Data	Number of Data	Mean Weighted Error (m or kg/s)	Maximum Weighted Residual	Minimum Weighted Residual	Error Standard Deviation (m or kg/s)
Wells	152	-0.74	20 (ER-OV-06a)	-21 (UE-20n #1) (1,005.84 m)	7.4
Springs	28	5.2	19 (Torrance Spring)	-6.5 (Spring id 159)	8.5
Oasis Valley Discharge	7	-5.0	62 (Zone 5)	-104 (Zone 4)	51
Boundary Flow	4	-9.1	38 (West)	-33 (South)	29

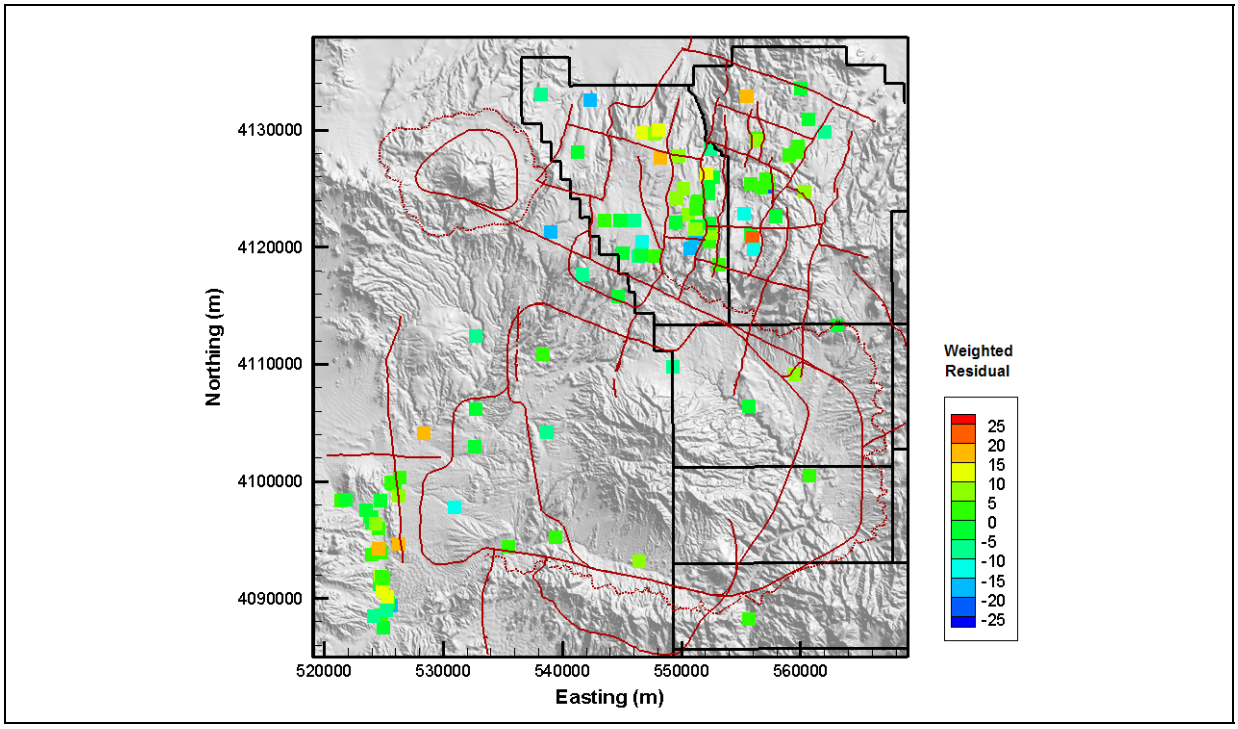

Figure 6-82
Post Plot of Weighted Well and Spring Head Residuals for BN-MME-SDA Reduced LCCU1 Permeability Alternative with 5:1 North-South Anisotropy

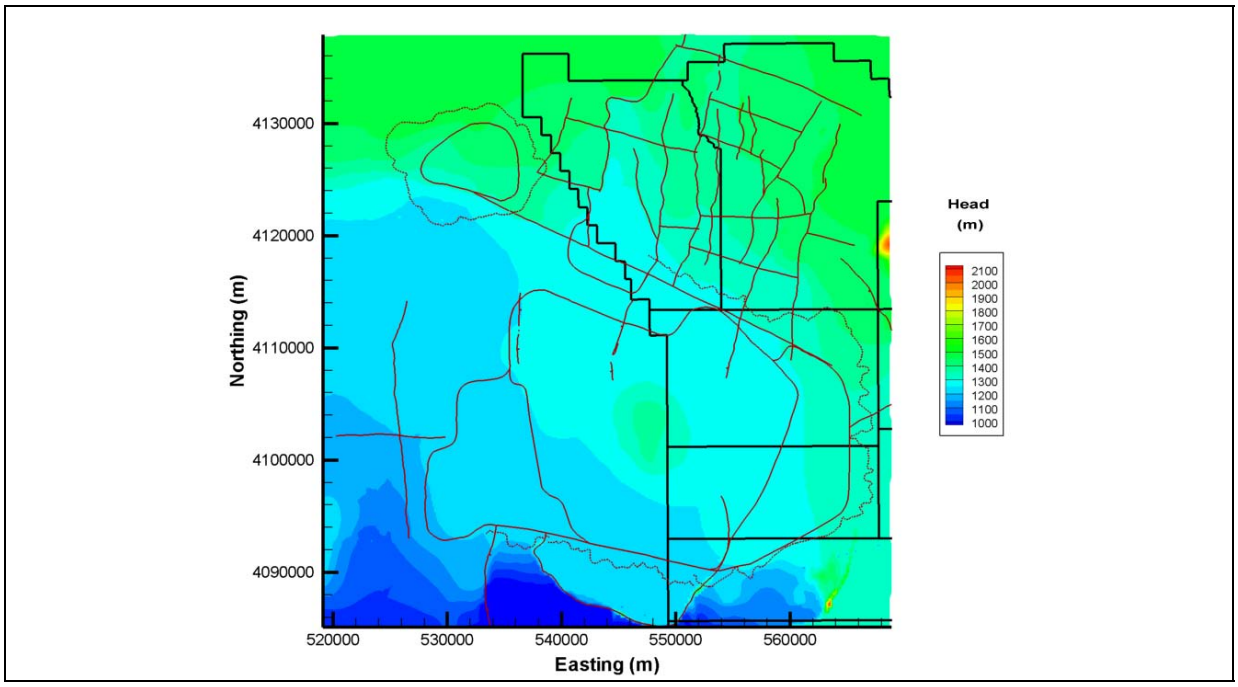

Figure 6-83
Simulated Water Table for BN-MME-SDA Reduced LCCU1 Permeability Alternative with 5:1 North-South Anisotropy

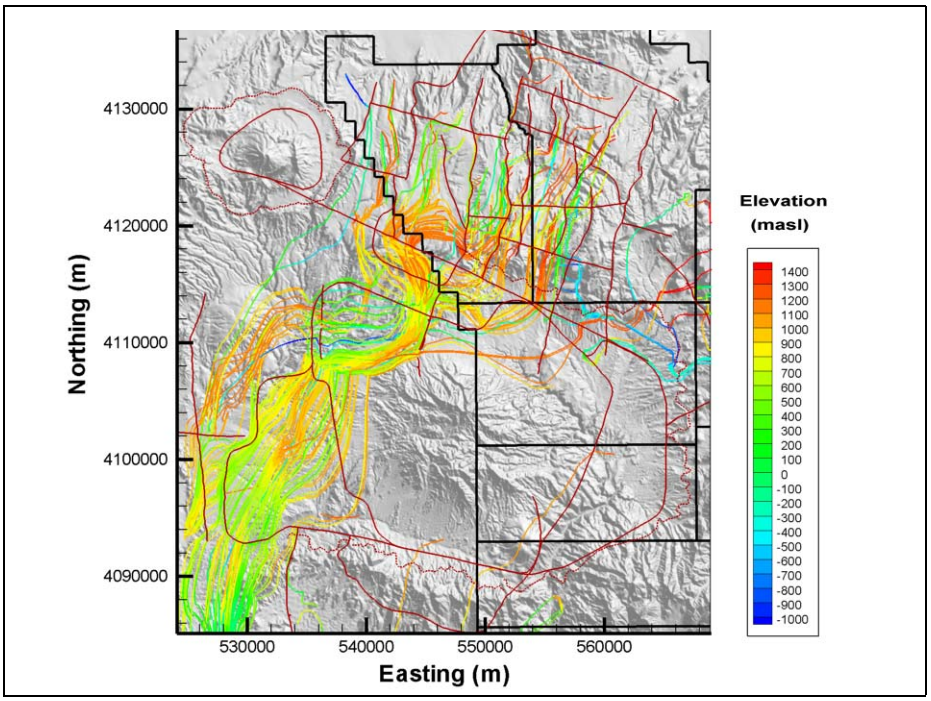

Figure 6-84
Particle Tracks for BN-MME-SDA Reduced LCCU1 Permeability with 5:1 North-South Anisotropy

The HSUs with changed permeability are shown in Figure 6-85. The geometric mean permeability (including reference permeability for HSUs with depth decay) was computed for the anisotropy case and subtracted from the LCCU1-MME-SDA permeability. The display is in log space; thus, a difference of 1.0 is an order of magnitude, and a negative value is an increase from the isotropic case. Figure 6-85 shows that there is a ubiquitous increase in effective permeability when north-south anisotropy is added. This is interpreted to arise because the flow system in the area, while showing a distinct north-south trend, is not strictly north-south like the anisotropy and higher effective permeabilities are required to move water in off-strike directions.

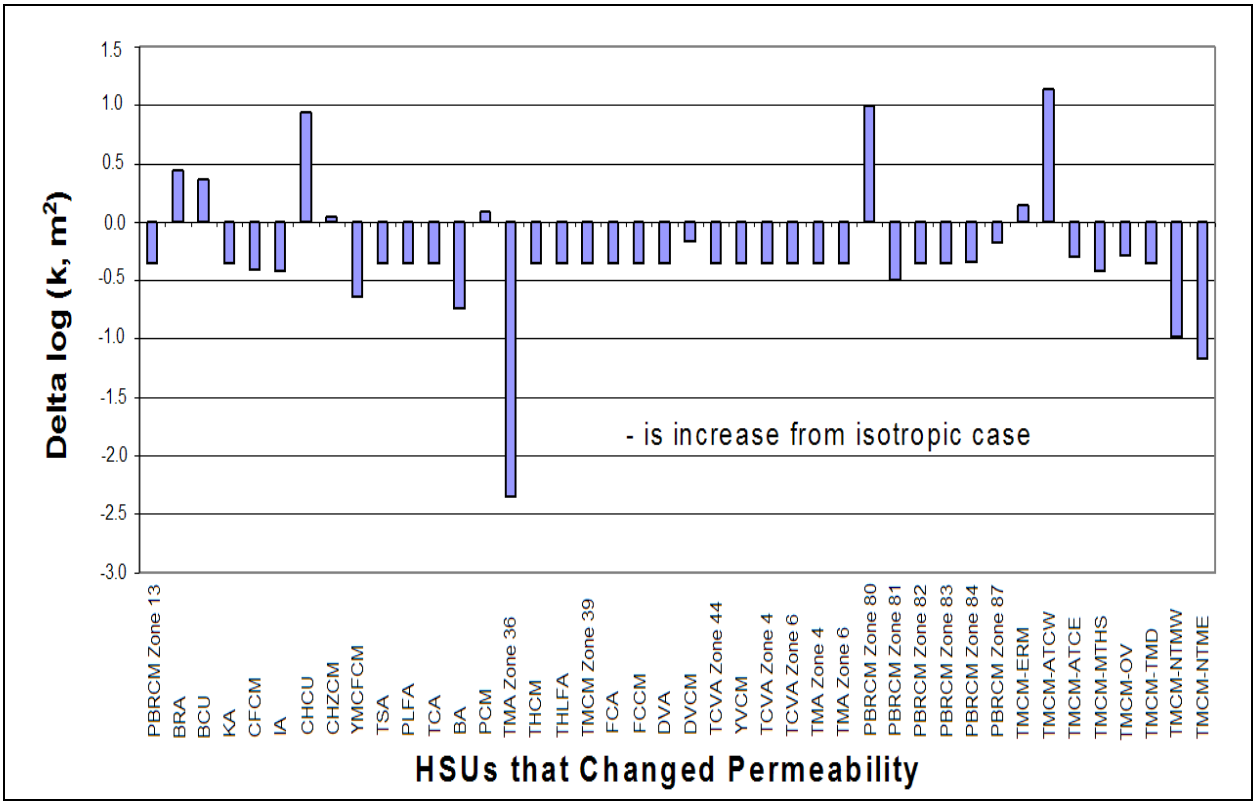

Figure 6-85
HSU Permeability Changes for BN-MME Reduced LCCU1 Permeability with 5:1 North-South Anisotropy

6.2.4.6 Timber Mountain Hydraulic Effects

All of the Pahute Mesa flow models, to some degree and by design, show the effect of a recharge mound under Timber Mountain. This feature is inferred from first principles and only suggested by the observation well data. Because the mound is an interpreted feature, it is important to understand its impact on the flow model. In addition, the Timber Mountain Composite (TMCM) HSU was subdivided during calibration, and the final impact of the subdivision should be investigated (individual parameter sensitivity is described earlier in Section 6.0). Three cases were investigated: 1) material 74, which represents the Timber Mountain Dome area (the area with the highest recharge in Timber Mountain) in Figure 5-6 and is used to control the height of the mound, reference permeability was increased 10 times; 2) the Timber Mountain Dome subdivision of the TMCM reference permeability was increased 100 times; and 3) a single value of the TMCM reference permeability was used.

In each case, the parameter change was made (and stayed fixed in the first two cases) and the model recalibrated. The reduced LCCU1 permeability alternative with MME recharge and selected depth decay as described in Section 6.2.4.2 was used as the starting point for these analyses.

Figures 6-86 through 6-89 show the observed and unweighted simulated values for the calibration wells, springs, Oasis Valley discharge, and boundary flows for all three cases. In general, the differences are mild, and the single TMCM-material case shows the largest errors.

Table 6-18 summarizes the calibration statistics. The objective functions are 16,690, 18,156, and 24,180 (recall the calibration of the case from which these analyses were derived was 16,623) for cases 1 through 3, respectively. The impact of adjusting Timber Mountain Dome and TMCM is generally the same for all cases; model agreement at WW-8 degrades, Torrance Spring is misfit, west and north boundary flows are misfit, as is ET Zone 3 in Oasis Valley.

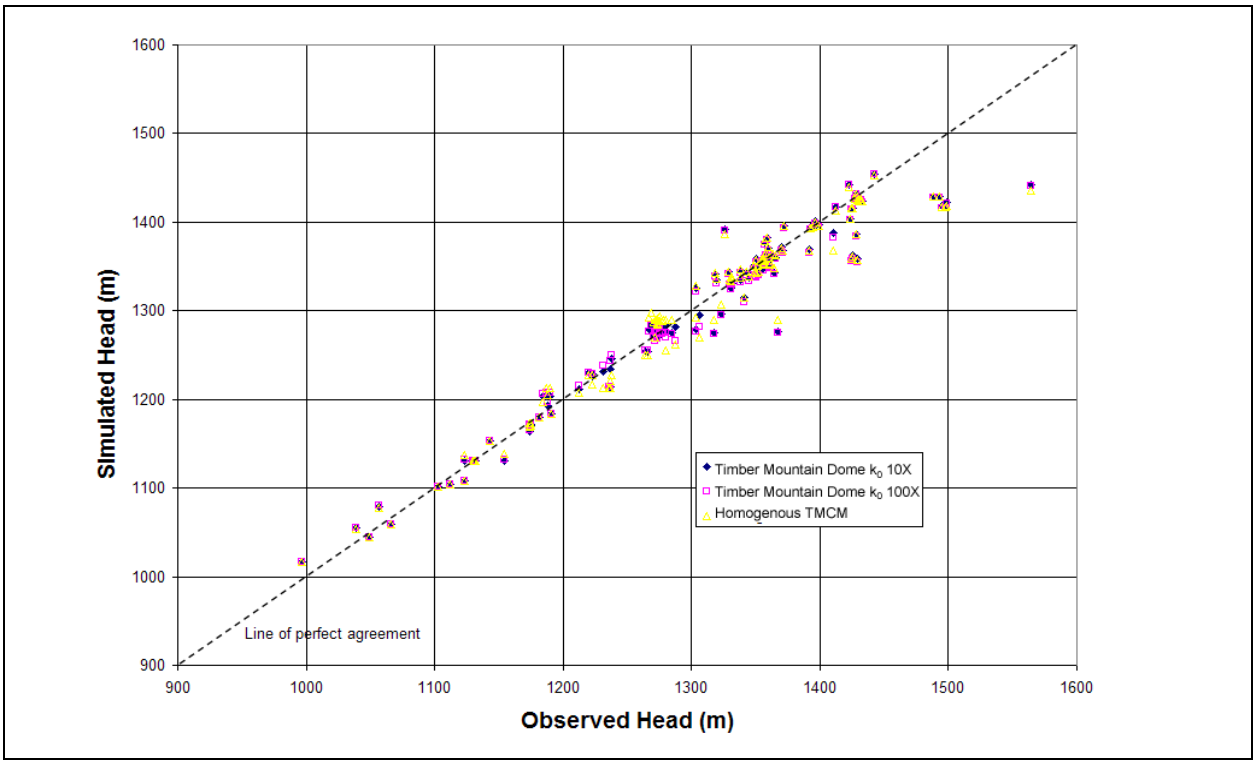

Figure 6-86
Observed Versus Simulated Observation Well Head for TMCM-MME-SDA

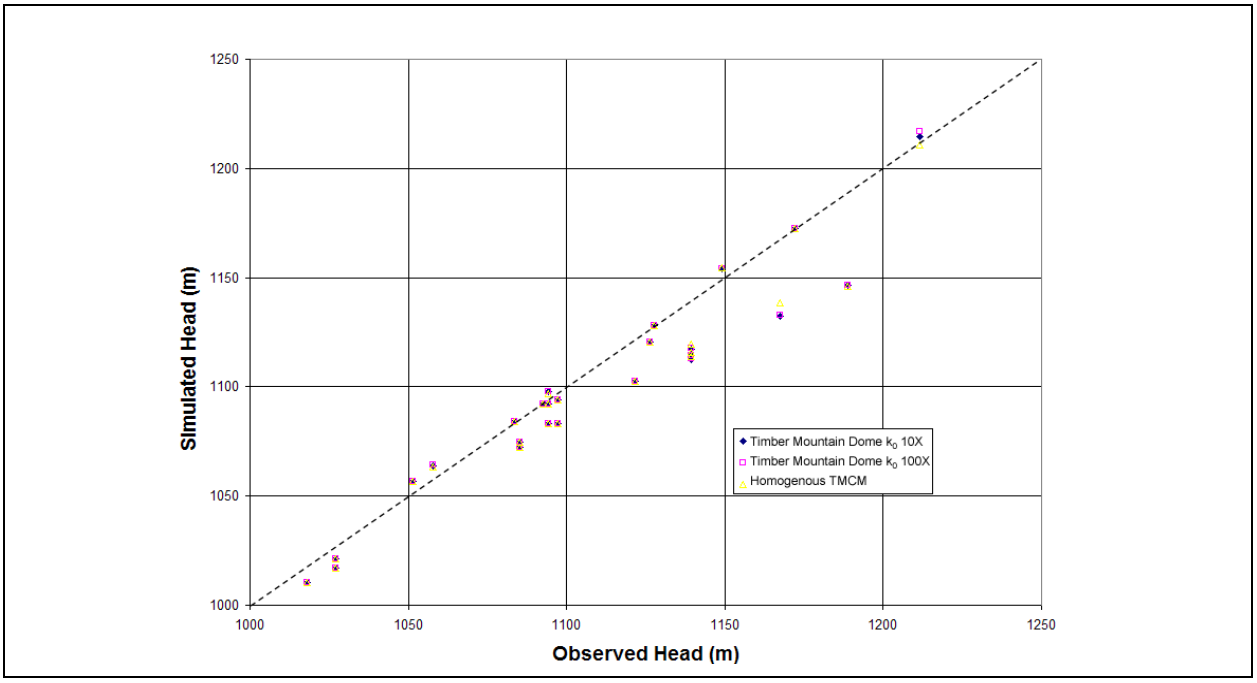

Figure 6-87
Observed Versus Simulated Spring Head for TMCM-MME-SDA

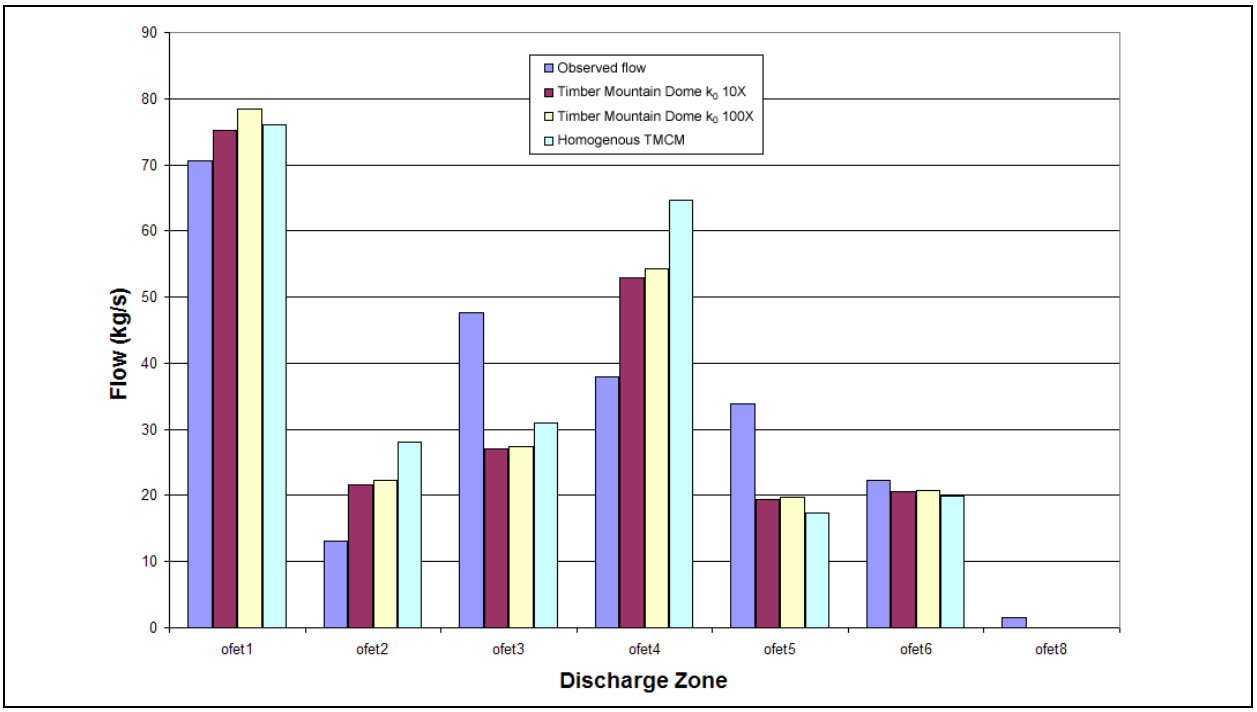

Figure 6-88
Observed and Simulated Oasis Valley Discharge for TMCM-MME-SDA

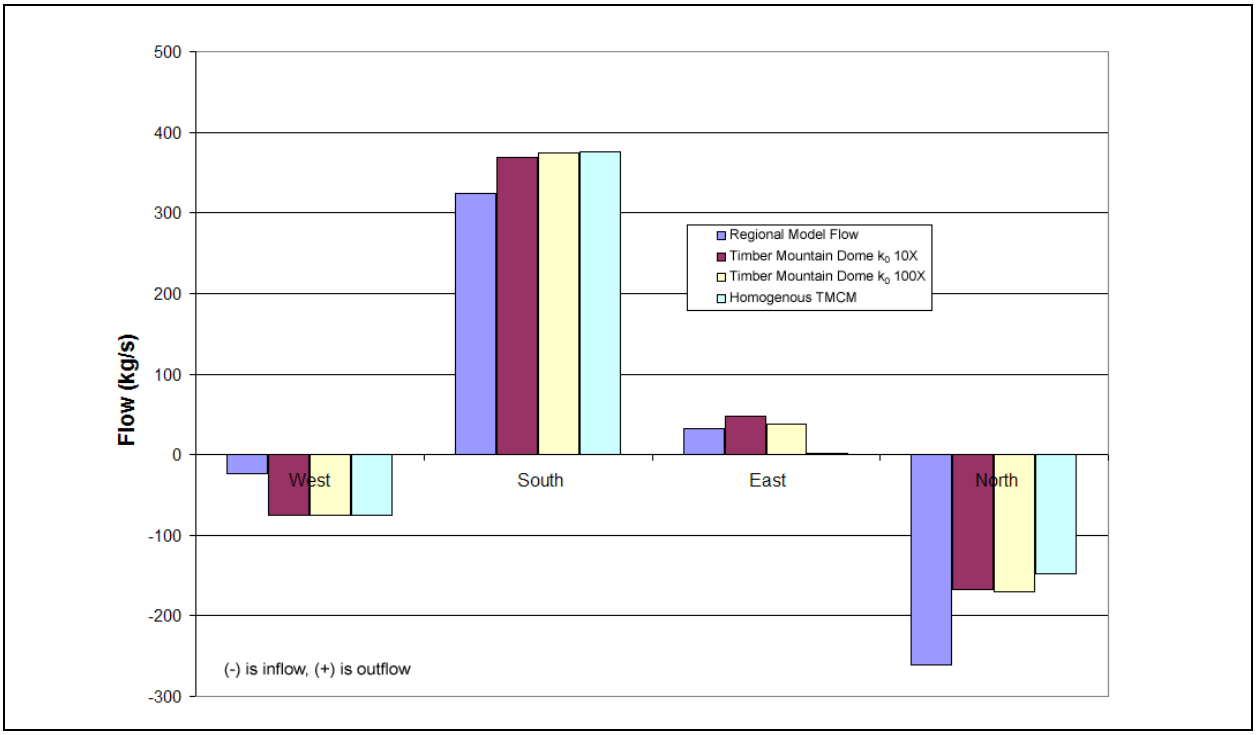

Figure 6-89
Observed and Simulated Boundary Flows for TMCM-MME-SDA

Table 6-18
Calibration Summary Statistics for Timber Mountain Dome Sensitivity

Calibration Data	Number of Data	Mean Weighted Error (m or kg/s)	Maximum Weighted Residual	Minimum Weighted Residual	Error Standard Deviation (m or kg/s)
Wells	152	0.44[a] 1.4[b] 0.12[c]	23 (WW-8) 27 (WW-8) 41 (WW-8)	-23 (U-19ad) -21 (U-19ad) -24 (UE-20n #1 1,005.84 m)	7.3 7.8 8.8
Springs	28	2.6 2.5 2.7	19 (Torrance Spring) 19 (Torrance Spring) 19 (Torrance Spring)	-6.4 (Spring id 159) -6.3 (Spring id 159) -5.5 (Spring id 159)	6.8 6.9 6.8
Oasis Valley Discharge	7	2.8 1.1 -2.9	41 (Zone 3) 40 (Zone 3) 33 (Zone 3)	-30 (Zone 4) -33 (Zone 4) -53 (Zone 4)	23 24 29
Boundary Flow	4	-12.7 -11.9 -10.3	26 (West) 26 (West) 26 (West)	-47 (North) -45 (North) -57 (North)	29 29 35

[a] Material 74 Timber Mountain Dome x 10
[b] Material 74 Timber Mountain Dome x 100
[c] Homogenous TMCM

Figure 6-90 shows the posted weighted residuals. The most notable change is the increasing underprediction in the area of WW-8 as the Timber Mountain Dome reference permeability increases, and in the homogenous case. Forming the mound under Timber Mountain clearly has an effect in this area, although less so elsewhere. Figure 6-91 shows the simulated water table, and Figure 6-92 shows the simulated flow paths. As the Timber Mountain Dome reference permeability increases, decreasing the simulated mound, the potentiometric surface grows flatter (as it conceptually should). The flow paths become more diffuse through the Timber Mountain area as the mound diminishes and no longer focuses flow on its northwest and northeast shoulders.

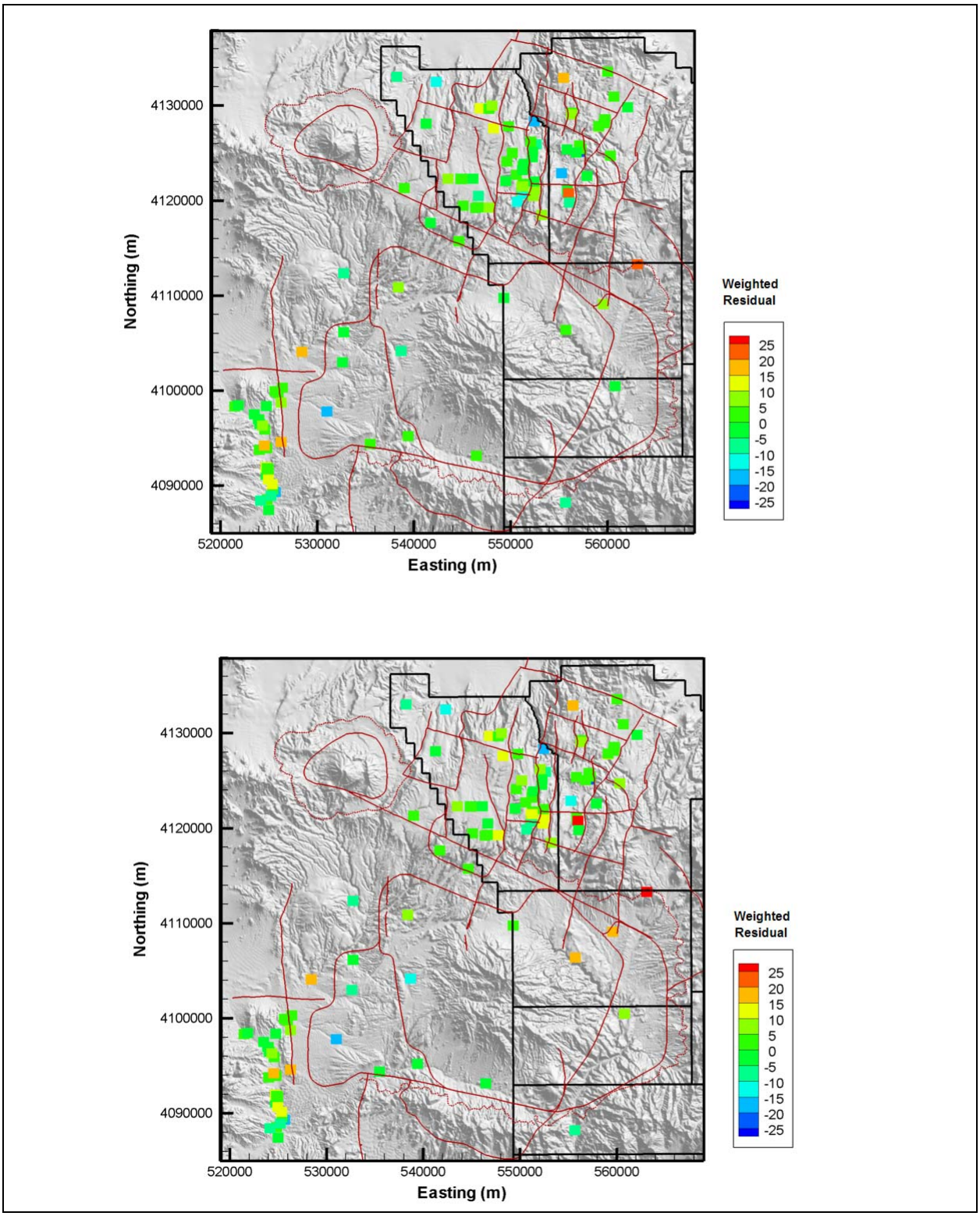

Figure 6-90
Post Plots of Weighted Well and Spring Head Residuals for Timber Mountain Dome k_0 10x (Upper) and 100x (Lower)

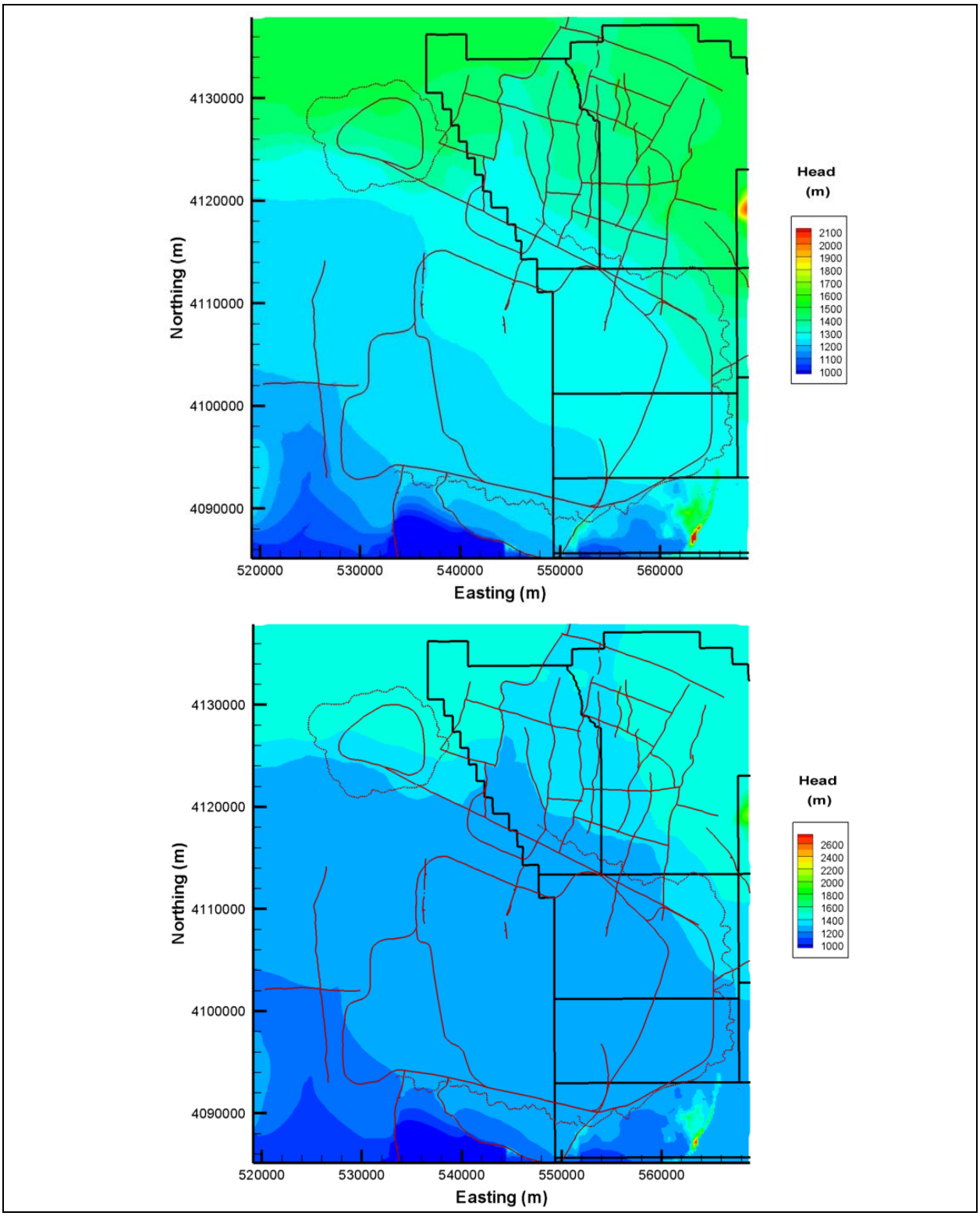

Figure 6-91
Simulated Water Tables for Timber Mountain Dome k_0 10x (Upper) and 100x (Lower)

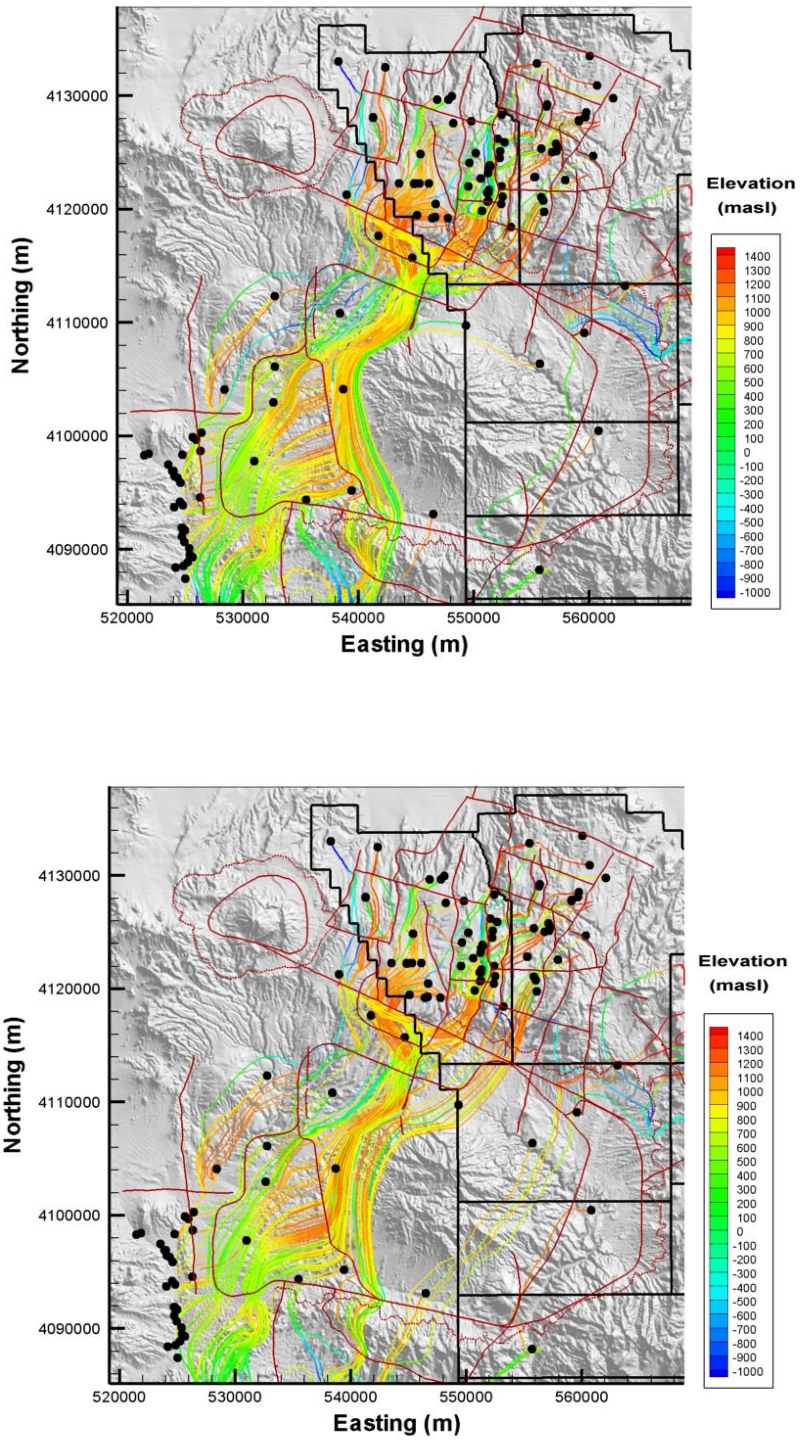

Figure 6-92
Particle Tracks for Timber Mountain Dome k_0 10x (Upper) and 100x (Lower)

6.2.5 Summary of Parameter Sensitivity Analysis

Parameter sensitivity analysis, as is customary practice and specified in the Pahute Mesa CAIP (DOE/NV, 1999), was performed on the two major HFMs in the Pahute Mesa CAU-scale groundwater model using a complementary suite of techniques. Two different approaches to parameterizing the base HFM (selected and all HSU depth decay and anisotropy) were further considered in order to investigate the consequences of choosing one approach or the other. Local sensitivity analyses were carried out using sensitivity coefficients computed by PEST and perturbation analysis around the calibration point. In addition, global sensitivity analyses were carried out using classification tree and entropy analysis to determine parameter importance conditioned over the entire range of parameter variations. For the global sensitivity analysis, a Monte Carlo simulation-based sampling methodology was used to generate multiple parameter combinations to evaluate each model.

The analysis combining a more conventional local sensitivity analysis with a global approach provided important insights about model input/output relationships, with each technique adding information to the overall perspective. In the local sensitivity analysis, the PEST sensitivity coefficients provided a look at relationships very near the point of calibration. This information is somewhat limited because it does not consider the model parameter uncertainty ranges; however, these coefficients provide some of the best insight into what is happening in the final stages of calibration. The perturbation analysis provided an intuitive visualization of the effects of varying individual parameters, with the caveat that combined parameter effects are not captured. In the global sensitivity analysis, the classification tree provided insight into what parameters affect the output over the entire parameter space. The classification tree also showed how particular combinations of parameters interact to produce a particular result. The entropy analysis not only served to corroborate results from the classification tree analysis, but also quantified the relative importance of particular parameters. Also, these global analyses provided information not only about the sensitivity of the objective function (the overall measure of how well the flow model is calibrated) to the input parameters, but also insight into what parameters are most important to the individual components of the objective function. An additional benefit of the Monte Carlo analysis is that it also provides information about which components of the objective function are most important to the total behavior.

The key findings from this analysis are summarized in Table 6-19. Importance rankings are presented with respect to the total objective function, head measurements, and Oasis Valley discharge. Note that the perturbation analyses used the mean difference between heads at target locations as a surrogate for the observation well component of the objective function. The results from the classification tree analysis and entropy analysis are integrated because of their general consistency across all model versions.

Table 6-19
Summary of Key Sensitivity Analysis Findings

Model Case	Sensitivity Analysis Technique	Key Parameters[a]			Comments
		PHI	Oasis Valley Discharge[b]	WELL	
Base HFM – Selected HSU depth decay and anisotropy (BN-MME-SDA)	Global	LCCU1 DVCM	DVCM PBRCM Zone 84[c]	YMCFCM PCM	
	Perturbation	LCCU1 DVCM	DVCM TMA	YMCFCM PCM	
	PEST	Depth decay assigned to selected volcanic HSUs Carbonate depth decay	N/A	N/A	PEST results only for PHI
Base HFM – All HSU depth decay and anisotropy (BN-MME-ADA)	Global	LCA Zone 1 DVCM	PBRCM Zone 13[d] DVCM	FCCM CHCU	
	Perturbation	DVCM LCA Zone 1	DVCM PBRCM Zone 13[d]	YMCFCM LCA3a	
	PEST	LCA3a LCA Zone 1	N/A	N/A	PEST results only for PHI
SCCC HFM – Selected HSU depth decay and anisotropy (SCCC-MME-SDA)	Global	LCCU1 DVCM	DVCM PBRCM	BRA PBRCM CHCU[e]	
	Perturbation	LCCU1 DVCM	DVCM PBRCM	PCM CHCU[e]	
	PEST	Depth decay assigned to selected volcanic HSUs Carbonate depth decay	N/A	N/A	PEST results only for PHI

[a]The top two parameters influencing model calibration
[b]Parameters most important in replicating Oasis Valley discharge
[c]Western PBRCM, see Figure 5-5
[d]PBRCM under Areas 19 and 20, see Figure 5-5
[e]CHCU is all Calico Hills units found in base HFM lumped together in SCCC HFM

The sensitivity analysis confirmed what was observed during flow model calibration: that the major controls on the groundwater flow system are not necessarily all the HSUs on Pahute Mesa. For instance, while it appears that the PBRCM, and to a lesser extent the BRA, have noticeable role in calibration, the fact that the DVCM, PCM, YMCFCM, and LCCU1 dominate (and that the TMCM had any role at all) calibration was unexpected. The underground nuclear tests were all conducted in Areas 19 and 20; hence, the observation well data tend to be clustered there, and the base HFM is also relatively complex in this area. Figure 6-93 shows the PHI perturbation results for the BN-MME-SDA case from 15 HSUs found only on Pahute Mesa: CFCU, CFCM, KA, BFCU, IA, CHCU, CHZCM, CHVCM, CHVTA, TSA, LPCU, PLFA, TCA, UPCU, and BA (see Table 4-1 for HSU descriptions). Remembering that the BN-MME-SDA case had a final objective function of about 17,000 (to the nearest thousand), it is seen that the BFCU, IA, CFCU, and CHZCM have a noticeable effect on calibration over their range of uncertainty. The TCA and CHVTA have a modest effect on model calibration, and the remaining nine HSUs (KA, CFCM, CHCU, TSA, LPCU, PLFA, UPCU, BA, and PVTA) are, practically speaking, of no consequence for model calibration.

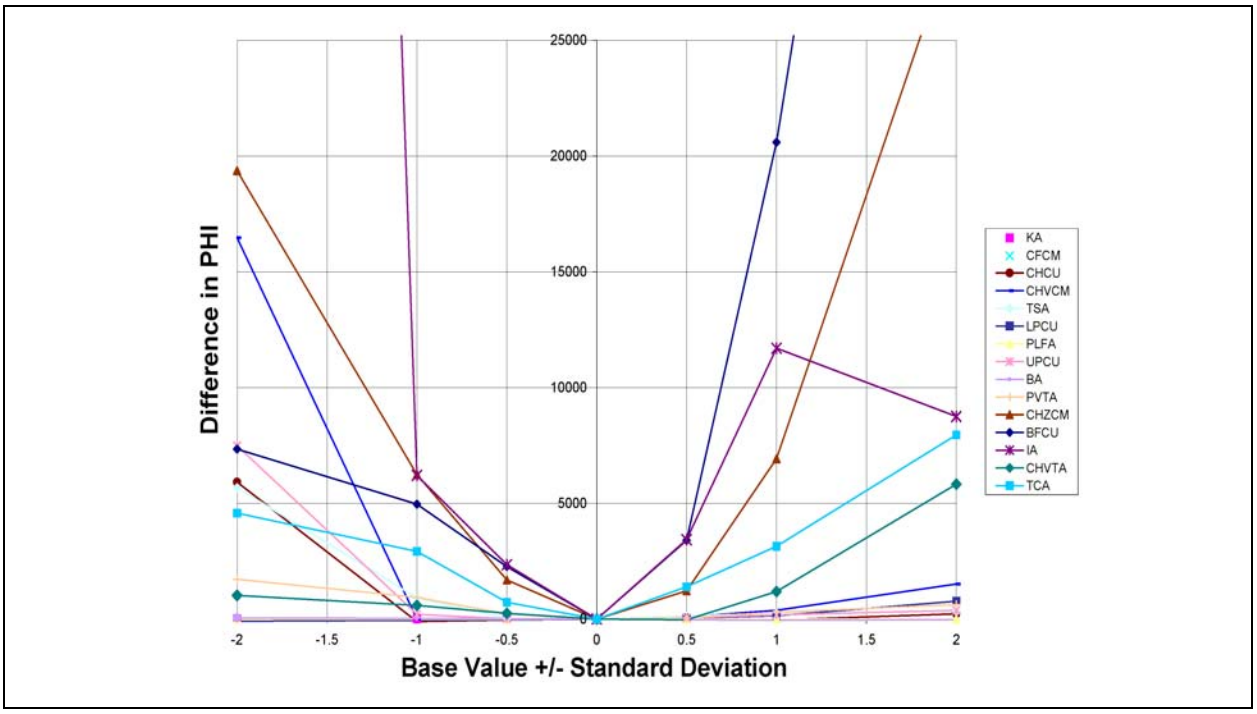

Figure 6-93
PHI Perturbation Results for Selected HSUs in BN-MME-SDA

Conceptually, the BFCU should be a sensitive HSU because it underlies most of Areas 19 and 20, separating the shallower volcanic HSUs from the PBRCM and BRA, as does the CFCU, and the correlation coefficient confirms that this relationship is true; the BFCU and CFCU permeabilities are strongly (greater than 0.95) negatively correlated (see Section 6.2.1.1), the effects of reducing the permeability in one can be offset by increasing the permeability in the other. The CHZCM, as previously noted, has sensitivity in the model because of the 23 observation wells completed in it. The IA is a thick rhyolite present near much calibration data but has no observation wells completed specifically in it. The IA does, however, connect with the CHZCM in a complex way, and this may be the reason for model sensitivity. Lastly, some of the remaining HSUs have relatively small-saturated extents, and the arrangement of the rest is concluded to be such as to not generate much effect. For instance, the TCA is nearly completely strata-bound by the LPCU and UPCU; changing its permeability has little effect because it is the lower permeability LPCU and UPCU that control the TCA ability to influence the flow system.

The Pahute Mesa HFMs, base and SCCC, incorporate a number of faults and other structural features (Appendix B assesses their likely properties in more detail). The Purse and Boxcar Fault systems have been previously identified as having sealing properties (Wolfsberg et al., 2002). Many others though, are unknown. The sensitivity analysis only revealed the Claim Canyon Caldera Structural Margin as a consistently sensitive feature due to its location on the southern edge of the model. Perturbation analysis showed the Hogback and the Rainier Mesa Caldera Structural Margin have a strong effect at a permeability multiplier of 100 (the response between 10 and 100 appears very nonlinear and shows little effect at 10). The Ribbon Cliff Structural Zone (fault 16) that runs east-west between Black Mountain and the Purse Fault is strongly sensitive at low values because it can restrict flow through the area, the North Timber Mountain Moat Structural Zone (Moat Fault, fault 15), Rainier Mesa Caldera Structural Margin, and Ammonia Tanks Caldera Structural Margin are sensitive for the same reason. Fault sensitivity tends to be one-sided; only lower values have any impact. Conceptually, this is sensible because a low (or high) permeability feature located in line with a flow path would have little obvious effect; the faults noted above all tend to lie across groundwater flow paths.

Oasis Valley and UGTA-regional model estimated boundary flow are used as a flow model calibration constraint. This use of boundary flows help further limit the inherent non-uniqueness in a

steady-state flow model with constant-head boundaries. Oasis Valley and western boundary flow are very sensitive to the DVCM, partly because the northern two-third or so of the western model boundary was treated as a no flow. If this conceptualization is revised, this conclusion may change to include additional HSUs, but because of the location of the DVCM near calibration data, it would likely still be sensitive even if the western boundary has a more extensive constant-head specified along its edge. The major inflow on the north is controlled by the LCCU1 at higher permeabilities and LPCU west of the Purse Fault at lower permeabilities. The LCCU1 effect is because at the higher permeability the high head near the Gold Meadows stock is easily propagated to the northern edge-creating outflow where the LCCU1 connects to the northern constant heads that are at lower potential than those near Gold Meadows stock. For the LPCU, at lower permeabilities it hinders flow through the "throat" between the lower permeability rocks in the Black Mountain caldera and the Purse Fault.

On the east, the PBRCM controls flow because it is connected to the boundary and of relatively large areal extent, with the LCA depth decay less important, but still contributing, because of its presence along the eastern edge of the model. The PCM is also sensitive in an analogous manner as the LCCU1, only oriented south, because it is connected to the boundary along the east and south edges. Finally, on the south, DVCM is important once again, presumably because whatever flow in excess of that supplied to Oasis Valley discharges through LCA3 directly to the south past Beatty. To some extent, the specific conclusions drawn are related only to the BN-MME-SDA alternative boundary flows examined via global sensitivity analysis; however, the broad conceptual understanding should still be transferable to the other cases.

6.3 HFM Uncertainty Analysis

It has been noted (Carrera and Neuman, 1986a and b) that inadequate model conceptualization is more detrimental to model predictive ability than parameter uncertainty. The Pahute Mesa CAIP (DOE/NV, 1999) recognizes this uncertainty and has propagated it by developing alternative geologic models for Pahute Mesa. The following section tests the major alternatives described by BN (2002) as summarized in Table 6-19 by implementing them in the FEHM flow model.

As previously described in Section 4.0, meshes for the base and SCCC HFMs were explicitly constructed. However, additional HFM alternatives were addressed using the mesh developed for the

base HFM. This is judged to be reasonable because all the alternatives were closer in initial conception to the base HFM than the SCCC HFM, and the base HFM had a slightly higher grid resolution. The base HFM also fully incorporated faults (as did the other alternatives), which were shown to be important in the previous sections. The procedure for approximating the alternative HFMs using the base HFM mesh is as follows:

- Identify the HSU for every node in the base HFM.
- Identify the HSU for every node in each alternative HFM.
- Using a relational database, find only the nodes in each alternative that are different from the base HFM.
- Construct FEHM input to change the nodes' HSU material type, and run FEHM.

The procedure is approximate because no consideration was (or can be) given to maintaining HSU continuity. Practically, it is more likely (but still unknown) that the uncertainty in actual HSU location in any alternative is greater than the error occurred in this approach, particularly when the depth of the changes is considered. For instance, in the raised Paleozoic (or pre-Tertiary) case, the uncertainty (thought to be large by BN [2002]) in the depth of basement rocks from gravity and well data was considered. Some units were shifted upward by as much as 800 m, with many areas raised 750 m.

In addition, BN (2002) suggested other possible modifications to the geologic model. Table 6-20 shows the suggestions and a brief comment on how they were or were not dealt with.

Table 6-20
Abridged List of Alternative Scenarios for the Pahute Mesa/Oasis Valley 3-D Hydrostratigraphic Model
(Page 1 of 10)

Alternative		Priority Group[a]	Comment
1.0	**HYDROSTRATIGRAPHY-RELATED ALTERNATIVES**		
1.1	**Alternatives to Simplify Hydrostratigraphy**		
1.1.1	Combine intra-caldera intrusives into a single HSU.	**D**	Are all the intra-caldera intrusives the same hydrologically? Can we combine the intrusives beneath the Ammonia Tanks and Rainier Mesa calderas?
	Response		The intrusives were assigned identical properties during calibration and their sensitivity investigated and found to be minimal.
1.1.2	Simplify HSUs above the water table.	**D**	Can HSUs in the unsaturated zone be lumped, simplified, or ignored?
	Response		The CAU model, by definition, is for the saturated zone only. HSUs in the unsaturated zone were ignored.
1.1.3	Decrease the depth of the model.	**D**	Is there any merit in raising the bottom of the model? Work on the regional model demonstrated that even after removing the lowest 2 km (1.2 mi) from the bottom of the model, there was no difference in the outcome compared to the original model. The elevation of the bottom of the framework model is now consistent with the regional model.
	Response		This was not investigated.
1.2	**Alternatives to Add Hydrostratigraphic Detail**		
1.2.1	Include all alluvium (AA) as mapped on USGS surface geologic maps.	**D**	In parts of the current base model, alluvium (typically, thin surficial deposits) is lumped with an underlying HSU. Thick deposits of AA, however are differentiated. Could this affect recharge (e.g., alluvium filling a wash or small structural valley)?
	Response		The effects of AA would have been apparent only in the USGS recharge estimates. MME does not consider soil texture, and DRI CMB masked the alluvium. These estimates were generated independently by the USGS, and it would be arbitrary to modify them.
1.2.2	Add collapse breccias along (within) caldera margins.	**D**	We do not know how permeable the breccias are, and we do not know exactly where they are located. Are they confining or conductive units? To explore this, collapse breccias would be added as another HSU. One way to do this is to symbolically add a wedge-shaped volume along the inside of the caldera.

Table 6-20
Abridged List of Alternative Scenarios for the Pahute Mesa/Oasis Valley 3-D Hydrostratigraphic Model
(Page 2 of 10)

Alternative		Priority Group[a]	Comment
	Response		This feature would require a fair amount of effort to modify the mesh because a digital geologic model was not created. This was not investigated further.
1.2.3	Subdivide the Fortymile Canyon composite unit (FCCM).	**A**	For example, this unit consists of lavas in the southeastern Timber Mountain moat area, but welded ash-flow tuffs become more common in the lower portion of the FCCM in Oasis Valley. These units may also become saturated in the deepest portion of the valley. A separate unit would allow more vertical resolution in the model.
	Response		As noted by BN (2002), category A items were implemented in the geologic models.
1.2.4	Differentiate units of the Twisted Canyon caldera.	**D**	The Twisted Canyon caldera (after Fridrich et al., 1999a) is relatively small and generally above the SWL. The Timber Mountain units are currently included with the detached volcanics composite units (DVCM) but could be differentiated to permit more detailed modeling.
	Response		The DVCM was found to be an important HSU in controlling flow in Oasis Valley. Further subdivision may have diluted this effect and was not considered further.
1.2.5	Subdivide the detached volcanics composite unit.	**A**	Is there enough information (e.g., in Fridrich et al., 1999a and b), and are the differences significant and/or predictable enough to warrant subdividing these units?
	Response		As noted by BN (2002), category A items were implemented in the geologic models.
1.2.6	Define areas of hydrothermal alteration.	**D**	Should we treat alteration as another HSU? This may be possible where there is evidence of alteration on the surface and in drill holes. Drill holes where hydrothermal alteration is documented include: ER-EC-1, ER-EC-6, PM-2 (deep), UE-20f (below 10,000 ft), UE-19w1 (shallowest; the hole cuts through Area 20 caldera margin, where the foot wall is hydrothermally altered but the hanging wall is not), ER-EC-7 and ER-EC-2A, all at various depths. To define hydrothermal alteration without evidence does not make sense. Are occurrences of hydrothermal alteration predictable?
	Response		It is not within the scope of the flow model to decide whether hydrothermal alteration is predictable. While it is a process, the sparse data do not lend themselves to generalization. This was not addressed.
1.2.7	Map caldera moat-filling units.	**D**	Differentiate moat gravels from other alluvium, though these units typically are not saturated.

Table 6-20
Abridged List of Alternative Scenarios for the Pahute Mesa/Oasis Valley 3-D Hydrostratigraphic Model
(Page 3 of 10)

Alternative		Priority Group[a]	Comment
	Response		Further mapping of geologic units is not in the flow model scope. The CAU flow model is for the saturated zone only.
1.2.8	Subdivide the Paintbrush composite unit (PCM) in the southern end of the model.	**C**	Though dominated by the Paintbrush Group, the PCM also includes remnants of the Rainier Mesa and Ammonia Tanks welded ash-flow tuffs and thin alluvium. In the north (the 1997 PM300 model area), the various Paintbrush tuffs are differentiated where drill hole data are available. We might be able to add more geologic detail, but we have almost no hydrologic data. Is the YMP information adequate to differentiate and map out various HSUs?
	Response		Assessment of YMP geologic data to refine HSUs is not in the scope of the flow model, and this was not addressed.
1.2.9	Subdivide the Kearsarge lavas identified in Well ER-EC-1.	**D**	The Kearsarge lava is a minor aquifer in the northwest corner of the model area and is currently modeled as the Kearsarge aquifer HSU. However, detailed petrographic analysis has identified the Kearsarge lava in Well ER-EC-1, farther south, which represents a newly recognized separate lobe of the lava. Currently, this lobe is lumped with the Crater Flat composite unit (CFCM), which contains lavas of uncertain thicknesses and extent.
	Response		This information is too sparse to be meaningfully addressed and was not considered further.
1.3 Alternatives to Develop Different Distributions for Pre-Tertiary HSUs			
1.3.1	LCCU in the southwestern portion of the model area.	**D**	Determine whether this outcrop is really LCCU (hydrologic “basement”) or LCCU1, with LCA beneath it
	Response		Additional mapping is beyond the scope of the flow model.
1.3.2	Outcrop of Paleozoic carbonate rocks west of Black Mountain.	**D**	It is currently modeled as LCA. Should it be LCA3?
	Response		LCA is assigned properties throughout the model domain, and those properties are adjusted as part of calibration. If the model had a systematic misfit in this area, then it may have been necessary to change properties, and identify geologic rationale. There are no head calibration data in this part of the model, and the need for this change could not be identified.
1.3.3	Continuity of LCA.	**D**	Model LCA as discontinuous from east to west across the model area. (Alternative 2.4.7 creates this geometry.)

Table 6-20
Abridged List of Alternative Scenarios for the Pahute Mesa/Oasis Valley 3-D Hydrostratigraphic Model
(Page 4 of 10)

Alternative		Priority Group[a]	Comment
	Response		Geometry addressed in HFM uncertainty analysis.
1.3.4	Basement subcrop.	**D**	Change the extent and thickness of LCA3 and LCCU1. Instead of only two small LCA3 subcrops in the southwestern corner, make a more extensive LCA3 plate(s)
	Response		Extensive geologic model alteration is beyond the scope of the flow model. Not addressed.
1.3.5	Vary the Paleozoic stratigraphy in the southern area.	**D**	Differentiate the LCA3 sandwiched between the two occurrences of UCCU, as in the YMP model.
	Response		The LCA3 was subdivided in the FEHM model into LCA3 and LCA3a to address this.
1.3.6	Vary the occurrence of the UCCU.	**A**	It was suggested to change the base model to have the western UCCU contact move eastward down along a line that goes through the middles of the calderas.
	Response		As noted by BN (2002), category A items were implemented in the geologic models.
1.3.7	LCCU1.	**A**	Depict as a continuous sheet in the southeastern portion of the model area.
	Response		As noted by BN (2002), category A items were implemented in the geologic models.
1.4 Other Hydrostratigraphy-Related Alternatives			
1.4.1	Intrusive confining unit beneath the Silent Canyon caldera.	**D**	Is this ICU different from that of the other resurgent calderas? What is the nature of this material? Can we define the hydrologic properties of a highly injected/altered rock mass?
	Response		It is beyond the scope of the flow model to address questions of volcanology. No data exist on the ICUs.
1.4.2	Composite units.	**D**	Change/divide composite units into aquifers and/or confining units.
	Response		The mesh is built using specific HSU geometries; thus, without a detailed geologic model describing such changes/divisions, a mesh was not constructed. Additional detailed geologic interpretation is beyond the scope of the flow model. This was not addressed further.
1.4.3	Pre-Belted Range composite unit (PBRCM).	**D**	Show PBRCM everywhere overlying the “basement.” Thin the younger units as necessary at basement highs to accommodate some added thickness of PBRCM.

Table 6-20
Abridged List of Alternative Scenarios for the Pahute Mesa/Oasis Valley 3-D Hydrostratigraphic Model
(Page 5 of 10)

Alternative		Priority Group[a]	Comment
	Response		The mesh is built using specific HSU geometries; thus, without a detailed geologic model describing such changes/divisions a mesh was not constructed. Additional detailed geologic interpretation is beyond the scope of the flow model. This was not addressed.
1.4.4	Mesozoic granite.	**D**	Make the Gold Meadows stock larger in the subsurface.
	Response		The stock is a low permeability feature, and no transport consequences of this change are apparent. Not addressed.
2.0 STRUCTURE-RELATED ALTERNATIVES			
2.1	Silent Canyon caldera alternative.	**B**	Develop an alternative based on McKee et al. (1999 and 2001) to explore a "structurally uncoupled" model for the SCCC.
	Response		This alternative was addressed in the SCCC HFM.
2.2	Simplify the model.	**D**	Omit all but the most profound structures and faults.
	Response		The SCCC HFM has fewer structures and faults, and partially addresses this.
2.3 Add More Structural Detail			
2.3.1	Faults and caldera margins.	**C**	Add width to these structures, modifying them from simple two-dimensional surfaces to a 3-D feature having some width. Can we predict where and why they might be a barrier and/or conduit to groundwater flow?
	Response		The numerical model requires that these features have a finite width. LANL reviewed the data and assessed whether individual faults may be barriers or conduits (see Appendix B).
2.3.2	Add more Tertiary faults or fault zones.	**D**	Perhaps begin by adding the mapped faults (shown on Slate et al. [1999] or the individual USGS quadrangle maps). Most reviewers thought that structurally the model contained the appropriate level of detail.
	Response		The mesh is built using specific HSU geometries; thus, without a detailed geologic model describing changes in faults such changes/divisions, revised conceptual model and mesh could not be constructed. Additional detailed geologic interpretation is beyond the scope of the flow model. This was not addressed.

Table 6-20
Abridged List of Alternative Scenarios for the Pahute Mesa/Oasis Valley 3-D Hydrostratigraphic Model
(Page 6 of 10)

Alternative		Priority Group[a]	Comment
2.3.3	Show several more older calderas.	**D**	Where is the source caldera for the Topopah Spring Tuff? If the gravity lows depicted on the USGS gravity maps are really older calderas, would it make any difference? Are they too deep to significantly affect groundwater flow?
	Response		Detailed geologic interpretation is not part of the scope of the flow model. This was not addressed further.
2.3.4	Add the CP thrust fault in the south.	**D**	The CP thrust is a poorly characterized, west-to-northwest-vergent thrust fault that appears to be mostly outside the boundaries of the model area. Do we really need to add this complexity to the southeastern margin of the model? Could the fault be elsewhere, too? The YMP geologic model includes the Calico Hills thrust, while the UGTA model shows a simpler variation without this thrust. Alternatively, the LCA3 might be more continuous in the southeast corner. In the southeast, there are potentially three versions of pre-Tertiary geometry: 1) As depicted in the current UGTA base model; 2) Alternative with LCA at the pre-Tertiary surface not covered with LCCU; 3) Base model with LCA3 as a continuous sheet, not as isolated islands.
	Response		The mesh is built using specific HSU geometries; thus, without a detailed geologic model describing such changes/divisions, a mesh was not constructed. Additional detailed geologic interpretation is beyond the scope of the flow model. This was not addressed further.
2.3.5	Juxtapose aquifers.	**C**	Deliberately juxtapose aquifer units across faults. See Alternative 2.5.3.
	Response		The mesh is built using specific HSU geometries; thus, without a detailed geologic model describing such changes/divisions, a mesh was not constructed. Additional detailed geologic interpretation is beyond the scope of the flow model. This was not addressed further.
2.4 Develop Different Structural Scenarios			
2.4.1	Vary fault dips.	**C**	The basin-and-range normal faults are modeled using an 80-degree dip. Varying fault dips would present more consequences in the source areas, where fault proximity to working points is important. This might be better addressed in sub-CAU-scale models.
	Response		The mesh is built using specific HSU geometries; thus, without a detailed geologic model describing such changes/divisions, a mesh was not constructed. Additional detailed geologic interpretation is beyond the scope of the flow model. This was not addressed.
2.4.2	Other fault variations.	**C**	Model faults as either present, a single plane, and/or a zone with multiple planes.

Table 6-20
Abridged List of Alternative Scenarios for the Pahute Mesa/Oasis Valley 3-D Hydrostratigraphic Model
(Page 7 of 10)

Alternative		Priority Group[a]	Comment
	Response		The numerical model requires that these features have a finite width and the mesh is specifically constructed to represent these features. It is not possible to modify fault geometries without a detailed digital geologic model and additional meshes. This was not addressed.
2.4.3	Vary the depth to basement rocks.	**B**	The uncertainty in depth to basement based on geophysical data is roughly 2,000 m (6,560 ft). This may not be geologically permissible in some areas. And where it is possible, what units would be thinned or thickened? Could the depth to the Ammonia Tanks and Rainier Mesa resurgent intrusive granites be raised or lowered?
	Response		This was addressed as the PZUP alternative.
2.4.4	Modify the shapes of calderas.	**D**	Do small differences in the shapes of calderas matter? Compare round vs. rectangular shapes; round the corners as a compromising geometry. The western and eastern lobes of the Timber Mountain caldera complex could be smaller, or extended. Separate the Rainier Mesa structural margin and the Ammonia Tanks structural margin in the north and south sides. Presently, the UGTA base model shows these structural margins merging together (the Ammonia Tanks margin as a reactivation of the Rainier Mesa margin) at those locations.
	Response		"Changes in caldera shape and HSUs were incorporated in the SCCC model."
2.4.5	Explore variations of the Thirsty Canyon Lineament.	**B**	Because of its northeast trend and the short distance from testing areas on Pahute Mesa to Oasis Valley, if this lineament exists, it would be the most direct path for migration. Could it be a single (or zone of) north-northeast trending features or faults rather than a series of en echelon, more north-south-trending faults and caldera margins?
	Response		This was addressed as the Thirsty Canyon Lineament alternative.
2.4.6	Model a "trap-door" caldera geometry.	**D**	"Trap-door" type collapse of the Ammonia Tanks caldera (hinge at the south side) may be another interpretation to explain the gravity inversion data.
	Response		Revision of geologic interpretation is not part of the flow model scope. This was not addressed.

Table 6-20
Abridged List of Alternative Scenarios for the Pahute Mesa/Oasis Valley 3-D Hydrostratigraphic Model
(Page 8 of 10)

Alternative		Priority Group[a]	Comment
2.4.7	Vary the geometry/position of the BRT fault.	**B**	The current UGTA base model depicts the BRT as not deeply rooted. An alternative interpretation developed by the USGS depicts the BRT as a very deeply rooted and through going thrust. What latitude do we have in moving this feature (what does it do between outcrops?)? The BRT is modeled as a low-dip feature except where it ramps up, especially at the top of the pre-Tertiary surface (e.g., 40 degrees as per Jim Cole).
	Response		This was addressed as the deeply rooted thrust alternative.
2.4.8	Model Oasis Valley as an extensional basin.	**D**	The preferred interpretation, based on drill hole MyJo Coffer #1 and mapped units in the Transvaal Hills, shows Oasis Valley as part of the Timber Mountain caldera and not an extensional basin. Some disagree. Magnetic data do show north-south faults.
	Response		Revision of geologic interpretation is not part of the flow model scope. This was not addressed.
2.5 Other Structure-Related Alternatives			
2.5.1	Add structural detail in Oasis Valley.	**D**	Study structural features in the Oasis Valley discharge area. There are indications of north south trending faults. Is Chris Fridrich's structural model best?
	Response		Revision of geologic interpretation is not part of the flow model scope. This was not addressed.
2.5.2	"Smooth" versus "rough" HSU surface.	**D**	Computer idiosyncrasies have produced "hills" and "indentations" on HSU surfaces where none were intended. Does it matter? A rough surface might better approximate the effect of faulting.
	Response		The mesh is constructed from the digital geologic model. It is not possible to add this detail after the fact, and such changes are almost certainly minor with respect to overall HSU parameter uncertainty. This was not addressed.
2.5.3	Explore interconnected groundwater pathways.	**C**	Consider increasing or decreasing fault displacements so aquifers are juxtaposed across faults. Conversely, if aquifers are juxtaposed, adjust relative fault displacement to prevent aquifer-aquifer juxtaposition. This may best be handled with sub-CAU-scale models. See Alternative 2.3.5.
	Response		This can only be addressed by creating an alternative mesh for an associated geologic model that was not presented.

Table 6-20
Abridged List of Alternative Scenarios for the Pahute Mesa/Oasis Valley 3-D Hydrostratigraphic Model
(Page 9 of 10)

Alternative		Priority Group[a]	Comment
2.5.4	Consider defining basin/lows with faults.	**D**	The UGTA base model portrays many of the gravity lows as syncline-type structures and not half-grabens related to basin-and-range extension (e.g., northeast of the Black Mountain caldera). However, most reviewers and modelers seem to feel that the present fault detail is about right.
	Response		Revision of geologic interpretation is not part of the flow model scope. This was not addressed.
3.0 OTHER ALTERNATIVES			
3.1	Explore variations of the gravity ridge between the TMCC and the SCCC.	**B**	This feature appears as a gravity high between two calderas. Possible explanations include an intrusive resurgent-type body, a hydrothermally altered area, etc.
	Response		This is addressed in the Ridge alternative.
3.2	Reposition the topographic margins of calderas.	**D**	In some areas their placement seems strange, such as too far removed from the inferred structural margin or not recognizable at all.
	Response		Revision of geologic interpretation is not part of the flow model scope. This was not addressed.
3.3	Account for lower hydraulic heads at Wells ER-EC-4 and ER-EC-2A.	**D**	These two wells show a significant downward gradient.
	Response		This is a model calibration issue, not a geologic model alternative.
3.4	Maximize detail within 1,000 m (3,280 ft) of the water table.	**D**	Add the water table to the model. Will detail above the SWL affect the model? Will small differences at or just beneath the water table make big differences in the flow and transport modeling results (e.g., raise or lower an HSU, or, add or remove HSUs)?
	Response		The CAU model considers saturated flow only, and the mesh is truncated at the water table.
3.5	Add spring locations.	**A**	Add the locations of springs, particularly those near the TCL and the western margin of the TMCM.
	Response		The springs are considered in the flow model.

Table 6-20
Abridged List of Alternative Scenarios for the Pahute Mesa/Oasis Valley 3-D Hydrostratigraphic Model
(Page 10 of 10)

Alternative	Priority Group[a]	Comment

Source: Modified from BN, 2002

[a]**Group A** comprises changes to the UGTA base model recommended by the alternative scenario-working group, and are already implemented.
Group B comprises considered viable alternative scenarios that will be modeled.
Group C comprises proposed alternatives that would be better addressed during the hydrologic modeling phase, rather than as alternatives to the base model.
Group D comprises proposed alternatives that were deemed to be low priority (due to minimal consequences to groundwater flow and contaminant transport), not cost-effective, impractical (e.g., no data, too complex), or simply unnecessary to model at this time.

The remainder of this section describes the calibration of the five major alternate models (those for which EV models were constructed) to the MME recharge and boundary flow targets. The selected HSU depth-decay and anisotropy approach described in Section 5.6.2 was used in parameterizing the models beginning with the calibrated parameters as shown in Section 5.6.2. Calibration was stopped when the objective function was less than the worst calibrated model described in Section 5.0, a value of about 30,000. It is computationally infeasible to investigate these alternatives with the other parameterization approaches discussed in Section 5.6.

6.3.1 Thirsty Canyon Lineament Alternative (TCL-MME-SDA)

The Thirsty Canyon Lineament is a geophysically inferred structure. Because of its northwest trend, presence in Oasis Valley, and short distance from western Area 20 if this feature is caused by faulting it could be an enhanced flow path, although it may also be a barrier. This alternative places more permeable fractured rocks in the area. See Section 6.4 in BN (2002) for more information.

Plots of observed versus simulated values for the calibration wells, springs, Oasis Valley discharge, and boundary flows are shown in Figures 6-94 through 6-97. The scatter around the line of perfect agreement is generally random in Figure 6-94, until an observed head of 1,450 m is exceeded. At the very highest observed observation well heads, the model has a tendency toward undersimulation. The remaining errors above 1,450 m are all in far eastern Area 19, where data become very sparse and uncertainty increases. Figure 6-98 shows a histogram of weighted observation well residuals. The bulk of the weighted errors (about 95) are less than 10 m. The errors are very symmetrically distributed around zero. The total errors above +10 m and below -10 m appear to be about the same.

The Oasis Valley discharge and boundary flow components provide the water-balance constraint on the model. The total estimated Oasis Valley discharge in the CAU model domain; the simulated discharge, shown in Figure 6-96, is 209 kg/s. The total error is within one standard deviation (30 kg/s) as reported by Laczniak et al. (2001). The model trends the same as the data with some scatter, showing that the general representation of the area is correct. The boundary flows, estimated from regional model analysis, all trend the correct way (e.g., have the proper sign), with the largest relative misfit on the western edge.

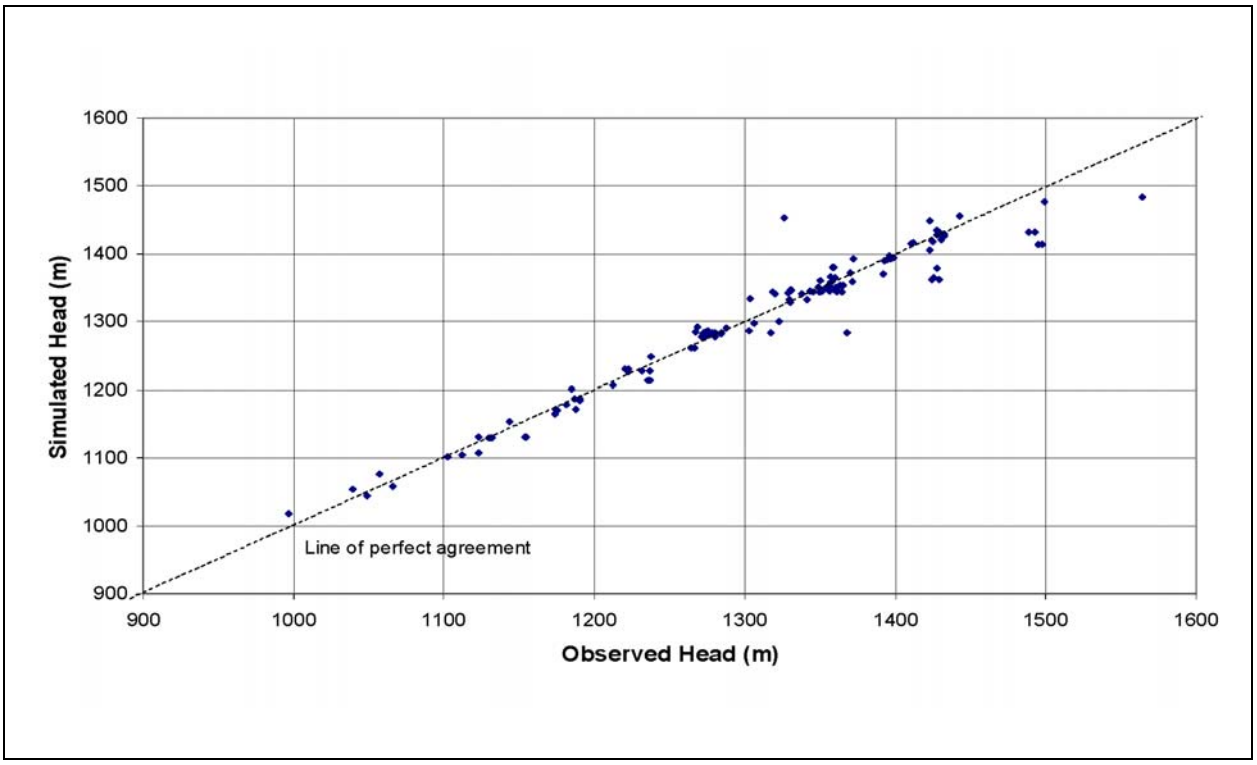

Figure 6-94
Observed Versus Simulated Observation Well Head for TCL-MME-SDA

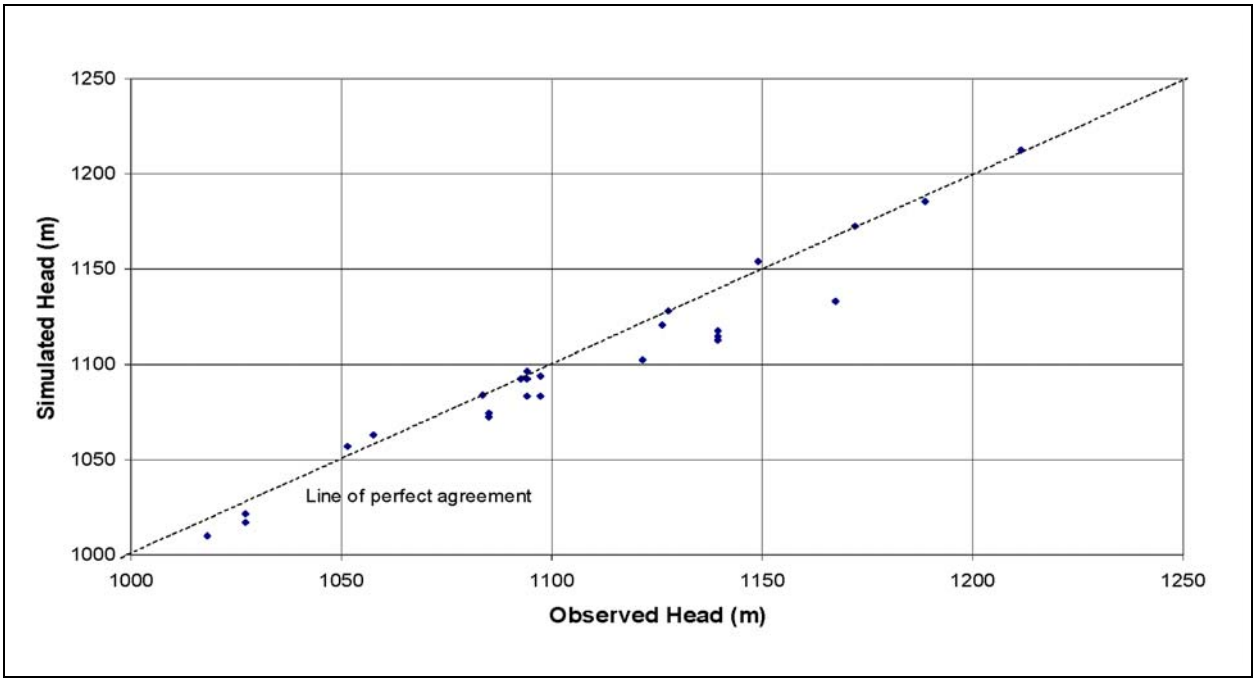

Figure 6-95
Observed Versus Simulated Spring Head for TCL-MME-SDA

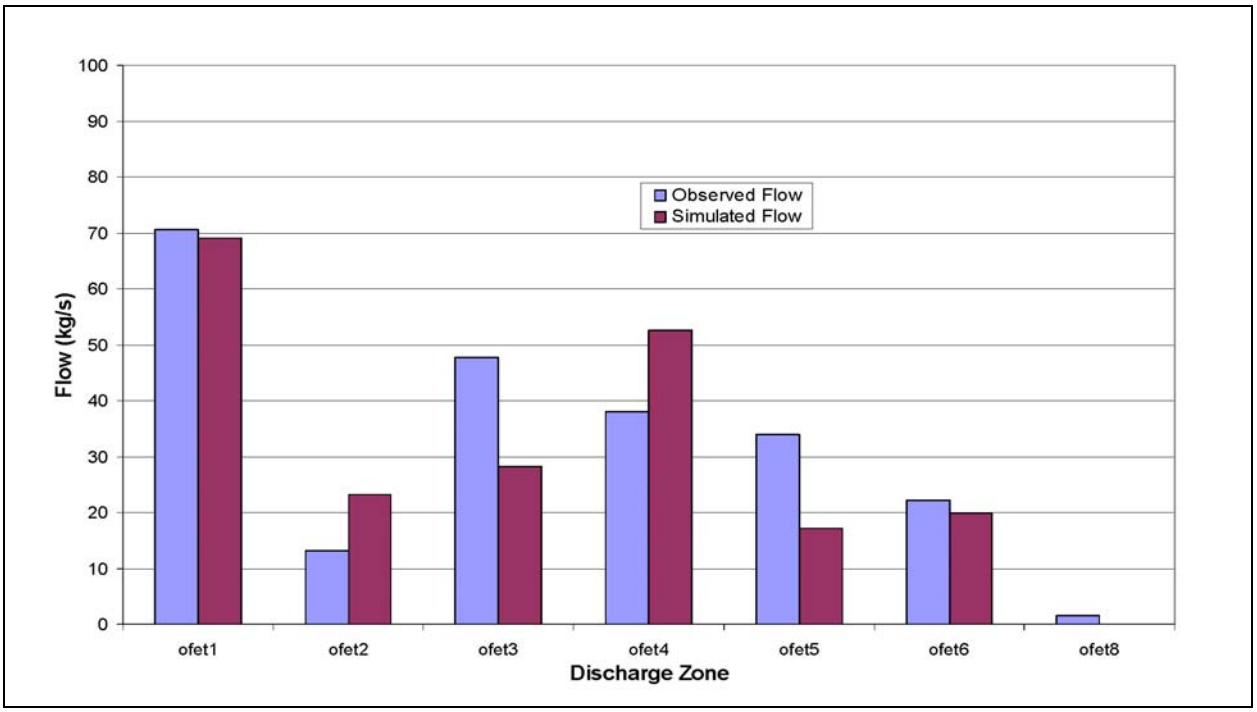

Figure 6-96
Observed and Simulated Oasis Valley Discharge for TCL-MME-SDA

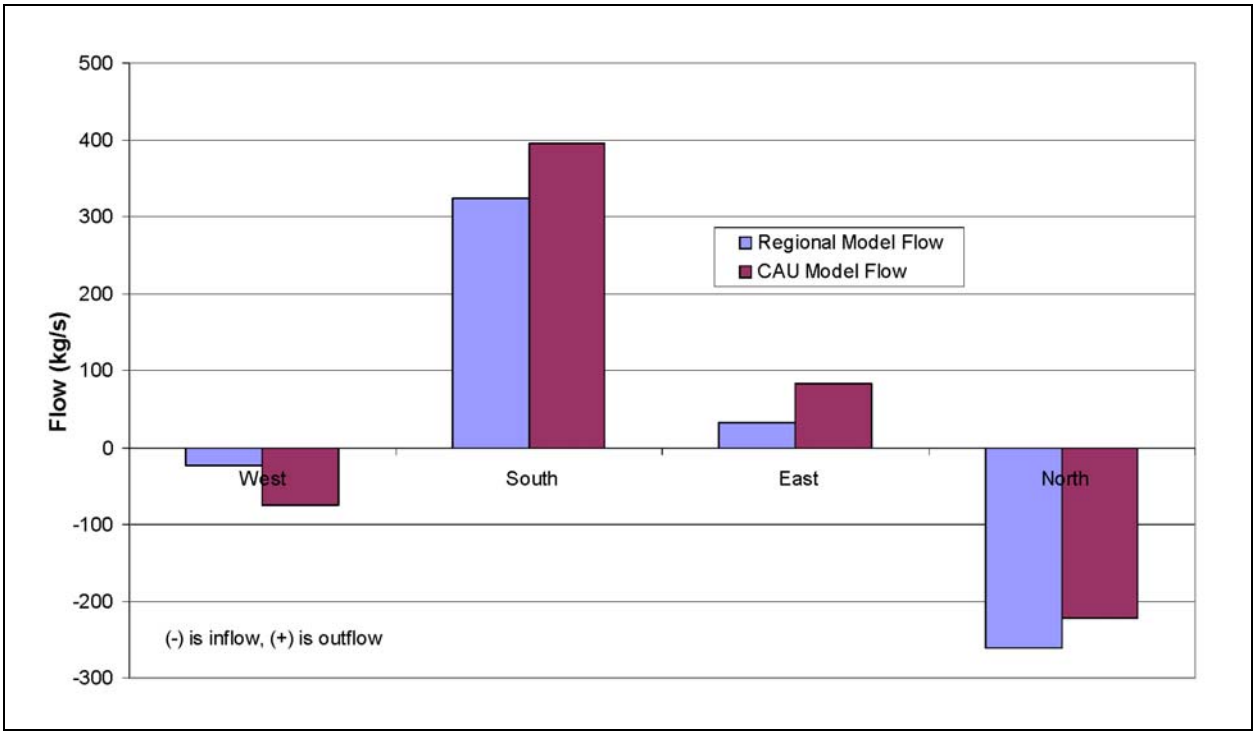

Figure 6-97
Observed and Simulated Boundary Flows for TCL-MME-SDA

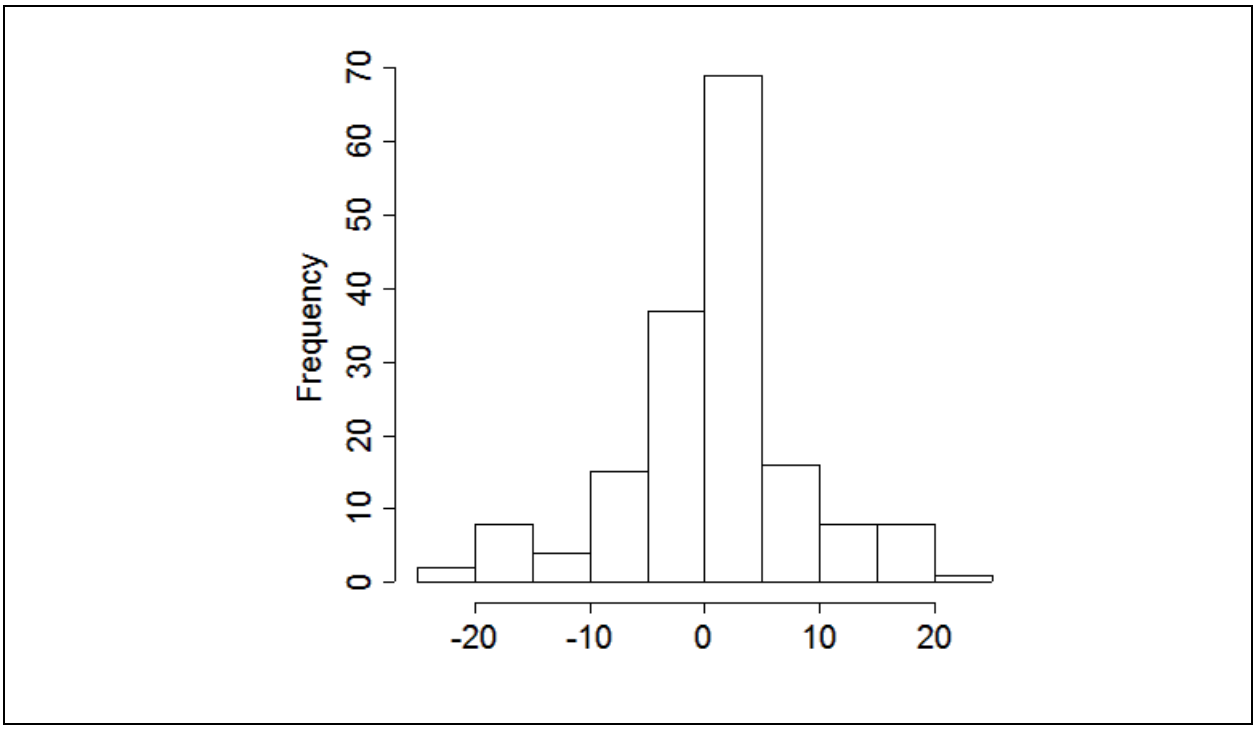

Figure 6-98
Histogram of Weighted Head Residuals for TCL-MME-SDA

The weighted head and spring errors are shown on Figure 6-99, color coded by value and sign. The driest, or undersimulated, well was U-19x. The single wettest well was UE-20n #1. In general, the errors are randomly distributed, although there is a slight dry bias in northern Area 20 at Easting and Northing of about 547,500 and 4,130,000 m, which includes Wells U-20i, UE-20e #1, U-20e, and U-20ar #1.

The quantitative measures of the model calibration are given by summary statistics shown in Table 6-21. These statistics alone are not used to judge model calibration; they are used to highlight errors in conjunction with the graphical approaches described previously. The mean error in well head is nearly zero (recall the symmetric residual histogram), a slight dry bias in the spring heads, with a slight overprediction bias for the flows. The total model objective function was 16,564; only 87 different than the base HFM (16,651). Table 6-22 shows the contribution of each data type to the total model goodness of fit.

Figure 6-100 shows the simulated water table for this model case. In the western part of Area 20, the influence of the Purse Fault is evident by the large offset in heads across it, with more subdued effects

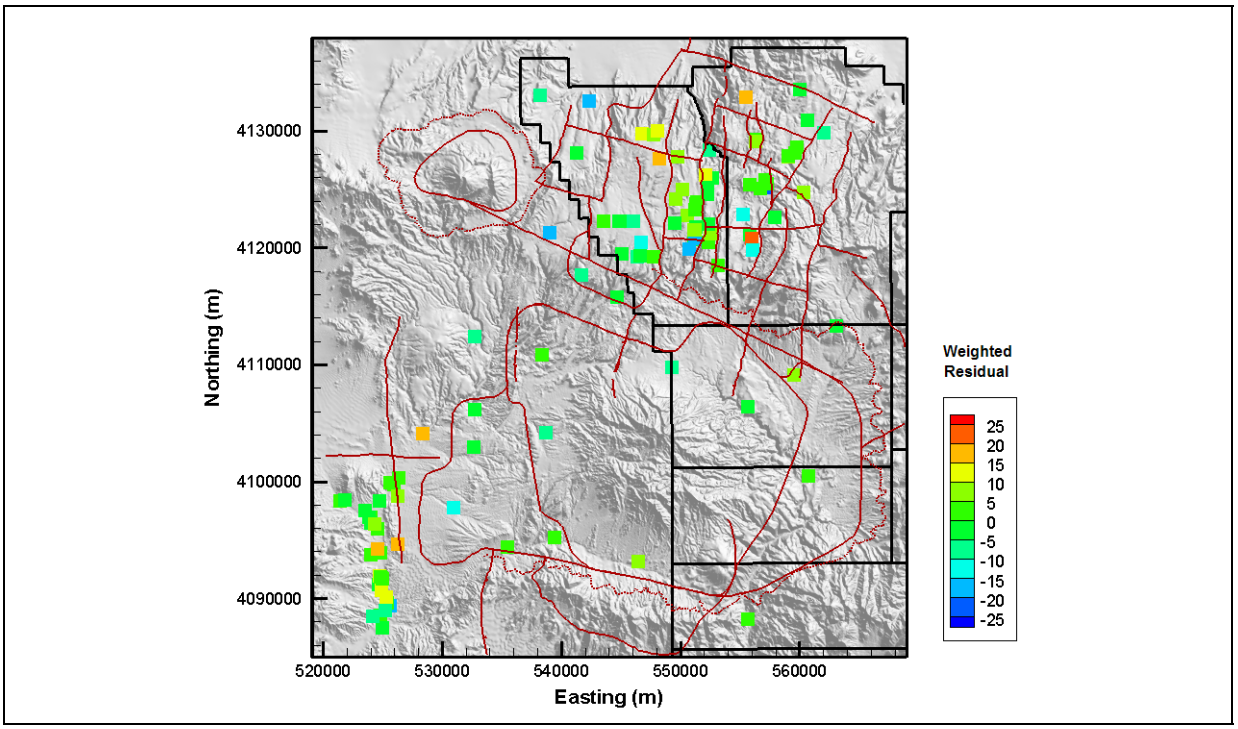

Figure 6-99
Post Plot of Weighted Well and Spring Head Residuals for TCL-MME-SDA

Table 6-21
Calibration Summary Statistics for TCL-MME-SDA

Calibration Data	Number of Data	Mean Weighted Error (m or kg/s)[a]	Maximum Weighted Residual	Minimum Weighted Residual	Error Standard Deviation (m or kg/s)
Well Head	152	-0.09	22 (U-19x)	-24 (UE-20n #1)	7.4
Spring Head	28	2.7	19 (Torrance Spring)	-5.5 (Spring id 159)	6.8
Oasis Valley Discharge	7	4.8	39 (Zone 3)	-29 (Zone 4)	24
Boundary Flow	4	-14	26 (West)	-35 (South)	27

[a]Positive sign is simulated less than target, negative is larger.

also present at West Boxcar Fault. Water flows from Areas 19 and 20 toward the southwest and Oasis Valley. Particle tracking (Figure 6-101) from each of the NTS wells shows the same generally noted flow paths as shown in Appendix A of the Pahute Mesa hydrologic data document (SNJV, 2004a).

Table 6-22
Contribution to Model Goodness of Fit by Data Type for TCL-MME-SDA

Data Type	Value (-)	Percent of Total
Well Head	8,342	50
Spring Head	1,285	8
Oasis Valley Discharge	3,966	24
Boundary Flow	2,971	18
Total	16,564	100

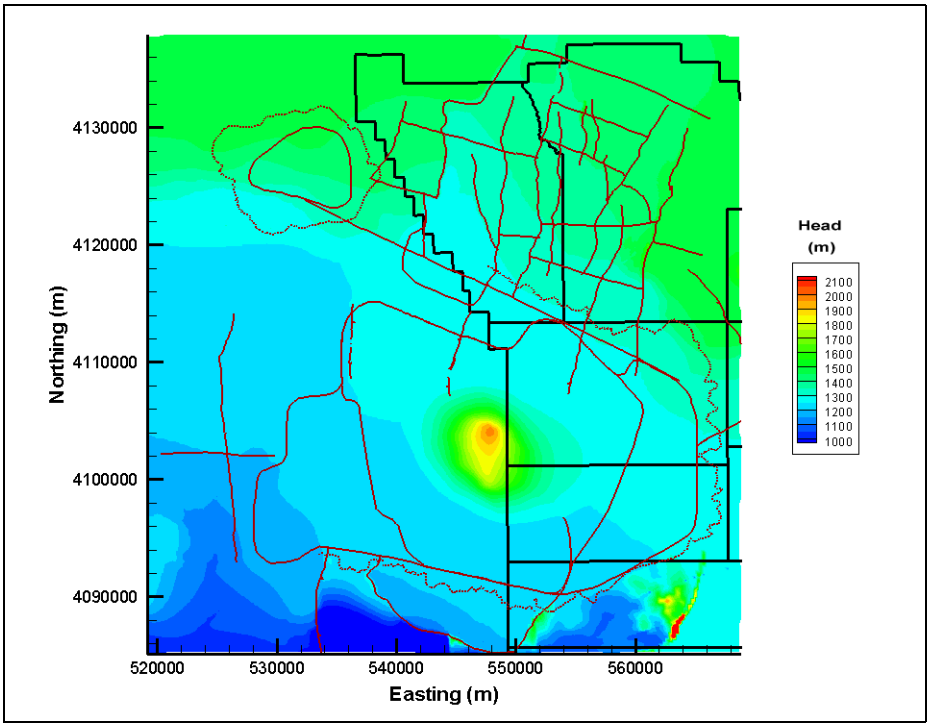

Figure 6-100
Simulated Water Table for TCL-MME-SDA

Relative to BN-MME-SDA, the particles exiting southern Area 20 near ER-EC-1 and ER-EC-6 dive a few hundred meters deeper and have a stronger tendency to discharge in southern Oasis Valley.

This alternative required no additional calibration; the BN-MME-SDA parameter values were mapped onto the HFM and the calibration shown obtained. With respect to flow, this alternative does not appear to be greatly different than the base HFM. The number of nodes that changed from the base HFM for this alternative, the HSU assigned in the base HFM and the changed HSU for the four

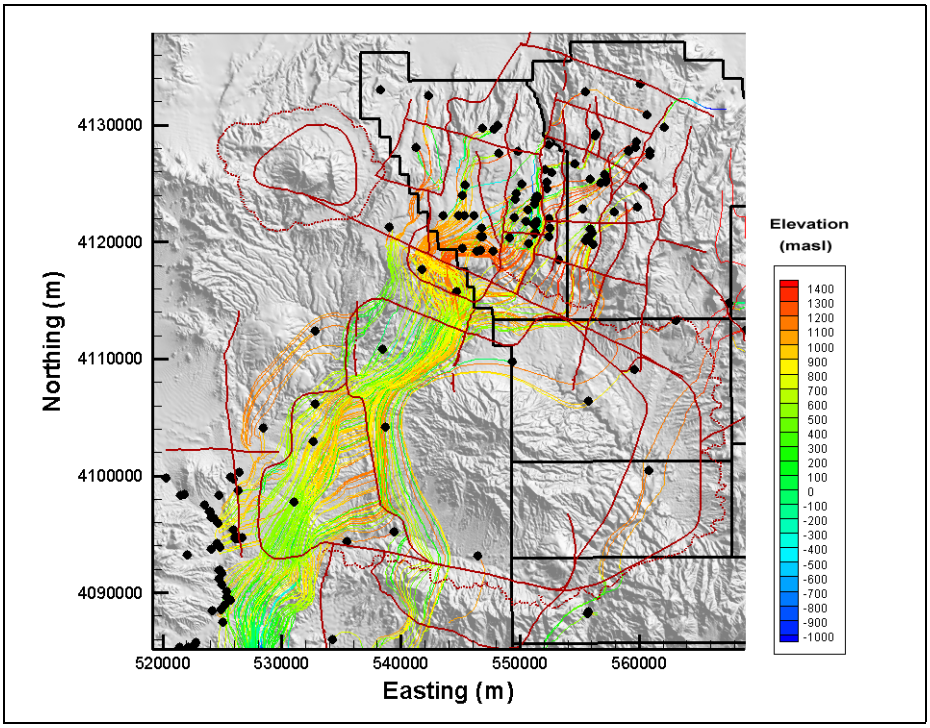

Figure 6-101
Particle Tracks for TCL-MME-SDA

largest node counts are shown in Table 6-23. Note that the change was generally from lower permeable to more permeable units. The total number of changed nodes was 49,013.

The properties used to parameterize this model are summarized in Section 6.3.6.

Table 6-23
Selected Node Changes for TCL HFM Alternative

Base HSU	Alternative HSU	Node Count
CHCU	TSA	4,878
CHCU	LPCU	2,217
LPCU	TCA	1,884
BFCU	CFCM	1,780

6.3.2 Basement Ridge Model Alternative (RIDGE-MME-SDA)

Water leaving the NTS from southwestern Area 20 tends to go southwest around the western edge of Timber Mountain. Data to define the bench between the Silent Canyon and Timber Mountain calderas are sparse. A higher gravity ridge has been measured in the area, which in the base model is

accounted for by LCA. This alternative distributes the BA, TCA, TSA, and CFCM further south so that they pinch out or truncate against the older, presumably less permeable units that form the bench, disrupting flow paths from Pahute Mesa. See Section 6.3 in BN (2002) for more information.

Plots of observed versus simulated values for the calibration wells, springs, Oasis Valley discharge, and boundary flows are shown in Figures 6-102 through 6-105. The scatter around the line of perfect agreement is generally random in Figure 6-102, until an observed head of 1,450 m is exceeded. At the very highest observed observation well heads, the model has a tendency toward undersimulation. On Figure 6-103, the line of perfect agreement is shown, and ideally the data would plot exactly onto this line. However, at the higher observed observation spring head, the model has a tendency toward undersimulation. The plot is not significantly different than those shown in Section 5.6.2. Figure 6-105 presents a plot of observed versus simulated values for boundary flows. Figure 6-106 shows a histogram of weighted observation well residuals. The bulk of the weighted errors (about 95) are less than ±10 m. The errors are not symmetrically distributed around zero, with larger oversimulated (negative sign) wells. The total errors above +10 m and below -10 m appear to be about the same.

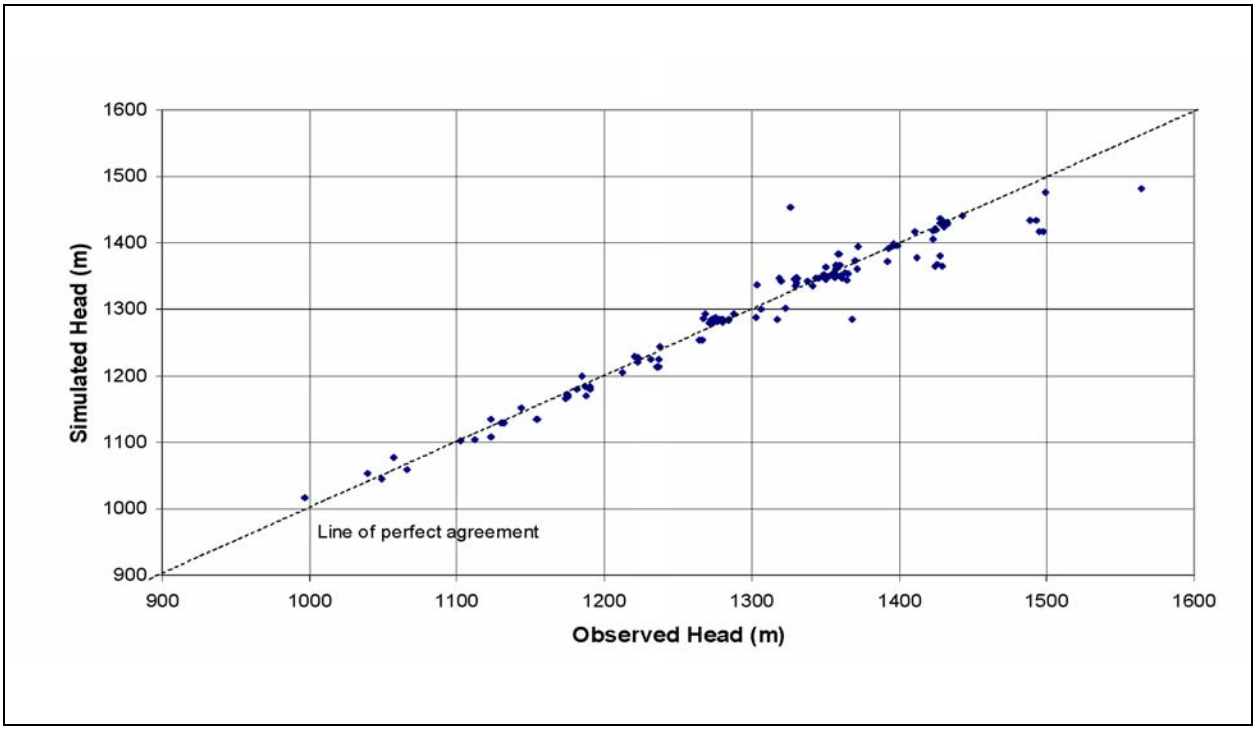

Figure 6-102
Observed Versus Simulated Observation Well Head for RIDGE-MME-SDA

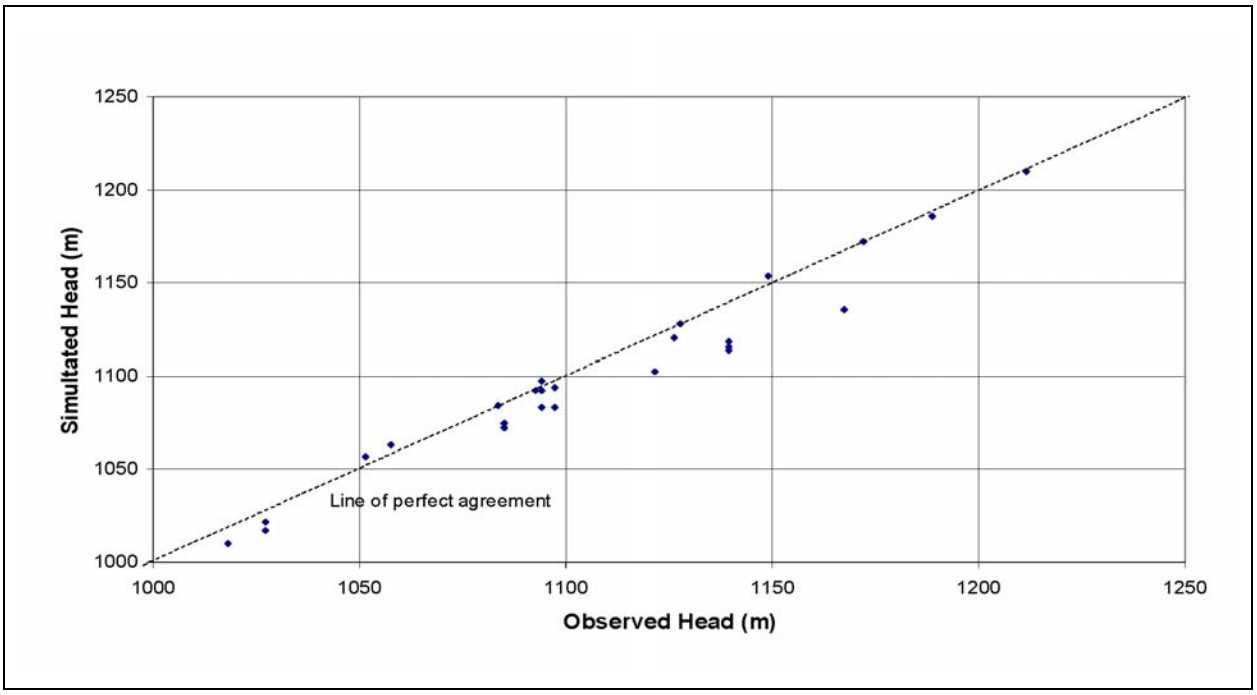

Figure 6-103
Observed Versus Simulated Spring Head for RIDGE-MME-SDA

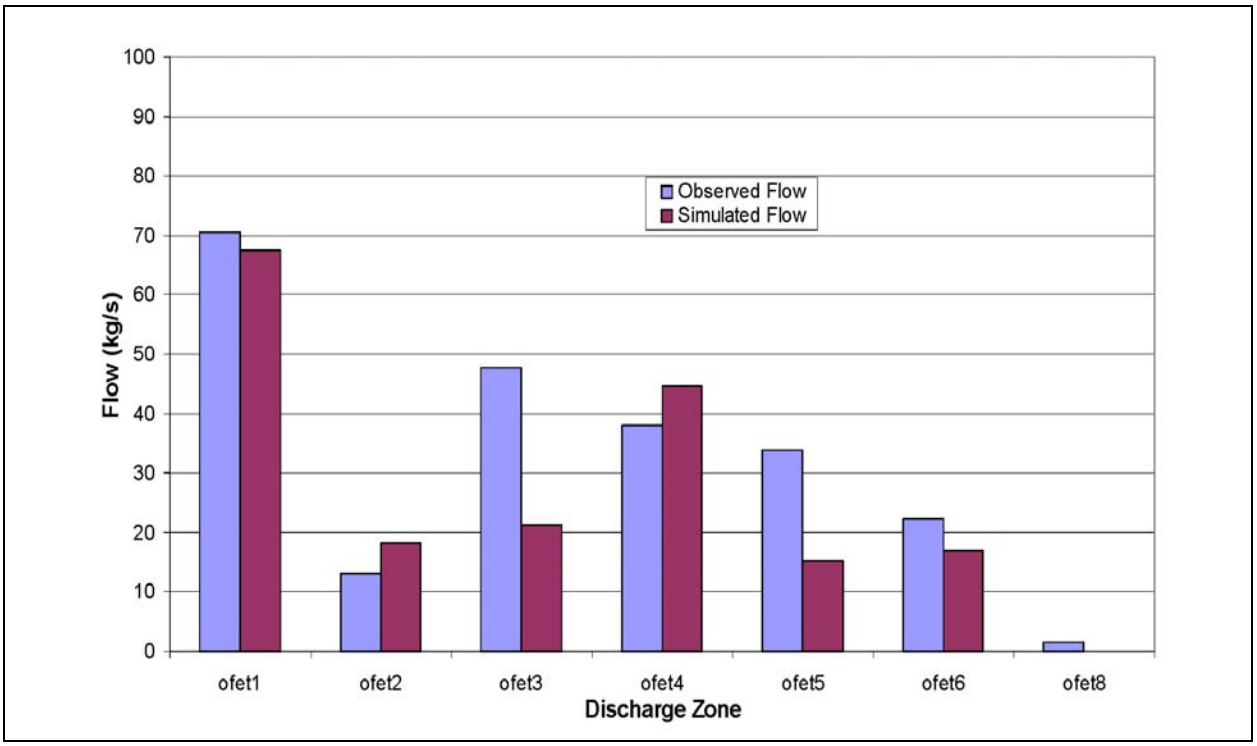

Figure 6-104
Observed and Simulated Oasis Valley Discharge for RIDGE-MME-SDA

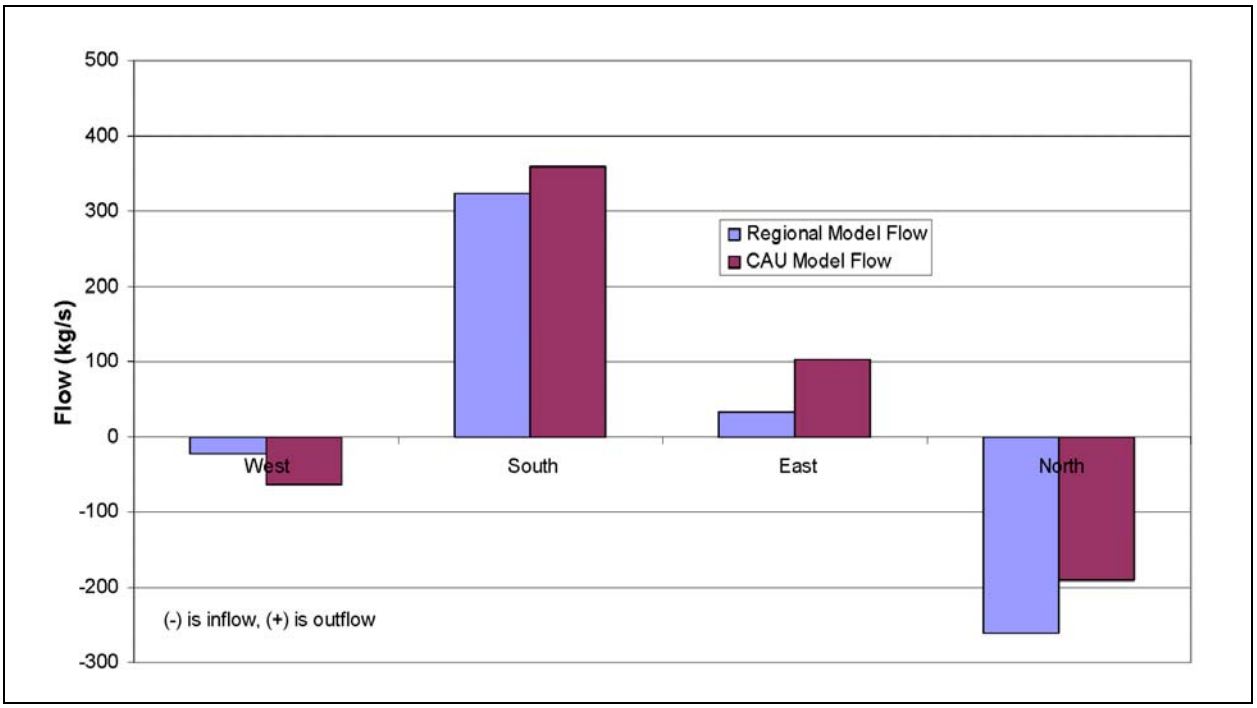

Figure 6-105
Observed and Simulated Boundary Flows for RIDGE-MME-SDA

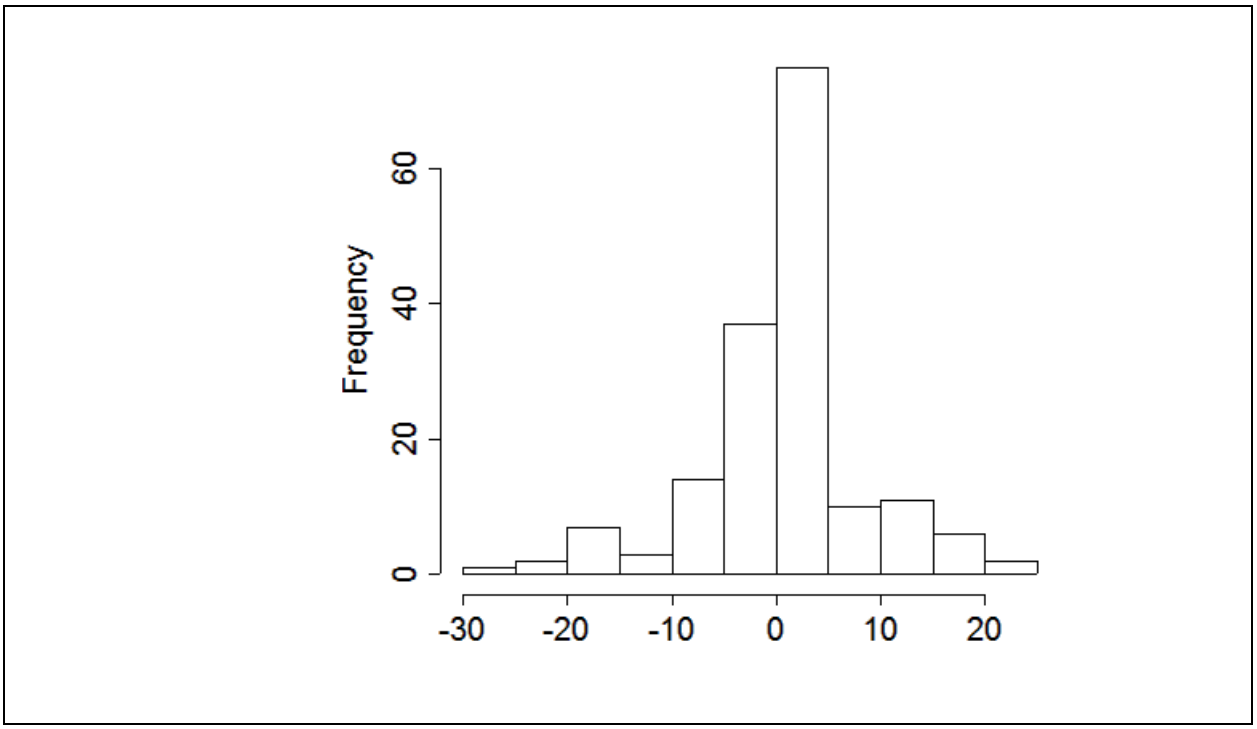

Figure 6-106
Histogram of Weighted Head Residuals for RIDGE-MME-SDA

The Oasis Valley discharge and boundary flow components provide the water-balance constraint on the model. The total estimated Oasis Valley discharge in the CAU model domain is 227 kg/s; the simulated discharge, shown in Figure 6-104, is 183 kg/s. This is about a 1.5 standard deviation less than the estimated value, which makes this model less good than most others in this regard. The model trends the same as the data with some scatter, showing that the general representation of Oasis Valley is correct. The boundary flows, estimated from regional model analysis, all trend the correct way (e.g., have the proper sign), with the largest relative misfit on the western edge.

The weighted head and spring errors are shown on Figure 6-107, color coded by value and sign. The driest, or undersimulated, well was U-20m. The most overpredicted head was at Well UE-20n #1. In general, the errors are randomly distributed, although there is a slight dry bias in northern Area 20 at Easting and Northing of about 547,500 and 4,130,000 m, which includes Wells U-20i, UE-20e #1, U-20e, and U-20ar #1.

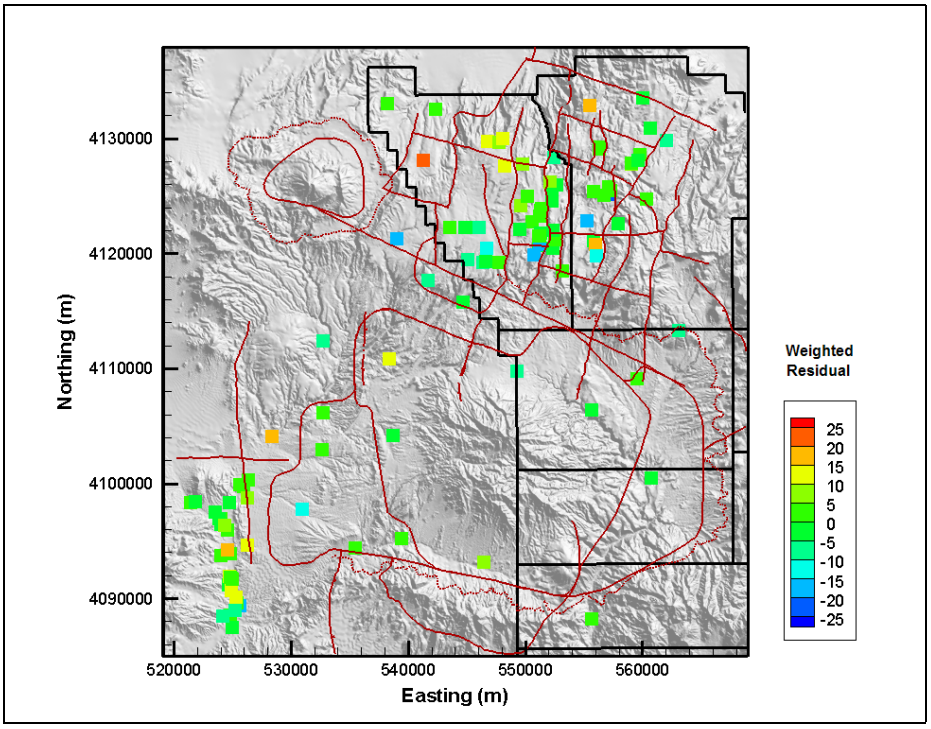

Figure 6-107
Post Plot of Weighted Well and Spring Head Residuals for RIDGE-MME-SDA

The quantitative measures of the model calibration are given by summary statistics shown in Table 6-24. There is a slight oversimulation bias for well heads. There is a slight dry bias in the

spring heads, with a slight overprediction bias for the flows. The total model objective function was 18,459, which is slightly worse than the best base HFM calibration (BN-MME-SDA). Table 6-25 shows the contribution of each data type to the total model goodness of fit.

Table 6-24
Calibration Summary Statistics for RIDGE-MME-SDA

Calibration Data	Number of Data	Mean Weighted Error (m or kg/s)[a]	Maximum Weighted Residual	Minimum Weighted Residual	Error Standard Deviation (m or kg/s)
Well Head	152	-0.07	23 (U-20m)	-27 (UE-20n #1)	7.8
Spring Head	28	2.8	19 (Torrance Spring)	-5.4 (Spring id 159)	6.8
Oasis Valley Discharge	7	12	53 (Zone 3)	-13 (Zone 4)	26
Boundary Flow	4	-17	20 (West)	-35 (East)	28

[a]Positive sign is simulated less than target, negative is larger.

Table 6-25
Contribution to Model Goodness of Fit by Data Type for RIDGE-MME-SDA

Data Type	Value (-)	Percent of Total
Well Head	9,351	51
Spring Head	1,289	7
Oasis Valley Discharge	4,665	25
Boundary Flow	3,154	17
Total	18,459	100

Figure 6-108 shows the simulated water table for this model case. In the western part of Area 20, the influence of the Purse Fault is evident by the large offset in heads across it, with more subdued effects also present at West Boxcar Fault. Particle tracking (Figure 6-109) from each of the NTS wells shows the same generally noted flow paths as shown by in Appendix A of the Pahute Mesa hydrologic data document (SNJV, 2004a). Relative to the base HFM calibration shown in Section 5.6.2, the particle tracks exit Area 20 further west and with a more even distribution. This is the effect of the truncation of BA, TCA, TSA, and CFCM against older, lower permeable units as described by BN (2002).

The parameters from BN-MME-SDA were mapped onto this HFM, and the calibration shown was obtained with no additional effort. Thus, the effects of this HFM on flow model metrics is modest.

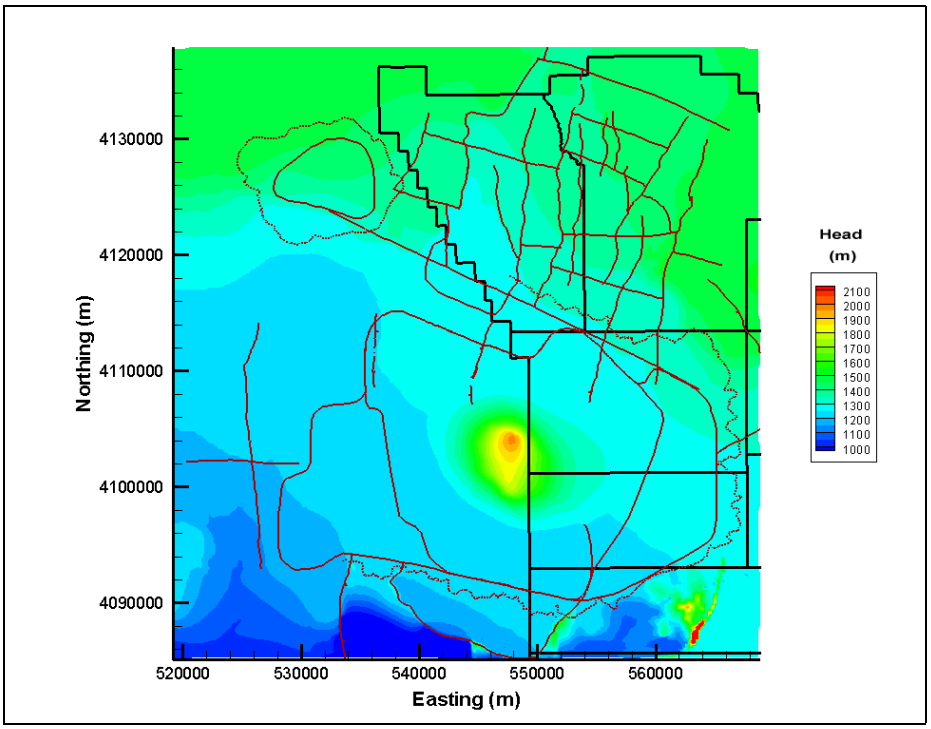

Figure 6-108
Simulated Water Table for RIDGE-MME-SDA

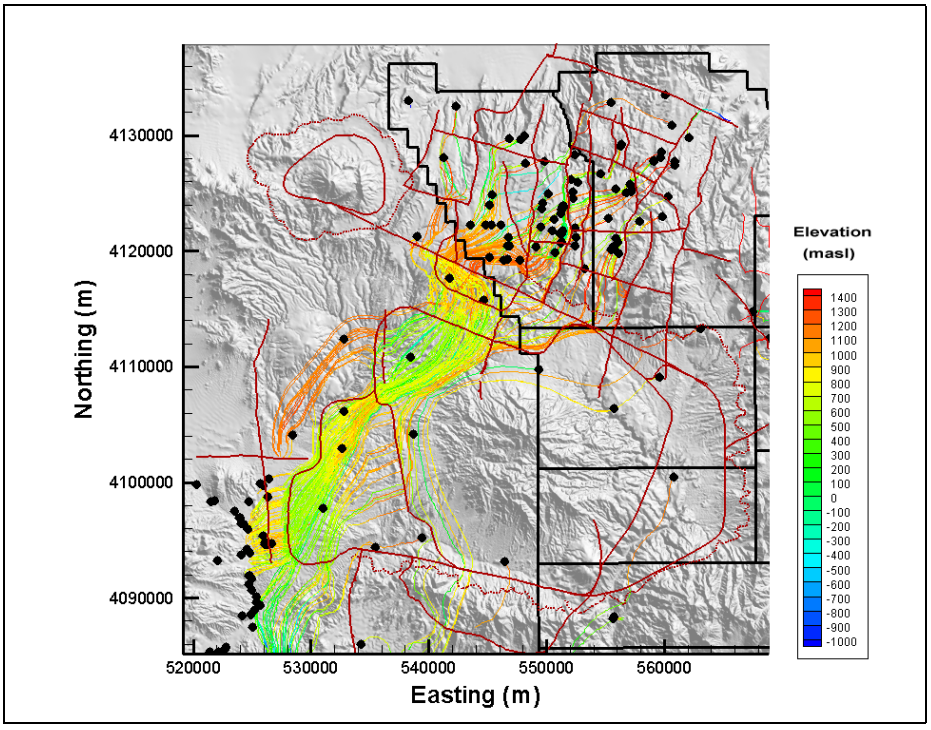

Figure 6-109
Particle Tracks for RIDGE-MME-SDA

The nodes that were changed from the base HFM for selected HSUs are summarized in Table 6-26. A total of 89,346 nodes were changed for RIDGE. The count is the largest of all the alternatives because this case makes changes in southern Pahute Mesa where the node spacing is relatively fine. The major change is from BA to FCCU; from high to low permeability. The TCA and TSA also change as described by BN (2002) and seen in Table 6-26 to less permeable HSUs. The properties used to parameterize this model are summarized in Section 6.3.6.

Table 6-26
Selected Node Changes for RIDGE HFM Alternative

Base HSU	Alternative HSU	Node Count
BA	FCCU	14,609
CHCU	CFCU	10,329
UPCU	CHCU	4,701
TCA	CHCU	4,568
TSA	CFCU	2,865

6.3.3 Raised Pre-Tertiary Surface Alternative (PZUP-MME-SDA)

The determination of depth to Paleozoic basement assumed a density/depth relation for gravity inversion. Two such distributions have been described for Pahute Mesa, which cause up to a 2-km variation in the position of the Paleozoic basement. This alternative raised the basement as much as possible and still remains in agreement with the hard data. The consequences were thought to be facilitation of groundwater flow around the eastern side of Timber Mountain. See Section 6.5 in BN (2002) for more information.

Plots of observed versus simulated values for the calibration wells, springs, Oasis Valley discharge, and boundary flows are shown in Figures 6-110 through 6-113. The scatter around the line of perfect agreement is generally random in Figure 6-110, until an observed head of 1,450 m is exceeded. At the very highest observed observation well heads, the model has a tendency toward undersimulation. On Figure 6-111, the line of perfect agreement is shown, and ideally the data would plot exactly onto this line. However, at the higher observed observation spring head, the model has a tendency toward undersimulation. The plot is not significantly different than those shown in Section 5.6.2. Figure 6-113 presents a plot of observed versus simulated values for boundary flows. Figure 6-114 shows a histogram of weighted observation well residuals. The bulk of the weighted errors (about 95)

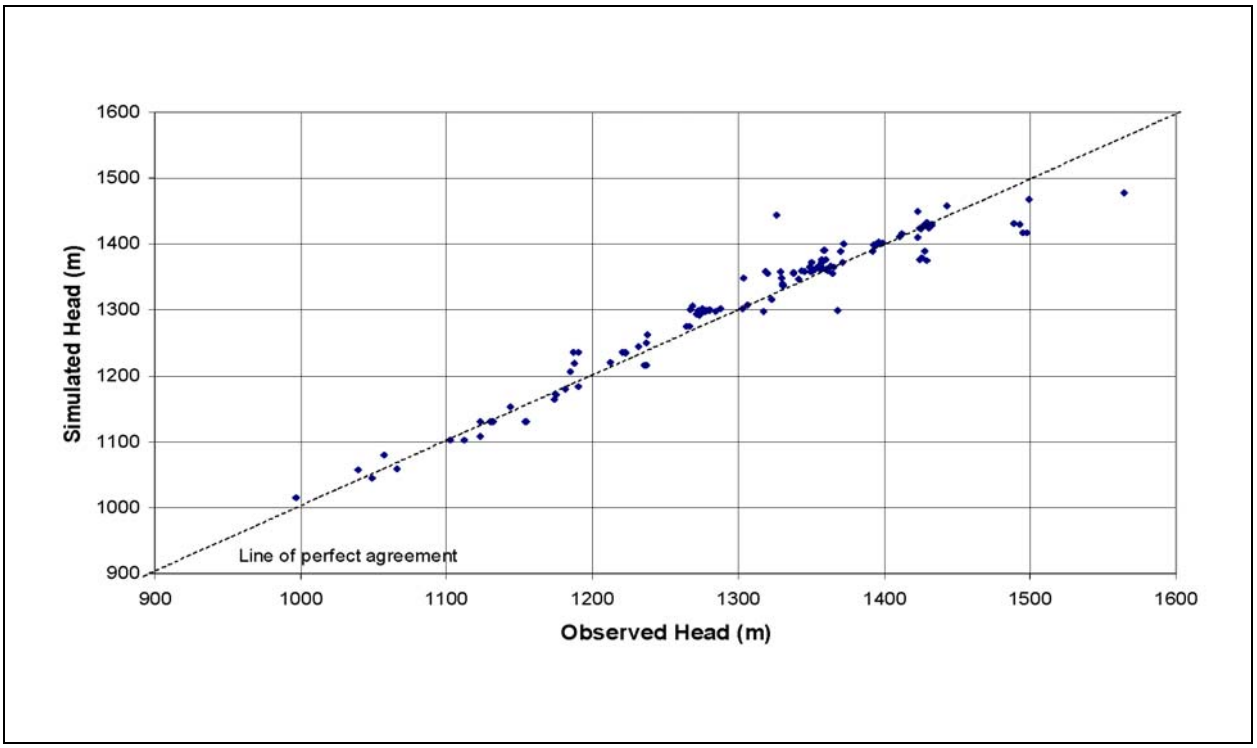

Figure 6-110
Observed Versus Simulated Observation Well Head for PZUP-MME-SDA

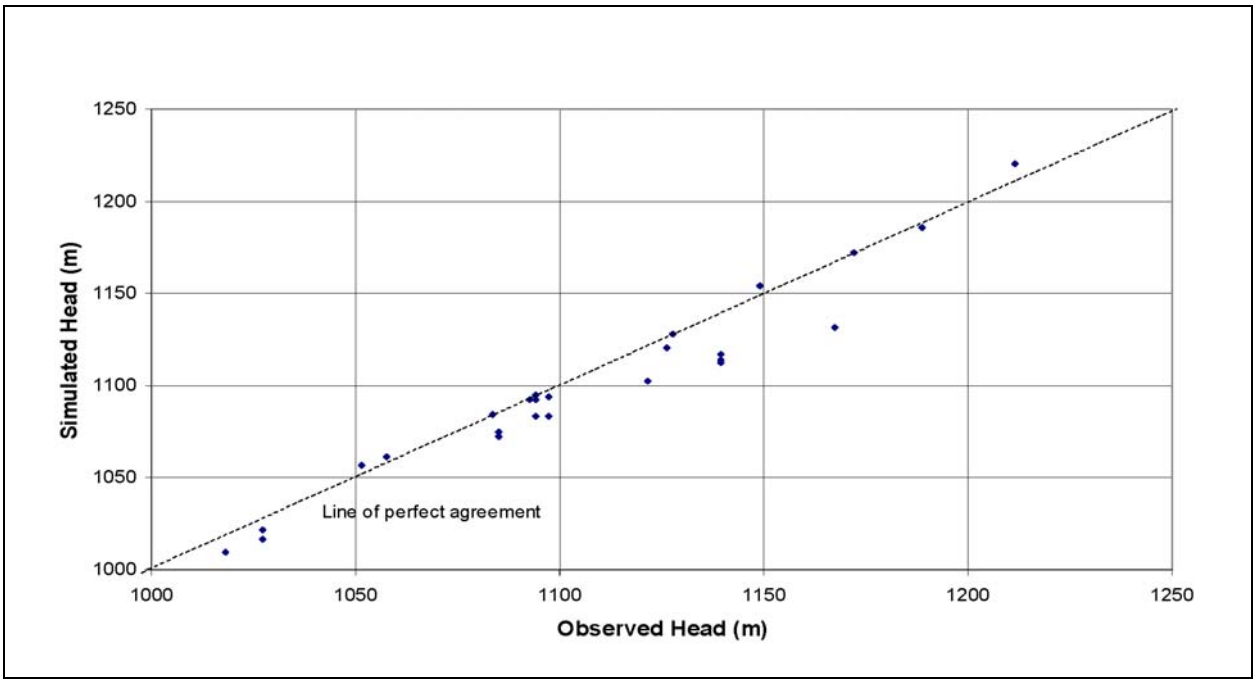

Figure 6-111
Observed Versus Simulated Spring Head for PZUP-MME-SDA

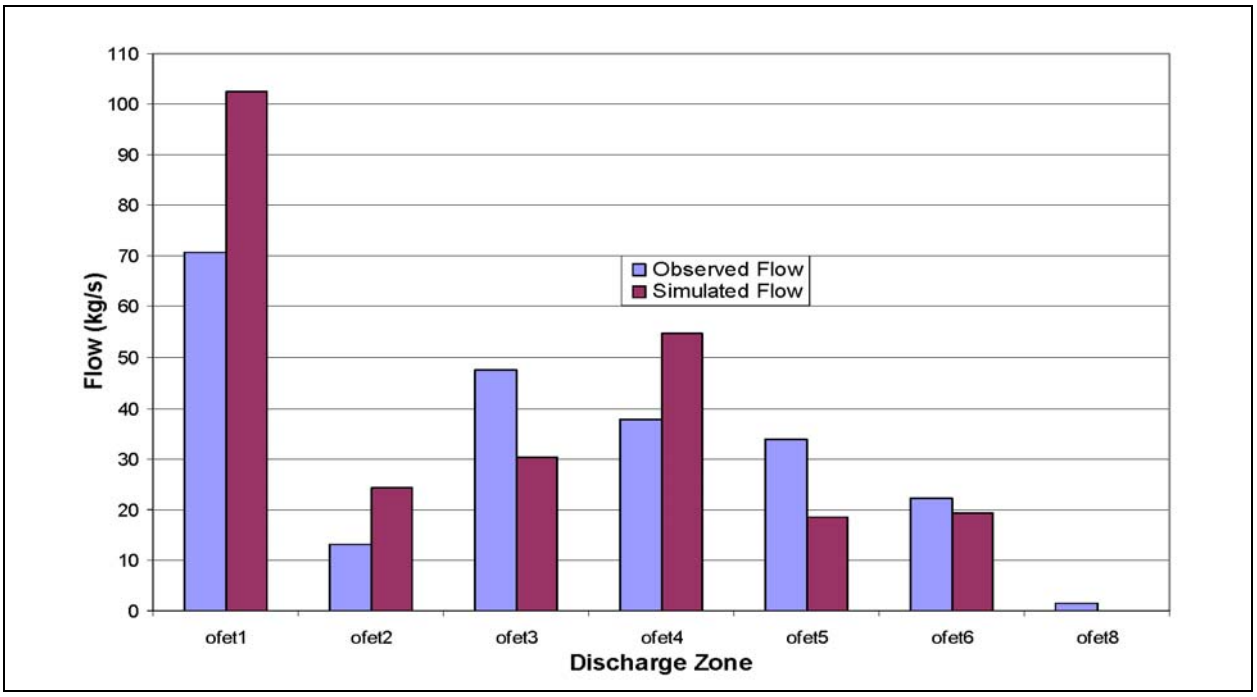

Figure 6-112
Observed and Simulated Oasis Valley Discharge for PZUP-MME-SDA

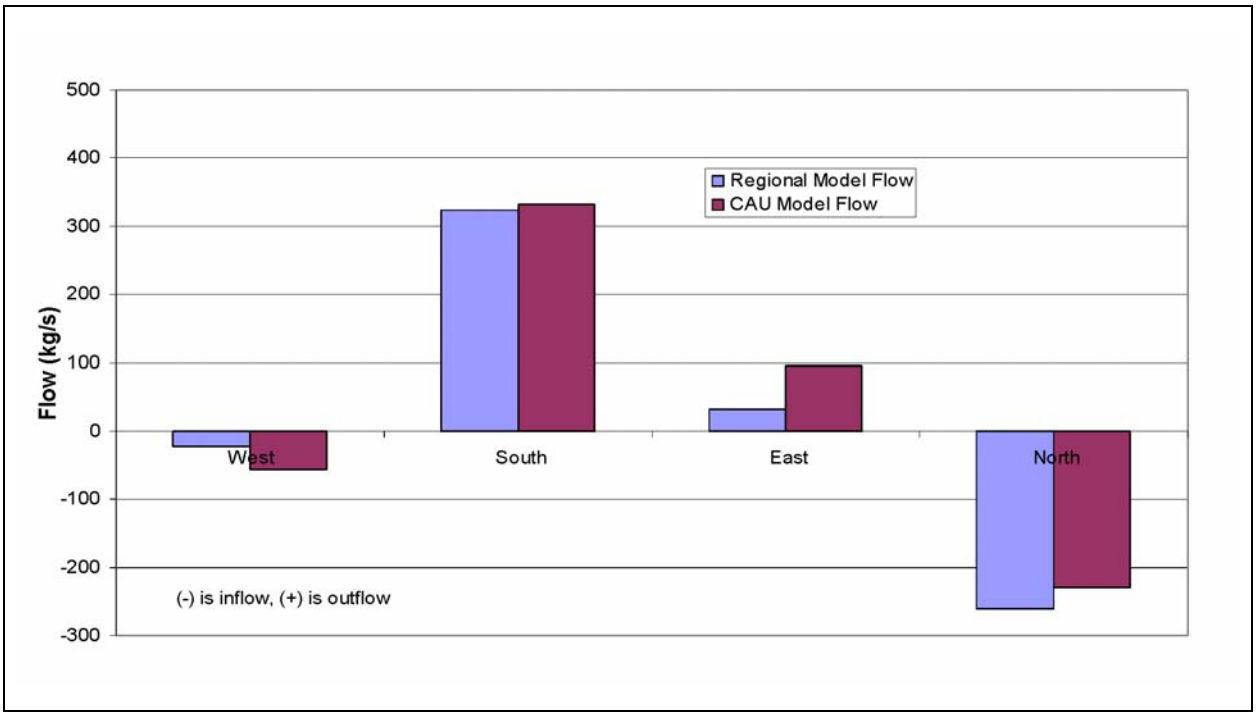

Figure 6-113
Observed and Simulated Boundary Flows for PZUP-MME-SDA

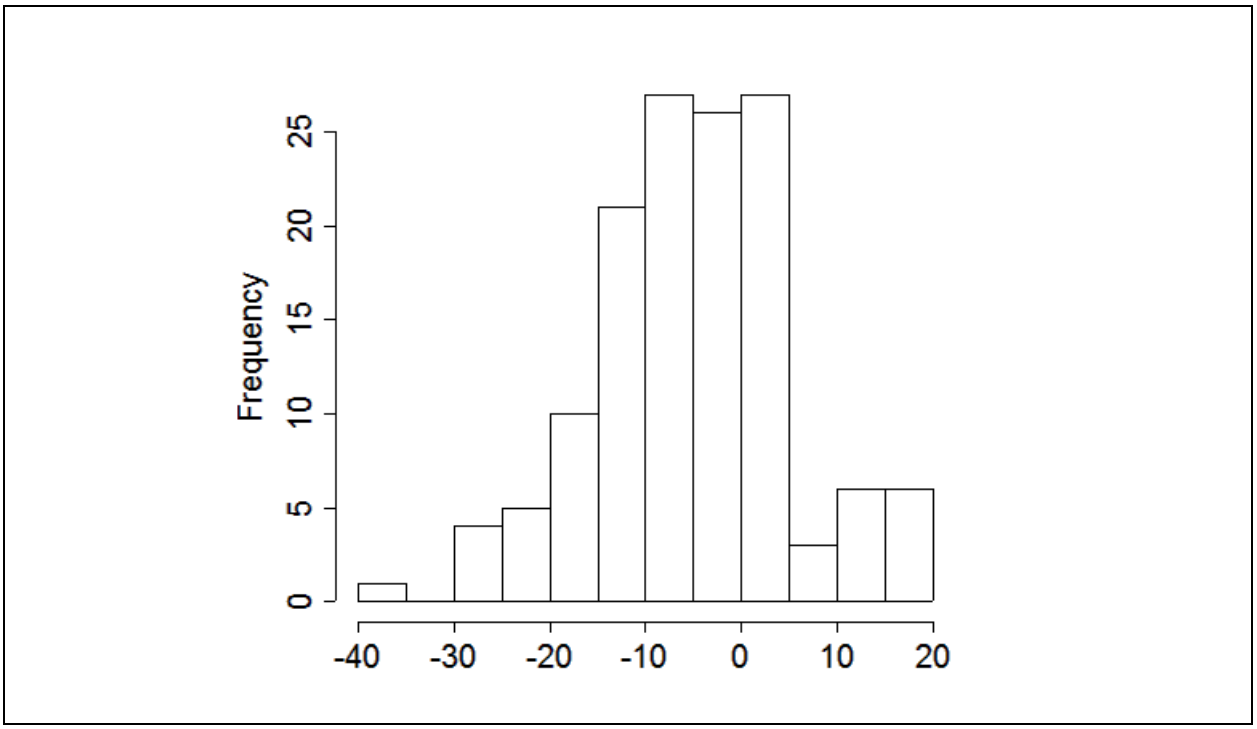

Figure 6-114
Histogram of Weighted Head Residuals for PZUP-MME-SDA

are less than ±10 m. The errors are not symmetrically distributed around zero, with a larger proportion of oversimulated (negative sign) wells.

The total estimated Oasis Valley discharge in the CAU model domain is 227 kg/s; the simulated discharge, shown in Figure 6-112, is 209 kg/s. The total error is within one standard deviation (30 kg/s) as reported by Laczniak et al. (2001). The model trends the same as the data with some scatter, showing that the general representation of the area is correct. The boundary flows, estimated from regional model analysis, all trend the correct way (e.g., have the proper sign), with the largest relative misfit on the western edge.

The weighted head and spring errors are shown on Figure 6-115, color coded by value and sign. There is a clear tendency to oversimulate heads, although this result is not associated with commensurate oversimulation of Oasis Valley discharge. The driest, or undersimulated, well was ER-OV-03a. The single wettest well was UE-20n #1.

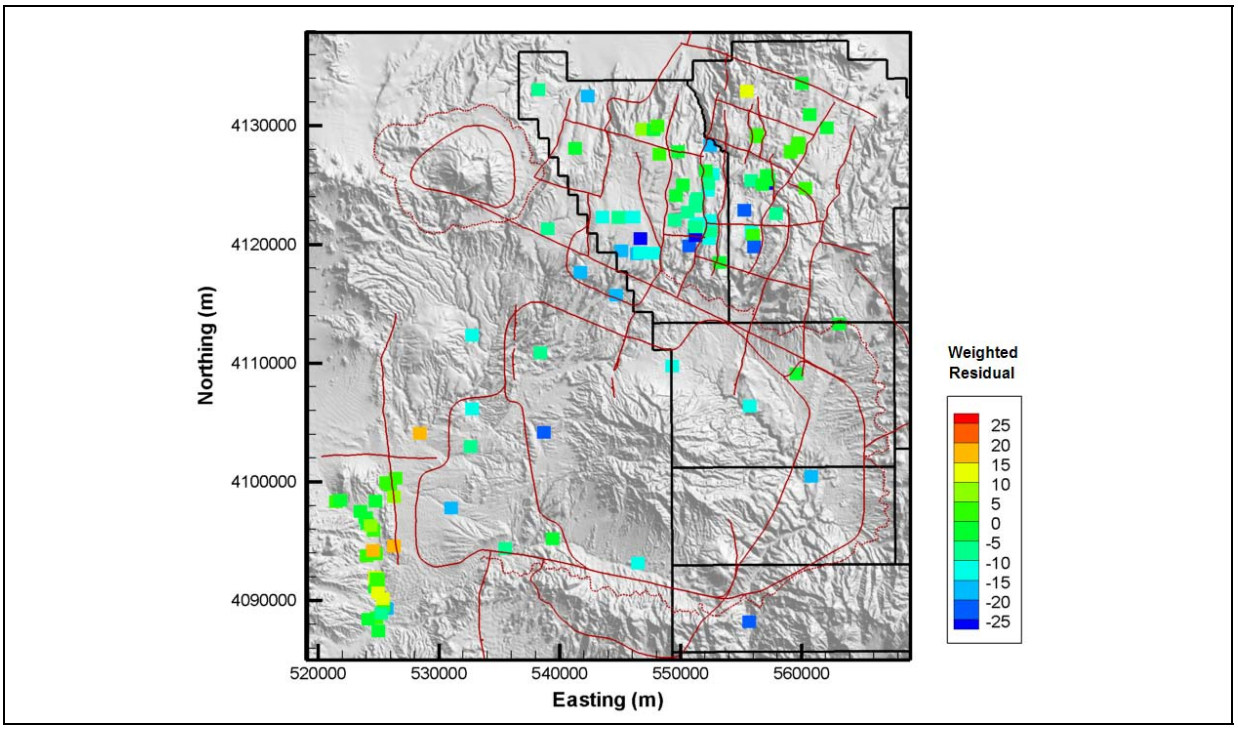

Figure 6-115
Post Plot of Weighted Well and Spring Head Residuals for PZUP-MME-SDA

The quantitative measures of the model calibration are given by summary statistics shown in Table 6-27. There is a slight dry bias in the spring heads, with a slight overprediction bias for the flows. The total model objective function was 22,513. Table 6-28 shows the contribution of each data type to the total model goodness of fit.

Figure 6-116 shows the simulated water table for this model case. In the western part of Area 20, the influence of the Purse Fault is evident by the large offset in heads across it, with more subdued effects also present at West Boxcar Fault. Water flows from Areas 19 and 20 toward the southwest and Oasis Valley. Particle tracking (Figure 6-117) from each of the NTS wells shows the same generally noted flow paths as shown in Appendix A of the Pahute Mesa hydrologic data document (SNJV, 2004a).

The initial results from this HFM were greatly different and required substantial effort to recalibrate. The number of changed nodes and associated HSUs for the four largest categories in this alternative are shown in Table 6-29. Notice that the changes are from higher permeability units to lower permeability units found at greater depth in the base HFM. Thus, the changes for this alternative are consistent with the intent of BN (2002) to raise the pre-Tertiary/Paleozoic contact and accentuate the

Table 6-27
Calibration Summary Statistics for PZUP-MME-SDA

Calibration Data	Number of Data	Mean Weighted Error (m or kg/s)[a]	Maximum Weighted Residual	Minimum Weighted Residual	Error Standard Deviation (m or kg/s)
Well Head	152	5.1	18 (U-19x)	-39 (ER-OV-03b)	10
Spring Head	28	2.6	19 (Torrance Spring)	-8.7 (Spring id 180)	6.9
Oasis Valley Discharge	7	-6.5	35 (Zone 3)	-64 (Zone 4)	34
Boundary Flow	4	-8.6	16 (West)	-31 (South)	19

[a]Positive sign is simulated less than target, negative is larger.

Table 6-28
Contribution to Model Goodness of Fit by Data Type for PZUP-MME-SDA

Data Type	Value (-)	Percent of Total
Well Head	16,416	61
Spring Head	1,337	5
Oasis Valley Discharge	7,865	29
Boundary Flow	1,500	5
Total	27,118	100

shallow flow system. The total number of changed nodes is 55,554. The properties used to parameterize this model are summarized in Section 6.3.6.

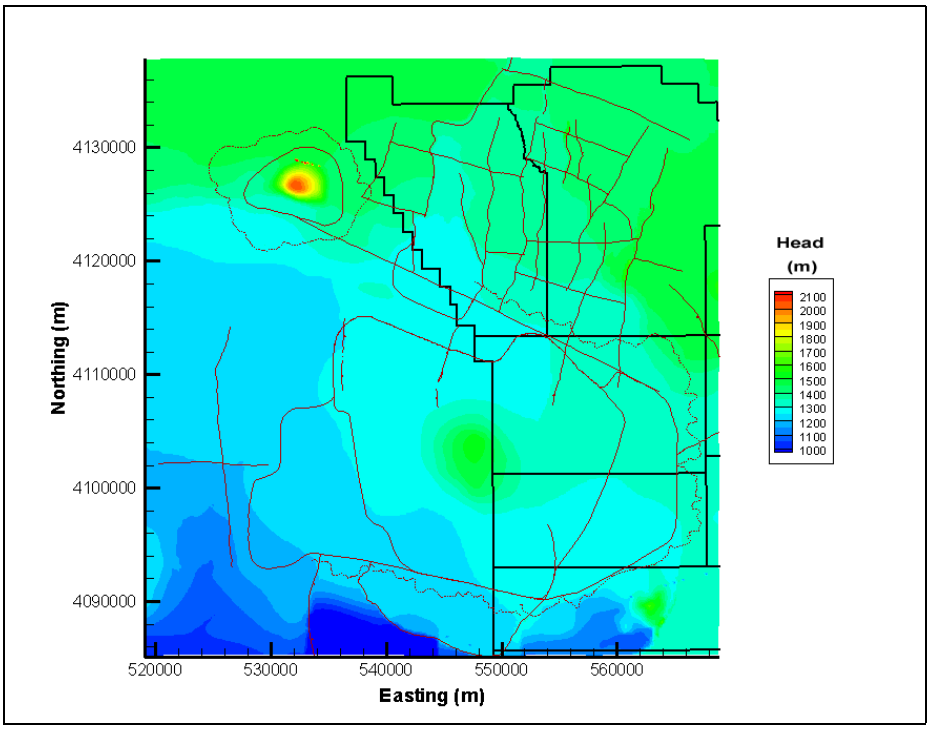

Figure 6-116
Simulated Water Table for PZUP-MME-SDA

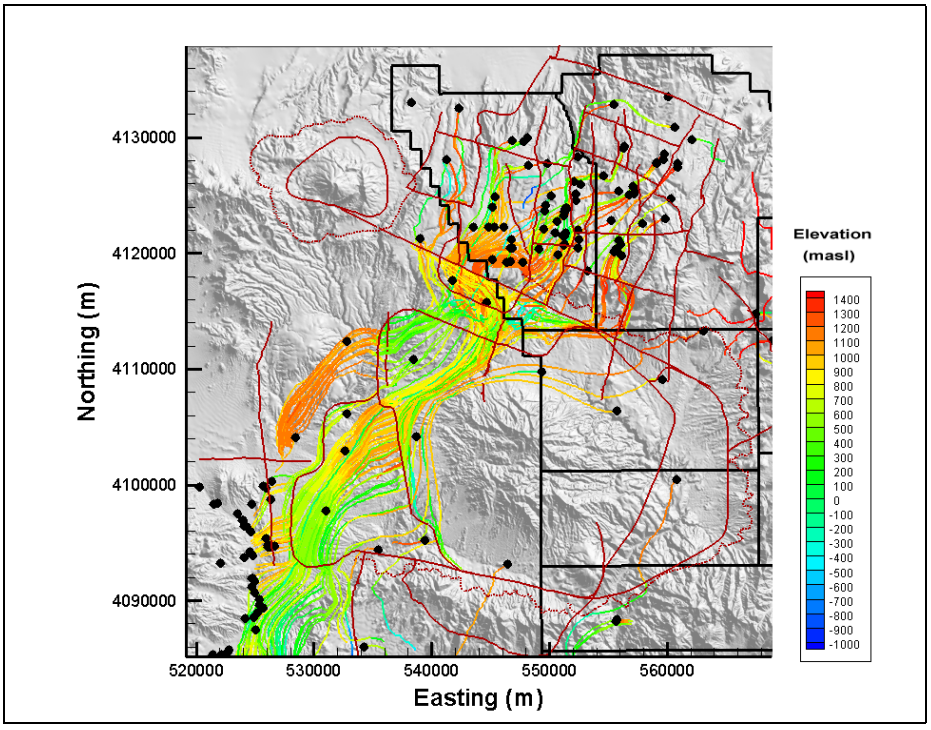

Figure 6-117
Particle Tracks for PZUP-MME-SDA

Table 6-29
Selected Node Changes for PZUP HFM Alternative

Base HSU	Alternative HSU	Node Count
TMCM	ATICU	10,637
PBRCM	LCA	9,576
TMCM	RMICU	5,388
PBRCM	LCCU1	5,188

6.3.4 Deeply Rooted Belted Thrust Fault Alternative (DRT-MME-SDA)

The Belted Range Fault is the principal pre-Tertiary structure in the model region and controls the distribution of pre-Tertiary rocks. The fault is poorly constrained over the model area, and an alternative was developed in which the fault extends deeper, resulting a thick sheet of LCCU over most of the model area. The anticipated consequence was the focusing of the flow system higher in the model from the reduction in the amount of permeable rocks, thus increasing flow velocity. See Section 6.7 in BN (2002) for more information.

Plots of observed versus simulated values for the calibration wells, springs, Oasis Valley discharge, and boundary flows are shown in Figures 6-118 through 6-121. The scatter around the line of perfect agreement is generally random in Figure 6-118, until an observed head of 1,450 m is exceeded. At the very highest observed observation well heads, the model has a tendency toward undersimulation. Moreover, on Figure 6-119, the line of perfect agreement is shown, and ideally the data would plot exactly onto this line. However, at the higher observed observation spring head, the model has a tendency toward undersimulation. The plot is not significantly different than those shown in Section 5.6.2. Figure 6-121 presents a plot of observed versus simulated values for boundary flows. Figure 6-122 shows a histogram of weighted observation well residuals. The bulk of the weighted errors (about 95) are less than ±10 m. The errors are not symmetrically distributed around zero, with a large proportion oversimulated (negative sign) wells and a single large (almost equal to 60 m) underprediction.

The total estimated Oasis Valley discharge in the CAU model domain is 227 kg/s; the simulated discharge, shown in Figure 6-120, is 214 kg/s. The total error is within one standard deviation (30 kg/s) as reported by Laczniak et al. (2001). The model trends the same as the data with some

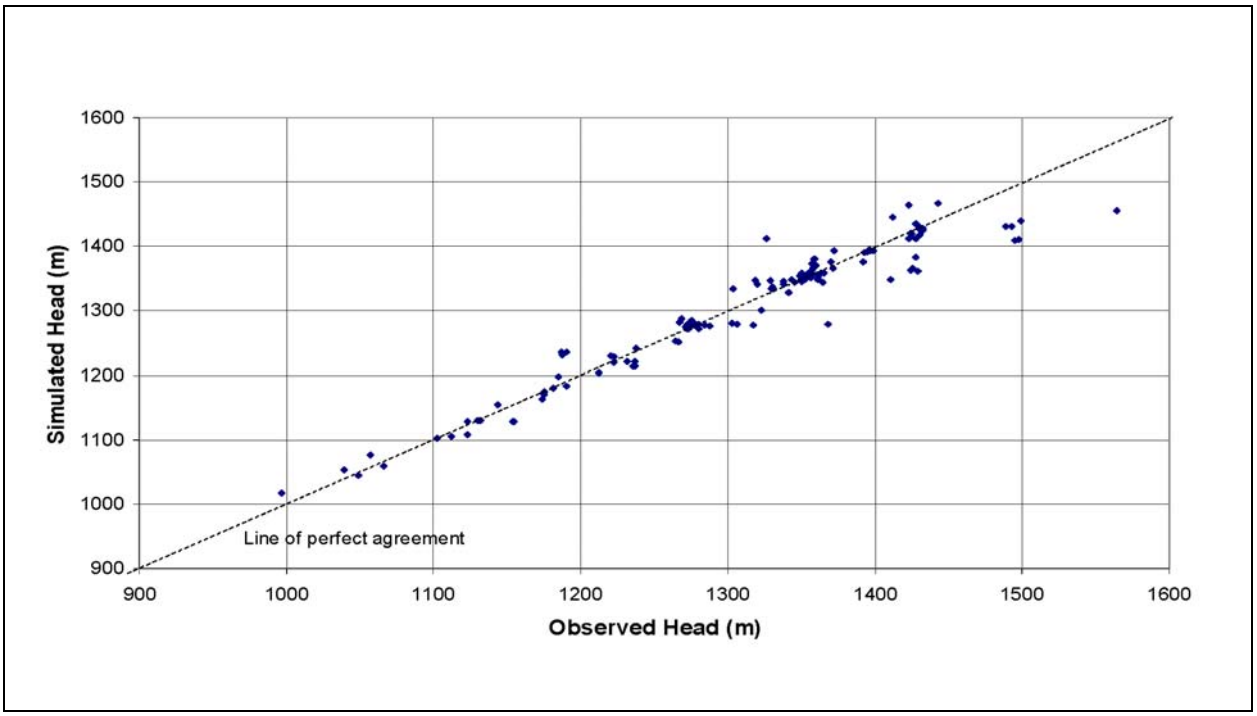

Figure 6-118
Observed Versus Simulated Observation Well Head for DRT-MME-SDA

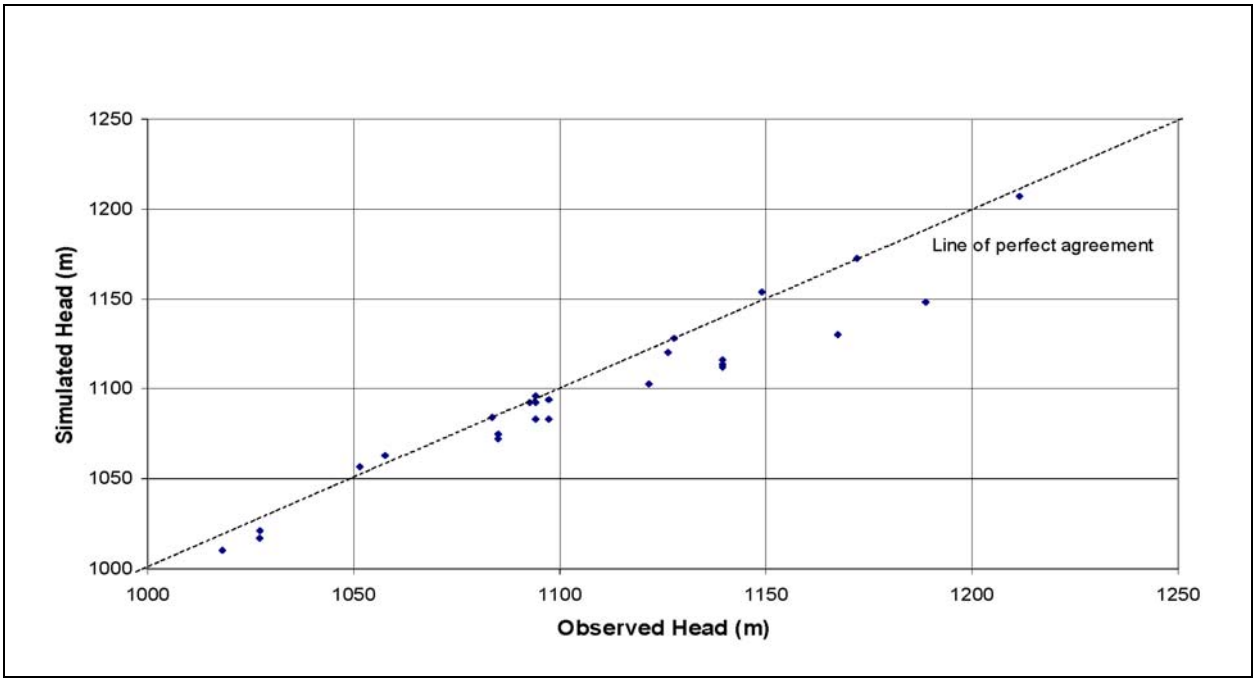

Figure 6-119
Observed Versus Simulated Spring Head for DRT-MME-SDA

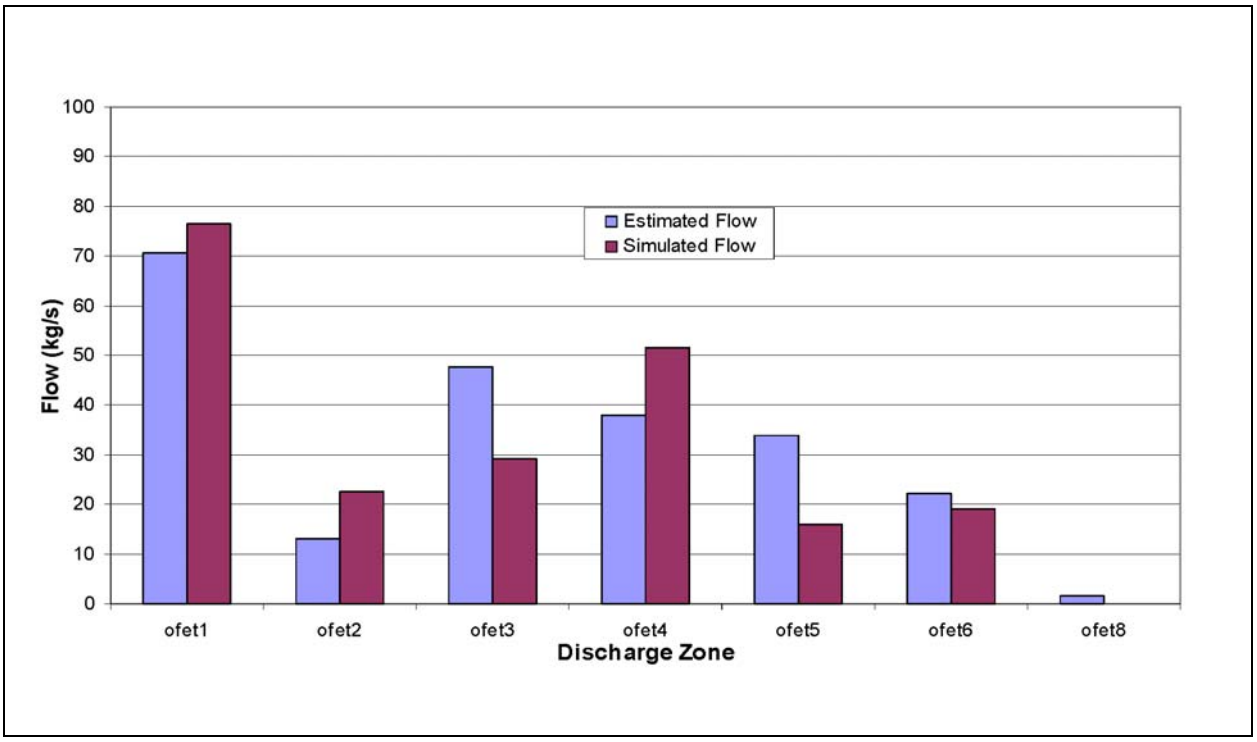

Figure 6-120
Observed and Simulated Oasis Valley Discharge for DRT-MME-SDA

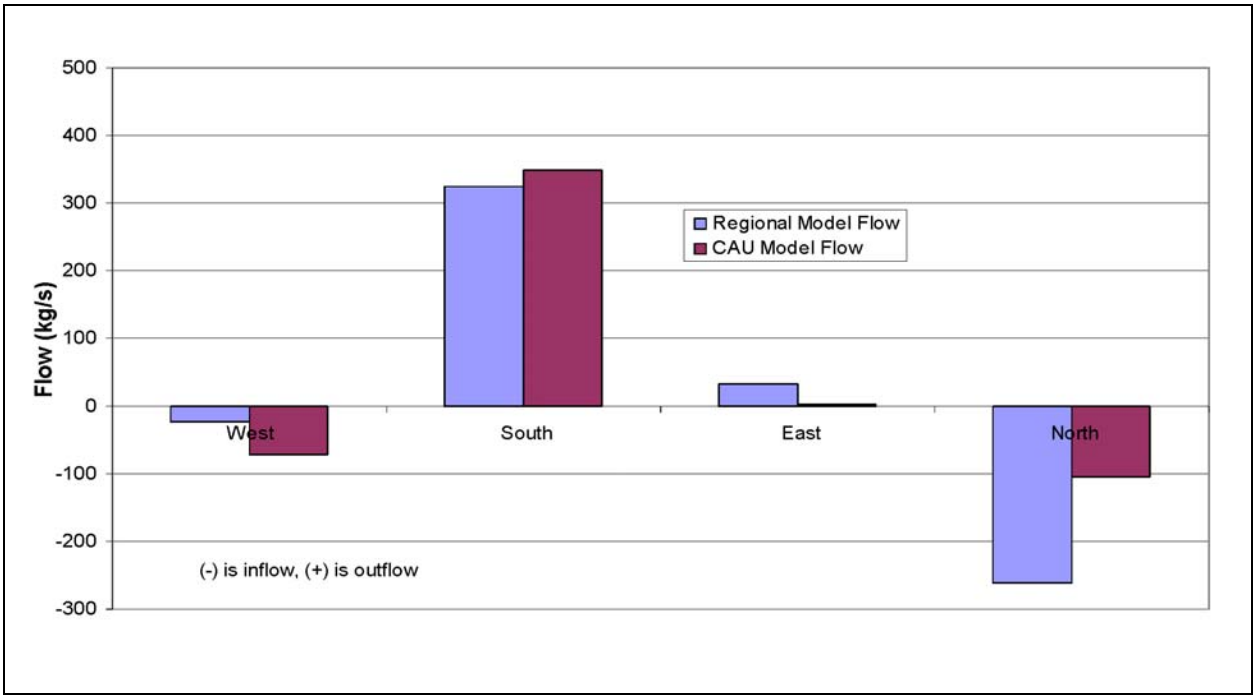

Figure 6-121
Observed and Simulated Boundary Flows for DRT-MME-SDA

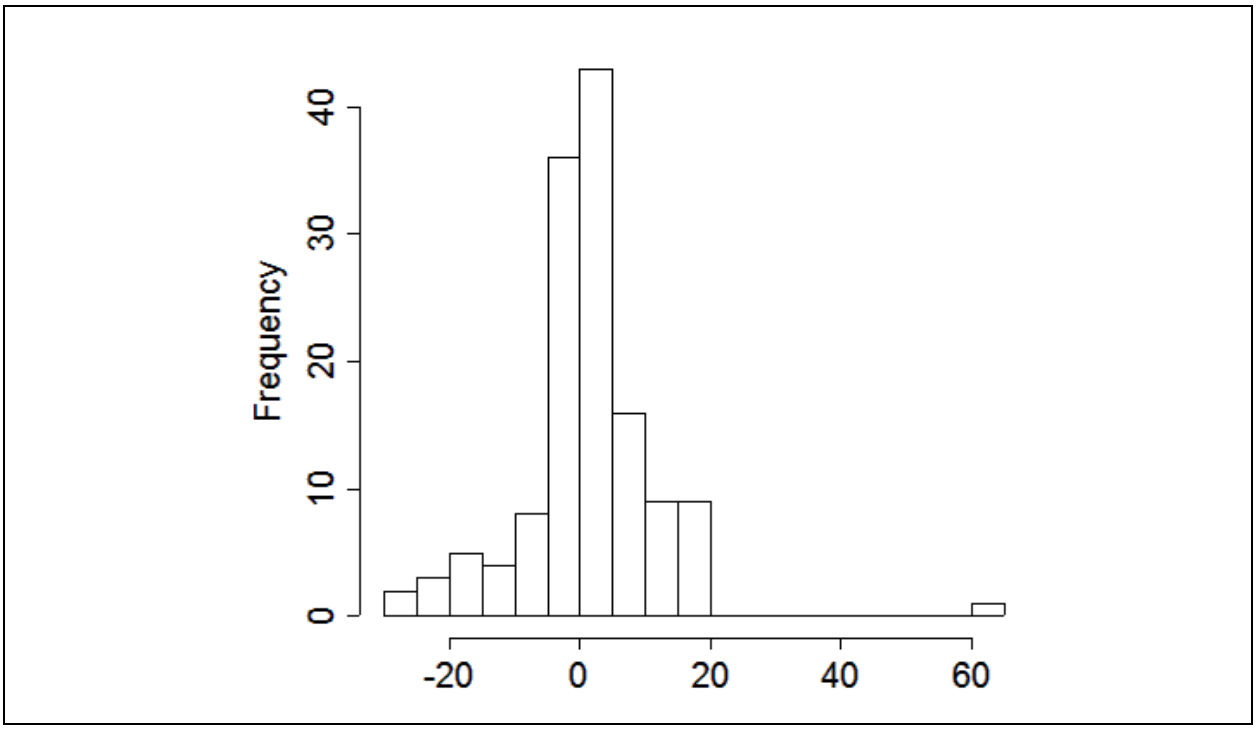

Figure 6-122
Histogram of Weighted Head Residuals for DRT-MME-SDA

scatter, showing that the general representation of the area is correct. The boundary flows, estimated from regional model analysis, all trend the correct way (e.g., have the proper sign), with the largest relative misfit on the eastern edge.

The weighted head and spring errors are shown on Figure 6-123, color coded by value and sign. The driest, or undersimulated, well was WW-8. The single wettest well was UE-20p. In general, the errors are randomly distributed, although there is a slight dry bias near WW-8 in the east-central model area, and an oversimulation bias in the north-central area (e.g., PM-2 and PM-3).

The quantitative measures of the model calibration are given by summary statistics shown in Table 6-30. The total model objective function was 26,240. Table 6-31 shows the contribution of each data type to the total model goodness of fit. Relative to other models in this section, the overall errors are clearly larger, but no worse than the SCCC HFM discussed in Section 5.7. While the model agreement with wells and boundary flow is clearly worse than the base HFM, the Oasis Valley discharge is only slightly affected. This may be because the deep-rooted thrust does not affect the units that control the flow of water into Oasis Valley.

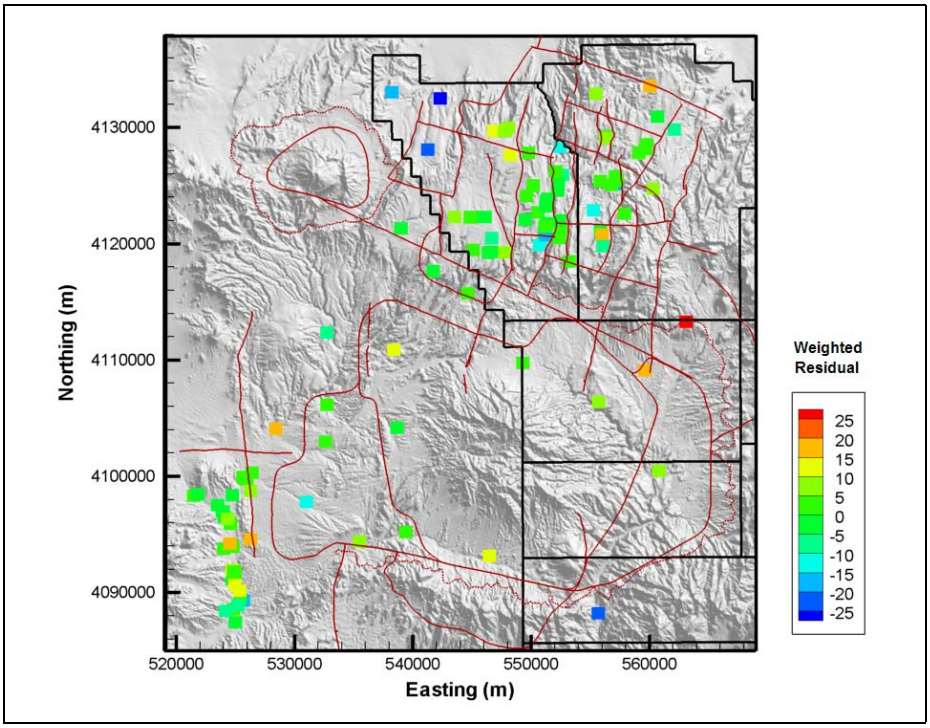

Figure 6-123
Post Plot of Weighted Well and Spring Head Residuals for DRT-MME-SDA

Table 6-30
Calibration Summary Statistics for DRT-MME-SDA

Calibration Data	Number of Data	Mean Weighted Error (m or kg/s)[a]	Maximum Weighted Residual	Minimum Weighted Residual	Error Standard Deviation (m or kg/s)
Well Head	152	0.27	61 (WW-8)	-27 (UE-20p)	9.6
Spring Head	28	2.9	19 (Torrance Spring)	-5.5 (Spring id 159)	6.8
Oasis Valley Discharge	7	3.5	37 (Zone 3)	-27 (Zone 4)	23
Boundary Flow	4	-13	24 (West)	-78 (North)	42

[a]Positive sign is simulated less than target, negative is larger.

Figure 6-124 shows the simulated water table for this model case. In the western part of Area 20, the influence of the Purse Fault is evident by the large offset in heads across it, with more subdued effects also present at West Boxcar Fault. Particle tracking (Figure 6-125) from each of the NTS wells shows the same generally noted flow paths as shown in Appendix A of the Pahute Mesa hydrologic data document (SNJV, 2004a).

Table 6-31
Contribution to Model Goodness of Fit by Data Type for DRT-MME-SDA

Data Type	Value (-)	Percent of Total
Well Head	13,886	53
Spring Head	1,301	5
Oasis Valley Discharge	3,946	15
Boundary Flow	7,106	27
Total	26,239	100

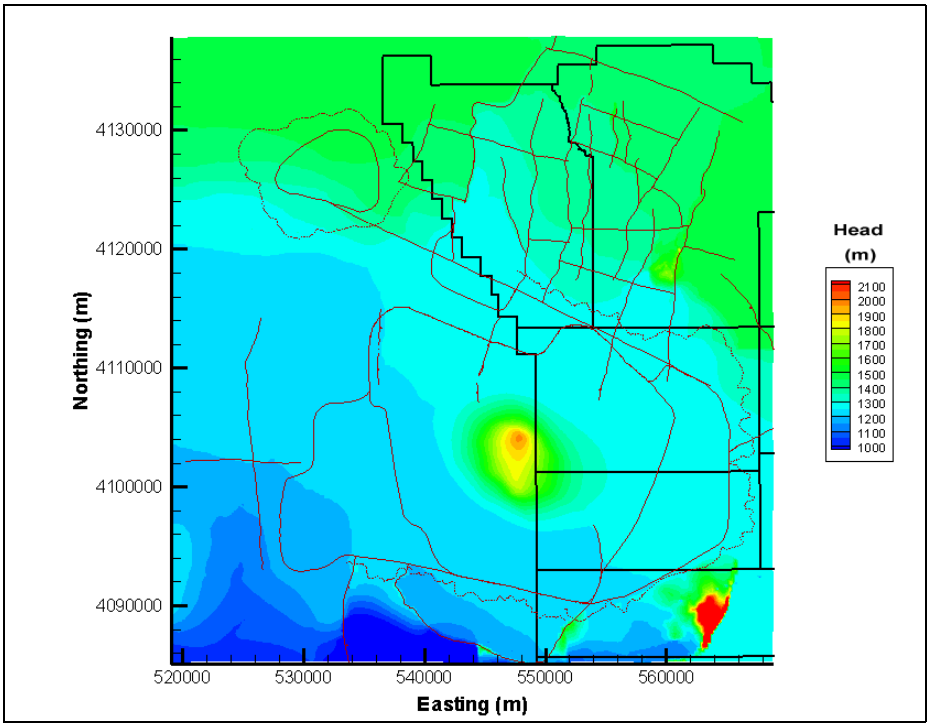

Figure 6-124
Simulated Water Table for DRT-MME-SDA

A summary of the major node HSU changes is shown in Table 6-32. The total node change count was 76,741. The changes are consistent with the propagation of the thrust westward as described by BN (2002). The properties used to parameterize this model are summarized in Section 6.3.6.

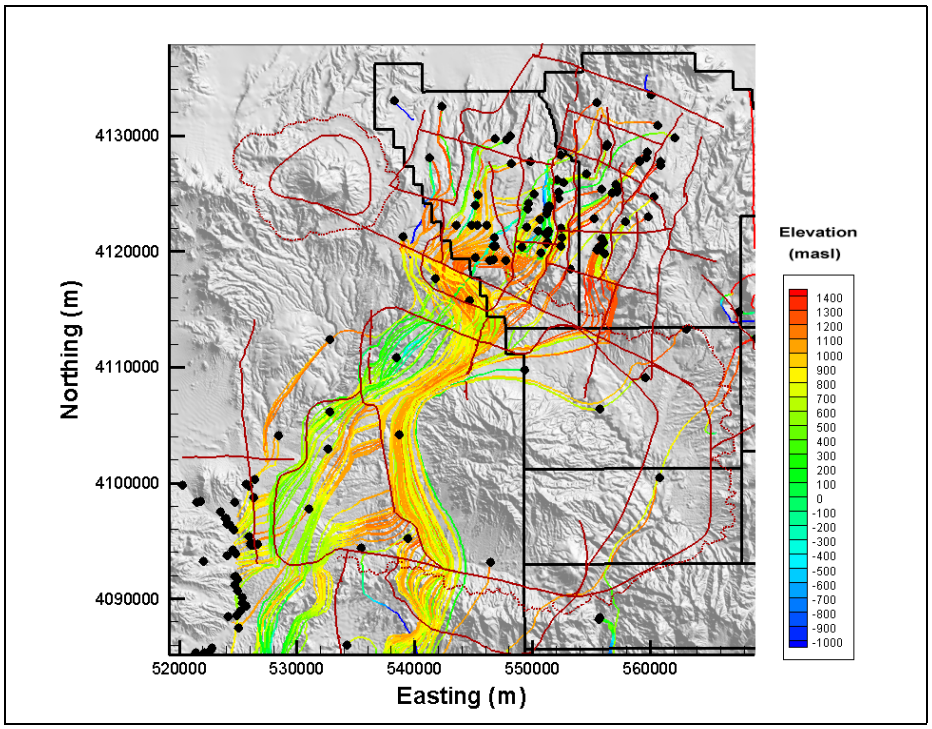

Figure 6-125
Particle Tracks for DRT-MME-SDA

Table 6-32
Selected Node Changes for DRT HFM Alternative

Base HSU	Alternative HSU	Node Count
LCA	LCA3	21,276
LCA	LCCU1	16,419
LCCU	LCCU1	10,165
UCCU	LCCU1	9,123

6.3.5 Contiguous Imbricate Thrust Sheet Alternative (SEPZ-MME-SDA)

In the eastern part of the model, an imbricate thrust fault is modeled that places LCA over UCCU. This relation is based on TW-1 and exposures east of the model area. A small surface exposure of the LCA occurs in this area that is thought to represent a small erosional remnant. This alternative explores the possibility that this feature is not a local remnant, but a continuous sheet. The expected consequence was to facilitate flow on the eastern side of Timber Mountain. See Section 6.6 in BN (2002) for more information.

Plots of observed versus simulated values for the calibration wells, springs, Oasis Valley discharge, and boundary flows are shown in Figures 6-126 through 6-129. The scatter around the line of perfect agreement is generally random in Figure 6-126, until an observed head of 1,450 m is exceeded. At the very highest observed observation well heads, the model has a tendency toward undersimulation. On Figure 6-127, the line of perfect agreement is shown, and ideally the data would plot exactly onto this line. However, at the higher observed observation spring head, the model has a tendency toward undersimulation. The plot is not significantly different than those shown in Section 5.6.2. Figure 6-129 presents a plot of observed versus simulated values for boundary flows. Figure 6-130 shows a histogram of weighted observation well residuals. The bulk of the weighted errors are less than ±10 m. The errors are not symmetrically distributed around zero, with a large proportion of oversimulated (negative sign) wells.

The Oasis Valley discharge and boundary flow components provide the water-balance constraint on the model. The total estimated Oasis Valley discharge in the CAU model domain is 227 kg/s; the simulated discharge, shown in Figure 6-128, is 210 kg/s. The total error is within one standard deviation (30 kg/s) as reported by Laczniak et al. (2001). The model trends the same as the data with some scatter, showing that the general representation of the area is correct. The boundary flows, estimated from regional model analysis, all trend the correct way (e.g., have the proper sign), with the largest relative misfit on the western edge.

The weighted head and spring errors are shown on Figure 6-131, color coded by value and sign. The two driest, or undersimulated, wells were ER-OV-06a and ER-OV-01. The single wettest well was U-19ad in northern Area 19. In general, the errors are randomly distributed, although there is a slight

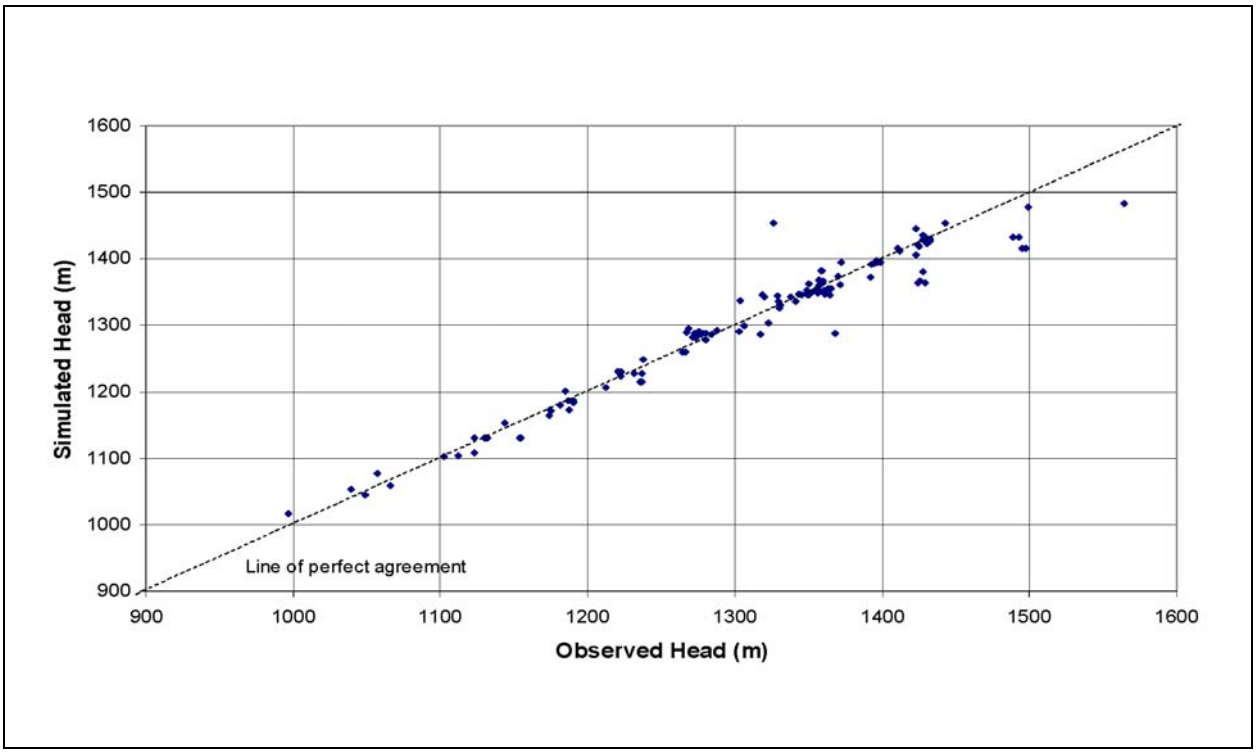

Figure 6-126
Observed Versus Simulated Observation Well Head for SEPZ-MME-SDA

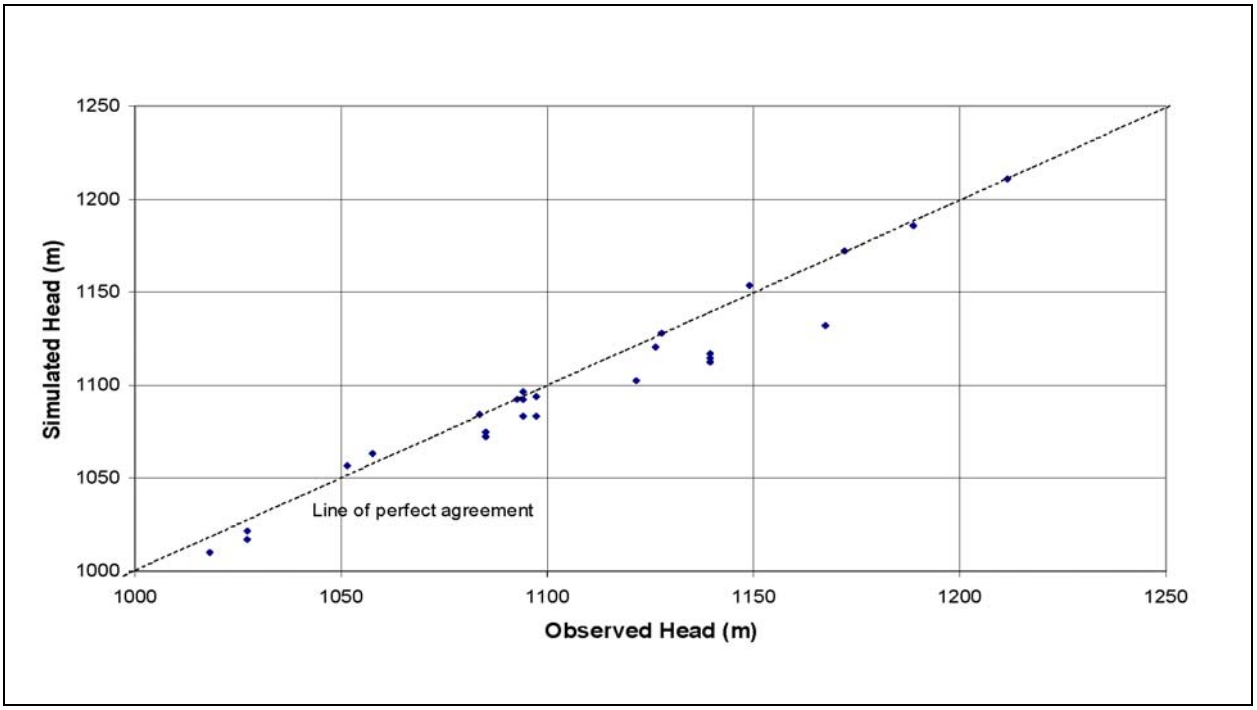

Figure 6-127
Observed Versus Simulated Spring Head for SEPZ-MME-SDA

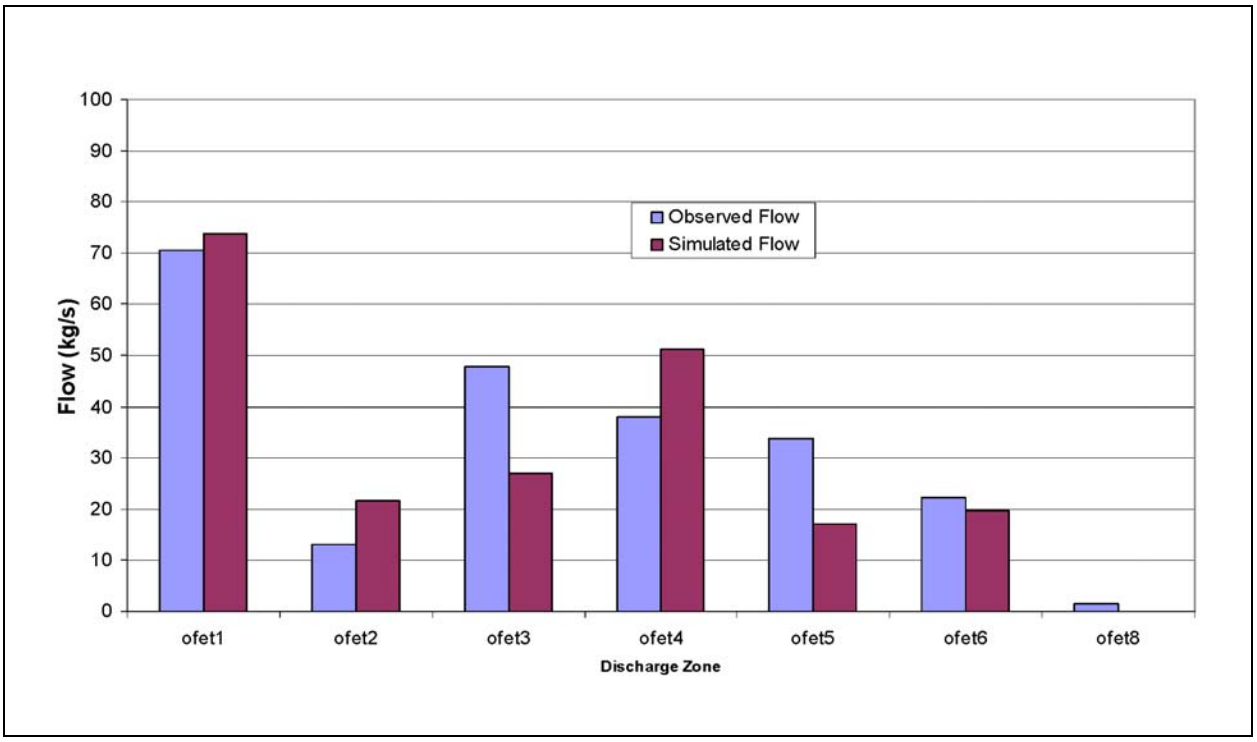

Figure 6-128
Observed and Simulated Oasis Valley Discharge for SEPZ-MME-SDA

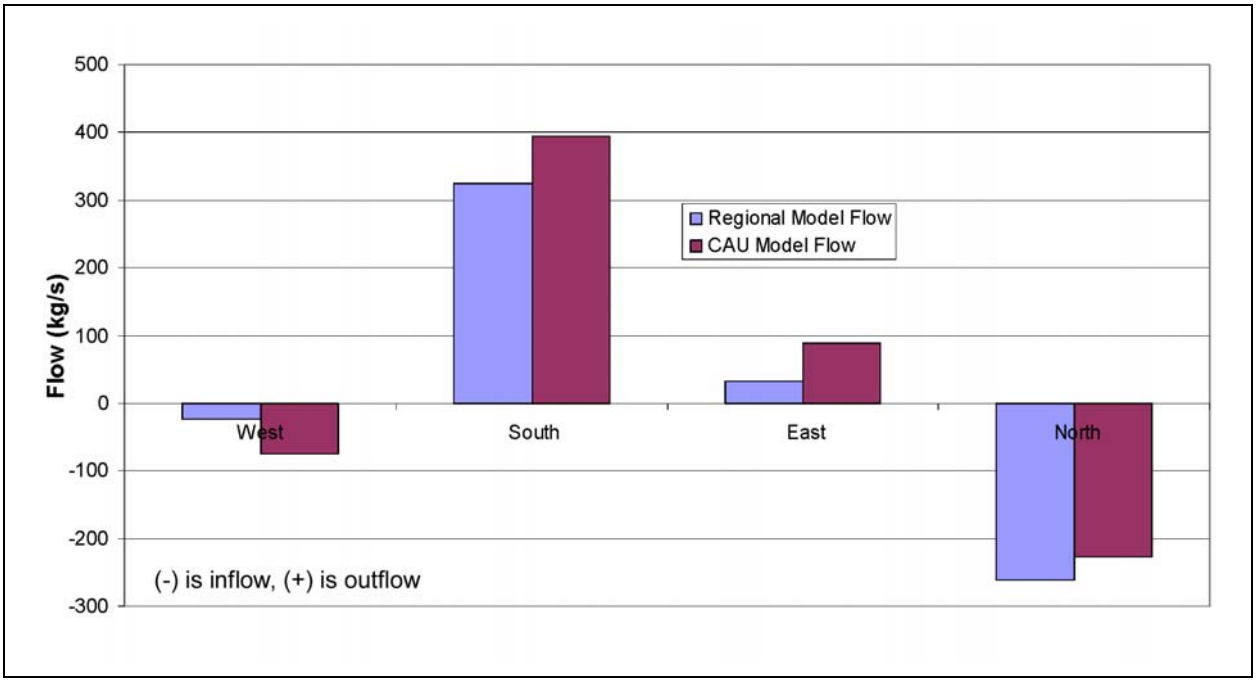

Figure 6-129
Observed and Simulated Boundary Flows for SEPZ-MME-SDA

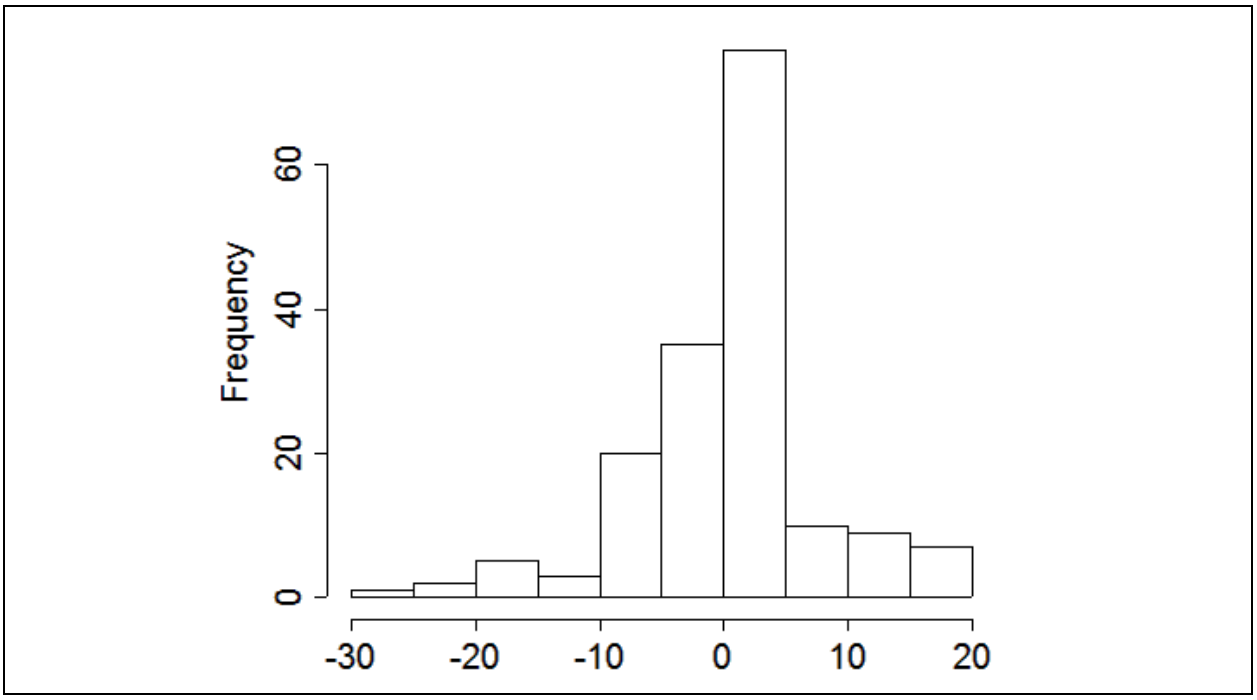

Figure 6-130
Histogram of Weighted Head Residuals for SEPZ-MME-SDA

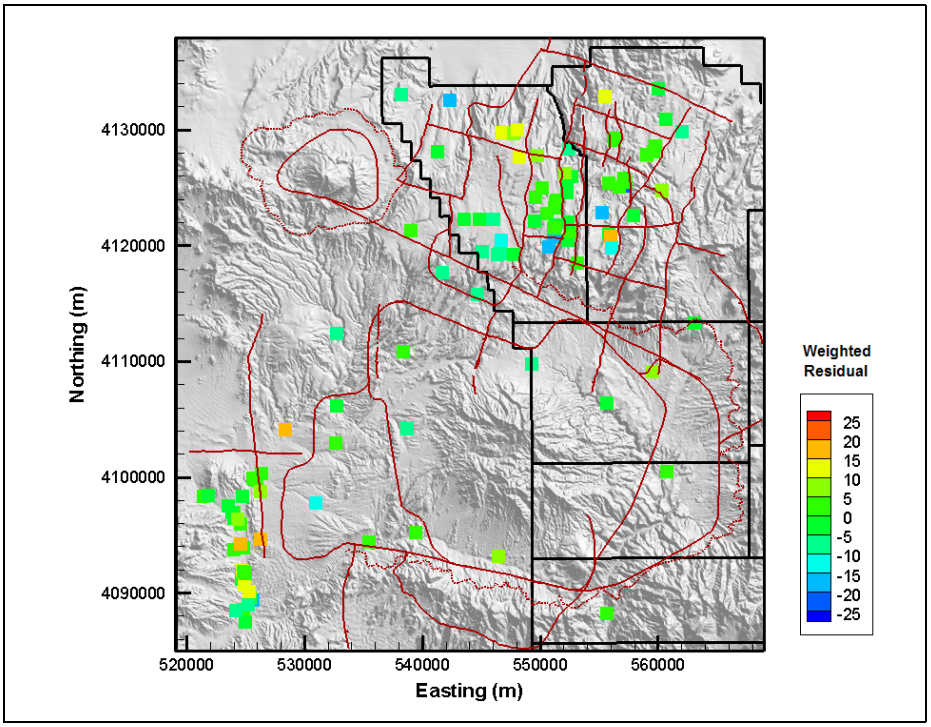

Figure 6-131
Post Plot of Weighted Well and
Spring Head Residuals for SEPZ-MME-SDA

dry bias in northern Area 20 at Easting and Northing of about 547,500 and 4,130,000 m, which includes Wells U-20i, UE-20e #1, U-20e, and U-20ar #1.

The quantitative measures of the model calibration are given by summary statistics shown in Table 6-33. These statistics are very similar to those shown in Section 5.6.2 for BN-MME-SDA. There is a slight dry bias in the spring heads, with a slight overprediction bias for the flows. The total model objective function was 16,159; slightly better than the best HFM calibration described in Section 5.6.2. Table 6-34 shows the contribution of each data type to the total model goodness of fit.

Table 6-33
Calibration Summary Statistics for SEPZ-MME-SDA

Calibration Data	Number of Data	Mean Weighted Error (m or kg/s)[a]	Maximum Weighted Residual	Minimum Weighted Residual	Error Standard Deviation (m or kg/s)
Well Head	152	-0.46	20 (U-19x)	-27 (UE-20n #1)	7.2
Spring Head	28	2.8	19 (Torrance)	-5.5 (Spring id 159)	6.8
Oasis Valley Discharge	7	4.6	41 (Zone 3)	-26 (Zone 4)	24
Boundary Flow	4	-13	26 (West)	-36 (South)	27

[a]Positive sign is simulated less than target, negative is larger.

Table 6-34
Contribution to Model Goodness of Fit by Data Type for SEPZ-MME-SDA

Data Type	Value (-)	Percent of Total
Well Head	7,979	49
Spring Head	1,284	8
Oasis Valley Discharge	3,898	24
Boundary Flow	2,999	19
Total	16,160	100

Figure 6-132 shows the simulated water table for this model case. In the western part of Area 20, the influence of the Purse Fault is still evident by the large offset in heads across it, with more subdued effects also present at West Boxcar Fault. Particle tracking (Figure 6-133) from each of the NTS wells shows the same generally noted flow paths as shown in Appendix A of the Pahute Mesa hydrologic data document (SNJV, 2004a).

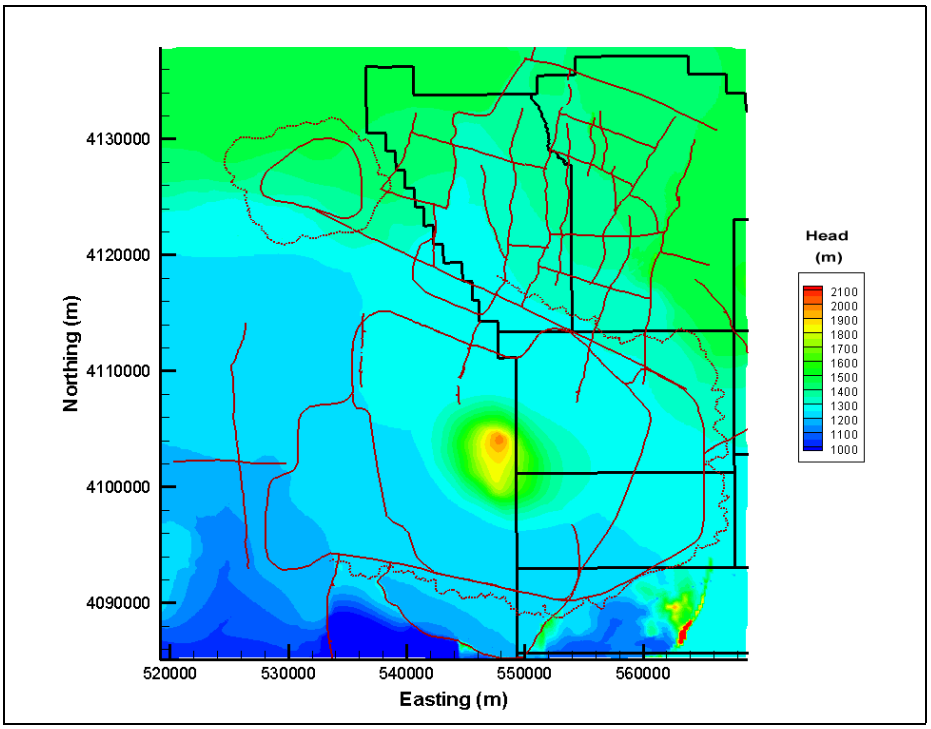

Figure 6-132
Simulated Water Table for SEPZ-MME-SDA

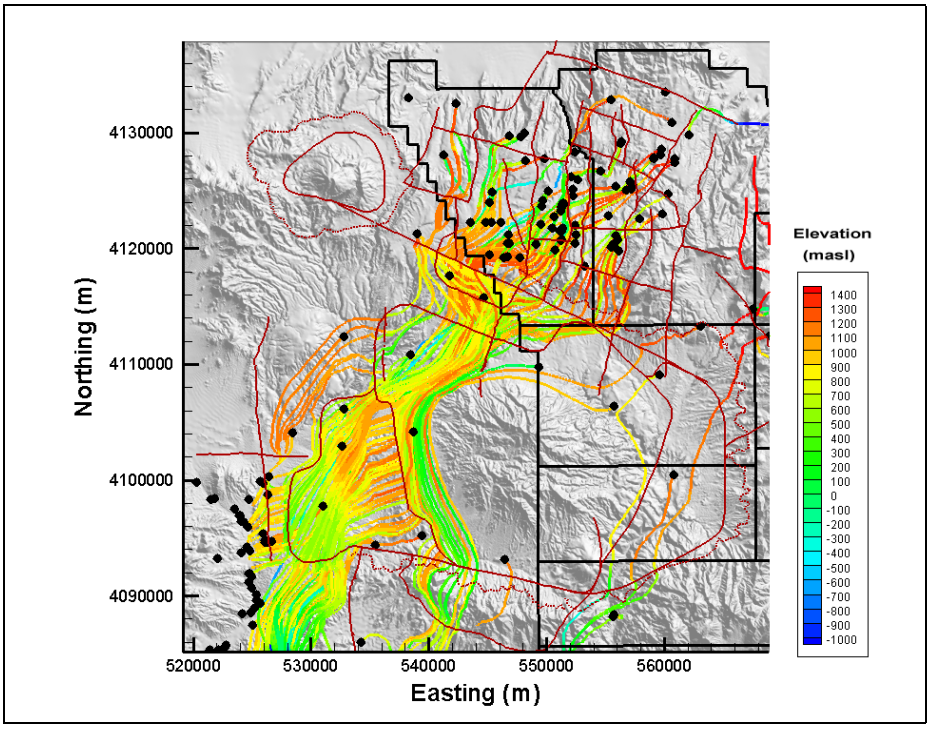

Figure 6-133
Particle Tracks for SEPZ-MME-SDA

The alternative HFM required no additional effort to recalibrate, and appears to have little impact on flow model metrics. A summary of the major node HSU changes is shown in Table 6-35. The total node change count was 8,425. The changes are consistent with increasing the continuity of the LCA in the southeast corner of the domain as described by BN (2002). The properties used to parameterize this model are summarized in Section 6.3.6.

Table 6-35
Selected Node Changes for SEPZ HFM Alternative

Base HSU	Alternative HSU	Node Count
UCCU	LCA3a	6,148
LCA	UCCU	2,277

6.3.6 HFM Uncertainty Analysis Summary

The calibrated HSU parameters for all five HFMs considered are shown in Table 6-36. In the case of TCL, RIDGE, and SEPZ alternatives, they are nearly identical to those used for the selected HSU depth-decay and anisotropy model (see Section 5.6.2) because the effects of the HSU changes required minimal parameter adjustment. However, DRT and PZUP caused dramatic changes in model output and required substantial effort to calibrate. A summary of flow model results for HFM uncertainty is presented in Table 6-37.

The estimates of HSU permeability used to guide the calibration were developed from the interpretation of hydraulic tests. As a qualitative model check, permeability from the model nodes associated with each test was extracted and arithmetically averaged in the case of a test zone with more than one associated node. These are shown in Figures 5-51 and 5-52 with the estimated values. Also shown is the mean permeability estimated for the test HSU as given by SNJV (2004a). Wells ER-EC-1, ER-EC-4, UE-19e, UE-19h, UE-20f, and UE-20h had noisy test data, and the estimated permeability should be considered to have larger uncertainty. The model calibrated permeabilities at the two observation wells from the BULLION FGE (ER-20-6 #1 and ER-20-6 #2) are about an order of magnitude and a half lower than the test values and lower than the value estimated (1.13×10^{-13} m^2) from model calibration by Wolfsberg et al. (2002) for the CHZCM, although within the range of uncertainty (at 2σ) estimated from the mean and standard deviation published by SNJV (2004a) between about 7×10^{-12} to 7×10^{-14} m^2. The permeability calibrated at UE-19h has the largest scatter among the HFMs, but the test value is fairly uncertain. There is some observed scatter that appears to be related to HFM. For instance, at ER-EC-7 the SCCC HFM has a permeability an order of magnitude and a half less than the base HFMs, which themselves are half an order of magnitude less than the estimated test value, but in good agreement with the estimated mean value. Similar results are also seen at Wells ER-EC-1 and ER-EC-6, and at ER 18-2 the SCCC HFM is actually quite a bit lower than the other data. However, no general conclusions can be drawn from the permeability comparison about the goodness of the HFMs because at Wells ER-EC-8, ER-EC-4, UE-19c, and UE-19gS the selected depth-decay and SCCC cases compare better to each other than the all depth-decay case (two different HFMs that were parameterized the same way).

All the alternative HFMs described here were parameterized with the selected HSU depth-decay and anisotropy approach (applied to the same HSUs as well) described in Section 5.6.2. They also were

Table 6-36
Calibrated HSU Parameters for All Five HFMs
(Page 1 of 3)

HSU	Notes log (k or k_0) (m^2)	BN-MME-SDA	TCL	SEPZ	RIDGE	DRT	PZUP
LCCU	k	-18	-25.00	-25.00	-25.00	-18.00	-25.00
LCA	**k_0**	**-14.20**	**-14.24**	**-14.24**	**-14.24**	**-14.24**	**-14.24**
UCCU	k	-16.78	-16.78	-16.78	-16.78	-16.78	-16.78
LCCU1	k	-12.43	-12.43	-12.43	-12.39	-15.54	-12.44
LCA3	**k_0**	**-13.38**	**-13.38**	**-13.38**	**-13.38**	**-13.38**	**-12.37**
MGCU	k	-18.38	-18.38	-18.38	-18.38	-18.38	-18.38
SCICU	k	-18.38	-18.38	-18.38	-18.38	-18.38	-18.38
CHICU	k	-18.38	-18.38	-18.38	-18.38	-18.38	-18.38
CCICU	k	-18.38	-18.38	-18.38	-18.38	-18.38	-18.38
RMICU	k	-18.38	-18.38	-18.38	-18.38	-18.38	-18.38
ATICU	k	-18.38	-18.38	-18.38	-18.38	-18.38	-18.38
BMICU	k	-18.38	-18.38	-18.38	-18.38	-18.38	-18.38
PBRCM Zone 13	**k_0**	**-11.91**	**-11.91**	**-11.91**	**-11.75**	**-13.15**	**-11.82**
BRA	**k_0**	**-11.51**	**-11.47**	**-11.47**	**-11.47**	**-11.47**	**-11.74**
BCU	k	-13.67	-13.80	-13.80	-13.80	-13.80	-13.80
KA	k	-11.78	-11.78	-11.78	-11.78	-11.78	-11.78
CFCU	k	-12.60	-12.60	-12.60	-12.60	-12.60	-12.60
CFCM	k	-15.07	-15.25	-15.25	-15.25	-15.39	-15.25
IA	k	-13.56	-13.48	-13.48	-13.48	-13.48	-13.48
CHCU	k	-14.61	-14.61	-14.61	-14.61	-14.61	-14.61
CHZCM	k	-13.49	-13.75	-13.75	-13.75	-14.22	-13.93
CHVCM	k	-13.39	-13.39	-13.39	-13.39	-13.39	-13.39
CHVTA	k	-11.81	-11.81	-11.81	-11.81	-11.81	-11.81
YMCFCM	**k_0**	**-14.54**	**-14.54**	**-14.54**	**-14.54**	**-14.54**	**-14.54**
TSA	k	-10.09	-10.26	-10.26	-10.26	-10.26	-10.26
LPCU	k	-13.04	-13.04	-13.04	-13.04	-13.04	-13.04
PLFA	k	-11.78	-11.78	-11.78	-11.78	-11.78	-11.78
TCA	k	-11.48	-11.48	-11.48	-11.48	-11.48	-11.48
UPCU	k	-15.33	-15.33	-15.33	-15.33	-15.33	-15.33
BA	k	-11.34	-11.34	-11.34	-11.34	-11.34	-11.34
PVTA	k	-12.33	-12.33	-12.33	-12.33	-12.33	-12.33
PCM	**k_0**	**-10.82**	**-10.82**	**-10.82**	**-10.88**	**-10.74**	**-11.00**

Table 6-36
Calibrated HSU Parameters for All Five HFMs
(Page 2 of 3)

HSU	Notes log (k or k_0) (m^2)	BN-MME-SDA	TCL	SEPZ	RIDGE	DRT	PZUP
LCA3a	**k_0**	**-14.03**	**-14.03**	**-14.03**	**-14.03**	**-14.03**	**-14.03**
FCCU	k	-12.98	-12.98	-12.98	-12.98	-12.98	-12.98
SCVCU	k	-16.28	-16.28	-16.28	-16.28	-16.28	-16.28
TMA	**k_0**	**-14.55**	**-14.53**	**-14.53**	**-14.53**	**-14.53**	**-14.31**
THCM	k	-12.88	-12.88	-12.88	-12.88	-12.88	-12.88
THLFA	k	-11.78	-11.78	-11.78	-11.78	-11.78	-11.78
TMCM	**k_0**	**-11.04**	**-11.04**	**-11.04**	**-11.04**	**-11.04**	**-11.04**
FCA	k	-11.50	-11.50	-11.50	-11.50	-11.50	-11.50
FCCM	k	-13.04	-13.04	-13.04	-13.04	-13.04	-13.04
DVA	k	-12.71	-12.71	-12.71	-12.85	-12.67	-12.66
DVCM	k	-13.23	-13.23	-13.23	-13.31	-13.25	-13.19
TCVA	**k_0**	**-10.65**	**-10.65**	**-10.65**	**-10.65**	**-10.65**	**-10.65**
YVCM	k	-10.08	-10.08	-10.08	-10.08	-10.08	-10.08
AA	k	-13.50	-13.50	-13.50	-13.50	-13.50	-13.50
LCA Zone 1	**k_0**	**-14.37**	**-14.37**	**-14.37**	**-14.37**	**-14.37**	**-14.37**
TCVA Zone 4	**k_0**	**-12.52**	**-10.65**	**-10.65**	**-10.65**	**-10.65**	**-10.65**
TCVA Zone 6	**k_0**	**-12.18**	**-12.52**	**-12.52**	**-12.52**	**-12.52**	**-12.03**
TMA Zone 4	**k_0**	**-10.42**	**-14.59**	**-14.59**	**-14.59**	**-14.59**	**-16.75**
TMA Zone 6	**k_0**	**-8.84**	**-12.18**	**-12.18**	**-12.18**	**-12.18**	**-12.33**
PBRCM Zone 80	**k_0**	**-11.30**	**-10.42**	**-10.42**	**-10.42**	**-10.42**	**-10.42**
PBRCM Zone 81	**k_0**	**-14**	**-8.84**	**-8.84**	**-8.84**	**-8.84**	**-8.84**
PBRCM Zone 82	**k_0**	**-11.49**	**-11.30**	**-11.30**	**-11.30**	**-11.30**	**-11.30**
PBRCM Zone 83	**k_0**	**-10.452**	**-13.10**	**-13.10**	**-13.10**	**-13.10**	**-13.10**
PBRCM Zone 84	**k_0**	**-11.26**	**-11.49**	**-11.49**	**-12.39**	**-11.07**	**-11.49**
PBRCM Zone 87	**k_0**	**-10.05**	**-10.45**	**-10.45**	**-10.45**	**-10.45**	**-8.58**
TMCM-ERM	**k_0**	**-11.05**	**-11.26**	**-11.26**	**-11.26**	**-11.26**	**-11.26**
TMCM-ATCW	**k_0**	**-11.94**	**-10.05**	**-10.05**	**-10.05**	**-10.05**	**-10.08**
TMCM-ATCE	**k_0**	**-10.76**	**-11.05**	**-11.05**	**-11.05**	**-11.05**	**-11.05**
TMCM-THS	**k_0**	**-12.5**	**-11.94**	**-11.94**	**-11.94**	**-11.94**	**-11.54**
TMCM-OV	**k_0**	**-9.40**	**-10.76**	**-10.76**	**-10.76**	**-10.76**	**-10.86**
TMCM-TMD	**k_0**	**-10.19**	**-12.50**	**-12.50**	**-12.50**	**-12.50**	**-12.00**
TMCM-NTMW	**k_0**	**-15.95**	**-9.40**	**-9.40**	**-9.40**	**-9.40**	**-9.42**

Table 6-36
Calibrated HSU Parameters for All Five HFMs
(Page 3 of 3)

HSU	Notes log (k or k_0) (m^2)	BN-MME-SDA	TCL	SEPZ	RIDGE	DRT	PZUP
TMCM-NTME	**k_0**	**-14.09**	**-10.19**	**-10.19**	**-10.19**	**-10.19**	**-9.95**
LPCU West of Purse Fault	k	**-10.80**	-15.95	-15.95	-15.95	-15.95	-15.95
UPCU West of Purse Fault	k	--	-14.09	-14.09	-14.09	-14.09	-14.09
BRA West of Purse Fault	k_0	--	-10.80	-10.80	-10.80	-10.80	-10.80

k = Permeability
k_0 = Reference permeability
See Table 4-1 for HSU descriptions.

Table 6-37
Summary of Flow Model Results for HFM Uncertainty Analysis

HFM	Water-Balance Condition	Calibration Observations Base HFM	Qualitative Flow Path Assessment Base HFM
TCL	MME	Almost identical calibration to BN. Required no additional effort to calibrate.	Particles go deeper near ER-EC-1 and ER-EC-6. Stronger tendency to go to Oasis Valley.
RIDGE	MME	Slightly poorer calibration than BN. Required no additional effort to recalibrate. Simulated low Oasis Valley discharge.	Particles exit Area 20 further west with a more even distribution than the base. Stronger tendency to go to Oasis Valley.
DRT	MME	Noticeably poorer calibration. Required substantial effort to recalibrate.	Fewer tracks go west into northern Oasis Valley. Tendency to exit at Easting 540,000 m.
PZUP	MME	Noticeably poorer calibration. Required substantial effort to recalibrate.	More particles go further west to exit at north Oasis Valley.
SEPZ	MME	Better calibration than base. Required no additional effort to recalibrate.	Very similar to base.

calibrated with the MME recharge map. Thus, a summary understanding can be developed of the relative HFM performance by considering the goodness of the respective calibrations. Figure 6-134 shows the objective function of each alternative HFM normalized by the results presented in Section 5.6.2. One alternative HFM (SEPZ) actually performed slightly better than the base HFM, with all of the improvement coming from a better agreement to the observation well data. The TCL alternative was nearly identical to the base HFM. The RIDGE case was mildly worse than the base HFM, primarily from increased misfit with the wells, although Oasis Valley flow was also noticeably

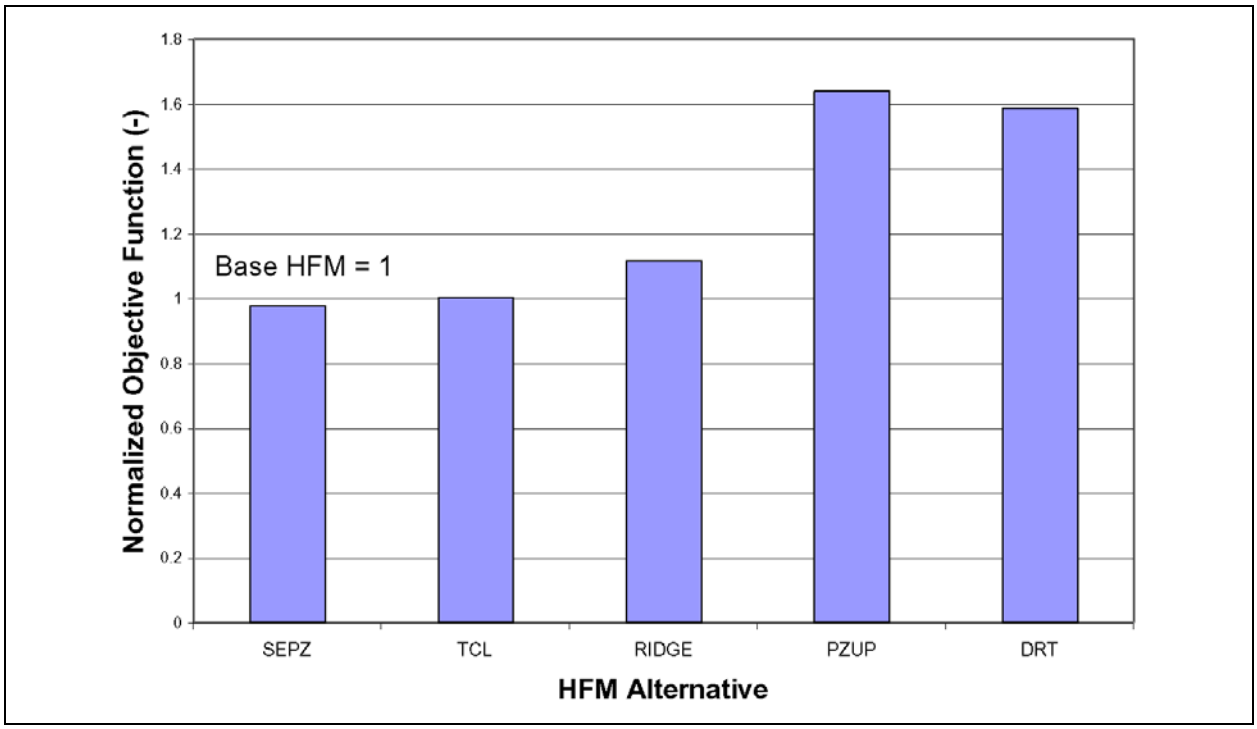

Figure 6-134
Normalized Objective Function of Alternative HFMs

undersimulated. The RIDGE case truncated the extent of VAs (BA, TCA, TSA) in southern Area 20 with older, lower permeability units. This results in more scatter in the model agreement with the observation well data, as shown by the increased error standard deviation in Table 6-24. Note that the mean error in Table 6-24 is improved over the base HFM, which if taken without the context of the error standard deviation would lead to the erroneous conclusion that the RIDGE-MME model was the better calibrated of the two models. The PZUP and DRT alternatives give far and away the most different results in comparison to the base HFM calibration, which relative to the degree of HFM changes is reasonable. The DRT alternative has significant misfit on the boundary flows because the large section of LCCU1 extending westward and northward into the model greatly reduces transmissivity along the northern boundary.

Relative to the prediction of radionuclide migration (the ultimate goal of the project), it is the differences in flow paths that is relevant. The SEPZ alternative, for instance, is so like the base HFM in all regards that it does not appear to provide any estimate of uncertainty useful to radionuclide migration. The PZUP alternative, however, has more particles exiting in the northern part of Oasis Valley, which is an issue of concern. The TCL and RIDGE alternatives have a tendency for more

particles to discharge in Oasis Valley, also a qualitative concern. Particle paths in the DRT alternative focus more along the western flank of Timber Mountain, a result that may be important to the ultimate delineation of the contaminant boundary, but is not readily identifiable as a risk to the biosphere.

6.4 Water-Balance Uncertainty Analysis

The Pahute Mesa CAIP (DOE/NV, 1999) states that boundary condition uncertainty must be considered in the flow model analysis, and that the two sources of boundary condition uncertainty are the recharge distribution and the model boundary flow derived from the regional model. These two factors control the water balance of the CAU-scale model, which in turns has a direct bearing on the overall flow rate, and hence groundwater velocity, through the model domain. This section briefly reviews the approach used to address water-balance uncertainty, and presents results for the base HFM and the SCCC HFM alternative.

6.4.1 Recharge Uncertainty

In arid systems with deep groundwater it is generally acknowledged that accurate estimation of recharge is difficult. There are some water-balance constraints for the entire regional flow system (e.g., discharge at Ash Meadows, Oasis Valley, Death Valley) but there is no perennial surface water flow in the Oasis Valley area that could be used to directly balance local inflow and outflow as is possible in other areas of the country.

In order to bound the possible recharge volumes, three recharge models were used. They are the chloride mass-balance approach of Russell and Minor (2002) (referred to as the DRI model hereafter), the MME empirical method (referred to as the MME hereafter) presented in the UGTA regional model (DOE/NV, 1997, IT, 1996a through f; IT, 1997a and b), and the distributed parameter watershed (referred to as the USGS hereafter) model of Hevesi et al. (2003). The chloride mass-balance recharge estimate was further subdivided to remove recharge in the alluvium (DRIA) and in the alluvium and below an elevation of 1,237 m (DRIAE). The distributed parameter watershed model had versions with (USGSD) and without runoff (USGSND) and run-on. The areal distribution and mass flows associated with these recharge models are shown in Section 4.3 and Table 4-5.

The base and SCCC HFMs were previously calibrated with the MME recharge model (see Sections 5.6 and 5.7). The DRI and USGS recharge models were then applied and the models recalibrated.

6.4.2 Lateral-Flow Uncertainty

The Pahute Mesa CAU flow model domain cannot be considered independently of the regional groundwater flow system. The inflow and outflows along the model edges are estimated from the regional model, but some uncertainty exists in these flows because they cannot be observed directly, and there are only large-scale constraints on the flow system.

In order to address the lateral-flow component of uncertainty, different combinations of recharge model and boundary flow are considered. It is possible to combine recharge models with boundary flows derived from using other recharge models in the regional model. For instance, the DRI recharge model could be used in conjunction with the boundary flows estimated using the USGS recharge model. However, the appropriateness of such combinations is difficult to interpret. The approach taken was to use a given recharge model with the regional model boundary flows derived from the same recharge model in the regional model. These combinations can be more readily interpreted to bound water-balance uncertainty as follows:

- The DRI recharge model has the highest mass flow and results in the highest CAU model boundary flows. Using these two datasets together results in a flow system with higher flow (and hence velocity) than the MME and USGS recharge models.
- The USGS model tends toward the lower range of recharge estimates. The overall flow of water through the system tends to be less than the MME or DRI models.

The base and SCCC HFMs were calibrated with the MME recharge model derived boundary flows in Sections 5.6 and 5.7, respectively; hence, this part of the analysis has already been completed. For the water-balance uncertainty analysis, the recharge model was changed, and then the flow model was recalibrated with the boundary flows that correspond to the same recharge model and regional model boundary flow.

6.4.3 Base Geologic Model Water-Balance Uncertainty Analysis

The base HFM with the selected HSU depth decay and anisotropy (BN-SDA) parameterization as described in Section 5.6.2 was used as the basis for analyzing water-balance uncertainty. Four combinations of recharge model and boundary flows are considered as follows:

1. DRIA recharge and boundary flow
2. DRIAE recharge and boundary flow
3. USGSD recharge and USGSND boundary flow (boundary flows with the USGSD recharge model were not calculated from the UGTA regional model)
4. USGSND recharge and USGSND boundary flow

In addition, the LCCU1 variation described in Section 6.2.4.2 is also investigated.

6.4.3.1 DRI Recharge Model

The base HFM - selected HSU depth-decay and anisotropy was calibrated with the DRIA and DRIAE recharge and boundary flows. Tables 6-38 and 6-39 summarize the calibration statistics for DRIAE and DRIA, respectively. The objective function is nearly the same, 21,407 versus 20,716. The results shown in Tables 6-38 and 6-39 are very similar, and only the DRIA recharge model will be carried for further analyses because it tends to spread recharge around the domain to a greater extent and the elevation screen only affects lower elevations.

Table 6-38
Calibration Summary Statistics for BN-DRIAE-SDA

Calibration Data	Number of Data	Mean Weighted Error (m or kg/s)	Maximum Weighted Residual	Minimum Weighted Residual	Error Standard Deviation (m or kg/s)
Well Head	152	-1.8	20 (ER-OV-03a)	-32 (UE-20n #1 1,005.84 m)	8.1
Spring Head	28	3.1	19 (Torrance Spring)	-5.4 (Spring id 159)	6.9
Oasis Valley Discharge	7	2.0	41 (Zone 3)	-18 (Zone 4)	21
Boundary Flow	4	-24	23 (West)	-60 (North)	42

[a]Positive sign is simulated less than target, negative is larger.

Table 6-39
Calibration Summary Statistics for BN-DRIA-SDA

Calibration Data	Number of Data	Mean Weighted Error (m or kg/s)[a]	Maximum Weighted Residual	Minimum Weighted Residual	Error Standard Deviation (m or kg/s)
Well Head	152	-1.5	20 (ER-OV-03a)	-31 (UE-20n #1 1,005.84 m)	7.9
Spring Head	28	3.1	19 (Torrance Spring)	-5.3 (Ute Springs Culvert)	6.9
Oasis Valley Discharge	7	3.1	42 (Zone 3)	-18 (Zone 4)	21
Boundary Flow	4	-23	23 (West)	-58 (North)	41

[a]Positive sign is simulated less than target, negative is larger.

Figure 6-135 shows the posted weighted residuals; there is a perceptible bias to oversimulate heads that is also suggested by the mean error. Simulated Oasis Valley discharge is 219 kg/s (versus an estimated discharge of 227 kg/s). Figure 6-136 shows the simulated water table, and Figure 6-137 shows the simulated flow paths from NTS wells. The water table and flow paths have the same general character seen in all the simulations, but there is an intensified flow path out to the south at Easting of about 540,000 m. The DVCM, PCM, BRA, and YMCFCM permeabilities (including k_0) all increased between a quarter and half an order of magnitude over the values used to calibrate the MME recharge in order to bleed off the additional recharge (nearly double that of the MME) imposed by the DRIA recharge model. This increase in permeability causes the increased flow across the southern boundary through the PCM and YMCFCM that is seen in the simulated flow paths.

The reduced LCCU1 permeability alternative variation of the model (Section 6.2.4.2) was also investigated with the DRIA recharge map. Table 6-40 shows the summary calibration statistics; the objective function is 27,712.

Figure 6-138 shows the posted weighted residuals; the error appears random with a slight oversimulation bias. Simulated Oasis Valley discharge is 216 versus 227 kg/s estimated. Figure 6-139 shows the simulated water table, and Figure 6-140 shows the simulated flow paths from NTS wells.

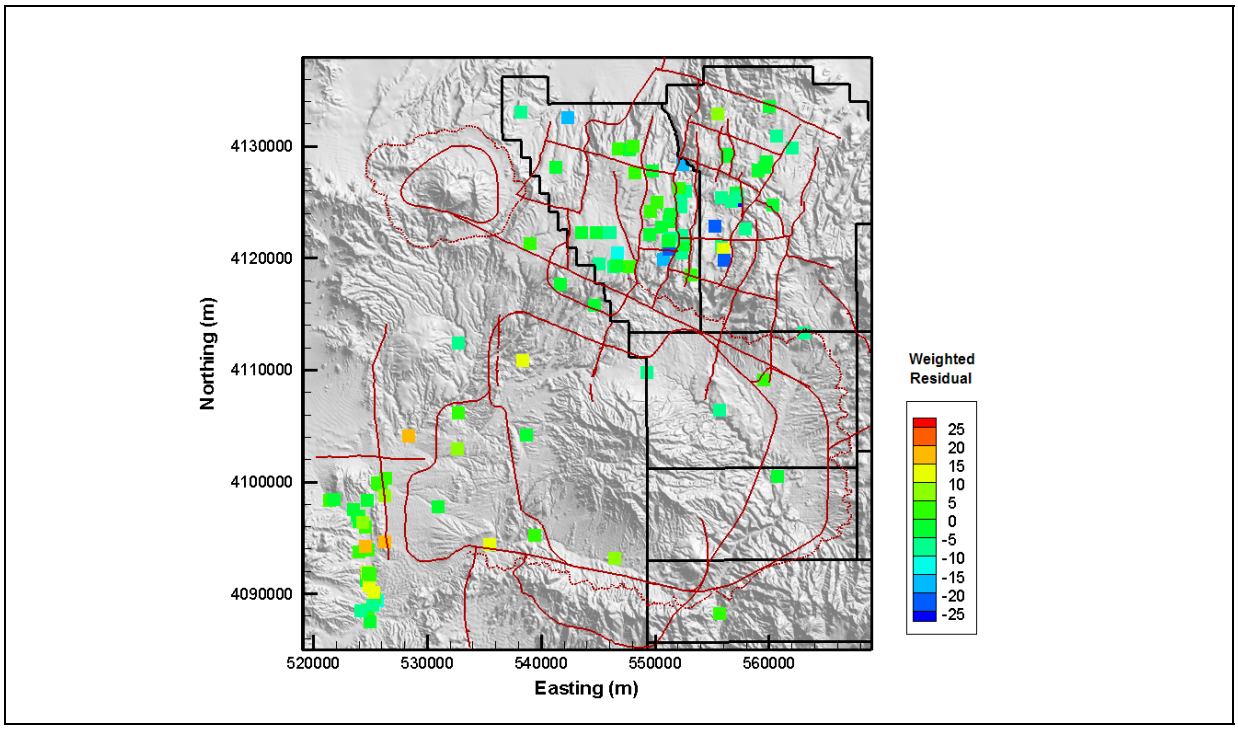

Figure 6-135
Posted Weighted Residuals for BN-DRIA-SDA

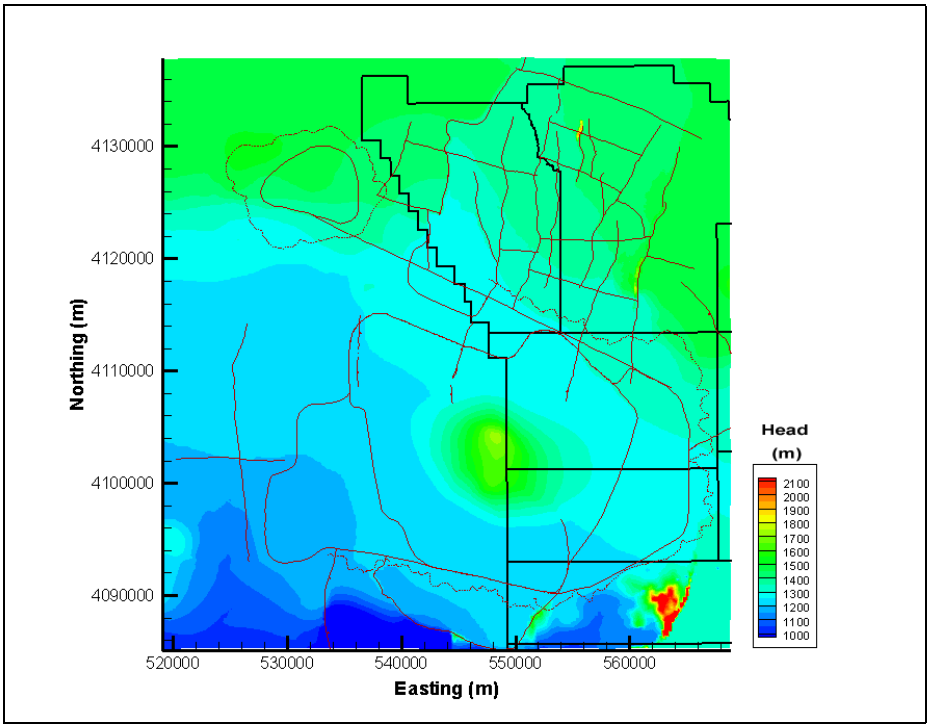

Figure 6-136
Simulated Water Table for BN-DRIA-SDA

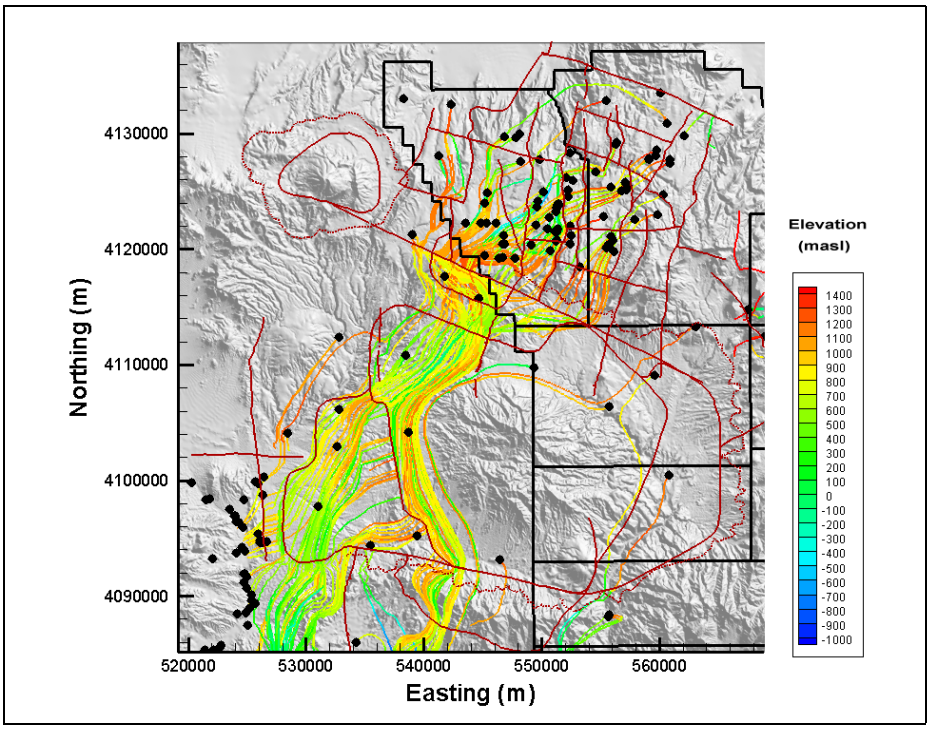

Figure 6-137
Particle Tracks for BN-DRIA-SDA

Table 6-40
Calibration Summary Statistics for BN-DRIA-SDA Reduced LCCU1 Permeability Alternative

Calibration Data	Number of Data	Mean Weighted Error (m or kg/s)[a]	Maximum Weighted Residual	Minimum Weighted Residual	Error Standard Deviation (m or kg/s)
Well Head	152	1.4	76 (WW-8)	-24 (UE-20n #1 1,005.84 m)	9.6
Spring Head	28	3.1	19 (Torrance Spring)	-6.0 (Spring id 159)	6.9
Oasis Valley Discharge	7	2.9	41 (Zone 3)	-19 (Zone 4)	20
Boundary Flow	4	-23	22 (East)	-70 (South)	49

[a]Positive sign is simulated less than target, negative is larger.

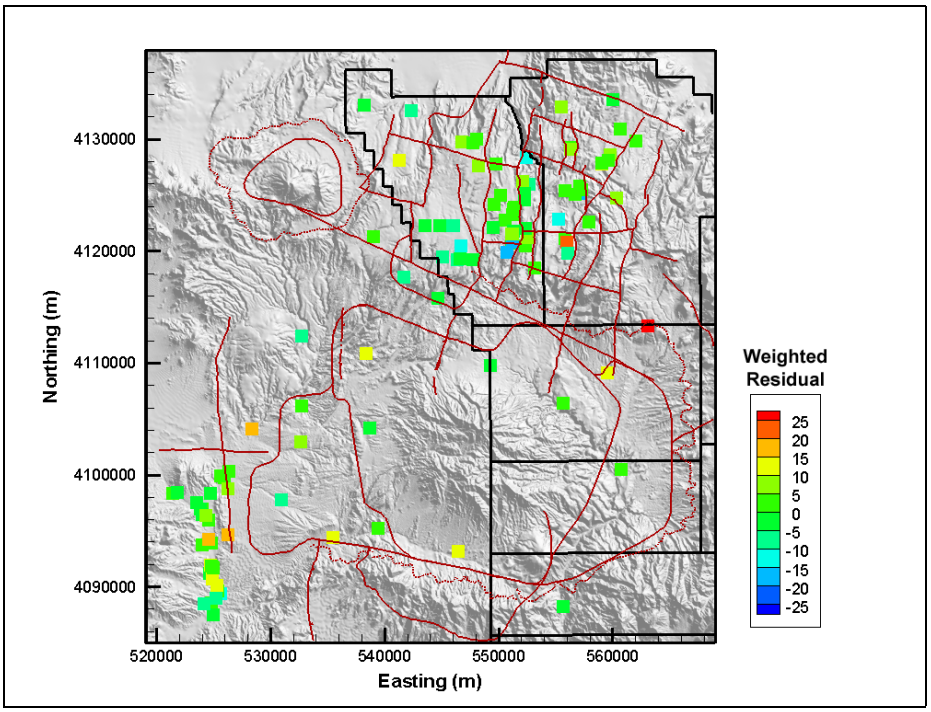

Figure 6-138
Post Plot of Weighted Well and Spring Head Residuals for BN-DRIA-SDA Reduced LCCU1 Permeability Alternative

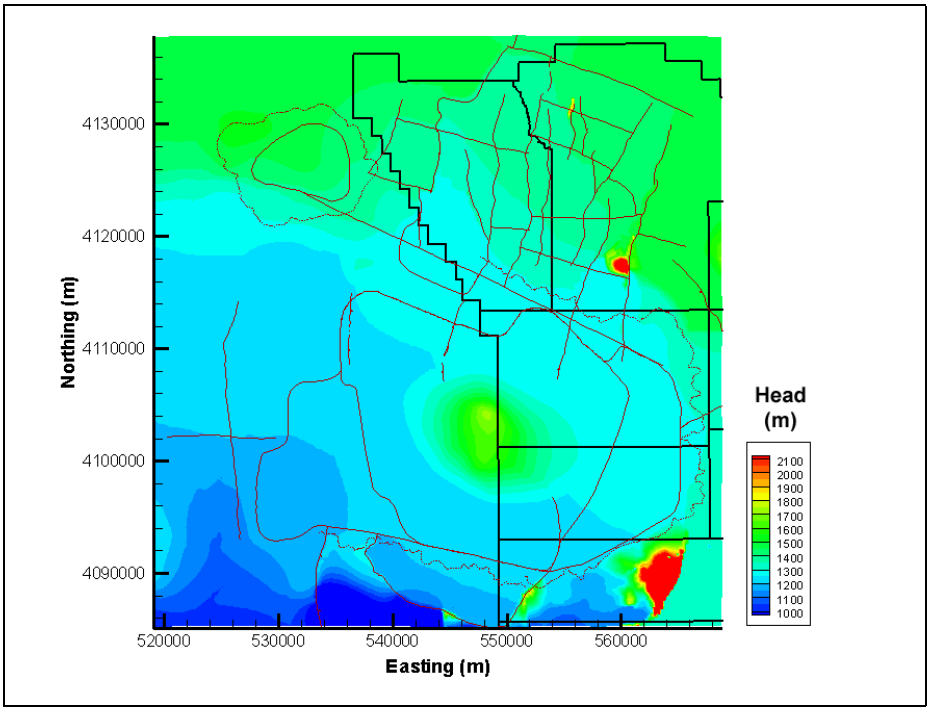

Figure 6-139
Simulated Water Table for BN-DRIA-SDA Reduced LCCU1 Permeability Alternative

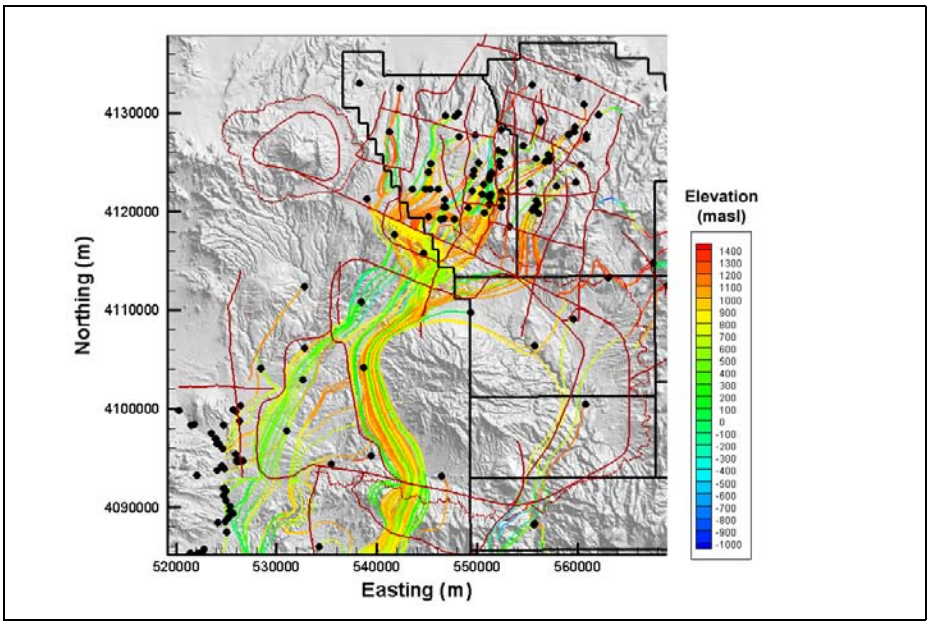

Figure 6-140
Particle Tracks for BN-DRIA-SDA Reduced LCCU1 Permeability Alternative

The clear change between the base calibrated HFM and lower reduced LCCU1 permeability alternative for both the MME and DRI recharge models is the poor matching of WW-8. It does seem not conceptually reasonable that the LCCU1 should support the hydraulic head in this area via its connection to the higher boundary heads, but again, there is no information as to the properties of the LCCU1.

6.4.3.2 USGS Recharge Model

The summary calibration statistics for the base HFM with the USGSND and USGSD recharge models are shown in Tables 6-41 and 6-42. The objective functions are 11,615 and 14,054, respectively. The USGSND model has the lowest recharge volume of all the alternatives and the best objective function. In general, the USGS recharge models calibrate far better than the MME and DRI recharge models. This is because the lower recharge results in fewer local changes in head from recharge accretion. The USGSND recharge model calibrates better than the USGSD model for similar reasons. However, conceptually it does not seem reasonable to neglect the basic watershed processes of runoff and run-on in estimating recharge; thus, the USGSND recharge model is not considered further. Furthermore, goodness of calibration is not the sole metric on which models should be judged.

Table 6-41
Calibration Summary Statistics for BN-USGSND-SDA

Calibration Data	Number of Data	Mean Weighted Error (m or kg/s)[a]	Maximum Weighted Residual	Minimum Weighted Residual	Error Standard Deviation (m or kg/s)
Well Head	152	0.42	19 (ER-OV-03a)	-24 (UE-20n #1 1,005.84 m)	6.2
Spring Head	28	2.8	19 (Torrance Spring)	-5.3 (Ute Springs Culvert)	6.7
Oasis Valley Discharge	7	7.9	43 (Zone 3)	-19 (Zone 4)	23
Boundary Flow	4	5.2	26 (West)	-5.8 (South)	14

[a]Positive sign is simulated less than target, negative is larger.

Table 6-42
Calibration Summary Statistics for BN-USGSD-SDA

Calibration Data	Number of Data	Mean Weighted Error (m or kg/s)[a]	Maximum Weighted Residual	Minimum Weighted Residual	Error Standard Deviation (m or kg/s)
Well Head	152	-1.9	18 (ER-OV-03a)	-30 (UE-20n #1 1,005.84 m)	7.0
Spring Head	28	2.7	19 (Torrance Spring)	-5.3 (Ute Springs Culvert)	6.8
Oasis Valley Discharge	7	3.2	42 (Zone 3)	-23 (Zone 1)	25
Boundary Flow	4	-1.7	26 (West)	-14 (East)	16

[a]Positive sign is simulated less than target, negative is larger.

Post plots of weighted well and spring head residuals are shown in Figures 6-141 and 6-142 for the USGSND and USGSD recharge models, respectively. The USGSND results show a more uniform degree of error, but there is a slight bias in central Area 20 to undersimulated heads. In contrast, the USGSD recharge model shows a systematic, but small, bias to oversimulated heads. The difference is entirely caused by differences in the recharge maps because the same set of hydraulic parameters was used for both cases. Figures 6-143 and 6-144 show the simulated water tables, which are very similar and show the broad features of the flow system correctly. Simulated Oasis Valley discharge is 199 and 215 kg/s for the USGSND and USGSD recharge models, respectively.

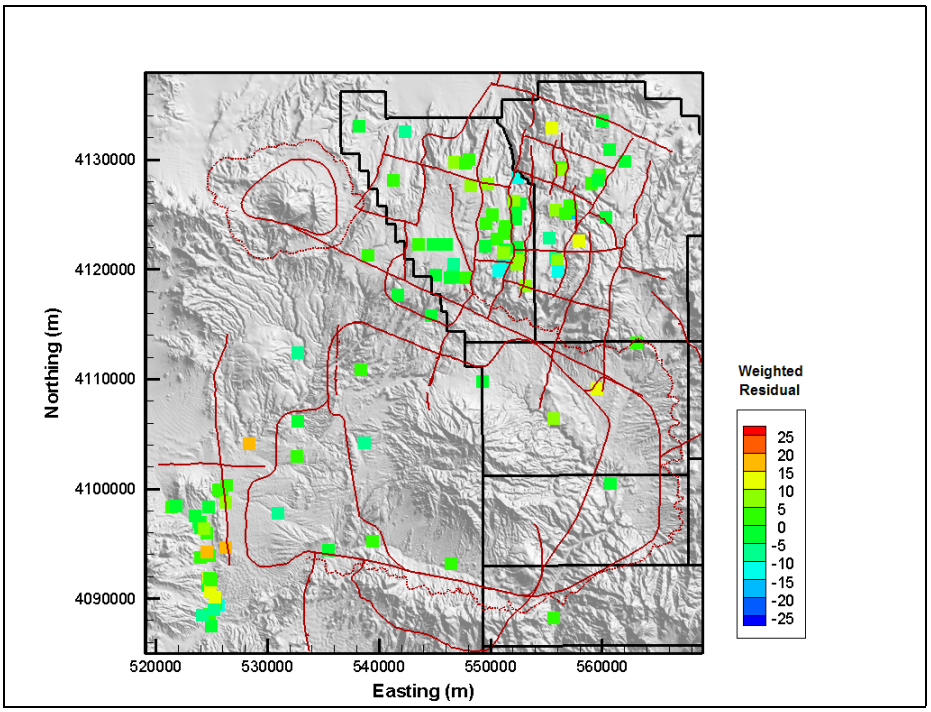

Figure 6-141
Post Plot of Weighted Well and Spring Head Residuals for BN-USGSND-SDA

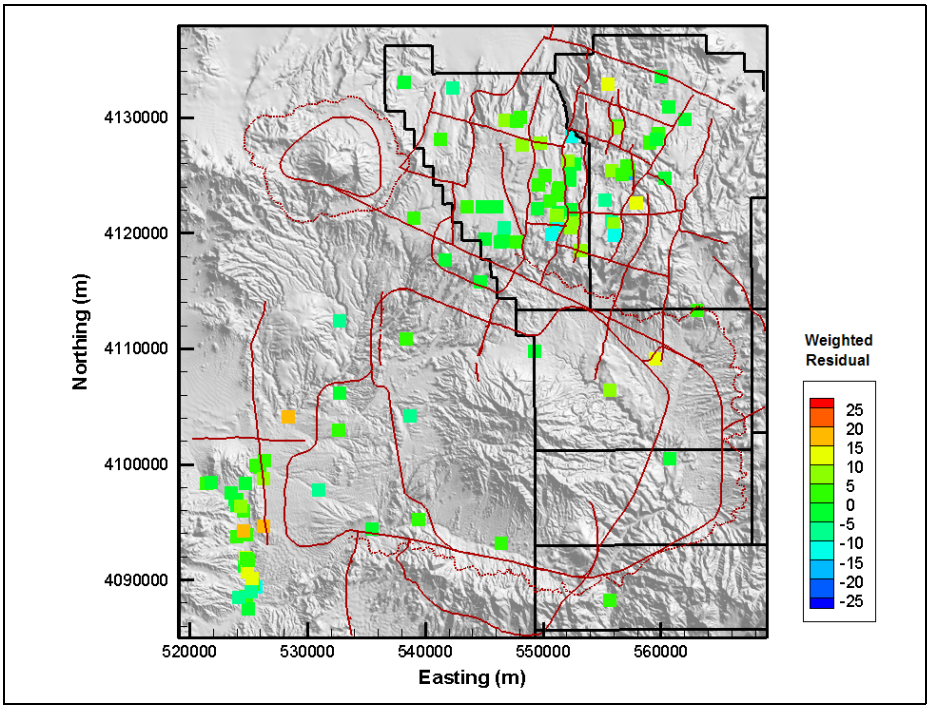

Figure 6-142
Post Plot of Weighted Well and Spring Head Residuals for BN-USGSD-SDA

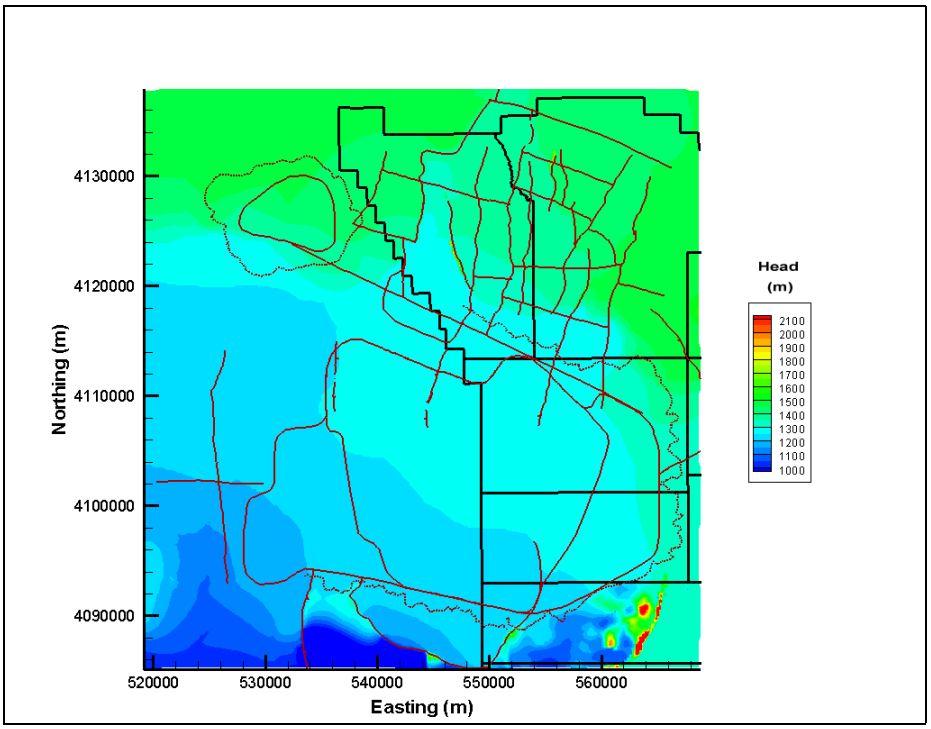

Figure 6-143
Simulated Water Table for BN-USGSND-SDA

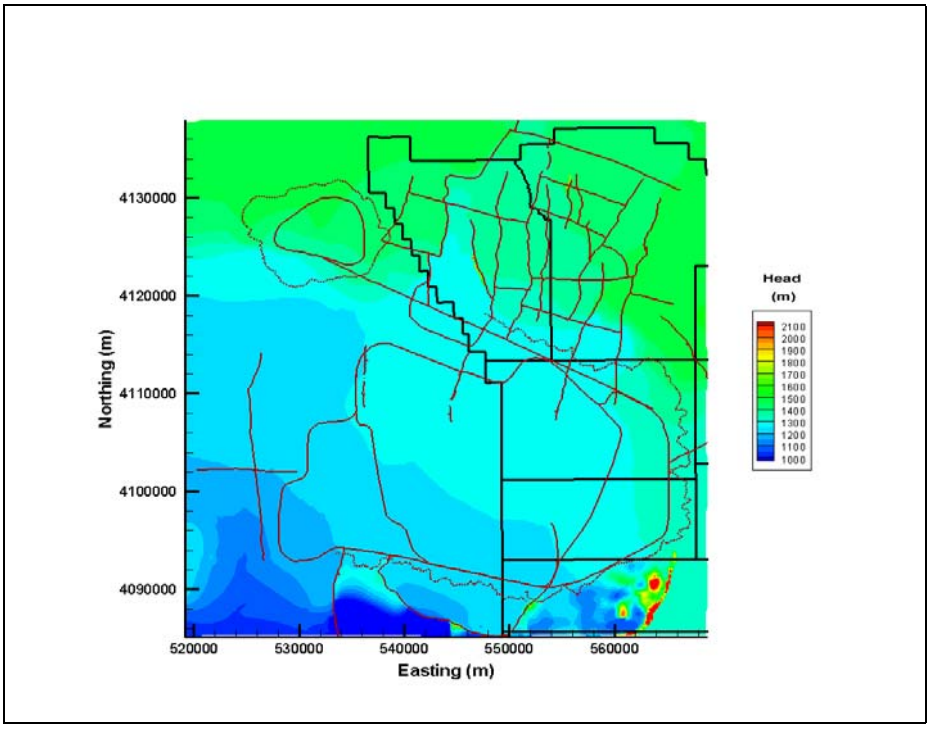

Figure 6-144
Simulated Water Table for BN-USGSD-SDA

Figures 6-145 and 6-146 show the simulated flow paths for the USGSND and USGSD recharge models. The simulated flow paths are very similar in trajectory. The main perceptible difference is in northeastern Area 19 where a few paths go to the northeast with the USGSD recharge versus west in the USGSND case. This difference is interpreted to arise from influence of local accretion of recharge on the flow paths. Table 6-43 shows the calibration summary statistics for the reduced LCCU1 permeability alternative case with the USGSD recharge model. The objective function is 10,304, the best of all the models presented in this report. The error standard deviation is markedly lower compared to the results of the DRIA simulations, and somewhat lower than the MME simulations. Simulated Oasis Valley discharge is 208 versus 227 kg/s estimated.

A post plot of weighted residuals for the reduced LCCU1 permeability alternative case shows a relatively homogenous scatter of error with the exception of UE-18t and ER-18-2, which are undersimulated (Figure 6-147). Figure 6-148 shows the simulated water table. The simulated flow paths (Figure 6-149) are very similar to the USGSD and USGSND results previously presented in this section. The major difference is more flow paths go down Fortymile Canyon (e.g., from ER-18-2 and UE-18t). A few particles exit deep along the southern boundary at about Easting 538,000 m that exit at Oasis Valley for the other cases.

The HSU permeabilities that changed the most between the MME and USGS recharge models are the BFCU, CFCM, IA, and CHZCM, which reduced by about an order of magnitude, three-quarters of an order of magnitude, two orders of magnitude, and one order of magnitude, respectively. Thus, the effect of dropping recharge rate was to require permeability to decrease in order to enhance the effect of the lower recharge in maintaining head. The two order of magnitude decrease in IA properties takes its permeability to the lowest bound thought plausible. The other reductions, particularly in the BFCU, appear reasonable.

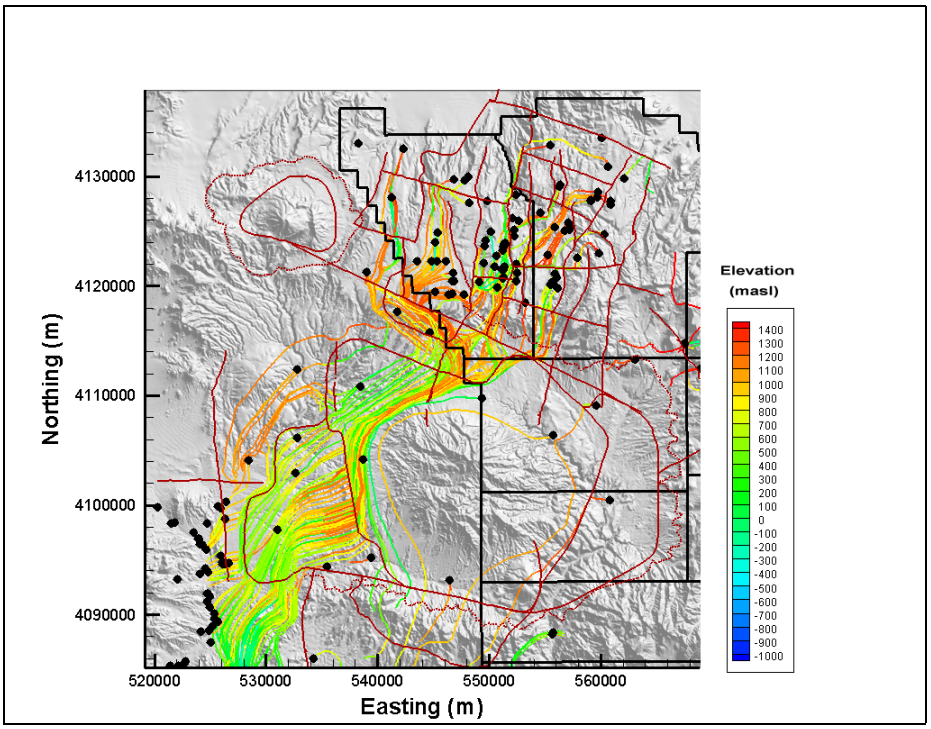

Figure 6-145
Particle Tracks for BN-USGSND-SDA

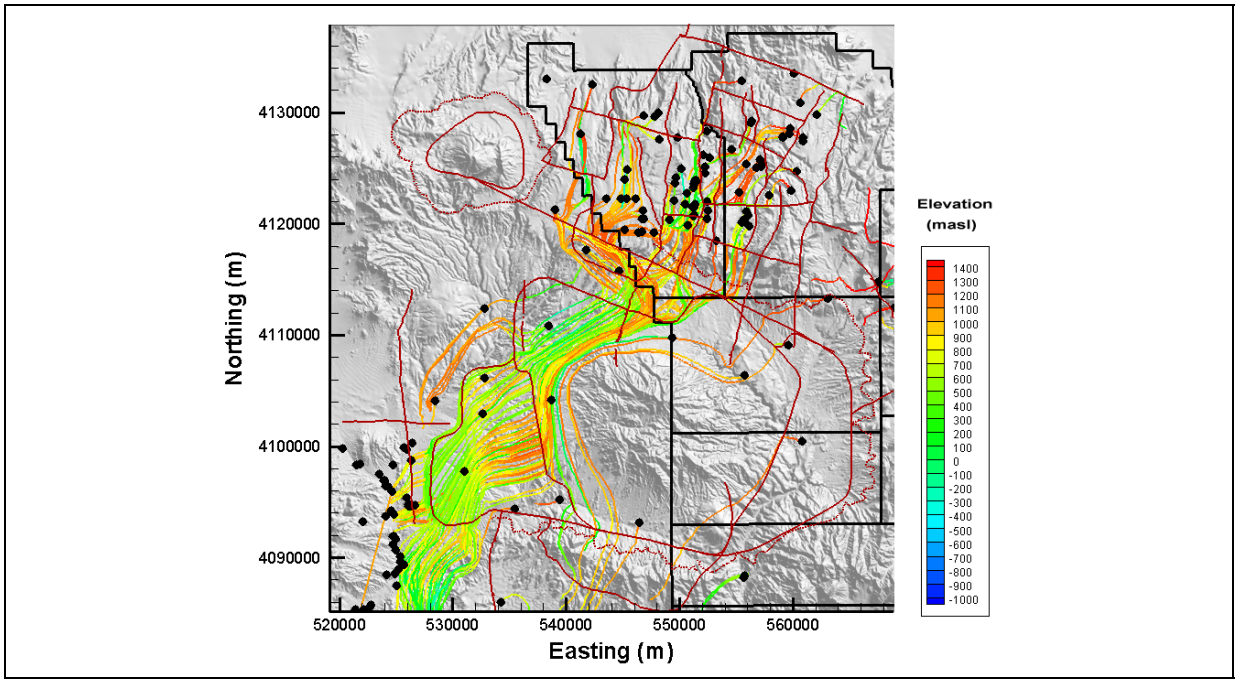

Figure 6-146
Particle Tracks for BN-USGSD-SDA

Table 6-43
Calibration Summary Statistics for BN-USGSD-SDA Reduced LCCU1 Permeability Alternative

Calibration Data	Number of Data	Mean Weighted Error (m or kg/s)[a]	Maximum Weighted Residual	Minimum Weighted Residual	Error Standard Deviation (m or kg/s)
Well Head	152	0.33	18 (ER-OV-06a)	-24 (UE-20n #1 1,005.84 m)	6.0
Spring Head	28	2.7	19 (Torrance Spring)	-7.2 (Spring id 159)	6.9
Oasis Valley Discharge	7	5.3	45 (Zone 3)	-18 (Zone 4)	21
Boundary Flow	4	5.1	21 (West)	-4.4 (North)	11

[a]Positive sign is simulated less than target, negative is larger.

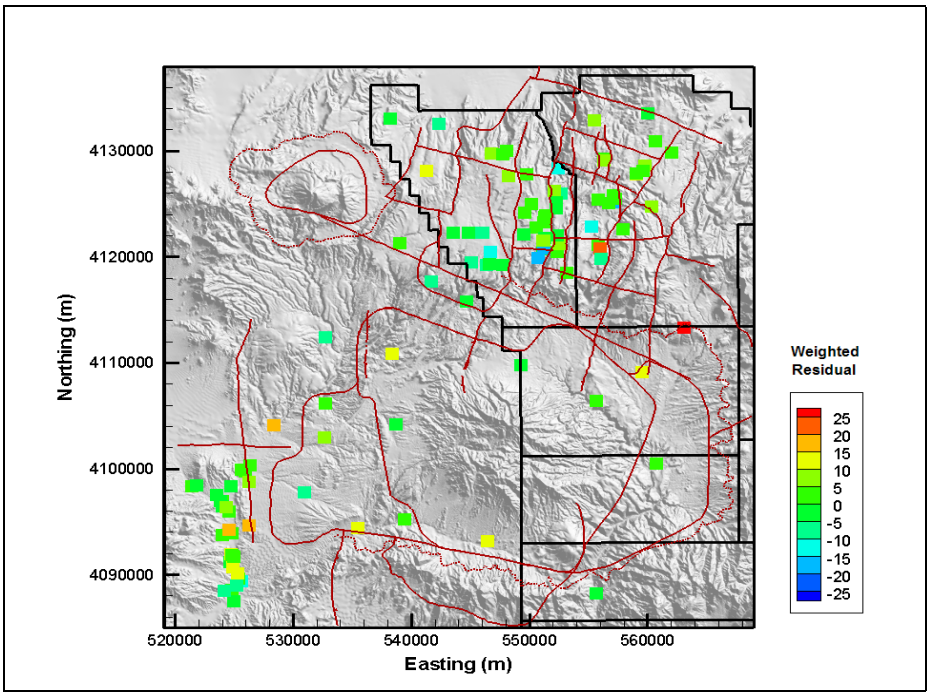

Figure 6-147
Post Plot of Weighted Well and Spring Head Residuals for BN-USGSD-SDA Reduced LCCU1 Permeability Alternative

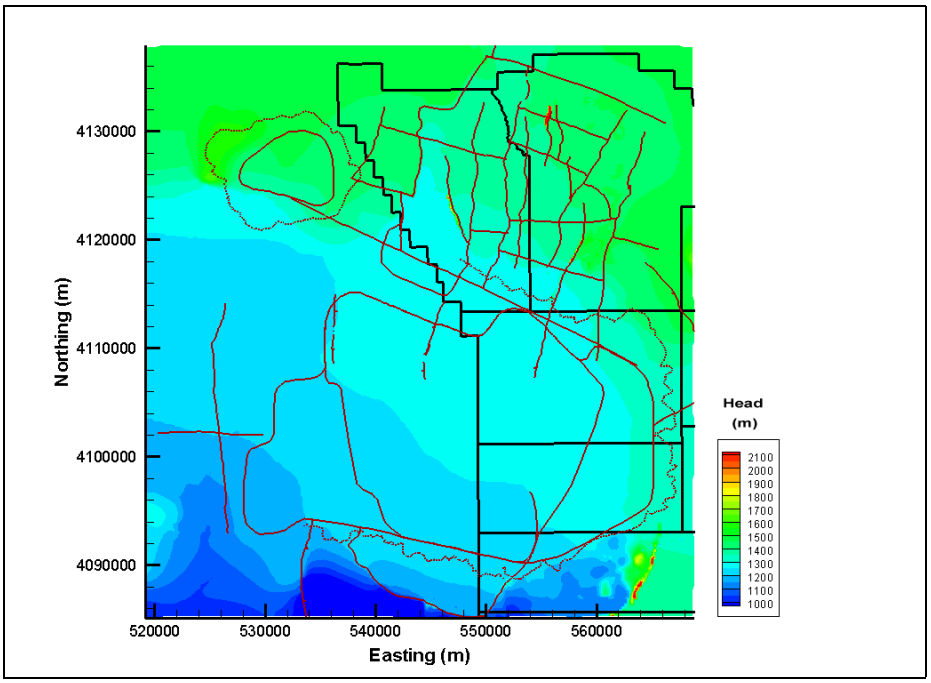

Figure 6-148
Simulated Water Table for BN-USGSD-SDA
Reduced LCCU1 Permeability Alternative

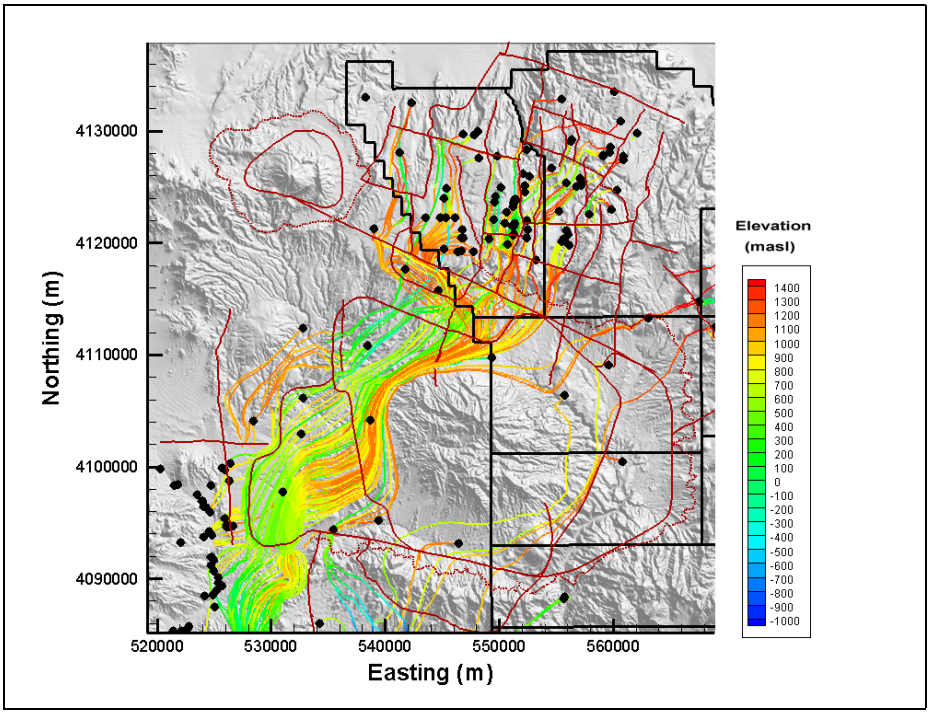

Figure 6-149
Particle Tracks for BN-USGSD-SDA
Reduced LCCU1 Permeability Alternative

6.4.4 SCCC Geologic Model Water-Balance Uncertainty Analysis

The SCCC HFM as described in Section 5.7 was used as the basis for analyzing water-balance uncertainty. Based on the results of Section 6.4.3, only two combinations of recharge model and boundary flows are considered as follows:

1. DRIA recharge and boundary flow
2. USGSD recharge and USGSND boundary flow

6.4.4.1 DRI Recharge Model

Calibration summary statistics for the SCCC HFM with the DRIA recharge model (SCCC-DRIA) are shown in Table 6-44. In spite of the high recharge associated with this map, the simulated observation well data are biased slightly low. The error standard deviations are slightly higher than those for the MME recharge calibration shown in Section 5.6. The model objective function is 31,086 versus 31,800 for calibration with the MME recharge model.

Table 6-44
Calibration Summary Statistics for SCCC-DRIA-SDA

Calibration Data	Number of Data	Mean Weighted Error (m or kg/s)[a]	Maximum Weighted Residual	Minimum Weighted Residual	Error Standard Deviation (m or kg/s)
Well Head	152	2.2	33 (PM-3 Piezometer 2)	-30 (U-20c)	11
Spring Head	28	2.5	19 (Torrance Spring)	-45 (Spring id 163)	11
Oasis Valley Discharge	7	9.0	42 (Zone 5)	-28 (Zone 4)	26
Boundary Flow	4	-27	-38 (North)	-64 (West)	35

[a]Positive sign is simulated less than target, negative is larger.

Figure 6-150 shows the posted weighted residuals; there is a strong underprediction in the east-central part of the model including Wells WW-8, ER-30-1, UE-18t, and ER-18-2 that is also suggested by the mean error. Wells WW-8 and PM-3 were undersimulated in the MME calibration as well, and this error is thus a consequence of the HFM, not the recharge model. Simulated Oasis Valley discharge is 195 kg/s. Figure 6-151 shows the simulated water table, and Figure 6-152 shows the simulated flow paths from NTS wells. The water table and flow paths have the same general character seen in all the simulations, but there is a large number of paths simulated as flowing around the eastern side of Timber Mountain. In the MME calibration, flow paths exit southern Area 20 on a nearly due south trajectory and then turn west around Timber Mountain. Slight shifts in head gradient were induced in the recalibration to the DRIA recharge model that caused a large amount of flow paths to go down Fortymile Canyon instead of into Oasis Valley. The parameter that changed the most was the permeability of the Calico Hills unit (recall that five HSUs from the base HFM were lumped into one Calico Hills HSU in the SCCC HFM), which increased nearly an order of magnitude. The PCM k_0 also increased by about half an order of magnitude. Sensitivity analysis showed that the PCM affected heads in the domain by controlling flow out to the south. The PCM increased permeability in this high recharge case is interpreted as being necessary in order to reduce heads elevated by the additional recharge in the DRIA recharge model. The TCVA and DVCM permeabilities also increased slightly. The increase in the DVCM permeability compensates for more flow apparently going down Fortymile Canyon by allowing more inflow from the west to maintain Oasis Valley discharge. This interpretation is supported by the result that the oversimulation of ET discharge Zone 4 is larger in this case than most others, and that Zone 5 in the southern part of Oasis Valley (which does not appear in any other model variation as a large error) has too low a discharge. This combination of HFM and recharge model does not appear to be reasonable.

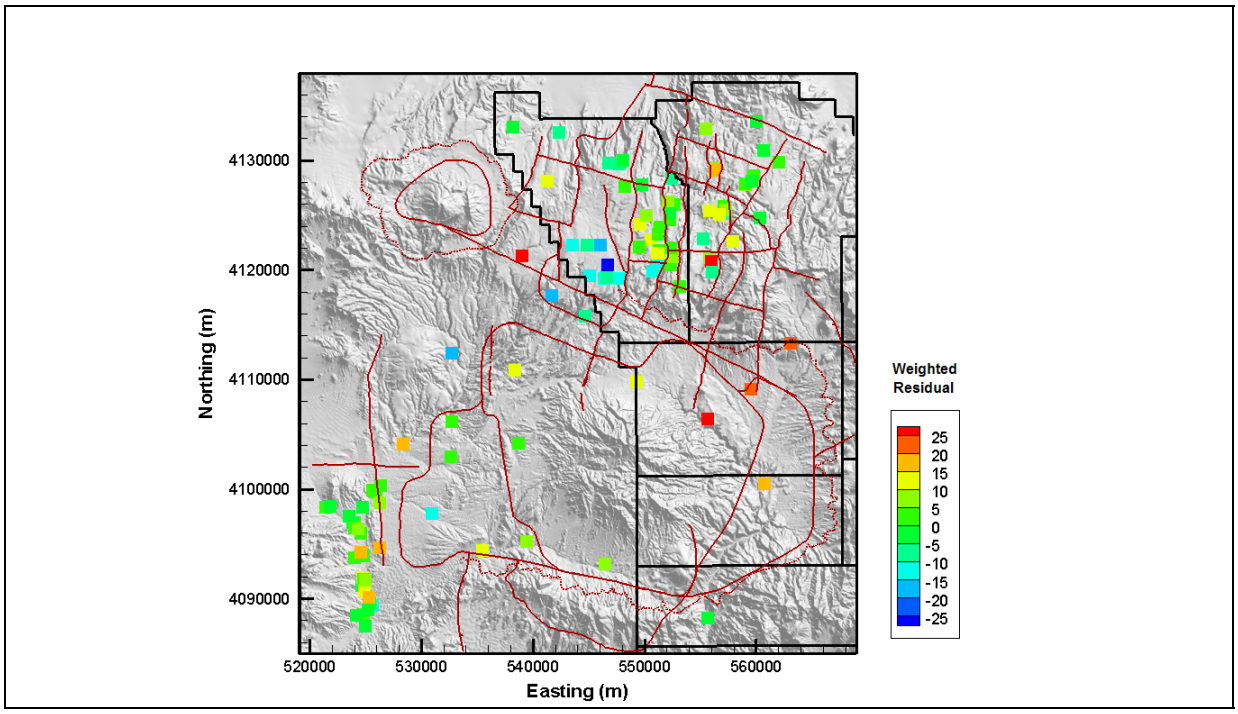

Figure 6-150
Post Plot of Weighted Well and Spring Head Residuals for SCCC-DRIA-SDA

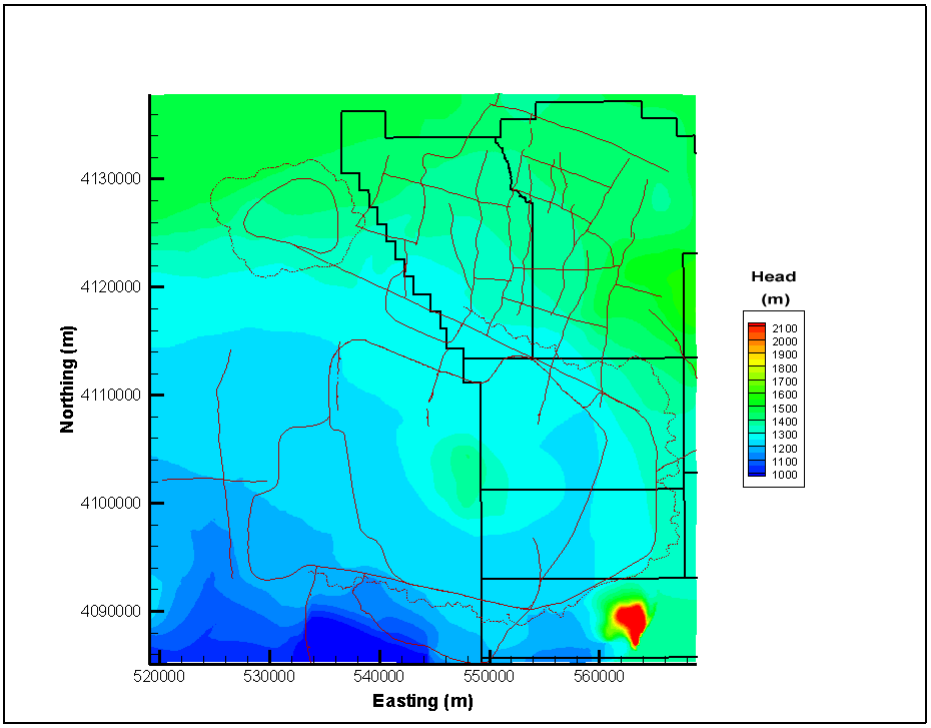

Figure 6-151
Simulated Water Table for SCCC-DRIA-SDA

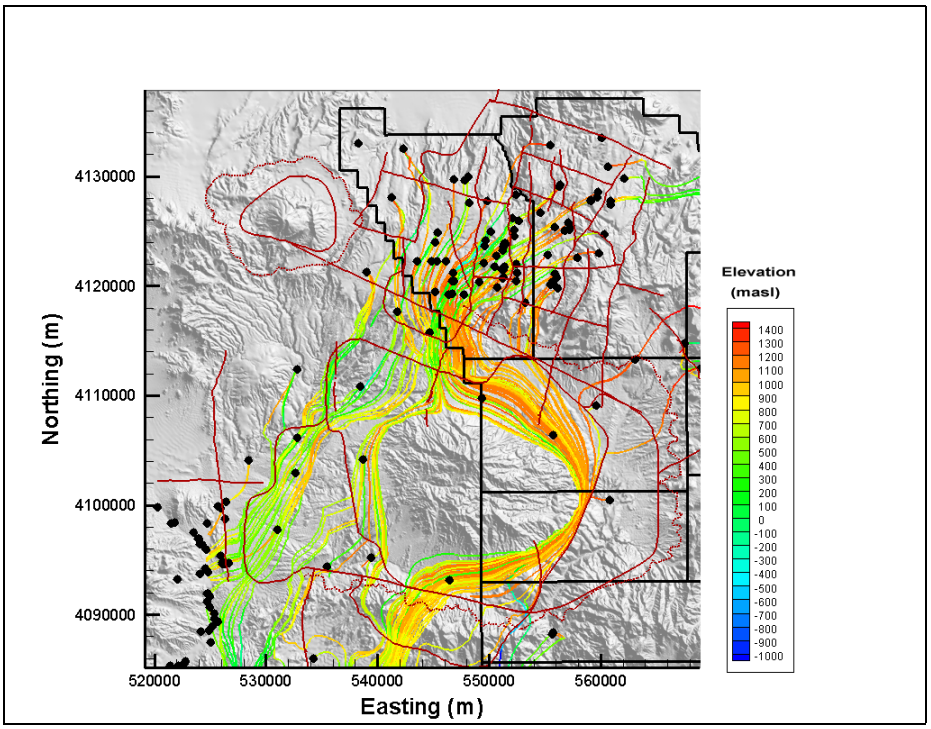

Figure 6-152
Particle Tracks for SCCC-DRIA-SDA

6.4.4.2 USGS Recharge Model

The calibration summary statistics for the SCCC HFM with the USGSD recharge model are shown in Table 6-45. The model objective function is 32,254 versus 31,800 for calibration with the MME recharge model.

Figure 6-153 shows the posted weighted residuals; there is a strong underprediction including WW-8 and PM-3 (which were also undersimulated in the MME calibration shown in Section 5.7). There is a bias to undersimulation in east-central Area 19. Simulated Oasis Valley discharge is 220 kg/s. Figure 6-154 shows the simulated water table, and Figure 6-155 shows the simulated flow paths from NTS wells. The water table and flow paths have the same general character seen in all the simulations, but there are more simulated flow paths around the eastern side of Timber Mountain, down Fortymile Canyon, and back around the southern part of Timber Mountain than with the MME recharge. The flow paths for the USGS recharge model are more like the DRIA recharge flow paths than the MME, which is surprising given that these two recharge models are at the opposite end of the spectrum of values. The parameters that changed the most in calibrating the SCCC HFM with the

Table 6-45
Calibration Summary Statistics for SCCC-USGSD-SDA

Calibration Data	Number of Data	Mean Weighted Error (m or kg/s)[a]	Maximum Weighted Residual	Minimum Weighted Residual	Error Standard Deviation (m or kg/s)
Well Head	152	-0.20	31 (U-19x)	-44 (U-20c)	12
Spring Head	28	2.7	19 (Torrance Spring)	-44 (Spring id 163)	11
Oasis Valley Discharge	7	1.9	34 (Zone 3)	-34 (Zone 4)	23
Boundary Flow	4	16	37 (East)	-14 (North)	25

[a]Positive sign is simulated less than target, negative is larger.

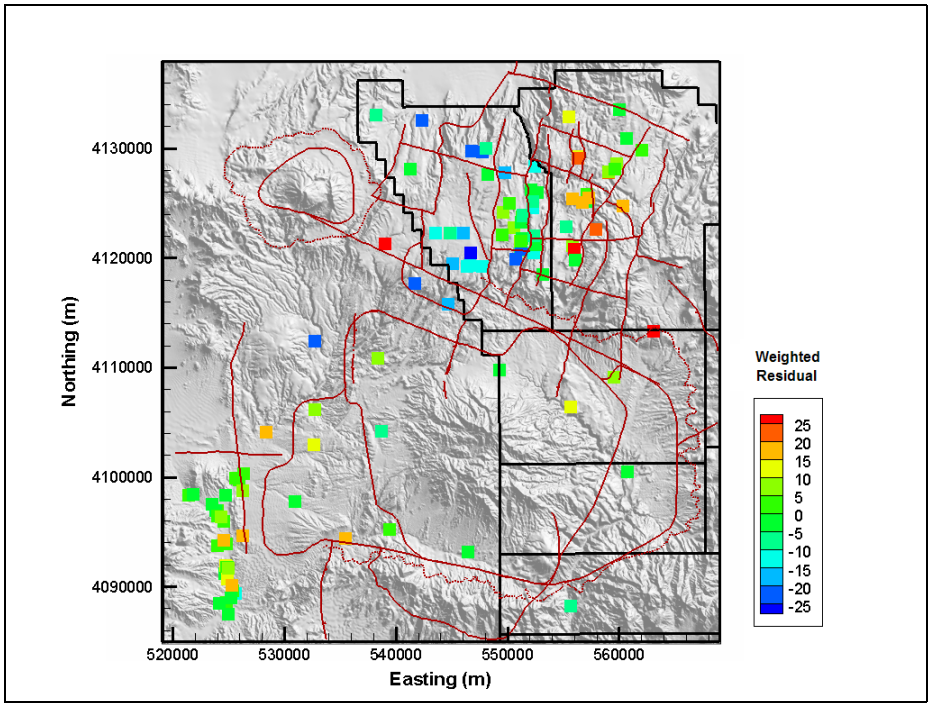

Figure 6-153
Post Plot of Weighted Well and Spring Head Residuals for SCCC-USGSD-SDA

USGSD recharge map include the permeability of the PBRCM, FCCM, DVCM, Calico Hills, LCA3, and PCM. The PBRCM permeability increased by an order of magnitude, with lesser increases in the PCM and DVCM, and LCA3. Physically, this is interpreted as being necessary to allow more flow in

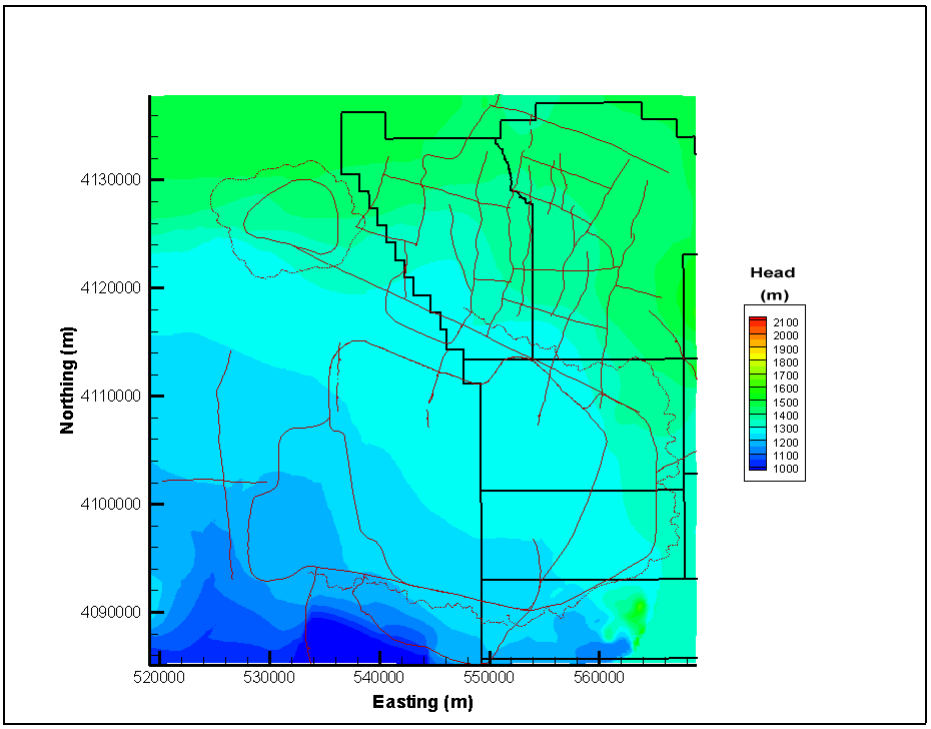

Figure 6-154
Simulated Water Table for SCCC-USGSD-SDA

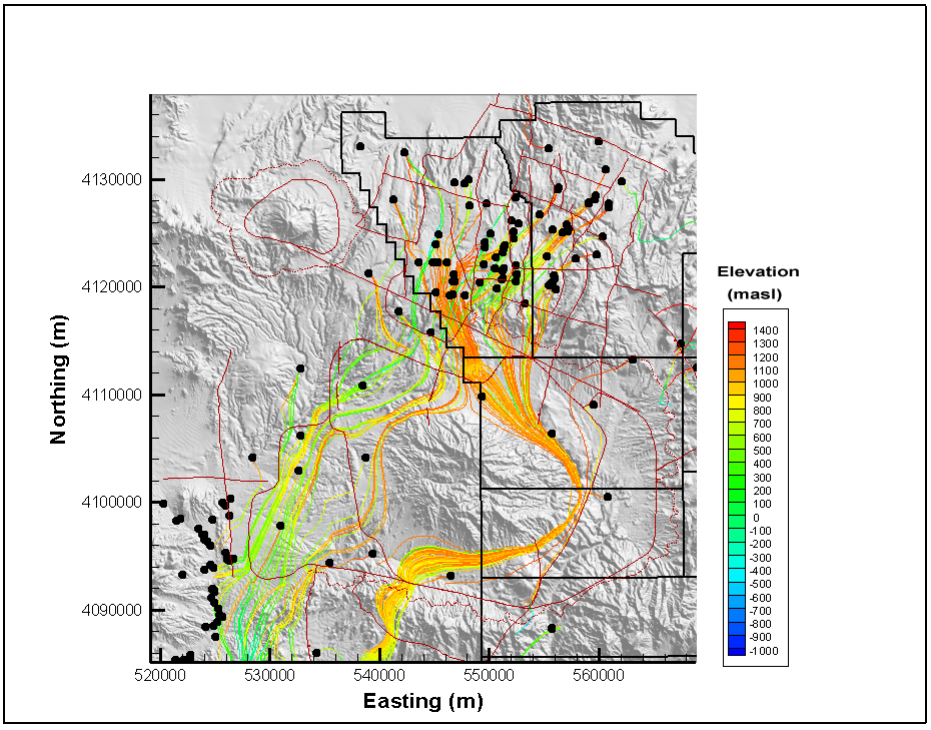

Figure 6-155
Particle Tracks for SCCC-USGSD-SDA

on the north and east model edges (through PBRCM and LCA3) and support the heads, and to allow more inflow from the west to maintain flow in Oasis Valley (through DVCM), and to balance out the increased flow and heads in the northern domain (through PCM). Because of the decreased recharge the FCCM permeability, which rings Timber Mountain, had to decrease to hold heads up, as did the Calico Hills permeability.

6.4.5 Summary of Water-Balance Uncertainty Analysis

Recalibrating the base and SCCC HFMs to a suite of recharge models and boundary flows addresses the water-balance component of flow model uncertainty. A total of eight combinations of recharge model, boundary flow, and HFM were considered (Table 6-46). Alternative recharge models included the two variations of the USGS distributed parameter model and two variations of the DRI chloride mass-balance model. In addition, a sub-variation of the base HFM with reduced LCCU1 permeability alternative was also considered. The boundary flows developed from the UGTA regional model (DOE/NV, 1997) analysis for the corresponding recharge models were used in conjunction with each respective recharge model. For example, the DRIA recharge model was used along with the UGTA regional model boundary flows resulting from the DRIA recharge model. In general, reducing recharge via the USGS recharge model had the effect of dropping permeability, with the converse resulting from the DRI recharge model. This is expected behavior in a steady-state model. Some of the downward changes, notably the IA for the USGS recharge model cases, are to the lower limit of estimated parameter uncertainty. No such issue was noted on the estimated upper end of parameter uncertainty with the DRI recharge model.

In general, all the combinations of HFM, recharge models, and boundary flows could be as well calibrated as with the MME recharge and boundary flow. This recalibration, however, can result in a few marginal parameter values as noted for the IA. The poorest-performing HFM considered under all recharge models was the SCCC alternative, as was also noted in Section 5.8. The lack of deep faults, particularly along the Purse Fault, limits the degree of freedom necessary to give a reasonable calibration. The SCCC HFM also showed the greatest sensitivity of simulated flow paths to recharge model, with significantly more flow paths down Fortymile Canyon for the DRIA and the USGSD recharges than for the MME recharge, or any other HFM and recharge combination. The combination of HFM and water-balance uncertainty is further addressed in Section 6.5.

Table 6-46
Summary of Flow Model Results for Water-Balance Uncertainty

HFM	Water-Balance Condition	Calibration Issues	Qualitative Flow Path Assessment
BN	DRIA	Slight oversimulation bias in Area 19	Fewer particles go west into northern Oasis Valley
BN	DRIAE	Slight oversimulation bias in Area 19	Fewer particles go west into northern Oasis Valley
BN	USGSD	Third-best calibration Slight oversimulation bias	Particles go deeper along northeastern Timber Mountain, but stay shallower after crossing Moat Fault than in base
BN	USGSND	Second-best calibration	Particles go deeper along northeastern Timber Mountain, but stay shallower after crossing Moat Fault than in base
BN Reduced LCCU1 Permeability Alternative	DRIA	Worst BN DRI calibration	Particle tracks concentrated on western flank of Timber Mountain, fewer go to Oasis Valley than in base
BN Reduced LCCU1 Permeability Alternative	USGSD	Best calibration	Very similar to base
SCCC	DRIA	Little change from MME	Particle tracks mainly go down Fortymile Canyon
SCCC	USGSD	Little change from SCCC with MME	Particle tracks mainly go down Fortymile Canyon

The particle paths, with the notable exception of the SCCC HFM, tend to behave similarly across all recharge alternatives, suggesting that HFM uncertainty plays a greater role than recharge uncertainty.

6.5 Combining HFM and Water-Balance Uncertainty

The Pahute Mesa CAIP (DOE/NV, 1999) requires that HFM and boundary condition uncertainty be considered in the flow model analysis. This section presents the approach used to address the joint effects of HFM and water-balance uncertainty and the results of the analysis.

Table 6-1 in Section 6.1.2 shows the matrix of HFM, recharge, and boundary flow uncertainties. Section 6.3 addresses HFM uncertainty by evaluating five alternative HFMs (in addition to base and SCCC) with the MME recharge model and associated boundary flows, and Section 6.4 addresses water-balance uncertainty by evaluated the USGSD, USGSND, DRIA, and DRIAE recharge models with the base and SCCC HFMs. The final assessment is the conjunction of HFM and water-balance uncertainty.

The first component of this assessment is the selection of alternative HFMs for evaluation. The SCCC HFM, the major alternative, has already been considered in Section 6.4, and its calibration is discussed in Section 5.7. The five alternative HFMs derived from the base HFM that were considered in Section 6.3 are also candidates for this evaluation. Of the five alternative HFMs considered in Section 6.3 two are distinctly different: the PZUP and DRT alternatives. Other, subtler differences were noticed between the remaining alternatives, but PZUP and DRT had pronounced differences. Therefore, the PZUP and DRT HFMs are chosen for additional water-balance uncertainty analysis.

The water-balance uncertainty was bounded by considering the DRIA and USGSD recharge models and associated UGTA regional boundary flows. The DRIAE and USGSND were assessed in Section 6.4, and it was decided that DRIA and USGSD have physical characteristics that make them desirable and that these two recharge alternates are sufficient to bound uncertainty. The areal distribution and mass flows associated with these recharge models is shown in Section 4.3.1.

The PZUP and DRT HFMs were calibrated with the MME recharge model in Section 6.3. The DRIA and USGSD recharge models were applied and the models recalibrated; the results are described in the following sections.

6.5.1 Raised Pre-Tertiary Surface (PZUP) HFM

The PZUP HFM with the selected HSU depth-decay and anisotropy (PZUP-MME-SDA) parameterization as described in Section 5.6.2 was used as the basis for analyzing the joint effects of HFM and water-balance uncertainty. Based on the results of Section 6.4.3, only two combinations of recharge model and boundary flows are considered as follows:

1. DRIA recharge and boundary flow
2. USGSD recharge and USGSND boundary flow

6.5.1.1 DRIA Recharge Model

Table 6-47 summarizes the calibration statistics. It is interesting to note that the mean head error is slightly positive, but with this high recharge model and potentially reduced transmissivity, the opposite result would be expected. The scatter of error as shown by the high error standard deviation in fitting the boundary flows is the worst of all models considered; MME recharge with this HFM

Table 6-47
Calibration Summary Statistics for PZUP-DRIA-SDA

Calibration Data	Number of Data	Mean Weighted Error (m or kg/s)[a]	Maximum Weighted Residual	Minimum Weighted Residual	Error Standard Deviation (m or kg/s)
Well Head	152	0.45	31 (USW UZ-N91)	-25 (UE-20n #1 1,005.84 m)	7.4
Spring Head	28	2.8	19 (Torrance Spring)	-5.3 (Spring id 159)	6.7
Oasis Valley Discharge	7	-17	27 (Zone 3)	-47 (Zone 1)	30
Boundary Flow	4	-34	59 (West)	-93 (East)	67

[a]Positive sign is simulated less than target, negative is larger.

also had some of the larger boundary flow errors. The increased volume of mainly lower permeability rocks limits the ability of this model to move water across the boundaries. The objective function is 33,713. Relative to the calibration with MME recharge this calibration is worse, but not greatly so.

Figure 6-156 shows the posted weighted residuals; there is a slight bias to undersimulate heads that is also suggested by the mean error. The visual impression of the residuals shows more scatter to high and low values than most other results. Simulated Oasis Valley discharge is 286 kg/s (versus 227 kg/s estimated), one of the highest simulated Oasis Valley discharges of all models. This is nearly two standard deviations above the estimated value (e.g., the upper 95 percent confidence limit on Oasis Valley discharge). This is interpreted as arising from the larger accretion of recharge that must move through shallower high-permeability HSUs, which can still satisfy Oasis Valley discharge while the boundary flows are otherwise more poorly matched than in other cases. Figure 6-157 shows the simulated water table, and Figure 6-158 shows the simulated flow paths. The water table and flow paths have the same general character seen in all the simulations. The mound under Black Mountain is from the substitution of TCVA with low permeability BMICU. The DVCM, BRA, LCA Zone 1, CHZCM, and YMCFCM permeabilities (including k_0) all increased between a quarter and an order of magnitude over the values used to calibrate the MME recharge in order to bleed off the additional recharge (nearly double that of the MME) imposed by the DRIA recharge model.

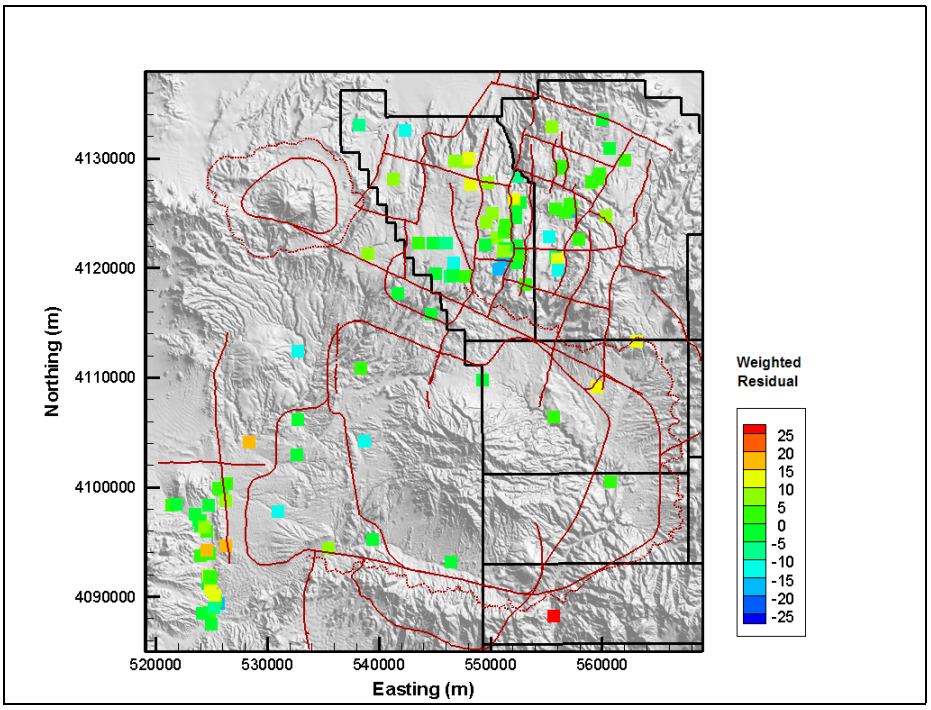

Figure 6-156
Post Plot of Weighted Well and Spring Head Residuals for PZUP-DRIA-SDA

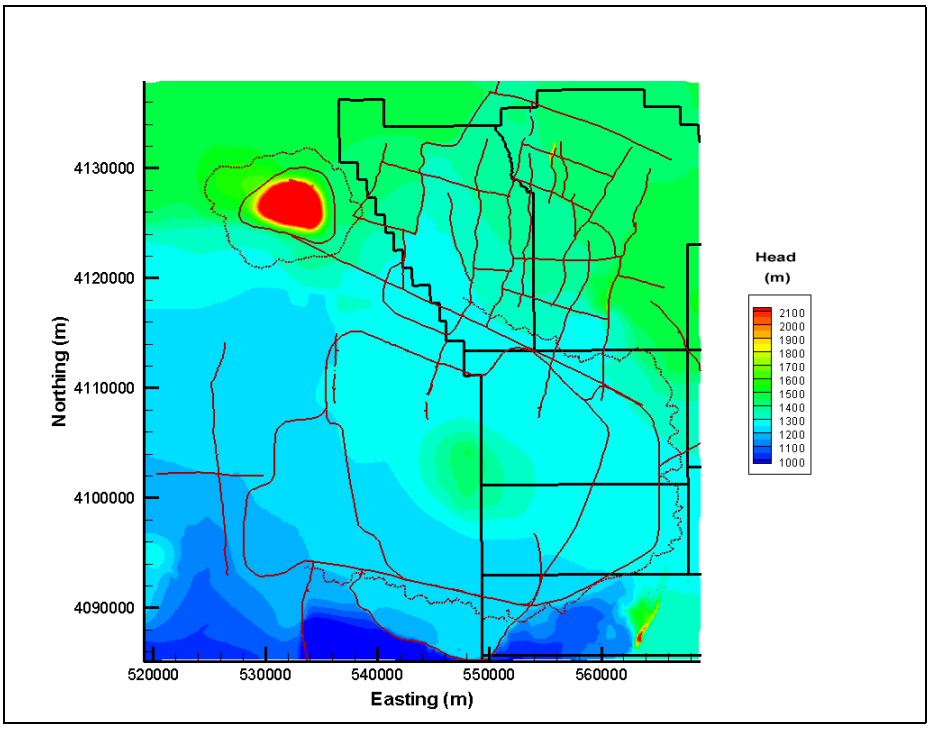

Figure 6-157
Simulated Water Table for PZUP-DRIA-SDA

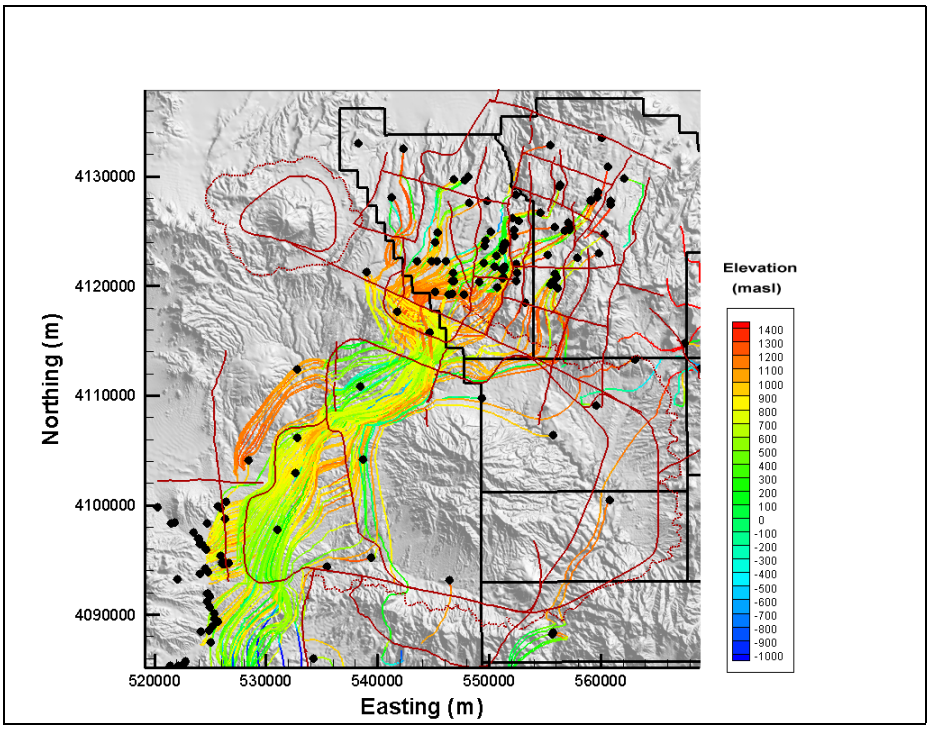

Figure 6-158
Particle Tracks for PZUP-DRIA-SDA

6.5.1.2 USGSD Recharge Model

The summary calibration statistics for the PZUP HFM and USGSD recharge model and USGSND boundary flows are shown in Table 6-48. There is a definite bias to undersimulate observation well heads. The objective function is 29,666, slightly worse than the calibration with the MME recharge model, but marginally better than the DRIA calibration.

Post plots of weighted well and spring head residuals are shown in Figure 6-159 for the USGSD recharge model. There is definite bias to undersimulate heads by 20 to 25 m in central Pahute Mesa that is also seen in the mean error. However, the boundary flows are matched well with an error standard deviation less than with both the MME and DRIA recharge models, although some of this effect may be artificial because the boundary flows for this recharge model are the lowest in magnitude. Figure 6-160 shows the simulated water table, which appears to show the broad features of the flow system correctly. Simulated Oasis Valley discharge is 208 kg/s. Thus, the controlling factor for Pahute Mesa head is not entirely the same as that which controls Oasis Valley discharge (which was noted in the sensitivity analysis as well). Figure 6-161 show the simulated flow paths,

Table 6-48
Calibration Summary Statistics for PZUP-USGSD-SDA

Calibration Data	Number of Data	Mean Weighted Error (m or kg/s)[a]	Maximum Weighted Residual	Minimum Weighted Residual	Error Standard Deviation (m or kg/s)
Well Head	152	5.8	42 (U-19x)	-17 (ER-OV-04a)	13
Spring Head	28	3.0	19 (Torrance Spring)	-5.3 (Ute Springs Culvert)	6.7
Oasis Valley Discharge	7	5.3	37 (Zone 3)	-26 (Zone 4)	23
Boundary Flow	4	6.0	15 (West)	-5.9 (East)	9.9

[a]Positive sign is simulated less than target, negative is larger.

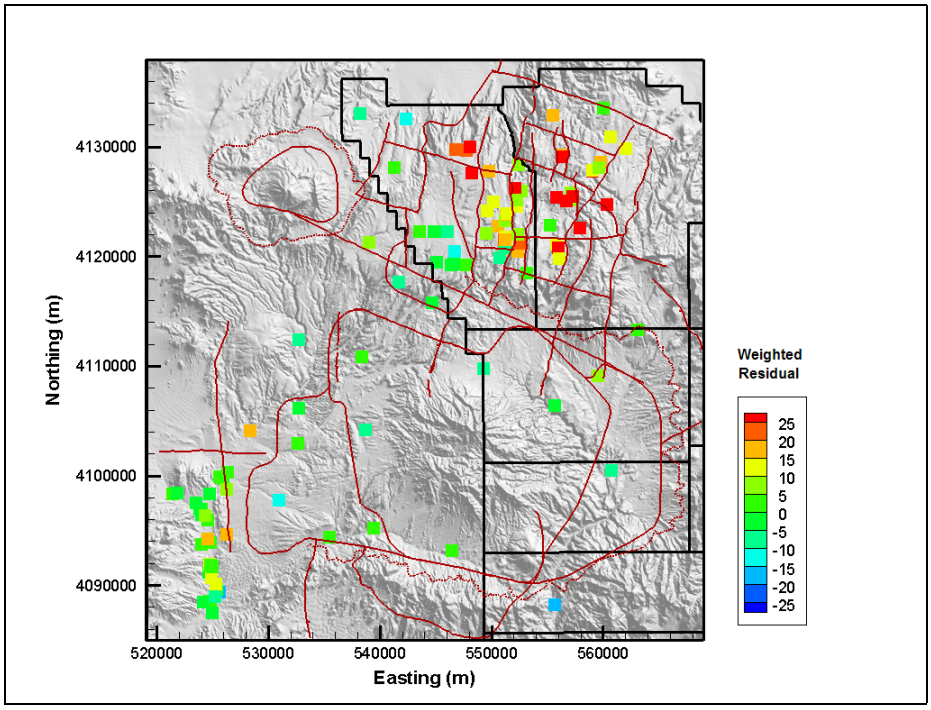

Figure 6-159
Post Plot of Weighted Well and Spring Head Residuals for PZUP-USGSD-SDA

which, in spite of the bias in head, show flow paths that appear quite reasonable. Hence, the overall direction of the hydraulic gradient is still reasonable in this case.

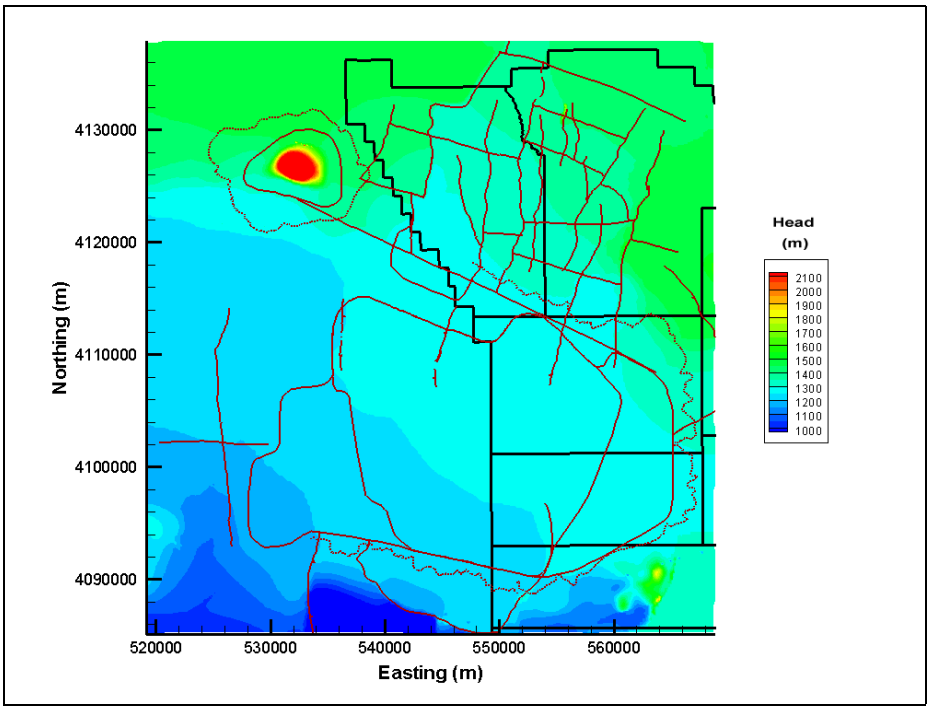

Figure 6-160
Simulated Water Table for PZUP-USGSD-SDA

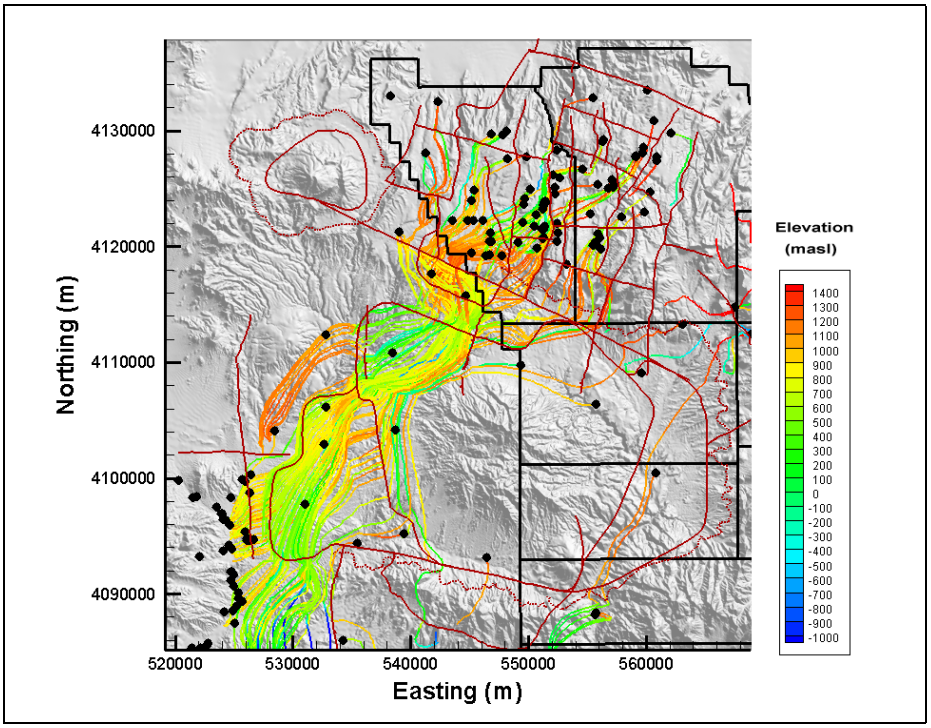

Figure 6-161
Particle Tracks for PZUP-USGSD-SDA

The HSU permeabilities that changed the most between the MME and USGS recharge models are the LCA3, PCM, TMA, and the various TMCM HSUs, all of which had modest decreases (a quarter an order of magnitude or less). Thus, the effect of dropping the recharge rate was to require permeability to decrease in order to enhance the effect of the lower recharge in maintaining head.

6.5.2 Deeply Rooted Belted Thrust Fault (DRT) HFM

The DRT HFM as described in Section 2.0 and Section 6.3 was also used for analyzing joint HFM and water-balance uncertainty. Based on the results of Section 6.4.3, only two combinations of recharge model and boundary flows are considered as follows:

1. DRIA recharge and boundary flow
2. USGSD recharge and USGSND boundary flow

6.5.2.1 DRIA Recharge Model

Calibration summary statistics for the DRT HFM with the DRIA recharge model are shown in Table 6-49. The error standard deviations are noticeably higher than those for the MME recharge calibration shown in Section 6.3. The scatter on boundary flows is comparable to the PZUP HFM and DRIA combination; this is because the LCCU1 is propagated extensively throughout the model and its low permeability makes it difficult to move water in and out of the model (similarly to the PZUP HFM). The model objective function is 37,630 versus 26,240 for calibration with the MME recharge model.

Figure 6-162 shows the posted weighted residuals; there is a strong underprediction at WW-8, although UE-18t and ER-18-2, which are often undersimulated when WW-8 is undersimulated, are reasonably matched. This is because of the higher recharge that applies more water locally that can correct bias. Simulated Oasis Valley discharge is 236 kg/s, one of the larger values from the suite of models tested, although not as large as the PZUP HFM and DRIA recharge. Figure 6-163 shows the simulated water table, and Figure 6-164 shows the simulated flow paths from NTS wells. The water table and flow paths have the same general character seen in all the simulations, but there is shift in flow paths such that many exit along the southern boundary at about 540,000 m Easting. This result is also noted in Section 6.3; thus, it is concluded that the shift in flow paths is due to the HFM and not the recharge model.

Table 6-49
Calibration Summary Statistics for DRT-DRIA-SDA

Calibration Data	Number of Data	Mean Weighted Error (m or kg/s)[a]	Maximum Weighted Residual	Minimum Weighted Residual	Error Standard Deviation (m or kg/s)
Well Head	152	-0.88	69 (WW-8)	-35 (U-19ad)	10
Spring Head	28	2.6	19 (Torrance Spring)	-6.0 (Spring id 159)	6.9
Oasis Valley Discharge	7	-2.8	45 (Zone 5)	-44 (Zone 4)	30
Boundary Flow	4	-40	6.6 (West)	-85 (South)	58

[a]Positive sign is simulated less than target, negative is larger.

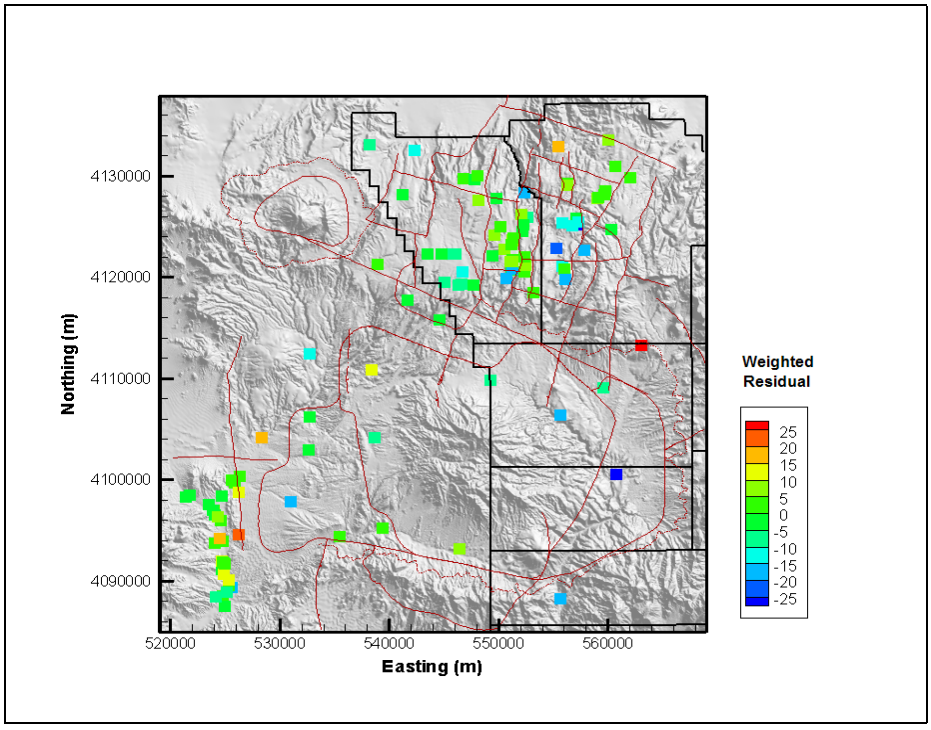

Figure 6-162
Post Plot of Weighted Well and Spring Head Residuals for DRT-DRIA-SDA

The HSU permeabilities that changed the most in calibrating the DRT HFM between the MME and DRIA recharge models include those of the CHZCM (an increase of just over an order of magnitude), DVCM (a slight decrease), LCA3 (an order of magnitude increase), CFCM (order of magnitude increase), PCM (slight increase), PBRCM Zone 84 (this zone controls flow from the north into Oasis

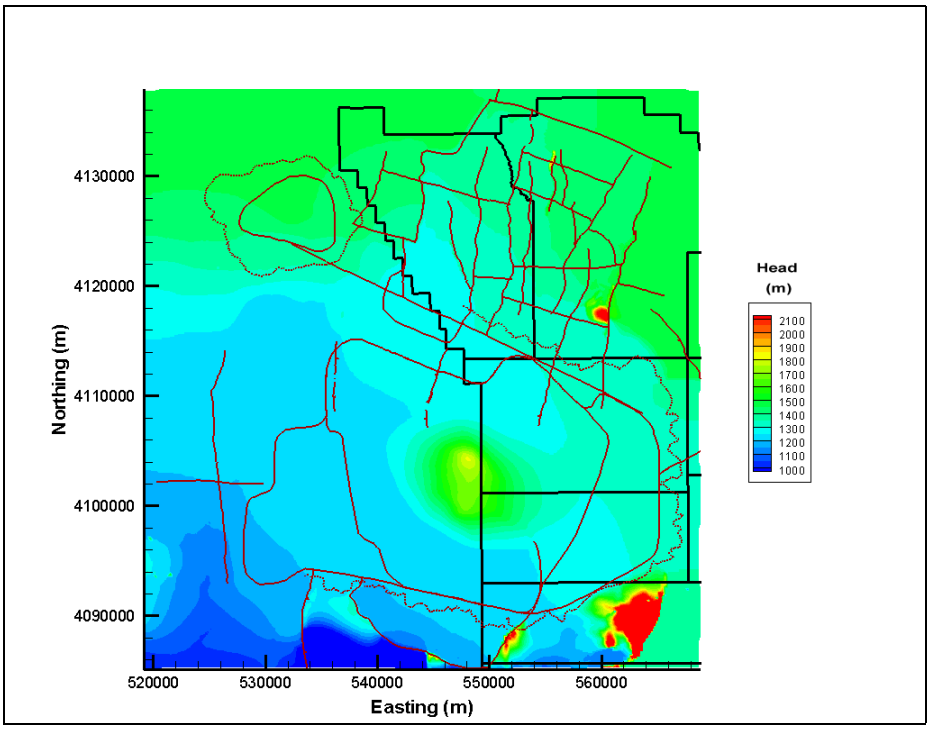

Figure 6-163
Simulated Water Table for DRT-DRIA-SDA

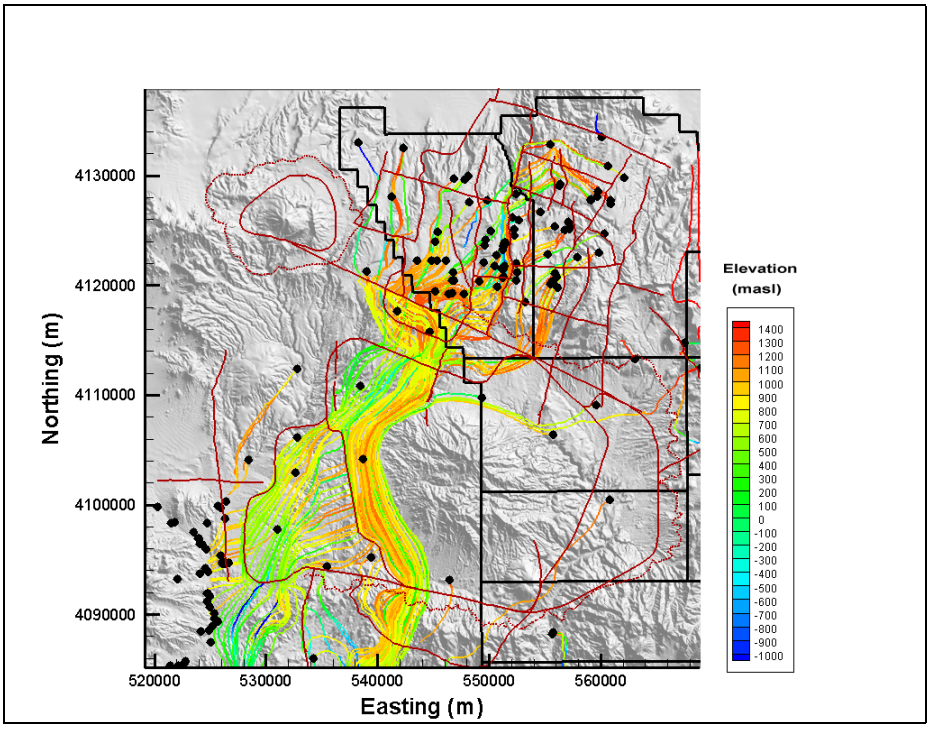

Figure 6-164
Particle Tracks for DRT-DRIA-SDA

Valley, about half an order of magnitude decrease). The interpretation of these changes is that the CHZCM and CFCM increased in permeability in order to move water out of Areas 19 and 20. Sensitivity analysis showed that PCM has a strong effect on average head in the domain, and its increased permeability is interpreted to be necessary to bleed off head by moving more water out of the system. The PBRCM Zone 84 and DVCM became tighter to limit flow to Oasis Valley from the north and west boundaries, respectively, because so much more is available from recharge accretion.

6.5.2.2 USGSD Recharge Model

The calibration summary statistics for the DRT HFM with the USGSD recharge model are shown in Table 6-50. The model objective function is 19,043 versus 26,240 for calibration with the MME recharge model. The calibration of this HFM and recharge model is much better than with the DRIA recharge model.

Table 6-50
Calibration Summary Statistics for DRT-USGSD-SDA

Calibration Data	Number of Data	Mean Weighted Error (m or kg/s)[a]	Maximum Weighted Residual	Minimum Weighted Residual	Error Standard Deviation (m or kg/s)
Well Head	152	1.3	37 (WW-8)	-32 (USW UZ-N91)	9.0
Spring Head	28	2.6	19 (Torrance Spring)	-6.3 (Spring id 159)	6.8
Oasis Valley Discharge	7	6.8	39 (Zone 3)	-21 (Zone 4)	22
Boundary Flow	4	-3.9	20 (West)	-33 (North)	23

[a]Positive sign is simulated less than target, negative is larger.

Figure 6-165 shows the posted weighted residuals; there is a strong underprediction including wells WW-8, UE-18t, and ER-18-2. There appears to be a modest bias to undersimulate heads in north-central Area 20, in central Area 19, and in the east-central area near the head of Fortymile Canyon. Simulated Oasis Valley discharge is 203 kg/s. Figure 6-166 shows the simulated water table, and Figure 6-167 shows the simulated flow paths from NTS wells. Flow paths are more concentrated with this recharge model than with the DRIA, and flow paths are also shallower than with the DRIA recharge model. This is interpreted as a consequence of the reduced permeabilities

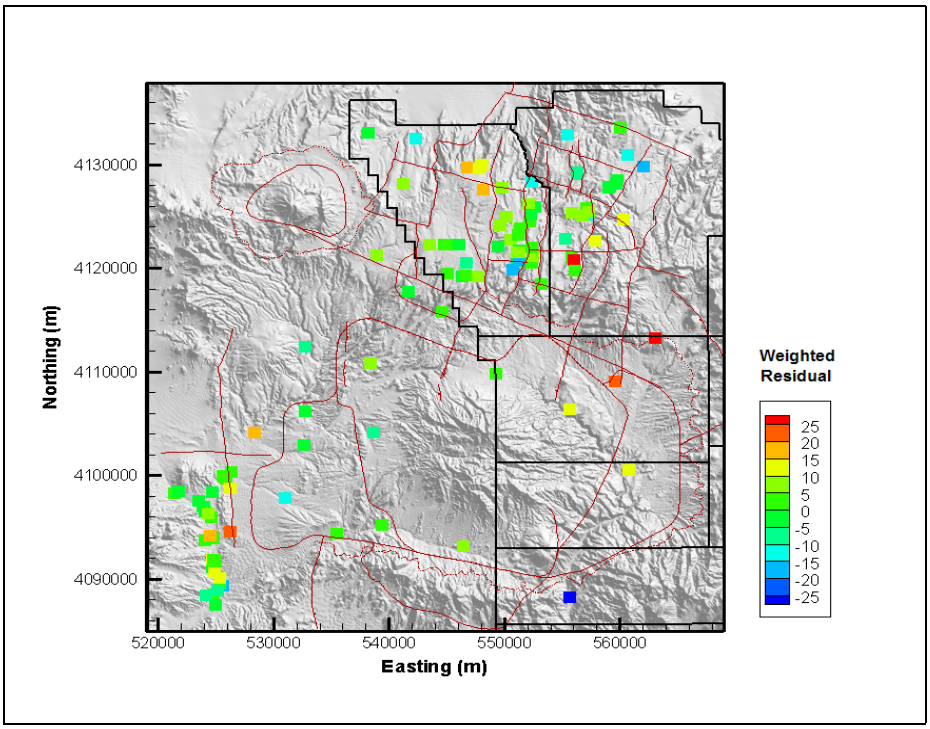

Figure 6-165
Post Plot of Weighted Well and Spring Head Residuals for DRT-USGSD-SDA

required to hold up model heads. The flow paths also show (like DRT-DRIA) a strong component of flow exiting the model at about Easting 540,000 m. In conclusion this is a function of HFM, not the recharge model.

The HSU permeabilities that changed between the DRIA and MME recharge models are the CFCU (two order of magnitude reduction), CFCM (one order of magnitude reduction), BRA (half an order of magnitude reduction), and CHZCM (one-quarter order of magnitude reduction). All these reductions are compensation for the reduced recharge in the USGSD model versus the MME model.

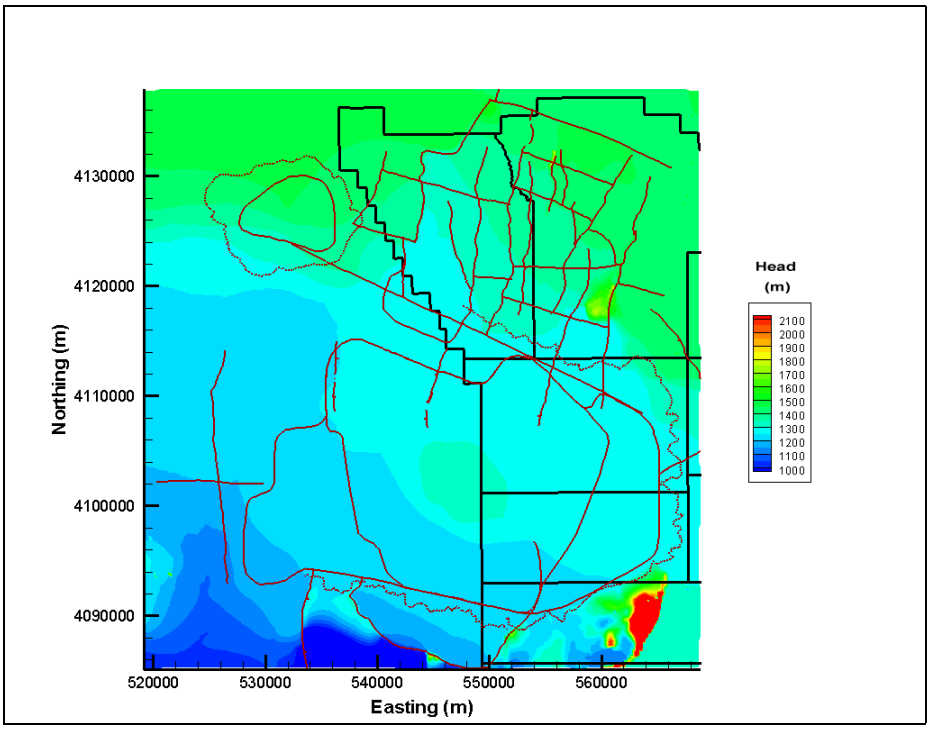

Figure 6-166
Simulated Water Table for DRT-USGSD-SDA

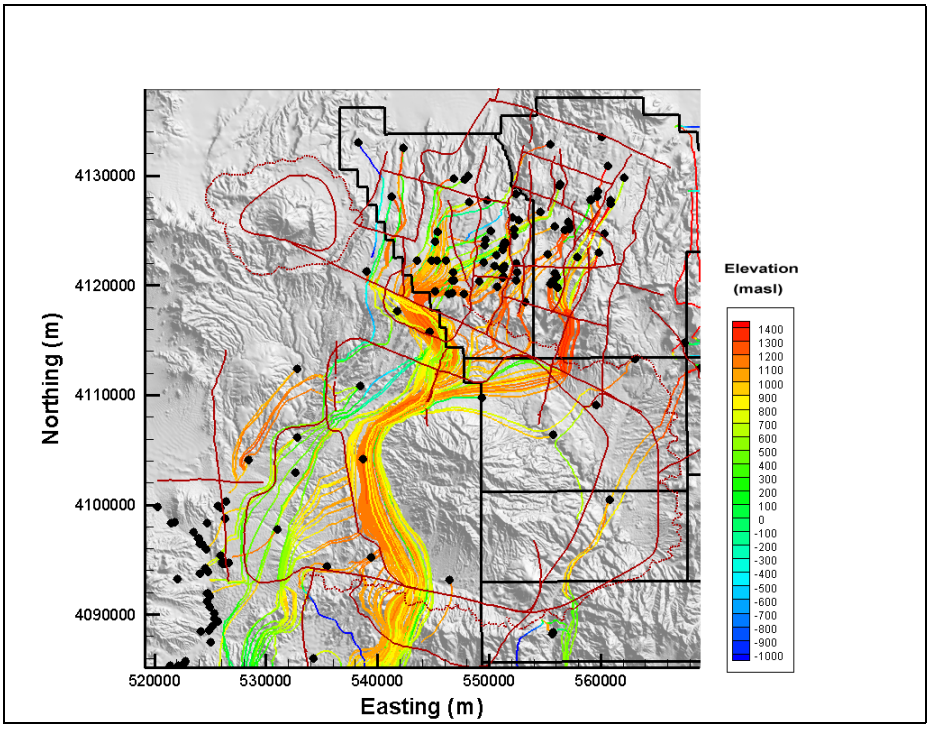

Figure 6-167
Particle Tracks for DRT-USGSD-SDA

6.5.3 Summary of HFM and Water-Balance Uncertainty Analysis

The two alternative HFMs most distinctly different than the base HFM (the DRT and PZUP cases) were combined with the DRIA and USGSD recharge models to further bound flow-system uncertainty. Both the DRT and PZUP HFMs have, by design, increased volumes of low permeability rock, although this is a consequence of the different conceptual models. Not surprisingly, both these alternatives do not perform well in matching boundary flows with the high volume (relative to the USGS and MME recharge models) DRIA recharge model simply because they do not have sufficient system transmissivity to move enough water across the boundaries. The simulated Oasis Valley flows tend to be on the high side, but not unreasonably so, and the heads are matched with a slight oversimulation bias. With respect to the boundary flows, these HFMs do perform reasonably with the USGSD recharge model, which is a direct consequence of the larger amount of lower permeability rocks in each HFM. However, there is a bias, modest for DRT and severe for PZUP, to undersimulate observation well head.

There are differences in the simulated flow paths, although not as great as might be expected. For instance, the PZUP HFM with the USGSD recharge model has a severe bias to undersimulate head on Pahute Mesa, but qualitatively the flow paths still appear reasonable. This is because the bias is ubiquitous; thus, the flow direction is maintained. The DRT HFM, in all cases, simulates a focused flow path that seems counterintuitive to the conceptual model of flow from Pahute Mesa to Oasis Valley, but still can match Oasis Valley discharge. With changing recharge models, the main simulated flow paths do not change in the DRT HFM, but at the highest recharge (DRIA) distinctly more paths exit in Oasis Valley than with the lowest recharge (USGSD). Thus, the large changes in flow paths from the DRT HFM are generated by the HFM itself, not the variation in recharge models. Conversely, the goodness of the calibrations varies in the PZUP case, but the flow paths show relatively minor variations. In both cases it appears that the HFM uncertainty dominates the recharge model uncertainty, although the models show different calibration pathologies.

It is clear from the results presented in this section that the combinations of HFM and recharge models do not perform similarly. Table 6-51 summarizes pertinent observations with respect to the flow model results. Section 7.0 explores these flow fields further in a more quantitative framework with respect to the observed geochemistry.

Table 6-51
Summary of Flow Model Results for HFM and Water-Balance Uncertainty

HFM	Water-Balance Condition	Calibration Issues	Qualitative Flow Path Assessment
PZUP	DRIA	Highest Oasis Valley discharge	Similar to MME
PZUP	USGSD	Approximately 20 m bias in Areas 19 and 20 Highest head undersimulation Largest residual standard deviation	Similar to MME
DRT	DRIA	WW-8 poorly matched Higher Oasis Valley discharge	Concentration of flow paths exiting at Easting 540,000 m
DRT	USGSD	Head undersimulation bias Poor fit in east-central model	Concentration of flow paths exiting at Easting 540,000 m

7.0 GEOCHEMICAL VERIFICATION

7.1 Approach

The calibrated flow models described in Sections 5.0 and 6.0 are evaluated with respect to independently developed groundwater mixing targets determined from geochemical analyses. The purpose of these comparisons is to determine whether the sources of groundwater at certain wells within the domain, as modeled, are consistent with the geochemical interpretation. In the comparisons, the sources of groundwater in the models are determined with reverse-particle simulations. In reverse mode, when a particle leaves the groundwater flow system, its location is documented. The top of the model has been discretized into eight separate recharge zones and the side boundaries have been discretized into seven separate inflow zones for a total of 15 unique source zones (Figure 7-1). With this method, the fraction of water from each of the recharge and boundary inflow zones that is present in the groundwater at the mixing target wells is computed. These fractions are compared with the mixing ratios estimated by interpreting geochemical compositions (Kwicklis et al., 2005).

The structure of Section 7.0 is such that after the methods are described in Section 7.1, substantial text is devoted to documenting the different behavior of each of the different flow models for each of the different geochemistry target wells (Sections 7.2 and 7.3). The quantitative comparison ranking all of the models does not come until Section 7.5. For a summary of the model comparison and ranking, the reader can skip to Section 7.5 after completing Section 7.1, and then return to the details of Sections 7.2 and 7.3 as needed.

7.1.1 Review of Verification Target Study Results

In an independent study, Kwicklis et al. (2005) estimated mixing ratios of water types at multiple boreholes in the Pahute Mesa CAU model domain. The specific objective conducted by Kwicklis et al. (2005) was to develop geochemical mixing targets for the CAU flow model. That report describes

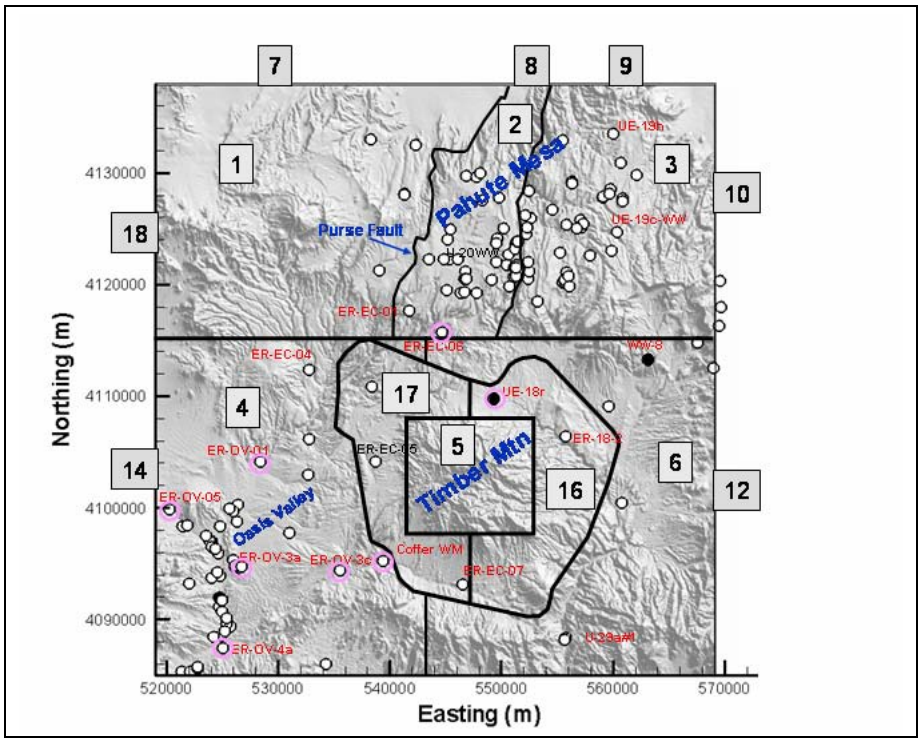

Figure 7-1
Zones Used To Identify Sources of Recharge and Inflow

in detail the methods and data that were used to estimate groundwater mixing ratios at target wells. This subsection provides a brief summary of that study.

7.1.1.1 Inverse Modeling Method

The inverse mixing model seeks to determine sources of water and their relative abundance in samples collected in various wells. The sources are identified as water types found in upgradient wells that are different from one another. The assessed mixing occurs as a result of dispersive interaction along flow pathways and through capture (and mixing) in a well, possibly from different depths.

Kwicklis et al. (2005) report that three distinct groundwater types can be identified in the Pahute Mesa/Oasis Valley flow system on the basis of their Cl^-, SO_4^{2-}, δD, and $\delta^{18}O$ compositions. Groundwaters in the northernmost Thirsty Canyon area, typified by groundwater samples from Wells ER-EC-1 and ER-EC-4, are characterized by relatively light δD and $\delta^{18}O$ compositions and high Cl^- and SO_4^{2-} concentrations compared to most other groundwaters in the flow system. Groundwaters in

Areas 19 and 20 of Pahute Mesa, typified by groundwaters at wells U-20WW, UE-19h and UE-19cWW, also have relatively light δD and $\delta^{18}O$ compositions, but have relatively low Cl^- and SO_4^{2-} concentrations compared to the northernmost Thirsty Canyon samples. Groundwater from Rainier Mesa, typified by groundwater from Well U-12s, and groundwater from the upper Fortymile Wash area, typified by groundwater from Wells UE-29a #1 and UE-29a #2 HTHs, are characterized by relatively low Cl^- and SO_4^{2-} concentrations and heavy δD and $\delta^{18}O$ compositions. Kwicklis et al. (2005) then add some additional distinctions such as identifying recharge on Timber Mountain as a water type represented by the composition of water found in Well ER-EC-7.

The wells whose sampled compositions are used to represent upgradient sources in the inverse modeling are ER-EC-1, ER-EC-4, Tolicha Peak, UE-29a #2, ER-EC-7, U-20 WW, UE-18r, UE-19h, UE-19 WW, Cedar Pass, WW-8, and ER-18-2 (see Figure 7-1). Their spatial relevance will be discussed in the next section. The wells at which mixing ratios of water represented by these upgradient sources are computed include UE-18r, ER-EC-6, ER-OV-05, ER-OV-01, ER-OV-04a, ER-OV-03a, and Coffer Windmill Well (see Figure 7-1). These wells, which help identify approximate flow paths, provide a counterclockwise sweep around the north flank of Timber Mountain, through Oasis Valley, and around to the southwest flank of Timber Mountain.

The geochemistry inverse modeling is conducted with the PHREEQC code (Parkhurst and Appelo, 1999) and described in detail by Kwicklis et al. (2005). The method seeks to identify optimal fractions of source water types in a mixed sample. Mathematically, PHREEQC seeks to optimize the following set of simultaneous algebraic equations:

$$C^j_{mixture} = f_1 C^j_1 + f_2 C^j_2 + \ldots. + f_n C^j_n \qquad (7\text{-}1)$$

$$f_1 + f_2 + \ldots. + f_n = 1 \qquad (7\text{-}2)$$

where C are the concentrations, j is the measured constituent (e.g., Cl^-, SO_4^{2-}, δD, and $\delta^{18}O$), and f_i are the volumetric fractions from the unique upgradient source types.

Mathematically, to identify n values of f_i, j must be equal to n-1. So, if only four non-reactive tracer concentrations are used, then only four upgradient source types can be used. Therefore, Kwicklis

et al. (2005) considered multiple different combinations in the simulations and they limited the process by requiring hydrologic plausibility between upgradient and downgradient sources.

7.1.1.2 Results at Boreholes Considered

At each of the target boreholes considered, several different plausible mixing ratios for source constituents were often simulated with PHREEQC. These different results provide ranges in uncertainty for the comparison with model results. The ranges are often quite large indicating significantly different plausible mixing compositions. The ranges of uncertainty reported by Kwicklis et al. (2005) indicate the differences between plausible models, but not the uncertainty associated with any given model or the data.

The results of the inverse mixing models are presented by Kwicklis et al. (2005, Tables 4 through 13, and 21 through 23). The key summary tables used for comparison with the flow models are reproduced in Section 7.2 as appropriate for the boreholes considered. Notes identify their number in the original document. The values in the tables provide input to the graphic comparisons between geochemistry analysis and flow model simulations.

Kwicklis et al. (2005) developed a series of figures based upon the mixing compositions and ranges of uncertainty to show the evolution of groundwater from different source areas (Kwicklis et al., 2005, Figures 12 through 17). For example, Figure 7-2 shows the sources and mixing ratio ranges for water at ER-OV-01. Along the path, water from the northwest (ER-EC-1) mixes with water from north-central Pahute Mesa (U-20 WW) to create a nearly equal mix at ER-EC-6. These components continue to be factored into ratios at downstream wells for which ER-EC-6 helps define the composition and mixing. Similarly, Figures 7-3 and 7-4 show the evolution and mixing source waters on Paths 4 and 6 (as defined by Kwicklis et al., 2005) with final targets in Oasis Valley or along the southwest flank of Timber Mountain.

Finally, a set of plausible flow paths that honor the mixing models are drawn. These are shown in Figure 7-5. For comparison, Figure 7-6 shows the simulated pathlines of particles originating within open screened intervals of the wells in the model domain in the base-case calibrated flow model. Qualitatively, this comparison shows great similarity between the two sets of flow paths.

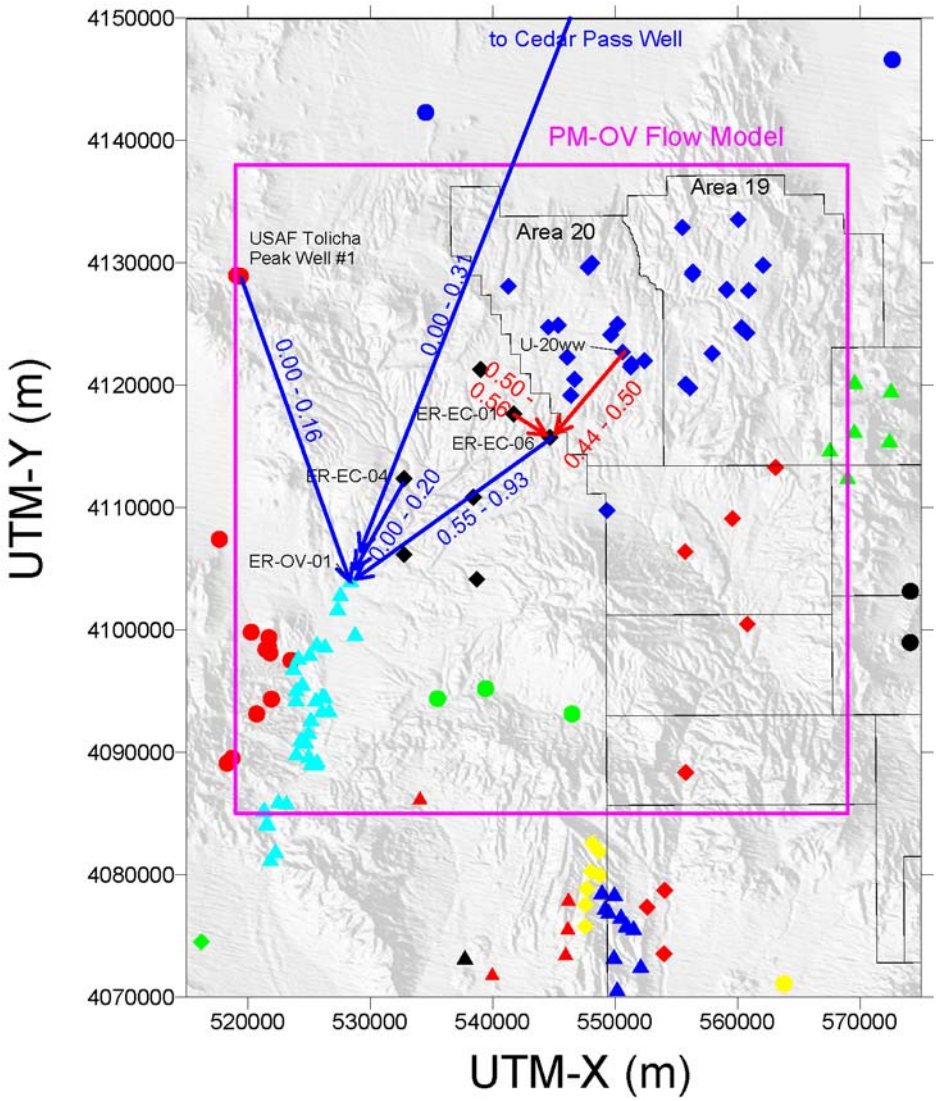

Figure 7-2
Schematic of Mixing Ratios from Upstream Source Wells Along Path 1 Toward ER-OV-01(from Kwicklis et al., 2005, Figure 13)

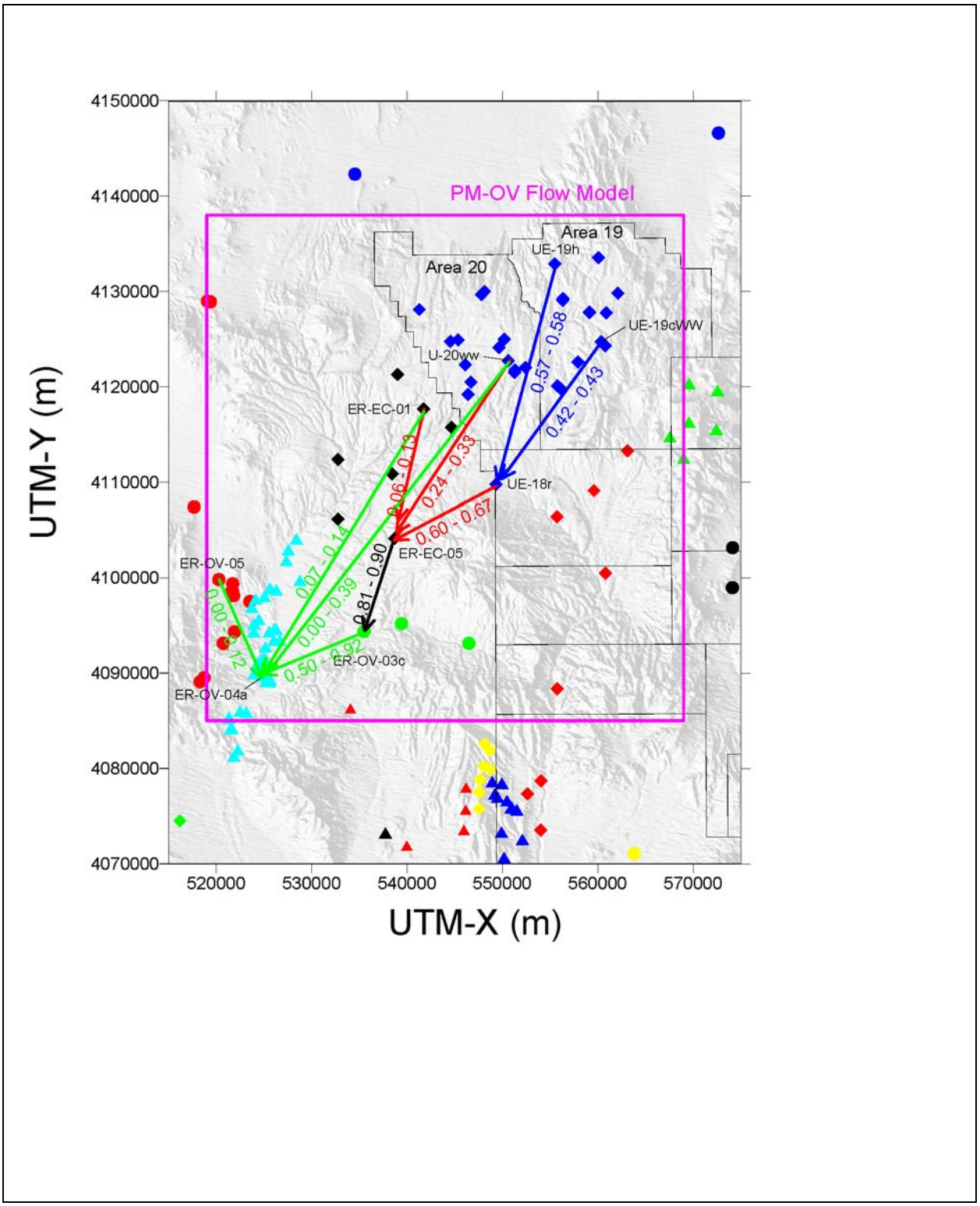

Figure 7-3
Schematic of Mixing Ratios from Upstream Source Wells Along Path 4 Toward ER-OV-04a (from Kwicklis et al., 2005, Figure 15)

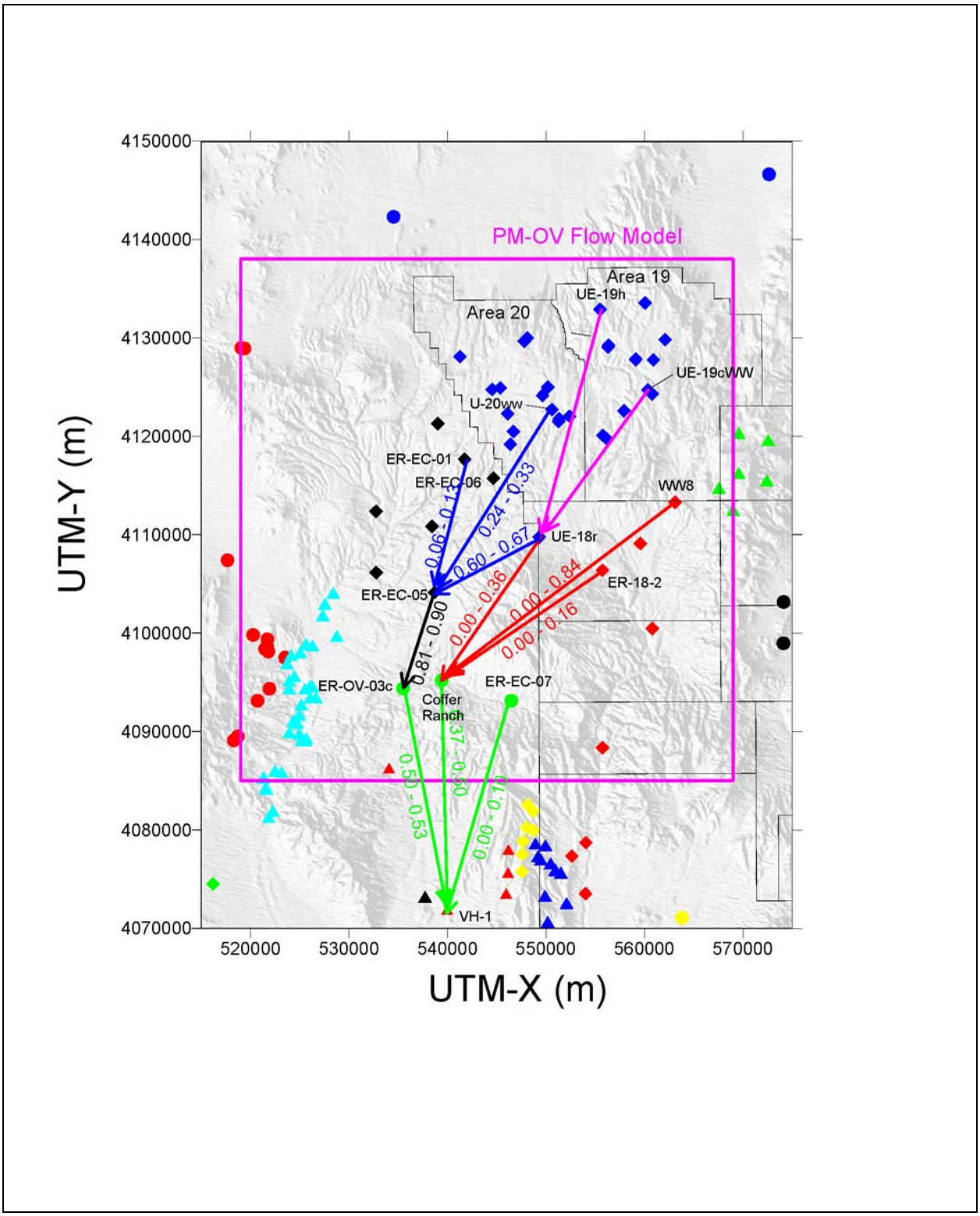

Figure 7-4
Schematic of Mixing Ratios from Upstream Source Wells Along Path 6 Toward Coffer Windmill Well (from Kwicklis et al., 2005, Figure 13)

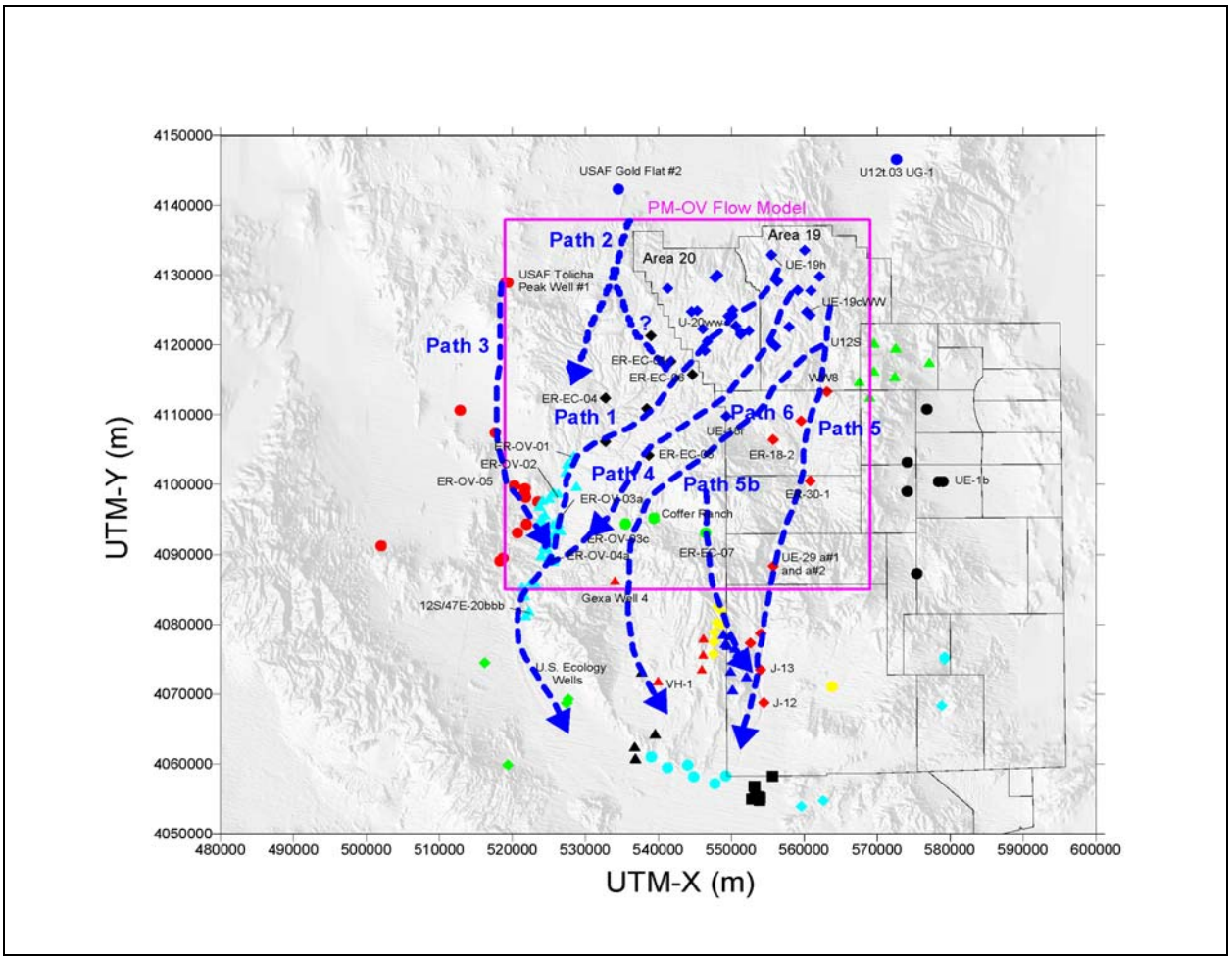

Figure 7-5
Flow Paths Estimated by Kwicklis et al. (2005) Based on Mixing Models

7.1.2 Reverse-Particle-Tracking Method

To compare the calibrated flow models with the mixing compositions quantitatively, reverse-particle tracking is used to identify fractions of water from different geographic source locations that are found at the target wells. In the reverse-particle-tracking method, the flow field in a calibrated steady-state flow model is simply reversed so particles released at a well of interest move upgradient and eventually leave the model at locations where water actually enters the model as either recharge or boundary flow.

In FEHM, two different particle-tracking algorithms are available. They are (a) the residence time transfer function particle-tracking method, PTRK (Robinson, 2004), and (b) the conventional streamline-particle-tracking method, SPTR, which is based on the standard method of Pollock (1988).

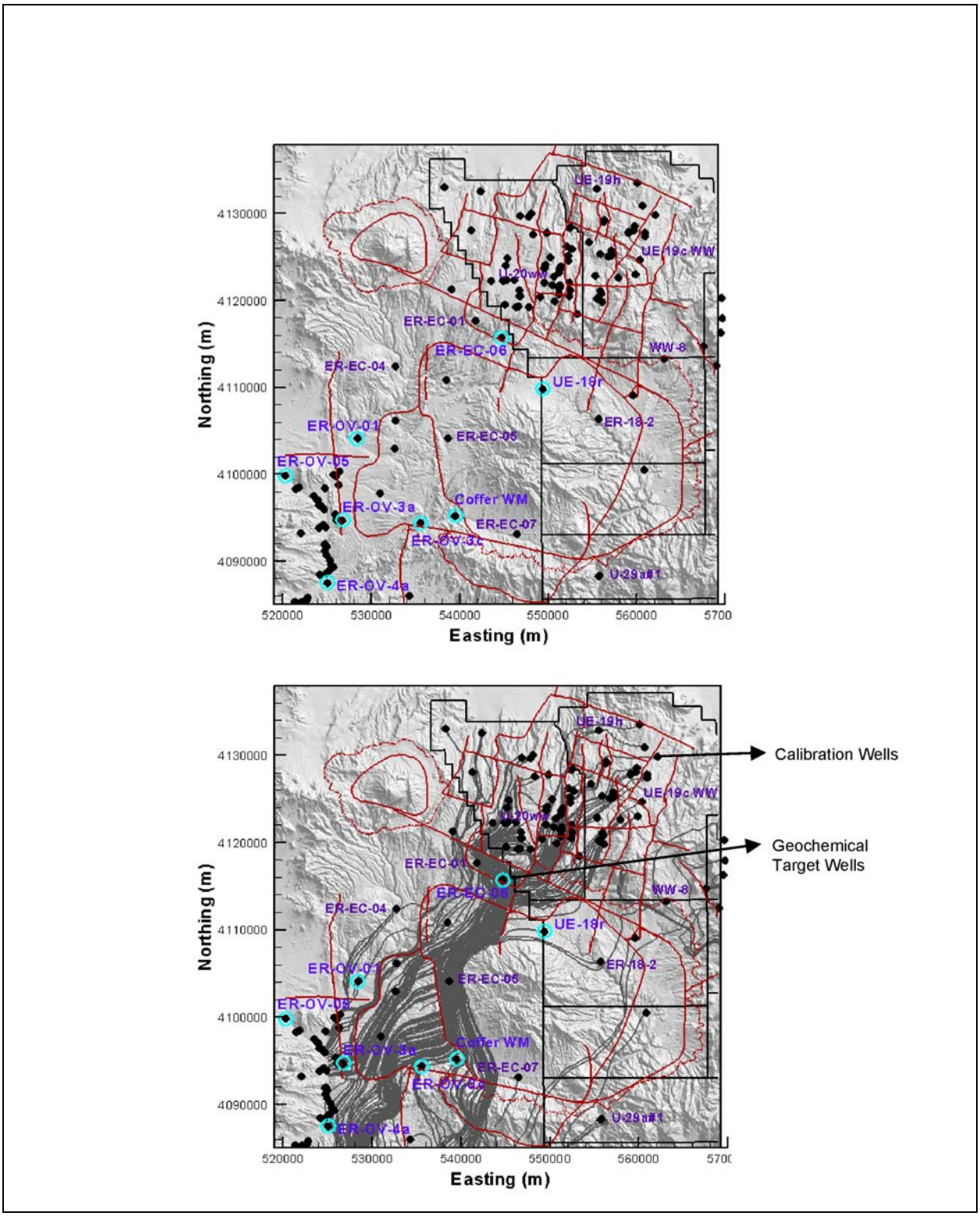

Figure 7-6
Locations of Flow Model Calibration Wells (black circles), Geochemical Target Wells (blue circles), and Pathlines for Forward SPTR Particles Originating in Open Screened Intervals of Wells in Model Domain

For mapping out the spatial origins of water in steady-state flow models, PTRK is used here due to its efficiency. In PTRK, particles simply move from cell to cell in proportion to the flux distribution across the different faces of the cell. Its efficiency comes from the algorithm in which no velocity interpolations are required. Thus, more particles can be simulated quickly with PTRK. The tradeoff is that lateral numerical dispersion is greater in PTRK than in SPTR due to the assumption of complete mixing in each cell. Whereas the SPTR method interpolates velocities within a cell to map out high-resolution pathways, the width of a PTRK pathway is no less than the width of a control volume in the model, and spreading occurs in all directions in which there is any flow out of a cell. However, for the purpose here of identifying the upgradient origin of groundwater in large geographic areas, that error is not considered to be of great importance. By contrast, the lateral dispersion associated with PTRK in a forward solute-transport simulation may not be acceptable because the point concentrations simulated at downstream wells of interest might be too dilute.

Figure 7-7 provides a comparison between the PTRK and SPTR particle-tracking models when used in reverse mode. This figure is particularly important because SPTR particles released from a small volume tend to find the diverse set of flow paths that converge and provide mixing at Well ER-OV-03a. Had all of the SPTR particles remained closely grouped together and exited the model in approximately the same location, there would have been greater cause for concern about the PTRK lateral dispersion. Instead, however, this comparison demonstrates that flow paths originating from geographically different upstream zones are identifiable. For the statistical comparison, PTRK is a more desirable methodology because 10 million particles can be easily tracked. As they spread to the different upstream source zones (see Section 7.1.3), a statistically significant number of particles are available for calculating the fractions originating in the different zones (Figure 7-1). Therefore, PTRK is used for all reverse transport modeling in Section 7.0.

7.1.3 Recharge and Inflow Zone Definitions

For comparison between the model results and the geochemical interpretations, groundwater source zones in the model domain are defined based on the location of the upgradient source wells used by Kwicklis et al. (2005). These groundwater source zones are used to bin the reverse-particle exit locations and calculate the fractions of groundwater at the target wells that originate in different areas of the model. These zones, listed in Table 7-1, are shown in Figure 7-1. Table 7-1 provides the

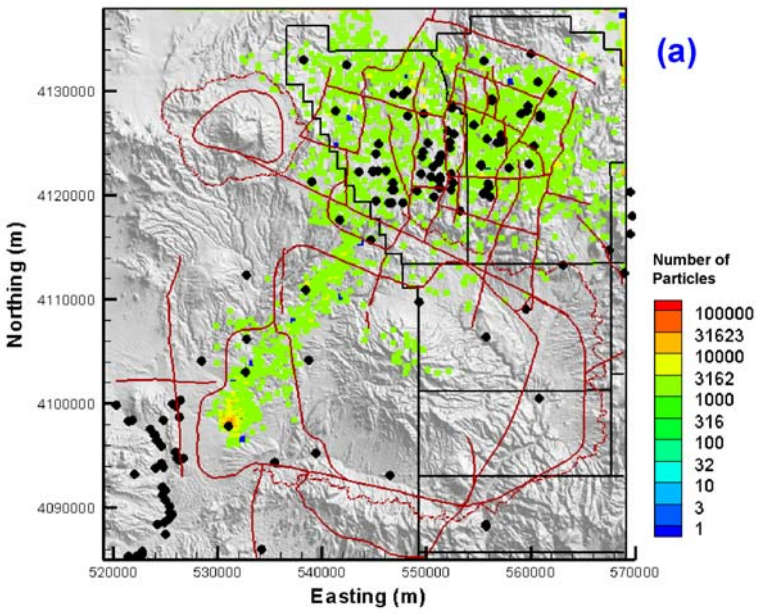

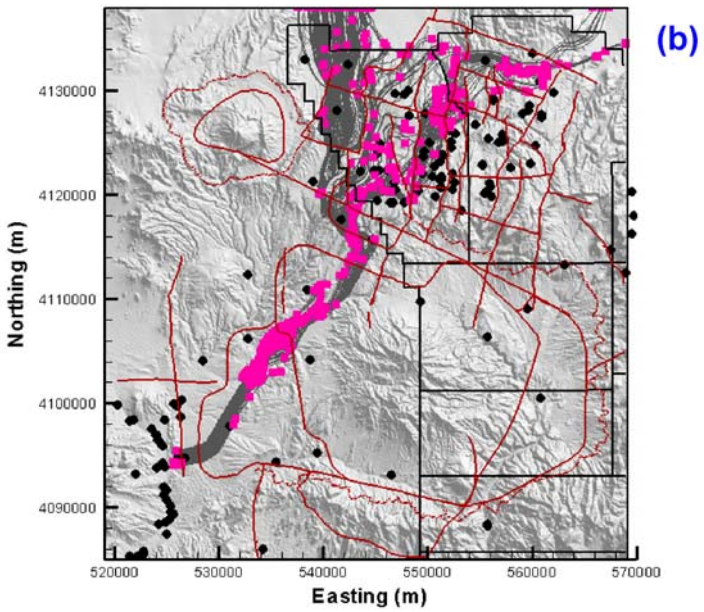

Figure 7-7
Comparison of Reverse PTRK and SPTR Particle-Tracking Methods for Particles Originating at Well ER-OV-03a

Figure (a) shows the exit locations and numbers (indicated by color scale) for 10 million PTRK particles. Figure (b) shows the reverse SPTR paths (grey lines) and exit locations (red squares) for 1,000 SPTR particles. The SPTR simulation is conducted with no dispersion. Black circles in both figures are wells in the domain.

Table 7-1
Spatial Association of Geochemistry Source Wells

Zone	ID Letter	Geochemistry Well	Model Zone
Northwest	A	ER-EC-1, Tolicha Peak, ER-EC-4	1, 7, 18
Recharge-washes	B	Local Recharge	17, 4
Recharge - TM	B	ER-EC-7	5
North Central	C	U-20 WW	2,8
Northeast	D	UE-18r, UE-19h, UE-19c WW, Cedar Pass	3,9
Southeast	E	WW-8	6,12
East (boundary flow)	E	WW-8	10
East (TM)	F	ER-18-2	16

spatial correlation between upstream source wells used in the geochemistry analysis and the recharge and boundary zones used in the reverse-particle-tracking simulations.

7.1.4 Method for Comparing Model Results to Targets

7.1.4.1 Comparison Zones

Starting with a calibrated steady-state flow model, the flow field is reversed and 10 million particles are released at the node or nodes representing the open interval of UE-18r, ER-EC-6, ER-OV-04a, ER-OV-05, ER-OV-01, ER-OV-03a, ER-OV-03c, and Coffer Windmill Well (a separate run is done for each well). The particles move upgradient and then leave the flow system. The number of particles exiting each zone, as identified in Figure 7-1 and Table 7-1, is documented for each simulation. These are then used to compute the mixing ratios by dividing the number of particles leaving each zone by 10 million. The model zones through which particles leave are combined, per Table 7-1, to represent eight geographic source zones. A few items in Table 7-1 require additional clarification. First, the geochemistry at ER-EC-1 and Tolicha Peak are different (Kwicklis et al., 2005), indicating that inflow across the northern boundary for this model domain is different from recharge in the northwest quadrant of the model domain. The purpose of the A grouping is to identify waters that are entirely different from those entering the model domain as recharge to the east of the Purse Fault, which is why they are grouped as such. Second, the Cedar Pass well source water is grouped in D. The actual flow path from Cedar Pass into the model domain is not known, particularly

whether it enters to the east or west of the Purse Fault intersection with the northern boundary. As will be shown later, this issue only applies at one of the nine target wells, ER-OV-01, and is relatively minor there. Comparisons between the model results and the mixing source wells are then made graphically as described below.

7.1.4.2 Explanation of Comparison Plots

For each target well in each flow field, a plot of the form in Figure 7-8 is created. The vertical lines represent the range of uncertainty in the fraction of groundwater from the indicated upgradient well that is present at the target well, as calculated by the geochemical model. The upgradient wells are grouped by geographic location (Table 7-1) and are color coded in the legend of the plots. For example, the northwest source zone can be represented by water types from ER-EC-1, Tolicha Peak, and/or ER-EC-4. In the model, the northwest source zone is represented by Zones 1 and 7. For each of the model zones, the symbol on the legend facilitates comparison with source wells. Thus, ER-EC-1, Tolicha Peak, and ER-EC-4 are followed by the model symbol for northwest source of groundwater (A), and so on for the other zones.

When multiple wells are present within a single source zone, the process of determining the geochemical ranges is somewhat more complicated. For the case where two source wells fall within the same zone, the target range is determined as the minimum and maximum of the combined fractions of the two wells in all plausible PHREEQC models. Figure 7-9 shows the 16 plausible mixing models developed for this example. The blue line shows the sum of NW1 and NW2 waters for each model. The range for the NW zone, then, is defined as the minimum and maximum values on the blue curve. In the comparison figure (b), the total possible range of all wells in this zone (0.14 to 0.37) is represented by adjacent lines for the individual wells, but each line spans the entire range.

7.2 Geochemical Verification Results for BN-MME-SDA

This section compares the base model results with the geochemistry mixing targets. The base model includes the BN HFM, the MME recharge map selected HSU depth decay and anisotropy, and lateral boundary fluxes from the regional model calibrated with the MME recharge map over the entire region (Section 4.2). This section provides a template for geochemical comparison results associated

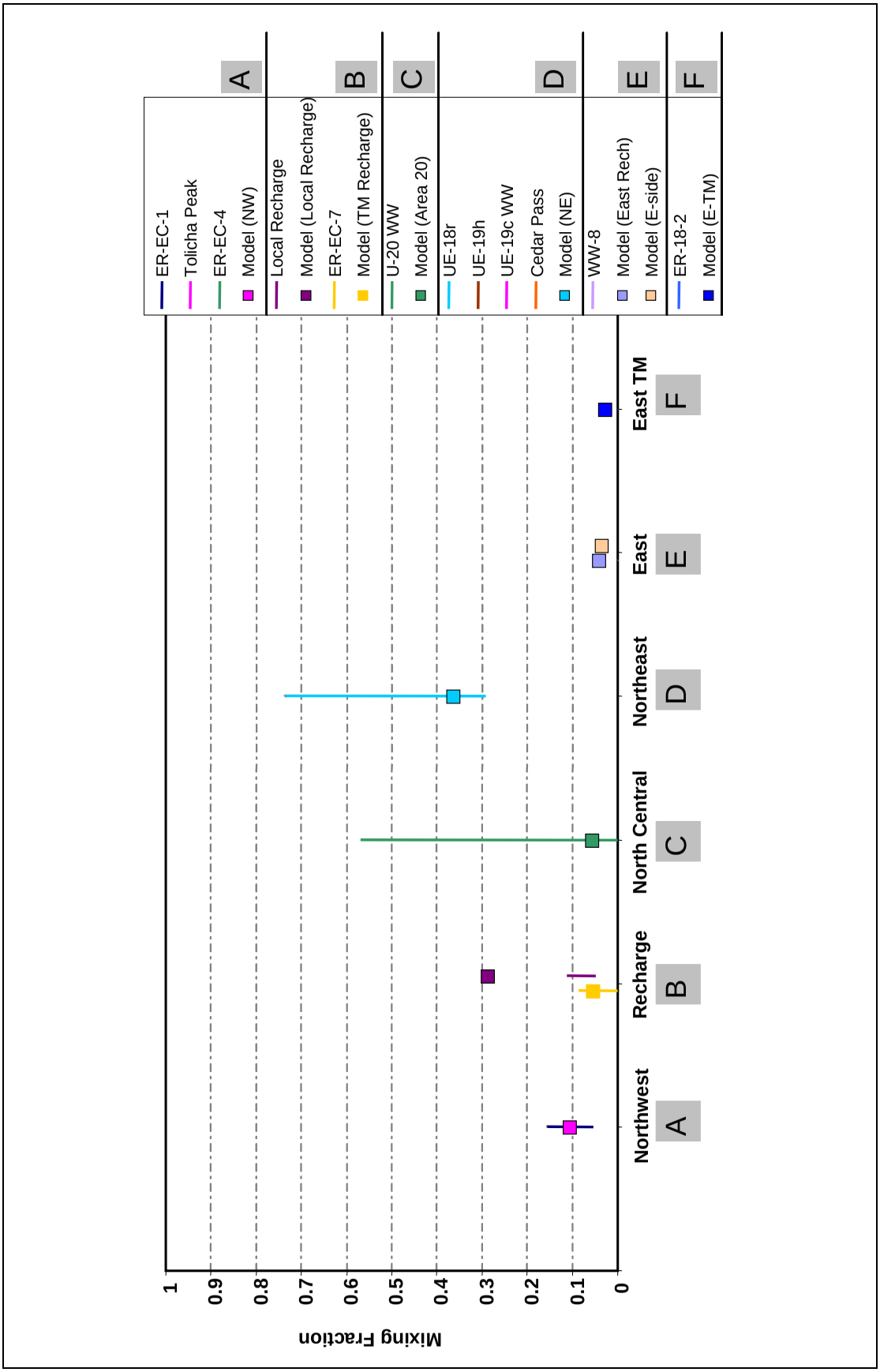

Figure 7-8
Example of Geochemistry Comparison Plot

Vertical lines represent mixing target uncertainties, and symbols represent model results.

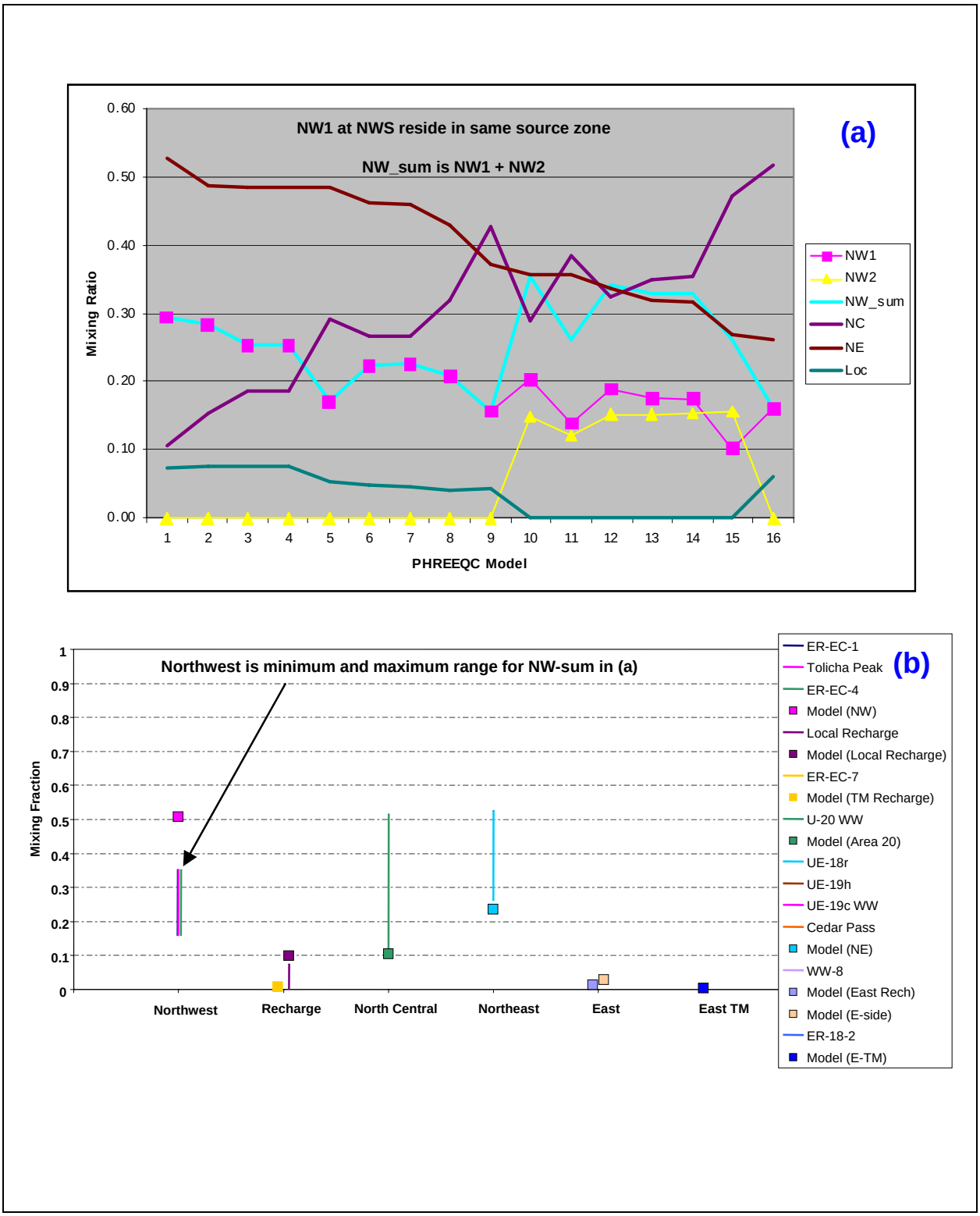

Figure 7-9
Example of PHREEQC and PTRK Results Comparison

Figure (a) shows 16 PHREEQC model results for mixing at a well. Figure (b) shows PTRK results.

with alternative HFMs and alternative recharge maps as listed in Table 6-1. Figure 7-6 shows the pathlines of particles originating at wells in the model domain as well as the locations and identities of the eight wells at which comparisons are made. The comparisons are made for target wells in the following order: UE-18r, ER-EC-6, ER-OV-05, ER-OV-01, ER-OV-03a, ER-OV-04a, ER-OV-03c, and Coffer Windmill Well. The sequence follows a somewhat counterclockwise path around Timber Mountain, sampling the different pathways described by Kwicklis et al. (2005).

7.2.1 UE-18r

Sitting just north of Timber Mountain, possible modeled source locations for water at UE-18r are from Areas 19 and 20 of Pahute Mesa, from Timber Mountain, and from the flow into the model across the eastern boundary. Figure 7-10 shows the flow paths for the BN-MME-SDA with forward particle paths (SPTR) colored in grey and the source locations for water at this well identified by reverse-particle-tracking (PTRK) exit densities (colored symbols), and the comparison between the model and the geochemistry mixing targets (b), developed from the data in Table 7-2. The two parts of this figure need to be considered together. The reverse-particle-tracking simulation shows a high density of particle exit locations in red along the eastern model boundary. In fact, in this model, 85 percent of all reverse PTRK particles originating at UE-18r leave the model along the eastern model boundary, as is shown in (b). In contrast, the geochemical interpretation (Table 7-2) suggests that most water at UE-18r is similar to that of the Area 19 wells with a small component resembling water in ER-18-2.

7.2.1.1 Simulated Rainier Mesa Recharge at UE-18r

This comparison raises the question of whether flow across the eastern model boundary at Gold Meadows Stock (near the water table) could be geochemically similar to the Area 19 wells. Kwicklis et al. (2005) determined that WW-8 type water and HTH-1-type water are not possible at UE-18r. Their analysis shows a small component of ER-18-2 water at UE-18r, but that ER-18-2 water indicates a source of old, deep origin, possibly from the regional carbonate aquifer. It does not represent local recharge as might occur in upper Fortymile Canyon (Kwicklis et al., 2005). Therefore, there is no geochemical evidence that would suggest the feasibility of shallow groundwater flow from Rainier Mesa recharge arriving at UE-18r.

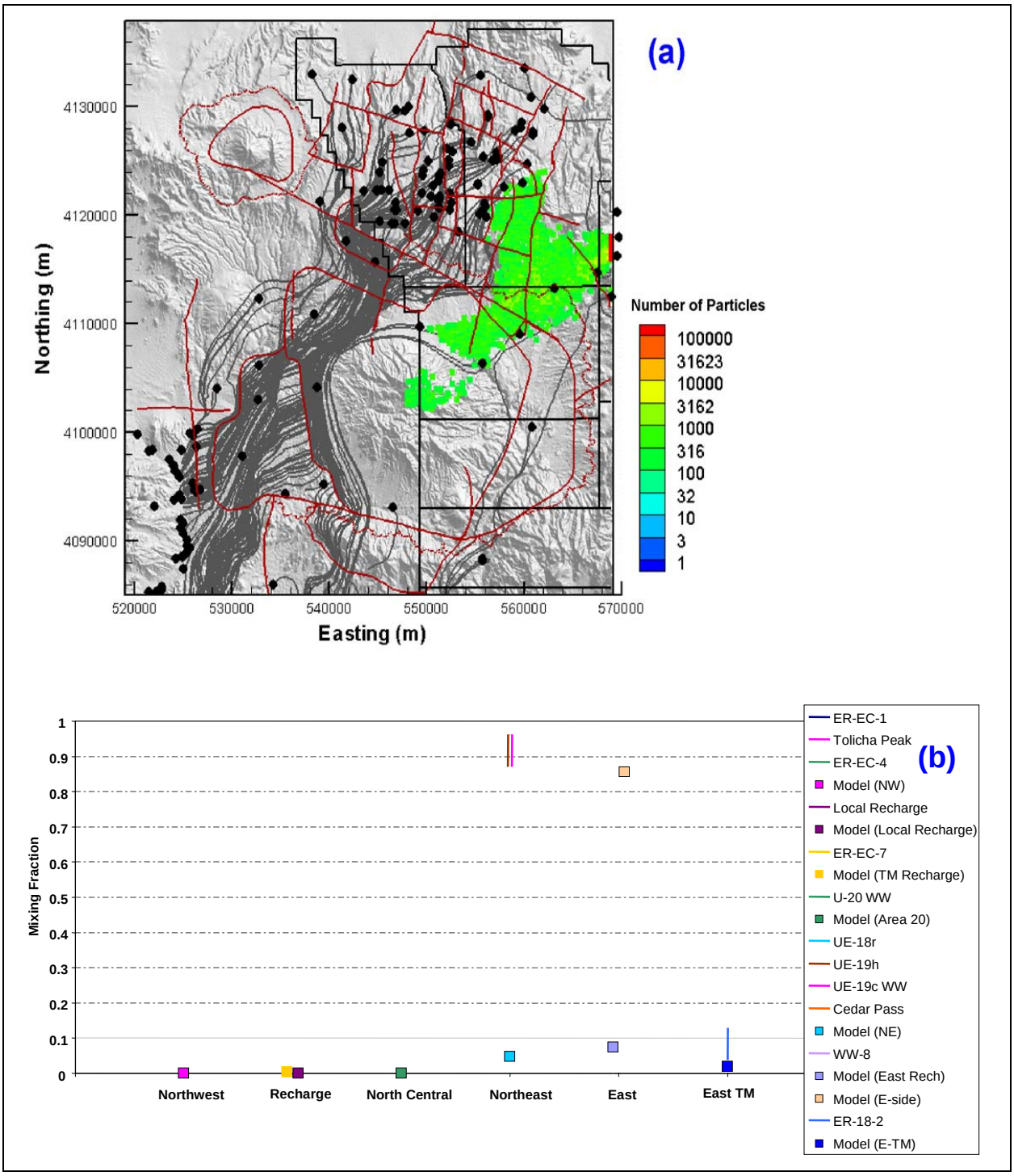

Figure 7-10
Comparison of Flow Model with Geochemical Mixing Targets at UE-18r for BN-MME-SDA

Figure (a) shows the flow paths as mapped by forward SPTR particles originating at wells (grey lines) and the source recharge locations identified by reverse PTRK particle tracking (colored squares). Figure (b) shows the model comparison with geochemical mixing target ranges.

Table 7-2
Fractions of Groundwater from Various Upgradient Wells Present in Groundwater at Well UE-18r

Mixing Component	Minimum Fraction	Maximum Fraction
ER-18-2	0.087	0.122
ER-EC-7	0.000	0.000
WW-8	0.000	0.000
Test Well #1	0.000	0.000
UE-19h	0.370	0.429
UE-19c WW	0.484	0.543

Note: Shallow groundwater from Well UE-29a #2 was used to represent local recharge from ephemeral surface runoff. Groundwater from ER-EC-7 was used to represent recharge from infiltration at Timber Mountain. See Kwicklis et al. (2005) for discussion of uncertainty tolerances and rock water reactions for the calculations represented in this specific table.

In some of the model simulations, highly localized, large flows across the eastern boundary at Gold Meadows near the water table are clearly due to the high fixed boundary heads at Gold Meadows coupled with relatively large calibrated LCCU1 permeabilities (see Sections 6.2 and 6.2.4.4). With a high boundary head and a high-permeability conduit, it is not surprising that significant simulated flow enters the model domain at this location. These flows do not adversely affect the head and flux calibrations, but they do result in unsupportable geochemical sources at UE-18r. Thus, this analysis serves to identify and quantify this error, as discussed in Section 7-5.

7.2.1.2 BN-MME-SDA Reduced LCCU1 Permeability Alternative

In the first alternative model, the LCCU1 permeability was fixed at about one order of magnitude lower than in the base case before recalibration of other HSU permeabilities, resulting in substantially less flow across the eastern boundary at Gold Meadows. For comparison, Figure 7-11 shows the reverse-particle-tracking simulation and the zone comparison to the geochemistry mixing targets for the BN-MME-SDA with reduced LCCU1 permeability alternative (described in Section 6.2.4.4). In this model, the reverse particles from UE-18r leave the system within the model domain in areas of high recharge in Area 19. Approximately 60 percent of the water at UE-18r originates within the northeast quadrant of the flow model domain in this simulation, but to the southeast of Wells UE-19h and UE-19c WW. In the absence of groundwater chemistry data in the area where the simulated recharge occurs (southeastern Area 19), it is assumed that the groundwater chemical composition is

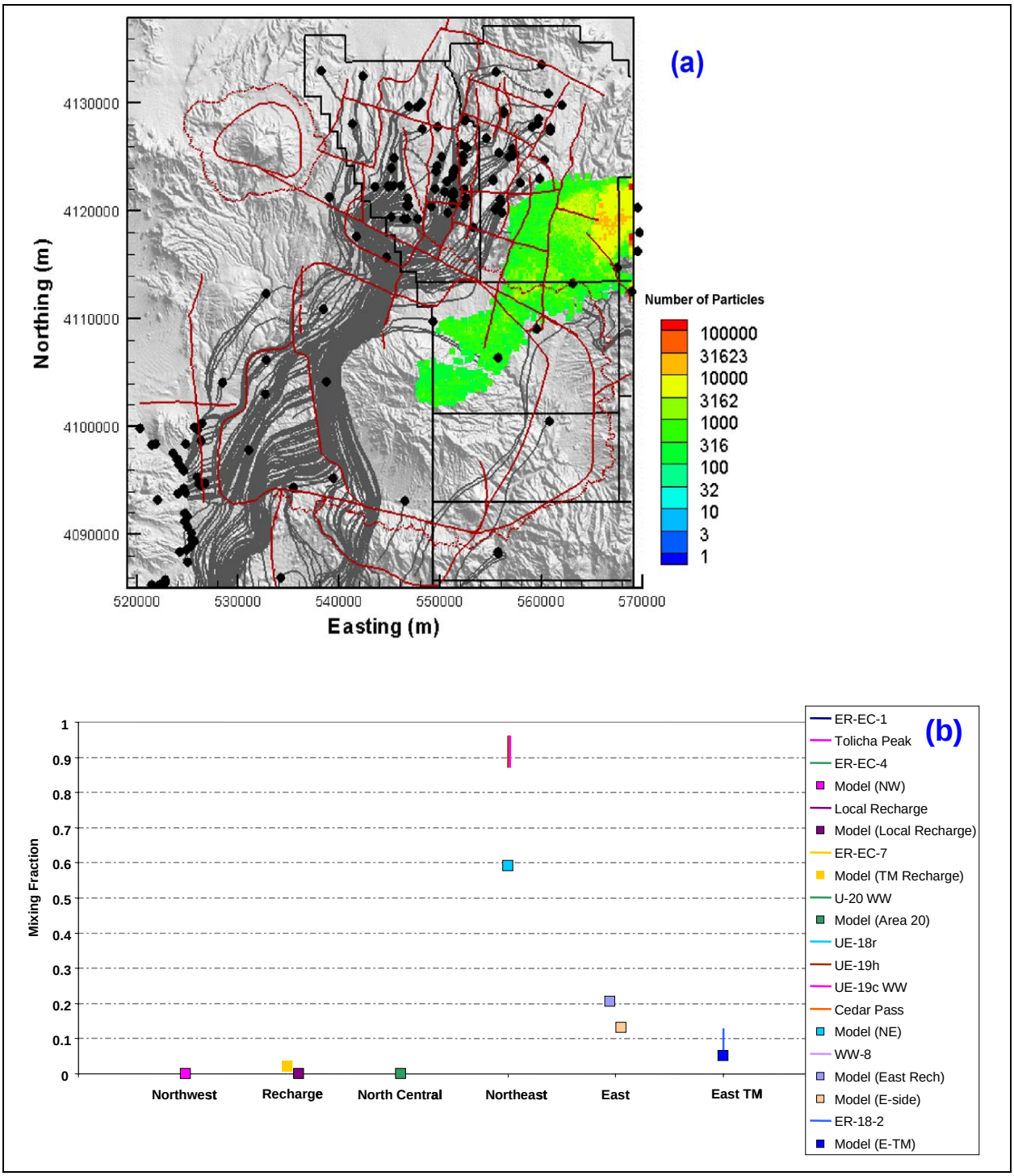

Figure 7-11
Comparison of Flow Model with Geochemical Mixing Targets at UE-18r in the Reduced LCCU1 Permeability Alternative

Figure (a) shows the flow paths as mapped by forward SPTR particles originating at wells (grey lines) and the source recharge locations identified by reverse PTRK particle tracking (colored squares). Figure (b) shows the model comparison with geochemical mixing target ranges.

similar to that of UE-19h and UE-19c WW. Further, Kwicklis et al. (2005) do not distinguish whether the source water identified by UE-19h and UE-19c WW originates as recharge within the model domain or as flow across the model boundary from the north. Another 20 percent of the mixed water (East) originates in Zone 6 (Figure 7-1). From Figure 7-11, it is clear that this component is all recharge from the northernmost portion of Zone 6, which may not be geochemically distinguishable from Zone 3. Also 13 percent (rather than 85 percent as in the base case, BN-MME-SDA) of the water at UE-18r in this model comes across the model boundary from the Gold Meadows. For comparison, Figure 7-12 shows the reverse-particle exit locations along the eastern boundary for the BN-MME-SDA and reduced LCCU1 permeability alternative models. Significantly more particles exit the eastern model boundary along a very short zone at the water table in the HSU LCCU1 in (a) compared to (b). It is important to note that the water in UE-18r does not resemble the water in WW-8 (Kwicklis et al., 2005), which could be along potential pathways from Rainier Mesa to UE-18r.

The geochemistry indicates that at UE-18r, there should be between 4 and 13 percent water with a signature like that found in ER-18-2. In the reduced LCCU1 permeability simulation, 5 percent of water found in UE-18r originates in Zone 16. However, considering that ER-18-2 water resembles deep, old groundwater rather than local recharge, the spatial correlation of BN-MME-SDA reduced LCCU1 permeability alternative particle exit locations to ER-18-2 is not significant. In the original BN-MME-SDA simulation, virtually no water originates from Zone 16. Further, the water entering the model as flow across the east boundary is shallow and therefore would not resemble ER-18-2 water.

7.2.1.3 UE-18r Summary

Summarizing the UE-18r comparison, the geochemistry indicates that most of the water should originate in the northeast with a small component resembling a deep source found in ER-18-2 on the east flank of Timber Mountain. The reduced LCCU1 permeability alternative simulations are consistent with this interpretation, whereas the BN-MME-SDA simulations are plagued with large volumes of flow into the model from Gold Meadows. The source of the water arriving at UE-18r in the reduced LCCU1 permeability alternative is consistent with specified boundary conditions on the model. Namely, the MME recharge prescribes a zone of high recharge where the source of the

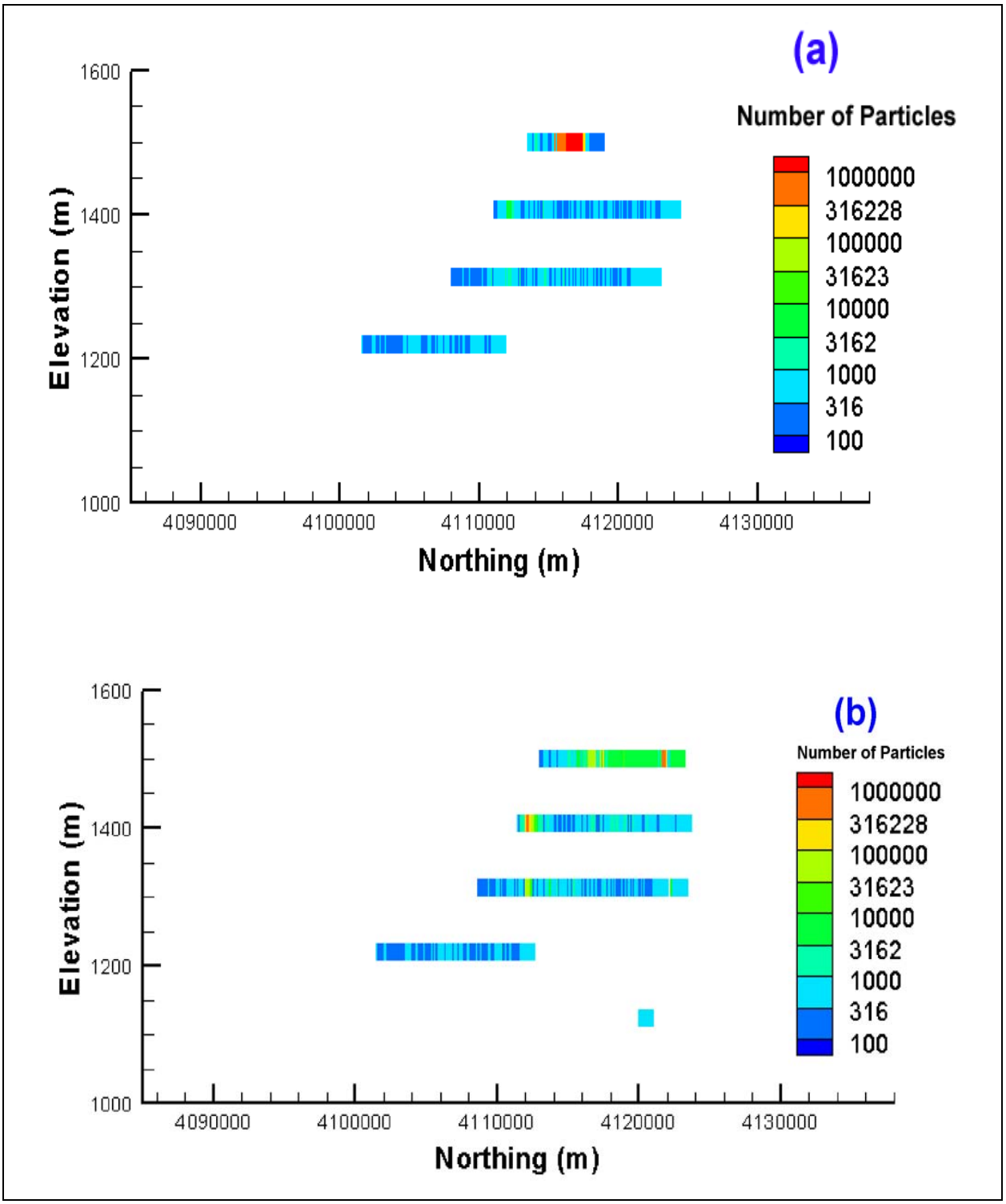

Figure 7-12
Particle Exit Locations on Model East Face for (a) BN-MME-SDA and (b) for BN-MME-SDA Reduced LCCU1 Permeability Alternative

Note the high density of exiting particles in (a) occurs within the LCCU1 HSU.

majority of water arriving at UE-18r is identified (Area 19 recharge zones). The combination of recharge occurring in Zones 3 and 6 is approximately in the range of Area 19-type water implied by the geochemistry. Kwicklis et al. (2005) do not distinguish whether the source water identified by UE-19h and UE-19c WW originates as recharge within the model domain or as flow across the model boundary from the north. The 13 percent of flow across the eastern boundary results from the boundary conditions reflecting the regionally high head at Gold Meadows Stock and, hence, large gradient into the Pahute Mesa CAU flow model domain, but is significantly less than the 85 percent flow from the east in BN-MME-SDA due to reduced LCCU1 permeability in this alternative.

7.2.2 ER-EC-6

Moving counterclockwise around Timber Mountain and away from the eastern boundary, the differences between BN-MME-SDA results and the reduced LCCU1 permeability alternative become far less differentiable; results for the two models are often nearly indistinguishable.

Well ER-EC-6 is just south of the termination of the Purse Fault; possible source locations for water at ER-EC-6 are from areas north on either side of the Purse Fault. The geochemistries of water from these two different zones are distinctly different (Kwicklis et al., 2005). The simulated flow paths in this region of the model domain are very complex as flow paths from the northwest and northeast converge in upper Thirsty Canyon (Figures 7-13 and 7-14).

The geochemical interpretation (Table 7-3) suggests that there should be approximately equal ratios of water from either side of the Purse Fault mixing at ER-EC-6. By comparison, the simulation results in Figures 7-13 and 7-14 for BN-MME-SDA and the reduced LCCU1 permeability alternative show that between 80 and 90 percent of the water source at ER-EC-6 is from west of the Purse Fault (although the plan view figures show approximately equal distribution of recharge from either side of the fault (a), most of the source water at ER-EC-6 is simulated to have originated as inflow along the northern boundary, which cannot be seen in the plan view).

The discrepancy between either of the flow model results and the geochemistry interpretation must be considered with regard to the structure of the flow paths at ER-EC-6. In this area, significant convergence of flow for highly different source areas occurs, as indicated by the geochemistry. In the model, at the exact location of ER-EC-6, most of the water is arriving from the northwest. However,

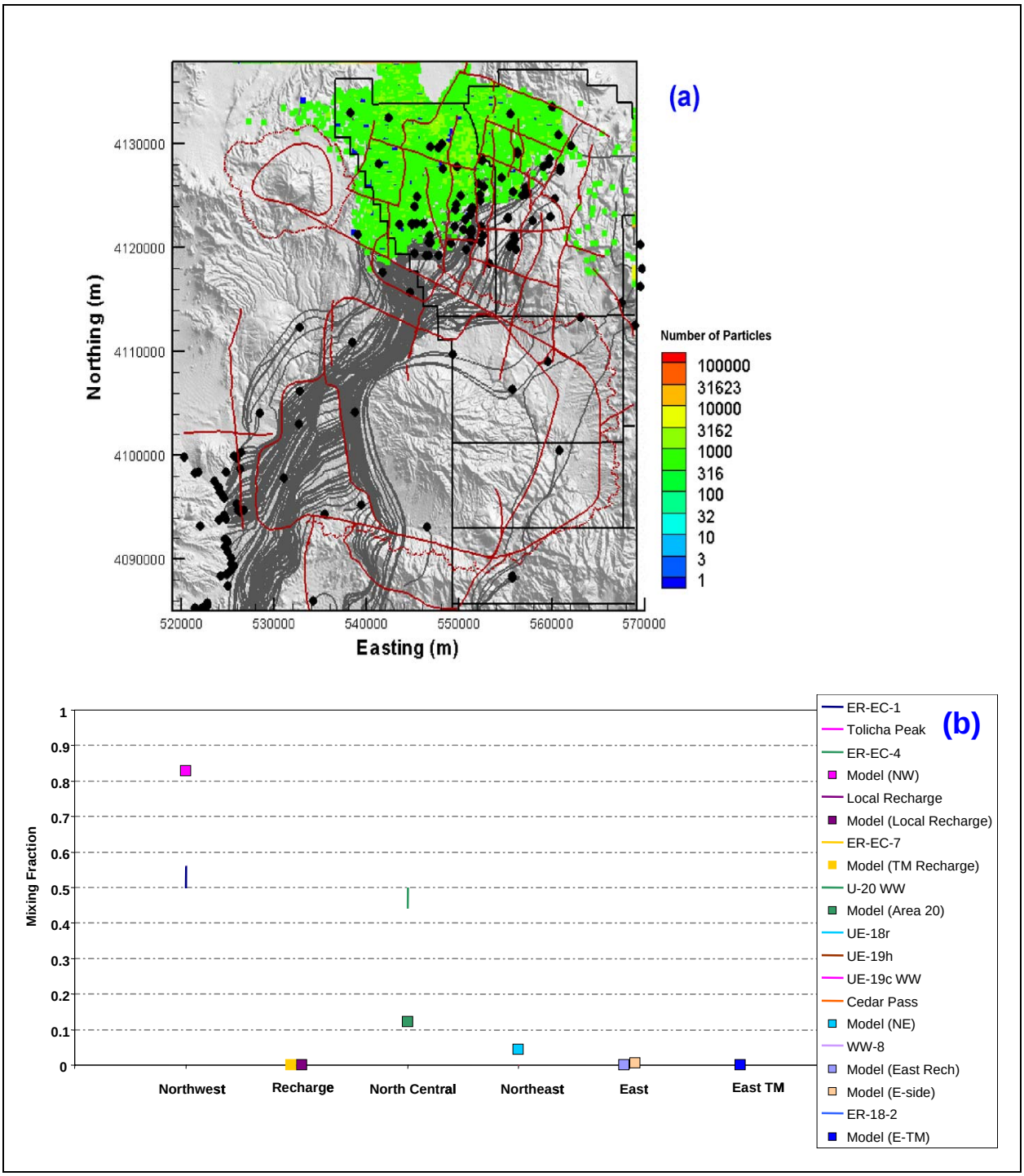

Figure 7-13
Comparison of Flow Model with Geochemical Mixing Targets at ER-EC-6 for BN-MME-SDA

Figure (a) shows the flow paths as mapped by forward SPTR particles originating at wells (grey lines) and the source recharge locations identified by reverse PTRK particle tracking (colored squares). Figure (b) shows the model comparison with geochemical mixing target ranges.

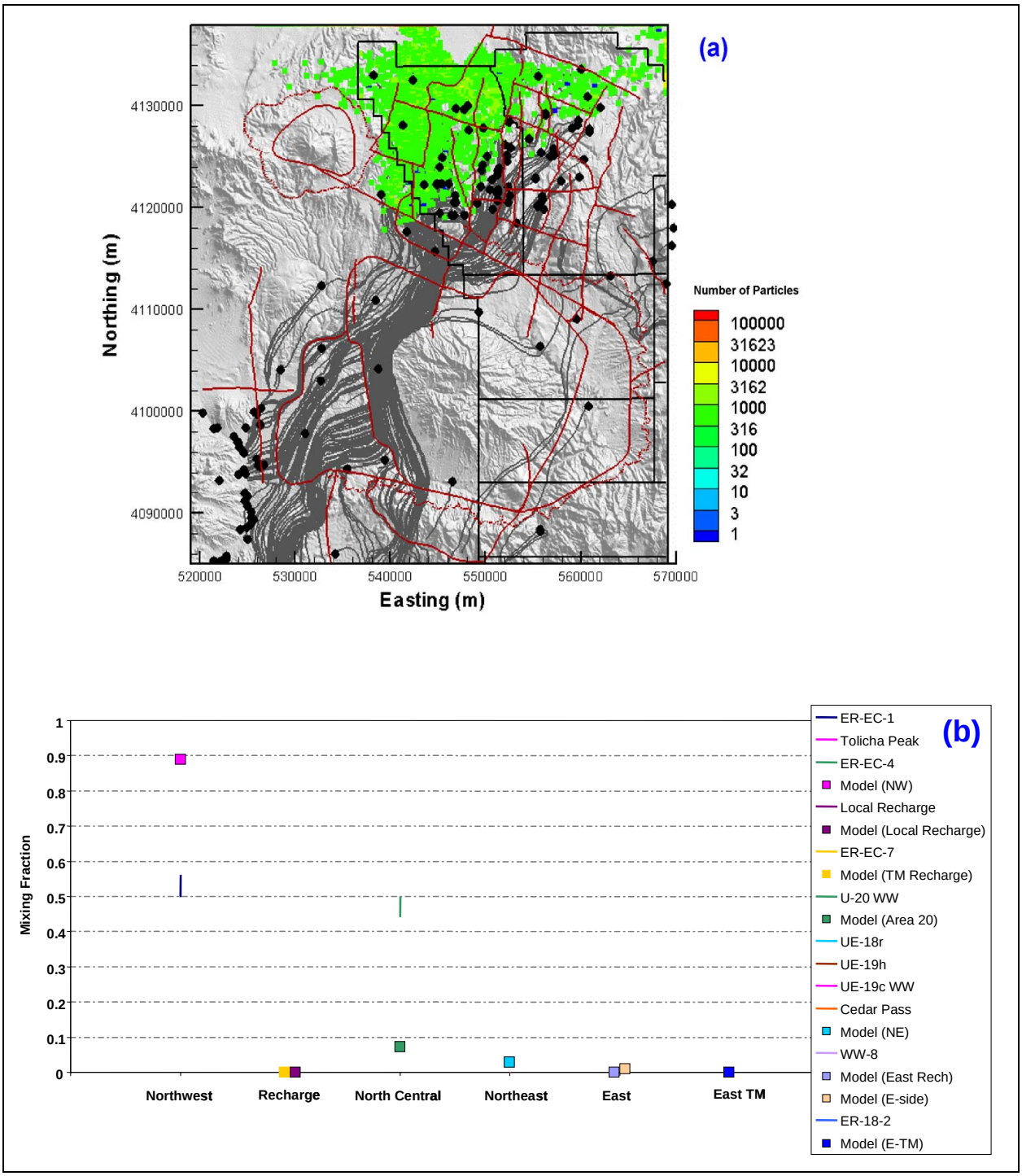

Figure 7-14
Comparison of Flow Model with Geochemical Mixing Targets at ER-EC-6 in the Reduced LCCU1 Permeability Alternative

Figure (a) shows the flow paths as mapped by forward SPTR particles originating at wells (grey lines) and the source recharge locations identified by reverse PTRK particle tracking (colored squares). Figure (b) shows the model comparison with geochemical mixing target ranges.

Table 7-3
Fractions of Groundwater from Various Upgradient Wells Present in Groundwater at Well ER-EC-6

Mixing Component	Minimum Fraction	Maximum Fraction
ER-EC-1	0.498	0.561
U-20 WW	0.440	0.502
UE-19h	0.000	0.000
Cedar Pass Well	0.000	0.000
UE-29a #2	0.000	0.000

Table 6 from Kwicklis et al. (2005). Note: Belted Range Aquifer minerals from Table 2 were used for this set of models. Shallow groundwater from Well UE-29a #2 was used to represent local recharge.

the figure shows that only a short distance to the east of ER-EC-6, the flow paths from the northeast enter this zone of convergence in upper Thirsty Canyon. Thus, although the quantitative comparison has discrepancies, the trend of the modeled flow paths and the geochemically inferred mixing are consistent.

A second explanation for the large ratio of northwest source water at ER-EC-6 in the simulations may be related to the no-flow conditions on the northern half of the western boundary. Eliminating the ability of water entering the system on the northern boundary from exiting on the western boundary could lead to translated flow paths to east. This explanation may hold for the mixing at ER-OV-01 as well.

This analysis highlights an additional consideration: Does too much water enter the model domain on the western half of the northern boundary? Data controls (basically nil) in this portion of the domain are not as good as to the east of the Purse Fault. If the head and subsequent gradient on the western northern boundary were lower, then inflow on that boundary would be less, and more flow from the northeast would mix at ER-EC-6. However, lowering the northern boundary heads would result in much poorer matches to internal model heads at wells west of the Purse Fault such as PM-2 and PM-3.

7.2.3 ER-OV-01

Well ER-OV-01 is in the transition zone from lower Thirsty Canyon into upper Oasis Valley. This is the target well where Cedar Pass Well source water plays a role in comparing the model results with the geochemical mixing targets. As mentioned previously, Cedar Pass Well source water is lumped with the other sources in the northeast, rather than the inflows from the northwest. Given how the source zones were defined, it is actually not clear whether water with Cedar Pass Well chemistry enters the model domain as inflow to the east or west of the Purse Fault. However, because there are greater differences in water chemistry between Cedar Pass and ER-EC-1 than UE-19h, Cedar Pass-type water inflows have been included with those coming into the model east of the Purse Fault. Well ER-OV-01 is the only target well where this distinction matters. For the analyses of ER-OV-01 water in this section, the Cedar Pass contribution (0 to 0.308) in the geochemical mixing targets is included with northeast waters for comparison with the model results. However, it can also be considered in the comparison with northwest source water. As will be shown later, the impact of this assignment on the comparisons is minor relative to other distinguishing differences for the different calibrated flow models.

The northwest contribution could be between 35 and 60 percent, the north-central component between 25 and 55 percent, and the northeast component as much as 30 percent (assuming Cedar Pass water can be associated with this zone). There is also a small contribution from local recharge of up to 6 percent. These target ranges are derived from Table 7-4. The model results for both BN-MME-SDA and the LCCU1 alternative show about a 60/40 split of source water between the northwest quadrant and recharge in Thirsty Canyon, with virtually no source water from the north-central or northeast zones (Figures 7-15 and 7-16). As with ER-EC-6 for these flow models, the flow paths from Areas 20 and 19 east of the Purse Fault do not extend quite as far west as the well. In these simulations, the impact of flow (or lack of flow) across the eastern boundary at Gold Meadows is not evident at this well dominated by northwestern flows.

One reason the northeast and north-central flow paths do not intersect this well in the simulation is that local recharge in Thirsty Canyon pushes those flow paths southeast, as shown in Figure 7-16. In the simulations, more than 30 percent of the source water at ER-OV-01 originates as recharge in Thirsty Canyon. However, the geochemical interpretation (Kwicklis et al., 2005) indicates that less than 10 percent of the water in the ER-OV-01 samples should be from local recharge. Considering

Table 7-4
Fractions of Groundwater from Various Upgradient Wells Present in Groundwater at Well ER-OV-01

Mixing Component	Minimum Fraction	Maximum Fraction
USAF Tolicha Peak #1	0.000	0.163
ER-EC-4	0.000	0.198
ER-EC-1	0.274	0.523
U-20 WW	0.242	0.468
Cedar Pass Well	0.000	0.308
UE-29 a #2	0.000	0.062

Table 22 from Kwicklis et al. (2005). Note: Paintbrush Aquifer minerals from Table 2 (Kwicklis et al., 2005) were used for this set of models. Shallow groundwater from Well UE-29 a #2 was used to represent local recharge. Minimum and maximum mixing fractions for Wells ER-EC-1 and U-20 WW were calculated by multiplying the minimum and maximum fractions of groundwater from these wells at ER-EC-6 (Table 6 in Kwicklis et al., 2005) by the minimum and maximum fractions of groundwater from Well ER-EC-6 at Well ER-OV-01 (Table 5 in Kwicklis et al., 2005).

the Thirsty Canyon recharge as shown in the flux map used in these base-case simulations (Figure 4-14), the fraction of local recharge at ER-OV-01 in the simulations is not surprising.

Another reason the northeast flow paths do not intersect ER-OV-01 may be due to the no-flow conditions on the northern half of the western boundary. That condition may force flow paths from the north to effectively push paths from the northeast away from this well. Finally, had Cedar Pass Well water been used in the target for northwest rather than northeast water, the differences between model and targets would have been slightly different. The model results would have been within range for northwest water, where they are slightly higher now. And, the northeast model results would be good because they are zero. However, this difference is relatively small and does not play a significant role in the model comparisons later in Section 7.3.3. Also, these models still underpredict flow from the north-central zone.

Summarizing the comparison, simulated flow paths from north-central and northeastern Pahute Mesa are east of ER-OV-01. The flow paths come close, but are pushed to the southeast by local recharge in Thirsty Canyon and possibly by high flow into the model along the western half of the northern boundary as indicated in the ER-EC-6 analysis. Qualitatively, the flow paths match those estimated from the geochemistry well, but quantitatively, the well is at least several kilometers west of the flow paths originating in eastern Area 20 and Area 19.

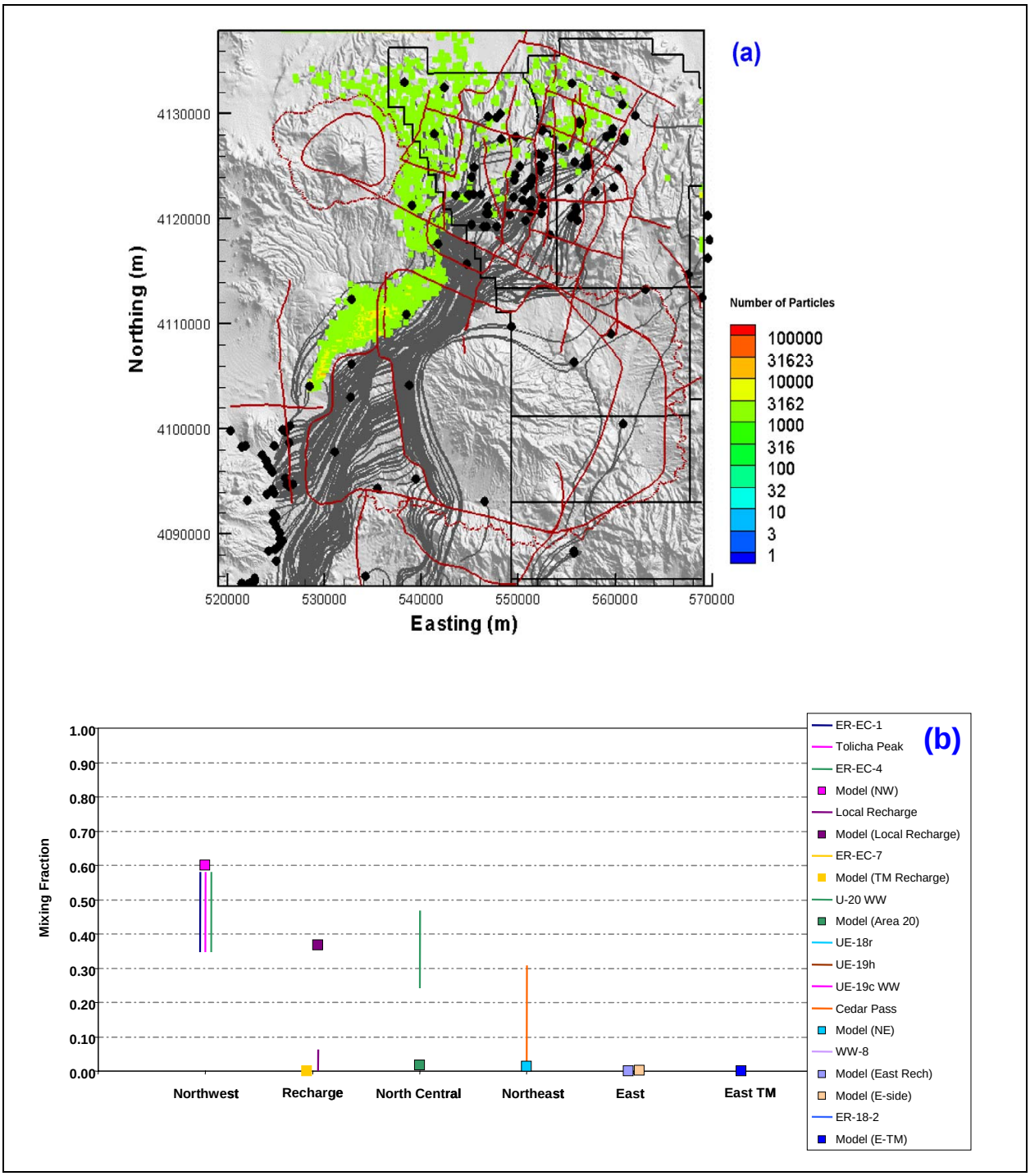

Figure 7-15
Comparison of Flow Model with Geochemical Mixing Targets at ER-OV-01 for BN-MME-SDA

Figure (a) shows the flow paths as mapped by forward SPTR particles originating at wells (grey lines) and the source recharge locations identified by reverse PTRK particle tracking (colored squares). Figure (b) shows the model comparison with geochemical mixing target ranges.

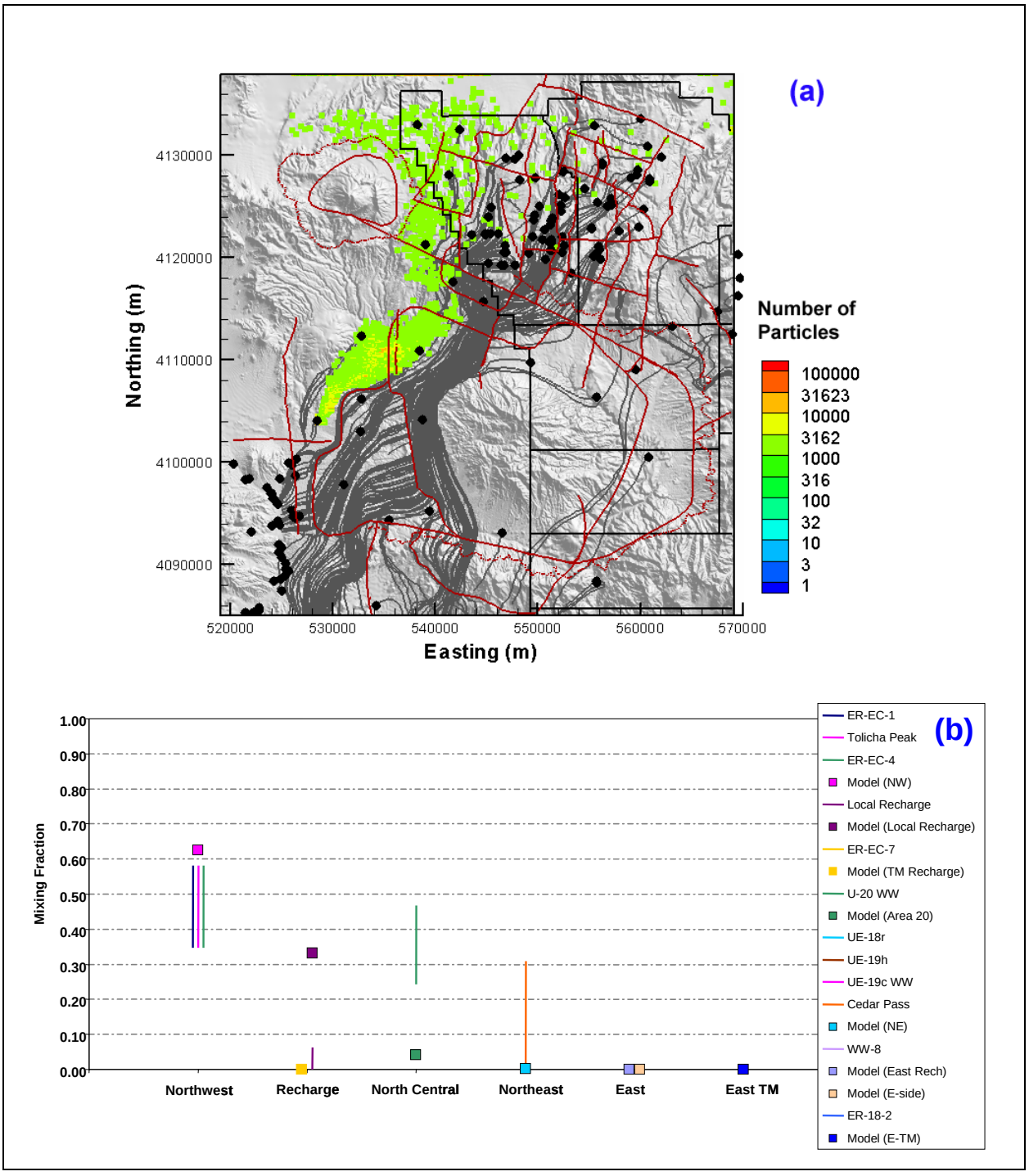

Figure 7-16
Comparison of Flow Model with Geochemical Mixing Targets at ER-OV-01 in the Reduced LCCU1 Permeability Alternative

Figure (a) shows the flow paths as mapped by forward SPTR particles originating at wells (grey lines) and the source recharge locations identified by reverse PTRK particle tracking (colored squares). Figure (b) shows the model comparison with geochemical mixing target ranges.

7.2.4 ER-OV-05

Well ER-OV-05 is in Oasis Valley near the western boundary of the model. The geochemistry and flow model simulations are consistent with each other, indicating the source of water found at the well is entirely from the northwest quadrant of the model domain (Table 7-5; Figures 7-17 and 7-18).

Table 7-5
Fractions of Groundwater from Various Upgradient Wells Present in Groundwater at Well ER-OV-05

Mixing Component	Model 2 Mean (Min, Max)
USAF Tolicha Peak	0.720 (0.717, 0.726)
Cedar Pass Well	0.000
ER-EC-4	0.280 (0.274, 0.283)
UE-29a #2	0.000

Table 7 from Kwicklis et al. (2005). Note: To obtain convergent models for this set of wells, it was necessary to increase the uncertainty tolerance on aluminum to 0.0001 moles/L or approximately 2.6 mg/L. Belted Range aquifer minerals from Table 2 were used for this set of models. Shallow groundwater from Well UE-29a #2 was used to represent local recharge. Only Model 2 from Kwicklis et al. (2005) is considered here. Model 1 is less certain due to the Cedar Pass water component, which cannot be accurately assigned to a specific zone in this domain. However, if it is assumed that Cedar Pass water enters this model domain on the western half of the northern boundary, then the two models are virtually identical.

There is virtually no difference between BN-MME-SDA and the LCCU1 alternative. It is interesting to note that the water of Tolicha Peak well and ER-OV-05 are nearly identical in chemical composition. In the geochemical mixing model, this water is also nearly a perfect mix of local recharge-type water (UE-29a #2) and ER-EC-1 water. Thus, this suggests an even split of local recharge in the northwest and flow into the model across the western half of the northern boundary.

7.2.5 ER-OV-04a

The geochemistry of ER-OV-04a, south and a little east of ER-OV-05, indicates a reduced component of the source originating in the northwest and increasing components from the north-central and northeast zones (Table 7-6). The BN-MME-SDA and the reduced LCCU1 permeability alternative flow model simulations follow this trend, as shown in Figures 7-19 and 7-20.

In the BN-MME-SDA model, the simulated northwest component is just slightly above its target, and the simulated fractions of the mixed water from the north central and northeast are at the low ends of the ranges suggested by the geochemistry. Most interesting is that there is a 9 percent contribution

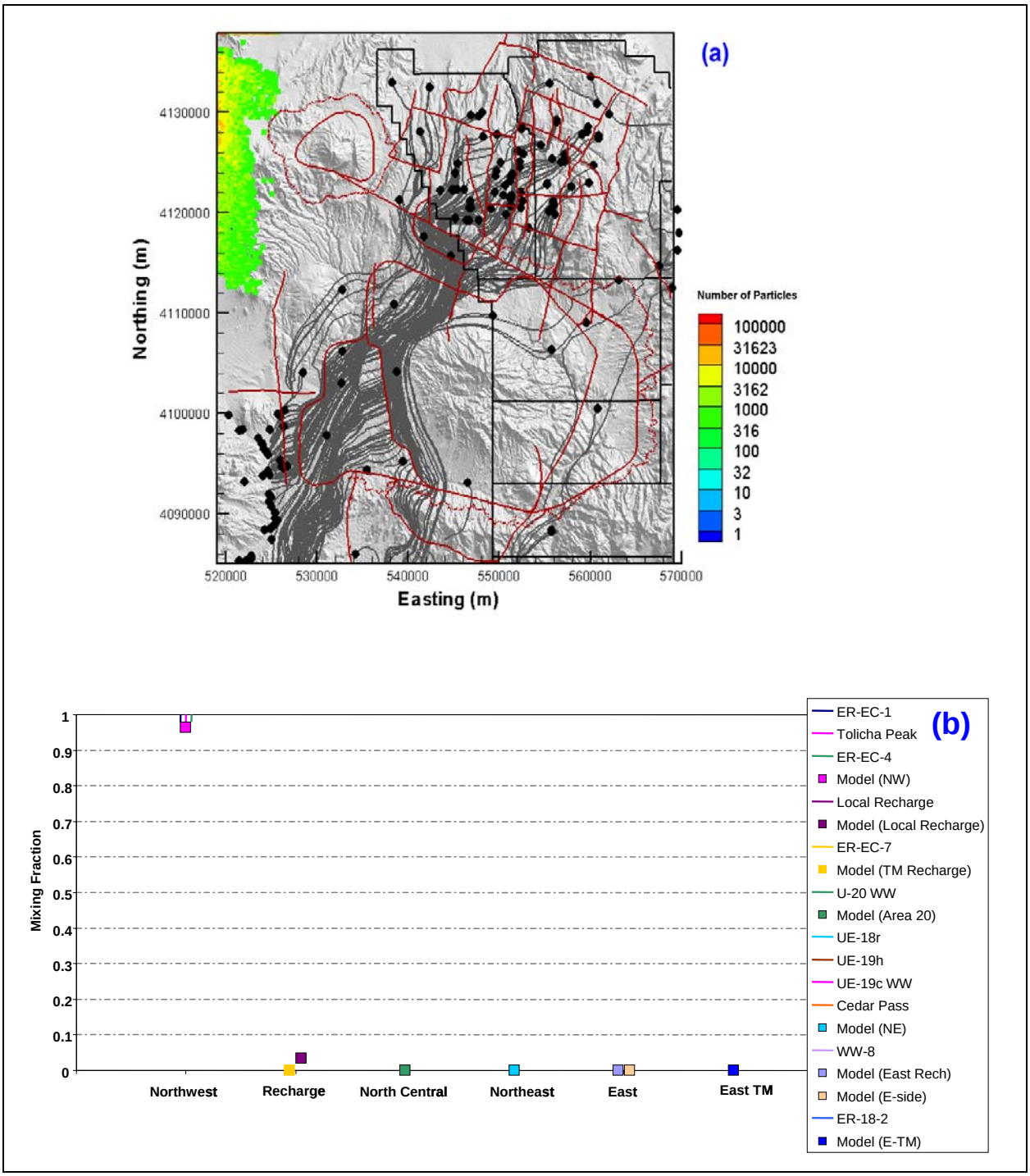

Figure 7-17
Comparison of Flow Model with Geochemical Mixing Targets at ER-OV-05 for BN-MME-SDA

Figure (a) shows the flow paths as mapped by forward SPTR particles originating at wells (grey lines) and the source recharge locations identified by reverse PTRK particle tracking (colored squares). Figure (b) shows the model comparison with geochemical mixing target ranges.

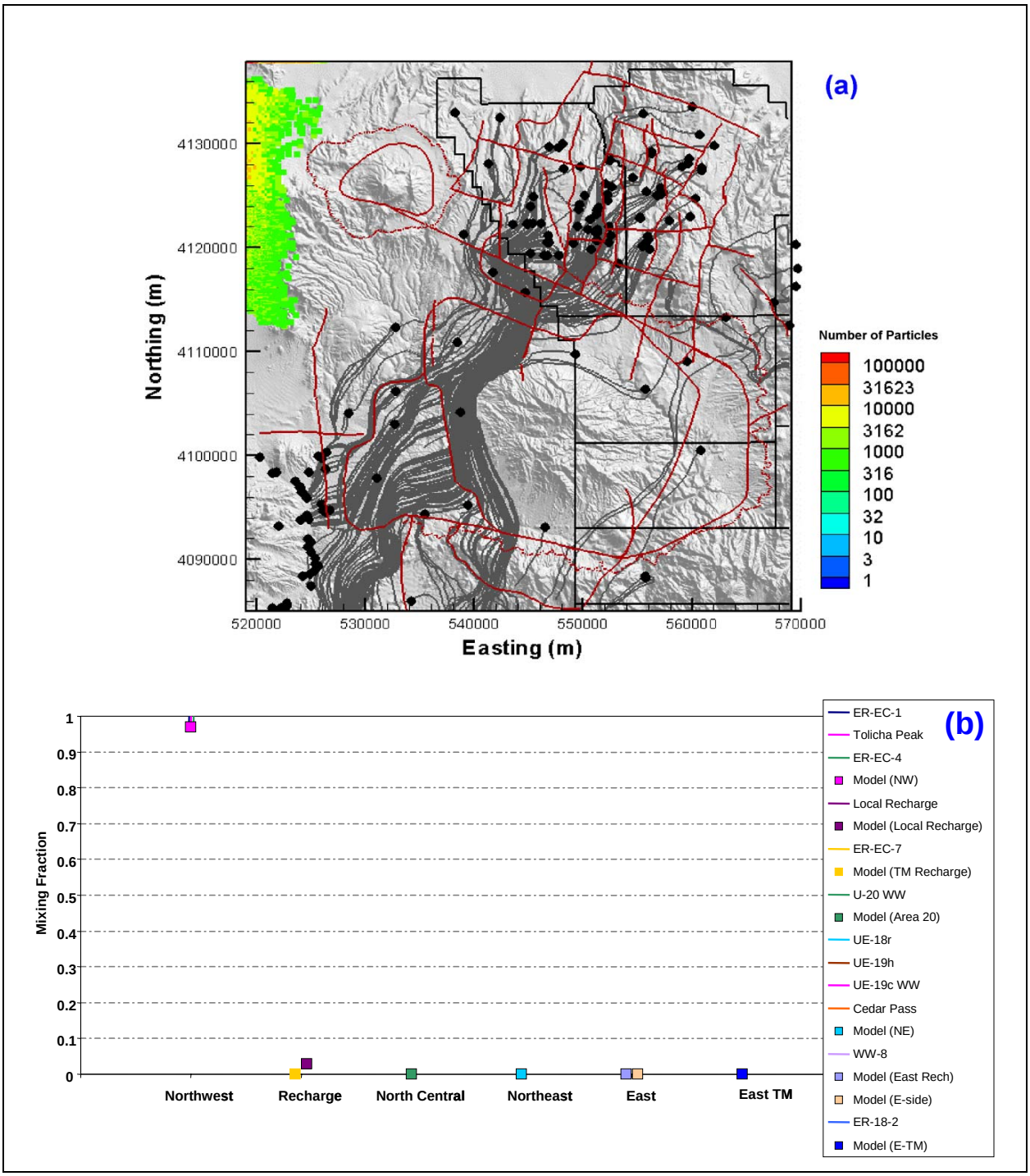

Figure 7-18
Comparison of Flow Model with Geochemical Mixing Targets at ER-OV-05 in the Reduced LCCU1 Permeability Alternative

Figure (a) shows the flow paths as mapped by forward SPTR particles originating at wells (grey lines) and the source recharge locations identified by reverse PTRK particle tracking (colored squares). Figure (b) shows the model comparison with geochemical mixing target ranges.

Table 7-6
Fractions of Groundwater from Various Upgradient Wells Present in Groundwater at Well ER-OV-04a

Mixing Component	Minimum Fraction	Maximum Fraction
U-20 WW	0.219	0.419
ER-EC-1	0.145	0.253
UE-18r	0.280	0.455
USAF Tolicha Peak	0.000	0.113
Cedar Pass Well	0.000	0.071
ER-EC-4	0.000	0.070
UE-29a #2	0.000	0.129

Table 23 from Kwicklis et al. (2005). Note: Timber Mountain Aquifer minerals from Table 2 were used for this set of models. Shallow groundwater from Well UE-29a #2 was used to represent local recharge. Note that the minimum fractions for the components from USAF Tolicha Peak, Cedar Pass and ER-EC-4 wells were determined by noting that the minimum contribution from Well ER-OV-05 in Table 13 is 0.00. The maximum component for these wells in Table 22 was determined by multiplying their maximum contributions in Table 7 by the maximum ER-OV-05 component in Table 13 (0.156). The UE-29a #2 contribution in Table 13 was augmented by 0.076 based on similar reasoning.

from inflow across the eastern boundary. Figure 7-19 shows that this inflow comes into the model at the high boundary head zone at Gold Meadows. Thus, the inflow that dominated the UE-18r water type in the base-case model is now showing up again in the southwest portion of the domain.

In the reduced LCCU1 permeability alternative, the low LCCU1 permeability reduces inflow to the model on the eastern boundary at Gold Meadows. The result at ER-OV-04a, by comparison to BN-MME-SDA results, is that there is a slight increase in northwest inflow contribution to the mixing ratio and a reduction in east boundary inflow. Comparison of Figures 7-19 and 7-20 along the eastern boundary clearly shows the location of high inflow for the base model.

Considering the complexity of flow paths and distances from source zones, the trend for either model, as compared with ER-OV-05 and ER-OV-03a, is encouraging in that the flow model results tend to track the changes suggested by the geochemistry in different areas of the model domain.

7.2.6 ER-OV-03a

Well ER-OV-03a is in lower Beatty Wash, east of ER-OV-03a, north of ER-OV-04a, and east of ER-OV-05; relative to groundwater at ER-OV-05, its source water as estimated by Kwicklis et al.

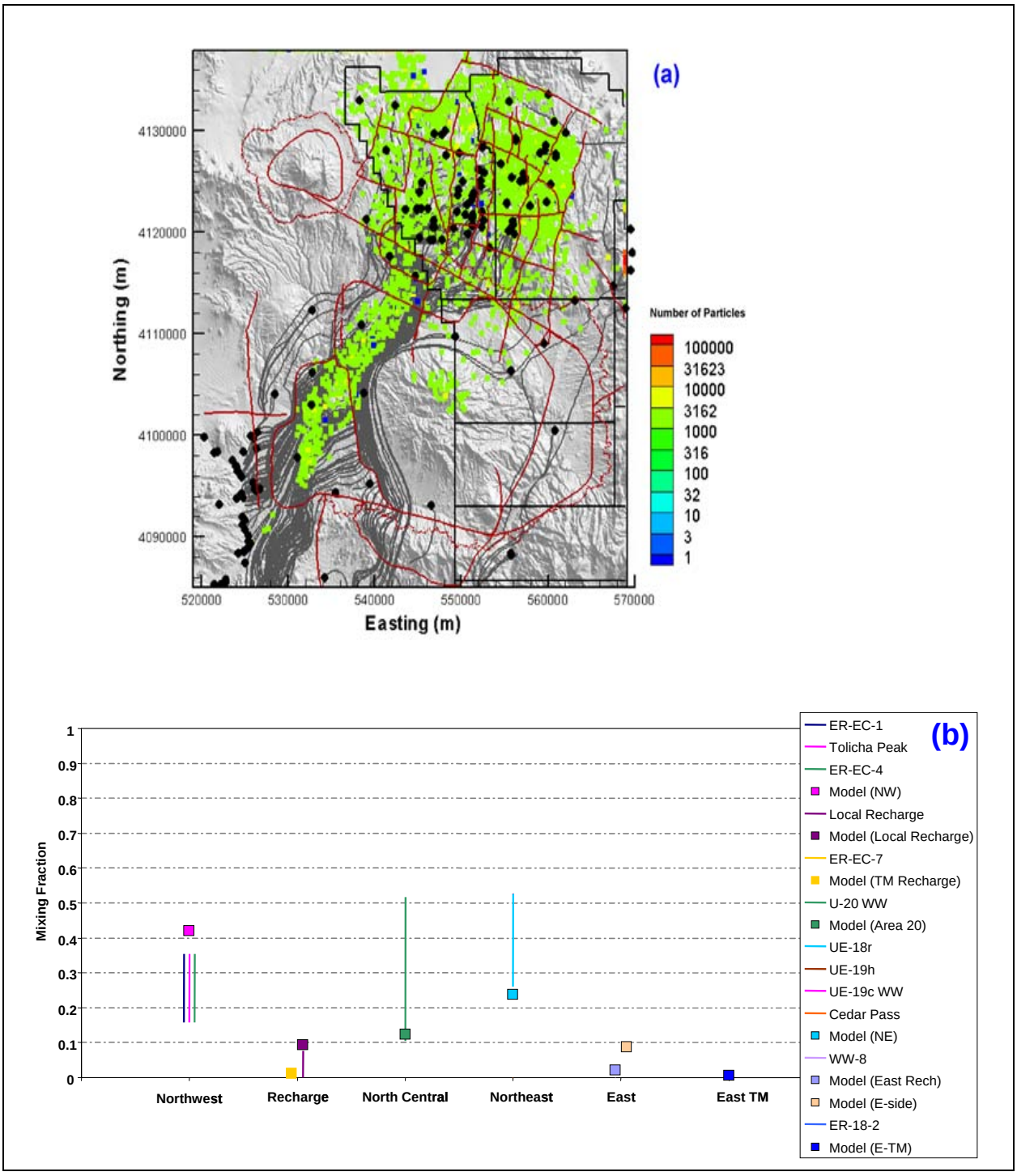

Figure 7-19
Comparison of Flow Model with Geochemical Mixing Targets at ER-OV-04a for BN-MME-SDA

Figure (a) shows the flow paths as mapped by forward SPTR particles originating at wells (grey lines) and the source recharge locations identified by reverse PTRK particle tracking (colored squares). Figure (b) shows the model comparison with geochemical mixing target ranges.

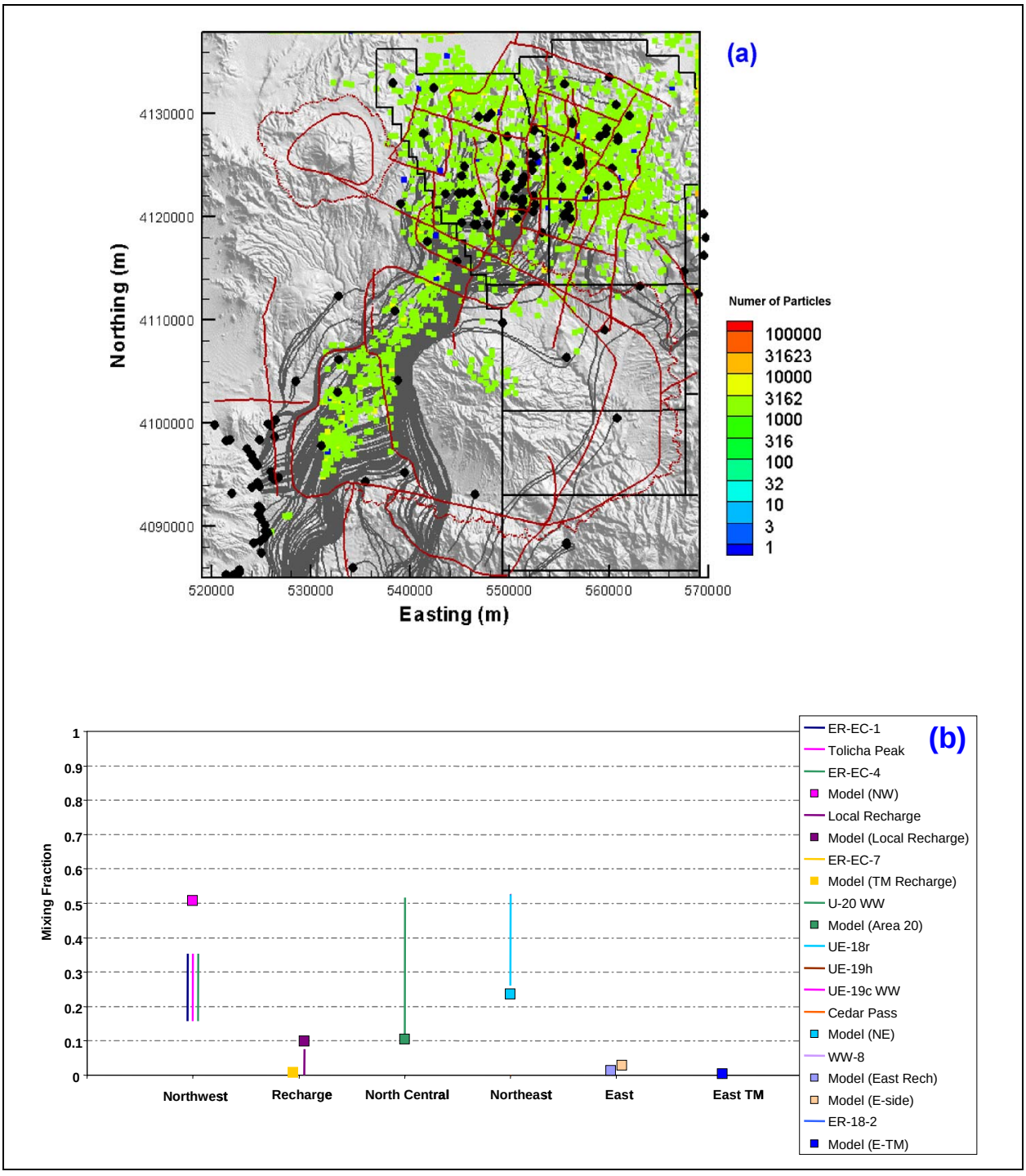

Figure 7-20
Comparison of Flow Model with Geochemical Mixing Targets at ER-OV-04a in the Reduced LCCU1 Permeability Alternative

Figure (a) shows the flow paths as mapped by forward SPTR particles originating at wells (grey lines) and the source recharge locations identified by reverse PTRK particle tracking (colored squares). Figure (b) shows the model comparison with geochemical mixing target ranges.

(2005) includes decreasing components from the northwest and increasing components from north-central and northeast Pahute Mesa (Table 7-7). The base-case flow model captures this change, with source fractions generally within the ranges estimated in the geochemistry analysis (Figure 7-21). As the source component from the northwest decreases in the simulations, the source component from the north-central and northeast zones increases. The only discrepancies between the flow model and the geochemistry for ER-OV-03a are that (a) the flow model estimates a slightly larger fraction of local recharge, as can be seen in the cluster of yellow exit counts in the reverse-particle-tracking figure, and (b) there is a small (less than 5 percent) contribution from the eastern model boundary at Gold Meadows. The component of recharge source is consistent with the specified local recharge flux in the MME map (Figure 4-14), and can be compared with results using different recharge maps later in this section. The east boundary source (Gold Meadows) is small but persistent and geochemically unexplainable.

Table 7-7
Fractions of Groundwater from Various Upgradient Wells Present in Groundwater at Well ER-OV-03a

Mixing Component	Minimum Fraction	Maximum Fraction
U-20 WW	0.000	0.482
UE-19h	0.145	0.648
ER-EC-1	0.289	0.469
UE-29a #2	0.000	0.081

Table 4 from Kwicklis et al. (2005). Note: Paintbrush Aquifer minerals from Table 2 were used for this set of models. Shallow groundwater from Well UE-29a #2 was used to represent local recharge.

The LCCU1 alternative (Figure 7-22) shows some interesting differences when compared to the base case. The small contribution from the eastern boundary to ER-OV-03a is gone in this model. Surprisingly, however, the northwest contribution has decreased, too, and the local recharge component has increased. This highlights the local and large-scale complexities in these simulated flow systems. With less inflow from the east in the LCCU1 alternative model, there is less westward flow to "push" local recharge away from ER-OV-03a, resulting in the increased local recharge component. Examination of the flow pathlines (grey) in the two figures shows the differences in flow direction relative to the same sources in these two models.

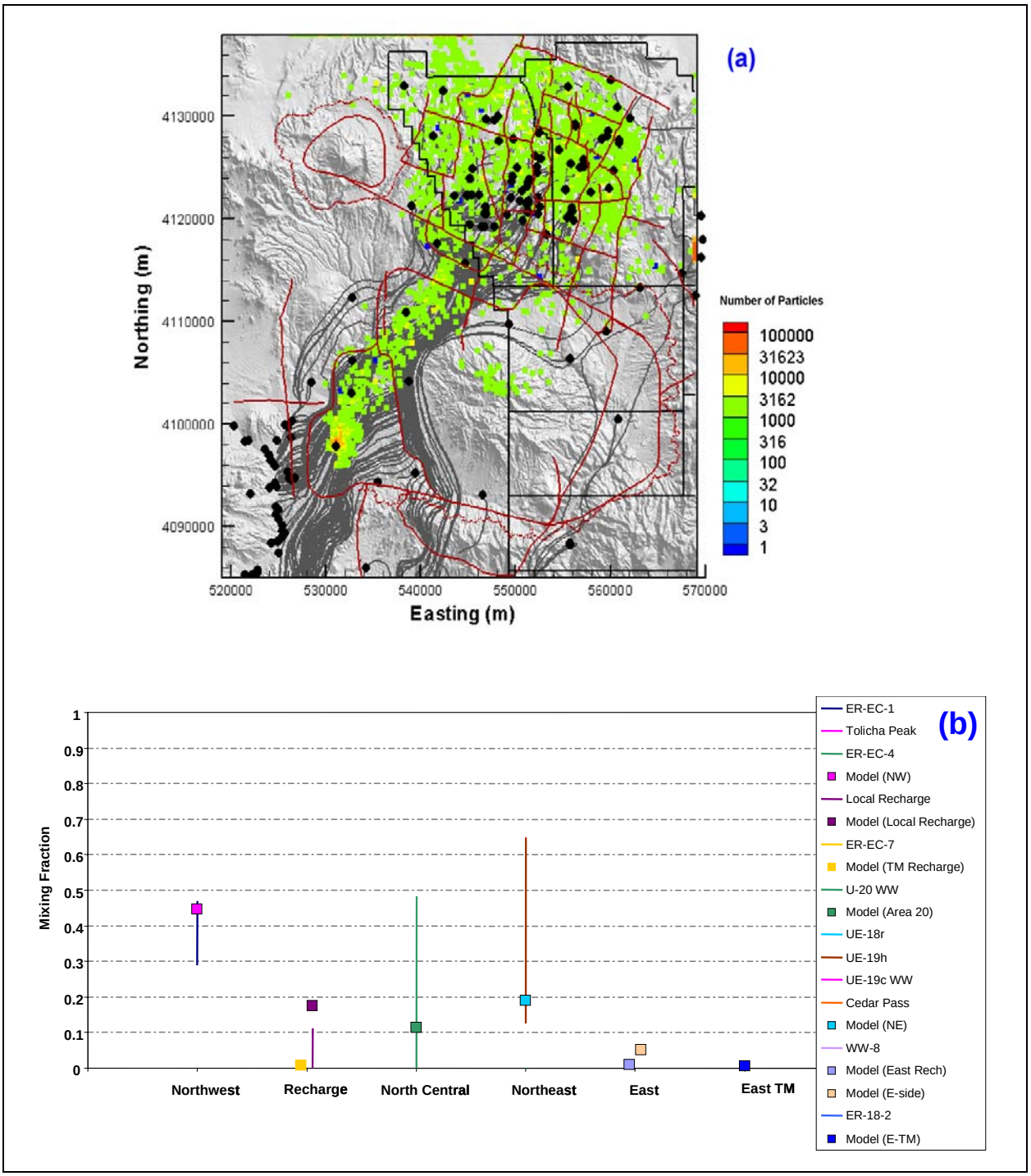

Figure 7-21
Comparison of Flow Model with Geochemical Mixing Targets at ER-OV-03a for BN-MME-SDA

Figure (a) shows the flow paths as mapped by forward SPTR particles originating at wells (grey lines) and the source recharge locations identified by reverse PTRK particle tracking (colored squares). Figure (b) shows the model comparison with geochemical mixing target ranges.

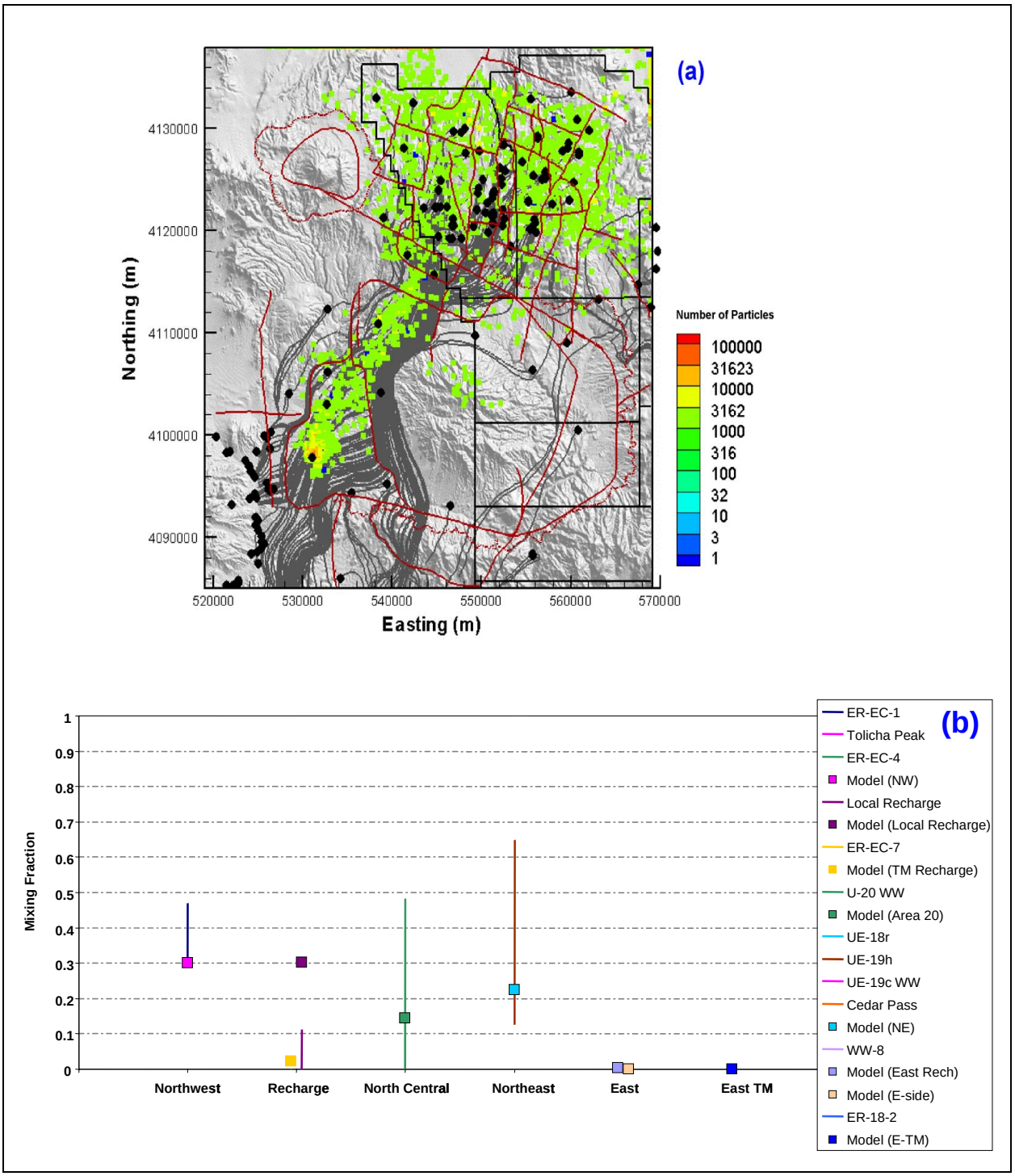

Figure 7-22
Comparison of Flow Model with Geochemical Mixing Targets at ER-OV-03a in the Reduced LCCU1 Permeability Alternative

Figure (a) shows the flow paths as mapped by forward SPTR particles originating at wells (grey lines) and the source recharge locations identified by reverse PTRK particle tracking (colored squares). Figure (b) shows the model comparison with geochemical mixing target ranges.

7.2.7 ER-OV-03c

Moving further east toward Timber Mountain, Well ER-OV-03c is in lower Beatty Wash. By comparison with the three previous wells, the geochemical analysis suggests a decreasing component of groundwater from the northwest, the appearance of a small amount of Timber Mountain recharge, some local recharge in the wash, and increasing source contributions from north-central and northeast Pahute Mesa (Table 7-8). As the geochemical interpretations indicate the presence of a larger groundwater component from the northeast, so does the simulation trend (Figure 7-23). However, the base-case model (a) substantially overpredicts local recharge from Beatty Wash, (b) underpredicts contributions from the northeast, and (c) has about a 15 percent contribution from the east boundary at Gold Meadows. With regard to (a), the model is consistent with the recharge map for this base case, which prescribes a considerable recharge flux into the model in the wash.

Table 7-8
Fractions of Groundwater from Various Upgradient Wells Present in Groundwater at Well ER-OV-03c, Including Sources for Groundwater at ER-EC-5

Mixing Component	Minimum Fraction	Maximum Fraction
ER-EC-1	0.054	0.157
U-20 WW	0.000	0.568
UE-18r	0.292	0.736
ER-EC-7	0.000	0.086
UE-29a #2	0.047	0.113

Table 11 from Kwicklis et al. (2005). Note: The uncertainty tolerance for aluminum was set to 0.00002 moles/kg or about 1 mg/L to reduce convergence problems. Timber Mountain aquifer minerals from Table 2 were used for this set of models. Shallow groundwater from Well UE-29a #2 was used to represent local recharge.

The reduced LCCU1 permeability alternative (Figure 7-24) shows good improvement on all three discrepancies listed for BN-MME-SDA listed above. The local recharge component is reduced from more than 40 percent to less than 30 percent. The northeast contribution increases to within the target range, and the east boundary contribution reduces to less than 3 percent. Further, the northwest component increases to the middle of the target range. Thus, for Well ER-EC-3c, the LCCU1 alternative appears to provide better matches to the targets than BN-MME-SDA.

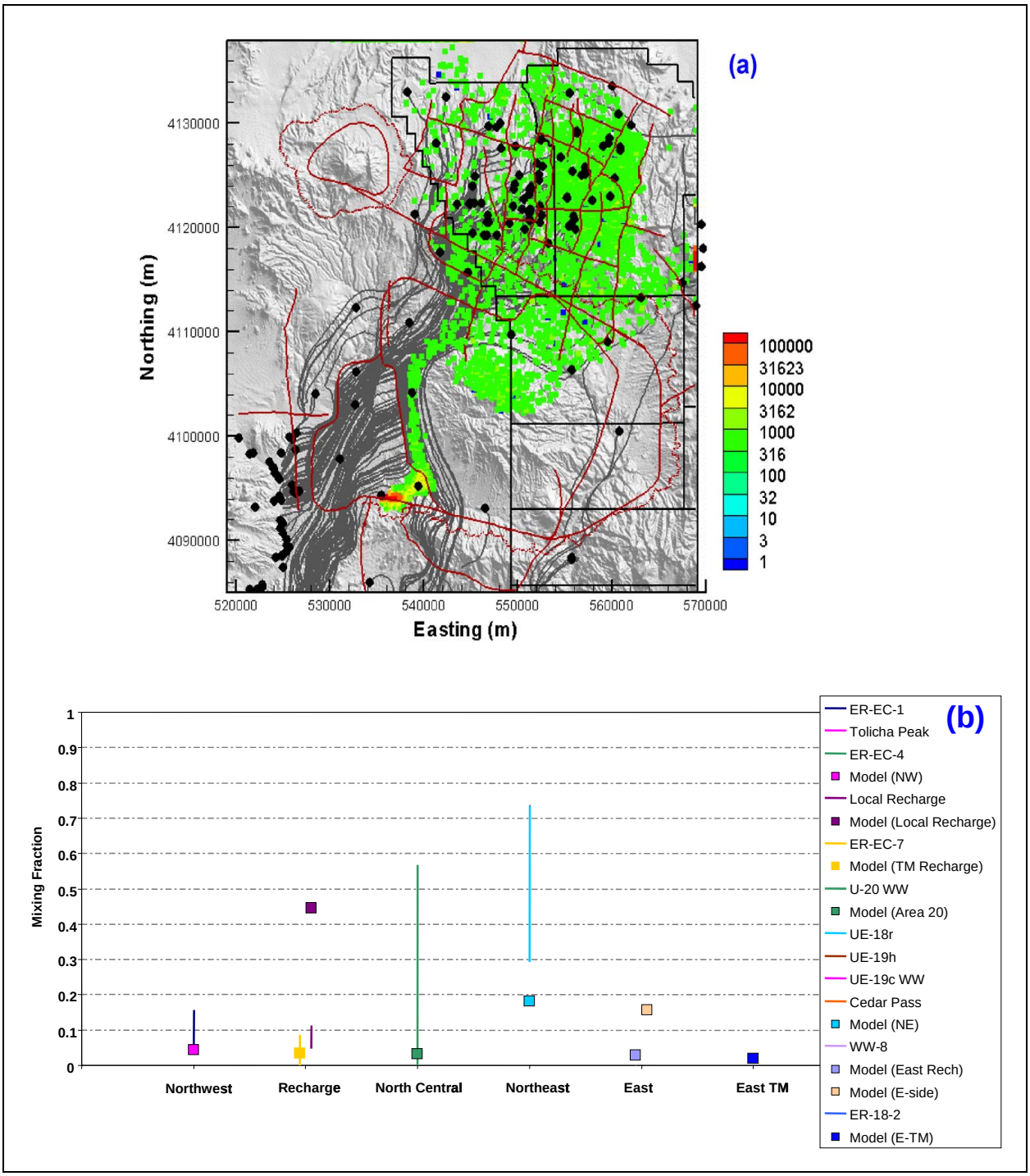

Figure 7-23
Comparison of Flow Model with Geochemical Mixing Targets at ER-OV-03c for BN-MME-SDA

Figure (a) shows the flow paths as mapped by forward SPTR particles originating at wells (grey lines) and the source recharge locations identified by reverse PTRK particle tracking (colored squares). Figure (b) shows the model comparison with geochemical mixing target ranges.

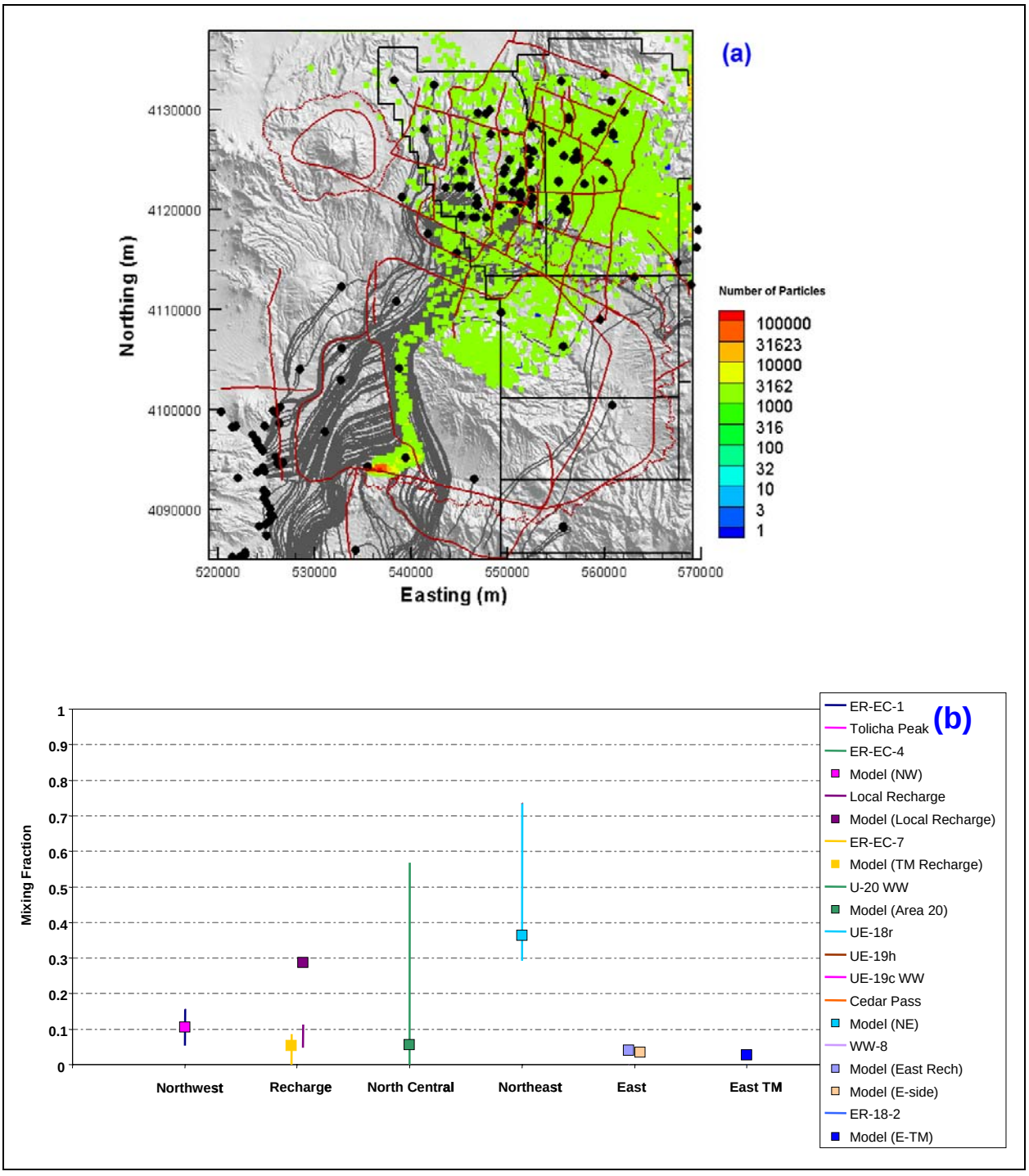

Figure 7-24
Comparison of Flow Model with Geochemical Mixing Targets at ER-OV-03c in the Reduced LCCU1 Permeability Alternative

Figure (a) shows the flow paths as mapped by forward SPTR particles originating at wells (grey lines) and the source recharge locations identified by reverse PTRK particle tracking (colored squares). Figure (b) shows the model comparison with geochemical mixing target ranges.

7.2.8 Coffer Windmill Well

Moving yet further east, the Coffer Windmill Well is on the southwest flank of Timber Mountain. Compared to nearby ER-OV-03c, the geochemical analysis suggests a marked difference in the source of water (Table 7-9). Not surprisingly, the component from Timber Mountain recharge can

Table 7-9
Fractions of Groundwater from Various Upgradient Wells Present in Groundwater at the Coffer Windmill Well

Mixing Component	Minimum Fraction	Maximum Fraction
UE-18r	0.000	0.357
ER-18-2	0.000	0.157
WW-8	0.000	0.843
ER-EC-7	0.000	0.643
UE-29a #2	0.000	0.000

Table 21 from Kwicklis et al. (2005). Note: Timber Mountain minerals from Table 2 were used for this set of models. Shallow groundwater from Well UE-29a #2 represents local recharge from stream-channel runoff in these models.

increase (represented by ER-EC-7). The northwest and north-central source components vanish and the potential northeast component decreases slightly. However, there could be a component from the east (upper Fortymile Canyon), with a signature like that found in WW-8. The large ranges suggest that these different sources must swap for each other in the PHREEQC model, which is confirmed in Figure 7-25. One possibility is a mixture of WW-8 and ER-18-2 waters, suggesting significant flow from Rainier Mesa. This is the only geochemical target well showing a potential Rainier Mesa signature, if WW-8 represents flow into Fortymile Canyon from the east rather than from Pahute Mesa to the north. However, UE-18r waters (Pahute Mesa source) and local recharge from Timber Mountain are equally likely. The BN-MME-SDA model shows a result intermediate to the two end members. Most of the source water is from the northeast or from local recharge, but 20 percent is from the east boundary at Gold Meadows (Figure 7-26). The reduced LCCU1 permeability alternative produces a match similar to one of the end members with no contribution from WW-8-type water (Figure 7-27).

In both models, the recharge occurs near the well rather than from the top of Timber Mountain. The geochemical control is likely not sufficient to rule this out, but it is important to note that UE-29a #2

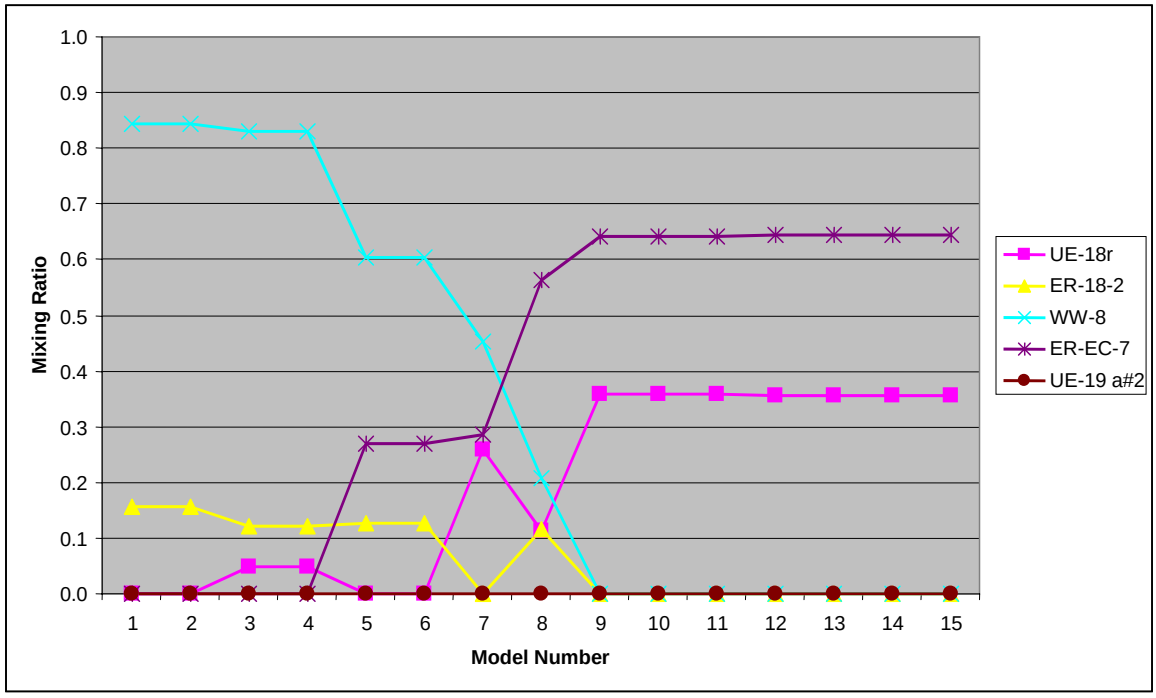

Figure 7-25
PHREEQC Models for Coffer Windmill Well

type water is not modeled to be present in the Coffer Windmill Well. The representative water for Timber Mountain is ER-EC-7, which could actually be a result of overland flow or interflow. Further, the MME map (Figure 4-14) explicitly redistributes water into washes and canyons. Thus, it is not surprising to have water from Timber Mountain recharging in the washes on the flanks in the simulation. The simulated northwest component of water at Coffer Windmill Well enters the model across the northern boundary. Its presence may be indicative of high inflows along that boundary resulting from the head boundary condition there.

The BN-MME-SDA model has a non-trivial component from Gold Meadows and has a large (38 percent) contribution from local recharge in washes instead of the top of Timber Mountain. The reduced LCCU1 permeability alternative model slightly overestimates the contribution from the northeast, has a large (25 percent) contribution from local recharge in washes instead from the top of Timber Mountain, and has an 11 percent contribution from the northwest, the latter of which is inconsistent with the geochemistry.

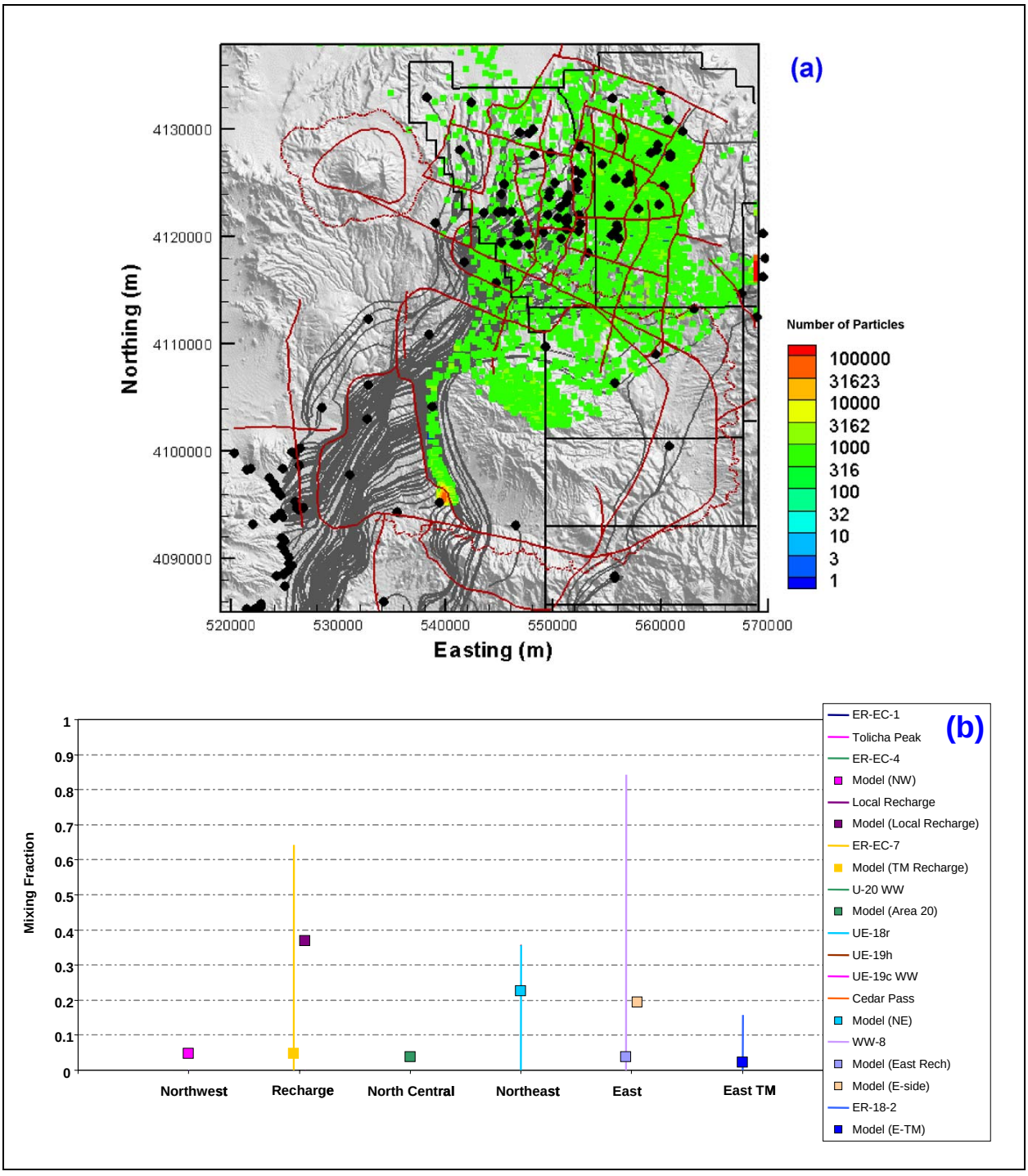

Figure 7-26
Comparison of Flow Model with Geochemical Mixing Targets at Coffer Windmill Well for BN-MME-SDA

Figure (a) shows the flow paths as mapped by forward SPTR particles originating at wells (grey lines) and the source recharge locations identified by reverse PTRK particle tracking (colored squares). Figure (b) shows the model comparison with geochemical mixing target ranges.

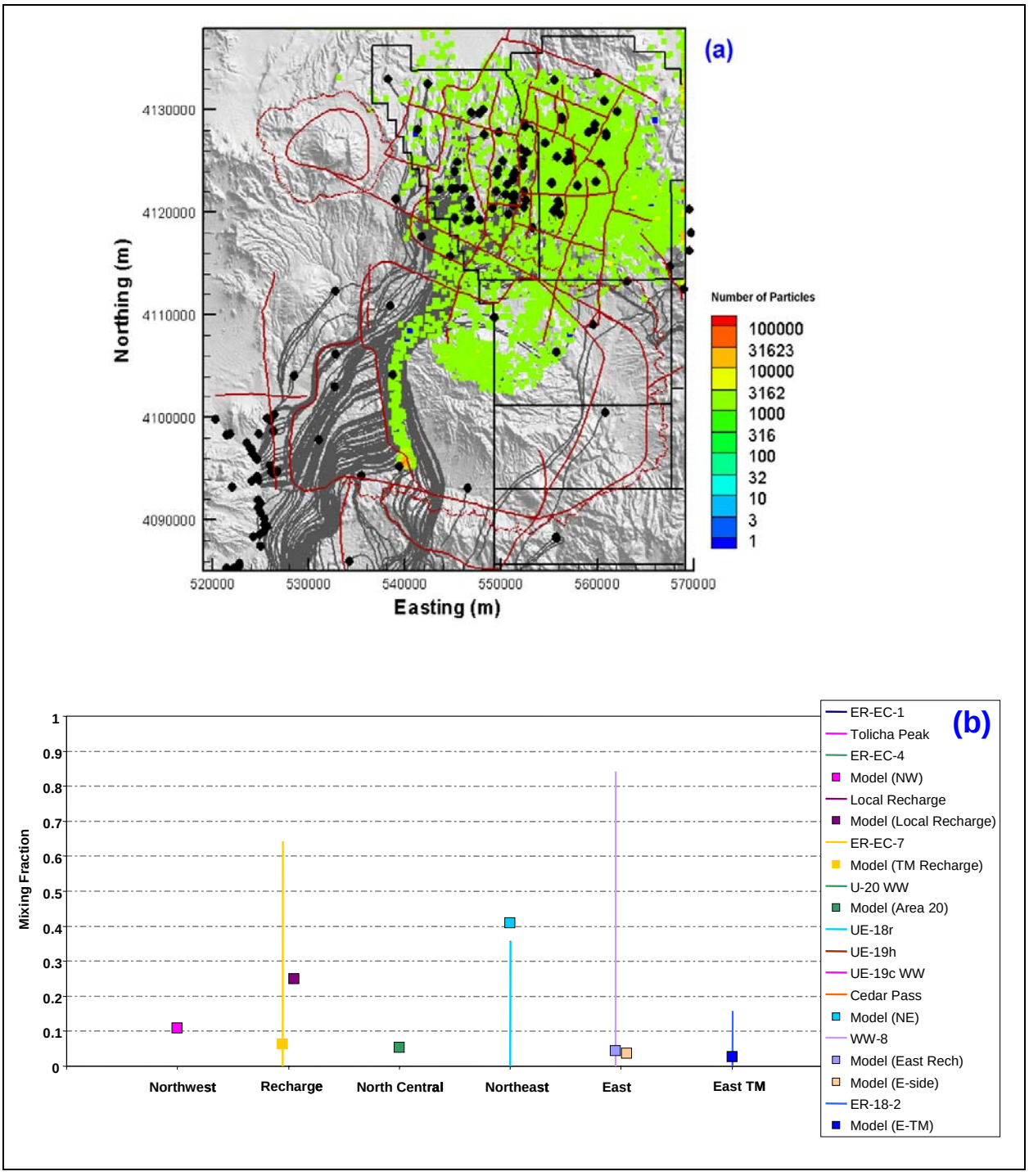

Figure 7-27
Comparison of Flow Model with Geochemical Mixing Targets at Coffer Windmill Well in the Reduced LCCU1 Permeability Alternative

Figure (a) shows the flow paths as mapped by forward SPTR particles originating at wells (grey lines) and the source recharge locations identified by reverse PTRK particle tracking (colored squares). Figure (b) shows the model comparison with geochemical mixing target ranges.

7.3 Geochemical Verification Results: Comparing Alternative Uncertain Models

In this section, the geochemical verification approach is applied for calibrated models with alternative water-balance conditions and alternative HFMs. The two alternative water-balance conditions include (a) the USGSD recharge map and associated boundary flux targets and (b) the DRIA recharge map and associated boundary flux targets. These two alternatives are described in detail in Section 4.3.1.

The alternative HFMs evaluated include SCCC, PZUP, DRT, RIDGE, TCL, and SEPZ as described in Table 2-5. For purposes of comparison, these are evaluated with the MME recharge map and associated boundary flux targets. Alternative water-balance conditions are also evaluated for PZUP and DRT.

Each of the water-balance alternatives and HFM alternatives represent conceptual model uncertainty. Therefore, they are compared with each other and to the BN-MME-SDA results described in the previous section for each of the target geochemical mixing wells. In each case, the alternative water-balance condition results are shown first followed by the alternative HFM results. As in the previous section, the comparison follows a counterclockwise tracking of target wells within the model domain, starting with UE-18r. For each target well considered, the geochemical mixing targets are shown graphically with the model results. The tables from Kwicklis et al. (2005) from which the graphic results are based are presented for each well discussed in Section 7.2.

In this section, different models for which results are compared at each target well are listed in Table 7-10. With this many different flow models, the primary purpose of this subsection is to provide visual comparison of the different model behaviors at each of the seven target wells.

Table 7-10
Hydrostratigraphic Models and Water-Balance Conditions Evaluated with Respect to Chemical Mixing Targets

HFM and Parameterization	Water-Balance Condition
BN-SDA reduced LCCU1 permeability alternative	MME
	USGSD
	DRIA
BN-SDA	MME
	USGSD
	DRIA
BN-ADA	MME
SCCC-SDA	MME
	USGSD
	DRIA
PZUP	MME
DRT	MME
RIDGE	MME
TCL	MME
SEPZ	MME
PZUP	USGSD
	DRIA
DRT	USGSD
	DRIA

7.3.1 UE-18r

7.3.1.1 Alternative Water-Balance Conditions, BN HFM

Figures 7-28 and 7-29 show the model results for the recalibrated flow models using the USGSD and DRIA alternative recharge maps, respectively, on the base HFM with reduced LCCU1 permeability alternative. The difference at first looks substantial. However, the sources of water at UE-18r, as estimated with reverse particles, for these two different recharge maps are actually quite similar, as shown in part (b) of the two figures. Most water comes from southeast Area 19, where high recharge is specified. The remaining sources are from the eastern flank of Timber Mountain (Zone 16) and the eastern model boundary at Gold Meadows. Slightly more water at UE-18r comes from Gold Meadows in the USGSD model (10 percent) than in the DRIA model (6 percent), probably because the gradient into the BN-USGSD model is greater due to lower total recharge flux. However, all HSU permeabilities are recalibrated in each model, leading to complex flow paths. The total component from Zones 10 and 16 is about similar for both models.

By comparison, model results for the BN-SDA (higher LCCU1 permeability alternative) with the USGSD and DRIA water-balance conditions lead to only small contributions from recharge within the model domain and 75 to 90 percent flow contributions from Gold Meadows on the eastern model boundary, respectively (Figure 7-30). Finally, the BN-MME-ADA model (Figure 7-31) shows a nearly even split between recharge within the model domain and simulated boundary flow from Gold Meadows at UE-18r. Section 7.5 addresses the differences between model results and geochemical target ranges and uses them to quantitatively rank the different flow models.

7.3.1.2 SCCC Alternative HFM

For the MME water-balance conditions and the SCCC alternative HFM, Figure 7-32 shows the forward pathlines for particles originating at wells (grey), the reverse-particle exits (colored), and the zone comparison for the mixing ratios between the model and the geochemistry targets. This model is substantially different from the base HFM and water-balance alternatives presented earlier in this section. Here, the source of water at UE-18r is from central and northern Area 19, with no contribution from anywhere near the eastern model boundary. The result is a very good fit to the geochemistry targets. However, the small component resembling ER-18-2 water is missing. Well

ER-18-2 water, however, is difficult to categorize in this spatial analysis. It is located on the eastern flank of Timber Mountain, but its chemistry is that of a deep groundwater, possibly from the carbonate aquifer. It is not representative of modern recharge.

The reason for the prominent difference between the SCCC model and other models based on the BN HFM is that there is a much stronger north-to-south flow component in Area 19, leading to greater flows into upper Fortymile Canyon. The southeast flow paths away from UE-18r beg the question of whether sufficient Area 19 water will be simulated in southwest wells, which will be addressed sequentially in this section.

The USGSD and DRIA water-balance conditions were also applied in calibrations of the SCCC model. In both of these alternatives, an unexplainable large component of the UE-18r water is simulated to originate in the northwest; on the other side of the Purse Fault (Figure 7-33), such results are not supported by any chemical mixing models for UE-18r, making those models suspect.

7.3.1.3 PZUP, DRT, RIDGE, TCL, and SEPZ Alternative HFMs

The other alternative HFMs with MME water-balance conditions are considered in this section with the quantitative comparisons in Figures 7-34 through 7-36. These can be broken into two groups with regard to their results at UE-18r. In the first group, PZUP and DRT both provide good matches at UE-18r, with most water originating in Area 19 and less than 20 percent coming from Zones 6 and 16, essentially on the east flank of Timber Mountain. In both of these cases, the inflow from Gold Meadows is very small. In the second group, RIDGE, TCL, and SEPZ show the primary contribution at UE-18r coming from Gold Meadows (east model boundary) and virtually no source anywhere in Area 19 within the model domain. Flow models with substantial inflow to the model at Gold Meadows with a path directly to UE-18r represent unlikely groundwater flow pathways as determined by Kwicklis et al. (2005). The geochemical mismatches between the model and verification targets for Gold Meadows inflow are quantified as errors in Section 7.5.

Alternative water-balance models USGSD and DRIA were also considered for the PZUP and DRT HFMs (Figures 7-37 and 7-38). For the PZUP model, both water-balance alternatives led to significantly more Gold Meadows source water at UE-18r than is simulated with the MME water balance. For DRT, however, the USGSD water-balance produces nearly identical results to the MME

water-balance model. The DRIA water-balance model with the DRT HFM, interestingly, simulates a majority of the source water at UE-18r originating as recharge within the model domain, thus avoiding the Gold Meadows inflow errors.

7.3.1.4 Summary: UE-18r

The most important issue at UE-18r is whether the simulated source of groundwater is from recharge within the model domain or from the eastern model boundary at Gold Meadows. The geochemistry analysis of Kwicklis et al. (2005) indicates that it is improbable for the source of water at UE-18r to originate at Rainier Mesa, east of the model domain. Table 7-11 separates the models based on this specific indicator.

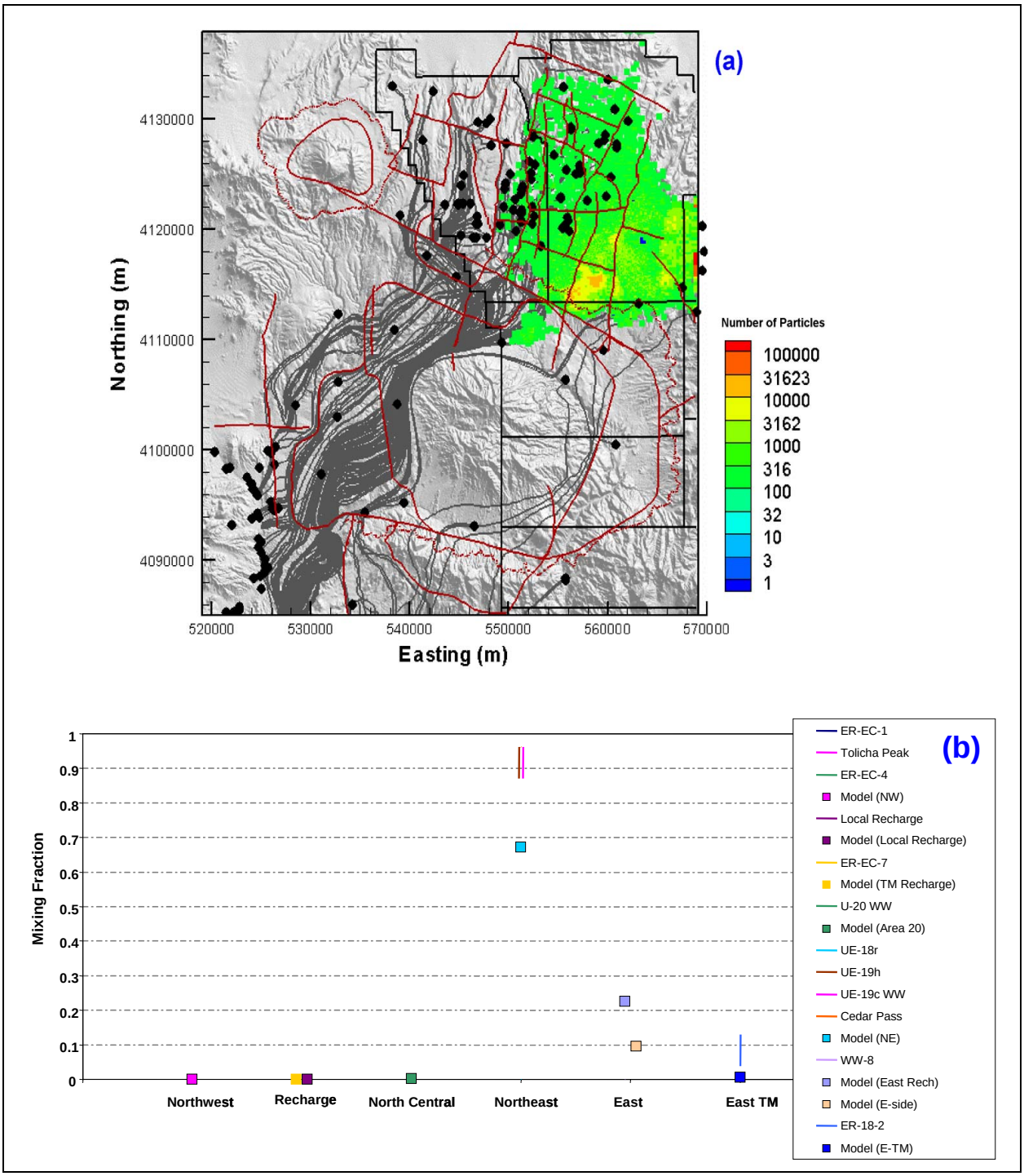

Figure 7-28
Comparison of Flow Model with Geochemical Mixing Targets at UE-18r for BN-USGSD-SDA in the Reduced LCCU1 Permeability Alternative

Figure (a) shows the flow paths as mapped by forward SPTR particles originating at wells (grey lines) and the source recharge locations identified by reverse PTRK particle tracking (colored squares). Figure (b) shows the model comparison with geochemical mixing target ranges.

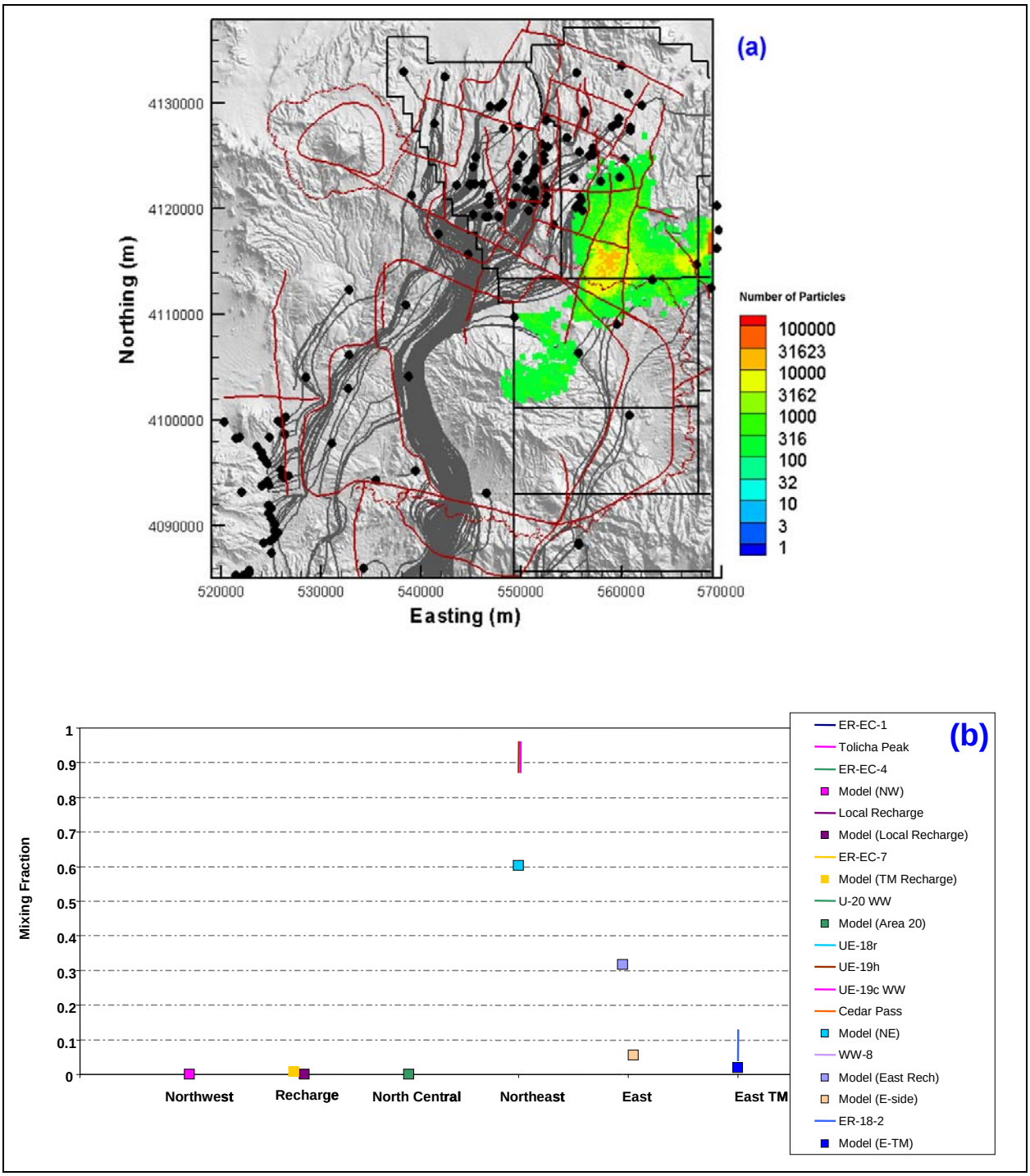

Figure 7-29
Comparison of Flow Model with Geochemical Mixing Targets for UE-18r for BN-DRIA-SDA in the Reduced LCCU1 Permeability Alternative

Figure (a) shows the flow paths as mapped by forward SPTR particles originating at wells (grey lines) and the source recharge locations identified by reverse PTRK particle tracking (colored squares). Figure (b) shows the model comparison with geochemical mixing target ranges.

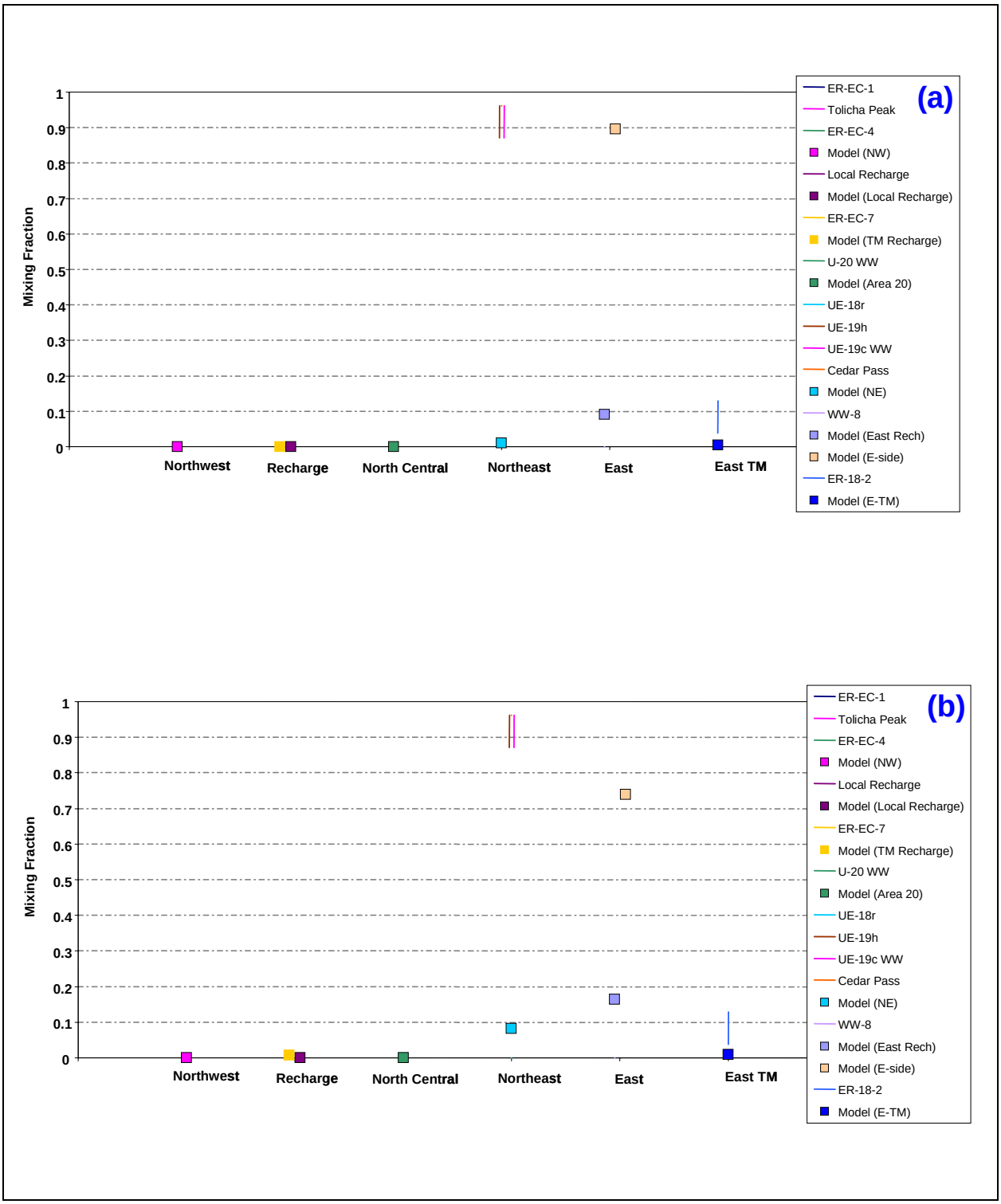

Figure 7-30
Quantitative Geochemical Comparison at UE-18r for (a) BN-USGSD-SDA and (b) BN-DRIA-SDA

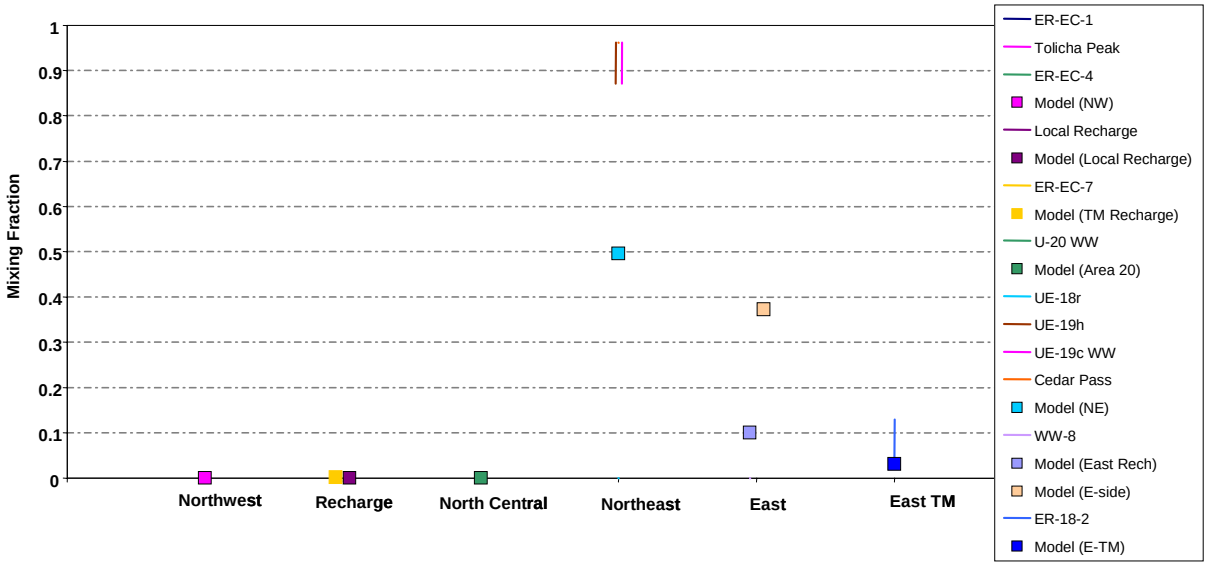

Figure 7-31
Comparison of Flow Model Geochemical Mixing Targets at UE-18r for BN-MME-ADA

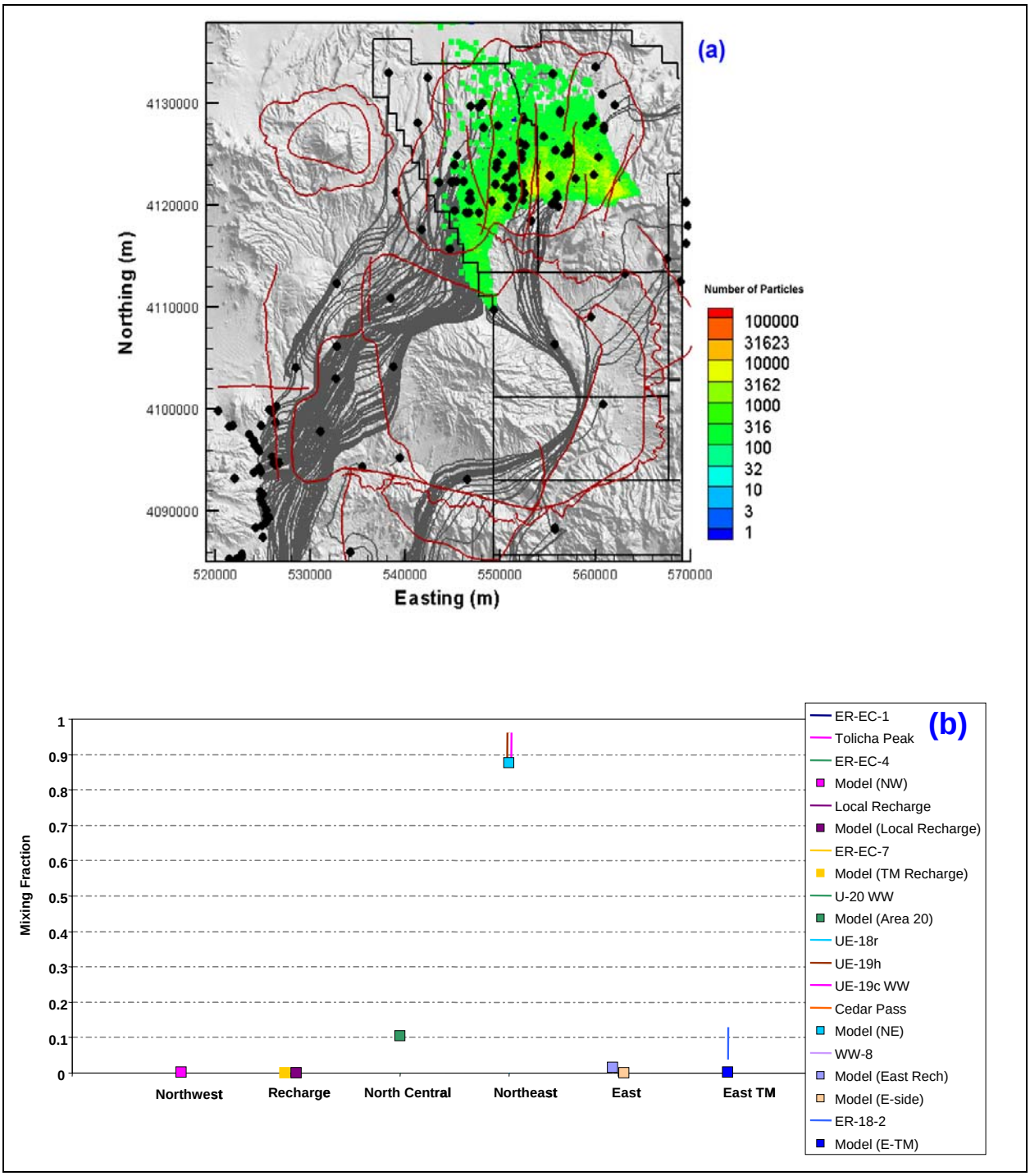

Figure 7-32
Comparison of Flow Model with Geochemical Mixing Targets at UE-18r for SCCC-MME-SDA

Figure (a) shows the flow paths as mapped by forward SPTR particles originating at wells (grey lines) and the source recharge locations identified by reverse PTRK particle tracking (colored squares). Figure (b) shows the model comparison with geochemical mixing target ranges.

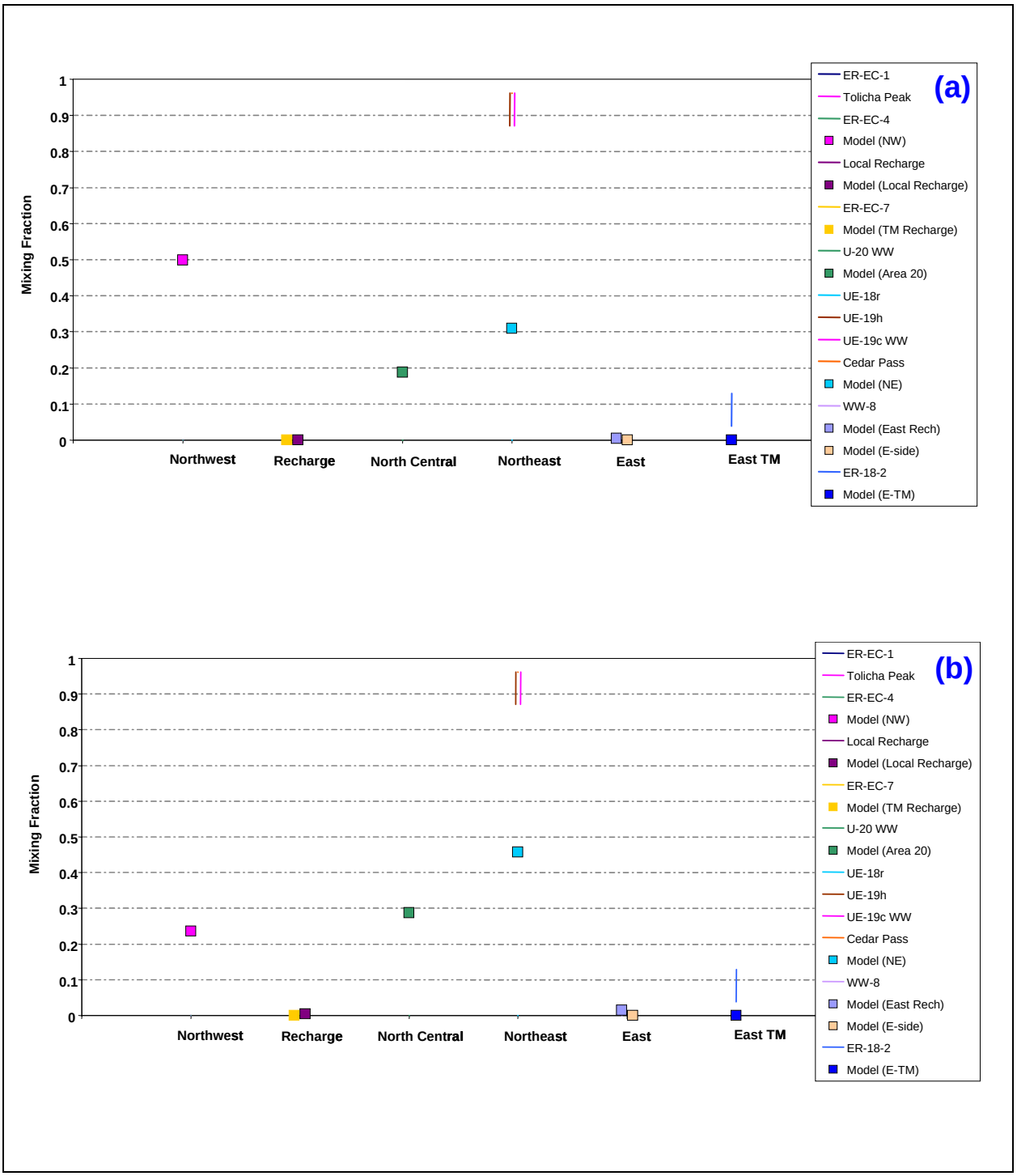

Figure 7-33
Quantitative Geochemical Comparisons at UE-18r for (a) SCCC-USGSD-SDA and (b) SCCC-DRIA-SDA

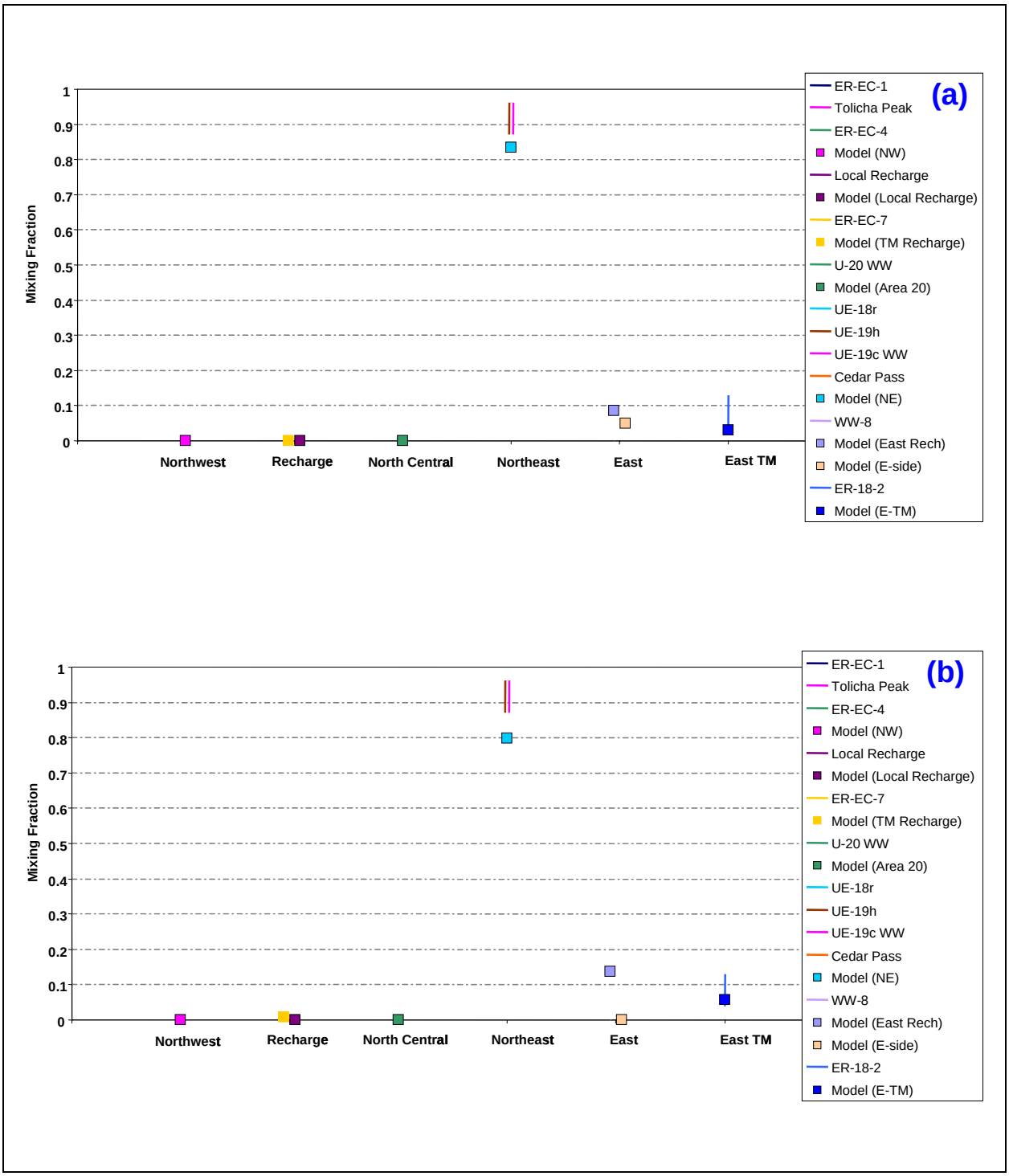

Figure 7-34
Quantitative Geochemical Comparisons at UE-18r for (a) PZUP-MME-SDA and (b) DRT-MME-SDA

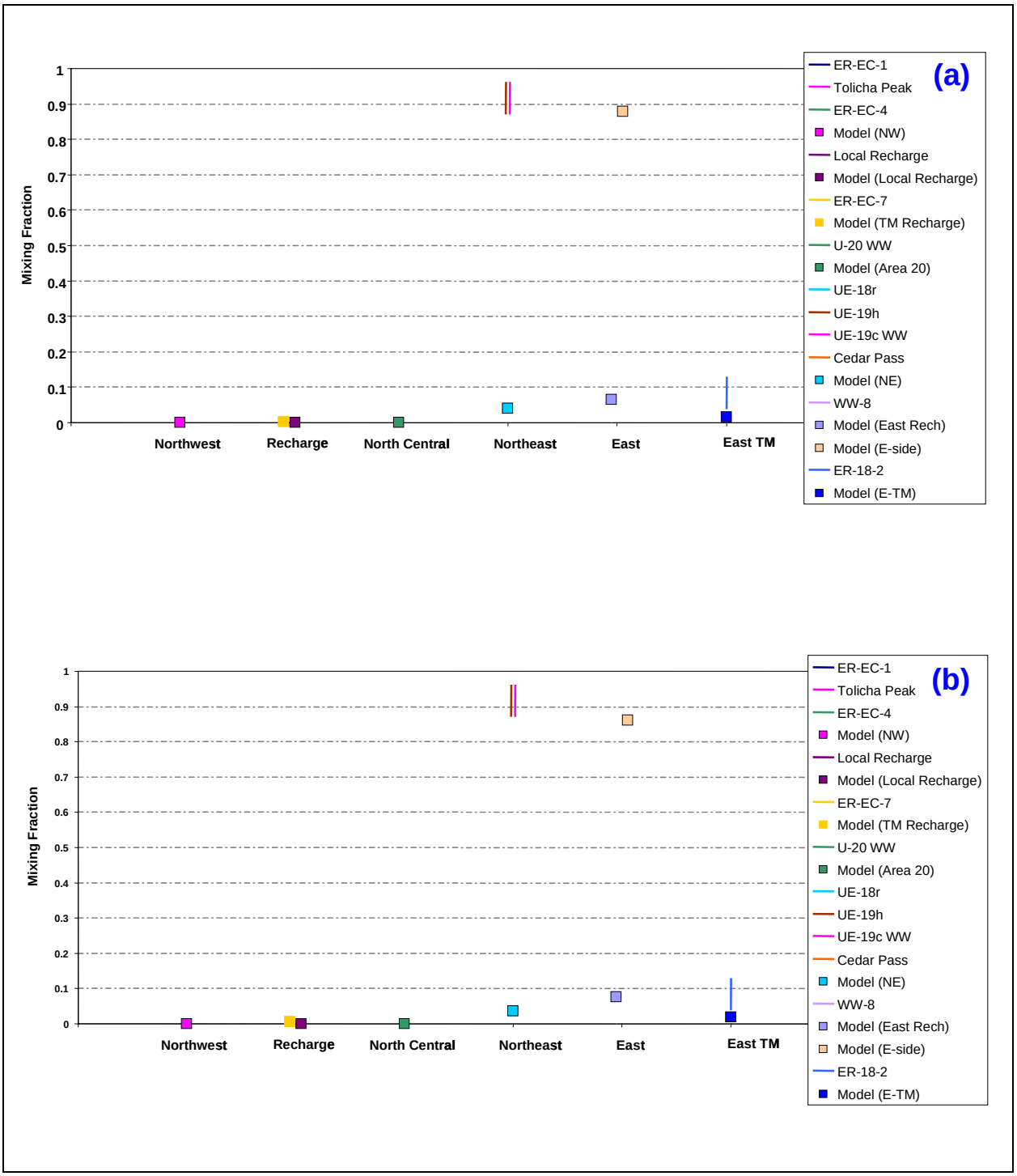

Figure 7-35
Quantitative Geochemical Comparisons at UE-18r for (a) RIDGE-MME-SDA and (b) TCL-MME-SDA

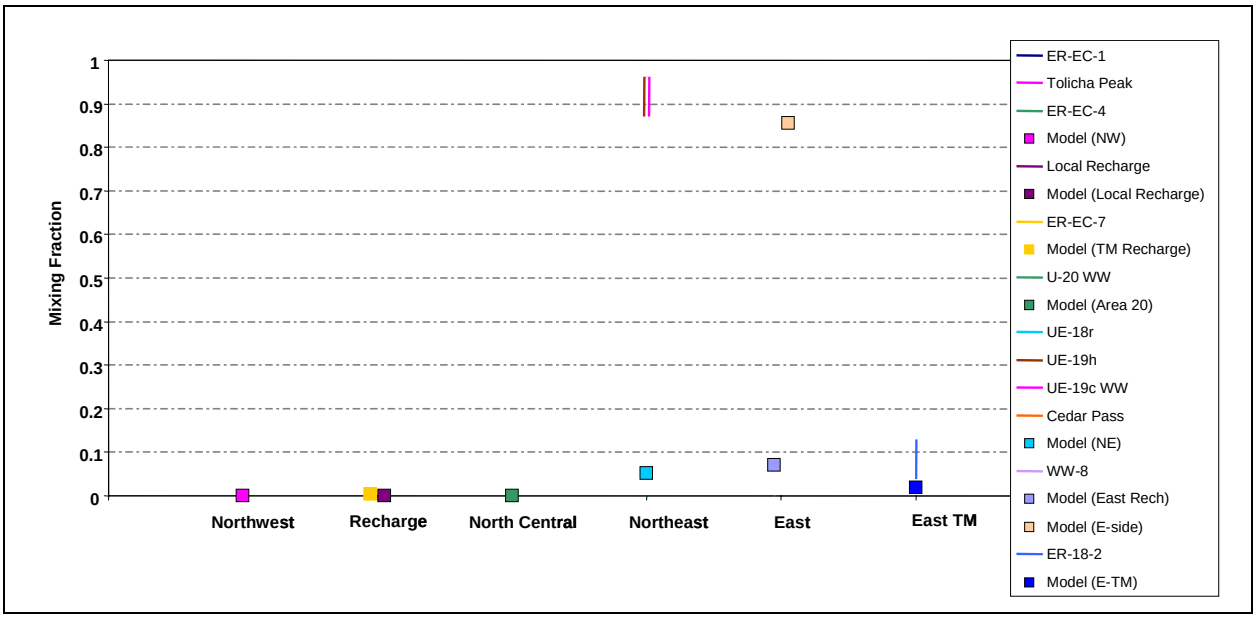

Figure 7-36
Quantitative Geochemical Comparison at UE-18r for SEPZ-MME-SDA

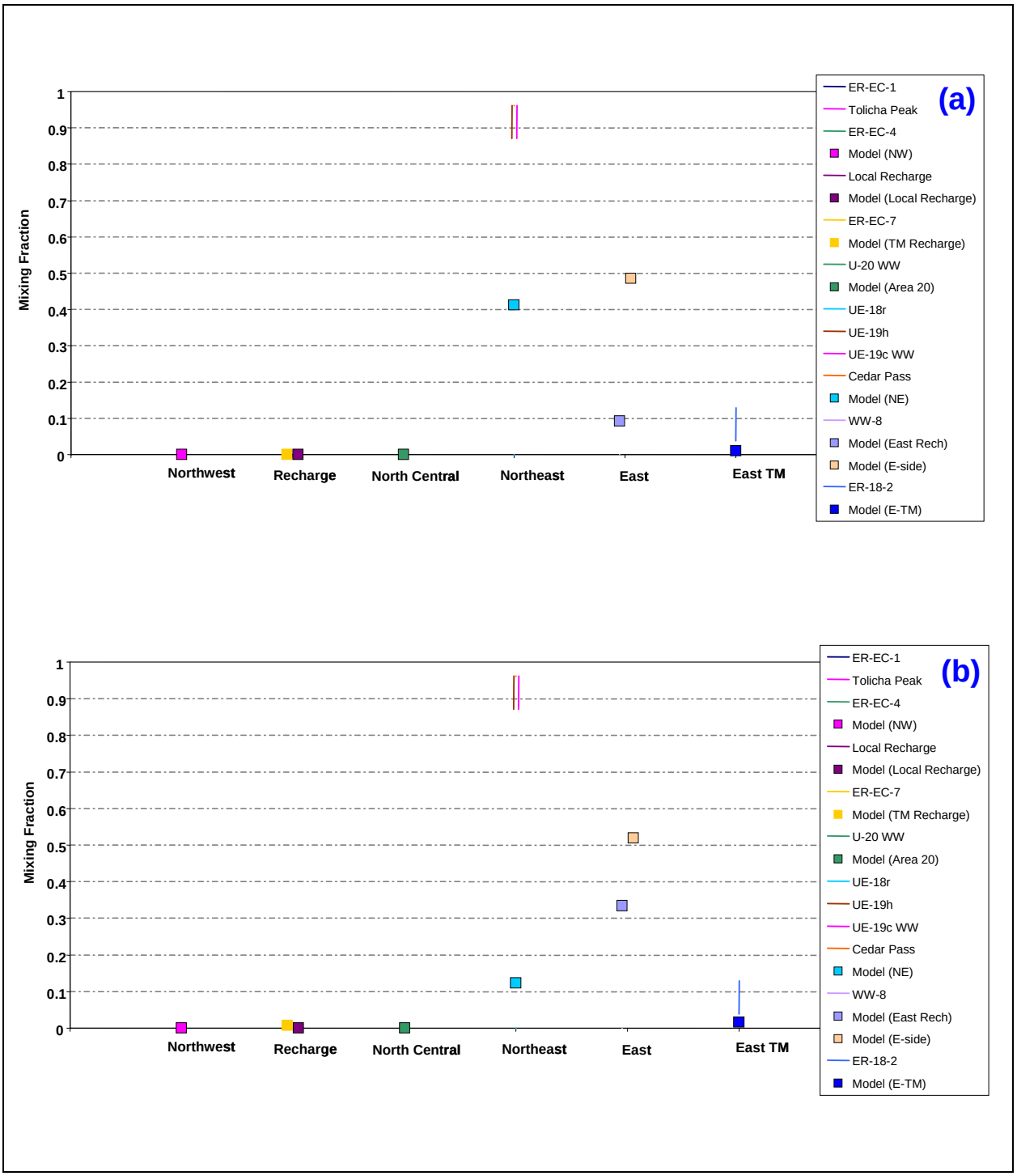

Figure 7-37
Quantitative Geochemical Comparisons at UE-18r for (a) PZUP-USGSD-SDA and (b) PZUP-DRIA-SDA

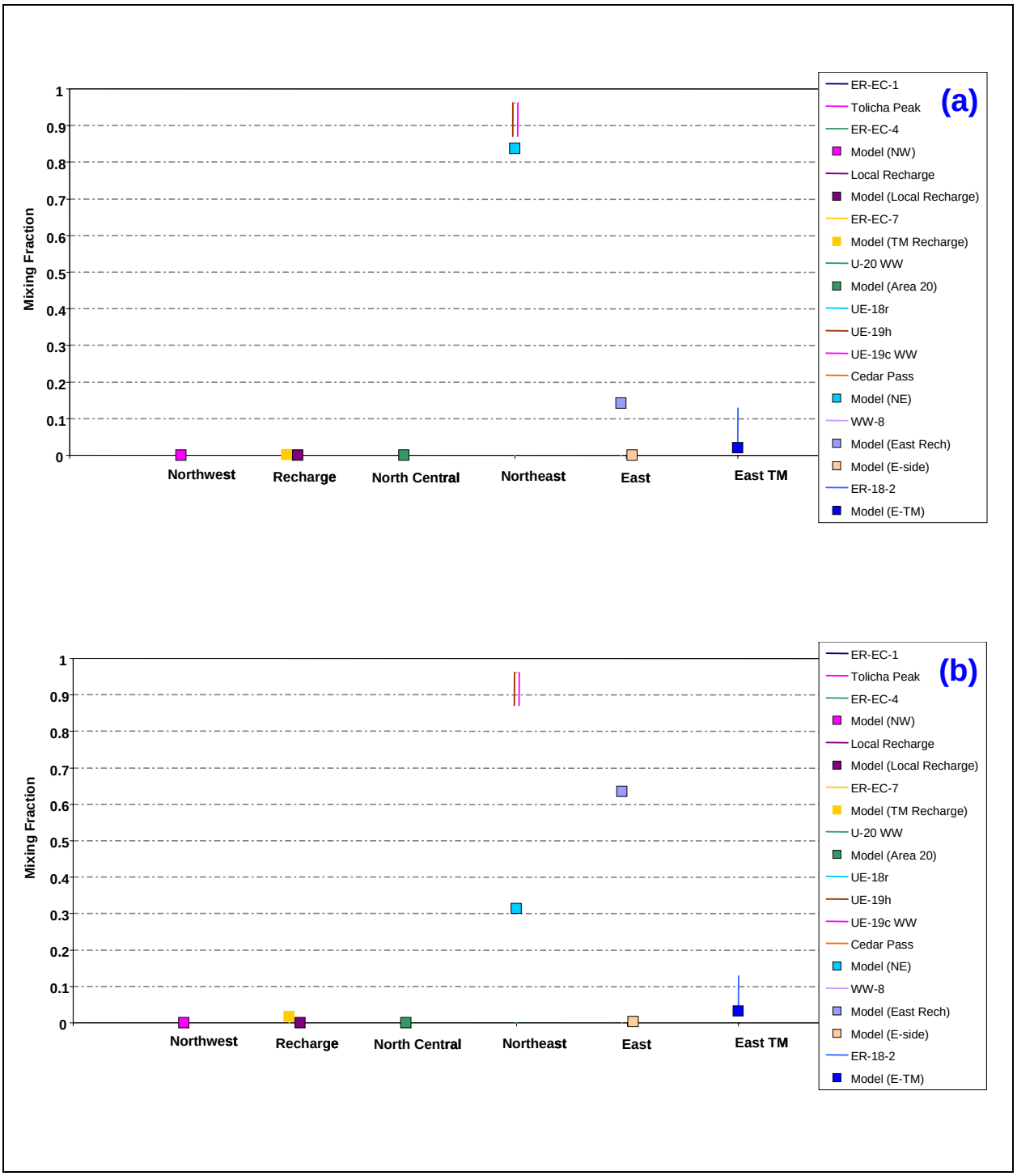

Figure 7-38
Quantitative Geochemical Comparisons at UE-18r for (a) DRT-USGSD-SDA and (b) DRT-DRIA-SDA

Table 7-11
Comparison of Alternative Models at UE-18r

HFM	Water-Balance Condition	Inflow from Gold Meadows?	Other Problems
BN-SDA reduced LCCU1 permeability alternative	MME		
	USGSD		
	DRIA		
BN-SDA	MME	X	
	USGSD	X	
	DRIA	X	
BN-ADA	MME		
SCCC-SDA	MME		
	USGSD		X
	DRIA		X
PZUP	MME		
DRT	MME		
RIDGE	MME	X	
TCL	MME	X	
SEPZ	MME	X	
PZUP	USGSD		
	DRIA	X	
DRT	USGSD		
	DRIA		

7.3.2 ER-EC-6

7.3.2.1 Alternative Water-Balance Conditions, BN HFM

Figures 7-39 and 7-40 show the model results for the recalibrated flow models using the USGSD and DRIA alternative recharge maps, respectively, on the reduced LCCU1 permeability alternative. For each recharge scenario, the simulated source of water at ER-EC-6 is primarily from the northwest. For the DRIA case, which is the "high" recharge flux scenario, about 15 percent of the ER-EC-6 source is from the recharge zone in Areas 20 and 19. For the USGSD case, recharge in the north-central and northeast areas is not large enough to produce a southwestward flow direction to ER-EC-6. However, as described in the base-case analysis, ER-EC-6 is in a highly complex local area where mixing from the northwest mixes with north-central and northeast water. Although the later sources do not show up in significant quantities in these simulations, they do mix with the northwest water at the top of Thirsty Canyon, not far from ER-EC-6.

Model results for BN-USGSD-SDA and BN-DRIA-SDA show an interesting difference (Figure 7-41). The USGSD model shows the entire source of water at ER-EC-6 coming from the northwest. By comparison, the DRIA model nearly matches the even split target between sources west and east of the Purse Fault, which is an improvement over the DRIA model with reduced LCCU1 permeability alternative. Finally, BN-MME-ADA (Figure 7-42) shows nearly all of ER-EC-6 water arriving from the northwest.

7.3.2.2 SCCC Alternative HFM

Given the way the Purse Fault is represented in the SCCC model, it was expected that ER-EC-6 would be dominated by northwest water. However, the SCCC-MME-SDA, as calibrated, produces a nearly perfect match to the geochemistry targets at ER-EC-6 (Figure 7-43). Flow to ER-EC-6 comes almost perfectly from the north. Because the well is due south of the Purse Fault, the mixing from either side of the fault is nearly even. The contribution from the northeast is not troubling because that water is so similar to the north-central water when compared with northwest water (Kwicklis et al., 2005).

The SCCC model calibrated with the DRIA water-balance conditions leads to a slight deterioration in the simulated mixing at ER-EC-6 from the MME water-balance conditions. Then, with the USGSD conditions, the mixing is lost as the entire source is from the northwest (Figure 7-44).

7.3.2.3 PZUP, DRT, RIDGE, TCL, and SEPZ Alternative HFMs

The other alternative HFMs with MME water-balance conditions are considered in this section with the quantitative comparisons in Figures 7-45 through 7-47. As with UE-18r, these can be broken into two groups with regard to their results at ER-EC-6. In the first group, PZUP, DRT, and SEPZ show a tendency similar to the base case, in which most water at ER-EC-6 arrives from the northwest. The SEPZ shows a further east source, although small, similar to BN-DRIA and SCCC.

In the second group, RIDGE-MME-SDA and TCL-MME-SDA show a drastic decrease in northwest source at ER-EC-6, with more than 80 percent coming from the north-central and northeast zones combined. This indicates the northwest inflow and recharge must be well to the west of ER-EC-6. Whereas all other models except the SCCC alternative HFM err on the side of too much northwest-type water at ER-EC-6, RIDGE-MME-SDA and TCL-MME-SDA err in the other direction with not enough northwest-type water.

The USGSD and DRIA alternative water-balance models were also considered for the PZUP and DRT HFMs (Figures 7-48 and 7-49). For both models, the USGSD water-balance alternative led to a nearly complete northwest source at ER-EC-6. The DRIA alternative, however, leads to an almost perfect mix of source water from either side of the Purse Fault. The BN-MME-ADA falls into the category of models with most source water at ER-EC-6 being to the northwest.

7.3.2.4 Summary: ER-EC-6

Nearly every model is unable to provide a 50/50 mix of water from west and east of the Purse Fault at ER-EC-6. This may be explainable by the complex zone of mixing near ER-EC-6 and the impact of the no-flow western boundary. The results may be acceptable in that the mixing generally does occur, just not right at ER-EC-6. Table 7-12 shows which models provide better estimates of the mixing right at ER-EC-6.

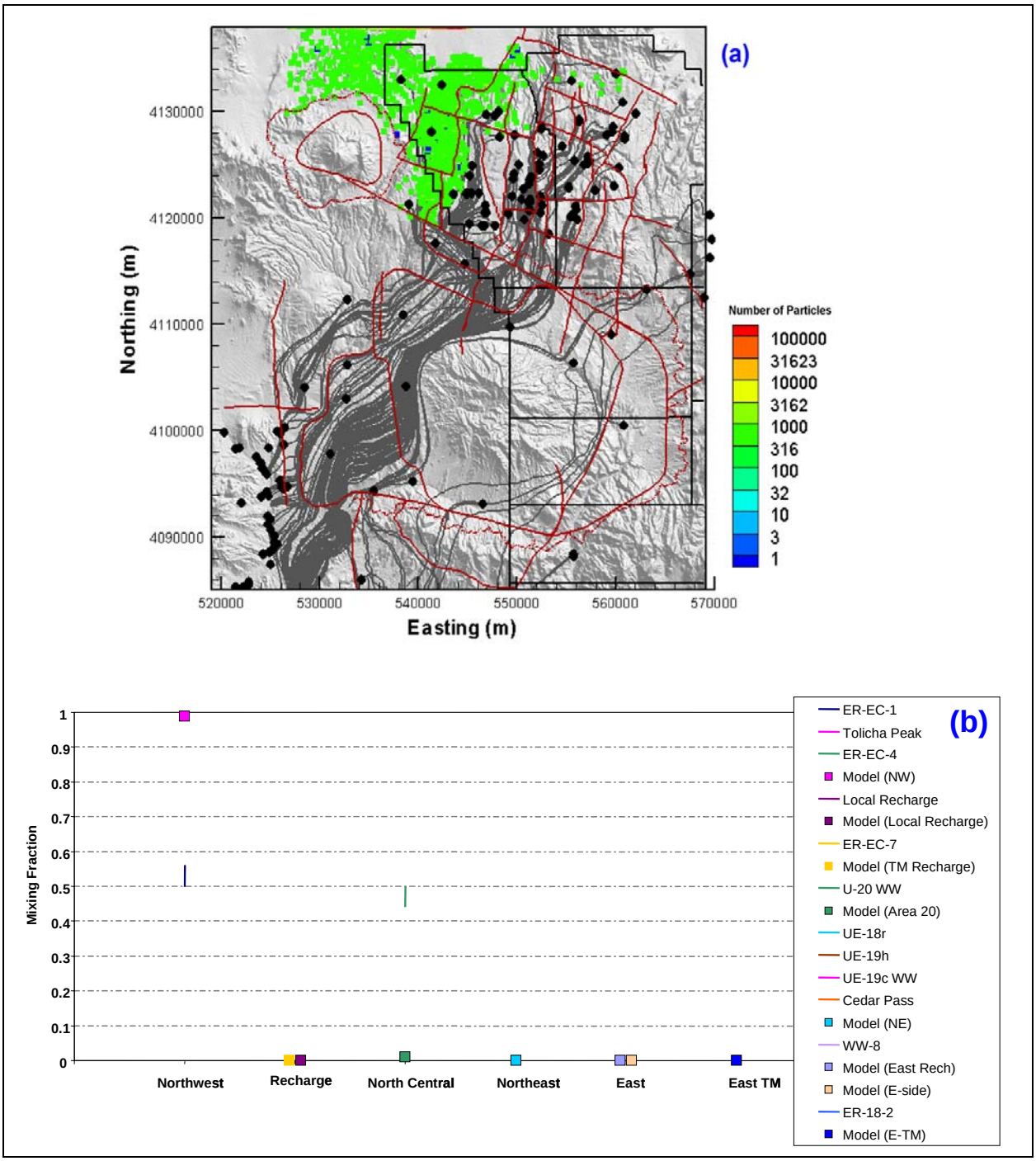

Figure 7-39
Comparison of Flow Model with Geochemical Mixing Targets at ER-EC-6 for BN-USGSD-SDA in the Reduced LCCU1 Permeability Alternative

Figure (a) shows the flow paths as mapped by forward SPTR particles originating at wells (grey lines) and the source recharge locations identified by reverse PTRK particle tracking (colored squares). Figure (b) shows the model comparison with geochemical mixing target ranges.

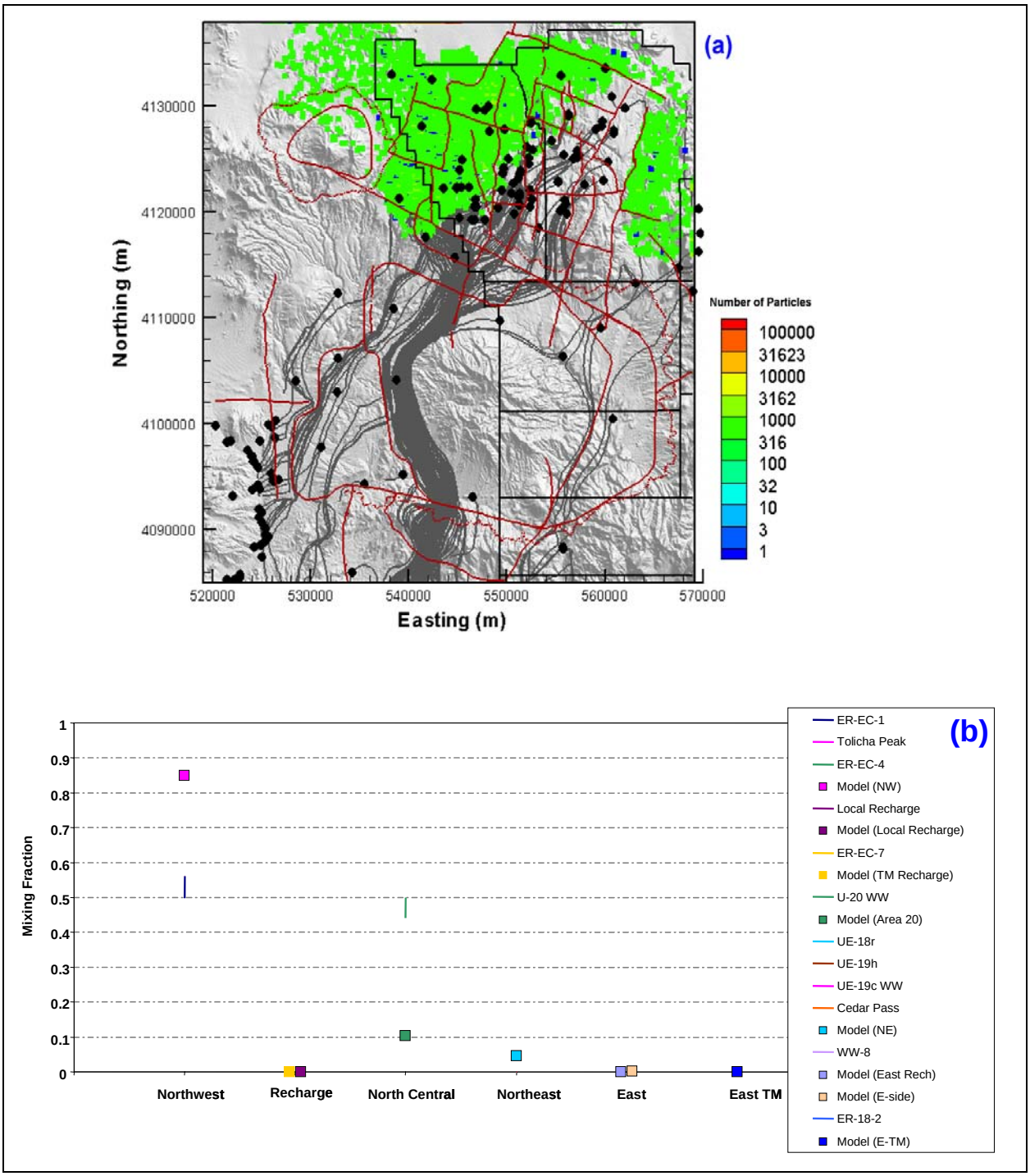

Figure 7-40
Comparison of Flow Model with Geochemical Mixing Targets at ER-EC-6 for BN DRIA-SDA in the Reduced LCCU1 Permeability Alternative

Figure (a) shows the flow paths as mapped by forward SPTR particles originating at wells (grey lines) and the source recharge locations identified by reverse PTRK particle tracking (colored squares). Figure (b) shows the model comparison with geochemical mixing target ranges.

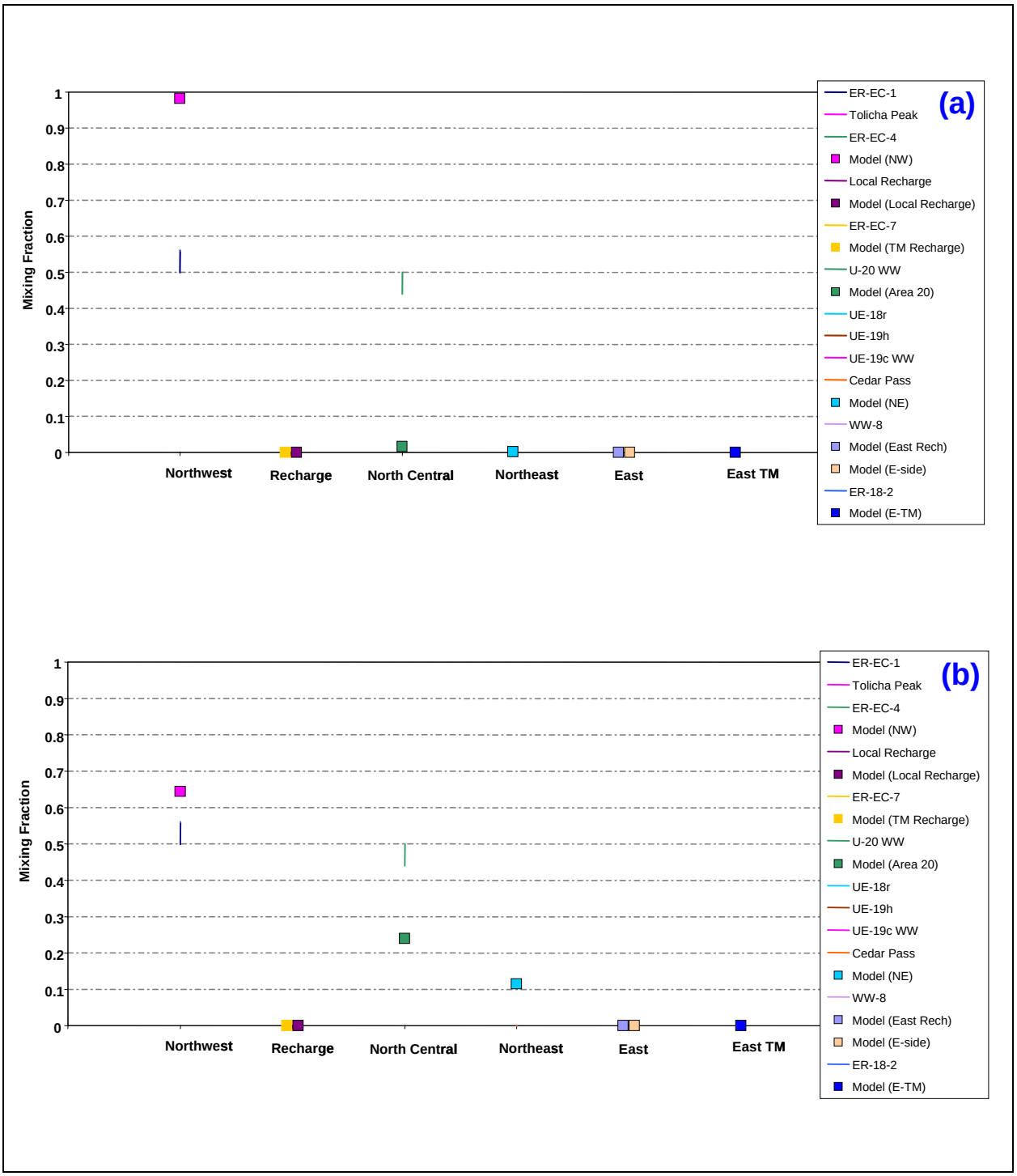

Figure 7-41
Quantitative Geochemical Comparison at ER-EC-6 for (a) BN-USGSD-SDA and (b) BN-DRIA-SDA

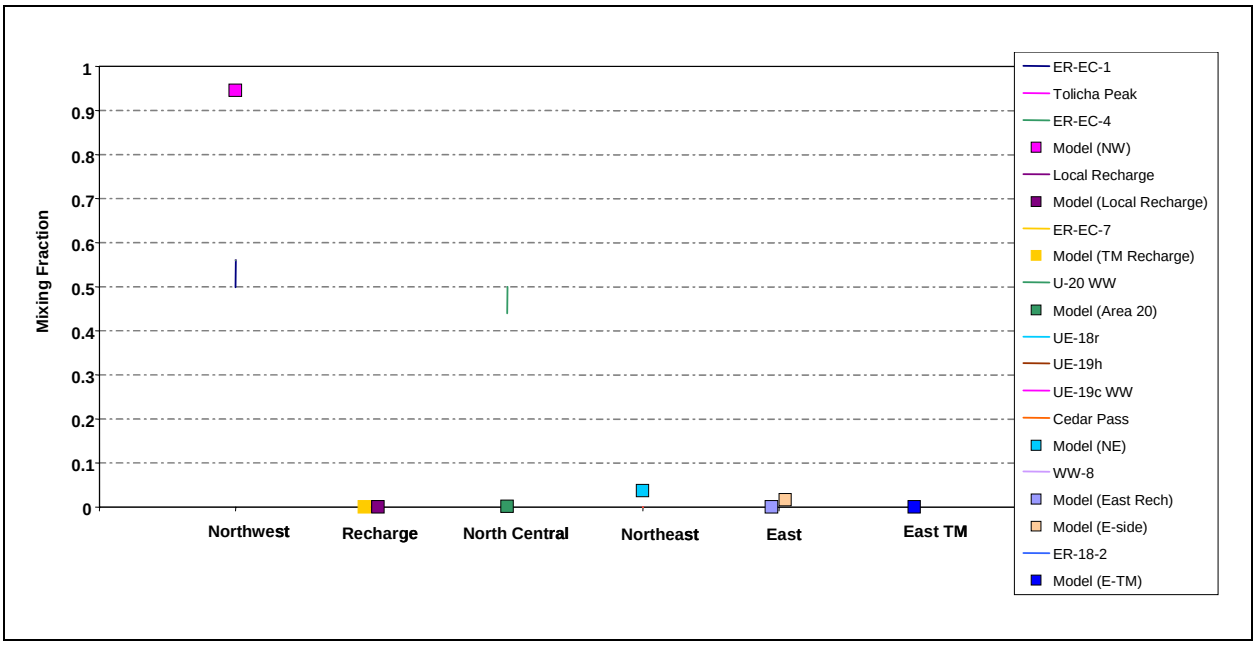

Figure 7-42
Comparison of Flow Model with Geochemical Mixing Targets at ER-EC-6 for BN-MME-ADA

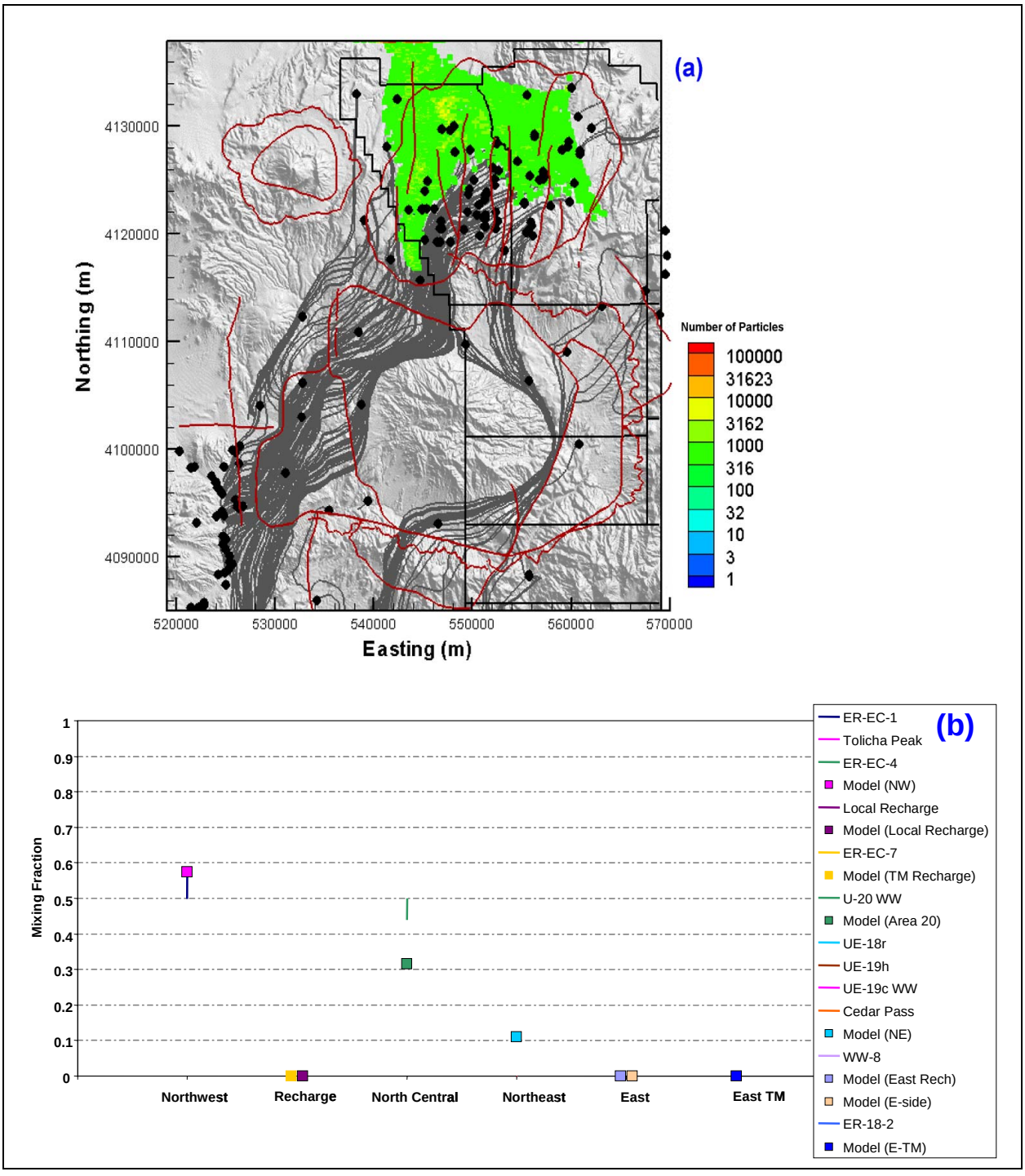

Figure 7-43
Comparison of Flow Model with Geochemical Mixing Targets at ER-EC-6 for SCCC-MME-SDA

Figure (a) shows the flow paths as mapped by forward SPTR particles originating at wells (grey lines) and the source recharge locations identified by reverse PTRK particle tracking (colored squares). Figure (b) shows the model comparison with geochemical mixing target ranges.

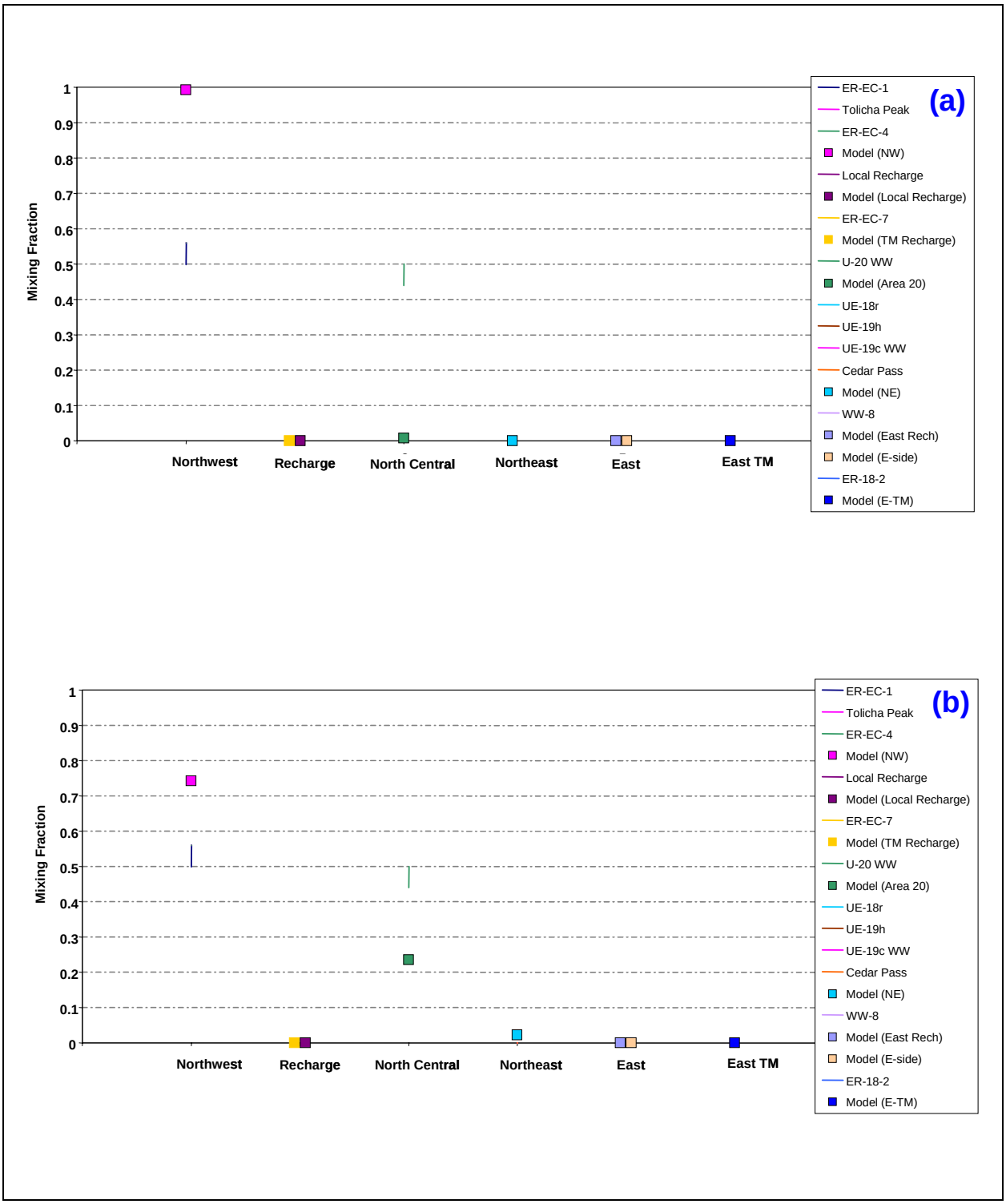

Figure 7-44
Quantitative Geochemical Comparisons at ER-EC-6 for (a) SCCC-USGSD-SDA and (b) SCCC-DRIA-SDA

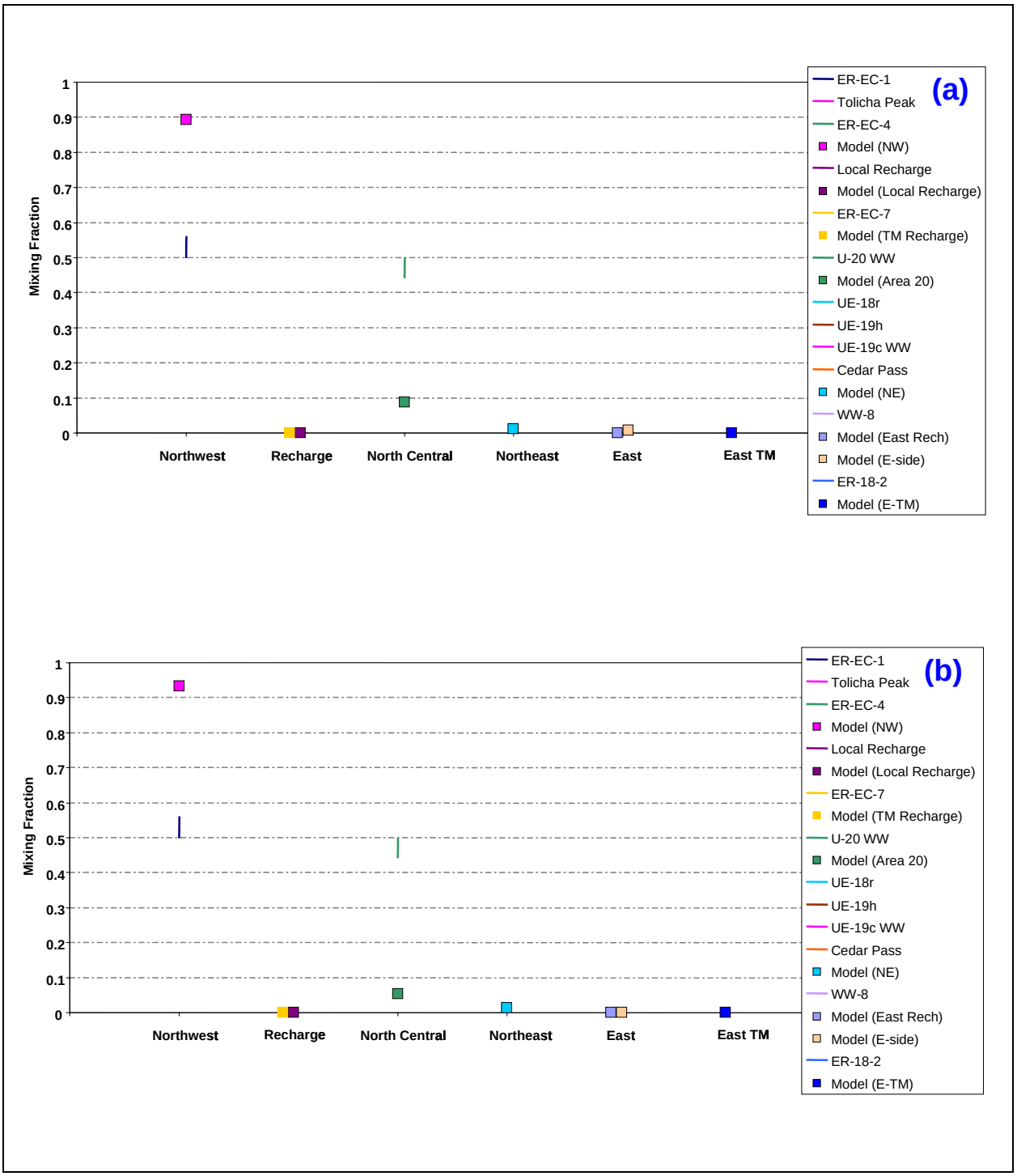

Figure 7-45
Quantitative Geochemical Comparisons at ER-EC-6 for (a) PZUP-MME-SDA and (b) DRT-MME-SDA

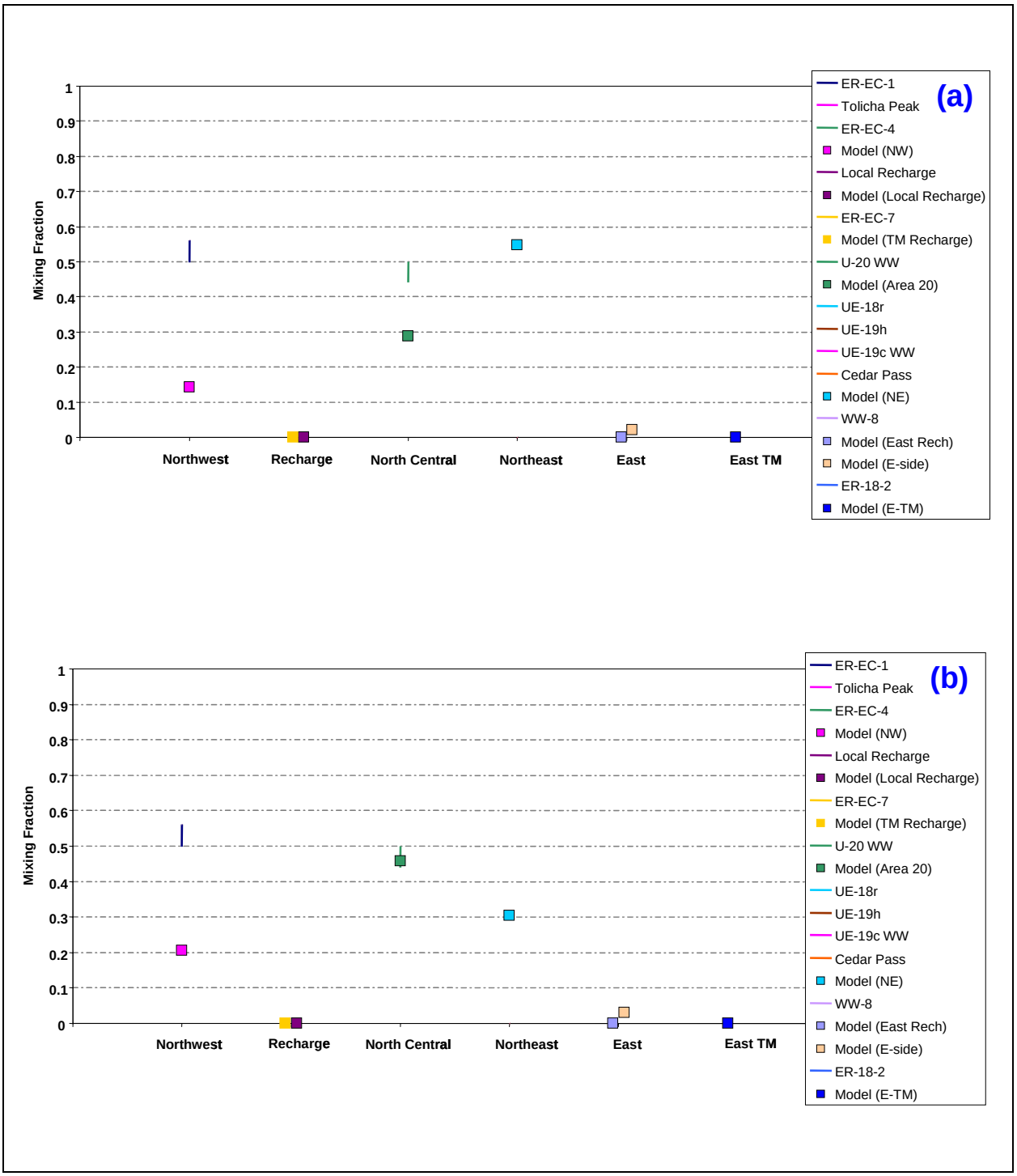

Figure 7-46
Quantitative Geochemical Comparison at ER-EC-6 for (a) RIDGE-MME-SDA and (b) TCL-MME-SDA

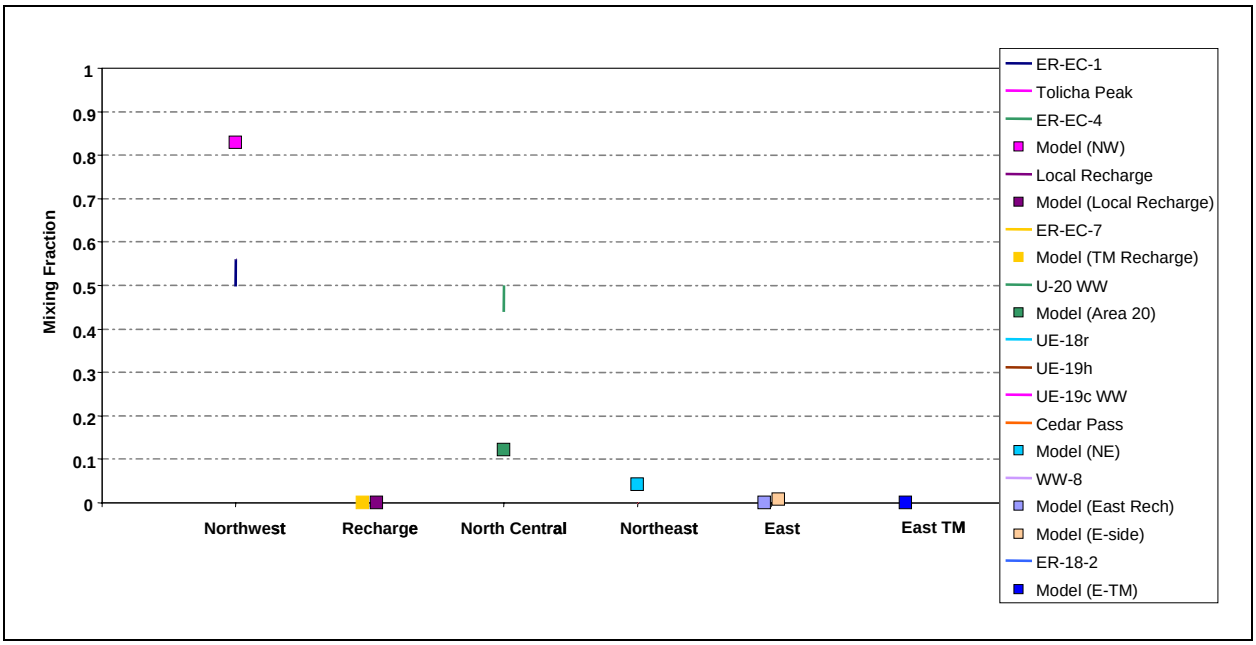

Figure 7-47
Comparison of Flow Model with Geochemical Mixing Targets at ER-EC-6 for SEPZ-MME-SDA

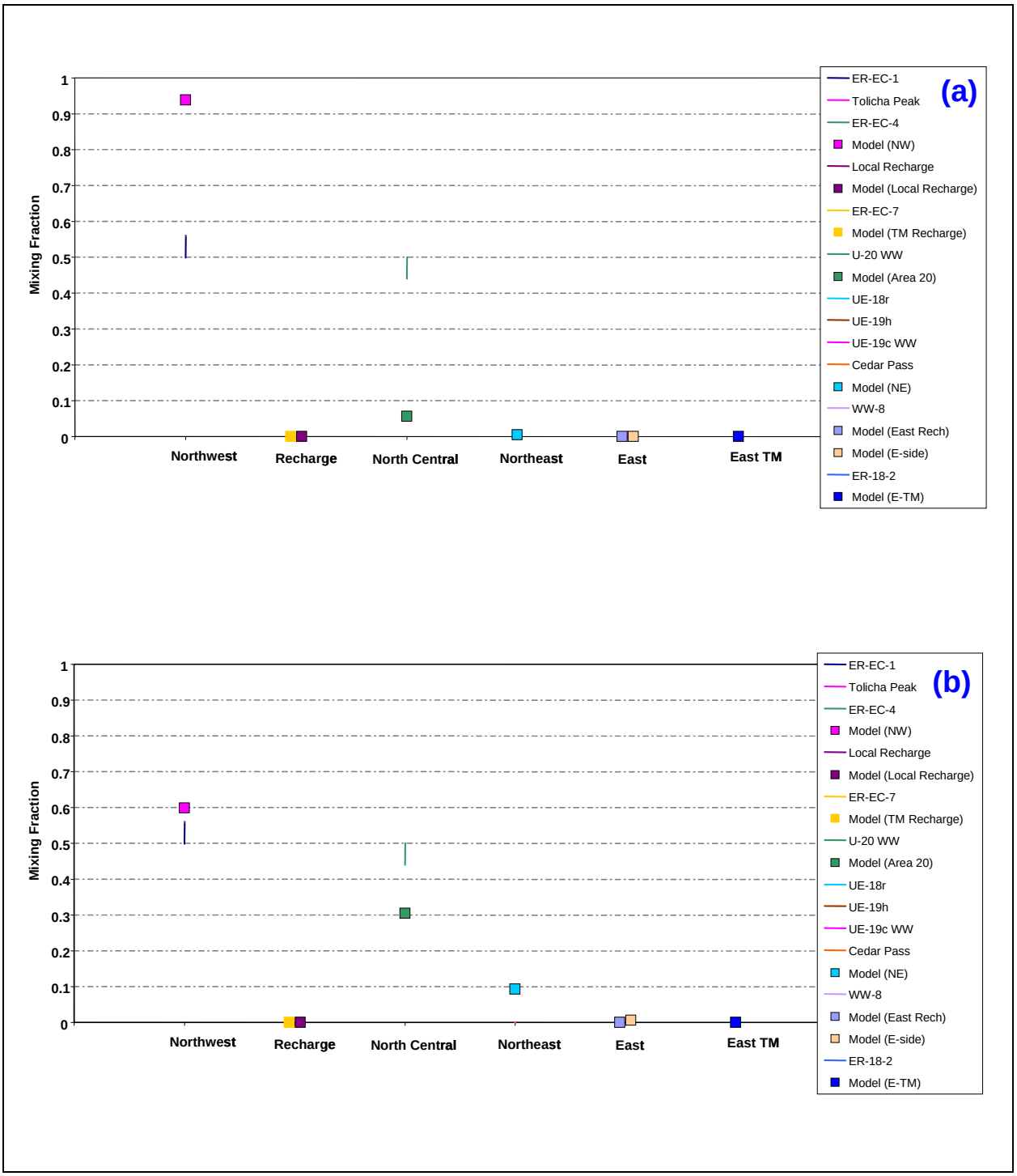

Figure 7-48
Quantitative Geochemical Comparisons at ER-EC-6 for (a) PZUP-USGSD-SDA and (b) PZUP-DRIA-SDA

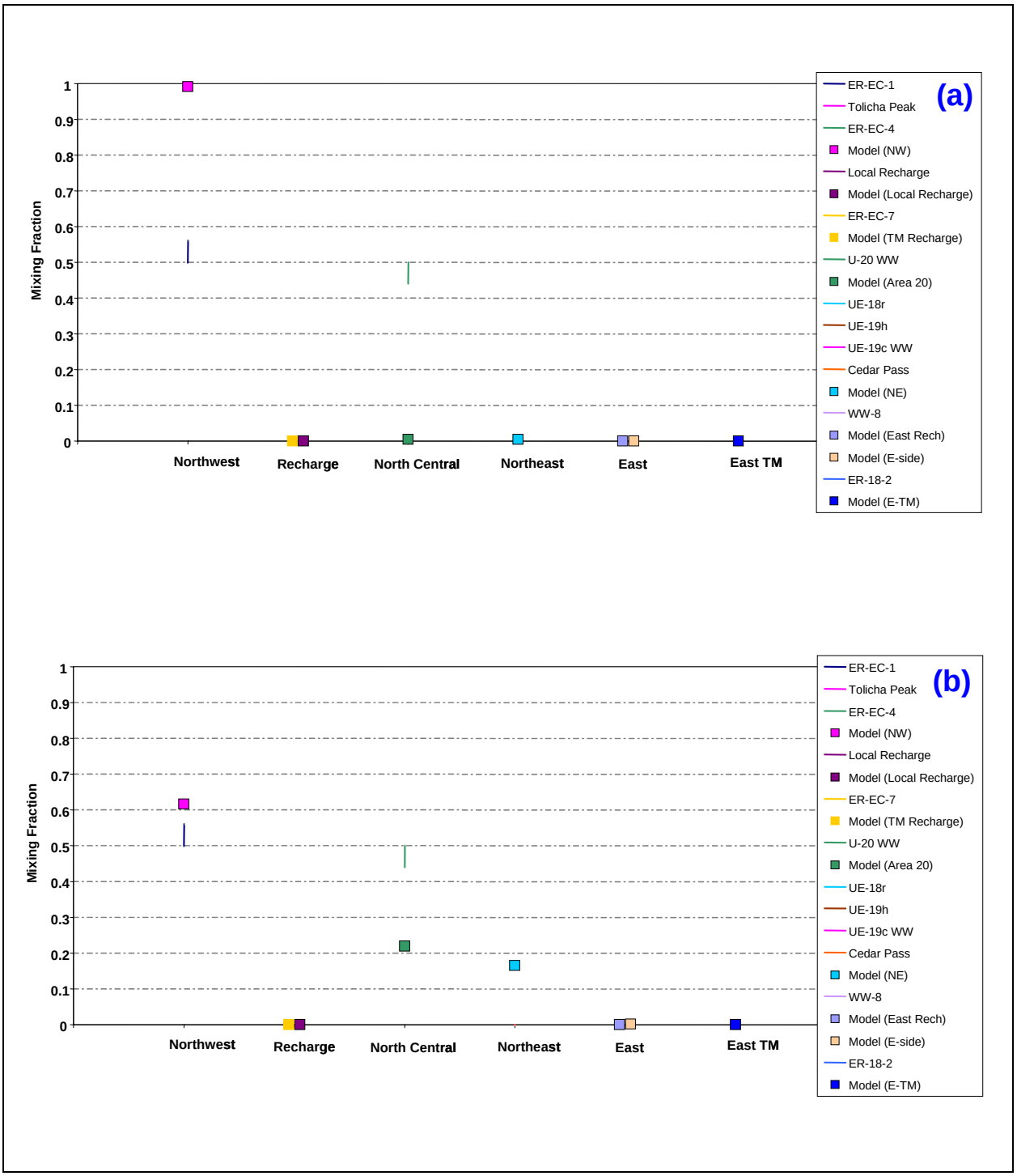

Figure 7-49
Quantitative Geochemical Comparisons at ER-EC-6 for (a) DRT-USGSD-SDA and (b) DRT-DRIA-SDA

Table 7-12
Comparison of Alternative Models at ER-EC-6

HFM	Water-Balance Condition	Overpredicts the Northwest Source Component	Other Issues
BN-SDA reduced LCCU1 permeability alternative	MME	X	
	USGSD	X	
	DRIA	X	
BN-SDA	MME	X	
	USGSD	X	
	DRIA		
BN-ADA	MME	X	
SCCC-SDA	MME		
	USGSD	X	
	DRIA	X	
PZUP	MME	X	
DRT	MME	X	
RIDGE	MME		X
TCL	MME		X
SEPZ	MME	X	
PZUP	USGSD	X	
	DRIA		
DRT	USGSD	X	
	DRIA		

7.3.3 ER-OV-01

7.3.3.1 Alternative Water-Balance Conditions, BN HFM

The simulated mixing at ER-OV-01 in the USGSD and DRIA recharge alternatives with the BN HFM with reduced LCCU1 permeability alternative is primarily between northwest water and local recharge, with little contribution from the north central and northeast (Figures 7-50 and 7-51). Whereas the northwest source overprediction was greater for the USGSD alternative at ER-EC-6, it is worse for the DRIA alternative here at ER-OV-01, where virtually no north-central or northeast contributions are simulated, yet again highlighting the complex mixing occurring along the Thirsty Canyon flow path. For both of these models, more local recharge is simulated than is called for by the geochemistry analysis, highlighting the impact of independent redistribution of flow into washes and canyons in the recharge map.

Model results for the BN HFM with the USGSD and DRIA water-balance conditions are nearly identical to each other and to the USGSD water balance with the reduced LCCU1 permeability alternative model described above (Figure 7-52). The BN-MME-ADA matches the northwest source component better than the alternative water-balance models, but at the expense of greater errors in local recharge estimates (Figure 7-53).

7.3.3.2 SCCC Alternative HFM

As with the BN models, the SCCC models also overpredict either local recharge or northwest sources at ER-OV-01, and they underpredict the component of north-central and northeast sources. The SCCC alternative HFM with MME water-balance conditions has the greatest local recharge overpredictions, but the northwest source component is nearly within the geochemical target range (Figure 7-54). Both the USGSD and DRIA water-balance conditions for this HFM lead to good local recharge estimates but very large overpredictions of the northwest source (Figure 7-55).

7.3.3.3 PZUP, DRT, RIDGE, TCL, and SEPZ Alternative HFMs

The other alternative HFMs with MME water-balance conditions are considered in this section with the quantitative comparisons in Figures 7-56 through 7-58. These five alternatives perform similarly and reasonably well with respect to the northwest source component, but they all overestimate the

local recharge and they underestimate the north-central and northeast source components, with the exception of RIDGE-MME-ADA. This model is notable because 20 percent of the sources for ER-OV-01 are from east of the Purse Fault. Due to the similarities of Area 20 and Area 19 water, this result can be interpreted as almost within range of the targets if the north-central and northeast zones are combined.

At ER-OV-01, the USGSD and DRIA water-balance conditions for PZUP calibrations both lead to small overestimates of the northwest source and local recharge, but they have favorable results for the north-central and northeast source components (Figure 7-59). The DRIA model produces the closest match to the north-central and northeast contributions, which is particularly interesting because that is where many of the calibrated models discussed thus far fail.

The DRT HFM model calibrated with both USGSD and DRIA water-balance conditions overestimates both the northwest source and the local recharge, and it has no source contribution from the north-central or northeast zones (Figure 7-60). The MME water-balance conditions for this HFM led to closer matches to the northwest component but worse matches to the local recharge.

7.3.3.4 Summary: ER-OV-01

Nearly every model is unable to provide a source from the north-central and northeast zones at ER-OV-01. This is due to high recharge in Thirsty Canyon forcing those pathlines to the east and possibly due to the no-flow western boundary. In the Table 7-13 comparison, model results that provide some northwest and north-central groundwater at ER-OV-01 are highlighted. Uppercase Xs indicate the issue is worse than lowercase x symbols.

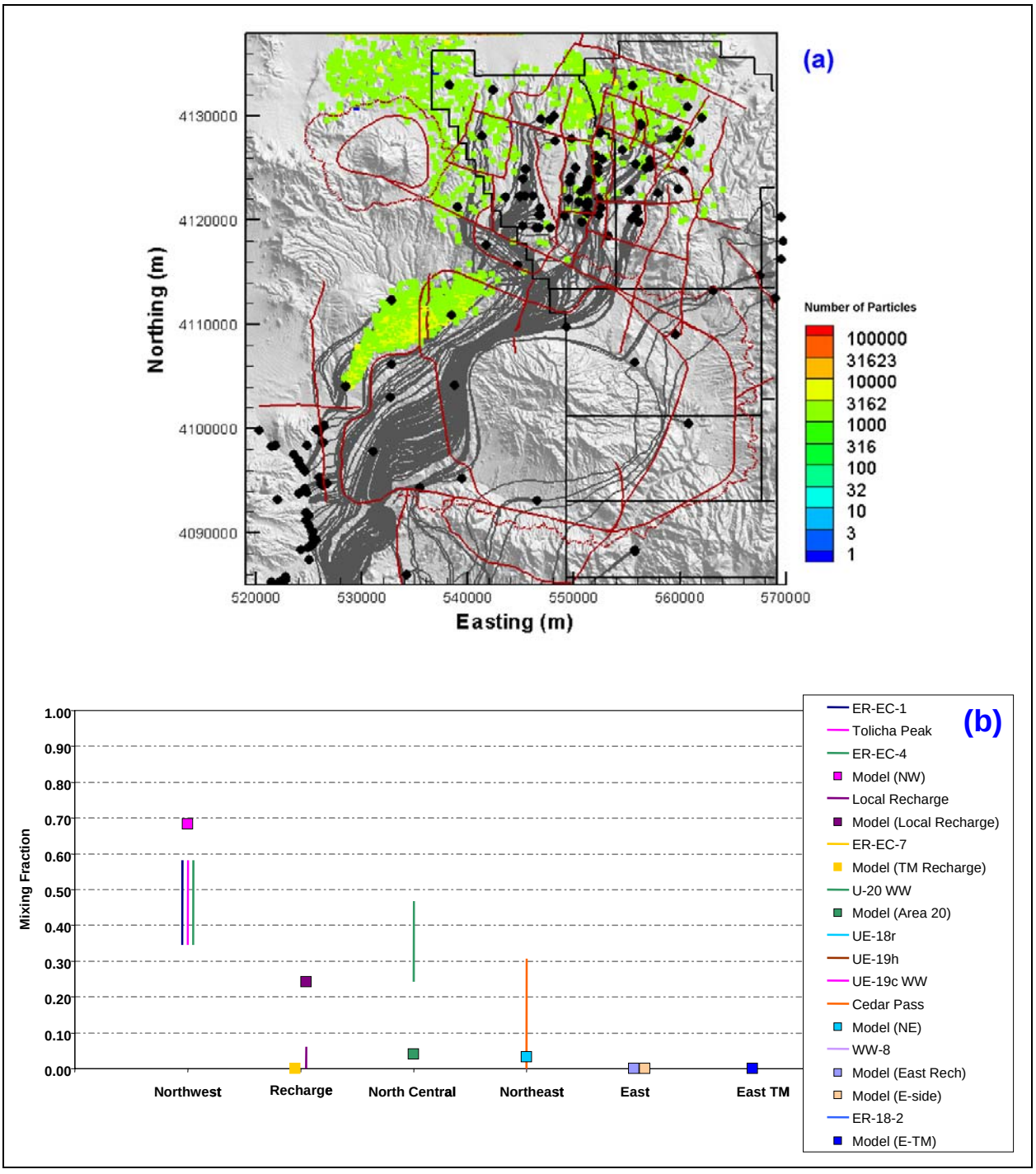

Figure 7-50
Comparison of Flow Model with Geochemical Mixing Targets at ER-OV-01 for BN-USGSD-SDA in the Reduced LCCU1 Permeability Alternative

Figure (a) shows the flow paths as mapped by forward SPTR particles originating at wells (grey lines) and the source recharge locations identified by reverse PTRK particle tracking (colored squares). Figure (b) shows the model comparison with geochemical mixing target ranges.

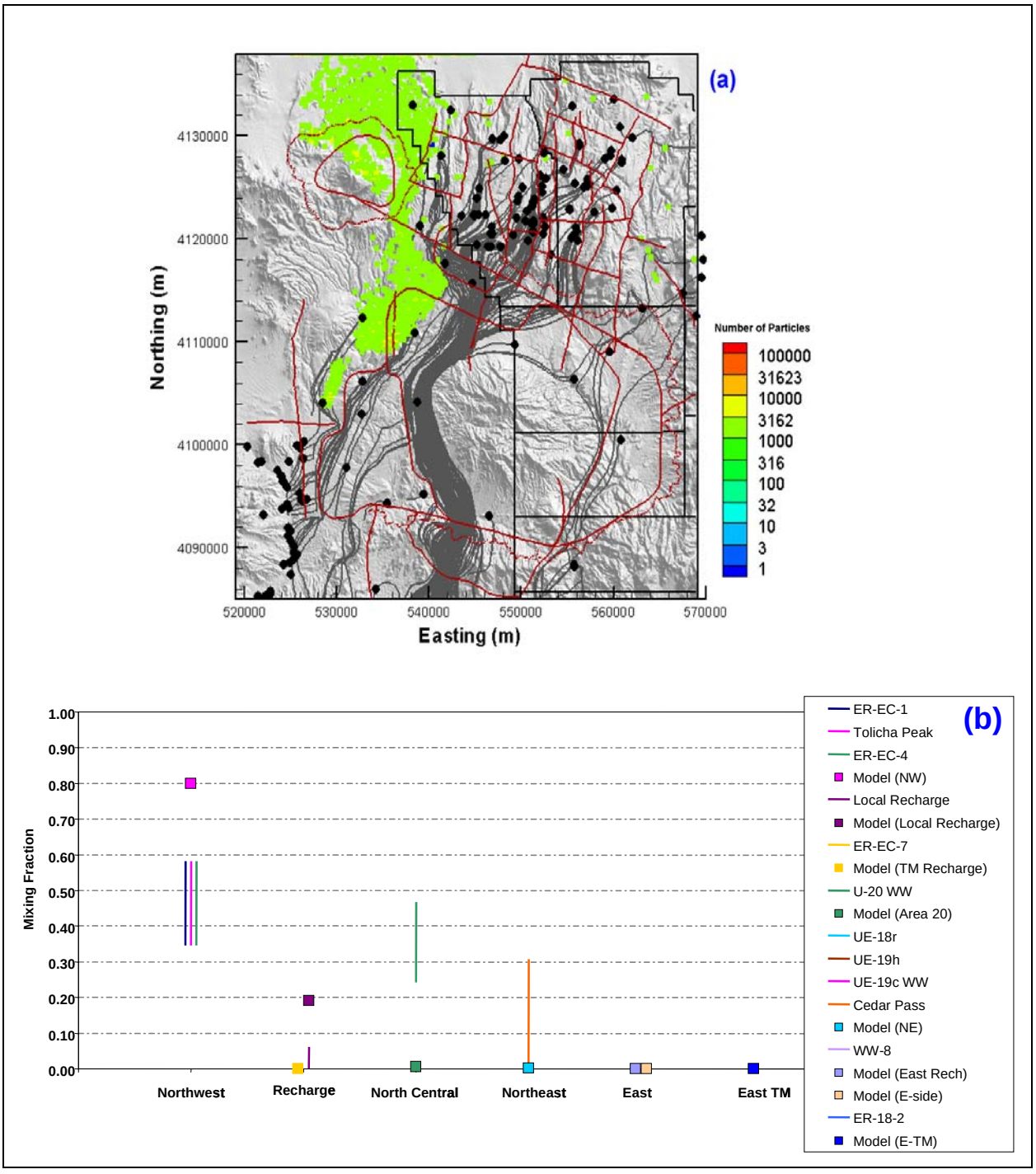

Figure 7-51
Comparison of Flow Model with Geochemical Mixing Targets at ER-OV-01 for BN-DRIA-SDA in the Reduced LCCU1 Permeability Alternative

Figure (a) shows the flow paths as mapped by forward SPTR particles originating at wells (grey lines) and the source recharge locations identified by reverse PTRK particle tracking (colored squares). Figure (b) shows the model comparison with geochemical mixing target ranges.

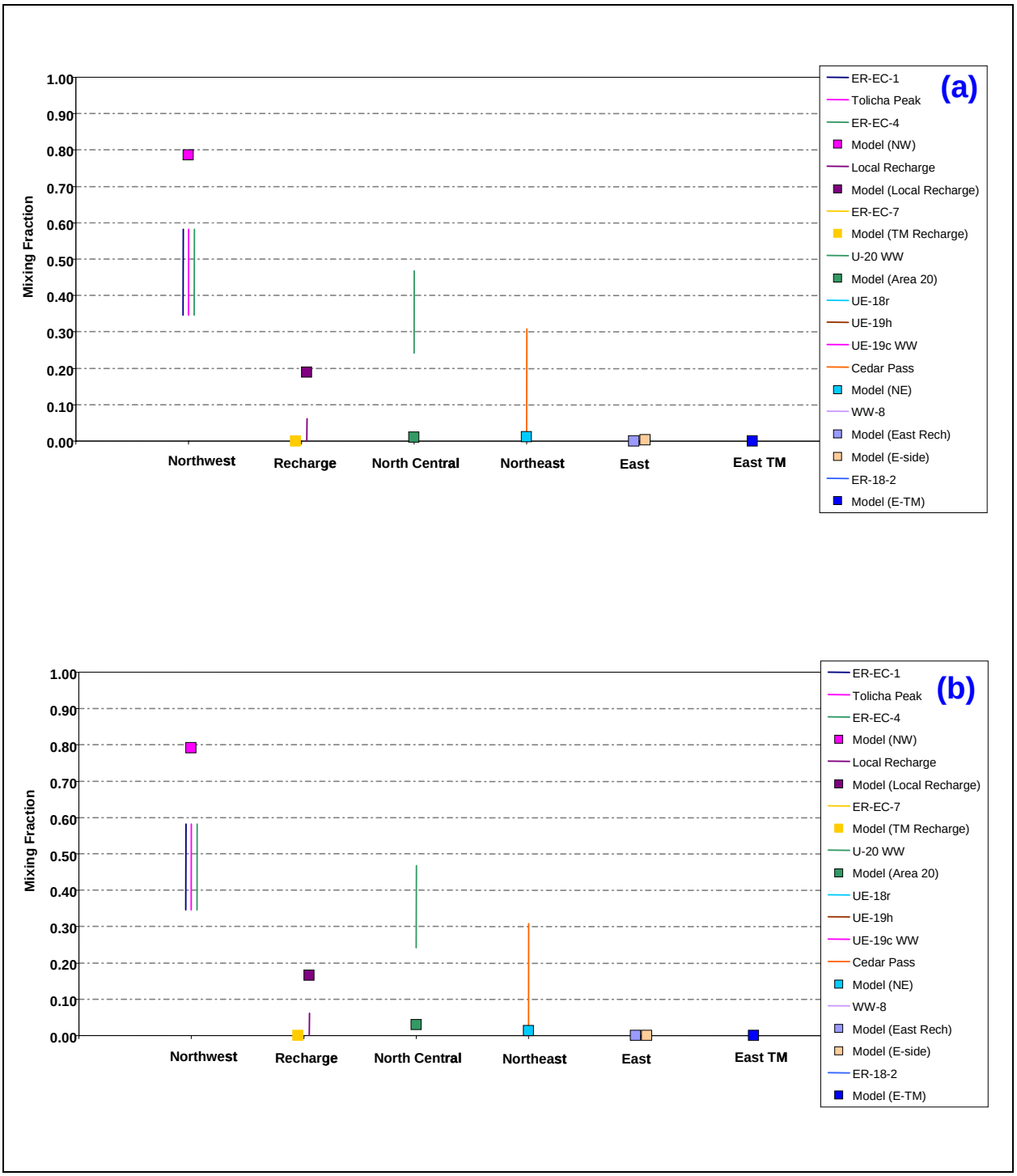

Figure 7-52
Quantitative Geochemical Comparison at ER-OV-01 for (a) BN-USGSD-SDA and (b) BN-DRIA-SDA

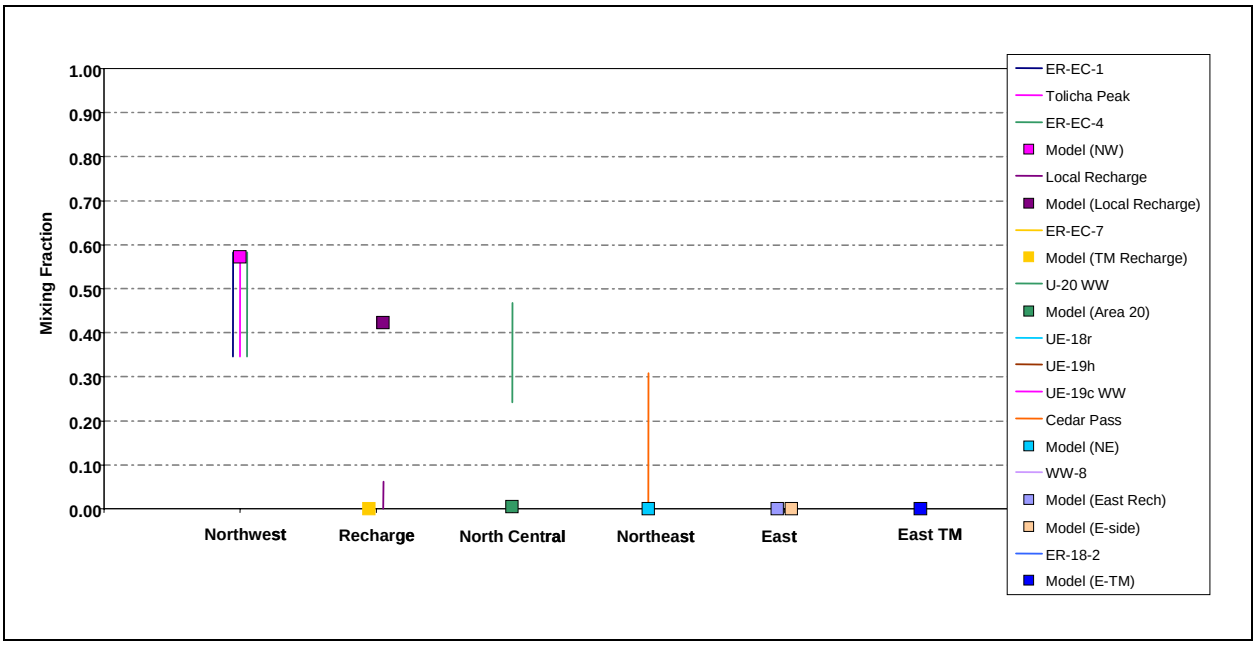

Figure 7-53
Comparison of Flow Model with Geochemical Mixing Targets at ER-OV-01 for BN-MME-ADA

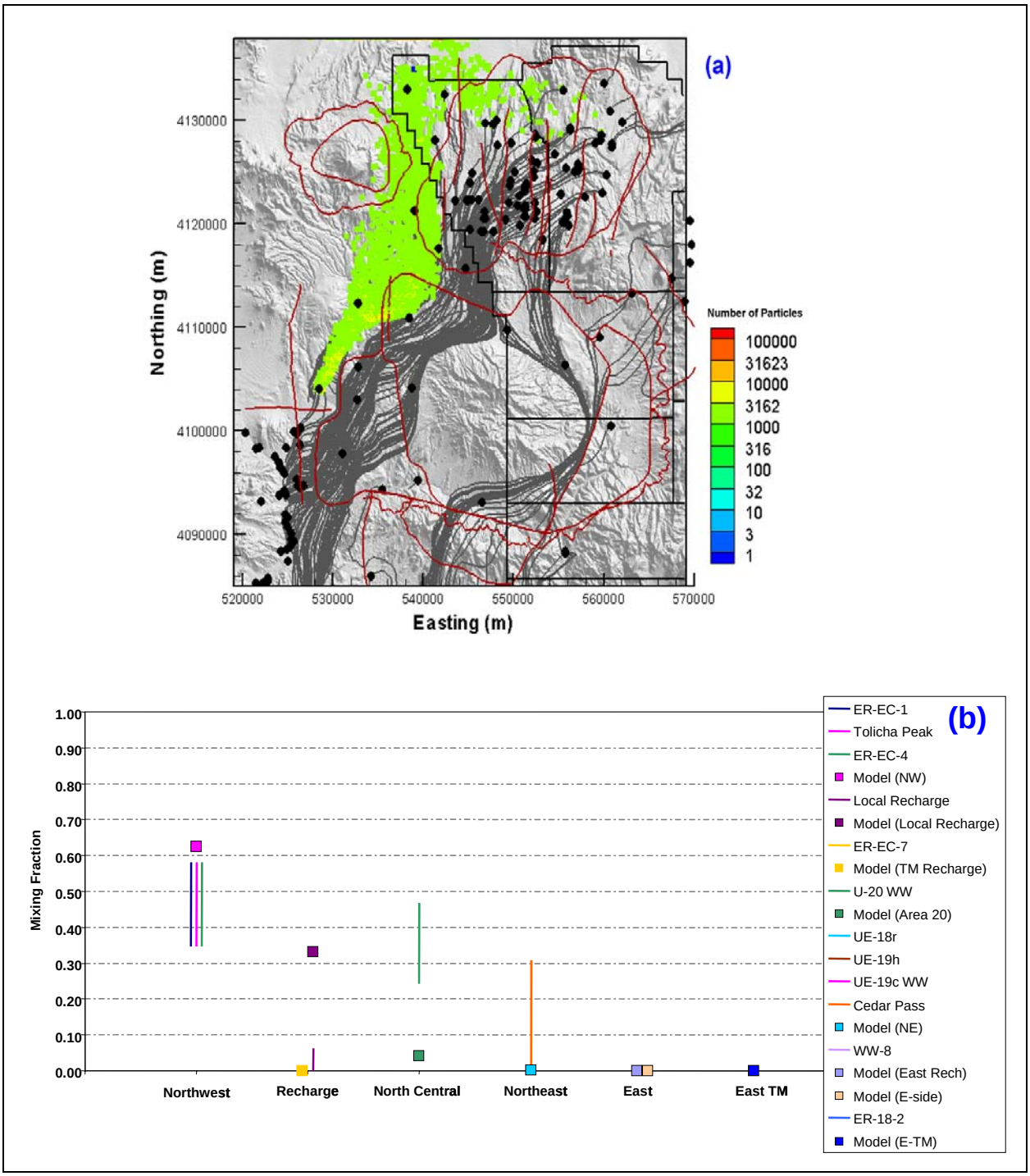

Figure 7-54
Comparison of Flow Model with Geochemical Mixing Targets at ER-OV-01 for SCCC-MME-SDA

Figure (a) shows the flow paths as mapped by forward SPTR particles originating at wells (grey lines) and the source recharge locations identified by reverse PTRK particle tracking (colored squares). Figure (b) shows the model comparison with geochemical mixing target ranges.

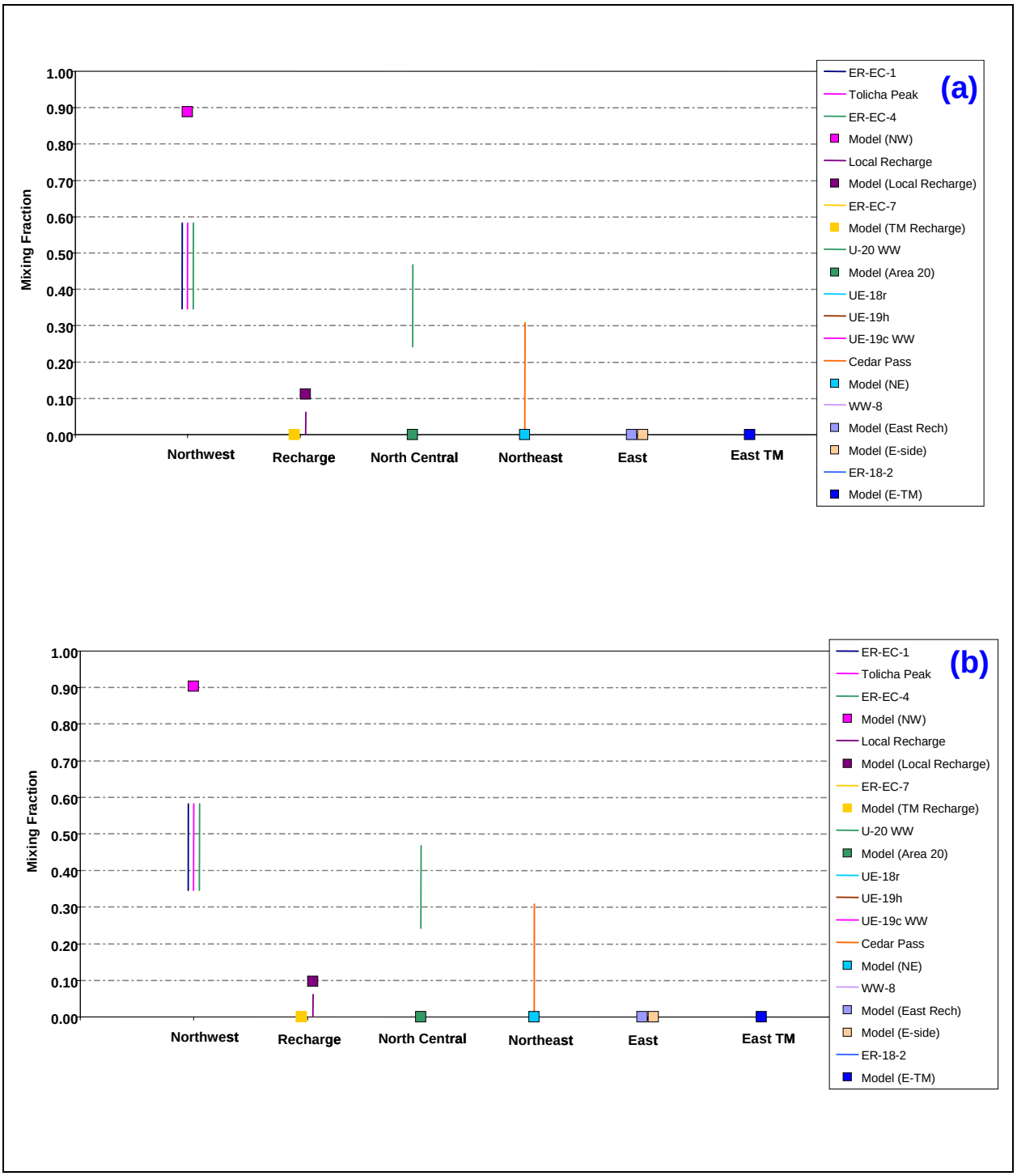

Figure 7-55
Quantitative Geochemical Comparisons at ER-OV-01 for (a) SCCC-USGSD-SDA and (b) SCCC-DRIA-SDA

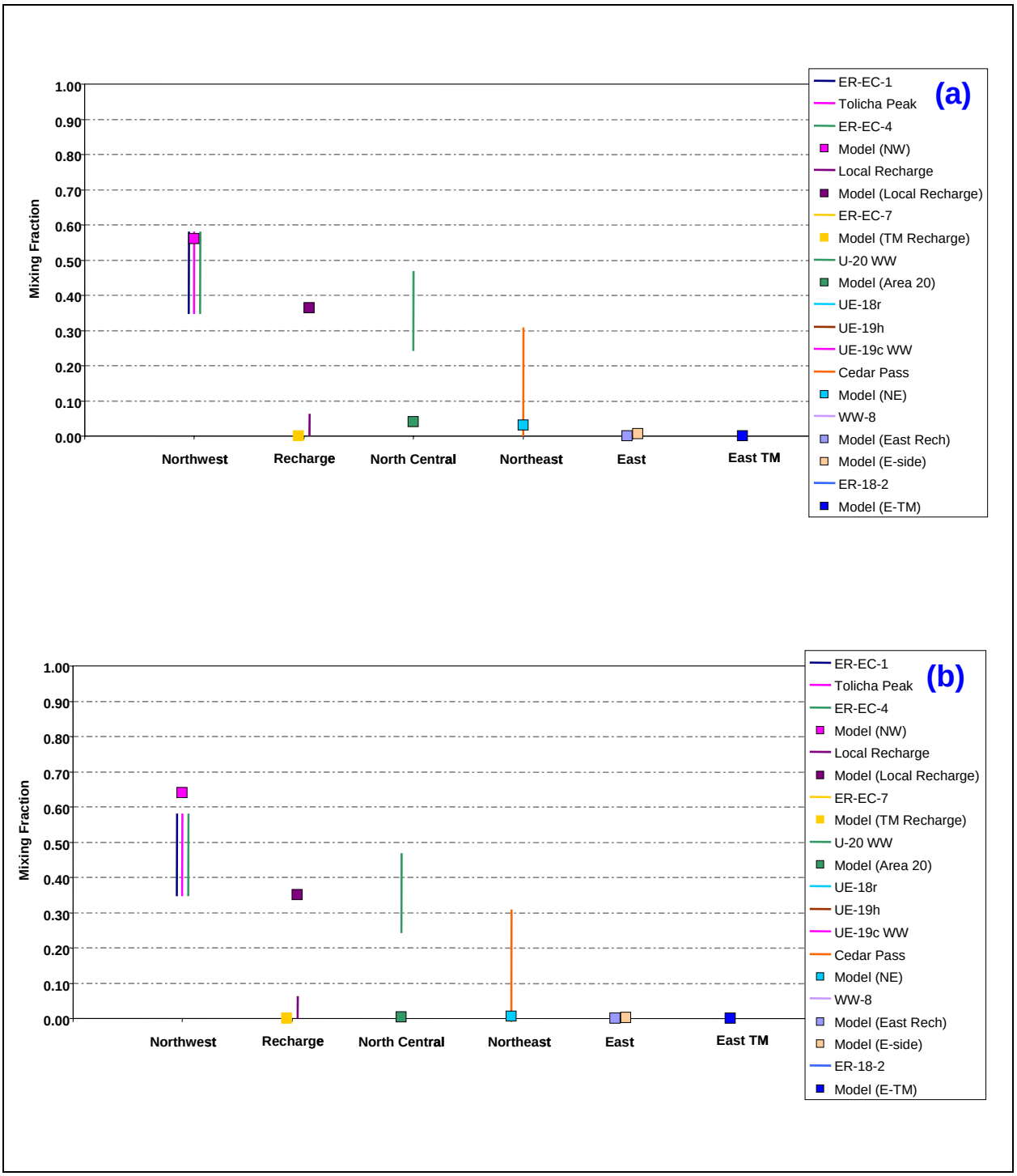

Figure 7-56
Quantitative Geochemical Comparison at ER-OV-01 for (a) PZUP-MME-SDA and (b) DRT-MME-SDA

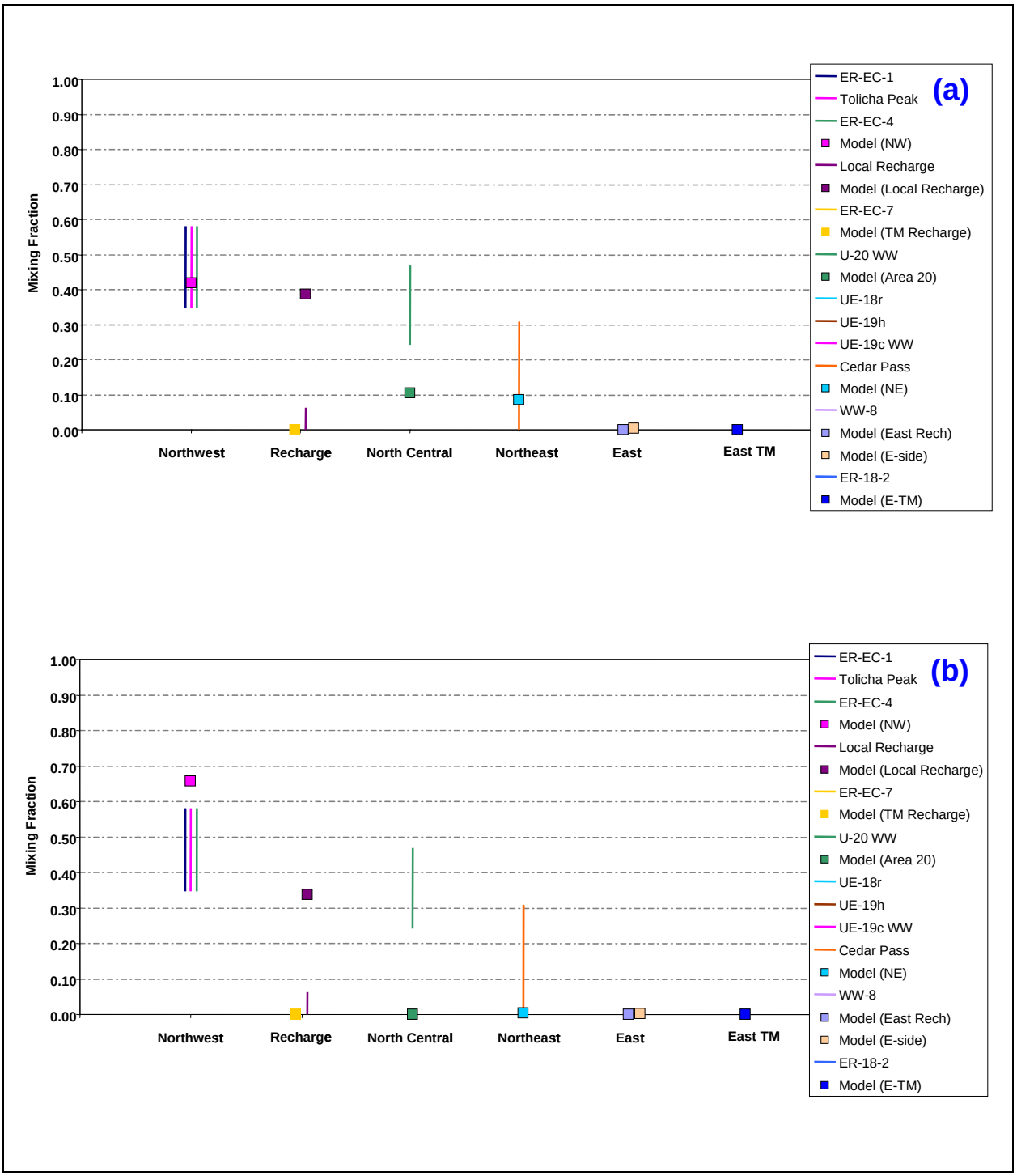

Figure 7-57
Quantitative Geochemical Comparisons at ER-OV-01 for (a) RIDGE-MME-SDA and (b) TCL-MME-SDA

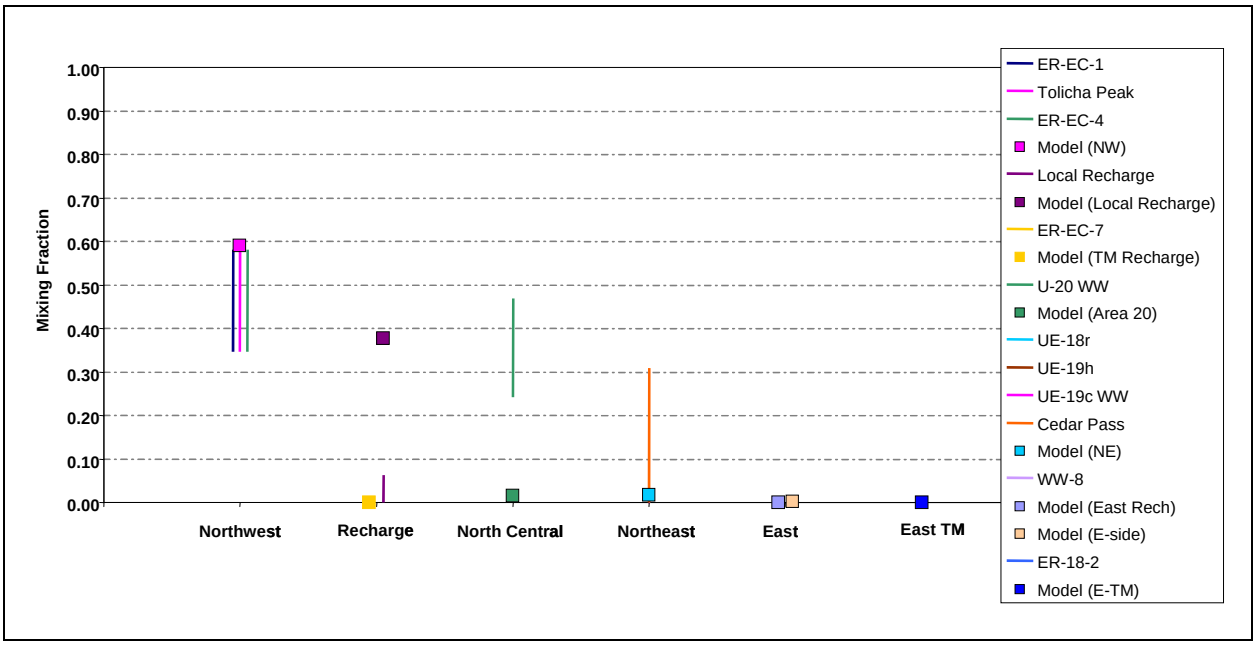

Figure 7-58
Comparison of Flow Model with Geochemical Mixing Targets at ER-OV-01 for SEPZ-MME-SDA

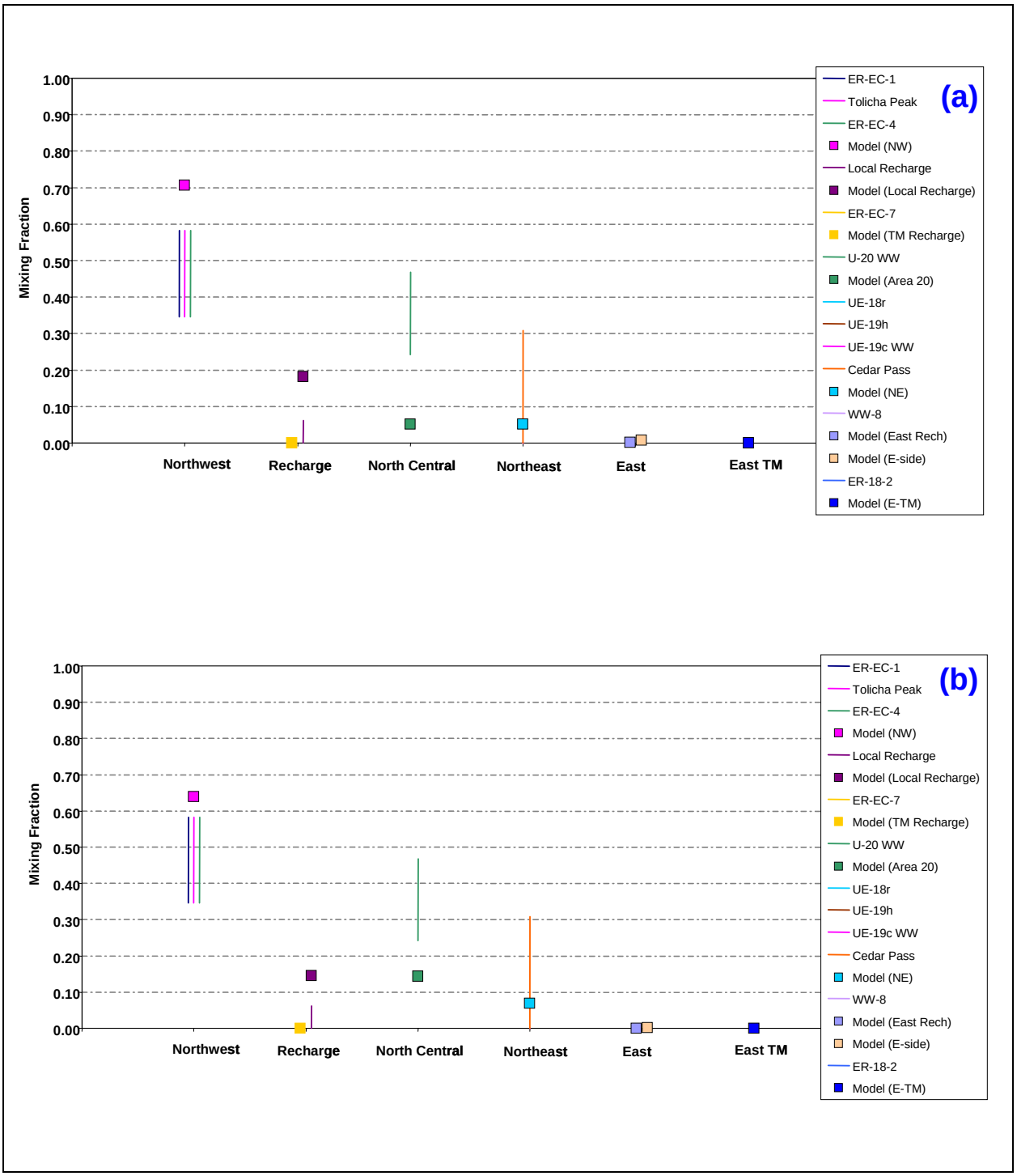

Figure 7-59
Quantitative Geochemical Comparisons at ER-OV-01 for (a) PZUP-USGSD-SDA and (b) PZUP-DRIA-SDA

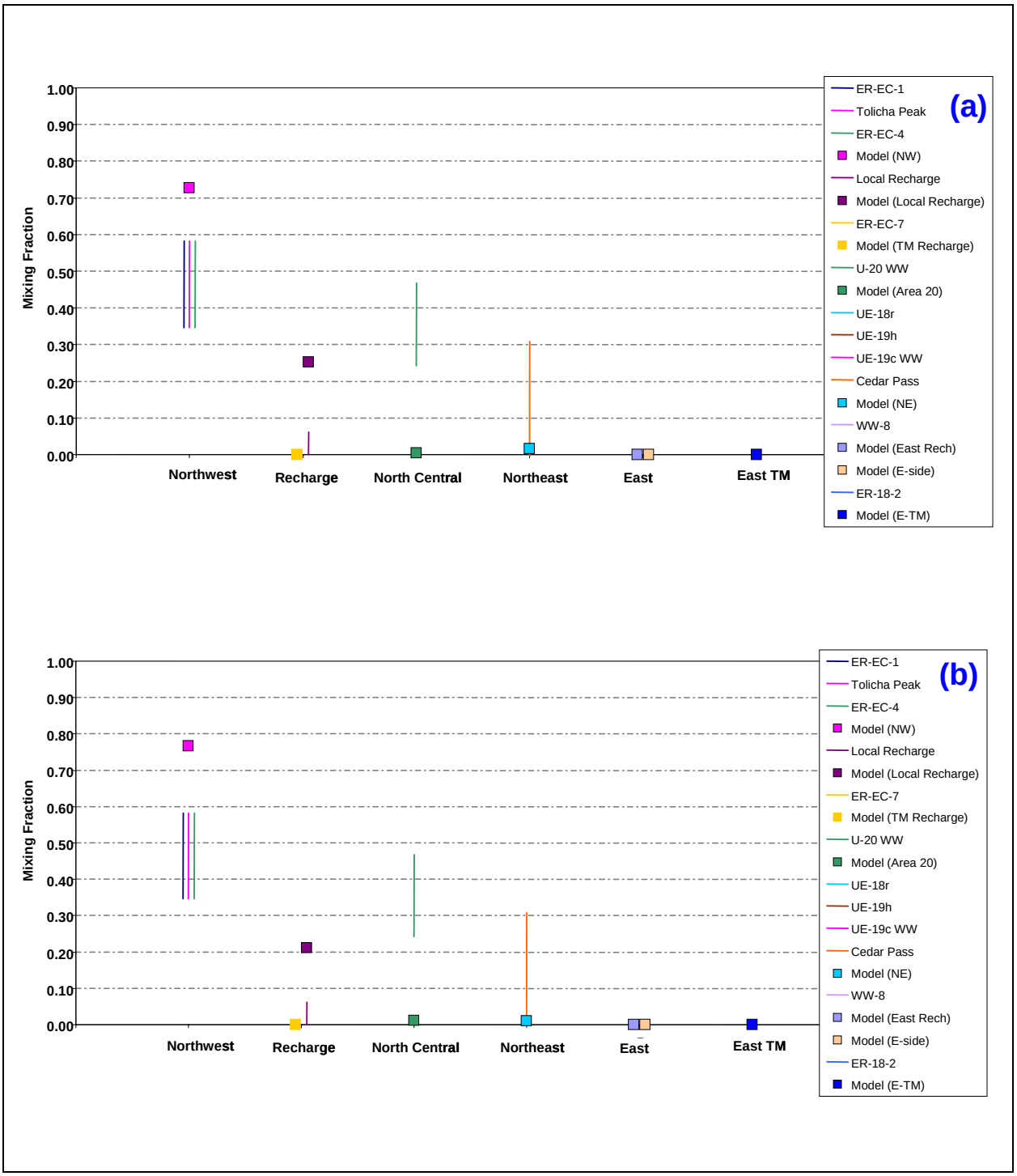

Figure 7-60
Quantitative Geochemical Comparisons at ER-OV-01 for (a) DRT-USGSD-SDA and (b) DRT-DRIA-SDA

Table 7-13
Comparison of Alternative Models at ER-OV-01

HFM	Water-Balance Condition	Underpredicts North-Central and/or Northeast Source	Overpredicts the Northwest Source	Overpredicts Local Recharge
BN-SDA reduced LCCU1 permeability alternative	MME	X		x
	USGSD	X	x	x
	DRIA	X	X	x
BN-SDA	MME	X		X
	USGSD	X	X	x
	DRIA	X	X	x
BN-ADA	MME	X		X
SCCC-SDA	MME	X		X
	USGSD	X	X	
	DRIA	X	X	
PZUP	MME	X		X
DRT	MME	X		X
RIDGE	MME			X
TCL	MME	X		X
SEPZ	MME	X		X
PZUP	USGSD		x	x
	DRIA			
DRT	USGSD	X	x	x
	DRIA	X	x	x

7.3.4 ER-OV-05

7.3.4.1 Alternative Water-Balance Conditions, BN HFM

As with the BN-MME-SDA reduced LCCU1 permeability alternative, the simulated mixing at ER-OV-05 for the USGSD and DRIA water-balance conditions match the targets well with a simple flow path from the northwest to the target well (Figures 7-61 and 7-62). It is interesting to note the effects of the different recharge maps, as represented by the locations and densities of reverse particles leaving the two different models. Not surprisingly, the BN-MME-SDA (high LCCU1 permeability) with both USGSD and DRIA water-balance conditions and the BN-MME-ADA model estimate the northwest source well (Figures 7-63 and 7-64).

7.3.4.2 SCCC Alternative HFM

Due to the boundary conditions and lack of HFM complexity on the west side of the model, flow is predominantly north to south. Thus, the SCCC alternative HFM model results with MME water-balance conditions are not significantly different from the BN HFM models (Figure 7-65). The only notable aspect of the alternative water-balance model calibrations with the SCCC HFM (Figure 7-66) is that when DRIA is used, a significant component of the mixing source is from local recharge. However, considering data control in this portion of the domain and the arbitrary boundaries for the different zones leads one to simply note that the recharge source for water at ER-OV-05 in this model is somewhat further south than in most other models.

7.3.4.3 PZUP, DRT, RIDGE, TCL, and SEPZ Alternative HFMs

As with all ER-OV-05a cases described thus far, there are no substantial differences between the alternative HFM and MME water-balance scenarios (Figures 7-67 through 7-69). When considering the alternative water-balance conditions for PZUP and DRT (Figures 7-70 and 7-71), the only notable features is that the location of some of the local recharge for the DRIA models is further south than the other water-balance condition models.

7.3.4.4 Summary: ER-OV-05

All of the models considered for ER-OV-05a produce reasonable results. There are no discriminating features in the geochemistry target matching that were identified for this well.

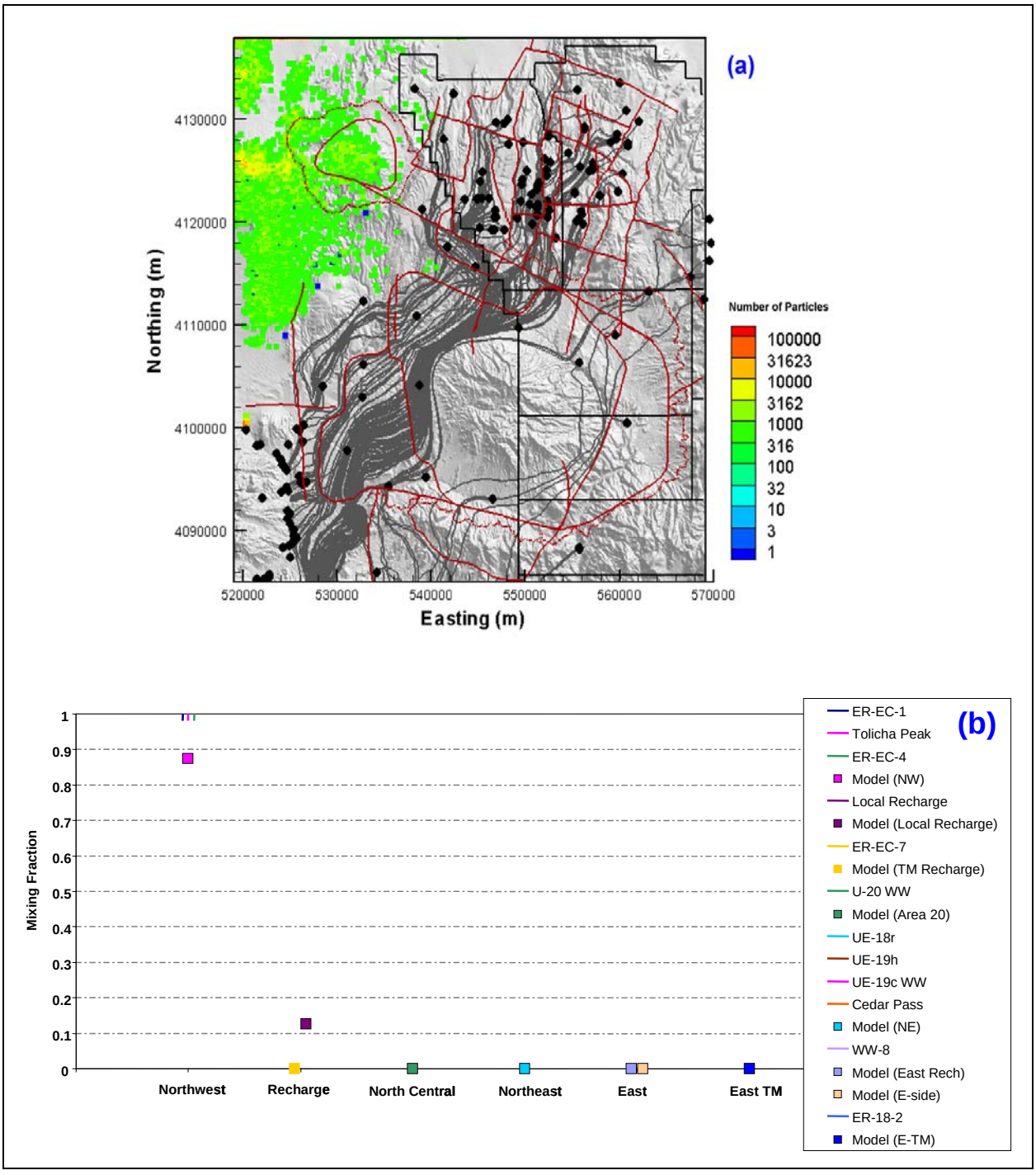

Figure 7-61
Comparison of Flow Model with Geochemical Mixing Targets at ER-OV-05 for BN-USGSD-SDA in the Reduced LCCU1 Permeability Alternative

Figure (a) shows the flow paths as mapped by forward SPTR particles originating at wells (grey lines) and the source recharge locations identified by reverse PTRK particle tracking (colored squares). Figure (b) shows the model comparison with geochemical mixing target ranges.

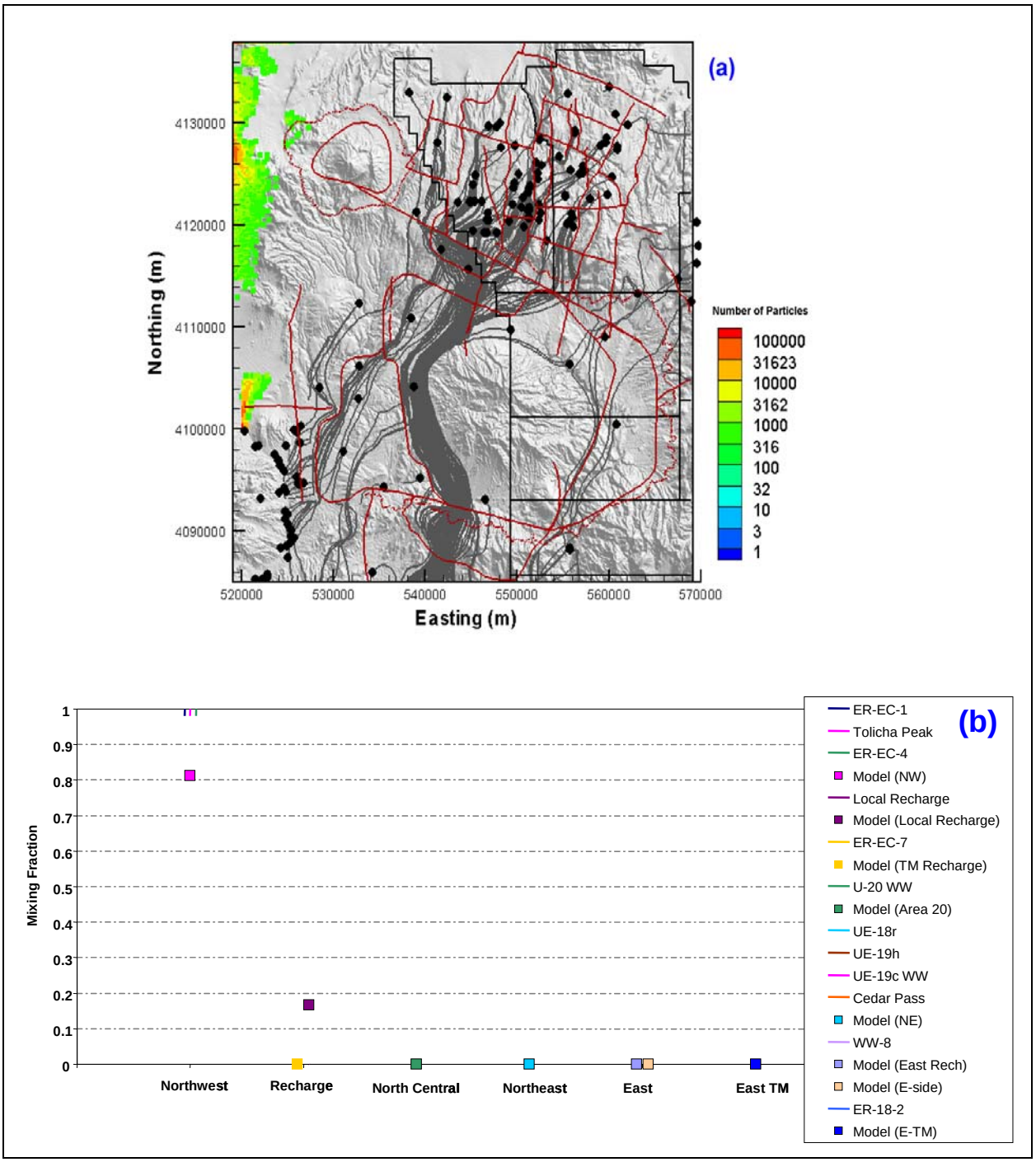

Figure 7-62
Comparison of Flow Model with Geochemical Mixing Targets at ER-OV-05 for BN-DRIA-SDA in the Reduced LCCU1 Permeability Alternative

Figure (a) shows the flow paths as mapped by forward SPTR particles originating at wells (grey lines) and the source recharge locations identified by reverse PTRK particle tracking (colored squares). Figure (b) shows the model comparison with geochemical mixing target ranges.

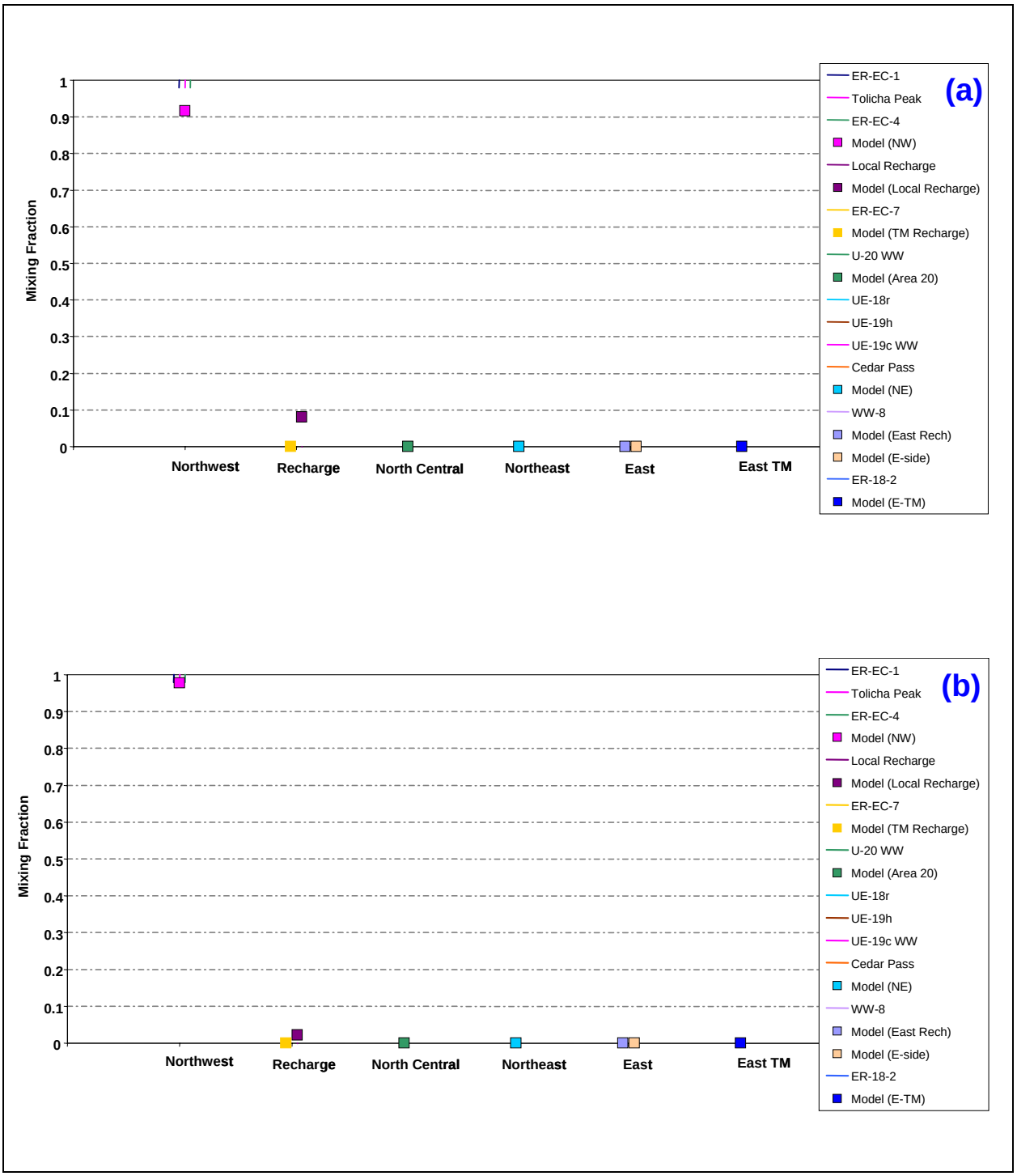

Figure 7-63
Quantitative Geochemical Comparisons at Well ER-OV-05 for (a) BN-USGSD-SDA and (b) BN-DRIA-SDA

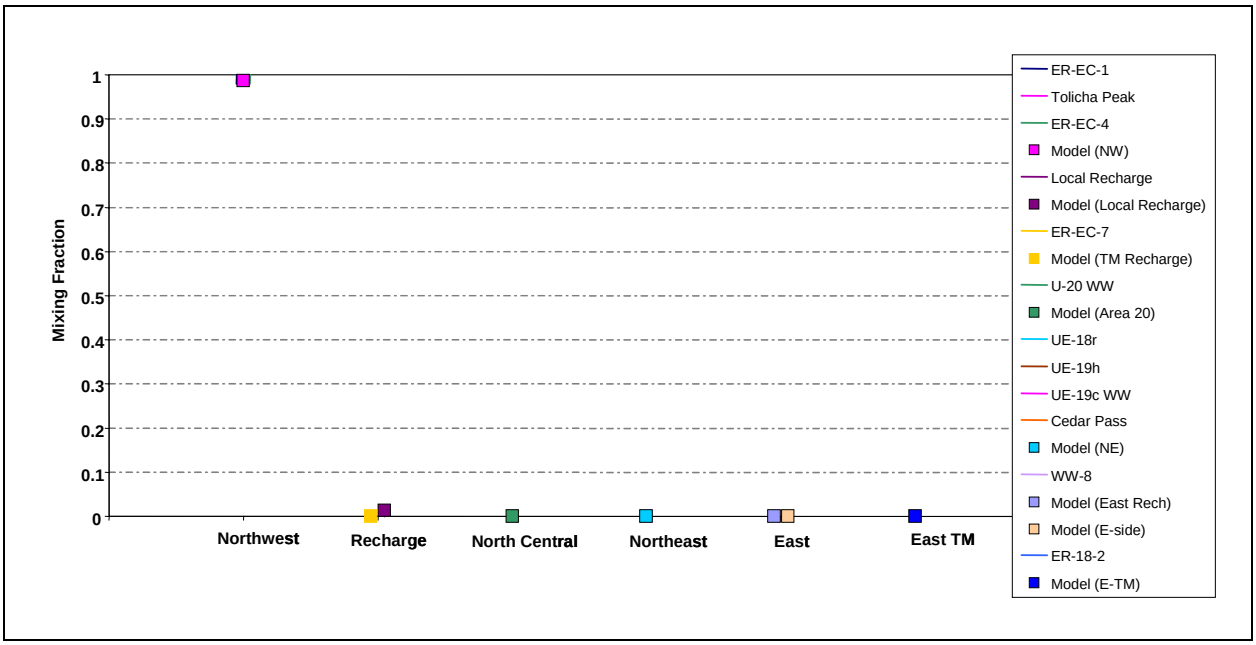

Figure 7-64
Comparison of Flow Model with Geochemical Mixing Targets at ER-OV-05 for BN-MME-ADA

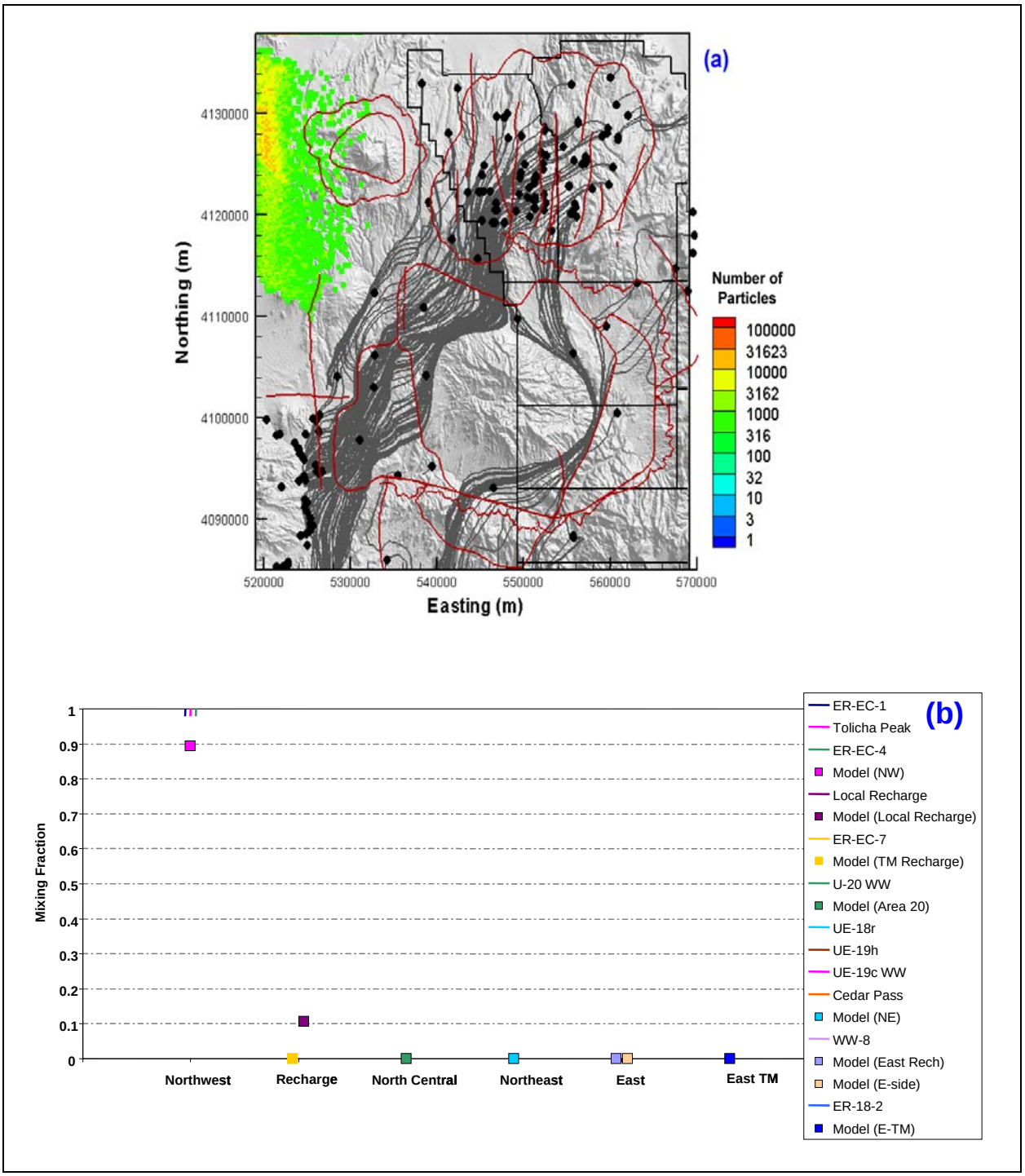

Figure 7-65
Comparison of Flow Model with Geochemical Mixing Targets at ER-OV-05 for SCCC-MME-SDA

Figure (a) shows the flow paths as mapped by forward SPTR particles originating at wells (grey lines) and the source recharge locations identified by reverse PTRK particle tracking (colored squares). Figure (b) shows the model comparison with geochemical mixing target ranges.

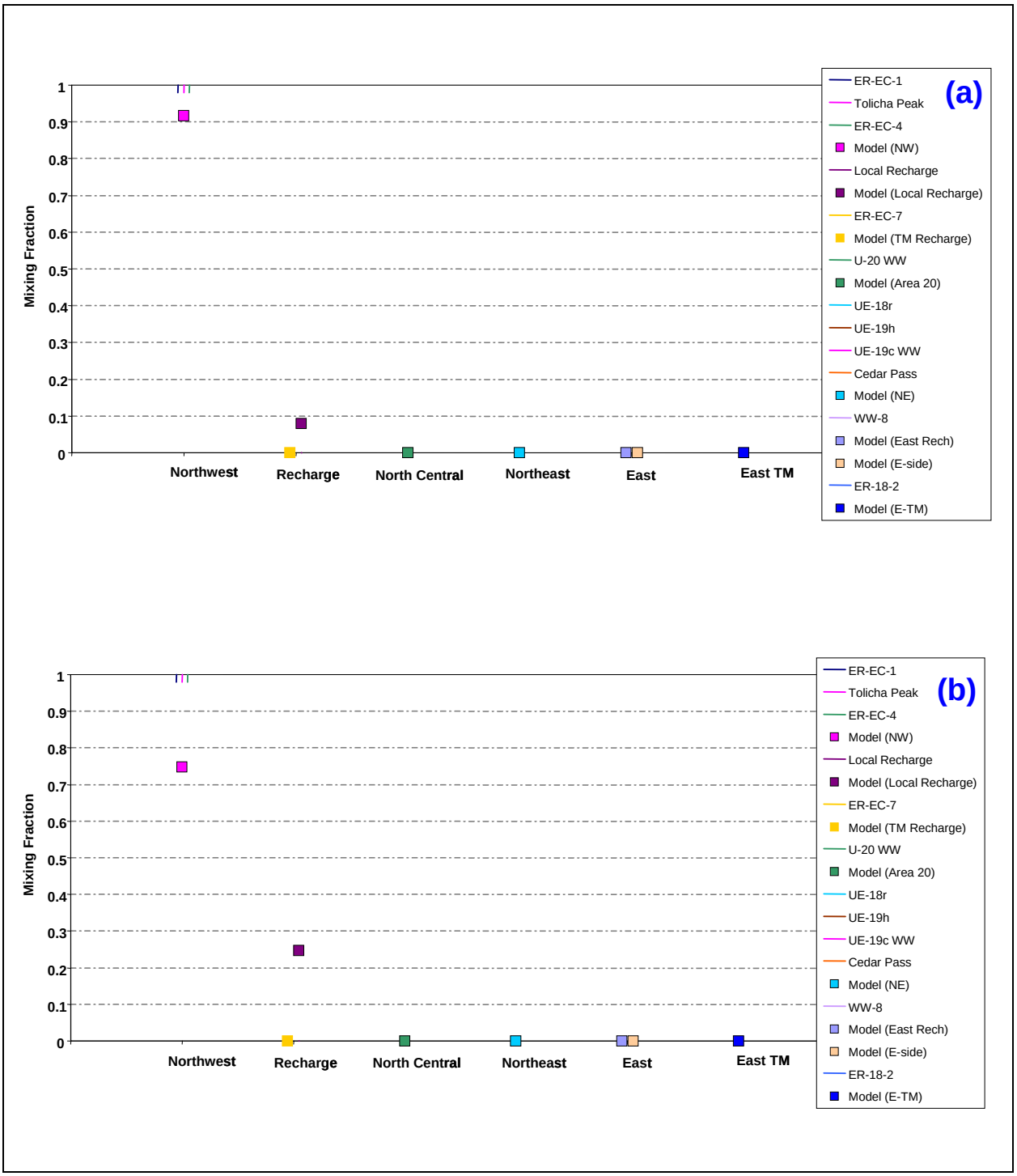

Figure 7-66
Quantitative Geochemical Comparisons at ER-OV-05 for (a) SCCC-USGSD-SDA and (b) SCCC-DRIA-SDA

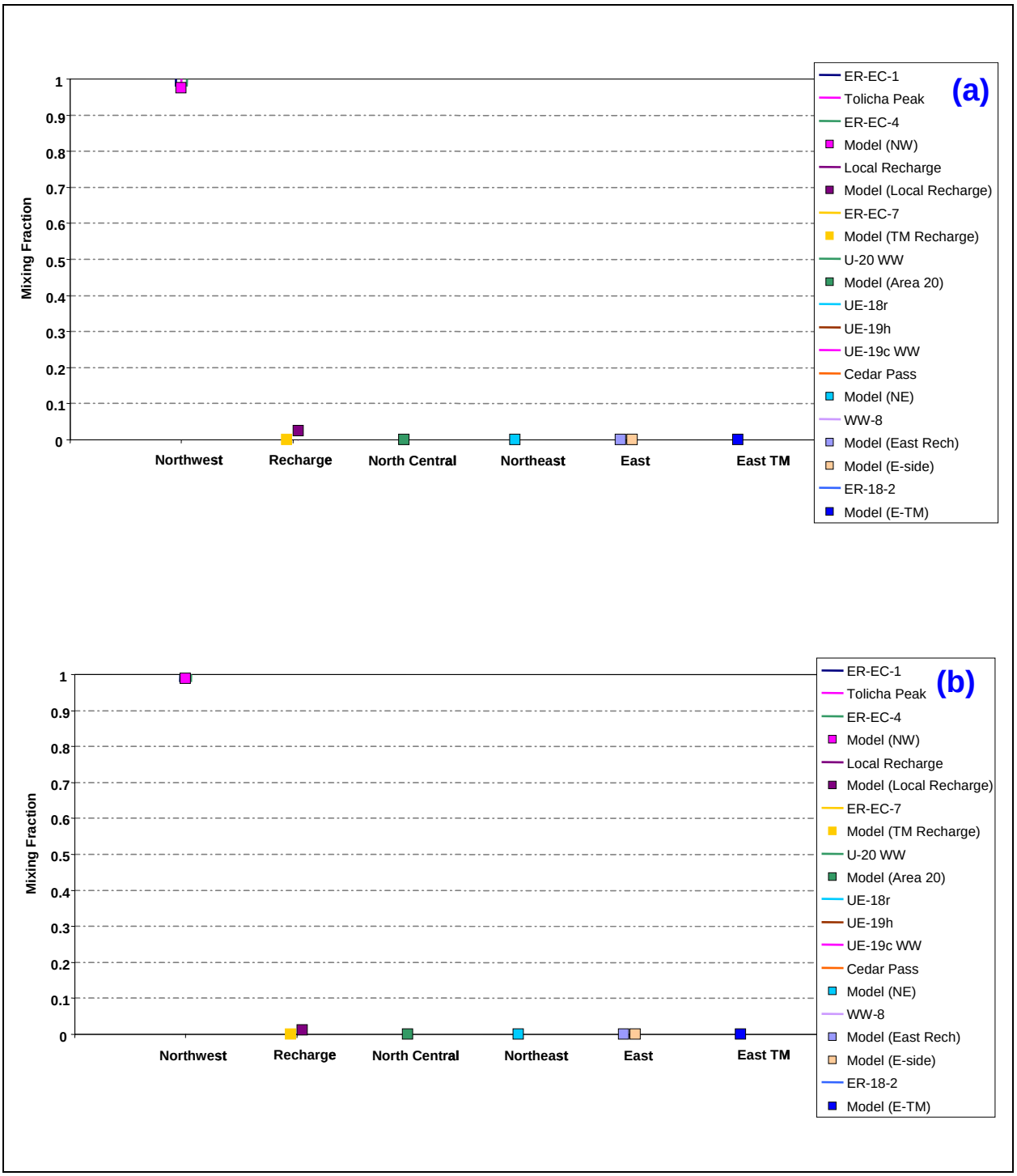

Figure 7-67
Quantitative Geochemical Comparison at ER-OV-05 for (a) PZUP-MME-SDA and (b) DRT-MME-SDA

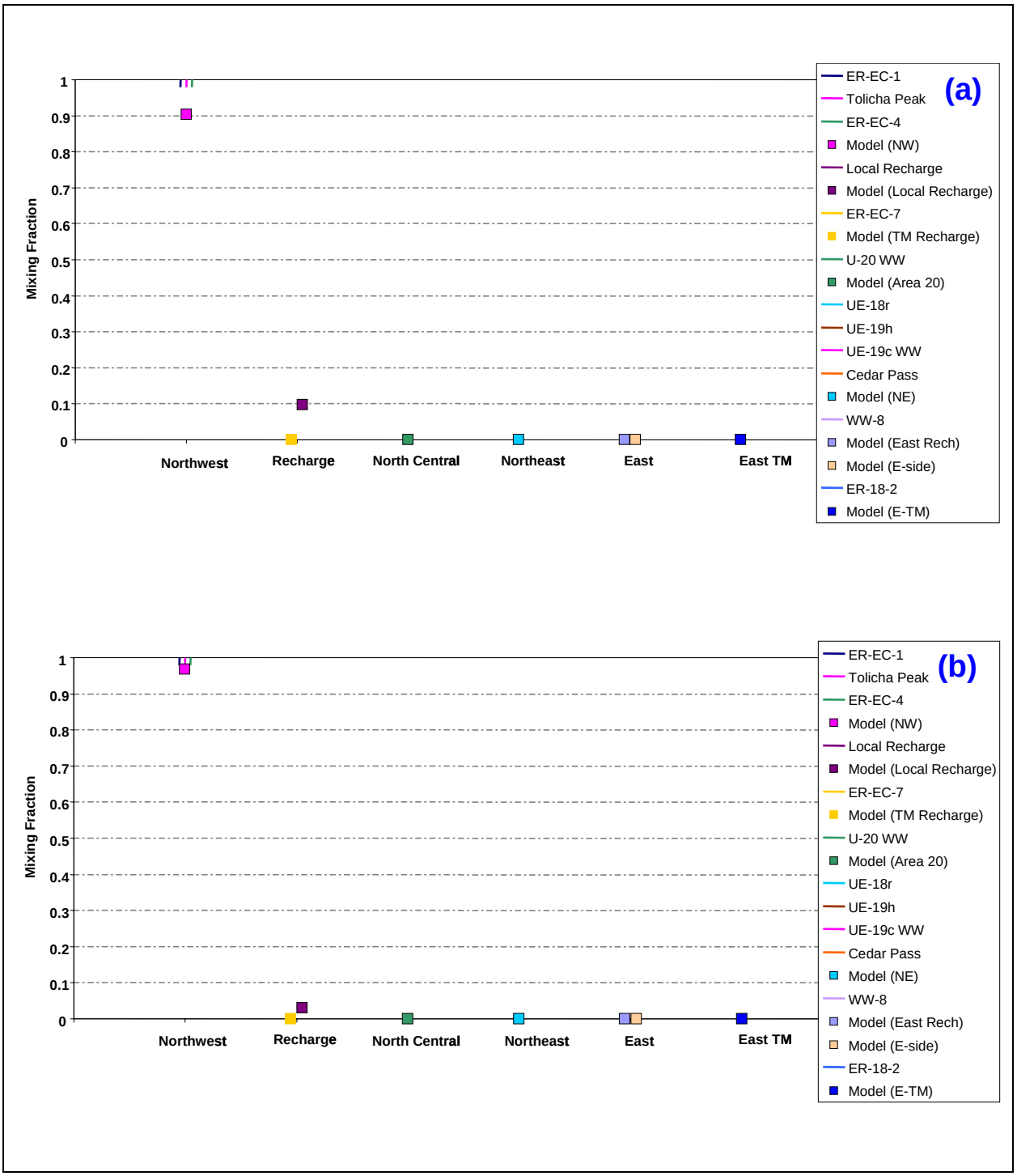

Figure 7-68
Quantitative Geochemical Comparisons at ER-OV-05 for (a) RIDGE-MME-SDA and (b) TCL-MME-SDA

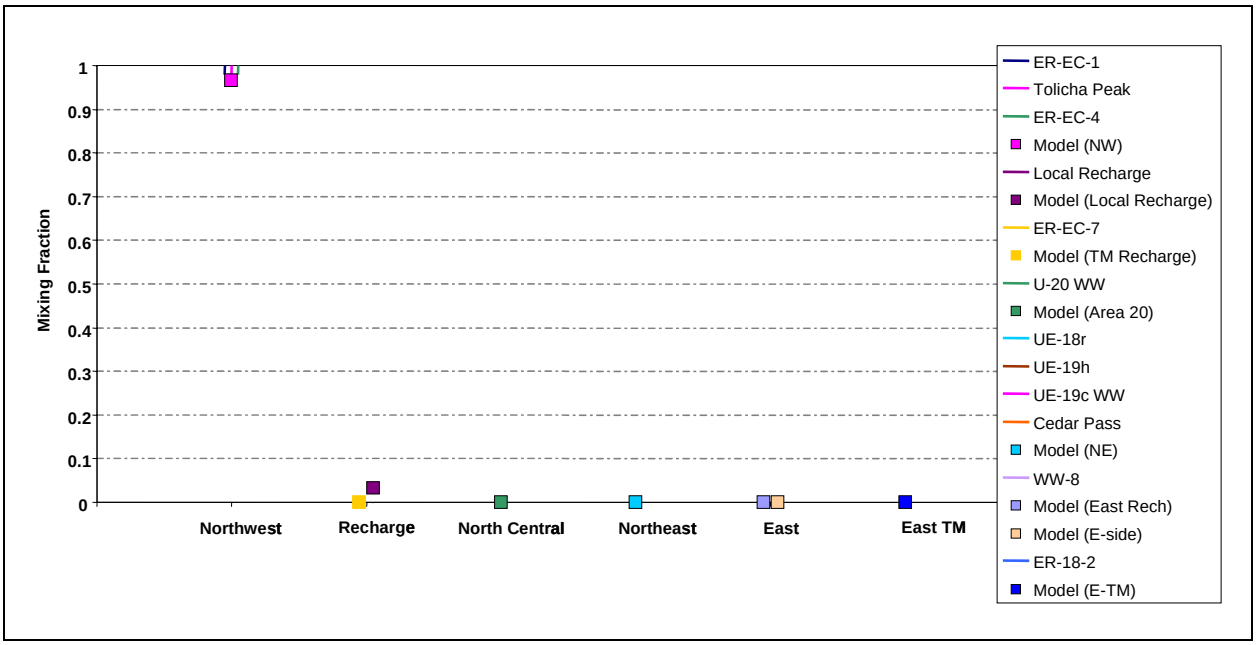

Figure 7-69
Comparison of Flow Model with Geochemical Mixing Targets at ER-OV-05 for SEPZ-MME-SDA

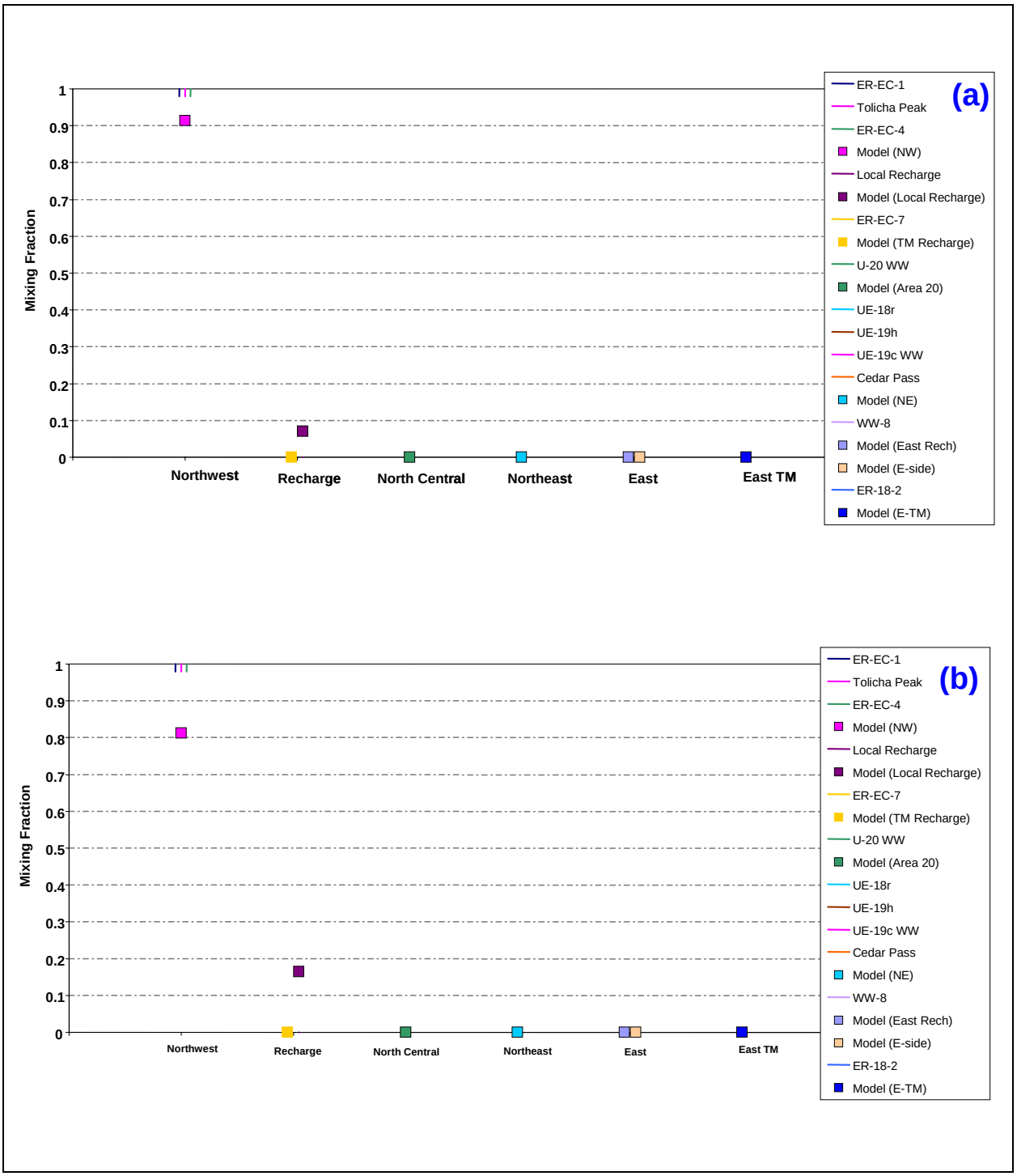

Figure 7-70
Quantitative Geochemical Comparisons at ER-OV-05 for (a) PZUP-USGSD-SDA and (b) PZUP-DRIA-SDA

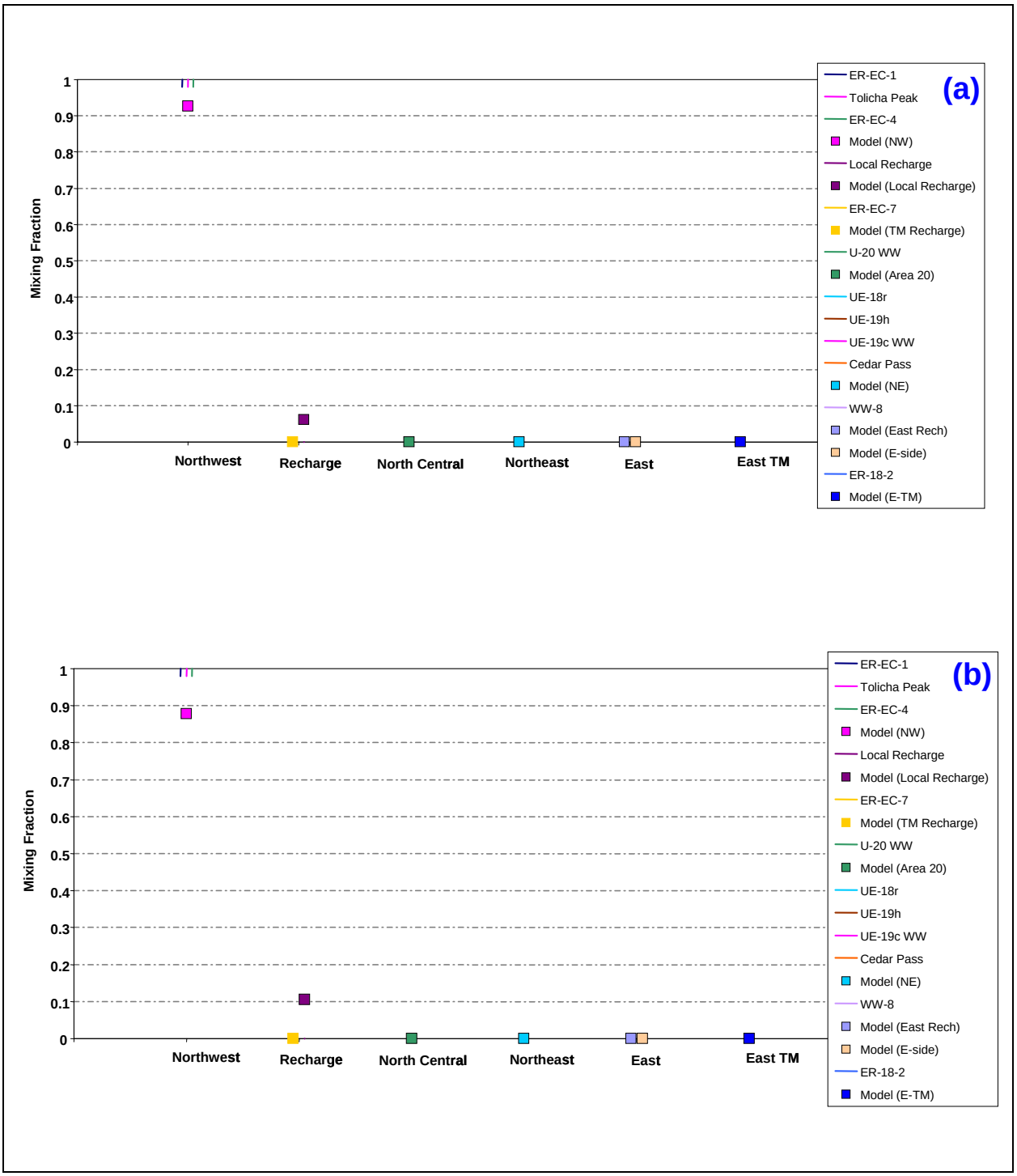

Figure 7-71
Quantitative Geochemical Comparisons at ER-OV-05 for (a) DRT-USGSD-SDA and (b) DRT-DRIA-SDA

7.3.5 ER-OV-04a

7.3.5.1 Alternative Water-Balance Conditions, BN HFM

Moving from ER-OV-05 to ER-OV-04a, the predominance of northwest source water at the target well decreases as more mixing occurs with water originating east of the Purse Fault. The greater total flux DRIA water-balance model does not capture the mixing trend as well, with excessive source water coming from the northwest and local recharge and almost no source water from east of the Purse Fault (Figure 7-72). The BN-USGSD-SDA reduced LCCU1 permeability alternative captures this trend well, but with an overestimation of northwest source water (Figure 7-73).

Examination of results at ER-OV-04a for the base HFM (with higher LCCU1 permeability) model with alternative water-balance conditions in Figure 7-74 shows that the USGSD model captures the trend well, with the exception of nearly 30 percent source contribution from Gold Meadows across the eastern model boundary. The DRIA model does not show the east boundary component, but does result in a greater overestimate of northwest source water. The DRIA model for the BN HFM is a significant improvement over the DRIA model for the reduced LCCU1 permeability alternative. Finally, the BN-MME-ADA model shows a very good match to the trend, but with a substantial overestimate of local recharge as a result of the MME recharge map (Figure 7-75).

7.3.5.2 SCCC Alternative HFM

The SCCC alternative HFM model produces a flow field that captures the geochemistry mixing trend quite well, with a slight overestimate of local recharge and a small contribution of Timber Mountain recharge not estimated in the geochemistry (Figure 7-76). Contrary to the MME model results with the SCCC HFM, both the USGSD and DRIA conditions lead to models with overestimates of either northwest sources or local recharge and no north-central or northeast components at ER-OV-04a (Figure 7-77).

7.3.5.3 PZUP, DRT, RIDGE, TCL, and SEPZ Alternative HFMs

The remaining alternative HFM scenarios with MME water-balance conditions show the mixing reasonably well (Figures 7-78 through 7-80), although some perform better with regard to inflow from the east model boundary and/or local recharge as listed below:

- PZUP – overall good match, similar to SCCC with slight overestimate of local recharge and Timber Mountain source.
- DRT – overestimates the northwest component and underestimates the northeast component, thus missing the dominant mixing trend, but matches local recharge well.
- RIDGE – matches the north-central and northeast components, but troublesome east model boundary inflow offsets underestimate of northwest component. Local recharge estimated well.
- TCL – overall good match, east model boundary component seems to offset underestimate of north-central component.
- SEPZ – very good match, but with slight east boundary component and slight northwest overestimate.

The PZUP model with USGSD and DRIA water-balance conditions also matches the geochemistry well, although the USGSD model shows a 20 percent contribution from the east model boundary at Gold Meadows and the DRIA model overestimates local recharge to this well (Figure 7-81). The DRT-USGSD models shows substantial overestimation of northwest inflow, whereas the DRI recharge map on DRT corrects that error at the expense of excessive local infiltration (Figure 7-82).

7.3.5.4 Summary: ER-OV-04a

At ER-OV-04a, there are four different, but often related, mismatches between the model simulations and the geochemistry targets. They are (a) overestimation of source groundwater from the northwest, (b) underestimation of source groundwater from the north central and northeast, (c) overestimation of source water from the eastern model boundary, and (d) overestimation of local recharge. In general, one would expect the overestimation of local recharge to be a function of the water-balance conditions. However, that is not necessarily the case. The inflow from the eastern model boundary is often related to the HFM. Table 7-14 identifies the mismatch issues for each simulation. Only those with more than a 10 percent mismatch are identified.

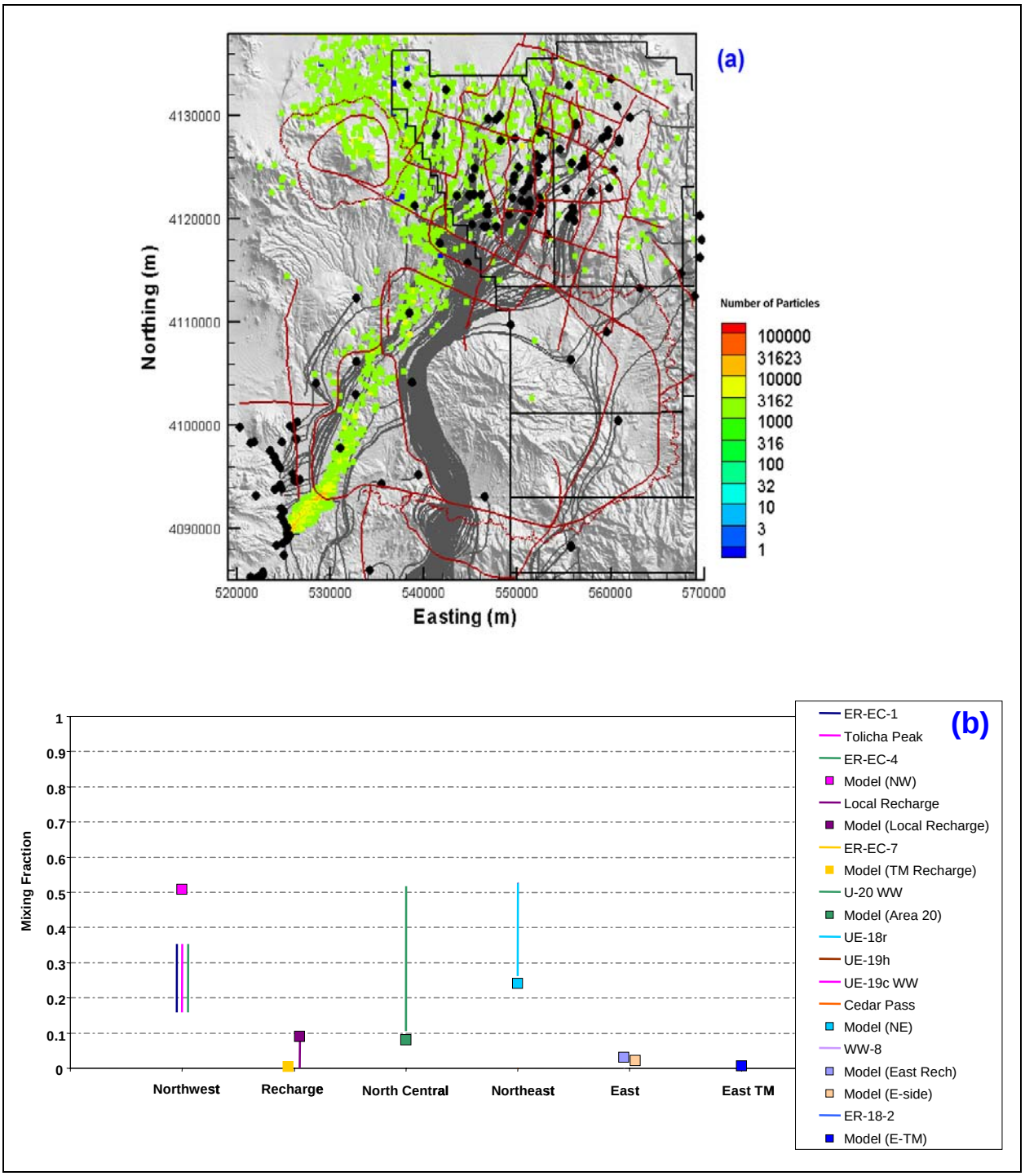

Figure 7-72
Comparison of Flow Model with Geochemical Mixing Targets at ER-OV-04a for BN-DRIA-SDA in the Reduced LCCU1 Permeability Alternative

Figure (a) shows the flow paths as mapped by forward SPTR particles originating at wells (grey lines) and the source recharge locations identified by reverse PTRK particle tracking (colored squares). Figure (b) shows the model comparison with geochemical mixing target ranges.

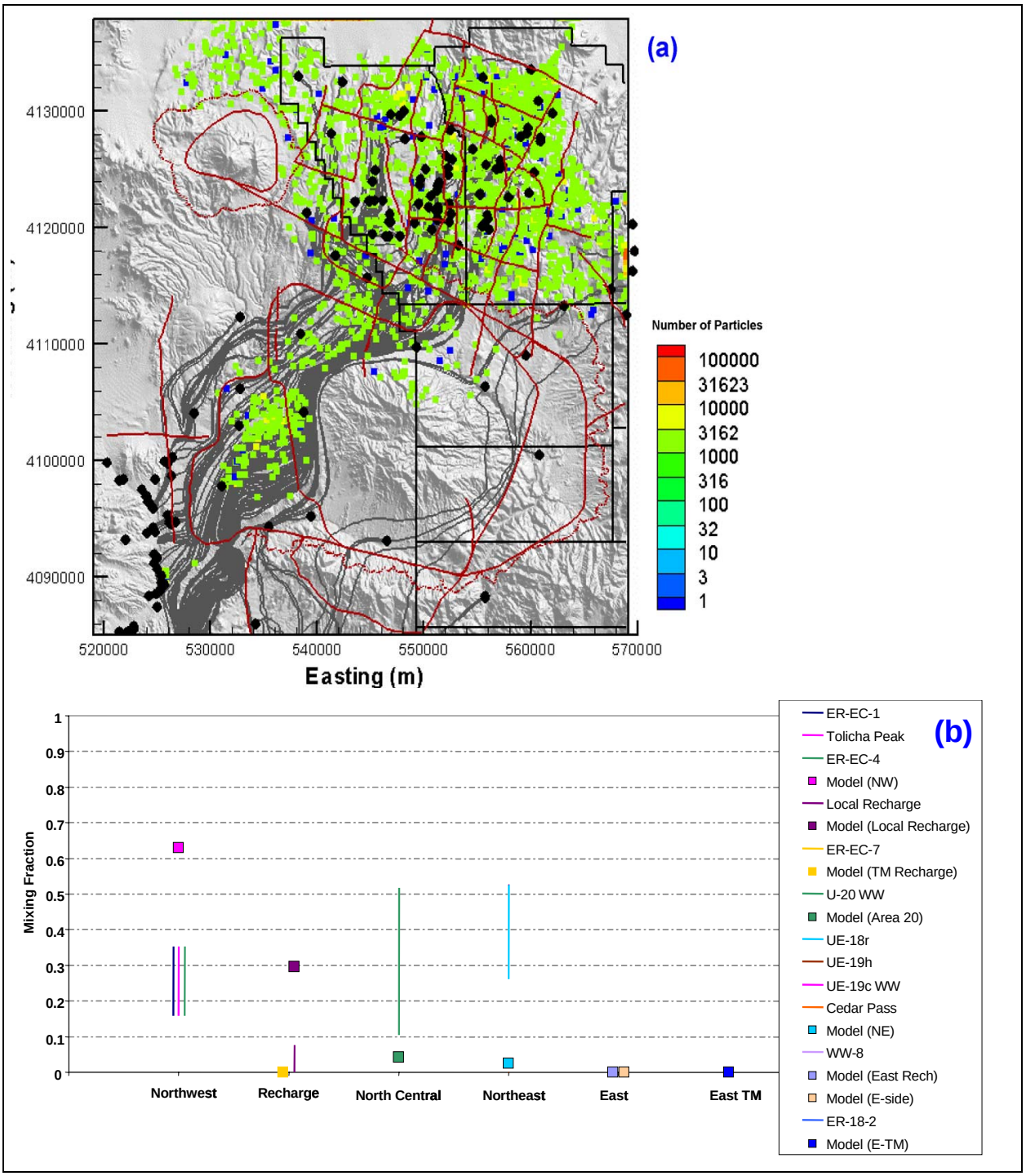

Figure 7-73
Comparison of Flow Model with Geochemical Mixing Targets at ER-OV-04a for BN-USGSD-SDA in the Reduced LCCU1 Permeability Alternative

Figure (a) shows the flow paths as mapped by forward SPTR particles originating at wells (grey lines) and the source recharge locations identified by reverse PTRK particle tracking (colored squares). Figure (b) shows the model comparison with geochemical mixing target ranges.

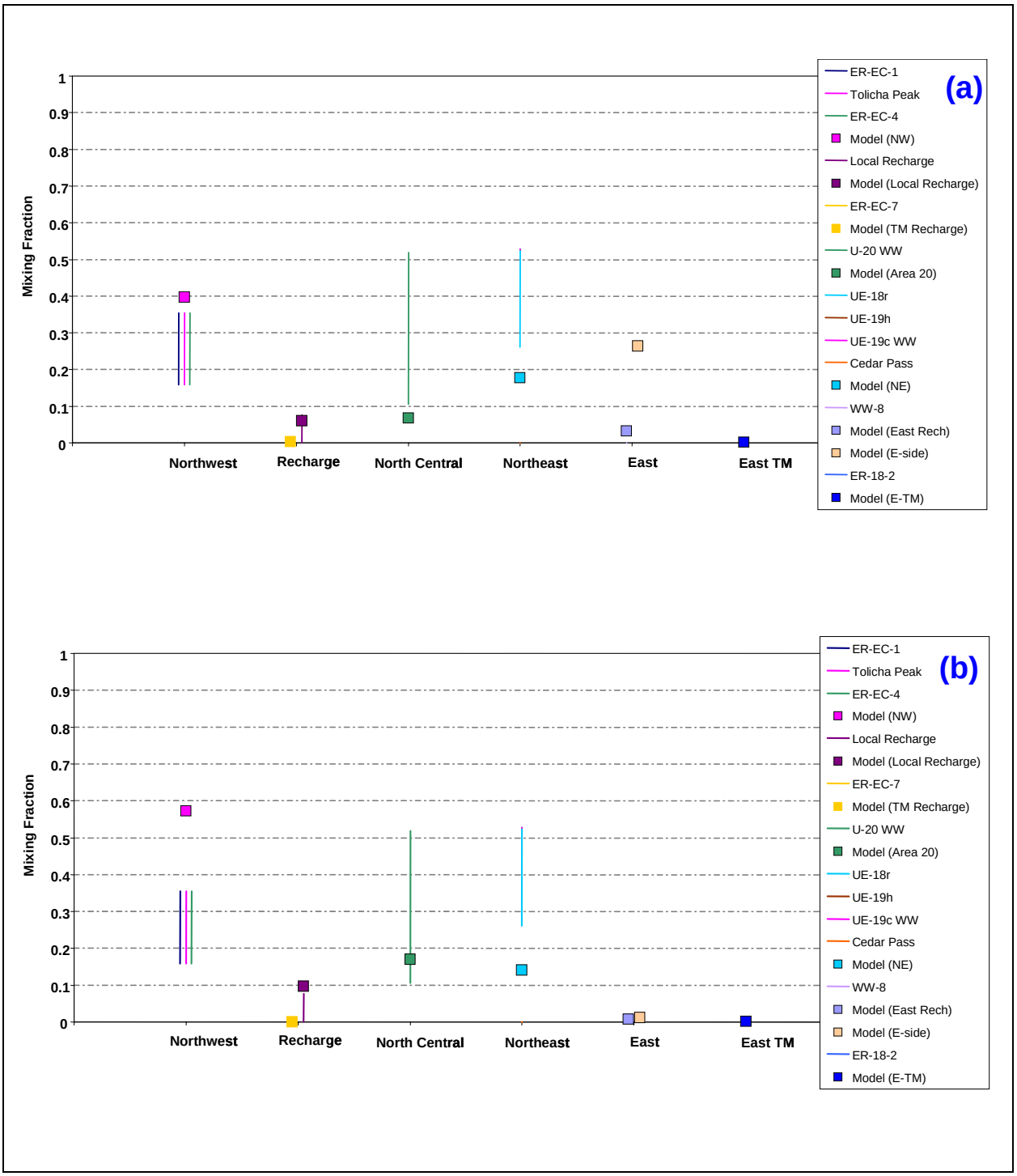

Figure 7-74
Quantitative Geochemical Comparison at ER-OV-04a for (a) BN-USGSD-SDA and (b) BN-DRIA-SDA

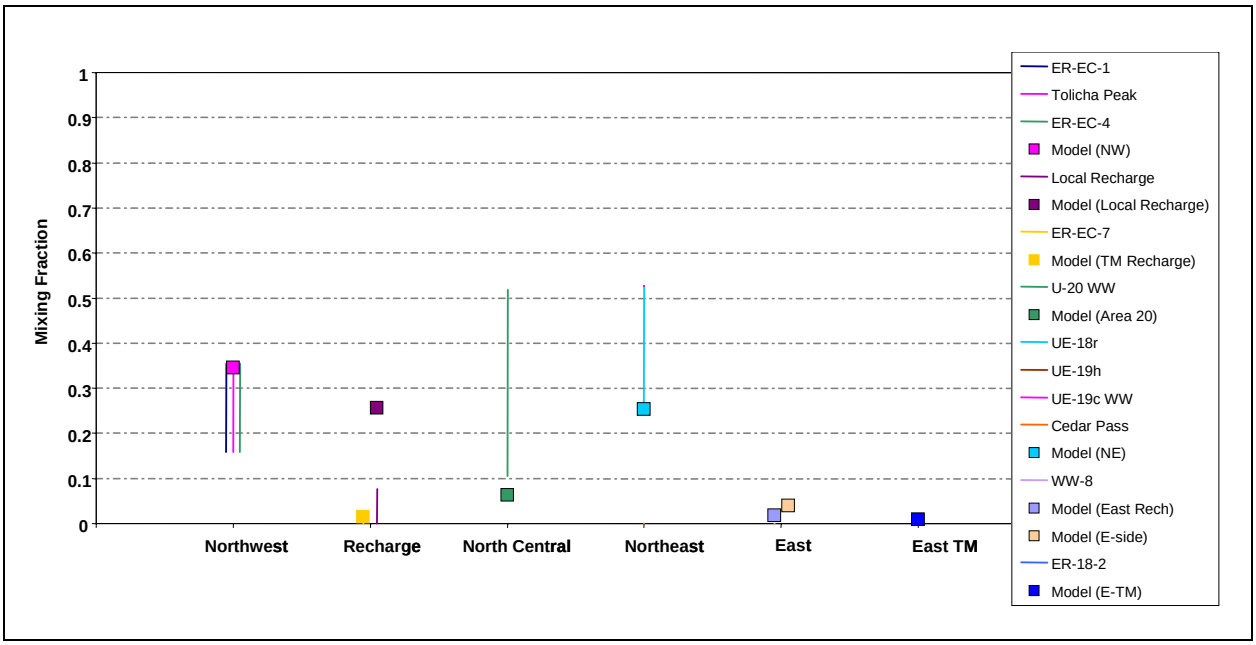

Figure 7-75
Comparison of Flow Model with Geochemical Mixing Targets at ER-OV-04a for BN-MME-ADA

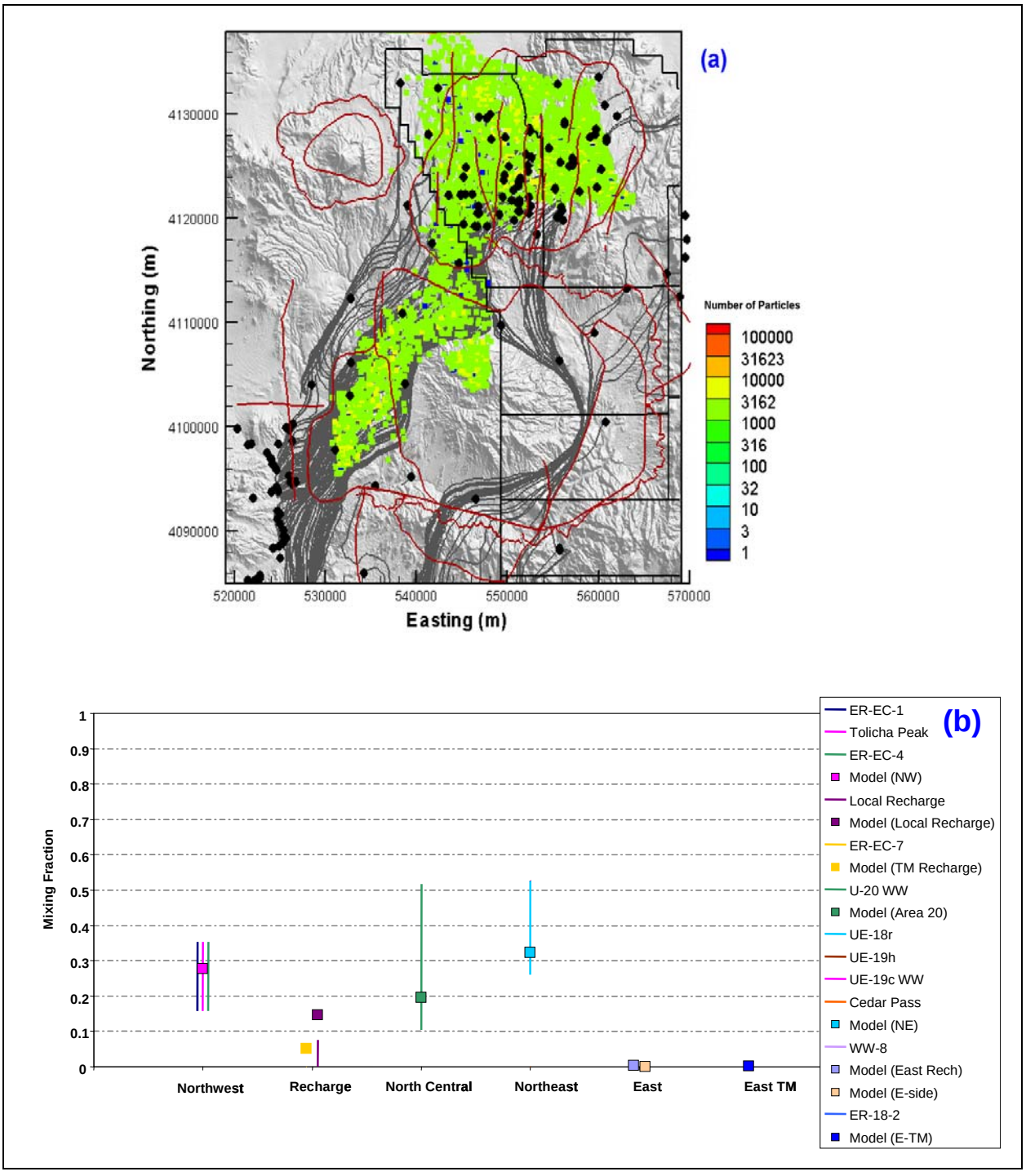

Figure 7-76
Comparison of Flow Model with Geochemical Mixing Targets at ER-OV-04a for SCCC-MME-SDA

Figure (a) shows the flow paths as mapped by forward SPTR particles originating at wells (grey lines) and the source recharge locations identified by reverse PTRK particle tracking (colored squares). Figure (b) shows the model comparison with geochemical mixing target ranges.

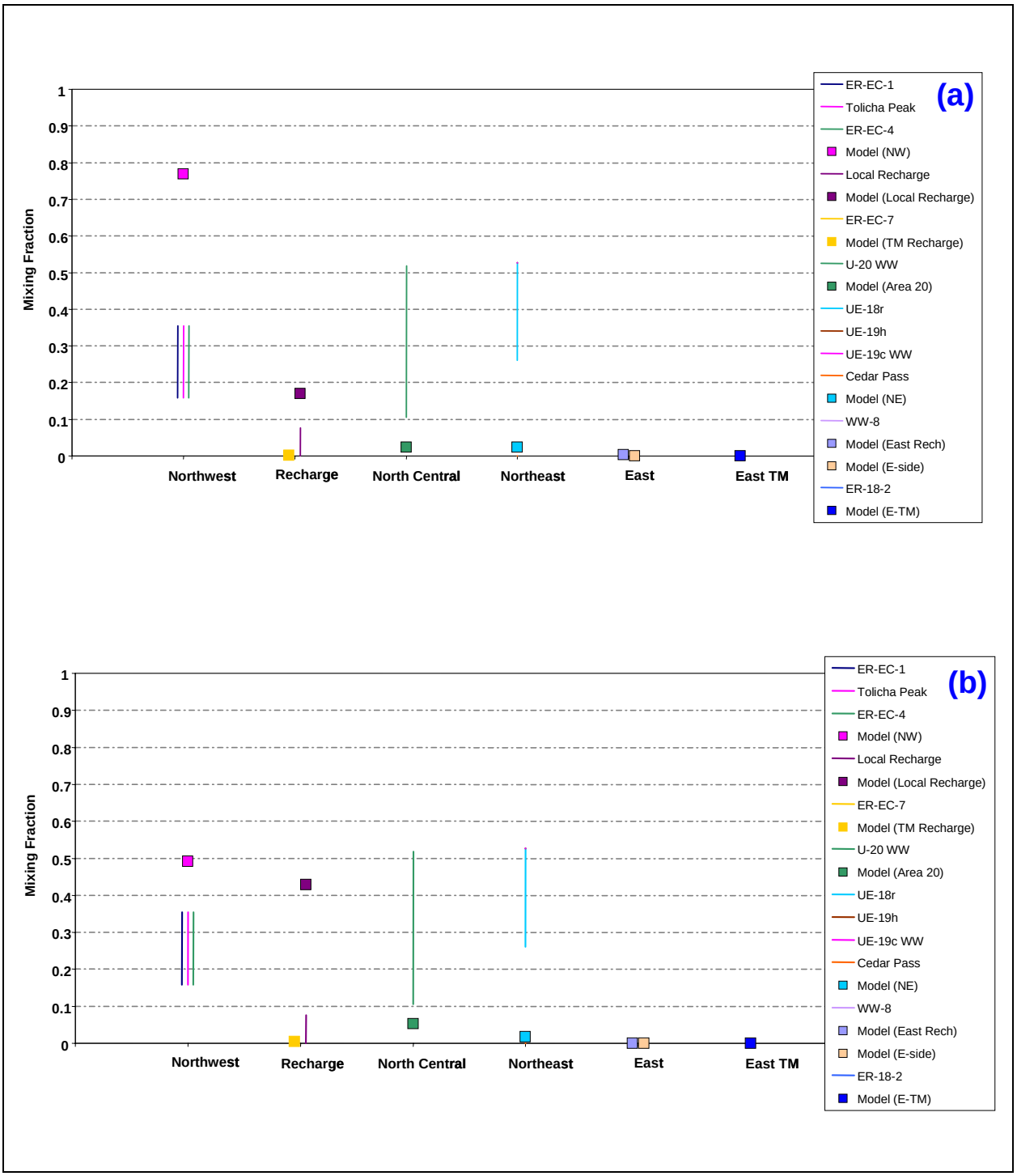

Figure 7-77
Quantitative Geochemical Comparisons at ER-OV-04a for (a) SCCC-USGSD-SDA and (b) SCCC-DRIA-SDA

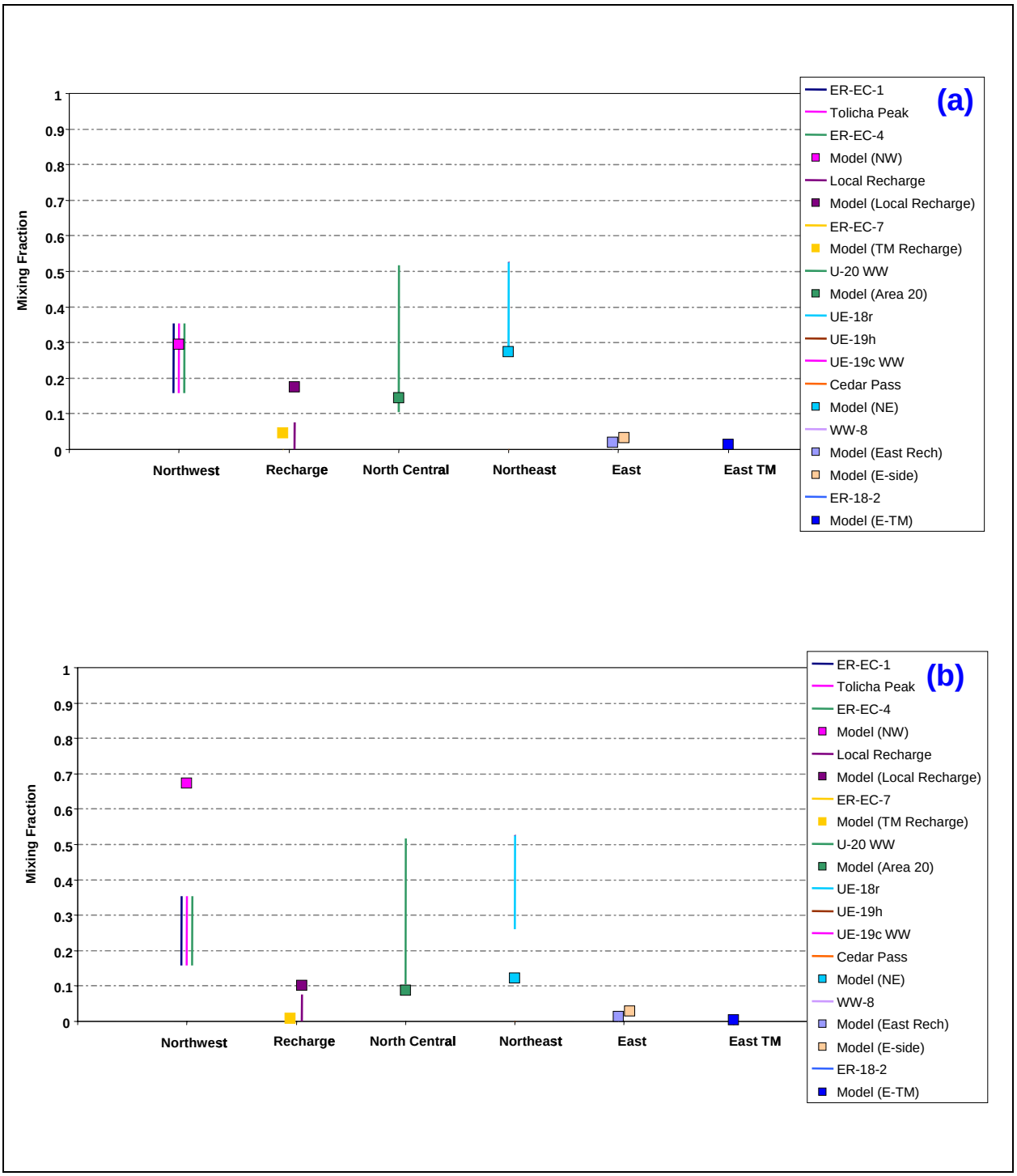

Figure 7-78
Quantitative Geochemical Comparisons at ER-OV-04a for (a) PZUP-MME-SDA and (b) DRT-MME-SDA

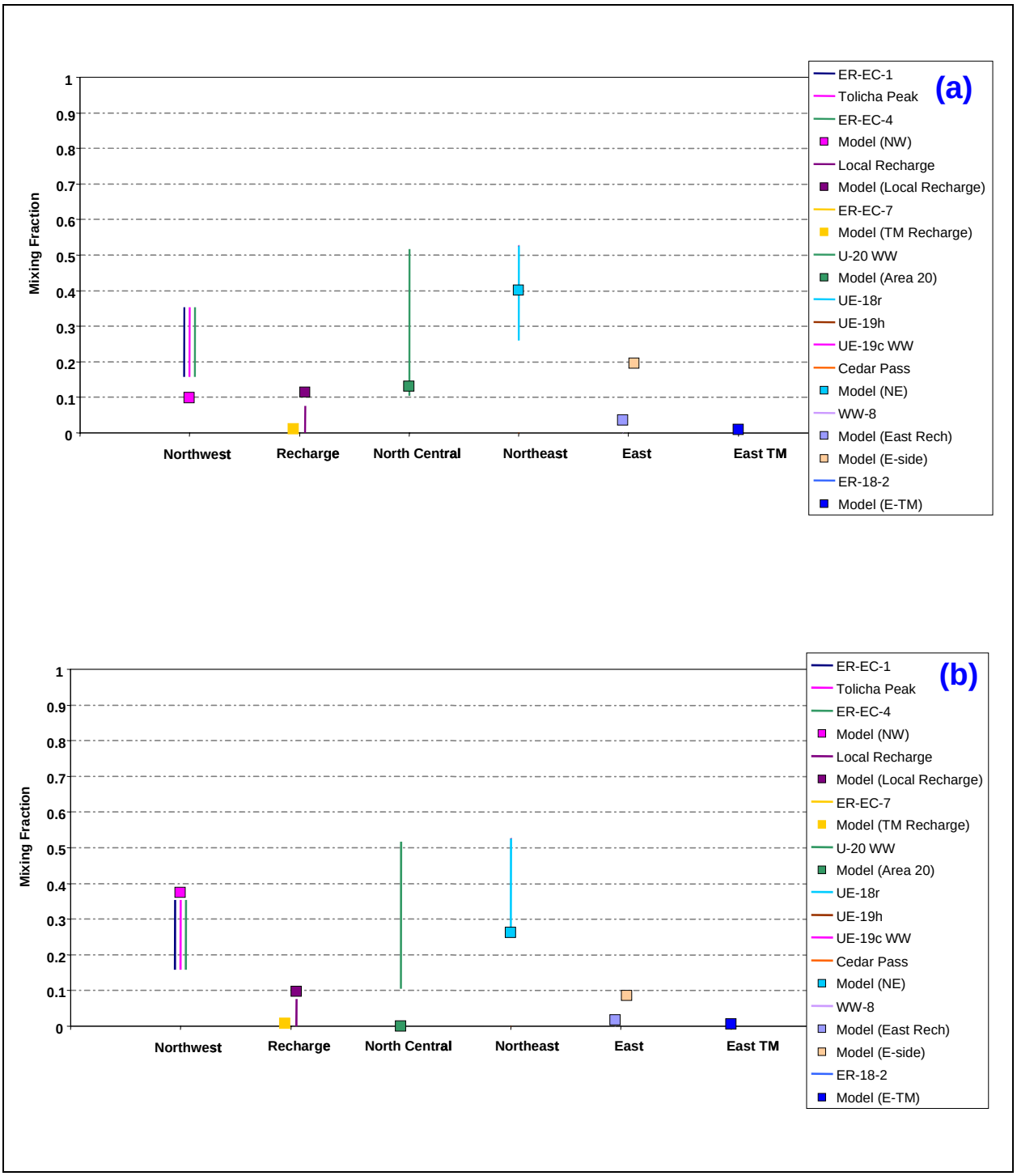

Figure 7-79
Quantitative Geochemical Comparisons at ER-OV-04a for (a) RIDGE-MME-SDA and (b) TCL-MME-SDA

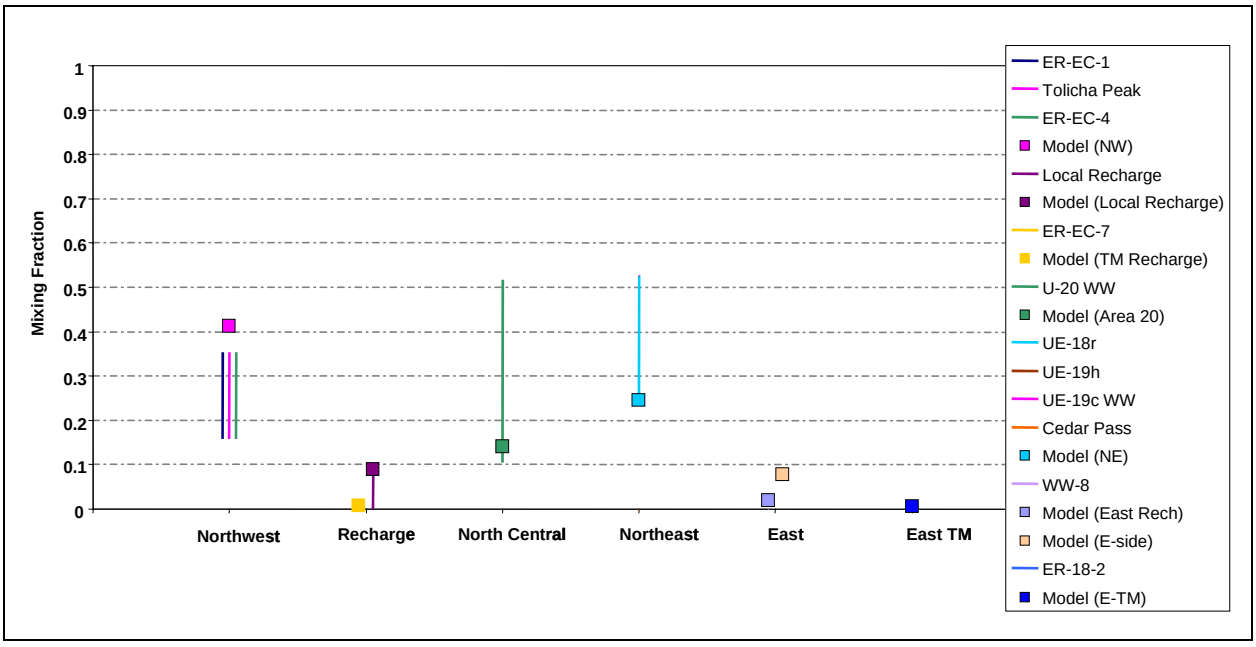

Figure 7-80
Comparison of Flow Model with Geochemical Mixing Targets at ER-OV-04a for SEPZ-MME-SDA

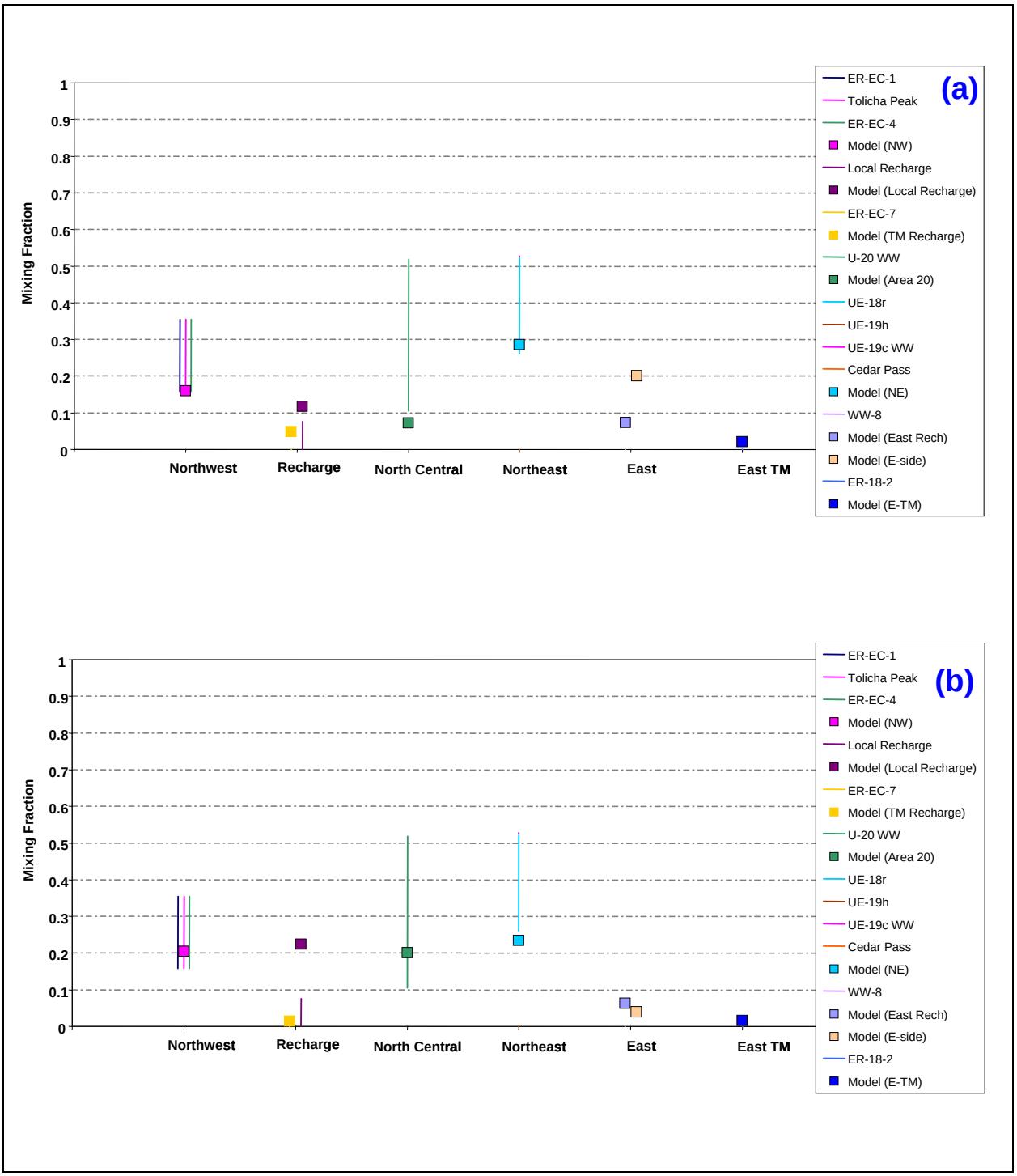

Figure 7-81
Quantitative Geochemical Comparisons at ER-OV-04a for (a) PZUP-USGSD-SDA and (b) PZUP-DRIA-SDA

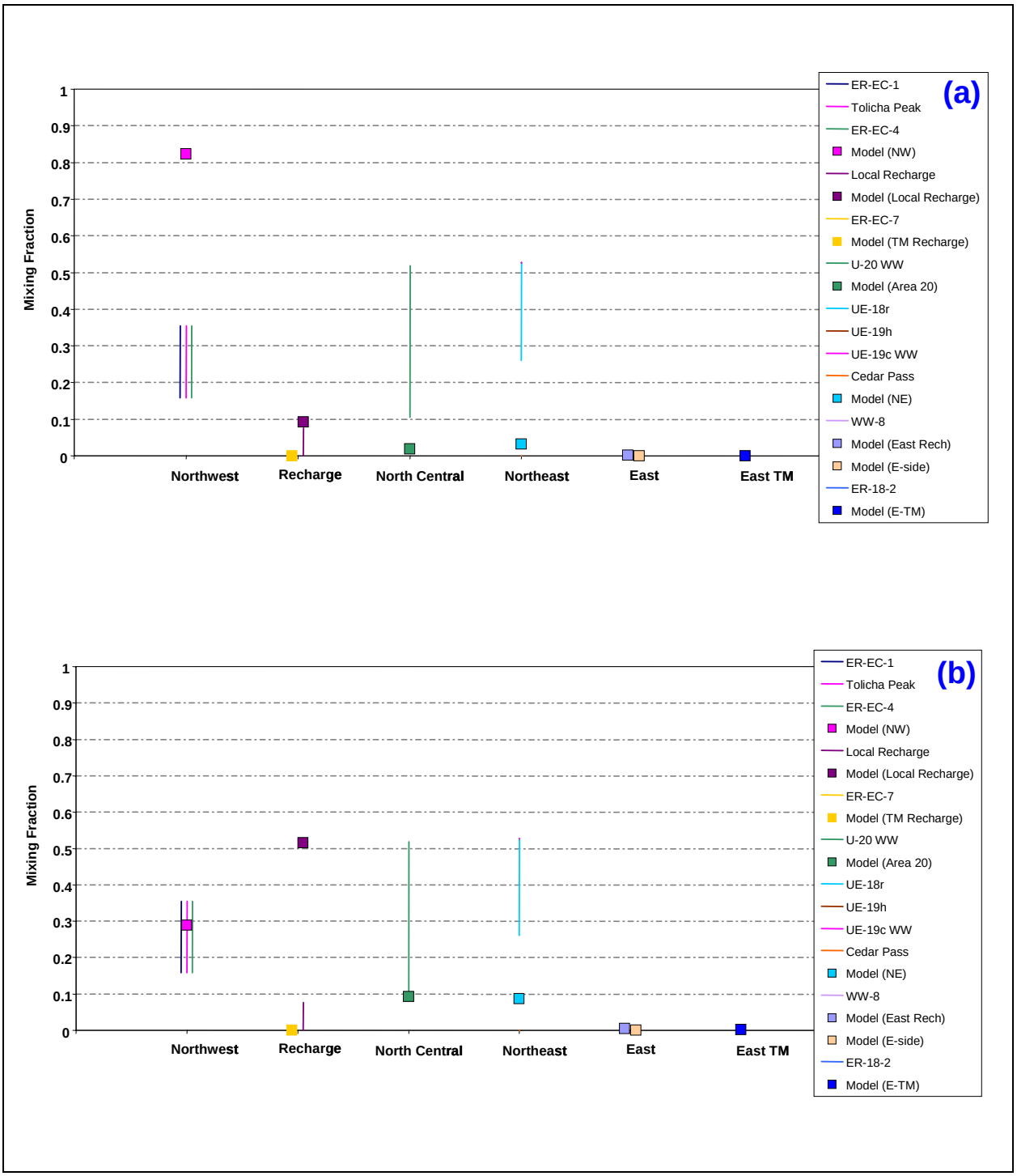

Figure 7-82
Quantitative Geochemical Comparisons at ER-OV-04a for (a) DRT-USGSD-SDA and (b) DRT-DRIA-SDA

Table 7-14
Comparison of Alternative Models at ER-OV-04a

HFM	Water-Balance Condition	Overestimation of Northwest Source	Underestimation of North-Central and Northeast Source	Overestimation of East Boundary Source	Overestimation of Local Recharge
BN-SDA reduced LCCU1 permeability alternative	MME	X			
	USGSD	X			
	DRIA	X	X		X
BN-SDA	MME				
	USGSD			X	
	DRIA	X	X		
BN-ADA	MME				X
SCCC-SDA	MME				
	USGSD	X	X		
	DRIA	X	X		X
PZUP	MME				
DRT	MME	X	X		
RIDGE	MME			X	
TCL	MME				
SEPZ	MME				
PZUP	USGSD			X	
	DRIA				X
DRT	USGSD	X	X		
	DRIA		X		X

7.3.6 ER-OV-03a

7.3.6.1 Alternative Water-Balance Conditions, BN HFM

The mixing ratios at ER-OV-03a for the BN-USGSD-SDA reduced LCCU1 permeability alternative case are similar to those of ER-OV-04a, although with somewhat larger uncertainty ranges. The USGSD simulation matches the targets very well, with only a small overestimate of source water from the northwest (Figure 7-83). By comparison, the BN-DRIA-SDA reduced LCCU1 permeability alternative simulation retains the same problem it had at ER-OV-04a; the only sources for ER-OV-03a water are from the northwest and from local recharge in Oasis Valley and Thirsty Canyon (Figure 7-84).

Similar to ER-OV-04a, the BN-USGSD-SDA (high LCCU1 permeability) matches the chemistry targets well at ER-OV-03a, with the exception of a 20 percent contribution from Gold Meadows (Figure 7-85). Results at ER-OV-03a for BN-DRIA-SDA are better than for the reduced LCCU1 permeability alternative because they match contributions from the north central, northeast, and northwest, but they overestimate the local recharge source. The BN-MME-ADA model also provides a good match at this well, with the exception of an overestimate in local recharge that is expected with the MME water-balance conditions (Figure 7-86).

7.3.6.2 SCCC Alternative HFM

The SCCC alternative HFM model produces a flow field that captures the geochemistry mixing trend quite well, but with an overestimation of local recharge and a small contribution of Timber Mountain recharge not estimated in the geochemistry (Figure 7-87).

Unlike the SCCC model calibrated with MME conditions, the USGSD and DRIA models produce mixing results with no sources from the north central or northeast (Figure 7-88). The USGSD model overestimates the northwest source and the DRIA model overestimates local recharge.

7.3.6.3 PZUP, DRT, RIDGE, TCL, and SEPZ Alternative HFMs

The remaining alternative HFM scenarios with MME water-balance conditions show the mixing reasonably well (Figures 7-89 through 7-91), although some perform better with regard to inflow from the east model boundary and/or local recharge as listed below:

- PZUP – very good match.
- DRT – overestimates the northwest component and local recharge, resulting in slight underestimation of the northeast source component.
- RIDGE – underestimates northwest source, which is offset by Gold Meadows Source Component.
- TCL – overall good match, but with slight east boundary component.
- SEPZ – overall good match, but with slight east boundary component and recharge overestimate.

Figures 7-92 and 7-93 show the comparisons for PZUP and DRT with alternative water-balance conditions. The PZUP with USGSD water-balance conditions provides a good match at ER-OV-03a, but with 12 percent source from Gold Meadows. The DRIA also provides a good match to targets; the overestimate in local recharge can likely be grouped with the underestimate of northwest source water to make a reasonable chemical match.

The DRT with USGSD water-balance conditions far overshoots the estimate for northwest groundwater sources and predicts almost none from the north central and northeast. These errors are corrected substantially with DRIA water-balance conditions, but the local recharge is then overestimated.

7.3.6.4 Summary: ER-OV-03a

At ER-OV-03a, there are four different, but often related, mismatches between the model simulations and the geochemistry targets. They are (a) overestimation of source groundwater from the northwest, (b) underestimation of source groundwater from the north central and northeast, (c) overestimation of source water from the eastern model boundary, and (d) overestimation of local recharge. Table 7-15 identifies the mismatch issues for each simulation. Only those with more than a 10 percent mismatch are identified.

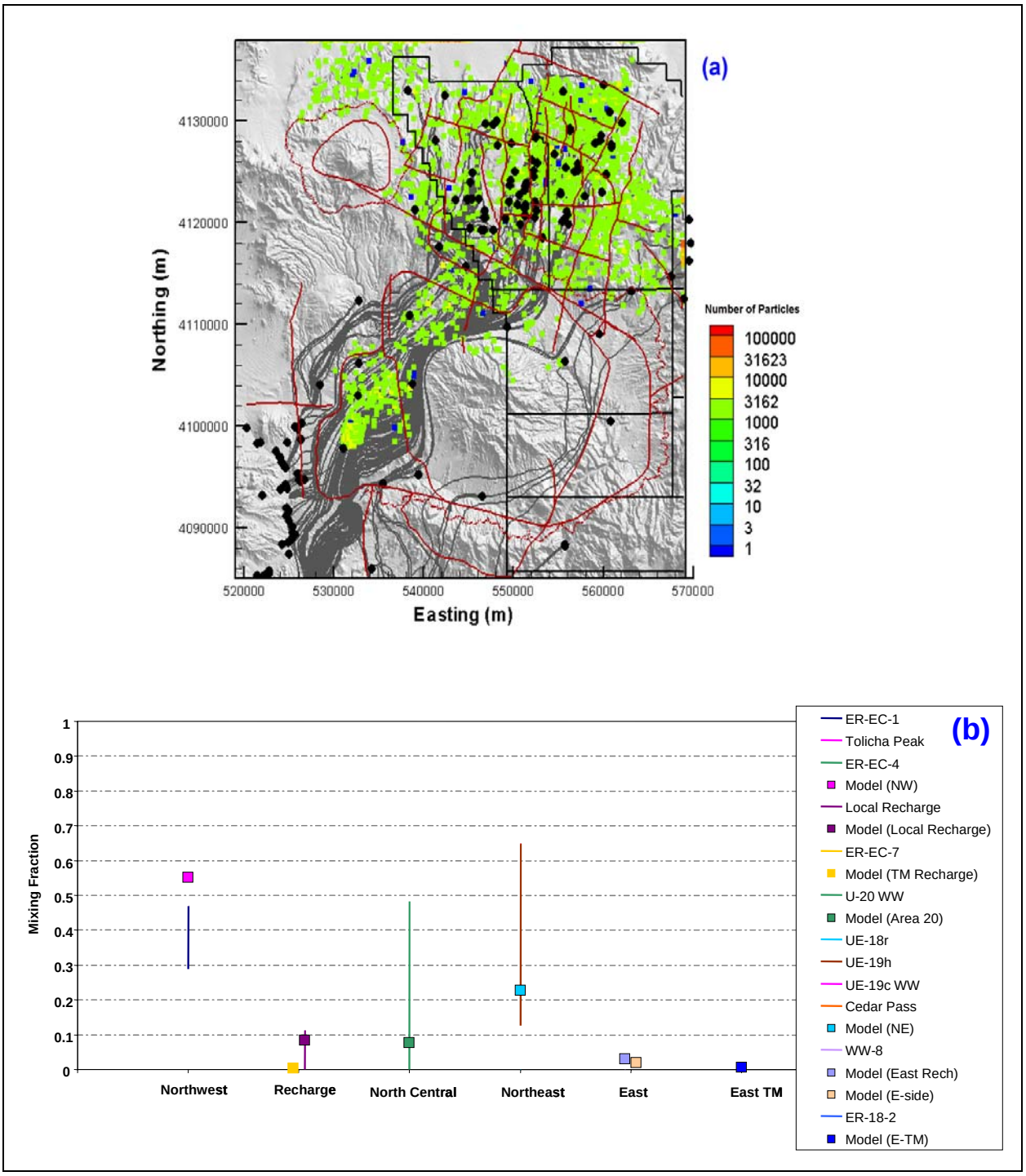

Figure 7-83
Comparison of Flow Model with Geochemical Mixing Targets at ER-OV-03a for BN-USGSD-SDA in the Reduced LCCU1 Permeability Alternative

Figure (a) shows the flow paths as mapped by forward SPTR particles originating at wells (grey lines) and the source recharge locations identified by reverse PTRK particle tracking (colored squares). Figure (b) shows the model comparison with geochemical mixing target ranges.

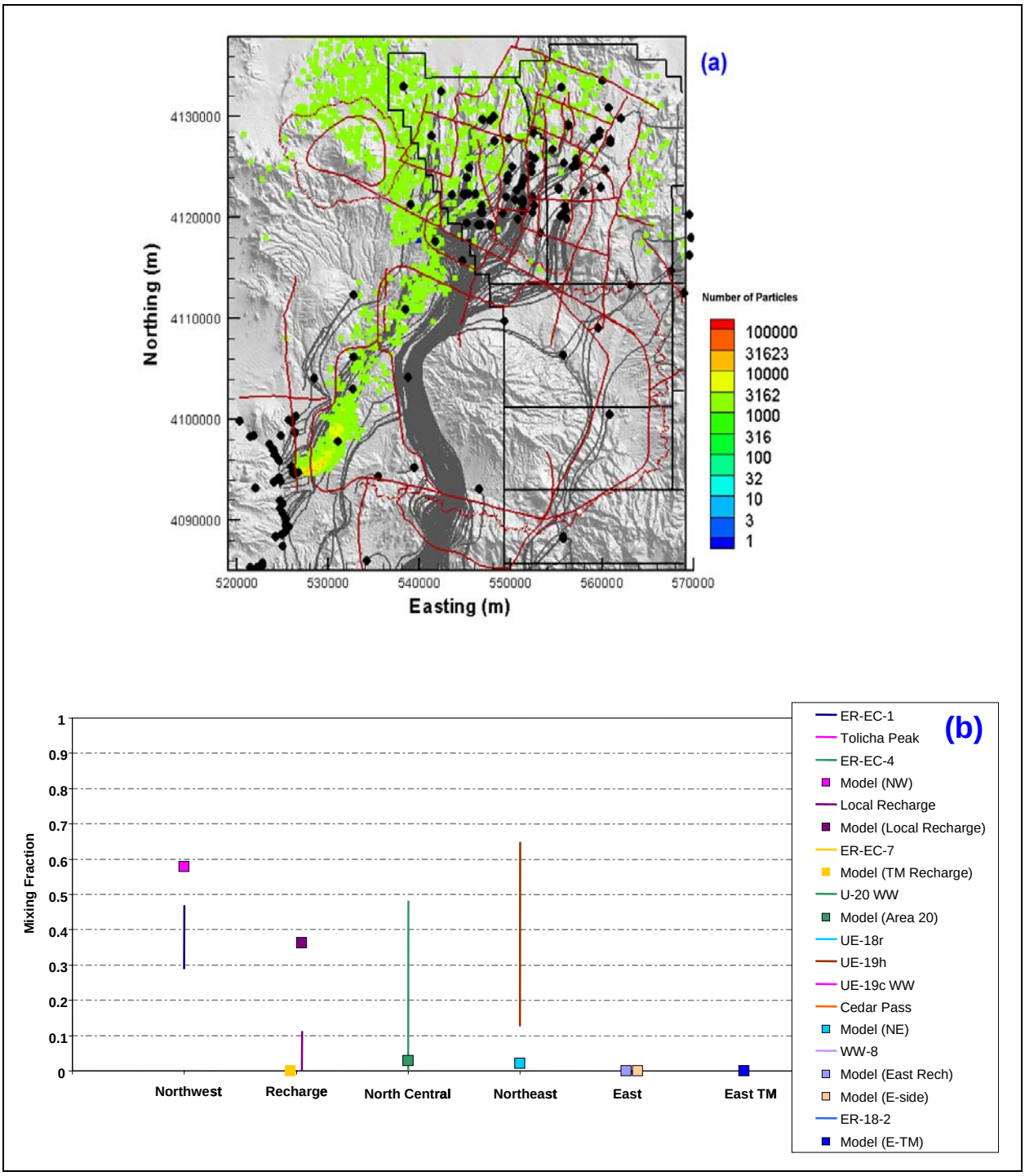

Figure 7-84
Comparison of Flow Model with Geochemical Mixing Targets at ER-OV-03a for BN-DRIA-SDA in the Reduced LCCU1 Permeability Alternative

Figure (a) shows the flow paths as mapped by forward SPTR particles originating at wells (grey lines) and the source recharge locations identified by reverse PTRK particle tracking (colored squares). Figure (b) shows the model comparison with geochemical mixing target ranges.

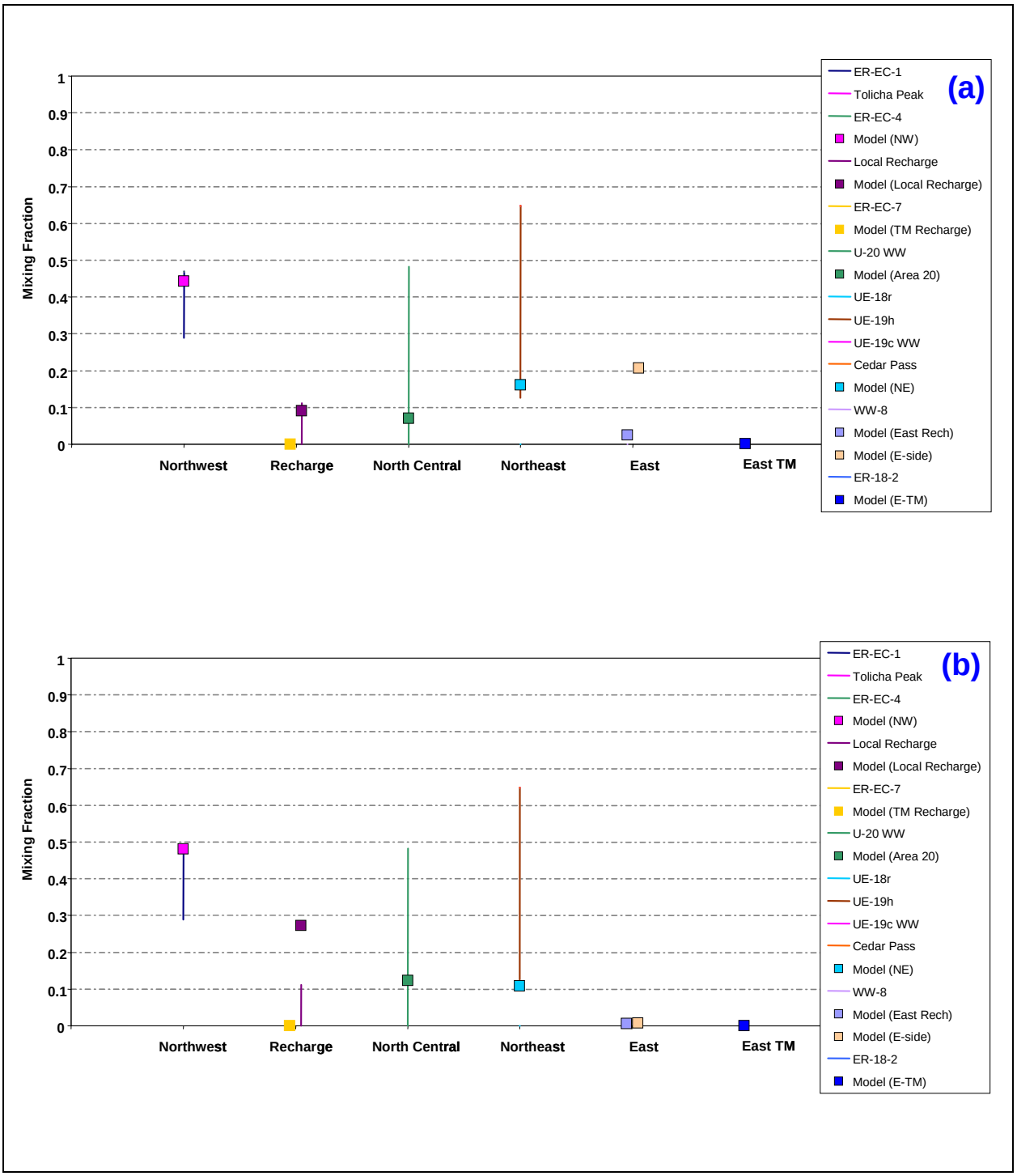

Figure 7-85
Quantitative Geochemical Comparisons at ER-OV-03a for (a) BN-USGSD-SDA and (b) BN-DRIA-SDA

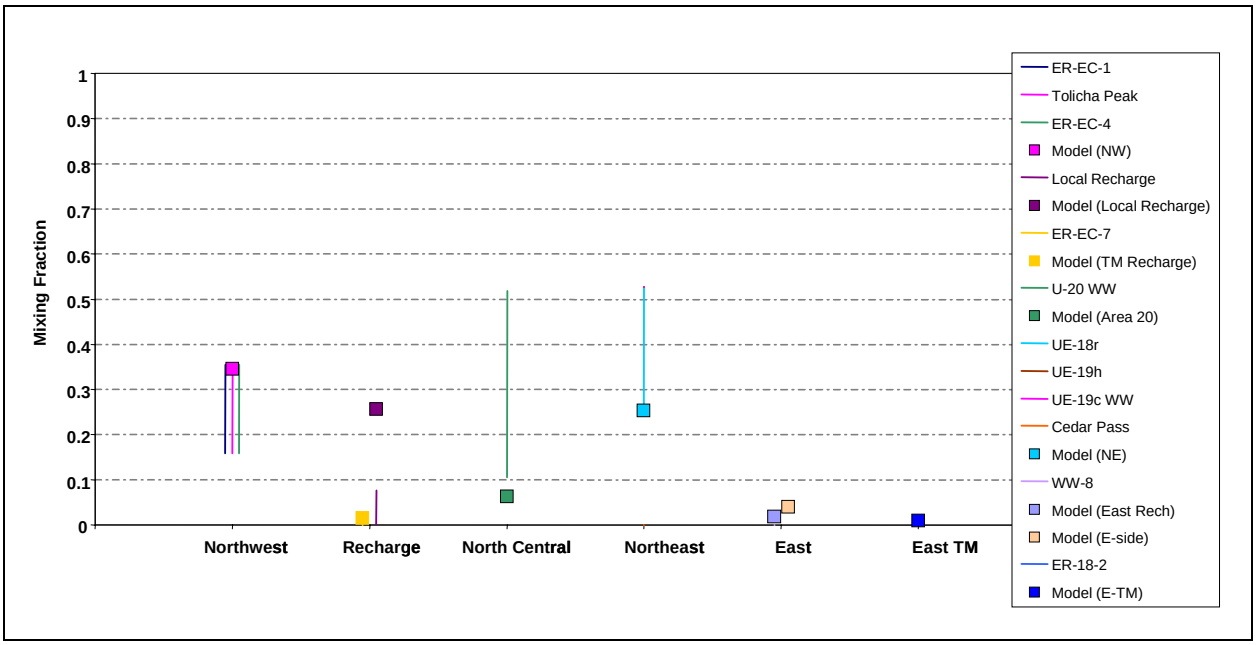

Figure 7-86
Comparison of Flow Model with Geochemical Mixing Targets at ER-OV-03a for BN-MME-ADA

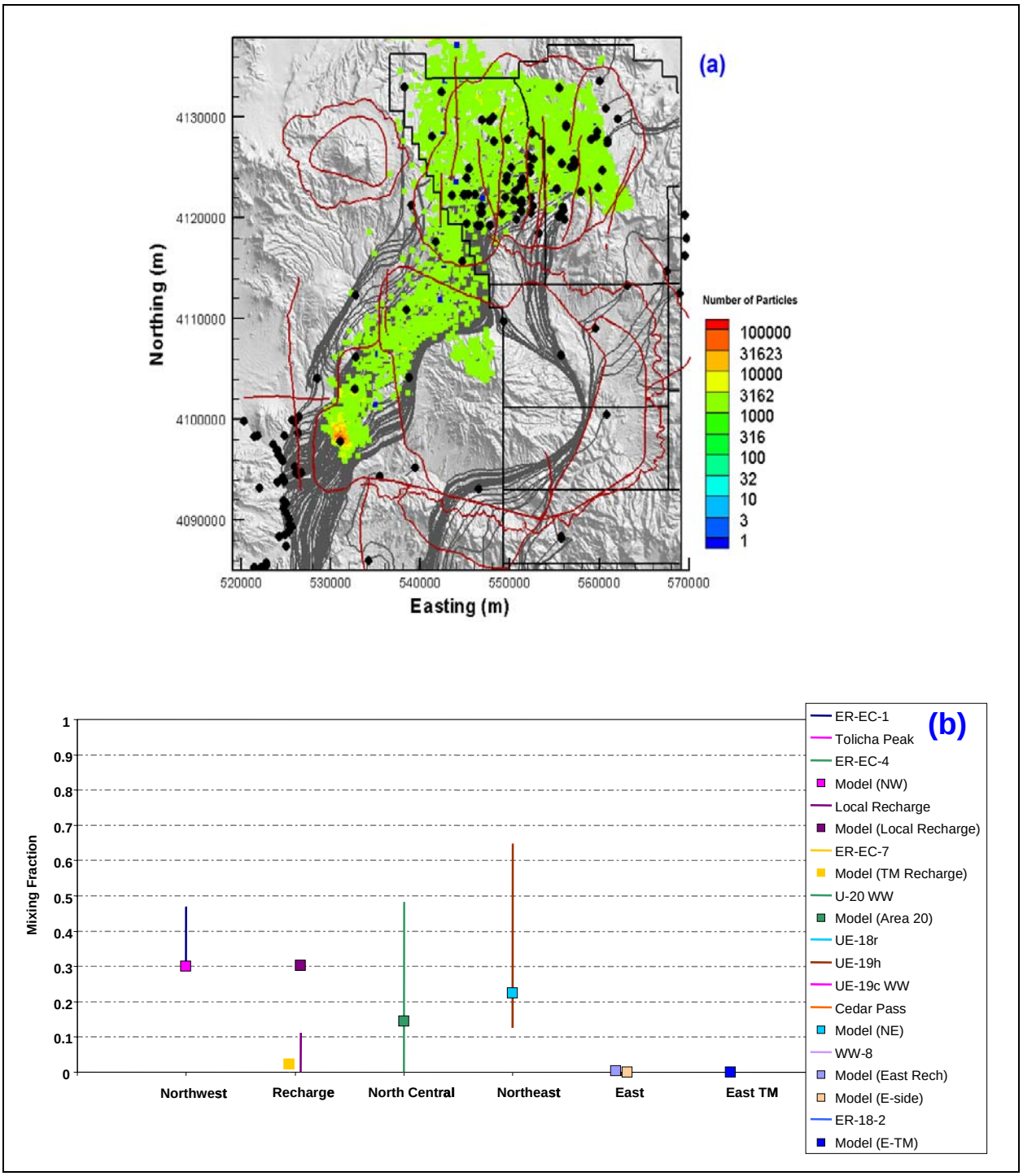

Figure 7-87
Comparison of Flow Model with Geochemical Mixing Targets at ER-OV-03a for SCCC-MME-SDA

Figure (a) shows the flow paths as mapped by forward SPTR particles originating at wells (grey lines) and the source recharge locations identified by reverse PTRK particle tracking (colored squares). Figure (b) shows the model comparison with geochemical mixing target ranges.

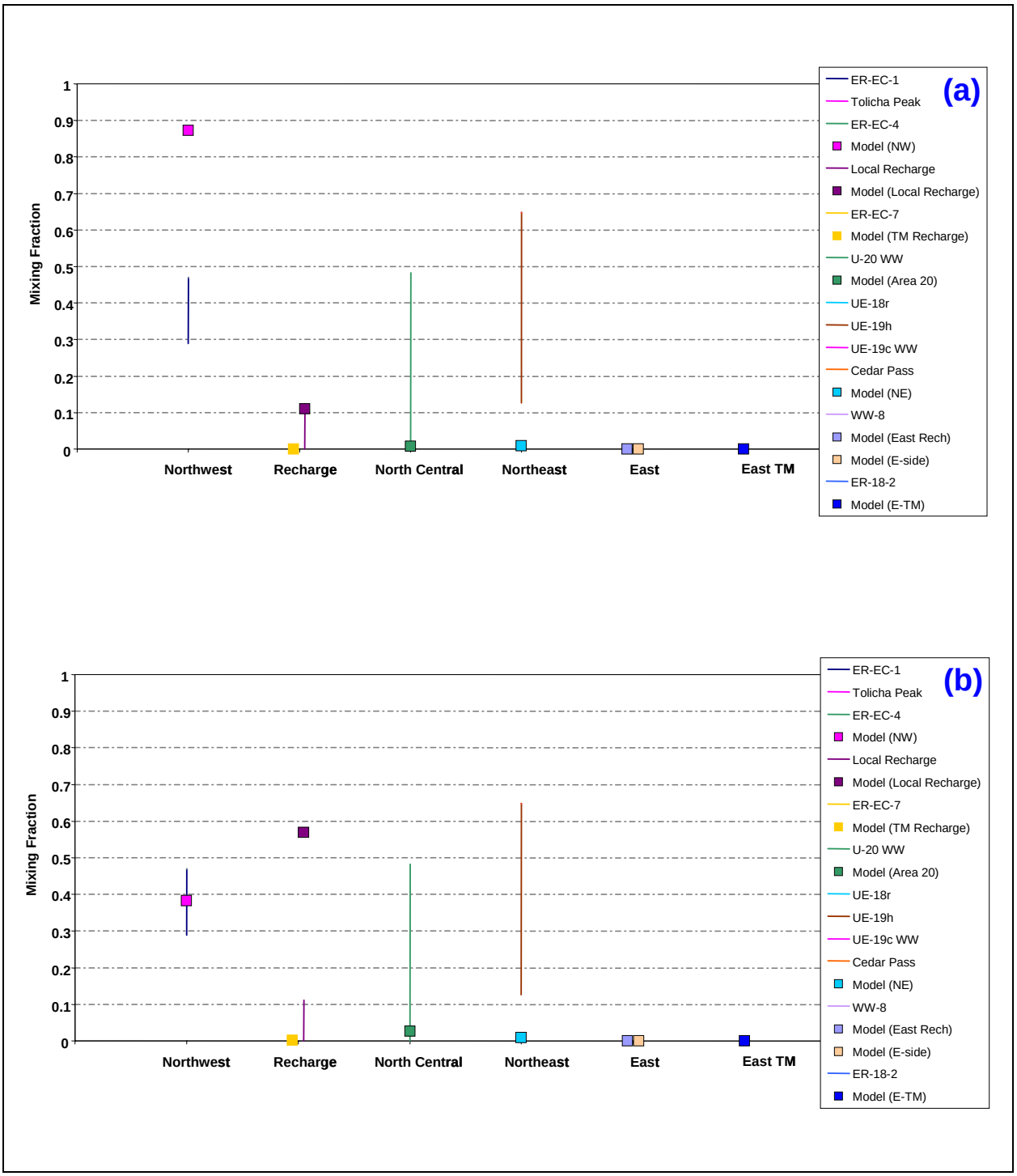

Figure 7-88
Quantitative Geochemical Comparisons at ER-OV-03a for (a) SCCC-USGSD-SDA and (b) SCCC-DRIA-SDA

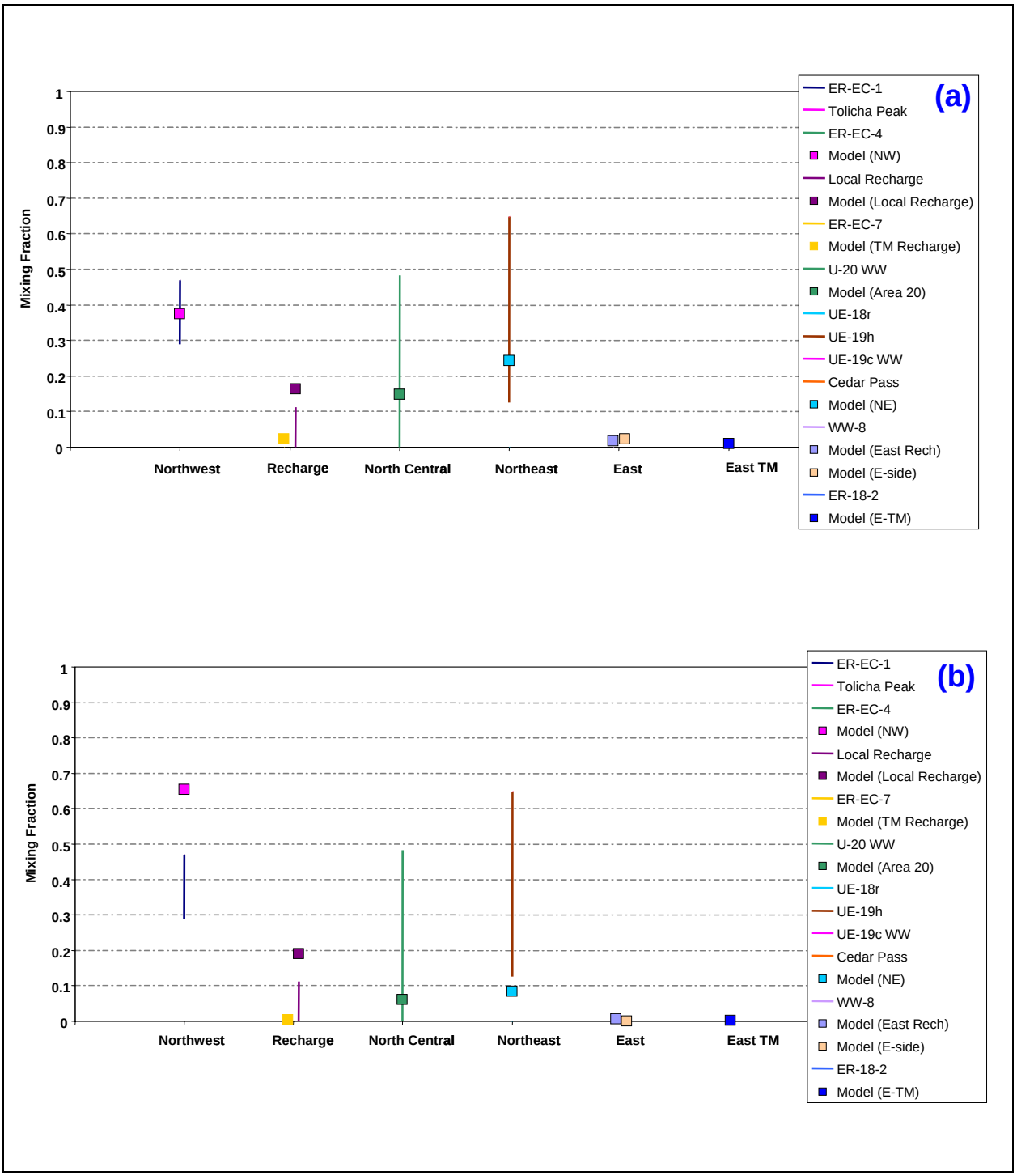

Figure 7-89
Quantitative Geochemical Comparisons at ER-OV-03a for (a) PZUP-MME-SDA and (b) DRT-MME-SDA

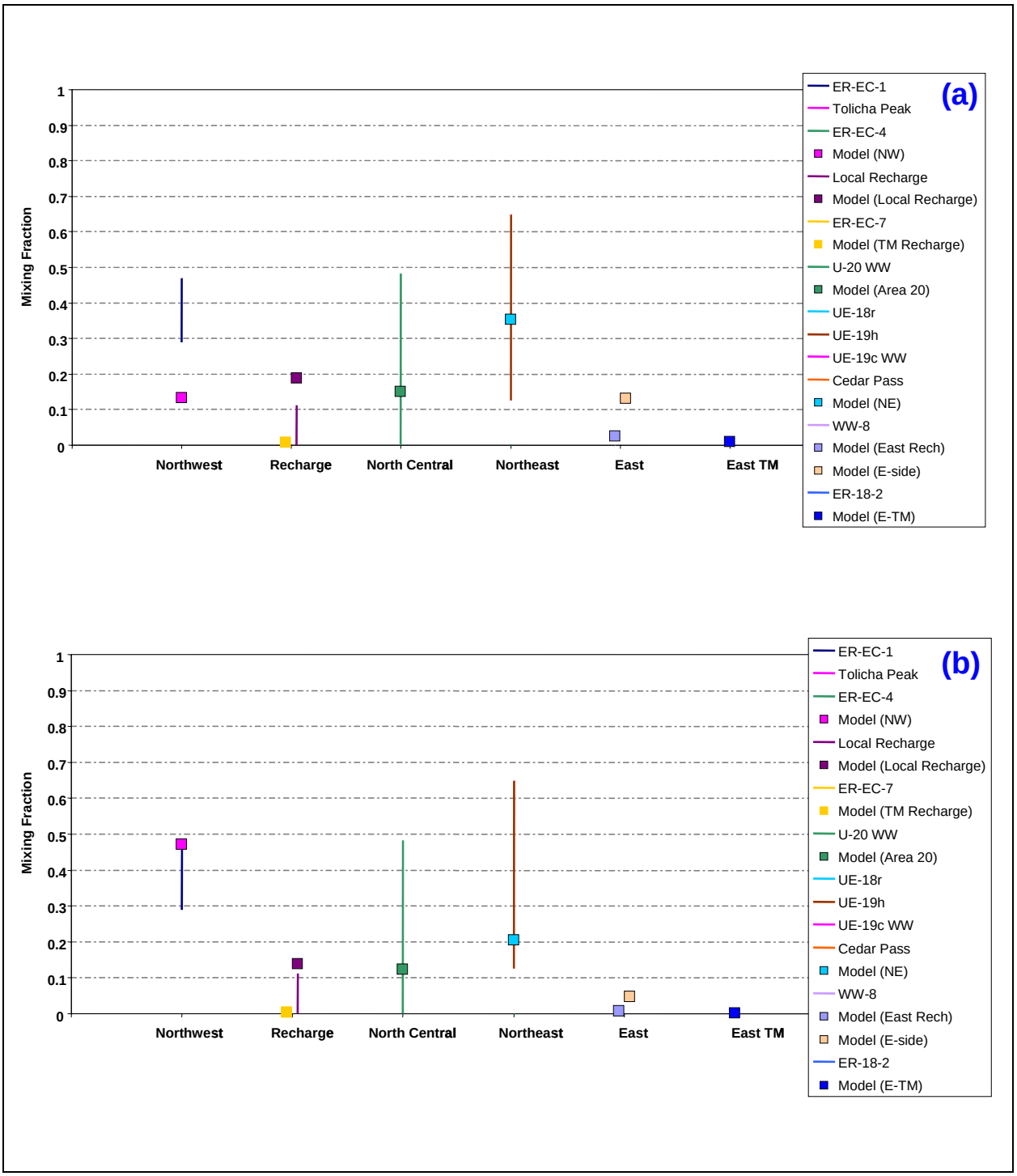

Figure 7-90
Quantitative Geochemical Comparisons at ER-OV-03a for (a) RIDGE-MME-SDA and (b) TCL-MME-SDA

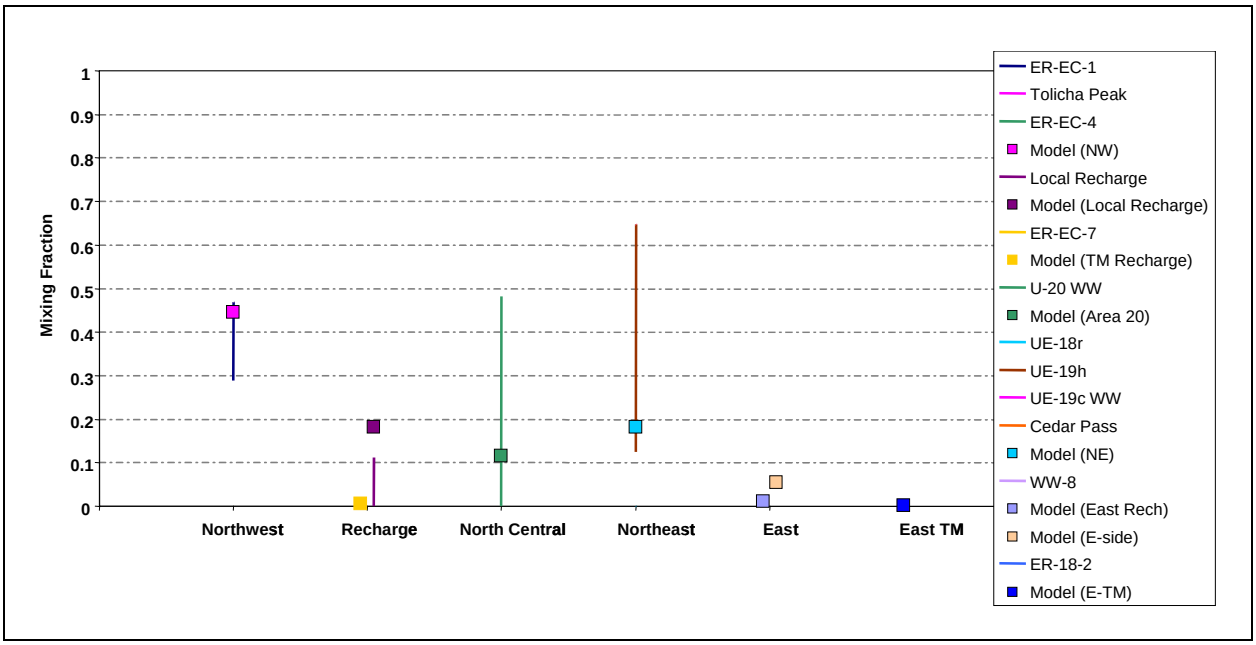

Figure 7-91
Comparison of Flow Model with Geochemical Mixing Targets at ER-OV-03a for SEPZ-MME-SDA

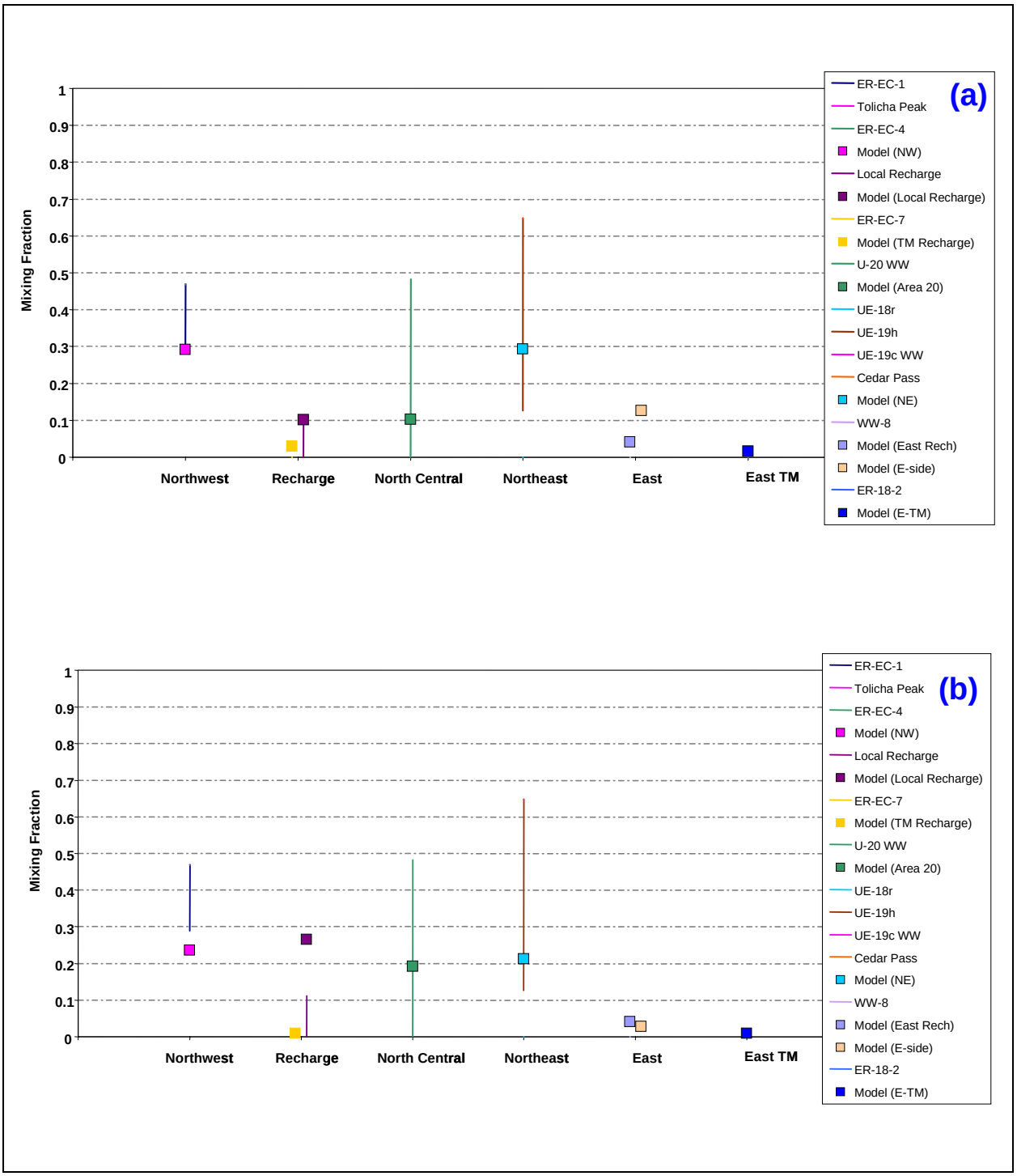

Figure 7-92
Quantitative Geochemical Comparisons at ER-OV-03a for (a) PZUP-USGSD-SDA and (b) PZUP-DRIA-SDA

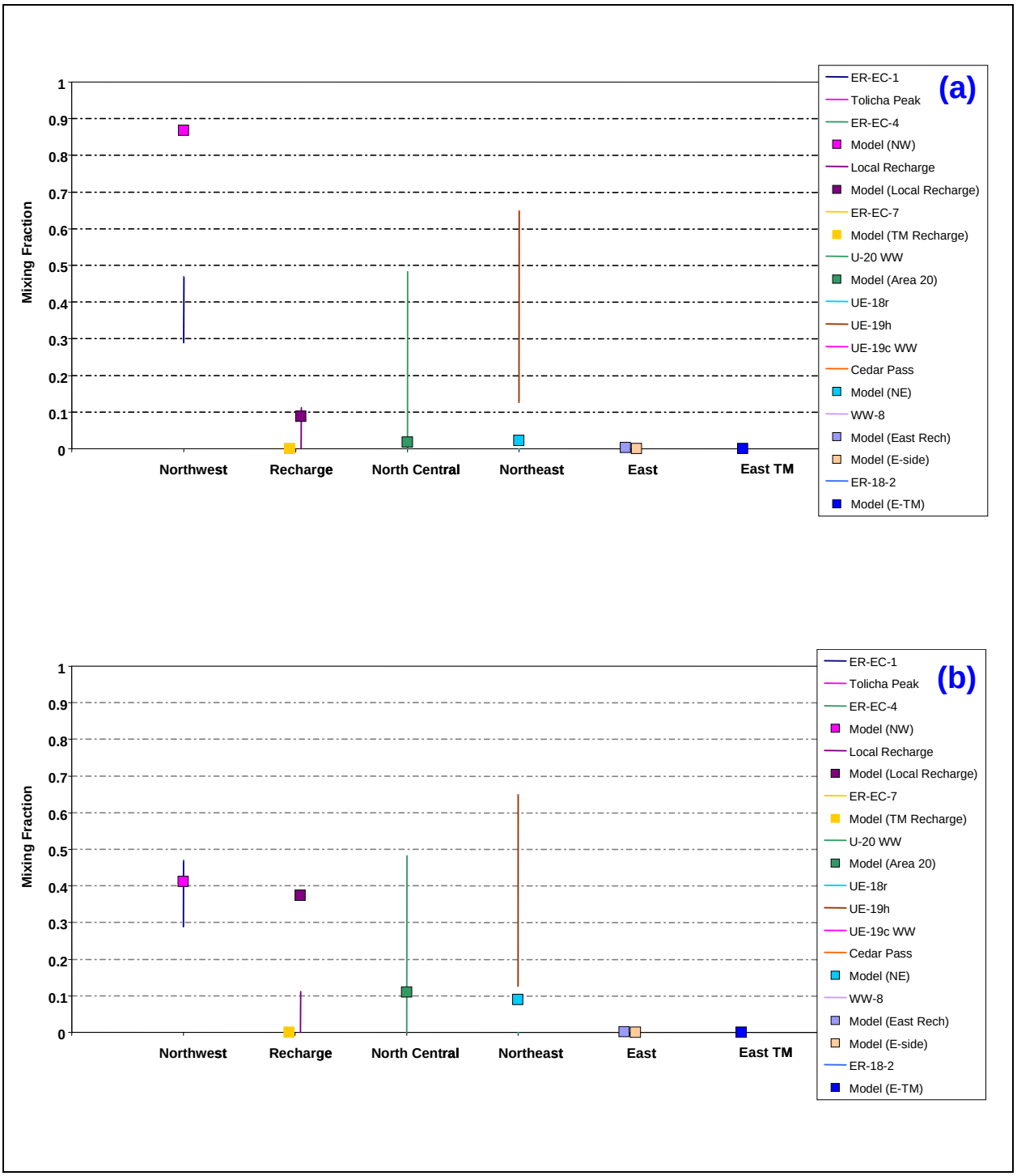

Figure 7-93
Quantitative Geochemical Comparisons at ER-OV-03a for (a) DRT-USGSD-SDA and (b) DRT-DRIA-SDA

Table 7-15
Comparison of Alternative Models at ER-OV-03a

HFM	Water-Balance Condition	Overestimation of Northwest Source	Underestimation of North-Central and Northeast Source	Overestimation of East Boundary Source	Overestimation of Local Recharge
BN-SDA reduced LCCU1 permeability alternative	MME				X
	USGSD				
	DRIA	X	X		X
BN-SDA	MME				
	USGSD			X	
	DRIA				X
BN-ADA	MME				X
SCCC-SDA	MME				X
	USGSD	X	X		
	DRIA		X		
PZUP	MME				
DRT	MME	X			
RIDGE	MME	-X[a]		X	
TCL	MME				
SEPZ	MME				
PZUP	USGSD			X	
	DRIA				X
DRT	USGSD	X	X		
	DRIA				X

[a]The actual discrepancy for this model is underestimation of northwest source.

7.3.7 ER-OV-03c

7.3.7.1 Alternative Water-Balance Conditions, BN HFM

The mixing ratios at ER-OV-03c show a reduction in northwest source water and an increase in source from the northeast. The results for the BN-USGS-SDA in the reduced LCCU1 permeability alternative nearly matches the targets, but with overestimates in Timber Mountain recharge and the east boundary at Gold Meadows (Figure 7-94). The DRIA calibration shows a very different picture with no Timber Mountain recharge, no problems with flow across the east model boundary, but an overestimate in northwest source water and local recharge, and an underprediction of northeast source water (Figure 7-95).

For the BN-USGSD-SDA (high LCCU1 permeability), an overestimate in east boundary flow leads to a reduction in sources at ER-OV-03c from the north central and northeast (Figure 7-96). The same model with DRIA conditions (Figure 7-96) shows a marked improvement on the inflow from Gold Meadows, but at the expense of increased local recharge. The BN-MME-ADA shows good agreement with targets, but with a small overestimate in east model boundary source water and local recharge (Figure 7-97).

7.3.7.2 SCCC Alternative HFM

The SCCC alternative HFM model (Figure 7-98) with MME water-balance conditions produces a flow field that captures the geochemistry mixing trend quite well at ER-OV-03c, but with an overestimate of local recharge in Beatty Wash as is expected with the MME recharge map. Figure 7-99 shows that the USGSD conditions for the model lead to poor results with no north-central or northeast sources and with overestimates in northwest, Timber Mountain, and local recharge sources. The DRIA model for SCCC suffers the same problem, with only a small increase in north-central source contribution (Figure 7-99).

7.3.7.3 PZUP, DRT, RIDGE, TCL, and SEPZ Alternative HFMs

The remaining alternative HFM scenarios with MME water-balance conditions show the similar results at ER-OV-03c (Figures 7-100 through 7-102), with the primary difference being the size of the local recharge and east boundary source overpredictions. The largest local recharge overprediction is

with DRT (60 percent) and the smallest is with PZUP (39 percent). The largest east boundary source estimate is with RIDGE (23 percent) and the smallest is with DRT (0 percent).

When the USGSD water-balance condition is used with PZUP, the east boundary flow contribution shoots up at the expense of the northwest and north-central components, which are pushed to the west of ER-OV-03c (Figure 7-103). The DRIA condition on the PZUP model maintains a northeast component at ER-OV-03c, but about 40 percent of the source comes from the east boundary and southeast quadrant of the model domain (Figure 7-103).

The DRT model with USGSD overestimates the northwest source and local recharge at the expense of underestimating the northeast source (Figure 7-104). With DRIA, the DRT model matches the target trend well, but with smaller northwest and local recharge source overestimates (Figure 7-104).

7.3.7.4 Summary: ER-OV-03c

As with the other wells southwest of Timber Mountain, at ER-OV-03c, there are four different mismatches between the model simulations and the geochemistry targets. They are (a) overestimation of source groundwater from the northwest, (b) underestimation of source groundwater from the north central and northeast, (c) overestimation of source water from the eastern model boundary, and (d) overestimation of local recharge. Table 7-16 identifies the mismatch issues for each simulation. Only those with more than a 10 percent mismatch are identified. Numerical quantification and comparison of this and all other target wells is presented in Section 7.5.

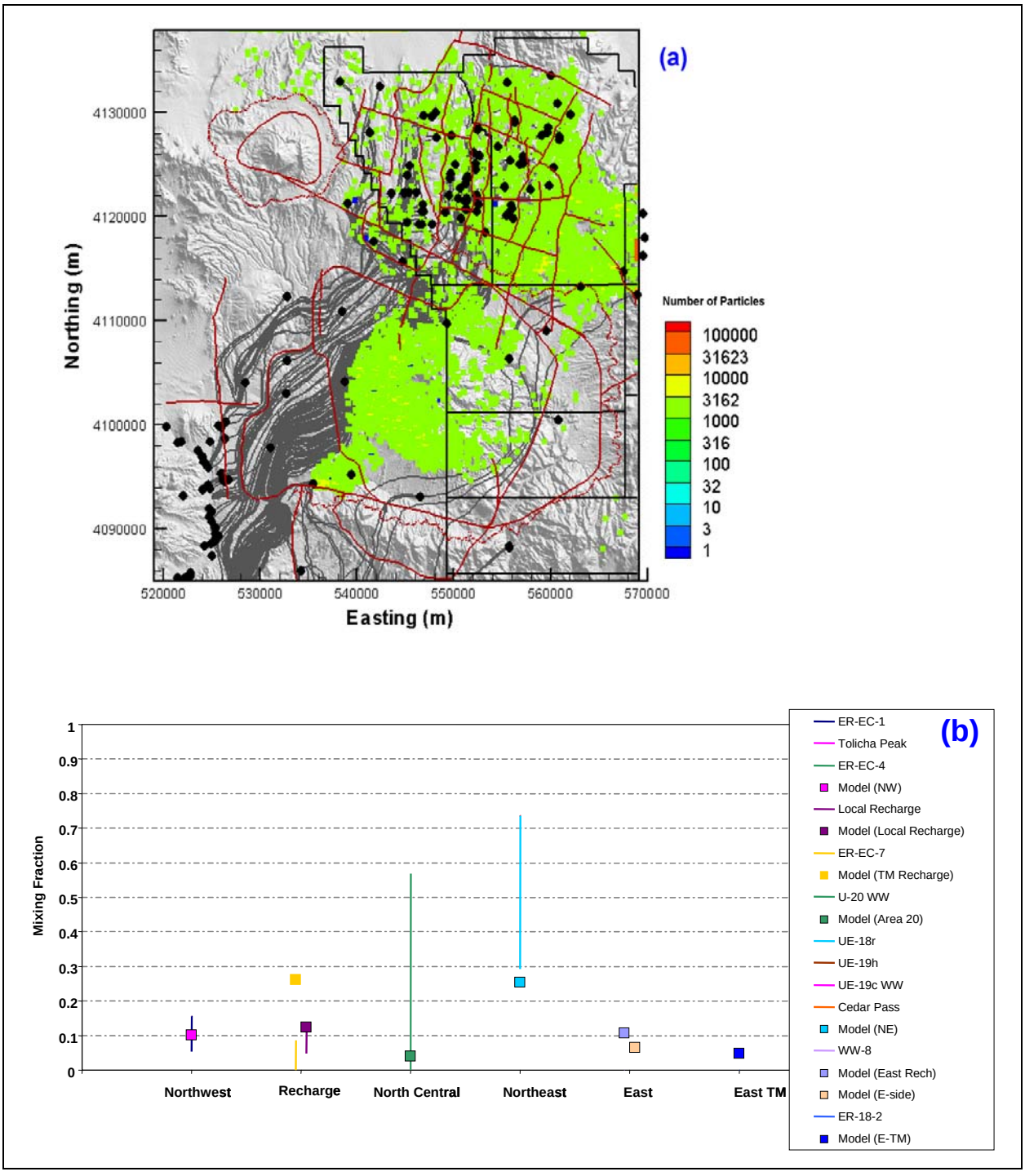

Figure 7-94
Comparison of Flow Model with Geochemical Mixing Targets at ER-OV-03c for BN-USGSD-SDA in the Reduced LCCU1 Permeability Alternative

Figure (a) shows the flow paths as mapped by forward SPTR particles originating at wells (grey lines) and the source recharge locations identified by reverse PTRK particle tracking (colored squares). Figure (b) shows the model comparison with geochemical mixing target ranges.

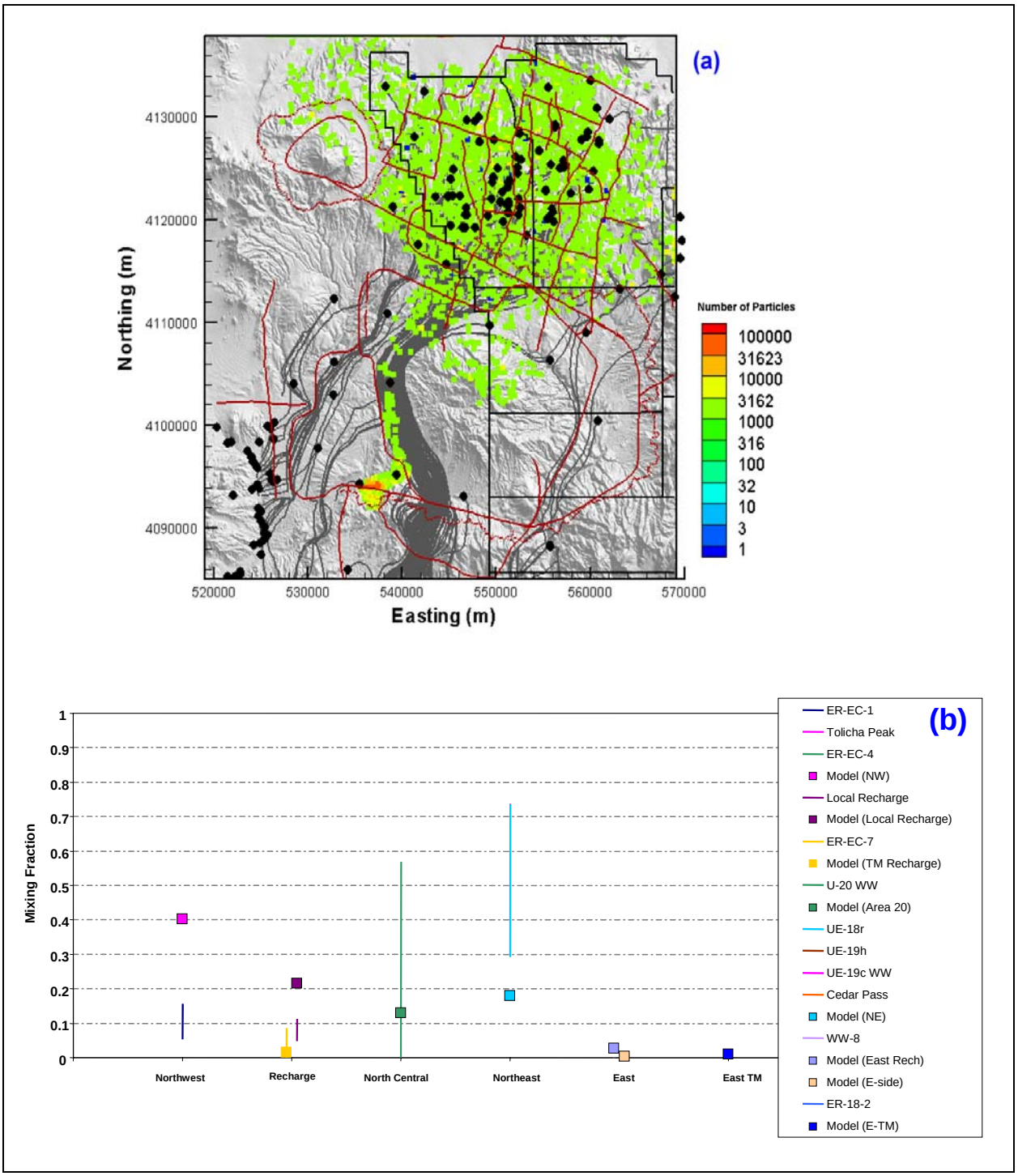

Figure 7-95
Comparison of Flow Model with Geochemical Mixing Targets at ER-OV-03c for BN-DRIA-SDA in the Reduced LCCU1 Permeability Alternative

Figure (a) shows the flow paths as mapped by forward SPTR particles originating at wells (grey lines) and the source recharge locations identified by reverse PTRK particle tracking (colored squares). Figure (b) shows the model comparison with geochemical mixing target ranges.

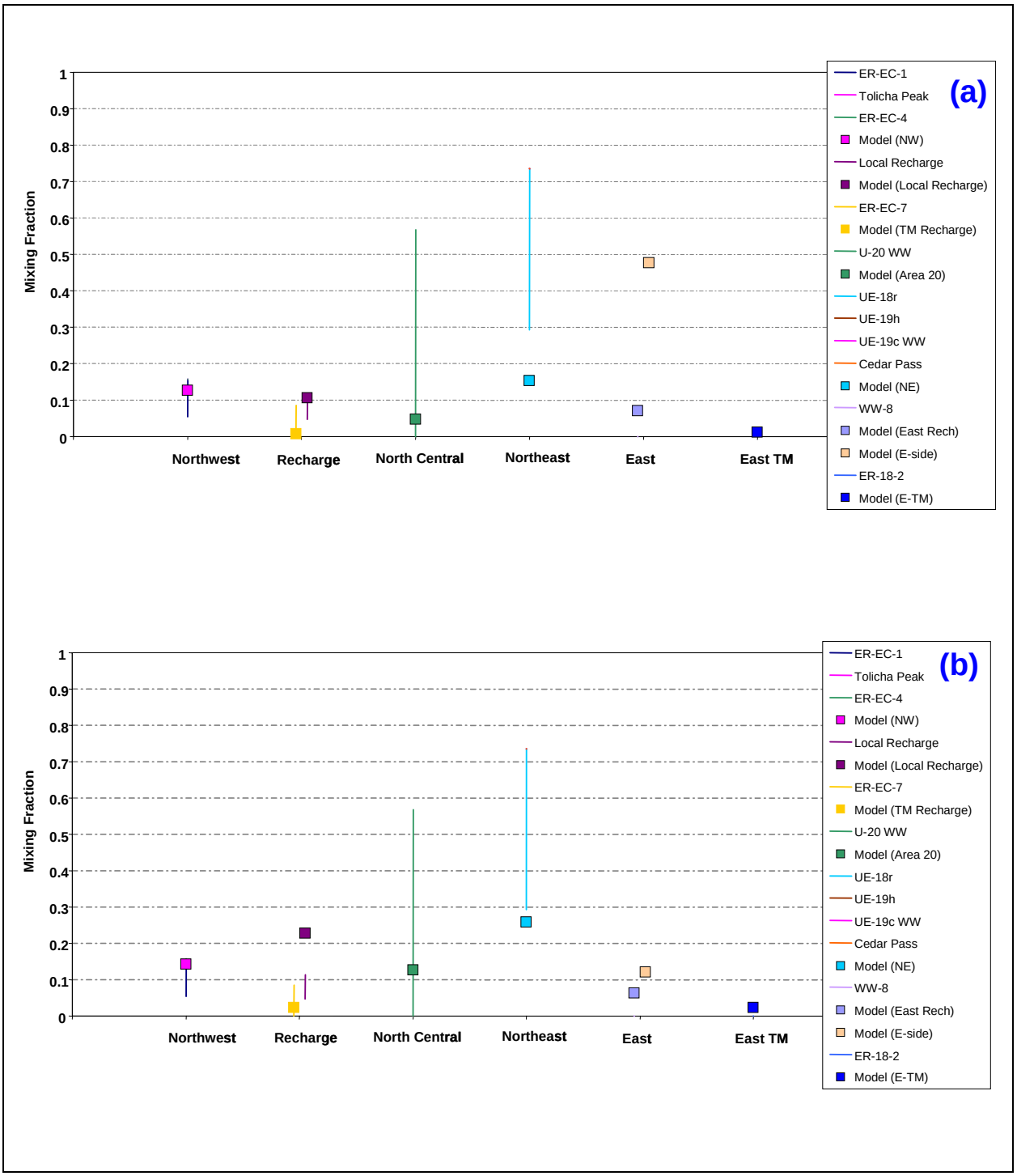

Figure 7-96
Quantitative Geochemical Comparisons at ER-OV-03c for (a) BN-USGSD-SDA and (b) BN-DRIA-SDA

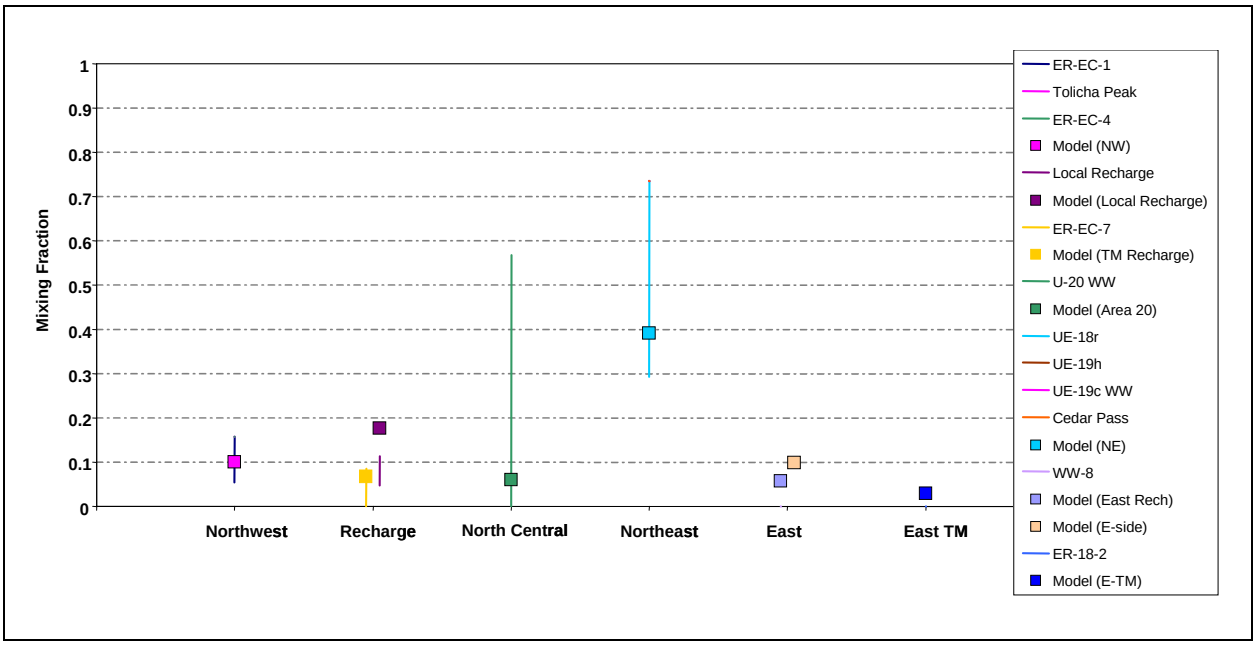

Figure 7-97
Comparison of Flow Model with Geochemical Mixing Targets at ER-OV-03c for BN-MME-ADA

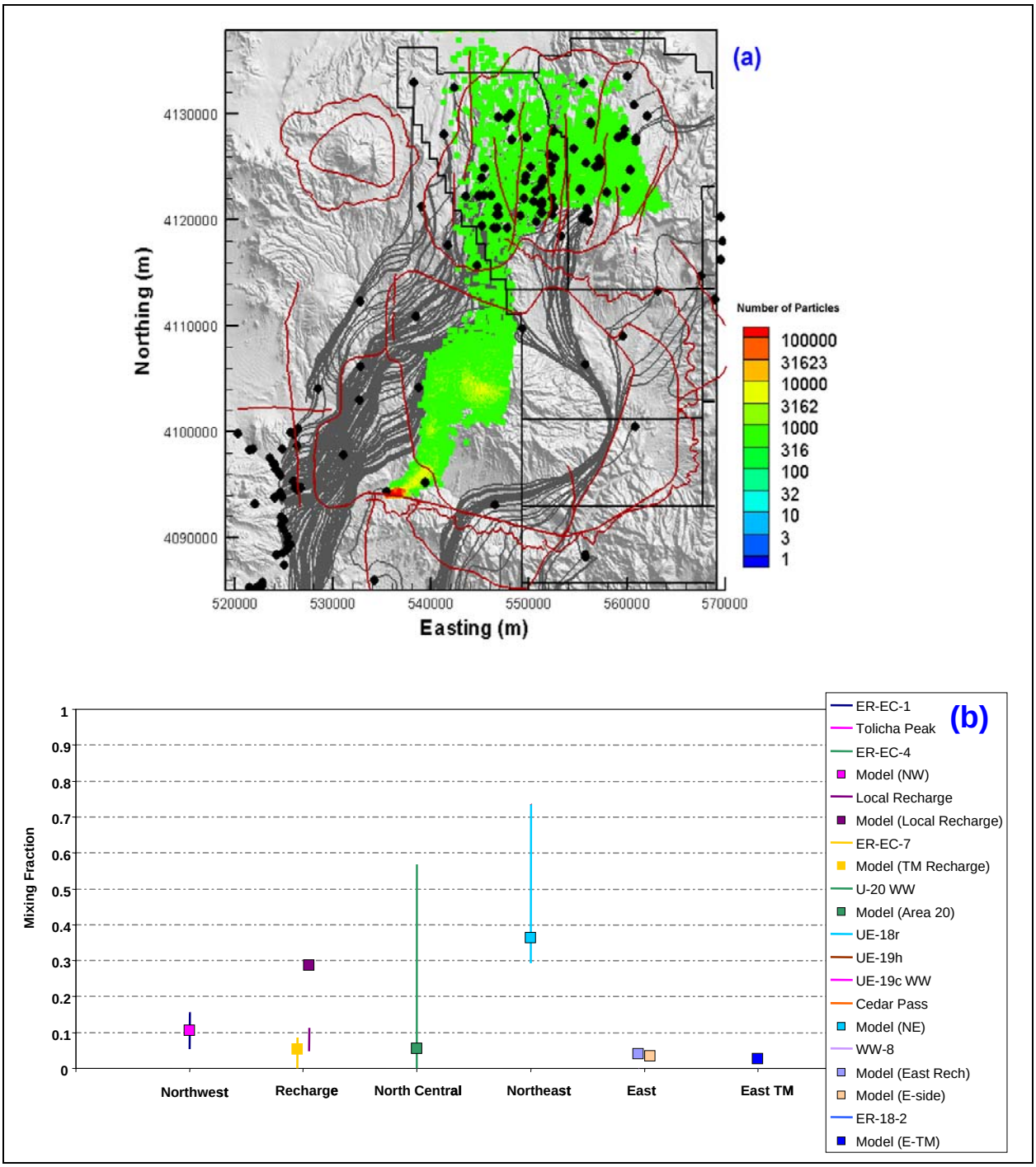

Figure 7-98
Comparison of Flow Model with Geochemical Mixing Targets at ER-OV-03c for SCCC-MME-SDA

Figure (a) shows the flow paths as mapped by forward SPTR particles originating at wells (grey lines) and the source recharge locations identified by reverse PTRK particle tracking (colored squares). Figure (b) shows the model comparison with geochemical mixing target ranges.

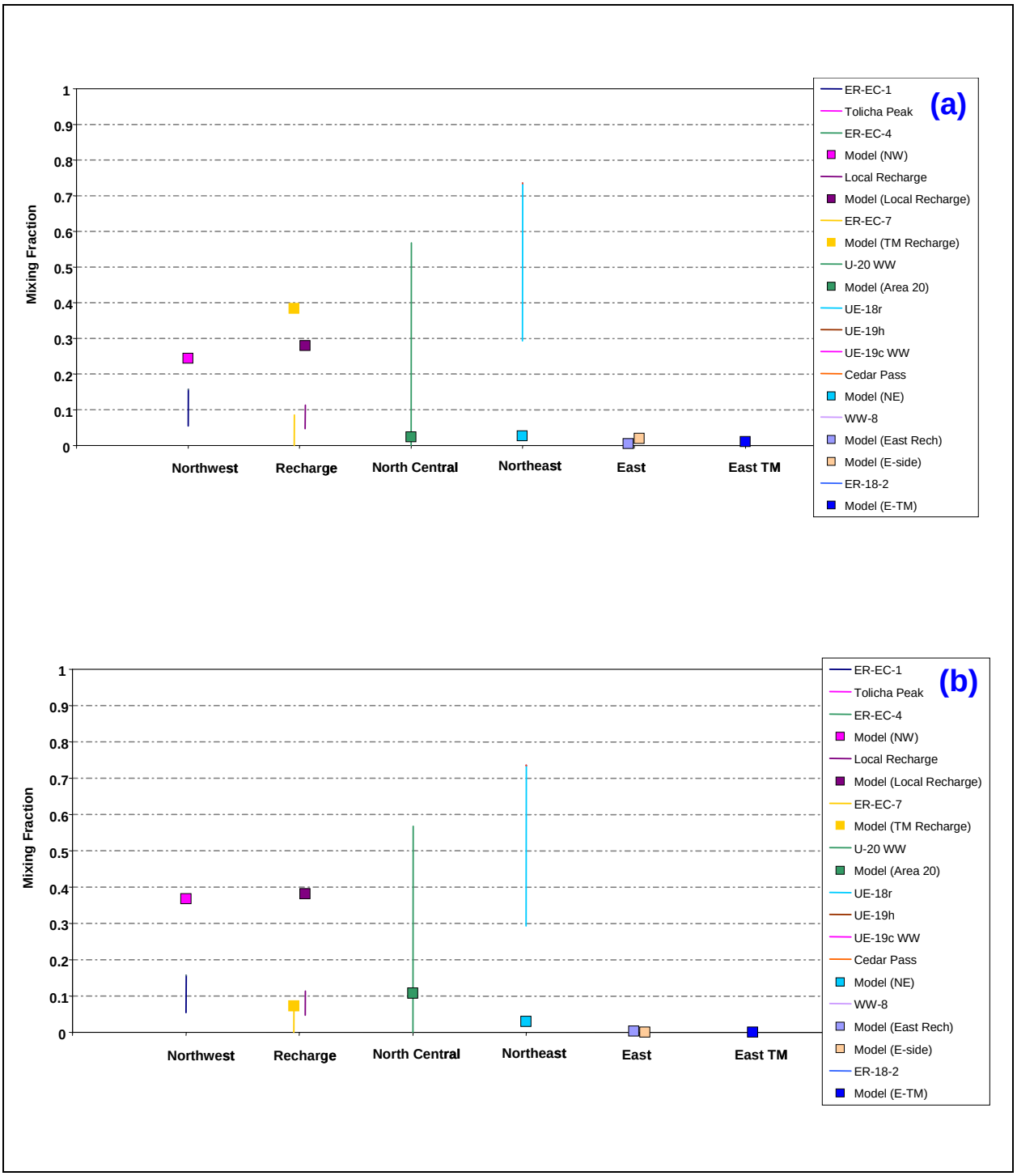

Figure 7-99
Quantitative Geochemical Comparisons at ER-OV-03c for (a) SCCC-USGSD-SDA and (b) SCCC-DRIA-SDA

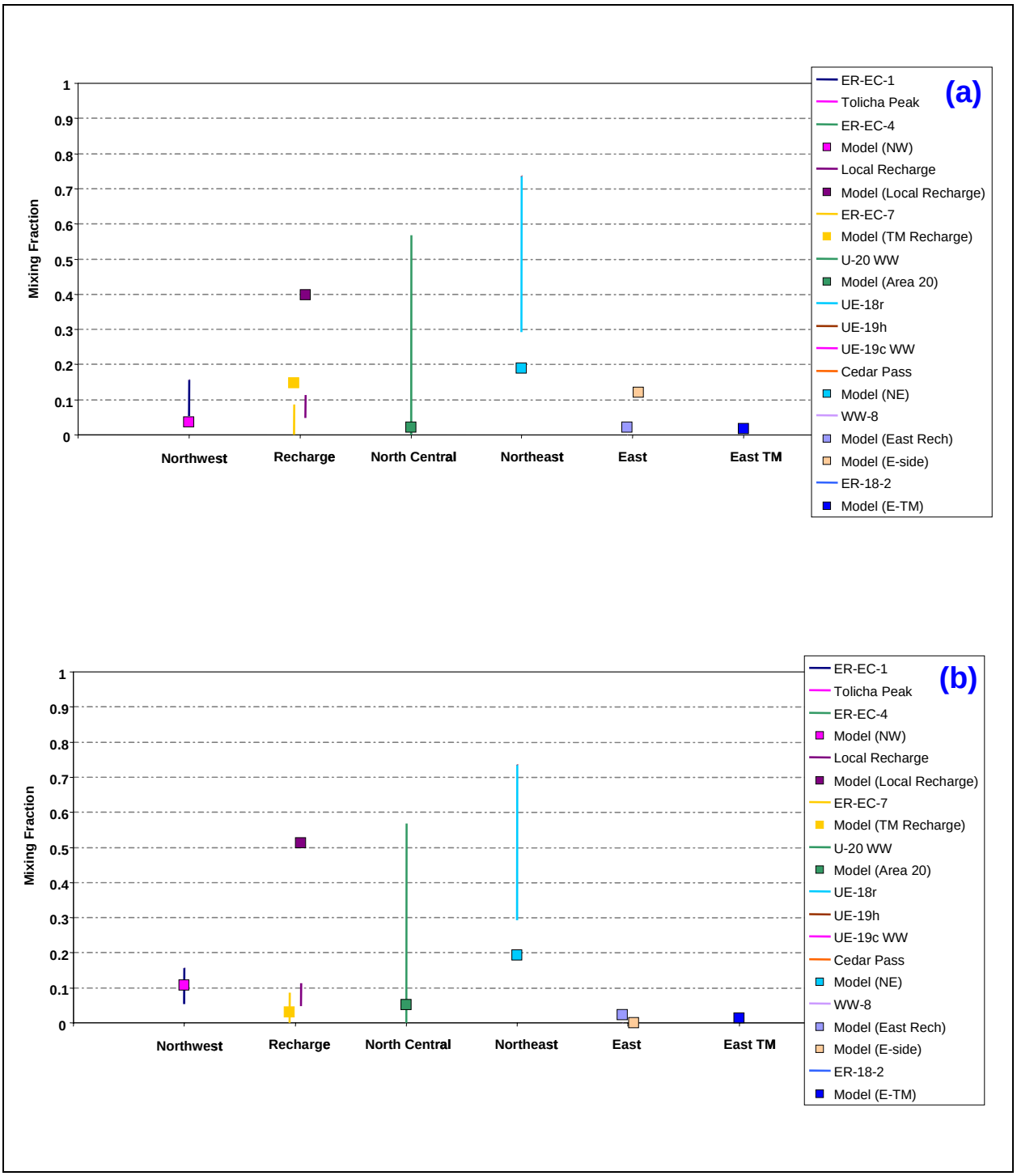

Figure 7-100
Quantitative Geochemical Comparisons at ER-OV-03c for (a) PZUP-MME-SDA and (b) DRT-MME-SDA

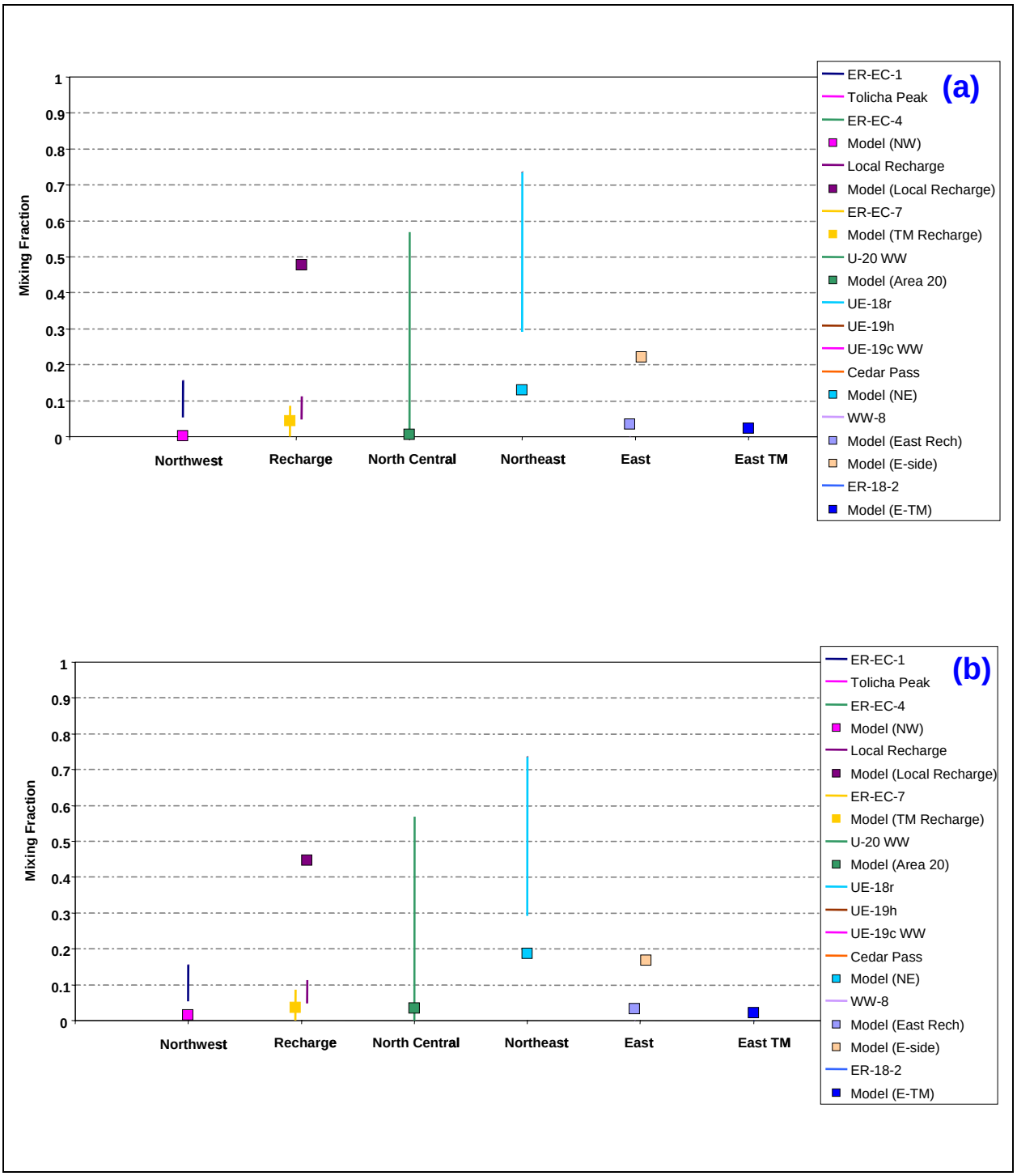

Figure 7-101
Quantitative Geochemical Comparisons at ER-OV-03c for (a) RIDGE-MME-SDA and (b) TCL-MME-SDA

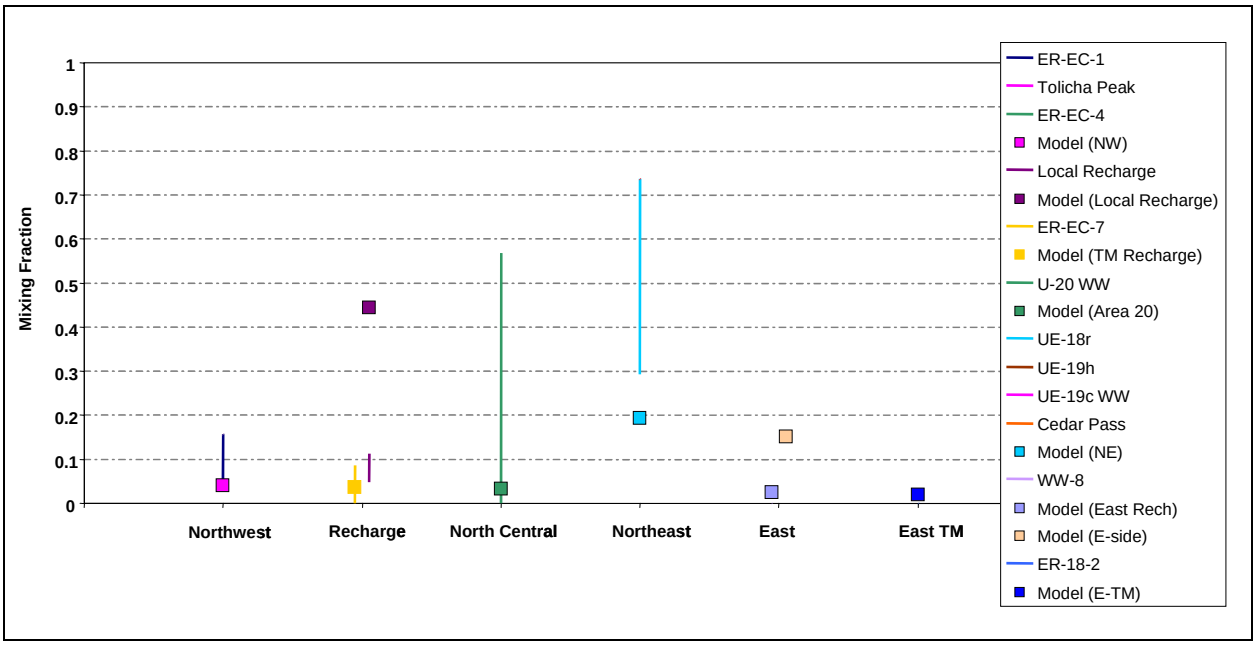

Figure 7-102
Comparison of Flow Model with Geochemical Mixing Targets at ER-OV-03c for SEPZ-MME-SDA

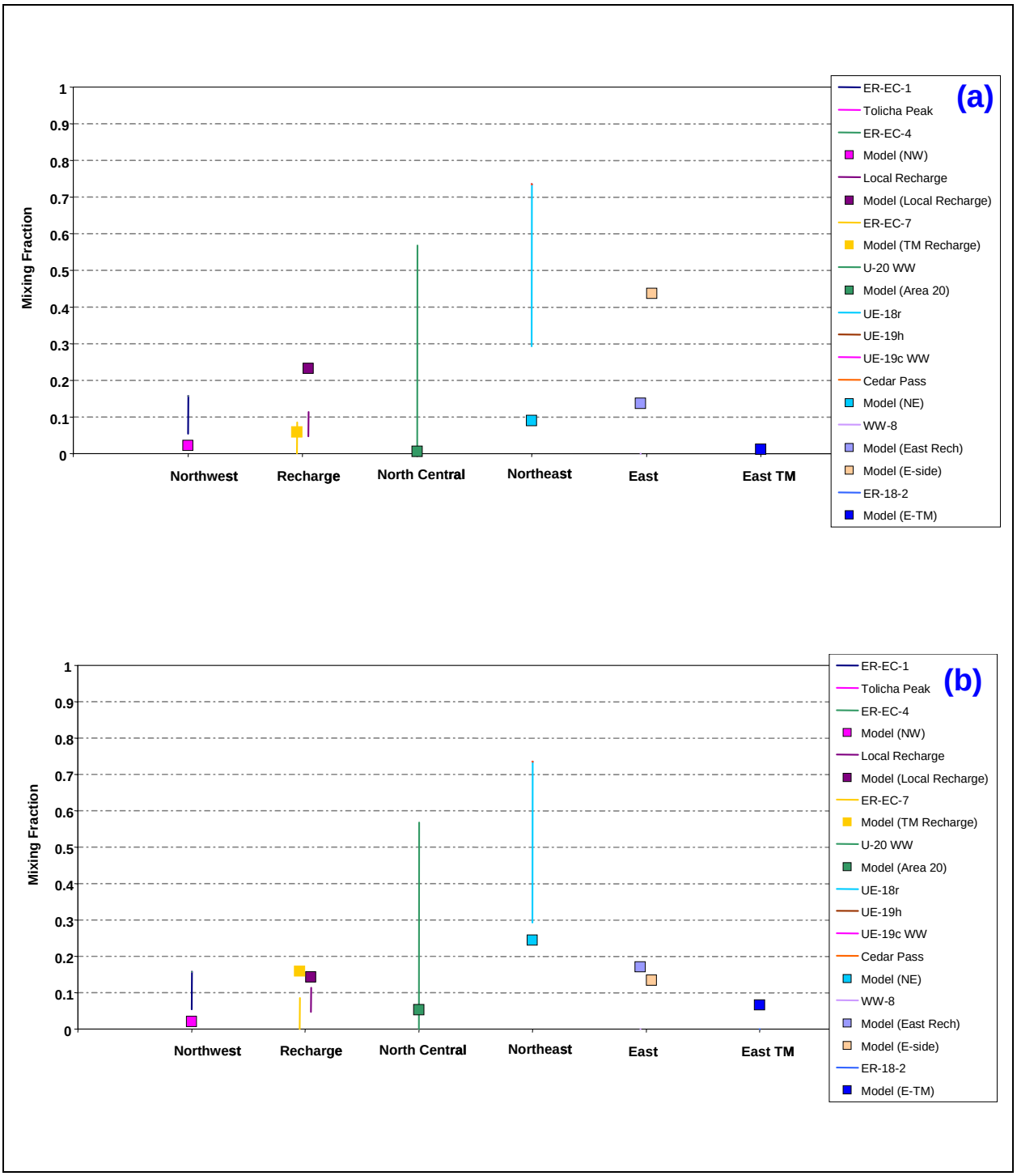

Figure 7-103
Quantitative Geochemical Comparisons at ER-OV-03c for (a) PZUP-USGSD-SDA and (b) PZUP-DRIA-SDA

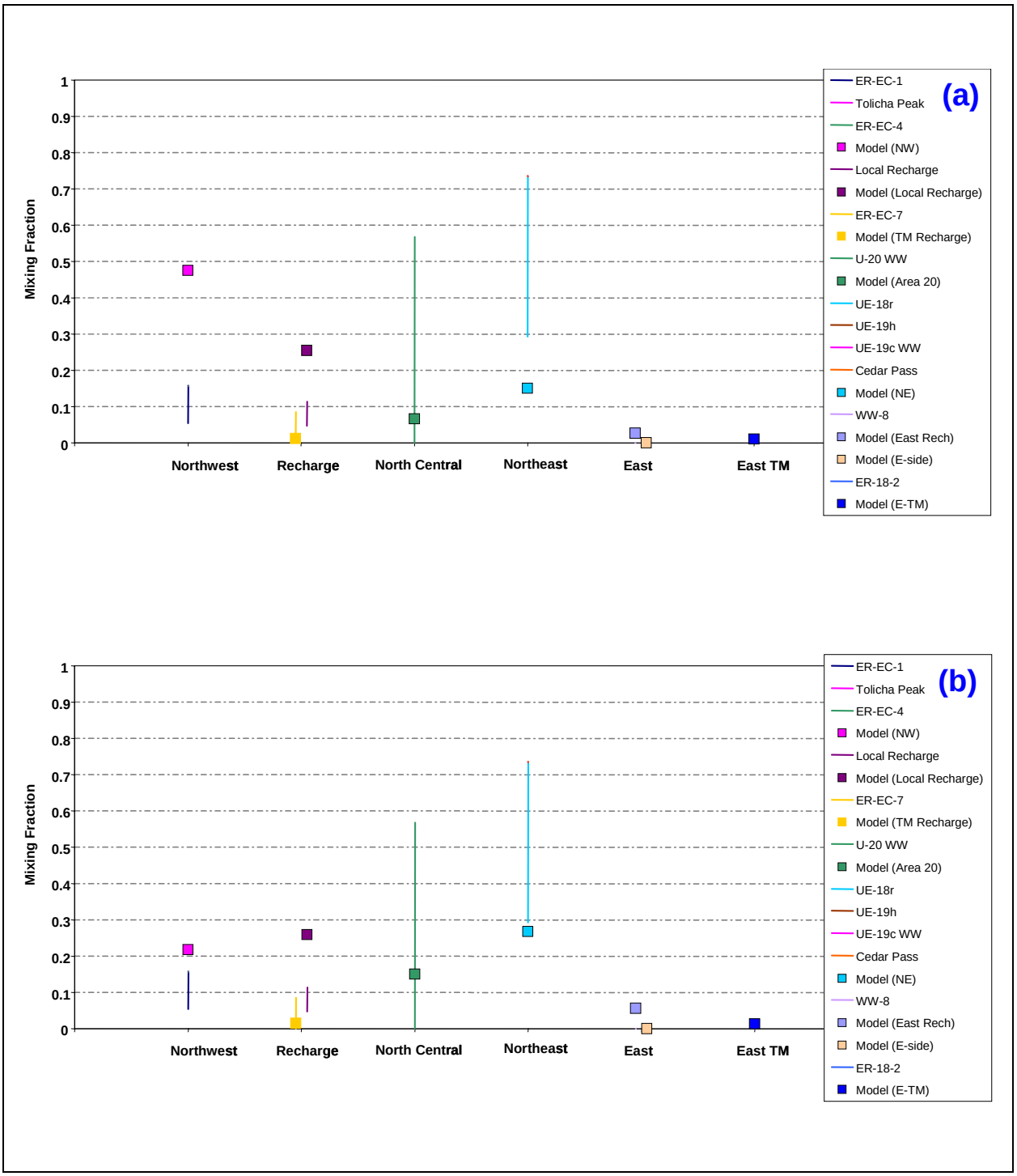

Figure 7-104
Quantitative Geochemical Comparisons at ER-OV-03c for (a) DRT-USGSD-SDA and (b) DRT-DRIA-SDA

Table 7-16
Comparison of Alternative Models at ER-OV-03c

HFM	Water-Balance Condition	Overestimation of Northwest Source	Underestimation of North-Central and Northeast Source	Overestimation of East Boundary Source	Overestimation of Local Recharge
BN-SDA reduced LCCU1 permeability alternative	MME				X
	USGSD				X (TM)
	DRIA	X			
BN-SDA	MME		X	X	X
	USGSD		X	X	
	DRIA			X	
BN-ADA	MME				
SCCC-SDA	MME				X
	USGSD		X		X
	DRIA	X	X		X
PZUP	MME			X	X
DRT	MME				X
RIDGE	MME		X	X	X
TCL	MME		X	X	X
SEPZ	MME		X	X	X
PZUP	USGSD		X	X	X
	DRIA			X	
DRT	USGSD	X	X		
	DRIA				X

7.3.8 Coffer Windmill Well

At the Coffer Windmill Well, the source of water has shifted to include greater contributions from either the northeast or even the eastern model boundary, as discussed in Section 7.2. As with the other seven target wells considered in this section, Figures 7-105 through 7-115 show the model comparisons with the geochemistry mixing targets for each alternative water balance and/or HFM considered. Because of the wide range in uncertainty for the sources of water at this well (Figure 7-25), the primary concern in comparing the models is whether too much northwest or local recharge source is simulated. These are clearly compared in Table 7-17.

7.3.8.1 Summary: Coffer Windmill Well

As described in Section 7.2, Coffer Windmill Well has a wide range of uncertainty in the chemical mixing targets. The groundwater looks like a mix of WW-8 and ER-18-2 water, like a mix of Timber Mountain Recharge (ER-EC-7) and Area 19 water (UE-18r), or some combination in between. Because WW-8 water is so similar to Rainier Mesa water in HTH-1 (Kwicklis et al., 2005), they are considered as equally possible in this comparison. Likewise, because it is unclear how different upper Beatty Wash recharge is from ER-EC-7 water they are both considered as equally possible local recharge, but their combination is considered with regard to the total local recharge estimate. Thus, the mismatches of greatest concern are (a) overestimation of source groundwater from the northwest and (b) overestimation of local recharge (e.g., no source water from the north-central, northeast or eastern zones). Table 7-17 identifies the mismatch issues for each simulation. Only those with more than a 10 percent mismatch are identified.

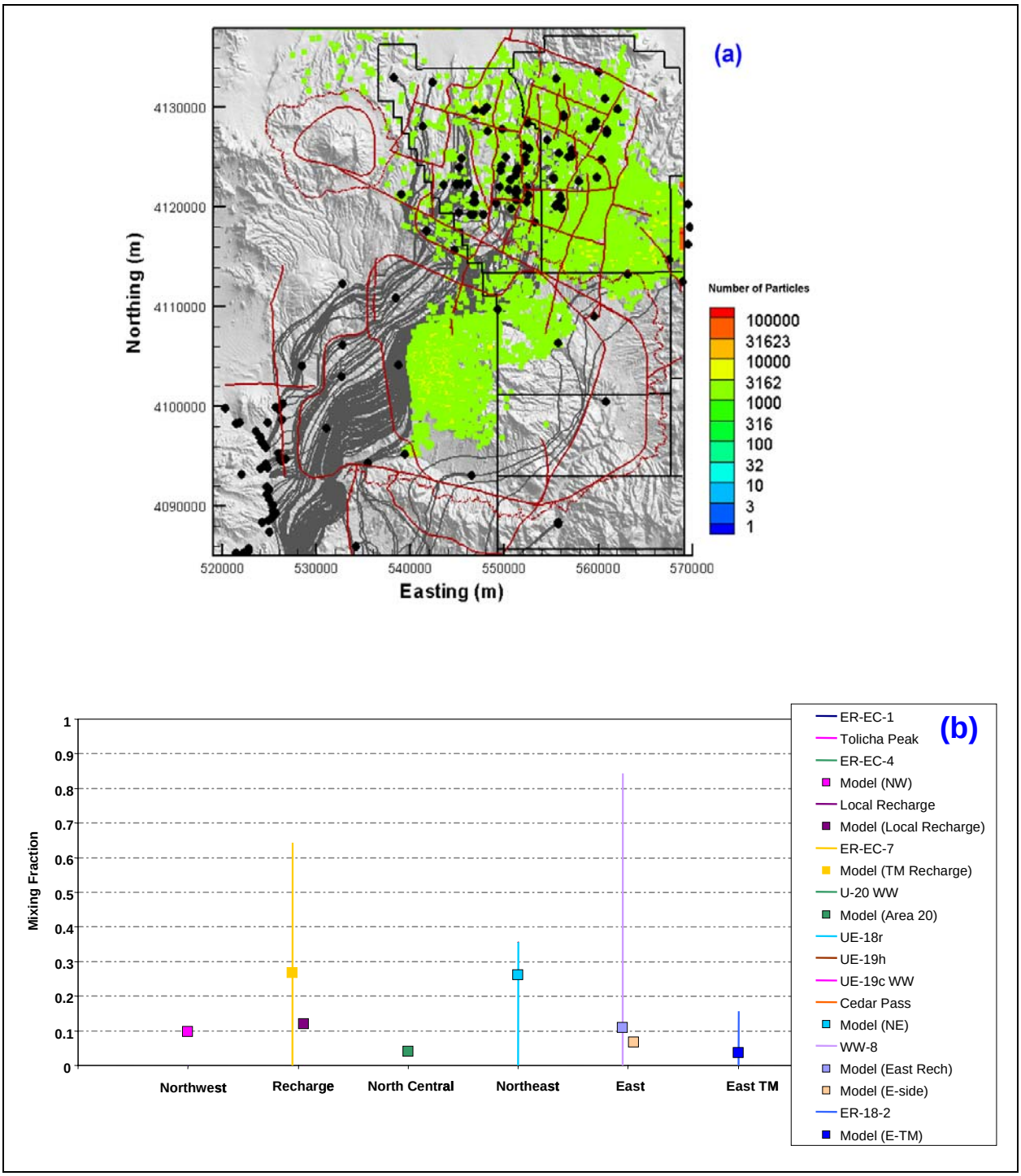

Figure 7-105
Comparison of Flow Model with Geochemical Mixing Targets at Coffer Windmill Well for BN-USGSD-SDA in the Reduced LCCU1 Permeability Alternative

Figure (a) shows the flow paths as mapped by forward SPTR particles originating at wells (grey lines) and the source recharge locations identified by reverse PTRK particle tracking (colored squares). Figure (b) shows the model comparison with geochemical mixing target ranges.

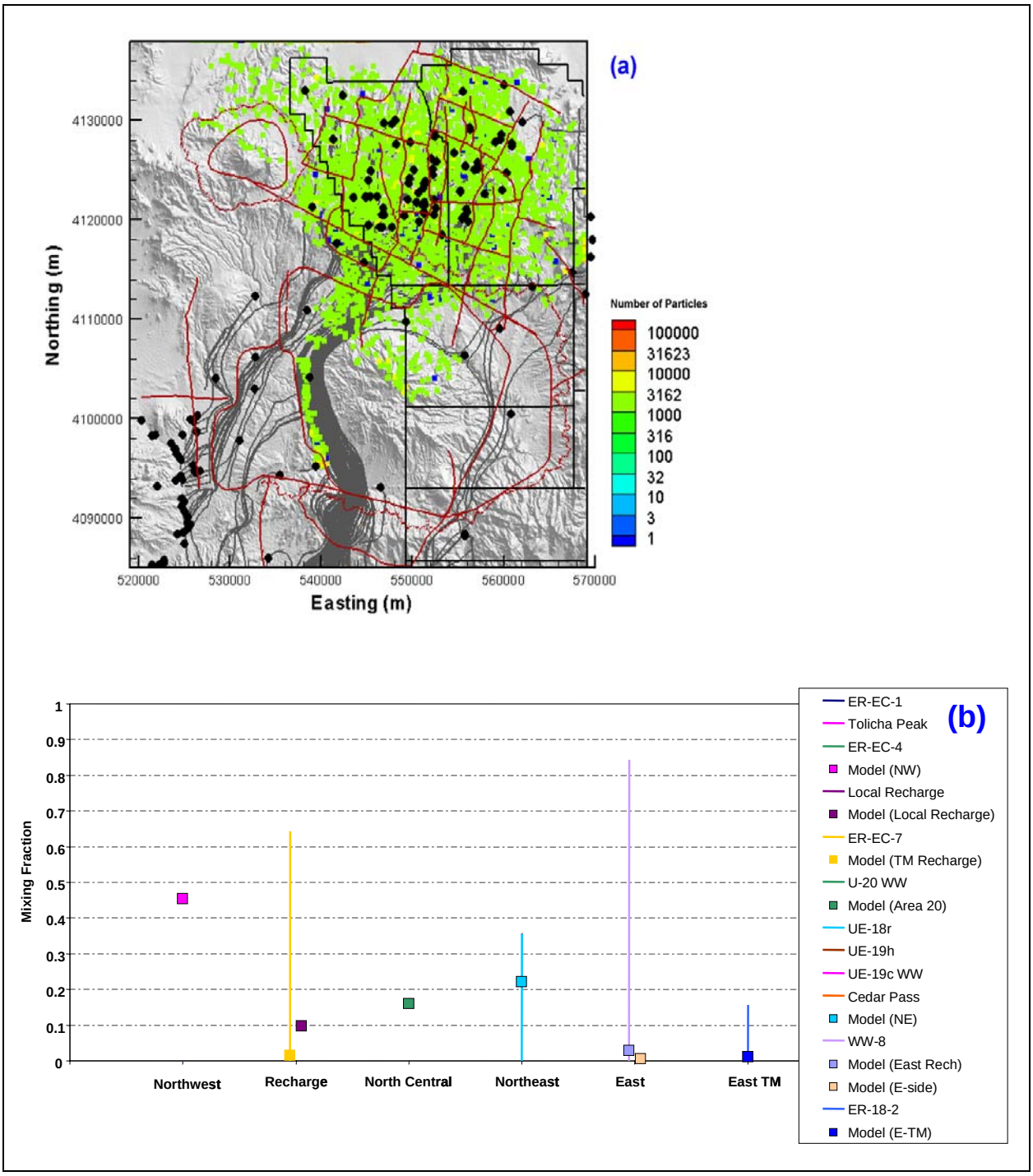

Figure 7-106
Comparison of Flow Model with Geochemical Mixing Targets at Coffer Windmill Well for BN-DRIA-SDA in the Reduced LCCU1 Permeability Alternative

Figure (a) shows the flow paths as mapped by forward SPTR particles originating at wells (grey lines) and the source recharge locations identified by reverse PTRK particle tracking (colored squares). Figure (b) shows the model comparison with geochemical mixing target ranges.

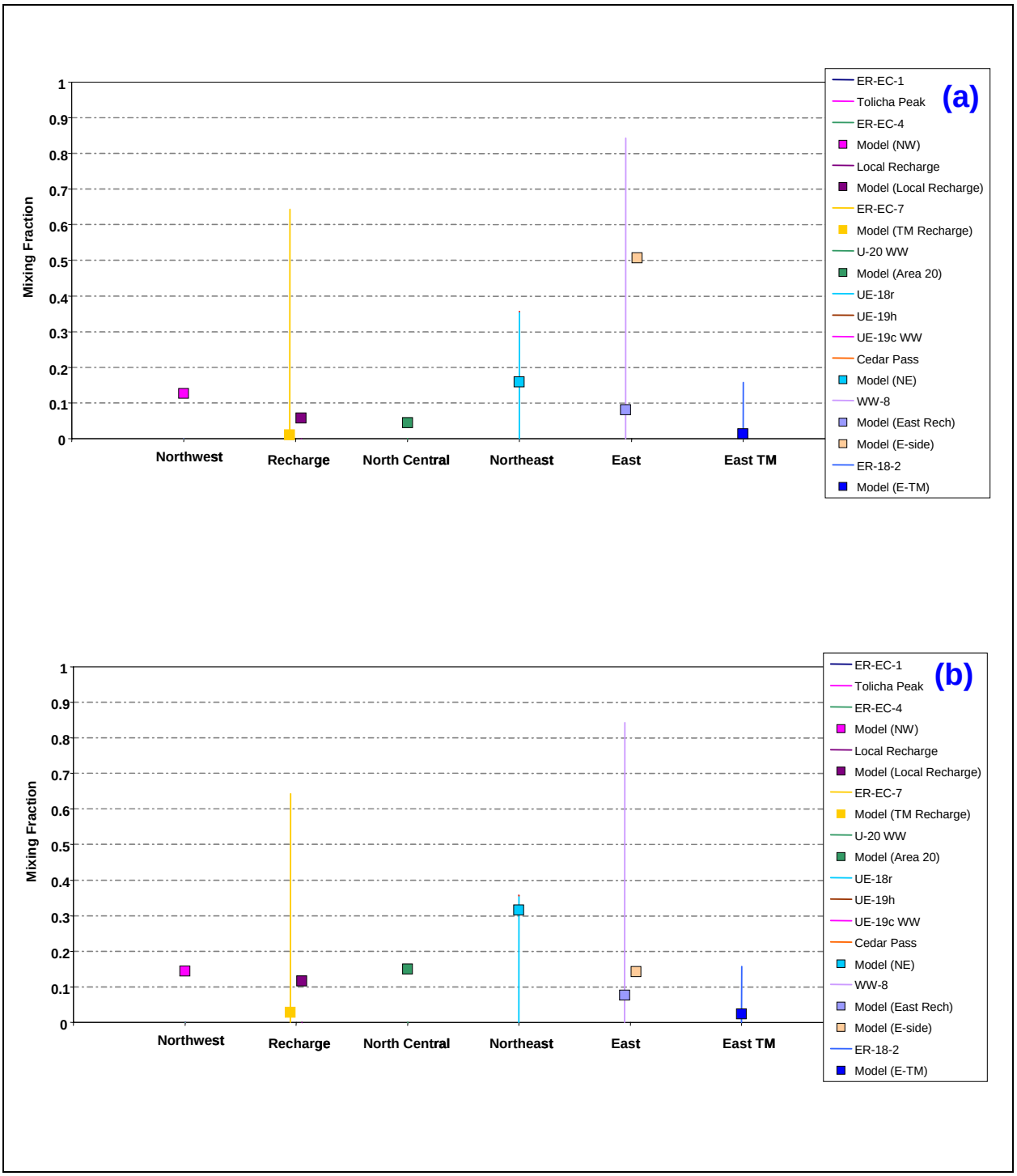

Figure 7-107
Quantitative Geochemical Comparisons at Coffer Windmill Well for (a) BN-USGSD-SDA and (b) BN-DRIA-SDA

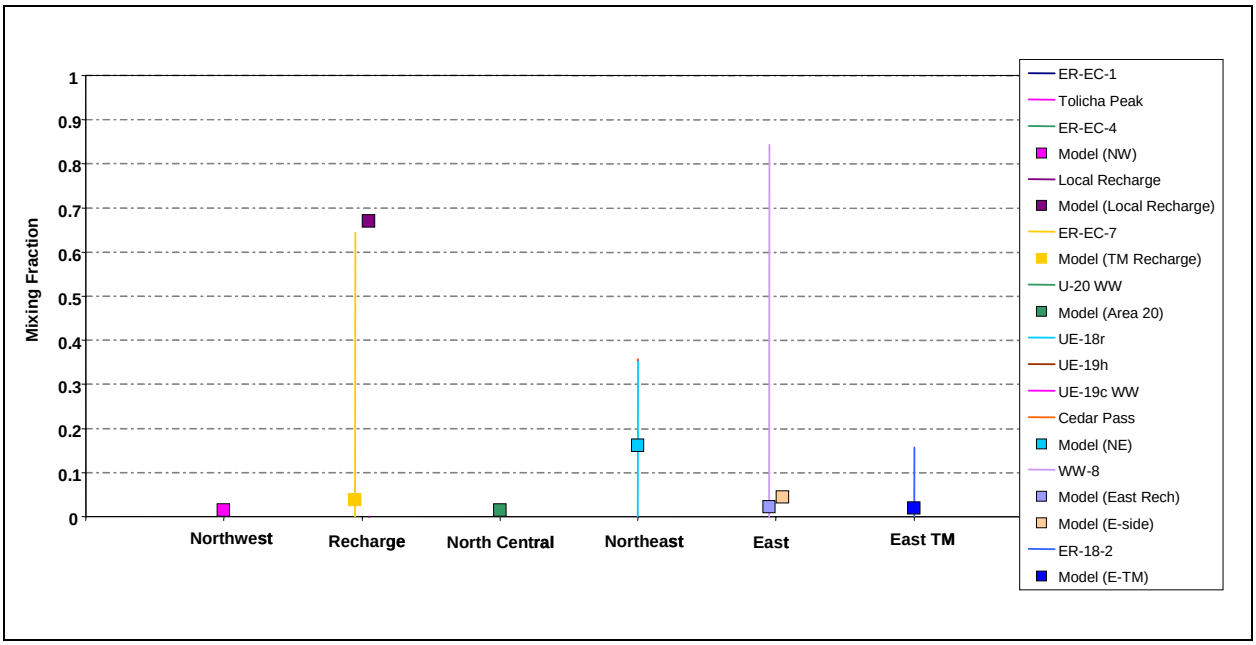

Figure 7-108
Comparison of Flow Model with Geochemical Mixing Targets at Coffer Windmill Well for BN-MME-ADA

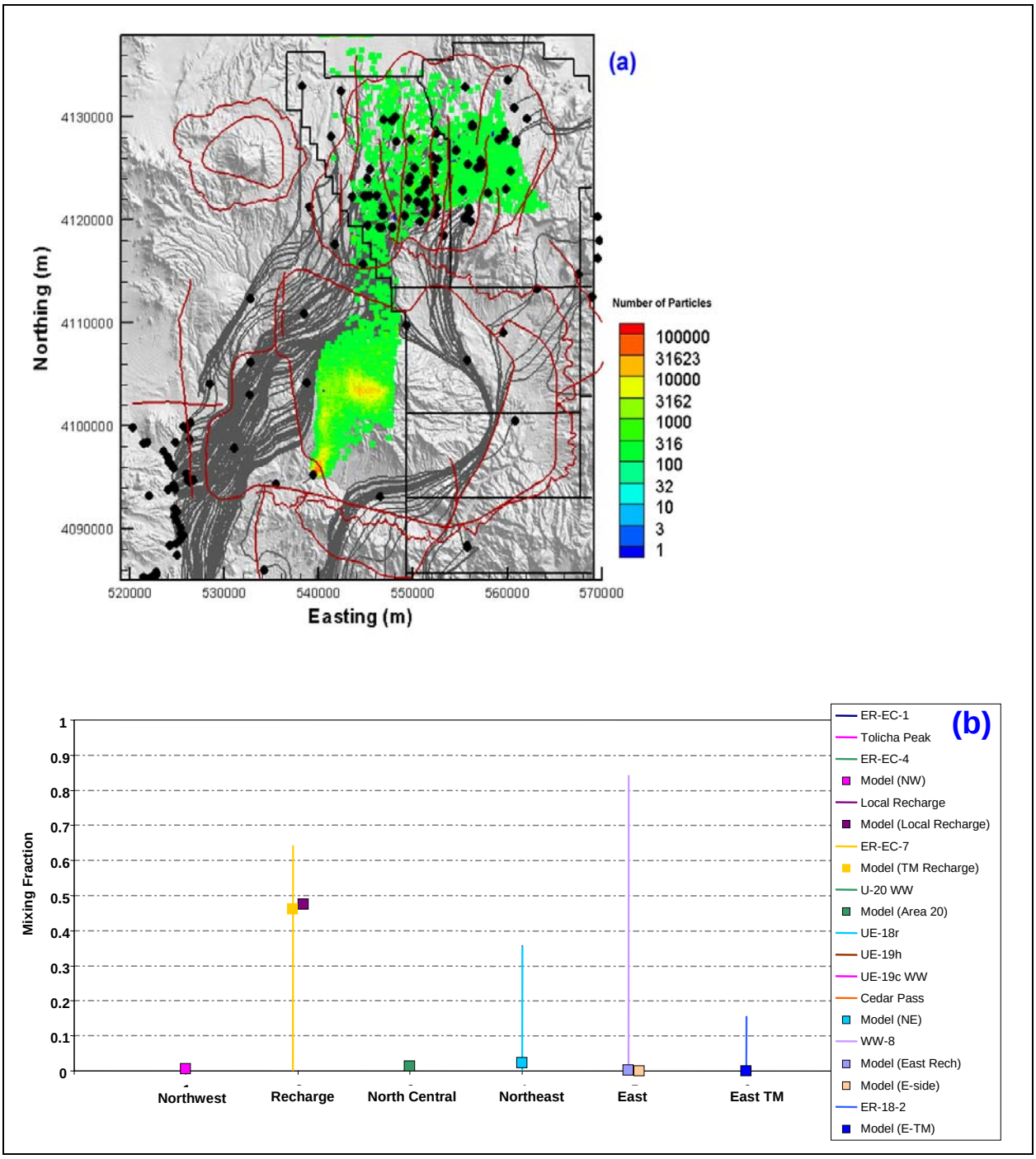

Figure 7-109
Comparison of Flow Model with Geochemical Mixing Targets at Coffer Windmill Well for SCCC-MME-SDA

Figure (a) shows the flow paths as mapped by forward SPTR particles originating at wells (grey lines) and the source recharge locations identified by reverse PTRK particle tracking (colored squares). Figure (b) shows the model comparison with geochemical mixing target ranges.

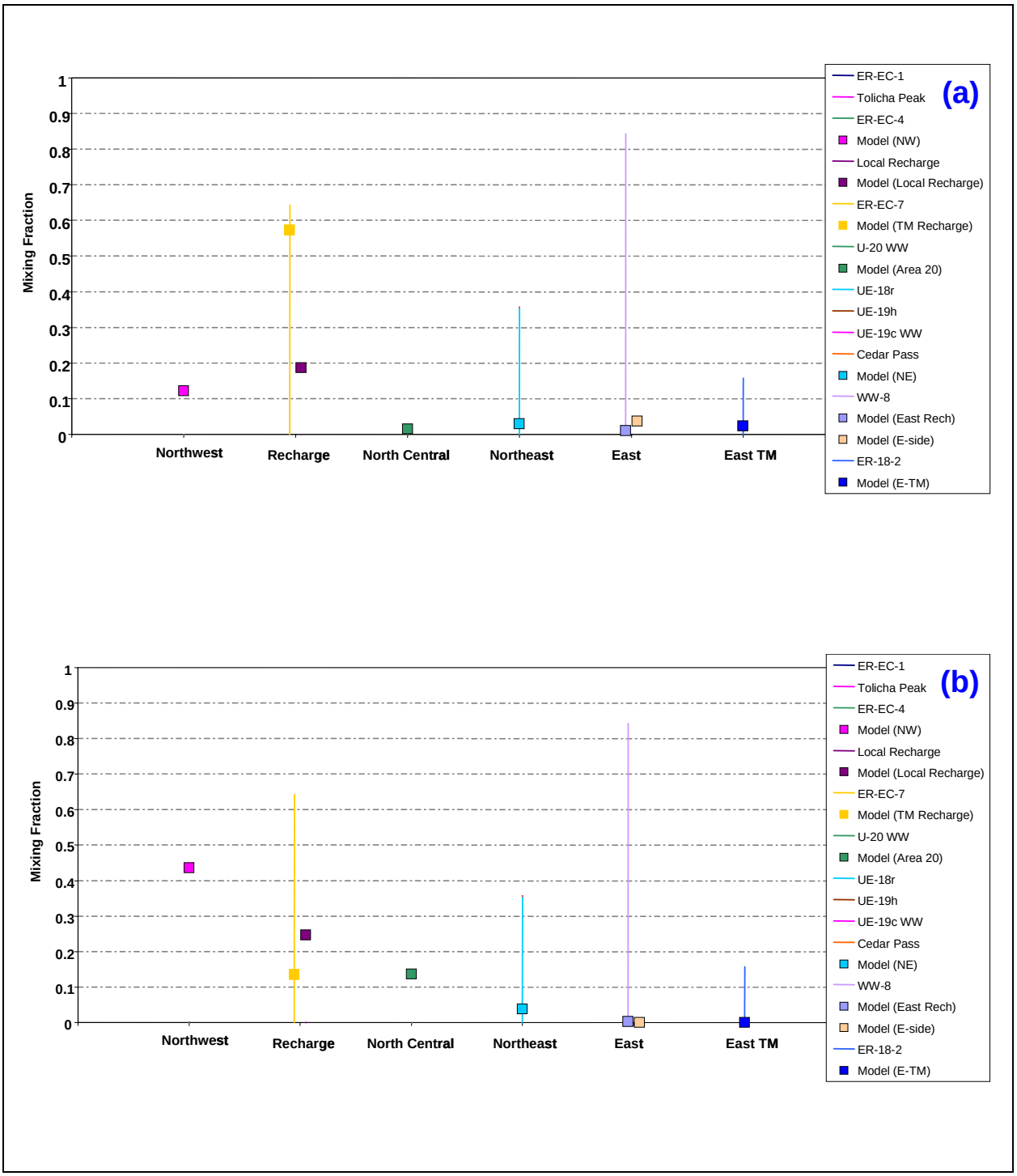

Figure 7-110
Quantitative Geochemical Comparisons at Coffer Windmill Well for (a) SCCC-USGSD-SDA and (b) SCCC-DRIA-SDA

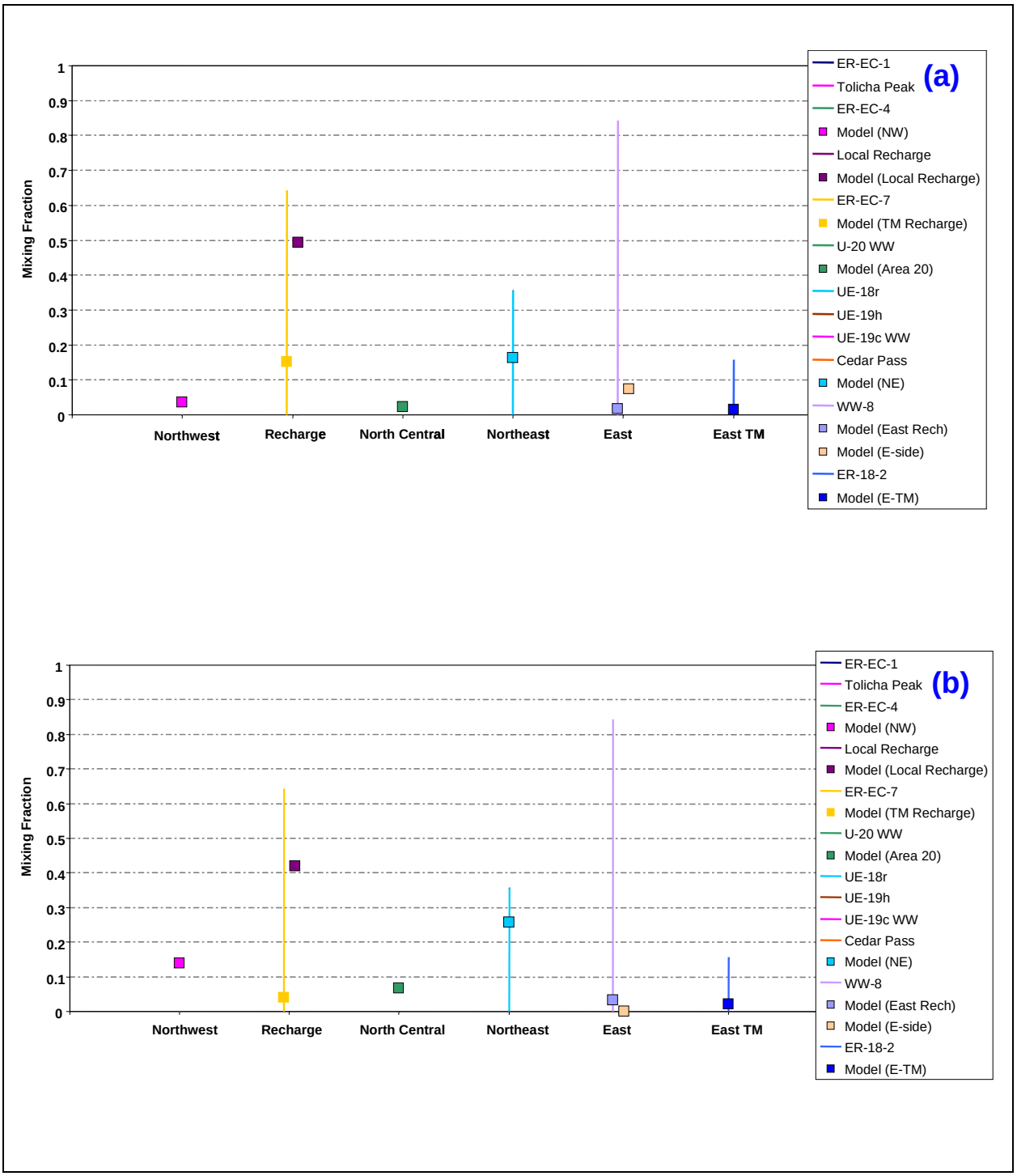

Figure 7-111
Quantitative Geochemical Comparisons at Coffer Windmill Well for (a) PZUP-MME-SDA and (b) DRT-MME-SDA

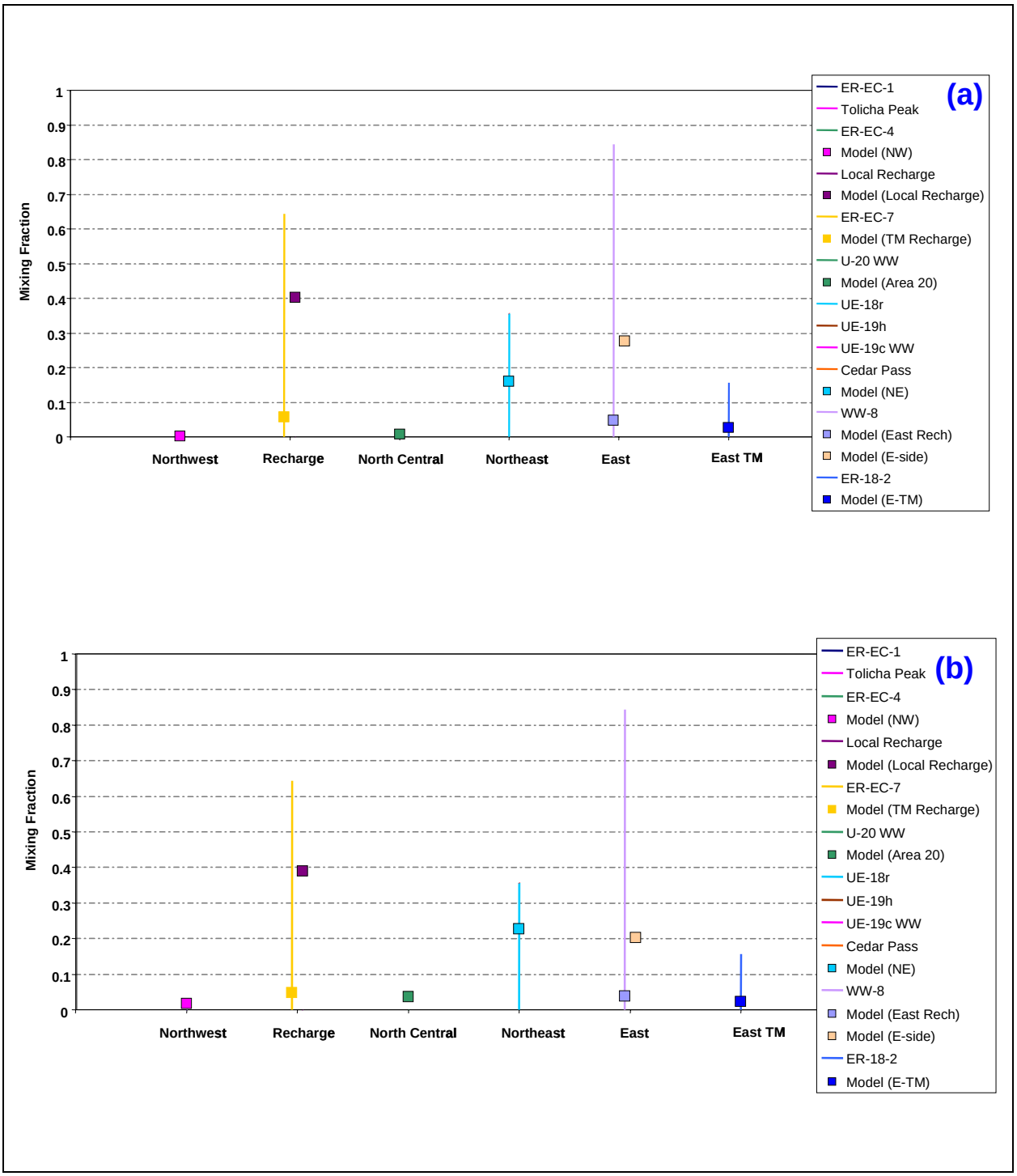

Figure 7-112
Quantitative Geochemical Comparisons at Coffer Windmill Well for (a) RIDGE-MME-SDA and (b) TCL-MME-SDA

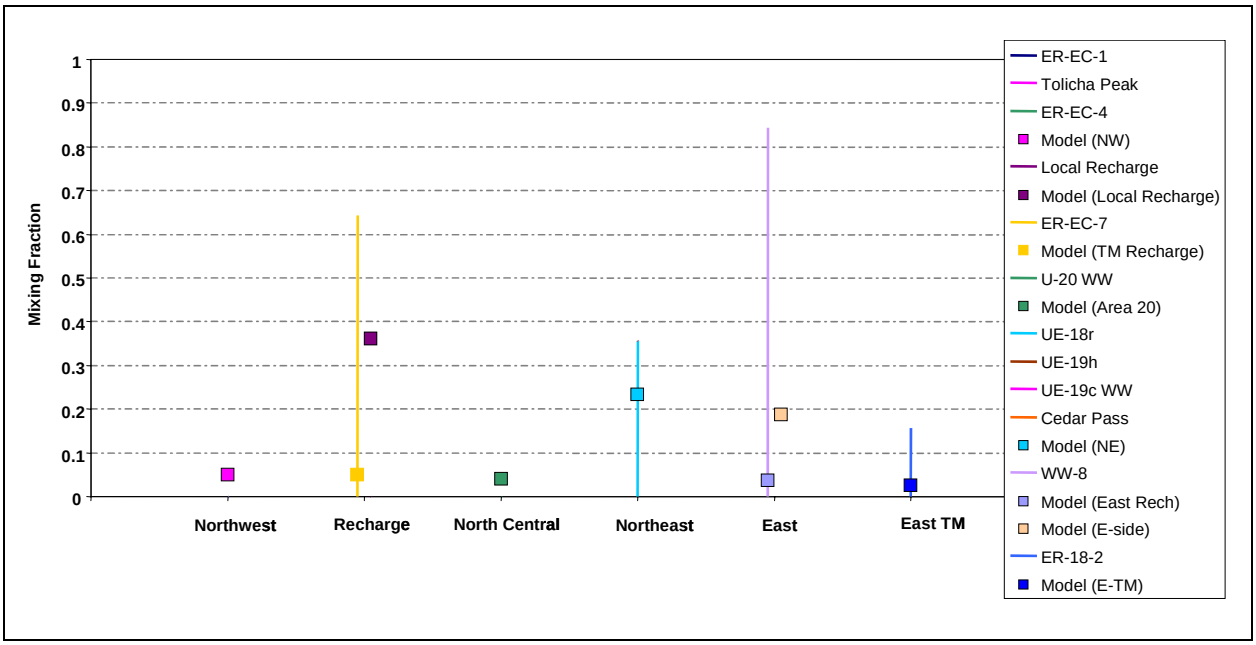

Figure 7-113
Comparison of Flow Model with Geochemical Mixing Targets at Coffer Windmill Well for SEPZ-MME-SDA

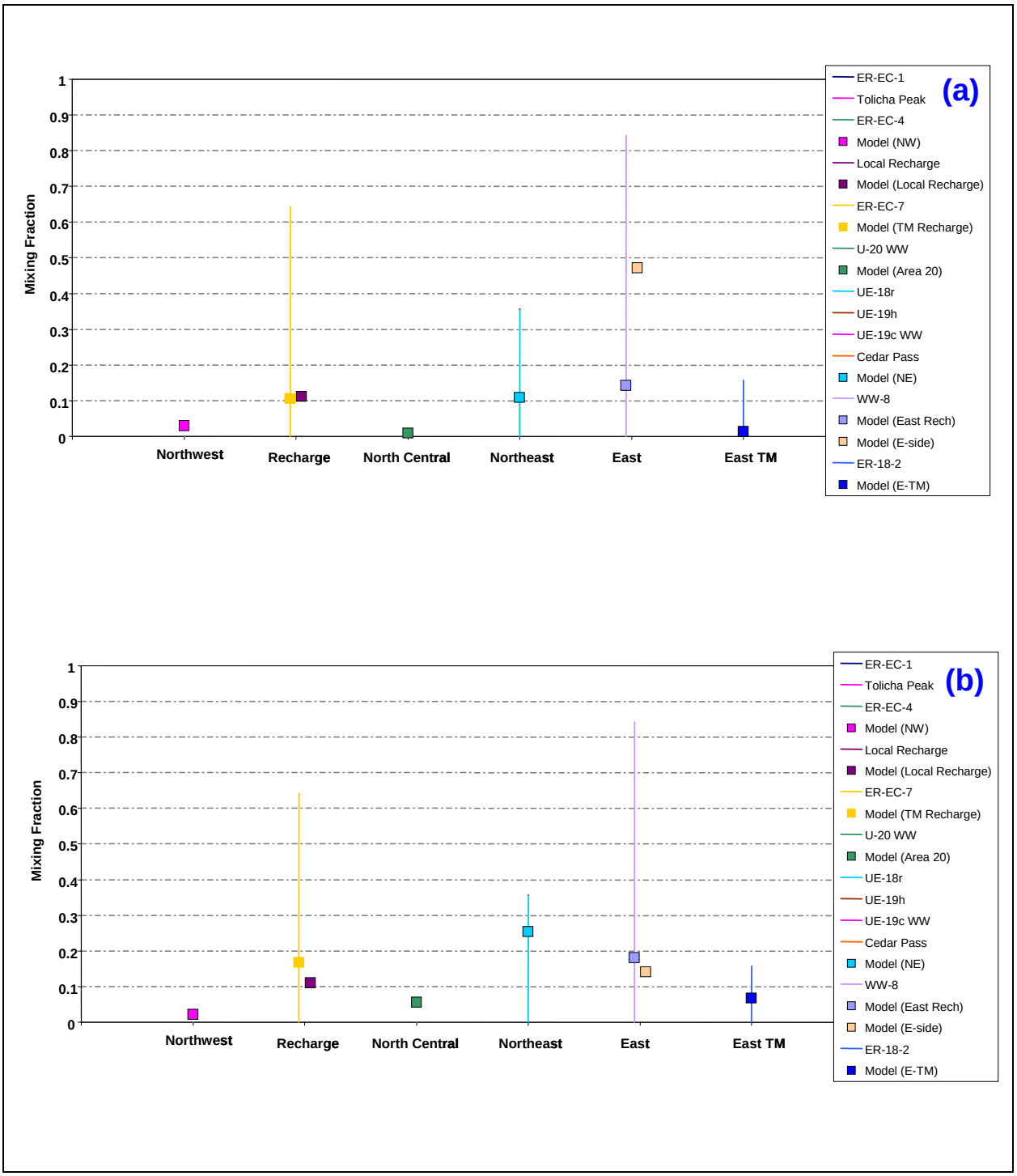

Figure 7-114
Quantitative Geochemical Comparisons at Coffer Windmill Well for (a) PZUP-USGSD-SDA and (b) PZUP-DRIA-SDA

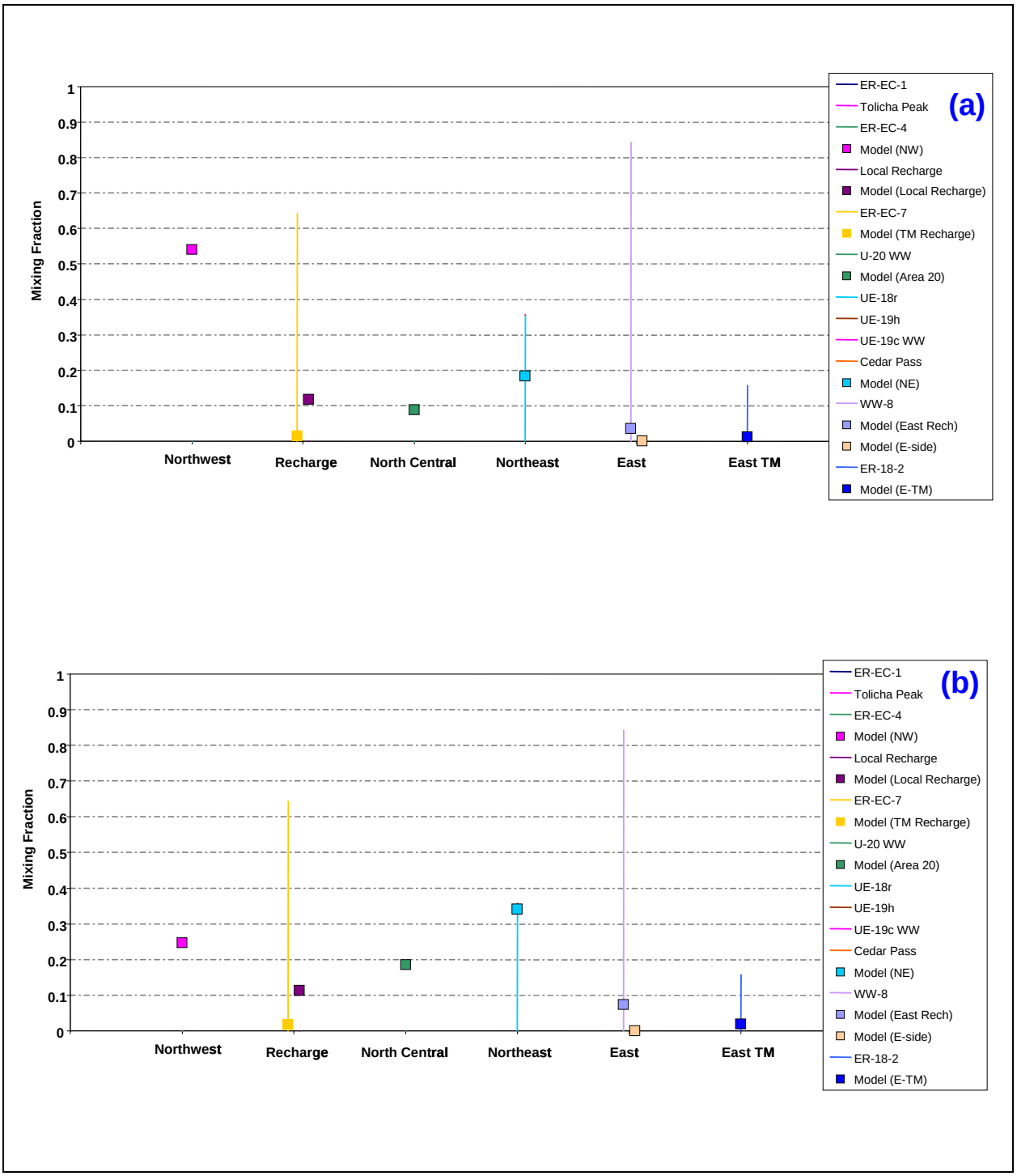

Figure 7-115
Quantitative Geochemical Comparisons at Coffer Windmill Well for (a) DRT-USGSD-SDA and (b) DRT-DRIA-SDA

Table 7-17
Comparison of Alternative Models at Coffer Windmill Well

HFM	Water-Balance Condition	Overestimation of Northwest Source	Overestimation of Local Recharge
BN-SDA reduced LCCU1 permeability alternative	MME	X	
	USGSD		
	DRIA	X	
BN-SDA	MME		
	USGSD	X	
	DRIA	X	
BN-ADA	MME		
SCCC-SDA	MME		
	USGSD	X	
	DRIA	X	
PZUP	MME		
DRT	MME	X	
RIDGE	MME		
TCL	MME		
SEPZ	MME		
PZUP	USGSD		
	DRIA		
DRT	USGSD	X	
	DRIA	X	

7.4 Geochemistry Performance of the Fortymile Canyon Alternate

One of the sensitivity simulations discussed in Section 6.2.4 involved manual intervention of a calibration to force a high permeability pathway southward along Fortymile Canyon. By increasing the permeabilities of the TMCM and reducing the LCCU1 permeability alternative and then recalibrating the flow model, a reasonable objective function was obtained, and the amount of flow originating on Pahute Mesa and flowing to the east of Timber Mountain was increased. Figure 7-116 shows the simulated pathlines highlighting the increased southward flow to the east of Timber Mountain. The quality of the comparison to geochemical mixing targets of this model decreases substantially from those discussed previously in this section. Figure 7-117 shows that nearly 80 percent of the source water for UE-18r in this simulation is from the northwest. However, the chemistry analysis indicates that there is no water source at UE-18r with such a signature. Figures 7-118 through 7-121 show a systematic error in overprediction of northwest source water at the Oasis Valley wells. This results from the northeast source water moving southward and to the east of Timber Mountain, rather than to Oasis Valley, where the geochemical analysis indicates it should be present.

The geochemistry verification study for this flow model, coupled with the calibration results, indicate that this flow model is not a good representation of the PM/OV flow system. Water from the northeast that should arrive in Oasis Valley moves southward below Fortymile Canyon instead. The increased permeabilities that make such flow possible in the model produce systematic errors in the calibration as well (Figure 6-76). The simulated heads along the east side of Timber Mountain are uniformly below observations, indicating at large-scale problem with the parameters and their impacts in groundwater flow.

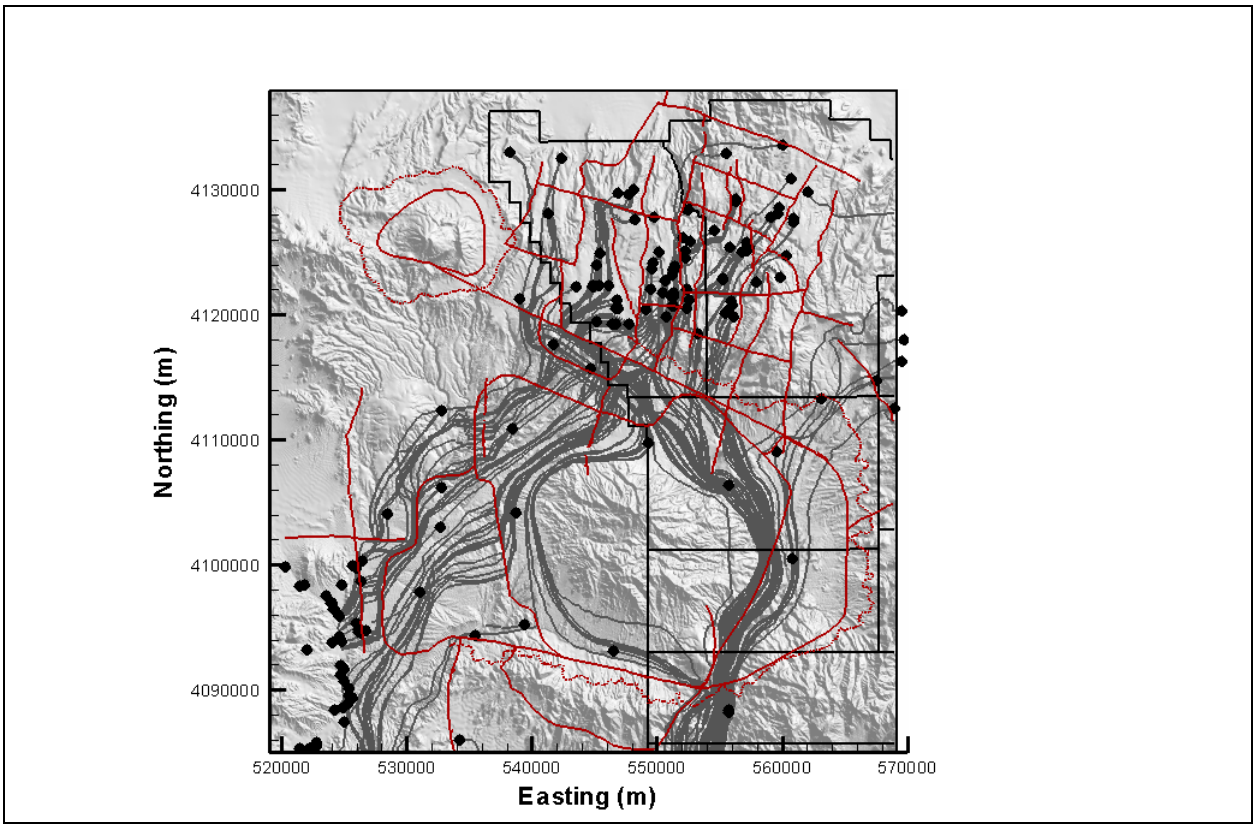

Figure 7-116
Paths of Particles Released in Wells for BN-USGSD-FMC Calibrated Flow Model

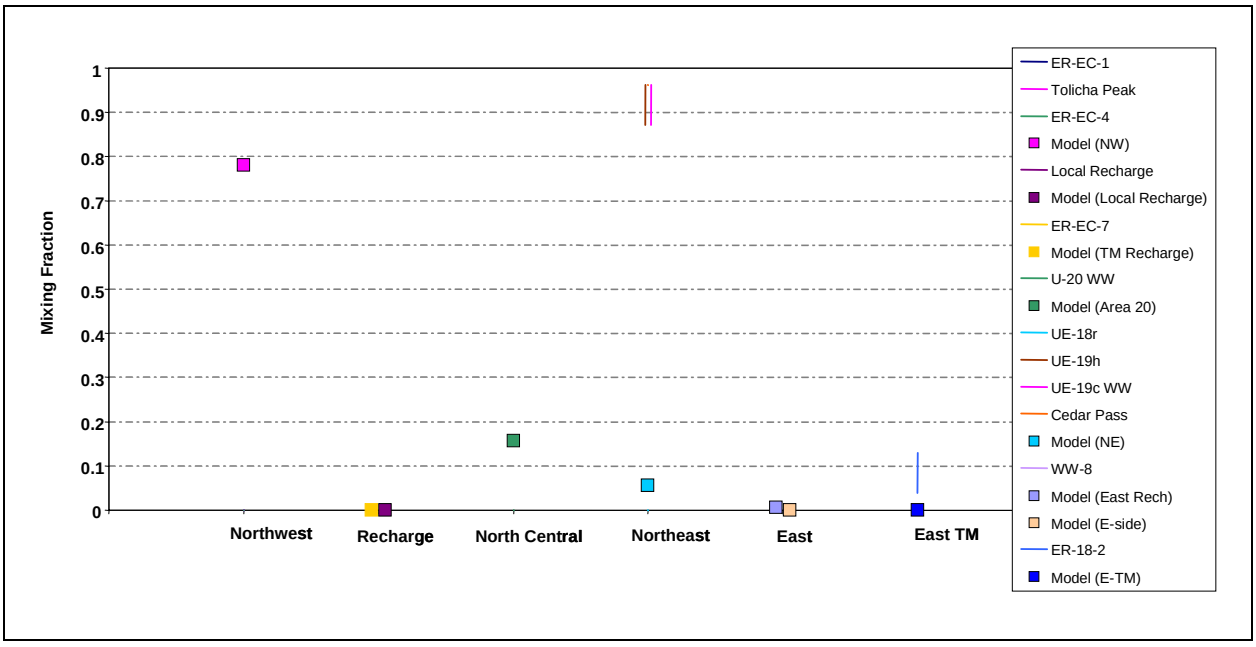

Figure 7-117
Comparison of Flow Model with Geochemical Mixing Targets for UE-18r with the BN-USGSD-FMC Flow Model

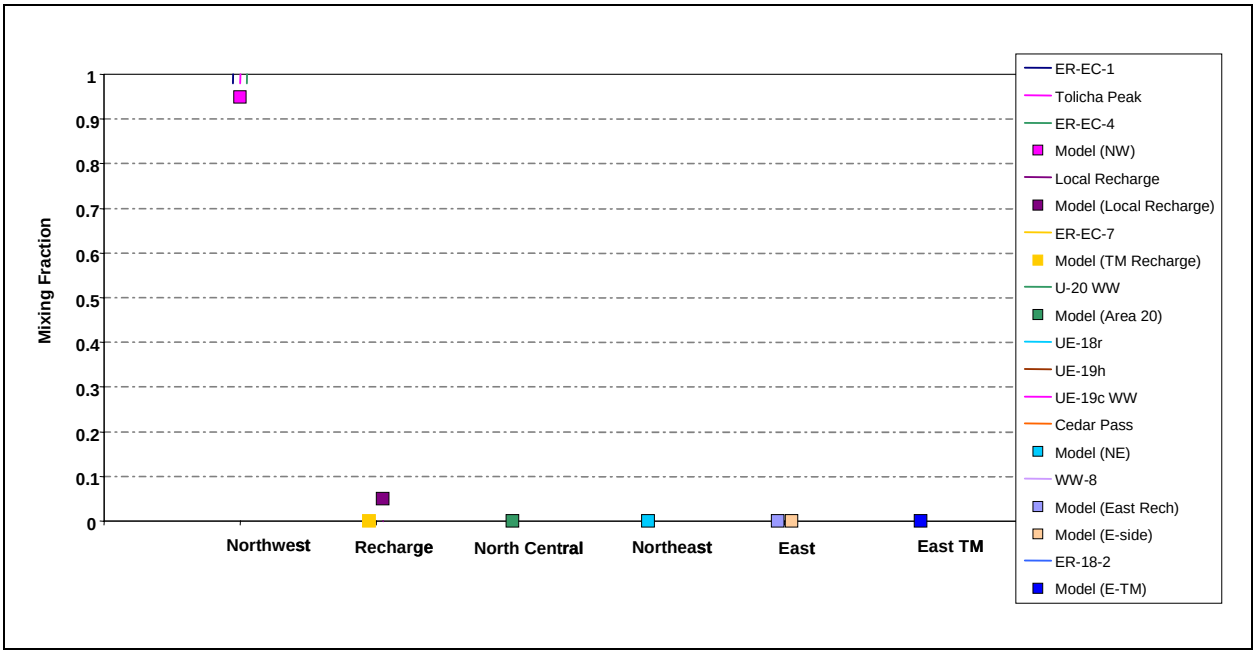

Figure 7-118
Comparison of Flow Model with Geochemical Mixing Targets for ER-OV-04a with the FMC-USGSD-SDA Flow Model

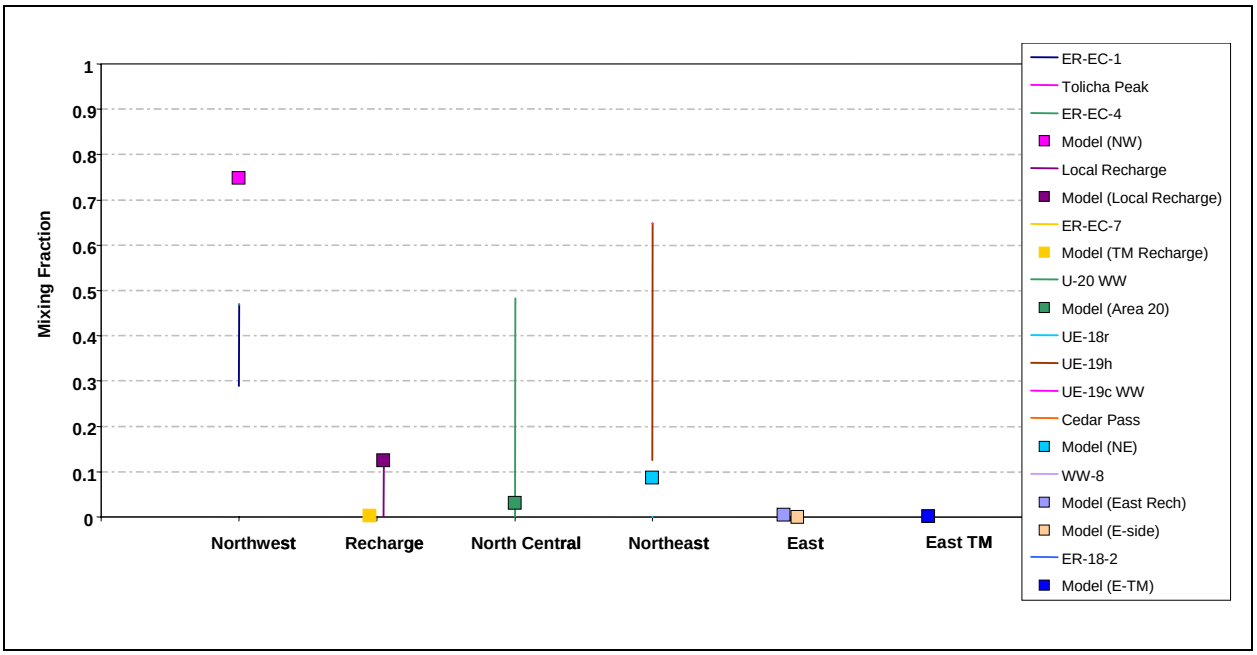

Figure 7-119
Comparison of Flow Model with Geochemical Mixing Targets for ER-OV-03a with the FMC-USGSD-SDA Flow Model

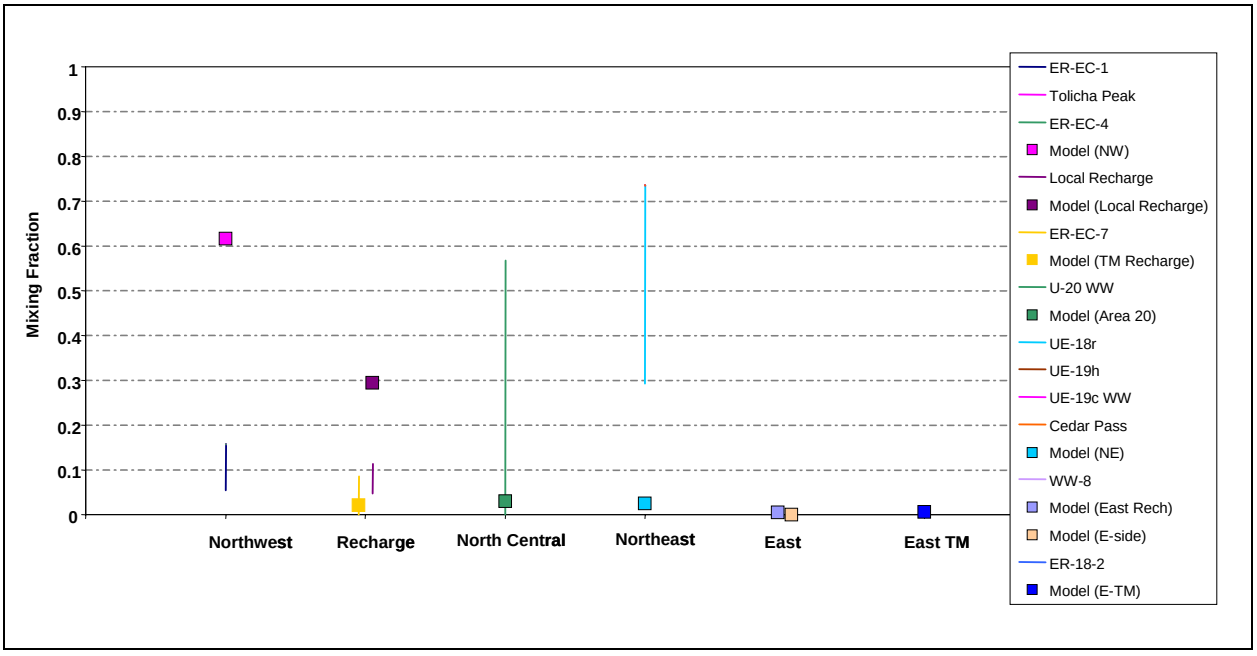

Figure 7-120
Comparison of Flow Model with Geochemical Mixing Targets for ER-OV-03c with the FMC-USGSD-SDA Flow Model

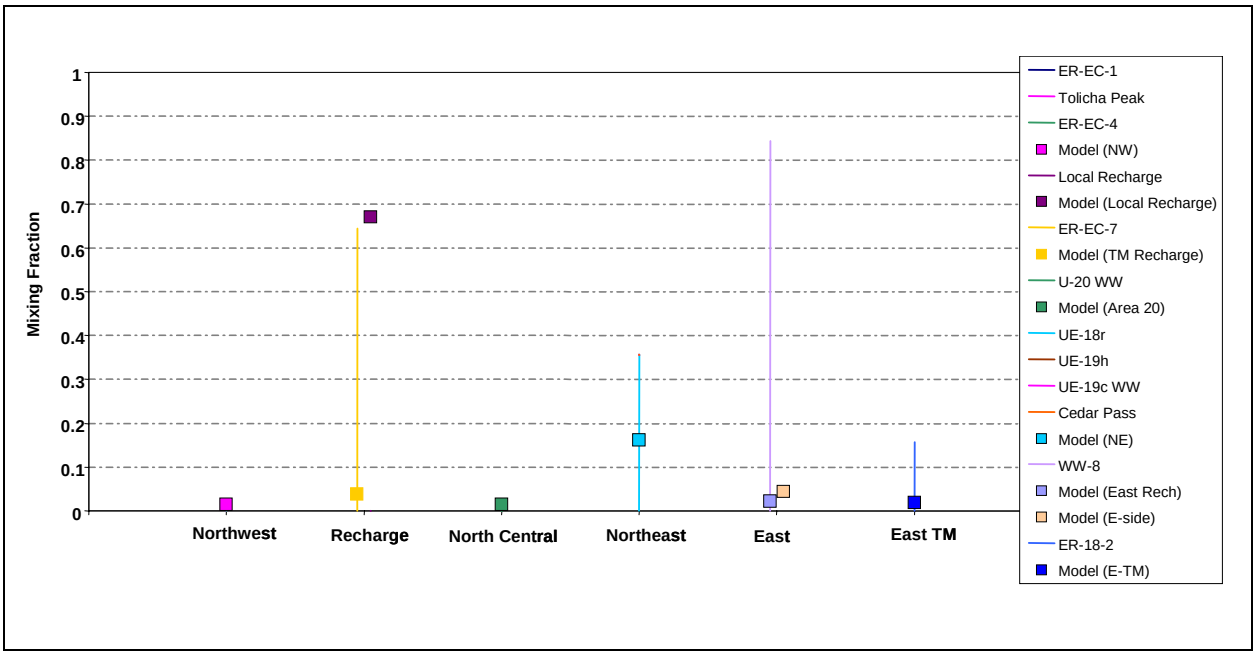

Figure 7-121
Comparison of Flow Model with Geochemical Mixing Targets for Coffer Windmill Well with the FMC-USGSD-SDA Flow Model

7.5 Quantitative Analysis and Ranking of Flow Models Based on Geochemistry

7.5.1 Quantifying the Flow Models

In Sections 7.2 and 7.3, each flow model was evaluated for each geochemical mixing target, graphically showing the ranges of source contributions from recharge/inflow zones in the domain as estimated by Kwicklis et al. (2005) (lines) compared with the fractions simulated with the reverse transport model (symbols), as shown in Figure 7-8. The geochemical residual for each recharge/inflow zone in the figures is the difference between the target range and the simulated fraction. However, visual inspection of figures in Sections 7.2 and 7.3 does not provide the quantitative analysis necessary to assess the performance of the different flow models.

For all target wells in each of the calibrated flow models, there are four potential types of error identified by the comparison of model results with geochemical mixing targets. These are:

- **RM:** Too much inflow across the eastern boundary from Rainier Mesa. Although the gradients suggest such flow might be possible, the geochemistry rules it out at all target wells except Coffer Windmill Well.
- **NW:** Too much inflow across the northern boundary west of the Purse Fault (Figure 7-1).
- **NCNE:** Not enough flow from the north-central and northeast areas east of the Purse Fault.
- **Rech:** Too much local recharge (lower Thirsty Canyon and Oasis Valley).

Eighteen of these residual types result at the target wells, forming the basis for a comparison and ranking of 19 different flow models. For example, UE-18r_RM is the error of too much inflow across the eastern model boundary (RM is notation for Rainier Mesa) as identified by differences between the geochemical target and model results at UE-18r. Its value is the difference between the symbol (model value) and the top of the line (geochemical mixing target range) in the first column of figures such as Figure 7-8. Another example is ER-OV-04a_Rech, which is excessive local recharge at ER-OV-04a. Apparent similarities in the errors among various models motivate a formal cluster analysis seeking to identify models with similar geochemical residuals. The clusters are developed with the objective of minimizing the intervariance within each cluster and maximizing the intervariance between different clusters. The analysis is achieved with a k-means clustering

algorithm, which is an iterative process for assigning models to different clusters and then testing the objective. This analysis highlights four distinct clusters of the 19 models considered (Table 7-18).

Table 7-18
k-Means Clusters of Flow Models Based on Geochemical Residuals

Cluster	1	2	3	4
Models	SCCC-DRIA SCCC-USGSD DRT-USGSD BN-DRIA-LCCU1	PZUP-USGSD BN-DRIA PZUP-DRIA BN-MME-ADA	BN-USGSD RIDGE-MME SEPZ-MME BN-MME TCL-MME	DRT-MME DRT-DRIA BN-MME-LCCU1 PZUP-MME BN-USGSD-LCCU1 SCCC-MME

Figure 7-122 shows the mean cluster value for each of the 18 geochemical residuals for each of the four clusters of the 19 models. The nomenclature for the residuals is such that the target well is listed first, followed by one of the four types of error listed above. Figure 7-123 shows the individual residual components of the total geochemical residual for each model, grouped by cluster. The four clusters can be summarized as follows:

- **Cluster 4:** Continuous problems with too much inflow from NW.
- **Cluster 3:** Substantial inflow from Rainier Mesa at UE-18r, ER-OV-04a, ER-OV-03a, and ER-OV-03c. Additional problems with local recharge at ER-OV-01 and ER-OV-03c
- **Cluster 2:** Inflow from Rainier Mesa, but not as bad as Cluster 3, particularly at UE-18r.
- **Cluster 1:** Local recharge issues at ER-OV-03a, ER-OV-03c, and ER-OV-01, however, not substantially different than other models at those locations.

The analysis in Figure 7-124 shows strong correspondence between the total geochemical residual and the type of model error(s) associated with the four clusters. Cluster 1 shows the strongest performance in total geochemical residual because these models are not plagued with NW inflow issues or Rainier Mesa inflow issues. The problems with local recharge in Cluster 1 are most indicative of local errors in the specified recharge models and less of the global flow solution. Generally, the recharge modes seem to apply more recharge in the washes than is consistent with the geochemisty. Cluster 4 models are characterized by incorrect assessment of inflow from the northwest and Cluster 3 models are characterized by excessive inflows from Rainier Mesa

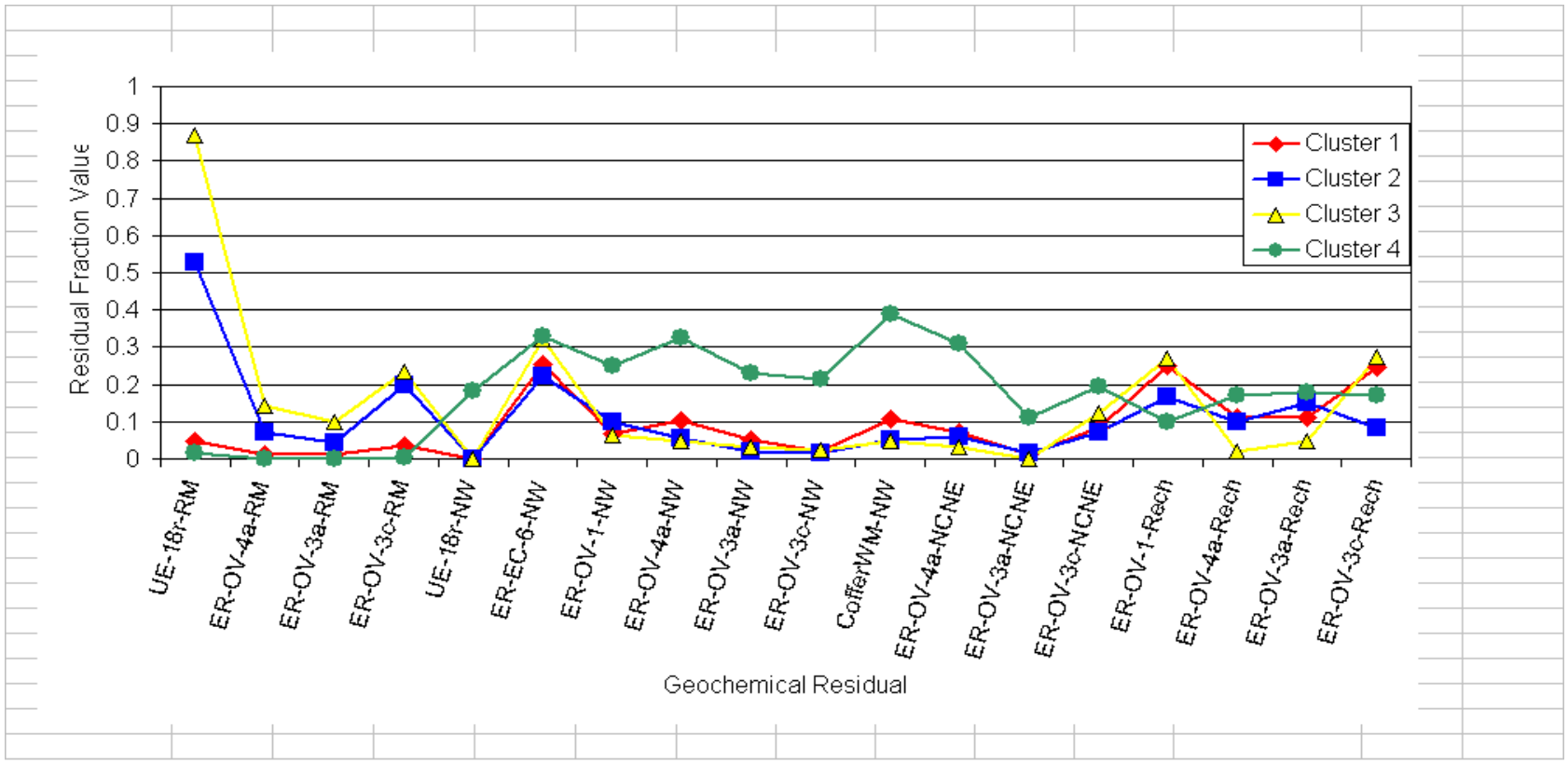

Figure 7-122
Geochemical Residual Means for Each Cluster

The residuals are defined as Well_name-Error_type and grouped by error type to highlight differences between the clusters.

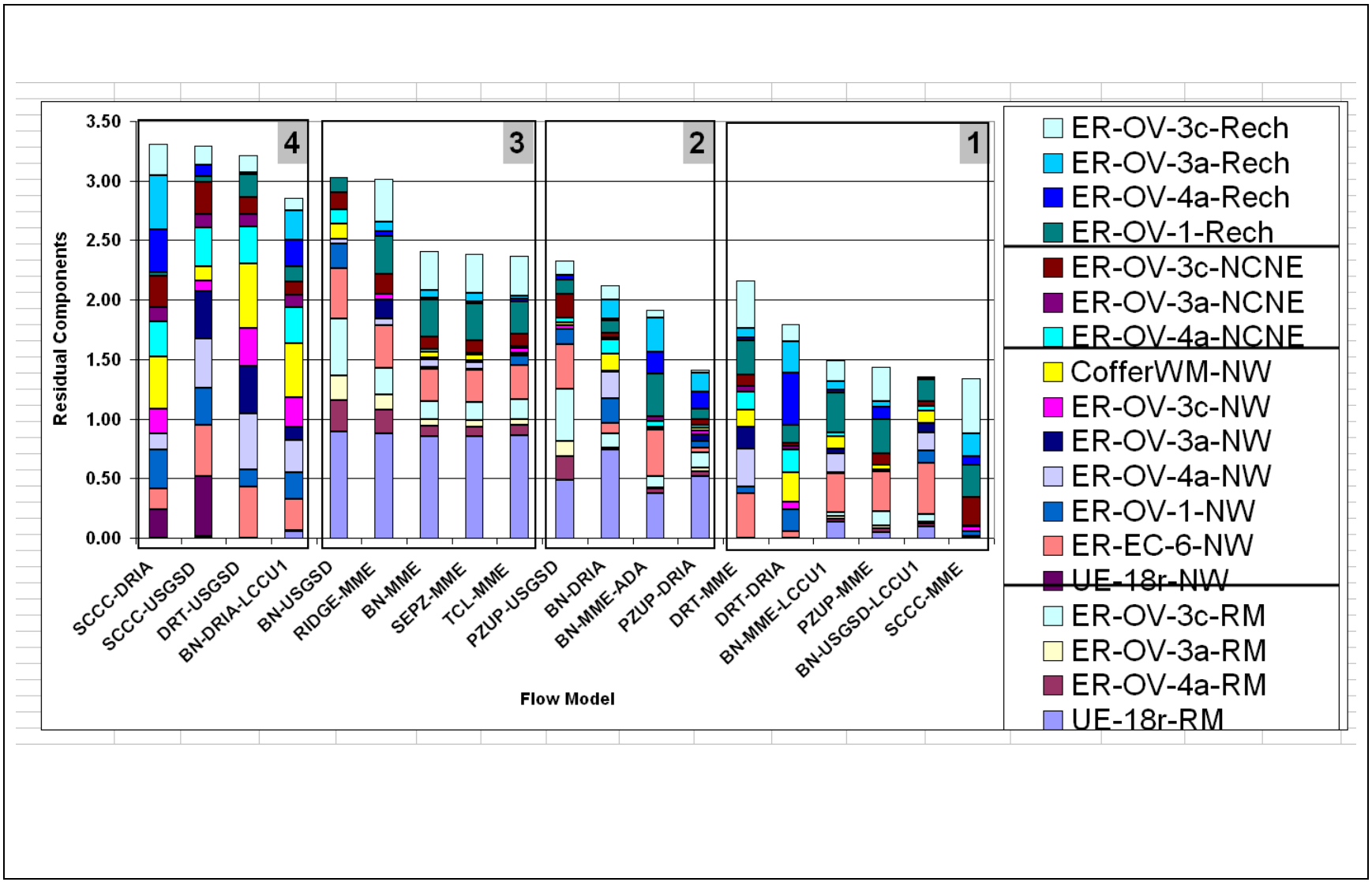

Figure 7-123
Components of the Total Geochemical Residual for Each Model

The models are grouped by the four clusters and the residuals are grouped by error type.

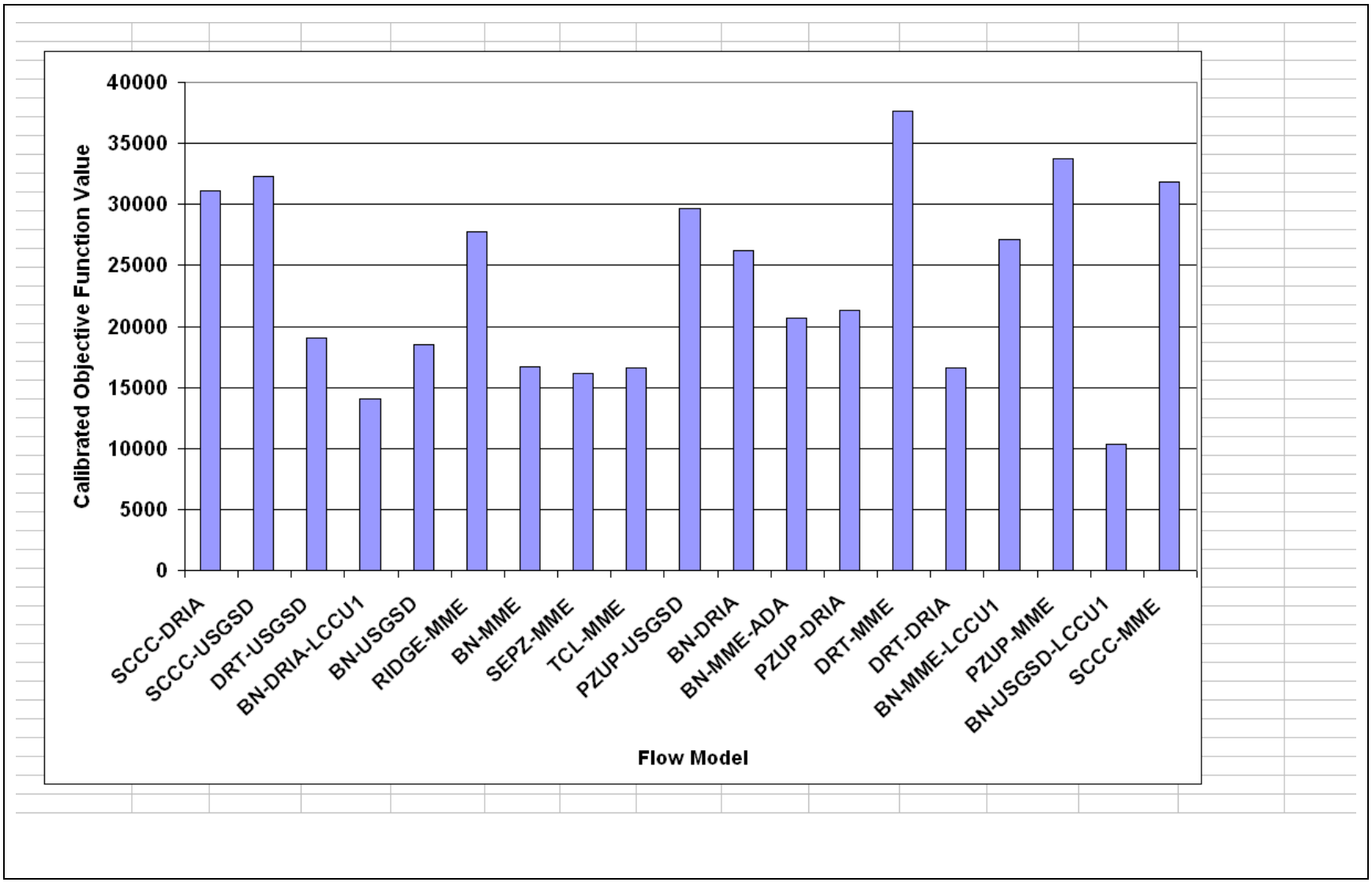

Figure 7-124
Flow Model Calibration Objective Functions, Sorted To Compare with Geochemical Residuals in Figure 7-123

(Gold Meadows to the east of the model domain). Cluster 2 models perform very well in all regards other than Rainier Mesa inflow, and they represent the better half of the models with Rainier Mesa inflow problems, the worse half being Cluster 3. It is also instructive to note that the total geochemical residual does not correspond with the final objective function of the head/flux calibrations (Figure 7-124). This is not surprising because the flow models were all calibrated by substantially reducing the flow/flux objective function from initial values more than an order of magnitude higher, with the assessment that they were all reasonably calibrated and ready for comparison.

7.5.2 Ranking the Flow Models

The total geochemical residual can be used to rank the quality of flow models relative to how well they represent inflow sources at downgradient wells (not their contaminant transport prediction capability). But first, flow models that do not perform well with regard to the verification data need to be eliminated from further consideration. Clusters 4 and 3 have systematic errors that are in direct conflict with the global flow system interpretation based on geochemistry. They have irreconcilably excessive inflows from the northwest at Gold Flat (Cluster 4) or from Gold Meadows on the eastern boundary (Cluster 3). Thus, they can be eliminated. At the other end of this analysis, the Cluster 1 models generally do not have such global flow errors. The Cluster 1 errors are dominated by excessive local infiltration as a direct result of the specified infiltration maps; these errors are similar in all four clusters. The impacts on flow and transport are local and generally downgradient from the sources, thus, they are far less significant than those errors in Clusters 3 and 4 when considering contaminant migration at the CAU scale. The Cluster 2 models have the Rainier Mesa inflow problems that characterize Cluster 3, but they are not as severe. They also have better performance than Cluster 1 models in almost all other regards. The PZUP-DRIA flow model in Cluster 2 has a total geochemical residual lower than all but one of the Cluster 1 models, and the remaining Cluster 2 models have total geochemical residuals similar to the worst two models in Cluster 1 (Figure 7-123). Thus, it is recommended, that these models be considered during transport modeling, at least in sensitivity analysis.

7.6 Summary

Multiple groundwater flow models were calibrated to minimize differences between simulated and observed heads as well as simulated and estimated boundary fluxes for the Pahute Mesa CAU at the NTS (Section 5.0 and Section 6.0). These models represent alternative conceptualizations for both geologic structure (faults and material thickness and extent), and water-balance conditions (recharge and boundary flux). Although all of the flow models are calibrated to minimize the residuals between simulated and target heads and fluxes, the resulting flow systems are different.

Kwicklis et al. (2005) developed an independent geochemical verification dataset with which to assess the various calibrated flow models. The geochemical analysis provides mixing ratios at wells within the domain, identifying the fractions of source water from upgradient zones present in groundwater samples collected at the target wells. Based upon the geochemical mixing targets, the calibrated flow models are interrogated with reverse transport simulations to identify how well they match the verification data in their predictions of mixing different upgradient sources.

Section 7.0 summarized the geochemical analysis, the reverse transport simulation methodology, and the quantitative comparison and ranking of the alternative flow model calibrations that are available for use in future assessments of contaminant migration.

8.0 THERMAL SENSITIVITY AND VERIFICATION

8.1 Introduction

The flow model calibration described in earlier sections utilizes a thermal field based upon calibration of the heat flux at the base of the model domain (Appendix C). In calibrating the heat fluxes with a conduction-only model to minimize residuals between observed and simulated temperatures in boreholes, certain anomalies were identified indicating convective flow. These anomalies indicate that cooler water from near the water table is likely flowing vertically downward, resulting in borehole temperatures cooler than would be explained with the pure convection model. Therefore, Section 8.2 investigates whether such downward flow is captured with the calibrated flow model, thus providing qualitative confirmation. Section 8.3 investigates the sensitivity (qualitatively again) of the variable heat-flux-based temperatures as compared to much simpler linear temperature profiles in the flow model.

8.2 Flow Model Verification to Vertical Flow Indicated by Temperature Analysis

The role and potential value of thermal data analysis for constraining groundwater flow models is presented in Appendix C. One of the primary results of that analysis is the identification of specific locations where pure vertical conduction of heat does not adequately explain thermal anomalies observed in borehole temperature profiles. The process of identifying such locations involved calibrating heat-conduction-only models to the thermal data in the Pahute Mesa CAU model domain (described in Appendix C). Then, following calibration, temperature datasets that still are not matched well and that show a systematic variance from the conduction-only simulations are examined with respect to other datasets and potential vertical groundwater (and hence heat) convection. Four locations within the CAU flow model domain where downward vertical flow would explain convective cooling are discussed in detail in Appendix C. They are summarized here, and the flow model is evaluated for consistency with respect to the hypothesized downward flow through the use of reverse-particle-tracking simulations. Only the BN-MME-LCCU1 reduced permeability

alternative is evaluated here, but the results are qualitatively representative for any of the calibrated flow models.

8.2.1 Southwestern Silent Canyon Caldera

In the southwestern part of the SCCC, it is likely that the deep heat flux is actually higher than the heat flux of 73 milliwatts per square meter (mW/m^2) estimated for the caldera complex as a whole with the variable heat-flux model described in Appendix C, and that cool groundwater from the shallow saturated zone flows downward through the upper units. These interpretations are supported by a detailed examination of temperature residuals from this area. The heat-conduction model with a uniform heat flux of 85 mW/m^2 provides a good match to the measured temperatures at borehole ER-EC-6, but underestimates the deepest measurement in the region – the temperature of 121 degrees Celsius (°C) measured at a 12,270 ft depth in borehole UE-20f. Conversely, simulated temperatures in nearby boreholes U-20c, U-20d, and ER-20-5 #3 in the southwest part of the caldera complex are warmer than the measured temperatures for deep heat fluxes of either 85 or 73 mW/m^2. A heat flux of 85 mW/m^2 would improve the match between simulated and measured temperatures at boreholes UE-20f, ER-EC-6, and ER-EC-1, where measured temperatures are underestimated by the model with a deep heat flux of 73 mW/m^2 for the SCCC. However, the use of a higher heat flux in the heat-conduction model would increase the mismatch between simulated and measured temperatures at boreholes U20c, ER-20-5 #3, and U-20d, which the model indicates are already too warm for a heat flux of 73 mW/m^2.

To offset the temperature increases that would result from higher deep heat fluxes, a mechanism to cool the subsurface temperatures in the southwestern part of the SCCC is required. The downward hydraulic gradient, dipping beds, and discontinuous HSUs across faults in the upper part of southwest Area 20 (Wolfsberg et al., 2002; BN, 2002, cross-sections J-J' and C-C') indicate that hydrogeologic conditions are favorable for cool groundwater near the water table to flow downward along the dipping beds or faults to deeper aquifers such as the IA, thereby reducing temperatures and heat fluxes below the wells in this region.

To test this hypothesis, a reverse streamline particle-tracking simulation (SPTR Module in FEHM simulation) was conducted for calibrated flow model BN-MME-LCCU1 reduced permeability alternative with 1,000 particles originating in the IA, below ER-20-5 #3 (which terminates in the

CHZCM). Figure 8-1 shows the particle paths moving upgradient and to higher elevations from their origin. This simulation confirms that cool shallow water from central and northern Areas 20 and 19 can flow vertically to deeper units. In this case, the primary elevation drop occurs at the West Greeley Fault, the Boxcar Fault, and within the block between the two faults. The movement of cool shallow water to depths below wells such as ER-20-5 #3 would result in the observed cooler temperatures, which lead to lower-than-expected estimations of deep thermal flux in conduction-only models.

8.2.2 Northeastern Silent Canyon Caldera

In the northeastern part of the SCCC, the simulated temperatures are higher than the measured temperatures at borehole U-19e for the calibrated variable heat-flux conduction model. Although the temperature data at borehole U-19e are reasonably well matched with a uniform heat flux of 45 mW/m^2, temperatures at borehole U19-i, located about 5 km (3 mi) to the south of borehole U-19e, are underestimated using this low heat flux, and better matched with a heat flux of 85 mW/m^2 (consistent with what is reasonable for other parts of the Silent Canyon Caldera). A hydrologic explanation is that downward groundwater movement through the Halfbeak Fault or Split Ridge Fault and along the down-dipping Belted Range Aquifer (BRA) (see BN, 2002, cross-section C-C') significantly cools the rocks and reduces heat flux near borehole U-19e.

To test this hypothesis, a reverse-particle-tracking simulation was conducted for calibrated flow model BN-MME-LCCU1 with 1,000 particles originating in the BRA below ER-19e. Figure 8-2 shows the reverse-particle paths moving upgradient to the Split Ridge Fault, which defines the Silent Canyon Caldera Margin, and then vertically upward to the water table. This simulation confirms that cool shallow water from the northeast can flow vertically to deeper HSUs along the Silent Canyon Caldera margin. In this case, the primary elevation drop occurs at the Split Ridge Fault, with additional elevation drop along dip with the BRA. The elevation drop of cool shallow water to depth below Well U-19e would result in the observed cooler temperatures, which lead to lower-than-expected estimations of deep thermal flux in conduction-only models at this well.

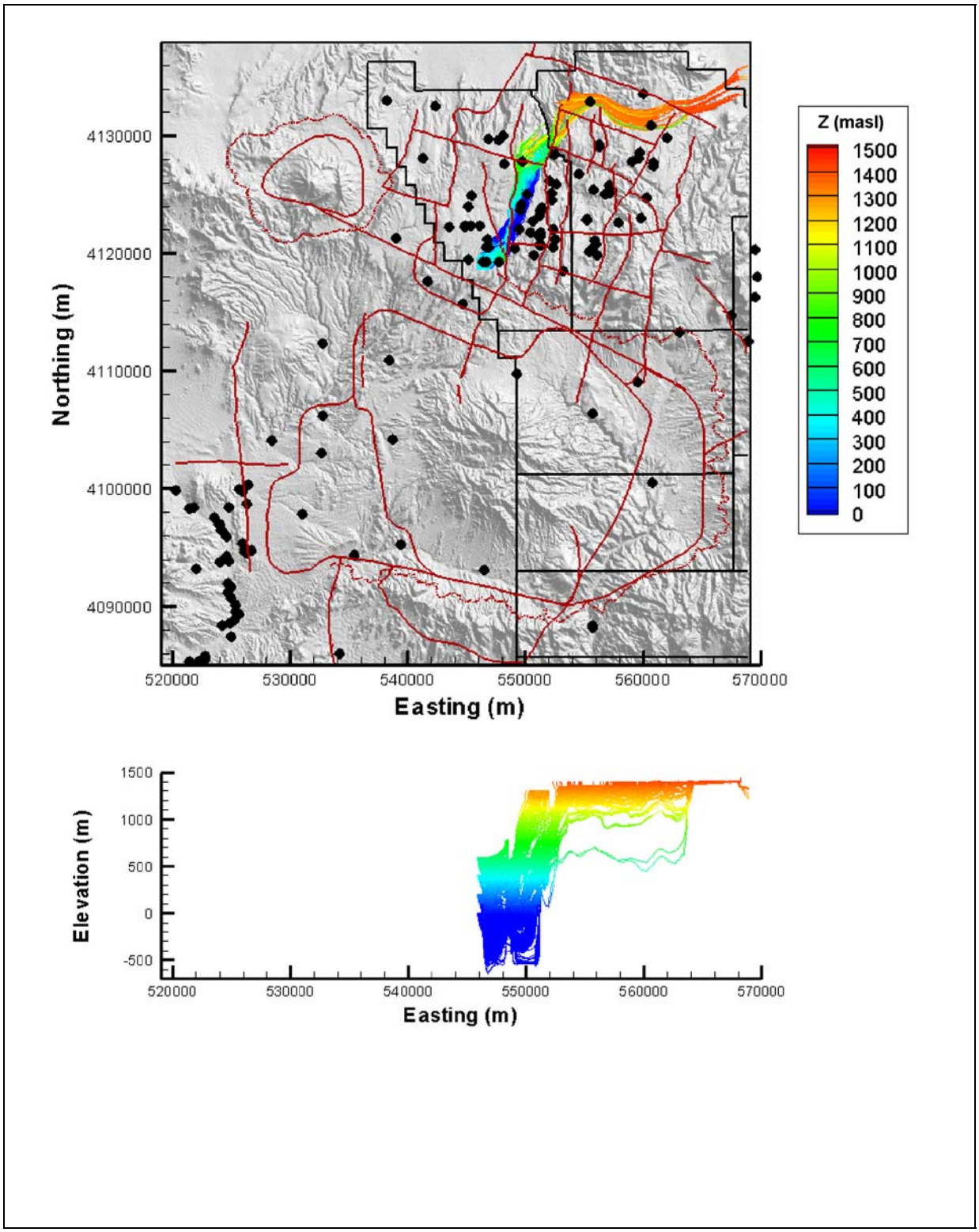

Figure 8-1
Reverse-Particle Paths Originating in Inlet Aquifer Below ER-20-5 #3
Simulated for the BN-MME-SDA Reduced LCCU1 Permeability Alternative Flow Model

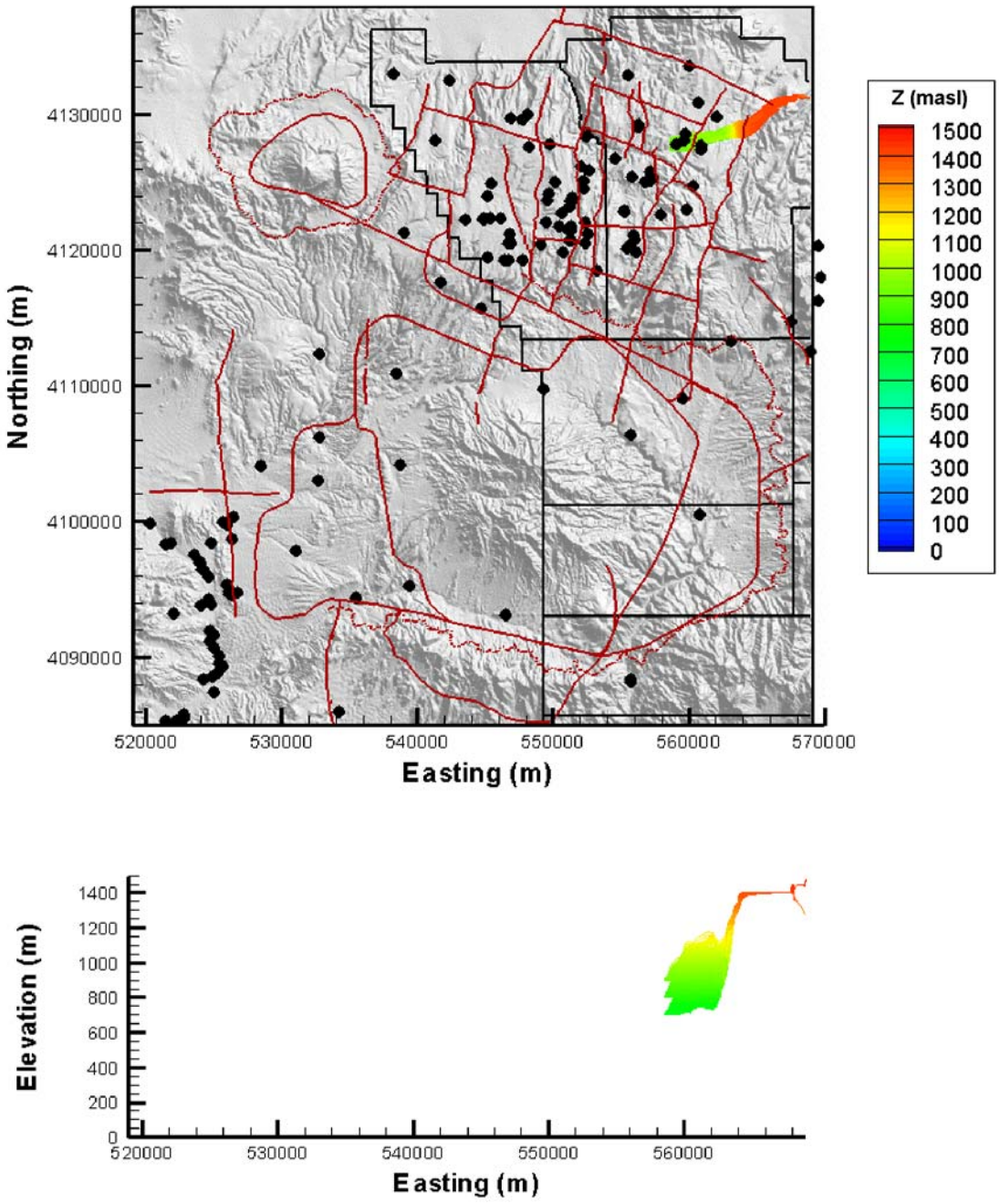

Figure 8-2
Reverse-Particle Paths Originating in UE-19e for BN-MME-SDA
Reduced LCCU1 Permeability Alternative Flow Model

8.2.3 Eastern Timber Mountain Caldera

Borehole UE-18r was characterized by Gillespie (2003) as having dominantly conductive heat flow (about 25 mW/m^2) and reliable temperature measurements above the bottom of the borehole casing at a depth of 496.5 m (elevation 1,192 m). Unfortunately, simulated temperatures at these elevations are dominated by the upper boundary conditions and are insensitive to the assumed thermal conductivity estimates and lower boundary conditions. Hence, it was necessary to use a deep temperature measurement from below the borehole casing as a calibration target in the inverse models. The simulated temperatures are significantly warmer than this deep measurement from borehole UE-18r for all lower boundary conditions considered in this report. The consistent overestimation of the measured temperature indicates that downward groundwater flow may have cooled the rocks near the bottom of the temperature profile. Borehole UE-18r penetrates a fault breccia at depth, which suggests that groundwater flow along the fault associated with this breccia or a nearby similar fault may have cooled nearby temperatures. This interpretation is also consistent with the relatively low heat flux of 25 mW/m^2 estimated by Gillespie (2003, Table 7) above elevations of 1,192 m and the much larger heat flux (greater than 75 mW/m^2) estimated below the elevation of 443 m. Based on one-dimensional scoping simulations (Appendix C), heat flux is expected to decrease with elevation in areas of downward groundwater flow. However, groundwater carbon-14 measured in the borehole is very low (Chapman et al., 1995), ruling out modern recharge as a likely influence on groundwater temperatures and suggesting that the downward movement of groundwater from laterally upgradient areas is a more likely explanation for the decrease in heat flux with elevation at borehole UE-18r.

Figure 8-3 shows the reverse-particle paths originating in the fault breccia zone of UE-18r for BN-MME-LCCU1 reduced permeability alternative. The paths show a major elevation change along the Timber Mountain Caldera structural margin fault (the fault intersected by UE-18r is not explicitly identified in the CAU flow model). As the reverse particles encounter the fault, they change elevation drastically. Also consistent with the age consideration mentioned above, the reverse particles do not leave the system immediately upon gaining shallow depths. Rather, they move laterally until finally leaving the flow model at higher elevations in Area 19. The combination of the distance between where the recharge occurs and UE-18r coupled with the permeability of the porous media may be sufficient to produce large residence times that would result in low carbon-14 signatures.

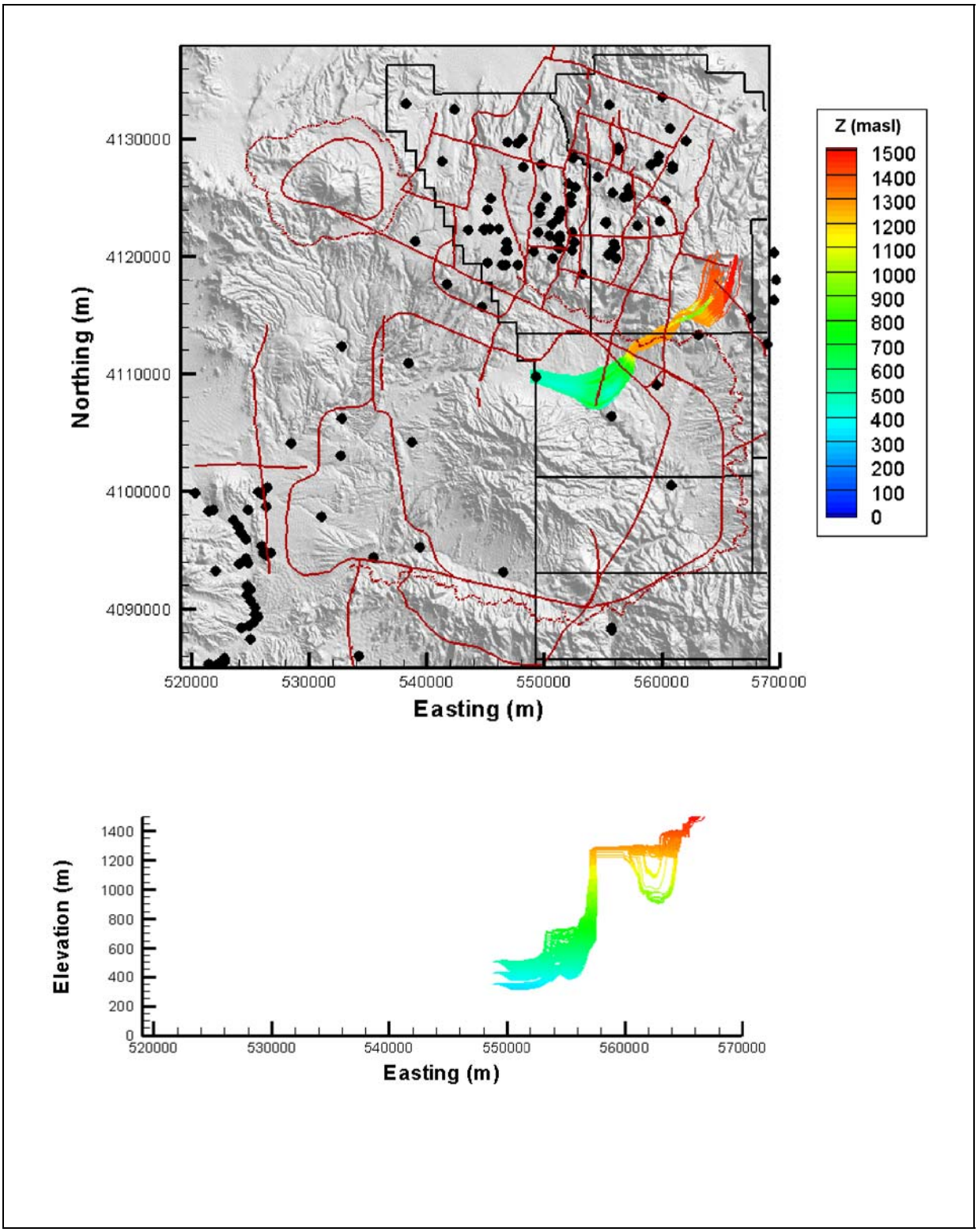

Figure 8-3
Reverse-Particle Paths Originating in the Fault Breccia Lithologic Subunit of the Timber Mountain Composite Unit at UE-18r for BN-MME-SDA Reduced LCCU1 Permeability Alternative Flow Model

8.2.4 Extra Caldera Zone Western Timber Mountain Caldera

Measured temperatures at borehole ER-EC-4 are consistently cooler than the temperatures calculated with the calibrated variable heat-flux model. These temperature differences, along with a decrease in the estimated heat flux from 54 to 28 mW/m^2 through the lower part of the borehole, indicate the presence of downward groundwater movement affecting temperatures below this borehole. One hypothesis that explains the low temperatures and heat flux at borehole ER-EC-4 is that cool shallow groundwater in the northwest flows to depth in this area within the southward dipping LCA (BN, 2002, cross-section G-G'). As groundwater moves southward through this area, the downward flow component induced by the dip of the beds causes the groundwater to become warmer, thereby consuming heat and decreasing the temperature and heat flux in the overlying rocks.

Figure 8-4 shows the complex origins of water in the LCA below ER-EC-4 as mapped with 1,000 reverse tracking particles in model BN-MME-LCCU1 reduced permeability alternative. The primary sources include: (a) a small component from the northeast, (b) inflow within the LCA along the northern boundary, and (c) shallow groundwater between the Black Mountain and Silent Canyon Calderas north of ER-EC-4. The latter source is consistent with the hypothesis that cool, shallow water flows to depth below ER-EC-4, reducing the temperature and giving and apparent lower heat flux for conduction-only models. Likewise, LCA water entering along the northern boundary has a shallower and, thus, cooler source to the north of the model domain.

8.2.5 Summary

Four different locations within the CAU model domain were identified as being affected by downward-groundwater flow. Identification was made for thermal profiles in wells that could not be explained with a heat conduction-only model. Following these identifications, reverse-particle-tracking simulations were conducted to investigate whether shallow groundwater sources were feasible at the depths indicated in the heat-conduction study. For two locations within the Silent Canyon Caldera, one within the Timber Mountain Caldera, and one to the west of the Timber Mountain Caldera, these simulations demonstrate that the flow model qualitatively captures the convective components identified, thus supporting the hypothesis that convective cooling explains the apparent low conductive fluxes.

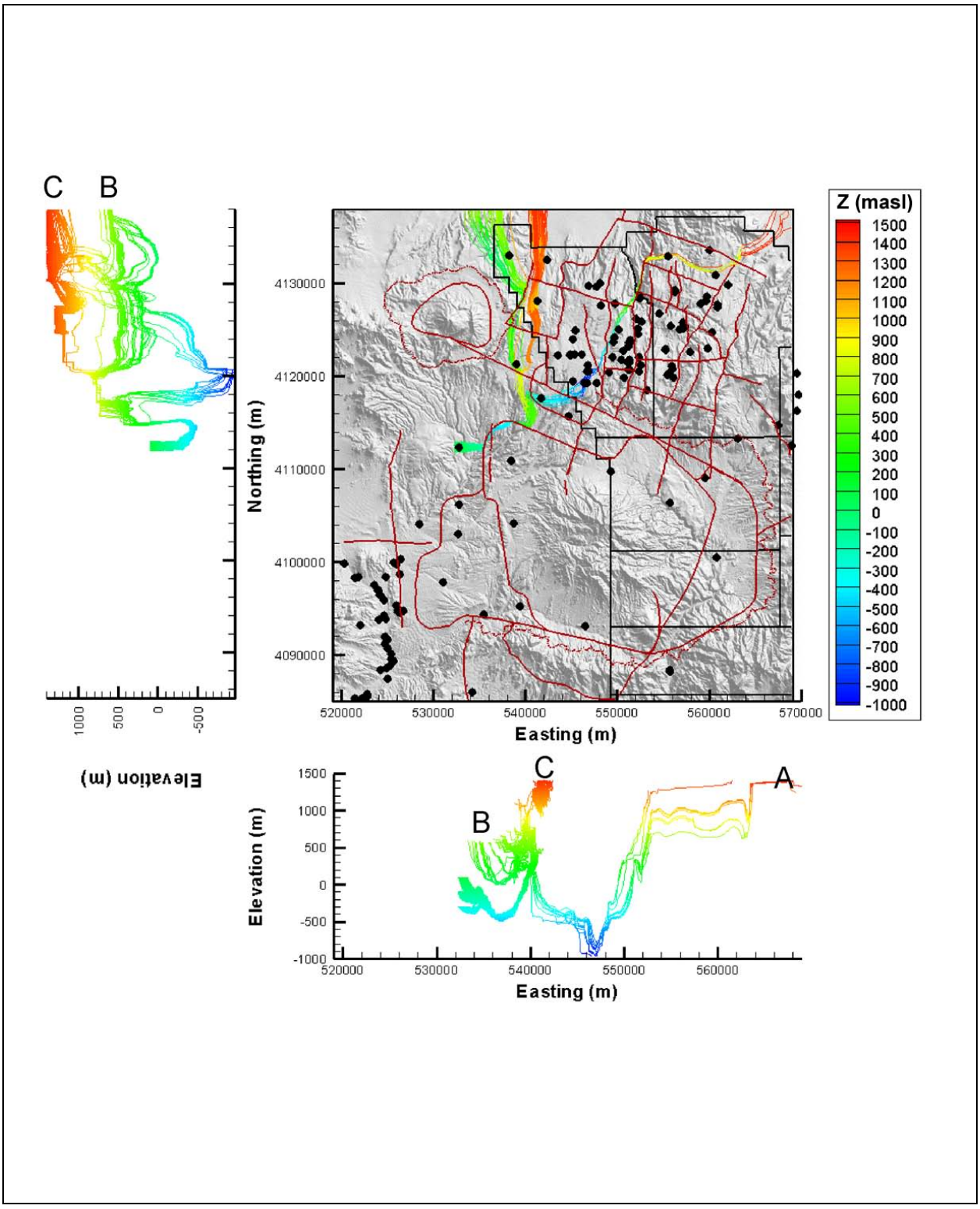

Figure 8-4
Reverse-Particle Paths Originating in the LCA Below ER-EC-4 for BN-MME-SDA Reduced LCCU1 Permeability Alternative Flow Model

8.3 Flow Model Sensitivity to Steady-State Temperature Distribution

8.3.1 Introduction

The Pahute Mesa CAU flow model spans an area 50 by 53 km with elevations between 3.5 km bmsl to 1.5 km amsl. Within the domain, there are three volcanic caldera complexes and extensive extra-caldera zones as well. Temperatures are not the same everywhere in this model domain.

In the flow model, spatial variations in temperature are set by specifying a steady-state, 3-D temperature distribution. The FEHM code accommodates changes in temperature through equations of state that relate viscosity and density to the specified temperature. Once set, however, the temperature distribution does not change over the course of a flow model or during flow model calibration.

The temperature field used in this study is derived from the calibrated, variable heat-flux model described in Appendix C. In that model, heat fluxes at -3,500 m elevation are calibrated to minimize the difference between simulated and observed temperatures in boreholes in the model domain. However, most of the temperature measurements are in the upper one-fifth of the model domain, leaving uncertainty in temperatures and, hence, water properties at depth in the model.

An alternative to simulating a temperature field, as described in Appendix C, is to simply specify a fixed geothermal gradient. Such an approach can match observed temperatures reasonably well if it is anchored to observations and extrapolates temperatures at depths below where the observations occur. Therefore, the thermal sensitivity here involves specifying temperatures at all depths in the model domain to correspond with thermal gradients of 10 degrees per kilometer (°/km) and 30°/km, representing low and high gradients for the system (Appendix C). The thermal fields for these sensitivity runs are anchored to the observed temperature of 47.7°C in Well ER-20-05 #3 at an elevation of 656.5 m amsl. Starting with the calibrated parameters for the BN-MME-SDA flow model, the temperature distribution is changed to reflect the low and high linear geothermal gradients. The flow model is not recalibrated and forward simulations are compared with the base-case model.

8.3.2 Sensitivity Results

For both the 10°/km and the 30°/km linear thermal gradient temperature fields, the model objective function increases from the calibrated model. Figure 8-5 shows the components of the objective function for each of the models considered. With the linear thermal gradients, temperatures at depth are greater than those computed with the heat conduction model. Thus, for the same permeability, hydraulic conductivity at depth increases. With increased hydraulic conductivity at depth, flow increases at greater depths, ET discharge in Oasis Valley decreases, and heads in shallow HSUs decrease.

It is interesting to note that although heads and fluxes in the sensitivity simulations change from those in the base model, simulated pathlines are about the same. Figure 8-6 shows forward paths originating at wells and reverse-particle exit locations for ER-OV-04a for the two thermal sensitivity runs. There is virtually no difference between the runs and they are nearly identical to the results shown in Figure 7-19 for the calibrated flow model with variable heat-flux-based temperatures. Quantitatively, the fractions of 10 million particle exits in the different source zones are nearly identical as well. This result holds for all eight of the geochemistry target wells considered.

8.3.3 Summary of Thermal Sensitivity Results

For all flow models used in this analysis, the temperature distribution resulting from the calibrated, variable base-flux conduction model is used. Here, as part of an assessment of model sensitivity to temperature, two different temperature distributions based on linear thermal gradients and extrapolation from a high-quality measurement are considered. It is not surprising that the model objective function increases with the two sensitivity runs because these fields are different than that used for calibration. The increased temperature at depth results in greater hydraulic conductivities for the same permeability developed in the calibrated base model. Thus, it is likely that the objective function could be reduced through calibration. It is possible that reasonable calibrated permeability fields could be achieved with linear thermal gradient. To offset the higher viscosities, lower rock permeabilities would be computed. However, it is unlikely that linear thermal gradients would lead to as good or better results than those achieved with the calibrated thermal field, which captures non-linear distributions of rock properties

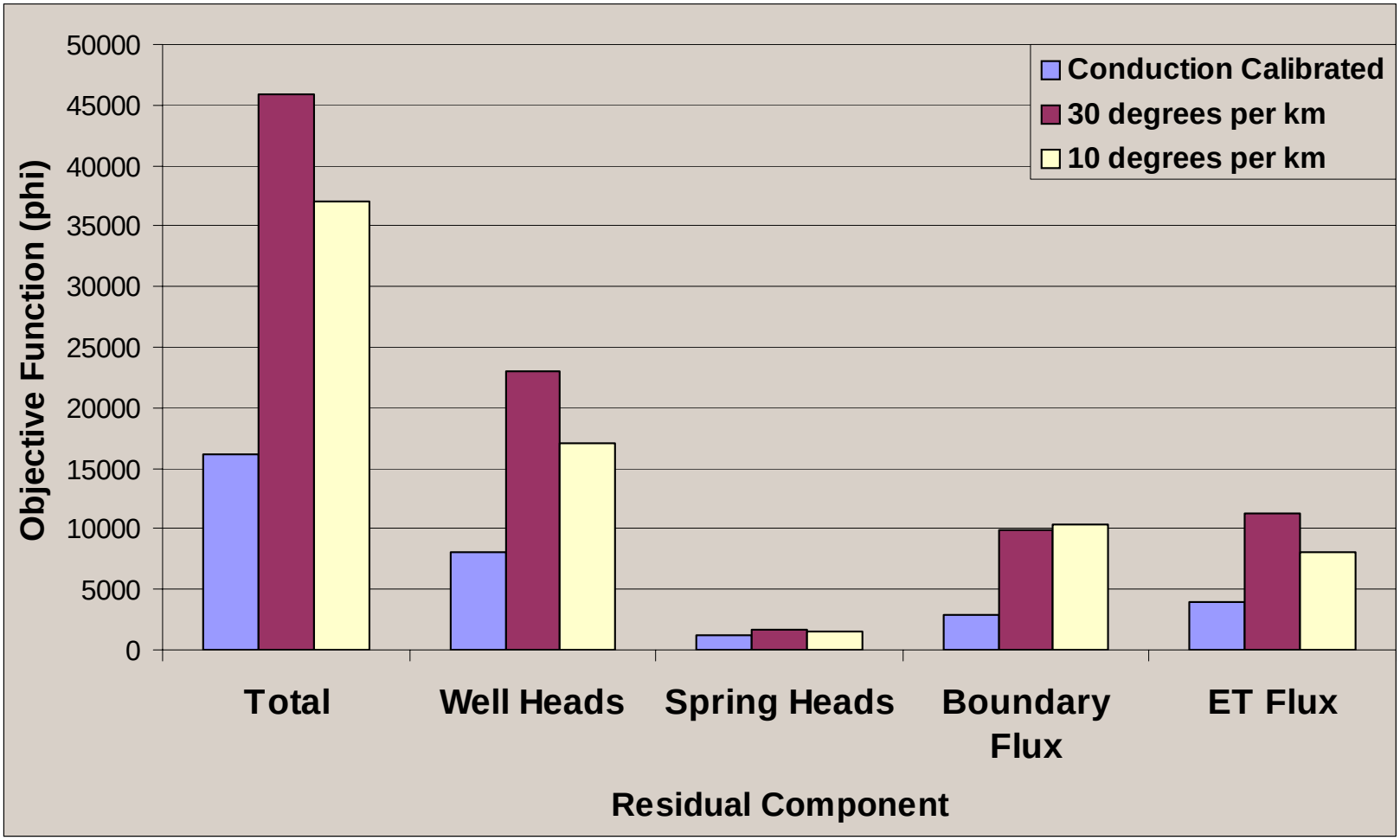

Figure 8-5
Comparison of Flow Model Objective Functions for Different Thermal Fields

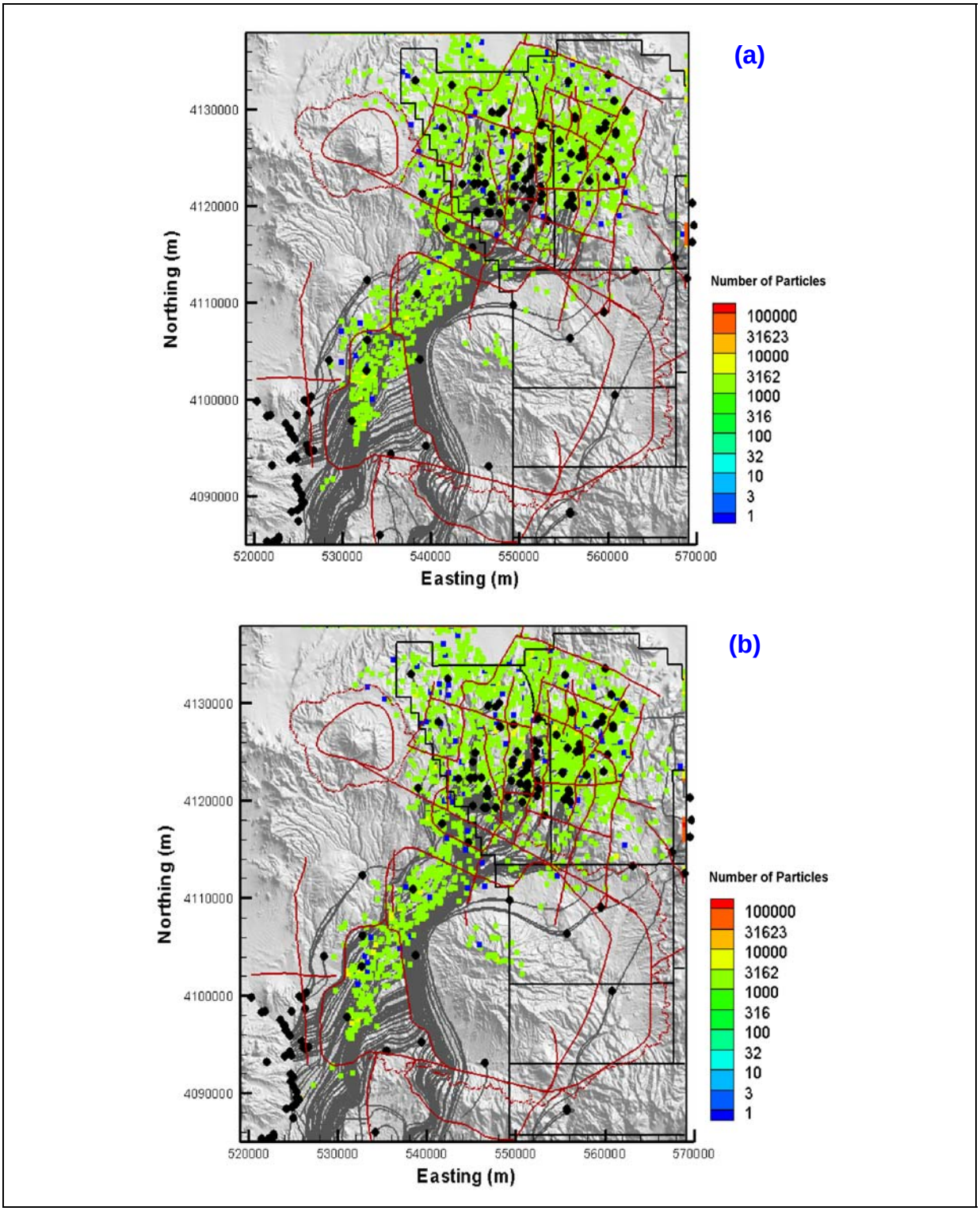

Figure 8-6
Comparison of Forward Flow Paths (Grey)
and Reverse-Particle Exits from ER-OV-04a
(a) the 10°/km Thermal Sensitivity Run (b) and the 30°/km Thermal Sensitivity Run

A curious result in this sensitivity analysis is that even with poorer matches to head and flux, the pathlines and reverse-particle-tracking simulations are nearly identical for the base model and the two thermal sensitivity runs. This is likely due to the fact that the models are most similar at the shallower depths where the forward particles are introduced. Recharge also enters the model at the shallower depths and is the same for each of the models. Thus, the reverse particles are likely to exit at the locations where recharge occurs.

9.0 SUMMARY AND CONCLUSIONS

To understand the potential for lateral and vertical radionuclide migration, a 3-D, finite element, steady-state groundwater flow model of the Central and Western Pahute CAUs was constructed. The model was created to allow for evaluation of conceptual model uncertainty. Different combinations of HFMs, recharge models, hydrologic boundary conditions, and application of permeability depth decay were considered in order to propagate the uncertainty associated with each of these elements of the model into the resulting flow fields. The approach resulted in several flow fields that were consistent with site-specific data and the conceptual understanding of the Pahute Mesa groundwater flow system. The modeling effort was able to synthesize an understanding of the regional hydrogeologic system and local data and observations while bounding flow-field uncertainty resulting from geologic and hydrologic uncertainty. This analysis was undertaken to satisfy the groundwater flow model required by the *Corrective Action Investigation Plan for Corrective Action Units 101 and 102, Central and Western Pahute Mesa, Nevada Test Site, Nevada* (DOE/NV, 1999).

Pahute Mesa is located in the northwestern part of the NTS; it includes NTS Areas 19 and 20. Pahute Mesa is an elevated plateau of about 500 km^2 (200 mi^2) at an altitude that ranges from 1,676 m (5,500 ft) on the western edge to over 2,134 m (7,000 ft) amsl throughout the eastern range (Blankennagel and Weir, 1973). The area of interest for the Pahute Mesa CAU is defined by the potentially affected portion of the regional groundwater flow system from the 82 underground nuclear tests conducted on Pahute Mesa, which includes a region stretching from the northern side of Pahute Mesa south and southwestward towards Oasis Valley.

Pahute Mesa geology is dominated by deposition of rock units from volcanic eruptions from nested calderas of the SWNVF. All rocks known to underlie Pahute Mesa are volcanic. The youngest caldera complex of hydrologic significance is the Timber Mountain Caldera. This caldera collapse and its filling with volcanic materials resulted in volcanic ash flows covering much of Pahute Mesa to the north. On Pahute Mesa, the rocks from Timber Mountain Caldera cover an older series of calderas that make up the SCCC. This caldera complex consists of at least two nested calderas, the

Area 20 Caldera and the older Grouse Canyon Caldera. Both calderas were formed and subsequently filled by voluminous eruptions of tuff and lava of generally rhyolitic composition. Total thickness of volcanic rocks beneath Pahute Mesa is on the order of 5 km (16,000 ft).

Groundwater beneath Pahute Mesa generally flows in a southwest direction, primarily through fractures in the lava-flow and tuff aquifers. Zeolitized bedded and nonwelded tuffs act as confining units that inhibit the flow of groundwater. The spatial distribution of permeable aquifers relative to the confining units is not well understood. Thickness variations of aquifers and confining units and their connectivity across faults or caldera boundaries are important hydrostratigraphic relationships that are also not well understood. A number of wells provide water-level information in the Pahute Mesa and Oasis Valley areas, but water levels in the area between Pahute Mesa and Oasis Valley are less well defined. However, what data are available suggest that groundwater elevations gently mimic the topography. Groundwater elevations are highest beneath northern Pahute Mesa, ranging in elevation from approximately 1,280 to nearly 1,500 m (~4,200 to 4,900 ft), with the depth to water on average of about 600 m (~2,000 ft). Groundwater elevations drop off gradually to the south and west, ranging from 1,100 to 1,250 m (~3,600 to 4,100 ft) in Oasis Valley. Some groundwater discharges to the surface within the Oasis Valley discharge area in the form of springs.

Groundwater recharge occurs locally from precipitation from areas located to the north of Pahute Mesa. Groundwater then flows south-southwestward to the Oasis Valley and Death Valley to the southwest. Several factors are believed to account for the flow around Timber Mountain. Due to its elevation, Timber Mountain receives more precipitation compared to surrounding areas of lower elevation, which leads to additional groundwater recharge at Timber Mountain. In addition, extensive zeolitization and clay alteration of the tuffs within the Timber Mountain Caldera causes these volcanic units to behave more like confining units than aquifers. Both of these factors are expected to lead to a mounding of the groundwater levels beneath the mountain, which affects groundwater flow paths from Pahute Mesa such that they would go around both sides of Timber Mountain rather than directly through the caldera.

The foundation of the flow model analysis is the Phase I HFM prepared and documented by BN (2002). The base (or BN) HFM incorporates all of the geologic data and evaluations deemed to provide the most viable interpretation of the hydrogeologic system. An additional major alternative

interpretation is the structurally uncoupled variant termed the SCCC. Major structural differences with the BN HFM include the margins of the caldera complex (single caldera ring-fracture system), locations of caldera-forming faults, and the number and depth of faults. To investigate the uncertainty in the BN HFM, five alternative geologic models were developed to assess the potential impact of alternative geologic interpretations on groundwater flow and the transport of contaminants in groundwater. The DRT alternative projects the Belted Range thrust LCCU1 through the model to the west. Effects of the TCL were developed by substituting more fractured rock HSUs. The depth of the basement rocks has an uncertainty of 2,000 m; the raised PZUP alternative brought the Paleozoic rocks to as high an elevation in the HFM as permitted by the drill-hole and geophysical data under the entire flow model area. An alternative geologic interpretation that attempts to account for the geophysical gravity anomaly between the Timber Mountain and Silent Canyon Calderas southwest of Area 20 was developed in the RIDGE alternative. Representation of the Paleozoic rocks as a continuous sheet in the southeast model domain was incorporated in the SEPZ alternative. Each of these HFMs was evaluated to determine uncertainty in the calibrated flow field of the BN HFM.

The hydrostratigraphy was translated into a computation model via finite-element meshes for use with the FEHM code to capture the complex HSU geometries and faults, and test chimneys for the two major HFMs: the BN base and SCCC. The mesh node spacing ranged from 67.5 m to 1 km, with refinement in thinner HSUs, around tests, and estimated flow paths from Areas 19 and 20 to Oasis Valley. About (depending on HFM) 46 HSUs and 37 faults are represented in the models. This resulted in two meshes with approximately 1.4 million and 1.3 million nodes for the BN and SCCC HFMs, respectively. The model area is 53.4 km (33.2 mi) north to south and 50.8 km (31.6 mi) west to east.

Once the meshes were constructed, heads interpolated from the UGTA regional model were assigned to the edges of the CAU as boundary conditions, and inside the CAU model as initial conditions. The calibrated thermal fields (see Appendix C) were specified as a fixed condition; that is, thermal transport was not simulated but the variable temperature field was specified. Five recharge models were prepared as input to investigate water-balance uncertainty: two based on the chloride mass-balance (called the DRI models) analysis of Russell and Minor (2002), one based on the modified Maxey-Eakin (MME) empirical approach developed for the UGTA regional model (DOE/NV, 1997), and two based on the distributed parameter model (called the USGS models) of

Hevesi et al. (2003). The USGS models had the lowest recharge flow, the DRI models the highest, and the MME model was intermediate between the USGS and DRI models.

Calibration data for well and spring head as published by SNJV (2004a) were assigned to the appropriate model nodes. In addition, Oasis Valley discharge as estimated by Laczniak et al. (2001) was represented by third-type boundary conditions in order to provide a flow constraint internal to the model. Flow on the CAU model edges was also output by FEHM and compared to the UGTA regional model. Thus, four datasets were used to calibrate the model: well head, spring head, Oasis Valley discharge, and UGTA regional model boundary flow. The goodness of the flow model is enhanced by considering these different types of data, especially flows (Hill, 1998). In particular, matching both head and flow in Oasis Valley increases confidence that the model behavior is correct in this area. A total of 191 calibration targets of head and flow were used in the model calibration. Once the necessary input and calibration data were mapped onto the model meshes, the files for the parameter estimation program PEST were created, and flow model calibration began.

Flow model calibration followed a generally accepted protocol in which model parameter sensitivities to calibration were evaluated and interpreted in light of the conceptual model of the system. The parameter estimation program PEST was used to streamline this process, providing sensitivity coefficients, model parameter correlation coefficients, and eigenvalue and eigenvectors. Discrete parameter changes were also investigated during the calibration process. In general, not all parameters that were sensitive were adjusted during calibration based upon their uncertainty. Parameters that were highly correlated were removed from the calibration process. A further constraint was the desire to honor, within the range of uncertainty, the estimated hydraulic properties for HSUs. Weights reflecting the uncertainty in the calibration target data were initially developed and then re-evaluated based on judgment about the importance of matching the type of data. Thus, the Oasis Valley discharge and UGTA regional model boundary flow weights were increased because it was judged important to match discharge to Oasis Valley (the closest biosphere access to source locations) and to honor the estimated regional water balance on the model domain (a particularly important constraint considering the model is mostly surrounded laterally with constant heads).

The starting point for the CAU model specified-head boundary conditions was the UGTA regional model results interpolated onto the mesh edges. Changes were made during calibration to address

inconsistencies to measured heads in the following areas: western part of the northern boundary, the north-central model edge near UE-20p and PM-2, southern edge of the model east of Oasis Valley, and eastern boundary near TW-1. Also, the northwest corner of the model (both north and west faces) was converted to a no-flow in conjunction with correction of heads in the vicinity of PM-2 and UE-20p.

A variety of parameterization approaches have been used to simulate groundwater flow in the NTS area (e.g., the UGTA regional model [DOE/NV, 1997], the USGS flow model of D'Agnese et al. [1997], and the YMP saturated-zone model [DOE/ORD, 2004]). The viability of four different parameterization approaches was tested: (1) no anisotropy and no depth decay of HSU permeability, (2) depth decay applied to selected HSUs, (3) anisotropy and depth decay applied to selected HSUs, and (4) anisotropy and depth decay applied to all HSUs. Approach (1) is a limiting case of simplicity; approaches (2) and (3) reflect parts of the USGS regional model (D'Agnese et al., 1997), the DVRFS model (Belcher et al., 2004), and the YMP saturated zone models (DOE/ORD, 2004); and approach (4) reflects the same approach used in the UGTA regional model. The BN HFM with MME recharge was calibrated with the four parameterization approaches above. The MME recharge model was selected because its value was in between the USGS and DRI models, and thus was approximately the central tendency of the recharge models. The no-anisotropy and no-depth-decay case was rejected as a reasonable approach because flow paths from Pahute Mesa tended to dive deep below Oasis Valley, reflecting the poor match of Oasis Valley discharge data. The selected HSU depth decay with no anisotropy was investigated briefly, but completely neglecting anisotropy was deemed unreasonable, and it was discarded. The application of anisotropy and depth decay to selected HSUs and to all HSUs approaches were carried to a final calibration. Both calibrated models could represent the flow system reasonably well, as defined by matching calibration targets. In addition, the SCCC HFM with MME recharge with the selected HSU anisotropy and depth-decay approach was also calibrated. This HFM did not calibrate as well as the two models calibrated using the BN HFM.

The change in observed hydraulic head over the Pahute Mesa CAU flow model is nearly 600 m. In general, the trend of model simulated and observed head is reasonable, however, there are a few areas of increased local error in all models. The SCCC HFM showed larger errors than the BN HFM.

The discharge in Oasis Valley was matched within one standard deviation of the estimated value by the BN-MME-SDA and BN-MME-ADA models, and not quite within one standard deviation by the SCCC-MME-SDA model. However, all models showed a mild spatial bias in discharge error with the highest flow at the northern end of Oasis Valley being reasonably matched with significant under simulation of flow for ET Zones 3 (located in the northwest part of Oasis Valley, see Figure 4-17) and 5 (in the central part of Oasis Valley, see Figure 4-17) in all cases. Thus, while the total Oasis Valley discharge is reasonably matched, it appears that some feature in either the HFM or the boundary condition itself needs refinement to better capture the spatial distribution of Oasis Valley discharge.

The UGTA regional model estimated boundary flows were also reasonably matched; the sense of the flow (e.g., in or out) was usually correct, and the error was typically within 20 percent. Thus, the general flow of water is in broad agreement with the regional understanding of the flow system. As an additional check on the CAU water balance the flow along the northern edge of the Yucca Mountain saturated zone model, which lies entirely within the Pahute Mesa CAU flow model, was compared to the CAU model results. The YMP saturated zone model (DOE/ORD, 2004) gives a value of 196 kg/s inflow. The calibrated models give values of 250, 300, and 218 kg/s for the BN-MME-SDA, BN-MME-ADA, and SCCC-MME-SDA cases, respectively. The DVRFM (Belcher et al., 2004) boundary flows were also estimated (see Table 5-5) for the Pahute Mesa CAU flow model, and were within the ranges developed from the UGTA regional model.

The BN and SCCC HFMs showed markedly different behavior along the Purse Fault, where a 100-m head discontinuity has been observed. The BN model has a long and deep representation of the Purse Fault, whereas the SCCC has a short and shallow Purse Fault representation. Thus, it is incapable of serving as a nearly impermeable barrier in the SCCC HFM between the northwest quadrant and the north-central portion of the model. This difference allowed the BN HFM to better represent the change in water levels across the fault. Juxtaposition of HSUs across the fault is incorporated in both HFMs; thus, the arrangement of HSUs alone is insufficient to capture the fault behavior.

At the Boxcar Faults, the BN and SCCC HFMs performed similarly. With a higher head to the east of the fault, a lower permeability is required along the fault itself to replicate the observed head drop, and both models improved as the fault permeability decreased. Wolfsberg et al. (2002) also noted

similar model behavior for the Boxcar Faults in their groundwater flow model of the area surrounding the TYBO and BENHAM underground nuclear tests.

Comparison of the calibrated permeabilities to those from single-well constant-rate tests showed a bias toward lower calibrated permeabilities. This is not unreasonable, because tested zones in fractured rock are those that typically have higher permeabilities while the model incorporates the entire thickness of rock. In addition, it has been shown that effective properties of a porous medium, especially permeability, decrease with the scale of analysis (Neuman, 1990); the so-called "scale effect." With the exception of ER-20-6 #1 and ER-20-6 #2, all the tests were single well, which would tend to have a relatively small sampling radius. Slug tests were not considered in this comparison because they are strongly affected by near-well mechanical disturbance (e.g., drilling) (Butler, 1997) and have an even smaller sample volume than single-well tests. Finally, the approach taken (and described in the Pahute Mesa CAIP [DOE/NV, 1999]) in parameterizing HSUs for the HFMs was to avoid specifying many small patches of different properties, but rather to use broad zones of constant properties that were developed from characterization data. Any individual test describes only a small volume of the zone in which it lies; thus, some misfit must be tolerated because the data density does not allow anything but a broad description of HSU properties.

The range of permeabilities estimated in the Pahute Mesa hydrologic data document (SNJV, 2004a) for the TMA, TMCM, PCM, YMCFCM, PBRCM, and LCA are compared to the ranges in the model, and are generally in reasonable agreement. The range of PCM permeabilities used in the models matches the estimated range well; the LCA less so, being biased low. For HSUs on Pahute Mesa, the KA, CHVTA, CHVCM, CFCU, and BFCU model-calibrated values are very similar to the estimated mean. The IA is about an order of magnitude lower than expected. The calibrated permeabilities for CHZCM, CFCM, and CHCU are toward the lower end of uncertainty (close to two orders of magnitude lower than the mean). Composite units are a mixture of HGUs, and because homogeneous parameters were used for these HSUs, it may be the heterogeneity of the HSU causing this variance. The THLFA, THCM, LPCU, TCA, PLFA, and FCCU all are close (less than half an order of magnitude variation) to the expected mean. The BA is close to the mean for BN-MME-SDA but an order of magnitude lower for SCCC-MME-SDA because it also includes the UPCU. The TSA has the greatest fluctuation among HFMs. The UPCU for BN-MME-SDA is about two orders of magnitude lower than the mean. The FCA, YVCM, DVCM, LCCU1, and PVTA are close (within a

half an order of magnitude), while FCCM and DVA are about an order of magnitude lower than expected. The AA and UCCU are lower than even the lower limit by 2 and 1.5 orders of magnitude, respectively. The estimated mean permeability for the UCCU of 3.7×10^{-13} m^2 seems somewhat high, and is based on two data points (see Figure 5-22 in SNJV, 2004a).

After calibration a formal sensitivity analysis was conducted. The sensitivity analysis used local techniques (all parameters are perturbed slightly or one at a time over their range of uncertainty) and global techniques (considered effects of joint parameter uncertainty over full range of uncertainty). The local approach used PEST to identify sensitive model parameters, sensitive observations, and parameter correlations. The perturbation analysis varied properties of HSUs and faults over their range of uncertainty, providing a comprehensive picture of model behavior (although without considering compensating effects). Major faults often showed a one-sided sensitivity behavior, where fault permeability multiplier ceased to have a noticeable effect below a certain value. The Purse Fault permeability multiplier, for instance, could be as high as 0.001 (that is, the fault permeability is 1,000 times less than the surrounding rock) before much model misfit was noticed – behavior that was similar in the BN HFM with depth decay applied to all HSUs (ADA) and only to selected HSUs (SDA). This behavior was not noticed in the SCCC HFM because the Purse Fault is not as long or as deep.

Global sensitivity analysis was conducted by generating 1,000 uncorrelated flow model parameter samples using Latin Hypercube sampling, computing flow model results for these samples, and recording the model results for the two calibrated versions of the base HFM (all and selected HSU depth decay and anisotropy) and SCCC HFM. This approach was taken to attempt to identify whether there were parameter combinations that were as good or better in calibrating the model than the chosen sets over the range of parameter uncertainty, and whether there were systematic effects of some model parameters. The results were analyzed using Spearman rank correlations, classification and regression trees, and entropy statistics. Similar sets of sensitive variables were identified in the local and perturbation analyses, notably the control of the PCM on model head and the DVCM on Oasis Valley discharge.

These sensitivity analyses led to the following findings:

- The PCM, YMCFCM, CHCU, and DVCM HSUs; and the Claim Canyon Caldera Structural Margin fault (fault 06 in the BN and fault 03 in the SCCC) were sensitive in controlling heads in the BN and SCCC HFMs. For the PCM and YMCFCM, this is because they are astride the southern boundary and control the influence of the strong head drop (observed regionally and incorporated in the CAU model) at the southern edge of the CAU model. Similarly, the Claim Canyon Caldera Structural Margin fault is convex open to the north with its apex at the southern boundary, which controls flow to the south. Finally, the DVCM is located in the southwest corner of the domain along the southern part of the western edge and western part of the southern edge, and controls both in and outflow to Oasis Valley. The CHCU controlled heads in the BN-MME-ADA case because of its location in an arc around the Silent Canyon Caldera structural margin causes it to act as a dam controlling head propagation west of the Greeley faults. In the SCCC, all the Calico Hills units were lumped into the CHCU (a model naming convention only; the unit was not parameterized as a confining unit), the properties of which are the effective properties of the combined BN Calico Hills units. In the SCCC HFM CHCU is several hundred meters thick and has many head observations, hence the model sensitivity.

- The thrusted LCCU, the LCCU1, controlled heads in the HFMs at higher permeabilities due to its connection to high heads along the northern part of the eastern edge (e.g., west of Rainier Mesa). The properties of this unit are not well known, the single test value is relatively high and may be biased (only permeable intervals are readily tested). The conceptual model of this unit is that its permeability is ubiquitously increased due to deformation from thrusting stresses.

- Reference permeability and depth decay have a nearly perfect correlation, which is expected considering the formulation of depth decay.

- Over their range of uncertainty, the reference permeability of HSUs with depth decay was more sensitive than the depth-decay parameter itself. It is important to note that this was recognized during calibration, and depth-decay coefficients as estimated for each type of HSU (e.g., volcanics and carbonates) were fixed and reference permeability calibrated; it is poor practice to attempt to adjust strongly correlated parameters simultaneously.

Perturbation analysis on HSUs localized on Pahute Mesa for the BN-MME-SDA case showed that the BFCU, IA, CHZCM, and TCA had noticeable control on model results over their estimated range of permeability uncertainty. The IA has no wells with calibration data in it, but the model is sensitive to its permeability probably because of its larger extent (relative to most other HSUs on Pahute Mesa) extent and complex connection to the CHZCM, which has head data for calibration. Several HSUs had practically no effect on model results because of the lack of calibration data, geometric isolation

or discontinuity, or small saturated extent including: KA, CFCM, CFCU, TSA, LPCU, PLFA, UPCU, BA, and PVTA.

Model calibration and sensitivity analysis revealed that at higher permeabilities the LCCU1 (thrusted LCCU relatively high in the geologic section on the northeastern edge of the HFM) routes pressure and flow into the domain exerting noticeable control on model results. The conceptual model of the LCCU1 is that thrusting stresses have ubiquitously enhanced its properties (SNJV, 2004a), which may be overly simplistic. Caine et al. (1996) studied a slip fault exposure in Paleozoic clastic rocks and found that where the rock was predominantly shale, the fault core lithology was dominated by clay-rich gouge with a localized damage zone that acted both as barrier and conduit features, respectively. The total fault zone width was only a few meters. Seaton and Burbey (2005) investigated a thrust fault and found that the fault plane itself had low permeability, and that the highly fractured zone (up to 10 m thick) was localized above the fault plane. Seaton and Burbey (2005) studied crystalline rocks in the Blue Ridge province of Virginia, and this observation may not be directly extensible to the sedimentary rocks of the NTS. However, a plausible conceptual model of the LCCU1 may be generally low permeability along the plane of the thrust fault and in undisturbed low-permeability rocks with thin zones of enhanced permeability from fracturing adjacent to the thrust plane, which would reconcile both the single hydraulic test result and model behavior.

Only three HSUs under Pahute Mesa were identified by the local and global sensitivity analyses as having ubiquitous influence on model calibration statistics: the PBRCM, BRA, and CHCU. These HSUs are extensive in area relative to most of the HSUs on Pahute Mesa proper, and to some degree, the sensitivity of model results to their permeability is probably related to their continuity and their updip extension to the water table. For instance, the CHCU has a relatively large areal extent and separates shallower volcanic HSUs (where much of the calibration data exist) from the deeper PBRCM and BRA. The DVCM also had ubiquitous influence on model results because of its control on flow into Oasis Valley from Sarcobatus Flat.

A set of discrete sensitivity analyses was also considered including the following: testing the effects of permeability enhancement of test chimneys; evaluating the effects of two additional plant rooting depths, or depth from which water can be transpired from the water table, on Oasis Valley discharge;

considering the effect of a reduced LCCU1 permeability alternative (suggested by the sensitivity analysis); and testing the consequences of trying to enhance flow down Fortymile Canyon. The effects of test chimneys were found to be negligible; the simulated Oasis Valley flows were mildly sensitive to the rooting depth, the model could still be calibrated well with lower LCCU1 permeability alternative, and enhancing flow down Fortymile Canyon does not look feasible.

The complexity of the geology in the area, and the resulting uncertainty in geologic interpretation, was addressed by the development of alternative framework models based on the BN HFM, and by quantitatively evaluating these alternative HFMs with FEHM. The flow models were calibrated for each of these alternative HFMs and the MME recharge model. Thus, the high-level uncertainty in geologic structure is addressed. Of the five alternatives, three (TCL, RIDGE, and SEPZ) required no additional effort over the base BN HFM to recalibrate, although the calibrations and simulated flow paths did show some differences. Two alternatives (DRT and PZUP), both involving raising or otherwise increasing the amount of low-permeability rocks in the domain, required extensive effort to recalibrate. The calibration process resulted in metrics similar to the base BN HFM calibration, with some modest changes in simulated flow paths.

Another component of model uncertainty is that associated with the water balance, which directly controls the flow rate (and hence velocity) of water through the domain. Having held the recharge model constant (MME) and changed HFMs, the opposite approach of using the BN and SCCC HFMs with alternative recharge models and associated boundary flows was also used. The base HFM (with anisotropy and depth decay applied to selected HSUs) was recalibrated using the two USGS and two DRI recharge models. The results were very similar between pairs of models (e.g., USGS with and without runoff). The USGS recharge model with run-on and runoff (USGSD) is conceptually more reasonable, so it was retained for further analysis. Likewise, the DRI recharge model with alluvial screen (DRIA) was retained because it has the highest flow rates and should bound the upper end of flow through the system. Thus, the SCCC HFM was tested with the DRIA and USGSD recharge models only. The USGSD recharge model provided some of the best calibrations, with the DRIA recharge giving results similar to or worse than the MME recharge models. The most noticeable effect was that flow paths in the SCCC HFM changed with different recharge models such that more paths were directed down Fortymile Canyon.

The final phase of uncertainty analysis was to combine HFM and recharge model uncertainty. This was accomplished by taking the alternative HFMs most different than the base (the DRT and PZUP HFMs) and analyzing them with the USGSD and DRIA recharge models. The PZUP HFM calibrated poorly with the USGSD recharge map because the increased volume of low-permeability rock and low recharge made it difficult to get enough water in the domain resulting in systematic under simulation of water levels. However, because the error was systematic, the flow directions remained very similar to other recharge models. The DRT HFM could be calibrated to similar degrees as other models, although superior to the PZUP under the USGSD and DRIA recharge models. The DRT HFM, under all recharge conditions, simulates a focused flow path around the northern edge of Timber Mountain at the highest consistent elevations (~1,100 m [~3,600 ft]) in the flow system. All the HFMs show such a path, but the DRT HFM shows the greatest concentration of flow lines in this area.

The Pahute Mesa CAIP states that flow model verification will be conducted (DOE/NV, 1999). Because of head data sparseness, no head or flux information was held out of the calibration for later use in verification (as described in the Pahute Mesa CAIP [DOE/NV, 1999]). However, Kwicklis et al. (2005) analyzed geochemical signatures of various waters in the area and generated mixing targets at key points in the model domain that were used for model verification. A reverse-particle-tracking methodology was developed that allowed identification of the sources of water at eight target wells for comparison to geochemical estimates. These estimates were used for geochemical flow model verification. Nineteen alternative models were tested with the geochemical mixing targets. The target wells at the higher parts of the flow system were more difficult to match because there is less distance for mixing to occur, and very complex flow paths (at ER-EC-6, for instance) produce poor comparisons because of narrow flow path deviations. In general, the geochemical trends are captured.

Cluster (K-means) analysis of the geochemical verification results was used to further group the combinations of calibrated HFM and recharge models. Four clusters resulted with four, four, five, and six flow models in the ranking of worst to best clusters. The best cluster of calibrated models with respect to the geochemical verification included the DRT HFM with MME and DRIA recharge models, the reduced LCCU1 alternative with the MME and USGSD recharge models, the PZUP HFM with the MME recharge model, and the SCCC HFM with the MME recharge model. The eight

models in the two worst clusters are judged to be in direct conflict with the interpreted geochemistry, and are to be eliminated from further consideration in future transport analyses. The remaining cluster of five calibrated models has less severe problems than the worst two clusters, and for some metrics even performs better than the best cluster. These models will be considered in less detail during transport calculations, perhaps in sensitivity analysis.

Thermal analysis was also used as a qualitative test of model consistency. Thermal analysis suggested areas where flow of cooler water downward could explain temperature anomalies. Reverse-particle tracking was conducted at the four locations of cooler thermal anomalies to test whether simulated flow paths were such that cooler water from upgradient could be seen to flow to the well. The results used the BN-MME-SDA reduced LCCU1 permeability alternative were positive with the model simulating such flow paths.

Bredehoeft (2005) suggests that selecting the proper conceptual model (that is, addressing conceptual model uncertainty) is a major problem in groundwater modeling analysis. He suggests that this can be overcome by collecting as much data as feasible using all applicable methods, and by leaving the conceptual model open to change. Recently, Nishikawa (1997) and Harrar et al. (2003) present analyses where alternative geologic conceptual models are tested in simulating groundwater flow and transport results. Nishikawa (1997) found that some conceptual alternatives better explained reality, while Harrar et al. (2003) found that while all the alternative models could replicate the calibration data, their performance in predicting capture zones and breakthrough were quite different, and inverse modeling coupled with alternative geologic models (such as that described in this report) could be used to assess predictive uncertainty. A total of 26 individual flow model calibrations for the Pahute Mesa CAU, and geochemical verification of most of them, were conducted and are presented in this report. These calibrations reflect a variety of combinations of alternative HFMs, recharge models, and water-balance conditions. Thus, the approach taken for the Pahute Mesa flow model attempts to bound the proper conceptualization of HFM and water balance, and at least addresses the high-level uncertainty associated with the conceptual model.

The Pahute Mesa CAU flow model is calibrated to hydraulic head and estimates of boundary flow and Oasis Valley discharge. This information is utilized to give the direction and velocity of groundwater flow, which will be used to compute contaminant transport in conjunction with the

appropriate processes (e.g., advection, dispersion, retardation, and radioactive decay). However, the solute transport process has profoundly different characteristics than groundwater flow alone (Anderson, 1979). Mathematically, the steady-state saturated groundwater flow equations are elliptic, with smoothly varying head, while the solute transport equations range from parabolic (with smoothly varying concentrations) in the case of dispersion-diffusion dominated system to hyperbolic (with sharp concentration fronts) in the case of advection-dominated systems. Consequently, calibration to head and flow does not necessarily inform or constrain solute transport. Thus, there may be additional uncertainty associated with the flow model when it is used to make predictions of radionuclide transport. The effects of concentration data on flow model calibration were examined by Weiss and Smith (1993 and 1997). They examined how head and concentration data interact in model calibration with eigenspace and response surface analysis. They showed that, depending on the flow model structure, concentration data could range from being unbeneficial to very beneficial in supplying additional flow model constraint. Scheibe and Chien (2003) showed that calibration of a flow and transport model with a large number of small-scale measurements of concentration and formation properties does not necessarily yield improved predictions, but that broader scale data do. Thus, simply collecting radionuclide or other concentration data does not guarantee improved transport predictions; the data must be collected with an understanding of how the hydrogeologic system (represented by the model) behaves.

The FFACO (1996) requires that the contaminant transport model predict the contaminant boundary at 1,000 years and "at a 95% level of confidence." The Pahute Mesa Phase I flow model described in this report provides, through the flow fields derived from alternative HFMs and recharge models, one part of the data required to compute the contaminant boundary. Other components include the simplified source term model, which incorporates uncertainty and variability in the factors that control radionuclide release from an underground nuclear test (SNJV, 2004a), and the transport model with the concomitant parameter uncertainty as described in Shaw (2003). The uncertainty in all the above model components will be analyzed to produce the final contaminant boundary.

10.0 REFERENCES

ASTM, see American Society for Testing and Materials.

American Society for Testing and Materials. 1993a. *Standard Guide for Application of a Ground-Water Flow Model to a Site-Specific Problem,* ASTM D 5447-93. Philadelphia, PA.

American Society for Testing and Materials. 1993b. *Standard Guide for Comparing Ground-Water Flow Model Simulations to Site-Specific Information,* ASTM D 5490-93. Philadelphia, PA.

American Society for Testing and Materials. 1994a. *Standard Guide for Defining Boundary Conditions in Ground-Water Flow Modeling Designation*, ASTM D 5609-94. Philadelphia, PA.

American Society for Testing and Materials. 1994b. *Standard Guide for Defining Initial Conditions in Ground-Water Flow Modeling,* ASTM D 5610-94. Philadelphia, PA.

American Society for Testing and Materials. 1994c. *Standard Guide for Conducting a Sensitivity Analysis for a Ground-Water Flow Model Application,* ASTM D 5611-94. Philadelphia, PA.

American Society for Testing and Materials. 1996. *Standard Guide for Calibrating a Ground-Water Flow Model Application*, ASTM D 5981-96. Philadelphia, PA.

Anderson, M.P. 1979. "Using Models To Simulate the Movement of Contaminants Through Groundwater Systems." In *Critical Reviews in Environmental Control,* v. 9(2): 97-156. CRC Press.

Anderson, M.P., and W.W. Woessner. 1992. *Applied Groundwater Modeling*. San Diego, CA: Academic Press.

Ashby, S.F. 1996. *ParFlow Project*. Livermore, CA: Lawrence Livermore National Laboratory.

BN, see Bechtel Nevada.

Bechtel Nevada. 2002. *A Hydrostratigraphic Model and Alternatives for the Groundwater Flow and Contaminant Transport Model of Corrective Action Units 101 and 102: Central and Western Pahute Mesa, Nye County, Nevada,* DOE/NV/11718--706. Las Vegas, NV.

Belcher, W.R., J.B. Blainey, F.A. D'Agnese, C.C. Faunt, M.C. Hill, R.J. Laczniak, G.M. O'Brien, C.J. Potter, H.M. Putnam, C.A. San Juan, and D.S. Sweetkind. 2004. *Death Valley Regional Model Ground-Water Flow System, Nevada and California - Hydrogeologic Framework and Transient Ground-Water Flow Model,* Scientific Investigations Report 2004-5205. U.S. Geological Survey.

Blankennagel, R.K., and J.E. Weir, Jr. 1973. *Geohydrology of the Eastern Part of Pahute Mesa, Nevada Test Site, Nye County, Nevada*, Professional Paper 712-B. Denver, CO: U.S. Geological Survey.

Bonnlander, B.V., and A.S. Weigend. 1994. "Selecting Input Variables Using Mutual Information and Nonparametric Density Estimation," Proc., *International Symposium on Artificial Neural Networks* (ISANN'94), 42-50. Tainan, Taiwan.

Bredehoeft, J.D. 2005. "The Conceptualization Model Problem — Surprise." In *Hydrogeology Journal,* v. 13(1): 37-46.

Breiman, L., J.H. Friedman, R.A. Olshen, and C.J. Stone. 1984. *Classification and Regression Trees*. Monterrey, CA: Wadsworth and Brooks/Cole.

Butler, J.J., Jr. 1997. *The Design, Performance, and Analysis of Slug Tests*. Campus West, University of Kansas. CRC Press.

CRWMS M&O, see Civilian Radioactive Waste Management System Management and Operating Contractor.

Caine, J.S., J.P. Evans, and C.B. Forster. 1996. "Fault Zone Architecture and Permeability Structure." In *Geology*, v. 24(11): 1025-1028.

Carrera, J., and S.P. Neuman. 1986a. "Estimation of Aquifer Parameters Under Transient and Steady State Conditions: 1. Maximum Likelihood Method Incorporating Prior Information." In *Water Resources Research* v. 22(2): 199-210.

Carrera, J., and S.P. Neuman. 1986b. "Estimation of Aquifer Parameters Under Transient and Steady State Conditions: 3. Application to Synthetic and Field Data." In *Water Resources Research*, v. 22(2): 228-242.

Chapman, J.B., R.L. Hershey, and B.F. Lyles. 1995. *Groundwater Velocities at the Nevada Test Site: ^{14}Carbon-Based Estimates*, DOE/NV/11508-03 UC-703; Publication No. 45135. Las Vegas, NV: Desert Research Institute.

Civilian Radioactive Waste Management System Management and Operating Contractor. 1997. *ISM2.0: A 3D Geologic Framework and Integrated Site Model of Yucca Mountain,* B00000000-0717-5700-004, Rev. 00. Las Vegas, NV.

Civilian Radioactive Waste Management System Management and Operating Contractor. 2000. *Integrated Site Model Process Report,* TDR-NBS-GS-000002, REV 00, ICN 01. Las Vegas, NV: TRW Environmental Safety Systems, Inc.

Cook, P., and J.K. Bohlke. 2000. "Determining Timescales for Groundwater Flow and Solute Transport." In *Environmental Tracers in Subsurface Hydrology,* pp.1-30. Boston, MA: Kluwer.

Cover, T.M., and J.A. Thomas. 1991. *Elements of Information Theory.* New York, NY: John Wiley & Sons, Inc.

DOE/NV, see U.S. Department of Energy, Nevada Operations Office.

DOE/ORD, see U.S. Department of Energy, Office of Civilian Radioactive Waste Management, Office of Repository Development.

D'Agnese, F.A., C.C. Faunt, A.K. Turner, and M.C. Hill. 1997. *Hydrogeologic Evaluation and Numerical Simulation of the Death Valley Regional Ground-water Flow System, Nevada and California:* Water-Resources Investigations Report 96–4300, p. 124. Denver, CO: U.S. Geological Survey.

Dash, Z.V. 2000. *Validation Test Report (VTR) for the FEHM Application Version 2.10, Yucca Mountain Project Identification Numbers SAN: LANL-1999-046; STN: 10086-2.10-00.* Los Alamos, NM: Los Alamos National Laboratory.

Dash, Z.V. 2001. *Validation Test Report (VTR) for the FEHM Application Version 2.12, Yucca Mountain Project Identification Numbers SAN: LANL-2001-133; STN: 10086-2.12-00.* Los Alamos, NM: Los Alamos National Laboratory.

Dash, Z.V., B.A. Robinson, and G.A. Zyvoloski. 1997. *Software Requirements, Design, and Verification and Validation for the FEHM Application - A Finite-Element Heat- and Mass-Transfer Code,* LA-13305-MS. Los Alamos, NM: Los Alamos National Laboratory.

Drellack, S.L., and L.B. Prothro. 1997. *Descriptive Narrative for the Hydrogeologic Model of Western and Central Pahute Mesa Corrective Action Units*. Las Vegas, NV: Bechtel Nevada.

Duffield, G.M., J.J. Benegar, and D.S. Ward. 1996. *MODFLOWT, A Modular Three-Dimensional Groundwater Flow and Transport Model, User's Manual,* Version 1.1. Sterling, VA: HSI GeoTrans, Inc.

Dynamic Graphics, Inc. 2002. *EarthVision 5.1: Software for 3-D Modeling and Visualization*. Alameda, CA.

FFACO, see *Federal Facility Agreement and Consent Order.*

Faunt, C.C. 1997. *Effect of Faulting on Ground-Water Movement in the Death Valley Region, Nevada and California*, Water-Resources Investigations Report 95-4132. Denver, CO: U.S. Geological Survey.

Faunt, C.C., F.A. D'Agnese, and G.M. O'Brien 2004. *Death Valley Regional Ground-Water Flow System, Nevada and California--Hydrogeologic Framework and Transient Ground-Water Flow Model,* Scientific Investigations Report 2004-5205, Chapter D, Hydrology, pp. 137-163. U.S. Geological Survey.

Federal Facility Agreement and Consent Order. 1996, as amended. Agreed to by the State of Nevada, the U.S. Department of Energy, and the U.S. Department of Defense. Appendix VI, which contains the Underground Test Area strategy, was last amended December 7, 2000, Revision No. 1.

Fenelon, J.M. 2000. *Quality Assurance and Analysis of Water Levels in Wells on Pahute Mesa and Vicinity, Nevada Test Site, Nye County, Nevada*, Water-Resources Investigations Report 00-4014. Carson City, NV: U.S. Geological Survey.

Ferguson, J.F., A.H. Cogbill, and R.G. Warren. 1994. "A Geophysical- Geological Transect of the Silent Canyon Caldera Complex, Pahute Mesa, Nevada." In *Ground Water*, v. 99(B3): 4323-4339. Columbus, OH: Groundwater Publishing Co.

Freyberg, D.L. 1988. "An Exercise in Ground-Water Model Calibration and Prediction." In *Ground Water,* v. 26(N3): 350-360.

Fridrich, C.J., S.A. Minor, and E.A. Mankinen. 1999a. *Geologic Evaluation of the Oasis Valley Basin, Nye County, Nevada.* U.S. Geological Survey Open-File Report 99-533-A.

Fridrich, C.J., S.A. Minor, P.L. Ryder, and J.L. Slate. 1999b. *Geologic Map of the Oasis Valley Basin and Vicinity Nye County, Nevada.* U.S. Geological Survey Open-File Report 99-533-B, scale 1:62,500.

GeoTrans, see HSI GeoTrans.

Gable, C., and T. Cherry. 2001. *Technical Note on Interpolation of MODFLOW Flux onto a Piecewise Linear Surface*. Los Alamos, NM: Los Alamos National Laboratory.

Gelhar, L. 1986. "Stochastic Subsurface Hydrology From Theory to Applications." In *Water Resources Research*, v. 22(9): 135S-145S. Washington, DC: American Geophysical Union.

Gentleman, R., and R. Ihaka. 2005. *An Integrated Suite of Software Facilities for Data Manipulation, Calculation and Graphical Display.* Auckland, New Zealand: University of Auckland.

George, D.C. 1997. *Unstructured 3D Grid Toolbox for Modeling and Simulation,* LA-UR-97-3052. Los Alamos, NM: Los Alamos National Laboratory.

Gillespie, D. 2003. *Temperature Data Evaluation*, DOE/NV/13609-22. Las Vegas, NV: Desert Research Institute.

Granger, C.W.J., and J. Lin. 1994. "Using Mutual Information To Identify Lags in Nonlinear Models." In *Journal of Time Series Analysis*, v. 15: 371-384.

Grauch, V.J.S., D.A. Sawyer, C.J. Fridrich, and M.R. Hudson. 1997. *Geophysical Interpretations West of and Within the Northwestern Part of the Nevada Test Site.* U.S. Geological Open-File Report 97-476. Denver, CO.

Gupta, S. 1996. *CFEST, Flow and Solute Transport, Draft User's Manual*. Irvine, CA: Consultant for Environmental System Technologies (CFEST).

Harrar, W.G. T.O. Sonnenborg, H.J. Henriksen. 2003. "Capture Zone, Travel Time, and Solute-Transport Predictions Using Inverse Modeling and Different Geological Models." In *Hydrogeology Journal,* v. 11: 536–548.

Hevesi, J.A., A.L. Flint, and L.E. Flint. 2003. *Simulation of Net Infiltration and Potential Recharge Using a Distributed Parameter Watershed Model for the Death Valley Region, Nevada and California*, Water-Resources Investigations Report 03-4090. Sacramento, CA: U.S. Geological Survey.

Hill, M.C. 1998. *Methods and Guidelines for Effective Model Calibration,* Water-Resources Investigations Report 98-4005. Denver, CO: U.S. Geological Survey.

HSI GeoTrans. 1990. *Data Input For Swift III, The Sandia Waste-Isolation Flow and Transport Model for Fractured Media, Release 2.32.* Based on original report by: Reeves, M., D.S. Ward, N.D. Johns, and R.M. Cranwell. Originally prepared: December 1985. Herndon, VA: Modifications to Report NUREG/CR-3162.

HSI GeoTrans. 1998. *Theory and Implementation for SWIFT-98: The Sandia Waste-Isolation Flow and Transport Model for Fractured Media*. Sterling, VA: HSI GeoTrans.

Iman, R.L., and W.J. Conover. 1979. "The Use of Rank Transform in Regression." In *Technometrics*, v. 21(4): 499-509.

Iman, R.L., J.M. Davenport, and D.K. Ziegler. 1980. *Latin Hypercube Sampling Program User's Guide*, SAND79-1473. Albuquerque, NM: Sandia National Laboratories.

Intercomp. 1976. *A Model for Calculating Effects of Liquid Waste Disposal in Deep Saline Aquifer*, Water-Resources Investigations Report 76061. Prepared for the U.S. Geological Survey: Reston, VA.

IT, see IT Corporation.

IT Corporation. 1996a. *Groundwater Recharge and Discharge Data Documentation Package (Phase I Data Analysis Documentation,* Volume III), ITLV/10972-181. Las Vegas, NV.

IT Corporation. 1996b. *Hydrologic Parameter Data Documentation Package (Phase 1 Data Analysis Documentation, Volume IV),* ITLV/10972-181. Las Vegas, NV.

IT Corporation. 1996c. *Potentiometric Data Documentation Package (Phase 1 Data Analysis Documentation, Volume II),* ITLV/10972-181. Las Vegas, NV.

IT Corporation. 1996d. *Regional Geologic Model Data Documentation Package (Phase 1 Data Analysis Documentation, Volume I),* ITLV/10972-181. Las Vegas, NV.

IT Corporation. 1996e. *Transport Parameter and Source Term Data Documentation Package (Phase I Data Analysis Documentation, Volume V),* ITLV/10972-181. Las Vegas, NV.

IT Corporation. 1996f. *Tritium Transport Model Documentation Package (Phase 1 Data Analysis Documentation, Volume VII),* ITLV/10972-181. Las Vegas, NV.

IT Corporation. 1997a. *Groundwater Flow Model Documentation Package (Phase I Data Analysis Documentation, Volume VI),* ITLV/10972-181. Las Vegas, NV.

IT Corporation. 1997b. *Risk Assessment Documentation Package (Phase I Data Analysis Documentation, Volume VIII),* ITLV/10972-181. Las Vegas, NV.

IT Corporation. 1998a. *Report and Analysis of the BULLION Forced-Gradient Experiment,* ITLV/13052-042, DOE/NV-13-52. Las Vegas, NV.

IT Corporation. 1998b. *Value of Information Analysis for Corrective Action Units Nos. 101 and 102: Central and Western Pahute Mesa, Nevada Test Site, Nevada,* ITLV/13052-041. Las Vegas, NV.

IT Corporation. 1998c. *Western Pahute Mesa – Oasis Valley Hydrogeologic Investigation Wells Drilling and Completion Criteria,* Rev. 0, ITLV/13052-049, p. 439. Las Vegas, NV.

IT Corporation. 1999. *Underground Test Area Project Corrective Action Unit 98: Frenchman Flat, Vol. II, Groundwater Data Documentation Package,* Rev. 0, DOE/NV/13052-044-V2. Las Vegas, NV.

IT Corporation. 2001. *Underground Test Area Fracture Analysis Report: Analysis of Fractures in Volcanic Rocks of Western Pahute Mesa-Oasis Valley*, ITLV/13052-150. Las Vegas, NV.

Katyal, A.K. 1995. *CSMoS Online Model Information for BIOF&T-3D*. U.S. Environmental Protection – Ada Oklahoma Laboratory. Blacksburg, VA: Draper Aden Environmental Modeling, Inc.

Kersting, A.B., D.W. Efurd, D.L. Finnegan, D.J. Rokop, D.K. Smith, and J.L. Thompson. 1999. "Migration of Plutonium in Groundwater at the Nevada Test Site." In *Nature,* v. 397: 56-59.

Kipp, K.L., Jr. 1986. *HST3D: A Computer Code for Simulation of Heat and Solute Transport in Three-Dimensional Ground-water Flow Systems*, Water-Resources Investigations Report 86-4095. Denver, CO: U.S. Geological Survey.

Kwicklis, E.M., T.P. Rose, and F.C. Benedict. 2005. *Evaluation of Groundwater Flow in the Pahute Mesa – Oasis Valley Flow System Using Groundwater Chemical and Isotopic Data,* LA-UR 05-4344. Los Alamos, NM: Los Alamos National Laboratory.

Laczniak, R.J., J.C. Cole, D.A. Sawyer, and D.A. Trudeau. 1996. *Summary of Hydrogeologic Controls on Ground-Water Flow at the Nevada Test Site, Nye County, Nevada,* Water-Resources Investigations Report 96-4109. Denver, CO: U.S. Geological Survey.

Laczniak, R.J., J.L. Smith, P.E. Elliott, G.A. DeMeo, M.A. Chatigny, and G. Roemer. 2001. *Ground-Water Discharge Determined from Estimates of Evapotranspiration, Death Valley Regional Flow System, Nevada and California*, Water-Resources Investigations Report 01-4195. Denver, CO: U.S. Geological Survey.

Maxey, G.B., and T.E. Eakin. 1949. "Groundwater in White River Valley, White Pine, Nye and Lincoln Counties, Nevada." In *Water Resources,* Bulletin No. 8. Carson City, NV: State of Nevada, Office of the State Engineer.

McDonald, M.G., and A.W. Harbaugh. 1988. *Techniques of Water-Resources Investigations of the United States Geological Survey, A Modular Three-Dimensional Finite-Difference Ground-Water Flow Model,* Book 6, Chapter A1. Washington, DC: U.S. Geological Survey.

McKay, M.D., W.J. Conover, and R.J. Beckman. 1979. "A Comparison of Three Methods for Selecting Values of Input Variables in the Analysis of Output from a Computer Code." In *Technometrics*, v. 21(3): 239-245.

McKee, E.H., T.G. Hildenbrand, M.L. Anderson, P.D. Rowley, and D.A. Sawyer. 1999. *The Silent Canyon Caldera Complex: Three Dimensional Model Based on Drill-Hole Stratigraphy and Gravity Inversion,* Open-File Report 99-555, p. 38. Las Vegas, NV: U.S. Geological Survey.

McKee, E.H., G.A. Phelps, and E.A. Mankinen. 2001. *The Silent Canyon Caldera: Three-Dimensional Model as Part of a Pahute Mesa-Oasis Valley, Nevada Hydrogeologic Model,* Open-File Report 01-297. Las Vegas, NV: U.S. Geological Survey.

Mishra, S., and R.G. Knowlton. 2003. "Testing for Input-Output Dependence in Performance Assessment Models," Proc., *Tenth International High-Level Radioactive Waste Management Conference*, March 30 - April 2. Las Vegas, NV.

Mishra, S., N.E. Deeds, and B.S. RamaRao. 2003. "Application of Classification Trees in the Sensitivity Analysis of Probabilistic Model Results." In *Reliability Engineering & System Safety*, v. 73: 123-129.

Moddemeijer, R. 1989. "On the Estimation of Entropy and Mutual Information of Continuous Distributions." In *Signal Processing*, v. 16(3): 233-248.

NRC, see National Research Council.

Naff, R.L. 1978. *A Continuum Approach to the Study and Determination of Field Longitudinal Dispersion Coefficients,* PhD Dissertation. Socorro, NM: New Mexico Institute of Mining and Technology.

National Research Council. 1996. *Rock Fractures and Fluid Flow: Contemporary Understanding and Applications*. Washington, DC: National Academy Press.

Neuman, S.P. 1990. "Universal Scaling of Hydraulic Conductivities and Dispersivities in Geologic Media." In *Water Resources Research,* v. 26 (8): 1749-1758. American Geophysical Union.

Nishikawa, T. 1997. "Testing Alternative Conceptual Models of Seawater Intrusion in a Coastal Aquifer Using Computer Simulation, Southern California, USA." In *Hydrogeology Journal,* v. 5(3): 60-74.

Nitao, J.L. 1998. *User's Manual for the USNT Module of the NUFT Code,* Version 2.0, UCRL-MA-130653. Livermore, CA: Lawrence Livermore National Laboratory.

Noble, D.C., G.D. Bath, R.L. Christiansen, and P.P. Orkild. 1968. *Zonal Relations and Paleomagnetism of the Spearhead and Rocket Wash Members of the Thirsty Canyon Tuff, Southern Nevada,* Professional Paper 600C: C61-65. Denver, CO: U.S. Geological Survey.

O'Hagan, M.D., and R.J. Laczniak. 1996. *Ground-Water Levels Beneath Eastern Pahute Mesa and Vicinity, Nevada Test Site, Nye County, Nevada,* Water- Resources Investigations Report 96-4042. Denver, CO: U.S. Geological Survey.

Orkild, P.P., K.A. Sargent, and R.P. Snyder. 1969. *Geologic Map of Pahute Mesa, Nevada Test Site and Vicinity, Nye County, Nevada,* Map I-567, scale: 1: 48,000. Denver, CO: U.S. Geological Survey.

Parkhurst, D.L., and C.A.J. Appelo. 1999. *User's Guide to PHREEQC (Version 2) — A Computer Program for Speciation, Batch-Reaction, One-Dimensional Transport, and Inverse Geochemical Calculations,* Water-Resources Investigations Report 99-4259, p. 312. U.S. Geological Survey.

Pawloski, G.A., A.F.B. Tompson, and S. Carle, eds. 2001. *Evaluation of the Hydrologic Source Term from Underground Nuclear Tests on Pahute Mesa at the Nevada Test Site*: *The CHESHIRE Test,* UCRL-ID-147023. Livermore, CA: Lawrence Livermore National Laboratory.

Plummer, L.N., E.C. Prestemon, and D.L. Parkurst. 1994. *An Interactive Code (NETPATH) for Modeling Net Geochemical Reactions Along a Flow Path,* Version 2.0, Water-Resources Investigations Report 94-4169. Denver, CO: U.S. Geological Survey.

Poeter, E.P., and M.C. Hill. 1997. "Inverse Models: A Necessary Next Step in Ground-Water Modeling." In *Ground Water*, v. 35(N2): 250-260.

Pollock, D.W. 1988. "Semianalytical Computation of Path Lines for Finite-Difference Models." In *Ground Water*, v. 26: 743-750.

Press, W.H., S.A. Teukloksky, W.T. Vetterling, and B.P. Flannery. 1992. *Numerical Recipes in FORTRAN*, LBL-29400. Cambridge University Press: London.

Prothro, L.B., and R.G. Warren. 2001. *Geology in the Vicinity of the TYBO and BENHAM Underground Nuclear Test, Pahute Mesa, Nevada Test Site.* Los Alamos National Laboratory and Bechtel Nevada Report DOE/NV11718--305.

Pruess, K. 1991. *TOUGH2 - A General Purpose Numerical Simulator for Multiphase Fluid and Heat Flow.* Berkeley, CA: Lawrence Berkeley Laboratory.

Reeves, M., D.S. Ward, N.D. Johns, and R.M. Cranwell. 1986. *Theory and Implementation for SWIFT II, The Sandia Waste-Isolation Flow and Transport Model for Fractured Media,* NUREG/CR3328. Albuquerque, NM: Sandia National Laboratories.

Reiner, S.R., R.J. Laczniak, G.A. DeMeo, J. LaRue Smith, P.E. Elliott, W.E. Nylund, and C.J. Fridrich. 2002. *Ground-Water Discharge Determined from Measurements of Evapotranspiration, Other Available Hydrologic Components, and Shallow Water-Level Changes, Oasis Valley, Nye County, Nevada,* Water-Resources Investigations Report 01-4239. Carson City, NV: U.S. Geological Survey.

Robinson, B.A. 2004. *Particle Tracking Model and Abstraction of Transport Processes,* MDL-NBS-HS-000020, REV 01, BSC LLC. Las Vegas, NV.

Russell, C.E., and T. Minor. 2002. *Reconnaissance Estimates of Recharge Based on an Elevation-Dependent Chloride Mass-Balance Approach,* DOE/NV/11508-37. Las Vegas, NV: Desert Research Institute.

Shaw, see Shaw Environmental, Inc.

SNJV, see Stoller-Navarro Joint Venture.

Saltelli, A., K. Chan, and M. Scott. 2000. *Sensitivity Analysis*. New York, NY: John Wiley & Sons Inc.

Sawyer, D.A., and K.A. Sargent. 1989. "Petrologic Evolution of Divergent Peralkaline Magmas from the Silent Canyon Caldera Complex, Southwestern Nevada Volcanic Field." In *American Geophysical Union, Journal of Geophysical Research*, v. 94(B5): 6021-6040.

Scheibe, T.D. and Y.-J. Chien. 2003. "An Evaluation of Conditioning Data for Solute Transport Prediction." In *Groundwater*, v. 41(2): 128.

Scientific Software Group. 1998. *Information relating to the MT3D96 and 3DFEMFAT Computer Codes*. Sandy, UT.

Scott, R.B., T.J. Smales, R.E. Rush, and A.S. Van Denburgh. 1971. "Water for Nevada, Nevada's Water Resources." In *State of Nevada Department of Conservation and Natural Resource, Water for Nevada Report 3*. Carson City, NV: Nevada Division of Water Resources.

Seaton, W.J., and T.J.Burbey. 2005. "Influence of Ancient Thrust Faults on the Hydrogeology of the Blue Ridge Province." In *Groundwater*, v. 43(3): 301-314.

Shaw Environmental, Inc. 2003. *Contaminant Transport Parameters for the Groundwater Flow and Contaminant Transport Model of Corrective Action Units 101 and 102: Central and Western Pahute Mesa, Nye County, Nevada,* Rev. 0, Shaw/13052-201-CD. Las Vegas, NV.

Slate, J.L., M.E. Berry, P.D. Rowley, C.J. Fridrich, K.S. Morgan, J.B. Workman, O.D. Young, G.L. Dixon, V.S. Williams, E.H. McKee, D.A. Ponce, T.G. Hildenbrand, W.C. Swadley, S.C. Lundstrom, E.B. Ekren, R.G. Warren, J.C. Cole, R.J. Fleck, M.A. Lanphere, D.A. Sawyer, S.A. Minor, D.J. Grunwald, R.J. Laczniak, C.M. Menges, J.C. Yount, and A.S. Jayko. 1999. *Digital Geologic Map of the Nevada Test Site and Vicinity, Nye, Lincoln, and Clark Counties, Nevada, and Inyo County, California,* Open-File Report 99-554-A. Denver, CO: U.S. Geological Survey.

Stoller-Navarro Joint Venture. 2004a. *Hydrologic Data for the Groundwater Flow and Contaminant Transport Model of Corrective Action Units 101 and 102: Central and Western Pahute Mesa, Nye County, Nevada*, Rev. 0, S-N/99205-002; Shaw/13052-204. Las Vegas, NV.

Stoller-Navarro Joint Venture. 2004b. *Modeling Approach/Strategy for Corrective Action Units 101 and 102, Central and Western Pahute Mesa*, *Nye County, Nevada*, S-N/99205-008. Las Vegas, NV.

Stoller-Navarro Joint Venture. 2004c. *Unclassified Source Term and Radionuclide Data for the Groundwater Flow and Contaminant Transport Model of Corrective Action Units 101 and 102: Central and Western Pahute Mesa, Nye County, Nevada,* Rev. 0, S-N/99205--022. Las Vegas, NV.

Thomas, J.M., F.C.Benedict, Jr., T.P. Rose, R.L. Hershey, J.B. Paces, Z.E. Peterman, I.M. Farnham, K.H. Johannesson, A.K. Singh, K.J. Stetzenbach, G.B. Hudson, J.M. Kenneally, G.F. Eaton, and D.K. Smith. 2002. *Geochemical and Isotopic Interpretations of Groundwater Flow in the Oasis*

Valley Flow System, Southern Nevada, DOE/NV/11508-56; Publication No. 45190. Las Vegas, NV: Desert Research Institute.

Tompson, A.F.B., C.J. Bruton, and G.A. Pawloski, eds. 1999. *Evaluation of the Hydrologic Source Term from Underground Nuclear Tests in Frenchman Flat at the Nevada Test Site*: *The CAMBRIC Test,* UCRL-ID-132300. Livermore, CA: Lawrence Livermore National Laboratory.

U.S. Department of Energy, Nevada Operations Office. 1996. *Recompletion Report and Summary of Well History for Well PM-3*, DOE/NV-437 UC700. Las Vegas, NV.

U.S. Department of Energy, Nevada Operations Office. 1997. *Regional Groundwater Flow and Tritium Transport Modeling and Risk Assessment of the Underground Test Area, Nevada Test Site, Nevada,* DOE/NV--477. Las Vegas, NV.

U.S. Department of Energy, Nevada Operations Office. 1999. *Corrective Action Investigation Plan for Corrective Action Units 101 and 102, Central and Western Pahute Mesa, Nevada Test Site, Nevada,* DOE/NV--516, Rev. 1. Las Vegas, NV.

U.S. Department of Energy, Nevada Operations Office. 2000. *United States Nuclear Tests, July 1945 through September 1992,* DOE/NV-209, Rev. 15. Las Vegas, NV.

U.S. Department of Energy, Office of Civilian Radioactive Waste Management, Office of Repository Development. 2004. *Site-Scale Saturated Zone Transport*, MDL-NBS-HS-000010, ICN 00, Rev. 1. Las Vegas, NV.

Vatnaskil Consulting Engineers. 1988. *AQUA3D Groundwater Flow and Transport Model*. Sudurlandsbraut 50, 108 Reykjavik, Iceland.

Watermark, see Watermark Numerical Computing and Waterloo Hydrogeologic.

Ward, D.S., M. Reeves, and L.E. Duda. 1984. *Verification and Field Comparison of the Sandia Waste-Isolation Flow and Transport Model (SWIFT)*, NUREG/CR3316. Albuquerque, NM: Sandia National Laboratories.

Warren, R.G, D.A. Sawyer, F.M. Byers, and G.L. Cole. 2003. *A Petrographic, Geochemical, and Geophysical Database, and Stratigraphic Framework for the Southwestern Nevada Volcanic Field,* LA-UR-03-1503. Albuquerque, NM: Los Alamos National Laboratory.

Waterloo Hydrogeologic, Inc. 1998. *FRAC3DVS: Variably-Saturated Groundwater Flow and Transport in Discretely Fractured Porous Media*. Waterloo, Ontario, Canada.

Watermark Numerical Computing. 2004. *PEST Model-Independent Parameter Estimation Software*. Brisbane, Australia.

Watrus, J. 2004. Personal communication to G. Ruskauff (SNJV) regarding Spot Springs, 24 March. Las Vegas, NV.

Weiss, R., and L. Smith. 1993. "Parameter Estimation using Hydraulic Head and Environmental Tracer Data." Proc. of the Groundwater Modeling Conference, June 9-12, 1993. Golden, CO.

Weiss, R., and L.Smith. 1997. "Efficient and Responsible Use of Prior Information in Inverse Methods." In *Groundwater*, v. 36(1): 151.

Westinghouse Hanford Company. 1991. *PORMC: A Model for Monte Carlo Simulation of Fluid Flow, Heat, and Mass Transport in Variably Saturated Geologic Media*, WHC-EP-0445. Richland, WA.

White, A.F. 1979. *Geochemistry of Ground Water Associated with Tuffaceous Rocks, Oasis Valley, Nevada*, Professional Paper 712-E. Denver, CO: U.S. Geological Survey.

Winograd, I.J., and W. Thordarson. 1975. *Hydrogeologic and Hydrochemical Framework, South-Central Great Basin, Nevada-California, with Special Reference to the Nevada Test Site,* Professional Paper 712-C. Denver, CO: U.S. Geological Survey.

Wolfsberg, A., L. Glascoe, G. Lu, A. Olson, P. Lichtner, M. McGraw, T. Cherry, and G. Roemer. 2002. *TYBO/BENHAM: Model Analysis of Groundwater Flow and Radionuclide Migration from Underground Nuclear Tests in Southwestern Pahute Mesa, Nevada,* LA-13977. Los Alamos, NM: Los Alamos National Laboratory.

Zyvoloski, G.A., B.A. Robinson, Z.V. Dash, and L.L. Trease. 1996. *User's Manual for the FEHM Application,* LA-UR--94-3788, Rev. 1. Los Alamos, NM: Los Alamos National Laboratory.

Zyvoloski, G.A., B.A. Robinson, Z.V. Dash, and L.L. Trease. 1997a. *Summary of Models and Methods for the FEHM Application - A Finite-Element Heat- and Mass-Transfer Code*, LA-13307-MS. Los Alamos, NM: Los Alamos National Laboratory.

Zyvoloski, G.A., B.A. Robinson, Z.V. Dash, and L.L. Trease. 1997b. *User's Manual for the FEHM Application - A Finite-Element Heat- and Mass-Transfer Code,* LA-13306-M. Los Alamos, NM: Los Alamos National Laboratory.

Zyvoloski, G.A., E. Kwicklis, A.A. Eddebbarh, B. Arnold, C. Faunt, and B.A. Robinson. 2003. "The Site-Scale Saturated Zone Flow Model for Yucca Mountain: Calibration of Different Conceptual Models and Their Impact on Flow Paths." In *Journal of Contaminant Hydrology,* v. 62-63: 731-750.

Appendix A

Evaluation of Flow and Transport Codes for Application to the Western Pahute Mesa Corrective Action Unit

This appendix contains the letter report documenting the evaluation of flow and transport codes for application to the Western Pahute Mesa Corrective Action Unit. This letter report was completed on September 2, 1999, and provided the basis for a presentation to the Technical Working Group Modeling Subcommittee on September 23, 1999.

A.1.0 INTRODUCTION

The code evaluation task consists of the selection and evaluation of three numerical codes in support of the Western Pahute Mesa Corrective Action Unit (CAU) modeling effort. The subtasks consist of identification of code attributes consistent with the key physical and chemical processes that must be simulated by the CAU scale model, identification of candidate codes, selection of three codes from the candidate codes for testing, development of a test problem, development of testing criteria, and evaluation against determined criteria of the performance of candidate codes in simulating the test problem. A quantitative evaluation of flow and transport on Western Pahute Mesa was not within the scope of work of this task. The test problem was simulated without calibration in some cases using extreme values of properties and hydrologic source terms in order to test the capabilities of the codes. With this in mind, it is important to note that the results of the test problem simulations should not in any way be interpreted as accurately representing the magnitudes of flow and transport processes occurring on Western Pahute Mesa.

A.2.0 CODE ATTRIBUTES

A number of attributes or capabilities of the CAU model were defined to satisfy the modeling objectives. The first objective requires the CAU model to have the ability to represent the important physical and chemical features of the CAU groundwater flow system. The features include faulting, stratigraphy, sources and sinks of water, the distribution of contaminants and their rates of introduction into the groundwater flow system, and other physical or chemical features unique to the CAU. The second objective requires the CAU model to simulate the movement of a variety of contaminants for which their distribution and abundance serve to define the contaminant boundary. The third objective requires flexibility in the CAU model to allow grid changes, placement of additional wells, and boundary condition variations. The required code attributes that were defined consistently with the three modeling objectives were categorized under "general," "flow model," and "transport model." Each of these attributes will be described and assessed with respect to importance for the CAU modeling. In addition, six non-essential but desirable attributes were identified. These include: finite-element formulation, steady-state capability, double-porosity/double-permeability formulation, the ability to simulate the transport of multiple solutes and daughter products, and established pre- and post-processors.

A.2.1 General Attributes

Fully Three-Dimensional

The groundwater flow system is controlled by the distribution of geologic units as well as the location of sources and sinks of water. Additionally, transport properties including source location and strength, porosity, and diffusion may vary in space. The three-dimensional (3-D) nature of the groundwater flow system requires that the CAU model will need to be 3-D to adequately simulate migration of the potential contaminants within the CAU-model area.

Large Numbers of Nodes Capability

For a given formulation, the greater the number of nodes in the CAU model, the greater the detail that can be included. Given the anticipated large geographic area of the Pahute Mesa CAU model, the ability of the CAU model to simulate many nodes will control the amount of detail that can be included. In general, each of the selected codes will only be limited by the capacity of the hardware, not by the software used.

Multiple Boundary Condition Options

Options for specified pressure and specified flux boundary conditions for fluids, as well as specified temperature or specified heat flow, may be required in implementing the CAU model.

Transient Capability

The initial flow simulations for the CAU model will be steady-state with possible transient runs to follow. The contaminant transport simulations will all be performed under transient conditions.

Efficient Solver

To simulate in sufficient detail, the CAU model will require a large number of nodes as mentioned above. To make a large model practical, the codes must run efficiently. Generally, a code has a selection of solvers available. The solvers must be efficient enough to allow for more than one run per day. A code that requires more than six hours per simulation would be eliminated. A six-hour run time allows two runs per day on a single computer.

Acceptable Numerical Accuracy

The numerical solution of the transport equation is typically more difficult than the solution of the flow equation. This attribute requires the results of the code for a given test problem to have been checked against analytical solutions and against the results of other numerical codes for the same problem. Documentation of this quality assurance (QA) checking must be available.

Minimal Numerical Dispersion

Under certain circumstances, the error in the numerical approximation of a value can become as large as the value being approximated. When this occurs, the numerical solution combines an exclusively

numerical dispersion with the real hydrodynamic dispersion producing an overestimate of the actual dispersion. Solution techniques that minimize numerical dispersion are required.

Acceptable Verification and Validation

The degree of computer code verification and validation varies widely depending on the code being considered. The extent to which this process has been documented for a particular code varies even more. Thoroughly documented testing is required to ensure that the code satisfies requirements specified for its options and features.

Access to Source Code

Computer codes are initially written by humans in a high-level language such as FORTRAN and then translated into machine language for execution on the computer. The high-level version of the code is called the "source code," and can be read and modified by humans. The machine-language version is called the "executable code," can be deciphered only by the computer. Many distributors of computer codes provide only the executable version of the code to the user. During the course of the development or application of the CAU model, it may be necessary to examine or modify the step-by-step procedure implemented in the computer code. To accomplish this, access to the source code will be required.

A.2.2 Groundwater Flow Model Attributes

Saturated Groundwater Flow

The codes must be able to simulate saturated groundwater flow.

Heterogeneous and Anisotropic Hydraulic Conductivity

Aquifer heterogeneity reflects the natural variability in the subsurface. The CAU model must be capable of simulating flow through aquifers in which the hydraulic conductivity may vary from location to location. Anisotropy is a directional dependence of the hydraulic conductivity. In fractured aquifers, it is common for hydraulic conductivity to be larger in a direction parallel to fracturing and smaller perpendicular to fracturing.

Point and Distributed Sources and Sinks of Water

Recharge may occur over a large spatial area due to precipitation or may be concentrated into washes or craters. Discharge may occur at wells or individual springs or may occur over larger areas such as playas. The CAU model should have the capability to simulate these various cases.

Temperature Dependence

The flow of groundwater may be influenced by water temperature variations. Warm water is more buoyant than colder water and tends to rise. Additionally, warm water is less viscous and tends to move more easily than cold water. These processes may be important in some portions of the CAU where naturally occurring sources of heat have caused elevated groundwater temperatures. An additional source of warm water may be the underground test cavities. It may be important to account for these temperature effects in the simulations.

Simulate Complex Geology

The geology of Pahute Mesa is complex. It consists of multiple stratigraphic units, some of which are truncated by faults and other structural features. Even within units, changes in facies result in spatial variations in material properties. The flow of groundwater (amount and direction) is governed, in large part, by the distribution of geologic units. The code must be able to include important features of the geology such as lateral and vertical changes in material properties. Much of this attribute is similar to earlier general attributes related to number of grid nodes and simulation speed. The greater the number of nodes, the more detail that can be incorporated into the CAU model.

A.2.3 Transport Model Attributes

Advection, Dispersion, Sorption, and Matrix Diffusion

It is expected that advection (via the groundwater flux) and matrix diffusion will be the primary factors influencing tritium transport. It is expected that sorption will also be important for reactive contaminants, but this may not be the dominant contributor to the location of contaminant boundary. Dispersion is included because it may be important at smaller scales.

Radioactive Decay

Most, but not all, of the potential contaminants of interest are radionuclides. The activity per volume of radionuclides decreases via the process of radioactive decay.

A.2.4 Desirable Attributes

These are attributes of the computer codes that were considered valuable but not essential to satisfying the CAU-modeling objectives.

Finite Element Formulation

A finite element formulation allows much more flexibility in representing the geology being modeled. Grids can be developed to represent complex structures such as faults, pinch outs and layer truncations. In addition, grid refinement allows the grid to be modified to provide more resolution in the area of interest.

Steady-State Capability

Some of the codes do not include a steady flow option, but rather reach steady-state by leaving parameters fixed in time and performing transient simulations over large periods of time until steady-state is reached. This approach is adequate, but somewhat slower than if a true steady-state option were available.

Double-Porosity/Double-permeability Formulation

The double-porosity/double-permeability method is similar to the double-porosity method in that it allows for communication between fractures and matrix material. The term dual porosity/dual permeability is often used in the literature. In this report, dual is used interchangeably with double depending on the usage in the model documentation. This feature allows for the modeling of matrix diffusion. The double-porosity/double-permeability method differs in that it allows matrix cells that communicate with fractures to also communicate with other matrix cells. While this method provides a more realistic simulation, its use is more important for unsaturated flow problems.

Multiple Solutes

Many codes are designed to provide a simulation of the migration of a single solute in a given run. Using a code with the ability to model transport for multiple solutes in a single run may be more efficient.

Daughter Products

A radionuclide may decay into another radionuclide (called a daughter product) or into a stable isotope. More accurate estimates of dose can be obtained if the code is capable of simulating the ingrowth and transport of a radionuclide and daughter product(s).

Established Pre- and Post-Processors

The task of creating the input datasets for any model is simplified by having pre-processors take data and put it into a form that is required by the model. Post-processors take model output and typically create graphic images of some simulated parameter such as water level or solute concentration. Pre- and post-processors generally speed up the modeling task.

A.3.0 Code Identification and Preliminary Selection

The following list includes the codes initially screened for the Pahute Mesa CAUs:

- AQUA3D (Vatnaskil Consulting Engineers, 1988)
- BIOF&T-3D (Katyal, 1995)
- CFEST (Gupta, 1996)
- FEHM (Zyvoloski, et al., 1997a)
- FRAC3DVS (Waterloo Hydrogeologic Inc., 1998)
- HST3D (Kipp, 1986)
- MODFLOWT (Duffield, et al., 1996)
- MT3D96 (Scientific Software Group, 1998)
- NUFT (Nitao, 1998)
- PARFLOW (Ashby, et al., 1996)
- PORMC (Westinghouse Hanford Co., 1991)
- SWIFT-1998 (HSI-GeoTrans, 1998)
- TOUGH2 (Pruess, 1991)
- 3DFEMFAT (Scientific Software Group, 1998)

An initial comparison of the codes was performed with respect to the attributes. The results of the comparison are presented in Table A.11-1 where the required code attributes have been grouped into the categories of general, flow model, and transport model. Comparisons of attributes considered desirable, but not required, are also shown.

Of this list, ten codes were eliminated from further consideration. Seven codes: CFEST, HST3D, MT3D96, PARFLOW, PORMC, TOUGH2, AND 3DFEMFAT were eliminated because they do not have the ability to simulate matrix diffusion explicitly. BIOF&T-3D and AQUA3D were eliminated because access to the source codes was not available. NUFT was eliminated because current documentation (Nitao, 1998) indicated that hydrodynamic dispersion was not implemented in the code and in addition, the source code was not accessible.

Of the remaining four codes, only FEHM and SWIFT-98 have all of the required attributes. FRAC3DVS and MODFLOWT lacked only the ability to simulate thermal effects. FRAC3DVS was

ranked above MODFLOWT and retained for testing because its finite element formulation would allow a more accurate representation of the complex geology. Therefore, the three codes that were retained for further evaluation are FEHM, FRAC3DVS, and SWIFT-98.

A.4.0 DESCRIPTION OF THE CANDIDATE CODES

Features of the three codes identified as possible candidates for use in the Pahute Mesa CAU model are described below.

FRAC3DVS

FRAC3DVS (Waterloo Hydrologic, Inc., 1998) is a 3-D, finite element code for simulating steady-state or transient, variably-saturated groundwater flow, and advective-dispersive solute transport in porous or discretely-fractured porous media. The code was developed by E.A. Sudicky, at the Waterloo Centre for Groundwater Research, and R. Thierren at Laval University. Specific capabilities of this code include:

- 3-D
- flow of water
- multi-species transport of either straight or branching decay chains
- sorption according to a linear Freundlich isotherm
- control-volume finite element, Galerkin finite element, or finite difference formulation
- saturated and unsaturated media
- conjugate-gradient-like solver
- dual porosity and discrete fracture capabilities
- irregular, layered grids composed of blocks or prisms

SWIFT-98

The SWIFT-98 (Sandia Waste Isolation Flow and Transport) computer code (Reeves et al., 1986; Ward et al., 1984; Ward and Benegar, 1998) is a 3-D ground water flow and transport code designed to simulate the advective-dispersive transport of solutes, including radionuclides, in groundwater. The code is based on a block-centered finite-difference scheme. SWIFT evolved from the USGS SWIP (Survey Waste Injection Program). The current version, SWIFT-98 (Ward and Benegar, 1998), contains the following capabilities:

- 3-D
- advective-dispersive solute transport

- first-order decay and adsorption/desorption based on linear or nonlinear Freundlich isotherms
- inclusion of up to three daughter products for radionuclide transport simulations
- dual-porosity/dual-permeability
- brine and heat transport in porous or fractured media
- planar or spherical matrix block geometries
- transient and steady-state flow options
- centered or backwards differencing schemes in both time and space
- direct solver and two-line successive over-relaxation scheme

FEHM

The FEHM code (Zyvoloski et al., 1997a), developed by Los Alamos National Laboratory (LANL), simulates 3-D, time-dependent, multiphase, multicomponent, nonisothermal, reactive groundwater flow through porous and fractured media. FEHM's finite element formulation provides an accurate representation of complex 3-D geologic media and structures and their effects on subsurface flow and transport. Specific capabilities include:

- 3-D
- flow of gas, water, oil, and heat
- flow of air, water, and heat
- multiple chemically reactive and sorbing tracers
- colloid transport
- finite element/finite volume formulation
- coupled stress module
- saturated and unsaturated media
- preconditioned conjugate gradient solution of coupled nonlinear equations
- double porosity and double porosity/double-permeability capabilities
- complex geometries with unstructured grids

A number of documents supporting the FEHM code are readily available from LANL. Documentation includes a description of the mathematical models and numerical methods used by FEHM (Zyvoloski, et al., 1997b), the user's manual (Zyvoloski, et al., 1997a), documentation of the functional and performance requirements for FEHM, description of the FEHM software, the verification and validation plan, and description of the verification and validation activities (Dash et al., 1997).

A.5.0 TESTING CRITERIA

The criteria used to assess the codes range from a somewhat subjective assessment of ease of use to more quantifiable assessments such as the run time for a sample problem. The testing criteria are as follows:

Portability

The CAU model may be sent to independent reviewers as well as the State of Nevada. Each of these stakeholders may want to run the code themselves. This requires that the code, when complete, should require minimal special equipment or software in order to make it usable. Additionally, the CAU model will likely need to be run on a classified computer at the DOE Nevada Support Facility or another secure location to produce a final estimate of the contaminant boundary (results based on classified data will be reported in a classified report). The code and associated pre- and post-processors must be portable to the selected secure location to allow for efficient classified simulations.

QA Evaluation

The chosen code must have been appropriately verified to ensure the output is accurate. The QA evaluation refers to the level of documentation and testing for a code. The ability of the code to simulate the processes of interest is a function of the formulation of the equations and the quality of the programming. A code meets the QA requirements if its results have been verified against those of other codes as well as compared with analytical solutions. These comparisons must be documented before a code will be used for the Pahute Mesa model.

Ease of Use

The ease of use is a subjective judgment that assesses the modeler's degree of difficulty in getting the model running. This is, by necessity, a value judgment of the modeler and reflects the modeler's experience and background. A great deal of energy will be spent calibrating the CAU model and

setting up sensitivity and uncertainty analyses. A code that is difficult to use makes the job of calibration more difficult and reduces the code's portability. Ease of use includes factors such as the structure of the input datasets used in the model and the flexibility of pre-and post-processors.

Ability To Represent the CAU Hydrogeology

The primary geologic features that control flow need to be represented in the CAU model. These features include the hydrostratigraphy, physical boundaries, and structural features such as faults. In addition, the ability to model physical processes of concern (advection, dispersion, matrix diffusion, adsorption, and radioactive decay) is also important. The criteria also include an assessment of the ability of the model to include sufficient detail and stay within the memory limitations of the computer platform chosen for simulation.

Speed of Simulation

The time required for a solution is also of importance to the evaluation of the codes. The faster the code, the shorter the time to complete each model run. As calibration normally requires many (often greater than 100) model runs, the simulation time becomes a problem if it is too long. For the purposes of the CAU model, simulation times less than six hours for a steady-state flow simulation are acceptable. This length of simulation time will allow for two or three runs per day, which provides sufficient time to perform the calibration assuming up to 200 runs to calibrate.

A.6.0 TEST PROBLEM

A test problem was created to evaluate the candidate codes. The features of the test problem were chosen to mimic the conditions expected in the Pahute Mesa model area. By doing so, the effort to set up and run the problem could be evaluated as well as the assessment of the run times of the model. The features to be included in the test problem are: complex caldera geology such as lithologic and structural features, temperature-dependent flow, radionuclide migration from a cavity, and matrix diffusion.

The test problem was designed to mimic the expected level of complexity anticipated for Pahute Mesa. The Pahute Mesa hydrogeologic model developed by Bechtel Nevada (Drellack and Prothro, 1997) provided the definition and distribution of hydrostratigraphic units (HSU) for the test problem. The Pahute Mesa hydrogeologic model consists of structure contour maps of the top of hydrostratigraphic units in the Pahute Mesa area mapped at a resolution of 300 meters (m). A portion of the Pahute Mesa hydrogeologic model, approximately 21 kilometers (km) by 19.5 km by 5,500 m in depth, and rotated 5 degrees to the east was selected for the comparison The locations of the test problem boundaries are shown in Figure A.11-1. The 3-D hydrogeologic model is shown in Figure A.11-2 as viewed from the southwest corner of the test problem area. The complexity of the hydrostratigraphic layering and occurrence of non-vertical faults is illustrated in a cross section of the model shown in Figure A.11-3.

The hydrogeologic model for the test problem included all the hydrostratigraphic layers in the Pahute Mesa hydrogeologic model as well as many of the faults. When using finite-element codes, the grid flexibility is used to attempt to reproduce the stratigraphic contacts and fault contacts. Finite-difference codes do not offer this flexibility; several identical horizontal and uniform grids must be stacked vertically to represent the model layers. Because of this limitation, faults must be represented as vertical. Thus, to use the finite-difference grid in the test problem, the faults will be approximated as vertical.

Each of the HSUs were assigned a hydraulic conductivity, porosity, and fracture volume fraction consistent with current best estimates of these properties.

Boundary conditions for the test problem were obtained from the MODFLOW regional model. The process used was to average the properties of the Pahute Mesa hydrogeologic model to the same resolution as the regional model. The hydrostratigraphic units from the Pahute Mesa hydrogeologic model were then added to the regional model. A visualization application, earthVision (eV), was used to examine the correspondence between the CAU scale model and the regional model. All layers were checked for inversions of layers, and that a constant thickness of at least 1 m vertically was maintained in the hydrogeologic model layering. Using this modified regional hydrogeologic model, the MODFLOW regional flow model was run, without re-calibration, to obtain the heads along the boundaries of the test problem.

Two nuclear tests were chosen for consideration as sources in the test problem, SERENA (U20an) and SCOTCH (U19as). The locations of these tests are shown in Figure A.11-1. SERENA was chosen because of its location on a fault and SCOTCH was chosen because of the depth of the working point and the absence of faults in the immediate vicinity in the Pahute Mesa hydrogeologic model. While SCOTCH is in fact adjacent to the Scotch fault (Warren and LaDelfe, 1991), this fault is not currently included in the Pahute Mesa hydrogeologic model. Since the location of SCOTCH is within the Bullfrog Confining Unit (BFCU) very little transport was expected. To provide a better test for the code, additional simulations considered the source to be translated vertically upward to a location in the Calico Hills Vitric Tuff Aquifer (CHVTA).

The unclassified hydrologic source term used for these sources in the test problem was developed at Lawrence Livemore National Laboratory (LLNL) by Tompson et al. (1999) for CAMBRIC. Of the radionuclides modeled by Tompson et al. (1999), four radionuclides were considered, tritium, Sr-90, Pu-239, and Am-241. 2.04 moles of tritium were introduced instantaneously as a pulse. The other radionuclides entered the flow system as a time-varying flux as determined by Tompson et al. (1999). Tritium and Sr-90 were treated as non-sorbing. Pu-239 and Am-241 were assigned sorption coefficient (Kd) values of 50 and 100 liters/kilogram respectively. These values are consistent with the Frenchman Flat CAU model. Analysis of the BULLION Forced-Gradient Experiment (IT, 1998) suggested values of dispersivities of 10/3/2 m for longitudinal, transverse, and vertical directions

respectively. Since this experiment involved transport on the scale of 100 m, dispersivities were increased to 50 and 5 m for longitudinal and transverse directions for the Frenchman Flat CAU model. Consistent with the Frenchman Flat CAU model, dispersivities used for the Pahute Mesa test problem were 50 and 5 m.

The local geothermal gradient was included in the test problem for the two codes that account for temperature dependence. The value of the geothermal gradient used was 0.011 degrees Centigrade/m.

A.7.0 FRAC3DVS TEST

The development and evaluation of the FRAC3DVS model for the Pahute Mesa (PM) test problem is described in the following section. Details of grid development, incorporation of faults, and flow and transport results are provided. Following the results, the use of FRAC3DVS for the test problem is evaluated with respect to the testing criteria. The FRAC3DVS evaluation was done by an individual with considerable experience with this code.

A.7.1 Grid Development

Around the perimeter of the Pahute Mesa test problem nodes were located so that the heads or fluxes through faces would align directly with the regional model, thus simplifying input of either type of boundary condition from the regional model. Subdivisions around the perimeter of the Pahute Mesa test problem were made at 300-m intervals within the 1,500-m cell spacing of the regional model. Within the PM model limits, a regular grid of nodes at 300-m spacing was constructed using eV. This base array of nodes was then altered along the faults so that at 300-m distances along each fault trace a set of nodes 1-m apart were added. These 1-m node sets straddle the fault. Within 1.6 km of the tests SCOTCH and SERENA the node array including nodes straddling a fault were refined to 150-m node spacing. Within one km of the two events the nodes, including fault node sets were further refined to a 75-m spacing. The nodes were triangulated using Groundwater Modeling System (GMS) and edited so that the 1X300/150/75 m two-dimensional (2-D) elements straddling a fault corresponded correctly to the fault traces. The vertical spacing of nodes varied in the grid and the number of layers varied from 22 to 33 depending on the simulation. The number of nodes and elements also varied depending on the simulation.

In order to accommodate the requested vertical faults, the non-vertical offsets in the base PM geologic Voxel model had to be edited. This conversion was labor intensive and required hand editing of hydrostratigraphic layer top elevations at nodes near or on a fault to lower the geologic model (now converted to eV) in those areas. All layers were checked for inversions of layers, and

that a constant thickness of at least 1-m vertically was maintained in the geologic model layering. eV was then used to back interpolate from the areal model node array/mesh to the elevations on the 300-m eV geologic model layers resulting in definition of the easting, northing, and elevation for each node for each layer in the finite element model mesh. GMS was used to stack the 3D slices representing each hydrostratigraphic layer into FRAC3DVS input format. This completed the initial mesh generation.

A.7.2 Model Properties

A combination of eV and GMS was then used to assign the hydraulic properties to each prismatic element in the completed mesh. This was accomplished by using the eV geologic model of the area and lowering the 1-m thick portions of the base Voxel grid that represent areas where a unit is absent to an elevation slightly lower than the next unit encountered vertically. This was easily accomplished using the eV formula processor and yielded a "clean" (no 1-m spacer units) geologic model of the area. The eV model geologic units, called zones, were then removed one by one to reveal what geologic unit actually occupied the 1-m thick spacer sections of the grid. A *.tiff format figure was made for each layer and imported into GMS as a backdrop from which to assign the correct hydraulic properties to the elements in each flow and transport model layer.

Discrete faults/fractures can be defined within FRAC3DVS in three ways: (1) as an element face with an aperture width (fracture based equations); (2) as an element face with a hydraulic conductivity (fracture based equations); and (3) as a thin element with a high or low hydraulic conductivity (fracture flow approximated). This allows great flexibility in defining faults that, in reality, may be discrete faults/fractures, breccia zones, or otherwise acting as flow barriers or conduits.

The FRAC3DVS preprocessor NP is used to select which faces are chosen by defining the fault traces as selection criteria for the faces in the mesh. Properties such as aperture width for sets of faces are also input.

A.7.3 Boundary and Initial Conditions

Two types of boundary conditions were implemented in the test model, constant head (type 1) and flux (type 3). The constant head boundaries were used around the perimeter of the test model and

were defined areally and vertically from the MODFLOW regional model simulation after incorporation of the Pahute Mesa revisions. The assignment of the perimeter constant heads was done using eV. First the regional model head distribution at the block centered node locations was input as a data set to eV and a high density interpolated grid was generated. The locations of the PM model perimeter nodes were then input and the heads at these finite element locations were backinterpolated from the gridded regional model head distribution.

Constant flux boundaries were used to represent areal recharge to the model. eV was used to convert the flux from the regional model input data for input to the PM test model. GMS was used to select the element faces and assign fluxes for the test model element faces corresponding to the mapped recharge distribution from the eV 2-D regional model based grids. The GMS preprocessor then directly outputs the files required to run NP and FRAC3DVS.

A.7.4 Simulation Results

Flow

A noncalibrated simulation was made using the predesignated hydraulic conductivities for each unit, and a fracture aperture width of 0.00005 m for all faults except the North Timber Mountain Moat fault, which was set to 0.000001 m. It is important to note that no calibration effort was made to match the regional model results.

Radionuclide Transport

High constant concentration sources (1,000 kg/m^3) with no retardation or decay were specified at the location of the SERENA and SCOTCH tests in order to test the areal and vertical numerical stability/dispersion in the transport model. The sources were specified at a number of model nodes (on the order of 10 per test) roughly corresponding to the location of the test cavities. Simulations of 1,000 years were conducted.

Numerical dispersion was not observed. Numerical stability was good; only small negative concentrations (typically < 5kg/ m^3) were predicted areally and vertically at nodes along the periphery of the modeled plume. Beyond these nodes, alternating bands of very small positive and negative

concentrations were present. The solute mass balance error ranged from ~3% at 1 year to ~10% at 1,000 years.

High constant concentration sources (1,000 kg/m3), with no retardation or decay, were specified at a location in the aquifer unit (CHVTA) above the SCOTCH test and near the water table above the SERENA test in order to test the areal and vertical numerical stability/dispersion in the transport model. The sources were specified at a number of model nodes (on the order of 10 per test) roughly corresponding to the location of the test cavities. Simulations of 1,000 years were conducted. Numerical dispersion was not observed. Numerical stability was good; only small negative concentrations (typically < 5kg/m3) were predicted areally and vertically at nodes along the periphery of the modeled plume. Beyond these nodes, alternating bands of very small positive and negative concentrations were present. The solute mass balance error ranged from <1% initially to ~5% by 75 years to ~100% by 1,000 years. The error in mass balance is due to transport above the water table as the model was run in saturated mode.

Low constant concentration sources (2.0×10^{-7} kg/m^3) with no retardation nor decay were specified at a location in the aquifer unit (CHVTA) above the SCOTCH test in order to test the areal and vertical numerical stability in the transport model. Simulations of 1,000 years were conducted. The simulated concentrations grade down over several orders of magnitude moving away from the source. Beginning at the periphery of the modeled plume and moving outward, alternating bands of very small positive and negative concentrations were present. Solute mass balance errors ranged from less than ~0.01% initially to ~2.5% at ~200 years to ~100% at 1,000 years.

In the simulations with sources in the aquifer units, transport was observed from source nodes upward to nodes where the nodal elevations exceed the calculated heads. To address this, simulations were attempted in variably, rather than fully, saturated mode. Once in variably saturated mode, difficulties were experienced in achieving flow field convergence. The authors of the code have suggested that the flow field may converge better if the variably saturated parameters are specified using the van Genuchten function option rather than using the tabular data option. This suggestion has not yet been implemented.

Tritium sources for the SERENA and SCOTCH tests corresponding to the LLNL unclassified hydrologic source term (Tompson et al., 1999) were specified at a number of model nodes (on the

order of 10 per test) roughly corresponding to the location of the test cavities. Initial concentrations were designated for these nodes so as to yield a total initial mass in the system of ~0.006 kg (2.0 moles), consistent with the LLNL hydrologic source term described in Section A.6.0.

To determine the mass balance error, the computed nodal mass change for a given time step (i.e., the 'ins' and 'outs' at various types of boundary nodes) is compared to the change in mass stored in the domain for that time step (calculated from the total mass in the system at the end of the time step minus the total mass in the system at the beginning of the time step). For the tritium simulations, the first term was essentially zero (~$1x10^{-12}$ kg) throughout the simulation, as there is no further mass input after the initial pulse and the initial pulse does not reach any model boundaries. The second term (the change in mass stored in the domain for the time step) was typically $1x10^{-5}$ to $1x\ 10^{-7}$ kg, depending upon the time step size. Comparing these two terms ($1x10^{-12}$ vs. $1x10^{-7}$), the mass balance error is large (5 orders of magnitude). However, as a percentage of the mass in the system, these masses are small. The change in mass stored during any given time step was typically 2 to 3 orders of magnitude less than the mass in the domain at the beginning of the time step.

Numerical stability was not adequate. Moving areally and vertically away from the source, nodal concentrations oscillated between positive and negative values. Altering timestep size did not have any effect towards correcting the output.

Pu-239, Am-241, and Sr-90 sources for the SERENA and SCOTCH tests were specified as one model node per test, with the node location roughly corresponding to the bottom of the test cavities. The sources were specified so as to approximate the pre-designated mass flux profile of the LLNL unclassified hydrologic source term (Tompson, et al., 1999). FRAC3DVS does not currently support specification of constant solute flux nodes in the interior of the model domain (the authors indicate that this can be remedied, but were unavailable to do so for these simulations). Consequently, the desired mass flux was approximated using multiple panel constant concentration source nodes. The concentration was increased relatively quickly in the beginning of the simulation and then slowly thereafter to approximate the desired mass flux profile for each of the three solutes. The solute mass balance error was typically 0.l% to 1.0% per time step.

Numerical stability was not adequate. Moving areally and vertically away from the source, nodal concentrations oscillated between positive and negative values as discussed above for tritium.

A.7.5 Performance Evaluation

Portability

The preprocessor GMS and codes NP/FRAC3DVS can run on both Personal Computer (PC) and UNIX based machines. The computer should have a fast processor (e.g., Pentium II 300MHz or faster) and have 256 Mb of RAM. The earthVision software runs only on UNIX based platforms to date, however within a year the eV software will be ported to PC based machines.

GMS is available free to government projects. The NP/FRAC3DVS software and source code is $3,000. The earthVision software is very expensive to purchase ($70,000+) but can be leased. For most applications involving a calibrated model and its review the use of earthVision is not necessary. It is only during the model construction phase that eV is extremely helpful.

QA Evaluation

All codes have been verified and documentation of the comparisons are included in the software user manuals.

Ease of Use

The FRAC3DVS code itself is a moderately difficult code to use. With the proper preprocessors the code is much more manageable. The input files for NP the pre-run processor are in ASCII format and therefore easy to check and manipulate if necessary. International System (SI) units are preferable for input structure, however other units can be used as long as they are dimensionally appropriate. GMS and eV are very user friendly and require only the self-tutorial to become familiar with the rudiments of the software.

Ability To Represent the CAU Hydrogeology

The FRAC3DVS code can simulate all of the pertinent hydrogeologic features of the mesa area and has good flexibility to represent faults in three ways. The code also has the built-in ability to generate random fractures/faults within the model for variability assessments. The code does not currently have the ability to do nonisothermal-based calculations, but the authors could add this feature given about six months to a year.

Speed of Simulation

Transport simulations on a Pentium II 300 MHz machine for one radionuclide in a steady-state flow field take one to two hours depending on the timestep size. The time required for a steady-state flow simulation is less than six hours, but is highly variable due to various factors such as good starting heads and variable saturation parameters.

A.8.0 SWIFT-98 TEST

The development and evaluation of the SWIFT-98 model for the Pahute Mesa test problem is described in the following section. Details of grid development, incorporation of faults, and flow and transport results are provided. Following the results, the use of SWIFT-98 for the test problem is evaluated with respect to the testing criteria. The SWIFT-98 evaluation was done by an individual with considerable experience with this code.

A.8.1 Model Assumptions

For the code comparison, a Pahute Mesa submodel was constructed based on Dirichelet (constant-head) boundary conditions interpolated from the MODFLOW regional model. For simplification, properties within each formation were assumed to be homogeneous. Radionuclide sources were defined in the vicinity of the SERENA and SCOTCH tests using source terms based upon the LLNL unclassified hydrologic source term model (Tompson, et al., 1999). The SWIFT-98 model was modeled as a water-table aquifer, which allows for nonlinear updating of transmissive and storage terms. The flow system was assumed to be at steady-state over the time-scale of the transport analyses. The base-case was simulated under isothermal conditions. Since large-scale faulting represents a major control on the flow system, two separate flow models were considered. For the SWIFT-98 simulations, the first model implements the fault effects, explicitly, by revising the hydraulic conductivities in each block that the fault traverses. The second model does not consider separate properties for fault blocks. Note that to some degree, faulting is considered, implicitly, since the geometry of the geologic model is also a function of the faulting.

A.8.2 Grid Development

The Pahute Mesa finite-difference grid used in the SWIFT-98 simulations, contains 224,952 rectangular prismatic blocks and is discretized into 103 columns, 104 rows and 21 horizontal layers. Spacings of the grid in the X and Y directions ranged from 75 m near the sources to 300 m on the

boundaries. The block elevations and thicknesses are equivalent to those used in the regional model. Vertical spacing was 150 m at the source elevations.

The northwest corner of the grid is located at the UTM easting and northing coordinates of 542772 and 4132833 m, respectively, and the grid is rotated 5 degrees clockwise at that corner. The top of the model is at an elevation of 2,000 m above mean sea level (amsl).

A.8.3 Model Properties

Flow

The porous media and fracture-zone hydraulic-conductivities used for all the models in the code comparison are described above in Section A.6.0. The exact nature of the application of the properties and property-zones differs for each code. For the SWIFT-98 simulations properties were generated separately for each model block using a FORTRAN-90 pre-processing code, GEO2MOD.for, which uses the Pahute Mesa hydrogeologic model to assemble data files for the simulation model. The hydrogeologic model defines the surfaces for each of the HSUs at the site. GEO2MOD uses the HSU geometry comprising the geologic model in conjunction with a zone file (allowing for varied properties within each HSU) and property files defining properties for each zone within each HSU to assemble the input files for SWIFT-98. A vertical profile of HSU thicknesses is generated at simulation-block centers and properties are then generated assuming parallel combinations of horizontal properties for each block and series combination of vertical properties for each block (i.e., hydraulic conductivities). For isotropic properties (i.e., storage coefficients), an arithmetic average is used). GEO2MOD also considers the influence of faults and fault zones by combining fault properties with the porous media properties generated from the geologic model. Fault properties are combined in parallel to porous-media block properties in the direction of the faults and in series perpendicular to the fault. The trace of all faults is assumed to follow a path from block center to block center parallel (or perpendicular to the block faces). For SWIFT-98, the end product of the GEO2MOD simulation is a binary R1-21 input-card type file (Ward and Benegar, 1998). The faults were explicitly modeled as 20 m wide zones with hydraulic conductivities of 75 m/day.

Radionuclide Transport

Except for porosity data, which are assembled using GEO2MOD as described above, the solute-transport properties, assumed to be homogeneous in these code-testing efforts, are included in the main ASCII input file. The longitudinal and transverse dispersivities used in the simulations were 25 m and 2.5 m respectively. The molecular diffusivity, which includes the effects of diffusion and tortuosity, used in the simulations was 1.3×10^{-10} m^2/s. A description of the source terms for the four radionuclides can be found in Section A.6.0.

A.8.4 Model Boundary and Initial Conditions

Flow

The lateral boundaries of the numerical model are defined using SWIFT-98's steady-state aquifer influence functions (AIF). The steady-state AIF boundary conditions represent an additional flux term added to the finite difference equations that is based upon the hydraulic-gradient between the unknown block pressure and a user-given pressure applied to the outer block-edge and the block transmissivity. The boundary pressures used are based on the linear interpolation of hydraulic-heads generated by the regional MODFLOW model. SWIFT-98's infiltration option was used to apply infiltration to the surface of the model equivalent to that applied in the regional model. The infiltration was apportioned to the blocks based upon the position and surface area of local-model blocks relative to the regional model blocks.

Since the flow simulations were steady-state, the initial conditions were only needed to define the initial transmissivities used in the iterative solution of the non-linear water-table option. The initial condition used to define the flow system was assumed to be static with the water table located at the top of the model.

Radionuclide Transport

For solute transport, the steady-state AIF boundary conditions represent an additional advective flux term added to the finite difference equations. For boundaries with water leaving the system, the flux term is based upon the amount of mass that would be advected out of the system with that water. Water entering the system is assumed to have negligible contaminant concentrations (Reeves et al.,

1986). SWIFT-98's infiltration option assumes water entering the system is clean. For the radionuclide transport, the initial concentrations in the system were considered to be negligible.

A.8.5 Simulation Results

Flow

Two separate steady-state flow models were considered in the simulations. The first model explicitly considers the influence of the faults on the flow-field, by updating the hydraulic conductivities in any blocks traversed by faults. The second model does not include updated conductivities for the fault blocks. For purposes of testing, the inclusion of fault blocks assumed the highest hydraulic conductivity in the expected range allowing a check on the influence of high-velocity zones on the codes ability to efficiently solve the problem. The results showed the marked degree of influence that the fault blocks have on the flow system. The faults are acting as conduits and obscure some of the features of the flow field generated by heterogeneities as reflected in the geologic model.

Radionuclide Transport

Four sets of radionuclide transport simulations were performed using SWIFT-98 in the code comparison. Simulations were performed using each of the two steady-state runs and two different source conditions. For all the SWIFT-98 simulations, the SERENA source was placed in the third layer, but the SCOTCH source was simulated in the third layer for half of the runs and in the fifth layer for half of the runs. The actual working point elevation would place the SCOTCH source in the fifth layer but it was of interest to see how much change in results and solution efficiency would occur if the source was moved from a low conductivity to a higher conductivity zone. Results are presented for the following cases:

- Case 0: Explicit-fault model with the SCOTCH source located at its working point in layer 5,
- Case 1: Explicit-fault model with the SCOTCH source translated vertically upward to the aquifer (CHVTA) in layer 3,
- Case 2: No-fault model with the SCOTCH source located in layer 5,
- Case 3: No-fault model with the SCOTCH source translated vertically upward to the aquifer (CHVTA) in layer 3,

Simulations were performed for the four radionuclides tritium, Am-241, Pu-239 and Sr-90. In total a combination of 16 transient transport simulations were performed using SWIFT-98. Mass balance errors for all simulations were less than 0.01 percent.

Simulation results were compared graphically at 50, 100, and 200 years for all radionuclides and for Am-241 and Pu-239 at 1,000 years. Note results for tritium and Sr-90 at 1,000 years are not considered due to their short half-lives.

Fault-controlled transport for tritium leaving the SERENA site was observed and the lesser spreading of tritium from the SCOTCH site which is located in a lower, less conductive layer further from any fault zones. With fracture flow and decay there was relatively rapid dissipation of the tritium mass from the SERENA site over 100 years. The SCOTCH source tritium levels also show the effects of decay, but are not as influenced by the dilution effects associated with the fault controlled spreading. When the source is placed in layer 3 there is a marked increase in horizontal transport for the SCOTCH source. The increased horizontal transport in the upper layers also combined with the vertical mixing to create a mechanism for a farther distribution of mass in layer 5.

When faults are not included, the tritium transport is more contained than when the faults are explicitly modeled. The need to examine the nature of the fault zones in Pahute Mesa is seen. When the SCOTCH source is moved up into the third layer the degree of spreading increases for the porous-medium (no-fault) model. This is indicative of the need to examine the vertical flow in the source areas.

The pattern for Sr-90 distribution at 50 years is similar to that for the tritium transport, but the more long-term nature of the source and the lesser quantities of material tend to accentuate the degree of fault control of the transport. When the source is moved up to the aquifer, spreading increases.

Little transport is noted at 200 years for Am-241 for Case 3 and 1,000 years for Pu-239 due to the strongly absorptive nature of the radionuclides. Results are similar for all times and cases for these two species.

In addition to simulating Case 3 with the four test radionuclides, Case 3 was also simulated for a conservative (non-decaying and non-sorbing) species subject to matrix diffusion. This allowed for

testing of the dual-porosity option in SWIFT-98. SWIFT-98 also has a dual-permeability option, but since matrix-diffusion is the process of concern, advection in the matrix was ignored in these simulations. The parallel fracture option of the code was used. The matrix blocks were considered to be 2.5 m apart. Two cases were simulated, one using an effective diffusivity of 3×10^{-11} m^2/s, and the second using a diffusivity of 0, for comparison. The potential retarding effects of matrix-diffusion was verified in these simulations.

A.8.6 Nonisothermal Test

In order to test flow and transport under nonisothermal conditions, a test problem was designed that included the local geothermal gradient. There was some difficulty with the nonisothermal model translating the heads from the isothermal MODFOW model to the boundaries of the nonisothermal model. After numerous attempts to obtain a steady-state flow field failed, this test was abandoned. The problem of taking a head from an isothermal model and mapping it in as a boundary condition for a nonisothermal model is discussed further in Section A.9.0.

A.8.7 Performance Evaluation

Portability

The SWIFT-98 code is designed to run on Pentium processors. This version is specifically designed for use in conjunction with the Lahey LF90 Fortran compiler. Since a compiled version of the code is available, the user does not need to have this compiler unless his problem dimensions exceed the present dimensions of the code. The Pahute Mesa test problem needed 256 MB of RAM to avoid paging. The associated pre- and post- processors are also designed to run on Pentium processors. The only restriction on these codes involves GEO2MOD, which generates a binary input file for SWIFT-98 and would need the Lahey LF90 Fortran compiler for compatibility if recompilation was necessary. All the other codes could be compiled with any Fortran compiler. As with SWIFT-98, compiled versions of the pre- and post-processors are available. Results of the simulations are saved in ASCII map files which can be converted to a format that can used in any standard contouring package. For this study, *.CSV (comma separated variables) files that can be used in conjunction with SURFER for Windows were generated by one of the post-processing codes. Window-based EXCEL macro programs were then used to plot the results of simulations from the *.CSV files. The macro programs need to be run on a PC containing Excel and Surfer.

QA Evaluation

The SWIFT genre of codes have undergone verification and field comparison (validation) testing during their development and maintenance by Sandia National Laboratories (Ward et al., 1984). SWIFT-98, which is maintained by HSI-GeoTrans, Inc., has also undergone the same testing procedure as described in Ward et al. (1984). Additionally, all changes made to the code have been tested. The testing was concluded March 1998. All test problems are included on the CD release of the code.

Ease of Use

SWIFT-98 is a difficult code to use, relative to standard groundwater flow and solute transport such as MODFLOW/MODFLOWT. The major difficulties are associated with the rigorous nature of the code, which allows the user to couple density-dependent heat and brine transport with the groundwater flow model. In addition, the user's manual is sometimes unclear as to input needed, but the documented sample problems help (Ward, et al., 1984). Still, for a fully coupled model, the model would probably have to be considered average in difficulty of usage. Some observations noted during this project and the Frenchman Flat modeling project are mentioned below.

Because most of the solute transport parameters needed for radionuclide transport in a steady-state flow field are required in the steady-state flow data set, SWIFT-98 is not always amenable to performing multiple transport simulations based on a single steady-state flow simulation. For problems where the steady-state flow simulation takes an excessive number of iterations to converge, the need to rerun the flow problem for different sets of transport parameters in the same flow-field is inefficient. This can be a problem since upwards to 100,000 iterations may be need to solve a 3-D isothermal flow problem when the system is extremely heterogeneous and the boundary conditions are mainly flux boundary conditions. SWIFT-98 was updated to allow for a change in half-life and absorption coefficient for each transport simulation. This update was easy to implement in the code because these parameters are used in assembling the equations each time step. For parameters such as dispersivity the terms are assembled in conjunction with the steady-state flow run and used as composite terms thereafter (even in restart runs). Updating SWIFT-98 to reassemble the composite terms would be a more difficult procedure. For complex 3-dimensional problems where heat flow is considered, boundary conditions other than no-flux and infiltration must be generated from

larger-scale simulations. Field-study based temperature and pressure profiles from which boundary conditions for the coupled thermal problems can be derived are unlikely to be available. Implementation of the dual-porosity mode in SWIFT-98 is quite easy.

Ability To Represent CAU Hydrogeology

SWIFT-98 is a block-centered finite-difference program and as such is not as flexible in its ability to explicitly incorporate the geometric aspects of the Pahute Mesa geologic model as some finite-element models (i.e., reproducing the shapes of the individual HSUs). Note that this is not true of finite-element models with the assembled equations directly integrated (as opposed to numerically integrated). Finite element codes, which utilize pre-spatially-integrated rectangular prismatic elements, would tend to be no more flexible in defining the geometry of the system than SWIFT-98. With SWIFT-98, the rectangular prism-type blocks can be defined by rows, columns and horizontal layers or in a stair-step fashion by rows, columns, the top elevation of the uppermost block of column i and row j, and the thickness of each block in column/row (i, j). The latter method allows for flexibility in defining the layering of a system, but not the discretization in the plan view. In the plan-view, all blocks along a column or a row must have the same width. In our test simulations, the simpler horizontal layering scheme was utilized. The change of hydrologic properties with depth as defined by HSU's was implicitly considered in block properties. When a block contained material from more than one HSU, a composite property was generated using a preprocessor. The process worked quite well as could be seen by comparing the SWIFT-98 flow model results with the FEHM flow model results. The ability of this methodology to represent the influence of the HSU heterogeneities and fault structures was seen in the SWIFT-98 results.

Speed of Simulation

Table A.11-2 contains a compilation of simulation CPU times for the flow and transport runs. The steady-state flow simulation of the explicit fault model took 23.4 minutes to solve as opposed to 13.1 minutes to solve the "no-fault" flow simulations. These results show that explicit inclusion of faults reduced the efficiency of the L2SOR solver. It should be noted when comparing the solution times to those for the other codes, that the SWIFT-98 simulations also included nonlinear iterations used to adjust physical properties that are a function of the water-table position.

For transport, the differences in simulation times are a function of the number of time steps used in the analysis and the number of linear iterations used in the indirect L2SOR solution scheme. The time stepping schemes used in the Am-241, Pu-239 and Sr-90 analyses were all the same. This was only for convenience, as much larger time steps could have been used for the Pu-239 and Am-241 analyses due to the slower retarded velocities. The short half-life of tritium dictated a need for a smaller time step in the analysis. The time stepping scheme used for the other species generated an oscillatory behavior in the tritium runs that obscured the concentrations at a level of interest.

As can readily be discerned from Table A.11-2, the tritium simulations were slower than most of the other simulations. The solution time was longer for Sr-90 with the source in layer 3 than Sr-90 with the source in layer 5, but the positioning of the SCOTCH source in layer 3 markedly slows down the solution process. The slow rate of solution for Sr-90 is due to an increased number of iterations needed for convergence.

A.9.0 FEHM TEST

The development and evaluation of the FEHM models for the Pahute Mesa test problem is described in the following section. Details of grid development, incorporation of faults, and flow and transport results are provided. Following the results, the use of FEHM for the test problem is evaluated with respect to the testing criteria. The FEHM evaluation was done by an individual with only minor previous experience with this code applied to small one-dimensional flow problems. The time required to set up and run the models for the test problem included training.

A.9.1 Model Assumptions

Flow

Assumptions for the flow and energy transport models discussed by Zyvoloski et al. (1997b) include fluid flow governed by Darcy's law, thermal equilibrium between fluid and rock, immovable rock phase, and negligible viscous heating. An additional assumption not required by the FEHM code but imposed on the test problem was modeling the test problem as a confined aquifer.

Radionuclide Transport

General assumptions discussed by Zyvoloski et al. (1997b) for the reactive transport model are summarized here. Concentrations of solutes are assumed to be low enough that their presence does not affect the properties of the fluid or the flow fields. Chemical reactions do not influence the energy balance and reactions between fluid and solid phases do not affect the hydrologic properties of the rock. Specific assumptions are discussed further by Zyvoloski, et al. (1997b).

Transport in FEHM can be simulated with either finite-element continuity equations (advection-dispersion-reaction equations) or with either of two particle tracking models. With the continuity approach, full reactive transport of multiple interacting reactive solutes can be simulated with either a single or dual continuum model formulation. In the particle-tracking model in the version of FEHM tested, matrix diffusion is solved with a semi-infinite boundary condition between

the fractures. This approach is limited to conditions where the diffusion distance is small with respect to the fracture spacing. A newer version of FEHM recently released incorporates finite fracture spacings into the particle tracking modules to more accurately simulate diffusion when distances between fractures is small.

Additional assumptions not required by the FEHM code but imposed on the test problem include the assumption that the flow system is at steady-state for the transport simulations and that the matrix porosities and fracture volume fractions are homogeneous within a hydrostratigraphic unit. In addition, linear distribution coefficients are dependent only on the radionuclide, and molecular diffusivities and dispersivities are constants, independent of radionuclide or hydrostratigraphic unit. The LLNL unclassified hydrologic source term developed by Tompson et al. (1999) discussed in Section A.6.0 was used at each source location.

A.9.2 Grid Development

Grid Generation Tools

Computational mesh generation tools for this model include the LaGriT Los Alamos Grid Toolbox (George, 1997) suite of grid meshing tools. Developed at LANL, this software provides an integrated system for all grid generation steps, from initial model import, to quality checking and postprocessing of input data, mesh optimization, 3-D mesh post-processing and quality checking, and mesh interfacing with the FEHM flow and transport code, and fault property inclusion into the model.

LaGriT is a library of user callable tools that provide mesh generation, mesh optimization and dynamic mesh maintenance in three dimensions for a variety of applications. Geometric regions within arbitrarily complicated geometries are defined as combinations of bounding surfaces, where the surfaces are described analytically or as collections of points in space. A variety of techniques for distributing points within these geometric regions are provided. Mesh generation uses a Delaunay tetrahedralization algorithm that respects material interfaces and assures that there are no negative coupling coefficients. A specialized subset of LaGriT has been developed specifically for hydrogeologic applications. The LaGriT code is documented in LaGriT User's Manual, LA-UR-95-3608, and maintained online at www.t12.lanl.gov/~lagrit.

Input Data - Surfaces

All grids for the test model are built using the Bechtel Nevada hydrogeologic model of Drellack and Prothro (1997). Whereas the test model is rotated 5 degrees from UTM coordinates to coincide with the MODFLOW regional flow model, the Bechtel Nevada hydrogeologic model is not rotated. The finite-element grid is generated from a point distribution associated with the tops of each HSU, so a new point distribution for each HSU was generated to be consistent with the rotated test domain. The test problem point distribution consists of a rectangle with the corners NW (542909.12, 4132671.15), NE (563530.36, 4130867.03), SE (561856.97, 4111740.08), SW (541235.73, 4113544.2) with 300 m spacing. The entire set of points is a rectangle translated 5 degrees off the x-axis.

The input surface files for the model are created using the test problem point distribution, a ray-shooting technique, and contoured surface files of HSUs in the Pahute Mesa area as developed by Drellack and Prothro (1997). To create a new surface, the test problem point distribution is positioned above a HSU surface and rays are projected through each x,y point on to the HSU surface to find the elevation for each point. This is done with each HSU surface to create the x,y,z coordinate points for each test problem surface. The points are then connected into triangular elements, creating a Triangular Irregular Network (TIN) for each surface of the test problem. Each surface is represented by a TIN sheet of 4,550 x,y,z coordinates and the connectivity for 8,832 triangles.

Input Data – Refinement and Quality Checking

For this model, there are two regions with increased grid resolution representing SCOTCH and SERENA sites. SCOTCH is represented with the x,y polygon with corners at (554833., 4124400.), (556626., 4124243.), (554990., 4126193.), (556783., 4126036.). SERENA has corners at (548714., 4126742.), (550507., 4126585.), (548897., 4128834.), (550690., 4128677.). Each TIN surface for the test problem is refined so that each site has elements of edge size 75 m, surrounded by a transitional buffer with elements of size 150 m. The remaining elements have edge size of 300 m. The final test problem refined surface has 5,275 points and 10,282 triangles. The surface files are tested to ensure that there are no holes, that no triangles overlap, and all triangles are ordered to have their normal vector on the same side of the TIN.

Building the 3-D Tetrahedral Mesh-Create Volumes Between Surfaces

The 3-D model is developed by effectively stacking all the contoured surfaces and populating the volume between the layers with test problem attributes. The TIN sheets are stacked from lowest elevation to highest elevation. The volumes between the surfaces are converted to prism elements (6 nodes, 2 triangle faces, 4 quadrilateral faces) with vertical connections between adjacent layers. Each prism is converted to three tetrahedra so that the final representation is in the form of a 3-D tetrahedral mesh.

Building the 3-D Tetrahedral Mesh-Refinement and Quality Checking

In preparation of a computational grid, thick units are subdivided vertically to provide a more gradual transition to the thinner layers, and to keep the horizontal edges in proportion to the vertical edges. The interfaces are buffered by a lower and upper surface of a distance of 15 m to be able to capture the unit geometry with Voronoi cells after the computational grid is created. A minimum unit thickness of 14 m is chosen so that large aspect ratio tetrahedral and triangular elements are avoided. The grid is checked to ensure there are no holes, and that the geometry correctly represents the Bechtel Nevada hydrogeologic model.

Delaunay Computational Grid

Numerical solution techniques for flow and transport calculations with finite volume and integrated finite difference methods place geometric constraints on the quality of a mesh. To optimize the mesh, reconnection algorithms enhance the quality while preserving the geometry. Reconnection can be done without adding points by allowing connections to flip. In the final mesh, points may be added or removed as needed to create a Delaunay grid with positive coupling coefficients.

The FEHM flow and transport code uses finite volume control volumes for solution of flow and transport equations. Part of the grid generation process is to calculate the Voronoi control volume associated with each node in the grid and the area of the polygonal faces of the Voronoi control volumes. In addition to control volumes, lists are created containing the surface area of each node on the surface of the grid, for use in scaling constant flux boundary conditions. Node sets for each material property are also written, including outside, top and bottom locations for each node.

The final Delaunay computational grid for 3-D calculations contains 138,680 nodes and 839,289 tetrahedral elements and accurately represents the geometry of the Bechtel Nevada hydrogeologic model.

Fault Zones

For the test model, a method developed by LANL was used to model the intersections of fault zones with the predetermined stratigraphy. The new capability provides a way to create fault planes from the surface maps of faults. This routine has the ability to offset a surface map of faults and to connect the original and offset maps to create a fence diagram defined by two-dimensional elements. The offset can be arbitrary, allowing for angled faults or for faults that have moved multiple times in different directions creating a new catalog of elements in the fault zones. In an unstructured grid, the width of the fault zone will vary depending on local resolution. The new routine gives LaGriT the capability to find the intersection of a grid containing two-dimensional elements representing the faults with the stratigraphic grid of tetrahedral elements and catalog which elements (if any) are intersected. This procedure is well documented, and is relatively robust.

A.9.3 Model Properties

Flow

The FEHM model consisted of 22 HSUs. The nodes in a given zone were assigned parameter values for hydraulic conductivity, fracture volume fraction, and porosity. Nodes assigned to faults were given a hydraulic conductivity of 75 m/day consistent with the highest value of the range estimated for fault conductivity. Isotropic hydraulic conductivities were used for the isothermal models and anisotropic hydraulic conductivities for the nonisothermal model.

Radionuclide Transport

The hydrologic source term is described in Section A.6.0 as well as values used for linear sorption coefficients and dispersivities. Source locations for simulations were chosen for each test as the node closest to the working point of the SCOTCH and SERENA tests. The SERENA working point is located in the Calico Hills Zeolitized Composite Unit (CHZCM). Since the location of SCOTCH is within the Bullfrog Confining Unit (BFCU) very little transport was expected. To provide a better test for the code, additional simulations considered the source to be translated vertically upward to a

node in the Calico Hills Vitric Tuff Aquifer (CHVTA). An additional scenario considered in the FEHM test kept the SCOTCH source in the BFCU and prescribed a high permeability chimney extending upwards to the water table.

A.9.4 Boundary and Initial Conditions

Flow

The lateral boundaries of the model were set as specified head boundaries. Values of hydraulic head from the MODFLOW regional model for the test problem area were obtained as described in Section A.6.0. A simple approach was taken for mapping the MODFLOW regional model heads onto the boundaries of the test problem. For every MODFLOW regional model cell along the boundaries of the test problem area, the value of the steady-state hydraulic head at the regional cell center was mapped onto the FEHM boundary nodes that were positioned within the borders of the regional cell face. The top (the water table) and bottom (top of the Pre-Tertiary unit) of the model were considered no-flow boundaries. For simplicity, recharge due to infiltration was not incorporated in the FEHM test but could be included as required. Initial conditions were set at a value of 1,400 m of head for every node in the grid. Simplified boundary conditions were used for the nonisothermal simulations imposing an approximately 200 m head gradient from north to south and no-flow boundaries on the east and west sides. Initial conditions were uniform fluid pressure and temperature distribution determined by a geothermal gradient of 0.011 degrees Centigrade/m.

Radionuclide Transport

For the FEHM test problem the concentration of solute in water entering the system was set to zero, but could be specified as a non-zero concentration. Internal sources can be specified as fixed concentration, instantaneous mass input, or time-dependent mass flux or concentration. For the test problem sources were specified as instantaneous mass input for tritium and as time-dependent mass fluxes for Am-241, Pu-239, and Sr-90.

A.9.5 Simulation Results

A number of situations were considered to provide a range of circumstances for testing the code. Five flow scenarios were considered and 14 transient transport simulations were performed. The number

of transport simulations could be reduced to 14 due to the ability of FEHM to treat multiple chemical species simultaneously. Mass balance errors for all simulations were less than 0.05 percent.

Flow

Five distinct steady-state flow models were developed for the FEHM test. These flow models were:

1. Isothermal, no faults
2. Isothermal, faults included
3. Isothermal, no faults, chimney included
4. Isothermal, faults included, chimney included
5. Nonisothermal, no faults, chimney included.

Inclusion of faults set to a hydraulic conductivity at the high end of the estimated range had a noticeable influence on the flow field. Presence of the chimney either with or without faults did not affect the flow field at the scale of the model domain.

Radionuclide Transport

Four sets of isothermal radionuclide transport simulations were conducted using an instantaneous injection of 2.04 moles of tritium as the source. These correspond to the first four steady-state flow models listed above; no faults, faults included, no faults chimney included, and faults and chimney included. Sources were located at the SCOTCH and SERENA working points and in the aquifer (CHVTA) above SCOTCH.

For the no fault case, tritium did not move far from the source nodes since the working points are located in low permeability units. When the source was moved up to the higher permeability unit, more movement occurred. The model captured the dissipation of tritium concentrations at 200 years due to decay. Time step control was checked to assure the accuracy of the simulations.

When faults were included at the maximum estimated permeability, simulations showed tritium moving from the SERENA cavity into the Boxcar Fault (Figure A.11-1) and away from the source. The sensitivity of transport to fault zone properties was evident. The effect of including a high permeability chimney above the SCOTCH working point was to allow tritium to move upwards from the confining unit into the permeable aquifer above. Once in the CHVTA, tritium spread downgradient.

The ability of the code to simulate multiple sorbing species simultaneously was tested by assigning the time varying fluxes of Sr-90, Am-241, and Pu-239 obtained from the LLNL unclassified hydrologic source term model to the nodes used for the SCOTCH and SERENA working points and the source in the CHVTA. Sorption coefficients were given to Am-241 and Pu-239; Sr-90 was treated as non-sorbing. Only the model that included faults was used. The first simulation considered all three radionuclides being injected at the SCOTCH and SERENA working points. At 50 years, little movement occurred for the sorbing radionuclides; however Sr-90 moved along the faults and downwards. Simulations for the three radionuclides at 200 years showed some small movement for Pu-239 and Am-241 with the shorter-lived Sr-90 concentrations decreasing due to decay. At 1,000 years, Pu-239 and Am-241 moved further along the faults and Sr-90 decayed away. Even when the source was moved upwards to the CHVTA, transport distances were small for the sorbing radionuclides. The non-sorbing Sr-90 moved several kilometers by 50 years but the front retreated at 200 years due to decay.

The capability of representing matrix diffusion processes was evaluated using one of FEHM's particle tracking models. Two simulations were conducted for comparison. In the first, a non-sorbing, non-decaying tracer was released in the CHVTA considering only advection and dispersion but not matrix diffusion. In the second, the same conditions were maintained but in addition, matrix diffusion was modeled. Results showed the code was able to represent the reduction of transport distance due to matrix diffusion. While not included in this evaluation, this particle tracking model does have additional options for sorption and decay. The particle tracking method is also used to represent colloid transport in fractured media.

A.9.6 Nonisothermal Test

In order to test flow and transport under nonisothermal conditions, a test problem was designed which uses slightly simpler boundary conditions than those used in the isothermal test cases. This is due to the effort that would have been required to convert isothermal heads to nonisothermal pressures. Because the density of water depends on its temperature, the conversion would have required several days investment in developing and testing a pre-processor. Therefore, a simpler case with a 200m head gradient north to south and 0.011 degree/m geothermal gradient was specified. A steady-state pressure and temperature field was obtained from the simulation.

Transport under nonisothermal conditions was evaluated using the nonisothermal flow model for the case without faults but including a high permeability chimney extending upwards from the SCOTCH working point to the water table. Sources consisting of 2.04 moles of tritium injected instantaneously were located at the SCOTCH and SERENA working points. Tritium movement was greater as compared with the isothermal case possibly due to increased hydraulic conductivity with temperature.

A.9.7 Performance Evaluation

Portability

Computational mesh generation tools for this model include the LaGriT Los Alamos Grid Toolbox (George, 1997) suite of grid meshing tools. LaGriT is a library of user callable tools that provide mesh generation, mesh optimization and dynamic mesh maintenance in three dimensions for a variety of applications. LaGriT and associated applications require a UNIX based platform. The software, users manuals, and examples are available at no cost from LANL. However, since considerable training is required to use these tools effectively, the grid for this test was developed by staff at LANL. All transfers of data files were done electronically through e-mail attachments or the LANL ftp site.

FEHM is available for a number of platforms including PC. This test was conducted on a Dell Precision Workstation 610 with twin 400 MHz Pentium II Xeon processors and 1 GB of physical memory. A post-processor that runs on a PC is available to convert FEHM output files into a format readable by visualization software such as Tecplot.

QA Evaluation

The FEHM code continues to be subjected to an extensive verification and validation effort and is maintained in a software configuration management system. The verification and validation plan are provided in detail by Dash et al. (1997). The objective of the verification is to test the options and features of the code. This is accomplished by comparing the results of simulations with published analytical solutions and results from other codes. Every time a modification is made to the code, it is tested with a suite of verification problems to insure no errors were introduced or capabilities eliminated. Validation will include modeling of a number of field tests when data become available.

The tests considered in the verification effort are described in detail by Dash et al. (1997) and test results are discussed. A number of additional documents supporting the FEHM code are readily available from LANL. These documents include the user's manual (Zyvoloski, et al., 1997a), and a description of the mathematical models and numerical methods used by FEHM (Zyvoloski, et al., 1997b).

Ease of Use

As discussed above, grid development was done at LANL. The hydrogeologic model and coordinates for source zone refinements were transferred electronically from IT to LANL. The completed grid was transferred electronically back to IT. This process was efficient and LANL staff were responsive to requested modifications.

Since the FEHM test was conducted by an evaluator with only limited previous exposure to FEHM, the five flow models and the fourteen transport simulations presented above were completed with technical support from LANL by telephone. With the availability of LANL technical support, all the simulations presented in this section were completed in seven weeks.

The users manual for FEHM is clearly written describing in detail all the data files, input data, and output files and includes examples for many of the macro control statements. Combining the available documentation with some training and telephone access to an experienced user, FEHM is surprisingly easy to use.

There was little difficulty getting isothermal flow and transport models running. There was some difficulty with the nonisothermal model translating the heads from the isothermal MODFOW model to the boundaries of the nonisothermal model. This was the same problem encountered in the SWIFT-98 test and is not code specific. Namely, one cannot simply take a head from an isothermal model and map it in as a boundary condition for a nonisothermal model. This is due, in part, to the density variation with temperature. Since the non-isothermal model tested here uses a geothermal gradient of increasing temperature with depth, then the pressure at any depth on a boundary needs to account for the variation in density of the water above that location. A pre-processor could be written to effectively integrate the pressure for each nonisothermal model boundary cell. This would entail choosing a reference temperature for the isothermal model from which the boundary pressures are

interpolated. This problem could have been solved with an investment of several days work to write and test a pre-processor. However, for the purposes of demonstrating the nonisothermal capability of FEHM, it was more efficient to use simpler boundary conditions.

Ability To Represent the CAU Hydrogeology

The unstructured 3-D finite-element mesh provided by LANL accurately represents to the resolution of the hydrogeologic model the complex geometry and distribution of the hydrostratigraphic units for the Pahute Mesa test problem. Faults were included through a method that creates fault planes from surface maps of faults. The specific offset across a fault, however, is only as accurate as the resolution of the hydrogeologic model. Faults may be specified as non-vertical, although for comparability with the finite difference code SWIFT-98, vertical faults were used for the test problem. The finite-element mesh was further improved for the test problem to provide higher resolution in the source regions. In addition to the ability of the mesh generating tools to represent complex geometry, the ability of FEHM to represent other attributes and processes characteristic of the CAU hydrogeology were demonstrated in this evaluation. These are, the capabilities to simulate a 3-D system, heterogeneous and anisotropic hydraulic conductivity, point and distributed sources and sinks of water, advection, dispersion, sorption, matrix diffusion and temperature dependent flow.

Speed of Simulation

CPU times in minutes for flow, finite-element transport, and particle tracking transport simulations are shown in Table A.11-3. Times for the steady-state flow simulations with or without faults were similar ranging from 15 to 19 minutes. Times for 200 year tritium simulations increased from 77 to 103 minutes when the source at SCOTCH was moved up to the CHVTA. Similar results were seen for the 1,000-year simulations of the simultaneous transport of three radionuclides, Am-241, Pu-239, and Sr-90. As anticipated, the particle tracking transport model was much faster.

A.10.0 CONCLUSIONS

The first criteria that must be met by the codes as a minimum standard prior to evaluating other criteria is whether or not plausible flow fields and transport results could be produced for the test problem. All three codes produced reasonable representations of steady-state flow fields, Differences between the codes became apparent for the transport simulations.

While FRAC3DVS shows promise for applications such as conceptual model testing of fracture-matrix interactions at smaller scales, difficulties were encountered applying the code to a problem of the scale used for this test. Problems with simulations of non-decaying, non-sorbing tracers included alternating bands of positive and negative concentrations and solute mass balance errors as high as 10 percent when the sources were modeled in confining units. When the source was translated upward to the aquifer unit, mass balance errors were as large as 100 percent due to the model simulating movement of the tracer into the unsaturated zone. The code authors have suggested that this problem could be resolved by using the variably saturated mode and specifying parameters for an unsaturated hydraulic conductivity model. This approach would increase simulation times and memory requirements. Simulations of an instantaneous pulse of tritium as specified by the LLNL unclassified hydrologic source term model showed significant oscillations between positive and negative concentrations. Since reducing the time step did not resolve the problem, the proposed solution is to further refine the grid down gradient from the source. This would increase the number of nodes required for the model. Simulation of the fluxes of Am-241, Pu-239, and Sr-90 from the working points revealed a previously unidentified limitation of FRAC3DVS. The current version does not support time varying solute flux at source nodes in the interior of the model domain. The code authors have stated that this limitation could be removed with further development. Considerable time was spent on this test problem by a modeler with significant experience. Using the LLNL source term, plausible transport results with acceptable mass balance were never achieved with FRAC3DVS. While these problems may be resolved with an investment of additional time and effort, the results of this test argue for eliminating FRAC3DVS from further consideration.

The results of SWIFT-98 simulations conducted for this test were satisfactory and demonstrated the required code capabilities. The only difficulty encountered was for nonisothermal conditions. The problem of translating boundary conditions from an isothermal model to a nonisothermal model was also experienced for nonisothermal simulations with FEHM. A pre-processor can easily be written to map the boundary conditions more accurately, as described in Section A.9.0. The results of the FEHM simulations were satisfactory and demonstrated the required code capabilities.

Criteria set out for evaluating the codes were portability, QA evaluation, ease of use, ability to represent the CAU hydrogeology, and speed of simulation. Portability and the ability to represent the CAU hydrogeology are linked and will be addressed first.

Portability/Ability To Represent CAU Hydrogeology

A major difference between FEHM and SWIFT-98 is how the hydrogeologic model is represented by the computational grid. SWIFT-98 is a finite-difference program and, as such, is not as flexible as a finite-element model at capturing the geometric shape of the individual hydrostratigraphic units. The rectangular prism-type blocks used for the SWIFT-98 grid can be defined by rows, columns and horizontal layers or in a stair-step fashion by rows, columns, the top elevation of the uppermost block of column i and row j, and the thickness of each block in column/row (i, j). The latter method allows for flexibility in defining the layering of a system, but not the discretization in the plan view. In plan-view, all blocks along a column or a row must have the same width. In the SWIFT-98 test simulations, the simpler horizontal layering scheme was utilized. The change of hydrologic properties with depth as defined by HSUs was implicitly considered in block properties by averaging all of the different HSU properties contained in each finite difference block. When a block contained material from more than one HSU a composite property was generated using a preprocessor. The pre-processor also considers the influence of faults and fault zones by combining fault properties with the porous media properties generated from the hydrogeologic model. Fault properties are combined in parallel to porous-media block properties in the direction of the faults and in series perpendicular to the fault. The trace of all faults is assumed to follow a path from block center to block center parallel (or perpendicular to the block faces). The block structure of the grid does not allow for non-vertical faults.

The grid generation tools interfaced with the FEHM code allowed for the accurate representation of the complexities of the hydrogeologic model for Pahute Mesa. The hydrostratigraphic structure as provided by the hydrogeologic model was captured in the finite-element grid. This included units of variable thickness and units that pinch out. Faults were included through a method that creates fault planes from surface maps of faults. With this method the specific offset across a fault was only as accurate as the resolution of the geologic model. While faults for the test problem were vertical, faults may be specified as non-vertical. Higher resolution of the grid was provided in source and down gradient regions. The exact specification of hydrostratigraphic units eliminated the need to use composite properties in the model.

The tradeoff for the finite difference approach is that while there is a loss of resolution and an averaging of properties in some cases, the methodology used to develop the grid is easy to implement and is more portable. The finite-element approach using unstructured grids accurately represents the hydrogeologic model but at the cost of requiring sophisticated grid generation tools. However, FEHM can also be applied to simple structured grids; it is distributed with a structured grid generation program.

Given the available methods, portability and accuracy of representation of the hydrogeology appear to be inversely related performance measures. Methods for developing the model grid and assigning model properties that require only a PC and easy to implement software produce models that average hydrogeologic features and properties. Methods for producing accurate representations of the hydrogeology and assigning model properties more accurately require less common hardware and software capabilities. As such, the measures of portability and accuracy need to be ranked in terms of their relative weights in the decision process. This relative weighting can be interpreted from the discussion of modeling issues provided by the Frenchman Flat CAU model peer reviews. The reviews emphasized the need for modeling approaches that would provide accurate representation of hydrostratigraphic units, accurate representation of faults, higher grid resolution in source areas and accurate transport predictions.

For the purposes of this evaluation, the conclusions of the peer reviews will be considered valid and accuracy will be given more weight than portability. In that case, FEHM with a better ability to represent the CAU hydrogeology but less portability would be ranked above SWIFT-98 for these two

criteria. If the relative importance between portability and accuracy is reversed, a comparison of FEHM and SWIFT using only simple, structured grids would be warranted. Such a comparison was not performed. However, FEHM may have more sophisticated transport capabilities with more options including two particle tracking methodologies as well as finite-element transport.

QA Evaluation

Both SWIFT-98 and FEHM have appropriate verification and validation documentation. In addition, FEHM is maintained in a software configuration management system. Both codes would receive the same ranking for the QA evaluation measure.

Ease of Use

The evaluator for SWIFT-98 described the code in Section A.8.0 as difficult to use and mentioned the vagueness of the users manual. The evaluator for FEHM (Section A.9.0) found the code relatively easy to implement for this problem and the users manual helpful. However, ease of use is a subjective measure and probably provides little distinction between the codes. Based on the quality of the users manuals FEHM would be ranked slightly higher than SWIFT-98 for ease of use.

Speed of Simulation

The CPU times required by FEHM and SWIFT-98 for specific simulations are shown in Tables A.11-2 and A.11-3. Comparing first the time required for simulation of a steady-state flow field with the presence of faults, FEHM required 15 minutes and SWIFT-98, 23 minutes. Transport simulations were consistently faster for SWIFT-98 than for FEHM. The time required to simulate 200 years of tritium transport with faults for sources located at the working points of SCOTCH and SERENA was 64 minutes for SWIFT-98 and 77 minutes for FEHM. When the source was moved up to the CHVTA, SWIFT-98 required 58 minutes and FEHM, 103 minutes. For the simulations with time-varying fluxes the times for simulation of individual radionuclides required by SWIFT-98 must be added for comparison to the multi-species FEHM simulations. Total times required to simulate 1000 years of transport for Am-241, Pu-239, and Sr-90 with faults for sources located at the working points were 106 minutes for SWIFT-98 and 142 minutes for FEHM. When the source was moved up to the CHVTA, simulation times were 120 minutes for SWIFT-98 and 153 minutes for FEHM.

While the transport simulation times for SWIFT-98 were somewhat faster than for FEHM an additional characteristic of SWIFT-98 must be considered when evaluating the speed of simulation for the CAU modeling effort. As discussed in Section A.8.0, SWIFT-98 requires that most of the solute transport parameters required for radionuclide transport in a steady-state flow field be input into the steady-state flow simulation data set. As a result, if a change is desired in the transport parameters, the flow field must be simulated again. This makes it difficult to perform multiple transport simulations based on a single steady-state flow simulation. FEHM does not have this limitation. For the Frenchman Flat CAU model, SWIFT-98 was updated to allow for changes in half-life and adsorption coefficient for each transport simulation without rerunning the flow problem. For parameters such as dispersivity the terms are assembled in conjunction with the steady-state flow run and used as composite terms thereafter (even in restart runs). Updating SWIFT-98 to reassemble the composite terms would be a more difficult procedure. With this limitation, FEHM would be ranked above SWIFT-98 for speed of simulation. If SWIFT-98 was updated to allow changes in all transport parameters without rerunning the flow problem, the rankings would be reversed.

Given the relative rankings of SWIFT-98 and FEHM for the five measures discussed above, FEHM is the code recommended for the Pahute Mesa CAU modeling effort.

A.11.0 REFERENCES

Ashby, S.F. 1996. Par-Flow Home Page: http://www.llnl.gov/CASC/ParFlow/.

Dash, Z.V., B.A. Robinson, and G.A. Zyvoloski. 1997. Software requirements, design, and verification and validation for the FEHM application - A finite-element heat- and mass-transfer code. Los Alamos National Laboratory report LA-13305-MS.

Drellack, S.L., Jr., and L.B. Prothro. 1997. Descriptive narrative for the hydrogeologic model of Western and Central Pahute Mesa Corrective Action Units. Prepared for the U.S. Department of Energy of Energy, Nevada Operations Office. Las Vegas, NV.

Duffield, G.M., J.J. Benegar, and D.S. Ward. 1996. MODFLOWT, A modular three-dimensional groundwater flow and transport model, user's manual version 1.1. Sterling, VA: HSI GeoTrans, Inc.

George, D. 1997. Unstructured 3D grid toolbox for modeling and simulation. Los Alamos National Laboratory Report. LA-UR-97-3052.

Gupta, S. 1996. CFEST, Flow and solute transport, Draft user's manual. Irvine, CA: Consultant for Environmental System Technologies (CFEST).

HSI GeoTrans. 1998. Theory and implementation for SWIFT-98: The Sandia waste-isolation flow and transport model for fractured media. HSI GeoTrans. Sterling, VA.

IT, see IT Corporation.

IT Corporation. 1998. Report and analysis of the BULLION forced-gradient experiment. DOE/NV/13052-042. Prepared for the U.S. Department of Energy of Energy, Nevada Operations Office. Las Vegas, NV.

Katyal, A.K. 1995. CSMoS online model information for BIOF&T-3D. U.S. Environmental Protection – Ada Oklahoma Laboratory. Blacksburg, VA: Draper Aden Environmental Modeling, Inc.

Kipp, K.L., Jr. 1986. HST3D: A computer code for simulation of heat and solute transport in three-dimensional ground-water flow systems. U.S. Geological Survey Water-Resources Investigations Report 86-4095.

Nitao, J.L. 1998. User's manual for the USNT module of the NUFT code, version 2.0. Lawrence Livermore National Laboratory report. UCRL-MA-130653.

Pruess, K. 1991. TOUGH2 - A General Purpose Numerical Simulator for Multiphase Fluid and Heat Flow. Lawrence Berkeley Laboratory Report LBL-29400. Lawrence Berkeley Laboratory. Berkeley, CA.

Reeves, M., D.S. Ward, N.D. Johns, and R.M. Cranwell. 1986. Theory and implementation for SWIFT II. The Sandia Waste-Isolation Flow and Transport model for fractured media. Sandia National Laboratories, NM, NUREG/CR3328.

Scientific Software Group. 1998. Scientific Software Group Home Page: http://www.scisoftware.com.

Tompson, A.F.B., C.J. Bruton, G.A. Pawloski, eds. 1999. Evaluation of the Hydrologic Source Term from Underground Nuclear Tests in Frenchman Flat at the Nevada Test Site. Lawrence Livermore National Laboratory Report UCRL-ID-132300.

Vatnaskil Consulting Engineers. 1988. AQUA3D groundwater flow and transport model. Sudurlandsbraut 50, 108 Reykjavik, Iceland. Vatnaskil Consulting Engineers Home Page: http://www.huglist.is/vatnaskil/index.htm.

Ward, D.S., M. Reeves, and L.E. Duda. 1984. Verification and field comparison of the Sandia Waste-Isolation Flow and Transport model (SWIFT), Sandia National Laboratories. Albuquerque, NM. NUREG/CR3316.

Ward, D.S., and J. Benegar. 1998. Data input guide for SWIFT-98. The Sandia Waste-Isolation Flow and Transport model for fractured media. Release 2.57. HSI-GeoTrans. Sterling VA.

Warren, R.G., and C.M. LaDelfe. 1991. Constraints on a basin-range fault at Pahute Mesa, Southwestern Nevada Volcanic Field. In 6th Symposium on Containment of Underground Nuclear Explosions, Conf-9109114-vol.2. C.W. Olsen, ed. Lawrence Livermore National Laboratory. Livermore, CA.

Waterloo Hydrogeologic, Inc. 1998. FRAC3DVS: Variably-saturated groundwater flow and transport in discretely fractured porous media. Waterloo, Ontario, Canada. Waterloo Hydrogeologic Inc. Home Page: http://www.flowpath.com.

Westinghouse Hanford Company. 1991. PORMC: A model for Monte Carlo simulation of fluid flow, heat, and mass transport in variably saturated geologic media. Report WHC-EP-0445. Richland, Washington.

Zyvoloski, G.A., B.A. Robinson, Z.V. Dash, and L.L. Trease . 1997a. User's manual for the FEHM application - A finite-element heat- and mass-transfer code. Los Alamos National Laboratory report LA-13306-M.

Zyvoloski, G.A., B.A. Robinson, Z.V. Dash, and L.L. Trease. 1997b. Summary of models and methods for the FEHM application - A finite-element heat- and mass-transfer code, Los Alamos National Laboratory report LA-13307-MS.

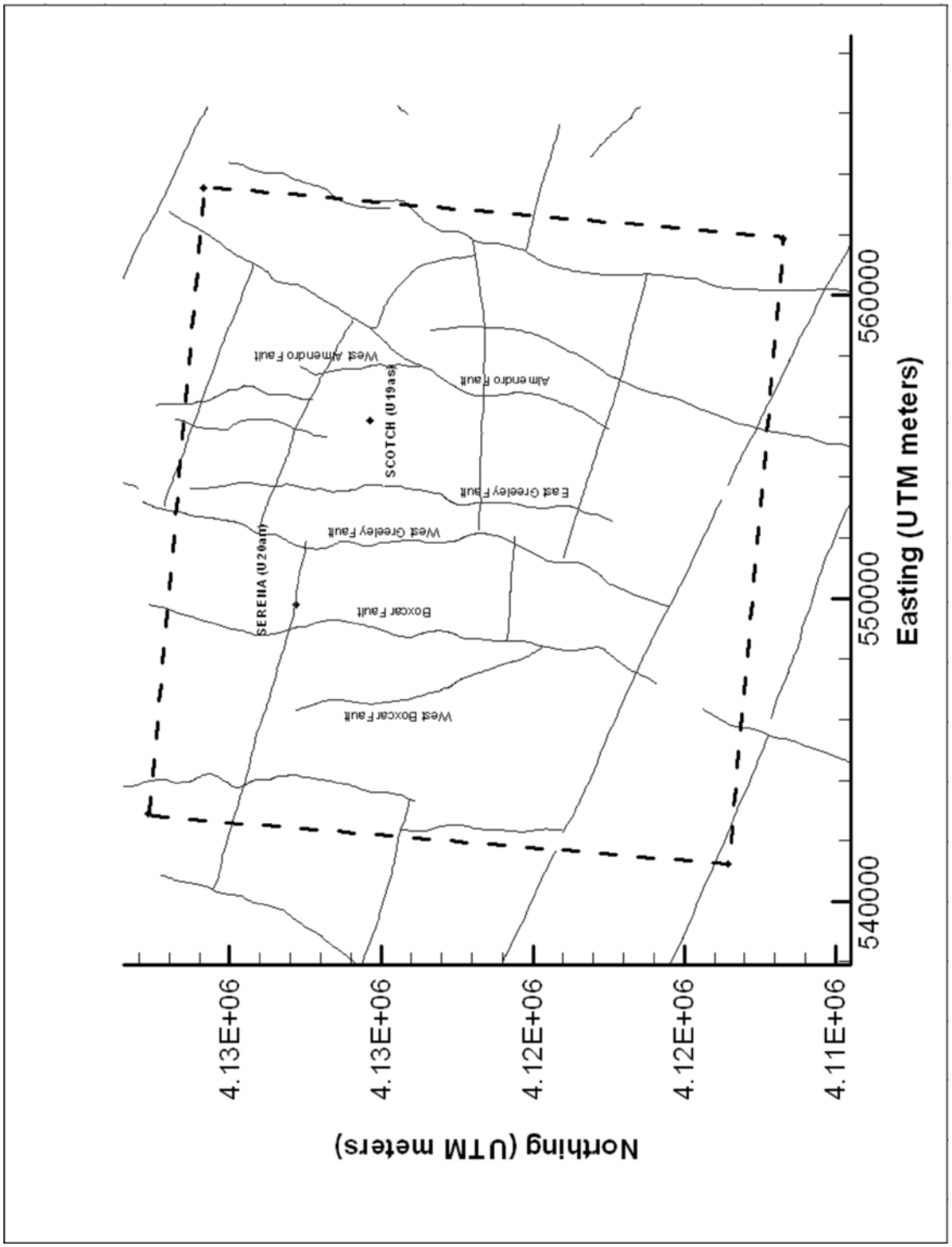

Figure A.11-1
Code Evaluation Test Problem Boundaries, Selected Faults, and Locations of SERENA (U20an) and SCOTCH (U19as) Tests

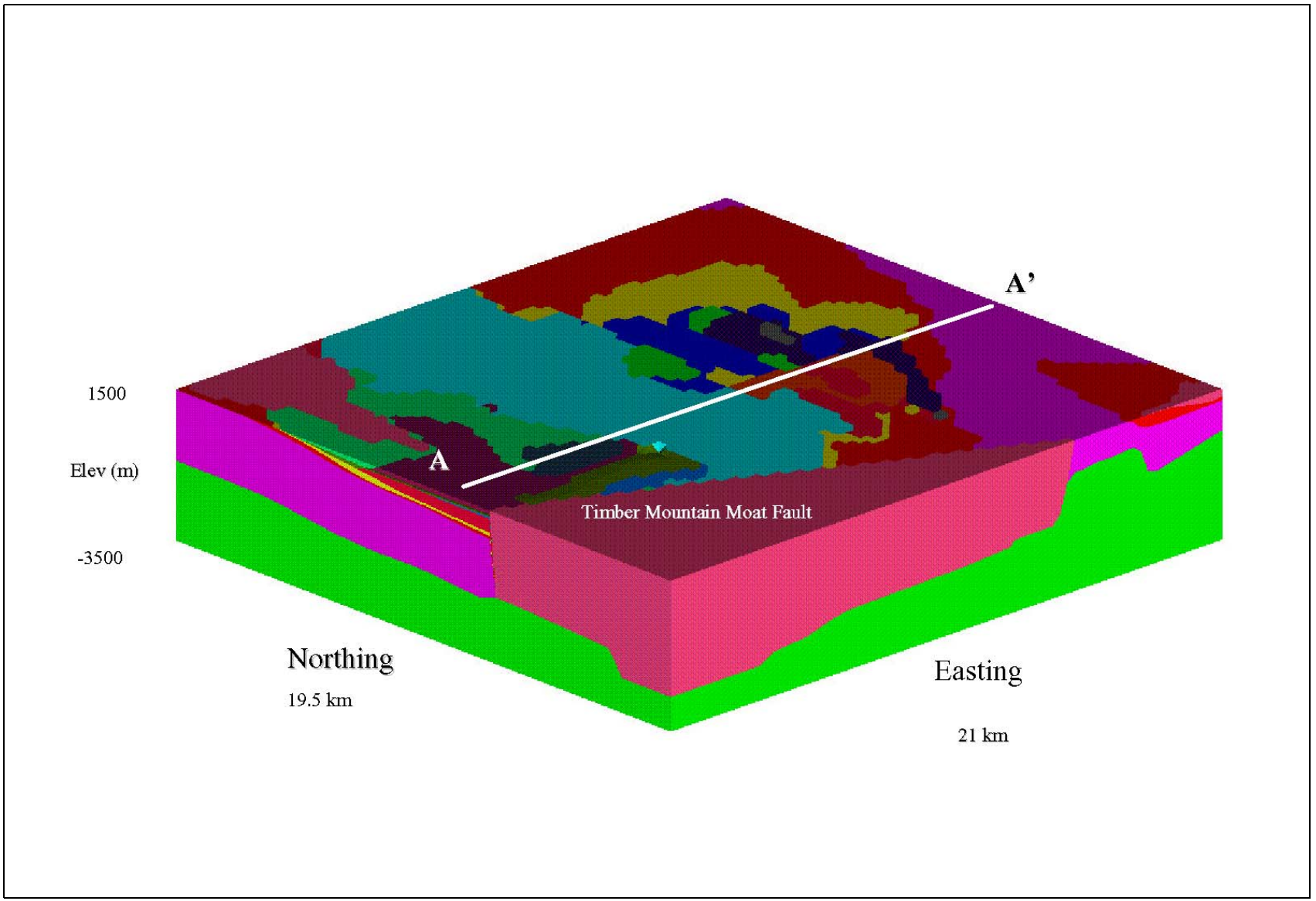

Figure A.11-2
Schematic Representation of the Three-Dimensional Hydrogeologic Model Used for the Code Evaluation Test Problem as Viewed from the Southwest Corner of the Test Problem Area

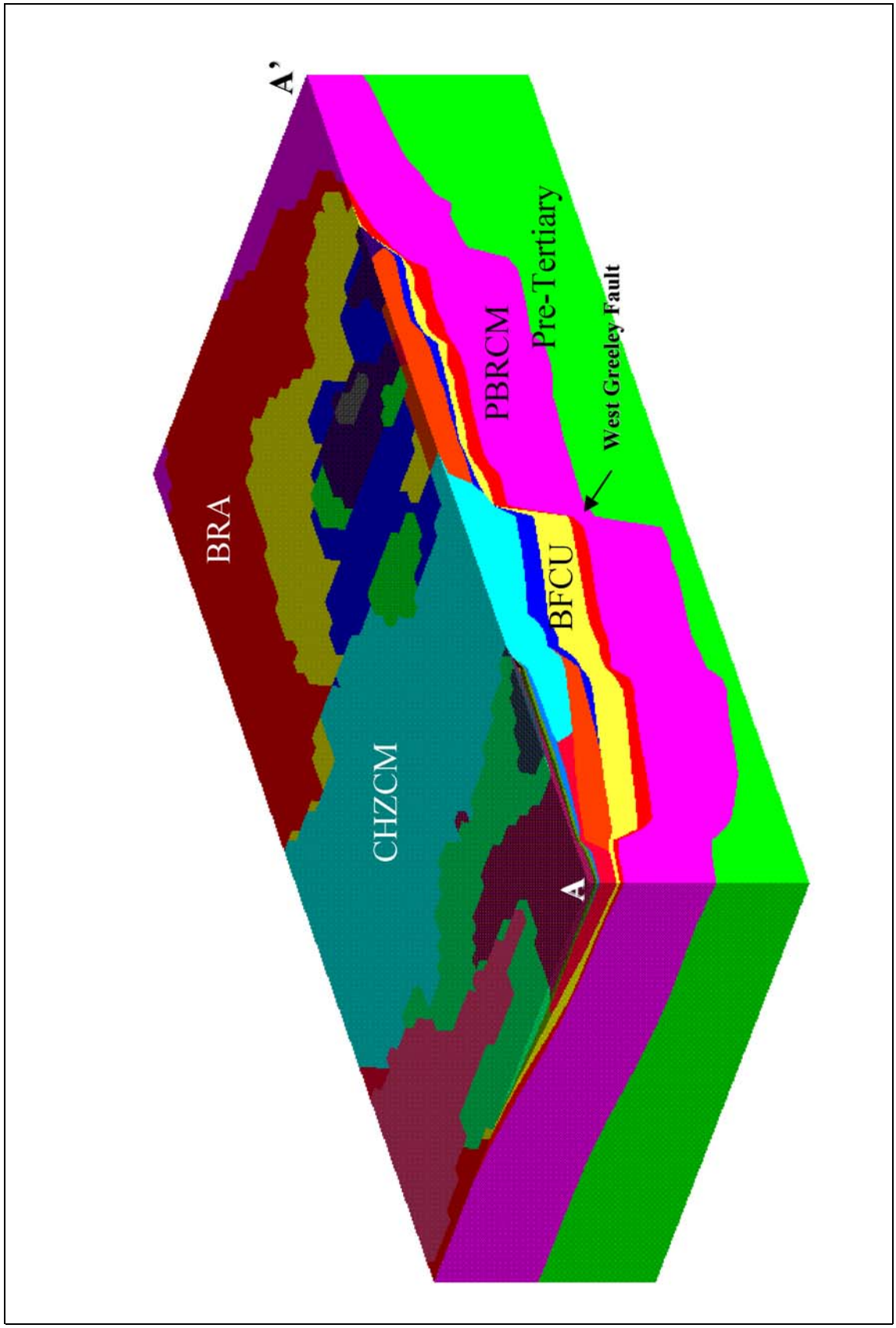

Figure A.11-3
Schematic Representation of a Cross Section Through Test Problem Domain as Viewed from the Southwest
Units identified are Bullfrog Confining Unit (BFCU), Belted Range Aquifer (BRA), Calico Hills Zeolitized Composite Unit (CHzCM), Pre-Belted Range Composite Unit (PBRCM), and Pre-Tertiary Rocks (PreT).

Table A.11-1
Comparison of Candidate Codes by Attribute
(Page 1 of 3)

	AQUA3D	BIOF&T-3D	CFEST	FEHM	FRAC3DVS	HST3D	MODFLOWT
Required Code Attribute							
GENERAL							
Fully three-dimensional	Y	Y	Y	Y	Y	Y	Y
500,000 nodes	?	Y	Y	Y	Y	?	Y
Transient capability	Y	Y	Y	Y	Y	Y	Y
Multiple boundary condition options	Y	Y	Y	Y	Y	Y	Y
Efficient solver	Y	Y	Y	Y	Y	?	Y
Acceptable numerical accuracy	Y	Y	Y	Y	Y	?	Y
Minimal numerical dispersion	Y	Y	Y	Y	Y	?	Y
Acceptable verification and validation	Y	Y	Y	Y	Y	?	Y
Access to source code	N	N	N	Y	Y	Y	Y
FLOW MODEL							
Saturated groundwater flow	Y	Y	Y	Y	Y	Y	Y
Heterogeneous hydraulic conductivity	Y	Y	Y	Y	Y	?	Y
Anisotropic hydraulic conductivity	Y	Y	Y	Y	Y	?	Y
Point/distributed sources/sinks of water	Y	Y	Y	Y	Y	Y	Y
Temperature dependence	Y	N	Y	Y	N	Y	N
Ability to simulate complex geology	Y	Y	Y	Y	Y	?	Y
TRANSPORT MODEL							
Advection	Y	Y	Y	Y	Y	Y	Y
Dispersion	Y	Y	Y	Y	Y	Y	Y
Sorption	Y	Y	Y	Y	Y	Y	Y
Matrix diffusion	Y	Y	N	Y	Y	N	Y
Radioactive decay	Y	Y	Y	Y	Y	Y	Y

Table A.11-1
Comparison of Candidate Codes by Attribute
(Page 2 of 3)

	AQUA3D	BIOF&T-3D	CFEST	FEHM	FRAC3DVS	HST3D	MODFLOWT
Desirable Code Attribute							
Finite element formulation	Y	Y	Y	Y	Y	N	N
Steady state capability	N	N	N	Y	Y	?	Y
Double porosity/double permeability	N	N	N	Y	N	N	N
Multiple solutes	N	Y	?	Y	Y	N	N
Daughter products	N	Y	N	Y	Y	N	Y
Established pre- and post-processors	Y	Y	Y	Y	Y	?	Y

Y = Yes, N = No, ? = no data

	MT3D96	NUFT	PARFLOW	PORMC	SWIFT-98	TOUGH2	3DFEMFAT
Required Code Attribute							
GENERAL							
Fully three-dimensional	Y	Y	Y	Y	Y	Y	Y
500,000 nodes	Y	Y	Y	Y	Y	Y	Y
Transient capability	Y	Y	Y	Y	Y	Y	Y
Multiple boundary condition options	Y	Y	Y	Y	Y	Y	Y
Efficient solver	Y	Y	Y	Y	Y	Y	Y
Acceptable numerical accuracy	Y	Y	Y	Y	Y	Y	Y
Minimal numerical dispersion	Y	Y	Y	Y	Y	Y	Y
Acceptable verification and validation	Y	Y	Y	N	Y	Y	N
Access to source code	Y	N	Y	Y	Y	Y	N

Table A.11-1
Comparison of Candidate Codes by Attribute
(Page 3 of 3)

Required Code Attribute	MT3D96	NUFT	PARFLOW	PORMC	SWIFT-98	TOUGH2	3DFEMFAT
FLOW MODEL							
Saturated groundwater flow	N*	Y	Y	Y	Y	Y	Y
Heterogeneous hydraulic conductivity	N*	Y	Y	Y	Y	Y	Y
Anisotropic hydraulic conductivity	N*	Y	Y	Y	Y	Y	Y
Point/distributed sources/sinks of water	N*	Y	Y	Y	Y	Y	Y
Temperature dependence	N	Y	N	Y	Y	Y	N
Ability to simulate complex geology	Y	Y	Y	Y	Y	Y	Y
TRANSPORT MODEL							
Advection	Y	Y	N	Y	Y	Y	Y
Dispersion	Y	N	N	Y	Y	N	Y
Sorption	Y	Y	N	Y	Y	N	Y
Matrix diffusion	N	Y	N	N	Y	N	N
Radioactive decay	Y	Y	N	Y	Y	N	Y
Desirable Code Attribute							
Finite element formulation	N	N	N	N	N	N	Y
Steady state capability	Y	N	N	Y	Y	N	N
Double porosity/double permeability	N	Y	N	N	N	Y	N
Multiple solutes	N	Y	N	N	N	N	N
Daughter products	Y	Y	N	N	Y	N	N
Established pre- and post-processors	Y	Y	Y	Y	Y	Y	Y

Y = Yes, N = No, ? = no data
*Transport code only. It requires specific discharge information provided by an external finite-difference code, such as MODFLOW.

Table A.11-2
CPU Times in Minutes for SWIFT-98 Test Problem Simulations

Model	Faults	Radionuclides	Source Location	Matrix Diffusion	Simulation Time (Yrs)	CPU Time (min)
Flow	No	-	-	-	-	13
Flow	Yes	-	-	-	-	23
Transport	No	Tritium	SCOTCH/SERENA*	No	200	16
Transport	No	Tritium	SCOTCH CHVTA**	No	200	54
Transport	Yes	Tritium	SCOTCH/SERENA	No	200	64
Transport	Yes	Tritium	SCOTCH CHVTA	No	200	58
Transport	No	Am	SCOTCH/SERENA	No	1000	29
Transport	No	Pu	SCOTCH/SERENA	No	1000	29
Transport	No	Sr	SCOTCH/SERENA	No	1000	31
Transport	No	Am	SCOTCH CHVTA	No	1000	29
Transport	No	Pu	SCOTCH CHVTA	No	1000	29
Transport	No	Sr	SCOTCH CHVTA	No	1000	31
Transport	Yes	Am	SCOTCH/SERENA	No	1000	29
Transport	Yes	Pu	SCOTCH/SERENA	No	1000	29
Transport	Yes	Sr	SCOTCH/SERENA	No	1000	48
Transport	Yes	Am	SCOTCH CHVTA	No	1000	29
Transport	Yes	Pu	SCOTCH CHVTA	No	1000	33
Transport	Yes	Sr	SCOTCH CHVTA	No	1000	58

*Sources were located at the SCOTCH and SERENA working points.
**Source was located in the CHVTA (Calico Hills Vitric Tuff Aquifer) above the SCOTCH working point.

Table A.11-3
CPU Times in Minutes for FEHM Test Problem Simulations

Model	Faults	Radionuclides	Source Location	Matrix Diffusion	Simulation Time (Yrs)	CPU Time (min)
Flow	No	-	-	-	-	19
Flow	Yes	-	-	-	-	15
F-E Transport	No	Tritium	SCOTCH/SERENA*	No	200	71
F-E Transport	No	Tritium	SCOTCH CHVTA**	No	200	82
F-E Transport	Yes	Tritium	SCOTCH/SERENA	No	200	77
F-E Transport	Yes	Tritium	SCOTCH CHVTA	No	200	103
F-E Transport	Yes	Am,Pu,Sr	SCOTCH/SERENA	No	1000	142
F-E Transport	Yes	Am,Pu,Sr	SCOTCH CHVTA	No	1000	153
Ptrk Transport***	Yes	Tracer	SCOTCH CHVTA	No	200	5
Ptrk Transport	Yes	Tracer	SCOTCH CHVTA	Yes	200	5

*Sources were located at the SCOTCH and SERENA working points.
**Source was located in the CHVTA (Calico Hills Vitric Tuff Aquifer) above the SCOTCH working point.
***Particle tracking solute transport model

Appendix B

Investigation of the Influence of Faults on Groundwater Movement in the Pahute Mesa/Oasis Valley Flow Model Domain

(As provided by Los Alamos National Laboratory)
Edward Kwicklis, David Broxton, David Vaniman, and Andrew Wolfsberg

B.1.0 PURPOSE AND SCOPE

The base case hydrostratigraphic model for the Pahute Mesa/Oasis Valley (PM/OV) flow system includes roughly forty-five structural features, including faults, caldera margins, and structural zones of unknown origin (Bechtel, 2002). Calibration of the groundwater flow model for the PM/OV area will require estimates for the hydraulic properties of these features, which by virtue of their considerable spatial extent, exert a potentially important influence on groundwater movement. This influence may arise through the juxtaposition of hydrostratigraphic units (HSUs) with contrasting hydrologic properties or through the hydraulic properties of the features themselves. In view of the large number of hydrostratigraphic units and structural features in the model, a desirable goal is to reduce the number of independent model parameters by obtaining an independent, if qualitative, understanding of the influence of these features on the hydrology of the area before formal calibration of the model is underway.

This report is intended to provide a preliminary assessment for the impact of these features on groundwater movement in the PM/OV flow domain. To make this assessment, an overview for the structural and tectonic/volcanic history of the area is provided, along with a brief narrative describing each of the features in the model domain. This summary includes a qualitative evaluation for the severity of hydrothermal alteration in various areas of the model, a process that would tend to seal features with alteration products and possibly cause them to be barriers rather than conduits for flow. Afterwards, examples of the influence of faults on groundwater movement from the vicinity of the Nevada Test Site (NTS) are reviewed to provide a perspective on the expected range of hydraulic properties and possible hydrologic behaviors. Finally, a more direct assessment of the hydraulic behavior of faults in the PM/OV flow domain is provided by comparing the map of the structural features in the PM/OV flow domain with maps of the potentiometric surface and of the distribution of conservative solutes like chloride and sulfate. Together these maps may indicate the potential and actual groundwater flow directions and suggest the influence of the structural features on these flow patterns. Although the focus of the present investigation is the hydraulic characteristics of the

features themselves, evaluation of the features' hydraulic properties will also necessarily involve a preliminary assessment of the effects of stratigraphic juxtaposition. It is believed, however, that to the extent the hydrostratigraphic model accurately reflects the juxtaposition of various HSUs across these features, the effects of stratigraphic offsets across features is already explicitly incorporated into the PM/OV flow model.

The analysis presented in this appendix focuses on faults and caldera structures associated with the base case hydrostratigraphic framework model (HFM) with the Thirsty Canyon Lineament added. This HFM was chosen because it contains most of the same shallow structural elements that are found in the other alternative HFMs (except for the SCCC HFM), which differ mainly at depth. The selection of the base case HFM for analysis was based solely on the fact that most of its structural features are shared by other HFMs and does not indicate a preference for this geologic interpretation relative to the others. The analysis that follows does not attempt to discriminate between the alternative HFMs and is believed to be general enough that the interpretations presented have applicability to more than just the base case HFM.

B.2.0 HYDROGEOLOGIC SETTING

The Nevada Test Site is located within the southern Great Basin region, an internally drained part of the Basin and Range physiographic province (Laczniak et al., 1996). The region is characterized by a complex geologic history in which episodes of sedimentation, tectonism, igneous activity, and erosion are overprinted in space and time.

B.2.1 Pre-Cenozoic Tectonic, Depositional, and Igneous History

The NTS region is located near the western margin of the Proterozoic craton where up to 11.5 km of Late Proterozoic and Paleozoic clastic and carbonate sequences were deposited in miogeoclinal and foreland basins (Frizzell and Shulters, 1990; Laczniak et al., 1996; Cole and Cashman, 1999). The miogeoclinal deposits include 3,000 m of Late Precambrian to Middle Cambrian quartzite, micaceous quartzite, and siltstone which together form the lower clastic aquitard of Winograd and Thordarson (1975) and the basement confining unit of Laczniak et al. (1996). This widespread confining unit is the hydrologic basement in southern Nevada, and it is a major barrier to lateral groundwater flow in northeastern Yucca Flat, south of Oasis Valley near Beatty, and south of Ash Meadows. Though generally an aquitard, it yields substantial water from fractured quartzite or fault zones in northern Yucca Flat (Laczniak et al., 1996).

The lower clastic sequence is overlain by 4,600 m of Middle Cambrian to Middle Devonian dolomite, limestone, and thin shale and quartzite layers (Laczniak et al., 1996; Cole and Cashman, 1999). This sequence, which is the most productive water-producing zone in the NTS region, forms the lower carbonate-rock aquifer of Winograd and Thordarson (1975) and Laczniak et al. (1996). It conveys most groundwater in the Yucca Flat and Frenchman Flat areas and along the Rock Valley fault system, and it is a significant aquifer southward from the southern part of Yucca Mountain into the Alkali Flat-Furnace Creek Ranch subbasin (Laczniak et al., 1996).

The region remained a stable continental shelf until Late Devonian time when tectonism in the Antler orogenic highland resulted in the emplacement of deep-water sediments over miogeoclinal deposits. This highland, which formed to the west and north of the NTS, was the source of up to 2,400 m of Late Devonian and Mississippian siltstone, sandstone, and conglomerate to the NTS region; minor limestone was also deposited at this time (Frizzell and Shulters, 1990; Cole and Cashman, 1999). Because of their generally low permeability, Winograd and Thordarson (1975) termed these rocks the upper clastic aquitard, and Laczniak et al. (1996) called them the Eleana confining zone. The upper clastic aquitard occurs in a narrow arcuate band in the subsurface that extends southward along the west side of Yucca Flat to CP Hills and then westward across northern Jackass Flats and the north end of Yucca Mountain to Bare Mountain (Laczniak et al., 1996). It is the major confining unit along the boundary between the Alkali Flat-Furnace Creek Ranch and the Ash Meadows subbasins in western Yucca Flat and northern Jackass Flats (Laczniak et al., 1996). Locally it yields water from fracture zones in quartzite and limestone.

A stable platform shelf was re-established during the Early Pennsylvanian and persisted until the Early Permian; 1,100 m of shallow-water carbonates were deposited on this platform in the NTS region (Frizzell and Shulters, 1990). This sequence and older carbonates thrust on top of the UCCU form the upper carbonate-rock aquifer of Winograd and Thordarson (1975) and Laczniak et al. (1996). The upper carbonate aquifer is a local aquifer in western Yucca Flat, but generally has a limited areal extent and does not substantially effect regional groundwater flow (Laczniak et al., 1996).

Late Permian and Mesozoic sedimentary rocks are absent in the NTS region and probably were never deposited there (Stewart, 1980). Small Cretaceous granite stocks intrude Early Paleozoic deposits north of Rainier Mesa and Yucca Flat, but are of limited extent. These stocks locally yield water from fracture zones, but they are relatively impermeable and are classified as aquitards (Laczniak et al., 1996).

The main pre-Cenozoic structures in the NTS include the east-verging Belted Range thrust fault and the west-to northwest-verging CP thrust system (Cole and Cashman, 1999). The Belted Range thrust is the principal contractional structure at the NTS with Late Proterozoic and Cambrian clastic rocks transported eastward over clastic and carbonate rocks as young as Late Mississippian. The fault trace

extends eastward from Bare Mountain to Shoshone Mountain before turning northward to Rainier Mesa and the Belted Range (Potter et al., 2002). The thrust plate is generally simple and displays little folding or internal disruption (Cole and Cashman, 1999). The nominal stratigraphic throw on the thrust is about 7 km. Both the fault and rocks in the hanging wall generally dip at a moderate angle to the west. The footwall of the Belted Range thrust is characterized by a broad zone of duplex faulting with east-verging folds and by imbricate thrust faults (Cole and Cashman, 1999). The amount of lateral displacement along the Belted Range thrust is not known, but juxtaposition of laterally equivalent miogeoclinal facies across the fault indicates significant lateral shortening (Cole and Cashman, 1999). The timing of compressional deformation in the NTS region is poorly constrained, ranging from Late Permian to Late Cretaceous (Cole and Cashman, 1999).

The west-to northwest-verging CP thrust system forms a parallel zone of thrusts and folds east and south of the Belted Range thrust (Cole and Cashman, 1999; Potter et al., 2002). Folds in the CP thrust system are typically overturned and developed kink-style bands. Thrust faults tend to be local in nature, and they are characterized by large stratigraphic throws and extreme overturning of footwall strata (Cole and Cashman, 1999). The thrust faults appear to be steep structures that flatten upwards. CP folds and thrusts deform the leading edge of the pre-existing Belted Range thrust system (Cole and Cashman, 1999).

B.2.2 Cenozoic Volcanic and Tectonic History

The Middle to Late Miocene southwestern Nevada volcanic field is the erosional remnant of an extensive volcanic plateau broken locally by normal faults; the plateau once covered an area of more than 11,000-km^2 (Christiansen et al., 1977). Volcanism from a complex of overlapping calderas and smaller eruptive centers was centered on Timber Mountain and Pahute Mesa (Byers et al., 1976, Christiansen et al., 1977). The volcanic field is dominated by metaluminous and peralkaline high-silica rhyolites and subordinate trachytes, dacites and basalts (Christiansen et al., 1977) erupted between >15 and 7.1 Ma (Sawyer et al., 1994; Fleck et al., 1996). Pahute Mesa and the two youngest calderas, Timber Mountain and Black Mountain, are the largest intact remnants of the volcanic plateau (Christiansen et al., 1977).

The southwestern Nevada volcanic field has been hypothesized to lie along a right-stepped zone within the NW trending Walker Lane Belt, a continental-scale lineament that separates areas of the

Great Basin with north-south structural features from those in the southwest with predominantly northwest structural trends (Carr, 1990). The most intense period of volcanism occurred from 15 to 11.5 Ma (Sawyer et al., 1994) with major ash-flow sheets erupted from the central caldera complexes (Byers et al., 1976, Christiansen et al., 1977). The locations and approximate geometries of the Silent Canyon caldera complex, the Claim Canyon caldera, the Timber Mountain caldera complex, and the Black Mountain caldera are reasonably well known through a combination of surface mapping, geophysical investigations, and subsurface data from drilling (e.g., Healey, 1968; Orkild et al., 1969; Byers et al., 1976; Christiansen et al., 1977; Noble et al., 1984; Ferguson et al., 1994, Hildenbrand et al., 1999; Grauch et al., 1999). Calderas older than the Claim Canyon caldera are completely buried by younger rocks or were partly destroyed where they coincide with younger caldera structures. The locations of source calderas for older major ash-flow sheets, including the Topopah Spring, Tram, Lithic Ridge, Tub Spring, and Redrock Valley Tuffs, are either unknown or poorly constrained (Byers et al., 1976, Christiansen et al., 1977; Sawyer et al., 1994). In addition to calderas, smaller vents were sources of numerous small-volume ash flows and lavas throughout the area.

Because of its youth and moderate level of erosion, the structure of the Timber Mountain caldera complex is better known than other calderas in the Southwestern Nevada volcanic field. This caldera complex formed during two major eruptions. The Rainier Mesa caldera formed during the initial collapse of the Timber Mountain caldera complex with eruption of 1200 km^3 of the ash-flow tuffs that make up the 11.6 Ma Rainier Mesa Member of the Timber Mountain Tuff (Byers et al., 1976, Christiansen et al., 1977; Sawyer et al., 1994). About 250,000 years later, the Ammonia Tanks caldera formed during eruption of an additional 900 km^3 of ash-flow tuffs that make up the Ammonia Tanks Member of the Timber Mountain Tuff (Byers et al., 1976, Christiansen et al., 1977). The Timber Mountain caldera complex consists of a central cauldron block approximately 24 km in diameter that subsided 1.3 to 3.8 km along a continuous ring fracture fault or series of faults (Christiansen et al., 1977). The central cauldron block probably collapsed in piecemeal fashion with ash-flow tuffs accumulating above cauldron blocks simultaneously with subsidence (Carr and Quinlivan, 1968; Christiansen et al., 1977). During and after collapse of the central cauldron block, the steep, unstable walls of the caldera slumped as a series of intact foundered blocks, megabreccias of various sizes, and debris slides and flows that are intercalated with intracaldera tuffs and bury the caldera floor (Byers et al., 1976; Christiansen et al., 1977). Shortly after collapse, resurgence of magma caused the floor of the caldera to rise at least 1220 m as a 19 x 13 km structural dome,

elongated to the northwest (Carr and Quinlivan, 1968; Byers et al., 1976, Christiansen et al., 1977). Some of the uplift occurred along the inner edge of the pre-existing caldera ring fracture zone, which in places is intruded by granite porphyry, basalt, rhyolite, and silicic tuff dikes (Carr and Quinlivian, 1968). The resurgent dome is broken by a complex system of normal faults, including an apical graben system that parallels the long axis of the dome.

Volcanism in the southwestern Nevada volcanic field coincided with the Miocene peak of extensional deformation in adjoining parts of the Great Basin (Sawyer et al., 1994). Aerial distributions and thickness variations of volcanic rocks of the field show that Basin and Range normal faulting occurred before, during, and after eruption of the major ash-flow sheets (Christiansen et al., 1977). Most of the extensional deformation in the NTS regional probably occurred between 8 and 16 Ma (Sawyer et al., 1994). Table 5 of Warren et al. (2000) shows that systematic, progressive offset occurred from >13.1 Ma to <9.6 Ma along the West Boxcar and West Greeley faults. This offset totals nearly a kilometer across each of these Basin and Range normal faults. Within the southwestern Nevada volcanic field, most of the extensional strain was accommodated in areas marginal to the central complex of overlapping calderas (Christiansen et al., 1977; Sawyer et al., 1994). For example, displacement and tilting along generally north-trending normal faults have produced features such as the Belted Range, Yucca Flat, Yucca Mountain, Crater Flat, and Bare Mountain. Although broken by north-south normal faults, the central complex of calderas is not overlapped by fault controlled alluvial basins (Christiansen et al., 1977; Sawyer et al., 1994). In addition, detachment faulting in the Bullfrog Hills area with upper plate movement to the west and northwest occurred approximately between 12.7 and 9.5 Ma. Taken together, these features indicate that structural activity was most intense within the central complex of overlapping calderas during their formation, but faulting shifted to the periphery of the central complex following the period of intense volcanism, possibly because of the greater mechanical strength of the granitic intrusive rocks underlying the calderas.

B.2.3 Description of Major Structural Features

Table B.7-1 lists the names, types, and abbreviations used for structural components of the Pahute Mesa – Oasis Valley Model Area, along with notes relating to orientation, offset, and measures of reactivation by underground testing. The locations of these structural features are shown in

Figure B.7-1. The data in this table are based largely on Bechtel (2002) with supporting information from other sources. Estimates of the fault offset of near-surface units are cited from McKee et al. (2001) and evidence for reactivation by underground testing follows the summary by Frizzell and Shulters (1990). These additional sources are added in order that the evidence of offset may be compared with fault offsets represented at depth in the model, and because recent fault reactivation reflects likely localization of upper crustal weakness but also likely zones where new fault and fracture openings might enhance groundwater flow.

B.2.3.1 Architecture and Mineralization of Faults

The surface geometry of small-scale faults (<10 m offset) has been characterized within the region surrounding Yucca Flat (Minor, 1995), which borders the eastern part of the model area. Measurements for 906 of these small-scale faults, shown in Figure 3 of Minor (1995), show two equal populations, a narrow one with a dip of 90 degrees, and a broader population with a dip of 77°. Very few of these faults have dips <60 degrees. But geometric details, including the width of fractured and pulverized zones, attitudes of fault zones, and movement direction along fault zones, have not been determined for major faults within the southwestern Nevada volcanic field (SWNVF). Warren and LaDelfe (1991) found an average dip of 82° degrees from the surface to 500 m depth for an en-echelon major fault system at Pahute Mesa, based on comparison of stratigraphic units on opposite sides of these faults.

Geologists and hydrogeologists have identified two primary components, or architectural elements, for faults in rocks of high strength. These elements are an impermeable core zone that has accommodated most of the fault slip and a highly permeable damage zone that brackets the core zone (Goodwin et al., 1999; Caine and Forster, 1999; Evans et al., 1997; Forster and Evans, 1991). In contrast, the single primary element for faults in rocks of low strength is typically an impermeable deformation band (Goodwin et al., 1999; Antonelli et al., 1999). In the PM/OV flow domain, lavas and welded tuffs are relatively high strength rocks, whereas nonwelded tuffs are of relatively low strength (Blankennagel and Weir, 1973).

In volcanic terrains, faults are potential conduits for hydrothermal fluids, whose past movement is recorded by the presence of hydrothermal minerals within the faults. Such mineralization is well studied for the Yucca Mountain region of the SWNVF (e.g., Levy et al., 1999; Carlos et al., 1995;

Carlos et al., 1993), and within the Pahute Mesa source region (Benedict et al., 2001). This generally associated hydrothermal alteration, depending on its intensity, can completely fill the permeable portions of faults, converting them to impermeable barriers (Reiter, 1999). Such mineralized, now impermeable faults can be broken by subsequent events to become permeable once again (Tamanyu, 1999). Little is known about the distribution and timing of such hydrothermal alteration as related to structures of the SWNVF, and whether that alteration may caused faults that were once conduits to become barriers to fluid flow. However, in most instances, clay formation, carbonate cementation, and zeolitization localized along faults and other deep structures are likely to reduce hydraulic conductivity while increasing the retention of solutes within the advancing groundwater. Within the SWNVF, caldera formation provides the most likely source for hydrothermal alteration (Noble et al., 1991), although intense, hydrothermal alteration is also associated with detachment faulting within the Bullfrog Hills (Jorgensen et al., 1990). Known calderas within the Oasis-Valley Pahute Mesa flow path include the Ammonia Tanks and Rainier Mesa calderas of the Timber Mountain caldera complex, and the Area 20 and Grouse Canyon calderas of the Silent Canyon caldera complex.

B.2.3.2 Alternative Structural Treatments

Several structural alternatives to the present structural construction within the Pahute Mesa – Oasis Valley Model are described in Bechtel (2002) and summarized in their Table 6-1. These alternatives were presented to acknowledge the uncertainty in some facets of the hydrostratigraphic model. These uncertainties relate to the shape of the caldera margins (arcuate versus rectilinear), the continuity and offset of hydrostratigraphic units across faults at depth, changes in the dip of the faults with depth, the distribution of collapse breccias along caldera margins, the depth to basement rock, and the need for more (or less) structural and hydrostratigraphic detail, among other issues. The present report does not consider the potential impact of alternative interpretations of the structure and hydrostratigraphy in the PM/OV flow domain nor does it attempt to discriminate between these alternatives. The analyses of fault behavior is limited to structural interpretations presented in the basecase model, with the addition of the Thirsty Canyon lineament as presented in Figure 6-5 of Bechtel (2002).

B.2.3.3 Normal Faults (NF)

Normal faults of the modeled area trend generally between N 30º E and N 47º W; dips on all of these faults are to the west, with the exception of the Bare Mountain fault, Claim Canyon fault #2, and the

Hogback fault, which dip to the east (Table B.7-1). Note that the dip angle on all of these faults is assigned a nominal value of 80º; in the absence of direct evidence to the contrary this is a reasonable average dip angle for the shallow segments of normal faults in the Basin and Range (McKee et al., 2001). Warren and LaDelfe (1991) found that average dip to 500 m depth along a pair of en-echelon faults at Pahute Mesa was 82º, in line with the general use of a nominal 80º dip. Some studies of Basin and Range structure indicate that dips on normal faults tend to flatten with depth, but the depths at which this occurs are below the modeled volume.

Many of the normal faults within Pahute Mesa are named for nearby underground tests that were conducted beneath the mesa (Halfbeak, Rickey, Estuary, Almendro, Greeley, Boxcar, Handley, and Purse). Most of these faults were reactivated by underground testing, as summarized by Frizzell and Shulters (1990). Faults and other structural features are numbered so that they can be more easily located on Figure B.7-1.

Almendro Fault (1) and West Almendro Fault (2)

The Almendro and West Almendro normal faults occur in the eastern part of the Silent Canyon Caldera Complex. As designated within the Hydrostratigraphic Model, the Almendro fault terminates to the south at the Southern Pahute Mesa Structural Zone (41) and is continuous to the north with the buried Halfbeak Fault (15). The West Almendro fault branches from the Almendro approximately where this transition occurs and trends more northerly. The Almendro and West Almendro fault segments have experienced some degree of reactivation as a result of underground testing (Table B.7-1), with most of this reactivation centered on the Almendro fault where it crosses Silent Canyon caldera structural margin (29) and extending about 3 km south of this margin. The near-surface offset of ~150 m is equal to the maximum cited across the Silent Canyon Caldera Complex by McKee et al. (2001).

Bare Mountain Fault (3)

The Bare Mountain fault extends south from the Hot Springs Lineament (34) and extends beyond the southern margin of the modeled block. This is one of the few normal faults in the model that dips to the east. This fault defines the western margin of Crater Flat, a basin bounded on the west by Bare Mountain (one of the few exposures of Paleozoic rocks within the modeled area) and to the east by a complex series of east-tilted tuff blocks. The Bare Mountain fault may have originally been a

strike-slope fault that has been reoccupied by a younger and mostly north-trending normal fault (Fridrich, 1998). The Bare Mountain fault juxtaposes a thick sequence of lower carbonate aquifer (LCA and LCA3) on the west against the Yucca Mountain – Crater Flat Composite Unit (YMCFCM) and Pre-Belted Range Composite Unit (PBRCM) on the east (Bechtel, 2002, Cross-section A-A').

Beatty Fault (4)

The Beatty fault is a short, buried normal fault segment in the southwestern portion of the modeled area. Its limited extent (<6 km) makes it a relatively minor contributor to the structural system within the modeled area.

Big Burn Valley Fault (5)

This NW-trending, SW-dipping normal(?) fault is shown in Figure 3-1 of Bechtel (2002), crossing the Belted Range thrust (31) and passing out of the eastern margin of the modeled area. However, this fault is not described in Table 3-1 of that report. Frizzell and Shulters (1990) show this fault as a NW-trending normal fault, down to the SW, with only minimal offset since the Oligocene.

Black Canyon Fault (6)

This fault is listed in Table 3-1 of Bechtel (2002) but could not be located on Figure 3-1 in that report.

Boxcar Fault (7) and West Boxcar Fault (8)

The Boxcar fault extends from the Northern Timber Mountain Moat Structural Zone (38) north across the western part of the Silent Canyon Caldera Complex. This is a major normal fault that drops the Trail Ridge Member of the Thirsty Canyon Tuff to the west against older Thirsty Canyon and Timber Mountain units to the east (Frizzell and Shulters, 1990). The West Boxcar fault branches from the Boxcar fault and trends to the NNW. Both of these fault segments have experienced extensive reactivation as a result of underground testing. Near-surface offset of ~60 m is cited for both the Boxcar and West Boxcar faults by McKee et al. (2001); these offsets are maintained in the Pahute Mesa – Oasis Valley Model (e.g., cross-section C-C' in Bechtel 2002). However, Table 5 of Warren et al. (2000) shows that offset increases to ~1,100 m for deeper units that predate the Area 20 caldera. The increase in offset with depth indicates reactivation of fault movement over long time spans, a process that may occur along many of the normal faults within the modeled area.

Claim Canyon Fault #1(9) and Claim Canyon Fault #2 (10)

The Claim Canyon normal faults are listed as #1 and #2 in Table 3-1 of Bechtel (2002); one of these faults is marked as "Claim Canyon B" on Figure 3-1 in that report but has the approximate azimuth (5º E) attributed to Claim Canyon #1. The other Claim Canyon fault is not labeled in Figure 3-1 of Bechtel (2002).

Estuary Faults (East [11] and West [12])

The East Estuary fault (buried) and West Estuary fault (exposed) are short, parallel fault segments that lie within the north-central part of the Silent Canyon Caldera Complex. Although within the area of extensive underground testing, there is no evidence for reactivation along either of these fault segments. McKee et al. (2001) cite near-surface offset of ~60 m on the East Estuary fault.

Greeley Faults (East [13] and West [14])

The West Greeley fault crosses the entire Silent Canyon Caldera Complex; the East Greeley fault parallels the West Greeley but is less extensive and partially buried. Both faults have experienced some reactivation as a result of underground testing (Table B.7-1). Cross-section C-C' of Bechtel (2002) indicates that the West Greeley fault has more significant displacement of hydrostratigraphic units than the East Greeley fault, particularly in disruption of continuity within the Belted Range Aquifer (BRA). This variation in fault offset and stratigraphic juxtaposition is in accord with the analysis by McKee et al. (2001), which lists ~150 m of near-surface offset along the West Greeley fault but only ~30 m along the East Greeley. Table 5 of Warren et al. (2000) indicates that offset along the East Greeley fault increases to ~850 m for units that predate the Area 20 caldera. As with the Boxcar faults, the increase in offset with depth indicates reactivation of fault movement over long time spans.

Halfbeak Fault (15)

The Halfbeak fault extends north from the Almendro fault (1) across the northeastern portion of the Silent Canyon Caldera Complex. Cross sections of the modeled area in Bechtel (2002) indicate only moderate offset of the Bullfrog Confining Unit (BFCU) along this fault, without significant juxtaposition of hydrostratigraphic units beneath the water table within the caldera complex.

Handley Fault (16)

The Handley fault includes an exposed segment northeast of the Black Mountain Caldera topographic margin and a buried segment within the margin. The exposed segment has experienced extensive reactivation as a result of underground testing (Frizzell and Shulters, 1990). Cross sections of the modeled area in Bechtel (2002) indicate only moderate offset of hydrostratigraphic units beneath the water table along this fault; McKee et al. (2001) report only ~30 m of near-surface offset along the exposed fault segment.

Hogback Fault (17)

The Hogback fault is a buried fault that extends along the southwestern margin of the modeled area. At depth, this fault separates Pre-Tertiary sedimentary rocks on the west from the volcanic aquifer system to the east (Grauch et al., 1999). At higher stratigraphic levels, the northern portion of this fault places the Pre-Belted Range Composite Unit (PBRCM) on the west against the Timber Mountain Aquifer (TMA) and younger units of Timber Mountain on the east; higher stratigraphic levels along the southern portion of the fault place the Detached Volcanics Aquifer (DVA) on the west against the TMA and overlying Fortymile Canyon Composite Unit (FCCM) on the east (Bechtel, 2002).

Paintbrush Canyon Fault (18)

The Paintbrush Canyon fault extends south from the Timber Mountain Caldera Complex margin and passes beyond the southern edge of the modeled area. Cross section A-A' in Bechtel (2002) indicates that this fault cuts the Belted Range Thrust (31) and places Paleozoic carbonate aquifer (LCA) and confining-unit (LCCU1) rocks on the east against the Yucca Mountain – Crater Flat Composite Unit (YMCFCM) on the west.

Purse Fault (19) and West Purse Fault (20)

The Purse fault and West Purse fault are *en-echelon* normal faults, offset from each other along the Ribbon Cliff Structural Zone (35), that lie within of the western margin of the Silent Canyon Caldera Complex. With depth these faults probably intersect and may offset the buried western structural margin of the Silent Canyon Caldera Complex (29,30), a major structure that creates significant east-to-west discontinuities in all of the principal hydrostratigraphic units ranging from the

Pre-Belted Range Composite Unit (PBRCM) upward through the Calico Hills Intrusive Confining Unit (CHICU) but not of the younger Timber Mountain units (Timber Mountain Aquifer, TMA). The Purse fault and West Purse fault both break through these younger units, although the near-surface offset along each is limited to ~30 m (McKee et al., 2001).

Rickey Fault (21)

The Rickey fault defines the northeastern margin of the Silent Canyon Caldera Complex and may be continuous with the Split Ridge Fault (23) beyond the caldera margin to the south. Because it is associated with a major caldera margin, with significant displacement down to the west, the Rickey fault represents an extensive discontinuity in hydrostratigraphy, placing an exceptionally thick sequence of the lower carbonate aquifer (LCA) against the Silent Canyon Intrusive Confining Unit (SCICU) and the Pre-Belted Range Composite Unit (PBRCM) on the west (Bechtel, 2002, cross-section C-C'). At higher stratigraphic levels, just below the water table, the Belted Range Aquifer on the west is juxtaposed against the Pre-Belted Range Composite Unit (PBRCM) on the east.

Scrugham Peak Fault (22)

The Scrugham Peak Fault extends from within the moat zone of the Timber Mountain Caldera Complex northward to define the southeastern margin of the Silent Canyon Caldera Complex. Offsets along this fault in the model are minor to the south, but may be extensive where the fault coincides with the margin of the Silent Canyon Caldera Complex north of the Southern Pahute Mesa Structural Zone (41). McKee et al. (2001) cite an offset of ~150 m along the Scrugham Peak fault, supporting the suggestion that offset increases significantly to the north along this fault.

Split Ridge Fault (23)

The Split Ridge fault runs north from the northeastern portion of the buried Rainier Mesa Caldera Structural Margin (27) and trends toward the Rickey fault (21), which defines the northeastern edge of the Silent Canton Caldera Complex (29,30). The Split Ridge fault is buried along most of its length but is exposed for about 6 km just north of the Timber Mountain Caldera Complex Topographic Margin. Offsets along this fault are likely to be far less significant than those along the Rickey fault (21), which bounds the northeastern edge of the Silent Canyon Caldera Complex

(29,30), and the Scrugham Peak Fault (22) where it forms the southeastern edge of the Silent Canyon Caldera Complex. McKee et al. (2001) cite near-surface offset of only ~30 m along the Split Ridge fault.

B.2.3.4 Caldera Margins (CM)

Caldera margins of the modeled area are typically circular to elliptical volcano tectonic basins that have accumulated very thick deposits of volcanic rocks compared to areas outside the caldera structures. In Table B.7-1 caldera margin features are divided into two categories: (1) structural margins comprised of faults and ring fracture zones that accommodated displacement of central cauldron block(s) and (2) topographic margins that represent syn- and post-collapse widening of the caldera depression by landslide and mass-wasting processes. Caldera structural margins of the Hydrostratigraphic Model are based on a structural-block conceptual model in which caldera subsidence was largely controlled by segments of pre-existing north-trending Basin and Range faults (Ferguson et al., 1994; Warren et al., 2000) as well as inherited northwest trending structures associated with the Walker Lane Belt (Carr, 1990). An alternative conceptual model treats caldera structural margins as arcuate ring fractures that form more or less independently of pre-existing Basin and Range faults (McKee et al., 2001). Despite the differences in these interpretations, locations and amount of subsidence for calderas are similar in both conceptual models.

Except for a few rare cases, as noted below, younger volcanic rocks cover the structural margins of calderas at the NTS, and there is little direct field evidence about the deformational characteristics of these structures. Nonetheless, some generalizations about these structures can be made based on models of caldera formation and on evidence collected from eroded calderas in other parts of the western US (e.g., Smith and Bailey, 1968; Lipman, 1976 and 1984). Regardless of origin, dips on caldera faults and ring fractures are expected to be steep (80° to 90°) based on the displacement of an irregular piston-like block into the partially evacuated magma chamber below. Collapse may occur along a single vertical or inward-dipping fault, or it may be distributed across a compound structure a kilometer or more in diameter that progressively steps down towards the deepest part of the caldera (e.g., Frizzell and Shulters, 1990, section B-B'). Some marginal caldera structures acted as conduits during eruptions of major ash-flow sheets, and in some cases these structures are filled with welded tuff dikes that merge upward with an ash-flow sheet (e.g., Carr and Quinlivian, 1968; Ekren and

Byers, 1976). Caldera resurgence often reactivates faults along which collapse occurred. In the southeast part of Timber Mountain, the inner zone of caldera ring faults is intruded by granite porphyry, basalt, and rhyolite, presumably during the influx of fresh magma into subcaldera magma chambers (Carr and Quinlivian, 1968). Modification of caldera structures by dikes and hydrothermal deposits would tend to decrease their transmissivity with respect to groundwater. Transmissivity is probably enhanced in areas where structures are reactivated by subsequent collapse, resurgence, or Basin and Range faulting.

The topographic walls of NTS calderas are marked by unconformities between pre-caldera rocks outside the collapse area and the syn- and post-collapse deposits that fill the caldera. Typically, the bounding fault scarps have enlarged by slumping or erosion, producing a topographic boundary that is larger in diameter than the structural boundary (Lipman, 1984). Debris from the caldera walls is commonly intercalated with intracaldera tuffs and buries the caldera floor (Byers et al., 1976, Christiansen et al., 1977). In some cases shallow listric faults bound sections of the wall that slumped en masse onto the caldera floor. The Hydrostratigraphic Model treats the area between the structural margin and the topographic margin as an inward-dipping erosional surface that extends from the topographic wall to the bounding caldera fault.

Calderas are well known worldwide as active sites for mineralization and hydrothermal alteration, for example within the Valles caldera (Hulen et al., 1988; Goff et al., 1989) and within the southwestern Nevada volcanic field (Noble et al., 1991). Such alteration seals fractures that pervade calderas, and also emplaces generally fine-grained, reactive secondary minerals within the "plumbing system" of the caldera. These minerals include clay minerals that typically form at much higher temperatures than those within extracaldera rocks, and carbonates and pyrite, both generally absent within extracaldera rocks. Pyrite may serve as a source for aqueous SO_4, or may act as a strong local reductant to interact with aqueous actinides. Data from Warren (2003) show striking differences among known calderas in the intensity of caldera-related hydrothermal alteration, indicating a great range in fracture-coating mineralogy encountered along the Oasis Valley-Pahute Mesa flow path, depending on the specific caldera, as discussed below. Although the alteration intensity of phenocryst feldspar is inconsequential in itself, it serves as a very sensitive and easily recognizable index for hydrothermal alteration, and is described below to characterize the intensity of hydrothermal alteration associated with calderas along the flow path.

Black Mountain Caldera Structural Margin (24)

Black Mountain is a relatively small caldera in the northwest part of the model area that formed during the eruption of the Thirsty Canyon Group 9.4 Ma (Noble et al., 1984; Sawyer et al., 1994). The structural margin is not exposed, but is interpreted in the model as being a generally circular structure 6 to 8 km in diameter. The topographic wall is well defined and is 1 to 4 km outside the structural margin.

The principal hydrostratigraphic unit beneath the water table within the Black Mountain caldera is the Thirsty Canyon volcanic aquifer (TCVA), which is made up of thick lavas and densely-welded ash-flow tuffs. TCVA is juxtaposed against a thick sequence of lower carbonate aquifer (LCA) rocks across the caldera structural and topographic margins. TCVA overlies rocks of the pre-Belted Range composite unit (PBRCM). The Black Mountain intrusive confining unit (CCICU) is modeled as a large intrusion of silicic magma injected beneath the caldera.

Timber Mountain Caldera Complex Topographical Margin (25)

The combined topographical expression formed by the nearly coincident collapse of the Rainier Mesa and Ammonia Tanks calderas is one of the most conspicuous features of the southwestern Nevada volcanic field. The topographical margin is easily recognized for more than half of the circumference of the caldera complex (Bechtel, 2002), extending as a continuous feature along the south, east, and northeast side of the caldera. The prominent north-trending normal faults on Pahute Mesa are truncated by the northern topographical margin, and the Claim Canyon caldera is truncated by the southern topographic margin. Where the northern and southern structural margins of the Rainier Mesa and Ammonia Tanks coincide, the distance between the topographical and structural margins is generally 1 to 6 km. On the east side of the complex, the Rainier Mesa topographical (25) and structural (27) margins are typically separated by 1 to 2 km, and the Ammonia Tanks topographical (25) and structural (26) margins are up to 6.5 km apart. There is some uncertainty about the actual location of the western topographic margin of the Timber Mountain caldera; based on more recent drill-hole data, Warren et al. (2000) place it between drill hole ER-EC-02A and drill holes ER-EC-01 and ER-EC-06, in contrast to the location shown on earlier regional maps (e.g., Wahl et al., 1997).

The model treats the topographic margin as an inward- moderately- to steeply-dipping unconformity that places precaldera volcanic rocks against the intracaldera Timber Mountain composite unit

(TMCU) and the overlying Fortymile Canyon Composite Unit (FCCM) and Alluvial Aquifer (AA) Unit. The FCCM and AA Units generally lie above the water table along the caldera complex topographical margin (25).

Ammonia Tanks Caldera Structural Margin (26)

The Ammonia Tanks caldera formed during the eruption of the Ammonia Tanks Tuff 11.45 Ma (Byers et al., 1976; Christiansen et al., 1977; Sawyer et al., 1994). The 21- to 24-km diameter caldera is nested inside the related Rainier Mesa caldera. The Hydrostratigraphic Model indicates that the southern and northern structural margins of the Ammonia Tanks (26) and Rainier Mesa (27) calderas coincide (Bechtel, 2002), indicating reactivation of older caldera structures in those areas during the Ammonia Tanks collapse. The Ammonia Tanks caldera is bound on the west by the Thirsty Canyon lineament (42) and by a north-trending fault. The eastern structural margin is poorly constrained, and it is treated in the model as a north to northeast-trending normal fault. A prominent feature of the Ammonia Tanks caldera is the resurgent dome centered on Timber Mountain.

The principal hydrostratigraphic unit beneath the water table within the Ammonia Tanks caldera is the Timber Mountain composite unit (TMCU), which consist of densely-welded intracaldera Ammonia Tanks and Rainier Mesa Tuffs as well as closely-related small-volume tuffs and lavas and landslide deposits. TMCU is juxtaposed against the lower carbonate aquifer (LCA) on the north side of the caldera. The TMCU lies above poorly-constrained units including the subcaldera volcanic confining unit (SCVCU) and the Ammonia Tanks intrusive confining unit, which is modeled as a large intrusion of silicic magma injected beneath the Ammonia Tanks caldera. Caldera-filling units such as the Fortymile Canyon Composite Unit and Alluvial Aquifer are confined to the caldera moat between the resurgent dome and the topographical margin.

The densely-welded tuffs of TMCU are typically considered to be fractured aquifers, but it is considered a composite unit in the model because fractures may be sealed by hydrothermal alteration (Bechtel, 2002). Recent data from drill hole ER-EC-02A indicate that TMCU units in the northern part of the caldera are hydrothermally altered (Table B.7-2; Warren et al, 2003). In addition to pervasive alteration throughout the borehole, a hot spring deposit containing chalcedony, dolomite, ankerite, and fluorite was identified between 950 and 960 m depths. Quartzofeldspathic alteration is common in rocks as shallow as 300 m deep within drill hole ER-EC-02A (Warren et al, 2003). Drill

hole ER-EC-06, located just north of the Ammonia Tanks caldera, is also characterized by hydrothermally- altered units (Warren et al, 2003). Alteration principally occurs in Tiva Canyon Tuff and older units, and may be temporally related to development of older volcanism. Alternatively, the Tiva Canyon Member may have formed an impermeable cap for hydrothermal fluids associated with the Ammonia Tanks caldera. Drill hole ER-EC-01, which is also located just north of the Ammonia Tanks caldera penetrated similar stratigraphic units that are little altered (Warren et al, 2003), suggesting that the distribution of hydrothermal alteration near the northern margin of the caldera is locally variable.

Rainier Mesa Caldera Structural Margin (27)

The Rainier Mesa caldera formed during the eruption of the Rainier Mesa Tuff 11.6 Ma (Byers et al., 1976; Christiansen et al., 1977; Sawyer et al., 1994). The structural margin is 21 x 37 km in diameter and is elongated in an east-west direction. Intracaldera rocks associated with the Rainier Mesa caldera are combined with the Ammonia Tanks Tuff as part of the Timber Mountain composite unit (TMCU). Intracaldera Rainier Mesa Tuff is exposed only at Transvaal Hills; elsewhere, younger volcanic rocks bury these rocks. The structurally-high Rainier Mesa Tuff at Transvaal Hill may represent the western flank of a resurgent dome that was downfaulted to the east by the Ammonia Tanks caldera (Bechtel, 2002).

The structural margin of the Rainier Mesa caldera is completely buried. The limit of the northern margin is fairly well constrained by drill hole and gravity data and by outcrops of precaldera rocks exposed on the south side of Pahute Mesa. The southern margin is less well constrained, but it must lie north of pre-Rainier rocks that crop out south of Beatty Wash. The southern margin is modeled as a west-northwest striking normal fault that parallels the topographical wall of the caldera complex (25). The southwest structural margin is coincident with the Hot Springs fault (34). The western structural margin is poorly constrained and is modeled as three north-trending en-echelon faults that step eastward from south to north. The eastern margin is also poorly constrained, but it must lie west of pre-Rainier rocks that crop out east of Fortymile Wash. The eastern margin is modeled as north-striking normal fault that parallels the topographical wall of the caldera complex (25).

The principal hydrostratigraphic unit beneath the water table within the Rainier Mesa caldera is the Timber Mountain composite unit (TMCU). The caldera structural margin juxtaposes TMCU against

subcrops of the lower carbonate aquifer (LCA) on all sides of the caldera. The TMCU lies above poorly-constrained units including the subcaldera volcanic confining unit (SCVCU) and the Rainier Mesa intrusive confining unit (RMICU), which is modeled as a large intrusion of silicic magma injected beneath the Rainier Mesa caldera. Caldera-filling units such as the Fortymile Canyon Composite Unit are particularly thick in the western part of the caldera and locally extend well below the water table.

Major north-trending faults on Pahute Mesa are shown on geologic maps to be truncated by the north caldera margin, but structural data for the Ammonia Tanks tuff (Warren et al., 2000) show that the Boxcar fault (7) continues into the caldera, where it is largely covered by the Beatty Wash Formation. Preferential groundwater pathways might occur where these intersecting structural features coincide with thick subcrops of lower carbonate aquifer. Similarly, north-northwest trending faults in Fortymile Wash and the Paintbrush Canyon Fault (18) south of Beatty Wash are truncated by the southern structural margin. The Belted Range thrust fault (31) is truncated by the caldera structural margins. The intersection of the Rainier Mesa caldera structural margin with the Belted Range thrust fault might be an important hydrological pathway, particularly in the southwest part of the caldera where the thrust fault occurs within a thick sequence of lower carbonate aquifer rocks (see cross section J-J' in Bechtel, 2002).

Intracaldera tuffs in the Rainier Mesa caldera appear to be only slightly altered compared to those in the Ammonia Tanks caldera (Table B.7-2). In drill hole UE-18t, where a thick section of intracaldera Rainier Mesa Tuff was penetrated from 524 m to 792 m TD, sanidine is strongly altered within a thin argillic bedded tuff at the top of the unit, but is unaltered below (Warren et al., 2003). Plagioclase has been strongly altered or destroyed within samples to 580 m depth, but is unaltered within samples 622 to 792 m depths. Plagioclase has been completely destroyed in a sample of argillic bedded tuff from 480 m depth near the base of Ammonia Tanks Tuff, and feldspar is progressively less altered upward to slightly altered in a sample of welded tuff from 291 m depth. The upward decrease in alteration intensity within Ammonia Tanks Tuff, coupled with a downward decrease in alteration intensity within Rainier Mesa Tuff indicates that alteration is associated primarily with the nearby Ammonia Tanks caldera, and that alteration associated with the Rainier Mesa caldera, exhibited by samples from 622 to 792 m depths, is slight. As in drill hole ER-EC-02A described above, dolomite is the primary carbonate associated with the hydrothermal activity, with calcite detected in some

samples, but only dolomite present in most (Warren et al., 2003). Dolomite is the dominant carbonate to TD from the shallowest sample analyzed by XRD, from Beatty Wash Formation at 171 m depth.

Claim Canyon Caldera Structural Margin (28)

The Claim Canyon caldera formed during the eruption of the Tiva Canyon Tuff 12.7 Ma (Byers et al., 1976; Sawyer et al., 1994). The Timber Mountain caldera complex in the southern part of the model area truncates a segment of the southern structural margin of the caldera. Except for limited exposures north and northwest of Yucca Mountain, younger volcanic rocks cover the structural margin of the caldera. The caldera is defined by thick sequence of densely-welded intracaldera Tiva Canyon Tuff (Tuff of Chocolate Mountain of Byers et al., 1976). Because of their structurally-high position, these tuffs may represent the southern flank of a resurgent dome (Byers et al., 1976).

The principal hydrostratigraphic units beneath the water table within the Claim Canyon caldera are the Paintbrush composite unit (PCM) and the underlying Yucca Mountain/Crater Flat composite unit (YMCFCM). On the north side of the caldera segment, PCM and YMCFCM are juxtaposed against TMCU across the Rainier Mesa caldera structural margin. On the southeast side of the Claim Canyon caldera, PCM and YMCFCM are probably juxtaposed against subcrops of the lower carbonate aquifer (LCA). PCM and YMCFCM lie above the poorly-constrained Claim Canyon intrusive confining unit (CCICU), which is modeled as a large intrusion of silicic magma injected beneath the caldera.

Basin and Range normal faults extend into the Claim Canyon caldera from the extended terrain to the south. Subordinate east-west faults within the caldera displace post-caldera volcanic rocks and may be related subsidence of the Timber Mountain caldera complex (Christiansen et al., 1977). The Belted Range thrust fault (31) probably truncates against the eastern and western caldera structural margin.

Silent Canyon Caldera Structural Margin (29 and 30)

The Silent Canyon caldera complex is comprised of the overlapping and temporally associated but petrologically unrelated Grouse Canyon (29) and Area 20 (30) calderas. The caldera complex is buried by younger volcanic rocks beneath Pahute Mesa, but it is reasonably well constrained by drill hole data and gravity measurements. Rocks of the Silent Canyon caldera complex overlie a

considerable thickness of older volcanic rocks that were probably erupted from older undefined calderas.

The Hydrostratigraphic Model is based on the interpretations of Ferguson et al. (1994) who presented geophysical, borehole, and surface geology evidence suggesting that caldera collapse was accommodated by Basin and Range normal faults and by buried west-northwest trending structural zones. Collapse along these structures resulted in calderas with rectilinear boundaries. An alternative conceptual model of caldera structure is presented by McKee et al. (2001) who use gravity inversion data to suggest that an elliptical ring fracture system bounds the caldera complex.

The Grouse Canyon caldera (29) formed during the eruption of the Grouse Canyon Tuff 13.7 Ma (Orkild et al., 1968; Noble et al, 1968; Sawyer et al., 1994). The caldera is bounded on the east by the Scrugham Peak (22) and Rickey (21) faults, on the west by the West Greeley fault (14), on the north by the Moor Hen Meadow structural zone (37), and the south by the East Thirsty Canyon structural zone (36) (Bechtel, 2002). Geophysical and borehole data suggest that collapse was asymmetric with the greatest accumulation of tuffs occurring in the northeast portion of the caldera (Ferguson et al., 1994). Additional collapse in the north and east part of the caldera may have accompanied eruption of the caldera-filling Dead Horse Flat Formation.

The principal hydrostratigraphic units beneath the water table within the Grouse Canyon caldera are, in descending order, the Crater Flat confining unit (CFCU), the Bullfrog confining unit (BFCU), the Belted Range aquifer (BRA), and the pre-Belted Range composite unit (PBRCM). The BRA is made up of up to 1981 m of lavas and densely-welded ash-flow tuffs. BRA is juxtaposed against a thick sequences of confining units across the caldera structural margins; the confining units include the lower and upper clastic confining units (LCCU and UCCU) on the north, the pre-Belted Range composite unit (PBRCM) on the east, and the Calico Hills zeolitic composite unit (CHZCM), Crater Flat confining unit (CFCU), the Bullfrog confining unit (BFCU) on the west. The lower part of the caldera complex is modeled as the Silent Canyon intrusive confining unit (SCICU), a large intrusion of silicic magma injected beneath the caldera.

Hydrothermal alteration has affected caldera-forming and caldera-filling units within the Grouse Canyon caldera. In contrast to intracaldera rocks of the Ammonia Tanks caldera, feldspar phenocrysts have not been as severely altered within the Grouse Canyon caldera (Table B.7-2;

Warren et al., 2003). Pyrite, generally lacking in the Ammonia Tanks caldera, is ubiquitous within the Grouse Canyon caldera (Warren et al., 2003). Within the caldera, the lavas and densely-welded tuffs of BRA are classified as a fractured aquifer. However, the hydrological character of these rocks may be more composite in nature because fractures may be sealed by hydrothermal alteration (Bechtel, 2002). For example, in UE-19gS, where the 577-m-thick intracaldera Grouse Canyon Tuff was completely penetrated between depths of 1,631 to 2,208 m, alteration of feldspar persists upward well into the thick caldera-filling Dead Horse Flat formation (Warren et al., 2003). The first hydrothermally altered sample of caldera-filling rock occurs about 2/3rds of the way downhole, marked by a consistent partial alteration of feldspar and by increasingly abundant pyrite. Feldspar, virtually entirely sanidine within this peralkaline unit, is not completely destroyed within any single sample of Dead Horse Flat formation. The caldera-forming Grouse Canyon Tuff is more strongly altered, with feldspar completely destroyed within most but not all samples, and pyrite is generally abundant. The single sample of comendite of Quartet Dome, a peralkaline unit that floors the caldera, has a similar style of alteration as Grouse Canyon Tuff. In borehole UE-19E, which penetrated the Dead Horse Flat formation, trachyte of Muenster, and uppermost Grouse Canyon Tuff, feldspars are unaltered except the single samples available for the trachyte and for Grouse Canyon Tuff (Warren et al., 2003).

The Area 20 caldera (30) formed during the eruption of the Bullfrog Tuff 13.25 Ma (Sawyer et al., 1994). The caldera is bounded by numerous separate structural elements, most of which coincide with Basin and Range normal faults and various linear structural zones (Ferguson et al., 1994).

The principal hydrostratigraphic units beneath the water table within the Area 20 caldera are lithologically diverse and include, in descending order, the Calico Hills zeolitic composite unit (CHZCM), the Inlet Aquifer (IA), the Crater Flat composite unit (CFCM), the Crater Flat confining unit (CFCU), the Bullfrog confining unit (BFCU), the Belted Range aquifer (BRA), and the pre-Belted Range composite unit (PBRCM). The lower part of the caldera complex is modeled as the Silent Canyon intrusive confining unit (SCICU), a large intrusion of silicic magma injected beneath the caldera. However, the very limited alteration of caldera fill to depths of 3 km in the Area 20 caldera places some doubt on the presence of such a large intrusion (Warren et al., 2003).

Intracaldera rocks within the Area 20 caldera are generally much less hydrothermally altered than within other calderas of the region (Table B.7-2; Warren et al., 2003). However, hydrologic properties are strongly affected by low-temperature diagenetic alteration. Feldspar is completely unaltered within caldera-filling units, which consist predominantly of glassy, devitrified, and zeolitic lavas and zeolitic nonwelded tuffs. The caldera-filling unit is uniformly zeolitic, generally with analcime at depths >1,500 m, with the top well below that level in drill hole UE-20F (Warren et al., 2003). Drill hole UE-20F penetrates the caldera floor, which consists of units marginal to the adjacent Grouse Canyon caldera. Feldspar alteration ranges from complete destruction to mild alteration within these flooring units, but feldspars are completely destroyed in pre-Grouse Canyon units, below approximately 3,000 m depth. This very strong alteration of pre-Grouse units suggests that pre-Area 20 rocks were altered in association with the Grouse Canyon caldera. Faults within the source region of Area 20 of Pahute Mesa should be poorly mineralized where the Area 20 caldera represents the latest volcanotectonic event.

B.2.3.5 Thrust Faults (TF)

Belted Range Thrust Fault (31)

The Belted Range thrust fault is the principal pre-Tertiary structural feature in the model area (Bechtel, 2002). The Belted Range fault is an east-verging thrust that generally places late Proterozoic to early Cambrian rocks over rocks as young as Mississippian. The fault is present over most of the model region except beneath the caldera complexes where the model indicates the destruction of pre-Cenozoic rocks by the intrusion of silicic batholiths into the floors of the calderas following their collapse (Bechtel, 2002). Because the Belted Range thrust fault is buried and only penetrated by one borehole (ER-19-1) in the model region, its depth and the thickness of the upper thrust sheet are poorly constrained. In most cross sections (Bechtel, 2002), the Belted Range thrust is underlain by the upper clastic confining unit (UCCU), which is in turn underlain be the lower carbonate aquifer (LCA) at depths of ~1 to 2 km along the eastern margin of the modeled area.

CP Thrust Fault (32)

The west-to northwest verging CP thrust system forms a parallel zone of thrusts and folds east and south of the Belted Range thrust (Cole and Cashman, 1999; Potter et al., 2002). The thrust faults appear to be steep structures that flatten upwards. CP folds and thrusts deform the leading edge of the

pre-existing Belted Range thrust system (31) (Cole and Cashman, 1999). The CP Thrust lies along the eastern and southern margin of the model area and is probably not an important contributor to structure-related hydrology.

B.2.3.6 Structural Zones (TSZ)

Structural zones that trend approximately E-W were first described by Warren et al. (1985) to explain significant north-south structural differences that postdate caldera formation at Pahute Mesa. Some of these differences can be explained by erosion or deposition, but the generally consistent increase in these differences within older stratigraphic units certainly requires a structural cause, which Warren et al. (1985) attributed to regional subsidence related to caldera formation south of Pahute Mesa. North-south profiles yield sawtooth patterns, with the breaks corresponding to southward-down structural zones, and blocks dipping northward, with tilts and displacements both increasing downward. The Ribbon Cliff (35) and Southern Pahute Mesa (41) structural zones are down to the north. This structural complexity is further described in Warren et al. (2000).

Gold Meadows Structural Zone (33)

The Gold Meadows structural zone is a west-northwest-trending structure located east of the Silent Canyon caldera complex in the northeast part of the model area. It is depicted as a steep growth fault with a maximum displacement of about 400 m of offset down to the south. It is a buried structure and does not displace units younger than the pre-Belted Range composite unit (PBRCM). The Gold Meadows structural zone displaces the Belted Range thrust fault (31) at a depth of about 2,000 m.

Hot Springs Lineament (34)

The Hot Springs lineament is a west-northwest-trending buried structure located in Beatty Wash in the southwest part of the model area. It is depicted as the southwest structural margin to the Rainier Mesa caldera (27). Stratigraphic relations across the Hot Springs lineament are poorly constrained.

Ribbon Cliffs Structural Zone (35)

The Ribbon Cliffs structural zone is a buried west-northwest-trending structure located between the Black Mountain caldera (24) and the Silent Canyon caldera complex in the north-central part of the model area (30). The Ribbon Cliffs structural zone is truncated on the west by the northeast trending

Handley fault (16). The eastern end of this feature truncates the north-trending West Purse fault (20) causing an eastward jog in the Area 20 caldera boundary (30). It interrupts the trend of the Thirsty Canyon lineament (42) and accounts for pronounced eastward structural alignment of comendite of Ribbon Cliff (Ttr) from the Black Mountain caldera (24) (see Figures A-4 and A-5 in Warren et al., 2000). Ribbon Cliff (RBCF) and Southwestern Gold Flat (SWGF) structural blocks may represent southward-tilted blocks separated by this northward-down structural zone. The similar structural relief for Pahute Mesa Tuff and Rainier Mesa Tuff indicates that the feature is post-Pahute Mesa and thus is probably related to the adjacent Black Mountain caldera (24). However, structural control is very poor for the Rainier Mesa Tuff, so structural relief ascribed to the Ribbon Cliff Arch might simply represent draping of Pahute Mesa Tuff over underlying lava.

East Thirsty Canyon Structural Zone (36)

The East Thirsty Canyon structural zone is an east-northeast-trending structure within the Silent Canyon caldera complex in the northeast part of the model area. It forms the southern structural margin for the inner zone of collapse associated with the Grouse Canyon caldera (29). It is crossed by the north-trending East Greeley (13), Almendro (1), and Scrughum Peak (22) faults, and it terminates against the West Greeley fault (14) on the west and the Split Ridge fault (23) on the east. It is a buried structure and may not displace intracaldera units younger than Grouse Canyon Tuff and the Dead Horse Flats Formation. This structure has been buried without reactivation by Tiva Canyon Tuff and younger units, and has displacements down to the south. It explains marked southward decreases in elevations for the top of rhyolite of Silent Canyon (Warren et al., 2000). This structural feature could represent the northern topographic wall of the Topopah Spring caldera.

Moor Hen Meadow Structural Zone (37)

The Moor Hen Meadow structural zone is a west-northwest-trending structure on the northeast corner of the Silent Canyon caldera complex in the northeast part of the model area. It forms the northern structural margin for the outer zone of collapse associated with the Grouse Canyon caldera (29). It has at least 1,600 m of displacement down to the south. Below the water table, pre-caldera rocks including the lower carbonate aquifer (LCA) are displaced against intracaldera units including, in descending order, the Calico Hills confining unit (CHCU), Belted Range aquifer (BRA), pre-Belted Range composite unit (PBRCM), and Silent Canyon intrusive confining unit (SCICU).

North Timber Mountain Moat Structural Zone (38)

The North Timber Mountain moat structural zone is a major west-northwest- trending structure that extends across the central part of the model area from the northeast corner of the Timber Mountain caldera complex (26, 27) to the southern structural margin of the Black Mountain caldera (24). It is depicted in the model as a normal fault with a maximum displacement of about 200 m of offset down to the south. It is a buried structure and does not displace extra-caldera volcanic units of the Black Mountain caldera.

Silent Canyon Northern Structural Zone (39)

The Silent Canyon northern structural zone is west-northwest-trending structure within the Silent Canyon caldera complex in the northeast part of the model area. It crosses the collapse zone associated with the Grouse Canyon caldera. It is a buried structure that has displacements down to the south and accounts for small north-south structural differences within units with excellent control (e.g., Pahute Mesa Tuff); displacements become larger with depth for units penetrated in drill hole. These structural differences probably reflect only regional subsidence related to caldera formation south of Pahute Mesa.

Silent Canyon Structural Zone (40)

The Silent Canyon structural zone is west-northwest-trending structure within the Silent Canyon caldera complex in the northeast part of the model area. It forms the northern structural margin for the inner zone of collapse associated with the Grouse Canyon caldera (29). It is crossed by the north-trending East Greeley (13), West Estuary (12), East Estuary (11), and West Almendro (2) faults, and it terminates against the West Greeley fault (14) on the west and the Half Beak fault (15) on the east. It displaces hydrostratigraphic units as young as the Timber Mountain aquifer (TMA), indicating recurrent activation following caldera collapse. It is depicted in the model as a normal fault with a maximum displacement of about 600 m of offset down to the south.

Southern Pahute Mesa Structural Zone (41)

The Southern Pahute Mesa structural zone is west-northwest-trending structure that marks the southern structural margin of the Silent Canyon caldera complex (29, 30). It is crossed by a number of major north-trending faults, including the West Greeley (14), East Greeley (13), Almendro (1), and

Scrughum Peak (22) faults, and it terminates against the Boxcar fault (7) on the west and the Split Ridge fault (23) on the east. This structural zone has displacements down to the north with increasingly larger structural differences for increasingly older units, and accounts for the structural relief resulting from formation of the Area 20 caldera. The northward-down geometry, and strong activation during formation of the Area 20 caldera accommodates the 600 m thick intracaldera rhyolite of Inlet without thinning the overlying Paintbrush Group, as recognized from structure contours in Warren et al. (2000).

Thirsty Canyon Lineament (42)

The Thirsty Canyon lineament is a major north-northeast-trending feature that has been identified on regional gravity and aeromagnetic maps (Mankinen et al., 1999). The lineament extends at least 35 km south-southwestward from western Pahute Mesa to the west-central margin of the Rainier Mesa caldera (27). The Thirsty Canyon lineament approximately coincides with a water-level discontinuity that Blankennagel and Weir (1973) and Laczniak et al. (1996) interpret as a limited barrier to groundwater flow near Area 20. Blankennagel and Weir (1973) believed that part of the water-level discontinuity coincided with the western structural margin of the Silent Canyon caldera complex (29, 30). The Thirsty Canyon lineament is one of the shortest and most direct routes for groundwater from the NTS to reach inhabited areas, and as such, deserves special attention for monitoring purposes (Mankinen et al., 1999).

Western East Thirsty Canyon Structural Zone (43)

The Western East Thirsty Canyon structural zone is west-northwest-trending structure that occurs within the south-central part of the Area 20 caldera (30). It has a strike length of about 3000 m, and it is truncated by the Boxcar fault (7) on the west and the West Greeley fault (14) on the east. Intracaldera units of the Silent canyon caldera complex are juxtaposed across this structure. It is clear that north-south structural breaks of the East Thirsty Canyon structural zone do not continue uninterrupted across the West Greeley fault (14). In the 1994 version of the Structural Block Model, the East Thirsty Canyon structural zone was thought to possibly continue westward about 1.2 km south from its westward termination against the West Greeley fault, dividing the Eastern Area 20 block in two. Structure contours of Warren et al. (2000) indeed suggest that the East Thirsty Canyon structural zone continues westward, but 2.5 km south from its westward termination against the West

Greeley fault (14). The structural differences across this southward-down structure, although moderately large, probably reflect only regional intumescence related to caldera formation south of Pahute Mesa.

Western Silent Canyon Structural Zone (44)

The Western Silent Canyon structural zone is west-northwest-trending structure that forms a shared structural margin for the northwest part of the Area 20 caldera (30) and the southwest part of the Grouse Canyon caldera (29). It extends between the Purse fault on the west and the West Greeley fault (14) on the east. It is crossed by the north-trending Boxcar Fault (7).

B.2.3.7 Detachment Faults (DFS)

Fluorspar Canyon-Bullfrog Hills Detachment Fault (45)

The Fluorspar Canyon-Bullfrog Hills detachment fault is a shallow, low-angle fault that underlies the Tertiary rocks in the southwest part of the model area (Bechtel, 2002) (Not [shown] on Figure B.7-1). The fault is assumed to have developed along the surface of pre-Tertiary rocks. Westward to northwestward movement occurred between 12.7 and 9.5 Ma, resulting in extreme eastward tilting of upper plate rocks (Fridrich et al., 1999). The model generally depicts the detachment fault as low-angle fault separating Tertiary volcanic rocks in the hanging wall from Paleozoic and Precambrian sedimentary and metasedimentary rocks in the footwall. Locally, the lower carbonate aquifer (LCA) forms the upper part of the sequence of Paleozoic rocks that underlie the detachment fault. Maldonado (1990) indicates that this aquifer is underlain by less permeable Paleozoic clastic sediments, providing a confined transmissive unit below the detachment fault.

B.2.4 Hydrologic Effects of Major Structural Features Within SWNVF

The discussion above summarizes features of faults to consider for their hydrologic effects within the Pahute Mesa/Oasis Valley flow model. Graduating from simple to complex below, we pose questions or state suppositions that, if answered, might explain observed changes in water levels and/or aqueous geochemistry.

1. Are there intrinsic differences among the types of structures identified in Table B.7-1? Although published studies indicate that thrust faults and normal faults have similar

architectures, their different geometries may accommodate different groundwater fluxes and provide different environments within fault systems that have been episodically sealed by hydrothermal alteration and episodically reopened. Structural zones may have intrinsic differences related to their typical E-W dominant strikes, as discussed below.

2. Does the length of a vertical structure, including faults, structural zones, and caldera structural margins, correlate with hydrologic characteristics? In the absence of complicating factors, it would seem that the longer the vertical structure, the more pronounced the effects.

3. Is the length of a fault activated by weapons testing relevant, being an indication of the openness of the vertical structure?

4. Is the orientation of each structure relative to the regional stress field important? Most normal faults, formed normal to the least stress axis of the regional field, probably have the most permeable and widest damage zones, whereas most structural zones, formed normal to the greatest stress axis, probably have the least permeable and narrowest damage zones.

5. What is the effect of juxtaposing rocks with different hydrologic properties across a structure? In the strict sense where offset refers only to a mismatch of hydrostratigraphic units, then offset can only result in a structural barrier. Note the offset is also complicated by episodic reactivation of faults, well known for Pahute Mesa (Figure 25 of Warren et al., 1985).

6. Is hydrothermal alteration that can be associated with the formation of a particular caldera characteristic of permeability? Although data are sparse, such characteristic alteration was introduced along caldera structural margins, and spread outside each caldera towards the topographic margins, but it probably was localized within such structures, likely at structural intersections.

7. Are buried structures least transmissive, with burial reflecting lack of late reactivation? An early episode of hydrothermal activity may have "plugged" a buried fault, producing a barrier, which might have been broken by an episode that faulted the burying units, transforming the fault into a conduit.

B.3.0 Evidence of Fault Behavior from Other Areas of the NTS and Vicinity

A summary of the possible effects of faults on groundwater movement in the Death Valley region was presented by Faunt (1997). The transmissivity of faults was described by Faunt (1997, p. 30) to be a function of many factors, including (1) the orientation of the fault relative to the minimum horizontal stress in the region, (2) the amount and type of fill material in the fault, (3) the relative transmissivities of hydrogeologic units juxtaposed by offset across the fault, (4) the solubility and deformation behavior of the rock adjacent to the fault, and (5) recent seismic history.

As noted by Faunt (1997, Figure 16), where faults juxtapose hydrogeologic units with contrasting permeabilities, the hydrologic effects caused by juxtaposition may be difficult to isolate from the effects of the fault properties themselves. In particular, a drop in head across a fault can occur if (1) the fault is closed, thereby blocking flow, (2) the fault is open, thereby redirecting flow, (3) the permeability of the material downgradient of the fault is low compared to the upgradient material, so that flow across the fault is blocked, or (4) the permeability of the material downgradient of the fault is high compared to the upgradient material, so that flow can drain away from the fault faster than it can be delivered by the upgradient material. In order to understand the hydrologic behavior of a fault, it is necessary to consider the potential effect of hydrostratigraphic offsets across the fault.

The following sections provide some examples in both non-tuffaceous and tuffaceous rocks that illustrate the effects of some of the factors described in the preceding paragraphs.

B.3.1 Evidence of Fault Behavior in Non-Tuffaceous Rocks

Although tuffs comprise the shallow aquifers and confining units in the PM/OV flow domain, the type and distribution of basement rocks and their structural features has the potential to influence flow patterns at shallower depths. For instance, groundwater flow may be diverted around areas where confining units are structurally high, or diverted toward areas where aquifers like the LCA are

shallow and laterally continuous. Non-tuffaceous rocks are juxtaposed against tuffaceous rocks along many caldera margins in the PM/OV hydrostratigraphic model (Bechtel, 2002) and, additionally, the Belted Range thrust fault (31) (Section B.2.3.5) is laterally continuous through the model domain and juxtaposes various non-tuffaceous rocks against each other. Therefore, observations regarding fault behavior in non-tuffaceous rocks elsewhere near the NTS are highly relevant to the discussion of faults in the PM/OV flow domain.

In the vicinity of the PM/OV model domain, the mean orientation of the minimum horizontal stress is currently approximately northwest/southeast (see Stock et al., 1985, table 3 and references therein), although the regional stress field may have rotated clockwise though time (Zoback and Zoback, 1980). Therefore, faults with traces oriented north/northeast are expected to be more open and permeable than faults with traces oriented in directions that place them in either a shear or compressive state. Faults oriented northwest, or perpendicular to the maximum horizontal stress direction, would be expected to be least transmissive, all other factors being equal. One example cited by Faunt (1997, p. 34-35) to illustrate that northeast-southwest trending structures may have relatively high transmissivity is the "megachannel" formed in the Spotted Range-Mine Mountain shear zone between Frenchman Flat and Ash Meadows. The presence of a highly transmissive zone in the carbonate aquifer was indicated by a potentiometric trough in this area and relatively young carbon-14 ages of groundwater discharging from springs at the distal end of the trough (Winograd and Pearson, 1976).

Fine-grained gouge or clayey fill material and deformation can cause faults to become poorly transmissive, even if their orientation relative to the stress field indicates they have the potential to be highly transmissive. The effects of deformation behavior, solubility, and fill material in the clastic aquitards and carbonate aquifer were discussed by Winograd and Thordarson (1975). These authors pointed out that, although the lower clastic aquitard is highly fractured, the fractures probably do not substantially augment the interstitial permeability of the unit on a regional scale because (1) the argillaceous formations within the unit have a tendency to deform plastically, (2) micaceous partings and argillaceous laminae tend to seal the fractures in the brittle quartzite parts of the unit, and (3) the clastic rocks which constitute the unit have a low solubility, and solution channels, common in the carbonate rocks, are therefore not likely to be present in this unit (Winograd and Thordarson,1975, p. C43). In support of these arguments, they noted that in the Spring Mountains, the total discharge

issuing from springs in the lower clastic aquitard is only a small fraction of the total discharge of the springs in the lower carbonate aquifer (Winograd and Thordarson, 1975, p. C42-C43; p. C53). Similarly, Winograd and Thordarson (1975, p. c43) argued that fractures in the Upper Clastic Confining Unit (Eleana Formation) were unlikely to remain open in the rock at depth because of the plastic deformation behavior of the rock, evidenced by tight folds and the fact that the formation serves as a glide plane for several thrust faults at the NTS. To further illustrate their arguments, they noted that a trough in the potentiometric surface appears to coincide with the north-trending Yucca Fault in Yucca Flat. The hydraulic gradient in the carbonate aquifer ranges from 5.9 ft or less per mile along the axis of the potentiometric trough in Yucca Flat to 20 ft per mile along the flanks of the trough (Winograd and Thordarson, 1975, p. C71), suggesting that the fault is quite permeable. Conversely, hydraulic gradients in the northwestern and northeastern parts of Yucca Flat are several hundred feet per mile across the upper and lower clastic confining units, respectively, indicating that there is little large-scale fracture or fault permeability in these units.

Evidence that springs in Ash Meadows are caused by the juxtaposition of poorly permeable sediments and rocks downgradient from carbonate aquifer across the Gravity Fault was presented in Winograd and Thordarson (1975, p. C82). Hydraulic data in southern Indians Springs Valley were interpreted by Winograd and Thordarson (1975, p. C67-68) to indicate the presence of two hydraulic barriers related to the Las Vegas shear zone: (1) a northern barrier caused by the juxtaposition of the lower clastic aquitard and lower carbonate aquifer; and (2) a southern barrier, that was attributed to the presence of gouge along a major fault zone.

B.3.2 Evidence of Fault Characteristics in Tuff from Yucca Mountain

The evidence for fault characteristics cited in the previous section were for non-tuffaceous rocks, so their relevance to the tuffs that constitute the shallow aquifers and aquitards in the PM/OV flow domain is uncertain. A more relevant analog for faults in the PM/OV flow domain may exist at Yucca Mountain, where the hydraulic properties of faults in welded and nonwelded tuffs above and below the water table have been estimated. As noted by Carr (1990, p. 290), similarities exist between the normal faults on Yucca Mountain and Pahute Mesa in terms of strike, spacing and direction of displacement, suggesting a genetic association that makes hydrologic data from faults at Yucca Mountain particularly relevant to faults at Pahute Mesa. The tectonic setting of Yucca

Mountain was discussed by Scott (1990), who hypothesized that the dips of major normal faults decrease with depth beneath Yucca Mountain and ultimately merge with a master low-angle normal fault along the contact between the pre-Tertiary and Tertiary rocks at depths between 1 and 4 km. However, subsequent seismic reflection studies across Yucca Mountain rule out a major low-angle detachment along this contact and indicate that moderate- to high-angle faults extend to 12 to 15 km depths beneath Yucca Mountain and Crater Flat with only modest changes in dip (Brocher et al., 1998). This last conclusion indirectly supports the dips assumed for normal faults in the PM/OV domain.

The tuffs at Yucca Mountain include many of the same formations that are found in the PM/OV flow domain, such as the Tiva Canyon Tuff, the Topopah Spring Tuff, the Calico Hills Formation, the Bullfrog Tuff and other tuffs of the Crater Flat group. Most of these units are lithologically similar between the two regions, and should therefore show similar hydrologic character. An important exception is the Bullfrog Tuff, which is a welded tuff aquifer beneath most of Yucca Mountain and a major confining unit beneath Pahute Mesa (Warren, 1983; Laczniak et al., 1996; Luckey et al., 1996).

In the unsaturated zone at Yucca Mountain, estimates of fault properties have been made by direct pneumatic testing of unfaulted and faulted rock (LeCain, 1997; LeCain et al., 2000), through numerical inversion of the subsurface pneumatic pressure variations that occur in response to barometric pressure variations at the ground surface (Ahlers et al., 1999; Rousseau et al., 1999), and by the modeling the faults properties required to reproduce the observed occurrences of bomb-pulse ^{36}Cl measured in an 8 km long tunnel at depths of several hundred meters below ground surface (Wolfsberg et al., 2000). Collectively, these studies indicate that the permeability of both nonwelded vitric tuffs and welded, devitrified tuffs in the unsaturated zone can be increased by several times to several orders of magnitude in the presence of faults. Although these observations provide a useful benchmark for estimating the behavior of faults in relatively unaltered, shallow rocks, the saturated tuffs at greater depths in the PM/OV flow domain have, in general, undergone more pervasive and severe degrees of alteration, which would tend to close the faults. The observations from the unsaturated zone at Yucca Mountain therefore might provide only an upper bound on the fault permeabilities expected at greater depths in the PM/OV flow domain.

In the saturated zone at Yucca Mountain, permeabilities have been estimated for welded and nonwelded tuffs from single- and cross-hole hydraulic tests. The nonwelded tuffs in the saturated zone have undergone substantial alteration to zeolites, with zeolite mineral assemblages largely a function of depth and proximity to the Timber Mountain caldera complex (Broxton et al, 1987). Evidence that the hydraulic conductivity of altered, nonwelded tuffs can be substantially enhanced by faulting is provided by data summarized by Loeven (1993) for boreholes UE-25 a#1 and UE-25 b#1. These nearby boreholes are located on the same drillpad near the intersection of the "imbricate fault zone" with the Drillhole Wash fault. The term "imbricate fault zone" refers to a series of closely spaced north and northwest striking normal faults in the hanging wall of the block-bounding Bow Ridge Fault, whereas the Drillhole Wash fault is a northwest-trending fault with probable strike-slip motion (Day et al., 1998b). Within the nonwelded tuffs, hydraulic conductivity estimates based on single-hole hydraulic tests at borehole UE-25 b#1 were several orders-of-magnitude higher than hydraulic conductivities measured on unfractured cores from the same depth interval in the two boreholes. The higher hydraulic conductivities associated with the field tests presumably reflect the increased fracturing associated with the nearby faults.

Single-hole and cross-hole test data reported by Geldon (1996) and Geldon et al. (1997; 1998) for the Calico Hills and Crater Flat Tuffs from the c-well testing complex at Yucca Mountain likewise indicate that the Midway Valley Fault is a permeable feature. The Midway Valley Fault is a northeast-trending, down-to-the-west normal fault that intersects the c-wells in the lower part of the Crater Flat Group tuffs (Geldon, 1996). Despite indications from single-hole test data elsewhere at Yucca Mountain that indicate permeabilities generally decrease with depth, the cross-hole test data from the c-wells complex indicates that permeabilities locally increase with depth and with increasing proximity to the fault (Zyvoloski et al., 2003, Figure 4).

Evidence from Yucca Mountain suggesting faults may create barriers to groundwater flow comes from hydraulic head data in the vicinity of the Solitario Canyon Fault, which borders the western edge of Yucca Mountain. The Solitario Canyon Fault is a north-trending "scissors" fault with variable displacement along its strike, ranging from down-to-the-east displacement of about 70 m along its northern part to as much as 500 m of down-to-the-west displacement along its southern part. A deformation zone about 550 m wide consisting of anastamosing faults and highly brecciated rock characterizes the southern part of the fault, where hydraulic heads decline by as much as 45 m across

the fault (Day et al., 1998b; Luckey et al., 1996). It is unclear, however, if the drop in hydraulic head is related to the intrinsic properties of the fault zone or to stratigraphic disruption across the fault. The largest head drop across the fault occurs in an area where the most permeable tuffs have been downdropped below the water table on the upgradient side of the fault, but have been tilted above the water table on the downgradient side of the fault (see geologic cross-sections in Day et al., 1998a). Very little head drop exists near the hinge point of the fault where no stratigraphic offset occurs, or across other normal faults located parallel to and downgradient from the Solitario Canyon fault.

In summary, the evidence from Yucca Mountain generally supports a conceptual model in which the permeabilities of both welded and nonwelded tuffs are enhanced by one- to two-orders of magnitude in the vicinity of normal faults. Data are ambiguous as to whether observed head declines across the Solitario Canyon fault are due to a complex fault structure that includes anastamosing fault strands and highly brecciated rock or to stratigraphic offset across the fault.

B.4.0 Evidence of Fault Behavior in the PM/OV Flow Domain

Discussions of the anticipated effects of faults on groundwater movement in the PM/OV flow domain are presented in Blankennagel and Weir (1973) and Grauch et al. (1999). Blankennagel and Weir (1973) discussed fault properties in the context of different rock types noting that, despite overall differences in their water yields and the greater tendency of faults in zeolitic nonwelded tuffs to reseal, nonwelded tuffs, like welded tuffs and lavas, can be quite productive where locally cross-cut by faults. Grauch et al. (1999) speculated that the amount of the stratigraphic offset across a structural feature will largely determine whether it exerts a significant influence on groundwater flow. Because of pronounced stratigraphic offset along caldera margins, Grauch et al. (1999) anticipate that these features will have the largest impact on groundwater flow. Conversely, because offset across the northwest trending structural zones is generally small in comparison, the northwest trending structural zones will have relatively minor impact on groundwater flow.

In this report, patterns in the distribution of hydraulic heads and conservative groundwater solutes (Cl, SO_4) in the PM/OV model domain are examined to evaluate the effect of structural features on groundwater flow patterns and infer their expected hydraulic properties. The hydraulic head gradients provide an indication of the potential for flow in a particular direction, whereas the conservative solute species provide an indication of the actual flow directions. Together, the hydraulic and chemical datasets can indicate the anisotropy introduced by faults in the flow system, whether because of the fault properties or because of the effects of stratigraphic disruption across the faults. To help isolate the effects introduced by fault properties from those caused by stratigraphic dislocation, frequent reference is made to hydrostratigraphic cross-sections in Bechtel (2002, Appendix D) that are reproduced in this report in Appendix A. In general, these cross-sections indicate that geologic dislocations across caldera boundaries can be profound and that the possible importance of stratigraphic offsets for individual HSUs on flow patterns can be quite variable across similar types of faults because of different amounts of offset.

B.4.1 Comparison of Structural Feature Map with the Potentiometric Surface Map

A preliminary analysis done in support of the PM/OV flow model project used numerical simulations to help identify patterns in hydraulic heads near faults that might be useful for diagnosing fault characteristics (Kwicklis and Sulley, 2005). In plan view, these simulations considered permeable, impermeable, and complexly-zoned faults oriented in various aspects relative to the regional flow field to explore the effect of these faults on nearby hydraulic heads. In cross-sectional view, these simulations considered the complicating effects of layering and the juxtaposition of layers with contrasting hydraulic properties. Pathlines were traced with particle tracking methods in both the plan view and the cross-sectional simulations. Based on their highly schematic simulations of fault behavior, Kwicklis and Sulley (2005) concluded that:

1. High permeability features oriented parallel to the regional gradient act as drains, so that hydraulic head contours bend toward the feature in a manner consistent with convergent flow toward the feature.

2. High permeability features of limited extent that are oriented perpendicular or oblique to the regional hydraulic gradient exert little observable effects on the gradient, although pathlines are displaced laterally across obliquely oriented features. Complexly zoned faults in which an outer zone of high permeability material surrounds an inner low-permeability zone also have little observable effect on the hydraulic gradient when the features are of limited extent and oriented obliquely to the regional gradient.

3. Low permeability features of limited extent oriented obliquely to the regional gradient result in local hydraulic head contours that intersect the features at high angles and cause the water-level contours to appear to be "discontinuous" across the feature. Complexly-zoned faults of similar extent and orientation in which an outer zone of low permeability material surrounds an inner high-permeability zone exert similar effects.

4. Groundwater flow is diverted around low permeability features of limited extent that are perpendicular to the regional hydraulic gradient, so that flow diverges upgradient from the barrier and converges downstream of the barrier.

5. Where high-permeability rocks are juxtaposed against low-permeability rocks with no distinct structural feature present, the hydraulic gradient in the high permeability rocks can be very small and heads decrease linearly through the low permeability material. This relationship is maintained regardless of whether the low-permeability rocks are the upgradient or the downgradient member. The inclusion of a very low-permeability structural feature between the two rock types causes some of the head loss through the moderately low-permeability rock to occur through the feature instead.

6. Where groundwater flow through layered aquifer/aquitard systems is blocked by low-permeability features, both upward and downward hydraulic gradients exist near the fault as groundwater moves out of the aquifers into the adjacent aquitards and through the faults.

Hydraulic heads in and near the PM/OV model domain are shown with the structural feature map from Bechtel (2002, Figures 3-1 and 6-5) for the model domain in Figure B.7-2. To produce the contour map of hydraulic heads, the measured hydraulic heads in Excel file *final_map_wl_headsv31.xls* (Shaw, 2003) were contoured using a linear kriging algorithm contained in SURFER 7.0 and a 500-m grid spacing. The hydraulic heads in this file included some outside the PM/OV flow domain to provide some constraints on heads along the model boundaries. In wells where measurements at multiple depths exist, only the lowest measured heads were included in the excel file, primarily to eliminate the possibility that the heads might represent perched water. To help constrain the contouring algorithm in data-poor areas in the northwest corner of the model domain, several (6) estimated heads at fictitious "control points" were contained in the original Excel file (Shaw, 2003). These fictitious control points were retained when the measurements were kriged onto a regular grid for contouring, but only actual measurement locations are plotted with the contours in Figures B.7-2 and B.7-3.

In addition to the data limitations mentioned in the preceding paragraph, it is important to note that hydraulic heads are generally measured in open boreholes and thus represent a composite of the heads in the formation intersecting the borehole. Where more detailed profiles of hydraulic head versus depth exist in individual boreholes, these profiles have indicated head variations of up to several tens of meters over the depth range of the borehole (e.g., Blankennagel and Weir, 1973, Table 7; Wolfsberg et al., 2002, Figures 3-5 and 4-4). Thus, these composite measurements bear an uncertain relation to the heads in any particular formation. Additionally, the composite heads originate from relatively shallow depths compared to many of the water-bearing formations in the hydrostratigraphic model.

Ignoring the possible effects of vertical head variations and assuming that permeability is isotropic within the model domain, the hydraulic head contours indicate that flow from area 20 and the western part of area 19 will be southwestward through the Timber Mountain caldera complex toward Oasis Valley, with some of this groundwater potentially turning southward toward Crater Flat before reaching Oasis Valley. The central part of area 19 coincides with a groundwater divide, with

groundwater in the western part flowing toward Oasis Valley and groundwater in the eastern part flowing toward Yucca Flat. Hydraulic head contours in Oasis Valley display a curvature that indicates convergent flow toward this area, as expected for an important regional discharge area. Hydraulic head contours are poorly constrained by actual data in the northwest part of the model domain, and the linear aspect of the contour lines there reflects the predominantly southerly flow assumed when assigning heads to the control points in this part of the model.

In some parts of the model domain, the hydraulic head contours are constrained well enough by the data that localized changes in the regional hydraulic gradient can be used to make inferences about the possible effects of nearby faults on groundwater flow. The following sections discuss the occurrence and possible structural causes of four such hydraulic features identified on the contour map (Figure B.7-2).

Hydraulic Feature #1

Hydraulic feature #1 is a southwest trending trough in the potentiometric surface. In the vicinity of area 20, this trough is located east of the western margin of the Silent Canyon caldera complex and the Thirsty Canyon lineament (42). Further south, this trough is coincident with, or west of, the western margin of the Timber Mountain caldera complex (26, 27) and the Thirsty Canyon lineament (42). Based on the simulation results summarized above, the trough in the potentiometric surface near Area 20 may have originated from several causes: (a) The potentiometric surface trough coincides with a zone of higher transmissivity, either because of fracturing associated with the caldera margin, or because it coincides with a thick accumulation of intra-caldera tuffs in a structural trough between the western caldera margin and the West Greeley Fault (14) (see Blankennagel and Weir, 1973, Plate 2). (b) The Purse (19) and West Purse (20) Faults on the western margin of the trough and the Boxcar (7) and West Boxcar (8) Faults on the eastern part of the structural trough, combined with the Western Silent Canyon Structural Zone (44) on the northern end of the trough, collectively limit groundwater flow into the potentiometric trough, so that the small flux of groundwater through this area can move under a relatively small hydraulic gradient. In addition to these explanations, the UGTA regional model (DOE/NV, 1997) suggested that this groundwater trough was caused, in part, by reduced permeability in the Black Mountain caldera area.

Distinguishing between alternative explanations for this feature is difficult. Blankennagel and Weir (1973, p. 18-19) suggested that the westernmost margin of the Silent Canyon Caldera functions as a barrier, while caldera ring fractures form a drain on the east side of the margin, therefore effectively combining aspects of explanations (a) and (b). Their hand-drawn representation of hydraulic heads near the barrier represent the potentiometric surface as discontinuous across the barrier (Blankennagel and Weir, 1973, Plate 1). The similarity between their depiction of the potentiometric surface near the Purse (7) and West Purse (8) Faults and the simulation results described by *summary result #3* above suggest that a barrier fault is part of the explanation for hydraulic feature # 1. Part of the barrier effect may also be due to the extreme stratigraphic dislocation across the western margin of the Silent Canyon Caldera Hydrostratigraphic cross-section C-C' of Bechtel (2002) through the Black Mountain Caldera and the Silent Canyon Caldera Complex). The cross-section also indicates that important aquifers like the Belted Range Aquifer (BRA) thin toward the west, so that they are more prone to stratigraphic disruption along faults in the western part of the caldera. However, cross-section C-C' shows that stratigraphic disruption of the BRA is complete across the West Greeley Fault (14) and the BRA is only partially disrupted across the Box Car Fault (7), indicating that hydraulic gradients should be steeper across the West Greeley Fault (14) if stratigraphic disruption is the principal cause of steep gradients in this area. Conversely, hydraulic head contours indicate relatively large hydraulic gradients across the East Greeley Fault (13) and the Boxcar (7) and West Boxcar (8) Faults and relatively small gradients across the West Greeley Fault (14) (Figure B.7-3).

Hydraulic Feature #2

Hydraulic feature #2 on Figure B.7-2 identifies a sharp break in the hydraulic gradient across the southern part of the combined Ammonia Tanks (26) and Rainier Mesa (27) caldera structural margins (henceforth referred to as ATS/RMS). Hydraulic gradients are small through the Timber Mountain Complex north of the ATS/RMS, whereas gradients increase substantially south and southeast of the ATS/RMS and moderately to the southwest of the ATS/RMS margins. Moreover, the curvature of the 1,250 m head contour appears to parallel the southern ATS/RMS boundary, as if this boundary were acting as a barrier to groundwater flow. The absence of a large hydraulic gradient across the northern ATS/RMS margin, the apparent coincidence of a potentiometric trough with the western ATS/RMS margin, and simulation summary result #5 described previously in this section,

collectively indicate that stratigraphic disruption across the southern ATS/RMS or RMS margins may be the cause of these changes in the hydraulic gradient. Hydrostratigraphic unit cross-sections support the concept that stratigraphic juxtaposition, rather than hydraulic properties of the ATS/RMS margin, is the dominant control on hydraulic gradients. Cross-section H-H' of Bechtel (2002) indicates that groundwater flow directly south across the ATS/RMS may be partially blocked by intrusive rocks associated with the Claim Canyon Caldera (CCICU). Similarly, cross-section I-I' of Bechtel (2002) indicates that groundwater flow southeast across the RMS boundary may be partially blocked by the Upper Clastic Confining Unit (UCCU). The more moderate gradient across the southwest RMS margin may arise from the juxtaposition of permeable carbonate rocks on the downgradient side of the southwestern RMS margin (Cross-section J-J' of Bechtel, 2002). In summary, the head patterns associated with the northern, southern and western parts of the ATS/RMS margins indicate that these structural features are not inherently groundwater barriers, and that the southern ATS/RMS or RMS margins functions as barriers largely because of the local stratigraphic juxtaposition of low permeability rocks on the downgradient side.

Hydraulic Features #3 and #4

The remaining hydraulic head features discussed in this section pertain to areas 19 and 20, and are best seen in Figure B.7-3. Hydrologic feature #3 refers to the southward hydraulic gradient indicated by the 1,350 to 1,300 m contours between the Boxcar (7) and West Greeley Faults (14) in the vicinity of the Western East Thirsty Canyon Structural Zone (43) (Western ETCSZ). The direction of the gradient could indicate that groundwater flow is redirected southward by the Boxcar Fault, whereas the steepness of the gradient in the vicinity of the Western ETCSZ could indicate that this feature, or nearby features like the southern Area 20 Caldera Margin (30), are barriers to groundwater flow. Wolfsberg et al. (2002) found through model calibration that permeabilities lower than those of the surrounding rocks were needed in the Boxcar (7) and West Boxcar (8) faults to preserve a steep SW gradient. However, the structural HSU model used in that study did not represent stratigraphic offsets and disruption explicitly, as the current model does.

The nearest available north-south hydrostratigraphic cross-section located to the west of this area indicates significant stratigraphic disruption across the southern Area 20 caldera margin (30), but only slight stratigraphic displacement across the Northern Timber Mountain Structural Zone (38) (Cross section H-H'). Although data are sparse, there is little evidence that, in general, the southern

Area 20 caldera margin, the Northern Timber Mountain Structural Zone, or other east-west structural zones exert much influence on hydraulic head patterns in this area. The steepness of the southward hydraulic gradient east of the Boxcar Fault (7) may simply reflect the deflection and accumulation of groundwater flow parallel to the fault. This interpretation is supported by the observation that the 1,400 and 1,375 m hydraulic head contours between the West Almendro Fault (2) and the East Greeley Fault (13) display a similar pattern (Hydrologic feature # 4), but, in this case, an east-west structural feature is absent.

B.4.2 Comparison of Structural Feature Map with Dissolved Chloride and Sulfate Distributions

The present study uses chloride (Cl) and sulfate (SO_4) to trace the movement of groundwater within the study area. These species were chosen as groundwater tracers because (1) they have relatively high solubilities and are unlikely to precipitate, (2) Cl- and S-bearing minerals are generally absent or sparse in the rocks, so large increases in Cl and SO_4 concentrations due to water/rock interaction are unlikely, and (3) both historic and UGTA-project related data are available for these species, thereby increasing the areal coverage and level of detail relative to less commonly measured isotopic species like delta deuterium (δD) and delta oxygen-18 ($\delta^{18}O$). Although the sampling density of these isotopic species was not sufficient to provide detailed information about the hydrologic properties of individual faults, δD has proven useful for interpreting regional flow patterns (SNJV, 2004a). It should also be noted that potential sources of SO_4 in the rock include pyrite in hydrothermally altered areas, such as that associated with the granitic intrusion encountered in borehole PM-2 in the extreme northwest corner of Area 20 (Warren et al, 2003; Blankennagel and Weir, 1973, p. 28).

Chloride, SO_4 and δD have previously been used by SNJV (2004a) to estimate regional flow paths in the PM/OV flow domain. The results of their analyses (SNJV, 2004a) indicated that groundwater from western Pahute Mesa flows southwest toward Oasis Valley, roughly parallel to the Thirsty Canyon lineament. At Oasis Valley, the groundwater from Pahute Mesa mixes with groundwater flowing southward from Gold Flat and local recharge in the highlands adjacent the discharge area. Groundwater from the western part of NTS area 19 flows southwest across Timber Mountain before turning southward toward Crater Flat, and groundwater in the eastern part of area 19 is estimated to flow southward toward western Jackass Flats through Fortymile Canyon. The flowpaths depicted in SNJV (2004a) were intended to provide an overview of regional flow directions and not intended to

demonstrate the effects of individual faults or structural features on flow patterns. However, it is interesting to note that these flow paths are closely aligned with the hydraulic gradient, implicitly implying that flow directions are not affected by anisotropy associated with structural features in any regionally consistent way.

The groundwater Cl and SO_4 concentration data used in the present study were obtained by querying the Department of Energy's comprehensive water quality database for the vicinity of the NTS (*geochem02.mdb*) for data within the map area shown in Figure B.7-2. The areal distributions of groundwater Cl and SO_4 concentrations obtained from this query show several trends (Figures B.7-4 to B.7-7). As noted by SNJV (2004a), groundwater Cl and SO_4 concentrations east of the Purse (19) and West Purse (20 Faults are substantially more dilute than concentrations of these species to the west of these faults. This suggests that groundwater flow eastward across these faults is small, despite the relatively large hydraulic gradient in this area. A small amount of leakage across the Purse Fault may be indicated by the relatively large Cl and SO_4 concentrations (32 and 73 mg/L, respectively) at well UE-20ai (Egmont) located east of the Purse Fault and the Area 20 caldera margin. However, evidence for significant mixing between these groundwaters exists only south of the southern end of the West Purse Fault (20), where groundwater concentrations in the vicinity of the Thirsty Canyon lineament indicate roughly subequal contributions of the groundwater found west and east of the Purse Fault (19) further north in area 20. The presence of relatively high concentrations of Cl and SO_4 east of the Thirsty Canyon Lineament (42) indicates it is not a barrier to groundwater flow, at least southwest of the Area 20 caldera margin (30). The disappearance of east-west chemical differences southwest of the Purse (19) and West Purse (20) Faults suggests that these faults act as barriers primarily because they coincide with the western boundary of the Area 20 caldera (29, 30).

In order to distinguish between possible alternative flowpaths using geochemical tracers, it is necessary that the alternative flow paths be characterized by different chemistries. Because only Cl and SO_4 concentrations are examined in this report, and their variability is insufficient to distinguish between alternative flowpaths in the vicinity of most faults, it is possible to distinguish between flowpaths in only a few instances. The first instance involves Hydrologic Feature #4, the north-south hydraulic gradient between the East Greeley (13) and West Almendro (2) Faults (Figure B.7-3). Direct north-south flow is precluded in this instance by the differences in the SO_4 concentrations north and south of this feature (Figure B.7-7). More northeast to southwest flow near Hydrologic

Feature #4 is indicated by the relative constancy in SO_4 concentrations along the NE/SW direction in this area. However, the sparsity of data also allows a more tortuous groundwater flow path involving southward flow along north-trending East Greeley Fault (13) and westward flow along East Thirsty Canyon Structural Zone (36), thus producing the apparent southwest flow direction. The SO_4 data, in general, preclude direct north to south flow from area 20 and the northwest part of area 19 into areas 18 and 30 (Figures B.7-6 and B.7-7). The moderately high SO_4 concentrations in the northwest part of area 19 and most of area 20 are compatible with flow from the northwest part of area 19 into area 20 across the West Greeley (14) and Boxcar (7) Faults and into the potentiometric trough associated with Hydrologic Feature #1 (Figures B.7-2 and B.7-6).

B.4.3 Evidence for Fault Behavior from Permeability Data

Hydraulic conductivities estimated for different HSUs in the PM/OV flow domain and surrounding areas indicate substantial overlap in their values (Figure B.7-8) (Shaw, 2003). Excluding data for the Volcanic Confining Units (VCU), the combined data indicate an overall trend of decreasing hydraulic conductivity with increasing depth, with hydraulic conductivities spanning an approximate 2 order of magnitude range at any particular depth. In contrast, hydraulic conductivities in the VCU vary over an almost 4 order of magnitude range at any particular depth and show, albeit with considerable scatter, a somewhat more rapid decrease with depth. Average conductivities are similar for VCU and non-VCU at 400 m depth [log10 (K) ~0], but at 1 km, the mean hydraulic conductivities of the VCU and non-VCU are about –2 and -0.5, respectively

In lavas, welded tuffs, and zeolitized nonwelded tuffs, hydraulic conductivity is dominated by fractures and faults. The variability in the hydraulic conductivity for any particular HSU at a given depth therefore probably reflects differences among the fracture and fault characteristics that exist at individual test locations. In general, lavas and welded tuffs have higher fracture densities than the zeolitized nonwelded tuffs (Drelleck et al., 1997). Thus, in densely fractured welded tuffs and lavas, most tests intersect conductive fractures and few test zones test only the rock matrix, so the variability in test results is relatively small. In sparsely fractured rock like the zeolitized nonwelded tuffs that comprise the VCU, test intervals may or may not intersect conductive fractures or faults, so the variability in hydraulic conductivity is larger than in the other units. The lowest hydraulic conductivities in the VCU presumably reflect tests done in unfractured or unfaulted zones, while the

highest conductivities were done in intervals that contain fractures or faults. The highest hydraulic conductivities for the VCU in the depth interval between 400 and 1,200 m depth are comparable to those found in aquifers and composite units in the area, supporting the notion that fractures and faults in the VCU can remain open and transmissive. However, the more rapid decrease in hydraulic conductivity with depth in the VCU may reflect the lower compressive strength of the nonwelded tuffs that comprise the VCU, a factor that would allow fractures and faults in the VCU to close more readily with increasing lithostatic stresses than fractures and faults in lavas or welded tuffs (Blankennagel and Weir, 1973).

The relatively high hydraulic conductivity values of 1 to 100 m/day evident in Figure B.7-8 are comparable to the permeabilities of 1.0×10^{-12} to 1.0×10^{-10} m^2 that have been measured in fault zones in welded and nonwelded tuffs at Yucca Mountain (LeCain et al., 2000; Loeven, 1993; Geldon et al., 1997). This similarity suggests that faults and fault zones in the PM/OV flow domain may have hydraulic conductivities parallel to their strike that are at least as high as those measured at Yucca Mountain.

B.4.4 Examination of the Role of Feature Orientation, Hydrothermal Alteration, Reactivation, Amount of Hydrostratigraphic Offset, and Feature Type on Feature Hydraulic Properties

In this section, hydraulic gradients near faults and structural zones in the vicinity of NTS areas 19 and 20 are examined in the context of the attributes of the structural features (Table B.7-1) and the intensity of hydrothermal alteration associated with the different calderas (Table B.7-2). The purpose of this examination is to determine whether head gradients across faults and structural zones can be correlated even qualitatively with the observed attributes of these features.

This examination focuses on the Boxcar (7), West Boxcar (8), West Greeley (14) and East Greeley (15) faults. These faults were selected because they are potential groundwater pathways from the testing areas and because hydraulic head contours near these faults are relatively well constrained by measurements. Hydraulic head contours in the vicinity of these faults (Figure B.7-3) indicate that the hydraulic gradient is relatively large across the Boxcar (7) and West Boxcar (8) faults, moderate across the northern part of the East Greeley fault (13), and small across the West Greeley fault (14). Because each of these faults trends northward, the effect of fault orientation as a possible cause for

the differences in their associated hydraulic gradients can be discounted. An examination of the relative intensities of alteration (Table B.7-2) indicates that the Area 20 caldera is less intensely altered than the Grouse Canyon caldera, so that the West and East Greeley Faults, which are within or bounding the Grouse Canyon caldera, would be expected to be less permeable and have steeper hydraulic gradients across them than the Boxcar and West Boxcar Faults. Because the reverse relation between alteration intensity and magnitude of hydraulic gradient is observed, alteration intensity related to caldera formation apparently does not control fault hydrologic behavior in these cases. Intense alteration associated with the Grouse Canyon caldera may not have been associated with the West and East Greeley Faults. More likely, nearly a km of offset has occurred along the West Greeley fault subsequent to formation of the Grouse Canyon caldera (Table 5 in Warren et al., 2000), so that any initial modification of its character by caldera activity has been overwhelmed during subsequent reactivation. Likewise, reactivation of the Boxcar (7) and West Boxcar (8) Faults by nuclear weapons tests is near 100 percent, whereas only 50 percent of the West (14) and East (13) Greeley Faults have been reactivated (Table B.7-1). Therefore, if reactivation percentage is the controlling variable, head gradients would be less across the Boxcar and West Boxcar faults compared to the West and East Greeley Faults. It is possible, of course, that reactivation has taken place too recently to have a measurable effect on heads near the Boxcar and West Boxcar Faults, but that long-term hydraulic readjustment may be underway.

Near-surface hydrostratigraphic offset across the West Greeley fault (150 m) is larger than estimated for the East Greeley Fault (30 m) or the Boxcar and West Boxcar Faults (60 m) (Table B.7-1), so there may be a correlation between stratigraphic offset and fault permeability. This relation suggests that, with increasing stratigraphic offset, any permeability reductions that result from gouge formation are secondary compared to permeability increases associated with the additional fracturing.

Caldera boundaries are generally thought of as normal faults, but with greater stratigraphic offset and a broader range of orientations than most other north-trending normal faults in the PM/OV area. The West Greeley Fault (14) forms the eastern boundary of the Area 20 caldera, whereas the Purse (19) and West Purse (20) Faults coincide with the western boundary of the caldera. The large hydraulic gradient associated with Purse and West Purse Faults and the small gradient associated with the West Greeley Fault suggests that stratigraphic offsets may be the dominant difference between head gradients in these areas. The West Greeley Fault juxtaposes a thick stratigraphic sequence of aquifers

and confining units entirely within a complex trough, whereas the Purse and West Purse Faults define the western boundary of this trough. Terrain west of the trough has remained structurally high throughout caldera formation within the Silent Canyon caldera complex, accumulating alteration from all nearby calderas within the PM/OV area. Thus this terrain, where the Pre-Belted Range Composite Unit (PBRCM) lies at shallow depths beneath the water table, contains no stratigraphic layers that are hydraulically conductive, and so provides a major barrier to westward flow of groundwater (Blankennagel and Weir, 1973, p. 18-19).

The geologic origins of many of the W- and NW-trending structural zones in the PM/OV flow domain are uncertain, but some may be the structural margins of buried calderas (Bechtel, 2002), in which case they would be normal faults. Because the direction of minimum horizontal stress is NW-SE in the PM/OV flow domain, these structural zones would be in a state of relative compression compared to N-trending normal faults, a condition that would tend to make them less permeable than N-trending faults in the area, other factors being equal. Furthermore, since many structural zones are buried by younger unfaulted rocks, the structural zones have clearly not been reactivated by recent weapons testing or other seismic events. The relatively steep N-S hydraulic gradients associated with the West Silent Canyon Structural Zone in hydrologic feature #1 and the Western East Thirsty Canyon Structural Zone in hydrologic feature #3 support the inference that these NW-trending structural zones may be barriers to southerly groundwater movement.

B.5.0 SUMMARY AND CONCLUSIONS

Preliminary interpretations regarding the hydrologic properties of selected faults, caldera margins, and structural zones have been made where hydrologic and geochemical data are sufficiently numerous to make interpretations of hydraulic gradients and flow patterns near these features. In these instances, estimates are made of the permeability of these features relative to the surrounding unfaulted rocks. Furthermore, in many instances the observed hydraulic gradients and interpreted flow patterns are not necessarily controlled by single structural features, but are the complex hydrologic response to multiple structural features, so unique interpretations may not be possible without the aid of a numerical model. Integrating the discussion presented in this report, the remainder of this summary provides a summary of inferred fault behavior that can help guide development of the PM/OV groundwater flow model.

As a first approximation, the PM/OV flow model should be run with all faults assigned permeabilities equal to the permeabilities of the HSUs they intersect. This model formulation, which considers faults as having no effect on groundwater flow, will allow for testing of hydraulic response to HSU offsets across fault zones and indicate whether the shallow composite head measurements are sensitive to offsets of HSUs at greater depths. Then, faults should be grouped based upon the following guidelines for permeability and considered with the numerical model.

Caldera structural margins may be relatively high permeability features because of considerable offset and brecciation of the rock near these faults. A trough in the potentiometric surface inside the western margin of the Area 20 caldera (30) and roughly coinciding with the western margin of the Timber Mountain caldera (27) is consistent with this interpretation. The relatively steep hydraulic gradients downgradient from the southern margin of the Timber Mountain caldera complex (26, 27) may have resulted from the juxtaposition of low permeability intrusive and clastic rocks on the downgradient side of the caldera margin. The absence of a comparably steep hydraulic gradient across the northern margin of the Timber Mountain caldera complex also indicates that the caldera margin is not an inherently low permeability feature.

Aside from two possible exceptions, the W- and NW-trending structural zones do not appear to be either barriers or conduits for groundwater flow. The two possible exceptions involve the steep hydraulic gradients south of the West Silent Canyon Structural Zone (44) and the steep hydraulic gradient near the Western East Thirsty Canyon Structural Zone (43). In both cases, however, other nearby structural features or stratigraphic offsets could be contributing to these apparent effects. The West Silent Canyon Structural Zone coincides with the northern margin of the Area 20 caldera (30), across which there is considerable stratigraphic offset (Bechtel [2002] – Cross-section J-J'). The nearby N-trending Purse (19) and West-Boxcar (14) faults may also be contributing to the apparent steep N-S gradient by blocking west-to-east and east-to-west flow south of the West Silent Canyon Structural Zone (44). Likewise, an apparent head drop near the Western East Thirsty Canyon Structural Zone (43) could be the result of influence of the nearby N-trending Boxcar (7) and West Greeley (14) faults, stratigraphic offsets across the nearby southern margin of the Area 20 caldera (30), and the lack of control on hydraulic heads. These two particular features should be modeled first as low-permeability features. However, where the northwest trending structural zones coincide with caldera margins, they can first be modeled as high-permeability features.

Normal faults in Areas 19 and 20 should be modeled first as relatively low permeability features, except where they coincide with caldera margins. However, differences in the hydraulic gradients across several of the many N-trending faults in areas 19 and 20 are not readily explainable in terms of differences in alteration intensity associated with the Grouse and Area 20 calderas or by differences in the percent of the fault trace length reactivated by nuclear weapons tests. Hydraulic gradients across these faults may be inversely related to the amount of offset across the fault, a possibility that is consistent with the inference that faults with considerable offset along caldera margins are essentially high-permeability features. This concept is also supported by the small hydraulic gradient across the West Greeley Fault (14), which coincides with the western boundary of the Grouse Canyon caldera (29) and which has 150 m of near-surface offset. However, the Purse (19) and West Purse (20) Faults are modeled as coinciding with the western margin of the Area 20 caldera (although each has only 30 m of near-surface offset) and a large hydraulic gradient coincides with this margin. If the head gradient across the Purse (19) and West Purse (20) Faults is not accurately reproduced using this conceptual model and the modeled hydrostratigraphic offsets, it may be necessary to make different assumptions regarding the permeability of the western margin of the Area 20 caldera.

The Thirsty Canyon Lineament (42) appears to coincide with a trough in the potentiometric surface over most of its length and to be a zone in which high and low salinity groundwaters mix. These characteristics suggest it is a high permeability feature over most or all of its length.

In general, the flow directions inferred from conservative geochemical tracers like chloride and sulfate are nearly coincident with those that would be inferred from the hydraulic gradient assuming that large-scale hydraulic conductivities are isotropic. This agreement implies that the many structural features present in the model domain do not impart a large-scale anisotropy to the flow system in any regionally consistent manner. However, this does not eliminate the possibility that flow patterns may be more complex and tortuous on a more local scale due to the influence of the structural features. Finally, hydraulic head and geochemical data are sparse beneath the resurgent dome and moat zone of the Timber Mountain caldera complex, and so the effects of faults and other structures on groundwater flow in this part of the model domain are poorly understood relative to other areas using the methods of analysis applied in this report.

B.6.0 ACKNOWLEDGEMENTS

Sincere thanks to Rick Warren of Los Alamos National Laboratory who reviewed this report and who directed the authors to important references. His suggestions and insights have greatly improved the quality of this report.

B.7.0 REFERENCES

Ahlers, C.F., S. Finsterle, and G.S. Bodvarsson, Characterization and prediction of subsurface pneumatic response at Yucca Mountain, Nevada, Journal of Contaminant Hydrology, vol. 38, no. 1-3, p. 47-68, 1999.

Antonelli, M., A. Aydin, and L. Orr, Outcrop-aided characterization of a faulted hydrocarbon reservoir: Arroyo Grande Oil Field, California, USA, American Geophysical Union Monograph 113, "Faults and Subsurface Fluid Flow in the Shallow Crust" (W. Haneberg, et al., eds.), pp. 7-26, 1999.

Bechtel, Nevada, A Hydrostratigraphic Model and Alternatives for the Groundwater Flow and Contaminant Transport Model of Corrective Action Units101 and 102: Central and Western Pahute Mesa, Nye County, Nevada, DOE/NV/11718-70, 2002.

Benedict, F.C., Jr., T.P. Rose, and X. Zhou, Mineralogical, Chemical, and Isotopic Characterization of Fracture-Coating Minerals in Borehole Samples from Western Pahute Mesa and Oasis Valley, Nevada, Lawrence Livermore National Laboratory Report UCRL-ID-152919, 2001.

Blankennagel, R.K., and J.E. Weir, Jr., Geohydrology of the eastern part of Pahute Mesa, Nevada Test Site, Nye County, Nevada, U.S. Geol. Survey Prof. Paper 712-B, 35 pp., 1973.

Brocher, T.M., W.C. Hunter, and V.E. Langenheim, Implications of seismic reflection and potential field geophysical data on the structural framework of the Yucca Mountain – Crater Flat region, Nevada, GSA Bulletin, v. 110, no. 8, p. 947-971, 1998

Broxton, D.E., D.L. Bish, and R.G. Warren, Distribution and chemistry of diagenetic minerals at Yucca Mountain, Nye County, Nevada, Clays and Clay Minerals, v. 35, p. 89-110, 1987.

Byers, F.M., Jr., W.J. Carr, P.P. Orkild, W.D. Quinlivan, and K.A. Sargent, Volcanic suites and related cauldrons of Timber Mountain-Oasis Valley caldera complex, southern Nevada, U.S. Geol. Survey Prof. Paper 919, 70 pp., 1976.

Caine, J.S., and C.B. Forster, Fault zone architecture and fluid flow: Insights from field data and numerical modeling, American Geophysical Union Monograph 113, "Faults and Subsurface Fluid Flow in the Shallow Crust" (W. Haneberg, et al., eds.), pp. 101-127, 1999.

Carlos, B.A., S.J. Chipera, D.L. Bish, and S.J. Craven, "Fracture-lining manganese oxide minerals in silicic tuff, Yucca Mountain, Nevada, USA," Chemical Geology, v. 107, pp. 47-69, 1993.

Carlos, B.A., S.J. Chipera, and D.L. Bish, "Distribution and chemistry of fracture-lining minerals at Yucca Mountain, Nevada," Los Alamos National Laboratory Report LA-12977-MS, 92 p., 1995.

Carr, W.J., and W.D. Quinlivan, Structure of Timber mountain resurgent dome, in Eckel, E. B., ed., Nevada Test Site. Geological Society of America Memoir 110, pp. 99-108, 1968.

Carr, W.J., Styles of extension in the Nevada Test Site region, southern Walker Lane Belt; An integration of volcano-tectonic and detachment fault models, in Basin and Range Extensional Tectonics Near the Latitude of Las Vegas, Nevada, Geological Society of America Memoir 176, Boulder Colorado, p. 283-303, 1990.

Christiansen, R.L., P.W. Lipman, W.J. Carr, F.M. Byers, Jr., P.P. Orkild, and K.A. Sargent, Timber Mountain-Oasis Valley caldera complex of southern Nevada, Geol. Soc. Amer. Bull., 88, 943-959, July 1977.

Cole, J.C., and P.H. Cashman, Structural relationships of pre-Tertiary rocks in the Nevada Test Site region, southern Nevada, U.S. Geol. Survey Prof. Paper 1607, 39 pp., 1999.

DOE/NV, see U.S. Department of Energy, Nevada Operations Office.

Day, W.C., R.P. Dickerson, C.J. Potter, D.S. Sweetkind, C.A. San Juan, R.M. Drake, and C.J. Fridrich, Bedrock geologic map of the Yucca Mountain area, Nye County, Nevada, Geologic Investigations Series I-2627, 1998a.

Day, W.C., C.J. Potter, D.S. Sweetkind, R.P. Dickerson, and C.A. San Juan, Bedrock geologic map of the central block area, Yucca Mountain, Nye County, Nevada, U.S. Geological Survey, Miscellaneous Investigations Series Map I-2601, 1998b.

Drellack, S.L., Jr., L.B. Prothro, K.E. Roberson, B.A. Schier, and E.H. Price, 1997. Analysis of fractures in volcanic cores from Pahute Mesa, Nevada Test Site. DOE/NV/11718 160. Bechtel Nevada. Las Vegas, NV.

Ekren, E.B., and F.M. Byers, Jr., Ash-flow fissure vent in west-central Nevada, Geology, 4, pp. 247-251, 1976.

Evans, J.P., C.B. Forster, and J.V. Goddard, Permeability of fault-related rocks, and implications for hydraulic structure of fault zones, Journal of Structural Geology, v. 19, no. 11, pp. 1393-1404, 1997.

Faunt, C.C., Effect of faulting on ground-water movement in the Death Valley Region, Nevada and California, U.S. Geological Survey Water-Resources Investigations Report 95-4132, 42 p., 1997.

Ferguson, J.F., A.H. Cogbill, and R.G. Warren, "A geophysical and geological transect of the Silent Canyon caldera complex, Pahute Mesa, Nevada," J. Geophys. Res., Vol. 99, No. B30, p. 4323-4339, 10 March 1994.

Fleck, R. J., B.D. Turrin, D.A. Sawyer, R.G. Warren, D.E. Champion, M.R. Hudson, and S.A. Minor, "Age and character of basaltic rocks of the Yucca Mountain region, southern Nevada," J. Geophys. Res., Vol. 101, No. B4, pp. 8205-8228, 10 April 1996.

Forster, C.B., and J.P. Evans, Hydrogeology of fault zones and crystalline thrust sheets: Results of field and modeling studies, Geophysical Research Letters, V. 18, pp. 979-982, 1991.

Fridrich, C.J., Tectonic evolution of Crater Flat basin, Yucca Mountain region, Nevada: U.S. Geological Survey Open-File Report 98-33, 43 p, 1998.

Fridrich, C.J., S.A. Minor, and E.A. Mankinen, Geologic evaluation of the Oasis Valley basin, Nye County, Nevada, U.S. Geol. Survey Open-file Report 99-533-A, 55 pp., 1999.

Frizzell, V.A., and J. Shulters, *Geologic Map of the Nevada Test Site, Southern Nevada,* U.S. Geological Survey Miscellaneous Investigation Series Map I-2046, scale 1:100,000, Washington, D.C., 1990.

Goff, F., J.N. Gardner, W.S. Baldridge, J.B. Hulen, D.L. Nielson, D. Vaniman, G. Heiken, M.A. Dungan, and D. Broxton, Excursion 17B: Volcanic and hydrothermal evolution of Pleistocene Valleys caldera and Jemez volcanic field, in Field Excursions to Volcanic Terrains in the Western United States, Volume I: Southern Rocky Mountain Region, C.E. Chapin and J. Zidek, eds., New Mexico Bureau of Mines and Mineral Resources Memoir 46, p. 381-435, 1989.

Goodwin, L.B., P.S. Mozely, J.C. Moore, and W.C. Haneberg, Introduction, American Geophysical Union Monograph 113, "Faults and Subsurface Fluid Flow in the Shallow Crust" (W. Haneberg, et al., eds.), pp. 1-5, 1999.

Geldon, A.L., Results and interpretation of preliminary aquifer tests in boreholes UE-25c #1, UE-25c #2, and UE-25 C #3, Yucca Mountain, Nye County, Nevada, U.S. Geological Survey Water-Resources Investigations Report 94-4177., Denver, CO, 199 p., 1996.

Geldon, A.L., A.M.A. Umari, M.F. Fahy, J.D. Earle, J.M. Gemmell, and J. Darnell, Results of hydraulic and conservative tracer tests in Miocene tuffaceous rocks at the C-hole complex, 1995 to 1997, Yucca Mountain, Nye County, Nevada. USGS Milestone Report SP23PM3. Denver, Colorado: U.S. Geological Survey, 1997.

Geldon, A.L., A.M.A. Umari, M.F. Fahy, J.D. Earle, J.M. Gemmell, and J. Darnell, Analysis of a multiple-well interference test in Miocene tuffaceous rocks at the C-hole complex, May-June 1995, Yucca Mountain, Nye County, Nevada, U.S. Geological Survey Water-Resources Investigations Report 97-4166, Denver, CO, 33 p., 1998.

Grauch, V.J.S., D.A. Sawyer, C.J. Fridrich, and M.R. Hudson. *Geophysical Framework of the Southwestern Nevada Volcanic Field and Hydrologic Implications.* U.S. Geological Survey Professional Paper 1608, 39 p., 1999.

Healey, D.L., *Application of Gravity Data to Geologic Problems at the Nevada Test Site*, in Eckel, E. B., ed., Nevada Test Site. Geological Society of America Memoir 110, pp. 65-74, 1968.

Hildenbrand, T.G., V.E. Langenheim, E.A. Mankinen, and E.H. McKee, *Inversion of Gravity Data to Define the Pre-Tertiary Surface and Regional Structures Possibly*

Influencing Ground-Water Flow in the Pahute Mesa - Oasis Valley Region, Nye County, *Nevada*. U.S. Geological Survey Open-File Report 99-49. Menlo Park, CA, 1999.

Hinrichs, E.N., R.D. Krushensky, and S.J. Luft, "Geologic Map of the Ammonia Tanks Quadrangle, Nye County, Nevada," U.S. Geol. Surv. Map GQ-638, scale 1:24 000, 1967.

Hulen, J.B., J.N. Gardner, D.L. Nielson, and F.E. Goff, Stratigraphy, structure, hydrothermal alteration and ore mineralization encountered in CSDP corehole VC-2A, Sulphur Springs area, Valleys caldera, New Mexico: A detailed overview, DOE/ER/13555-1 (ESL-88001-TR), 55 pp., Earth Sci. Lab., Univ. of Utah Res. Inst., Salt Lake City, February 1988.

Jorgensen, D.K., J.W. Rankin, and J. Wilkins, Jr., Geology, alteration, and mineralogy of Bond Gold's Bullfrog deposit, Mining Engineering, pp. 681-686, 1990.

Kwicklis, E.M. and Sulley, M., 2005, Effects of Fault Geometry and Properties on Groundwater Flow and Transport: A Simulation Study, Los Alamos National Laboratory report LA-UR-05-3952, Los Alamos, NM.

Laczniak, R.J., J.C. Cole, D.A. Sawyer, and D.A. Trudeau, "Summary of hydrogeologic controls on ground-water flow at the Nevada Test Site, Nye County, Nevada," U.S. Geological Survey Water-Resources Investigations Report 96-4109, 59 pp., 1996.

LeCain, G.D., Air-injection testing in vertical boreholes in welded and nonwelded tuff, Yucca Mountain, Nevada, U.S. Geological Survey Water-Resources Investigations Report 96-4262, Denver, CO, 33 p., 1997.

LeCain, G.D., L.O. Anna, and M.F. Fahy, Results from geothermal logging, air and core-water chemistry sampling, air-injection testing, and tracer testing in the northern Ghost Dance Fault, Yucca Mountain Nevada, November 1996 to August 1998, U.S. Geological Survey Water-Resources Investigations Report 99-4210, Denver, CO, 47 p., 2000.

Levy, S.S., S.J. Chipera, G. WoldeGabriel, J. Fabryka-Martin, J. Roach, and D. Sweetkind, Flow-path textures and mineralogy in tuffs of the unsaturated zone, American Geophysical Union Monograph 113, "Faults and Subsurface Fluid Flow in the Shallow Crust" (W. Haneberg, et al., eds.), pp. 159-184, 1999.

Lipman, P.W., Caldera-collapse breccias in the western San Juan Mountains, Colorado, Geol. Soc. Amer. Bull., 872, pp. 1397-1410, 1976.

Lipman, P.W., The roots of ash flow calderas in western North America: Windows into the tops of granitic batholiths, Journ. Geophys. Res., Vol. 89, No. B10, pp. 8801-8841, 1984.

Loeven, C., A summary and discussion of hydrologic data from the Calico Hills nonwelded hydrogeologic unit at Yucca Mountain, Nevada, LA-12376-MS (UC-814), Los Alamos National Laboratory, Los Alamos, NM, 102 p., 1993.

Luckey, R.R., P. Tucci, C.C. Faunt, E.M. Ervin, W.C. Steinkampf, F.A. D'Agnese, and G.L. Patterson, Status of understanding of the saturated-zone ground-water flow system at Yucca Mountain, Nevada, as of 1995, U.S. Geological Survey Water-Resources Investigations Report 96-4077, 71 p., 1996.

Maldonado, F., Structural geology of the upper plate of the Bullfrog Hills detachment fault system, southern Nevada, Geol. Soc. Amer. Bull., 102, 992-1006, July 1990.

Mankinen, E.A., T.G. Hildenbrand, G.L. Dixon, E.H. McKee, C.J. Fridrich, and R.J. Laczniak, *Gravity and Magnetic Study of the Pahute Mesa and Oasis Valley Region, Nye County, Nevada.* U.S. Geological Survey Open-File Report 99-303. Menlo Park, CA, 1999.

McKee, E.H., G.A. Phelps, and E.A. Mankinen, *The Silent Canyon Caldera – A Three-Dimensional Model as part of a Pahute Mesa - Oasis Valley, Nevada, Hydrogeologic Model,* U.S. Geological Survey Open-File Report 01-297, 21 p. 2001.

Minor, S.A., "Superposed local and regional paleostresses: Fault-slip analysis of Neogene extensional faulting near coeval caldera complexes, Yucca Flat, Nevada", J. Geophys. Res., Vol. 100, No. B6, p. 10507-10528, 10 June 1995.

Noble, D.C., R.D. Krushensky, E.J. McKay, and J.R. Ege, "Geologic Map of the Dead Horse Flat Quadrangle, Nye County, Nevada," U.S. Geol. Surv. Map GQ-614, scale 1:24 000, 1967.

Noble, D.C., G.D. Bath, R.L. Christiansen, and P.P. Orkild, "Silent Canyon volcanic center, Nye County, Nevada," in Nevada Test Site, E. B. Eckel, ed., Geol. Soc. Amer. Memoir 110, p. 67-75, 1968.

Noble, D.C., T.A. Vogel, E.H. McKee, S.I. Weiss, J.W. Erwin, and L.W. Younker, Stratigraphic relations and source areas of ash-flow sheets of the Black Mountain and Stonewall Mountain volcanic centers, Nevada, Journ. Geophys. Res., Vol. 89, No. B10, p. 8593-8602, Sept. 1984.

Noble, D.C., S.I. Weiss, and E.H. McKee, Magmatic and hydrothermal activity, caldera geology, and regional extension in the western part of the southwestern Nevada volcanic field, in G.L. Raines, R.E. Lisle, R.W. Shafer, and W.W. Wilkinson, eds., Geology and Ore deposits of the Great Basin: Symposium Proceedings, Geol. Soc. of Nevada, p. 913-934, 1991.

Orkild, P.P., F.M. Byers, Jr., D.L. Hoover, and K.A. Sargent, "Sub-surface Geology of Silent Canyon Caldera, Nevada Test Site, Nevada," in Nevada Test Site, E.B. Eckel, ed., Geol. Soc. Amer. Memoir 110, p. 77-86, 1968.

Orkild, P.P., K.A. Sargent, and R.P. Snyder, "Geologic Map of Pahute Mesa, Nevada Test Site and Vicinity, Nye County, Nevada," U.S. Geol. Surv. Misc. Geol. Invest. Map I-567, scale 1:48 000, 1969.

Potter, C.J., D.S. Sweetkind, R.P. Dickerson, and M.L. Kilgore, Hydrostructural Maps of the Death Valley Regional Flow System, Nevada and California; Map A Structural framework, Neogene Basins, and potentiometric Maps, 2002.

Reiter, M., Hydrothermal studies on the southern part of Sandia National Laboratories/Kirtland Air Force Base – Data regarding groundwater flow across the boundary of an intermountain basin, American Geophysical Union Monograph 113, "Faults and Subsurface Fluid Flow in the Shallow Crust" (W. Haneberg, et al., eds.), pp. 207-222, 1999.

Rose, T.P., F.C. Benedict, J.M. Thomas, W.S. Sicke, R.L. Hershey, J.B. Paces, I.M. Farnham, and Z.E. Peterman. 2002. *Geochemical Data Analysis and Interpretation of the Pahute Mesa - Oasis Valley Groundwater Flow System, Nye County, Nevada. Lawrence Livermore National Laboratory.* Report attached to a memorandum to files by W. Drici (Stoller-Navarro Joint Venture), February 23, 2004. Las Vegas, NV.

Rousseau, J.P., E.M. Kwicklis, and D.C. Gillies, eds., Hydrogeology of the unsaturated zone, North Ramp Area of the Exploratory Studies Facility, Yucca Mountain, Nevada, U.S. Geological Survey Water-Resources Investigations Report 98-4050, Denver, CO., 244 p., 1999.

Sawyer, D.A., R.J. Fleck, M.A. Lanphere, R.G. Warren, D.E. Broxton, and M.R. Hudson, "Episodic caldera volcanism in the Miocene southwestern Nevada volcanic field: Revised stratigraphic framework, 40Ar/39Ar geochronology, and implications for magmatism and extension," Geol. Soc. Amer. Bull., Vol. 106, p. 1304-1318, October 1994.

Scott, R.B., Tectonic setting of Yucca Mountain, southwest Nevada, in Basin and Range Extensional Tectonics Near the Latitude of Las Vegas, Nevada, Geological Society of America Memoir 176, Boulder Colorado, p. 251-282, 1990.

Shaw, Inc., Unpublished report on hydrologic data documentation for the Pahute Mesa-Oasis Valley Corrective Action Unit, Las Vegas, Nevada, 2003.

Smith, R.L., and R.A. Bailey, Resurgent cauldrons, in Studies in Volcanology, R.R. Coats, R.L. Hay, and C.A. Anderson, eds., Geol. Soc. Amer. Memoir 116, p. 613-662, 1968.

Stewart, J.H., Geology of Nevada – A discussion to accompany the geologic map of Nevada, Nevada Bur. Mines and Geology Special Publication 4, 136 p., 1980.

Stock, J.M., J.H. Healy, S.H. Hickman, and M.D. Zoback, Hydraulic fracturing stress measurements at Yucca Mountain, Nevada and relationship to the regional stress field, Journal of Geophysical Research vol. 90, no. B10, p. 8691-8706, 1985.

Tamanyu, S., How do fracture-vein systems form in a geothermal reservoir? Examples from northern Honshu, Japan, American Geophysical Union Monograph 113, "Faults and Subsurface Fluid Flow in the Shallow Crust" (W. Haneberg, et al., eds.), pp. 185-205, 1999.

U.S. Department of Energy, Nevada Operations Office. 1997. *Regional Groundwater Flow and Tritium Transport Modeling and Risk Assessment of the Underground Test Area, Nevada Test Site, Nevada,* DOE/NV--477. Las Vegas, NV.

Wahl, R.R., D.A. Sawyer, S.A. Minor, M.D. Carr, J.C. Cole, W.C. Swadley, R.J. Laczniak, R.G. Warren, K.S. Green, and C.M. Engle, Digital geologic map database of the Nevada Test Site area, Nevada, U.S. Geological Survey Open-file Report 97-140, 1997.

Warren, R.G., Geochemical Similarities between Volcanic Units at Yucca Mountain and Pahute Mesa: Evidence for a Common Magmatic Origin for Volcanic Sequences that Flank Timber Mountain Caldera, Proceedings of the Second Symposium on Containment of Underground Nuclear Explosions, Lawrence Livermore National Laboratory, CONF-830882, Vol. 1, p. 213-244, 1983.

Warren, R.G., and C.M. LaDelfe, "Constraints on a Basin-Range fault at Pahute Mesa, southwestern Nevada volcanic field," 6th Symposium on Containment of Underground Nuclear Explosions, Lawrence Livermore National Laboratory, CONF-9109114-Vol. 2, p. 289-305, September 1991.

Warren, R.G., F.M. Byers, Jr., and P.P. Orkild, "Post-Silent Canyon Caldera Structural Setting for Pahute Mesa," Proceedings of the Third Symposium on Containment of Underground Nuclear Explosions, Lawrence Livermore National Laboratory, CONF-850953, Vol. 2, p. 3-30, September 1985.

Warren, R.G., G.L. Cole, and D. Walther, A structural block model for the three-dimensional geology of the southwestern Nevada volcanic field, Los Alamos National Laboratory Report LA-UR-00-5866, 84 pp., December 2000.

Warren, R.G., D.A. Sawyer, F.M. Byers, Jr., and G.L. Cole, A petrographic, geochemical, and geophysical database and stratigraphic framework for the southwestern Nevada volcanic field, Los Alamos National Laboratory Report LA-UR-03-1503, 54 pp., March 2003.

Winograd, I.J., and F.J. Pearson, Jr., Major Carbon 14 anomaly in a regional carbonate aquifer: Possible evidence for megascale channeling, south central Great Basin, Water Resources Research, vol. 12, no. 6, p. 1125 – 1143, 1976.

Winograd, I.J., and W. Thordarson, "Hydrogeologic and hydrochemical framework, south-central Great Basin, Nevada-California, with special reference to the Nevada Test Site," U.S. Geological Survey Professional Paper 712-C, 126 pp., 1975.

Wolfsberg, A., K. Campbell, and J. Fabryka-Martin, Use of chlorine-36 data to evaluate fracture flow and transport models at Yucca Mountain, Nevada, in Dynamics of Fluids in Fractured Rock, Geophysical Monograph 122, ed. by B. Faybishenko, P.A. Witherspoon, and S.M. Benson, American Geophysical Union, Washington, D.C., p. 349-362, 2000.

Wolfsberg, A., L. Glascoe, G. Lu, A. Olson, P. Lichtner, M. McGraw, T. Cherry, and G. Roemer. TYBO/BENHAM: Model Analysis of Groundwater Flow and Radionuclide Migration from Underground Nuclear Tests in Southwestern

Pahute Mesa, Nevada, Los Alamos National Laboratory LA-13977, Los Alamos, NM, 2002.

Zoback, M.L., and M.D. Zoback, State of stress in the conterminous United States, Journal of Geophysical Research, v. 85, p. 6113-6156, 1980.

Zyvoloski, G., E. Kwicklis, A.A. Eddebbarh, B. Arnold, C. Faunt and B.A. Robinson, The site-scale saturated zone flow model for Yucca Mountain: calibration of different conceptual models and their impact on flow paths, Journal of Contaminant Hydrology, 62-63, p. 731-750, 2003.

Table B.7-1
Structures of the Pahute Mesa/Oasis Valley Model Area
(Page 1 of 4)

(1) Structure Name	(2) Map no.	(3) Type	(4) Symbol	(5) Fault Strike	(6) Dip Azimuth	(7) Dip Amount	(8) Notes	(9) Offset (m)	(10) Activated?	(11) Active Length (Km)	(12) Percent Active Length
Ammonia Tanks caldera structural margin	26	CM	ATCSM			-80		(~800)			
Ammonia Tanks caldera topographical margin	25	CM	ATCTM				Inward variable dip	minor			
Black Mountain caldera structural margin	24	CM	BMSM				Variable inward dip	(~750)			
Claim Canyon caldera structural margin	28	CM	CCCSM				Variable inward dip	(~600)			
Rainier Mesa caldera structural margin	27	CM	RMCSM			-80	Inward dip	(>2,000)			
Rainier Mesa caldera topographical margin	25	CM	RMCTM			-80	Inward dip	minor			
Silent Canyon caldera structural margin	29,30	CM	SCCCSM				Variable inward dip	(>2,500)			
Silent Canyon caldera complex topographical margin	---	CM	SCCCTM				Variable inward dip	minor			
Fluorspar Canyon – Bullfrog Hills detachment fault	---	DF	FC-BH DF	90	180	-3	Strike approximate; dip <5				
Almendro Fault	1	NF	AL	15	285	-80		150	Y	5.5	80
Bare Mountain fault	3	NF	BM	343	73	-80	Actual dip 45° in model?	(~2,000)			
Beatty fault	4	NF	BF	0	270	-80		(>500)			
Big Burn Valley fault	5	NF	?	325	235	-80	Offset from Hinrichs et al., 1967	45			

Table B.7-1
Structures of the Pahute Mesa/Oasis Valley Model Area
(Page 2 of 4)

(1) Structure Name	(2) Map no.	(3) Type	(4) Symbol	(5) Fault Strike	(6) Dip Azimuth	(7) Dip Amount	(8) Notes	(9) Offset (m)	(10) Activated?	(11) Active Length (Km)	(12) Percent Active Length
Black Canyon fault	6	NF	BC	352	262	-80		?			
Boxcar fault	7	NF	BX	3	273	-80	Strike range 0-5	60	Y	16	100
Claim Canyon fault 1	9	NF	CC1	5	275	-80		?			
Claim Canyon fault 2	10	NF	CC2	313	43	-80		?			
East Estuary fault	11	NF	EE	0	270	-80		60			
East Greeley fault	13	NF	EG	0	270	-80		30	Y	7	55
Halfbeak fault	15	NF	HB	30	300	-80		(~100)			
Handley fault	16	NF	HA	30	300	-80		30	Y	5	45
Hogback fault	17	NF	HOG	355	85	-80		(~200-1000)			
Paintbrush Canyon fault	18	NF	PC	352	262	-80		(~200)			
Purse fault	19	NF	PU	8	278	-80		30	Y	7.5	60
Rickey fault	21	NF	RY	16	286	-80		(~2,000)			
Scrugham Peak fault	22	NF	SP	16	286	-80		150			
Split Ridge fault	23	NF	SR	5	275	-80		30			
West Almendro fault	2	NF	WAL	356	266	-80		(~100)			
West Boxcar fault	8	NF	WB	342	252	-80		60	Y	8.5	100
West Estuary fault	12	NF	WE	0	270	-80	Offset from Noble et al., 1967	30			
West Purse fault	20	NF	WP	0	270	-80		30	Y	3.5	70
West Greeley fault	14	NF/CM	WG	0	270	-80		150	Y	10.5	50
Thirsty Canyon lineament	42	NF?	TCL	10	100	-80		(>2,000)			
Belted Range thrust fault	31	TF	BRT	45	315	-20	Dip range 0-40				

Table B.7-1
Structures of the Pahute Mesa/Oasis Valley Model Area
(Page 3 of 4)

(1) Structure Name	(2) Map no.	(3) Type	(4) Symbol	(5) Fault Strike	(6) Dip Azimuth	(7) Dip Amount	(8) Notes	(9) Offset (m)	(10) Activated?	(11) Active Length (Km)	(12) Percent Active Length
CP thrust fault	32	TF	CPT	315	?	-5	Dip <10, azimuth varies				
Colson Pond fault	46	TSZ	CPF	90	180	-80		(<30)			
Fleur de Lis fault	47	TSZ	FDL	90	180	-80	Azimuth approximate	(<100)			
Gold Meadows structural zone	33	TSZ	GMSZ	285	195	-80		(~100)			
Hot Springs lineament	34	TSZ	HSL	87	357	-80		(>2.000)			
Ribbon Cliff structural zone	35	TSZ	RCSZ	285	15	-80		150			
East Thirsty Canyon structural zone	36	TSZ/CM	ETCSZ	90	180	-80		0-300			
Moor Hen Meadow structural zone	37	TSZ/CM	MHMSZ	290	200	-80		(~1800)			
North Timber Mountain moat structural zone	38	TSZ/CM	NTMMSZ	296	206	-80		(~100)			
Silent Canyon northern structural zone	39	TSZ/CM	SCNSZ	292	202	-80		15-250			
Silent Canyon structural zone	40	TSZ/CM	SCSZ	297	207	-80		50-1300			
Southern Pahute Mesa structural zone	41	TSZ/CM	SPMSZ	286	16	-80		25-500			
Western East Thirsty Canyon structural zone	43	TSZ/CM	WETCSZ	90	180	-80		75-400			
Western Silent Canyon structural zone	44	TSZ/CM	WSCSZ	285	?	-80	Dips both SSW and NNE	(~200)			

Table B.7-1
Structures of the Pahute Mesa/Oasis Valley Model Area
(Page 4 of 4)

(1) Structure Name	(2) Map no.	(3) Type	(4) Symbol	(5) Fault Strike	(6) Dip Azimuth	(7) Dip Amount	(8) Notes	(9) Offset (m)	(10) Activated?	(11) Active Length (Km)	(12) Percent Active Length

Notes to Table B.7-1: Column 1 lists the name of the structure; column 2 lists the type of structure (CM = caldera margin, DF = detachment fault, NF = normal fault, TF = thrust fault, TSZ = transverse fault or structural zone); column 3 lists the abbreviation used to mark the structure in this report and in Bechtel (2002); column 4 lists the fault strike in northern-sector 360° coordinates; column 5 lists the dip azimuth; column 6 lists the dip angle below horizontal (note that all normal faults are assigned an arbitrary dip of -80°), column 7 provides explanatory notes; column 8 lists the offset of faults near-surface as summarized by McKee et al. (2001) or other references as noted, with additional interpretations from cross sections in Bechtel (2002) in parentheses, ranges of offset in italics reflecting increase in offset with depth where such information can be deduced from Warren et al. (2000), and "?" indicating offsets that could not be estimated; columns 9-11 provide information on whether a fault has been reactivated by underground testing and if so the total length reactivated and the percentage of reactivated length relative to total mapped length (calculated from Frizzell and Shulters, 1990).

Table B.7-2
Hydrothermal Alteration Associated with Calderas of the SWNVF

Caldera	Age	Feldspar	Pyrite	Altn	Location	Caldera Fill
Ammonia Tanks	11.45	Destroyed	Trace	High	ER/EC2A	Overlying Beatty Wash formation strongly altered to 400 m above Ammonia Tanks Tuff
Rainier Mesa	11.65	Slightly altered	Slight	Slight	UE18T	Overlying Ammonia Tanks Tuff is unaltered
Claim Canyon	12.7	Unaltered	None	None	Chocolate Mtn	Basal unit, rhyolite of Vent Pass, is unaltered
Area 20	13.2	Unaltered	None	None	UE20F	Basal unit, rhyolite of Jorum, is unaltered
Grouse Canyon	13.7	Strongly altered	Abundant	High	UE19G\S	Overlying Dead Horse Flat formation strongly altered to 240 m above Grouse Canyon Tuff

Data are from tables strat and pa_measure in database of Warren et al. (2003), or from petrographic analyses planned for addition to database. Feldspar phenocrysts have been altered as described within drill hole or outcrop location designated. Alteration indicates intensity (severity) of hydrothermal alteration suggested for caldera. Caldera-filling units are altered in same style as caldera-forming unit upward to the level within the indicated drill hole.

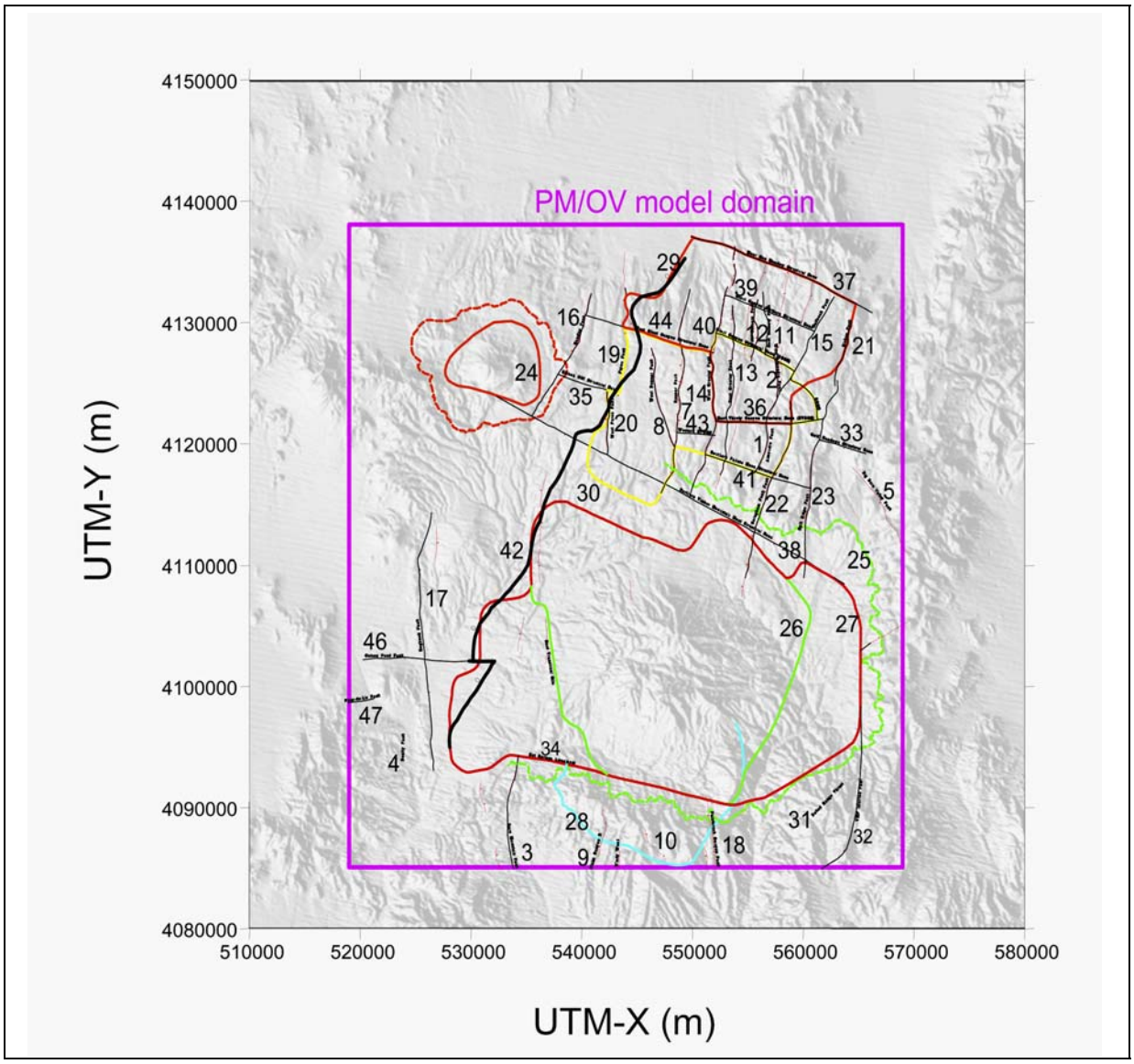

Figure B.7-1
Map Showing Structural Features and Model Boundaries for the PM/OV Flow Model
(Structural features are from Figures 3-1 and 6-5 of Bechtel, 2002). Identification numbers are defined within Section B.2.3 in descriptions of each feature and in Table B.7-1.

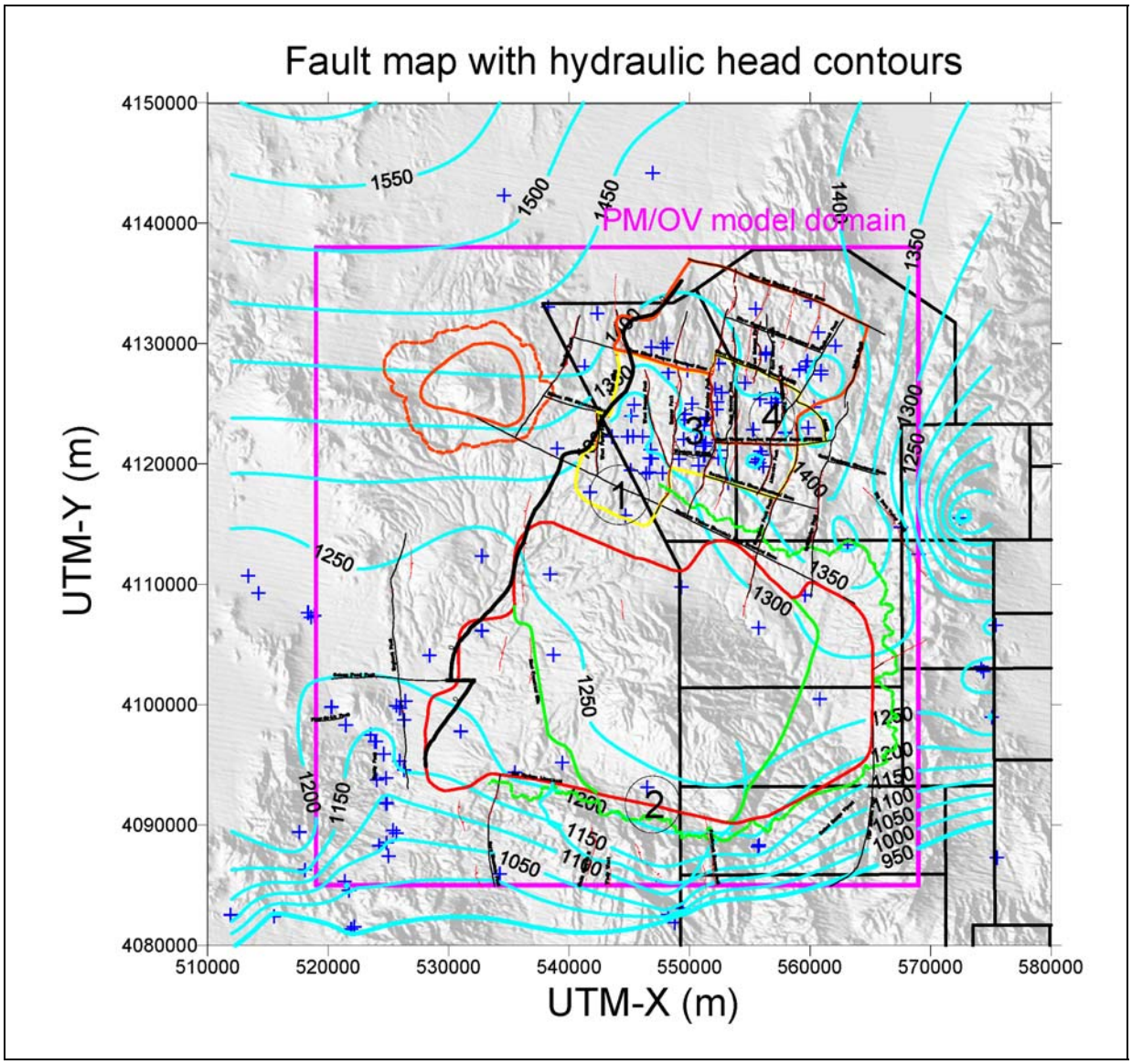

Figure B.7-2
Map Showing Hydraulic Head Measurements and Contours, Including Structural Features in the Vicinity of the PM/OV Flow Model

Hydraulic heads are expressed in meters above sea level. Numbered hydraulic features are discussed in text.

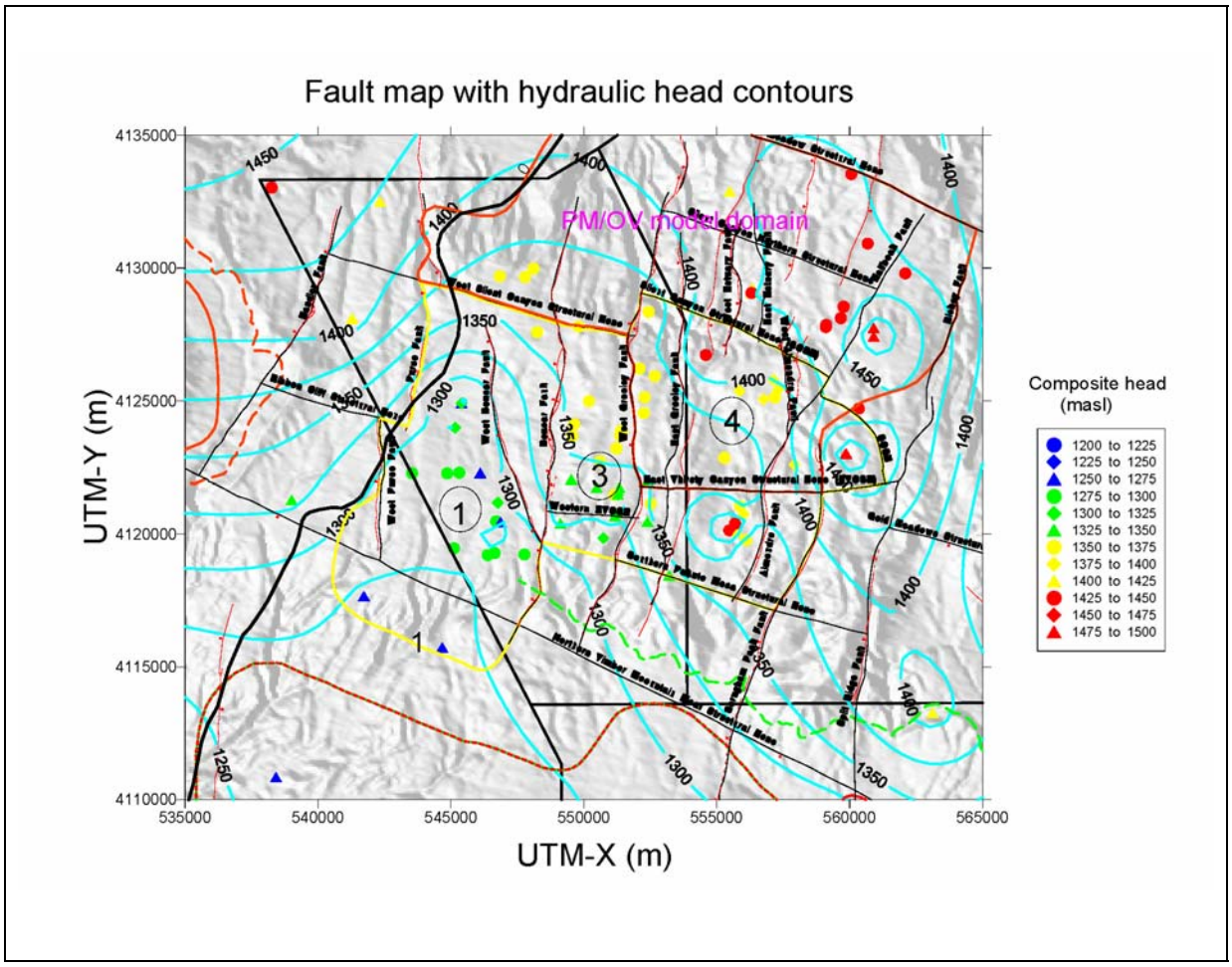

Figure B.7-3
Map Showing Hydraulic Heads Measurements and Contours with Structural Features in the Vicinity of NTS Areas 19 and 20

Hydraulic heads are expressed in meters above sea level. Numbered hydraulic features are discussed in text.

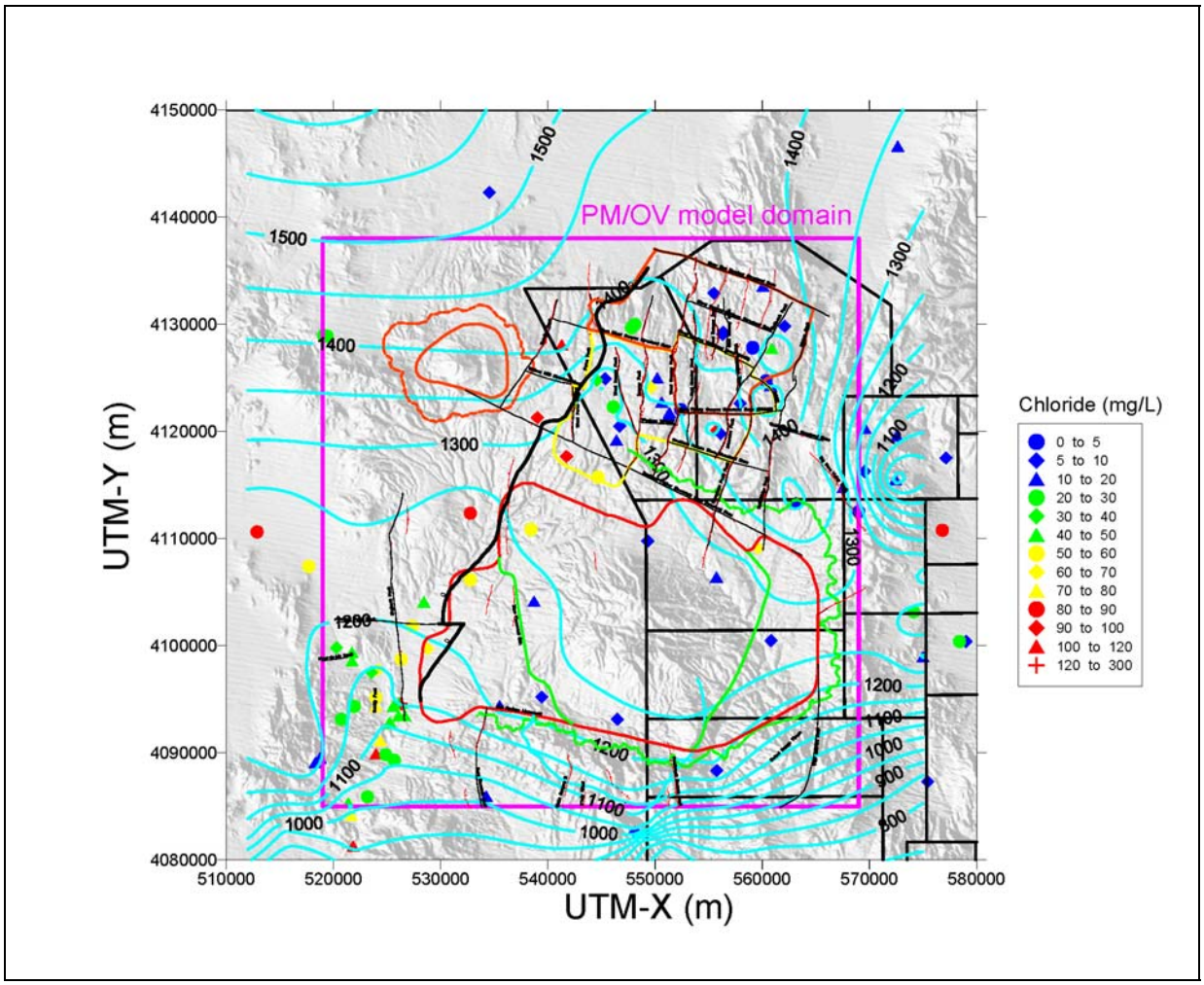

Figure B.7-4
Map Showing Groundwater Chloride Concentrations, Hydraulic Head Contours, and Structural Features in the PM/OV Flow Domain

Hydraulic heads are expressed in meters above sea level. Chloride concentrations are in milligrams per liter.

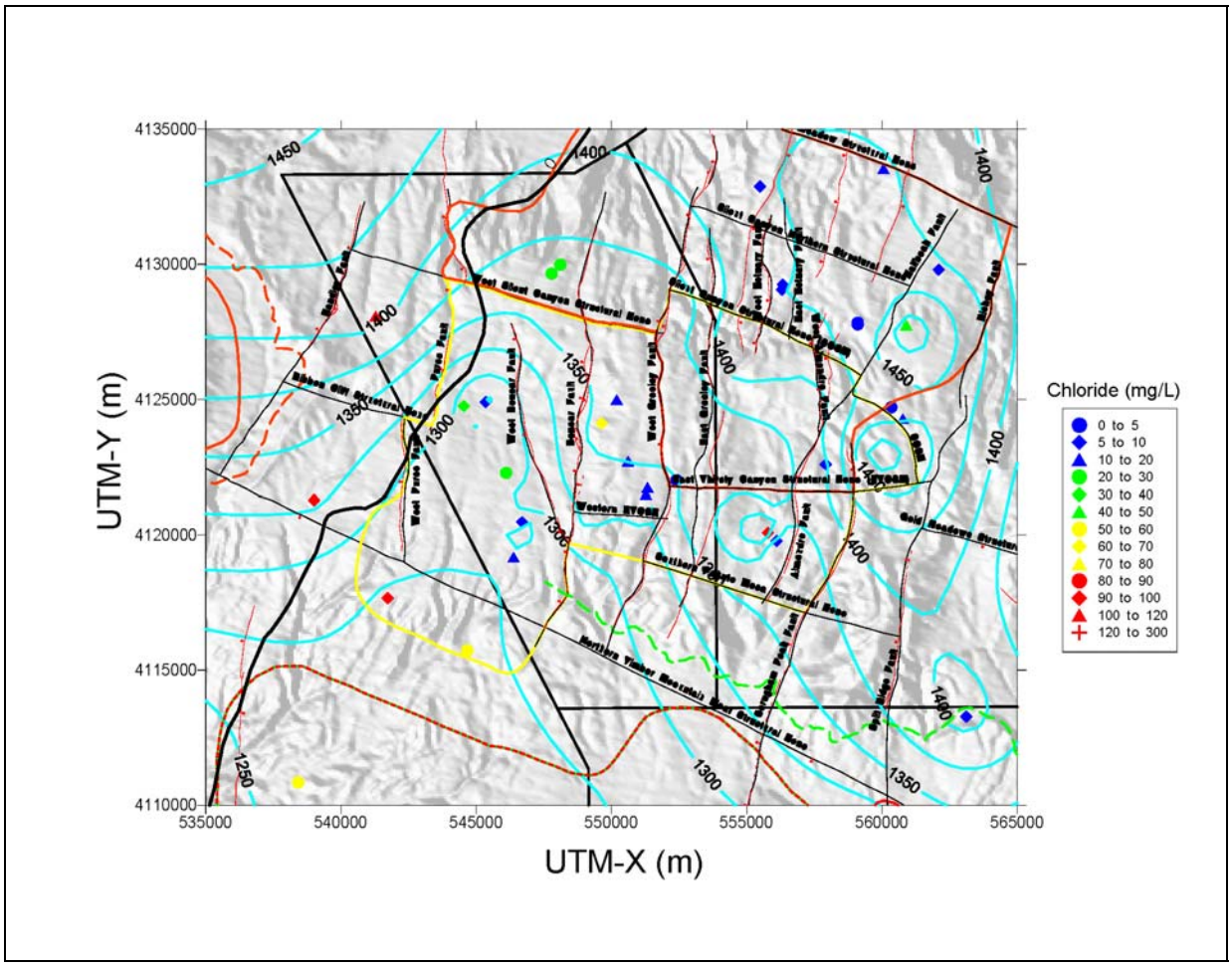

Figure B.7-5
Map Showing Groundwater Chloride Concentrations, Hydraulic Head Contours, and Structural Features in the Vicinity of NTS Areas 19 and 20

Hydraulic heads are expressed in meters above sea level. Chloride concentrations are in milligrams per liter.

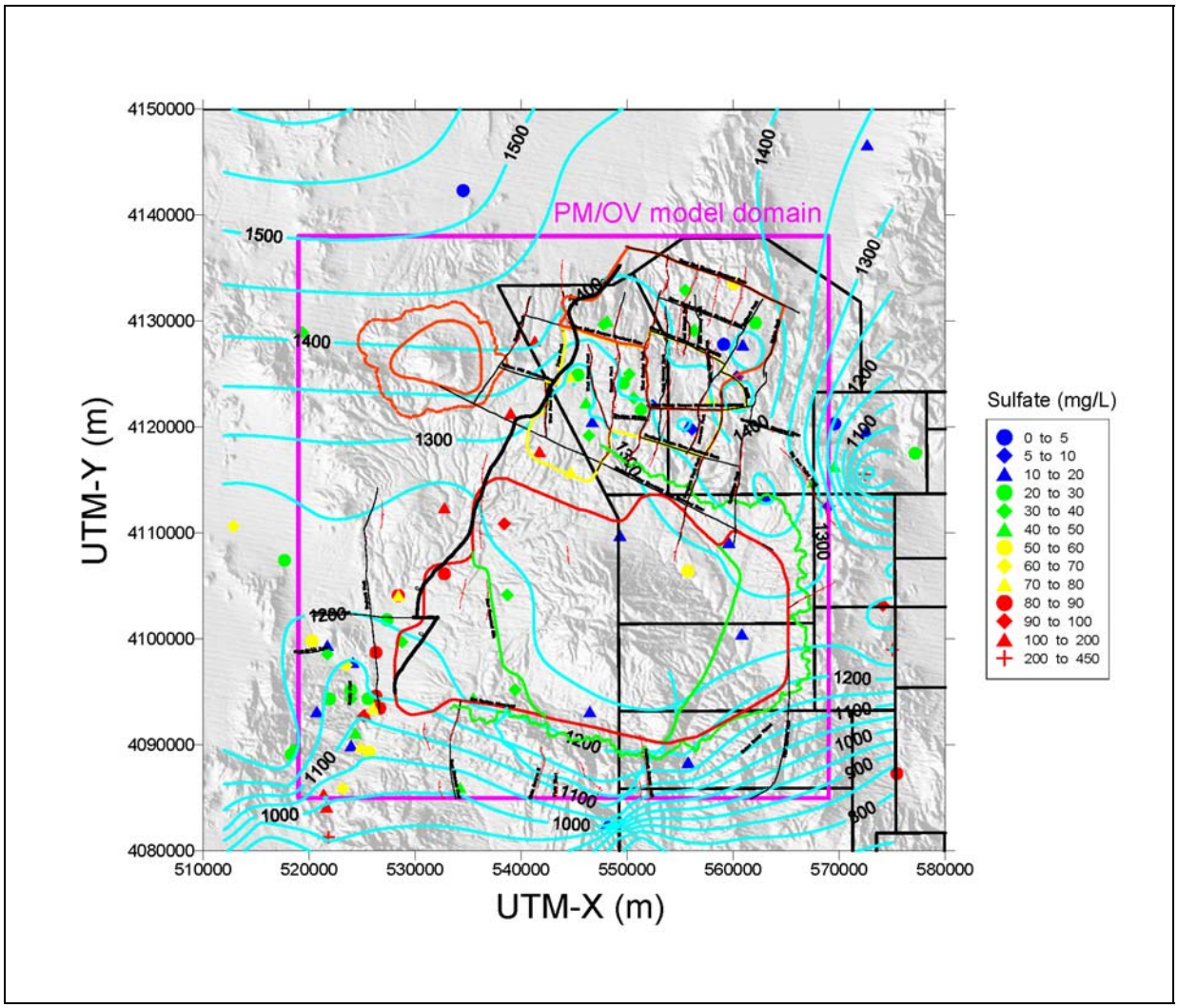

Figure B.7-6
Map Showing Groundwater Sulfate Concentrations, Hydraulic Head Contours, and Structural Features in the PM/OV Flow Domain

Hydraulic heads are expressed in meters above sea level. Sulfate concentrations are in milligrams per liter.

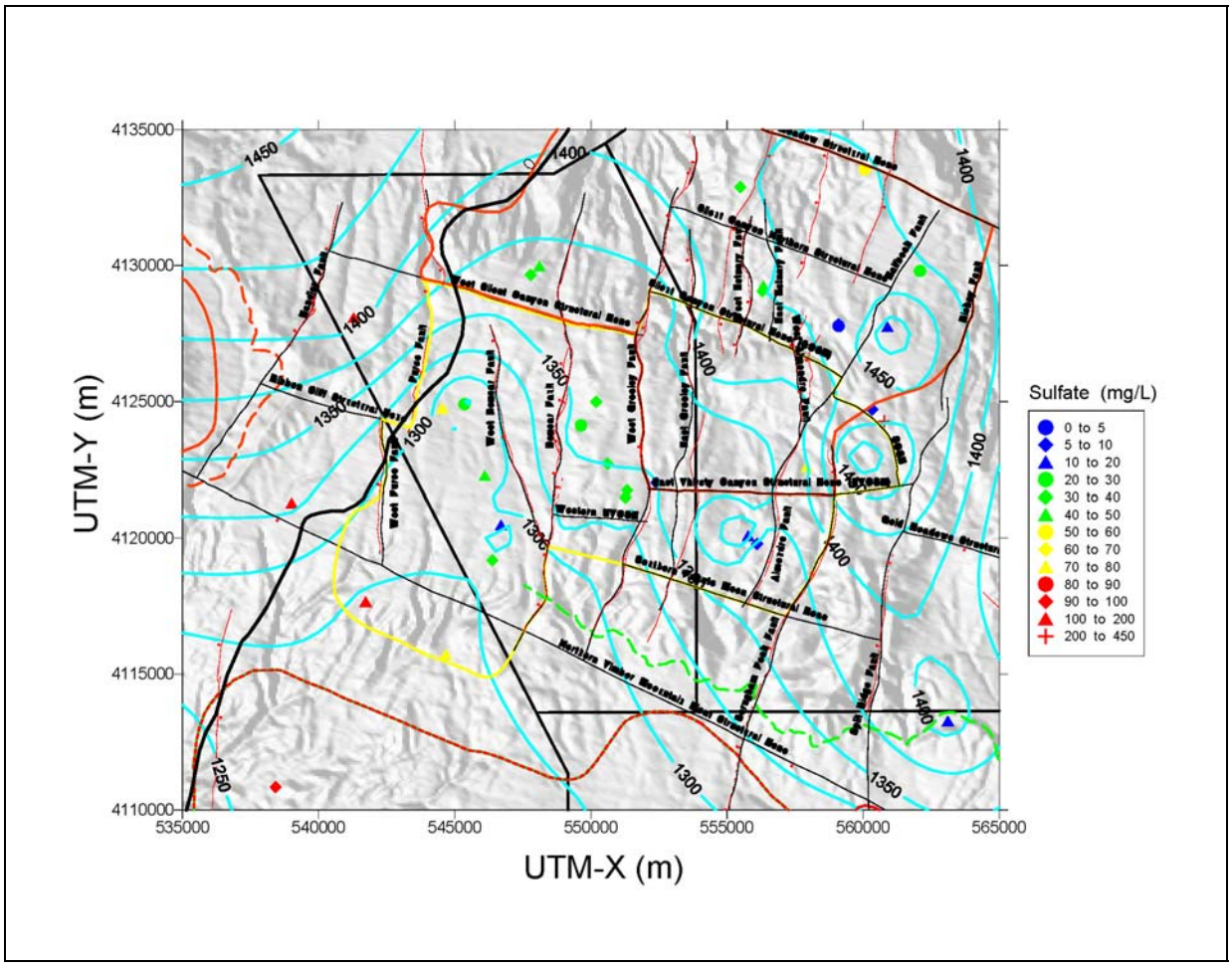

Figure B.7-7
Map Showing Groundwater Sulfate Concentrations, Hydraulic Head Contours, and Structural Features in the Vicinity of NTS Areas 19 and 20
Hydraulic heads are expressed in meters above sea level. Sulfate concentrations are in milligrams per liter.

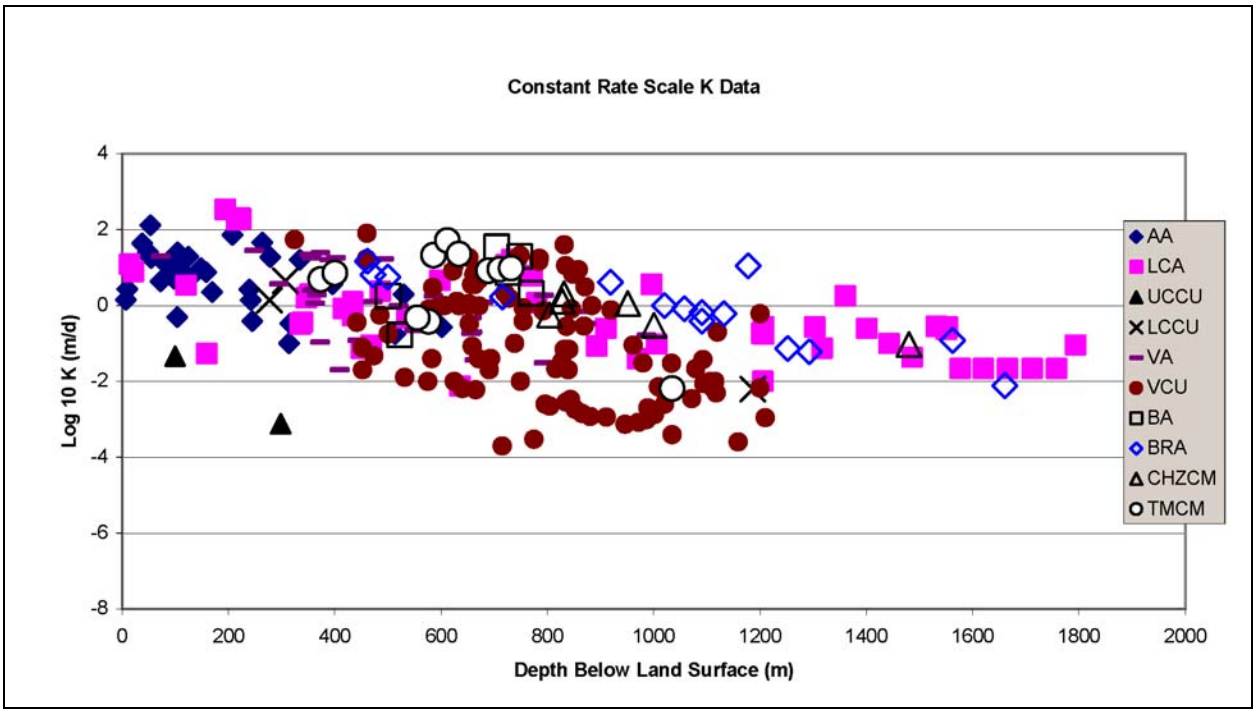

Figure B.7-8
Figure Showing Hydraulic Conductivities as a Function of Hydrostratigraphic Unit and Depth in the PM/OV Flow Domain and Surrounding Areas
Data and figure are from Shaw (2003).

Appendix C

Development of a Steady-State Thermal Field and Evaluation of the Potential Use of Temperature Data To Constrain Pahute Mesa CAU Groundwater Flow Models

(As provided by Los Alamos National Laboratory)
Edward Kwicklis, Jenny Boryta, and Andrew Wolfsberg

C.1.0 INTRODUCTION

In geologically complex environments, groundwater head and spring discharge data by themselves may not sufficiently constrain groundwater flow patterns. In the PM/OV area, this geologic complexity is associated with tuffs and lavas having varying degrees of welding and fracturing, faults with little known and possibly varying hydraulic properties, caldera boundaries, and other features recognized from geophysical investigations of unknown geologic origins (e.g., Grauch et al., 1999). Consequently, there has been a growing interest in the use of other types of data to help identify, or at least constrain, patterns of groundwater movement in these environments. These data have included groundwater geochemical and isotopic tracers and subsurface temperature data to help delineate flow patterns (SNJV, 2004; Fridrich et al., 1994; Gillespie, 2002). The use of groundwater geochemistry is described in detail in Section 2.4 of this report. In this appendix, we investigate the use of heat (a) for developing a steady-state thermal field for use in the groundwater flow models and (b) as a tracer for which departures of measured temperature from temperatures simulated by purely conductive heat-flow models provide information about groundwater flow patterns. The purpose of this thermal study is to develop a heat conduction-only model that matches temperature observations in boreholes and estimates steady-state temperatures at every node in the flow model domain. Then, by examining specific locations where the conduction model fails to adequately match temperature profiles, advective processes are identified for further investigation with the calibrated flow models.

Because temperatures increase with depth in response to geothermal heating, groundwater temperature patterns may be useful for identifying vertical flow components. Relatively warm groundwater compared to other areas at the same elevation may indicate that groundwater has flowed upward from depth; conversely, relatively cool groundwater may indicate downward flow. Because aquifer temperature data are sensitive to vertical groundwater movement, temperature data may be helpful in identifying whether groundwater is actually flowing in response to vertical head gradients that have been identified. Alternatively, if the distribution of hydraulic heads with depth is unknown,

groundwater temperature data may provide indirect indications of the likely changes of head with depth.

Two approaches involving the use of subsurface temperature data in groundwater flow models have been discussed in the literature. In the first approach, a coupled groundwater flow and heat transport model is calibrated to hydraulic head and temperature data using either a formal parameter optimization method (Woodbury et al., 1987; Woodbury and Smith, 1988) or through trial-and-error (Painter et al., 2003). In the second approach, the effects of groundwater flow on subsurface temperatures are not modeled explicitly, but are inferred based on the differences between the measured subsurface temperatures and temperatures simulated with a pure heat-conduction model (Arnold et al., 2003). This report uses the second approach to infer groundwater flow patterns in the PM/OV flow domain.

To assess the possible influence of groundwater on subsurface temperatures, a three-dimensional, steady-state thermal conduction model was developed for the PM/OV flow domain. As described below, identification of a set of high-quality temperature observations for modeling required careful screening of scores of digitized temperature profiles to eliminate portions of temperature logs where flow within the borehole appeared to have disturbed *in situ* temperatures. The model attempts to simulate borehole temperature measurements by adjusting either the thermal conductivities of individual HSUs or groups of HSUs while also adjusting lower boundary temperatures or heat fluxes. Both automated calibration using the PEST code and manual adjustments to thermal conductivities and boundary conditions are used. Temperatures measured at the composite water level, or in the unsaturated-zone just above the composite water level were used as the upper thermal boundary condition in the model. Areas of the model domain where the conduction model could not match the measured borehole temperatures are interpreted to be areas where groundwater flow may have affected the borehole temperature data.

C.2.0 BACKGROUND

To help evaluate borehole temperature logs from the PM/OV area, it is useful to conduct some simple one-dimensional, heat-transport simulations to illustrate the expected effects of groundwater movement on borehole temperature profiles. Although their one-dimensional nature make these results somewhat idealized, these simulations nonetheless help both to identify borehole temperature measurements that have been perturbed by the presence of the borehole or by hydraulic tests, and to develop hydrologic interpretations for borehole temperature measurements that appear to reflect actual formation temperatures. The departures from purely conductive heat flow resulting from advective heat flow described here are used to interpret field measurements described later in this appendix.

At steady-state in a homogeneous medium, the temperature gradient resulting from purely conductive heat-flow processes would be linear (Figure C.2-1) and heat flux would be constant with elevation (Figure C.2-1). A steady, downward groundwater flux would result in cooler temperatures at any elevation compared to the conduction-only profile, resulting in a concave-upwards profile. For downward flux, the concave-upward profile implies a decrease in the geothermal gradient (and, hence, in the heat flux), with elevation (Figure C.2-1). This decrease in heat flux occurs because, with increasing elevation, more and more of the heat flux existing at depth has been consumed by warming the downwardly moving groundwater. Conversely, where groundwater flow is upward, rock temperatures at any elevation are warmer than those that would result from heat conduction alone (Figure C.2-1). In this case, the steepening of the temperature profile with elevation implies an increase in the upward heat flux with elevation (Figure C.2-1). This increase occurs because the upward moving groundwater loses heat to the surrounding rock, so that with increasing elevation, more and more heat must be transmitted conductively through the rock.

At steady-state in a layered medium, the temperature profile resulting from purely conductive heat-flow processes would have linear segments within a layer, and the temperature gradient associated with each linear segment would be inversely related to the thermal conductivity of that

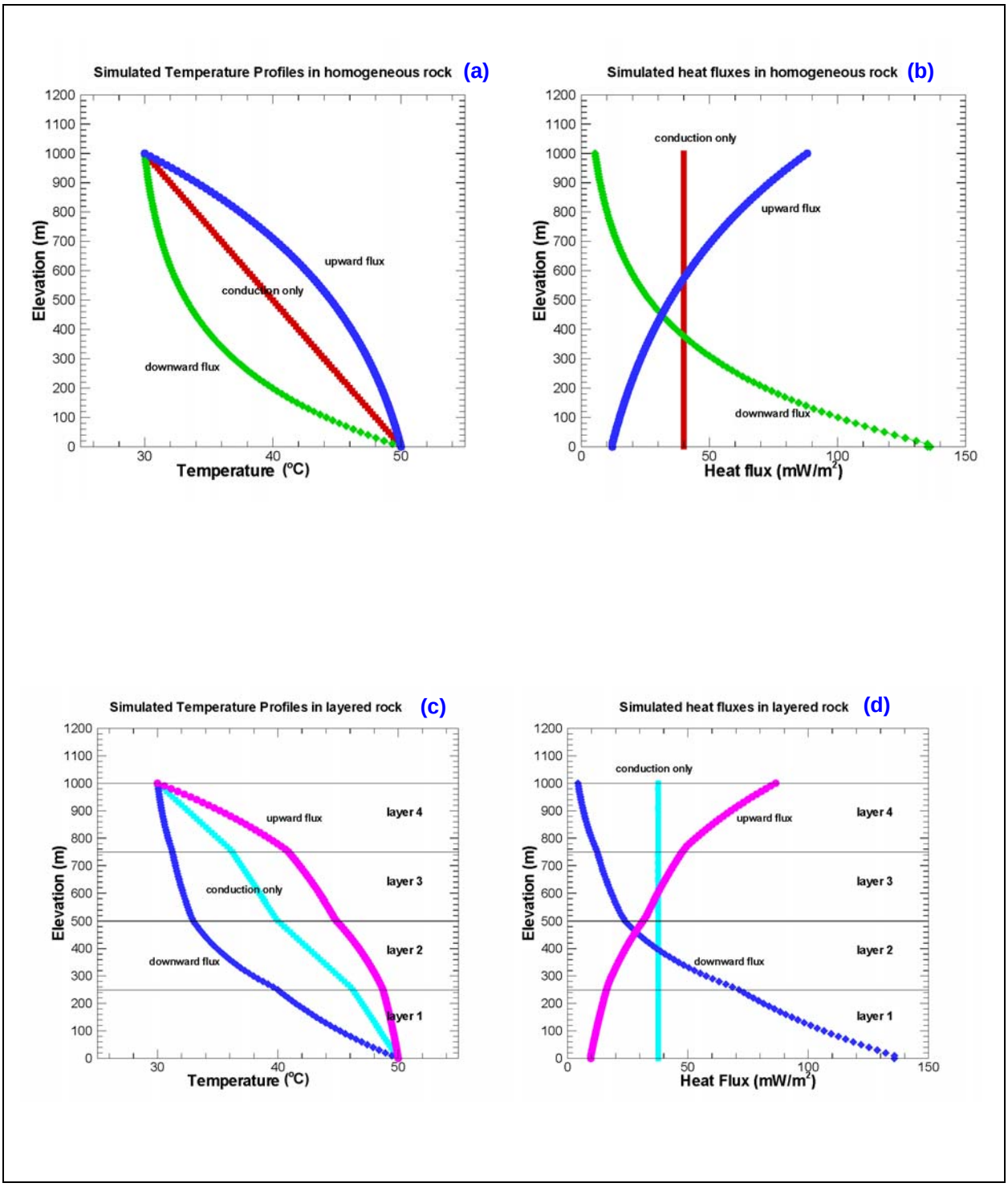

Figure C.2-1
Simulated (a) Temperature and (b) Heat Flux Profiles in Homogenous Rock
Simulated (c) Temperature and (d) Heat Flux Profiles in Layered Rock

layer (Figure C.2-1). For pure heat conduction, the thermal conductivity and thermal gradient within each layer result in a constant heat flux with elevation (Figure C.2-1). As in the case of homogeneous rock, a downward groundwater flux results in cooler temperatures at any elevation compared to the pure conduction profiles, with the segments within each layer having an upward concavity. In this case, the heat flux changes with elevation in a way that is similar to that found for a homogenous medium with downward groundwater flow (Figure C.2-1). An upward groundwater flux through a layered medium results in higher temperatures compared to temperatures associated with a pure conduction profile, with each segment in the profile for the layered rock having a downward concavity (Figure C.2-1). The heat flux associated with downward groundwater flow through the layered rock resembles the heat flux profile for downward groundwater flow through a homogeneous medium.

The heat flux qH at some elevation, z2, can be expressed as a function of q_H at a lower elevation z1 by

$$q_{H-z2} = q_{H-z1} - q_l C_l \Delta T \qquad \text{(C.2-1)}$$

where:

q_H = the heat flux (J s^{-1} m^{-2});
q_l = the liquid mass flux (kg s^{-1} m^{-2});
C_l = the specific heat capacity of water (4,187 J kg^{-1} $°C^{-1}$);
ΔT = the temperature difference between elevations z_2 and z_1 (°C);
z = the elevation (m), positive upwards.

Fluxes are positive when upwards and negative when downward. As the equation indicates, the heat flux at the higher elevation z_2 depends on the heat flux at the lower elevation z_1, on the direction and magnitude of the liquid flux, and on the change in the temperature the water undergoes as it moves through the rock. If heat flux can be estimated at two distinct elevations and assumed to be one-dimensional, the vertical groundwater flux can be calculated from these heat fluxes and corresponding temperature difference between these elevations. The equation also indicates that heat flux between two elevations would not be changed by horizontal groundwater movement where the temperature of the water did not change. However, in some instances, temperature at a given elevation varies spatially because of spatial variations in heat flux or due to the insulating effects

associated with variable thickness of the overburden. In this case, horizontal groundwater flow could alter the heat flux because the groundwater would warm or cool as it moved from one area to another area at a different temperature.

Other factors can also cause the interpretation of temperature profiles to be more complicated than described above. The three-dimensional distribution of temperatures (and heat flux) in a rock mass is a function of the spatial variability in heat flux at depth, topography, and the variability in rock thermal properties, as well as groundwater flow. In the PM/OV area, variability in heat flux could potentially arise because of the presence of now-dormant volcanic centers coinciding with the Timber Mountain, Silent Canyon and Black Mountain caldera complexes. Model calculations indicate that in a homogeneous medium, subsurface temperature distributions are a subdued reflection of the topography (Rousseau et al., 1999). Heat flux vectors tend to diverge under ridges and converge toward washes, resulting in decreasing heat fluxes with elevation beneath ridges and increasing heat fluxes with elevation beneath washes. Likewise, the subsurface distribution of rocks with different thermal conductivities can concentrate heat flow toward some areas and away from others. A preliminary analyses of heat flux in the vicinity of the NTS (Gillespie, 2003) has indicated that heat flux tends to be redirected around low thermal conductivity alluvium in basins like Yucca Flat and Frenchman Flats and into the higher thermal conductivity rocks beneath ridges bordering the basins. The deflection of heat flux from beneath the alluvium into the surrounding rock is possible because the insulating properties of the alluvium cause temperatures to be higher beneath the alluvium than in rocks at the same elevation beneath the ridges.

One difficulty in using temperature measurements as a constraint on hydrologic models is that only after all of these processes and their uncertainties are accounted for can the hydrologic significance of temperatures measurements be reliably identified. The foregoing discussion indicates that borehole temperature profiles should be interpreted with a three-dimensional model that incorporates all of the relevant processes and their uncertainties. Even then, however, features of the temperature profiles that cannot be explained by the 3-D conduction model may have hydrologic significance or they may simply be the result of an inadequate thermal conduction model.

C.3.0 MODEL OVERVIEW

C.3.1 Modeling Approach

Although a desirable goal, the development of models that explicitly couple groundwater flow and heat transport for the entire PM/OV flow domain was beyond the scope of this study. In this report, the effects of groundwater flow on subsurface temperatures in the PM/OV flow system are inferred indirectly from the differences between temperatures simulated with a pure heat-conduction model and measured temperatures. These differences, or residuals, are interpreted in terms of the possible hydrologic processes that may have produced them, based on analyses from past hydrologic studies that use temperature data (Gillespie, 2003; Rousseau et al., 1999; Constantz et al, 2003; Reiter, 1999) and simple scoping simulations of coupled flow and heat transport (Figure C.2-1). However, other factors, such as uncertainty in boundary conditions and thermal conductivities, are also considered in the interpretation of model results.

The heat-conduction models described in this report include a combination of forward models, in which boundary conditions and thermal properties were systematically varied to evaluate the sensitivity of simulated temperatures to these parameters, and inverse models in which either thermal properties or boundary conditions were optimized by minimizing the differences between simulated and measured temperatures.

C.3.2 The PM/OV Heat-Conduction Model

The numerical model of heat conduction in the PM/OV flow domain was created with the finite-element heat and mass transport code FEHM (Zyvoloski et al., 1997). This model uses the hydrostratigraphic framework model (BN, 2002) and the computational grid developed for the base-case PM/OV flow model. The computational grid includes nearly 1.5 million nodes and over 7 million finite elements to represent faults and HSUs in a volume that is approximately 50 km by 50 km in area and 5 km deep. The grid has variable spatial resolution, with the highest resolution applied to fault zones, thin HSUs, and nuclear test locations (see Section C.4.0).

Borehole temperature data from the PM/OV area are used as observations for model calibration and to estimate upper and lower boundary conditions. The selection of temperature data to calibrate the PM/OV heat-conduction model is discussed in Section C.4.0 of this report and the use of temperature data to estimate boundary conditions is discussed in Section C.6.0. The data used in this study were carefully selected from a much larger dataset of uncertain quality to ensure that the temperature data were reliable indicators of actual formation temperatures.

The simulated temperatures within the PM/OV heat-conduction model depend on the distribution of thermal properties in the model and on the boundary conditions imposed along the upper and lower surfaces of the model. The distribution of thermal conductivities in the model depends on both the thermal conductivities estimated for individual HSUs and the spatial distribution of different HSUs in the HFM (BN, 2002). As described in Section C.5.0, thermal conductivities were estimated for individual HSUs based on previous compilations of thermal conductivities for rocks from the vicinity of the NTS (e.g., Gillespie, 2003; Sass et al., 1987) and thermal conductivities reported in the literature for similar rock types.

Boundary conditions are discussed in Section C.6.0 of this report. The upper boundary of the heat-conduction model coincides with the potentiometric surface, which in this report is taken to be synonymous with the water table. The upper boundary was assigned constant, but spatially variable temperatures that were determined by contouring shallow groundwater temperatures measured at boreholes within the model domain. Lower boundary conditions in the forward models are assumed to be either uniform, constant temperature or uniform, constant heat flux. Additionally, one inverse model described in this report is used to calibrate heat fluxes at the base of the model in six different intra- and extra-caldera areas.

The following sections describe these aspects of the model in greater detail.

C.4.0 TEMPERATURE OBSERVATIONS

Borehole temperature data in the PM/OV flow domain have been collected by various investigators over a four-decade period under a variety of conditions (see Attachment A). These data are widely distributed throughout the model domain (Figure C.4-1; Table C.4-1), suggesting that temperature data could provide an important constraint for estimating temperatures and potentially flow processes. However, as previous reports have indicated (Pottoroff et al., 1987; Rehfeldt, 2002; Gillespie, 2003), measured borehole temperatures may not reflect the actual formation temperatures to varying degrees because of residual drilling effects, hydraulic tests conducted prior to temperature logging, and either intra-borehole flow or flow within the annular space between the casing and formation. Building on an earlier report (Kwicklis et al., 2003), this report eliminates temperature data that are suspected to be unrepresentative of actual formation temperatures to derive a set of reliable temperature measurements that can be used in model calibration. The disqualification of data was based on temperature logging dates relative to drilling and hydraulic testing history, borehole completion information and, most importantly, the temperature data itself. Data was avoided from depth intervals where temperatures varied erratically or in ways incompatible with known physical processes, in favor of depth intervals where temperature profiles were approximately linear. During this evaluation, a very conservative approach towards data retention was applied, so that some valid data may have been excluded from use as calibration targets. However, the possible rejection of valid measurements was considered preferable to the more likely possibility that erroneous conclusions would be made based on data affected by intra-borehole flow or the other factors listed above.

Ultimately, a subset of 67 temperature measurements were selected as calibration targets from the over 800 temperature measurements listed in Attachment A, Table A2. This subset of borehole temperature measurements (Table C.4-2) was chosen based on (1) the aforementioned criteria that measured temperatures reflect actual formation temperatures, (2) the resolution of the numerical grid near the measurement locations, and (3) the need to obtain as broad a geographic distribution in as many structural domains (Figure C.4-2) as possible, given the constraints imposed by the first two

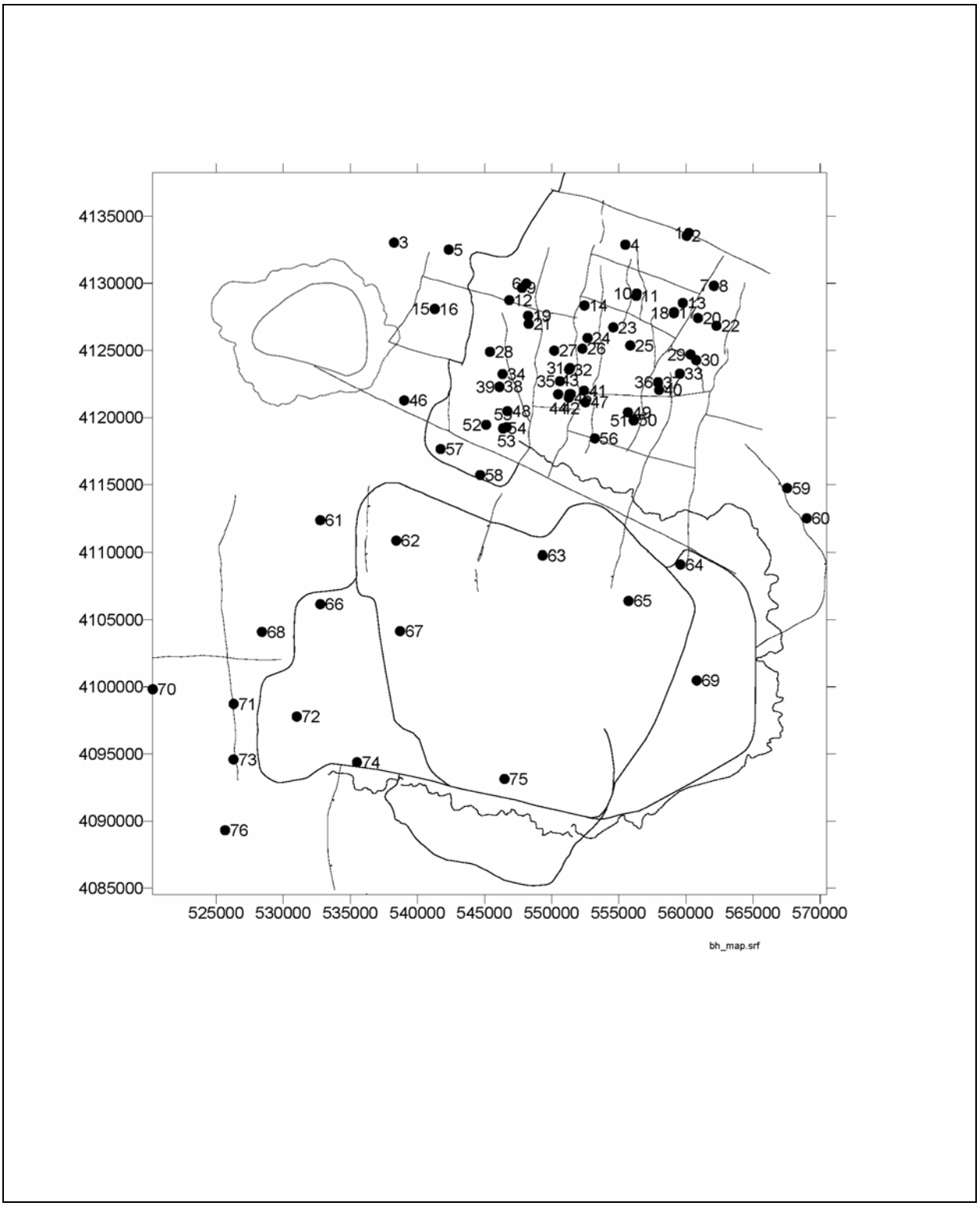

Figure C.4-1
Location of Boreholes Used in Study
Numbers correspond to boreholes listed in Table C.4-1.

Table C.4-1
Borehole Names and Locations (see Figure C.4-1)
(Page 1 of 3)

Map No.	Borehole	UTM-Easting	UTM-Northing
1	U-19u	560207.3	4133751.4
2	U-19d#2	560056.3	4133534.8
3	PM-2	538256.7	4133028.2
4	UE-19h	555488.4	4132881.8
5	UE-20p	542331.4	4132503.2
6	UE-20e#1	548110.5	4129980.7
7	UE-19b	562088.5	4129826.5
8	UE-19b1	562090.7	4129796.6
9	U-20e	547789.2	4129655.1
10	U-19g	556340.5	4129244.0
11	UE-19gS	556306.1	4129056.8
12	U-20aa	546837.4	4128745.2
13	U-19aj	559768.3	4128539.1
14	U-20g	552440.2	4128343.5
15	U-20m	541289.6	4128104.3
16	UE-20j	541285.3	4128082.0
17	UE-19e	559111.7	4127849.3
18	U-19e	559100.9	4127774.9
19	U-20i	548242.9	4127580.9
20	U-19bj	560900.4	4127416.2
21	UE-20ad	548286.2	4126975.0
22	U-19t	562271.5	4126843.3
23	U-19bk	554585.6	4126723.0
24	PM-1	552668.1	4125925.1
25	U-19aS	555856.8	4125370.8
26	UE-20ab	552284.5	4125130.3
27	UE-20h	550191.7	4124986.5
28	UE-20f	545400.8	4124900.4
29	UE-19c WW	560338.9	4124701.6
30	U-19c	560769.4	4124276.5
31	ER-20-6#1	551362.9	4123691.8
31	ER-20-6#2	551328.0	4123662.0
32	ER-20-6#3	551295.7	4123578.8

Table C.4-1
Borehole Names and Locations (see Figure C.4-1)
(Page 2 of 3)

Map No.	Borehole	UTM-Easting	UTM-Northing
33	U-19p	559541.6	4123266.9
34	UE-20ae	546339.7	4123243.6
35	U-20ww	550614.0	4122711.7
36	U-19i	557922.1	4122637.7
37	UE-19i	557922.3	4122592.0
38	U-20d	546102.6	4122300.8
39	UE-20d	546102.7	4122275.3
40	U-19v	558003.1	4122055.1
41	UE-20bh#1	552402.2	4122007.3
42	U-20n	551424.4	4121743.1
43	U-20a2	551333.2	4121743.0
44	U-20a	550480.6	4121740.0
45	UE-20n#1	551273.2	4121483.8
46	PM-3	539011.8	4121281.3
47	U-20bg	552511.9	4121139.3
48	U-20c#1	546698.7	4120477.7
49	U-19bh	555683.6	4120389.3
50	U-19f	556107.4	4119811.5
51	UE-19fS	556107.5	4119780.7
52	ER-20-1	545113.1	4119467.8
53	U-20y	546651.3	4119290.9
54	ER-20-5#1	546385.9	4119208.3
55	ER-20-5#3	546384.8	4119177.0
56	ER-20-2#1	553210.6	4118447.1
57	ER-EC-1	541729.8	4117659.5
58	ER-EC-6	544673.5	4115728.5
59	ER-19-1	567541.6	4114743.3
60	HTH-1	569000.3	4112499.0
61	ER-EC-4	532759.6	4112355.8
62	ER-EC-2A	538420.8	4110841.2
63	UE-18r	549322.0	4109762.0
64	UE-18t	559591.0	4109095.0
65	ER-18-2	555724.6	4106388.7

Table C.4-1
Borehole Names and Locations (see Figure C.4-1)
(Page 3 of 3)

Map No.	Borehole	UTM-Easting	UTM-Northing
66	ER-EC-8	532763.8	4106141.8
67	ER-EC-5	538701.8	4104136.9
68	ER-OV-6a2	528416.9	4104084.5
69	ER-30-1	560804.7	4100463.0
70	ER-OV-5	520280.1	4099808.5
71	ER-OV-2	526310.0	4098715.8
72	ER-OV-3b	531007.6	4097776.6
73	ER-OV-3a3	526298.8	4094586.9
74	ER-OV-3c2	535494.2	4094374.1
75	ER-EC-7	546483.5	4093127.3
76	ER-OV-4a	525671.4	4089315.7

criteria. The second criterion limited the number of data from borehole intervals with reliable measurements to the number of model nodes coinciding with that interval. Grid resolution varies considerably with location and depth, and occasionally imposes significant limitations on the number of temperature measurements that could be used. The third criterion ensures that spatial bias in the calibration will be minimized, given the inherent bias that the uneven distribution of wells in the model domain imparts to the analysis.

Of all the boreholes with temperature observations used to evaluate the results of the forward and inverse models, only boreholes PM-1, UE-18r, and HTH-1 were considered by Gillespie (2003) to have reliable temperature measurements throughout the entire borehole. Measurements in these boreholes were made in depth intervals where the casing was grouted to the formation, eliminating the possibility of flow in the annular space surrounding the casing. Additionally, at least one year had elapsed after drilling before the temperature measurement were made, thereby allowing time for the effects of drilling on formation temperatures to dissipate. However, as described above, careful screening of temperature data from other boreholes in the PM/OV flow domain allowed parts of temperature profiles from other boreholes to be used in this study. The inclusion of data from additional wells was necessary to achieve the geographic coverage that was considered essential for model calibration.

Table C.4-2
Observed Temperature and Elevation in Boreholes that Correlate with Elevation in Model Simulations
Observed Temperature and Elevations Used in Calibration Shown in Grey
(Page 1 of 6)

Borehole	Easting	Northing	Observed Temperature (C°)	Elevation of Observed Temperature (m)	Stratigraphy[a]	Class/ Rock Type[a]	HGU[a]	HSU[a]	Temperature Log (date)	No.	Mean Residual (HF85)	Mean Residual (T160)	Mean Residual (HF Subregional)
Purse Fault-W. Boxcar Fault (1)													
ER-20-5#3	546385	4119177	43.8	750.1	Thp	PL	TCU	CHZCM	2/6/1996				
ER-20-5#3	546385	4119177	47.7	656.5	Thr[e]	NWT	TCU	CHZCM	2/6/1996	2	7.88	4.93	1.93
U-20c#1	546699	4120478	44.9	609.4	Thp	LA	LFA	CHZCM	9/27/1968				
U-20c#1	546699	4120478	45.8	562.5	Th	BED	TCU	CHZCM	9/27/1968				
U-20c#1	546699	4120478	47.1	515.7	Th	BED	TCU	CHZCM	9/27/1968	3	13.08	8.48	6.11
U-20d	546103	4122301	37.3	939.4	Tptm	NWT	unk	TSA	1/31/1967	4	8.7	5.80	5.00
U-20d	546103	4122301	38.1	890.6	Thp	BED	TCU	CHZCM	1/31/1967				
U-20d	546103	4122301	38.9	844.9	Thp	BED	TCU	CHZCM	1/31/1967				
U-20d	546103	4122301	40.4	750.4	Thp	BED	TCU	CHZCM	1/31/1967				
UE-20d	546103	4122275	43.0	564.5	Thr[e]	LA	LFA	CHZCM	7/28/1964	1	16.3	11.16	9.66
UE-20f	545401	4124900	121.0	-1876	To	LA	LFA	PBRCM	6/25/1964				
			124-128	-2000						1	21.90	0.90	-4.10
W. Boxcar Fault-Boxcar Fault (2)													
UE-20e#1	548110	4129981	51.5	471.5	Tcps	LA	LFA	CFCM	6/2/1964	3	15.93	9.50	10.26
UE-20e#1	548110	4129981	53.4	377.0	Tcps	LA	LFA	CFCM	6/2/1964				
UE-20e#1	548110	4129981	57.2	29.6	Tbdk	LA	LFA	BRA	5/27/1964				
			58.0	0.0									
Boxcar Fault-W. Greeley Fault (3)													
ER-20-6#1	551363	4123692	34.1	1125.2	Thp	LA	LFA	CHZCM	3/8/1996	1	0.80	0.90	1.10
U-20a2	551333	4121743	41.1	601.7	Tmw	IN	ICU	CHZCM	2/17/1964	1			
UE-20h	550192	4124987	50.0	-194.5	unk	unk	unk	CFCM	8/16/1964	1			

Table C.4-2
Observed Temperature and Elevation in Boreholes that Correlate with Elevation in Model Simulations
Observed Temperature and Elevations Used in Calibration Shown in Grey
(Page 2 of 6)

Borehole	Easting	Northing	Observed Temperature (C°)	Elevation of Observed Temperature (m)	Stratigraphy[a]	Class/ Rock Type[a]	HGU[a]	HSU[a]	Temperature Log (date)	No.	Mean Residual (HF85)	Mean Residual (T160)	Mean Residual (HF Subregional)
S of Silent Canyon Caldera Structural Margin-N of Timber Mountain Caldera Topographic Margin (4)													
ER-EC-1[h]	541730	4117660	43.6	797.2	Tptm	VT	WTA	TSA	2/17/2000	7	7.55	5.54	-1.98
ER-EC-1[h]	541730	4117660	45.7	750.4	Tptm	NWT-PWT	unk	TSA	2/17/2000				
ER-EC-1[h]	541730	4117660	47.7	703.5	Thr[e]	BED	TCU	CHCU	2/17/2000				
ER-EC-1[h]	541730	4117660	50.0	656.4	Thr[e]	BED	TCU	CHCU	2/17/2000				
ER-EC-1[h]	541730	4117660	54.3	562.8	Thr[e]	BED	TCU	CHCU	2/17/2000				
ER-EC-1	541730	4117660	60.5	468.8	Tcpe	LA/FB	LFA	CFCM	4/20/1999				
ER-EC-1	541730	4117660	61.7	375.0	Tcpe	BED	TCU	CFCM	4/20/1999				
ER-EC-6[i, j]	544673	4115729	45.0	938.0	Tpcm	PWT	WTA	TCA	3/8/2000	12	1.93	0.22	-6.92
ER-EC-6[i, j]	544673	4115729	46.7	890.8	Tpcm	PWT	WTA	TCA	3/8/2000				
ER-EC-6[i, j]	544673	4115729	48.6	843.9	Thr[e]	NWT	TCU	LPCU	3/8/2000				
ER-EC-6[i, j]	544673	4115729	50.4	797.0	Thr[e]	NWT	TCU	LPCU	3/8/2000				
ER-EC-6[i, j]	544673	4115729	52.4	750.4	Tptm	PWT	WTA	TSA	3/8/2000				
ER-EC-6[i, j]	544673	4115729	54.2	703.2	Tptm	MWT	WTA	TSA	3/8/2000				
ER-EC-6[i, j]	544673	4115729	56.1	656.5	Tptm	PWT	WTA	TSA	3/8/2000				
ER-EC-6[i, j]	544673	4115729	58.1	609.5	Thr[e]	NWT	TCU	CHCU	3/8/2000				
ER-EC-6[i, j]	544673	4115729	60.0	562.7	Thr[e]	NWT	TCU	CHCU	3/8/2000				
ER-EC-6[i, j]	544673	4115729	62.3	516.0	Thr[e]	NWT	TCU	CHCU	3/820/00				
ER-EC-6[i, j]	544673	4115729	64.4	469.2	Tcpe	LA	LFA	CFCM	3/8/2000				
ER-EC-6[i, j]	544673	4115729	68.7	375.5	Tcpe	LA	LFA	CFCM	3/8/2000				
Handley Fault-Purse Fault (5)													
PM-3#1	539012	4121281	33.8	1218.8	Tpcx	TB	TCU	UPCU	12/15/1999[c]	3	5.00	4.73	2.70
PM-3#1	539012	4121281	34.7	1172.0	Tpcm	MWT	WTA	TCA	12/15/1999[c]				
PM-3#1	539012	4121281	35.5	1125.0	Tpcm	PWT	WTA	TCA	12/15/1999[c]				

Table C.4-2
Observed Temperature and Elevation in Boreholes that Correlate with Elevation in Model Simulations
Observed Temperature and Elevations Used in Calibration Shown in Grey
(Page 3 of 6)

Borehole	Easting	Northing	Observed Temperature (C°)	Elevation of Observed Temperature (m)	Stratigraphy[a]	Class/ Rock Type[a]	HGU[a]	HSU[a]	Temperature Log (date)	No.	Mean Residual (HF85)	Mean Residual (T160)	Mean Residual (HF Subregional)
NW of Handley Fault (6)													
PM-2	538257	4133028	39.8	1315.5	Tbq	NWT	unk	PBRCM	7/11/1964	4	-0.75	-0.65	-1.50
PM-2	538257	4133028	46.0	1126.5	Tor	NWT	unk	PBRCM	7/11/1964				
PM-2	538257	4133028	60.2	751.6	Tqm	LA	LFA	PBRCM	7/11/1964				
PM-2	538257	4133028	83.8	45.1	Tqm	LA	LFA	PBRCM	8/10/1964				
PM-2	538257	4133028	85.5-85.7	0.0									
W. Greeley Fault-E. Greeley Fault (7)													
PM-1	552668	4125925	34.2	1265.6	Thp	BED	TCU	CHZCM	8/3/1994[c]	7	1.88	-0.06	0.34
PM-1	552668	4125925	35.5	1218.9	Thp	BED	TCU	CHZCM	8/3/1994[c]				
PM-1	552668	4125925	36.7	1172.0	Thp	BED	TCU	CHZCM	8/3/1994[c]				
PM-1	552668	4125925	38.0	1125.0	Thr	BED	TCU	CHZCM	8/3/1994[c]				
PM-1	552668	4125925	39.3	1078.2	Tcj	BED	TCU	CFCU	8/3/1994[c]				
PM-1	552668	4125925	40.5	1031.2	Tcblr	NWT	TCU	BFCU	8/3/1994[c]				
PM-1	552668	4125925	42.7	937.7	Tcblp	NWT	TCU	BFCU	8/3/1994[c]				
PM-1	552668	4125925	65.5	-381.0	unk	unk	unk	BRA	5/1/1964				
UE-20bh#1	552402	4122007	35.3	1265.6	Thp	LA,GL	LFA	CHZCM	10/1/1991[c]	3	0.98	0.18	-0.02
UE-20bh#1	552402	4122007	36.7	1218.8	Thp	LA,GL	LFA	CHZCM	10/1/1991[c]				
UE-20bh#1	552402	4122007	38.2	1171.9	Thp	LA,ZE,DV	LFA	CHZCM	10/1/1991[c]				

Table C.4-2
Observed Temperature and Elevation in Boreholes that Correlate with Elevation in Model Simulations
Observed Temperature and Elevations Used in Calibration Shown in Grey
(Page 4 of 6)

Borehole	Easting	Northing	Observed Temperature (C°)	Elevation of Observed Temperature (m)	Stratigraphy[a]	Class/ Rock Type[a]	HGU[a]	HSU[a]	Temperature Log (date)	No.	Mean Residual (HF85)	Mean Residual (T160)	Mean Residual (HF Subregional)
Silent Canyon Structure Zone-W and E Estuary Faults (8)													
U-19e[m]	559101	4127775	38.5	938.5	Tbdl	MWT	WTA	BRA	3/6/1966	8	7.22	4.36	2.75
U-19e[m]	559101	4127775	39.4	892.8	Tbdl	NWT	unk	BRA	3/6/1966				
U-19e[m]	559101	4127775	40.5	844.0	Tbdl	BED	unk	BRA	3/6/1966				
U-19e[m]	559101	4127775	41.8	798.3	Tbdl	MWT	WTA	BRA	3/6/1966				
U-19e[m]	559101	4127775	42.8	752.6	Tbdl	DWT	WTA	BRA	3/6/1966				
U-19e[m]	559101	4127775	44.4	703.8	Tbdl	BED	unk	BRA	3/6/1966				
U-19e[m]	559101	4127775	47.0	655.0	Tbdk	PWT	WTA	BRA	3/6/1966				
U-19e[m]	559101	4127775	49.1	612.3	Tbds	LA	LFA	BRA	3/6/1966				
UE-19e	559112	4127849	46.6	621.5	Tbdk	LA	LFA	BRA	8/23/1964				
UE-19gS	556306	4129057	61.6	-238.0	Tbq	NWT	unk	PBRCM	5/4/1965				
E. Greeley Fault-Almendro Fault (9)													
UE-19fS	556107	4119781	41.1	711.7	Tcj	NWT	TCU	CFCU	8/20/1965		8.80	6.50	2.00
Almendro Fault-Scrugham Peak Fault (11)													
U-19i[g]	557922	4122638	35.3	1266.7	Tcps	NWT	TCU	CFCU	8/24/1967	4	-1.22	-2.14	-3.07
U-19i[g]	557922	4122638	37.1	1221.0	Tcps	NWT	TCU	CFCU	8/24/1967				
U-19i[g]	557922	4122638	40.0	1126.5	Tcblp	NWT	TCU	BFCU	8/24/1967				
U-19i[g]	557922	4122638	44.9	937.6	Tcbx	LA	LFA	BFCU	8/24/1967				
UE-19i	557922	4122592	73.8	-344.1	Tbgs	LA	LFA	BRA	9/3/1965				
Scrugham Peak Fault-Split Ridge Fault (12)													
U-19p	559542	4123267	31.5	1218.9	Tcblp	NWT	TCU	BFCU	10/29/1975	2	3.91	3.31	2.11
U-19p	559542	4123267	32.0	1173.2	Tcblp	NWT	TCU	BFCU	10/29/1975				

Table C.4-2
Observed Temperature and Elevation in Boreholes that Correlate with Elevation in Model Simulations
Observed Temperature and Elevations Used in Calibration Shown in Grey
(Page 5 of 6)

Borehole	Easting	Northing	Observed Temperature (C°)	Elevation of Observed Temperature (m)	Stratigraphy[a]	Class/ Rock Type[a]	HGU[a]	HSU[a]	Temperature Log (date)	No.	Mean Residual (HF85)	Mean Residual (T160)	Mean Residual (HF Subregional)
Halfbeak Fault-Rickey Fault-Moor Hen Meadow Structure Zone (13)													
U-19t	562271	4126843	38.9	1218.9	Tcpk	"FB"	LFA	KA	9/27/1993[c]	2	-6.40	-6.70	-8.70
U-19t	562271	4126843	45.1	1125.1	Tcpk	"FB"	LFA	KA	9/27/1993[c]				
UE-19cWW[k]	560339	4124702	35.8	1312.5	Tbdl	LA	LFA	BRA	11/13/1992[c]	3	-1.00	-1.96	-3.76
UE-19cWW[k]	560339	4124702	36.6	1221.9	Tbdl	LA	LFA	BRA	11/13/1992[c]				
UE-19c	560339	4124702	46.6	769.0	Tbdl	LA	LFA	BRA	5/7/1964				
			47.0	750.0									
Split Ridge Fault-Rainier Mesa/Ammonia Tanks Caldera Topographic Margin (14)													
ER-19-1	567542	4114743	23.3	1312.5	Tor	PWT	WTA	PBRCM	12/6/1993[d]	4	14.69	15.81	6.54
ER-19-1	567542	4114743	25.9	1125.0	Tor	MWT-DWT	WTA	PBRCM	12/6/1993[d]				
ER-19-1	567542	4114743	31.2	937.6	CZw	SLT/QTZ/SS	SCU	LCCU1	12/6/1993[d]				
ER-19-1	567542	4114743	34.8	779.4	MDc	SLT	SCU	UCCU	12/6/1993[d]				
			34.9-37.7	750.0									
HTH-1[f]	569000	4112499	22.5	1312.8	Tor	PWT	WTA	PBRCM	8/19/1991[c]	4	12.95	14.27	6.55
HTH-1[f]	569000	4112499	24.9	1125.0	Tor	MWT	WTA	PBRCM	8/19/9191[c]				
HTH-1[f]	569000	4112499	27.9	938.5	Tot	NWT	TCU	PBRCM	8/19/1991[c]				
HTH-1[f]	569000	4112499	**29.9**	**750.7**	Tot	BED	TCU	PBRCM	8/19/1991[c]				
E of Thirst Canyon Lineamint-S of Silent Canyon Caldera Structural Margin (15)													
ER-EC-2A	538421	4110841	43.7	375.5	Tmaw	NWT	TCU	TMCM	2/9/2000	2	23.36	19.76	5.86
ER-EC-2A	538421	4110841	50.2	0.3	Tmar	MWT	WTA	TMCM	2/9/2000				
Ammonia Tanks Caldera Structural Margin-W of Scrugham Peak Fault (16)													
UE-18r	549322	4109762	33.4	375.1	Tmrx	NWT	VTA	TMCM	3/16/1993[c]	1	22.26	19.56	12.86
Ammonia Tanks Caldera Structural Margin-E of Scrugham Peak Fault (17)													
ER-18-2	555725	4106389	52.7	937.5	Tmar	MWT-DWT	WTA	TMCM	7/14/1999	1	-1.14	-2.35	-1.24

Table C.4-2
Observed Temperature and Elevation in Boreholes that Correlate with Elevation in Model Simulations
Observed Temperature and Elevations Used in Calibration Shown in Grey
(Page 6 of 6)

Borehole	Easting	Northing	Observed Temperature (C°)	Elevation of Observed Temperature (m)	Stratigraphy[a]	Class/ Rock Type[a]	HGU[a]	HSU[a]	Temperature Log (date)	No.	Mean Residual (HF85)	Mean Residual (T160)	Mean Residual (HF Subregional)
E of Ammonia Tanks Caldera Structural Margin-Within Rainier Mesa Caldera Structural Margin (18)													
UE-18t	559591	4109095	38.4	1126.1	Tmrb	NWT	TCU	TMCM	12/12/1999[c]	1	-1.66	-1.86	-1.86
E of Thirst Canyon Lineamint-Hogback Fault-Ammonia Tanks Caldera Structural Margin (19)													
ER-EC-8	532764	4106142	36.8	750.0	Tmap	MWT	WTA	TMCM	7/22/1999	1	12.08	11.68	4.38
W of Thirst Canyon Lineamint-SW of Silent Canyon Caldera Structural Margin (20)													
ER-EC-4[i]	532760	4112356	38.0	844.2	Tmap	PWT	WTA	TMA	8/25/2000[c]	3	16.72	17.32	11.52
ER-EC-4[i]	532760	4112356	38.6	750.3	Tmap	MWT	WTA	TMA	8/25/2000[c]				
ER-EC-4[i]	532760	4112356	42.1	562.7	Tmab	BED	TCU	TMA	8/25/2000[c]				
Claim Canyon Caldera Structure Margin (21)													
ER-EC-7[n]	546484	4093127	25.9	1125.5	Tfbr	BED	TCU	FCCM	6/1/2000	1	1.49	0.99	-0.01

[a] Explanation of abbreviations can be found at the end of Attachment A.
[b] HSUs in gray have linear (possibly dominantly conductive) temperature profiles; temperature gradients are listed in Table A2.
[c] Temperature logged more than one year after drilling.
[d] Temperature logged about 5 months after drilling.
[e] Basalt/mafic-rich composition.
[f] Casing perforated over five intervals from 582.2 to 740.7 m depth; cased to 1,131.1 m depth.
[g] May not have been cased to 1,220.4 m depth at time of temperature log.
[h] Casing perforated over three intervals between depths of 700.4 to 860 m, 1,020.3 to 1,146.2 m, and 1,355.9 to 1,447.6 m. Analcime found at depth.
[i] Intense low-temperature hydrothermal alteration below the Rhyolite of Benham of the Paintbrush Group (analcime is the zeolite in minor amounts).
[j] Casing perforated over four intervals between depths of 496.3 to 570 m, 668.9 to 764 m, 1,047.8 to 1161.5 m, and 1,347.4 to 1,494.6 m.
[k] Cased to 737.9 m.
[l] Casing perforated over three intervals between depths of 301.5 to 372.1 m, 582.2 to 686.7 m, and 945.9 to 1,037.8 m. Temperature gradients low throughout borehole, approximately one week after hydraulic tests. Is this borehole significantly affected by pumping? Is there not-yet-equilibrated borehole mixing between intervals?
[m] May not have been cased to 1,529 m depth at time of temperature log.
[n] Borehole gravel packed and casing perforated over two intervals between depths of 278 to 312.1 and 360.9 to 399.3 m.

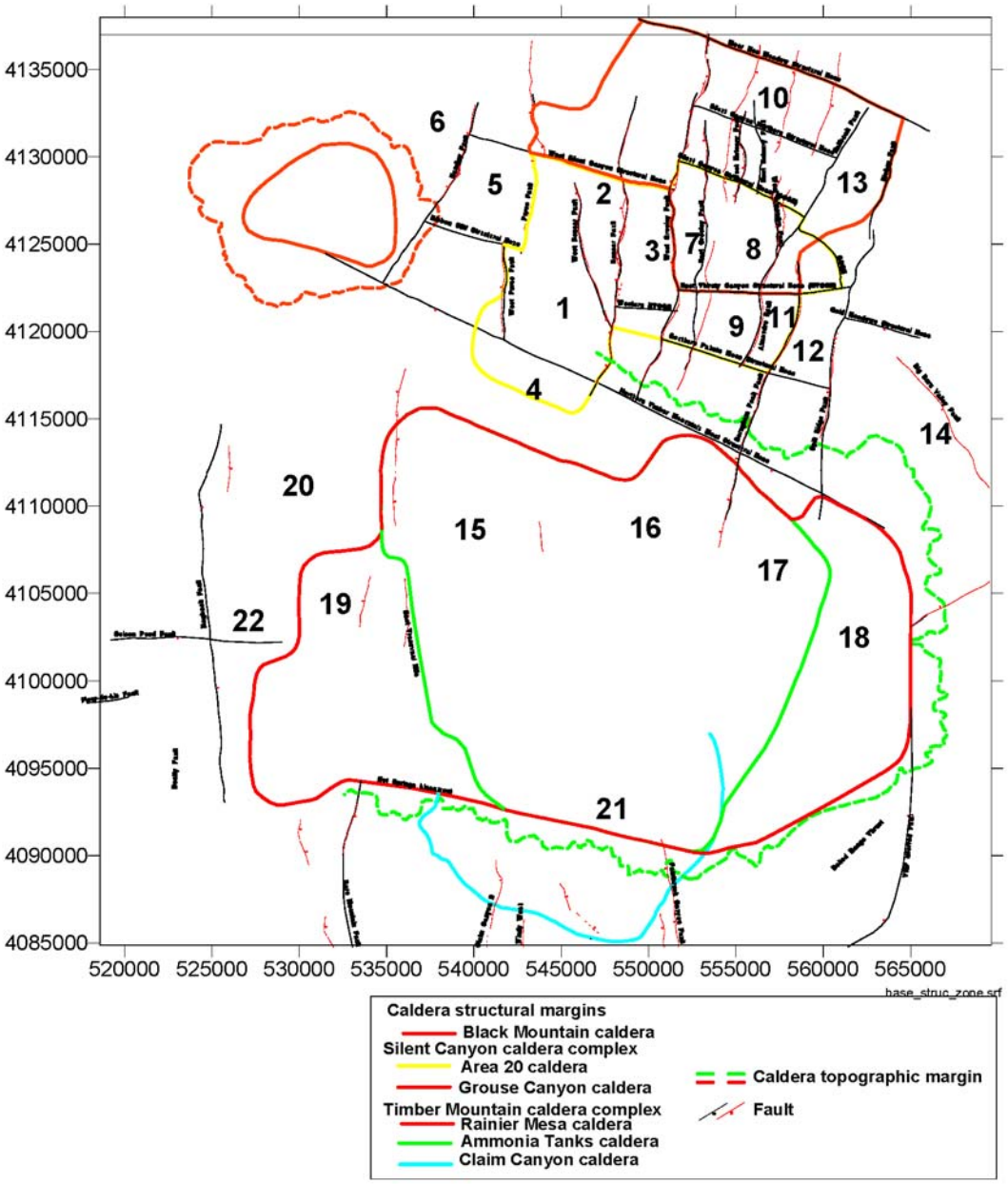

Source: BN, 2002

Figure C.4-2
Location of Structural Zones Used in Study
See Attachment A, Tables A1 and A2.

C.5.0 THERMAL CONDUCTIVITY ESTIMATES

The distribution of temperatures within the PM/OV heat-conduction model is determined by the boundary conditions and the distribution of thermal conductivities within the model. The model described in this report uses the base case HFM described in BN (2002) to distribute thermal conductivities throughout the model. The following sections describe the basis for assigning thermal conductivities to each of the 46 HSUs in the PM/OV model domain, as listed in BN (2002, Table 4-4). Thermal conductivity estimates are described below, grouped by HSU type (Table C.5-1).

Table C.5-1
Range of SZ Thermal Conductivity Estimates for Rock Types in HSU
(Based on Attachment A, Tables B1, B2, and B3)
(Page 1 of 2)

HSU #	Group #[a]	HSU[b]	λ low (W/m °C)[c]	λ Base (W/m °C)[c]	λ high (W/m °C)[c]
1	1	LCCU	2.23	3.9	5.8
2	2	LCA	4.67	4.95	5.23
3	3	UCCU	2.47	3.1	3.66
4	1	LCCU1	2.23	3.9	5.8
5	2	LCA3	4.67	4.95	5.23
6	4	MGCU	2.26	2.26	2.6
7	4	SCICU	2.6	2.6	2.9
8	4	CHICU	2.6	2.6	2.9
9	4	CCICU	2.6	2.6	2.9
10	4	RMICU	2.6	2.6	2.9
11	4	ATICU	2.6	2.6	2.9
12	5	BMICU	2.1	2.1	2.41
13	6	**PBRCM**	1.71	2.13	2.71
14	6	**BRA**	1.84	2.63	3.06
15	6	**BFCU**	1.57	2.61	2.95
16	7	KA	1.77	1.85	1.89
17	8	CFCU	1.43	1.61	1.79
18	7	CFCM	1.78	1.87	1.96

Table C.5-1
Range of SZ Thermal Conductivity Estimates for Rock Types in HSU
(Based on Attachment A, Tables B1, B2, and B3)
(Page 2 of 2)

HSU #	Group #[a]	HSU[b]	λ low (W/m °C)[c]	λ Base (W/m °C)[c]	λ high (W/m °C)[c]
19	7	IA	1.65	1.86	2.06
20	7	CHCU	1.56	1.84	2.12
21	7	CHZCM	1.67	1.81	1.95
22	7	CHVCM	1.48	1.7	1.93
23	8	CHVTA	1.42	1.5	1.61
24	7	YMCFCM	1.66	1.86	2.16
25	8	TSA	1.57	1.69	1.81
26	8	LPCU	1.52	1.69	1.86
27	7	PLFA	1.58	1.75	1.92
28	7	TCA	1.7	1.75	1.8
29	8	UPCU	1.59	1.69	1.8
30	7	BA	1.7	1.9	2.11
31	8	PVTA	1.54	1.68	1.82
32	7	PCM	1.42	1.95	2.16
33	2	LCA3a	4.67	4.95	5.23
34	8	FCCU	1.42	1.58	1.73
35	6	**SCVCU**	2.16	2.61	2.79
36	8	TMA	1.46	1.59	1.73
37	7	THCM	1.67	1.81	1.95
38	7	THLFA	1.66	1.86	2.16
39	6	**TMCM**	1.7	2.79	2.98
40	7	FCA	1.66	1.86	2.16
41	7	FCCM	1.58	1.74	1.89
42	7	DVA	1.66	1.86	2.16
43	8	DVCM	1.43	1.56	1.68
44	8	TCVA	1.42	1.64	1.78
45	7	YVCM	1.67	1.81	1.95
46	9	AA	1.2	1.44	1.44

[a]Group number used to assign lumped thermal conductivities for calibration purposes.
[b]HSU in bold is more indurated, intracalera tuff.
[c]Tuff HSU thermal conductivity estimated from harmonic mean of tuff rock types in boreholes (Attachment A, Table B3).

C.5.1 LCA, LCA3, LCAA, and UCCU

Laboratory measurements of saturated thermal conductivity reported for the carbonate aquifer (LCA, LCA3, LCA3a) and upper clastic confining unit (UCCU) were used as initial estimates of thermal conductivity for these HSUs (Sass et al., 1980; Sass et al., 1987) (Attachment A, Tables B1 and B3). Thermal conductivities of the LCA, LCA3, and LCA3a were estimated from the arithmetic average of 4.95 W/m•^{o}K calculated by Gillespie et al. (2003) from measurements on the Lone Mountain Dolomite and Roberts Mountain Formation in Well UE-25 p#1 at Yucca Mountain (Sass et al.,1987, Table 3-5). The harmonic average of 3.1 W/m•^{o}K estimated by Sass et al. (1980) for the Eleana Formation argillite unit in borehole UE-25 a-3 in the Calico Hills was used for the UCCU. This thermal conductivity is similar to the value of 3.3 W/m•^{o}K estimated by Gillespie et al. (2003) for the UCCU based on values for other argillites reported in the literature.

C.5.2 LCCU

Thermal conductivity measurements for the lower clastic confining unit (LCCU and LCCU1) in the NTS area have not been reported in the literature. This unit includes the late Proterozoic to early Cambrian Wood Canyon, Stirling Quartzite, and Johnnie Formations, rocks described as having a siltstone to quartzite lithology. Gillepsie et al. (2003) estimated an average thermal conductivity for the LCCU of 5.8 W/m•^{o}K, based on thermal conductivities of 4.5 to 7.1 W/m•^{o}K (pure quartzite) reported in the literature for rocks with dominantly quartzite lithologies. However, a thermal conductivity of 3.9 W/m•^{o}K is considered as the base case thermal conductivity of the LCCU in this report, a value that is an average of typical values for a quartzite (5.8 W/m•°K) and a muddy sandstone (2.23 W/m•^{o}K) (Gillespie, 2003).

The thermal conductivity of the LCCU was initially allowed to vary in the inverse THERMAL models, but was later fixed at 3.9 W/m•^{o}K because simulated temperatures at the observation points were insensitive to its value. The insensitivity of the simulated temperatures to the thermal conductivity of the LCCU is a consequence of its small volume in the flow model domain, despite its widespread presence at greater depths in the hydrostratigraphic model (BN, 2002). However, where present at the base of the model domain, the LCCU influences the distribution of calculated temperatures using specified heat flux boundary conditions.

C.5.3 Intrusive Confining Units

Thermal conductivity measurements for the granitic plutons that comprise the Mesozoic Granitic Confining Unit (MGCU) in the NTS area have not been reported in the literature. Neither were they available for the deep granitic intrusive rocks (the SCICU, CHICU, CCICU, RMICU and ATICU HSUs) thought to be present at depth beneath the caldera complexes, areas that may also include older volcanic rocks and sedimentary rocks (BN, 2002, Table 4-4). Thermal conductivities of 1.77 to 2.40 W/m•^{o}K were reported by Sass et al. (1987) for extrusive latitic lavas encountered in boreholes at Yucca Mountain; however, the relation of these values to the thermal conductivities of more widespread intrusive rocks at depth are unknown. In this study, a base-case thermal conductivity of 2.6 W/m•^{o}K is used for the intrusive confining units, based on the compilation for granodiorite reported by Gillespie (2003). For comparison, Morgan et al. (1996) reported a thermal conductivity of 2.26 W/m•^{o}K for quartz monzonite in the Jemez Mountains, New Mexico and Lin et al., (2000) used a thermal conductivity value of 2.9 W/m•^{o}K for granite in the Ozark Mountains, Arkansas.

Thermal conductivity laboratory measurements for the trachytic (more basaltic) intrusive rocks thought to be present beneath the Black Mountain caldera (the BMICU) were not found in the literature. Gillespie (2003) reported a thermal conductivity estimate of 2.1 W/m•^{o}K for basalt extrusive, and this estimate was used as both a lower bound and base case thermal conductivity for the BMICU in this study. A thermal conductivity of 2.41 W/m•^{o}K was estimated as an upper bound thermal conductivity for the BMICU, based on the possibility that greater alteration or induration at depth may have increased its thermal conductivity relative to the lavas.

C.5.4 Volcanic Rocks

The volcanic HSUs in the BN (2002) HFM were defined in an attempt to group lithologic units that had similar degrees of welding and alteration history, and would therefore be likely to have relatively similar hydrologic and solute transport properties. However, this was not always possible where lithologic units were relatively thin or where the scarcity of subsurface data precluded more detailed definition of the hydrostratigraphy. In some cases, the inclusion of different types of rock in a single HSU is explicitly acknowledged through the definition of "composite" units. However, detailed borehole stratigraphic logs indicate that even HSUs characterized as aquifers or confining units can have considerable variability in rock types.

In this report, thermal conductivities for individual volcanic HSUs were estimated by considering the percentages of different rocks types that are typically present in the HSU, as indicated by borehole stratigraphic logs. First, arithmetic averages of thermal conductivity were calculated for different rock types (e.g., welded devitrified tuff, lava, nonwelded zeolitic tuff) using data reported for those rock types (Gillespie, 2003; Sass and Lachenbruch, 1982; Sass et al., 1987) (see Attachment A, Table B1). Second, the borehole stratigraphic logs were examined and the thickness-weighted harmonic means of thermal conductivity were calculated for each HSU in individual boreholes using the saturated thickness of different rock types present in the HSU at that borehole (see Attachment A, Table B2). Lastly, the harmonic mean thermal conductivities for an HSU at individual boreholes were arithmetically averaged to produce the final estimate of the thermal conductivity for the HSU (Attachment A, Table B3). In general, these last estimates constitute the base-case thermal conductivity value for different HSUs used in this report. However, in some cases, other factors were also considered, as described in the following sections.

C.5.4.1 Extra-Caldera Volcanic Rocks

The thermal conductivities compiled by Gillespie et al. (2003) were based on measurements of extra-caldera volcanic rocks near Yucca Mountain, and are assumed to be representative of thermal conductivity values for similar rock types within the extra-caldera HSUs of the PM/OV flow domain. The methodology for estimating the thermal conductivity of individual HSUs was outlined previously in Section C.5.4.

C.5.4.2 Intra-Caldera Volcanic Rocks

The intra-caldera HSUs in the PM/OV model domain are by definition within the structural margins of calderas and include the PBRCM, BRA, BFCU, and TMCM HSUs (BN, 2002). These HSUs contain lavas, welded tuffs, bedded and nonwelded tuffs, debris flows and dikes (Byers et al., 1976; Sawyer et al., 1994). The thermal conductivities compiled by Gillespie et al. (2003) were based on measurements of extra-caldera volcanic rocks near Yucca Mountain, which may be less indurated and hence have lower thermal conductivities than rocks found within the calderas of the PM/OV model. This hypothesis is supported by laboratory data from Morgan et al. (1996) that indicate the thermal conductivities of indurated intra-caldera volcanic rocks in the Jemez Mountains, New Mexico, are typically 1.7 to 2.9 times higher than the thermal conductivities of their extra-caldera counterparts.

Based on these data, it is assumed that the constituent rock types of intra-caldera HSUs within the PM/OV domain have thermal conductivities that are 1.7 times higher than the values reported by Gillespie (2003) for their extra-caldera analogs (Attachment A, Tables B1 and B2).

C.5.5 Alluvium

Thermal conductivity measurements for alluvium (AA) in the NTS area were not available in the literature. However, because of its high porosity at Yucca Mountain, the nonwelded and bedded Calico Hills Formation (CHZCM) was considered suitable as an analog for alluvium. Thermal conductivity measurements reported in Sass et al. (1987) from Yucca Mountain indicate that the Calico Hills Formation has thermal conductivities that range from 0.8 to 1.3 W/m•°K at ambient saturations above the water table, and from 1.1 to 1.6 W/m•°K in the saturated zone. An average unsaturated-zone thermal conductivity of 1.2 W/m•°K is reported for these tuffs at Yucca Mountain (Bodvarsson et al., 2003). The thermal conductivity of all types of tuff at Yucca Mountain increases by an average factor of 1.2 as the tuffs go from unsaturated to saturated conditions (Attachment A, Table B3). Based on these values, the base-case saturated thermal conductivity of alluvium derived from rocks like the Calico Hills Formation is estimated to be 1.44 W/m•°K with a lower bound of 1.2 W/m•°K. For comparison, an average saturated thermal conductivity of 1.5 W/m•°K was reported for Basin and Range tuffaceous alluvium (Wollenberg et al., 1983) and Olmsted and Rush (1987) reported that the saturated thermal conductivity of tuffaceous alluvium at a site in northern Nevada varies between 1.33 to 1.83 W/m•°K based on laboratory measurements of clay-, sand-, and gravel-sized alluvium.

The thermal conductivity of alluvium in the PM/OV heat conduction model was initially allowed to vary in the inverse model calibration, but was later fixed at 1.44 W/m•°K after determining that simulated temperatures at the observation points were insensitive to this parameter. Temperatures were probably insensitive to the assumed thermal conductivity of the alluvium because of its relatively small volume in the model and proximity of the alluvium to the upper boundary where temperatures were held constant.

C.5.6 Summary of Thermal Conductivity Estimates

The range in thermal conductivity estimates for HSUs in the PM/OV flow domain and sources for these estimates are summarized in Table C.5-1. These estimates are based primarily on a thermal conductivity data measured on extra-caldera tuffs and lavas at Yucca Mountain (Sass et al., 1982; 1987), supplemented by measurements made elsewhere in the vicinity of the NTS (Sass et al., 1980; Sass et al., 1995) and values for analogous rocks reported in the literature (Morgan, 1996; Gillespie, 2003).

In the vicinity of the NTS, the thermal conductivities of volcanic rocks in the NTS depend on the degree of welding and alteration of the rock. Because volcanic HSUs in the PM/OV flow domain often contain multiple rock types, a methodology was developed to estimate representative thermal conductivities that considered variability in rock types within an HSU. In this methodology, the thickness-weighted harmonic mean thermal conductivities of different rock types in the HSU at individual boreholes were first calculated. These harmonic means were then averaged arithmetically across the multiple boreholes to estimate a representative thermal conductivity for the HSU that could be used throughout the model domain.

Other adjustments to the measured thermal conductivity values were made to provide estimates for HSUs in which measurements are lacking. To compensate for the lack of thermal conductivity measurements on intra-caldera tuffs, this study relies on observations from other sites (Morgan, 1996) which indicate that intra-caldera tuffs have thermal conductivities at least 1.7 times those of their extra-caldera analogs because of their greater alteration and induration. For alluvium, saturated thermal conductivity was estimated by analogy with porous bedded and nonwelded tuffs in the unsaturated zone at Yucca Mountain and by noting typical increases in thermal conductivity that accompany the transition from unsaturated to saturated conditions.

Although anisotropy in thermal conductivity was not explicitly analyzed as part of this study, its affect on heat transport may be less important than anisotropy of permeability is to groundwater flow (Phillips, 1991, p. 34). For this reason, together with the absence of anisotropic measurements, thermal conductivities were assumed isotropic in simulations.

C.6.0 Boundary Condition Estimates

C.6.1 Upper Boundary Condition

The upper boundary of the model coincides with the potentiometric surface, which in this report is taken to be synonymous with the water table. Constant, but spatially variable temperatures were estimated at the water table using borehole measurements of shallow groundwater temperature. These temperatures were kriged onto a uniform grid with 100 x 100 m cells using a linear variogram to approximate the covariance structure (Figure C.6-1). The kriged temperatures were then mapped onto the top nodes of the PM/OV CAU model grid using a nearest neighbor approach. By using measured temperatures to estimate temperatures along the upper boundary of the heat conduction model, the effects of unsaturated-zone hydrologic processes and variable unsaturated-zone thickness on water-table temperatures are implicitly taken into account.

In developing the dataset used to construct the map of water table temperatures, temperatures measured near the water table were evaluated against deeper temperature data and other nearby water table temperature measurements to determine their reliability as indicators of water table temperature. For example, the water table temperature for well UE-20e#1 measured on 6/2/1964 (immediately after drilling) was discarded due to possible upwelling in the borehole (Attachment A, Figure C6) and because it was anomalously warm temperatures relative to other wells in the area (Table C.6-1). By similar reasoning, the water table temperature at well U-19t measured on 9/27/1993 was included because a deeper, linear segment of the temperature profile at this well projected upward to this temperature, whereas a temperature measured on 6/7/1978 was discarded because it was anomalously cool for the area. An average of unpublished USGS temperatures measured 5 ft below the water table in various boreholes between the years 2000 and 2002 were used where available (Table C.6-1). Between the Handley Fault and the Purse Fault, the water table temperature from well U-20m was chosen as representative of this area because the water table temperature at nearby well UE-20j varied over time (Table C.6-1).

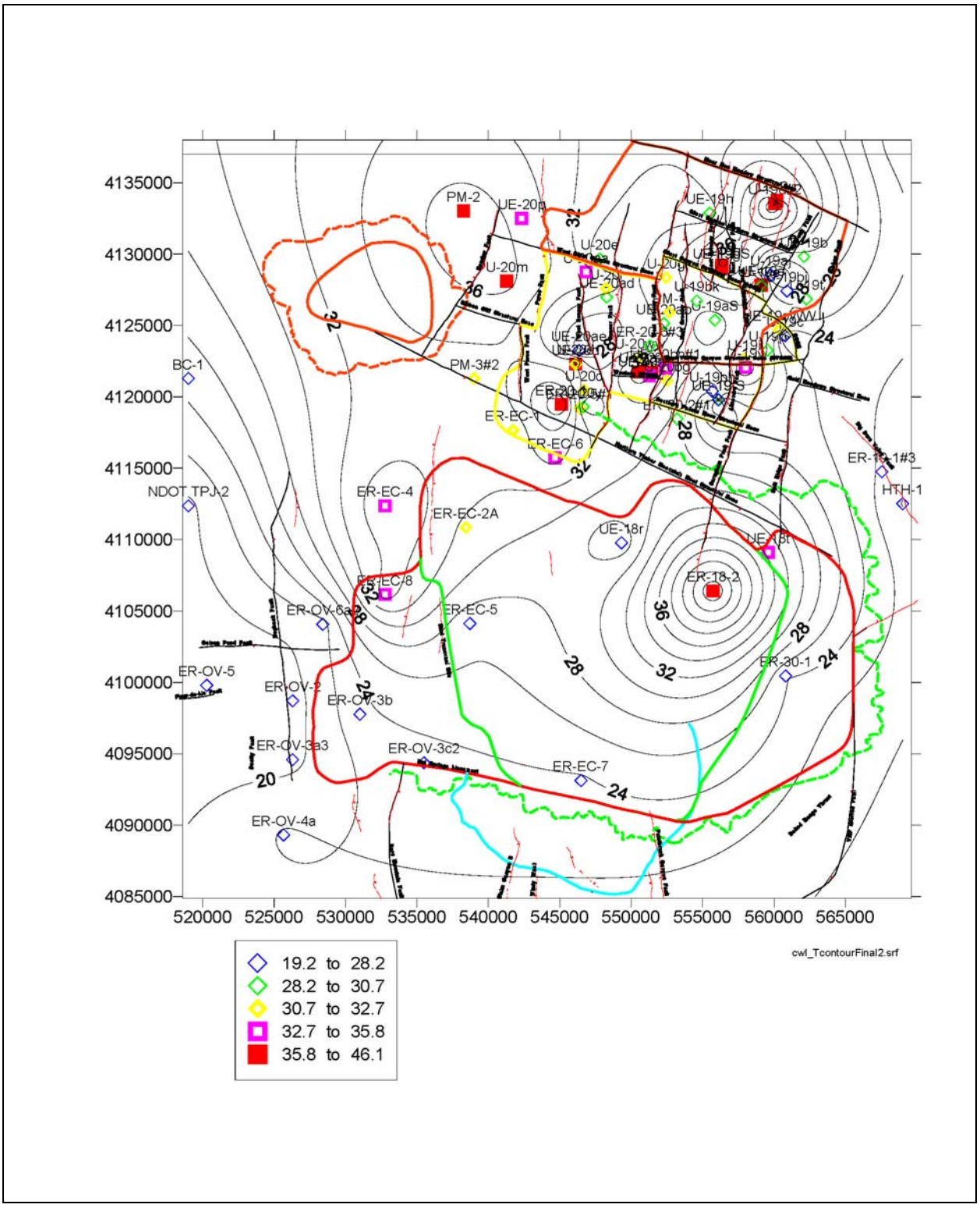

Figure C.6-1
Contour Map of Water Table Temperatures (°C) Used as Upper Boundary Conditions
See Table C.6-1.

Table C.6-1
Depth and Elevation Range, Hydrostratigraphic Unit, and Temperature of Borehole Composite Water Levels
Depth, Temperature, and Elevation of Composite Water Levels are Shown in Bold
(Page 1 of 5)

Easting	Northing	Composite Water Level Temperature (°C)	Standard Deviation (°C)	Borehole	Composite Water Level[a] Depth (m)	Standard Deviation (m)	Lower Depth (m)	Composite Water Level Elevation (m)	Lower Elevation (m)	Stratigraphic[b]	Class/ Rock Type[b]	HGU[b]	HSU[b]	Temperature Log (Date)
Purse Fault-W. Boxcar Fault (1)														
545113.1	4119468	**39.9**	0.2	ER-20-1	**606.2**	0.0	623.0	**1,277.8**	1,261.0	Tpcm	MWT	WTA	TCA	2000-2002
546385.9	4119208	**32.7**		ER-20-5#1	**626.4**			**1,276.1**		Tp	BED	TCU	LPCU	11/3/1995
546698.7	4120478	**31.2**		U-20c	**643.1**			**1,271.3**		Tpcm	tuf	unk	TCA	4/5/1965
546102.6	4122301	**35.8**		U-20d	**634.0**			**1,271.6**		Tpb	LA	LFA	BA	1/31/1967
546651.3	4119291	**28.8**		U-20y	**630.9**			**1,276.2**		Tp	BED	TCU	LPCU	1/2/1975
546339.7	4123244	**23.9**		UE-20ae	**609.6**			**1,276.8**		unk	BED	unk	PVTA/TCVA	7/19/1978
546102.7	4122275	**32.0**		UE-20d	**624.8**			**1,281.4**		Tpb	LA	LFA	BA	7/28/1964
W. Boxcar Fault-Boxcar Fault (2)														
546837.4	4128745	**33.3**		U-20aa	**570.0**			**1,361.5**		Thp	FB	LFA	CHZCM	8/18/1975
547789.2	4129655	**28.2**		U-20e	**566.9**			**1,358.2**		Thp	LA	LFA	CHZCM	12/20/1968
548242.9	4127581	**31.2**		U-20i	**582.2**			**1,359.4**		Thp	PL	unk	CHZCM	10/20/1967
548286.2	4126975	**28.9**		UE-20ad	**582.2**			**1,358.2**		Thp	LA	LFA	CHZCM	8/4/1978
Boxcar Fault-W. Greeley Fault (3)														
551362.9	4123692	29.1		ER-20-6#1[c]	618.4		633.7	1,355.1	1,339.8	Tpd	BED	TCU	UPCU	2002
551328	4123662	28.7		ER-20-6#2[d]	618.6		633.9	1,355.0	1,339.7	Tpd	BED	TCU	UPCU	2002
551295.7	4123579	**28.2**		ER-20-6#3[e]	**615.9**		631.1	**1,354.9**	1,339.7	Thp	LA	LFA	CHZCM	2002
550480.6	4121740	**35.9**		U-20a	**563.9**			**1,423.4**		Thp	LA	LFA	CHZCM	4/29/1964
551424.4	4121743	**36.3**		U-20n	**634.0**			**1,340.2**		Thp	LA	LFA	CHZCM	8/25/1968
550614	4122712	**31.5**	0.2	U-20ww	**626.2**	0.4	643.0	**1,345.3**	1,328.5	Thp	LA	LFA	CHZCM	2000-2002
551273.2	4121484	**33.9**	0.1	UE-20n#1	**622.2**	0.1	637.5	**1,347.1**	1,331.8	Thp	LA	LFA	CHZCM	2000-2002
S of Silent Canyon Caldera Structural Margin-N of Timber Mountain Caldera Topographic Margin (4)														
541729.8	4117660	**32.3**		ER-EC-1	**565.6**		580.9	**1,271.1**	1,255.9	Tmrf	NWT	TCU	FCCU	2000-2002
544673.5	4115729	**34.6**		ER-EC-6	**434.6**		449.8	**1,273.5**	1,258.3	Tmrf	BED	TCU	FCCU	2000-2002

Table C.6-1
Depth and Elevation Range, Hydrostratigraphic Unit, and Temperature of Borehole Composite Water Levels
Depth, Temperature, and Elevation of Composite Water Levels are Shown in Bold
(Page 2 of 5)

Easting	Northing	Composite Water Level Temperature (°C)	Standard Deviation (°C)	Borehole	Composite Water Level[a] Depth (m)	Standard Deviation (m)	Lower Depth (m)	Composite Water Level Elevation (m)	Lower Elevation (m)	Stratigraphic[b]	Class/ Rock Type[b]	HGU[b]	HSU[b]	Temperature Log (Date)
Handley Fault-Purse Fault (5)														
539011.8	4121281	32.3	0.2	PM-3#1	444.2	0.02	461.0	1,330.6	1,313.9		NWT	TCU	UPCU	2000-2002
539011.8	4121281	**32.7**	0.1	PM-3#2	**443.6**	0.02	458.9	**1,331.2**	1,316.0		NWT	TCU	UPCU	2000-2002
541289.6	4128104	**36.6**		U-20m	**381.0**			**1,418.2**		Tmrp	DWT	WTA	TMA	10/24/1968
541285.3	4128082	30.8-32.7-37.89[i]		UE-20j	390.1			1,409.1		Tmrp	MWT	WTA	TMA	9/5/1964 - 10/21/1964
NW of Handley Fault (6)														
538256.7	4133028	**36.9**	0.2	PM-2	**261.7**	0.03		**1,440.9**		Tqu	BED	unk	PBRCM	2000-2002
542331.4	4132503	**35.4**		UE-20p	**277.4**			**1,415.2**		Tmr	MWT	WTA	TMA	2/10/1968
W. Greeley Fault-E. Greeley Fault (7)														
553210.6	4118447	**29.5**	0.00	ER-20-2#1	**692.6**	0.1	709.4	**1,340.4**	1,323.6	Thp	BED	TCU	CHZCM	2000-2002
552668.1	4125925	**31.6**	0.1	PM-1	**639.2**	0.2	656.0	**1,359.6**	1,342.9	Thp	FB	LFA	CHZCM	2000-2002
552511.9	4121139	**32.1**	0.1	U-20bg	**651.5**	0.03	666.8	**1,350.1**	1,334.8	Thp	BED	TCU	CHZCM	2000-2002
552440.2	4128344	**31.2**		U-20g	**615.7**			**1,356.4**		Thp	LA	LFA	CHZCM	10/15/1964
552284.5	4125130	**30.1**		UE-20ab	**652.3**			**1,353.6**		Thp	FB	LFA	CHVCM	6/5/1978
552402.2	4122007	**33.6**	0.1	UE-20bh#1	**674.6**	0.1	689.9	**1,321.8**	1,306.6	Thp	BED	TCU	CHZCM	2000-2002
Silent Canyon Structural Zone-W and E Estuary Faults (8)														
559768.3	4128539	**22.8**		**U-19aj**	**667.5**			**1,432.9**		Tcblp	TB	TCU	BFCU	12/9/1980
555856.8	4125371	**29.0**		**U-19aS**	**673.6**			**1,387.1**		Thp	NWT	VTA	CHVTA	10/4/1964
554585.6	4126723	**30.7**	0.1	U-19bk	**604.9**	0.03	620.1	**1,428.1**	1,412.9	unk	unk	unk	unk	2000-2002
559100.9	4127775	**30.7**	3.4	**U-19e**	**678.2**	29.0		**1,430.7**		Tcblp	NWT	TCU	BFCU	1966-1968
556340.5	4129244	**39.0**		**U-19g**	**627.9**			**1,424.6**		Tcps	BED	TCU	CFCU	11/19/1965
556975.7	4125473	**13.1**	1.7	**U-19yS**	**627.9**	6.1		**1,412.1**		Tpr	LA/PL/FB	LFA	PLFA	1978
559100.4	4127836	**37.5**		**UE-19e**	**698.0**			**1,410.9**		Tcblp	NWT	TCU	BFCU	8/23/1964
556306.1	4129057	**36.9**	1.6	**UE-19gS**	**695.1**	55.0		**1,352.9**		Tcblp	NWT	TCU	BFCU	1965

Table C.6-1
Depth and Elevation Range, Hydrostratigraphic Unit, and Temperature of Borehole Composite Water Levels
Depth, Temperature, and Elevation of Composite Water Levels are Shown in Bold
(Page 3 of 5)

Easting	Northing	Composite Water Level Temperature (°C)	Standard Deviation (°C)	Borehole	Composite Water Level[a] Depth (m)	Standard Deviation (m)	Lower Depth (m)	Composite Water Level Elevation (m)	Lower Elevation (m)	Stratigraphic[b]	Class/ Rock Type[b]	HGU[b]	HSU[b]	Temperature Log (Date)
E. Greeley Fault-Almendro Fault (9)														
555683.6	4120389	**26.1**	0.1	U-19bh	**636.7**	0.4	651.9	**1,426.2**	1,411.0	Tpe	NWT	TCU	PLFA	2000-2002
556107.4	4119811	**29.4**		**U-19f**	**759.3**			**1,293.3**		Thp	BED	TCU	CHCU	7/5/1968
556107.5	4119781	**19.8**		**UE-19fS**	**731.5**			**1,321.3**		Tpe	NWT	TCU	CHCU	7/28/1965
Halfbeak Fault-Moor Hen Meadow-Silent Canyon Northern Structure Zones (10)														
560056.3	4133535	**44.8**		**U-19d#2**	**664.5**			**1,426.8**		Tbds	LA	LFA	BRA	6/25/1964
560207.3	4133751	**37.8**		**U-19u**	**661.4**			**1,433.5**		Tbdb	LA	LFA	BRA	5/6/1969
555488.4	4132882	**28.5**	0.05	UE-19h	**643.4**	0.1	658.7	**1,423.1**	1,407.9	Tbdl	LA	LFA	BRA	2000-2002
Almendro Fault-Scrugham Peak Fault (11)														
557922.1	4122638	**31.1**		**U-19i**	**728.5**			**1,355.1**		Tcps	NWT	VTA	CFCU	8/24/1967
558003.1	4122055	**33.8**		**U-19v**	**661.4**			**1,434.4**		Thp	NWT	VTA	CHVTA	5/27/1969
Scrugham Peak Fault-Split Ridge Fault (12)														
559541.6	4123267	**29.9**		**U-19p**	**670.6**			**1,432.3**		**Tcblp**	**NWT**	**TCU**	**BFCU**	10/29/1975
Halfbeak Fault-Rickey Fault-Moor Hen Meadow Structure Zone (13)														
560900.4	4127416	**26.3**	0.1	U-19bj	**650.9**	0.1	666.1	**1,493.4**	1,478.1	Tcpk	LA	LFA	KA	2000-2002
560769.4	4124277	**21.5**	9.4	**U-19c**	**454.2**	40.6		**1,689.2**		Tmt	BS	LFA	PVTA	1965
562271.5	4126843	**20.7**		U-19t	**588.3**			**1,542.6**		Tcbk	FB	LFA	KA	6/7/1978
562271.5	4126843	**29.5**		**U-19t**	**721.0**			**1,409.8**		Tcbk	FB	LFA	KA	9/27/1993
562088.5	4129826	**29.4**	2.7	**UE-19b**	**646.2**	0.0		**1,427.1**		Tbdl	LA	LFA	BRA	1964
		34.6		**UE-19c**	**716.3**			**1,427.4**		Tcbr	NWT	TCU	BFCU	5/2/1964
560338.9	4124702	**31.2**	0.2	UE-19cWW	**713.1**	0.1	728.4	**1,430.5**	1,415.3		NWT	TCU	BFCU	2000-2002
Split Ridge Fault-Rainier Mesa/Ammonia Tanks Caldera Topographic Margin (14)														
567541.6	4114743	**26.8**	0.2	ER-19-1#1[f]	**544.1**	0.7	559.3	**1,327.4**	1,312.1	Tor	BED	TCU	PBRCM	2000-2002
567541.6	4114743	**22.5**	0.2	ER-19-1#27[g]	**359.7**	3.6	374.9	**1,511.8**	1,496.6	Ton2	NWT	TCU	PBRCM	2000-2002
567541.6	4114743	**21.7**	0.3	ER-19-1#3[h]	**306.7**	0.0	321.9	**1,564.8**	1,549.6	Ton2	BED	TCU	PBRCM	2000-2002
569000.3	4112499	**19.9**	1.5	**HTH-1**	**165.1**	0.1	180.4	**1,711.2**	1,696.0	Tn	BED	unk	PBRCM	2001-2002

Table C.6-1
Depth and Elevation Range, Hydrostratigraphic Unit, and Temperature of Borehole Composite Water Levels
Depth, Temperature, and Elevation of Composite Water Levels are Shown in Bold
(Page 4 of 5)

Easting	Northing	Composite Water Level Temperature (°C)	Standard Deviation (°C)	Borehole	Composite Water Level[a] Depth (m)	Standard Deviation (m)	Lower Depth (m)	Composite Water Level Elevation (m)	Lower Elevation (m)	Stratigraphic[b]	Class/ Rock Type[b]	HGU[b]	HSU[b]	Temperature Log (Date)
E of Thirst Canyon Lineamint-S of Silent Canyon Caldera Structural Margin (15)														
538420.8	4110841	**31.5**		ER-EC-2A	**230.0**		245.2	**1,264.2**	1,248.9	Tfbw	BED	TCU	FCCM	2000-2002
538701.8	4104137	**26.5**	0.5	ER-EC-5	**309.9**	0.1	325.2	**1,237.5**	1,222.3	Tmar	DWT-VT	WTA	TMCM	2000-2002
Ammonia Tanks Caldera Structure Margin-W of Scrugham Peak Fault (16)														
549322	4109762	**26.5**	0.2	UE-18r	**415.8**	0.02	431.0	**1,272.2**	1,257.0	Tma	PWT	WTA	TMCM	2000-2002
Ammonia Tanks Caldera Structural Margin-E of Scrugham Peak Fault (17)														
555724.6	4106389	**46.1**	0.3	ER-18-2	**369.3**	0.1	384.6	**1,287.9**	1,272.6	Tmar	NWT	TCU	TMCM	2000-2002
E of Ammonia Tanks Caldera Structure Margin-Within Rainier Mesa Caldera Structure Margin (18)														
560804.7	4100463	**24.2**		**ER-30-1**	**137.5**			**1,279.0**		Tfdb	BS	LFA	FCCM	3/22/1994
559591	4109095	**33.5**	0.2	UE-18t	**278.7**	0.02		**1,306.6**		Tfbw	BED	TCU	FCCM	2000-2002
E of Thirst Canyon Lineamint-Hogback Fault-Ammonia Tanks Caldera Structure Margin (19)														
532763.8	4106142	**34.8**	0.1	ER-EC-8	**98.3**	0.1	113.6	**1,222.4**	1,207.1	Tfb	BED	TCU	FCCM	2000-2002
W of Thirst Canyon Lineamint-SW of Silent Canyon Caldera Structure Margin (20)														
532759.6	4112356	**35.7**	0.1	ER-EC-4	**228.3**	0.04	243.5	**1,222.6**	1,207.3	Ttr	BED	VTA	TCVA	2000-2002
Claim Canyon Caldera Structure Margin (21)														
546483.5	4093127	**23.8**	0.4	ER-EC-7	**228.0**	0.1	243.2	**1,236.6**	1,221.3	Tfbw	LA	LFA	FCCM	2000-2002
Oasis Valley (22)														
528416.7	4104084	**21.0**	0.3	ER-OV-1(?)	**5.5**	0.0	20.8	**1,235.9**	1,220.6	Tf	LA	LFA	FCCM	2000-2002
526310.0	4098716	**19.3**	0.2	ER-OV-2	**8.7**	0.02	23.9	**1,174.1**	1,158.8	Tgs	AL	AA	AA	2000-2002
526298.8	4094587	**19.8**	0.1	ER-OV-3a	**17.5**	0.03	32.7	**1,154.3**	1,139.0	Tf	PWT-MWT	WTA	DVCM	2000-2002
526298.8	4094587	**21.3**	0.2	ER-OV-3a2	**48.7**	0.1	64.0	**1,122.9**	1,107.6	Tf	MWT	WTA	DVCM	2000-2002
526298.8	4094587	**19.5**	0.1	ER-OV-3a3	**17.4**	0.03	32.7	**1,154.1**	1,138.9	Tf	PWT-MWT	WTA	DVCM	2000-2002
531007.6	4097777	**23.5**	0.2	ER-OV-3b	**105.6**	0.03	120.8	**1,184.5**	1,169.3	Tgs	AL	AA	AA	2000-2002
535494.2	4094374	**23.3**	0.1	ER-OV-3c	**65.3**	0.02	80.5	**1,212.3**	1,197.1	Tma	NWT-PWT	VTA	TMA	2000-2002
535494.2	4094374	**23.3**	0.2	ER-OV-3c2	**65.4**	0.02	80.6	**1,212.3**	1,197.1	Tma	NWT-PWT	VTA	TMA	2000-2002
525671.4	4089316	**22.2**	0.1	ER-OV-4a	**7.3**	0.1	21.8	**1,056.9**	1,042.4	Tgs	AL	AA	AA	2000-2002
520280.1	4099809	**19.3**	0.2	ER-OV-5	**9.7**	0.01	24.2	**1,190.5**	1,176.0	Tgs	AL	AA	AA	2000-2002
528416.9	4104085	**20.5**	0.1	ER-OV-6a	**4.9**	0.5	19.4	**1,236.6**	1,222.1	Tf	LA	LFA	FCCM	2000-2002
528416.9	4104085	**21.3**	0.1	ER-OV-6a2	**5.7**	0.01	17.9	**1,235.6**	1,223.4	Tf	LA	LFA	FCCM	2000-2002

Table C.6-1
Depth and Elevation Range, Hydrostratigraphic Unit, and Temperature of Borehole Composite Water Levels
Depth, Temperature, and Elevation of Composite Water Levels are Shown in Bold
(Page 5 of 5)

Easting	Northing	Composite Water Level Temperature (°C)	Standard Deviation (°C)	Borehole	Composite Water Level[a] Depth (m)	Standard Deviation (m)	Lower Depth (m)	Composite Water Level Elevation (m)	Lower Elevation (m)	Stratigraphic[b]	Class/ Rock Type[b]	HGU[b]	HSU[b]	Temperature Log (Date)

[a] USGS - Temperature collected by USGS in 2000, 2001, and 2002 at 5 ft below composite water level in well.
[b] Explanation of abbreviations can be found at the end of Attachment A
[c] Casing perforated and gravel packed over two intervals between depths of 742.8 to 843.4 m and 858 to 898.2 m.
[d] Casing perforated and gravel packed over two intervals between depths of 735.8 to 840.3 m and 851.3 to 897.6 m.
[e] Casing perforated and gravel packed between 755.9 to 855.6 m depth.
[f] Casing set to 1,090.4 m depth; gravel packed and casing perforated 988.5 to 1,008.5 m and 1,051.7 to 1.069.9 m depth.
[g] Casing set to 829.1 m depth; gravel packed and casing perforated 785.5 to 834.5 m depth.
[h] Casing set to 420.8 m depth; gravel packed and casing perforated 405.7 to 433.4 m depth.
[i] Temperature of composite water level increased as warmer water rose in open borehole due to artificial breaching of confining units by borehole.

C.6.2 Lower Boundary Condition

The PM/OV flow domain is located in an area with a long and complex thermal history. Local igneous activity or tectonism has affected the geothermal regime in this area of the NTS since at least the Mesozoic, when granitic plutons were intruded (HSU MGCU). In the Cenozoic, thrust faulting re-arranged the distribution of rocks and probably redirected heat flow through thickened sections of high thermal conductivity rock like the lower carbonate aquifer. These events were followed by the development of the southwestern Nevada volcanic field (SWNVF) and the extrusion of hundreds of cubic kilometers of tuff and related lavas, caldera collapse and resurgence by new infusions of magma, and basin-and-range normal faulting (Sawyer et al., 1994; Grauch et al., 1999; BN, 2002). The residual effect of past igneous and tectonic events on the present-day geothermal regime is uncertain and it is possible that geothermal heat fluxes remain spatially variable to this day. This conclusion is supported by recent work has indicated that the Timber Mountain caldera complex is located within an inherent structural weakness in the upper crust that has a higher than average regional heat flow (Faulds and Varga, 1998, Figure 1).

Due to the great depth of the lower model boundary relative to boreholes in the area, considerable uncertainty exists regarding thermal conditions at the base of the model. Because of this uncertainty and the expected influence of the lower boundary conditions on model results, several different approaches were used to assign thermal conditions along the base of the model. The first approach assumes that heat flux is uniform along the base of the model, and that temperatures are free to vary in response to variations in thermal conductivity and overburden thickness. The second approach assumes that temperatures along the base of the model are uniform, and that heat flux along the base of the model is free to vary in response to the same factors. The third approach subdivides the base of the model into a number of different intra- and extra-caldera areas and allows heat fluxes (and, indirectly, temperatures) to vary between these areas.

C.6.2.1 Specified Heat Flux Lower Boundary Conditions

Sass et al. (1995) reported that deep groundwater flow through the LCA and faults may influence the shallow geothermal regime in the NTS area. Because estimates of heat flow in many boreholes at the NTS may have been influenced by groundwater flow in the LCA, the value of 84 mW/m^2 measured in the LCCU beneath the LCA at well TW-5 (Rock Valley) was considered by Sass et al. (1995) to be

most representative of deep regional heat fluxes in the NTS area. The use of this relatively high value as representative of the deep regional heat flux is supported by data from other non-Pahute-Mesa wells where shallow heat fluxes are similarly high, such as TW-3 (Frenchman Flat) and TW-4 (Indian Springs Valley) (Sass et al., 1987, Table 7).

Based on these considerations, a uniform heat flux value of 85 mW/m^2 was initially applied to the base of the PM/OV heat-conduction model. Subsequent analyses used uniform heat fluxes of 45, 65 and 105 mW/m^2 as lower boundary conditions to investigate the sensitivity of simulated temperatures to the assumed heat fluxes. Additionally, one inverse model allowed heat fluxes at six different intra-caldera and extra-caldera areas to be estimated independently as part of the calibration process.

C.6.2.2 Specified Temperature Lower Boundary Conditions

The elevation of the lower boundary of the PM/OV CAU model domain is 3,500 m below sea level (bsl). Because no boreholes have been drilled deep enough to measure temperatures at this elevation, it is necessary to estimate temperatures at the base of the model by using borehole temperatures measured at shallower depths and extrapolating these temperatures to greater depths using Fourier's Law (q=kdt/dz) and assumptions about deeper thermal conductivity values and heat fluxes. These estimates (Table C.6-1) were made in three different structural zones using bottom-hole temperature data from boreholes UE-20f (121°C), PM-2 (83.8°C) and UE-19gs (61.6°C) (Blankennagel and Weir, 1973, Table 8). The calculations assume conductive vertical heat flow and a regional heat flux of 85 mW/m^2 and rely on structure contour maps for the PBRCM, LCA, and UCCU (BN, 2002), and thermal conductivity estimates for different rock types (summarized in Table C.5-1) to estimate the distribution of thermal conductivity values below the bottoms of these boreholes.

The estimated temperature at the base of the model for the three structural zones is ~172 to 179°C, assuming a range in the temperature gradient for the PBRCM (Table C.6-1). For comparison, the simulated temperatures at the base of the model using a specified heat flux of 85 mW/m^2 range from 107 to 204°C and average ~162°C (see Section C.7.1) (As described below, specification of a heat flux boundary condition generates spatially variable temperatures at the base of the PM/OV model domain.). For different assumed heat fluxes, temperatures along the lower boundary are, of course, also different.

The estimated temperatures at the base of the model are sensitive to the assumed thermal properties between the depth of the temperature measurement and the base of the model. The deep thermal properties, in turn, depend on the type of rocks interpreted to exist at depth, which can differ among alternative HFMs because of limited information at depth. As an example, BN (2002) reported an alternative structural interpretation (Alternative #6) for the eastern part of the PM/OV domain near borehole ER-19-1. Lower model boundary temperatures were estimated for both the base case and the Alternative #6 structural interpretations using a measured temperature of 31.5°C at ER-19-1, a range of thermal properties for the LCCU1, the UCCU and the LCA, and an assumed a regional heat flux of 85 mW/m^2. The average temperature estimated at the base of the model at well ER-19-1 is 112°C for the Alternative #6 structural interpretation and 131°C for the base-case structural interpretation (Table C.6-2). This comparison highlights the sensitivity of estimated bottom boundary temperatures to uncertainties in the HFM in this part of the model domain.

Table C.6-2
Temperature Estimates at the Base of the PM/OV Model (3.5 km Below Sea Level)
Assuming Dominantly Conductive 1D Heat Flow and Background Regional Heat Flux of 85 mW/m²
(Page 1 of 2)

Borehole	Area	Measured or Estimated Temperature[a] (°C)	HSU	Measured or Estimated Gradient Temperature[b] (°C/km)	Estimated Thickness (km)	Estimated Temperature at HSU Base (°C)	Estimated Temperature Increase (°C)	Estimated Elevation at HSU Base (km)	Estimated Heat Flux (Low λ) (mW/m²)	Estimated Heat Flux (Base λ) (mW/m²)	Average Estimated Temperature (mW/m²)	Estimated Temperature Using 3-D FEHM (85 mW/m²)
UE-20f	W. Boxcar Fault-Purse Fault (1)	**121.0**	PBRCM	22.2	0.73	137.2	16.2	-2.61	37.96	47.29		
		121.0	PBRCM	38.6	0.73	149.2	28.2	-2.61	66.01	82.22		
		121.0	PBRCM	58.2	0.73	163.5	42.5	-2.61	99.52	123.97		
UE-20f	W. Boxcar Fault-Purse Fault (1)	137.2	SCICU	32.7	0.89	166.3	29.1	-3.50		85.00	179.1	195.9
		149.2	SCICU	32.7	0.89	178.3	29.1	-3.50		85.00		
		163.5	SCICU	32.7	0.89	192.6	29.1	-3.50		85.00		
PM-2	NW of Handley Fault (6)	**83.8**	PBRCM	**38.6**	0.87	117.4	33.6	-0.82	66.01	82.22		
		83.8	PBRCM	**40.4**	0.87	118.9	35.1	-0.82	69.08	86.05		
		83.8	PBRCM	**41.8**	0.87	120.2	36.4	-0.82	71.48	89.03		
PM-2	NW of Handley Fault (6)	117.4	LCA	17.2	1.20	138.0	20.6	-2.02		85.00		
		118.9	LCA	17.2	1.20	139.6	20.6	-2.02		85.00		
		120.2	LCA	17.2	1.20	140.8	20.6	-2.02		85.00		
PM-2	NW of Handley Fault (6)	138.0	LCCU	21.8	1.48	170.2	32.3	-3.50		85.00	171.7	161.7
		139.6	LCCU	21.8	1.48	171.8	32.3	-3.50		85.00		
		140.8	LCCU	21.8	1.48	173.0	32.3	-3.50		85.00		
UE-19gS	SCStrucZone-W-E Estuary Faults (8)	**61.6**	PBRCM	22.2	1.26	89.7	28.1	-1.50	37.96	47.29		
		61.6	PBRCM	38.6	1.26	110.4	48.8	-1.50	66.01	82.22		
		61.6	PBRCM	58.2	1.26	135.2	73.6	-1.50	99.52	123.97		
UE-19gS	SCStrucZone-W-E Estuary Faults (8)	89.7	SCICU	32.7	2.00	154.9	65.2	-3.50		85.00	177.0	194.7
		110.4	SCICU	32.7	2.00	175.6	65.2	-3.50		85.00		
		135.2	SCICU	32.7	2.00	200.4	65.2	-3.50		85.00		

Table C.6-2
Temperature Estimates at the Base of the PM/OV Model (3.5 km Below Sea Level)
Assuming Dominantly Conductive 1D Heat Flow and Background Regional Heat Flux of 85 mW/m²
(Page 2 of 2)

Borehole	Area	Measured or Estimated Temperature[a] (°C)	HSU	Measured or Estimated Gradient Temperature[b] (°C/km)	Estimated Thickness (km)	Estimated Temperature at HSU Base (°C)	Estimated Temperature Increase (°C)	Estimated Elevation at HSU Base (km)	Estimated Heat Flux (Low λ) (mW/m²)	Estimated Heat Flux (Base λ) (mW/m²)	Average Estimated Temperature (mW/m²)	Estimated Temperature Using 3-D FEHM (85 mW/m²)
ER-19-1	Split Ridge Fault-RM/AT Caldera Topo Margin (14)	**31.5**	LCCU1	**40.5**		**31.5**		0.93	90.32	157.95		
		31.5	LCCU1	21.8		**31.5**		0.93	48.60	85.00		
		31.5	LCCU1	38.1		**31.5**		0.93	85.00	148.65		
ER-19-1	Split Ridge Fault-RW/AT Caldera Topo Margin (14)	**31.5**	UCCU	**18.8**	2.43	77.2	45.6	-1.50	46.44	58.28		
		31.5	UCCU	27.4	2.43	98.1	66.6	-1.50	67.73	85.00		
		31.5	UCCU	34.4	2.43	115.1	83.6	-1.50	85.00	106.68		
ER-19-1	Split Ridge Fault-RM/AT Caldera Topo Margin (14)	77.2	LCA	17.2	2.00	111.5	34.3	-3.50	80.19	85.00	131.1	147.0
		98.1	LCA	17.2	2.00	132.5	34.3	-3.50	80.19	85.00		
		115.1	LCA	17.2	2.00	149.4	34.3	-3.50	80.19	85.00		
ER-19-1[c] Alternative #6	Split Ridge Fault-RM/AT Caldera Topo Margin (14)	**31.5**	LCCU1	**40.5**		**31.5**		0.93	90.32	157.94		
		31.5	LCCU1	21.8		**31.5**		0.93	48.60	85.00		
		31.5	LCCU1	38.1		**31.5**		0.93	85.00	148.65		
ER-19-1[c] Alternative #6	Split Ridge Fault-RM/AT Caldera Topo Margin (14)	**31.5**	UCCU	**18.8**	0.43	39.6	8.0	0.50	46.44	58.28		
		31.5	UCCU	27.4	0.43	43.3	11.7	0.50	67.73	85.00		
		31.5	UCCU	34.4	0.43	46.3	14.7	0.50	85.00	106.68		
ER-19-1[c] Alternative #6	Split Ridge Fault-RM/AT Caldera Topo Margin (14)	39.6	LCA	17.2	4.00	108.3	68.7	-3.50	80.19	85.00	111.7	
		43.3	LCA	17.2	4.00	112.0	68.7	-3.50	80.19	85.00		
		46.3	LCA	17.2	4.00	114.9	68.7	-3.50	80.19	85.00		

[a] Measured temperatures from Attachment A or Blankennagel and Weir (1973).
[b] Estimated gradient temperature taken from range in temperature gradients for HSU reported in Attachment A.
[c] Structural interpretation alternative #6 (BN, 2002, Figure 6-14).

Table C.6-3
Temperature Estimates in ER-19-1 from Base of the PM/OV Model (3.5 km Below Sea Level)
Assuming Dominantly Conductive Heat Flow, Background Regional Heat Flow of 85 mW/m^2 Base Temperature of 147°C, and Two Structural Interpretations

PM/OV Model	HSU	Elevation at HSU Base (m)	Estimated Temperature at HSU Base (°C)	λ (W/m °C)	Estimated Gradient Temperature (°C/km)	Estimated Heat Flow (mW/m^2)	Estimated Thickness (km)	Measured Temperature at HSU Base (°C)
Grid g (base λ)	PBRCM	999	44.5	2.13	39.9	85		
	LCCU1	928	46.1	3.9	21.8	85	0.07	31.5
	UCCU	-1,500	112.7	3.1	27.4	85	2.43	
	LCA	-3,500	147.0	4.95	17.2	85	2.00	
Grid g (low λ)	PBRCM	999	24.3	1.71	49.7	85		
	LCCU1	928	27.0	2.23	38.1	85	0.07	31.5
	UCCU	-1,500	110.6	2.47	34.4	85	2.43	
	LCA	-3,500	147.0	4.67	18.2	85	2.00	
Grid g (best λ)	PBRCM	999	27.6	2.13	39.9	85		
	LCCU1	928	29.1	3.9	21.8	85	0.07	31.5
	UCCU	-1,500	112.7	2.47	34.4	85	2.43	
	LCA	-3,500	147.0	4.95	17.2	85	2.00	
Alt #6 (base λ)	PBRCM	999	65.0	2.13	39.9	85		
	LCCU1	928	66.6	3.9	21.8	85	0.07	31.5
	UCCU	500	78.3	3.1	27.4	85	0.43	
	LCA	-3,500	147.0	4.95	17.2	85	4.00	
Alt #6 (low λ)	PBRCM	999	56.8	1.71	49.7	85		
	LCCU1	928	59.5	2.23	38.1	85	0.07	31.5
	UCCU	500	74.2	2.47	34.4	85	0.43	
	LCA	-3,500	147.0	4.67	18.2	85	4.00	
Alt #6 (high λ)	PBRCM	999	71.0	2.71	31.4	85		
	LCCU1	928	72.1	5.8	14.7	85	0.07	31.5
	UCCU	500	82.0	3.66	23.2	85	0.43	
	LCA	-3,500	147.0	5.23	16.3	85	4.00	

C.6.2.3 Summary of Lower Boundary Conditions

Different boundary conditions were used at the base of the model in the models described in this report, including specified uniform heat fluxes and specified uniform temperatures. Specified uniform heat fluxes used in forward heat-conduction models ranged from 45 to 105 $mW/m^2$and encompassed the average deep heat flux of 85 mW/m^2 estimated for the vicinity of the NTS by Sass et al. (1995). Temperatures at the base of the model were calculated from Fourier's Law using measured bottom-hole temperatures reported in Blankennagel and Weir (1973, Table 8) and thermal properties estimated from the HFM (BN, 2002) and thermal conductivity data summarized in Gillespie (2003). Estimates of the temperature at the base of the PM/OV model (-3,500 m elevation) indicate an average temperature of at least 160°C. Simulation results discussed later in this report show that temperature distributions within the model domain are similar for models that use specified lower boundary temperatures of 160°C or specified lower heat fluxes of 65 mW/m^2. Inverse heat-conduction models were also done that consider variable intra- and extra-caldera heat fluxes. In these inverse models, heat fluxes are optimized by matching match model results with borehole temperature measurements.

C.7.0 MODEL RESULTS

This section describes the results of both forward models of steady-state heat conduction done with various thermal conductivity estimates and lower boundary conditions, and inverse models of heat conduction that optimize either thermal conductivities or deep heat flux at the base of the model. The forward models were used to determine if a uniform heat flux value at the base of the model, combined with the estimated thermal conductivities of the 46 HSUs, would be able to match the temperature observations or if a more complex distribution of heat flux along the lower boundary might be necessary. The inverse models investigated whether (1) grouped thermal conductivities could be optimized for a uniform heat flux to match the temperature data or (2) a simple, spatially variable distribution of heat flux could be found that, combined with the original 46 estimates of thermal conductivities, would provide an adequate match to the temperature data.

C.7.1 Forward Heat Conduction Models

Forward models of heat conduction in the PM/OV model domain were developed to investigate the sensitivity of simulated temperatures to thermal conductivity estimates and boundary conditions. Simulations considered upper, lower, and base-case thermal conductivity estimates (Table C.5-1) and either specified temperature (160°C) or specified heat flux (45, 65, 85 or 105 mW/m^2) conditions at the base of the model. In addition to using the base-case thermal conductivities, the simulations run with a lower boundary temperature of 160°C also considered cases where the thermal conductivities were set at their upper or lower limits. For all models, the upper boundary was determined by interpolating borehole temperatures measured near the water table onto the top nodes in the model (Figure C.6-1). The simulated and measured temperatures are compared on a borehole-by-borehole basis for different model runs in (Attachment A, Figures C1 to C-30). Only summary results and overall conclusions are presented in the paragraphs and figures that follow.

Based on estimates of deep regional heat flux by Sass et al. (1995), the initial forward models assumed a uniform heat flux of 85 mW/m^2. The results from this model are presented to illustrate the

three-dimensional nature of heat transport in the PM/OV model domain. Simulated temperatures at the base of the model (Figure C.7-1) vary from less than 120°C to over 200°C as a consequence of the spatial variability in thermal conductivity associated with the distribution of HSUs in the model. Generally, temperatures at the base of the model are highest beneath the calderas and lowest in areas adjacent to the calderas. Beneath the Timber Mountain caldera complex and the Black Mountain caldera, the high temperatures simulated at the base of the model may be related to the great thickness of low-thermal conductivity rocks such as the intra-caldera intrusive confining units (BN, 2002, Figure 4-43) and the absence of high thermal conductivity HSUs like the LCA and LCCU (BN, 2002, Figures 4-49 and 4-51). Beneath the SCCC, the high temperatures at the base of the model are attributed to the absence of the LCA and LCCU, and the great thickness of low thermal conductivity tuffs that fill the caldera (e.g., BN, 2002, Figures 4-31 and 4-37).

A series of maps of simulated temperatures at different elevations indicates that temperatures differences between the intra- and extra-caldera areas become less with increasing elevation (Figure C.7-2). The muted differences between intra- and extra-caldera temperatures at higher elevations are a consequence of the increasing influence of the specified upper boundary temperatures (Figure C.6-1) and the lateral as well as vertical flow of heat. Evidence for the lateral flow of heat is provided by cross-sections of simulated temperatures profiles taken along east-west (Figure C.7-3) and north-south transects (Figure C.7-4). Heat flows from areas of higher to lower temperature in a direction perpendicular to the temperature contours (isotherms), so the isotherms in these cross-sections indicate that some heat will move away from the caldera areas into the surrounding rock. An interesting consequence of this conclusion is that vertical heat flux will decrease with elevation within the calderas and increase with elevation in the adjacent extra-caldera areas, even in the absence of groundwater flow.

The temperatures simulated with a specified heat flux of 85 mW/m^2 are compared to the measured temperatures in Figure C.7-5. The scatterplot shown in Figure C.7-5 compares individual pairs of measured and calculated temperatures, coded with different symbols according to borehole. The figure indicates that although some of the simulated and measured temperatures fall on or near the "one-to-one" line (most notably temperatures for wells ER-EC-6, U-19i, and PM-1), most of the simulated temperatures are too warm relative to the measured temperatures. This suggests that, in general, a uniform specified heat flux of 85 mW/m^2 is too high compared with the actual heat flux.

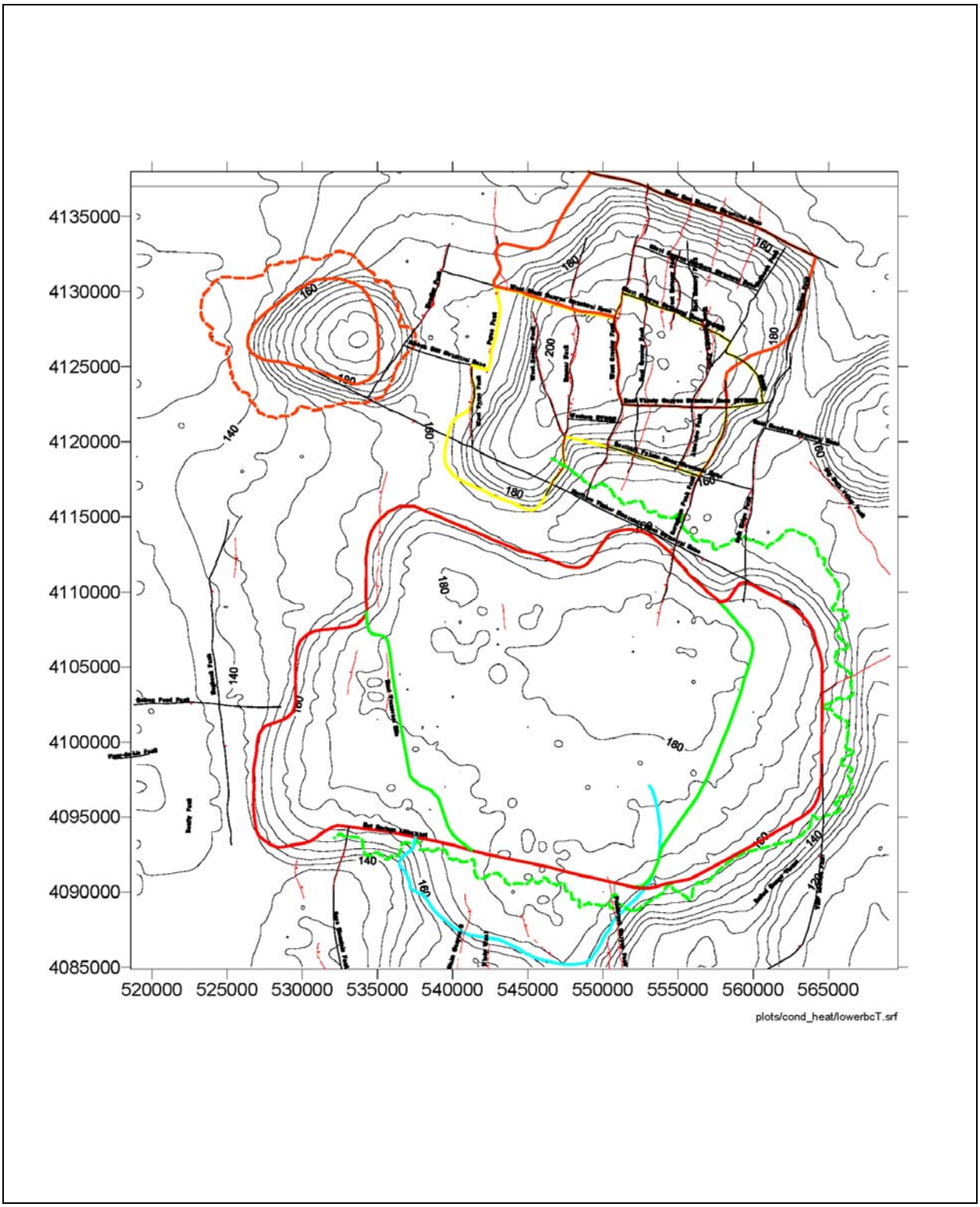

Figure C.7-1
Simulated Temperature (°C) at the Lower Boundary for a Uniform Heat Flux of 85 mW/m²

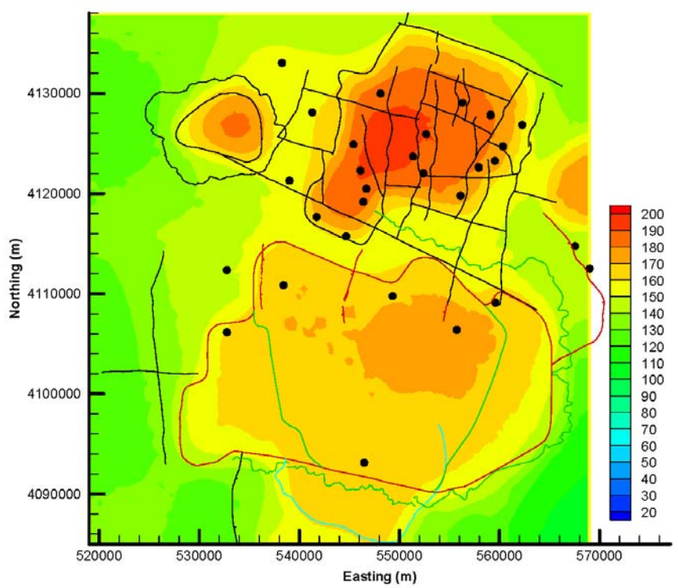

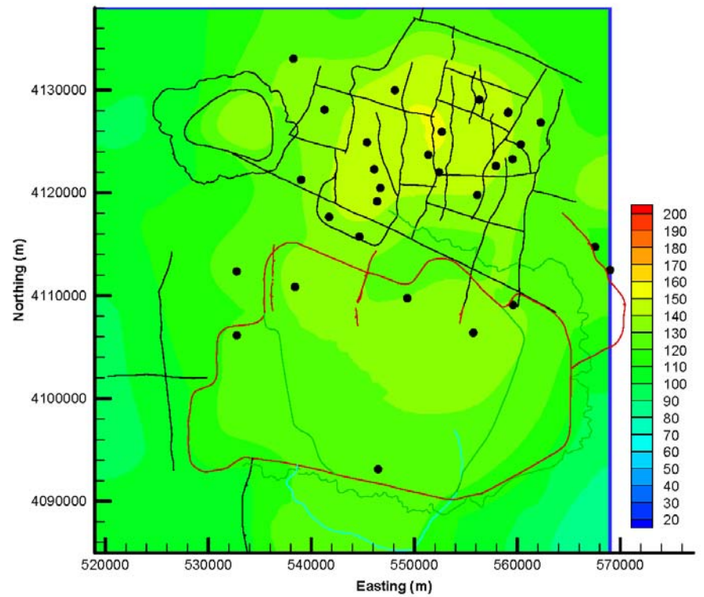

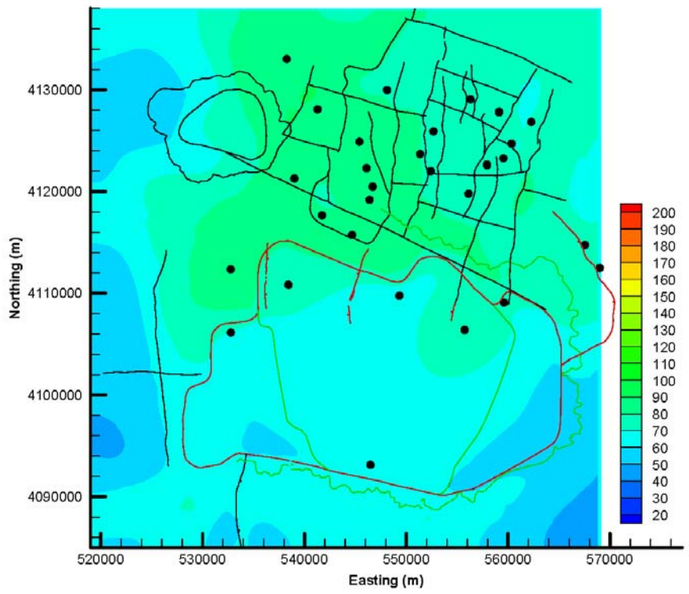

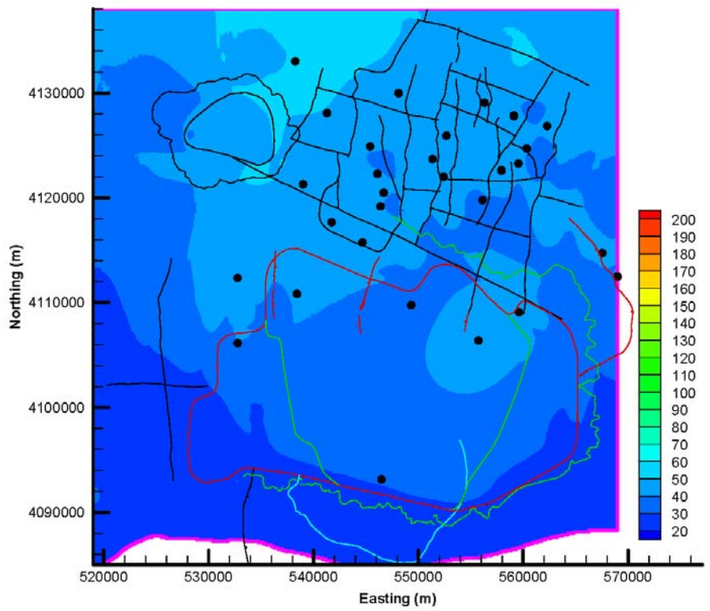

Figure C.7-2
Simulated Temperatures (°C) for a Specified Lower Heat Flux of 85 mW/m^2 at Four Elevations (a) z = -3,200 m, (b) z = -2,000, (c) z = 0 m, and (d) z = 1,000 m

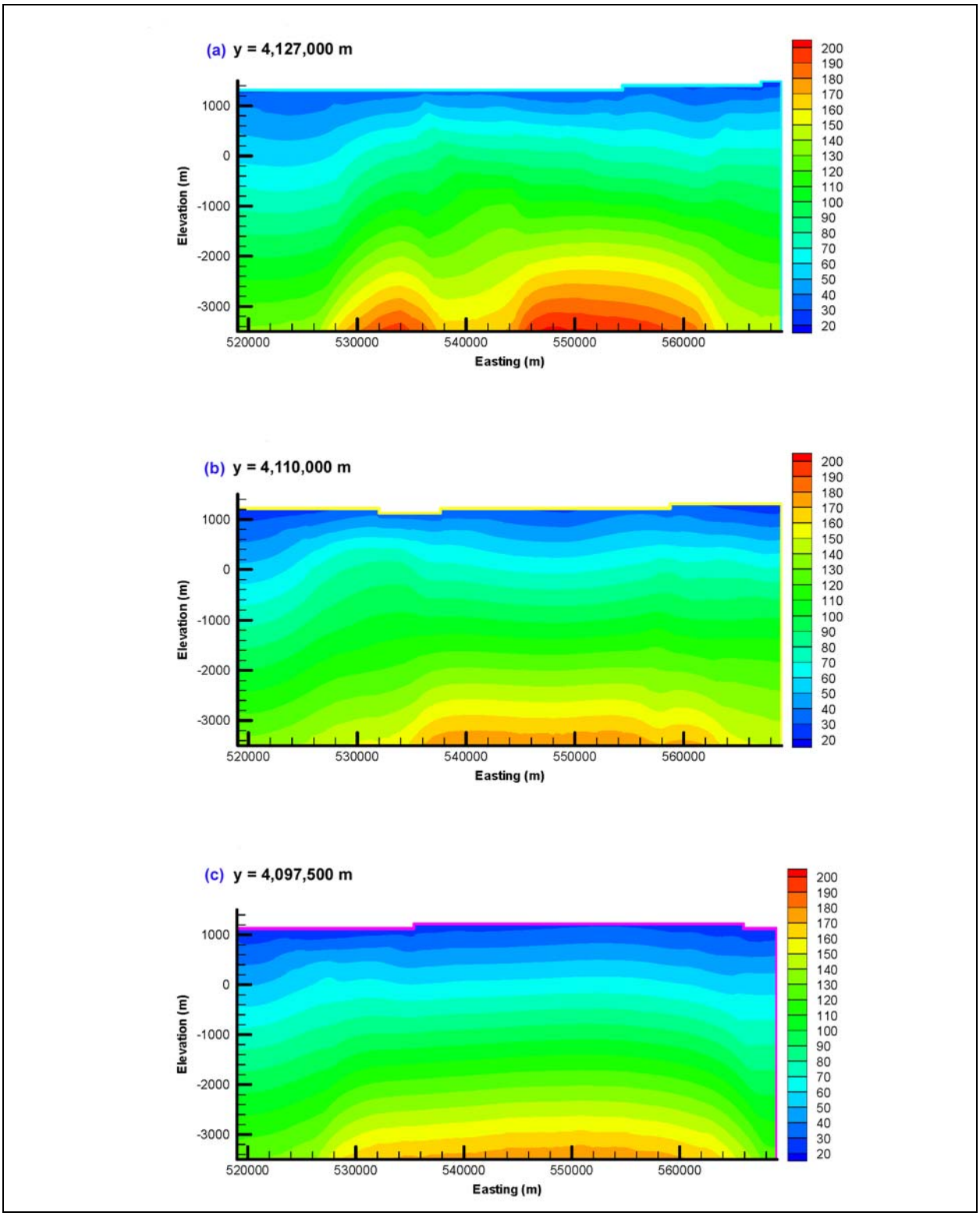

Figure C.7-3
East-West Transects for Uniform 85 mW/m² Lower Boundary Flux Simulation at (a) y = 4,127,000 m, (b) y = 4,110,000 m, and (c) y = 4,097,500 m, Corresponding Approximately to Transects C-C', E-E', and B-B' (BN, 2002)

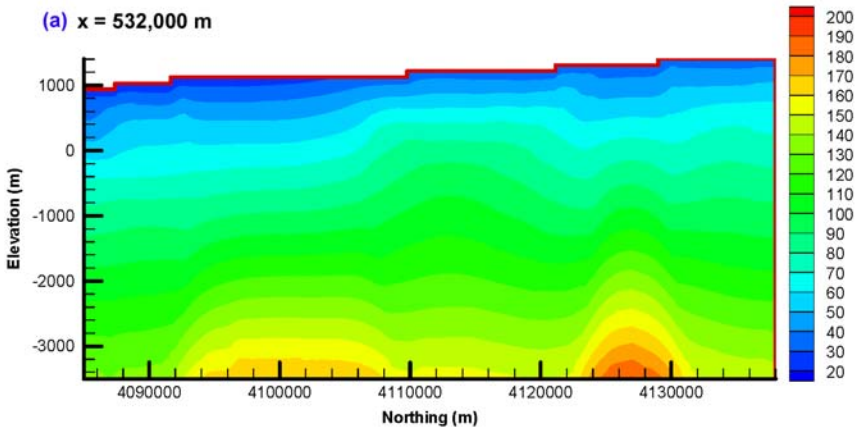

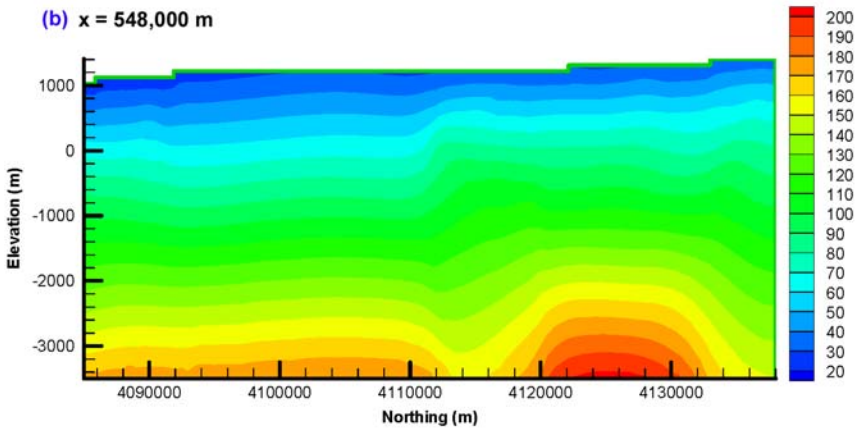

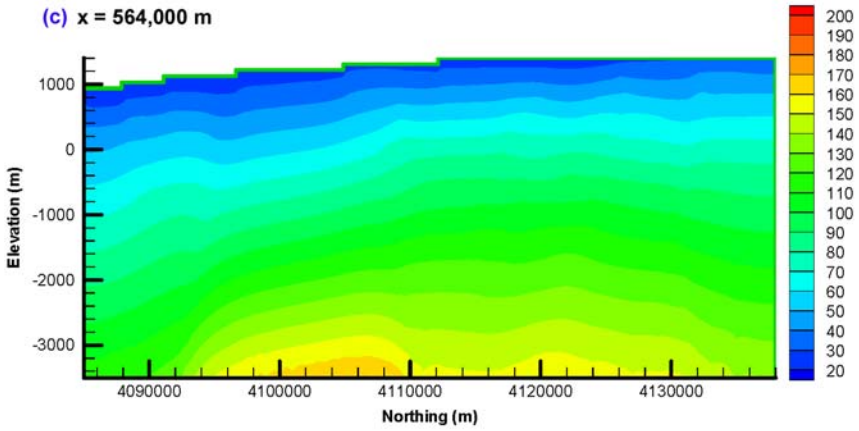

Figure C.7-4
North-South Transects for Uniform 85 mW/m² Lower Boundary Flux Simulation at (a) x = 532,000 m, (b) x = 548,000 m, and (c) x = 564,000 m, Corresponding Approximately to Transects G-G', H-H', and I-I' (BN, 2002)

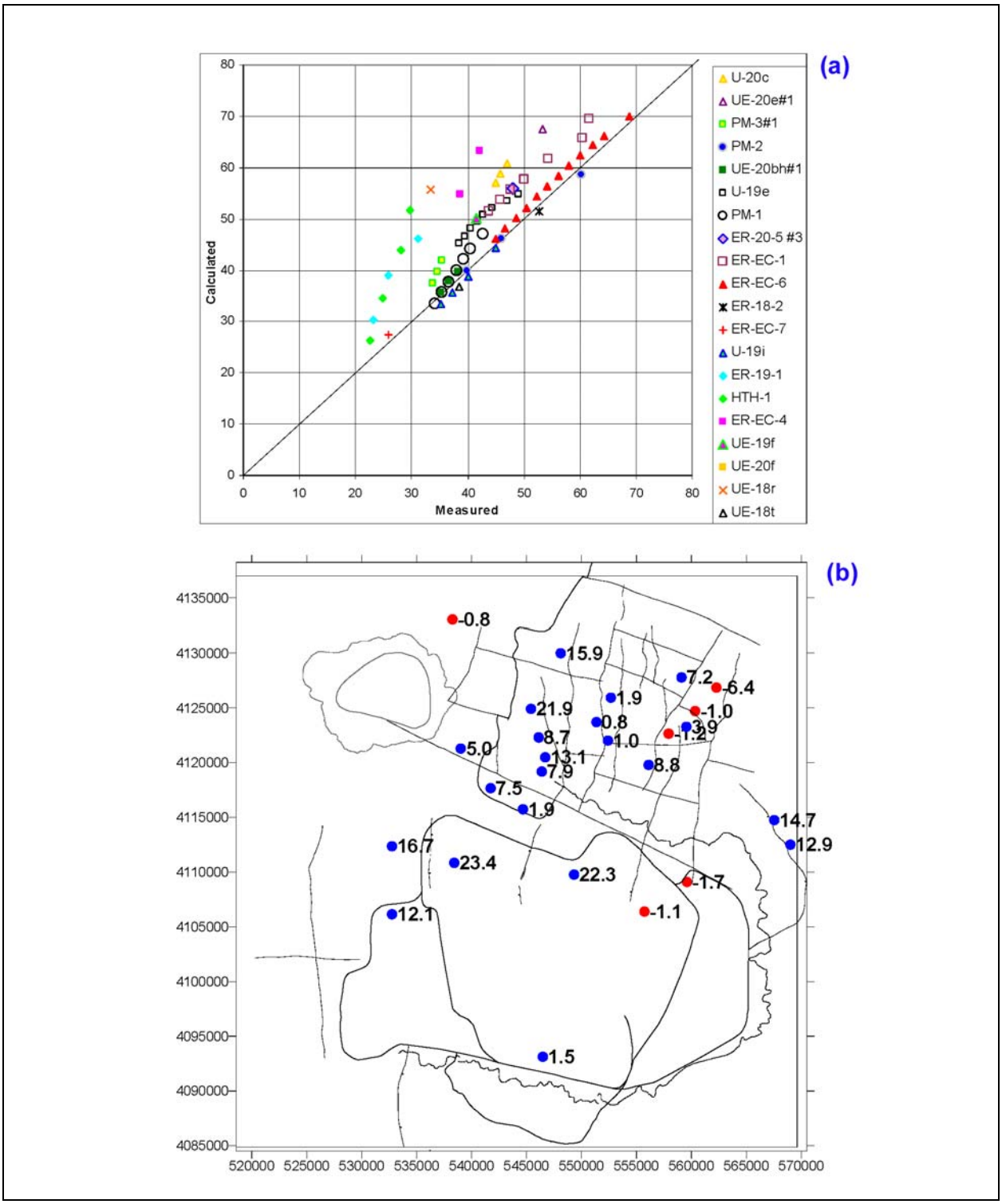

Figure C.7-5
Results from Forward Model with a Uniform Lower Heat Flux of 85 mW/m² and Base-Case Thermal Conductivities for all 46 HSUs Listed in Table C.5-1
(a) Simulated Versus Measured Temperatures and (b) Map of Average Residual Temperatures. Objective Function ϕ = 1308

The map shown in Figure C.7-5 displays the distribution of "average temperature residuals" for each borehole with reliable temperature measurements in the PM/OV flow domain. (The measurements are from depth intervals with linear temperature gradients highlighted in Attachment A, Table A2, and are identified by crosses in Attachment A, Figures C1 to C30). The average temperature residual is calculated as the average difference between all pairs of simulated and measured temperatures in a borehole. The root-mean square errors (RMSE) at individual boreholes were also computed and found to be similar to the average temperature residuals. However, average temperature residuals, rather than more standard measures of fit such as RMSE values, are shown to indicate where the simulated temperatures are generally higher (positive residuals) or lower (negative residuals) than the measured temperatures. The distribution of average borehole residuals supports the interpretation that the actual heat flux is lower than the specified heat flux of 85 mW/m^2 value at most locations throughout the model domain (Figure C.7-5 (b)).

Similar plots summarize the results from simulations that consider specified lower heat fluxes of 65 and 45 mW/m^2 (Figures C.7-6 and C.7-7) and a specified uniform lower boundary temperature of 160°C (Figure C.7-8). The temperatures simulated with a uniform lower heat flux of 65 mW/m^2 provide the best overall match to the measured temperatures, as indicated by the symmetry of the simulated and measured temperatures around the one-to-one line and the relatively low value of the objective function (a measure of the degree of mismatch between the simulated and measured temperatures), which is defined in the following section. The objective function drops from 1,308 to 339 when the heat flux at the base of the model decreases from 85 to 65 mW/m^2, indicating much better overall agreement between the calculated and measured temperatures at the smaller heat flux. However, the simulated temperatures at some boreholes (for example, ER-19-1, HTH-1, UE-18r, and ER-EC-4) remain much warmer than the measured temperatures at a heat flux of 65 mW/m^2, whereas the satisfactory match obtained at other boreholes for a heat flux of 85 mW/m^2 begins to deteriorate. Reducing the heat flux at the base of the model further to 45 mW/m^2 increases the objective function to 1,186 and results in an under-estimation of measured temperatures at most boreholes in the PM/OV model domain (Figure C.7-7). However, even for a heat flux of 45 mW/m^2, the heat conduction model overestimates the measured temperatures at boreholes ER-19-1, HTH-1, UE-18r and ER-EC-4, suggesting that either additional modifications must be made to the model parameters or boundary conditions, or that processes other than heat conduction are affecting the measured temperatures at these boreholes.

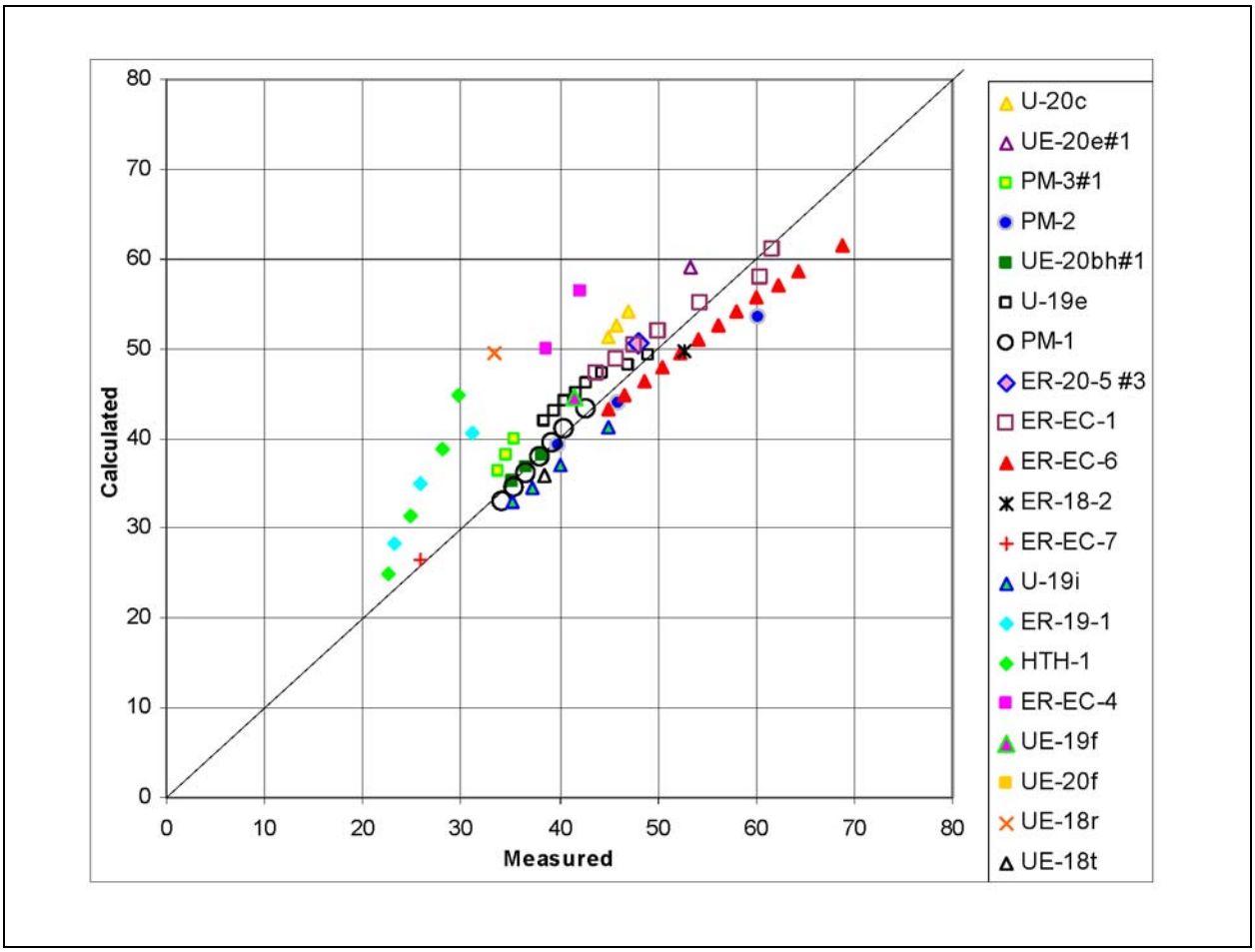

Figure C.7-6
Simulated Versus Measured Temperatures for Uniform Lower Heat Flux of 65 mW/m² and Base-Case Thermal Conductivities for all 46 HSUs Listed in Table C.5-1
Objective Function ϕ = 339

C.7.2 Inverse Modeling To Optimize Grouped Thermal Conductivities and Deep Heat Fluxes

C.7.2.1 Inverse Modeling Background Summary

Inverse modeling is used to estimate optimal values for uncertain model parameters that minimize the difference between simulated and observed system characteristics. In this study, the observations are temperatures measured in deep boreholes. The model parameters to be optimized are thermal conductivities for HSUs and specified heat fluxes at the base of the model. The objective function, ϕ, that the inversion seeks to minimize is the sum of the weighted square weighted residuals defined as

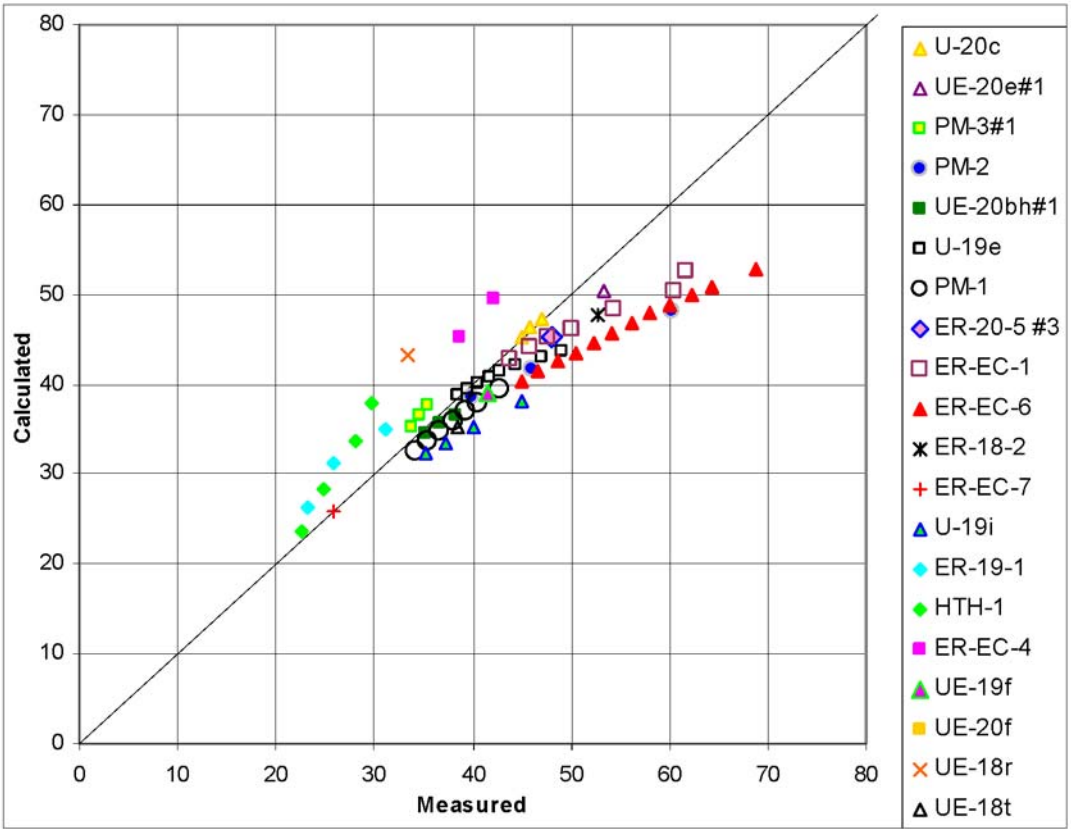

Figure C.7-7
Simulated Versus Measured Temperatures for Uniform Lower Heat Flux of 45 mW/m² and Base-Case Thermal Conductivities for all 46 HSUs Listed in Table C.5-1
Objective Function ϕ = 1,186

$$\phi = \sum_{i=1}^{m} (w_i r_i)^2 \qquad \text{(C.7-1)}$$

where: m is the number of observations,
w is the weight assigned to each observation, and
r is the residual between simulated and observed temperatures for each observation.

Temperature observations from multiple boreholes distributed throughout the domain are used in the calibration. The number of observations used per borehole varies between 1 and 12, depending on grid resolution at the location of the borehole and quality of data. In this study, the weights for each

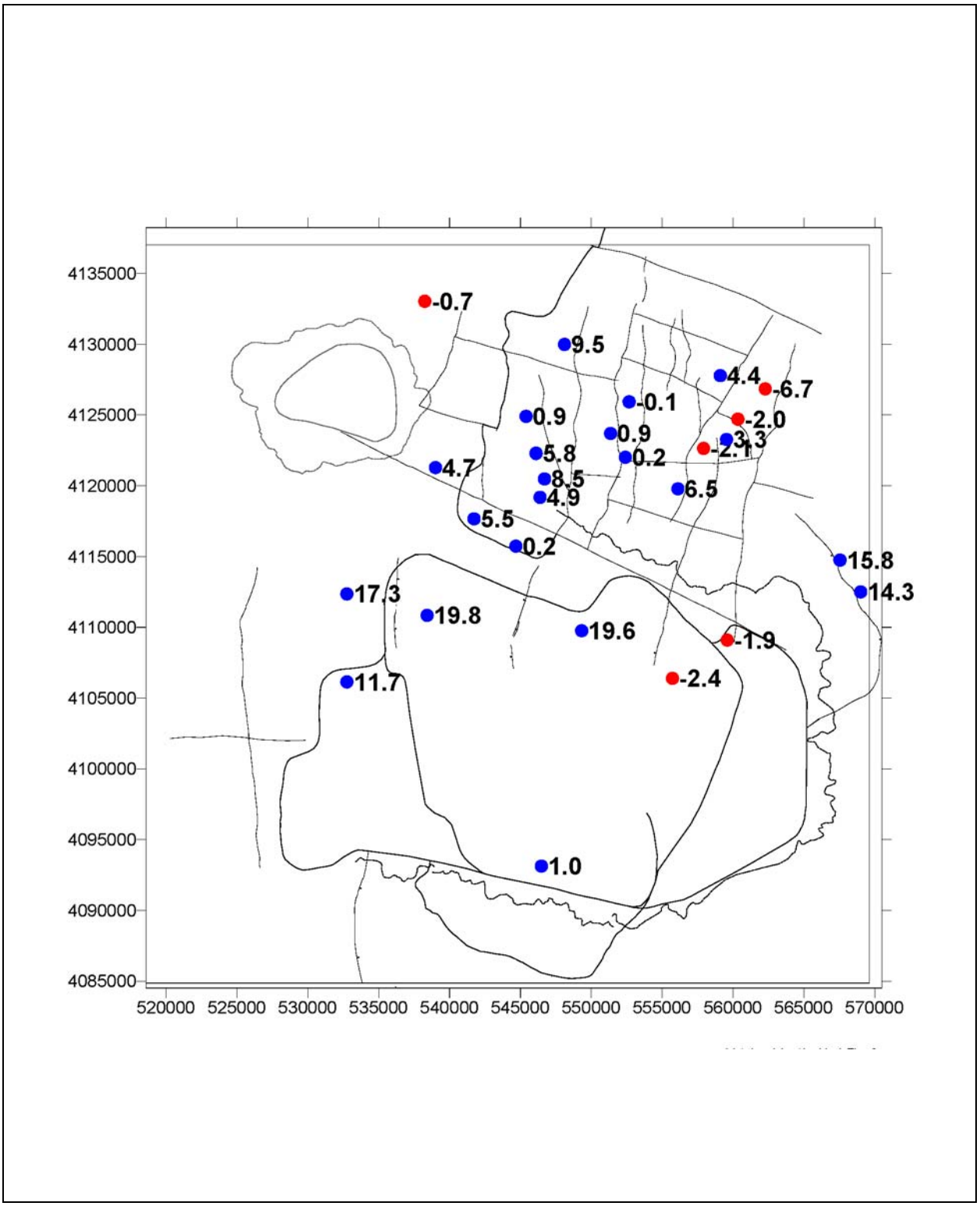

Figure C.7-8
Average Residual Temperature (°C) in Deep Saturated Boreholes
Simulations Use Specified Uniform Temperature at Lower Boundary of 160°C

observations (w_i) are assigned such that they add up to 1 for each borehole. This has the effect of weighting each borehole equivalently in the calibration, thereby emphasizing the importance of the geographic coverage in the data.

Parameter optimization is accomplished by coupling the PEST parameter estimation software (Doherty, 2000) with the FEHM heat conduction model for the PM/OV flow domain. The Gauss-Marquaardt-Levenberg algorithm used by PEST is described in detail in Chapter 2 of the PEST manual. Summarizing the process, PEST takes control of FEHM and conducts the necessary simulations to estimate derivatives of model-generated observations with respect to uncertain model parameters. The matrix containing these derivatives, known as the Jacobian matrix, is then used to estimate an improved parameter set that will reduce the objective function defined above. By comparing parameter changes and the reduction in the objective function achieved in an iteration with those achieved in the previous iteration, PEST determines whether to take another optimization iteration.

C.7.2.2 Inverse Models for the PM/OV Flow Domain

The analysis of model errors associated with the forward heat conduction models indicates that no single value of specified heat flux or temperature can be found that will allow the models which use the base case estimates of thermal conductivities to match all of the temperature data. This conclusion suggests that either the actual thermal conductivities are different than their initial estimates, or that boundary conditions are more complex than initially assumed. Initial attempts to optimize both thermal conductivities and boundary conditions with PEST indicated that the estimates of thermal conductivity and heat flux are strongly correlated and cannot be estimated simultaneously with confidence. Therefore, it is necessary to specify one when the other is being estimated. The two inverse models described in the remainder of this report (1) optimize thermal conductivities for nine groups of HSUs, assuming a specified uniform heat flux of 65 mW/m^2 at the base of the model (a value suggested by the forward model runs as the optimal uniform heat flux), and (2) optimize specified heat fluxes along the lower boundary in six independent intra- and extra-caldera areas of the model, using the initial estimates of thermal conductivity for each of the 46 HSUs (Table C.5-1).

C.7.2.2.1 Calibrating Thermal Conductivities of Volcanic HSUs with a Specified Heat Flux of 65 mW/m²

The first inverse model was calibrated under the assumption that a heat flux of 65 mW/m² at the base of the heat-conduction model adequately characterizes the deep heat flux within the PM/OV flow domain and that model errors, as represented by the temperature residuals, are entirely the result of uncertainty in the original thermal conductivity estimates (Table C.5-1). The goal of this inverse model is to find a set of thermal conductivity values that allows the model to match the temperature data for this uniform heat flux. In this inverse model, the thermal conductivities of the 46 HSUs were first grouped into 9 classes in order to minimize the number of thermal conductivity parameters that need to be estimated through inverse modeling. The nine groups (Table C.7-1) were defined based the similarity of thermal conductivity estimates in the original 46 HSUs (Table C.5-1). However, note that because HSUs were initially defined based on their hydraulic properties, whereas thermal conductivity is affected by somewhat unrelated lithologic and mineralogic characteristics, there is not always an exact correspondence between an HSUs classification as an aquifer, confining unit or composite unit and its assignment to a specific thermal conductivity group (Table C.7-1). As an example, volcanic HSUs were first sorted according to whether they represented intra-caldera (Group 6) or extra-caldera (Groups 7 and 8) rocks. Then, based on borehole stratigraphic logs, extra-caldera HSUs with a large percentage of high thermal conductivity lava were sorted into Group 7, whereas extra-caldera HSUs that contained only a small percentage of lava were sorted into Group 8.

Table C.7-1
Optimal Thermal Conductivity Estimates and Fixed Thermal Conductivities Used with a Heat Flux of 65 mW/m²

Class[a]	Type	Lambda (W/m•°K)
1	Fixed	3.9
2	Fixed	4.95
3	Fixed	3.1
4	Fixed	2.6
5	Fixed	2.1
6	Calibrated	2.0
7	Calibrated	2.1
8	Calibrated	4.7
9	Fixed	1.2

[a]For HSUs in class, refer to Table C.5-1.

An initial attempt to optimize the thermal conductivities of all 9 classes using a fixed value for heat flux of 65 mW/m^2 at the base of the model indicated that the calibration is most sensitive to the thermal conductivities of the volcanic units and that the measured temperatures provide little information about the thermal conductivities of the non-volcanic units. This result is understandable given that most of the observed temperatures used in the calibration were measured in the volcanic units. Therefore, the calibration strategy was modified so that only the thermal conductivities of Classes 6, 7, and 8 were allowed to vary during optimization. Thermal conductivities of the remaining classes were fixed at their base-case values.

The temperatures simulated with the calibrated model are compared to the measured temperatures in Figure C.7-9. The calibrated model has a better overall fit to the data compared to the forward model that used the base-case thermal conductivity estimates for the 46 HSUs and the same specified heat flux (compare Figures C.7-6 and C.7-9). The improved fit is indicated by the decrease in the objective function from 339 to 256 and the greater symmetry of the simulated and measured temperatures around the one-to-one line using the calibrated model. However, several other factors indicate that the calibrated model is unsatisfactory, despite its overall reduction in the objective function and the improved symmetry of its residuals. First, temperature data from some boreholes that had previously been well matched by the forward model (for example, data from boreholes PM-2, ER-EC-1 and ER-EC-6) are now farther from the one-to-one line, complicating the interpretation of data from locations that formerly were interpreted to be consistent with pure heat conduction. At the same time, only slight improvements in the match between simulated and measured temperatures were made for boreholes that lie furthest from the one-to-one line (HTH-1 and ER-19-1) which are more likely to be genuinely affected by non-conductive heat transport processes. Second, although the thermal conductivity values estimated for Classes 6 and 7 are reasonable (Table C.7-1), the thermal conductivity of 4.7 W/m•°K estimated for HSU Class 8 is approximately twice the value expected on the basis of its constituent rock types, calling into question the physical realism of the model. In conclusion, although the calibration procedure successfully reduced the objective function, it did so with non-plausible parameters, raising doubts about the overall reliability of these calibration results. Based on these results and those of the forward models that indicated different heat fluxes matched data from some areas better than others, the use of a single specified value of heat flux in model calibration was abandoned in order to pursue the approach described in the following section.

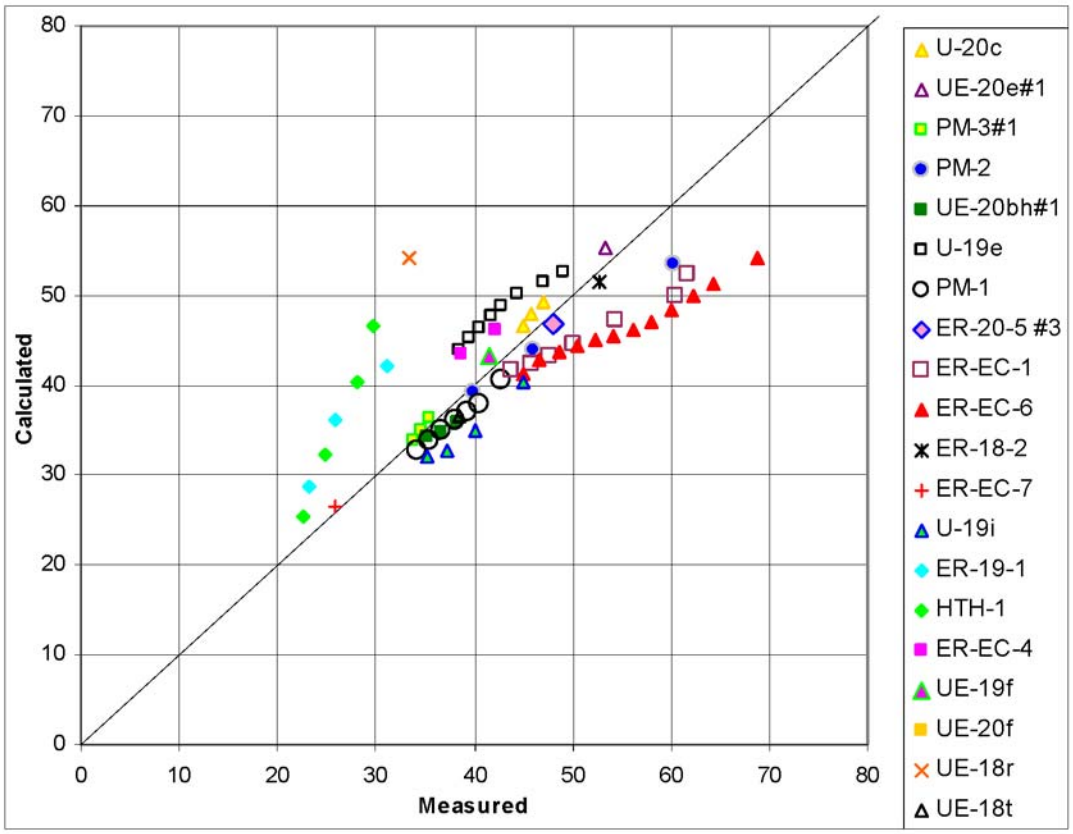

Figure C.7-9
Simulated Versus Measured Temperatures for Specified Lower Heat Flux of 65 mW/m² and Calibrated Thermal Conductivities for Volcanic HSU Groupings 6, 7, and 8 Listed in Table C.7-1
Objective Function $\phi = 256$

C.7.2.2.2 Calibrating Heat Fluxes at the Base of the Model Domain

Studies of geothermal systems in the western United States have concluded that deep heat flux can change dramatically over short distances due to anomalies in the upper crust (Barroll, 1989; Jiracek et al., 1996). In recognition that similar variability may exist in the PM/OV model domain, a second set of inverse models was created with PEST to estimate the heat-flux for different areas that were defined at the base of the model. These inverse models used the base-case thermal conductivities estimated for each of the 46 HSUs (Table C.5-1) and held these values fixed during the calibration.

The number of zones used to distribute heat flux at the base of the model was limited to seven because excessive refinement would lead to an unconstrained fit to the data (similar to the situation where too many degrees of freedom in a polynomial fit renders the physical significance of the fit meaningless). These zones were defined based on the hydrogeology of the system and a spatial analysis of temperature residuals from the forward models that indicates certain areas are regions of higher- or lower-than-average heat flux. The intra-caldera areas were divided into four zones, one each for the Black Mountain caldera and SCCC, and two for the Timber Mountain caldera complex. The definition of two separate zones for the Timber Mountain caldera complex was motivated by the sharp contrast in temperature profiles between the seven wells in the western two-thirds of the complex and the three wells in the eastern third. The distribution of HSUs in the stratigraphic framework model (BN, 2002) does not indicate any differences in the distribution of HSUs that can explain these differences, except that beds in the western and eastern parts of the Timber Mountain caldera complex dip in opposite directions. The extra-caldera area was divided into three zones: one east of the Timber Mountain caldera complex and SCCC, one north of the Black Mountain caldera, and a third containing all other extra-caldera areas.

The final calibrated heat fluxes for each of the seven zones at the base of the model are shown in Figure C.7-10. The estimated heat flux of 100 mW/m^2 in the eastern third of the Timber Mountain caldera complex is the highest of any zone in the model. (Note that the initial model results indicated the model is insensitive to the value of heat flux at the base of the Black Mountain caldera because of the lack of temperature data from that caldera, so the heat flux in this zone was subsequently tied to the estimate for the eastern third of the Timber Mountain caldera complex.). The estimated heat flux in the western two-thirds of the Timber Mountain caldera complex is approximately half (49 mW/m^2) the heat flux estimated for the eastern third. The SCCC has a relatively high estimated heat flux of 73 mW/m^2. Of the extra-caldera areas, the northwest zone also has a relatively high estimated heat flux (90 mW/m^2) that is exceeded only by the heat flux in eastern Timber Mountain. Other extra-caldera areas have estimated heat fluxes of 45 mW/m^2, a value that defines the lower limit of the range of possible heat fluxes to be searched by PEST for the optimal heat flux. This lower limit was imposed on the PEST calibration based on the results of the forward models.

The temperatures simulated with this model are compared to the measured temperatures in Figure C.7-11. The distribution of simulated and measured temperatures around the one-to-one line

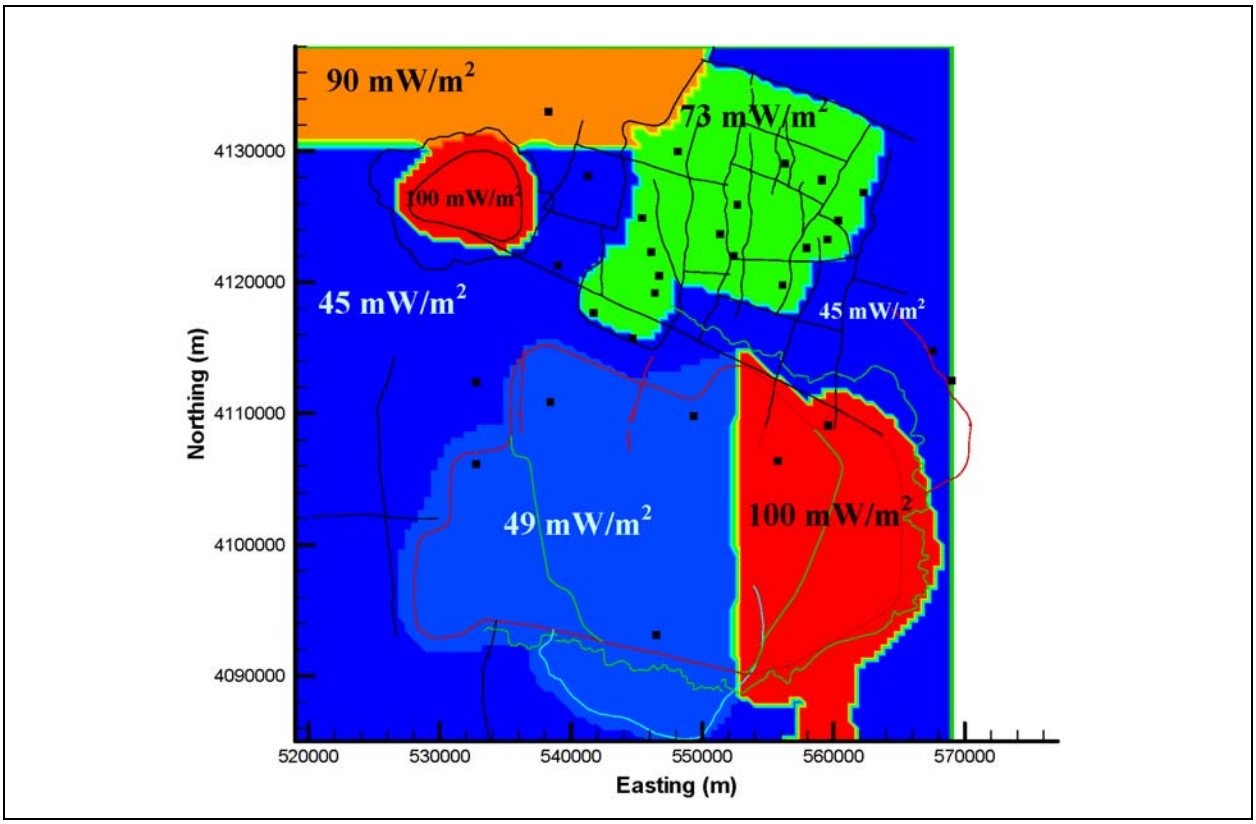

Figure C.7-10
Calibrated Heat Fluxes at Base of Model

is similar to that found for the inverse model with optimized thermal conductivities for the grouped HSU classes (Figure C.7-9). Likewise, the value of the objective function for this model ($\phi = 262$) is similar to that associated with the previous inverse model ($\phi = 256$). In spite of the general similarity between the results of the two inverse models, the model with variable heat flux at the base of the model is considered as the preferred model in this study because it does not obviously conflict with known data, whereas the previous inverse model required implausible thermal conductivity values for certain HSU groups to match the data.

The distribution of temperatures simulated with this inverse model is shown in map view in Figure C.7-12 and along east-west and north-south transects in Figures C.7-13 and C.7-14. The simulated temperature distribution displays many of the same characteristics that have been noted previously in connection with temperature distributions simulated with a uniform heat flux of 85 mW/m^2 (Figures C.7-2 to C.7-4). However, significant differences between results from these two simulations exist in the western part of the Timber Mountain caldera complex, where the

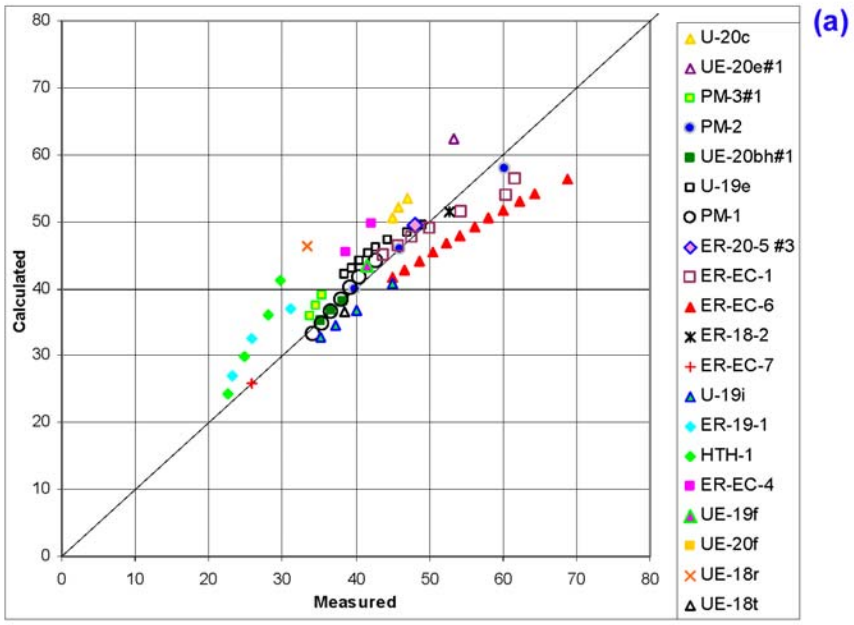

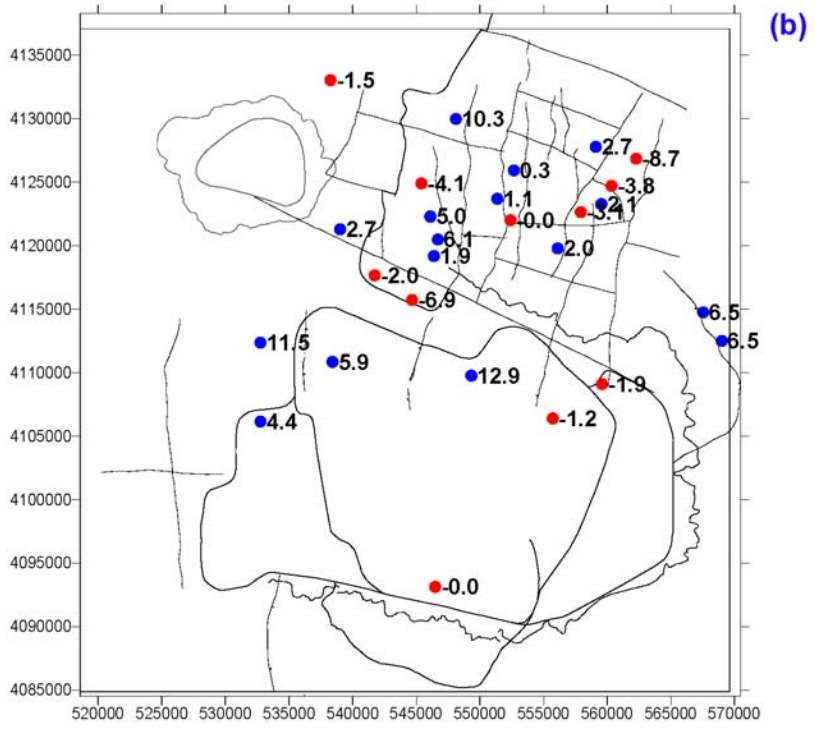

Figure C.7-11
Results from Inverse Model with Calibrated Heat Fluxes in Multiple Zones and Thermal Conductivities Assigned for all 46 HSUs Listed in Table C.5-1
(a) Simulated Versus Measured Temperatures and (b) Map of Average Residual Temperatures. Objective Function ϕ = 262

temperatures simulated with the inverse model are much lower because of the smaller heat flux value estimated with the inverse model in this area (Figures C.7-2 and C.7-12).

C.7.2.3 Evaluation of Deep Subregional Heat Flux Estimates

The deep heat fluxes of 45 to 100 mW/m^2 estimated with the inverse model described in Section C.7.2 were compared with heat flux estimates calculated directly from measured borehole temperature profiles and base case thermal conductivity values (Table C.5-1) to evaluate if the model estimates (Figure C.7-10) are reasonable. The heat fluxes estimated from borehole temperature profiles include data from the deep unsaturated zone, where the intra-borehole flow of groundwater is not a factor (Attachment A, Tables A1 and A2). Based on estimates of heat flux derived directly from the measured temperature profiles (Table C.7-2), the estimates of deep heat flux estimated with the inverse model generally seem reasonable. Each of the 6 distinct subregions defined at the base of the model are discussed briefly below.

C.7.2.3.1 Subregion (1), North of Black Mountain

Based on the heat fluxes of 54.8 and 57.3 mW/m^2 estimated directly from temperature logs at high elevations in borehole PM-2 (Table C.7-2), the model calibrated value of 90 mW/m^2 appears to be an overestimate of the deep heat flux in subregion (1). However, the simulated and measured temperatures at borehole PM-2 are in good agreement (Figure C.7-11 and Attachment A, Figure C11), indicating that the high heat flux of 90 mW/m^2 estimated for the base of the model in this area may have decreased with elevation because of the lateral spreading of heat from this subregion (Figure C.7-12).

C.7.2.3.2 Subregion (2), Silent Canyon Caldera Complex

Heat fluxes calculated directly from relatively linear parts of borehole temperature logs in subregion (2) are highly variable, ranging from about 22 to 162 mW/m^2 (Table C.7-2). However, within the individual structural zones of subregion (2) defined in Figure C.4-2, the variability of the heat flux estimates is generally smaller that the overall variability. For instance, heat flux estimates in structural Zones 1 and 7 are generally between 40-50 and 30-60 mW/m^2, respectively, whereas heat flux estimates in structural Zone 4 range between about 80 and 130 mW/m^2 (Table C.7-2). Given the variability of heat flux estimates within and between structural zones, and the difficulty of applying

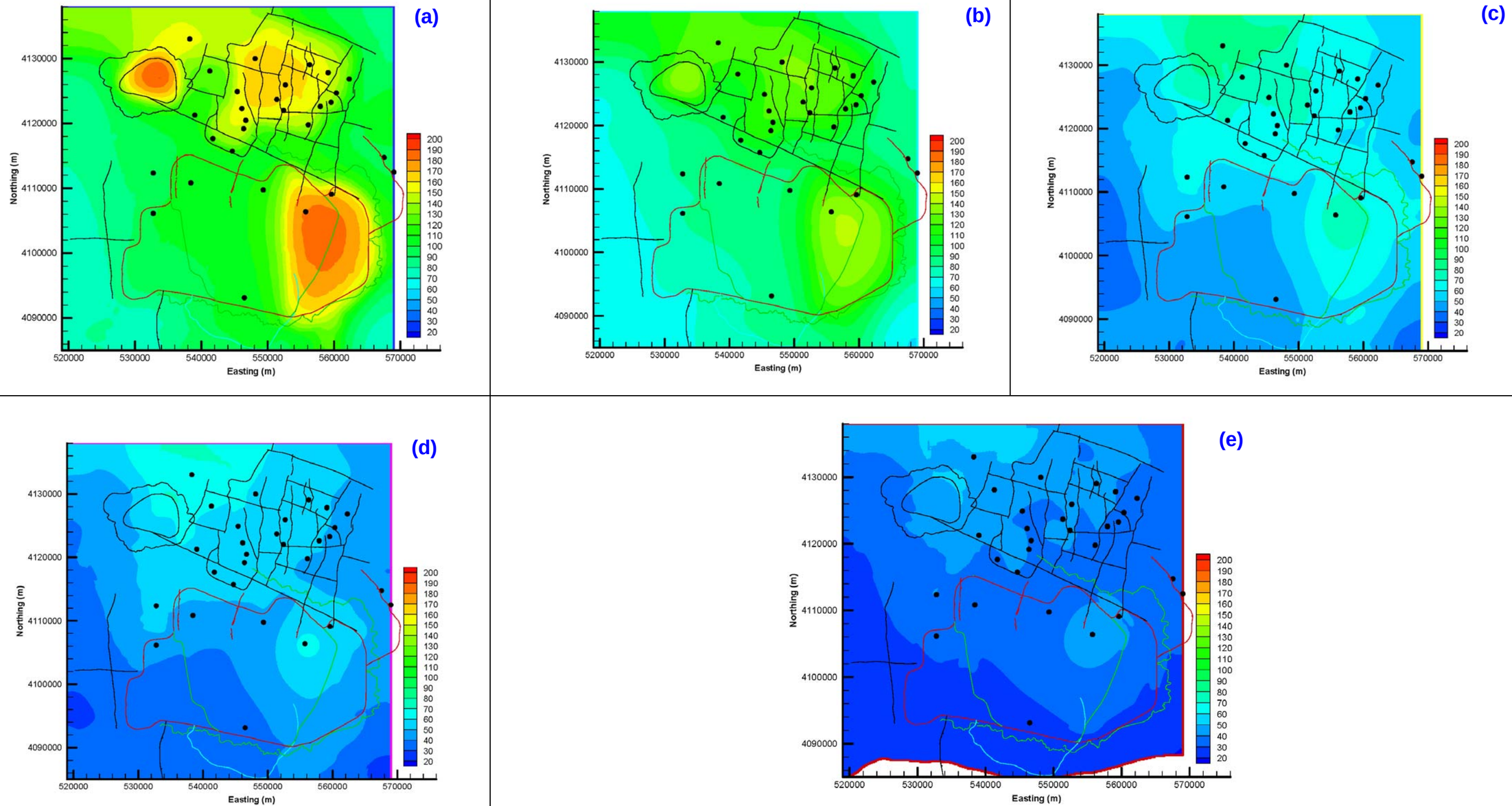

Figure C.7-12
Simulated Temperatures (°C) at 5 Elevations for Calibrated Thermal Fluxes in 6 Zones on Lower Boundary: (a) -3,200 m, (b) -2,000 m, (c) 0 m, (d) 500 m, and (e) 1,000 m

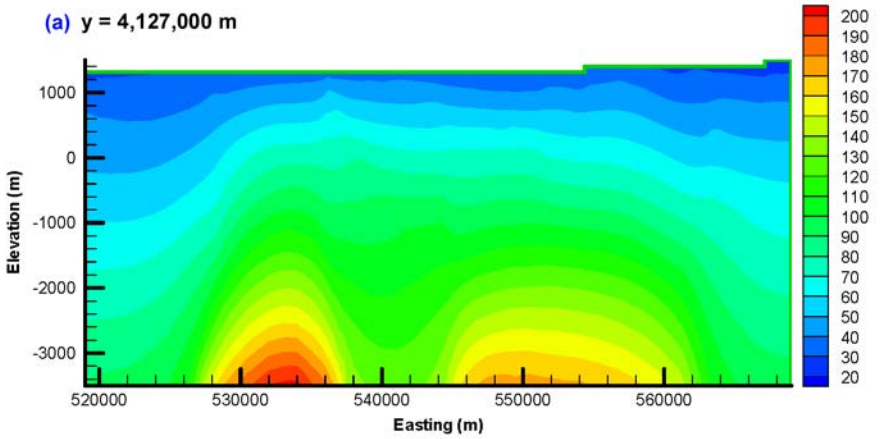

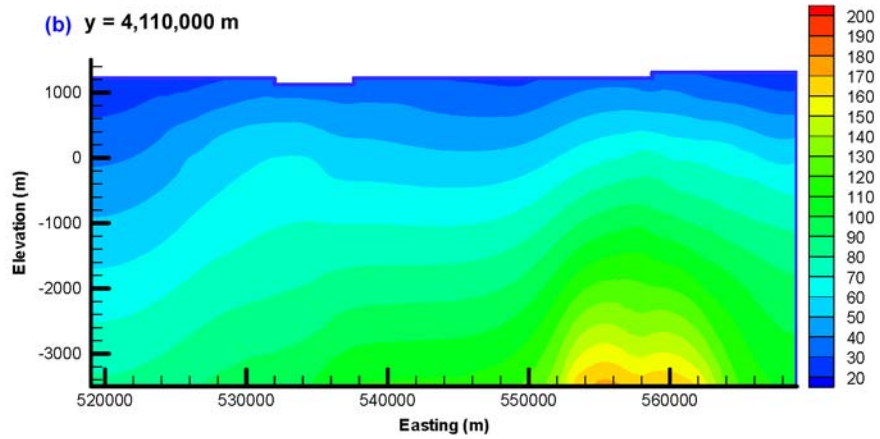

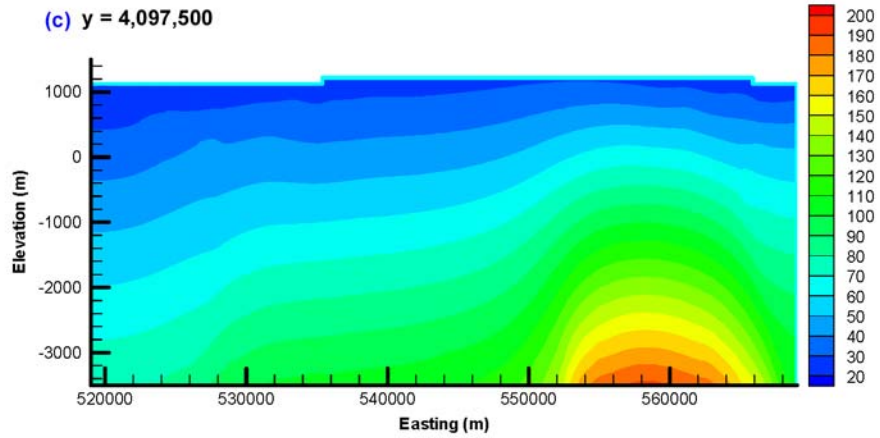

Figure C.7-13
East-West Transects for Calibrated Six-Zone Heat-Flux Model at (a) y = 4,127,000 m, (b) y = 4,110,000 m, and (c) y = 4,097,500 m, Corresponding Approximately to Transects C-C', E-E', and B-B' (BN, 2002)

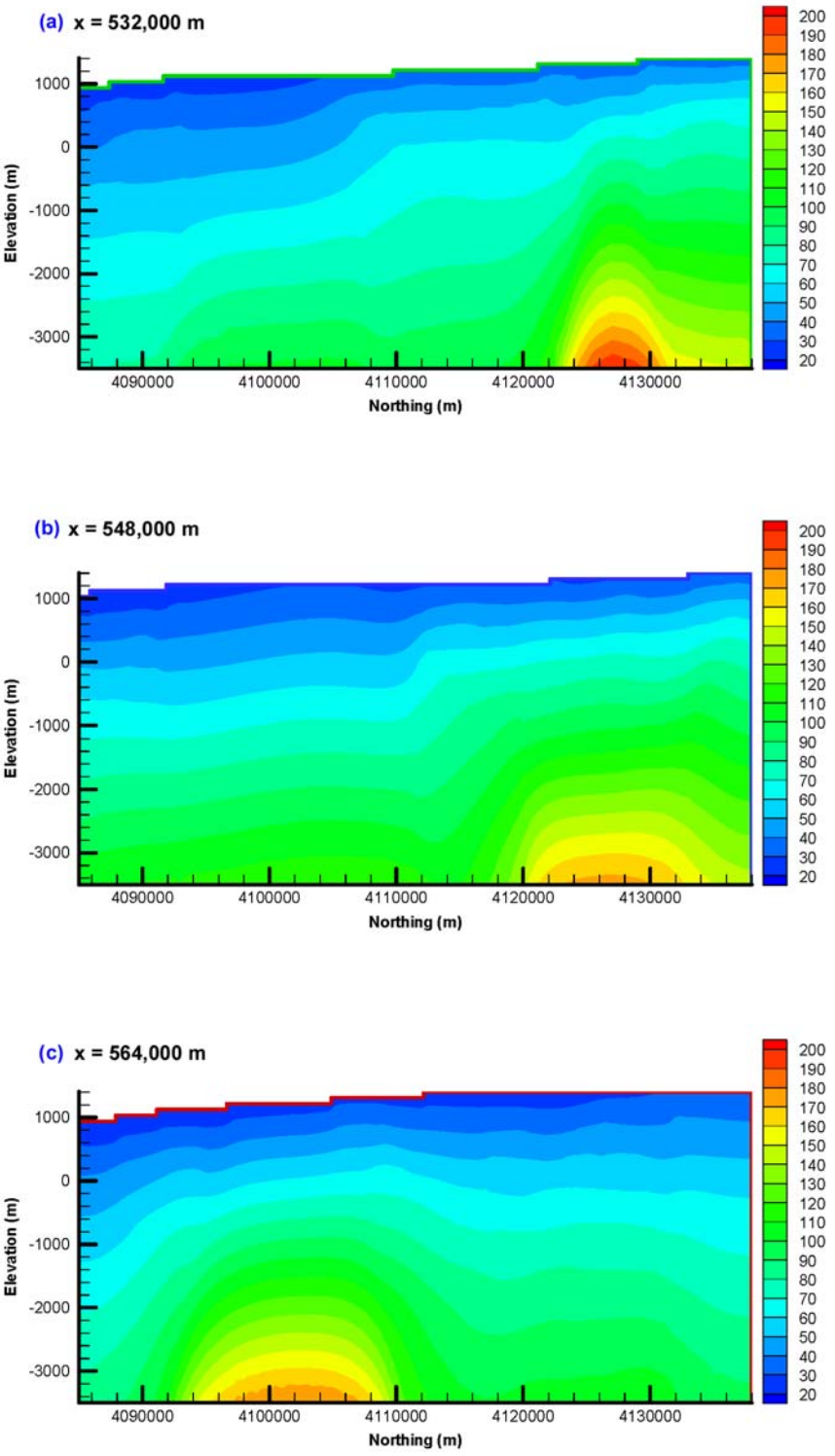

Figure C.7-14
North-South Transects for Calibrated Six-Zone Heat-Flux Model at (a) x = 532,000 m, (b) x = 548,000 m, and (c) x = 564,500 m, Corresponding Approximately to Transects G-G', H-H', and I-I' (BN, 2002)

Table C.7-2
Subregional Lower Boundary Heat Flux Estimates[a]
(Page 1 of 5)

Borehole	Elevation Range (m)	Structural Zone Number	HSU	Measured Type[b]	Estimated Heat Flow (mW/m^2)	Temperature Log (Date)	Calibrated Model Heat Flux (mW/m^2)
Subregion (1), North of Black Mountain							
PM-2	1,251.5 to 986.3	6	PBRCM	sz	54.8	7/11/1964	90
PM-2	983.3 to 949.8	6	PBRCM	sz	57.3	7/11/1964	90
Subregion (2), Silent Canyon Caldera Complex							
ER-20-5#3	1,275.0 to 1,242.98	1	LPCU	cwl	48.7	2/6/1996llnl	72.7
U-20c	1,301.8 to 1,277.4	1	BA	uz	49.1	4/5/1965	72.7
U-20c#1	576.4 to 481.9	1	CHZCM	sz	49.4	9/27/1968	72.7
U-20y	1,388.9 to 1,343.2	1	TCA	uz	42.1	1/2/1975	72.7
UE-20d	1,328.9 to 1,284.4	1	BA	uz	50.5	7/28/1964	72.7
UE-20e#1	370.9 to 352.7	2	BRA	sz	78.1	6/2/1964	72.7
ER-20-6#1	1,373.4 to 1,355.5	3	UPCU	uz	54.1	3/7/1996	72.7
ER-20-6#1	1,329.2 to 1,322.5	3	LPCU	sz	104.0	5/1/1996	72.7
ER-20-6#1	1,322.5 to 1,318.3	3	LPCU	sz	108.4	5/1/1996	72.7
ER-20-6#3	1,354.9 to 1,339.7	3	CHZCM	cwl	60.0	2002	72.7
U-20WW	1,345.3 to 1,328.5	3	CHZCM	cwl	53.1	2000-2002	72.7
UE-20n#1	1,347.1 to 1,331.8	3	CHZCM	cwl	70.9	2000-2002	72.7
ER-EC-1	1,270.3 to 1,212.5	4	FCCU	cwl	29.0	2/17/2000	72.7
ER-EC-1	535.1 to 503.7	4	CFCM	sz	85.3	2/17/2000	72.7
ER-EC-1	503.1 to 494.9	4	CFCM	sz	87.9	2/17/2000	72.7
ER-EC-6	1,271.6 to 1,240.5	4	FCCU	cwl	79.9	3/8/2000	72.7
ER-EC-6	754.0 to 742.2	4	TSA	sz	100.8	3/8/2000	72.7
ER-EC-6	741.7 to 663.2	4	TSA	sz	119.6	3/8/2000	72.7
ER-EC-6	546.4 to 529.3	4	CHCU	sz	116.6	3/8/2000	72.7
ER-EC-6	528.8 to 501.6	4	CHCU	sz	108.9	3/8/2000	72.7

Table C.7-2
Subregional Lower Boundary Heat Flux Estimates[a]
(Page 2 of 5)

Borehole	Elevation Range (m)	Structural Zone Number	HSU	Measured Type[b]	Estimated Heat Flow (mW/m^2)	Temperature Log (Date)	Calibrated Model Heat Flux (mW/m^2)
Subregion (2), Silent Canyon Caldera Complex, continued							
ER-EC-6	501.1 to 480.1	4	CFCM	sz	124.9	3/8/2000	72.7
ER-EC-6	479.5 to 455.9	4	CFCM	sz	126.6	3/8/2000	72.7
ER-EC-6	455.4 to 405.4	4	CFCM	sz	127.0	3/8/2000	72.7
ER-EC-6	404.9 to 367.1	4	CFCM	sz	131.5	3/8/2000	72.7
U-20bg	1,380.7 to 1,361.5	7	CHZCM	uz	28.9	6/22/1992	72.7
UE-20ab	1,487.7 to 1,426.8	7	CHVCM	uz	47.1	6/5/1978	72.7
ER-20-2#1	1,340.4 to 1,323.6	7	CHZCM	cwl	51.1	2000-2002	72.7
PM-1	1,358.5 to 1,330.4	7	CHZCM	cwl	46.1	8/3/1994	72.7
PM-1	1,042.1 to 1,029.9	7	BFCU	sz	60.2	8/3/1994	72.7
PM-1	1,029.8 to 972.6	7	BFCU	sz	56.9	8/3/1994	72.7
PM-1	972.3 to 931.4	7	BFCU	sz	55.9	8/3/1994	72.7
UE-20bh#1	1,321.7 to 1,306.4	7	CHZCM	cwl	51.1	2000-2002	72.7
UE-20bh#1	1,199.8 to 1,169.2	7	CHZCM	sz	48.7	10/1/1991	72.7
U-19aj	1,490.8 to 1,435.9	8	BFCU	uz	22.3	12/9/1980	72.7
U-19aS	1,496.9 to 1,393.2	8	CHVTA	uz	28.5	10/4/1964	72.7
U-19e	1,481.0 to 1,404.8	8	BFCU	uz	32.1	3/6/1966	72.7
U-19e	691.6 to 664.2	8	BRA	sz	162.1	3/6/1966	72.7
U-19e	661.1 to 642.8	8	BRA	sz	116.4	3/6/1966	72.7
U-19e	636.7 to 597.1	8	BRA	sz	119.0	3/6/1966	72.7
U-19g	1,464.3 to 1,427.7	8	CFCU	uz	32.6	11/19/1965	72.7
U-19f	1,302.7 to 1,296.6	9	CHCU	uz	43.3	7/5/1968	72.7
UE-19h	1,423.1 to 1,407.9	10	BRA	cwl	108.7	2000-2002	72.7

Table C.7-2
Subregional Lower Boundary Heat Flux Estimates[a]
(Page 3 of 5)

Borehole	Elevation Range (m)	Structural Zone Number	HSU	Measured Type[b]	Estimated Heat Flow (mW/m^2)	Temperature Log (Date)	Calibrated Model Heat Flux (mW/m^2)
Subregion (2), Silent Canyon Caldera Complex, continued							
U-19i	1,364.3 to 1,358.2	11	CFCU	uz	65.5	8/24/1967	72.7
U-19i	1,129.6 to 1,099.1	11	BFCU	sz	76.9	8/24/1967	72.7
U-19i	1,096.1 to 1,074.7	11	BFCU	sz	83.0	8/24/1967	72.7
U-19i	1,071.7 to 1,053.4	11	BFCU	sz	76.3	8/24/1967	72.7
U-19p	1,468.8 to 1,459.7	12	BFCU	uz	39.8	10/29/1975	72.7
U-19t	1,554.7 to 1,414.4	13	KA	uz	55.0	9/27/1993	72.7
U-19t	1,245.2 to 1,143.0	13	BRA	sz	92.8	9/27/1993	72.7
UE-19cWW	1,430.5 to 1,415.2	13	BFCU	cwl	62.1	2000-2002	72.7
Subregion (3), East Timber Mountain Caldera Complex and Black Mountain Caldera							
ER-18-2	1,287.8 to 1,272.5	17	TMCM	cwl	80.8	2000-2002	100
UE-18t	1,305.4 to 1,299.7	18	FCCM	cwl	58.7	12/12/1999	100
UE-18t	1,188.4 to 1,146.1	18	TMCM	sz	84.7	12/12/1999	100
UE-18t	1,143.9 to 1,088.1	18	TMCM	sz	58.8	12/12/1999	100
UE-18t	1,085.8 to 1,062.4	18	TMCM	sz	75.8	12/12/1999	100
UE-18t	1,059.9 to 1,008.6	18	TMCM	sz	86.2	12/12/1999	100

Table C.7-2
Subregional Lower Boundary Heat Flux Estimates[a]
(Page 4 of 5)

Borehole	Elevation Range (m)	Structural Zone Number	HSU	Measured Type[b]	Estimated Heat Flow (mW/m^2)	Temperature Log (Date)	Calibrated Model Heat Flux (mW/m^2)
Subregion (4), West Timber Mountain Caldera Complex							
ER-EC-2A	1264.2 to 1,248.9	15	FCCM	cwl	34.1	2000-2002	49
ER-EC-5	1225.5 to 1,212.7	15	TMCM	cwl	30.9	6/7/2000	49
UE-18r	1268.1 to 1,191.5	16	TMCM	cwl	31.5	3/16/1993	49
UE-18r	442.6 to 321.0	16	TMCM	sz	81.5	3/16/1993	49
UE-18r	321.0 to 267.6	16	TMCM	sz	78.0	3/16/1993	49
UE-18r	267.5 to 246.4	16	TMCM	sz	78.6	3/16/1993	49
UE-18r	246.3 to 181.6	16	TMCM	sz	74.4	3/16/1993	49
ER-EC-8	1,222.4 to 1,207.1	19	FCCM	cwl	104.0	2000-2002	49
ER-EC-7	1,333.3 to 1,237.0	21	FCCM	uz	40.3	8/8/1999	49
ER-EC-7	1,096 to 1,081.8	21	FCCM	sz	61.3	8/8/1999	49
Subregion (5), Extracaldera Area East of Timber Mountain and Silent Canyon Caldera Complexes							
ER-19-1#2	1,508.5 to 1,493.2	14	PBRCM	cwl	37.3	2000-2002	45
ER-19-1	999.2 to 929.2	14	LCCU1	sz	90.3	12/6/1993	45
ER-19-1	928.8 to 779.4	14	UCCU	sz	68.9	12/6/1993	45
HTH-1	1,427.4 to 1,331.7	14	PBRCM	cwl	33.2	8/19/1991	45
HTH-1	1,115.6 to 1,085.7	14	PBRCM	sz	28.1	8/19/1991	45
HTH-1	1,037.8 to 799.8	14	PBRCM	sz	30.9	8/19/1991	45
HTH-1	798.3 to 749.5	14	PBRCM	sz	26.8	8/19/1991	45
Subregion (6), Extracaldera Areas West of Silent Canyon Caldera Complex and West and South of Timber Mountain Caldera Complex							
PM-3#2	1,331.2 to 1,315.9	5	UPCU	cwl	55.6	2000-2002	45
UE-20j	1,369.5 to 1,271.9	5	PVTA	cwl	48.1	9/5/1964	45
ER-EC-4	1,237.4 to 1,222.9	20	TCVA	uz	88.9	6/2/1999	45
ER-EC-4	599.1 to 564.7	20	TMA	sz	28.5	8/25/2000	45

Table C.7-2
Subregional Lower Boundary Heat Flux Estimates[a]
(Page 5 of 5)

Borehole	Elevation Range (m)	Structural Zone Number	HSU	Measured Type[b]	Estimated Heat Flow (mW/m^2)	Temperature Log (Date)	Calibrated Model Heat Flux (mW/m^2)
Subregion (6), Extracaldera Areas West of Silent Canyon Caldera Complex and West and South of Timber Mountain Caldera Complex, continued							
ER-EC-4	564.2 to 539.4	20	TMA	sz	33.7	8/25/2000	45
ER-EC-4	518.2 to 505.2	20	TMA	sz	53.8	8/25/2000	45
ER-OV-3a2	1,122.9 to 1,107.6	22	DVCM	cwl	38.0	2000-2002	45
ER-OV-3b	1,184.5 to 1,169.3	22	AA	cwl	23.0	2000-2002	45
ER-OV-3c2	1,212.3 to 1,197.1	22	TMA	cwl	65.2	2000-2002	45

[a]See text for explanation of anomalous high heat fluxes (compiled from Attachment A, Tables A1 and A2).
[b]Temperatures measured at composite water level are prone to error; estimated heat flux represents minimum value.

more detail to the distribution of deep heat flux at the base of the model, the value of 72.7 mW/m^2 estimated for the SCCC as a whole seems to be a reasonable average value.

C.7.2.3.3 Subregion (3), East Timber Mountain Caldera Complex and Black Mountain Caldera

The number of calibration points for this subregion was severely limited by the quality of the temperature log for borehole ER-18-2 (Attachment A, Figure C26) and the grid resolution at borehole UE-18t (Attachment A, Figure C27). The calibrated heat flux of 100 mW/m^2 for subregion (3), which was constrained by only 2 temperature measurements in this subregion, appears to be high, based on the heat fluxes of 58 to 86 mW/m^2 estimated directly from the temperature logs. Again, however, lateral spreading of heat between the base of the model at –3,500 m and the much higher elevations (>1,000 m) at which the temperature-log based estimates were made may explain part of the difference in these estimates (Figure C.7-12).

C.7.2.3.4 Subregion (4), West Timber Mountain Caldera Complex

Grid resolution and the generally poor quality of the temperature logs limited the number of calibration points in subregion (4) to one each at boreholes UE-18r, ER-EC-8 and ER-EC-7 (Figure C.7-11; Attachment A, Figures C24, C25, C28, and C30). Moreover, the simulated temperature at the measurement elevation in borehole ER-EC-7 was relatively insensitive to heat flux because of its proximity to the fixed water table temperature and there was considerable uncertainty in the water table temperature at borehole ER-EC-8 (Attachment A, Figure C28). Even in light of these issues, however, the calibrated heat flux of 49 mW/m^2 may be somewhat low, based on the values of heat flux of 74 to 82 mW/m^2 calculated directly from deep portions of the temperature log at borehole UE-18r (Table C.7-2).

C.7.2.3.5 Subregion (5), Extra-Caldera Area East of the Timber Mountain and Silent Canyon Caldera Complexes

The calibrated heat flux of 45 mW/m^2 may be a reasonable estimate of heat flux in Subregion (5), based on the range in heat flux of 27 to 90.3 mW/m^2 estimated directly from temperature logs at boreholes ER-19-1 and HTH-1 (Table C.7-2). However, temperature logs at these boreholes are interpreted to have been strongly affected by groundwater flow (see Section C.8.0), so unbiased estimates of deep heat flux may not exist for this subregion.

C.7.2.3.6 Subregion (6), Extra-Caldera Areas West of Silent Canyon Caldera Complex and West and South of the Timber Mountain Caldera Complex

The heat flux of 45 mW/m^2 estimated by the model calibration was driven by the relatively cool temperatures measured in boreholes PM-3 (Attachment A, Figure C10) and ER-EC-4 (Attachment A, Figure C24). A heat flux of 45 mW/m^2 was the permissible lower limit allowed in the calibration; heat fluxes below this value were believed to be unrealistic, given the base-case estimate of 85 mW/m^2 for deep regional heat flux. The cool temperatures measured in boreholes PM-3 and ER-EC-4 are interpreted to be the result of groundwater flow processes (Section C.8.0). Based on this interpretation, unbiased estimates of deep heat flux may not exist for this subregion.

C.8.0 HYDROLOGICAL SIGNIFICANCE OF TEMPERATURE RESIDUALS

The differences (residuals) between the temperatures simulated with heat-conduction models described in this report and measured temperatures reflect the potential influence of many factors. These residuals may simply be the result of uncertainties in boundary conditions, thermal conductivity estimates, hydrostratigraphy, grid resolution and other aspects of the model's construction. Alternatively, the residuals may reflect the omission of advective heat-transport processes in the heat-conduction model and so, may be indirect indicators of groundwater flow patterns in the PM/OV flow system

The one-dimensional simulations presented earlier in this appendix that include both conductive and advective heat-transport indicate that in areas of vertical groundwater movement, conductive heat fluxes can be both larger and smaller than for conduction alone, depending on elevation (Figure C.2-1). This observation is true for both upward and downward groundwater movement. In areas of upward groundwater movement, however, conductive heat fluxes increase with elevation; conversely, in areas of downward groundwater movement, conductive heat fluxes decrease with elevation. Therefore, conductive heat flux is not diagnostic of the direction of groundwater movement unless heat-flux estimates are available at multiple elevations in a borehole. Discrepancies between simulated and measured temperatures provide a more unique interpretation of flow directions when measurements from only a single elevation (or narrow range of elevations) are available. Regardless of the elevation at which the measurements are made, temperatures in areas of downward groundwater flow are always cooler, and temperatures in areas of upward groundwater flow are always warmer, than temperatures produced by heat conduction alone. Therefore, except in rare instances where reliable heat flux estimates from multiple elevations are available, the interpretations in the following sections focus on the differences between simulated and measured temperatures.

Normal faults, caldera boundaries and other structural features disrupt the continuity of HSUs in the PM/OV flow system and may provide preferential pathways across confining units. Therefore, if significant vertical flow across confining units exists, it is most likely that it occurs through these structural features. To investigate this possibility, structural features are included on maps showing the distribution of borehole temperature residuals (Figures C.7-5, C.7-8, and C.7-11). These maps were analyzed jointly with summary plots of simulated versus measured temperatures from multiple boreholes (Figures C.7-5, C.7-6, C.7-7, C.7-9, and C.7-11) and plots of simulated and measured temperature profiles at individual Wells (Attachment A, Figures C1 to C30). The analyses that follow focus on the residuals produced with the inverse variable heat-flux model described in Section C.7.2.2.2. Calibrating heat fluxes at the base of the model domain in which heat flux was estimated at six distinct zones along the bottom boundary. However, when interpreting residuals from this model, it was also considered if these residuals could be explained by other factors, such as a poor estimate of water table temperature at the well, or if the residuals were considerably smaller for the alternative heat-conduction models described in this report. Temperature residuals in the variable heat-flux model, which arose because of poor estimates of water table temperature, or which were significantly smaller in other heat conduction models, were not interpreted in terms of their possible hydrologic significance.

C.8.1 Subregion (2) - Silent Canyon Caldera Complex

In the southwestern part of the SCCC, it is likely that the deep heat flux is actually higher than the heat flux of 73 mW/m^2 estimated for the caldera complex as a whole with the variable heat-flux model, and that cool groundwater from the shallow saturated zone flows downward through the upper units. These interpretations are supported by a detailed examination of temperature residuals from this area, as follows. The heat-conduction model with a uniform heat flux of 85 mW/m^2 provides a good match to the measured temperatures at borehole ER-EC-6 (Figure C.7-5 and Attachment A, Figure C9), but underestimates the deepest measurement in the region - the temperature of 121°C measured at a 12,270 ft depth in borehole UE-20f (not shown). Conversely, simulated temperatures in nearby boreholes U20c, U20d and ER-20-5 #3 in the southwest part of the caldera complex are warmer than the measured temperatures for deep heat fluxes of either 85 or 73 mW/m^2 (see residuals on Figures C.7-5 and C.7-11). A heat flux of 85 mW/m^2 would improve the match between simulated and measured temperatures at boreholes UE-20f, ER-EC-6 and ER-EC-1, where measured

temperatures are underestimated by the model with a deep heat flux of 73 mW/m^2 for the SCCC (Figure C.7-10). However, the use of a higher heat flux in the heat-conduction model would increase the mismatch between simulated and measured temperatures at boreholes U20c, ER-20-5#3, and U-20d, which the model indicates are already slightly too warm for a heat flux of 73 mW/m^2 (Figure C.7-10). To offset the temperature increases that would result from higher deep heat fluxes, a mechanism to cool the subsurface temperatures in the southwestern part of the SCCC is required. The downward hydraulic gradient, dipping beds and discontinuous confining units (e.g., the CHCU and LPCU) in the upper part of southwest Area 20 (Wolfsberg et al. 2002; BN, 2002, cross-section J-J') indicate that hydrogeologic conditions are favorable for cool groundwater near the water table to flow downward along the dipping beds or faults to deeper aquifers such as the IA, thereby reducing temperatures and heat fluxes below the wells in this region.

In the northeastern part of the SCCC, the simulated temperatures are higher than the measured temperatures at borehole U-19e for the calibrated variable heat-flux model (Figure C.7-11 and Attachment A, Figure C15). Although the temperature data at borehole U-19e are reasonably well matched with a uniform heat flux of 45 mW/m^2 (Figure C.7-7), temperatures at borehole U19-i, located about 5 km to the south of borehole U-19e, are underestimated using this heat flux, and better matched with a heat flux of 85 mW/m^2 (Figure C.7-5 and Attachment A, Figure C15). It is possible that heat flux varies significantly within the SCCC complex. However, an alternative hydrologic explanation is that downward groundwater movement, possibly through the Halfbeak Fault (see BN, 2002, cross-section C-C') significantly cools the rocks and reduces heat flux near borehole U-19e.

C.8.2 Subregion (4) - Western Timber Mountain Caldera Complex

Borehole UE-18r was characterized by Gillespie (2003) as having dominantly conductive heat flow (~ 25 mW/m^2) and reliable temperatures measurements above the bottom of the borehole casing at a depth of 496.5 m (elevation 1,192 m). Unfortunately, simulated temperatures at these elevations are dominated by the upper boundary conditions and are insensitive to the assumed thermal conductivity estimates and lower boundary conditions. Hence, it was necessary to use a deep temperature measurement from below the borehole casing as a calibration target in the inverse models. The simulated temperatures are significantly warmer than this deep measurement from borehole UE-18r

for all lower boundary conditions considered in this report (Figures C.7-5 through C.7-9 and C.7-11; Attachment A, Figures C24 and C25). The consistent overestimation of the measured temperature indicates that downward groundwater flow may have cooled the rocks near the bottom of the temperature profile. Borehole UE-18r penetrates a fault breccia (Tmrx) at depth, which suggests that groundwater flow along the fault associated with this breccia may have cooled nearby temperatures. This interpretation is also consistent with the relatively low heat flux of 25 mW/m^2 estimated by Gillespie (2003) above elevations of 1,192 m and the much larger heat flux (> 75 mW/m^2) estimated below a 443 m elevation (Table C.7-2). Based on one-dimensional scoping simulations (Figure C.2-1), heat flux is expected to decrease with elevation in areas of downward groundwater flow. However, groundwater carbon-14 measured in the borehole is very low (Chapman et al., 1995), ruling out modern recharge as a likely influence on groundwater temperatures and suggesting that the downward movement of groundwater from laterally upgradient areas is a more likely explanation for the decrease in heat flux with elevation at borehole UE-18r.

C.8.3 Subregion (5) - Extra-Caldera Area East of Timber Mountain and Silent Canyon Caldera Complexes

The simulated temperatures at boreholes HTH-1 and ER-19-1 in the eastern part of the PM/OV flow domain were significantly warmer than the measured temperatures for all models with specified deep heat fluxes discussed in this report (Attachment A, Figures C21 and C22), including the variable heat-flux model (Figure C.7-11). Several related hypotheses involving the downward movement of groundwater may explain the relatively cool temperatures measured in boreholes HTH-1 and ER-19-1. The first hypothesis involves the downward movement of groundwater recharge in this part of the NTS. Isotopic data were not available from boreholes HTH-1 or ER-19-1 to evaluate whether young recharge is present in the groundwater at these boreholes. However, relatively high groundwater carbon–14 activities of 25 to 75 pmc in nearby boreholes WW-8, ER-30-1 and 29a #2 may indicate that the Fortymile Canyon and surrounding areas are locations with comparatively high recharge rates (SNJV, 2004 Figure 5). Downward groundwater flow would result from locally high recharge rates and cause temperatures to be relatively cool at these boreholes. The second related hypothesis involves the Belted Range Thrust Fault. This thrust fault, which intersects the lower part of borehole ER-19-1, could help to focus downward groundwater movement and reduce the measured temperatures and heat fluxes at elevations above the fault.

C.8.4 Subregion (6) - Extra-Caldera Areas West of Silent Canyon Caldera Complex, and West and South of the Timber Mountain Caldera Complex

Measured temperatures at borehole ER-EC-4 are consistently cooler than the temperatures calculated with the calibrated variable heat-flux model (Figure C.7-11 and Attachment A, Figure C29). These temperature differences, along with a decrease in the estimated heat flux from 54 to 28 mW/m^2 through the lower part of the borehole (Table C.7-2), indicates the presence of downward groundwater movement near this borehole. One hypothesis that might explain the low temperatures and heat flux at borehole ER-EC-4 is that HSUs in this area, including the very thick and transmissive LCA, have an apparent southward dip (BN, 2002 cross-section G-G'). As groundwater moves southward through this area, the downward flow component induced by the dip of the beds causes the groundwater to become warmer, thereby consuming heat and decreasing the temperature and heat flux in the overlying rocks. Despite the location of borehole ER-EC-4 along a major canyon, there is no evidence from geochemical and isotopic data, such as delta deuterium or carbon-14, that groundwater near borehole ER-EC-4 receives significant recharge (SNJV, 2004 Figures 5 and 6).

C.9.0 SUMMARY AND CONCLUSIONS

A 3-D steady-state heat-conduction model was developed for the PM/OV flow domain in order to (a) provide a 3-D temperature distribution for steady-state flow modeling and (b) to investigate if borehole temperature data from this region might provide information about vertical groundwater movement by identifying locations in the model domain where temperatures could not be explained by conduction. The temperature observations that could not be satisfactorily explained by the conduction model were used as the basis for developing possible explanations involving groundwater flow.

Development of the model utilized the existing hydrostratigraphy of the PM/OV flow model as the starting point. Thermal conductivities were assigned to 46 individual HSUs present in the model, based on the thermal conductivities measured on various rock types and the proportions of those rock types present in the individual HSUs. Temperatures measured in the deep unsaturated zone or shallow saturated zone were used to develop a map of water table temperatures that was used as the upper thermal boundary condition in the model. The lower boundary condition was treated as either a constant temperature boundary (160 °C), or as a specified heat flux boundary. Forward heat-conduction models assumed uniform specified heat fluxes of 45, 65, 85 and 105 mW/m^2 along the lower boundary of the model. Based on these forward heat-conduction models, inverse heat-conduction models were created that either (1) optimize the thermal conductivities of three groups of volcanic HSUs for a specified lower heat flux of 65 mW/m^2, or (2) estimate the heat flux for six intra- or extra-caldera domains at the base of the model, using the base-case estimates of thermal conductivity in each of the 46 HSUs. Evaluation of the forward and inverse models was done by comparing simulated temperatures with borehole temperatures measured over a four-decade period by various investigators. The development of a sub-set of reliable temperature measurements to use as calibration targets required careful screening of scores of digitized temperature profiles to eliminate portions of temperature logs where flow within the borehole may have disturbed *in situ*

temperatures. Limited grid resolution in parts of the model domain also limited the number of temperature measurements that could be used for direct comparison with the simulated temperatures.

Differences between temperatures simulated with the heat-conduction models and the measured temperatures are potentially the results of many factors, including (1) uncertainty in the spatial variations in the deep heat flux, (2) uncertainty in the hydrostratigraphy (especially below depths sampled by boreholes), (3) uncertainty in thermal conductivities estimates, and (4) groundwater movement. The hydrologic interpretations of the differences between simulated and measured temperatures are therefore only one of several possible explanations of these differences.

Possible hydrologic explanations of temperature residuals within the PM/OV flow domain include (1) the downward flow of cool groundwater along the West Boxcar Fault or dipping beds in the southwest corner of the Area 20 caldera, (2) the downward flow of cool groundwater near the Halfbeak Fault (Area 20 structural margin) in the northeast part of the SCCC, (3) downward groundwater flow through the brecciated rocks along the northern structural margin of the Timber Mountain caldera complex near borehole UE-18r, (4) downward groundwater movement along the Belted Range Thrust Fault near the eastern model boundary, perhaps associated with higher recharge rates in this area, and (5) a downward groundwater flow component in rocks west of the Silent Canyon and Timber Mountain caldera complexes that is induced by the southerly apparent dip of rocks (including the highly transmissive LCA) in this area. Although the hydrologic interpretations of the temperature residuals are only one of several possible explanations, they indicate areas where the numerical model of groundwater flow in the PM/OV flow domain should be examined for consistency with these explanations.

C.10.0 REFERENCES

Beck, A.E., G. Garven, and Stegena, 1989, Hydrogeological regimes and their subsurface thermal effects, AGU Geophysical Monograph 47, IUGG v. 2.

Arnold, B.W., G. Zyvoloski, K. Economy, and M. Wallace, 2003, Thermal transport in the saturated zone site-scale model at Yucca Mountain, International High-level Radioactive Waste Management Conference, Las Vegas, Nevada.

Barroll, M.W., 1989, Analysis of the Socorro hydro-geothermal system, central New Mexico, Ph.D. Dissertation, 81 pp., Appendices.

Bechtel Nevada, 2002, A hydrostratigraphic model and alternatives for the groundwater flow and contaminant transport model of corrective action units 101 and 102: Central and Western Pahute Mesa, Nye County, Nevada, DOE/NV/11718-706.

Blankennagel, R.K., and J.E. Weir, Jr., 1973, Geohydrology of the Eastern Part of Pahute Mesa, Nevada Test Site, Nye County, Nevada: USGS Professional Paper 712-B, 35 pp.

Bodvarsson, G.S., S. Vonder Haar, M.J. Wilt, and C.F. Tsang, 1982, Preliminary studies of the reservoir capacity and generating potential of the Baca geothermal field, New Mexico, Water Resources Research, v. 18, p. 1713-1723.

Bodvarsson, G.S., E. Kwicklis, C. Shan, and Y.S. Wu, 2003, Estimates of percolation flux from borehole temperature data at Yucca Mountain, Nevada, Journal of Contaminant Hydrology, v.62-63, p. 3-22.

Brodsky, N.S., M. Riggins, J. Connolly, and P. Ricci, 1997, Thermal expansion, thermal conductivity, and heat capacity measurements for boreholes UE-25 NRG-4, UE25 NRG-5, USW NRG-6, and USW NRG-7/7A, SAND95-1955, 77 pp., Appendices

Byers, F.M., Jr., W.J. Carr, P.P. Orkild, W.D. Quinlivan, and K.A. Sargent, 1976, Volcanic suites and related cauldrons of Timber Mountain-Oasis Valley caldera complex, southern Nevada, U.S. Geol. Survey Prof. Paper 919, 70 pp.

Chapman, J.B., R.L. Hershey, and B.F. Lyles, 1995, Groundwater velocities at the Nevada Test Site: ^{14}Carbon-based estimates, technical report #45135, DOE/NV/11508-03 UC-703, Desert Research Institute, Las Vegas, NV.

Constantz, J., S.W. Tyler, and E. Kwicklis, 2003, Temperature-profile methods for estimating percolation rates in arid environments, Vadose-Zone Journal v.2, p. 12-24.

Doherty, J., 2000, PEST, Model-Independent Parameter Estimation Users Manual, Watermark Numerical Computing, http://members.ozemail. com.au/~wcomp/, distributed as freeware software with documentation from SS Popadopulos & Associates, Inc., http://www.sspa.com/pest (URL confirmed July, 2002).

Faulds, J.E., and R.J. Varga, 1998, The role of accommodation zones and transfer zones in the regional segmentation of extended terrains, in J.E. Faulds and J.H. Stewart, eds., Accommodation zones and transfer zones: the regional segmentation of the Basin and Range Province, GSA Special Paper 323, pp. 1-45.

Fridrich, C.J, W.W. Dudley, Jr, and J.S. Stuckless, 1994, Hydrogeologic analysis of the saturated zone ground-water system under Yucca Mountain, Nevada, Journal of Hydrology, v. 154, p. 133-168.

Giles, M.R., 1997, Diagenesis: A quantitative perspective, Kluwer Academic Publishers.

Gillespie, D., 2003, Temperature data evaluation, DOE/NV/13609-22; Publication No. 45194, 35 pp.

Grauch, V.J.S., D.A. Sawyer, C.J. Fridrich, and M.R. Hudson, 1999, Geophysical framework of the southwestern Nevada volcanic field and hydrogeologic implications, U.S. Geological Survey Professional Paper 1608, 39 pp.

Jiracek, G.R., C.L. Kinn, C.L. Scott, M.G. Kuykendall, W.S. Baldridge, S. Biehler, L.W. Braile, J.F. Ferguson, and B. Gilpin, 1996, Tracing crustal isotherms under the western margin of the Jemez Mountains using SAGE and industry magnetotelluric data, in NMGS Guidebook, 47th Field Conference, pp. 129-133.

Kwicklis, E., D. Broxton, D. Vaniman, and A. Wolfsberg, 2003, Investigation of the influence of faults on groundwater movement in the Pahute Mesa/Oasis Valley flow model domain, Letter Report to DOE.

Lappin, A.R., and F.B. Nimick, 1982, Thermal properties of the Grouse Canyon Member of the Belted Range Tuff and of Tunnel Bed 5, G-tunnel, Nevada Test Site, SAND82-2203. 47 pp.

Lin, G., J.A. Nunn, and D. Deming, 2000, Thermal buffering of sedimentary basins by basement rocks: implications arising from numerical simulations, Petroleum Geoscience, v. 6, pp. 299-307.

McKinley, P.W., M.P. Long, and L.V. Benson, 1991, Chemical analyses of water from selected wells and springs in the Yucca Mountain area, Nevada and southeastern California: USGS Open-file Report 90-355, 47 pp.

Morgan, P., J.H. Sass, and R.D. Jacobson, 1996, Heat flow in VC-2a and VC-2b, and constraints on the thermal regime of the Valles Caldera, New Mexico, in NMGS Guidebook, 47th Field Conference, pp. 231-236.

Olmsted, F.H., and F.E. Rush, 1987, Hydrogeologic reconnaissance of the Beowawe geysers geothermal area, Nevada: Geothermics, v. 16, no. 1, pp. 27-46.

Painter, S., J. Winterle, and A. Armstrong, 2003, Using temperature to test models of flow near Yucca Mountain, Nevada: Groundwater, v. 41, no. 5, pp. 657-666.

Phillips, O.M., 1991, Flow and reactions in permeable rocks, Cambridge University Press, New York, pp. 34-35.

Pottoroff, E.J., S.J. Erikson, and M.E. Campana, 1987, Hydrologic utility of borehole temperatures in areas 19 and 20, Pahute Mesa, Nevada Test Site, DOE/NV/10384-19, Publication No. 45060, 189 pp.

Rehfeldt, K.R., 2002, Assessment of groundwater temperature logs, Geotrans Inc.

Reiter, M., 1999, Hydrogeothermal studies on the southern part of Sandia National Laboratories/Kirtland Air Force Base—Data regarding ground-water flow across the boundary of an intermontane basin, in Faults and Subsurface fluid flow in the shallow crust, eds, L. Goodwin, P. Mosely, pp. 207-222.

Rose, T.P., F.C. Benedict, Jr., J.M. Thomas, W.S. Sicke, R.L. Hershey, J.B. Paces, I.M. Farnham, and Z.E. Peterman, 2002, Geochemical Data Analysis and Interpretation of the Pahute Mesa—Oasis Valley Groundwater Flow System, Nye County, Nevada, Preliminary report to the National Nuclear Security Administration, U.S. Department of Energy.

Rousseau, J.P., E.M. Kwicklis, and D.C. Gillies, eds., 1999, Hydrogeology of the unsaturated zone, North Ramp Area of the Exploratory Studies Facility, Yucca Mountain, Nevada, U.S. Geological Survey Water-Resources Investigations Report 98-4050, Denver, CO., 244 p.

Sass, J.H., and A.H. Lachenbruch, 1982, Preliminary interpretation of thermal data from the Nevada Test Site, USGS Open-file Report 82-973, 30 pp.

Sass, J.H., A.H. Lachenbruch, and C.W. Mase, 1980, Analysis of thermal data from drill holes UE25a-3 and UE25a-1, Calico Hills and Yucca Mountain, Nevada Test Site, USGS Open-file Report 80-826.

Sass, J.H., A.H. Lachenbruch, S.S. Priest, R.J. Munroe, and W.W. Dudley, Jr., 1987, Temperature, thermal conductivity, and heat flow near Yucca Mountain, Nevada: some tectonic and hydrologic implications, USGS Open-file Report 87-649, 96 pp.

Sass, J.H., W.W. Dudley, Jr., and A.H. Lachenbruch, 1995, Chapter 8: Regional thermal setting; in Major results of geophysical investigations at Yucca Mountain and vicinity, southern Nevada, eds. H.W. Oliver, D.A. Ponce, and W.C. Hunter, USGS Open-file Report 95-74, pp. 157-170.

Sawyer, D.A., R.J. Fleck, M.A. Lamphere, R.G. Warren, D.E. Broxton, and M.R. Hudson, 1994, Episodic caldera volcanism in the Miocene southwestern Nevada volcanic field: Revised stratigraphic framework, 40Ar/39Ar geochronology, and implications for magmatism and extension, GSA Bulletin, v. 106, p. 1304-1318.

Stoller-Navarro Joint Venture. 2004. *Hydrologic Data for the Groundwater Flow and Contaminant Transport Model of Corrective Action Units 101 and 102: Central and Western Pahute Mesa, Nye County, Nevada*, Rev. 0, S-N/99205-002; Shaw/13052-204. Las Vegas, NV.

White, A.F., 1979, Geochemistry of ground water associated with tuffaceous rocks, Oasis Valley, Nevada: USGS Professional Paper 712-E, 25 pp.

Wolfsberg, A., L. Glascoe, G. Lu, A. Olson, P. Lichtner, M. McGraw, T. Cherry, and G. Roemer, 2002, TYBO/BEHNAM: Model analysis of groundwater flow and radionuclide migration from underground nuclear tests in southwestern Pahute Mesa, Nevada, Los Alamos National Laboratory Report LA-13977, Los Alamos, New Mexico.

Wollenberg, H.A., J.S.Y. Wang, and G. Korbin, 1983. An appraisal of nuclear waste isolation in the vadose zone in arid and semiarid regions (with emphasis on the Nevada Test Site), Lawrence Berkeley National Laboratory technical report 15010, Berkeley, California.

Woodbury, A.D., L. Smith, and W.S. Dunbar, 1987, Simultaneous inversion of hydrogeologic and thermal data: 1 – Theory and application using hydraulic head data, Water Resources Research, v. 23, no. 8, p. 1586-1606.

Woodbury, A.D., and L. Smith, 1988, Simultaneous inversion of hydrological and thermal data, 2. Incorporation of thermal data, Water Resources Research, v. 24, no. 3, pp. 356-372.

Zyvoloski, G.A., B.A Robinson, Z.V Dash, and L. Trease, 1997. Summary of the Models and Methods for the FEHM Application – A Finite-Element Heat-and Mass-Transfer Code. Report LA-13307-MS, Los Alamos, New Mexico: Los Alamos National Laboratory.

Attachment A

Supporting Data, Calculations, and Figures for Appendix C

(As provided by Los Alamos National Laboratory)
Andrew Wolfsberg

Table A1. Depth and elevation range, hydrostratigraphic unit, and temperature gradients for deepest unsaturated-zone or cwl. Depth intervals with temperature gradients that may represent the ambient temperature gradient are shown in bold. Depth intervals with reasonable temperature gradients that are not consistent within an hsu or spatial location are bold italicized.

E	N	UZ or cwl temp (C)	Borehole	Elev range (m)	Strat[1]	Class/ rock type[1]	HGU[1]	HSU[1]	Grad T (C/km)	Std dev (C/km)	R^2	Saturation (u,s)[2]	Temp log (date)	l (W/m C)	Est. Heat Flow (mW/m^2)
Purse Fault-W. Boxcar Fault (1)															
545113.1	4119467.8	40.2	ER-20-1[24]	1277.8 - 1261.0	Tpcm	MWT	WTA	TCA	14.8	10.8		s, below cwl	2000-2002		
546386	4119208	29.5	*ER-20-5#1*	*1349.9 - 1301.1*	*Tpcm*	*MWT*	*WTA*	*TCA*	*28.2*	*1.5*	*0.99*	u, deep uz	11/3/95		
546386	4119208	30.2	***ER-20-5#1***	***1301.1 - 1276.5***	***Tp***	***BED***	***TCU***	***LPCU***	***30.3***	***2.3***	***0.97***	u, deep uz	11/3/95	**1.15**	**34.8**
546386	4119208	32.7	ER-20-5#1	1274.2 - 1242.9	Tp	BED	TCU	LPCU	15.9	1.0	0.99	s, below cwl	11/3/95		
546385	4119177	37.2	ER-20-5#3[5]	1301.1 - 1275.8	Tp	BED	TCU	LPCU	60.0	10.5	0.81	u, deep uz	2/6/96llnl		
546385	4119177	36.6	ER-20-5#3[5]	1291.0 - 1285.1	Tp	BED	TCU	LPCU	98.8	4.4	0.99	u, deep uz	2/6/96llnl		
546385	4119177	37.2	ER-20-5#3[5]	1284.9 - 1275.8	Tp	BED	TCU	LPCU	117.7	1.9	0.97	u, deep uz	2/6/96llnl		
546385	4119177	38.1	ER-20-5#3[5]	1275.0 - 1242.9	Tp	BED	TCU	LPCU	28.2	0.8	0.97	s, below cwl	2/6/96llnl	1.73	48.7
546699	4120478	27.1	U-20c	1667.5 - 1624.8	unk	BED	VTA	PVTA	33.2	1.8	0.95	u, deep uz	4/5/65		
546699	4120478	29.8	U-20c	1624.8 - 1310.9	Tpb	LA	LFA	BA	10.3	0.6	0.98	u, deep uz	4/5/65		
546699	4120478	30.6	**U-20c**	1301.8 **-** 1277.4	**Tpb**	**LA**	**LFA**	**BA**	**26.9**	**0.8**	**0.93**	u, deep uz	4/5/65	**1.95**	**52.6**
546699	4120478	31.2	U-20c	1271.3 - 1164.6	Tpcm	TUF	unk	TCA	10.0	1.0	0.94	s, below cwl	4/5/65		
546699	4120478	31.8	U-20c[3]	1310.9 - 1302.0	Tpb	LA	LFA	BA	24.1	0.8	0.93	u, deep uz	9/27/68		
546699	4120478	31.8	**U-20c[3]**	1301.8 **-** 1277.6	**Tpb**	**LA**	**LFA**	**BA**	**23.4**	**0.8**	**0.99**	u, deep uz	9/27/68	**1.95**	**45.7**
546699	4120478	32.4	U-20c[3]	1273.3 - 1249.1	Tpcm	TUF	unk	TCA	13.1	0.4	0.98	s, below cwl	9/27/68		
546699	4120478	33.2	U-20c[3]	1215.7 - 1164.8	Tpcm	TUF	unk	TCA	19.1	0.5	0.99	s, below cwl	9/27/68		
546103	4122301	27.6	U-20d	1506.3 - 1341.7	unk	BED	VTA	PVTA	18.7	1.3	0.96	u	1/31/67		
546103	4122301	28.0	*U-20d*	*1341.7 - 1332.6*	*unk*	*BED*	*VTA*	*PVTA*	59.2	1.4	0.83	u	1/31/67		
546103	4122301	35.8	***U-20d***	***1332.6 - 1271.6***	***Tpb***	***LA***	***LFA***	***BA***	***56.0***	***2.8***	***0.93***	u, deep uz	1/31/67	**1.95**	**109.3**
546103	4122301	35.8	U-20d	1271.6 - 1229.0	Tpb	LA[28]	LFA	BA	7.6	0.3	0.95	s, below cwl	1/31/67		
546103	4122301	37.5	U-20d	1229.0 - 1146.7	Tp	BED	TCU	UPCU	17.7	0.3	0.98	s, below cwl	1/31/67		
546103	4122301	39.1	U-20d	1146.7 - 1067.4	Tpcm	unk	unk	TCA	21.5	0.5	0.99	s	1/31/67		

Table A1. (continued)

E	N	UZ or cwl temp (C)	Borehole	Elev range (m)	Strat[1]	Class/ rock type[1]	HGU[1]	HSU[1]	Grad T (C/km)	Std dev (C/km)	R^2	Saturation (u,s)[2]	Temp log (date)	l (W/m C)	Est. Heat Flow (mW/m^2)
Purse Fault-W. Boxcar Fault (1), continued															
546103	4122301	37.8	***U-20d***	***1332.6 - 1271.6***	***Tpb***	***LA***	***LFA***	***BA***	***55.1***	***2.6***	***0.96***	u, deep uz	2/2/67	**1.95**	**107.5**
546103	4122301	37.8	U-20d	1271.6 - 1229.0	Tpb	LA[28]	LFA	BA	45.7	1.5		s, below cwl	2/2/67		
546103	4122301	40.9	U-20d	1229.0 - 1146.7	Tp	BED	TCU	UPCU	16.5	0.4		s, below cwl	2/2/67		
546103	4122301	42.3	U-20d	1146.7 - 1067.4	Tpcm	unk	unk	TCA	17.1	0.5		s	2/2/67		
546651	4119291	25.9	**U-20y**	**1388.9 - 1343.2**	**Tpcm**	**MWT**	**WTA**	**TCA**	**24.9**	**2.2**	**0.74**	u	1/2/75	**1.69**	**42.1**
546651	4119291	27.8	U-20y	1328.0 - 1276.2	Tp	BED	TCU	LPCU	17.6	2.8	0.74	u, deep uz	1/2/75		
546651	4119291	28.8	U-20y	1276.2 - 1267.0	Tp	BED	TCU	LPCU	140.3	2.5	0.94	s, below cwl	1/2/75		
546103	4122275	26.9	UE-20d	1510.0 - 1342.3	unk	BED	VTA	PVTA	17.2	1.1	0.98	u	7/28/64		
546103	4122275	27.0	UE-20d	1342.3 - 1328.9	unk	BED	VTA	PVTA	28.3	0.3	0.97	u	7/28/64		
546103	4122275	32.0	***UE-20d***	***1328.9 - 1284.4***	***Tpb***	***LA***	***LFA***	***BA***	***25.9***	***3.6***	***0.82***	u, deep uz	7/28/64	**1.95**	**50.5**
546103	4122275	32.0	UE-20d	1281.4 - 1229.6	Tpb	LA[28]	LFA	BA	33.5	3.0	0.65	s, below cwl	7/28/64		
546103	4122275	36.8	UE-20d	1229.6 - 1162.5	Tp	BED	TCU	UPCU	25.2	1.4	0.94	s, below cwl	7/28/64		
Boxcar Fault-W. Greeley Fault (3)															
551362.9	4123691.8	25.6	ER-20-6#1	1373.4 - 1355.5	Tpd	BED	TCU	UPCU	**44.7**	**4.4**	**0.93**	u, deep uz	3/7/96	**1.15**	**51.5**
551362.9	4123691.8	30.5	ER-20-6#1	1348.5 - 1329.2	Tpd	BED	TCU	UPCU	31.1	0.8	0.92	s, below cwl	3/7/96	1.73	53.8
551362.9	4123691.8	30.3	ER-20-6#1[21]	1353.2 - 1329.2	Tpd	BED	TCU	UPCU	33.0	0.7	0.99	s, below cwl	5/1/96	1.73	57.1
551362.9	4123691.8	29.9	ER-20-6#1[21]	1355.1 - 1339.8	Tpd	BED	TCU	UPCU	*54.6*			s, below cwl	2002	*1.73*	*94.5*
551328	4123661.8	29.4	ER-20-6#2[22]	1355.0 - 1339.7	Tpd,Tp	BED	TCU	UPCU,L	*47.6*			s, below cwl	2002	*1.73*	*82.3*
551295.7	4123578.8	28.7	ER-20-6#3[23]	1354.9 - 1339.7	Thp	LA[31]	LFA	CHZCM	34.7			s, below cwl	2002	1.73	60.0
550614	4122711.7	31.9	U-20WW	1345.3 - 1328.5	Thp	LA	LFA	CHZCM	24.6	9.7		s, below cwl	2000-2002	2.16	53.1
551273.2	4121483.8	34.5	UE-20n#1	1347.1 - 1331.8	Thp	LA[31]	LFA	CHZCM	41.0	5.4		s, below cwl	2000-2002	1.73	70.9

Table A1. (continued)

E	N	UZ or cwl temp (C)	Borehole	Elev range (m)	Strat[1]	Class/ rock type[1]	HGU[1]	HSU[1]	Grad T (C/km)	Std dev (C/km)	R^2	Saturation (u,s)[2]	Temp log (date)	l (W/m C)	Est. Heat Flow (mW/m^2)
S of Silent Canyon caldera structural margin-N of Timber Mountain caldera topographic margin (4)															
541730	4117660	36.5	ER-EC-1[16]	1294.7 - 1270.3	Tmrf	NWT	TCU	FCCU	2.7	5.6	0.55	u, deep uz	4/20/99		
541730	4117660	37.0	ER-EC-1[16]	1270.2 - 1211.8	Tmrf	NWT	TCU	FCCU	9.0	6.3	0.94	s, below cwl	4/20/99		
541730	4117660	32.6	ER-EC-1[17]	1271.1 - 1255.9	Tmrf	NWT	TCU	FCCU	19.7			s, below cwl	2000-2002	1.42	28.0
541730	4117660	33.8	ER-EC-1[17]	1270.3 - 1212.5	Tmrf	NWT	TCU	FCCU	21.1	3.3	0.74	s, below cwl	2/17/00	1.42	30.0
544673	4115729	40.0	ER-EC-6[18]	1296.7 - 1273.6	Tmrf	BED	TCU	FCCU	23.0	6.6	0.86	u, deep uz	3/20/99		
544673	4115729	40.6	ER-EC-6[18]	1267.7 - 1240.4	Tmrf	BED	TCU	FCCU	39.7	13.0	0.87	s, below cwl	3/20/99		
544673	4115729	35.3	ER-EC-6[19]	1273.5 - 1258.3	Tmrf	BED	TCU	FCCU	45.9			s, below cwl	2000-2002		
544673	4115729	35.7	**ER-EC-6[19]**	1271.6 - 1240.5	**Tmrf**	**BED**	**TCU**	**FCCU**	**46.2**	**3.7**	**0.92**	s, below cwl	3/8/00	**1.73**	79.9
Handley Fault-Purse Fault (5)															
539012	4121281	28.8	PM-3#1[4]	1348.1 - 1330.5	Tmrf	NWT	TCU	UPCU	37.1	0.7	0.99	u, deep uz	12/15/99	1.16	43.1
539012	4121281	32.5	PM-3#1[4]	1330.6 - 1315.3	Tmrf	NWT,BED	TCU	UPCU	54.1	9.7		s, below cwl	2000-2002	1.53	82.8
539012	4121281	28.8	PM-3#1[4]	1326.8 - 1320.1	Tmrf	BED	TCU	UPCU	48.4	0.6	0.99	s, below cwl	12/15/99	1.73	83.8
539012	4121281	28.8	PM-3#1[4]	1320.1 - 1258.0	Tmrf	NWT	TCU	UPCU	11.6	0.5	0.96	s	12/15/99		
539012	4121281	28.8	PM-3#1[4]	1258.0 - 1241.5	Tmrf	NWT	TCU	UPCU	32.1	0.5	0.99	s	12/15/99		
539012	4121281	31.8	PM-3#2[4]	1331.2 - 1315.9	Tmrf	NWT,BED	TCU	UPCU	36.1	7.3		s, below cwl	2000-2002	1.54	55.6
541285.3	4128082	29.7	UE-20j	1521.9 - 1412.1	Tmrp	MWT	WTA	TMA	-17.4		0.92	u, deep uz	9/5/64		
541285.3	4128082	32.7	UE-20j	1406.0 - 1393.9		MWT	WTA	TMA	-0.9		0.23	s, below cwl	9/5/64		
541285.3	4128082	33.2	UE-20j	1384.7 - 1372.5	Tmrp	NWT	unk	TMA	29.7		0.98	s, below cwl	9/5/64		
541285.3	4128082	35.6	UE-20j	1369.5 - 1271.9	Tptb	BED	VTA	PVTA	27.8		0.98	s, below cwl	9/5/64	1.73	48.1
541285.3	4128082	26.1	UE-20j	1521.9 - 1409.1	Tmrp	MWT	WTA	TMA	9.5		0.82	u, deep uz	10/10/64		
541285.3	4128082	23.9	UE-20j	1406.0 - 1393.9		MWT	WTA	TMA	-38.3		0.72	s, below cwl	10/10/64		
541285.3	4128082	23.9	UE-20j	1384.7 - 1372.5	Tmrp	NWT	unk	TMA	10.2		0.50	s, below cwl	10/10/64		
541285.3	4128082	27.1	UE-20j	1369.5 - 1271.9	Tptb	BED	VTA	PVTA	32.0			s, below cwl	10/10/64		

Table A1. (continued)

E	N	UZ or cwl temp (C)	Borehole	Elev range (m)	Strat[1]	Class/ rock type[1]	HGU[1]	HSU[1]	Grad T (C/km)	Std dev (C/km)	R^2	Saturation (u,s)[2]	Temp log (date)	l (W/m C)	Est. Heat Flow (mW/m^2)
Handley Fault-Purse Fault (5), continued															
541285.3	4128082	31.4	UE-20j	1521.9 - 1470.1	Tmrp	MWT	WTA	TMA	3.0		0.10	u, deep uz	10/21/64		
541285.3	4128082	36.0	UE-20j	1467.0 - 1415.2		MWT	WTA	TMA	-1.9		0.01	u, deep uz	10/21/64		
541285.3	4128082	38.6	UE-20j	1384.7 - 1372.5	Tmrp	NWT	unk	TMA	-8.4		0.25	s, below cwl	10/21/64		
541285.3	4128082	36.9	UE-20j	1369.5 - 1271.9	Tptb	BED	VTA	PVTA	-15.7			s, below cwl	10/21/64		
NW of Handley Fault (6)															
538256.7	4133028.2	35.3	**PM-2**	1538.0 - 1407.0	**Tqu**	**BED**	**unk**	**PBRCM**	**41.8**	**3.6**	**0.90**	u, deep uz	6/6/64	**1.15**	**48.1**
538256.7	4133028.2	35.6	PM-2	1403.9 - 1367.3	Tbq	NWT	unk	PBRCM	26.9	1.4	0.67	u, deep uz	6/6/64		
538256.7	4133028.2	37.6	PM-2	1364.3 - 1303.3	Tbq	NWT	unk	PBRCM	20.4	0.4	0.99	s, below cwl	6/6/64		
538256.7	4133028.2	37.6	PM-2[20]	1538.0 - 1407.0	Tqu	BED	unk	PBRCM	34.9	0.8	0.95	u, deep uz	7/11/64		
538256.7	4133028.2	39.8	PM-2[20]	1403.9 - 1303.3	Tbq	NWT	unk	PBRCM	22.5	0.5	0.98	u, deep uz	7/11/64		
538256.7	4133028.2	40.5	PM-2[20]	1300.3 - 1275.9	Tbq	BED	unk	PBRCM	27.2	0.4	0.97	u, deep uz	7/11/64		
538256.7	4133028.2	41.4	PM-2[20]	1272.8 - 1254.6		BED		PBRCM	20.6	0.4	0.96	s, below cwl	7/11/64		
538256.7	4133028.2	51.8	PM-2[20]	1251.5 - 986.3	Tor	NWT	unk	PBRCM	38.6	0.5	1.00	s, below cwl	7/11/64	**1.42**	54.8
538256.7	4133028.2	53.3	PM-2[20]	983.3 - 949.8	Tqm	NWT	unk	PBRCM	40.4	0.4	0.99	s, below cwl	7/11/64	**1.42**	57.3
W. Greeley Fault-E. Greeley Fault (7)															
553210.6	4118447.1	30.0	ER-20-2#1	1340.4 - 1323.6	Thp	BED	TCU	CHZCM	29.5	4.0		s, below cwl	2000-2002	1.73	51.1
552668.1	4125925.1	32.4	PM-1[27]	1358.5 - 1330.4	Thp	FB	LFA	CHZCM	24.4	4.0	0.99	s, below cwl	8/3/94	1.89	46.1
552668.1	4125925.1	32.3	PM-1[27]	1359.6 - 1342.9	Thp	FB	LFA	CHZCM	44.3	5.4		s, below cwl	2000-2002	1.89	83.7
552512	4121139	26.4	U-20bg	1546.5 - 1477.4	Thp	LA	LFA	CHZCM	20.7	1.2	1.00	u, deep uz	6/22/92		
552512	4121139	29.7	U-20bg	1477.4 - 1380.7	Thp	LA	LFA	CHZCM	34.5	1.9	1.00	u, deep uz	6/22/92		
552512	4121139	30.2	**U-20bg**	1380.7 - 1361.5	**Thp**	**BED**	**TCU**	**CHZCM**	**25.2**	**1.9**	**0.97**	u, deep uz	6/22/92	**1.15**	**28.9**
552512	4121139	32.1	U-20bg	1350.1 - 1334.8	Thp	BED	TCU	CHZCM	3.3	3.3		s, below cwl	2000-2002		

Table A1. (continued)

E	N	UZ or cwl temp (C)	Borehole	Elev range (m)	Strat[1]	Class/ rock type[1]	HGU[1]	HSU[1]	Grad T (C/km)	Std dev (C/km)	R^2	Saturation (u,s)[2]	Temp log (date)	l (W/m C)	Est. Heat Flow (mW/m^2)
W. Greeley Fault-E. Greeley Fault (7), continued															
552284.5	4125130.3	25.8	UE-20ab	1487.7 - 1426.8	Thp	LA	LFA	CHVCM	24.0	1.4	0.95	u, deep uz	6/5/78	**1.95**	46.7
552284.5	4125130.3	27.1	UE-20ab	1423.7 - 1396.3	Thp	LA[29]	LFA	CHVCM	45.9	1.2	0.96	u, deep uz	6/5/78	**1.15**	52.8
552284.5	4125130.3	27.9	UE-20ab	1393.2 - 1368.9	Thp	LA[30]	LFA	CHVCM	33.1	1.3	0.91	u, deep uz	6/5/78	**1.26**	41.7
552284.5	4125130.3	28.2	UE-20ab	1365.8 - 1356.7	Thp	FB	LFA	CHVCM	16.6		0.34	u, deep uz	6/5/78		
552284.5	4125130.3	32.1	UE-20ab	1350.6 - 1268.3		FB[28]		CHVCM	23.7		1.00	s, below cwl	6/5/78	1.89	44.9
552402	4122007	30.7	UE-20bh#1[6]	1410.2 - 1389.2	Thp	BED	TCU	CHZCM	28.3	2.2	0.98	u	10/1/91		
552402	4122007	32.0	**UE-20bh#1[6]**	1389.1 - 1350.1	**Thp**	**BED**	**TCU**	**CHZCM**	**33.9**	**1.9**	**1.00**	u, deep uz	10/1/91	**1.15**	**39.0**
552402	4122007	33.6	UE-20bh#1[6]	1348.5 - 1331.0	Thp	BED	TCU	CHZCM	32.8	1.2	1.00	s, below cwl	10/1/91		
552402	4122007	34.1	UE-20bh#1[6]	1321.7 - 1306.4	Thp	BED	TCU	CHZCM	29.5	7.3		s, below cwl	2000-2002	1.73	**51.1**
Silent Canyon Struc Zone-W and E Estuary Faults (8)															
559768	4128539	22.2	**U-19aj**	1490.8 - 1435.9	Tcbx	TB	TCU	BFCU	**11.5**	**1.6**	0.74	u, deep uz	12/9/80	**1.95**	**22.3**
555857	4125371	28.7	**U-19aS**	1496.9 - 1393.2	Thp	NWT	VTA	CHVTA	**24.6**	**0.4**	0.99	u, deep uz	10/4/64	**1.16**	**28.5**
554585.6	4126723	30.8	U-19bk	1428.1 - 1412.9	unk	unk	unk	unk	9.8	3.3		s, below cwl	2000-2002		
559101	4127775	28.1	***U-19e***	*1502.4* - *1484.1*	***Tcbx***	***LA*** [30]	***LFA***	***BFCU***	***29.3***	***2.0***	***0.81***	u, deep uz	3/6/66	**1.26**	**37.0**
559101	4127775	30.1	***U-19e***	*1481.0* - *1404.8*	***Tcblp***	***NWT***	***TCU***	***BFCU***	***23.5***	***2.2***	***0.94***	u, deep uz	3/6/66	**1.16**	**27.3**
559101	4127775	34.0	U-19e	1401.8 - 1340.8	Tcblp	NWT	TCU	BFCU	6.3	0.5	0.86	s, below cwl	3/6/66		
556340	4129244	35.9	U-19g[8]	1500.8 - 1491.7	Tcu	BED	TCU	CHVCM	19.9	0.4	0.91	u	11/19/65		
556340	4129244	36.3	U-19g[8]	1488.6 - 1467.3	Tcj	BED	TCU	CFCU	15.5	0.9	0.85	u	11/19/65		
556340	4129244	37.5	**U-19g[8]**	1464.3 - 1427.7	**Tcps**	**BED**	**TCU**	**CFCU**	**28.3**	**0.9**	**0.97**	u, deep uz	11/19/65	**1.15**	**32.6**
556340	4129244	39.0	U-19g[8]	1415.5 - 1403.3	Tcg	ITL	LFA	CFCU	7.3	1.1	0.17	s, below cwl	11/19/65		

Table A1. (continued)

E	N	UZ or cwl temp (C)	Borehole	Elev range (m)	Strat[1]	Class/ rock type[1]	HGU[1]	HSU[1]	Grad T (C/km)	Std dev (C/km)	R^2	Saturation (u,s)[2]	Temp log (date)	l (W/m C)	Est. Heat Flow (mW/m^2)
E. Greeley Fault-Almendro Fault (9)															
555683.6	4120389.3	26.3	U-19bh	1426.2 - 1411.0	Tpe,Tpr	NWT[31],L	TCU	PLFA[33]	9.8	3.3		s, below cwl	2000-2002	1.49	14.6
556107	4119811	26.4	U-19f	1394.2 - 1366.7	Tpe	VT[29]	WTA	PLFA	35.6	0.7	0.97	u	7/5/68	1.15	41.0
556107	4119811	28.5	U-19f	1357.6 - 1327.1	Tpe	BED	TCU	CHCU	33.3	1.0	0.96	u	7/5/68	1.15	38.3
556107	4119811	29.1	**U-19f**	1302.7 **-** 1296.6	**Thp**	**NWT**	**TCU**	**CHCU**	**43.7**	**1.3**	**0.98**	u, deep uz	7/5/68	**1.16**	**50.7**
556107	4119811	29.7	U-19f	1293.6 - 1281.4	Thp	NWT	TCU	CHCU	22.1	1.3	0.86	s, below cwl	7/5/68	1.42	31.3
Halfbeak Fault-Moor Hen Meadow-Silent Canyon Northern Struc Zones (10)															
555488.4	4132881.8	29.2	UE-19h	1423.1 - 1407.9	Tbdl	LA	LFA	BRA	50.3	6.2		s, below cwl	2000-2002	2.16	108.7
Almendro Fault-Scrugham Peak Fault (11)															
557922	4122638	30.9	U-19i	1379.5 - 1373.4	Tcu	NWT	VTA	CHVTA	31.0	1.2	0.90	u, deep uz	8/24/67		
557922	4122638	31.1	**U-19i**	1364.3 **-** 1358.2	**Tcps**	**NWT**	**VTA**	**CFCU**	**56.5**	**1.4**	**0.88**	u, deep uz	8/24/67	**1.16**	**65.5**
557922	4122638	32.6	U-19i	1352.1 - 1336.9	Tcps	NWT	VTA	CFCU	30.8	1.4	0.98	s, below cwl	8/24/67		
557922	4122638	37.5	U-19i	1333.8 - 1208.8	Tcps	NWT	TCU	CFCU	39.2	1.4	0.99	s, below cwl	8/24/67		
Scrugham Peak Fault-Split Ridge Fault (12)															
559542	4123267	28.0	U-19p[9]	1502.4 - 1435.3		DWT,NW	WTA, TCU	BFCU	42.3	2.1	0.95	u, deep uz, hsu	10/29/75		
559542	4123267	25.9	U-19p[9]	1502.4 - 1484.1	Tcbx	DWT[30]	WTA	BFCU	26.8	2.0	0.65	u, deep uz	10/29/75	1.26	33.8
559542	4123267	26.2	U-19p[9]	1478.0 - 1471.9	Tcblr	NWT[31]	TCU	BFCU	38.3	1.1	1.00	u, deep uz	10/29/75	1.16	44.4
559542	4123267	26.6	**U-19p[9]**	1468.8 **-** 1459.7	**Tcblp**	**NWT[31]**	**TCU**	**BFCU**	**42.7**	**1.4**	**0.95**	u, deep uz	10/29/75	**1.16**	**49.5**
559542	4123267	27.6	U-19p[9]	1453.6 - 1444.4	Tcblp	NWT[31]	TCU	BFCU	27.3	1.4	1.00	u, deep uz	10/29/75	1.16	31.7
559542	4123267	29.9	U-19p[9]	1429.2 - 1161.0	Tcblp	NWT	TCU	BFCU	8.0	1.4	0.97	s, below cwl	10/29/75		

Table A1. (continued)

E	N	UZ or cwl temp (C)	Borehole	Elev range (m)	Strat[1]	Class/ rock type[1]	HGU[1]	HSU[1]	Grad T (C/km)	Std dev (C/km)	R^2	Saturation (u,s)[2]	Temp log (date)	l (W/m C)	Est. Heat Flow (mW/m^2)
Halfbeak Fault-Rickey Fault-Moor Hen Meadow Struc Zone (13)															
560900.4	4127416.2	26.4	U-19bj	1493.4 - 1478.1	Tcpk	LA	LFA	KA	8.2	2.8		s, below cwl	2000-2002	2.16	17.7
		28.9	**U-19t**	1554.7 **-** 1414.4	**Tcpk**	**"FB"**	**LFA**	**KA**	**28.2**	**3.4**	**0.99**	u, deep uz	9/27/93	**1.95**	**55.0**
		29.6	U-19t	1414.3 - 1409.3	Tcpk	"FB"	LFA	KA	122.5	2.3	1.00	u, deep uz	9/27/93		
		32.1	U-19t	1408.2 - 1384.8	Tcpk	"FB"	LFA	KA	65.7	4.2	1.00	s, below cwl	9/27/93		
		33.6	U-19t	1384.8 - 1364.8	Tcpk	"FB"	LFA	KA	70.8	4.8	0.99	s	9/27/93		
560339	4124702	34.7	**UE-19cWW[7]**	1477.1 **-** 1448.9	**Tcps**	**BED**	**TCU**	**CFCU**	**38.8**	**1.2**	**1.00**	u,17-20 m above cwl	11/13/92	**1.15**	**44.6**
560339	4124702	34.8	UE-19cWW[7]	1448.9 - 1442.5	Tcps	BED	TCU	CFCU	20.3	1.0	0.99	u,11-14 m above cwl	11/13/92		
560339	4124702	34.8	UE-19cWW[7]	1435.1 - 1430.2	Tcps	BED	TCU	CFCU	5.5	0.9	0.89	u, deep uz	11/13/92		
560339	4124702	31.9	UE-19cWW[7]	1430.5 - 1415.2	Tcps	NWT	TCU	BFCU	43.7	6.2		s, below cwl	2000-2002	1.42	62.1
560339	4124702	34.8	UE-19cWW[7]	1426.2 - 1419.1	Tcbr	NWT	TCU	BFCU	7.2	1.1	0.96	s, below cwl	11/13/92		
Split Ridge Fault-Rainier Mesa/Ammonia Tanks Caldera Topographic Margin (14)															
567542	4114743	18.7	**ER-19-1**	1582.1 - 1565.5		**BED**	**TCU**	**PBRCM**	**56.1**	**4.9**	**0.89**	u, deep uz	11/17/93	**1.15**	**64.5**
567542	4114743	18.3	ER-19-1	1582.1 - 1571.1	Tn3D	BED	TCU	PBRCM	65.3	5.6	0.79	u, deep uz	11/17/93		
567542	4114743	18.7	ER-19-1	1571.0 - 1565.5	Ton2	BED	TCU	PBRCM	75.1	3.1	0.96	u, deep uz	11/17/93		
567542	4114743	21.9	ER-19-1	1561.9 - 1533.0	Ton2	BED	TCU	PBRCM	18.3	1.6	0.96	s, below cwl	11/17/93		
567542	4114743	27.1	ER-19-1#1	1326.6 - 1311.3	Tor	BED	TCU	PBRCM	26.3	10.7		s, below cwl	2000-2002	1.73	45.4
567542	4114743	22.7	ER-19-1#2	1508.5 - 1493.2	Ton2	NWT	TCU	PBRCM	26.3	5.4		s, below cwl	2000-2002	1.42	37.3
567542	4114743	22.0	ER-19-1#3	1564.8 - 1549.6	Ton2	BED	TCU	PBRCM	3.3	16.4		s, below cwl	2000-2002		
569000.3	4112499	22.6	HTH-1[34]	1427.4 - 1331.7	Toy	BED	unk	PBRCM	17.1	3.4	0.94	s, below cwl	8/19/91	1.73	29.6
569000.3	4112499	23.2	HTH-1[34]	1330.1 - 1298.1	Tor	PWT	WTA	PBRCM	22.2	3.3	0.78	s, below cwl	8/19/91	1.66	36.8

Table A1. (continued)

E	N	UZ or cwl temp (C)	Borehole	Elev range (m)	Strat[1]	Class/ rock type[1]	HGU[1]	HSU[1]	Grad T (C/km)	Std dev (C/km)	R^2	Saturation (u,s)[2]	Temp log (date)	l (W/m C)	Est. Heat Flow (mW/m^2)
E of Thirst Canyon Lineamint-S of Silent Canyon caldera Structural Margin (15)															
538421	4110841	18.6	ER-EC-2A[12]	1300.7 - 1286.9	Tfbw	VL	LFA	FCCM	83.3	9.5	0.99	u, deep uz	2/7/00		
538421	4110841	20.1	ER-EC-2A[12]	1286.8 - 1266.7	Tfbw	PL	LFA	FCCM	74.8	10.6	0.99	u, deep uz	2/7/00		
538421	4110841	22.8	ER-EC-2A[12]	1266.7 - 1237.3	Tfbw	BED	TCU	FCCM	88.7	14.1	0.99	u, deep uz	2/7/00		
538421	4110841	32.6	ER-EC-2A[12]	1262.5 - 1236.0	Tfbw	BED	TCU	FCCM	19.4	1.1	0.98	u, deep uz	2/9/00	1.15	22.3
538421	4110841	25.9	ER-EC-2A[12]	1237.2 - 1176.4	Tfbw	BED	TCU	FCCM	53.2	10.6	0.96	s, below cwl	2/7/00		
538421	4110841	36.0	ER-EC-2A[12]	1236.0 - 1095.0	Tfbw	BED	TCU	FCCM	25.6	1.2	0.91	s, below cwl	2/9/00		
538421	4110841	35.7	ER-EC-2A[12]	1176.2 - 1166.7	Tfbw	BED	TCU	FCCM	605.2	51.6	0.68	s, below cwl	2/7/00		
538421	4110841	36.3	ER-EC-2A[12]	1166.6 - 1094.9	Tfbw	BED	TCU	FCCM	6.2	14.6	0.37	s, below cwl	2/7/00		
538421	4110841	31.8	ER-EC-2A[13]	#REF! - #REF!	Tfbw	BED	TCU	FCCM	19.7			s, below cwl	2000-2002	1.73	34.1
538701.8	4104136.9	28.2	ER-EC-5[25]	1225.5 - 1212.7	Tmar	DWT-VT	WTA	TMCM	16.5		0.89	s, below cwl	6/7/00	1.86	30.6
538701.8	4104136.9	28.4	ER-EC-5[25]	1212.2 - 1186.4	Tmar	MWT	WTA	TMCM	17.5		0.96	s, below cwl	6/7/00	1.78	31.2
538701.8	4104136.9	26.9	ER-EC-5[25]	1237.5 - 1222.3	Tmar	DWT-VT	WTA	TMCM	26.2	14.2		s, below cwl	2000-2002		
Ammonia Tanks Caldera Struc Margin-W of Scrugham Peak Fault (16)															
549322	4109762	23.0	UE-18r[11]	1290.8 - 1272.2	Tma	PWT	WTA	TMCM	71.2	3.7	0.96	u, deep uz	3/16/93	1.26	89.8
549322	4109762	27.1	UE-18r[11]	1268.1 - 1191.5	Tma	PWT	WTA	TMCM	18.3	1.1	1.00	s, below cwl	3/16/93	1.66	30.4
549322	4109762	26.7	UE-18r[11]	1272.2 - 1256.9	Tma	PWT	WTA	TMCM	19.7	6.6			2000-2001	1.66	32.7
549322	4109762	26.7	UE-18r[11]	1272.2 - 1256.9	Tma	PWT	WTA	TMCM	10.9	13.5		s, below cwl	2000-2002		

Table A1. (continued)

E	N	UZ or cwl temp (C)	Borehole	Elev range (m)	Strat[1]	Class/ rock type[1]	HGU[1]	HSU[1]	Grad T (C/km)	Std dev (C/km)	R^2	Saturation (u,s)[2]	Temp log (date)	l (W/m C)	Est. Heat Flow (mW/m^2)
Ammonia Tanks Caldera Struc Margin-E of Scrugham Peak Fault (17)															
555725	4106389	31.0	ER-18-2[10]	1398.8 - 1394.6	Tmawr	NWT	TCU	TMCM	55.9	5.4	0.95	u	7/14/99		
555725	4106389	34.4	ER-18-2[10]	1394.6 - 1329.3	Tmawr	PWT-DW	WTA	TMCM	48.0	9.8	0.98	u	7/14/99		
555725	4106389	36.7	ER-18-2[10]	1329.3 - 1293.4	Tmawp	BED	TCU	TMCM	64.7	6.7	1.00	u	7/14/99		
555725	4106389	37.9	ER-18-2[10]	1293.4 - 1271.4	Tmar	NWT	TCU	TMCM	59.4	8.2	0.99	u	7/14/99		
555725	4106389	38.3	ER-18-2[10]	1271.4 - 1266.8	Tmar	PWT	WTA	TMCM	99.2	5.2	0.97	u	7/14/99		
555725	4106389	40.3	ER-18-2[10]	1264.0 - 1229.4	Tmar	MWT	WTA	TMCM	52.1	8.5	0.96	u, deep uz	7/14/99	1.69	88.0
555725	4106389	45.9	ER-18-2[10]	1227.0 - 1197.0	Tmar	MWT[28]	WTA	TMCM	68.9	9.1	0.97	s, below cwl	7/14/99	1.78	122.7
555725	4106389	46.5	ER-18-2[10]	1287.8 - 1272.5	Tmar	NWT	TCU	TMCM	56.9	16.4		s, below cwl	2000-2002	1.42	80.8
E of Ammonia Tanks Caldera Struc Margin-Within Rainier Mesa Caldera Struc Margin (18)															
560804.7	4100463	25.5	ER-30-1	1276.6 - 1199.1	Tfdb	BS	LFA	FCCM	17.3	4.3	0.99	s, below cwl		2.1	36.4
560804.7	4100463	25.9	ER-30-1	1198.9 - 1175.7	Tg	NWT	TCU	FCCM	18.4	5.4	0.94	s, below cwl		1.42	26.2
559591	4109095	33.6	UE-18t[24]	1305.4 - 1299.7	Tfbw	BED	TCU	FCCM	34.6	2.7	0.44	s, 20ftbelow	12/12/99	1.73	59.8
559591	4109095	34.0	UE-18t[24]	1293.6 - 1273.1	Tmar	MWT	WTA	TMCM	32.4	1.6	0.96	s, below cwl	12/12/99	1.78	57.7
E of Thirst Canyon Lineamint-Hogback Fault-Ammonia Tanks Caldera Struct Margin (19)															
532763.8	4106141.8	22.8	ER-EC-8	1266.0 - 1247.8	Tfb	NWT	TCU	FCCM	53.9		0.98	u, deep uz	7/22/99	1.16	62.6
532763.8	4106141.8	25.2	ER-EC-8	1247.7 - 1222.2	Tfb	BED	TCU	FCCM	88.5		0.99	u, deep uz	7/22/99	1.15	101.8
532763.8	4106141.8	36.1	ER-EC-8	1222.4 - 1207.1	Tfb	BED	TCU	FCCM	85.3	14.2		s, below cwl	2000-2002	1.73	147.6
W of Thirst Canyon Lineamint-SW of Silent Canyon Caldera Struc Margin (20)															
532760	4112356	21.2	ER-EC-4	1297.7 - 1263.4	Ttr	NWT	VTA	TCVA	51.6	8.0	1.00	u, deep uz	6/2/99		
532760	4112356	22.1	ER-EC-4	1263.3 - 1250.2	Ttr	PWT	WTA	TCVA	60.1	6.6	0.97	u, deep uz	6/2/99	1.26	75.7
532760	4112356	22.5	ER-EC-4	1250.2 - 1243.5	Ttr	MWT	WTA	TCVA	75.6	7.0	0.96	u, deep uz	6/2/99	1.69	127.7
532760	4112356	23.0	ER-EC-4	1243.5 - 1237.4	Ttr	PWT-MW	WTA	TCVA	78.8	7.9	0.93	u, deep uz	6/2/99	1.69	133.2
532760	4112356	23.8	**ER-EC-4**	1237.4 - 1222.9	**Ttr**	**BED**	**VTA**	**TCVA**	**55.0**	**7.6**	**0.98**	u, deep uz	6/2/99	**1.15**	**63.3**
532760	4112356	35.8	ER-EC-4	1216.0 - 1180.2	Ttr	MWT,NWT,PW		TCVA	29.8	6.7	0.66	s, below cwl	6/2/99		

Table A1. (continued)

E	N	UZ or cwl temp (C)	Borehole	Elev range (m)	Strat[1]	Class/ rock type[1]	HGU[1]	HSU[1]	Grad T (C/km)	Std dev (C/km)	R^2	Saturation (u,s)[2]	Temp log (date)	l (W/m C)	Est. Heat Flow (mW/m^2)
W of Thirst Canyon Lineamint-SW of Silent Canyon Caldera Struc Margin (20), continued															
532760	4112356	36.7	ER-EC-4[14]	1222.5 - 1207.4	Ttr	BED,NW	VTA,W	TCVA[33]	70.0	17.2		s, below cwl	2000-2002	1.66	115.9
532760	4112356	36.6	ER-EC-4[14]	1215.7 - 1210.2	Ttr	MWT	WTA	TCVA	22.6		0.89	s, below cwl	8/25/00		
532760	4112356	36.8	ER-EC-4[14]	1209.6 - 1188.8	Ttr	NWT	VTA	TCVA	7.1		0.62	s, below cwl	8/25/00		
532760	4112356	36.2	ER-EC-4[15]	1297.7 - 1263.4	Ttr	NWT	VTA	TCVA	62.2	8.7	0.98	u, deep uz	6/14/99		
532760	4112356	36.7	ER-EC-4[15]	1263.3 - 1250.2	Ttr	PWT	WTA	TCVA	50.1	13.7	0.89	u, deep uz	6/14/99		
532760	4112356	37.3	ER-EC-4[15]	1250.2 - 1243.5	Ttr	MWT	WTA	TCVA	74.4	9.4	0.90	u, deep uz	6/14/99		
532760	4112356	37.6	ER-EC-4[15]	1243.5 - 1237.4	Ttr	PWT-MW	WTA	TCVA	35.7	10.2	0.74	u, deep uz	6/14/99		
532760	4112356	37.4	ER-EC-4[15]	1237.4 - 1222.5	Ttr	BED	VTA	TCVA	-15.5	56.3	0.47	u, deep uz	6/14/99		
532760	4112356	43.5	ER-EC-4[15]	1216.0 - 1210.0	Ttr	MWT	WTA	TCVA	14.4	8.2	0.40	s, below cwl	6/14/99		
532760	4112356	43.4	ER-EC-4[15]	1209.9 - 1188.7	Ttr	NWT	VTA	TCVA	-7.9	8.1	0.72	s, below cwl	6/14/99		
Claim Canyon Caldera Struc Margin (21)															
546483.5	4093127.3	19.1	ER-EC-7	1333.3 - 1237.0	Tfbw	LA	LFA	FCCM	20.7		0.97	u, deep uz	8/8/99	1.95	40.3
546483.5	4093127.3	23.9	ER-EC-7	1236.6 - 1221.3	Tfbw	LA	LFA	FCCM	6.6	6.6		s, below cwl	2000-2002		
Oasis Valley (22)															
526298.8	4094586.9	21.6	ER-OV-3a2	1122.9 - 1107.6	Tf	MWT	WTA	DVCM	21.3	12.6		s, below cwl	2000-2002	1.78	38.0
526298.8	4094586.9	19.9	ER-OV-3a3[32]	1154.2 - 1138.9	Tf	PWT-MW	WTA	DVCM	27.9	5.4		s, below cwl	2000-2002	1.66	46.3
526298.8	4094586.9	20.5	ER-OV-3a[32]	1154.3 - 1139.0	Tf	PWT-MW	WTA	DVCM	41.0	12.6		s, below cwl	2000-2002	1.66	68.1
531007.6	4097776.6	23.7	ER-OV-3b	1184.5 - 1169.3	Tgs	AL	AA	AA	16.4	7.3		s, below cwl	2000-2002	1.4	23.0
520280.1	4099808.5	19.6	ER-OV-5[32]	1190.5 - 1176.0	Tgs	AL	AA	AA	22.6	9.7		s, below cwl	2000-2002	1.4	31.6

Table A1. (continued)

E	N	UZ or cwl temp (C)	Borehole	Elev range (m)	Strat[1]	Class/ rock type[1]	HGU[1]	HSU[1]	Grad T (C/km)	Std dev (C/km)	R^2	Saturation (u,s)[2]	Temp log (date)	l (W/m C)	Est. Heat Flow (mW/m^2)
Oasis Valley (22), continued															
528416.7	4104084.1	24.3	ER-OV-1[32]	1235.9 - 1220.6	Tf	LA[29,30]	LFA	FCCM	218.7	29.5		s, below cwl	2000-2002	1.66	363.1
526310	4098715.8	19.5	ER-OV-2[32]	1174.1 - 1158.8	Tgs	AL	AA	AA	15.3	11.2		s, below cwl	2000-2002	1.4	21.4
525671.4	4089315.7	22.8	ER-OV-4a[32]	1057.0 - 1042.4	Tgs	AL	AA	AA	36.1	7.3		s, below cwl	2000-2002	1.4	50.5
528416.9	4104084.5	23.6	ER-OV-6a[32]	1236.8 - 1222.1	Tf	LA[29]	LFA	FCCM	219.4	27.5		s, below cwl	2000-2002	1.73	379.6
528416.9	4104084.5	23.4	ER-OV-6a2[32]	1235.6 - 1223.4	Tf	LA[29,30]	LFA	FCCM	172.0	28.0		s, below cwl	2000-2002	1.66	285.6
535494.2	4094374.1	24.0	ER-OV-3c	1212.3 - 1197.1	Tma	↓WT-PW	VTA	TMA	47.6	7.2		s, below cwl	2000-2002	1.42	67.6
535494.2	4094374.1	24.0	ER-OV-3c2	1212.3 - 1197.1	Tma	↓WT-PW	VTA	TMA	44.3	9.7		s, below cwl	2000-2002	1.42	62.9

[1]Explanation of abbreviations can be found at the end of this attachment.
[2]u - unsaturated zone, s - saturated zone, uz - unsaturated zone, cwl - composite water level in well
[3]Cased to 1449 m depth.
[4]Cased to 653.8 m depth.
[5]Cased to 950 m depth on 1/22/96.
[6]Cased to 590.1 m depth on 8/27/91.
[7]Cased to 737.9 m depth.
[8]Cased to 978.5 m depth in 1/65.
[9]Cased to 921.1 m depth.
[10]Cased to 653.2 m depth in 4/99.
[11]Cased to 496.5 m depth.
[12]Cased to 415.7 m depth.

Table A1. (continued)

[13]Borehole gravel packed and casing perforated over three intervals betweeen depths of 498.3-681.5 m, 922-1081.6 m, and 1344.1-1511.9 m
[14]Casing perforated over three intervals between depths of 301.5-372.1 m, 582.2-686.7 m, and 945.9-1037.8 m
[15]Cased to 263.7 m depth.
[17]Casing perforated over three intervals between depths of 700.4-860 m, 1020.3-1146.2 m, and 1355.9-1447.6 m
[16]Cased to 667.4 m depth.
[18]Cased to 485.1 m depth.
[19]Casing perforated over four intervals between depths of 496.3-570 m, 668.9-764 m, 1047.8-1161.5 m, and 1347.4-1494.6 m
[20]Casing set to 762 m depth on 6/7/64
[21]Borehole gravel packed and casing perforated over two intervals between depths of 742.8.4-843.4 m and 858-898.2 m
[22]Borehole gravel packed and casing perforated over two intervals between depths of 735.8-840.3 m and 851.3-897.6 m
[23]Borehole gravel packed and casing perforated between 755.9-855.6 m depth
[24]Cased to 577.9 m depth.
[25]Borehole gravel packed and casing perforated over three intervals between depths of 361.8-439.8, 565.2-654.1, and 677.5-755.9 m.
[26]Cased to 590.4 m depth.
[27]Cased to 2299.1 m depth.
[28]Large rise in temperature at cwl suggests warm water convecting in along FB or LFA
[29]Alteration is vitric, bedded.
[30]Alteration is devitrified.
[31]Alteration is zeolitic.
[32]Shallow temperature measurement. Depth of measurement interval less than 35 m deep.
[33]Harmonic mean used to calculate λ.
[34]Casing set to 1131.1 m depth; casing perforated over five intervals between depths of 582.2-598 m, 622-625 m, 645-655 m,

Table A2. Depth and elevation range, hydrostratigraphic unit, and temperature gradients for deepest borehole temperatures. Depth intervals with deepest borehole temperature are shown in bold.

E	N	Deep bh temp (C)	Borehole	Diff from TD (m)	Elev range (m)	Strat[1]	Class/ rock type[1]	HGU[1]	HSU[1]	Grad T (C/km)	Std dev (C/km)	R^2	Total depth (m)	Temp log (date)	Sat l (W/m C)	Est. Heat Flow (mW/m^2)
Purse Fault-W. Boxcar Fault (1)																
546386	4119208	36.7	ER-20-5#1	31.5	1112.8 - 1073.6	unk	unk (NWT)	TCU	CHZCM (TSA)	7.4	1.0	0.97	860.5	11/3/95		
546386	4119208	36.5	ER-20-5#1	35.1	1112.8 - 1077.2	unk	unk (NWT)	TCU	CHZCM (TSA)	7.3	0.9	0.98	860.5	11/3/95		
546386	4119208	**36.7**	ER-20-5#1	31.5	1075.7 - **1073.6**	unk	unk (NWT)	TCU	CHZCM (TSA)	60.6	1.1	0.99	860.5	11/3/95	1.42	86.1
546385	4119177	43.0	ER-20-5#3[2]	*204.8*	829.0 - 798.5	Thp	LA	LFA	CHZCM	15.6	5.0	0.93	1308.8	2/6/96		
546385	4119177	44.6	ER-20-5#3[2]	*130.7*	798.5 - 724.5	Thp	PL	TCU	CHZCM	20.1	3.8	0.99	1308.8	2/6/96		
546385	4119177	47.9	ER-20-5#3[2]	70.7	724.5 - 664.4	Thp	NWT	TCU	CHZCM	59.4	4.4	0.97	1308.8	2/6/96	1.42	84.3
546385	4119177	49.9	ER-20-5#3[2]	14.6	664.4 - 608.4	Thr[24]	NWT	TCU	CHZCM	40.9	4.5	0.96	1308.8	2/6/96	1.42-2.1	58-85.8
546385	4119177	**49.8**	ER-20-5#3[2]	14.5	608.4 - **608.3**	unk	unk	TCU	CHZCM				1308.8	2/6/96		
546699	4120478	45.0	U-20c#1	*137.1*	660.2 - 588.6	Thp	LA	LFA	CHZCM	6.2	0.7	0.98	*1463.0*	9/27/68		
546699	4120478	45.4	U-20c#1	*125.1*	588.7 - 576.5	Thp	LA	LFA	CHZCM	39.1	0.7	0.98	*1463.0*	9/27/68		
546699	4120478	**48.2**	U-20c#1	30.4	576.4 - **481.9**	Th	BED	TCU	CHZCM	28.5	1.1	0.99	*1463.0*	9/27/68	1.73	49.4
546699	4120478	38.5	U-20c	*124.9*	660.1 - 576.3	Thp	LA	LFA	CHZCM	19.8	0.8	0.98	1463.0	4/5/65		
546699	4120478	**39.9**	U-20c	*0.0*	576.3 - **451.4**	Th	BED	TCU	CHZCM	13.4	0.6	0.97	1463.0	4/5/65		
546103	4122301	40.5	U-20d	*107.3*	933.3 - 735.2	Thp	BED	TCU	CHZCM	16.5	0.3	1.00	1277.7	1/31/67	1.73	28.6
546103	4122301	41.3	U-20d	32.9	735.2 - 660.8	Thr[24]	NWT	TCU	CHZCM	9.9	0.2	0.99	1277.7	1/31/67	2.10	20.8
546103	4122301	41.4	U-20d	9.7	660.8 - 637.6	Thp	LA	LFA	CHZCM	7.0	0.2	0.94	1277.7	1/31/67		
546103	4122301	**41.4**	U-20d	9.7	637.6 - **637.6**	Thp	LA	LFA	CHZCM				1277.7	1/31/67		
546651	4119291	32.9	U-20y	12.8	1160.3 - 1126.8	Tptm	NWT	unk	TSA	59.5	0.6	0.99	793.1	1/2/75	1.42	84.4
546651	4119291	**33.5**	U-20y	0.6	1126.8 - **1114.6**	Tptm	NWT	unk	TSA	25.7	0.3	0.98	793.1	1/2/75	1.42	36.5

Table A2. (continued)

E	N	Deep bh temp (C)	Borehole	Diff from TD (m)	Elev range (m)	Strat[1]	Class/ rock type[1]	HGU[1]	HSU[1]	Grad T (C/km)	Std dev (C/km)	R^2	Total depth (m)	Temp log (date)	Sat l (W/m C)	Est. Heat Flow (mW/m^2)
Purse Fault-W. Boxcar Fault (1), continued																
546103	4122275	39.5	UE-20d	*198.8*	748.0 - 735.8	Thp	BED	TCU	CHZCM	13.9	0.2	0.94	1369.2	7/28/64	1.73	24.0
546103	4122275	40.4	UE-20d	*124.4*	735.8 - 661.4	Thr[24]	NWT	TCU	CHZCM	12.1	0.3	0.99	1369.2	7/28/64	2.10	25.3
546103	4122275	40.6	UE-20d	*101.2*	661.4 - 638.3	Thr[24]	LA	LFA	CHZCM	11.5	0.3	0.94	1369.2	7/28/64	2.10	24.2
546103	4122275	43.4	UE-20d	37.2	638.3 - 574.2	Thr[24]	LA	LFA	CHZCM	15.4	0.4	0.99	1369.2	7/28/64	2.10	32.3
546103	4122275	**44.1**	UE-20d	3.7	552.9 - **540.7**	Thr[24]	LA	LFA	CHZCM	119.8	1.0	0.99	1369.2	7/28/64	2.10	251.5
546102.7	4122275.252	**46.1**	UE-20d	0.9	**537.7**	[5]Total borehole grad T				24.3			1369.5	8/14/64		
545400.83	4124900.362	**121.0**	UE-20f	*431.6*	**-1876**	[5]Total borehole grad T				28.9			4171.5	6/25/64		
W. Boxcar Fault-Boxcar Fault (2)																
548110.45	4129980.729	53.9	UE-20e#1	*382.5*	370.9 - 352.7	Tct,Tbd	NWT,LCU,LF	BRA[17,18]		29.4	1.7	0.68	1949.2	6/2/64	2.66	78.1
548110.45	4129980.729	**57.2**	UE-20e#1	59.4	**29.6**	[5]Total borehole grad T				23.6			1949.2	5/27/64		
Boxcar Fault-W. Greeley Fault (3)																
551362.94	4123691.827	30.8	ER-20-6#1[13]	*324.4*	1329.2 - 1322.5	Tpe	BED	TCU	LPCU	60.1	1.4	0.98	975.4	5/1/96	1.73	104.0
551362.94	4123691.827	31.0	ER-20-6#1[13]	*320.2*	1322.5 - 1318.3	Tpr	BED	TCU	LPCU	62.6	2.0	0.96	975.4	5/1/96	1.73	108.4
551362.94	4123691.827	32.6	ER-20-6#1[13]	*301.3*	1318.2 - 1299.4	Thp	BED	TCU	CHZCM	91.3	2.6	0.99	975.4	5/1/96	1.73	158.0
551362.94	4123691.827	32.0	ER-20-6#1[13]	*233.4*	1235.9 - 1231.5	Thp	LA	LFA	CHZCM	11.9	0.5	0.95	975.4	5/1/96	1.66	19.7
551362.94	4123691.827	**34.2**	ER-20-6#1	65.1	1075.6 - **1063.2**	Thp	BED	TCU	CHZCM	2.0		0.20	975.4	3/8/96		
551333.24	4121743.043	**41.1**	U-20a2	0.0	**601.7**	[5]Total borehole grad T				20.7			1371.6	2/17/64		
550191.74	4124986.54	**50.0**	UE-20h	3.7	**-194.5**	[5]Total borehole grad T				17.1			2196.7	8/16/64		

Table A2. (continued)

E	N	Deep bh temp (C)	Borehole	Diff from TD (m)	Elev range (m)	Strat[1]	Class/ rock type[1]	HGU[1]	HSU[1]	Grad T (C/km)	Std dev (C/km)	R^2	Total depth (m)	Temp log (date)	Sat [1] (W/m C)	Est. Heat Flow (mW/m^2)
S of Silent Canyon caldera structural margin-N of Timber Mountain caldera topographic margin (4)																
541730	4117660	59.2	ER-EC-1	*190.6*	535.1 - 503.2	Tcpe	PL	TCU	CFCM	39.2	11.5	0.99	1524.0	4/20/99		
541730	4117660	61.8	ER-EC-1	*118.3*	503.1 - 430.9	Tcpe	LA/FB	LFA	CFCM	37.0	9.2	1.00	1524.0	4/20/99		
541730	4117660	62.1	ER-EC-1	*103.6*	430.9 - 416.2	Tcpe	VL	LFA	CFCM	26.6	9.5	0.94	1524.0	4/20/99		
541730	4117660	61.8	ER-EC-1	67.4	416.2 - 380.0	Tcpe	PL	TCU	CFCM	-7.2	11.3	0.25	1524.0	4/20/99		
541730	4117660	61.7	ER-EC-1	54.6	380.0 - 367.2	Tcpe	BED	TCU	CFCM	-12.8	8.9	0.71	1524.0	4/20/99		
541730	4117660	**62.4**	ER-EC-1	18.6	367.2 - **331.2**	Tcpk	FB	LFA	CFCM	21.7	9.2	0.90	1524.0	4/20/99		
541730	4117660	57.3	ER-EC-1[8]	*191.1*	535.1 - 503.7	Tcpe	PL	TCU	CFCM	51.4	5.7	0.97	1524.0	2/17/00	1.66	85.3
541730	4117660	57.8	ER-EC-1[8]	*182.3*	503.1 - 494.9	Tcpe	LA/FB	LFA	CFCM	40.7	5.9	0.64	1524.0	2/17/00	2.16	87.9
544673	4115729	61.7	ER-EC-6[9]		576.5 - 529.3	Thr[24]	NWT	TCU	CHCU	43.2	8.7	0.99	1524.0	3/20/99	1.42-2.41	61.4-104.2
544673	4115729	62.9	ER-EC-6[9]		529.2 - 501.3	Thr[24]	NWT	TCU	CHCU	43.4	7.1	0.97	1524.0	3/20/99	1.42-2.41	61.7-104.7
544673	4115729	59.2	ER-EC-6[9]	*295.7*	501.2 - 480.0	Tcpe	PL	TCU	CFCM	44.4	10.1	0.96	1524.0	3/20/99	1.66-2.82	73.6-125.1
544673	4115729	60.0	ER-EC-6[9]	*271.3*	479.9 - 455.6	Tcpe	LA	LFA	CFCM	39.9	11.7	0.95	1524.0	3/20/99	2.16-2.81	86.1-112.0
544673	4115729	62.4	ER-EC-6[9]	*221.1*	455.5 - 405.3	Tcpe	PL	TCU	CFCM	44.1	8.2	0.99	1524.0	3/20/99	1.66-2.82	73.2-124.4
544673	4115729	65.4	ER-EC-6[9]	*163.1*	405.2 - 347.4	Tcpe	LA	LFA	CFCM	51.6	7.9	0.99	1524.0	3/20/99	2.16-2.81	111.5-145
544673	4115729	67.6	ER-EC-6[9]	*120.8*	347.3 - 305.0	Tcpe	NWT	TCU	CFCM	57.8	9.5	0.97	1524.0	3/20/99	1.42-2.41	82.1-139.3
544673	4115729	70.8	ER-EC-6[9]	64.7	304.9 - 248.9	Tcpk	LA	LFA	CFCM	53.7	9.9	0.99	1524.0	3/20/99	2.16-2.81	116-150.9
544673	4115729	71.6	ER-EC-6[9]	43.4	248.8 - 227.6	Tcpk	PL	TCU	CFCM	43.6	9.5	0.94	1524.0	3/20/99		
544673	4115729	**72.2**	ER-EC-6[9]	11.1	227.5 - **195.3**	Tcpk	LA	LFA	CFCM	14.0	9.9	0.81	1524.0	3/20/99		
544673	4115729	52.6	ER-EC-6[10,9]	*557.9*	754.0 - 742.2	Tptm	PWT	WTA	TSA	35.8	6.5	0.77	1524.0	3/8/00	1.66-2.82	59.4-100.8
544673	4115729	55.7	ER-EC-6[10,9]	*478.9*	741.7 - 663.2	Tptm	MWT	WTA	TSA	39.5	4.7	1.00	1524.0	3/8/00	1.78-3.03	70.3-119.6
544673	4115729	61.7	ER-EC-6[10,9]	*345.1*	546.4 - 529.3	Thr[24]	NWT	TCU	CHCU	48.4	4.7	0.95	1524.0	3/8/00	1.42-2.41	68.7-116.6
544673	4115729	62.9	ER-EC-6[10,9]	*317.4*	528.8 - 501.6	Thr[24]	NWT	TCU	CHCU	45.2	4.4	0.99	1524.0	3/8/00	1.42-2.41	64.1-108.9
544673	4115729	63.9	ER-EC-6[10,9]	*295.8*	501.1 - 480.1	Tcpe	PL	TCU	CFCM	44.3	4.2	0.97	1524.0	3/8/00	1.66-2.82	73.5-124.9
544673	4115729	64.9	ER-EC-6[10,9]	*271.7*	479.5 - 455.9	Tcpe	LA	LFA	CFCM	45.1	5.5	0.97	1524.0	3/8/00	2.16-2.81	97.3-126.6
544673	4115729	67.2	ER-EC-6[10,9]	*221.2*	455.4 - 405.4	Tcpe	PL	TCU	CFCM	45.0	6.6	0.99	1524.0	3/8/00	1.66-2.82	74.7-127.0
544673	4115729	69.0	ER-EC-6[10,9]	*182.8*	404.9 - 367.1	Tcpe	LA	LFA	CFCM	46.8	14.1	0.95	1524.0	3/8/00	2.16-2.81	101-131.5

Table A2. (continued)

E	N	Deep bh temp (C)	Borehole	Diff from TD (m)	Elev range (m)	Strat[1]	Class/ rock type[1]	HGU[1]	HSU[1]	Grad T (C/km)	Std dev (C/km)	R^2	Total depth (m)	Temp log (date)	Sat l (W/m C)	Est. Heat Flow (mW/m^2)
Handley Fault-Purse Fault (5)																
539012	4121281	34.4	PM-3#1	*335.0*	1200.4 - 1189.7	Tpcm	PWT	WTA	TCA	18.1	0.5	1.00	920.2	12/15/99[3]	1.66	30.0
539012	4121281	35.3	PM-3#1	*280.2*	1189.6 - 1134.8	Tpcm	MWT	WTA	TCA	16.4	0.5	0.99	920.2	12/15/99[3]	1.78	29.1
539012	4121281	35.6	PM-3#1	*268.0*	1134.8 - 1122.6	Tpcm	PWT	WTA	TCA	24.1	0.5	0.97	920.2	12/15/99[3]	1.66	39.9
539012	4121281	**35.6**	PM-3#1	*265.7*	1122.6 - **1120.4**	Tpd	BED	TCU	LPCU	9.2	0.0	0.66	920.2	12/15/99[3]		
541285.3	4128082.007	34.3	UE-20j	*746.8*	1006.8 - 811.7	Tbq	TB	TCU	PBRCM	-0.6		0.13	1734.3	10/10/64		
541285.3	4128082.007	35.0	UE-20j	*652.3*	808.6 - 717.2	Tqj	FB	LFA	PBRCM	6.8		0.92	1734.3	10/10/64		
541285.3	4128082.007	41.6	UE-20j	*566.9*	714.1 - 631.9	Tqj	FB	LFA	PBRCM	93.1		0.97	1734.3	10/10/64		
541285.3	4128082.007	44.4	UE-20j	*490.7*	628.8 - 555.7	Tqj	NWT	unk	PBRCM	37.2		0.88	1734.3	10/10/64	1.42	52.8
541285.3	4128082.007	46.3	UE-20j	*387.1*	552.6 - 452.0	Tqc	LA	LFA	PBRCM	16.3		0.97	1734.3	10/10/64		
541285.3	4128082.007	**46.3**	UE-20j	*359.7*	442.9 - **424.6**	Tqc	NWT	TCU	PBRCM	3.6		0.26	1734.3	10/10/64		
541285.3	4128082.007	45.5	UE-20j	*338.3*	421.5 - 403.3	Tor	NWT	TCU	PBRCM	-48.7		0.91	1734.3	10/10/64		
541285.3	4128082.007	46.1	UE-20j	*347.5*	412.4	[5]Total borehole grad T				24.0			1734.3	10/10/64		
541285.3	4128082.007	38.0	UE-20j	*746.8*	1006.8 - 811.7	Tbq	TB	TCU	PBRCM	2.8	0.5	0.95	1734.3	10/21/64		
541285.3	4128082.007	38.4	UE-20j	*652.3*	808.6 - 717.2	Tqj	FB	LFA	PBRCM	4.2	0.3	0.95	1734.3	10/21/64		
541285.3	4128082.007	47.3	UE-20j	*566.9*	714.1 - 631.9	Tqj	FB	LFA	PBRCM	132.4	3.1	0.93	1734.3	10/21/64		
541285.3	4128082.007	38.3	UE-20j	*652.3*	732.4 - 717.2	Tqj	FB	LFA	PBRCM	28.6		0.97	1734.3	11/8/64		
541285.3	4128082.007	41.0	UE-20j	*566.9*	714.1 - 631.9	Tqj	FB	LFA	PBRCM	29.9		0.99	1734.3	11/8/64		
541285.3	4128082.007	43.7	UE-20j	*490.7*	628.8 - 555.7	Tqj	NWT	unk	PBRCM	36.3		0.99	1734.3	11/8/64	1.42	51.6
541285.3	4128082.007	45.4	UE-20j	*387.1*	552.6 - 452.0	Tqc	LA	LFA	PBRCM	15.6		0.91	1734.3	11/8/64		
541285.3	4128082.007	45.2	UE-20j	*359.7*	442.9 - 424.6	Tqc	NWT	TCU	PBRCM	-4.6		0.62	1734.3	11/8/64		
541285.3	4128082.007	43.1	UE-20j	*286.5*	421.5 - 351.4	Tor	NWT	TCU	PBRCM	-35.1		0.97	1734.3	11/8/64		
541285.3	4128082.007	44.0	UE-20j	*265.2*	348.4 - 330.1	Tot	NWT	TCU	PBRCM	47.1		0.96	1734.3	11/8/64		

Table A2. (continued)

E	N	Deep bh temp (C)	Borehole	Diff from TD (m)	Elev range (m)	Strat[1]	Class/ rock type[1]	HGU[1]	HSU[1]	Grad T (C/km)	Std dev (C/km)	R^2	Total depth (m)	Temp log (date)	Sat [1] (W/m C)	Est. Heat Flow (mW/m^2)
NW of Handley Fault (6)																
538256.72	4133028.18	53.7	PM-2	45.7	1251.5 - 986.3	Tor	NWT	unk	PBRCM	58.2	2.0	0.89	762	6/6/64		
538256.72	4133028.18	54.2	PM-2	9.1	983.3 - 949.8	Tqm	NWT	unk	PBRCM	15.0	0.3	0.94	762	6/6/64		
538256.72	4133028.18	51.8	PM-2[7]	*807.7*	1251.5 - 986.3	Tor	NWT	unk	PBRCM	38.6	0.5	1.00	1524	7/11/64	1.42	54.8
538256.72	4133028.18	53.3	PM-2[7]	*771.1*	983.3 - 949.8	Tqm	NWT	unk	PBRCM	40.4	0.4	0.99	1524	7/11/64	1.42	57.3
538256.72	4133028.18	56.9	PM-2	*652.3*	946.7 - 830.9	Tot	NWT	unk	PBRCM	27.8	0.7	0.97	1524	7/11/64		
538256.72	4133028.18	62.3	PM-2	*493.8*	827.8 - 672.4	Tqm	FB,LA,I	LFA	PBRCM	33.5	0.6	0.99	1524	7/11/64		
538256.72	4133028.18	63.4	PM-2	*454.2*	669.3 - 632.8	Toh	NWT	unk	PBRCM	29.4	0.2	0.99	1524	7/11/64		
538256.72	4133028.18	64.0	PM-2	*426.7*	629.7 - 605.3	Toh	FB	LFA	PBRCM	21.8	0.3	0.99	1524	7/11/64		
538256.72	4133028.18	65.5	PM-2	*329.2*	602.3 - 507.8	Toh	NWT	unk	PBRCM	15.7	0.4	0.97	1524	7/11/64		
538256.72	4133028.18	65.5	PM-2	*307.8*	504.7 - 486.5	Toh	BED	unk	PBRCM	-2.8	0.1	0.68	1524	7/11/64		
538256.72	4133028.18	**83.8**	PM-2	*1019.3*	**45.1**	[5]Total borehole grad T				43.0			2676.8	8/10/64		
W. Greeley Fault-E. Greeley Fault (7)																
552668.11	4125925.142	**65.5**	PM-1	15.2	**-381.0**	[5]Total borehole grad T				22.3			2395.1	5/1/64		
552668	4125925	40.5	PM-1	*1426.2*	1042.1 - 1029.9	Tcblr	NWT	TCU	BFCU	25.0	1.1	0.99	2395.1	8/3/94[3]	1.42-2.41	35.5-60.2
552668	4125925	41.9	PM-1	*1368.8*	1029.8 - 972.6	Tcblp	NWT	TCU	BFCU	23.6	1.4	1.00	2395.1	8/3/94[3]	1.42-2.41	33.5-56.9
552668	4125925	**42.8**	PM-1	*1327.7*	972.3 - **931.4**	Tcblp	NWT	TCU	BFCU	23.2	2.8	1.00	2395.1	8/3/94[3]	1.42-2.41	32.9-55.9
552284.53	4125130.301	32.1	UE-20ab	30.2	1265.2 - 1259.1	Thp	LA	LFA	CHVCM	8.2		1.00	777	6/5/78		
552402	4122007	36.4	UE-20bh#1	61.0	1239.5 - 1227.4	Thp	LA,DV	LFA	CHZCM	26.9	1.2	1.00	856.5	10/1/91[3]	1.66	44.6
552402	4122007	37.2	UE-20bh#1	42.8	1227.3 - 1209.1	Thp	LA,GL	LFA	CHZCM	43.5	1.2	1.00	856.5	10/1/91[3]	1.73	75.3
552402	4122007	37.5	UE-20bh#1	33.5	1209.0 - 1199.9	Thp	LA,DV	LFA	CHZCM	36.3	1.3	0.99	856.5	10/1/91[3]	1.66	60.3
552402	4122007	**38.2**	UE-20bh#1	2.8	1199.8 - **1169.2**	Thp	LA,ZE,I	LFA	CHZCM	22.6	1.1	0.98	856.5	10/1/91[3]	2.16	48.7

Table A2. (continued)

E	N	Deep bh temp (C)	Borehole	Diff from TD (m)	Elev range (m)	Strat[1]	Class/ rock type[1]	HGU[1]	HSU[1]	Grad T (C/km)	Std dev (C/km)	R^2	Total depth (m)	Temp log (date)	Sat l (W/m C)	Est. Heat Flow (mW/m^2)
Silent Canyon Struc Zone-W and E Estuary Faults (8)																
559768	4128539	**23.8**	U-19aj	0.0	1432.9 - **1429.8**	Tcblp	TB	TCU	BFCU				670.6	12/9/80		
555857	4125371	30.9	U-19aS	*104.8*	1079.3 - 1073.2	Tcblr	BED	TCU	BFCU	29.2	0.1	1.00	1092.4	10/4/64	1.73-2.94	50.5-85.7
555857	4125371	31.3	U-19aS	71.3	1070.2 - 1039.7	Tcblr	NWT	TCU	BFCU	5.5	0.9	0.50	1092.4	10/4/64		
555857	4125371	**31.3**	U-19aS	65.2	1036.6 - **1033.6**	Tcblp	NWT	TCU	BFCU				1092.4	10/4/64		
559101	4127775	41.9	U-19e[20]	*222.5*	834.8 - 792.2	Tbdl	MWT	WTA	BRA	25.0	0.5	0.99	1539.2	3/6/66		
559101	4127775	42.7	U-19e[20]	*188.9*	789.1 - 758.6	Tbdl	BED	unk	BRA	23.1	0.6	0.98	1539.2	3/6/66		
559101	4127775	44.3	U-19e[20]	*138.1*	731.2 - 706.8	Tbdl	DWT	WTA	BRA	47.7	1.7	0.93	1540.2	3/6/66		
559101	4127775	46.6	U-19e[20]	96.4	691.6 - 664.2	Tbdl	PWT	WTA	BRA	57.5	1.1	0.98	1541.2	3/6/66	1.66-2.82	95.4-162.1
559101	4127775	47.5	U-19e[20]	76.1	661.1 - 642.8	Tbdk	PWT	WTA	BRA	41.3	0.8	0.97	1542.2	3/6/66	1.66-2.82	68.5-116.4
559101	4127775	49.4	U-19e[20]	32.4	636.7 - 597.1	Tbds	LA	LFA	BRA	42.3	1.2	0.97	1544.2	3/6/66	2.16-2.81	91.5-119.0
559101	4127775	**49.2**	U-19e[20]	4.0	636.7 - **569.7**	Tbds	LA	LFA	BRA				1543.2	3/6/66		
556340	4129244	**42.2**	U-19g	*21.9*	1089.4 - **1071.1**	Tbdl	LA	LFA	BRA	9.6	0.4	0.85	1003.4	11/19/65		
559111.73	4127849.312	**46.6**	UE-19e	*342.9*	**621.5**	[5]Total borehole grad T				22.6			1830.3	8/23/64		
556306.09	4129056.774	**61.6**	UE-19gS	1.8	**-238.0**	[5]Total borehole grad T				21.3			2287.8	5/4/65		
E. Greeley Fault-Almendro Fault (9)																
556107	4119811	**30.3**	U-19f	4.3	**1226.5**	Tci	LA	LFA	IA				830.3	7/5/68		
556107.49	4119780.695	**41.1**	UE-19fs	*777.2*	**711.7**	[5]Total borehole grad T				21.0			2118.4	8/20/65		

Table A2. (continued)

E	N	Deep bh temp (C)	Borehole	Diff from TD (m)	Elev range (m)	Strat[1]	Class/ rock type[1]	HGU[1]	HSU[1]	Grad T (C/km)	Std dev (C/km)	R^2	Total depth (m)	Temp log (date)	Sat l (W/m C)	Est. Heat Flow (mW/m^2)
Halfbeak Fault-Moor Hen Meadow-Silent Canyon Northern Struc Zones (10)																
		61.1	UE-19d	*344.1*		[5]Total borehole grad T				24.3			2343.6	6/25/64		
555488	4132882	28.2	UE-19h[19]	*460.9*	1421.0 - 1398.1	Tbdl	LA	LFA	BRA	47.9	0.6	1.00	1129.3	12/15/99[3]	2.16-2.81	103.5-134.6
555488	4132882	28.3	UE-19h[19]	*457.7*	1398.1 - 1394.9	Tbdl	LA	LFA	BRA	22.6	0.6	0.99	1129.3	12/15/99[3]		
555488	4132882	28.4	UE-19h[19]	*449.9*	1394.9 - 1387.1	Tbdl	LA	LFA	BRA	13.6	0.6	1.00	1129.3	12/15/99[3]		
555488	4132882	**28.4**	UE-19h[19]	*444.7*	1387.1 - **1382.0**	Tbdl	LA	LFA	BRA	4.6	0.4	0.95	1129.3	12/15/99[3]		
555488.44	4132881.785	**31.1**	UE-19h[19]	75.9	**1013.2**	[5]Total borehole grad T				17.4			1129.3	7/31/65		
Almendro Fault-Scrugham Peak Fault (11)																
557922	4122638	40.8	U-19i[22]	*238.6*	1129.6 - 1099.1	Tcblp	NWT	TCU	BFCU	31.9	0.5	0.99	1223.1	8/24/67	1.42-2.41	45.3-76.9
557922	4122638	41.6	U-19i[22]	*214.2*	1096.1 - 1074.7	Tcbx	NWT	TCU	BFCU	34.4	0.8	0.95	1223.1	8/24/67	1.42-2.41	48.9-83.0
557922	4122638	42.2	U-19i[22]	*192.9*	1071.7 - 1053.4	Tcbx	MWT	WTA	BFCU	25.2	0.2	0.99	1223.1	8/24/67	1.78-3.03	35.8-76.3
557922	4122638	45.1	U-19i[22]	64.9	1041.2 - 925.4	Tcbx	LA	LFA	BFCU	24.5	1.0	0.96	1223.1	8/24/67		
557922	4122638	**45.6**	U-19i[22]	0.9	916.2 - **861.4**	Tcbr	NWT	TCU	BFCU	6.8	0.4	0.95	1223.1	8/24/67		
557922.26	4122592.036	**73.8**	UE-19i	9.8	**-344.1**	[5]Total borehole grad T				25.3			2438.4	9/3/65		
Scrugham Peak Fault-Split Ridge Fault (12)																
559542	4123267	**32.6**	U-19p	84.2	1429.2 - **1161.0**	Tcblp	NWT	TCU	BFCU	8.0	1.4	0.97	1026.0	10/29/75		
Halfbeak Fault-Rickey Fault-Moor Hen Meadow Struc Zone (13)																
560769	4124277	36.0	U-19c	*267.3*	1454.5 - 1442.3	Tcps	BED	TCU	CFCU				968.3	3/11/65		
560769	4124277	**35.4**	U-19c	*270.3*	1454.5 - **1445.4**	Tcps	BED	TCU	CFCU	21.7	0.2	0.98	968.3	3/11/65	1.73	37.5
		42.9	U-19t		1245.2 - 1143.0	Tcpk	"FB"	LFA	KA	49.1	1.9	1.00	588.9	9/27/93[3]	1.89	92.8
		45.1	U-19t		1143.0 - **1125.1**	Tcpk	"FB"	LFA	KA	129.0	2.6	0.99	588.9	9/27/93[3]		

Table A2. (continued)

E	N	Deep bh temp (C)	Borehole	Diff from TD (m)	Elev range (m)	Strat[1]	Class/ rock type[1]	HGU[1]	HSU[1]	Grad T (C/km)	Std dev (C/km)	R^2	Total depth (m)	Temp log (date)	Sat l (W/m C)	Est. Heat Flow (mW/m^2)
Halfbeak Fault-Rickey Fault-Moor Hen Meadow Struc Zone (13), continued																
562090.74	4129796.621	**34.4**	UE-19b1	*134.1*	**835.8**	[5]Total borehole grad T				17.4			1371.6	6/15/64		
		35.6	UE-19cWW[2]	*1828.1*	1419.1 - 1384.3	Tbdl	LA	LFA	BRA	28.5	1.2	0.98	2587.4	11/13/92[3]	2.16-2.81	61.5-80.0
		36.6	UE-19cWW[2]	*1665.7*	1238.8 - 1221.9	Tbdl	LA	LFA	BRA	34.8	1.3	0.98	2587.4	11/13/92[3]	2.16-2.81	75.1-97.7
560338.88	4124701.599	**46.6**	UE-19c	*1212.8*	**769.0**	[5]Total borehole grad T				24.6			2587.4	5/7/64		
Split Ridge Fault-Rainier Mesa/Ammonia Tanks Caldera Topographic Margin (14)																
567542	4114743	28.6	ER-19-1	*223.6*	1283.4 - 999.3	MWT,DWT,NWT,PW			PBRCM	16.5		0.99	1095.8	12/6/93[4]		
567542	4114743	31.5	ER-19-1	*153.5*	999.2 - 929.2	CZw	SLT/QT	SCU	LCCU1	40.5		0.99	1095.8	12/6/93[4]	2.23-3.9	90.3-158.0
567542	4114743	**34.8**	ER-19-1	3.7	928.8 - **779.4**	MDc	SLT	SCU	UCCU	18.8	1.4	0.99	1095.8	12/6/93[4]	3.1-3.66	58.3-68.9
569000	4112499	24.4	HTH-1[6]	*583.4*	1201.8 - 1177.7	Tor	MWT	WTA	PBRCM	45.7	4.0	0.84	1282.0	8/19/91[3]	1.78	81.3
569000	4112499	25.1	HTH-1[6]	*522.7*	1147.0 - 1117.1	Tor	MWT	WTA	PBRCM	27.0	3.8	0.80	1282.0	8/19/91[3]	1.78	48.1
569000	4112499	25.7	HTH-1[6]	*491.3*	1115.6 - 1085.7	Tor	PWT	WTA	PBRCM	17.0	2.3	0.75	1282.0	8/19/91[3]	1.66	28.1
569000	4112499	29.3	HTH-1[6]	*205.4*	1037.8 - 799.8	Tot	NWT[23]	TCU	PBRCM	12.8	3.1	0.99	1282.0	8/19/91[3]	1.42-2.41	18.2-30.9
569000	4112499	**29.8**	HTH-1[6]	*155.1*	798.3 - **749.5**	Tot	BED[23]	TCU	PBRCM	9.1	3.5	0.66	1282.0	8/19/91[3]	1.73-2.94	15.8-26.8
E of Thirst Canyon Lineamint-S of Silent Canyon caldera Structural Margin (15)																
538421	4110841	46.7	ER-EC-2A	*115.9*	282.2 - 94.0	Tmaw[1]	NWT/B	TCU	TMCM	15.2	9.4	0.99	1516.1	2/7/00	1.73-2.94	26.7-44.6
538421	4110841	46.9	ER-EC-2A	*106.1*	93.9 - 84.2	Tmaw	MWT	WTA	TMCM	13.7	13.2	0.46	1516.1	2/7/00	1.78-3.03	24.4-41.5
538421	4110841	47.3	ER-EC-2A	64.1	84.1 - 42.1	Tmaw	NWT/R	TCU	TMCM	10.0	11.7	0.79	1516.1	2/7/00	1.42-2.41	14.2-24.1
538421	4110841	48.6	ER-EC-2A	-2.6	42.1 - -24.5	Tmar	MWT	WTA	TMCM	23.9	12.1	0.97	1516.1	2/7/00	1.78-3.03	42.5-72.3
538421	4110841	**48.6**	ER-EC-2A	-2.6	**-24.5**	Tmar	MWT	WTA	TMCM				1516.1	2/7/00		
538421	4110841	48.3	ER-EC-2A	*116.1*	281.8 - 94.2	Tmaw[1]	NWT/B	TCU	TMCM	16.2	2.8	0.99	1516.1	2/9/00	1.73-2.94	28-47.7
538421	4110841	48.4	ER-EC-2A	*106.4*	93.6 - 84.5	Tmaw	MWT	WTA	TMCM	24.6	2.8	0.76	1516.1	2/9/00	1.78-3.03	43.7-74.4
538421	4110841	49.4	ER-EC-2A	64.1	83.9 - 42.1	Tmaw	NWT/R	TCU	TMCM	21.3	2.5	0.99	1516.1	2/9/00	1.42-2.41	30.2-51.2
538421	4110841	**50.5**	ER-EC-2A	11.3	41.5 - **-10.7**	Tmar	MWT	WTA	TMCM	21.1	2.1	0.99	1516.1	2/9/00	1.78-3.03	37.5-63.9

Table A2. (continued)

E	N	Deep bh temp (C)	Borehole	Diff from TD (m)	Elev range (m)	Strat[1]	Class/ rock type[1]	HGU[1]	HSU[1]	Grad T (C/km)	Std dev (C/km)	R^2	Total depth (m)	Temp log (date)	Sat l (W/m C)	Est. Heat Flow (mW/m^2)
E of Thirst Canyon Lineamint-S of Silent Canyon caldera Structural Margin (15), continued																
538702	4104334	28.6	ER-EC-5	-0.6	1117.7 - 784.9	Tmar,T	MWT	WTA	TMCM	0.9		0.68	762.0	7/5/99		
538702	4104334	**30.1**	ER-EC-5	6.0	**791.4**	Tmap	VT	WTA	TMCM				762.0	7/7/99		
538702	4104334	29.9	ER-EC-5[14]	22.6	864.5 - 808.1	Tmap	MWT-L	WTA	TMCM	0.4		0.10	762.0	6/7/00		
Ammonia Tanks Caldera Struc Margin-W of Scrugham Peak Fault (16)																
549322	4109762	35.0	UE-18r	*158.2*	442.6 - 321.0	Tmrx	NWT	VTA	TMCM	33.8	1.2	1.00	1525.2	3/16/93[3]	1.42-2.41	48-81.5
549322	4109762	36.5	UE-18r	*104.8*	321.0 - 267.6	Tmr	MWT	WTA	TMCM	27.7	1.2	1.00	1525.2	3/16/93[3]	1.78-2.82	49.2-78
549322	4109762	37.0	UE-18r	83.6	267.5 - 246.4	Tmr	VT	WTA	TMCM	23.0	1.1	1.00	1525.2	3/16/93[3]	2.01-3.42	46.2-78.6
549322	4109762	**38.5**	UE-18r	18.8	246.3 - **181.6**	Tmrx	TB	WTA	TMCM	23.2	1.1	1.00	1525.2	3/16/93[3]	1.89-3.21	43.8-74.4
Ammonia Tanks Caldera Struc Margin-E of Scrugham Peak Fault (17)																
555725	4106389	50.9	ER-18-2	*201.9*	1188.1 - 1097.2	Tmar	WT-DW	WTA	TMCM	62.1	10.4	0.99	762.0	7/14/99	2.82	175.0
555725	4106389	**52.9**	ER-18-2	35.0	963.3 - **930.2**	Tmar	WT-DW	WTA	TMCM	53.2	10.8	0.99	762.0	7/14/99	2.82	150.0
E of Ammonia Tanks Caldera Struc Margin-Within Rainier Mesa Caldera Struc Margin (18)																
560804.66	4100462.968	**28.0**	ER-30-1	*145.5*	1165.8 - **1126.9**	Tfbw	BED	TCU	FCCM	42.5	4.1	0.96	435	3/22/94	1.73	73.4
559591	4109095	37.8	UE-18t	*353.3*	1188.4 - 1146.1	Tmab	BED	TA,TC	TMCM	28.8	1.3	0.99	792.5	12/12/99[3]	1.73-2.94	49.8-84.7
559591	4109095	39.3	UE-18t	*295.3*	1143.9 - 1088.1	Tmrb	NWT	TCU	TMCM	24.4	0.9	0.99	792.5	12/12/99[3]	1.42-2.41	42.2-58.8
559591	4109095	40.0	UE-18t	*269.6*	1085.8 - 1062.4	Tmrr[24]	MWT,VT	WTA	TMCM	31.4	0.8	0.96	792.5	12/12/99[3]	1.78-2.41	54.4-75.8
559591	4109095	**42.0**	UE-18t	*215.8*	1059.9 - **1008.6**	Tmrr[24]	MWT	WTA	TMCM	35.8	6.46*	0.99	792.5	12/12/99[3]	1.78-2.41	61.9-86.2
E of Thirst Canyon Lineamint-Hogback Fault-Ammonia Tanks Caldera Struct Margin (19)																
532764	4106142	**36.9**	ER-EC-8	-10.8	**700.4**	Tmap	MWT	WTA	TMCM				609.6	7/22/99		

Table A2. (continued)

E	N	Deep bh temp (C)	Borehole	Diff from TD (m)	Elev range (m)	Strat[1]	Class/ rock type[1]	HGU[1]	HSU[1]	Grad T (C/km)	Std dev (C/km)	R^2	Total depth (m)	Temp log (date)	Sat l (W/m C)	Est. Heat Flow (mW/m^2)
W of Thirst Canyon Lineamint-SW of Silent Canyon Caldera Struc Margin (20)																
532760	4112356	51.6	ER-EC-4	*176.8*	599.1 - 564.7	Tmap	NWT	VTA	TMA	45.3	7.5	1.00	1062.8	6/14/99	1.42	64.4
532760	4112356	52.9	ER-EC-4	*151.2*	564.7 - 539.1	Tmab	BED	TCU	TMA	52.2	8.5	1.00	1062.8	6/14/99	1.73	90.3
532760	4112356	53.4	ER-EC-4	*142.4*	539.1 - 530.3	Tmrb	RWT	TCU	TMA	59.9	8.6	0.96	1062.8	6/14/99	1.73	103.7
532760	4112356	54.0	ER-EC-4	*130.8*	530.2 - 518.7	Tmrb	BED	TCU	TMA	54.4	15.6	0.93	1062.8	6/14/99	1.73	94.0
532760	4112356	54.9	ER-EC-4	*116.2*	518.6 - 504.1	Tmrp	NWT	TCU	TMA	54.6	9.6	0.98	1062.8	6/14/99	1.42	77.5
532760	4112356	56.6	ER-EC-4	74.1	504.0 - 462.0	Tmrp	PWT	WTA	TMA	42.7	8.1	1.00	1062.8	6/14/99	1.66	70.9
532760	4112356	58.1	ER-EC-4	50.9	462.0 - 438.9	Tmrp	MWT	WTA	TMA	63.7	8.4	0.98	1062.8	6/14/99	1.78	113.5
532760	4112356	58.7	ER-EC-4	44.8	438.8 - 432.8	Tmrp	VT	WTA	TMA	100.8	8.5	0.95	1062.8	6/14/99		
532760	4112356	62.0	ER-EC-4	24.7	432.7 - 412.7	Tmrp	DWT	WTA	TMA	163.8	11.8	0.98	1062.8	6/14/99	1.66	271.9
532760	4112356	62.9	ER-EC-4	20.5	412.6 - 408.4	Tmrp	VT	WTA	TMA	244.1	10.9	0.97	1062.8	6/14/99		
532760	4112356	**64.2**	ER-EC-4	7.2	408.3 - **395.1**	Tmrp	NWT	TCU	TMA	112.7	11.9	0.92	1062.8	6/14/99	1.42	160.0
532760	4112356	**64.2**	ER-EC-4	-3.5	**384.4**	Tmrp	NWT	TCU	TMA				1062.8	6/14/99		
532760	4112356	42.1	ER-EC-4[12]	*176.8*	599.1 - 564.7	Tmap	NWT	VTA	TMA	20.0	2.1	0.99	1062.8	8/25/00[3]	1.42	28.5
532760	4112356	42.6	ER-EC-4[12]	*151.4*	564.2 - 539.4	Tmab	BED	TCU	TMA	19.5	2.4	0.97	1062.8	8/25/00[3]	1.73	33.7
532760	4112356	42.7	ER-EC-4[12]	*142.4*	538.9 - 530.3	Tmrb	RWT	TCU	TMA	19.5	2.7	0.82	1062.8	8/25/00[3]		
532760	4112356	43.0	ER-EC-4[12]	*130.8*	529.8 - 518.7	Tmrb	BED	TCU	TMA	24.7	3.0	0.88	1062.8	8/25/00[3]		
532760	4112356	43.5	ER-EC-4[12]	*117.3*	518.2 - 505.2	Tmrp	NWT	TCU	TMA	37.9	2.2	0.95	1062.8	8/25/00[3]	1.42	53.8
532760	4112356	44.6	ER-EC-4[12]	74.2	503.7 - 462.1	Tmrp	PWT	WTA	TMA	22.4	3.2	0.93	1062.8	8/25/00[3]		
532760	4112356	44.8	ER-EC-4[12]	51.3	461.6 - 439.2	Tmrp	MWT	WTA	TMA	8.0	2.9	0.70	1062.8	8/25/00[3]		
532760	4112356	44.9	ER-EC-4[12]	45.3	438.8 - 433.2	Tmrp	VT	WTA	TMA	23.2	2.5	0.71	1062.8	8/25/00[3]		
532760	4112356	45.8	ER-EC-4[12]	25.0	432.7 - 412.9	Tmrp	DWT	WTA	TMA	40.1	2.1	0.96	1062.8	8/25/00[3]		
532760	4112356	46.6	ER-EC-4[12]	20.9	412.4 - 408.8	Tmrp	VT	WTA	TMA	242.1	1.9	0.99	1062.8	8/25/00[3]		
532760	4112356	46.7	ER-EC-4[12]	19.9	408.3 - 407.8	Tmrp	NWT	TCU	TMA	<3			1062.8	8/25/00[3]		
Claim Canyon Caldera Struc Margin (21)																
546484	4093127	26.9	ER-EC-7[15]	53.5	1112.6 - 1095.6	Tfbr	LA	LFA	FCCM	21.8		0.97	422.5	8/8/99		
546484	4093127	**27.3**	ER-EC-7[15]	39.6	1096 - **1081.8**	Tfb	LA	LFA	FCCM	28.4		0.94	422.5	8/8/99	2.16	61.3
546484	4093127	26.6	ER-EC-7[16]	41.5	1095.5 - 1083.7	Tfb	LA	LFA	FCCM	33.0		0.98	422.5	6/1/00		

Table A2. (continued)

[1]Explanation of abbreviations can be found at the end of this attachment
[2]Depth corrected for borehole deviation from vertical by 13.18 ^{o} at bottom of well
[3]Temperature logged more than one year after drilling
[4]Temperature logged about 5 months after drilling
[5]Blankennagel and Weir (1973): total borehole temperature gradient for all hydrostratigraphic units from surface elevation to temperature measurement depth
[6]Casing perforated over five intervals from 582.2 to 740.7 m depth; cased to 1131.1 m depth.
[7]Cased to 762 m
[8]Casing perforated over three intervals between depths of 700.4-860 m, 1020.3-1146.2 m, and 1355.9-1447.6 m. Analcime found at depth.
[9]Intense low-temperature hydrothermal alteration below the Rhyolite of Benham of the Paintbrush Group (analcime is the zeolite in minor amounts)
[10]Casing perforated over four intervals between depths of 496.3-570 m, 668.9-764 m, 1047.8-1161.5 m, and 1347.4-1494.6 m
[11]Original description: Tmx, 948-1256 m depth, landslide breccia (argillite, interbedded sediments, limestone block, intracaldera tuff breccia in zeolitized tuff matrix)
[12]Casing perforated over three intervals between depths of 301.5-372.1 m, 582.2-686.7 m, and 945.9-1037.8 m. Temperature gradients low throughout borehole, approximately one week after hydraulic tests. Is this borehole significantly affected by pumping? Is there not-yet-equilibrated borehole mixing between intervals?
[13]Casing perforated and gravel packed over two intervals between depths of 742.8.4-843,4 m and 858-898.2 m
[14]Borehole gravel packed and casing perforated over three intervals between depths of 361.8-439.8, 565.2-654.1, and 677.5-755.9 m
[15]Cased to 265.8 m
[16]Borehole gravel packed and casing perforated over two intervals between depths of 278-312.1 and 360.9-399.3 m
[17]Harmonic mean used to calculate λ
[18]Deep intracaldera thermal conductivity used to estimate heat flux
[19]Cased to 707.4 m
[20]May not have been cased to 1529 m depth at time of temperature log
[21]Cased to 737.9 m
[22]May not have been cased to 1220.4 m depth at time of temperature log
[23]Low-temperature hydrothermal alteration (analcime is the zeolite in minor amounts; chalcedony present).
[24]Basalt/mafic-rich composition

Table B1. Range of SZ thermal conductivity estimates for rock types in HSU

HSU #	Group #[1]	HSU[2]	HGU	Alteration[3]	Rock type[3]	Representative Wells Penetrating HSU[4]	Stratigraphy[3]	Dominant lithology[3]	l low (W/m C)[5]	l base (W/m C)[5]	l high (W/m C)[5]
1	1	LCCU	CCU		SLT/QTZ/SS		CZ (Wood Canyon Fm, Stirling Qtzite, Johnnie Fm)	Qtzite,silica-cemented siltst	2.23	3.9	5.8
2	2	LCA	CA		DM		DSsl	Ds,ls	4.67	4.95	5.23
3	3	UCCU	CCU/SCU		SLT	ER-19-1	MDc (Eleana Fm, Chainman Shale)	Argillite, shale, limestone	2.47	3.1	3.66
4	1	LCCU1	CCU/SCU		SLT/QTZ/SS	ER-19-1	CZ (Wood Canyon Fm, Stirling Qtzite, Johnnie Fm)	Qtzite,silica-cemented siltst	2.23	3.9	5.8
5	2	LCA3	CA		DM	HTH-1	DSsl	Ds,ls	4.67	4.95	5.23
6	4	MGCU	GCU		IN			Qtz monzonite, granodiorite	2.26	2.26	2.6
7	4	SCICU	IICU		IN			Granite	2.6	2.6	2.9
8	4	CHICU	IICU		IN			Granite, marble, argillite	2.6	2.6	2.9
9	4	CCICU	IICU		IN			Granite	2.6	2.6	2.9
10	4	RMICU	IICU		IN			Granite	2.6	2.6	2.9
11	4	ATICU	IICU		IN			Granite	2.6	2.6	2.9
12	5	BMICU	IICU		IN			Diorite	2.1	2.1	2.41

Table B1. Range of SZ thermal conductivity estimates for rock types in HSU (continued).

HSU #	Group #[1]	HSU[2]	HGU	Alteration[3]	Rock type[3]	Representative Wells Penetrating HSU[4]	Stratigraphy[3]	Dominant lithology[3]	l low (W/m C)[5]	l base (W/m C)[5]	l high (W/m C)[5]
13	6	**PBRCM**	TCU, WTA, LFA	ZE, **DV**, **QC**, AR, **AB**	NWT, BED, PWT, MWT, DWT, TB, FB, LA, IN	**PM-2, PM-3**, U-19d #2, UE-19c, UE-19gS, U-20m, UE-20f, **UE-20j**, UE-20p, **ER-19-1 #1, #2, #3, HTH-1, WW 8**	Tbgb, Tbq, Tln, Tn, Tn3D, Tn4AF, Tn4J, Tn4K, To, Toa, Toh, Ton2, Tor, Tot, Toy, Tqc, Tqh, Tqj, Tqm, Tqu, Trg, Trl, Trpd, Trr, Tub, unk	**Zeolitic tuff, devitrified tuff, lava**	1.71	2.13	2.71
14	6	**BRA**	**LFA**, **WTA,** TCU, VTA,	**DV**, ZC, ZE, **AB**, **PY, QC, KF**	LA, FB, BED, NWT, MWT, PWT, DWT, PL	PM-1**, PM-3**, U-19c, U-19d #2, U-19g, U-19e, U-19u, UE-19b, UE-19b#1, UE-19c, UE-19e, UE-19h, UE-19fS, UE-19gS, UE-19i, U-20m, UE-20f, **UE-20j**, UE-20p, UE-20e #1, **WW-8**	Tbd, **Tbdb, Tbdc, Tbdk, Tbdl, Tbds, Tbg, Tbgb, Tbgm, Tbgp, Tbgr, Tbgs, Tbq**, Tcl, Tn4JK, Trl, Trr, unk	**Lava, devitrified tuff,** zeolitic tuff	1.84	2.63	3.06
15	6	**BFCU**	**TCU**	ZE, ZC, **DV**	BED, NWT, LA	**PM-3**, PM-1, U-19ab, U-19ab#2,#3, **U-19ai**, **U-19aj,** U-19aS, **U-19ba #1,#2,#3**, U-19e, **U-19g**, U-19i, U-19p, U-19v, UE-19c, **UE-19e**, UE-19fS, **UE-19gS**, UE-19i, **UE-19z**, U-20g, U-20m, UE-20f, UE-20h	Tbdl, **Tcblp, Tcblr**, Tcbp, **Tcbr, Tcbs, Tcbx**, Tct	**Zeolitic tuff,** lava	1.57	2.61	2.95
16	7	KA	**LFA**, TCU	**DV**, **GL**, ZE, ZC	LA, FB, PL	U-19ba, U-19ba #1, #2, U-19ba #3, U-19bj, U-19t	Tcg, **Tcpk**	**Lava,** Zeolitic tuff	1.77	1.85	1.89

Table B1. Range of SZ thermal conductivity estimates for rock types in HSU (continued).

HSU #	Group #[1]	HSU[2]	HGU	Alteration[3]	Rock type[3]	Representative Wells Penetrating HSU[4]	Stratigraphy[3]	Dominant lithology[3]	l low (W/m C)[5]	l base (W/m C)[5]	l high (W/m C)[5]
17	8	CFCU	**TCU,** LFA, VTA	ZC, ZE, **DV**, **GL**	LA, NWT, BED	PM-1, U-19ab, U-19ab#2,#3, U-19ae, U-19aS, U-19aS#1, U-19c, U-19g, U-19i, U-19v, UE-19c, UE-19fS, UE-19gS, UE-19i	**Tcg, Tci, Tcj**, Tcpk, **Tcps**, Tcu, unk	**Zeolitic tuff,** lava, vitric tuff	1.43	1.61	1.79
18	7	CFCM	Mostly **LFA,** some TCU	**DV**, QF, AR, **PY**, **CH**, **ZA**, ZC	LA, FB, BED, NWT	ER-EC-1, **ER-EC-6**, U-20aa, U-20g, U-20i, UE-20e #1, UE-20f, UE-20h, UE-20j	Tcbs, Tcf, **Tci, Tcj, Tcpe, Tcpk, Tcps**, Tcu, unk	**Lava,** Zeolitic tuff	1.78	1.87	1.96
19	7	IA	**LA**	**DV, GL**, ZC	LA, MWT, FB	U-19f, UE-19fS, UE-20f	**Tci**	**Lava**	1.65	1.86	2.06
20	7	CHCU	**TCU,** LFA	ZC	NWT, BED, PL	PM-3, ER-EC-1, **ER-EC-6**, U-19f, U-19ae, UE-19fS	Tcg, **Tci, Thp, Thr, Tpe, Tpr**, Tptb	**Zeolitic tuff,** Lava	1.56	1.84	2.12
21	7	CHZCM	**LFA, TCU,** VTA	ZC, ZE, **ZA**, **DV**, **GL**	LA, FB, PL, BED	ER-20-5#1,#3, **ER-20-2#1**, U-20a, U-20a#2WW, U-20aa, U-20ah, U-20ai, U-20an, U-20ar#1, U-20aw, U-20ax, U-20ay, U-20az, U-20bd, U-20bd#1, #2, U-20be, U-20bf, U-20bg, U-20c, U-20d, U-20e, U-20e#1, U-20g, U-20i, U-20n, U-20WW, UE-20ad, UE20av, UE-20c, UE-20d, UE-20e, UE-20e#1, UE-20f, UE-20h, UE-20n#1, UE-20bh#1	Tcj, Tcu, Th, **Thp, Thr,** Tmw, Tpr, Tpt, Tptm, unk	**Zeolitic tuff, Lava**	1.67	1.81	1.95
22	7	CHVCM	**VTA, LFA,** TCU	**GL**, **DV**, ZC, **ZA**	LA, FB, NWT, BED	U-19au, U-19au#1, U-20am, UE-20ab	Tcj, Tcps, **Tcu**, **Thp**, Tpt, unk	**Vitric tuff, Lava**	1.48	1.7	1.93

Table B1. Range of SZ thermal conductivity estimates for rock types in HSU (continued).

HSU #	Group #[1]	HSU[2]	HGU	Alteration[3]	Rock type[3]	Representative Wells Penetrating HSU[4]	Stratigraphy[3]	Dominant lithology[3]	l low (W/m C)[5]	l base (W/m C)[5]	l high (W/m C)[5]
23	8	CHVTA	**VTA,** TCU	**GL**, ZC	NWT, BED, PL	U-19aS, U-19aS#1, U-19bg#1, U-19bj, U-19c, U-19v, U-19yS, UE-19i	**Tcj**, Tcpk, Tcps, **Tcu**, Th, **Thp**, Tmt, **Tpe**, Tpr, Tptb, unk	**Vitric,** zeolitic tuff	1.42	1.5	1.61
24	7	YMCFCM	**TCU, LFA**, WTA, unk	ZE, ZM, ZC, **ZA**, AR, **QC**, **AB**, **CC**, **KF**, **DV**	NWT, BED, MWT, PWT, LA	UE-29a #2	**Tcby, Tcp, Tct, Thp, Thr**	**Zeolitic tuff, Lava**	1.66	**1.86**	**2.16**
25	8	TSA	**WTA**, TCU, unk	**DV**, QF, **GL**, ZE, unk	NWT, PWT, TUF, MWT, VT	ER-EC-1, **ER-EC-6**, ER-20-5 #1, ER-20-5 #3, U-20c, U-20d, U-20y, UE-20c, UE-20d	**Tptm**	**Devitrified tuff**	1.57	1.69	1.81
26	8	LPCU	**TCU**, unk	ZE, ZC, **ZA**, QZ, QF, **PY**, **CH**, unk	NWT, BED, TB, WBE	PM-3, ER-EC-1, **ER-EC-6**, ER-20-5 #1, ER-20-6 #1, #2, #3, U-20av, U-20bd, U-20bd #1, #2, U-20c, U-20d, U-20m, U-20y, UE-20av, UE-20c, UE-20f, UE-20d	Thr, Tp, Tpcm, Tpd, Tpe, Tpr, Tptb, Tptm, Tptx	**Zeolitic tuff**	1.52	1.69	1.86
27	7	PLFA	**LFA, WTA**, TCU, VTA, unk	**DV, GL,** ZC**,** ZE, VP, AR, unk	LA, FB, PL, NWT, BED, MWT, DWT, VT, PWT, unk	U-19ad, U-19aq, U-19ar, U-19ay, U-19az, U-19bg#1, U-19bg, U-19bh, U-19yS, U-19x	**Tpe, Tpr**, Tptb, unk	**Lava, Devitrified tuff,** Zeolitic tuff, Vitric tuff	1.58	1.75	1.92
28	7	TCA	**WTA**, unk	**DV**, QF, VP, QC, QZ, ZE, unk	MWT, PWT, DWT, VT, unk, TUF	PM-3, ER-EC-1, **ER-EC-6**, ER-20-1, U-20d, U-20c, UE-20d, UE-20c, UE-20f	**Tpcm**, Tpcr	**Devitrified tuff**	1.7	1.75	1.8

Table B1. Range of SZ thermal conductivity estimates for rock types in HSU (continued).

HSU #	Group #[1]	HSU[2]	HGU	Alteration[3]	Rock type[3]	Representative Wells Penetrating HSU[4]	Stratigraphy[3]	Dominant lithology[3]	l low (W/m C)[5]	l base (W/m C)[5]	l high (W/m C)[5]
29	8	UPCU	**TCU**, VTA, LFA, unk	ZC, ZE, **GL**, QF, **KF**, unk, **OP**	NWT, BED, unk, TUF, RWT, FB, BS, TB	PM-3, ER-EC-1, **ER-EC-6**, ER-20-6#2, ER-20-6#1, U-20as, U-20bb, U-20bb#1, U-20bc, U-20bd, U-20bd#2, U-20d, UE-20d, UE-20f, UE-20n #1	Tm, Tmrf, Tmrh, Tmt, Tmw, Tp, Tpb, Tpc, Tpcm, Tpcr, Tpcx, Tpcy, Tpcyp, Tpd, Tpe, unk	**Zeolitic tuff**, Vitric tuff, Basalt, Lava	1.59	1.69	1.8
30	7	BA	**LFA**, TCU, un	**GL, DV,** ZE**,** QZ**, unk**, QF, **OP**	**LA**, PL, FB, VL	ER-EC-6, ER-EC-1, U-20ak, U-20ao, U-20bb, U-20bb #1, UE-20d, U-20d	**Tpb**	**Lava**, Devitrified tuff, Zeolitic tuff	1.7	1.9	2.11
31	8	PVTA	**VTA, WTA,** LFA, TCU, unk	**GL, DV,** ZE**,** ZC, unk, VP, AR	MWT, PWT, DWT, VT, NWT, BED, TUF, unk, RWT, BS, PL	U-19c, U-20bb, U-20bb#1, U-20m, UE-20f, UE-20j	Tm, Tmra, Tmrd, Tmrf, Tmrh, Tmt, Tp, Tpb, Tpcm, Tpd, Tpe, Tpr, Tptb, unk	**Vitric tuff, Devitrified tuff, Zeolitic tuff,** Lava**,** Basalt	1.54	1.68	1.82
32	7	PCM	**WTA, VTA,** TCU**,** LFA**,** unk, AA	**DV,** VP, **GL**, ZC, ZE, unk, AR, **CC**, **QC**, **OP**	DWT, MWT, VT, PWT, NWT, BED, LA, AL	UE-29a #2	QTa, Tpcp, Tpg, Tpp, Tptbr, Tptp, Tptr, Tpv, Tpy	**Devitrified tuff, Vitric tuff**, Zeolitic tuff, Lava, Alluvium	1.42	1.95	2.16
33	2	LCA3a									
34	8	FCCU	**TCU**	ZE	NWT, BED	ER-EC-1, ER-EC-6	**Tmrf**	**Zeolitic tuff**	1.42	1.58	1.73

Table B1. Range of SZ thermal conductivity estimates for rock types in HSU (continued).

HSU #	Group #[1]	HSU[2]	HGU	Alteration[3]	Rock type[3]	Representative Wells Penetrating HSU[4]	Stratigraphy[3]	Dominant lithology[3]	l low (W/m C)[5]	l base (W/m C)[5]	l high (W/m C)[5]
35	6	**SCVCU**	NA	NA	NA	NA	NA	NA	2.16	2.61	2.79
36	8	TMA	**WTA, VTA,** unk, TCU, LFA, ICU, AA	**unk, GL, DV,** VP, ZE, ZC, QF, QZ, **CC**, **OP**, AR, **KF**	MWT, PWT, DWT, VT, unk, TUF, WT, NWT, BED, RWT, AL, BD, LA	ER-EC-4, ER-OV-3c, ER-OV-3c2, U-20m, UE-20j, UE-20p	Tfbr, Tfbw, Tg, Tm, Tma, Tmab, Tmap, Tmar, Tmay, Tmr, Tmra, Tmrb, Tmrp, Tmrr, Tt, Ttl, Ttp, Ttt, Tyb, unk	**Devitrified tuff, Vitric tuff**, Zeolitic tuff, Lava, Alluvium	1.46	1.59	1.73
37	7	THCM	**TCU, WTA,** VTA	ZE**, GL, DV**, QZ	BED, MWT	ER-EC-1, ER-EC-6	**Tmat**	**Zeolitic tuff**, **Vitric tuff**, Devitrified tuff	1.67	1.81	1.95
38	7	THLFA	**LFA**, AA	**DV,** QZ**, GL**, ZE, unk	**LA**, VL, PL, AL	ER-EC-1, ER-EC-6	**Tmat**, Qay	**Lava**, Alluvium	1.66	1.86	2.16
39	6	**TMCM**	**TCU**, **WTA**, VTA, LFA, AA	QF**, DV**, ZE, QZ, VP, **GL**, **ZA**, QZ, **QC**, **AB**, AR, **KF**, **KA**, **CC**, **CH**, **PY**	MWT, PWT, DWT, LB, VT, NWT, BED, LA, RWT, TB, TG, TS, TSS, FB	ER-EC-2a, ER-EC-5, ER-EC-8, ER-30-1, ER-18-2, UE-18r, UE-18t	Tma, Tmab, Tmac, Tmap, Tmar, Tmat, Tmaw, Tmawp, Tmawr, Tmay, Tmr, Tmrb, Tmrr, Tmrx, Tmx	**Zeolitic tuff**, **Devitrified tuff,** Lava, Vitric tuff, Alluvium	1.7	2.79	2.98
40	7	FCA	NA	NA	NA	NA	NA	NA	1.66	1.86	2.16
41	7	FCCM	**LFA**, **TCU**, WTA, unk, VTA, AA	ZE**, DV, GL**, QZ, QF, **QC**, **CC**, **AB**, Pl, MP, **CH**, **PY**, unk, AR	MWT, PWT, NWT, TB, unk, RWT, BED, TSS, PL, LA, FB, VL, BS, TSLT, WT, AL	ER-EC-2a, ER-EC-4, ER-EC-7, ER-EC-8, ER-OV-1, ER-OV-6a, ER-OV-6a2, UE 18t	Qay, **Tf, Tfb**, Tfbb, Tfbc, **Tfbr, Tfbw**, Tfdb, Tff, Tfl, Tfu, Tg, **Tgc**, unk	**Zeolitic tuff**, **Lava**, Devitrified tuff, Vitric tuff, Basalt, Alluvium	1.58	1.74	1.89

Table B1. Range of SZ thermal conductivity estimates for rock types in HSU (continued).

HSU #	Group #[1]	HSU[2]	HGU	Alteration[3]	Rock type[3]	Representative Wells Penetrating HSU[4]	Stratigraphy[3]	Dominant lithology[3]	l low (W/m C)[5]	l base (W/m C)[5]	l high (W/m C)[5]
42	7	DVA	NA	NA	NA	NA	NA	NA	1.66	1.86	2.16
43	8	DVCM	**TCU, WTA**	**DV**, AR, QF	NWT, MWT, PWT	ER-OV-03a2, ER-OV-03a3, ER-OV-03a	**Tf**, Tma	**Devitrified tuff**	1.43	1.56	1.68
44	8	TCVA	**WTA, VTA**, LFA, unk, TCU, AA	unk**, DV**, **GL**, VP, ZE, **CC**, QF	MWT, PWT, DWT, NWT, BED, RWT, WT, TUF, ITL, LA, AL, CL	ER-EC-4	Tfb, Tfbr, Tfbw, Tftr, Tmap, Tt, Ttc, Ttcl, Ttcm, Ttg, Ttp, Ttr, Ttt, unk	**Devitrified tuff, Vitric tuff,** Lava, Zeolitic tuff, Alluvium	1.42	1.64	1.78
45	7	YVCM	**LFA, WTA,** AA	unk**, DV**, VP	AL, BS, PWT	TP/AFB1, ER-18-2, ER-EC-4	QTa, Tg, Ts, Tsc, Ty	**Devitrified tuff, Basalt,** Alluvium	1.67	1.81	1.95
46	9	AA	**AA**, VTA, WTA, LFA, TCU	unk**, GL, VP**, AR, **CC**, ZE, ZC	AL, TS, RWT, BS, NWT, BED, PWT, MWT, PWT	ER-OV-02, ER-OV-03b, ER-OV-04a, ER-OV-05	**Qa, QTa, Tg**, Tgc, **Tgs**, Tt, Tte, Ttp, Ttt, Tyo	**Alluvium**, **Devitrified tuff**, **Vitric tuff**, Zeolitic tuff, Basalt	1.33	1.44	1.44

[1]Group number used to assign lumped thermal conductivities for calibration purposes

[2]HSU in bold is more indurated, intracaldera tuff

[3]Dominant lithology, alteration, rock type, or stratigraphy in bold

[4]Borehole in bold is located outside the caldera for intracaldera HSU or inside a caldera for extracaldera HSU

[5]Tuff HSU thermal conductivity estimated from harmonic mean of tuff rock types in boreholes (Table B3)

Table B2. Estimates of SZ HSU thermal conductivity. Estimates computed from harmonic mean of SZ thermal conductivity estimates (compiled in Table B3) for rock types in boreholes penetrating HSU.

HSU	Borehole	Depth range (m)	Elevation range (m)	Thickness (m)	Harmonic mean over rock types l (W/mC)	HSU l (W/mC)	Std dev l (W/mC)	Min l (W/mC)	Max l (W/mC)	Low l (W/mC)	High l (W/mC)
LCCU											
LCA											
UCCU	ER-19-1#1	942.8 - 1095.8	928.7 - 775.7	153.0	3.10 N=3	3.10		3.10	5.45	2.47	3.66
	ER-19-1#2	942.8 - 1095.8	928.7 - 775.7	153.0	3.10						
	ER-19-1#3	942.8 - 1095.8	928.7 - 775.7	153.0	3.10						
LCCU1	ER-19-1#1	872.3 - 942.7	999.1 - 928.7	70.4	3.90 N=3	3.90		2.23	5.80		
	ER-19-1#2	872.3 - 942.7	999.1 - 928.7	70.4	3.90						
	ER-19-1#3	872.3 - 942.7	999.1 - 928.7	70.4	3.90						
LCA3	HTH-1	1127.7 - 1282.0	748.6 - 594.4	154.2	4.95 N=1	4.95		4.95	4.95	4.45	5.47
MGCU								2.26	2.60		
SCICU								2.60	4.00		2.90
CHICU								2.60	5.00		2.90
CCICU								2.60	4.00		2.90
RMICU								2.60	4.00		2.90
ATICU								2.60	4.00		2.90
BMICU								2.10	2.41		
PBRCM	ER-19-1#1	544.0 - 872.3	1327.4 - 999.1	328.3	1.66 N=13	1.71-2.13	0.14,0.58	1.42	2.94	1.58	1.85-2.71
	ER-19-1#2	359.6 - 872.3	1511.8 - 999.1	512.7	1.64						
	ER-19-1#3	306.6 - 872.3	1564.8 - 999.1	565.7	1.63						
	HTH-1	165.2 - 1127.8	1711.2 - 748.6	962.6	1.91						
	PM-2	261.7 - 2676.8	1440.9 - -974.1	2415.0	1.83						
	PM-3	914.4 - 920.2	860.5 - 854.7	5.8	1.42						
	U-19d #2	2279.9 - 2343.6	-188.7 - -252.4	63.7	1.73 - 2.94						
	UE-19c	2401.9 - 2587.4	-258.2 - -443.8	185.6	1.95 - 2.86						
	UE-19gS	2002.6 - 2286.0	45.4 - -238.0	283.4	1.63 - 2.77						
	UE-20f	2974.3 - 4171.5	-1110.1 - -2307.3	1197.2	1.76 - 2.82						
	UE-20j	761.1 - 1734.3	1038.1 - 64.9	973.2	1.60						
	UE-20p	554.8 - 1524.0	1137.8 - 168.6	969.2	1.77 - 2.84						
	WW 8	612.6 - 1676.1	1123.2 - 59.7	1063.5	1.72						

Table B2. Estimates of SZ HSU thermal conductivity (continued).

HSU	Borehole	Depth range (m)	Elevation range (m)	Thickness (m)	Harmonic mean over rock types l (W/mC)	HSU l (W/mC)	Std dev l (W/mC)	Min l (W/mC)	Max l (W/mC)	Low l (W/mC)	High l (W/mC)
BRA	PM-1	1603.3 - 2395.1	395.6 - -396.2	791.8	1.86 - 2.81 N=21	1.84-2.63	0.19,0.43	1.62	3.09	1.65-2.20	2.03-3.06
	PM-3	899.2 - 914.4	875.7 - 860.5	15.2	1.67						
	U-19c	730.0 - 968.3	1413.4 - 1175.0	238.4	2.15						
	U-19d #2	664.4 - 2279.9	1426.8 - -188.7	1615.5	1.86 - 2.73						
	U-19e	894.0 - 1539.2	1214.9 - 569.7	645.2	1.76 - 2.91						
	U-19g	858.0 - 1003.4	1194.5 - 1049.1	145.4	1.58 - 2.68						
	U-19u	661.4 - 929.6	1433.5 - 1165.3	268.2	2.14 - 2.81						
	U-20m	565.4 - 704.1	1233.8 - 1095.1	138.7	1.67 - 2.84						
	UE-19b	646.2 - 710.2	1427.1 - 1363.1	64.0	2.16 - 2.81						
	UE-19b #1	645.3 - 1371.6	1427.9 - 701.6	726.3	2.08 - 2.84						
	UE-19c	724.5 - 2401.8	1419.1 - -258.2	1677.3	1.98 - 2.84						
	UE-19e	894.0 - 1830.6	1214.9 - 278.3	936.6	1.81 - 2.89						
	UE-19fS	1552.9 - 2118.4	499.9 - -65.5	565.4	1.76 - 2.87						
	UE-19gS	807.7 - 2002.5	1240.2 - 45.4	1194.8	1.71 - 2.82						
	UE-19h	643.4 - 1129.3	1423.1 - 937.3	485.8	2.07 - 2.80						
	UE-19i	1484.3 - 2438.4	600.2 - -353.9	954.1	1.99 - 2.81						
	UE-20e #1	1548.4 - 1949.2	370.9 - -29.9	400.8	1.62 - 2.76						
	UE-20f	2521.6 - 2974.2	-657.5 - -1110.1	452.6	1.82 - 3.09						
	UE-20j	573.3 - 761.1	1225.9 - 1038.1	187.8	1.67						
	UE-20p	451.0 - 554.7	1241.5 - 1137.8	103.7	1.66 - 2.82						
	WW 8	325.3 - 612.6	1410.5 - 1123.2	287.3	1.62						

Table B2. Estimates of SZ HSU thermal conductivity (continued).

HSU	Borehole	Depth range (m)	Elevation range (m)	Thickness (m)	Harmonic mean over rock types λ (W/mC)	HSU λ (W/mC)	Std dev λ (W/mC)	Min λ (W/mC)	Max λ (W/mC)	Low λ (W/mC)	High λ (W/mC)
BFCU	PM-1	956.7 - 1603.2	1042.1 - 395.6	646.5	1.42 - 2.41 N=26	1.57-2.61	0.19,0.35	1.42	3.21	1.39-2.26	1.76-2.95
	PM-3	874.8 - 899.2	900.1 - 875.7	24.4	1.56						
	U-19ab	637.4 - 685.8	1474.3 - 1425.9	48.4	1.44 - 2.44						
	U-19ab #2	643.2 - 731.5	1468.8 - 1380.4	88.4	1.42 - 2.41						
	U-19ab #3	641.3 - 731.5	1470.7 - 1380.4	90.3	1.48 - 2.51						
	U-19ai	626.1 - 632.5	1428.9 - 1422.5	6.4	1.73 - 2.94						
	U-19aj	668.0 - 670.6	1432.4 - 1429.8	2.6	1.89 - 3.21						
	U-19aS	978.6 - 1092.4	1082.2 - 968.3	113.9	1.44 - 2.45						
	U-19ba #1	657.1 - 713.2	1487.8 - 1431.6	56.2	1.86 - 3.17						
	U-19ba #2	657.1 - 713.2	1487.8 - 1431.6	56.2	1.86 - 3.17						
	U-19ba #3	655.9 - 713.2	1489.0 - 1431.6	57.4	1.87 - 3.17						
	U-19e	678.2 - 894	1430.7 - 1214.9	215.8	1.54 - 2.61						
	U-19g	651.3 - 858	1401.2 - 1194.5	206.7	1.42 - 2.41						
	U-19i	877.8 - 1223.2	1205.8 - 860.5	345.3	1.52 - 2.59						
	U-19p	670.6 - 1026.0	1432.3 - 1076.9	355.4	1.42 - 2.41						
	U-19v	832.1 - 1082.0	1263.7 - 1013.8	249.9	1.44 - 2.44						
	U-20g	887.0 - 1280.2	1085.1 - 691.9	393.2	1.42 - 2.41						
	U-20m	537.9 - 565.4	1261.3 - 1233.8	27.5	1.73 - 2.94						
	UE-19c	714.1 - 724.5	1429.5 - 1419.1	10.4	1.42 - 2.41						
	UE-19e	698.0 - 894	1410.9 - 1214.9	196.0	1.51 - 2.56						
	UE-19fS	1460.1 - 1553	592.8 - 499.9	92.9	2.04 - 2.84						
	UE-19gS	658.6 - 807.7	1389.3 - 1240.2	112.7	1.42 - 2.41						
	UE-19i	884.0 - 1484.4	1200.6 - 600.2	600.4	1.63 - 2.77						
	UE-19z	669.8 - 853.4	1429.7 - 1246.0	183.6	1.45 - 2.46						
	UE-20f	1859.2 - 2521.6	4.9 - -657.5	662.4	1.42 - 2.41						
	UE-20h	1653.9 - 2196.4	344.7 - -197.8	542.5	1.53 - 2.60						
KA											
	U-19ba	655.9 - 663.5	1489.0 - 1481.3	7.7	1.89 N=5	1.85	0.08	1.70	1.89	1.77	1.93
	U-19ba #1	655.9 - 657.1	1489.0 - 1487.8	1.2	1.89						
	U-19ba #2	655.9 - 657.1	1489.0 - 1487.8	1.2	1.89						
	U-19bj	641.0 - 656.2	1493.4 - 1478.1	15.3	1.70						
	U-19t	588.3 - 588.9	1542.6 - 1542.0	0.6	1.89						

Table B2. Estimates of SZ HSU thermal conductivity (continued).

HSU	Borehole	Depth range (m)	Elevation range (m)	Thickness (m)	Harmonic mean over rock types l (W/mC)	HSU l (W/mC)	Std dev l (W/mC)	Min l (W/mC)	Max l (W/mC)	Low l (W/mC)	High l (W/mC)
CFCU	PM-1	886.7 - 956.8	1112.2 - 1042.1	70.1	1.93 N=14	1.61	0.18	1.42	1.96	1.43	1.79
	U-19ab	616.8 - 637.3	1494.8 - 1474.3	20.5	1.42						
	U-19ab #2	614.0 - 643.1	1497.9 - 1468.8	29.1	1.75						
	U-19ab #3	614.1 - 641.3	1497.9 - 1470.7	27.2	1.59						
	U-19ae	786.4 - 832.1	1278.6 - 1232.9	45.7	1.49						
	U-19aS	725.5 - 978.6	1335.3 - 1082.2	253.1	1.54						
	U-19aS #1	685.8 - 1005.8	1375.3 - 1055.2	320.1	1.56						
	U-19c	688.9 - 730	1454.5 - 1413.4	41.1	1.73						
	U-19g	628.0 - 651.4	1424.6 - 1401.2	23.4	1.96						
	U-19i	728.5 - 877.8	1355.1 - 1205.8	149.3	1.42						
	U-19v	719.3 - 832.1	1376.5 - 1263.7	112.8	1.44						
	UE-19c	713.1 - 714.1	1430.5 - 1429.5	1.0	1.73						
	UE-19fS	1336.5 - 1460	716.3 - 592.8	123.5	1.55						
	UE-19i	730.9 - 883.9	1353.6 - 1200.6	123.1	1.43						
CFCM	ER-EC-1	1301.5 - 1524.0	535.1 - 312.6	222.5	1.79 N=9	1.87-1.97	0.09,0.29	1.73	2.75	1.78	1.96-2.26
	ER-EC-6	1207.0 - 1524.0	501.2 - 184.2	317.0	1.87 - 2.75						
	U-20aa	1063.7 - 1294.5	867.8 - 637.0	230.8	1.86						
	U-20g	874.8 - 887	1097.3 - 1085.1	12.2	1.90						
	U-20i	1149.1 - 1434.1	792.5 - 507.5	285.0	2.08						
	UE-20e #1	1269.8 - 1548.4	649.5 - 370.9	278.6	1.88						
	UE-20f	1644.4 - 1859.3	219.8 - 4.9	214.9	1.85						
	UE-20h	2196.4 - 2196.7	-197.8 - -198.1	0.3	1.89						
	UE-20j	530.3 - 573.3	1268.9 - 1225.9	43.0	1.73						
IA	U-19f	826.0 - 830.3	1226.5 - 1222.2	4.3	1.66 N=3	1.86	0.21	1.66	2.15	1.65	2.06
	UE-19fS	850.4 - 1336.5	1202.4 - 716.3	486.1	2.15						
	UE-20f	1323.8 - 1644.4	540.4 - 219.8	320.6	1.76						
CHCU	ER-EC-1	1097.3 - 1301.5	739.3 - 535.1	204.2	2.10 N=6	1.84-1.89	0.28,0.34	1.42	2.41	1.56	2.12-2.24
	ER-EC-6	1084.5 - 1207	623.7 - 501.2	122.5	2.10 - 2.41						
	PM-3	823.0 - 874.8	951.9 - 900.1	51.8	2.12						
	U-19ae	694.9 - 786.4	1370.1 - 1278.6	91.5	1.42						
	U-19f	759.2 - 826	1293.3 - 1226.5	66.8	1.63						
	UE-19fS	731.5 - 850.4	1321.3 - 1202.4	118.9	1.68						

Table B2. Estimates of SZ HSU thermal conductivity (continued).

HSU	Borehole	Depth range (m)	Elevation range (m)	Thickness (m)	Harmonic mean over rock types l (W/mC)	HSU l (W/mC)	Std dev l (W/mC)	Min l (W/mC)	Max l (W/mC)	Low l (W/mC)	High l (W/mC)
CHZCM	ER-20-2 #1	609.4 - 768.1	1340.4 - 1181.7	158.7	1.47 - 2.24 N=42	1.81	0.14	1.60	2.24	1.67	1.95
	ER-20-5 #1	789.7 - 860.5	1112.8 - 1042.1	70.7	1.78						
	ER-20-5 #3	902.2 - 1308.8	1000.3 - 593.7	406.6	1.64						
	ER-20-6 #1	655.3 - 975.4	1318.2 - 998.2	320.0	1.79						
	ER-20-6 #2	636.1 - 975.4	1337.5 - 998.3	339.2	1.64						
	ER-20-6 #3	615.9 - 975.4	1354.9 - 995.5	359.5	1.66						
	PM-1	639.3 - 886.7	1359.6 - 1112.2	247.4	1.70						
	U-20 WW	626.2 - 996.1	1345.3 - 975.4	369.9	1.81						
	U-20a	563.9 - 774.2	1423.4 - 1213.1	210.3	1.89						
	U-20a #2 WW	629.7 - 1371.6	1343.6 - 601.7	741.9	1.83						
	U-20aa	570.1 - 1063.8	1361.5 - 867.8	493.7	1.78						
	U-20ah	609.9 - 701.0	1354.5 - 1263.4	91.1	2.16						
	U-20ai	625.4 - 656.5	1356.7 - 1325.6	31.1	2.16						
	U-20an	606.7 - 617.5	1362.9 - 1352.1	10.8	1.66						
	U-20ar #1	601.9 - 696.5	1324.1 - 1229.6	94.5	1.87						
	U-20aw	635.8 - 640.1	1371.3 - 1367.0	4.3	1.73						
	U-20ax	662.3 - 670.6	1329.9 - 1321.6	8.3	1.73						
	U-20ay	626.6 - 640.1	1361.0 - 1347.5	13.5	1.73						
	U-20az	658.3 - 685.8	1345.1 - 1317.7	27.5	1.73						
	U-20bd	646.1 - 687.3	1330.8 - 1289.6	41.2	1.73						
	U-20bd #1	630.9 - 732.1	1346 - 1244.8	101.2	1.73						
	U-20bd #2	642.2 - 746.8	1335 - 1230.5	104.5	1.73						
	U-20be	675.1 - 676.7	1304.0 - 1302.4	1.6	1.73						
	U-20bf	650.6 - 685.8	1337.3 - 1302.1	35.2	1.73						
	U-20bg	650.4 - 670.6	1351.2 - 1331.1	20.1	1.73						
	U-20c	929.6 - 1463.0	984.8 - 451.4	533.4	1.86						
	U-20d	972.3 - 1277.7	933.3 - 627.9	305.4	1.84						
	U-20e	566.9 - 1174.4	1358.2 - 750.7	607.5	1.77						
	U-20e #1	566.9 - 1064.1	1358.2 - 861.1	497.1	1.81						
	U-20g	614.8 - 874.8	1357.3 - 1097.3	260.0	1.72						

Table B2. Estimates of SZ HSU thermal conductivity (continued).

HSU	Borehole	Depth range (m)	Elevation range (m)	Thickness (m)	Harmonic mean over rock types l (W/mC)		HSU l (W/mC)	Std dev l (W/mC)	Min l (W/mC)	Max l (W/mC)	Low l (W/mC)	High l (W/mC)
CHZCM (cont)	U-20i	580.4 - 1149.1	1361.2 - 792.5	568.7	1.94							
	U-20n	634.0 - 1301.2	1340.2 - 673.0	667.2	2.02							
	UE-20ad	582.2 - 777.2	1358.2 - 1163.1	195.1	1.60							
	UE-20av	688.8 - 796.7	1279.6 - 1171.7	107.9	1.87							
	UE-20bh #1	701.0 - 856.5	1321.8 - 1166.3	155.5	1.80							
	UE-20c	892.2 - 1630.1	1022.9 - 285.0	737.9	1.79							
	UE-20d	968.6 - 1369.2	937.6 - 537.1	400.5	1.90							
	UE-20e	556.6 - 743.7	1362.1 - 1175.0	187.1	2.03							
	UE-20e #1	556.6 - 1269.8	1362.7 - 649.5	713.2	1.85							
	UE-20f	899.1 - 1323.7	965 - 540.4	424.6	1.94							
	UE-20h	641.5 - 1653.8	1357.0 - 344.7	1012.3	1.85							
	UE-20n #1	634.0 - 1005.8	1335.3 - 963.5	371.8	1.69							
CHVCM	U-19au	633.1 - 670.6	1358.5 - 1321.0	37.5	1.46	N=4	1.70	0.22	1.46	1.96	1.48	1.93
	U-19au #1	633.1 - 660.5	1358.5 - 1331.1	27.4	1.50							
	U-20am	653.0 - 670.6	1356.6 - 1339.0	17.6	1.89							
	UE-20ab	652.3 - 777.2	1353.6 - 1228.6	125.0	1.96							
CHVTA	U-19aS	673.6 - 725.4	1387.1 - 1335.3	51.8	1.42	N=7	1.50	0.11	1.42	1.73	1.39	1.61
	U-19aS #1	668.1 - 685.8	1393.0 - 1375.3	17.7	1.42							
	U-19bg #1	667.5 - 685.8	1372.8 - 1354.5	18.3	1.42							
	U-19c	533.3 - 688.8	1610 - 1454.5	155.5	1.51							
	U-19v	661.4 - 719.3	1434.4 - 1376.5	57.9	1.42							
	U-19yS	682.7 - 716.3	1357.6 - 1324.1	33.5	1.73							
	UE-19i	688.2 - 730.9	1396.3 - 1353.6	42.7	1.58							
YMCFCM	UE-29a #2	65.0 - 421.5	1150.2 - 793.7	356.5	2.16	N=1	2.16		2.16	2.16		
TSA	ER-20-5 #1	659.6 - 789.7	1242.9 - 1112.8	130.1	1.78	N=9	1.69-1.82	0.12,0.41	1.42	2.94	1.57	1.81-2.24
	ER-20-5 #3	789.7 - 902.2	1112.8 - 1000.3	112.5	1.42							
	ER-EC-1	1030.5 - 1097.3	806.1 - 739.3	66.8	1.61							
	ER-EC-6	954.0 - 1084.5	754.2 - 623.7	130.5	1.73 - 2.94							
	U-20c	792.4 - 929.6	1122 - 984.8	137.2	1.86							
	U-20d	905.2 - 972.3	1000.4 - 933.3	67.1	1.65							
	U-20y	640.0 - 793.1	1267.1 - 1114.0	153.1	1.65							
	UE-20c	792.4 - 892.1	1122.6 - 1022.9	99.7	1.76							
	UE-20d	902.3 - 968.7	1004 - 937.6	66.4	1.74							

Table B2. Estimates of SZ HSU thermal conductivity (continued).

HSU	Borehole	Depth range (m)	Elevation range (m)	Thickness (m)	Harmonic mean over rock types l (W/mC)	HSU l (W/mC)	Std dev l (W/mC)	Min l (W/mC)	Max l (W/mC)	Low l (W/mC)	High l (W/mC)
LPCU	ER-20-5 #1	626.4 - 659.6	1276.1 - 1242.9	33.2	1.73 N=19	1.69-1.71	0.17,0.23	1.42	2.41	1.52	1.86-1.94
	ER-20-5 #3	626.4 - 789.7	1276.1 - 1112.8	163.3	1.42						
	ER-20-6 #1	644.3 - 655.3	1329.2 - 1318.2	11.0	1.73						
	ER-20-6 #2	623.9 - 636.1	1349.7 - 1337.5	12.2	1.73						
	ER-EC-1	894.9 - 1030.5	941.7 - 806.1	135.6	2.10						
	ER-EC-6	827.5 - 954	880.7 - 754.2	126.5	1.99 - 2.41						
	PM-3	652.3 - 823	1122.6 - 951.9	170.7	1.50						
	U-20av	632.6 - 640.1	1337.6 - 1330.1	7.4	1.73						
	U-20bd	637.1 - 646.2	1339.9 - 1330.8	9.1	1.73						
	U-20bd #1	621.4 - 630.9	1355.5 - 1346	9.5	1.42						
	U-20bd #2	627.2 - 642.2	1350.0 - 1335	15.0	1.73						
	U-20c	749.9 - 792.5	1164.6 - 1122	42.6	1.73						
	U-20d	838.3 - 905.3	1067.4 - 1000.4	67.0	1.62						
	U-20m	515.2 - 538	1284.1 - 1261.3	22.8	1.42						
	U-20y	631.0 - 640.1	1276.2 - 1267.1	9.1	1.73						
	UE-20av	648.6 - 688.8	1319.8 - 1279.6	40.2	1.73						
	UE-20c	749.8 - 792.5	1165.3 - 1122.6	42.7	1.73						
	UE-20d	836.7 - 902.2	1069.5 - 1004	65.5	1.73						
	UE-20f	830.0 - 899.2	1034.2 - 965	69.2	1.56						
PLFA	U-19ad	667.5 - 685.8	1372.2 - 1353.9	18.3	2.16 N=10	1.75	0.17	1.55	2.16	1.58	1.92
	U-19aq	642.8 - 662.9	1429.5 - 1409.4	20.1	1.69						
	U-19ar	645.9 - 670.6	1398.4 - 1373.7	24.7	1.85						
	U-19ay	648.9 - 657.1	1396.9 - 1388.7	8.2	1.73						
	U-19az	633.7 - 649.2	1424.6 - 1409.1	15.5	1.72						
	U-19bg	645.8 - 657.5	1394.5 - 1382.9	11.6	1.89						
	U-19bg #1	645.8 - 667.5	1394.5 - 1372.8	21.7	1.55						
	U-19bh	636.7 - 654.7	1426.2 - 1408.2	18.0	1.59						
	U-19x	674.8 - 679.7	1392.0 - 1387.1	4.9	1.66						
	U-19yS	628.3 - 682.8	1412.1 - 1357.6	54.5	1.66						

Table B2. Estimates of SZ HSU thermal conductivity (continued).

HSU	Borehole	Depth range (m)	Elevation range (m)	Thickness (m)	Harmonic mean over rock types l (W/mC)	HSU l (W/mC)	Std dev l (W/mC)	Min l (W/mC)	Max l (W/mC)	Low l (W/mC)	High l (W/mC)
TCA	ER-20-1	606.2 - 629.4	1277.8 - 1254.6	23.2	1.78 N=9	1.75-1.88	0.05,0.35	1.68	2.85	1.70	1.80-2.23
	ER-EC-1	821.7 - 894.9	1014.9 - 941.7	73.2	1.73						
	ER-EC-6	734.5 - 827.5	973.7 - 880.7	93.0	1.68 - 2.85						
	PM-3	574.6 - 652.3	1200.3 - 1122.6	77.7	1.74						
	U-20c	643.1 - 749.8	1271.3 - 1164.6	106.7	1.86						
	U-20d	758.9 - 838.2	1146.7 - 1067.4	79.3	1.73						
	UE-20c	648.0 - 749.8	1267.1 - 1165.3	101.8	1.76						
	UE-20d	759.5 - 836.7	1146.7 - 1069.5	77.2	1.68						
	UE-20f	793.7 - 830	1070.5 - 1034.2	36.3	1.78						
UPCU	ER-20-6 #1	618.4 - 644.3	1355.1 - 1329.2	25.9	1.73 N=15	1.69-1.76	0.11,0.21	1.47	2.46	1.59	1.80-1.97
	ER-20-6 #2	618.6 - 623.9	1355.0 - 1349.7	5.3	1.73						
	ER-EC-1	788.5 - 821.7	1048.1 - 1014.9	33.2	1.73						
	ER-EC-6	647.5 - 734.6	1060.8 - 973.7	87.1	1.45 - 2.46						
	PM-3	789.9 - 920.2	1330.6 - 1200.3	130.3	1.56						
	U-20as	613.6 - 640.1	1284.4 - 1257.9	26.5	1.73						
	U-20bb	658.4 - 676.7	1239.3 - 1221.0	18.3	1.73						
	U-20bb #1	657.8 - 714.8	1239.9 - 1182.9	57.0	1.86						
	U-20bc	570.4 - 609.6	1302.9 - 1263.7	39.2	1.73						
	U-20bd	621.1 - 637	1355.8 - 1339.9	15.9	1.47						
	U-20bd #2	621.3 - 627.2	1355.9 - 1350.0	5.9	1.73						
	U-20d	676.7 - 759	1229 - 1146.7	82.3	1.73						
	UE-20d	676.7 - 759.6	1229.6 - 1146.7	82.9	1.73						
	UE-20f	545.3 - 793.7	1318.9 - 1070.5	248.4	1.73						
	UE-20n #1	622.2 - 634	1347.1 - 1335.3	11.8	1.73						
BA	ER-EC-1	624.8 - 788.5	1211.8 - 1048.1	163.7	1.86 N=8	1.90	0.21	1.67	2.16	1.70	2.11
	ER-EC-6	467.8 - 647.4	1240.4 - 1060.8	179.6	1.75						
	U-20ak	622.4 - 640.1	1278.0 - 1260.3	17.7	1.67						
	U-20ao	596.5 - 655.3	1317.3 - 1258.5	58.8	1.73						
	U-20bb	644.1 - 658.4	1253.6 - 1239.3	14.3	1.73						
	U-20bb #1	637.7 - 657.8	1260 - 1239.9	20.1	2.16						
	U-20d	634.1 - 676.7	1271.6 - 1229	42.6	2.16						
	UE-20d	624.9 - 676.7	1281.4 - 1229.6	51.8	2.16						

Table B2. Estimates of SZ HSU thermal conductivity (continued).

HSU	Borehole	Depth range (m)	Elevation range (m)	Thickness (m)	Harmonic mean over rock types l (W/mC)	HSU l (W/mC)	Std dev l (W/mC)	Min l (W/mC)	Max l (W/mC)	Low l (W/mC)	High l (W/mC)
PVTA	U-19c	454.2 - 533.4	1689.2 - 1610	79.2	1.61 N=6	1.68	0.14	1.42	1.86	1.54	1.82
	U-20bb	619.9 - 644	1277.7 - 1253.6	24.1	1.73						
	U-20bb #1	617.6 - 637.6	1280.0 - 1260	20.0	1.86						
	U-20m	426.7 - 515.1	1372.5 - 1284.1	88.4	1.73						
	UE-20f	537.4 - 545.3	1326.8 - 1318.9	7.9	1.42						
	UE-20j	429.8 - 530.4	1369.5 - 1268.9	100.6	1.73						
PCM	UE-29a #2	27.6 - 65	1187.6 - 1150.2	37.4	1.95 N=1	1.95		1.42	2.16		
WWA											
FCCU	ER-EC-1	482.6 - 541.9	1271.1 - 1211.8	59.3	1.42 N=2	1.58	0.16	1.42	1.73	1.42	1.73
	ER-EC-6	434.8 - 467.9	1273.5 - 1240.4	33.1	1.73						
SCVCU											
TMA	ER-EC-4	585.8 - 1062.8	864.9 - 387.9	477.0	1.68 N=6	1.59	0.13	1.42	1.77	1.46	1.73
	ER-OV-03c	65.3 - 165.2	1212.3 - 1112.4	99.9	1.42						
	ER-OV-03c2	65.4 - 97.8	1212.3 - 1179.9	32.5	1.42						
	U-20m	381.0 - 426.7	1418.2 - 1372.5	45.7	1.69						
	UE-20j	390.2 - 429.8	1409.1 - 1369.5	39.6	1.59						
	UE-20p	277.4 - 451.1	1415.2 - 1241.5	173.7	1.77						
THCM											
THLFA											
TMCM	ER-18-2	369.4 - 762.0	1287.9 - 895.2	392.6	1.76 - 2.99 N=7	1.70-2.79	0.12,0.20	1.49	3.03	1.57-2.59	1.82-2.98
	ER-30-1	365.1 - 434.6	1051.3 - 981.8	69.5	1.78 - 3.03						
	ER-EC-2A	961.6 - 1516.1	532.5 - -21.9	554.4	1.49 - 2.54						
	ER-EC-5	309.9 - 762.0	1237.5 - 785.5	452.1	1.78 - 2.96						
	ER-EC-8	421.3 - 609.6	899.6 - 711.3	188.3	1.56 - 2.65						
	UE-18r	415.8 - 1525.2	1272.2 - 162.8	1109.4	1.64 - 2.79						
	UE-18t	286.1 - 792.5	1299.2 - 792.8	506.4	1.86 - 2.54						
FCA											

Table B2. Estimates of SZ HSU thermal conductivity (continued).

HSU	Borehole	Depth range (m)	Elevation range (m)	Thickness (m)	Harmonic mean over rock types l (W/mC)	HSU l (W/mC)	Std dev l (W/mC)	Min l (W/mC)	Max l (W/mC)	Low l (W/mC)	High l (W/mC)
FCCM	ER-30-1	137.5 - 365.2	1279.0 - 1051.3	227.7	1.90 N=9	1.74	0.15	1.45	2.02	1.58	1.89
	ER-EC-2A	229.9 - 961.6	1264.2 - 532.5	731.7	1.60						
	ER-EC-4	499.8 - 585.8	950.9 - 864.9	86.0	1.73						
	ER-EC-7	228.1 - 422.5	1236.6 - 1042.2	194.4	2.02						
	ER-EC-8	98.4 - 421.2	1222.4 - 899.6	322.8	1.45						
	ER-OV-01	5.5 - 54.9	1235.9 - 1186.5	49.3	1.74						
	ER-OV-06a	4.9 - 163.4	1236.6 - 1078.1	158.5	1.78						
	ER-OV-06a2	5.7 - 21.6	1235.6 - 1219.7	15.9	1.70						
	UE-18t	278.7 - 286.1	1306.6 - 1299.2	7.4	1.73						
DVA											
DVCM	ER-OV-03a	17.5 - 76.5	1154.3 - 1095.3	59.0	1.73 N=3	1.56	0.12	1.46	1.73	1.43	1.68
	ER-OV-03a2	48.7 - 250.2	1122.9 - 921.3	201.5	1.46						
	ER-OV-03a3	17.4 - 250.2	1154.1 - 921.3	232.8	1.48						
TCVA	ER-EC-4	228.2 - 499.9	1222.6 - 950.9	271.7	1.64 N=1	1.64		1.42	1.78		
YVCM											
AA	ER-OV-02	8.6 - 61.0	1174.1 - 1121.8	52.3	1.44 N=4	1.44		1.44	1.44		
	ER-OV-03b	105.6 - 121.9	1184.5 - 1168.2	16.3	1.44						
	ER-OV-04a	7.3 - 46.0	1056.9 - 1018.2	38.7	1.44						
	ER-OV-05	9.7 - 61.0	1190.5 - 1139.3	51.2	1.44						

Table B3. Thermal properties by lithology as reported for NTS and other rock types

	Extra Caldera				Intracaldera[3]			
Rock type	λ (W/m C)	Std dev	N	Source	λ (W/m C)[4]	Std dev	N	Source
Unsaturated zone								
Tuffaceous ss[1]	1.2			Sass et al. (1987), Bodvarrson et al. (2003)				
NWT	1.16	0.5	9	Sass et al. (1987, tables 3-1 to 3-4)				
PWT	1.26	0.37	6	Sass et al. (1987, tables 3-1 to 3-4)				
BT	1.15	0.12	4	Sass et al. (1987, tables 3-1 to 3-4)				
MWT	1.69	0.17	4	Sass et al. (1987, tables 3-1 to 3-4)				
V/WT	1.95	0.27	33	Sass et al. (1987, tables 3-1 to 3-4)				
WT, DV[2]	1.1		1	Moss et al. (1982)				
NWT, ZE[2]	0.68		1	Moss et al. (1982)				
Saturated zone								
Granite	1.7-4.0			Gillespie (2003)				
Granitic pluton	2.9			Lin et al. (2000)				
Diabase	2.1			Gillespie (2003)	2.41[6]			
Granodiorite	2.6			Gillespie (2003)				
LCA	4.95	0.28	13	Gillespie (2003)				
UCCU	2.47,3.1	0.56	18	Sass et al. (1980)				
Quartzite	5.8,4.5-7.1			Gillespie (2003)				
Qtz Monzonite	2.26	0.02	6	Morgan et al. (1996)				
Muddy ss	2.23			Gillespie (2003)				
Argillite	3.3			Gillespie (2003)				
Tuffaceous ss[3]	1.44				2.38			
Clay,ss,gravel (unconsolidated volcanic alluvium)	1.33-1.83			Olmsted and Rush (1987)				
Siltstone	1.91-2.15			Gillespie (2003)				
NWT	1.42	0.31	15	Gillespie (2003)	2.41			
PWT	1.66	0.29	37	Gillespie (2003)	2.82			
BT	1.73	0.45	8	Gillespie (2003)	2.94			
MWT	1.78	0.2	19	Gillespie (2003)	3.03			
WT	1.86	0.08	2	Gillespie (2003)	3.16			
FB	1.89	0.35	7	Gillespie (2003)	3.21			
V/WT	2.01	0.09	4	Gillespie (2003)	3.42			
WT, DV[2]	1.6		1	Moss et al. (1982)				
NWT, ZE[2]	1.1		1	Moss et al. (1982)				
MWT-WT[5]	1.75		16	Lappin & Nimick (1982)				
Rhyolitic Lava	2.16	0.24	7	Gillespie (2003)	3.67			
Qtz-rich WT**	1-1.2			Morgan et al. (1996)	2.52	0.11	4	Morgan et al. (1996)

[1]Calico Hills Formation [2]Grouse Canyon Tuff, BRA

[3]Alluvium (sandy gravel); gravel consists of welded tuff and rhyolite lava clasts. Sandy matrix is tuffaceous, partly zeolitized with quartz; λ assumed ~1.2 times UZ Calico Hills tuffaceous sandstone of Bodvarrson et al. (2003)

[4]Intracaldera thermal conductivities increase by 1.7 to 2.9 times flanking tuff units (Morgan et al.,1996), due to high degree of hydrothermal induration

[5]Average thermal conductivity of Grouse Canyon Tuff, BRA (porosity< 0.2)

[6]Estimate of indurated mafic-rich tuff/lava (with alteration minerals pyrite and chalcopyrite) assumed less than NWT

Table B4. Other thermal properties as reported for NTS and other areas

Rock type	Est. Heat flow (mW/m^2)	Matrix porosity	Heat capacity (J/kg C)	Density (g/cm^3)	SZ λ (W/m K)	Std dev	N	Source
Background NTS (Basin and Range)	85							Sass et al. (1995)
Granite	91			2.65				Turcotte and Schubert (1982, p.145)
Diorite				2.8				
BMICU				2.8				Bechtel Nevada (2002)
Basalt				2.9				
Granitic pluton		0.01	837		2.9			Olmsted and Rush (1987)
(MWT-WT) Grouse Canyon Tuff		0.1-0.2		2.58-2.65	1.75		16	Lappin and Nimick (1982)
TSA (TSw1)			718-972-922[1]					Brodsky et al. (1997)
TSA (TSw2)			814-1114-1086[1]					Brodsky et al. (1997)
Valles Caldera			950					Bodvarrson et al. (1982)

[1]Varies with temperature

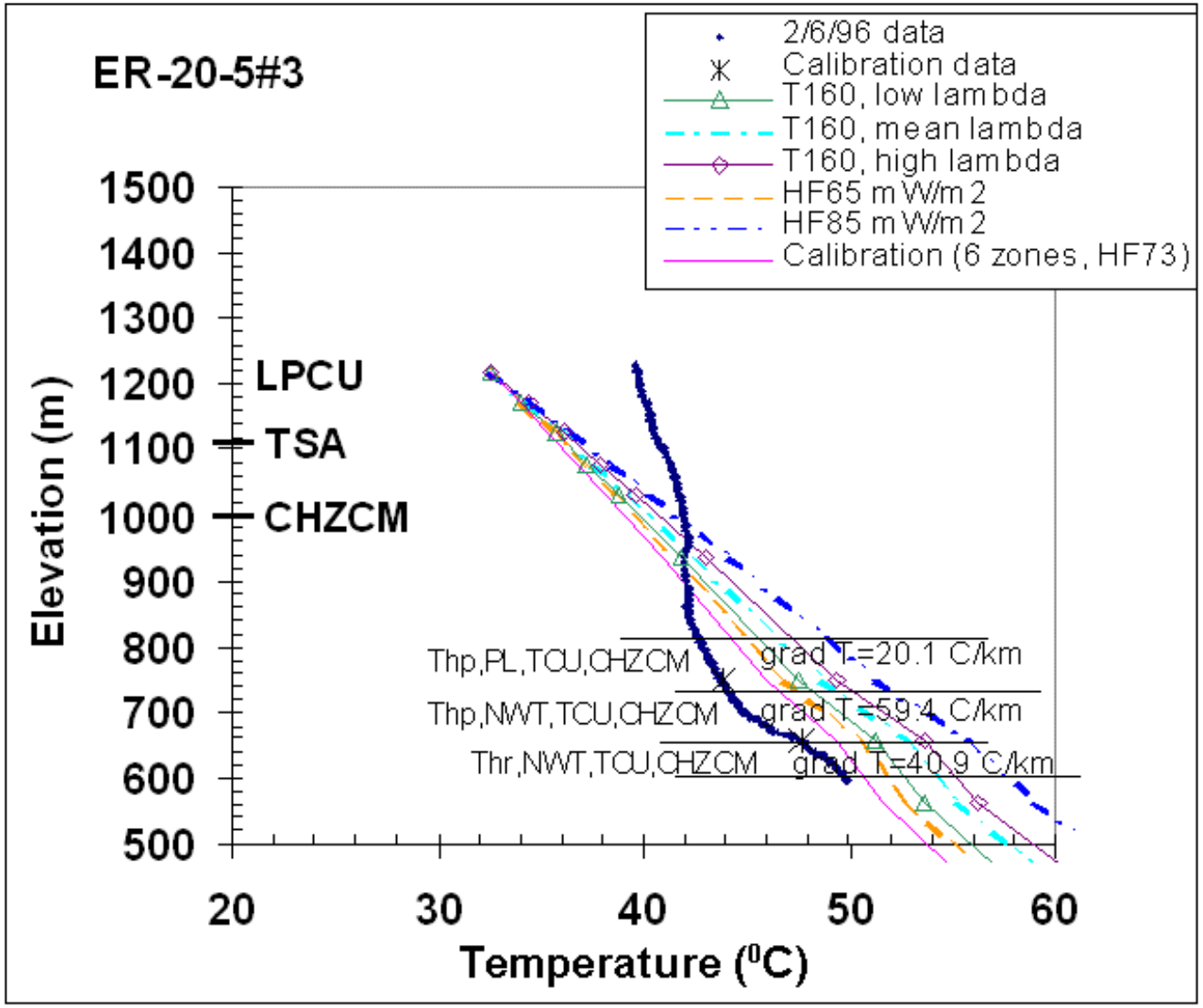
ER-20-5#3
2/6/96 data
Calibration data
T160, low lambda
T160, mean lambda
T160, high lambda
HF65 mW/m2
HF85 mW/m2
Calibration (6 zones, HF73)
1500
1400
1300
1200
1100
1000
900
800
700
600
500
LPCU
TSA
CHZCM
Elevation (m)
Thp,PL,TCU,CHZCM grad T=20.1 C/km
Thp,NWT,TCU,CHZCM grad T=59.4 C/km
Thr,NWT,TCU,CHZCM grad T=40.9 C/km
20
30
40
50
60
Temperature (0C)

Figure C1

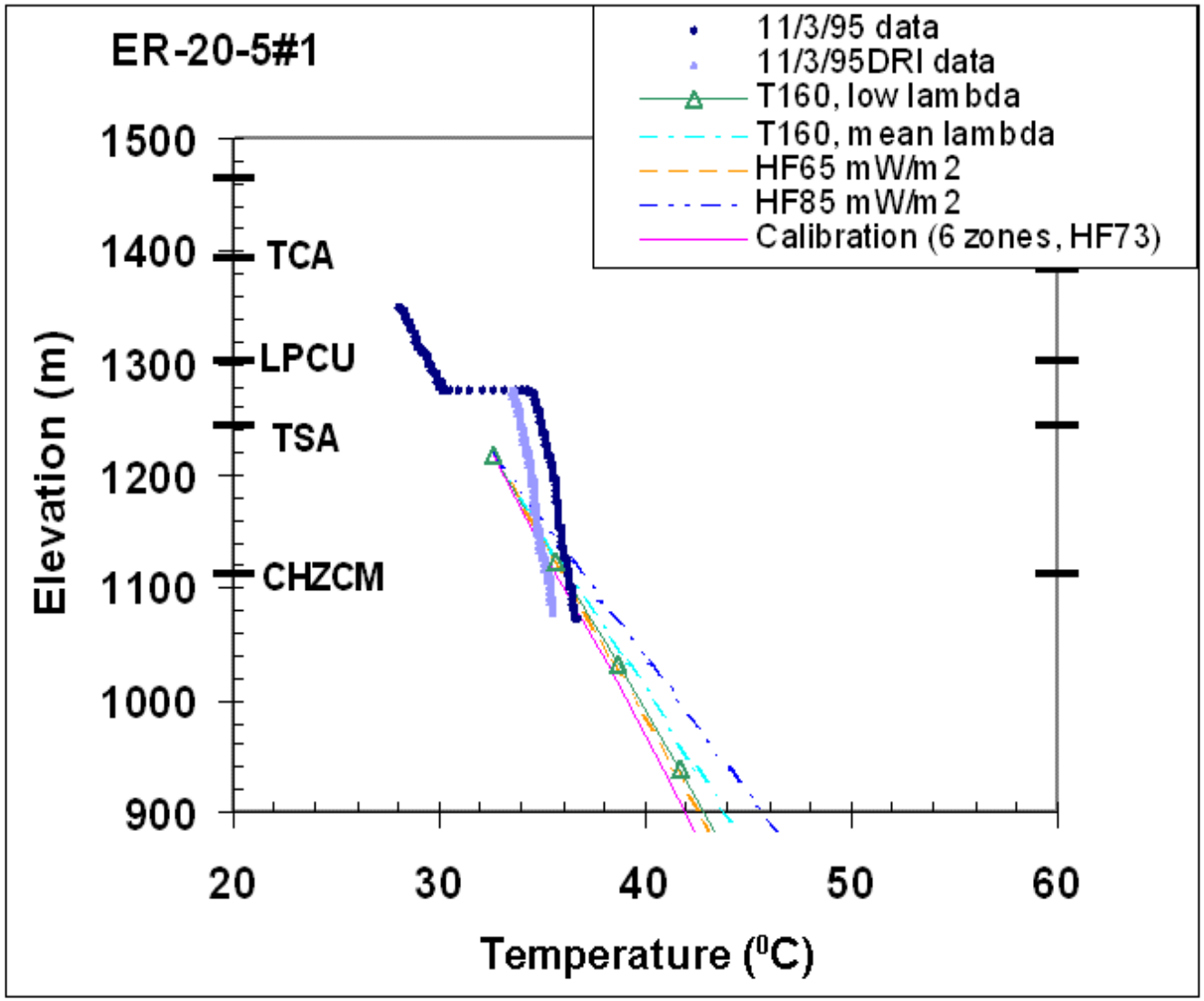
ER-20-5#1
11/3/95 data
11/3/95DRI data
T160, low lambda
T160, mean lambda
HF65 mW/m2
HF85 mW/m2
Calibration (6 zones, HF73)
1500
1400
1300
1200
1100
1000
900
TCA
LPCU
TSA
CHZCM
Elevation (m)
20
30
40
50
60
Temperature (0C)

Figure C2

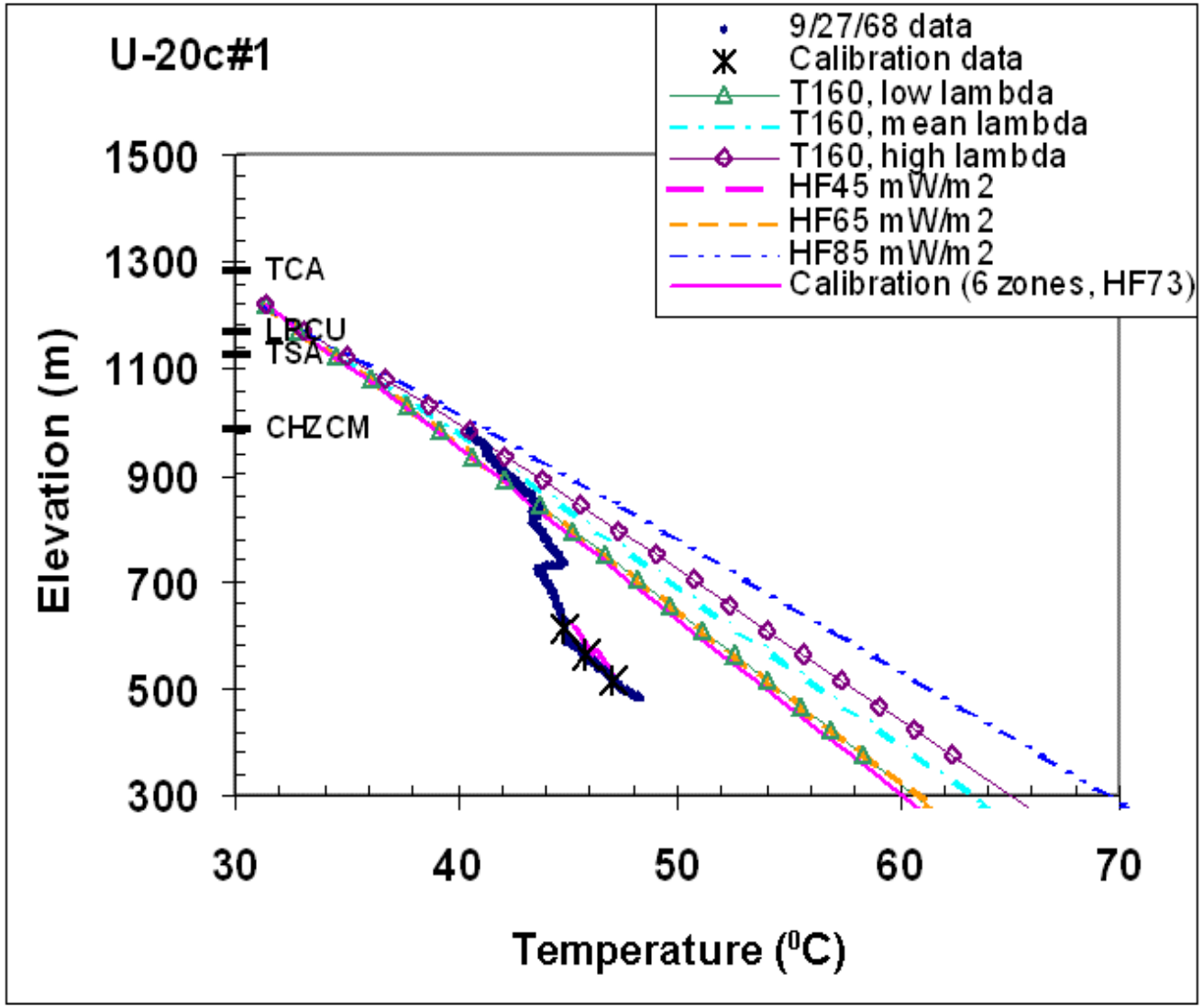
U-20c#1
9/27/68 data
Calibration data
T160, low lambda
T160, mean lambda
T160, high lambda
HF45 mW/m2
HF65 mW/m2
HF85 mW/m2
Calibration (6 zones, HF73)
1500
1300
1100
900
700
500
300
TCA
LRCU
TSA
CHZCM
Elevation (m)
30
40
50
60
70
Temperature (⁰C)

Figure C3

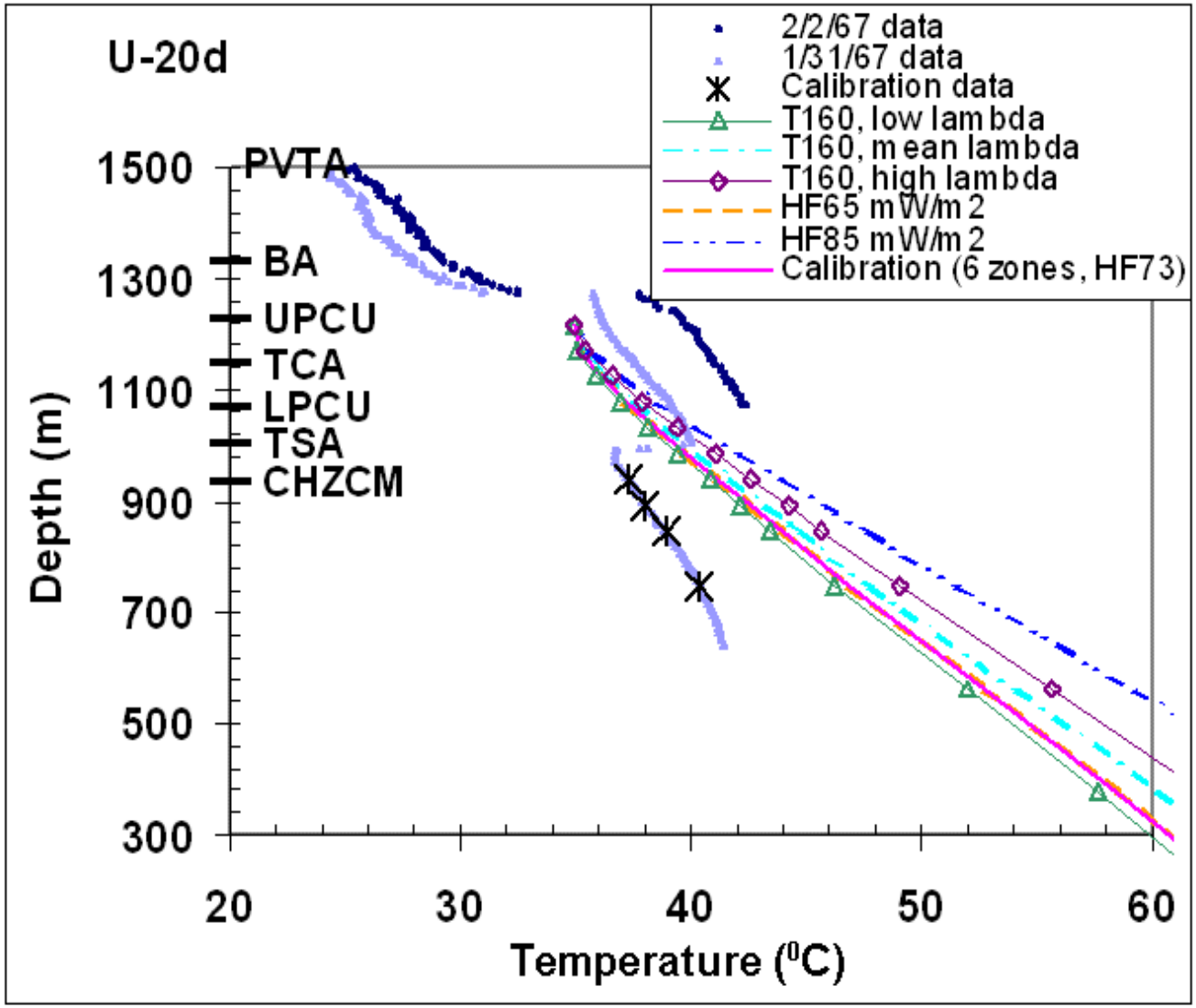
U-20d
2/2/67 data
1/31/67 data
Calibration data
T160, low lambda
T160, mean lambda
T160, high lambda
HF65 mW/m2
HF85 mW/m2
Calibration (6 zones, HF73)
PVTA
BA
UPCU
TCA
LPCU
TSA
CHZCM
Depth (m)
1500
1300
1100
900
700
500
300
20
30
40
50
60
Temperature (0C)

Figure C4

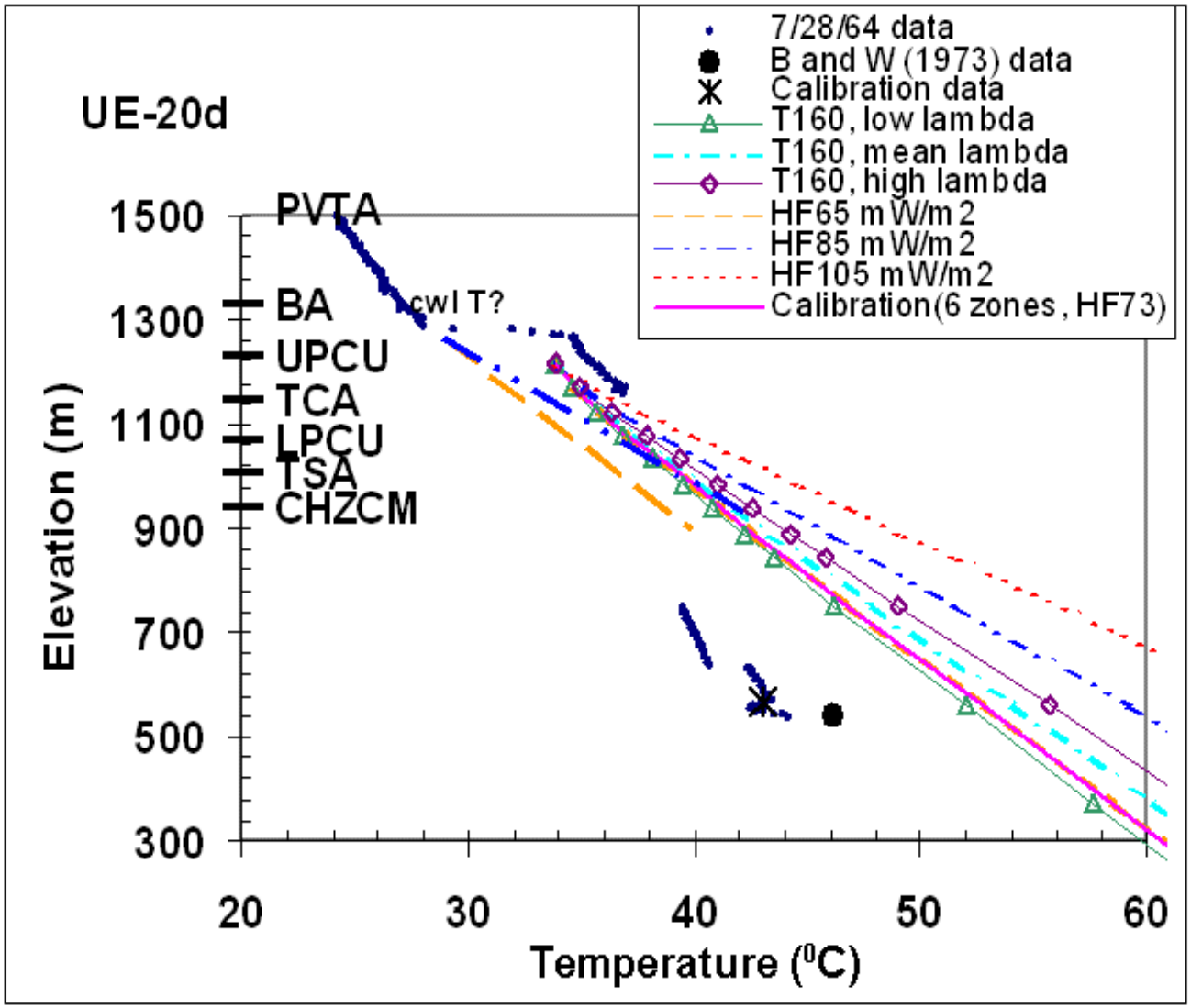
UE-20d
7/28/64 data
B and W (1973) data
Calibration data
T160, low lambda
T160, mean lambda
T160, high lambda
HF65 mW/m2
HF85 mW/m2
HF105 mW/m2
Calibration(6 zones, HF73)
PVTA
BA
UPCU
TCA
LPCU
TSA
CHZCM
cwl T?
Elevation (m)
1500
1300
1100
900
700
500
300
20
30
40
50
60
Temperature (0C)

Figure C5

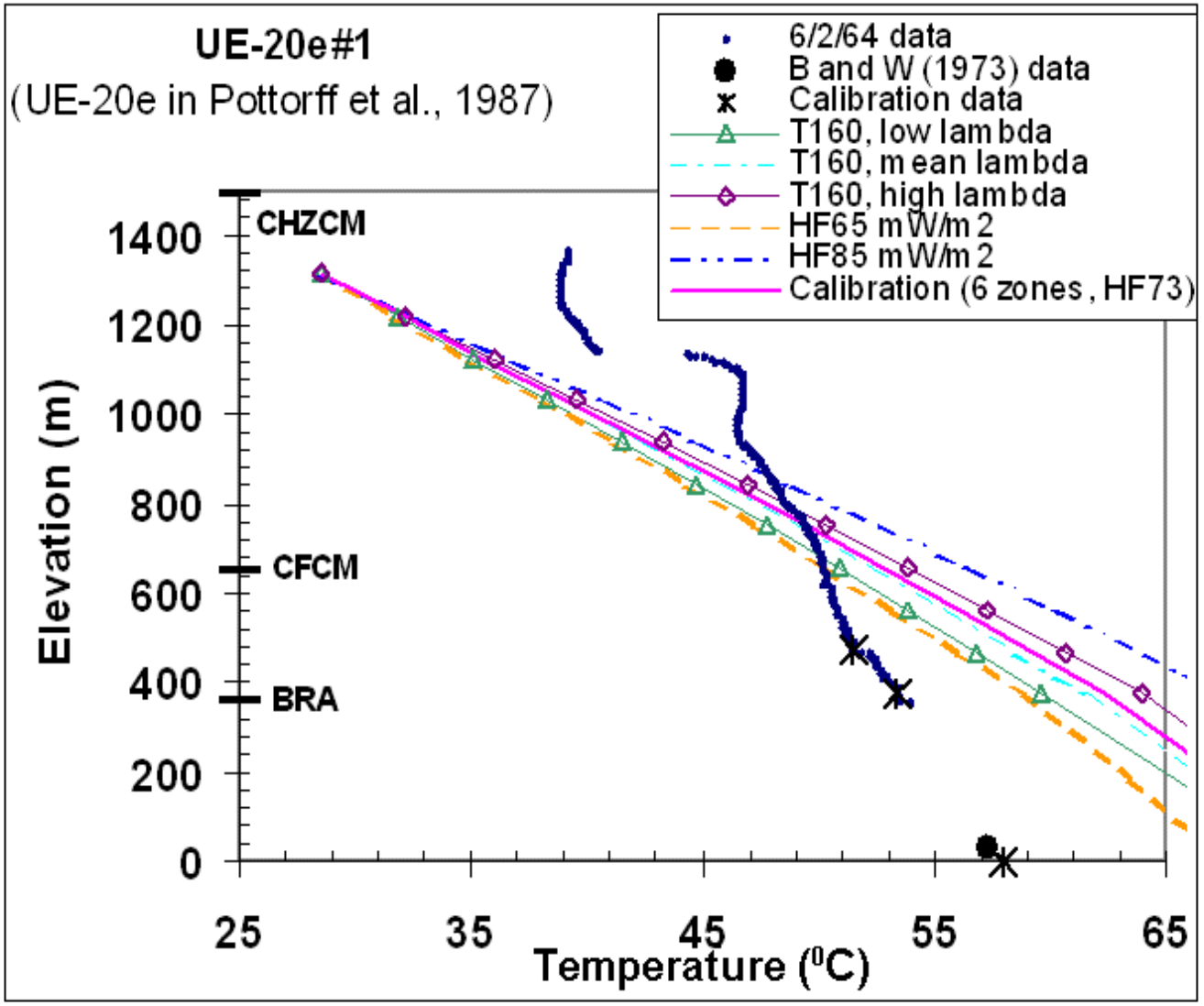
UE-20e#1
(UE-20e in Pottorff et al., 1987)
6/2/64 data
B and W (1973) data
Calibration data
T160, low lambda
T160, mean lambda
T160, high lambda
HF65 mW/m2
HF85 mW/m2
Calibration (6 zones, HF73)
CHZCM
CFCM
BRA
Elevation (m)
1400
1200
1000
800
600
400
200
0
25
35
45
55
65
Temperature (0C)

Figure C6

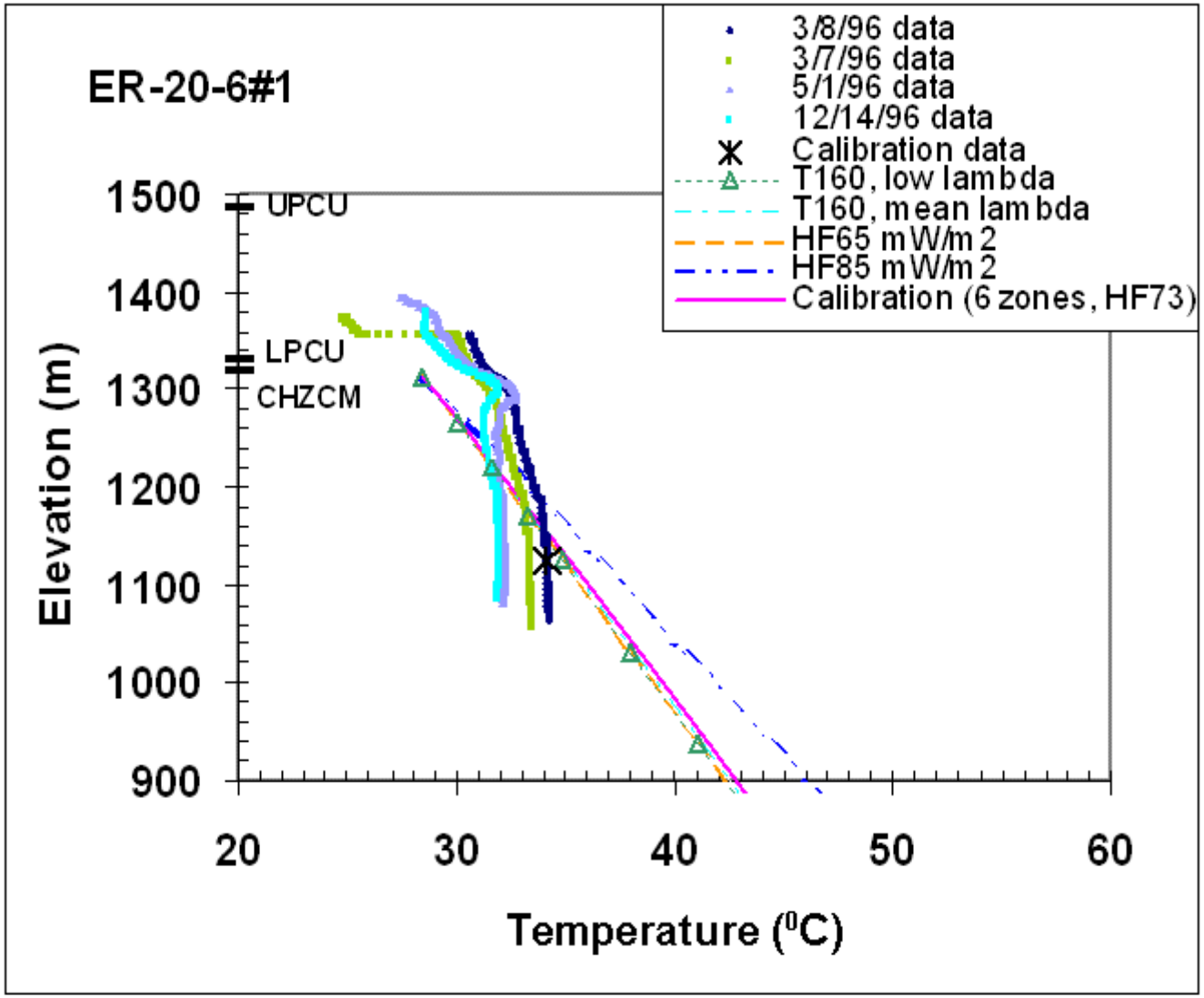
ER-20-6#1
3/8/96 data
3/7/96 data
5/1/96 data
12/14/96 data
Calibration data
T160, low lambda
T160, mean lambda
HF65 mW/m2
HF85 mW/m2
Calibration (6 zones, HF73)
UPCU
LPCU
CHZCM
Elevation (m)
1500
1400
1300
1200
1100
1000
900
20
30
40
50
60
Temperature (0C)

Figure C7

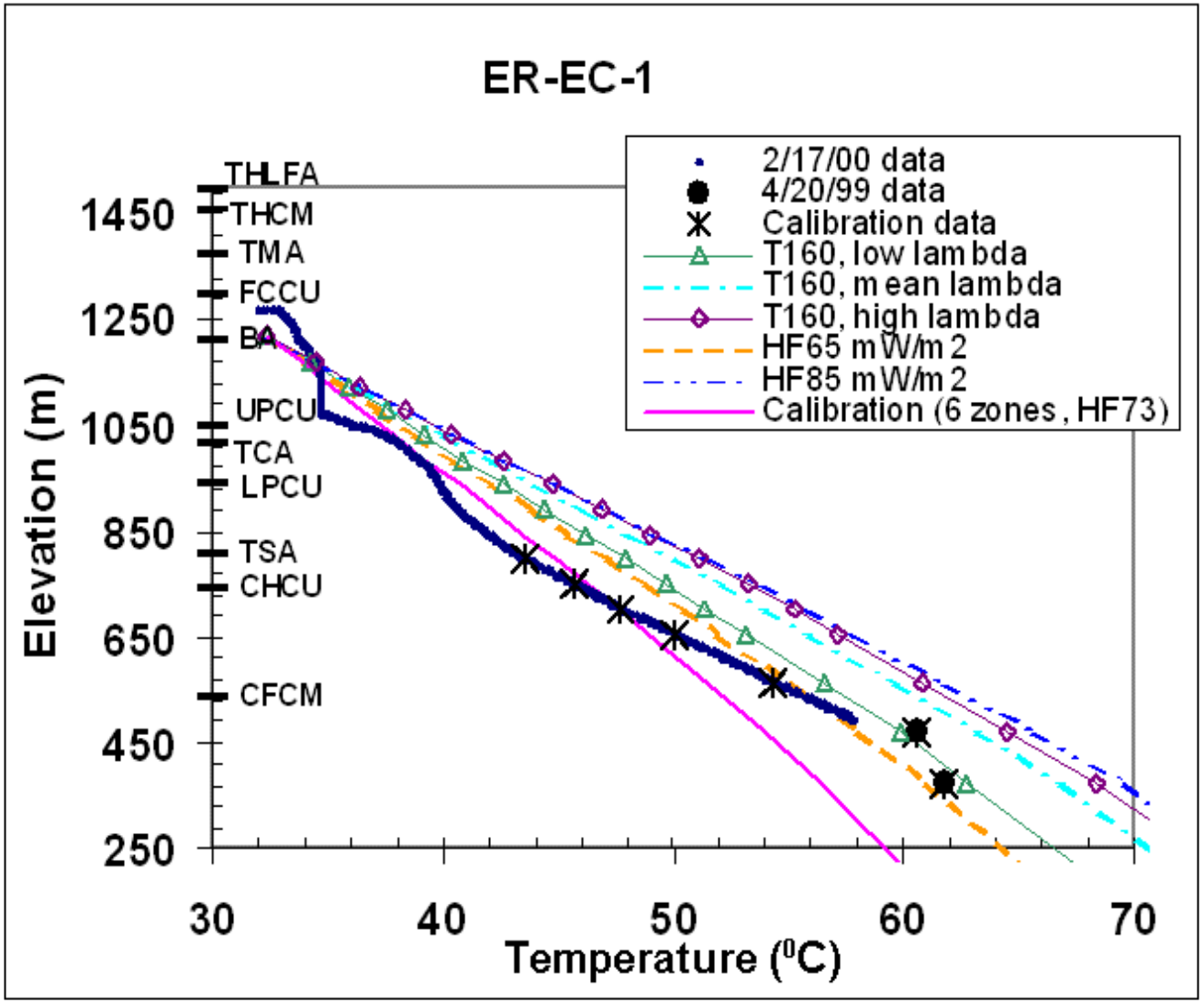
ER-EC-1
2/17/00 data
4/20/99 data
Calibration data
T160, low lambda
T160, mean lambda
T160, high lambda
HF65 mW/m2
HF85 mW/m2
Calibration (6 zones, HF73)
THLFA
THCM
TMA
FCCU
BA
UPCU
TCA
LPCU
TSA
CHCU
CFCM
Elevation (m)
1450
1250
1050
850
650
450
250
30
40
50
60
70
Temperature (0C)

Figure C8

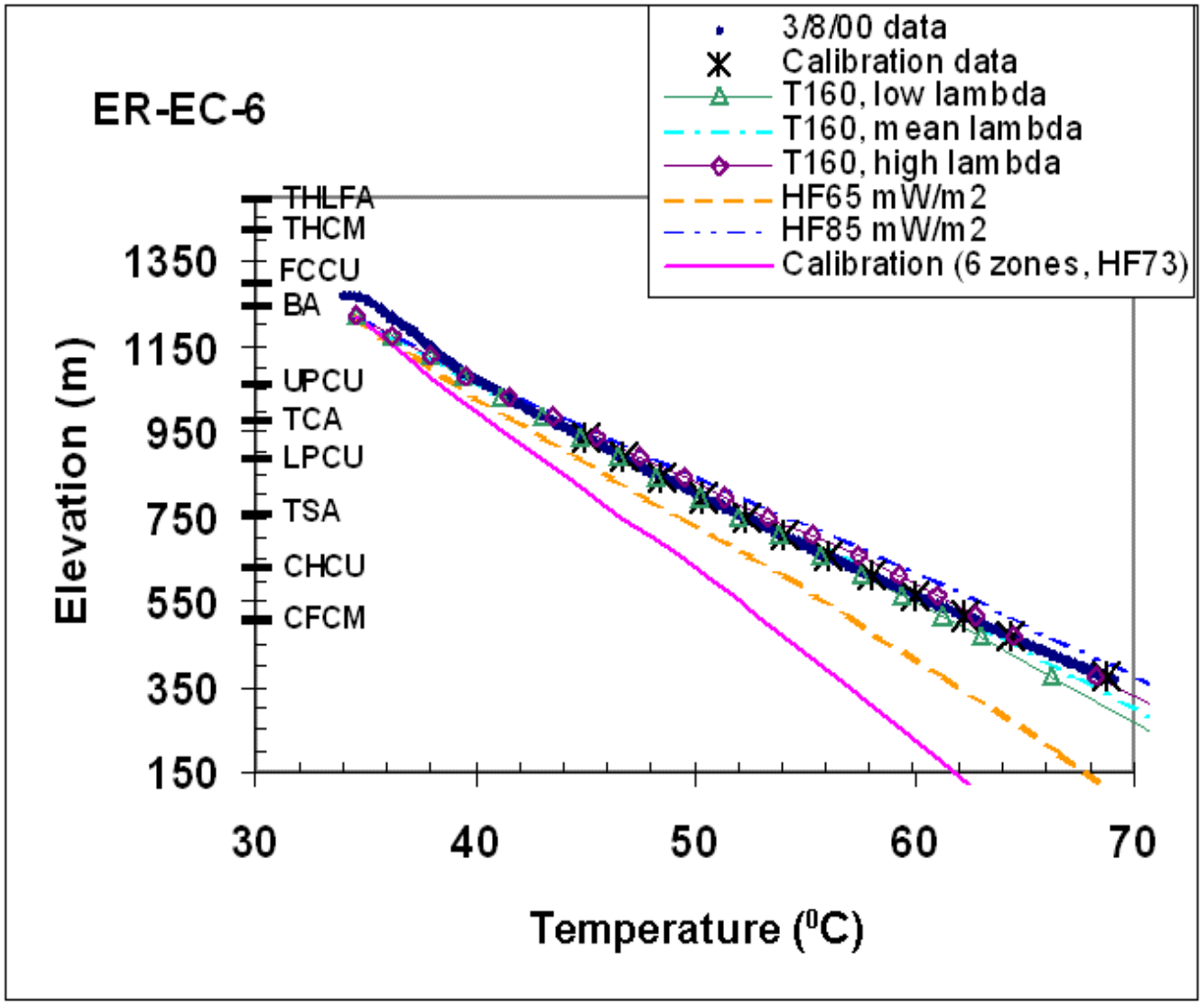
ER-EC-6
3/8/00 data
Calibration data
T160, low lambda
T160, mean lambda
T160, high lambda
HF65 mW/m2
HF85 mW/m2
Calibration (6 zones, HF73)
THLFA
THCM
FCCU
BA
UPCU
TCA
LPCU
TSA
CHCU
CFCM
1350
1150
950
750
550
350
150
Elevation (m)
30
40
50
60
70
Temperature (0C)

Figure C9

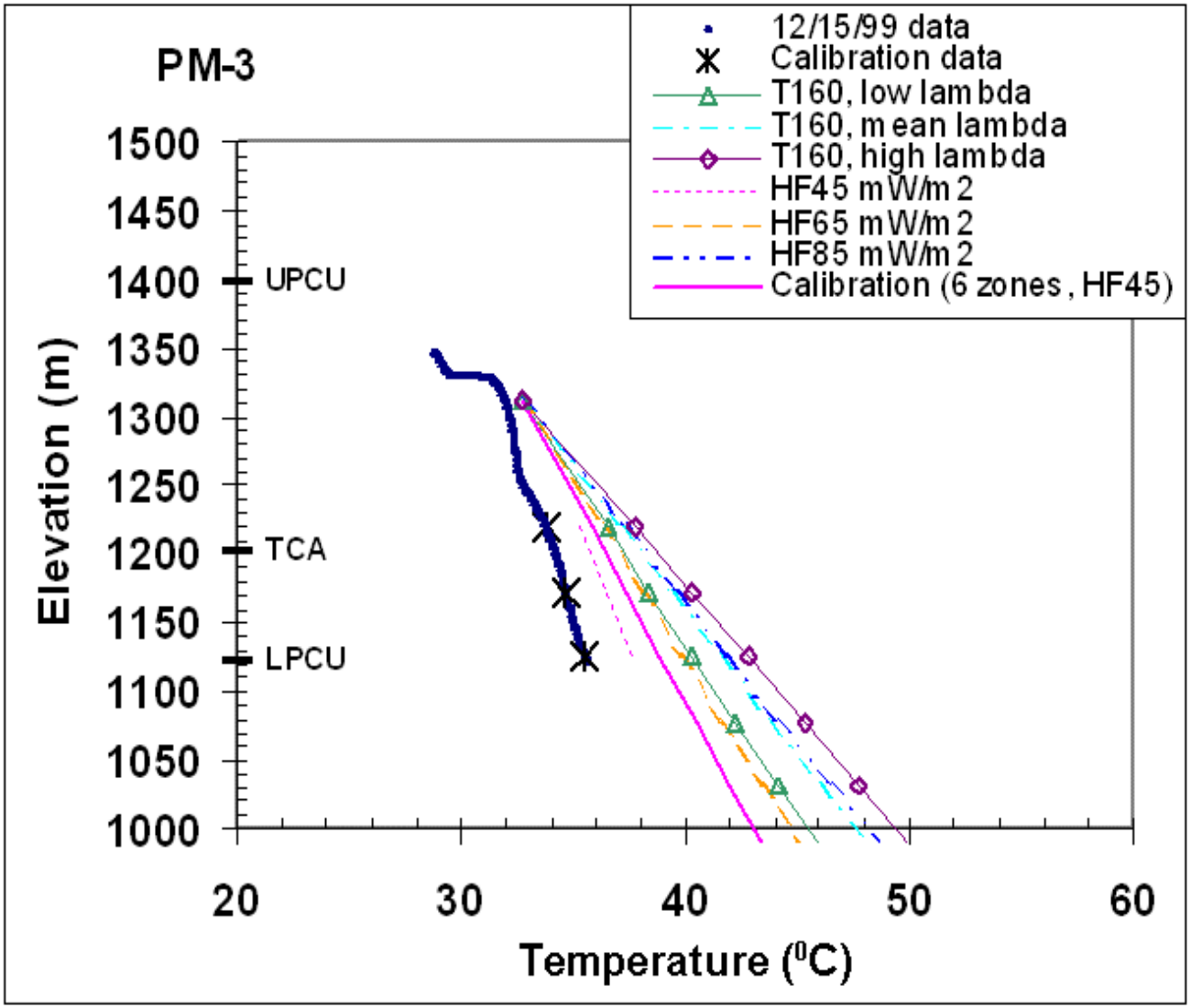
PM-3
12/15/99 data
Calibration data
T160, low lambda
T160, mean lambda
T160, high lambda
HF45 mW/m2
HF65 mW/m2
HF85 mW/m2
Calibration (6 zones, HF45)
Elevation (m)
1500
1450
1400
1350
1300
1250
1200
1150
1100
1050
1000
UPCU
TCA
LPCU
20
30
40
50
60
Temperature (0C)

Figure C10

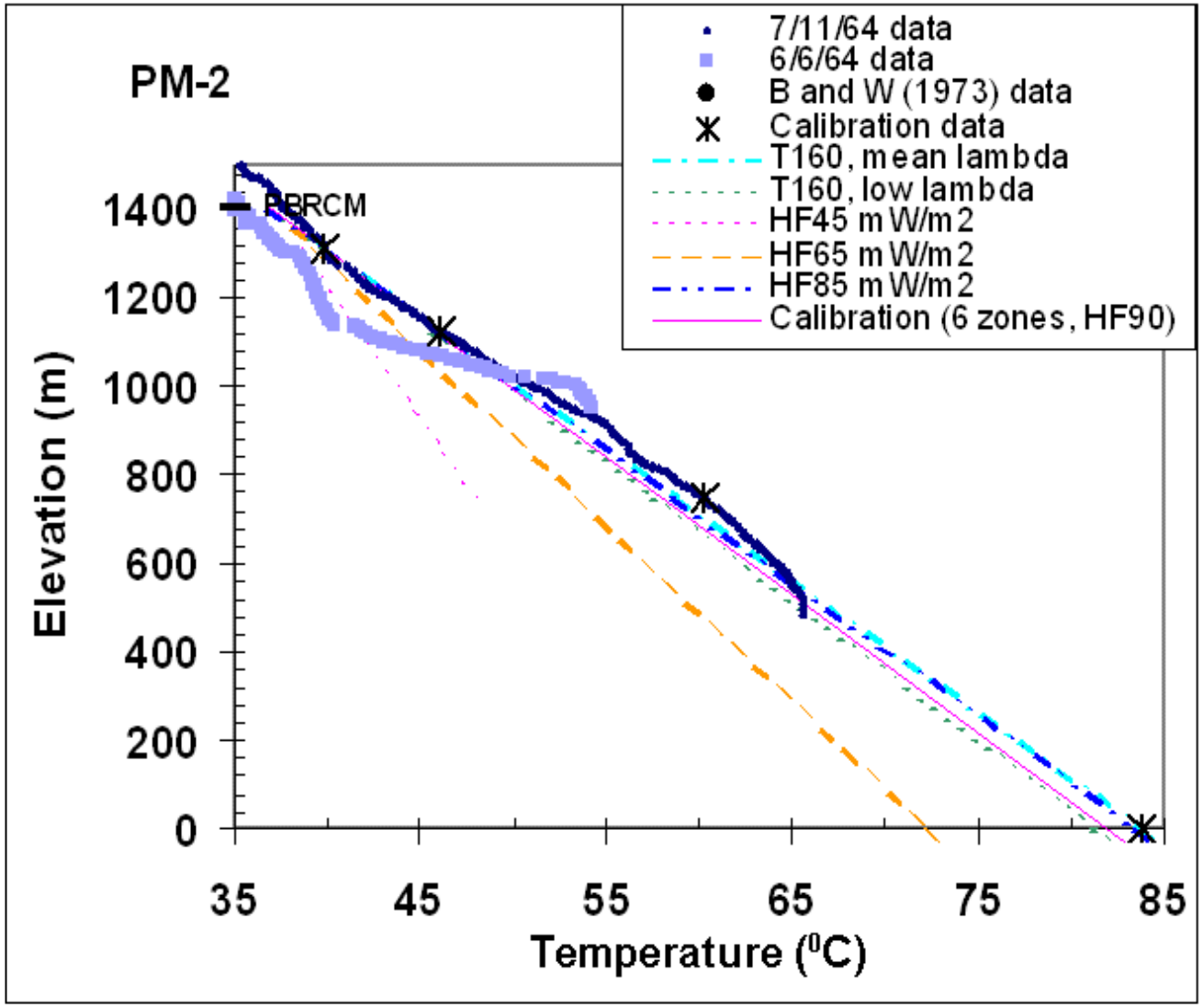
PM-2
7/11/64 data
6/6/64 data
B and W (1973) data
Calibration data
T160, mean lambda
T160, low lambda
HF45 mW/m2
HF65 mW/m2
HF85 mW/m2
Calibration (6 zones, HF90)
PBRCM
Elevation (m)
1400
1200
1000
800
600
400
200
0
35
45
55
65
75
85
Temperature (0C)

Figure C11

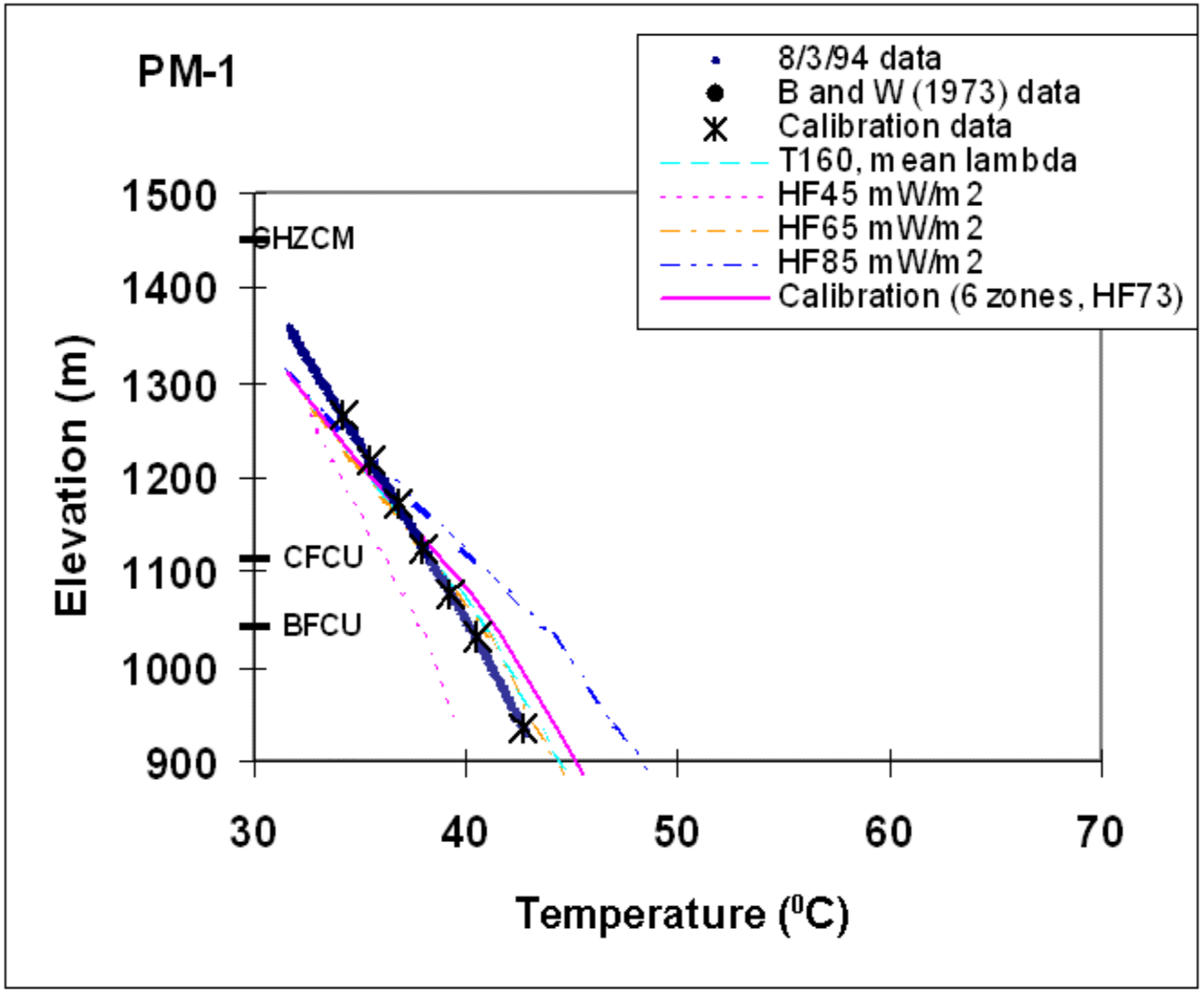
PM-1
8/3/94 data
B and W (1973) data
Calibration data
T160, mean lambda
HF45 mW/m2
HF65 mW/m2
HF85 mW/m2
Calibration (6 zones, HF73)
1500
1400
1300
1200
1100
1000
900
GHZCM
CFCU
BFCU
Elevation (m)
30
40
50
60
70
Temperature (0C)

Figure C12

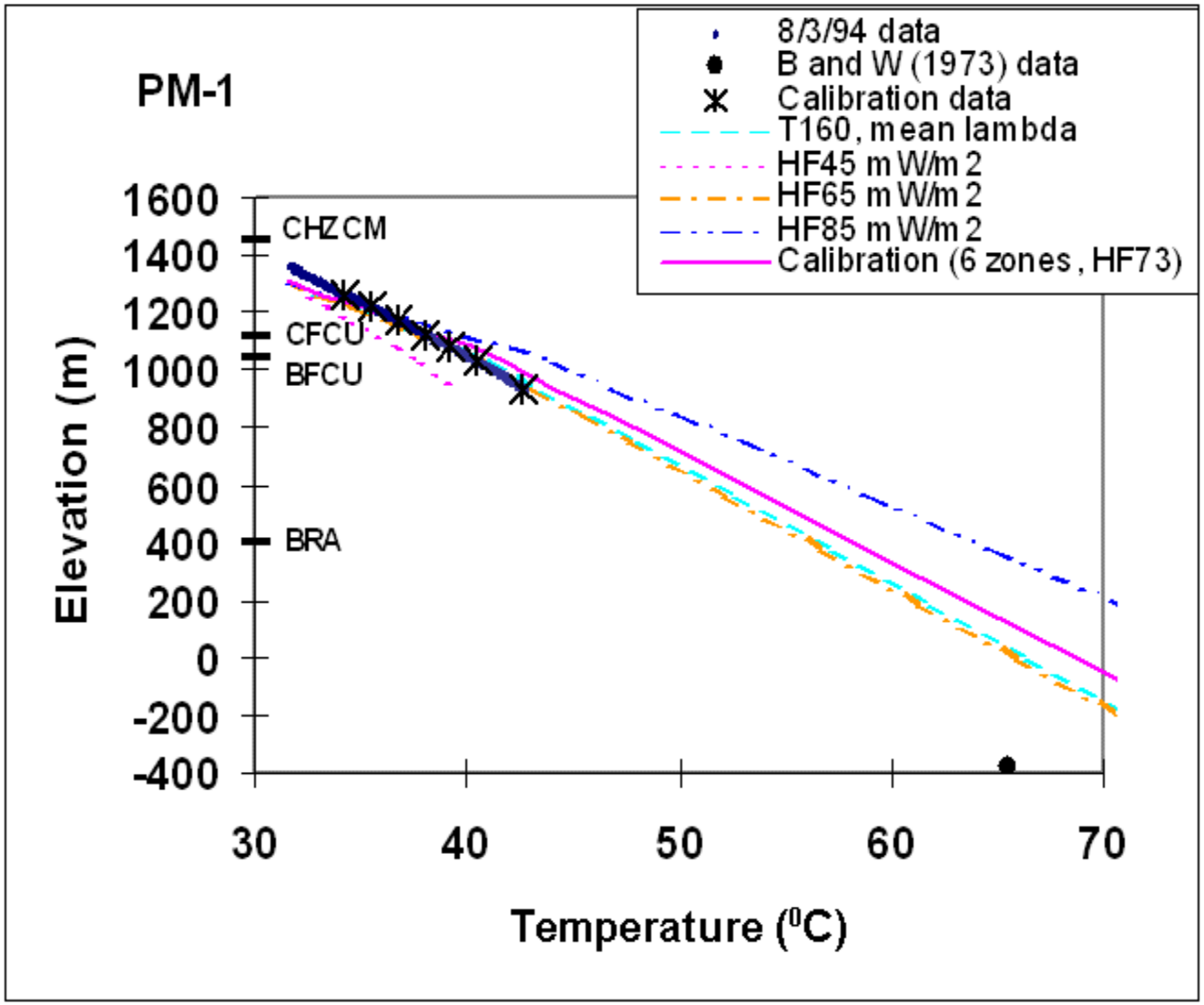
PM-1
8/3/94 data
B and W (1973) data
Calibration data
T160, mean lambda
HF45 mW/m2
HF65 mW/m2
HF85 mW/m2
Calibration (6 zones, HF73)
CHZCM
CFCU
BFCU
BRA
Elevation (m)
1600
1400
1200
1000
800
600
400
200
0
-200
-400
30
40
50
60
70
Temperature (0C)

Figure C13

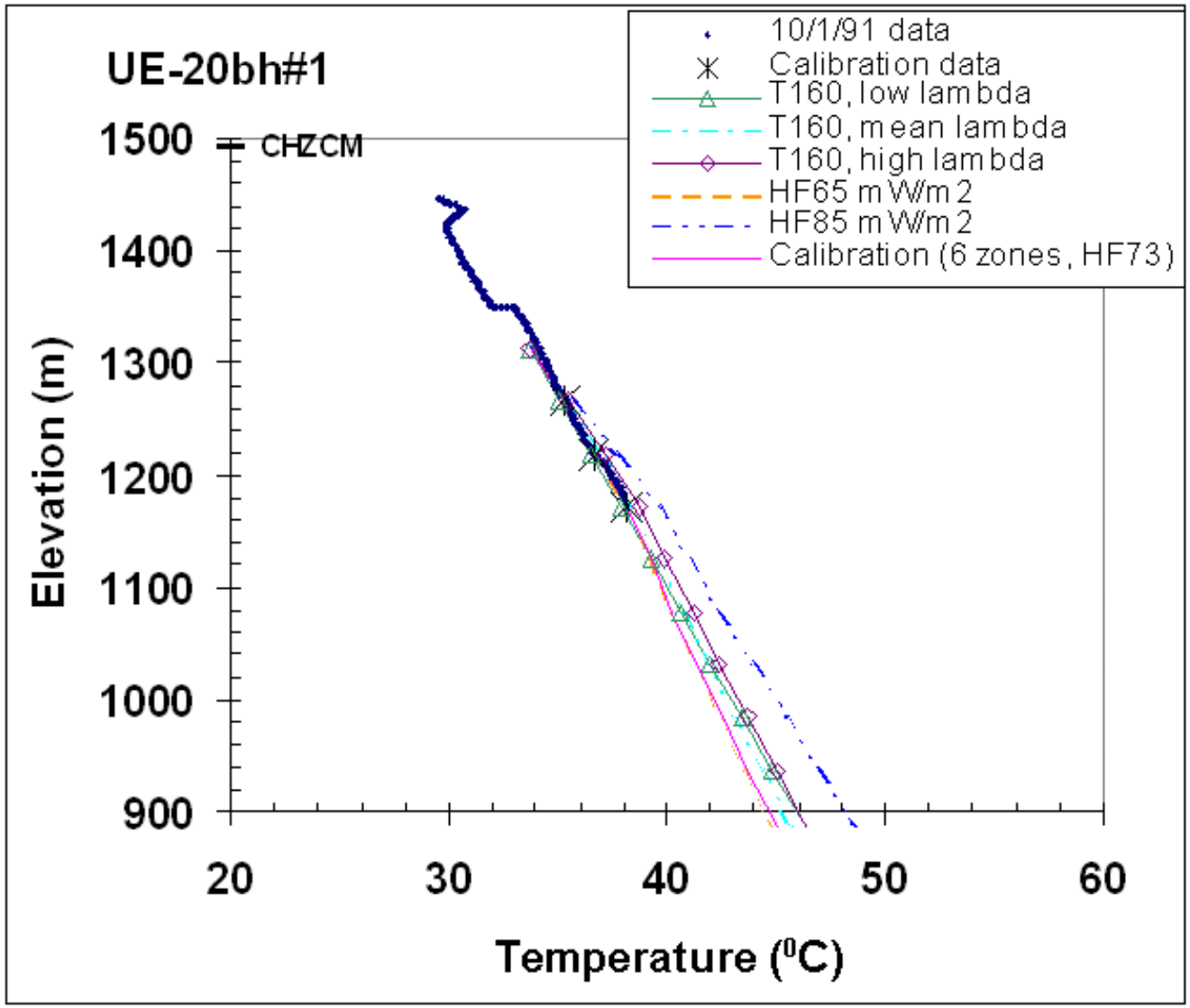
UE-20bh#1
10/1/91 data
Calibration data
T160, low lambda
T160, mean lambda
T160, high lambda
HF65 mW/m2
HF85 mW/m2
Calibration (6 zones, HF73)
CHZCM
1500
1400
1300
1200
1100
1000
900
Elevation (m)
20
30
40
50
60
Temperature (⁰C)

Figure C14

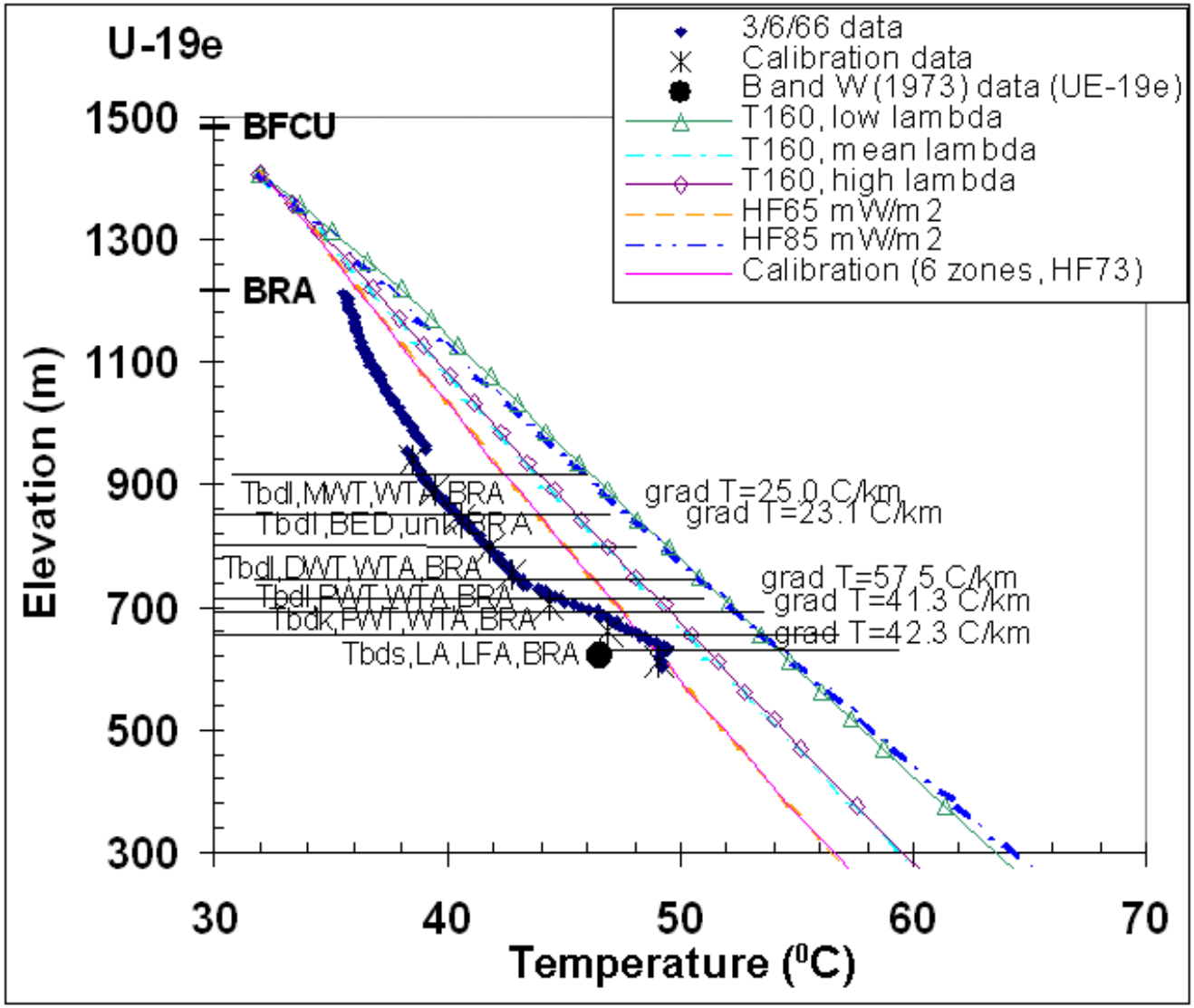
U-19e
3/6/66 data
Calibration data
B and W (1973) data (UE-19e)
T160, low lambda
T160, mean lambda
T160, high lambda
HF65 mW/m2
HF85 mW/m2
Calibration (6 zones, HF73)
BFCU
BRA
Tbdl,MWT,WTA,BRA
Tbdl,BED,unk,BRA
Tbdl,DWT,WTA,BRA
Tbdl,PWT,WTA,BRA
Tbdk,PWT,WTA,BRA
Tbds,LA,LFA,BRA
grad T=25.0 C/km
grad T=23.1 C/km
grad T=57.5 C/km
grad T=41.3 C/km
grad T=42.3 C/km
Elevation (m)
1500
1300
1100
900
700
500
300
30
40
50
60
70
Temperature (0C)

Figure C15

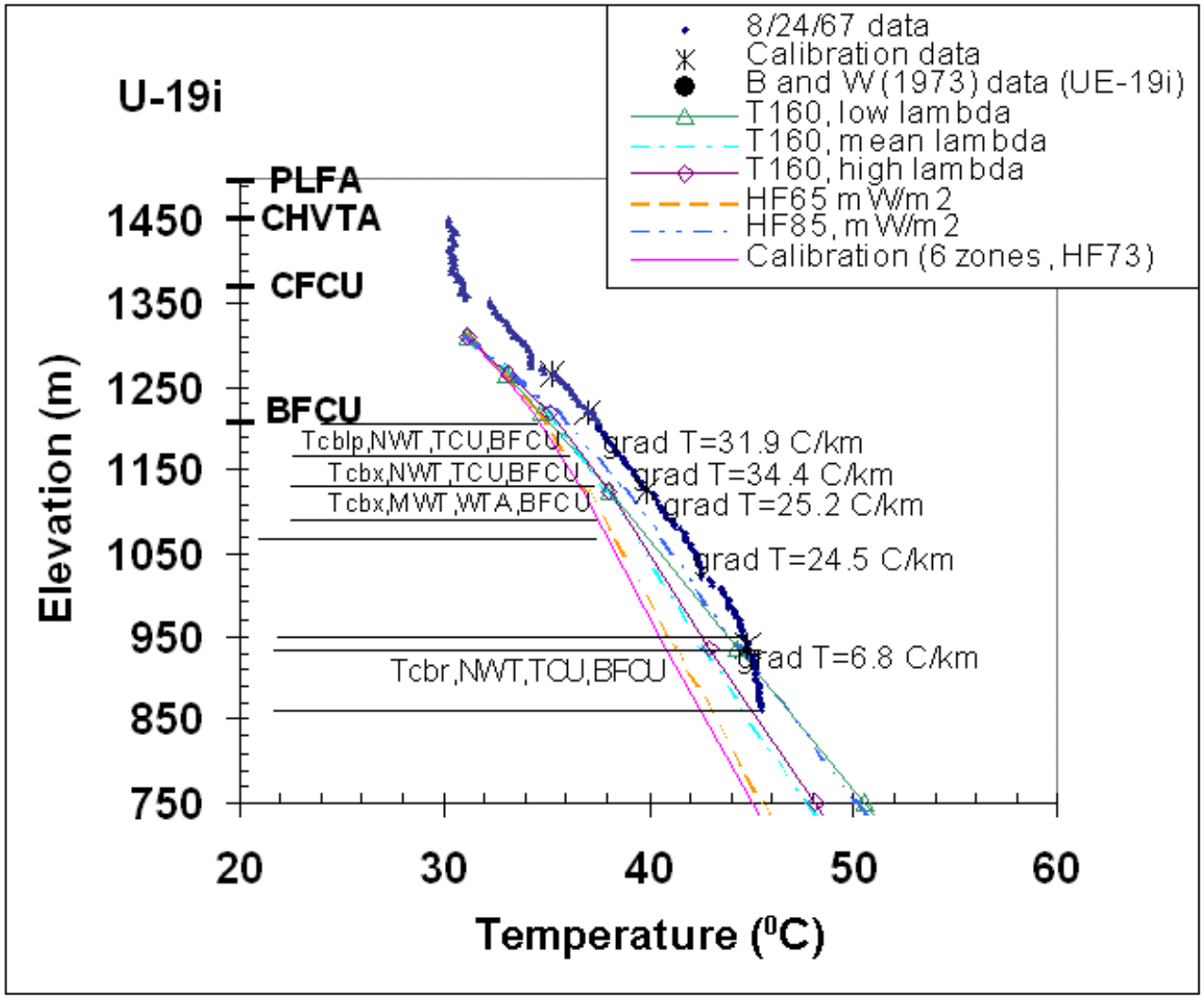
U-19i
8/24/67 data
Calibration data
B and W (1973) data (UE-19i)
T160, low lambda
T160, mean lambda
T160, high lambda
HF65 mW/m2
HF85, mW/m2
Calibration (6 zones, HF73)
PLFA
CHVTA
CFCU
BFCU
Tcblp,NWT,TCU,BFCU
Tcbx,NWT,TCU,BFCU
Tcbx,MWT,WTA,BFCU
Tcbr,NWT,TCU,BFCU
grad T=31.9 C/km
grad T=34.4 C/km
grad T=25.2 C/km
grad T=24.5 C/km
grad T=6.8 C/km
Elevation (m)
1450
1350
1250
1150
1050
950
850
750
20
30
40
50
60
Temperature (0C)

Figure C16

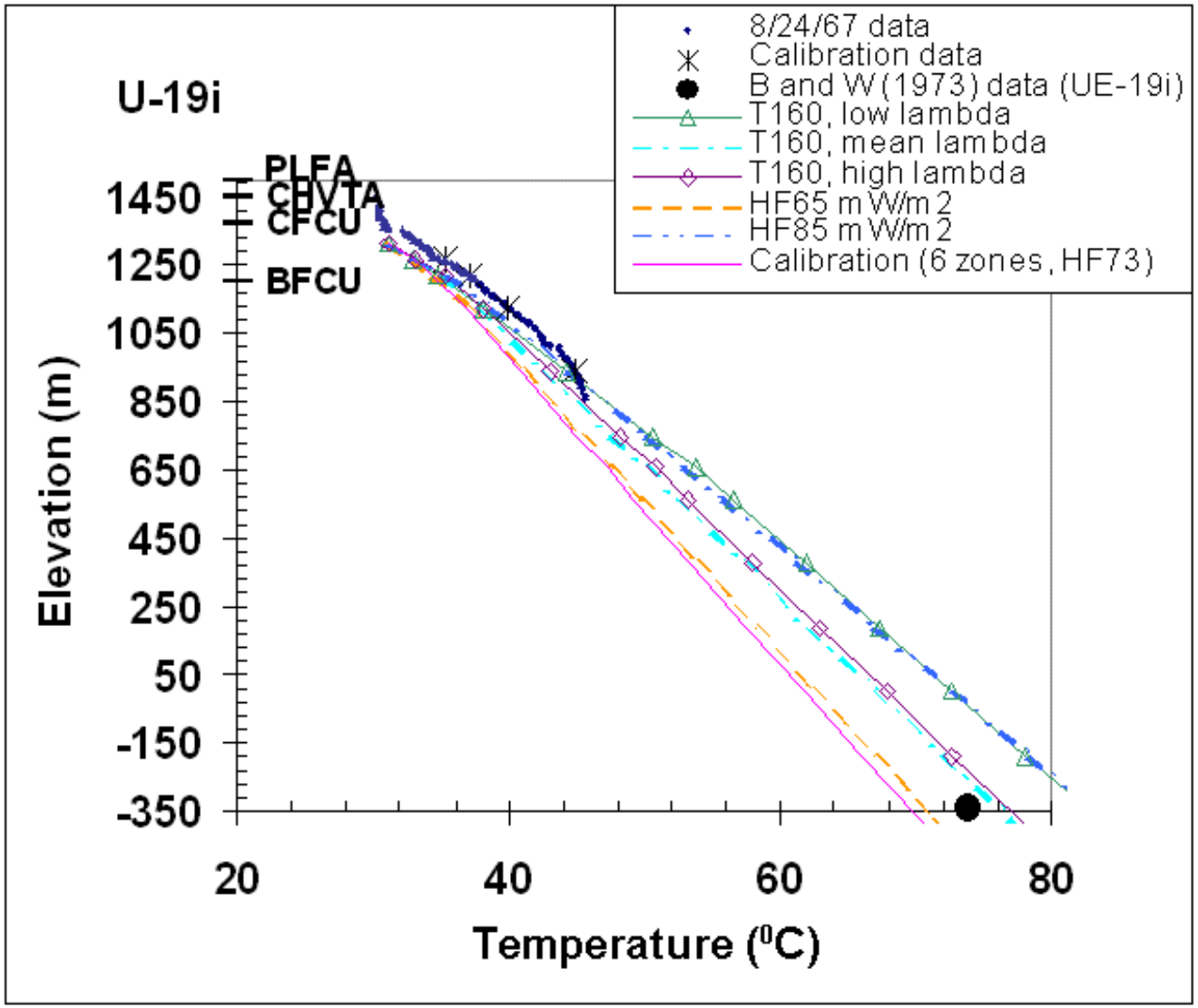
U-19i
8/24/67 data
Calibration data
B and W (1973) data (UE-19i)
T160, low lambda
T160, mean lambda
T160, high lambda
HF65 mW/m2
HF85 mW/m2
Calibration (6 zones, HF73)
PLFA
CDVTA
CFCU
BFCU
Elevation (m)
1450
1250
1050
850
650
450
250
50
-150
-350
20
40
60
80
Temperature (0C)

Figure C17

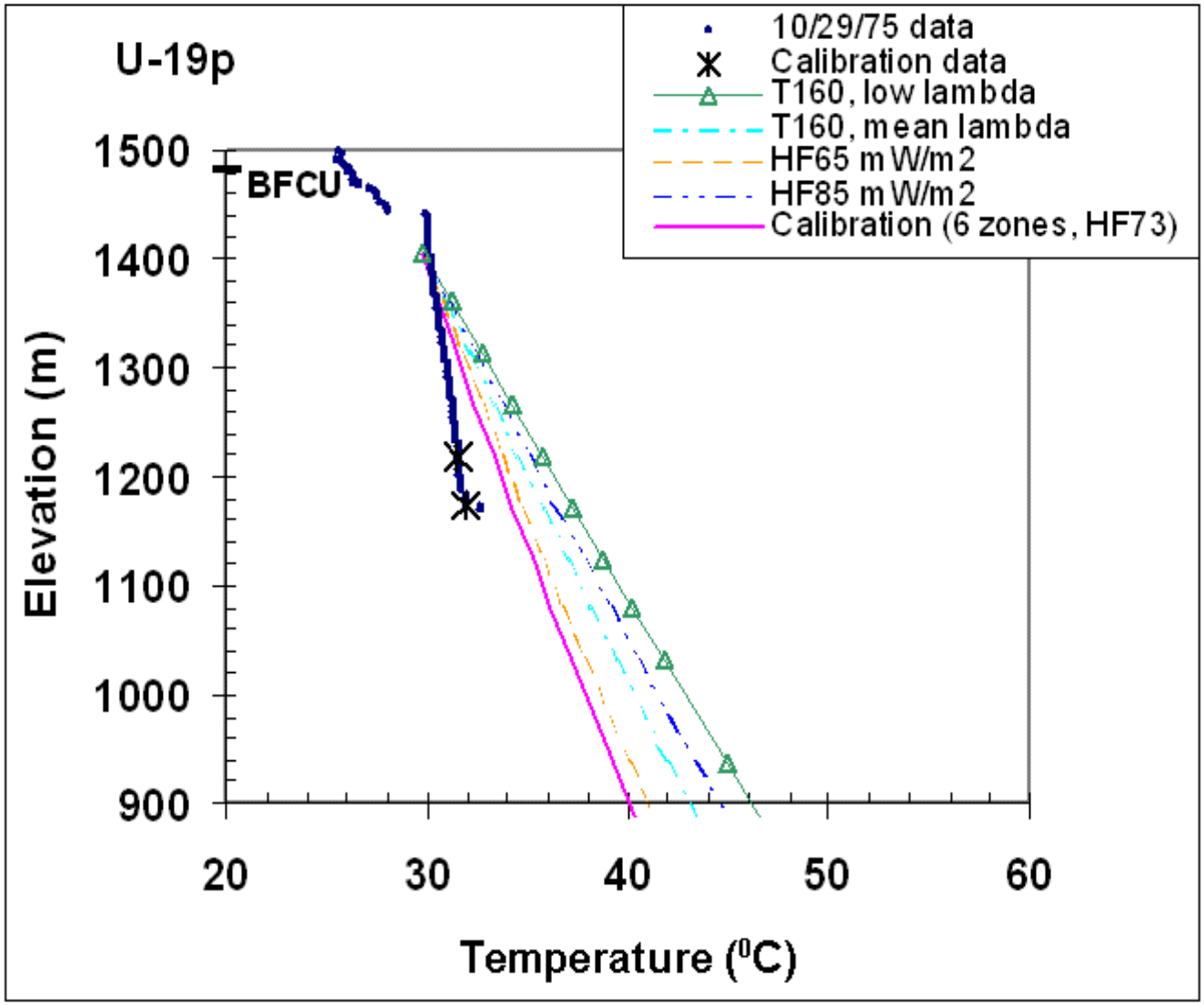
U-19p
10/29/75 data
Calibration data
T160, low lambda
T160, mean lambda
HF65 mW/m2
HF85 mW/m2
Calibration (6 zones, HF73)
BFCU
1500
1400
1300
1200
1100
1000
900
Elevation (m)
20
30
40
50
60
Temperature (⁰C)

Figure C18

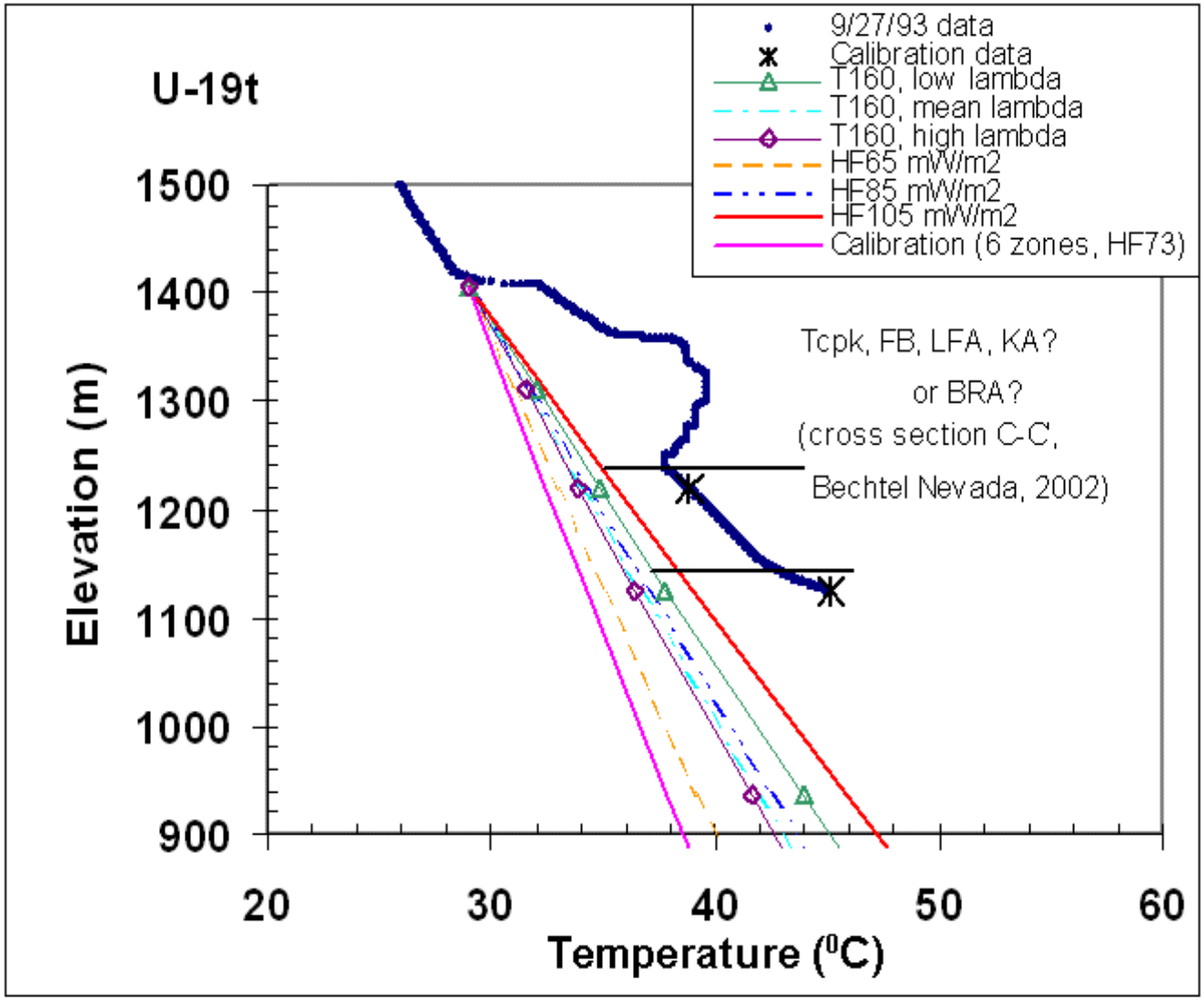
U-19t
9/27/93 data
Calibration data
T160, low lambda
T160, mean lambda
T160, high lambda
HF65 mW/m2
HF85 mW/m2
HF105 mW/m2
Calibration (6 zones, HF73)
Tcpk, FB, LFA, KA?
or BRA?
(cross section C-C',
Bechtel Nevada, 2002)
Elevation (m)
1500
1400
1300
1200
1100
1000
900
20
30
40
50
60
Temperature (0C)

Figure C19

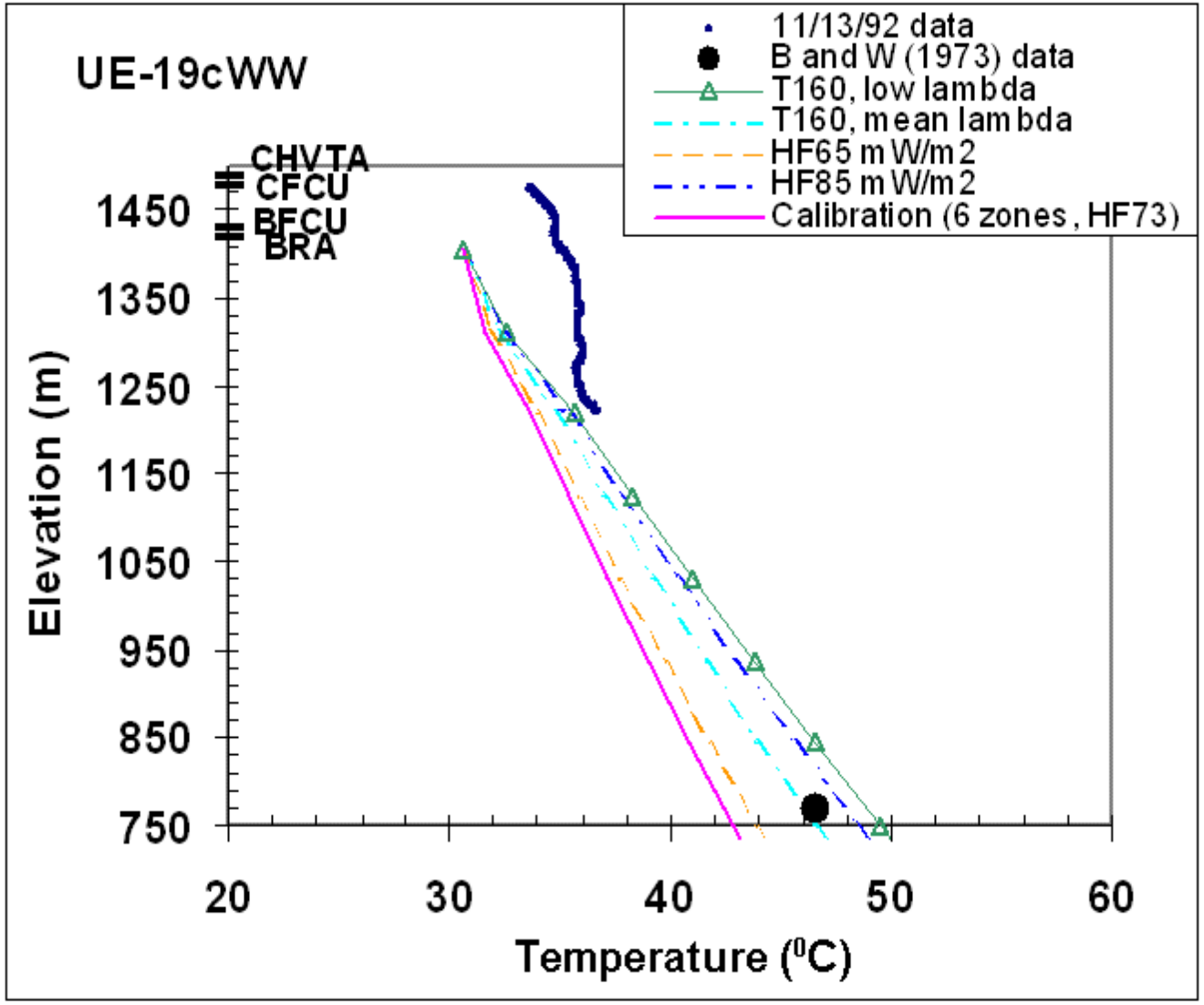
UE-19cWW
11/13/92 data
B and W (1973) data
T160, low lambda
T160, mean lambda
HF65 mW/m2
HF85 mW/m2
Calibration (6 zones, HF73)
CHVTA
CFCU
BFCU
BRA
Elevation (m)
1450
1350
1250
1150
1050
950
850
750
20
30
40
50
60
Temperature (⁰C)

Figure C20

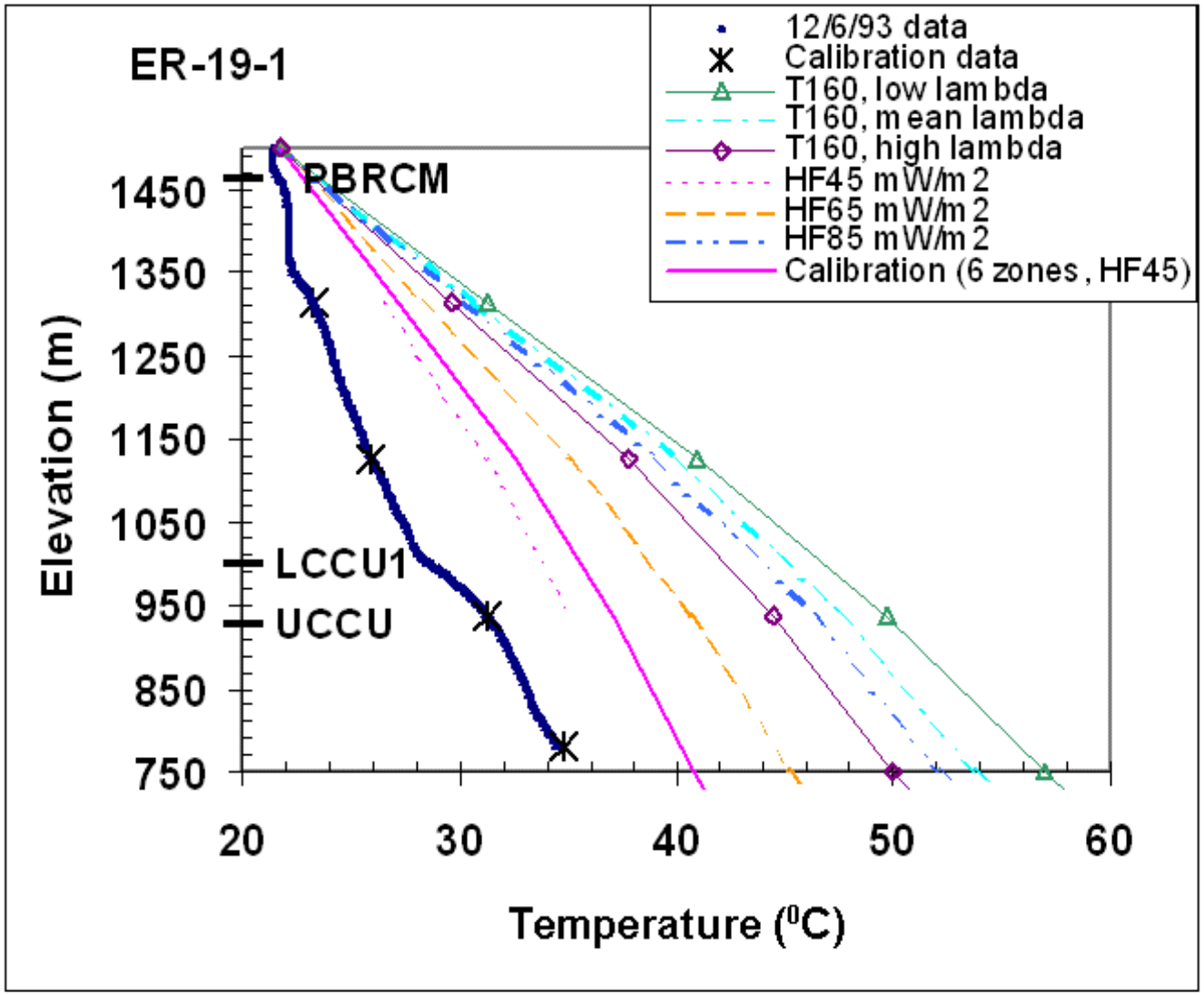
ER-19-1
12/6/93 data
Calibration data
T160, low lambda
T160, mean lambda
T160, high lambda
HF45 mW/m2
HF65 mW/m2
HF85 mW/m2
Calibration (6 zones, HF45)
PBRCM
LCCU1
UCCU
Elevation (m)
1450
1350
1250
1150
1050
950
850
750
20
30
40
50
60
Temperature (0C)

Figure C21

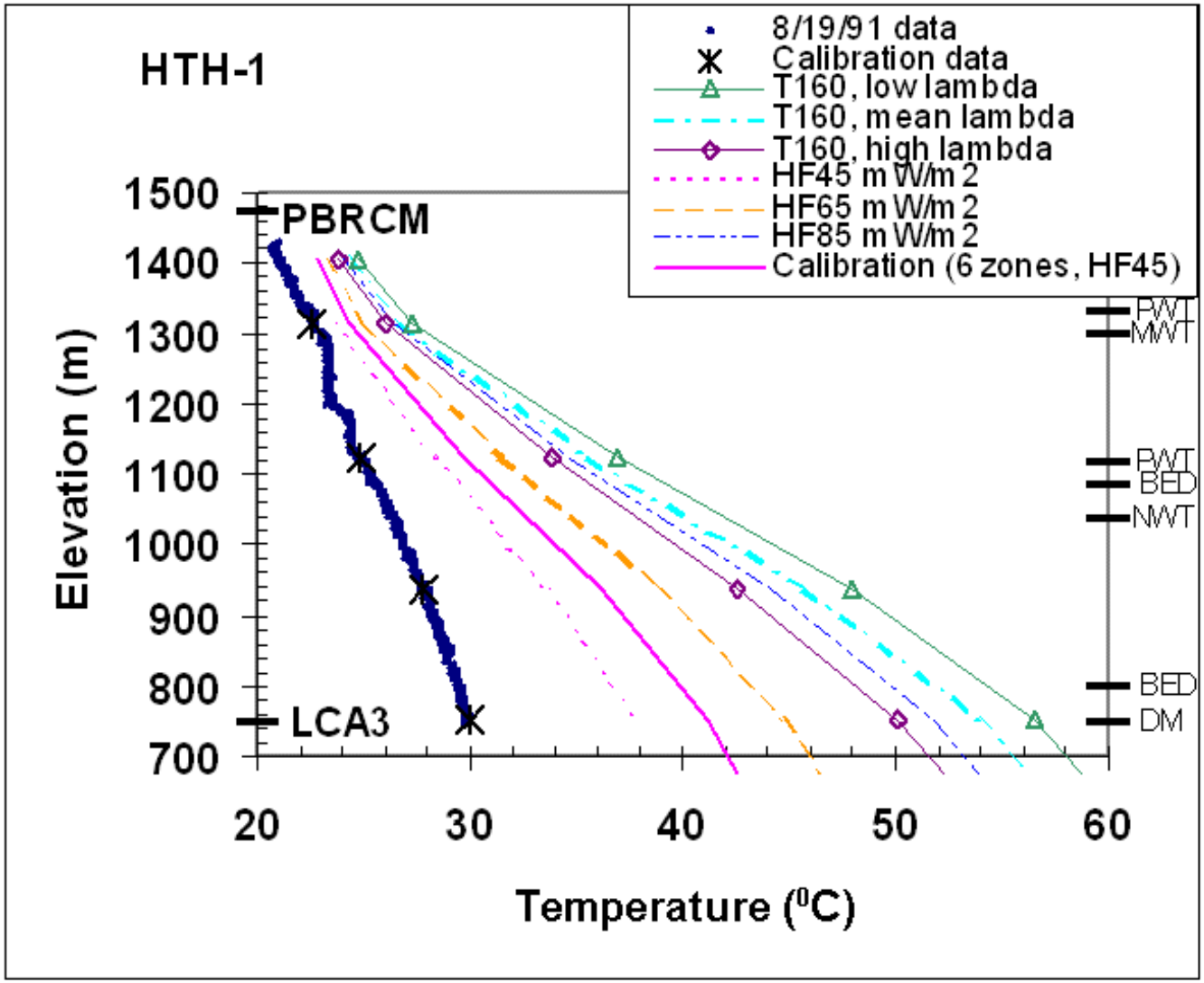
HTH-1
8/19/91 data
Calibration data
T160, low lambda
T160, mean lambda
T160, high lambda
HF45 mW/m2
HF65 mW/m2
HF85 mW/m2
Calibration (6 zones, HF45)
PBRCM
LCA3
PWT
MWT
PWT
BED
NWT
BED
DM
Elevation (m)
1500
1400
1300
1200
1100
1000
900
800
700
20
30
40
50
60
Temperature (0C)

Figure C22

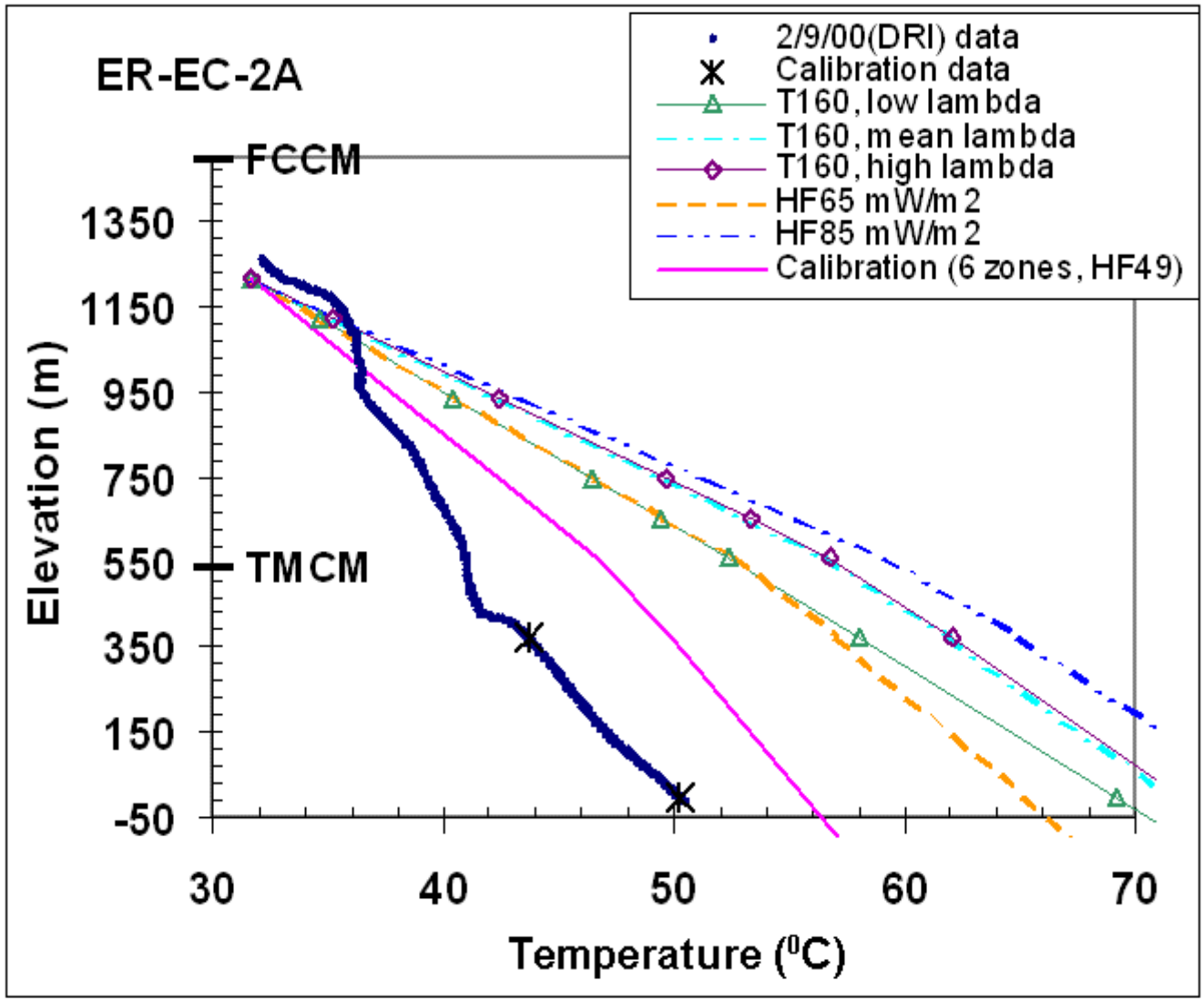
ER-EC-2A
2/9/00(DRI) data
Calibration data
T160, low lambda
T160, mean lambda
T160, high lambda
HF65 mW/m2
HF85 mW/m2
Calibration (6 zones, HF49)
FCCM
TMCM
Elevation (m)
1350
1150
950
750
550
350
150
-50
30
40
50
60
70
Temperature (0C)

Figure C23

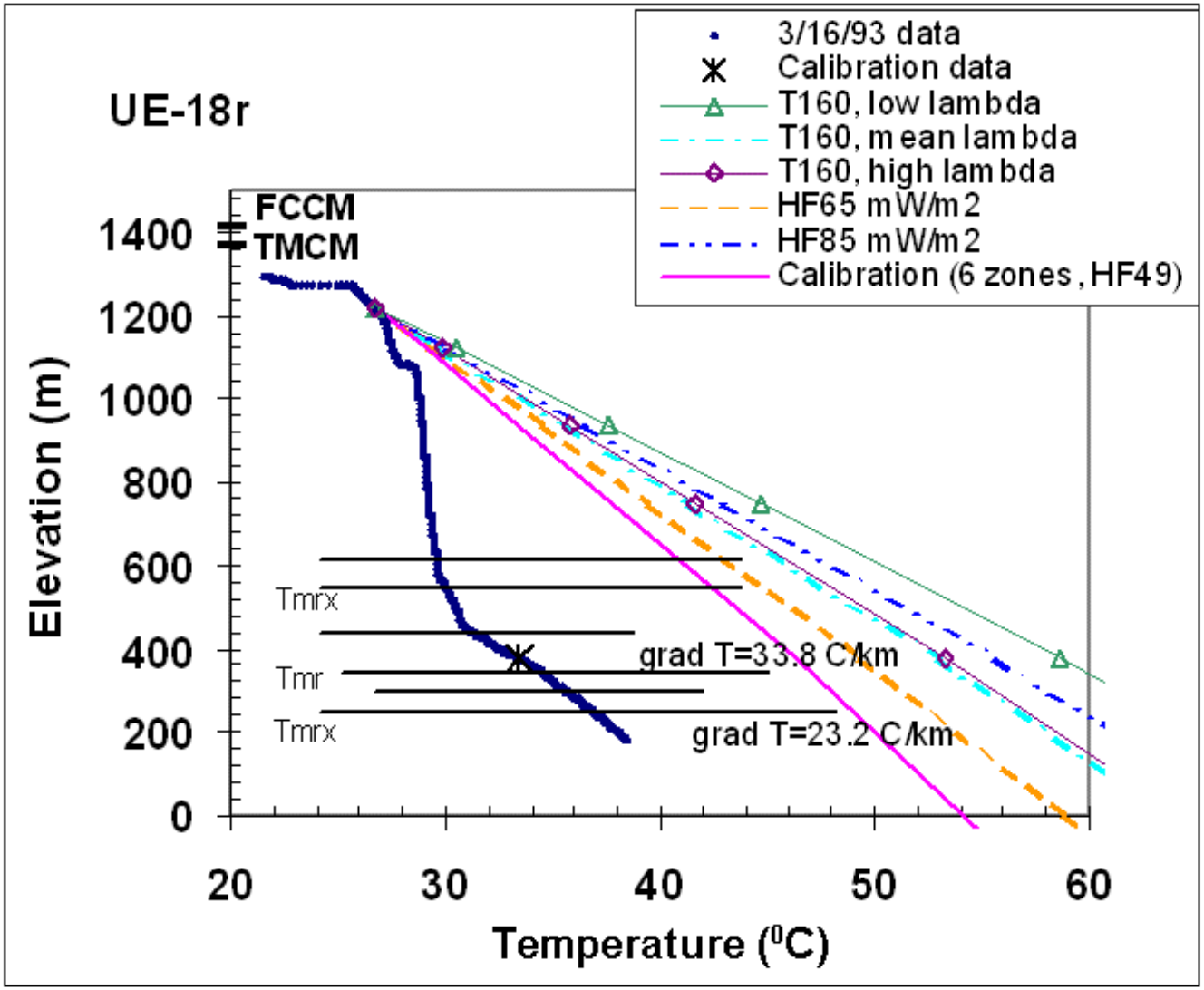
UE-18r
3/16/93 data
Calibration data
T160, low lambda
T160, mean lambda
T160, high lambda
HF65 mW/m2
HF85 mW/m2
Calibration (6 zones, HF49)
FCCM
TMCM
Tmrx
Tmr
Tmrx
grad T=33.8 C/km
grad T=23.2 C/km
Elevation (m)
1400
1200
1000
800
600
400
200
0
20
30
40
50
60
Temperature (0C)

Figure C24

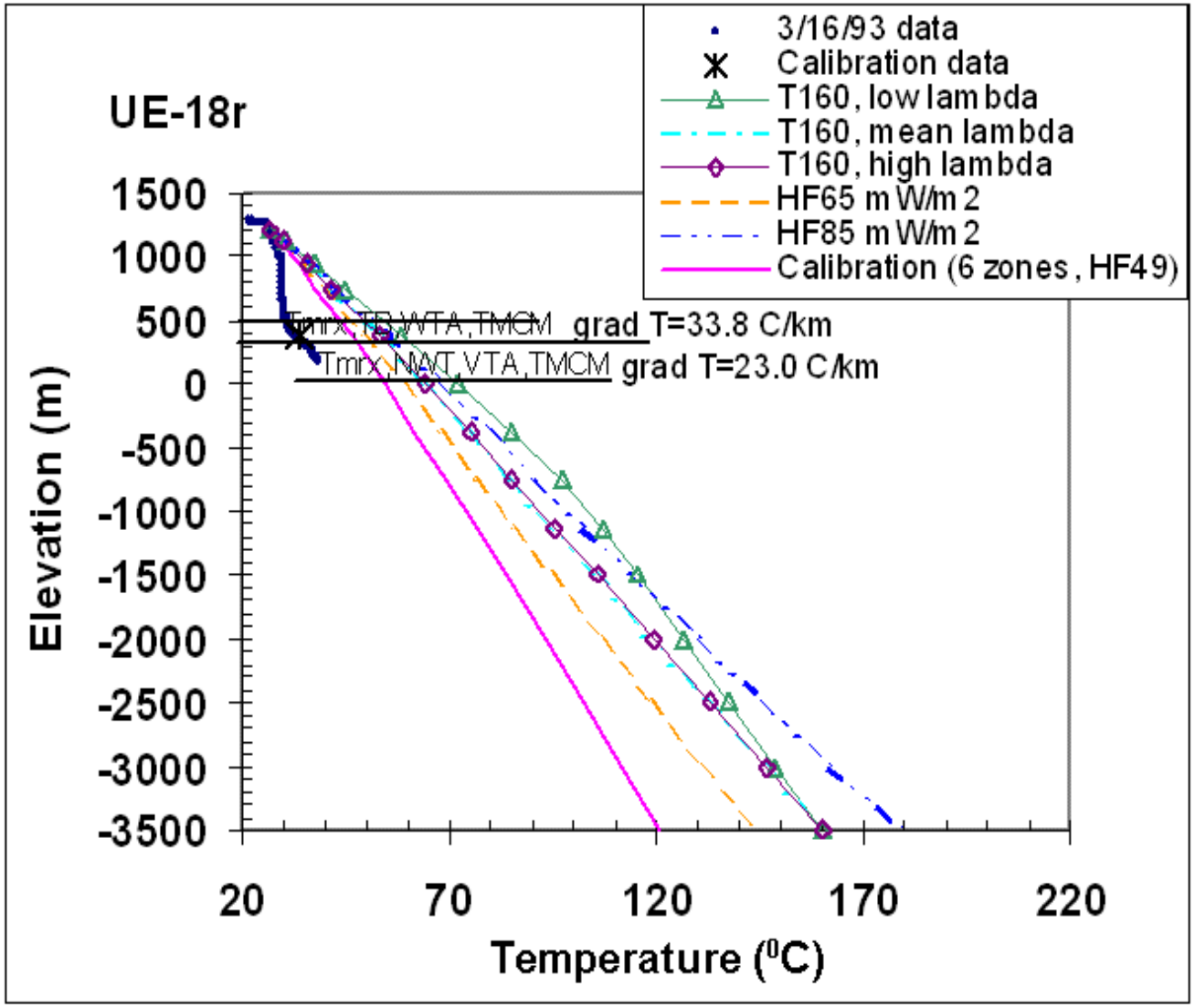
UE-18r
3/16/93 data
Calibration data
T160, low lambda
T160, mean lambda
T160, high lambda
HF65 mW/m2
HF85 mW/m2
Calibration (6 zones, HF49)
Tmrx,TB,VTA,TMCM grad T=33.8 C/km
Tmrx,NAT,VTA,TMCM grad T=23.0 C/km
Elevation (m)
1500
1000
500
0
-500
-1000
-1500
-2000
-2500
-3000
-3500
20
70
120
170
220
Temperature (0C)

Figure C25

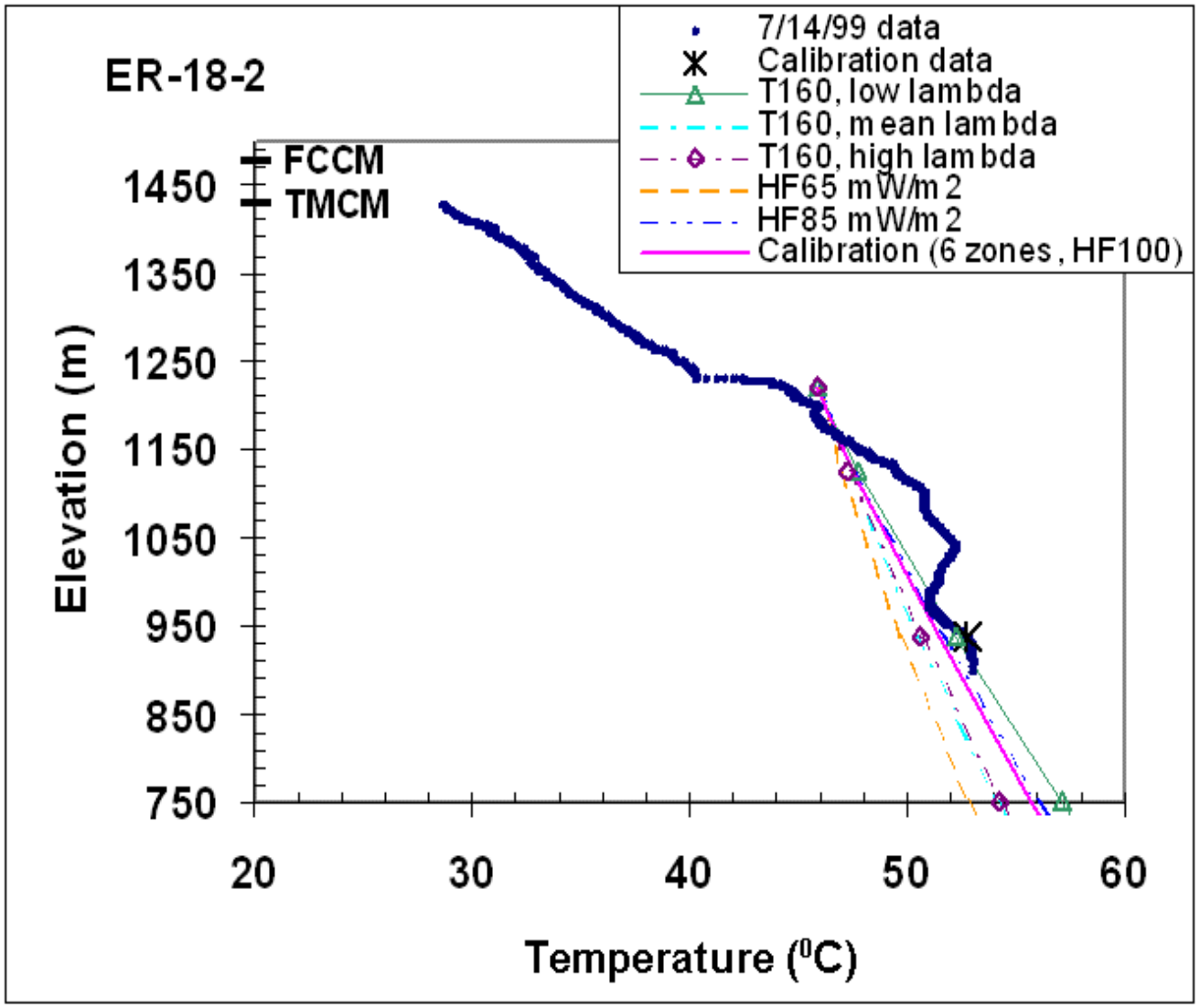
ER-18-2
7/14/99 data
Calibration data
T160, low lambda
T160, mean lambda
T160, high lambda
HF65 mW/m2
HF85 mW/m2
Calibration (6 zones, HF100)
FCCM
TMCM
1450
1350
1250
1150
1050
950
850
750
Elevation (m)
20
30
40
50
60
Temperature (0C)

Figure C26

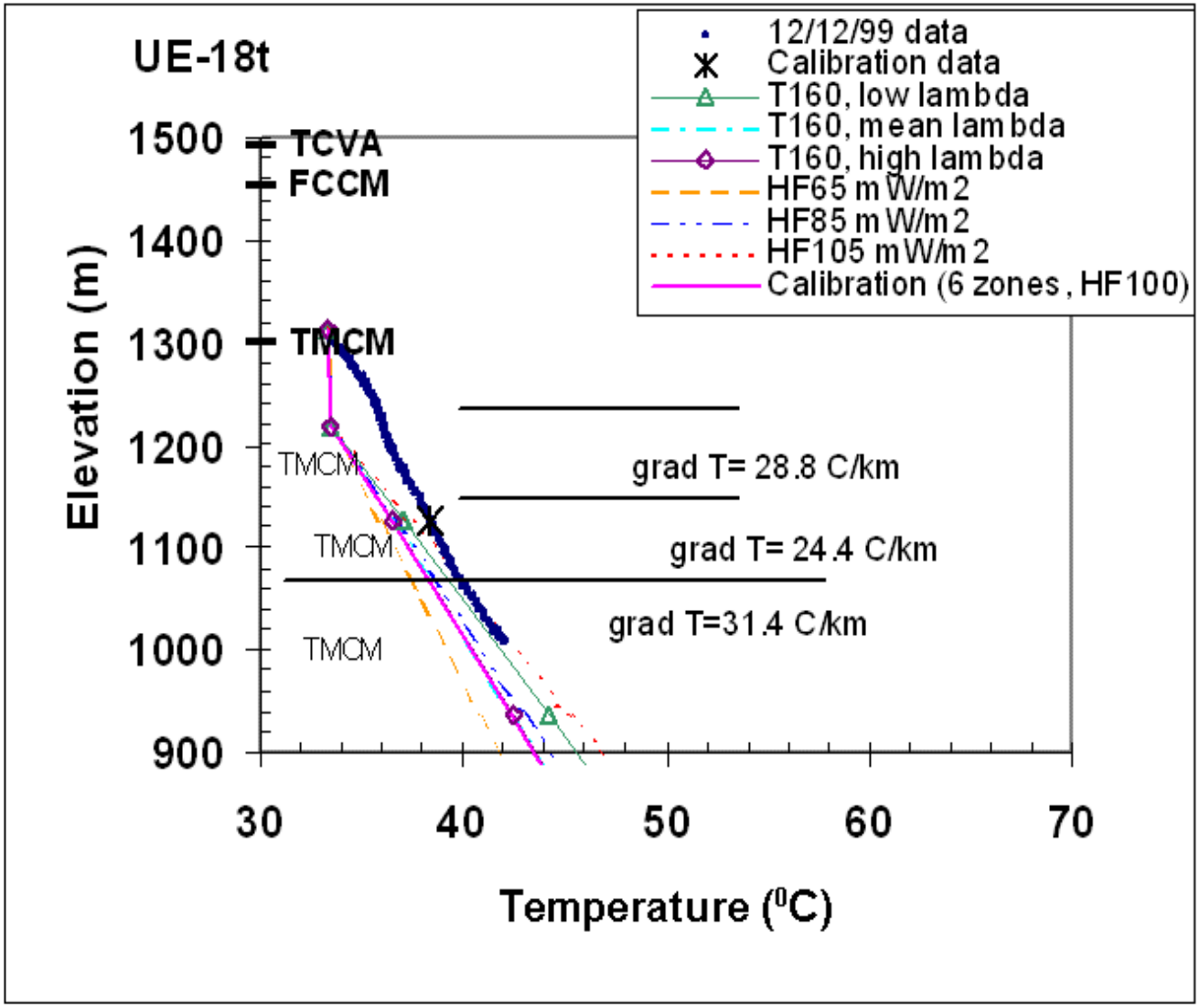
UE-18t
12/12/99 data
Calibration data
T160, low lambda
T160, mean lambda
T160, high lambda
HF65 mW/m2
HF85 mW/m2
HF105 mW/m2
Calibration (6 zones, HF100)
1500
1400
1300
1200
1100
1000
900
TCVA
FCCM
TMCM
TMCM
TMCM
TMCM
grad T= 28.8 C/km
grad T= 24.4 C/km
grad T=31.4 C/km
Elevation (m)
30
40
50
60
70
Temperature (0C)

Figure C27

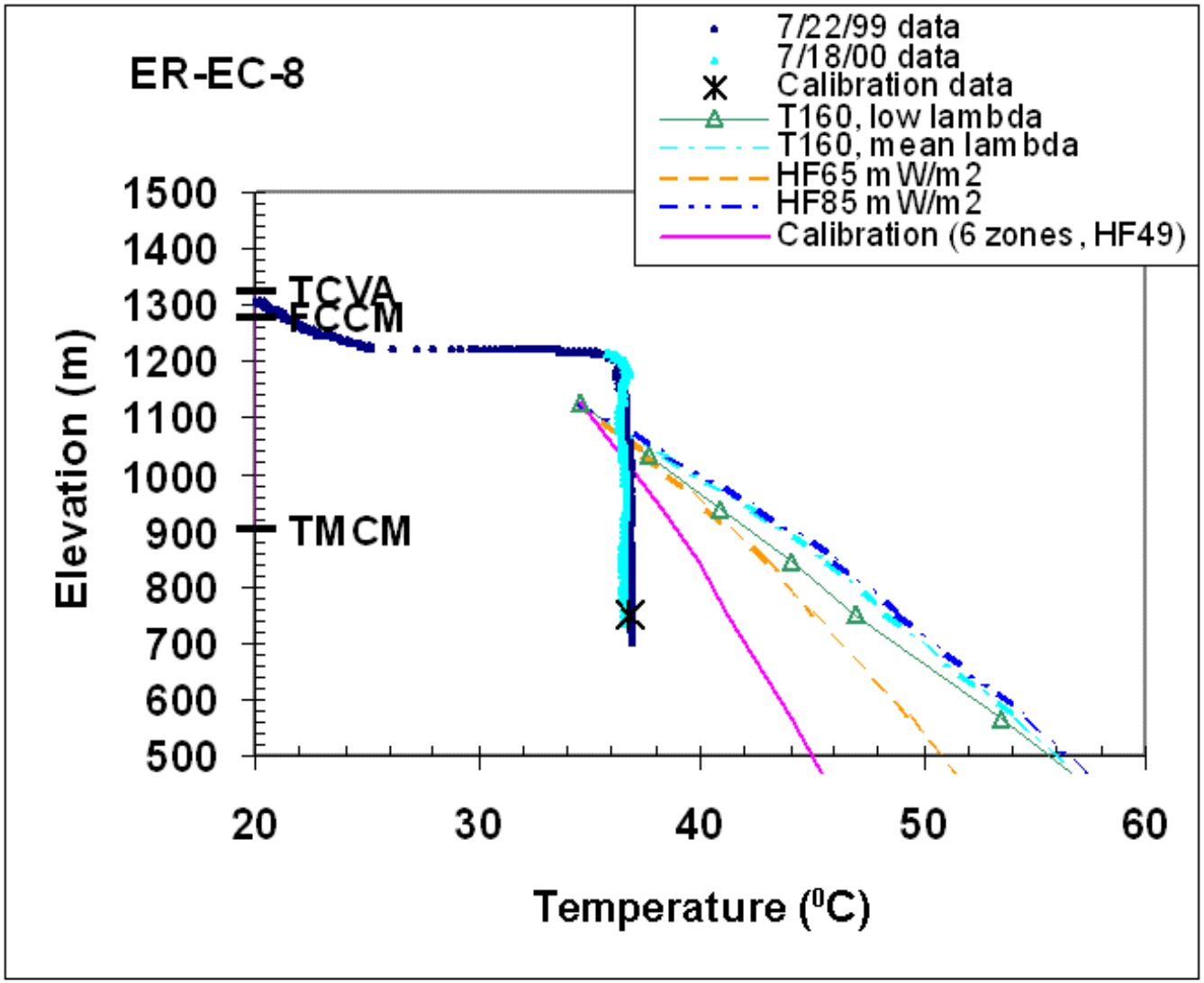
ER-EC-8
7/22/99 data
7/18/00 data
Calibration data
T160, low lambda
T160, mean lambda
HF65 mW/m2
HF85 mW/m2
Calibration (6 zones, HF49)
Elevation (m)
1500
1400
1300
1200
1100
1000
900
800
700
600
500
TCVA
TCCM
TMCM
20
30
40
50
60
Temperature (0C)

Figure C28

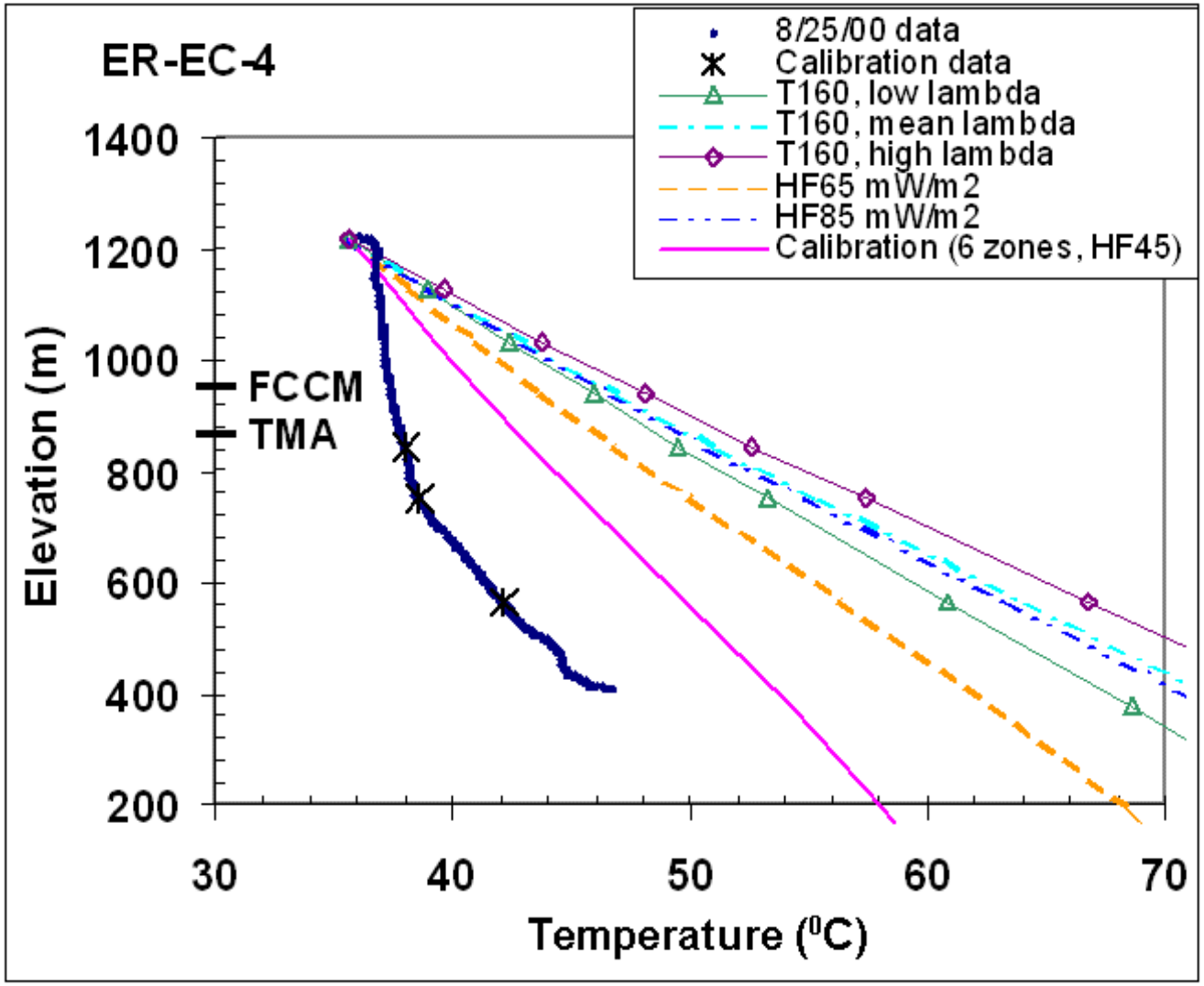
ER-EC-4
8/25/00 data
Calibration data
T160, low lambda
T160, mean lambda
T160, high lambda
HF65 mW/m2
HF85 mW/m2
Calibration (6 zones, HF45)
Elevation (m)
1400
1200
1000
800
600
400
200
FCCM
TMA
30
40
50
60
70
Temperature (0C)

Figure C29

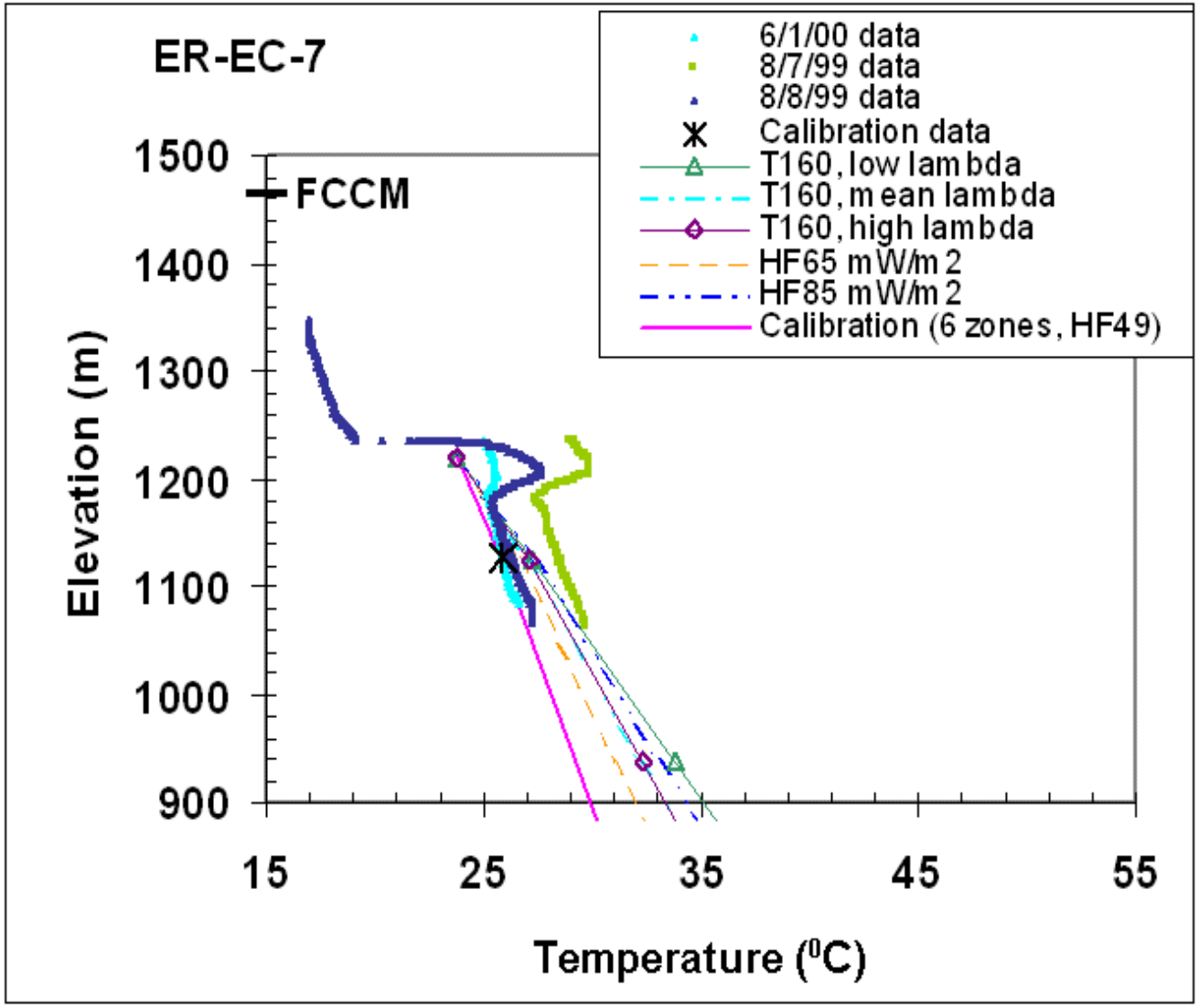
ER-EC-7
FCCM
6/1/00 data
8/7/99 data
8/8/99 data
Calibration data
T160, low lambda
T160, mean lambda
T160, high lambda
HF65 mW/m2
HF85 mW/m2
Calibration (6 zones, HF49)
Elevation (m)
1500
1400
1300
1200
1100
1000
900
15
25
35
45
55
Temperature (0C)

Figure C30

Explanation of stratigraphic symbols, rock types, alteration, and hydrogeologic units

Stratigraphy

unk = unknown
Tgs = Tertiary sediments
Tt = Thirsty Canyon Group
Ttr = Rocket Wash Tuff
Ttt = Trail Ridge Tuff
Ttp = Pahute Mesa and Rocket Wash Tuffs
Tf = Volcanics of Fortymile Canyon
Tfb = Beatty Wash Formation
Tfbr = Rhyolite of Chukar Canyon
Tfbw = Rhyolite of Beatty Wash
Tm = Timber Mountain Group
Tma = Ammonia Tanks Tuff
Tmab = bedded Ammonia Tanks Tuff
Tmap = mafic-poor Ammonia Tanks Tuff
Tmat = Rhyolite of Tannebaum Hill
Tmt = Basalt Rhyolite of Tannebaum Hill
Tmr = Rainier Mesa Tuff
Tmrb = Bedded Rainier Mesa Tuff
Tmrf = Rhyolite of Fluorspar Canyon
Tmrr = mafic-rich Rainer Mesa Tuff
Tmrp = mafic-poor Rainer Mesa Tuff
Tmrh = Tuff of Holmes Road
Tmrx = Landslide or eruptive breccia
Tmaw = Tuff of Buttonhook Wash
Tmw = Rhyolite of Windy Wash
Tp = Paintbrush Group
Tpb = Rhyolite of Benham
Tpc = Tiva Canyon Tuff
Tpd = Rhyolite of Delirium Canyon
Tpe = Rhyolite of Echo Peak
Tpr = Rhyolite of Silent Canyon
Tpt = Topopah Spring Tuff
Th = Calico Hills Formation
Tc = Crater Flat Group
Tcp = Prow Pass Tuff
Tci = Rhyolite of Inlet
Tcj = Andesite of Grimy Gulch
Tcpk = Rhyolite of Kearsarge
Tcb = Bullfrog Tuff
Tct = Tram Tuff
Tb = Belted Range Group
Tbd = Deadhorse Flat Formation
Tq =Volcanics of Quartz Mountain
To = Volcanics of Oak Spring Butte
Ton = Older tunnel beds
Tor = Redrock Valley Tuff
Tot = Tuff of Twin Peaks

Lithology/Rock type

AL = alluvium
BD = basaltic dike
BS = basalt
BED = bedded tuff
DM = dolomite
DWT = densely welded tuff
FB = flow breccia
IN = intrusive
ITL = intermediate to trachytic lava
LA = lava
MWT = moderately welded tuff
NWT = nonwelded tuff
PL = pumiceous (frothy) lava
PWT = partially welded tuff
QTZ = quartzite or sandstone
RWT = reworked tuff
SLT = siltstone
TS = tuffaceous sandstone
TUF = tuff
TB = tuff breccia
unk = unknown
VT = vitrophyric tuff, vitric bedded
WBE = welded bedded tuff
WT = welded tuff

Major Alteration

KA = kaolinitic
KF = potassic
MP = microporphyritic (holocrystalline)
OP = opalline
PI = pilotaxitic (holocrystalline)
PY = pyritic
QC = silicic (chalcedony)
QF = quartzo-feldspathic
QZ = silicic
SE = seriate (holocrystalline)
unk = unknown
VP = devitrified (vapor phase)
ZA = zeolitic (analcime)
ZC = zeolitic (clinoptilolite)
ZE = zeolitic
ZM = zeolitic (mordenite)

Hydrogeologic Units

AA = Alluvial aquifer
WTA = Welded tuff aquifer
VTA = Vitric Tuff aquifer
LFA = Lava flow aquifer
TCU = Tuff confining unit
CCU = Clastic confining unit

Appendix D

Perturbation Sensitivity Analysis Plots

D.1.0 INTRODUCTION

This appendix contains perturbation sensitivity analysis plots for the Pahute Mesa Oasis Valley area. Included are figures for Base HFM with Depth Decay and Anisotropy, Base HFM with Selected Depth Decay and Selected Anisotropy, and Silent Canyon Caldera Complex Selected Depth Decay and Selected Anisotropy.

D.2.0 DATA PRESENTATION

The data are presented in individual figures. These figures present the change in some model metric as a function of model parameters. The model metrics in each file are as follows:

- Average Head – change in calibration target head as defined in Section 6.1.1.
- Lateral Boundary west, south, east, and north – change in respective model edge flow objective function
- Lateral Boundary – Oasis Valley – change in objective function for each discharge zone in Oasis Valley
- Oasis Valley Discharge – change in objective function for entire Oasis Valley
- Boundary Flow Goodness of Fit – change in objective function for all boundary flows
- Total objective function – change in PHI, overall model goodness of fit
- Spring head – change in spring head component of model goodness of fit
- Observation well goodness of fit – change in observation well component of model goodness of fit

Model parameters are referred to in a shorthand that incorporates both the index number as given in Section 4.0 and the HSU name abbreviation (also given in Section 4.0). For instance, hsu01lccu is HSU index number 1, which is also the LCCU. Depth decay is referred to by "dd" to identify the parameter, by HSU type via "ca" for carbonate and "va" for volcanic, and by HSU number. Thus, ddca02 is for a carbonate that is also HSU 2 (the LCA proper). DDVA32 is depth decay for volcanic HSU number 32, which is the PCM. Faults are referred to by number and a brief abbreviation of the name.

D.3.0 ACCESS TO DATA

The perturbation sensitivity analysis plots can be found on the accompanying CD in pdf format. The data files are listed below.

D.3.1 Base HFM with Depth Decay and Anisotropy with MME Recharge

- Average Head.pdf
- Lateral Boundary – West Face Model Flow.pdf
- Lateral Boundary – South Face Model Flow.pdf
- Lateral Boundary – East Face Model Flow.pdf
- Lateral Boundary – North Face Model Flow.pdf
- Lateral Boundary – Oasis Valley Discharge Region 1 Flow.pdf
- Lateral Boundary – Oasis Valley Discharge Region 2 Flow.pdf
- Lateral Boundary – Oasis Valley Discharge Region 3 Flow.pdf
- Lateral Boundary – Oasis Valley Discharge Region 4 Flow.pdf
- Lateral Boundary – Oasis Valley Discharge Region 5 Flow.pdf
- Lateral Boundary – Oasis Valley Discharge Region 6 Flow.pdf
- Lateral Boundary – Oasis Valley Discharge Region 8 Flow.pdf
- Oasis Valley Discharge.pdf
- Boundary Flow Goodness of Fit.pdf
- Total Objective Function.pdf
- Spring Head.pdf
- Observation Well Goodness of Fit.pdf

D.3.2 Base HFM with Selected Depth Decay and Selected Anisotropy with MME Recharge

- Average Head.pdf
- Lateral Boundary – West Face Model Flow.pdf
- Lateral Boundary – South Face Model Flow.pdf
- Lateral Boundary – East Face Model Flow.pdf
- Lateral Boundary – North Face Model Flow.pdf
- Lateral Boundary – Oasis Valley Discharge Region 1 Flow.pdf
- Lateral Boundary – Oasis Valley Discharge Region 2 Flow.pdf
- Lateral Boundary – Oasis Valley Discharge Region 3 Flow.pdf
- Lateral Boundary – Oasis Valley Discharge Region 4 Flow.pdf
- Lateral Boundary – Oasis Valley Discharge Region 5 Flow.pdf

- Lateral Boundary – Oasis Valley Discharge Region 6 Flow.pdf
- Lateral Boundary – Oasis Valley Discharge Region 8 Flow.pdf
- Oasis Valley Discharge.pdf
- Boundary Flow Goodness of Fit.pdf
- Total Objective Function.pdf
- Spring Head.pdf
- Observation Well Goodness of Fit.pdf

D.3.3 Silent Canyon Caldera Complex Selected Depth Decay and Anisotropy with MME Recharge

- Average Head.pdf
- Lateral Boundary – West Face Model Flow.pdf
- Lateral Boundary – South Face Model Flow.pdf
- Lateral Boundary – East Face Model Flow.pdf
- Lateral Boundary – North Face Model Flow.pdf
- Lateral Boundary – Oasis Valley Discharge Region 1 Flow.pdf
- Lateral Boundary – Oasis Valley Discharge Region 2 Flow.pdf
- Lateral Boundary – Oasis Valley Discharge Region 3 Flow.pdf
- Lateral Boundary – Oasis Valley Discharge Region 4 Flow.pdf
- Lateral Boundary – Oasis Valley Discharge Region 5 Flow.pdf
- Lateral Boundary – Oasis Valley Discharge Region 6 Flow.pdf
- Lateral Boundary – Oasis Valley Discharge Region 8 Flow.pdf
- Oasis Valley Discharge.pdf
- Boundary Flow Goodness of Fit.pdf
- Total Objective Function.pdf
- Spring Head.pdf
- Observation Well Goodness of Fit.pdf

Appendix E

CAU Model Permeability Along Geologic Model Cross Sections

E.1.0 CAU Model Permeability Along Geologic Model Cross Sections

This appendix presents the CAU model intrinsic permeability along geologic cross sections A through J as desribed in BN (2002) for the base HFM (selected and all HSU depth decay and anisotropy), the SCCC HFM, and the RIDGE, TCL, PZUP, SEPZ, and DRT alternatives (see Section 2.0 for a description, and Sections 5.0 and 6.0 for calibration results). The sections for PZUP with DRI-A recharge, PZUP with USGS-D recharge, DRT with DRI-A recharge, and DRT with USGS-D recharge are also presented. Figure E.1-1 shows the location and names of the sections.

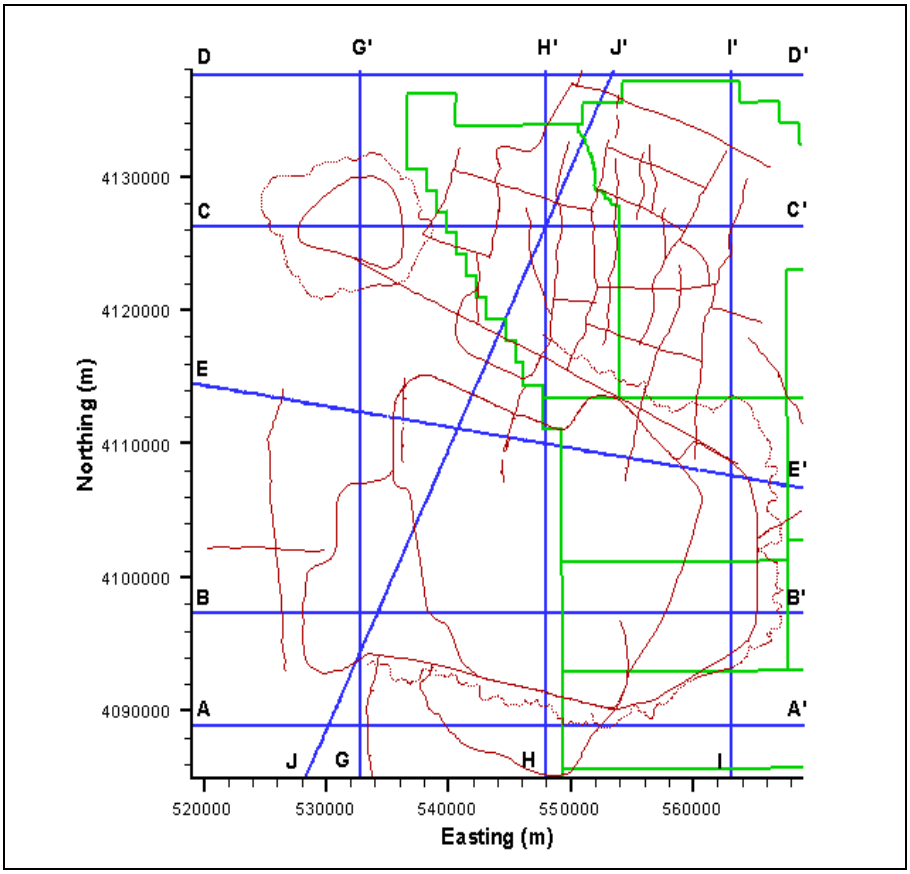

Figure E.1-1
Geologic Cross-Section Key

Base HFM - Selected HSU Depth Decay and Anisotropy (BN-MME-SDA)

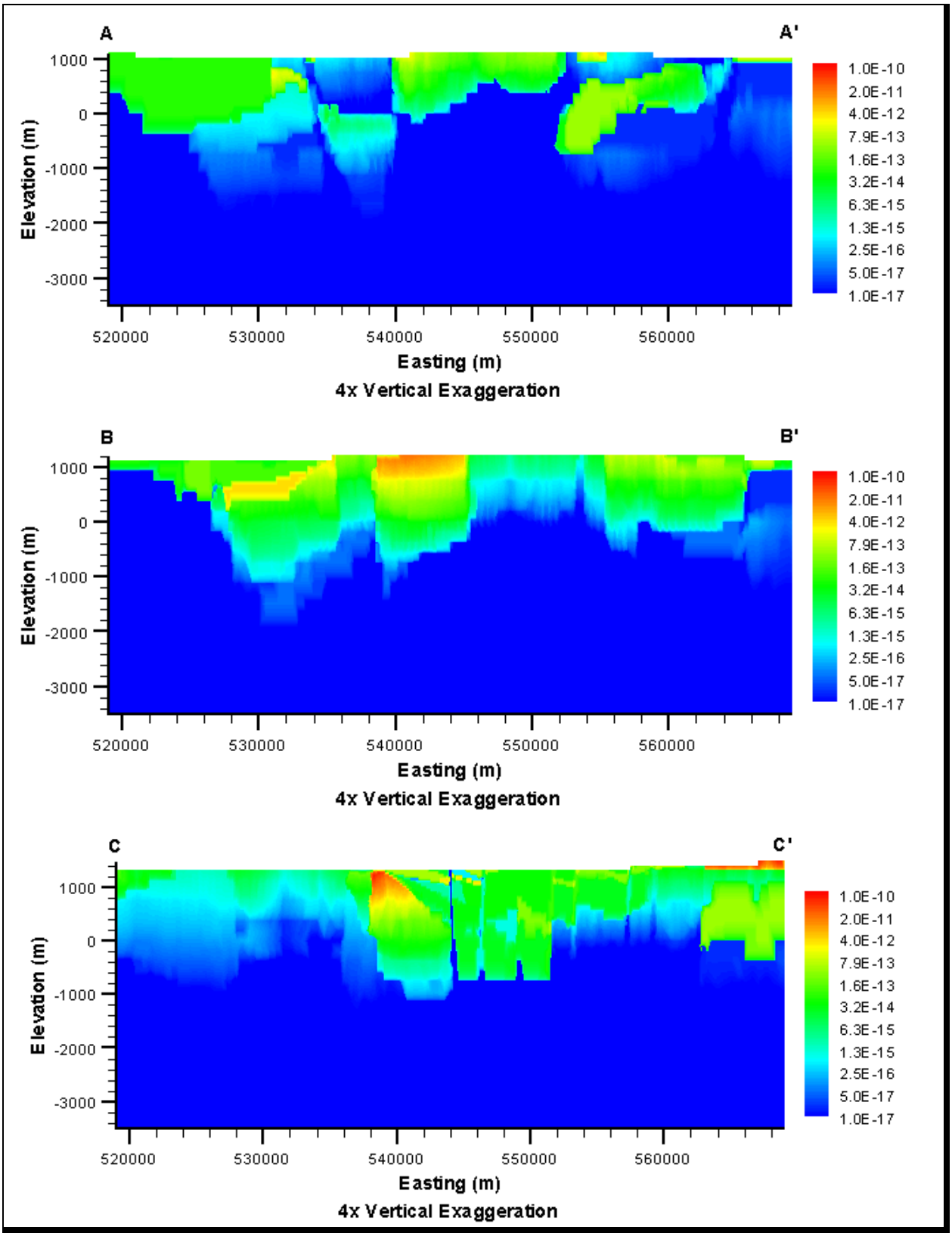
A
A'
1000
0
-1000
-2000
-3000
Elevation (m)
520000
530000
540000
550000
560000
Easting (m)
4x Vertical Exaggeration
1.0E-10
2.0E-11
4.0E-12
7.9E-13
1.6E-13
3.2E-14
6.3E-15
1.3E-15
2.5E-16
5.0E-17
1.0E-17
B
B'
1000
0
-1000
-2000
-3000
Elevation (m)
520000
530000
540000
550000
560000
Easting (m)
4x Vertical Exaggeration
1.0E-10
2.0E-11
4.0E-12
7.9E-13
1.6E-13
3.2E-14
6.3E-15
1.3E-15
2.5E-16
5.0E-17
1.0E-17
C
C'
1000
0
-1000
-2000
-3000
Elevation (m)
520000
530000
540000
550000
560000
Easting (m)
4x Vertical Exaggeration
1.0E-10
2.0E-11
4.0E-12
7.9E-13
1.6E-13
3.2E-14
6.3E-15
1.3E-15
2.5E-16
5.0E-17
1.0E-17

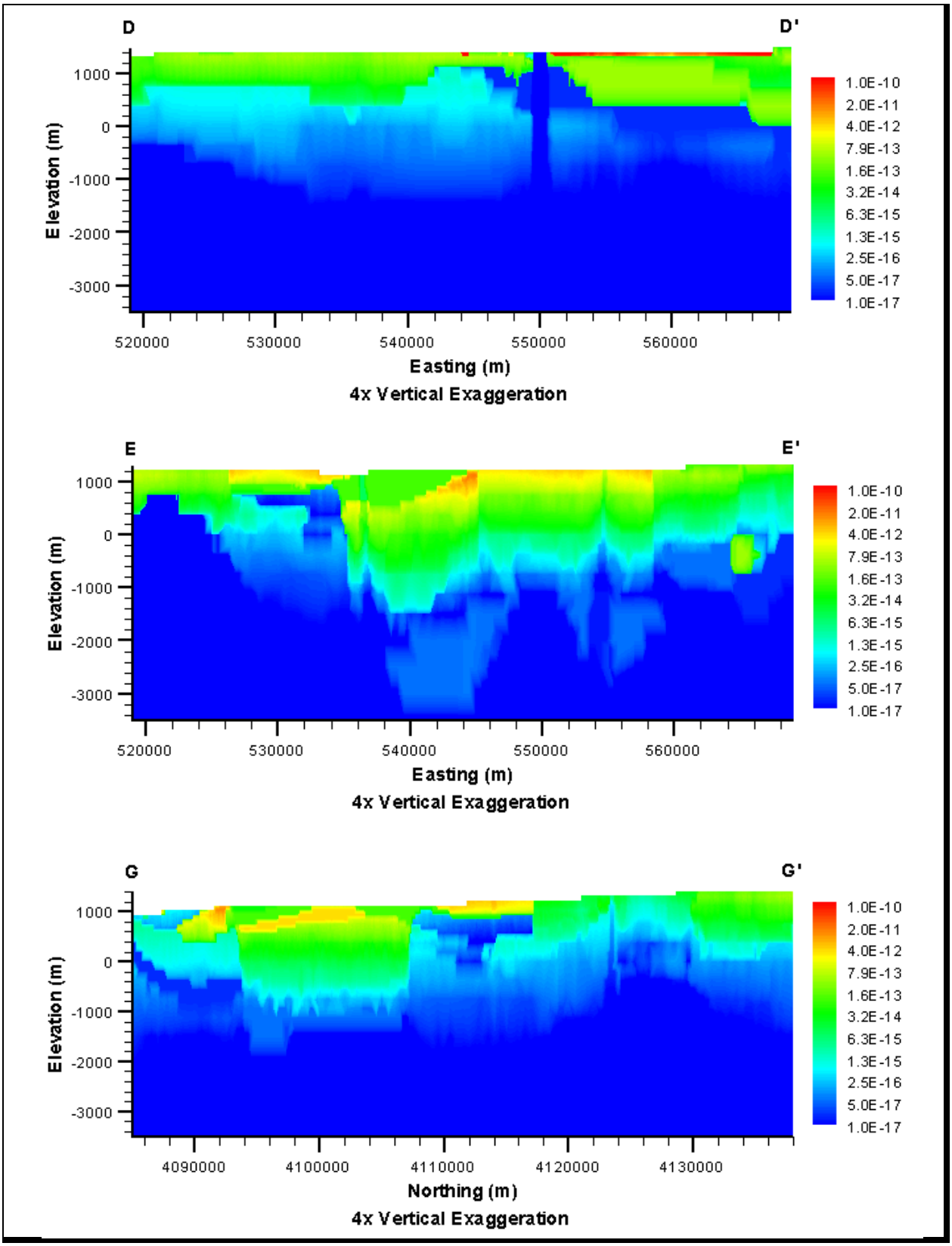
D
D'
1000
0
-1000
-2000
-3000
Elevation (m)
520000
530000
540000
550000
560000
Easting (m)
4x Vertical Exaggeration
1.0E-10
2.0E-11
4.0E-12
7.9E-13
1.6E-13
3.2E-14
6.3E-15
1.3E-15
2.5E-16
5.0E-17
1.0E-17
E
E'
1000
0
-1000
-2000
-3000
Elevation (m)
520000
530000
540000
550000
560000
Easting (m)
4x Vertical Exaggeration
1.0E-10
2.0E-11
4.0E-12
7.9E-13
1.6E-13
3.2E-14
6.3E-15
1.3E-15
2.5E-16
5.0E-17
1.0E-17
G
G'
1000
0
-1000
-2000
-3000
Elevation (m)
4090000
4100000
4110000
4120000
4130000
Northing (m)
4x Vertical Exaggeration
1.0E-10
2.0E-11
4.0E-12
7.9E-13
1.6E-13
3.2E-14
6.3E-15
1.3E-15
2.5E-16
5.0E-17
1.0E-17

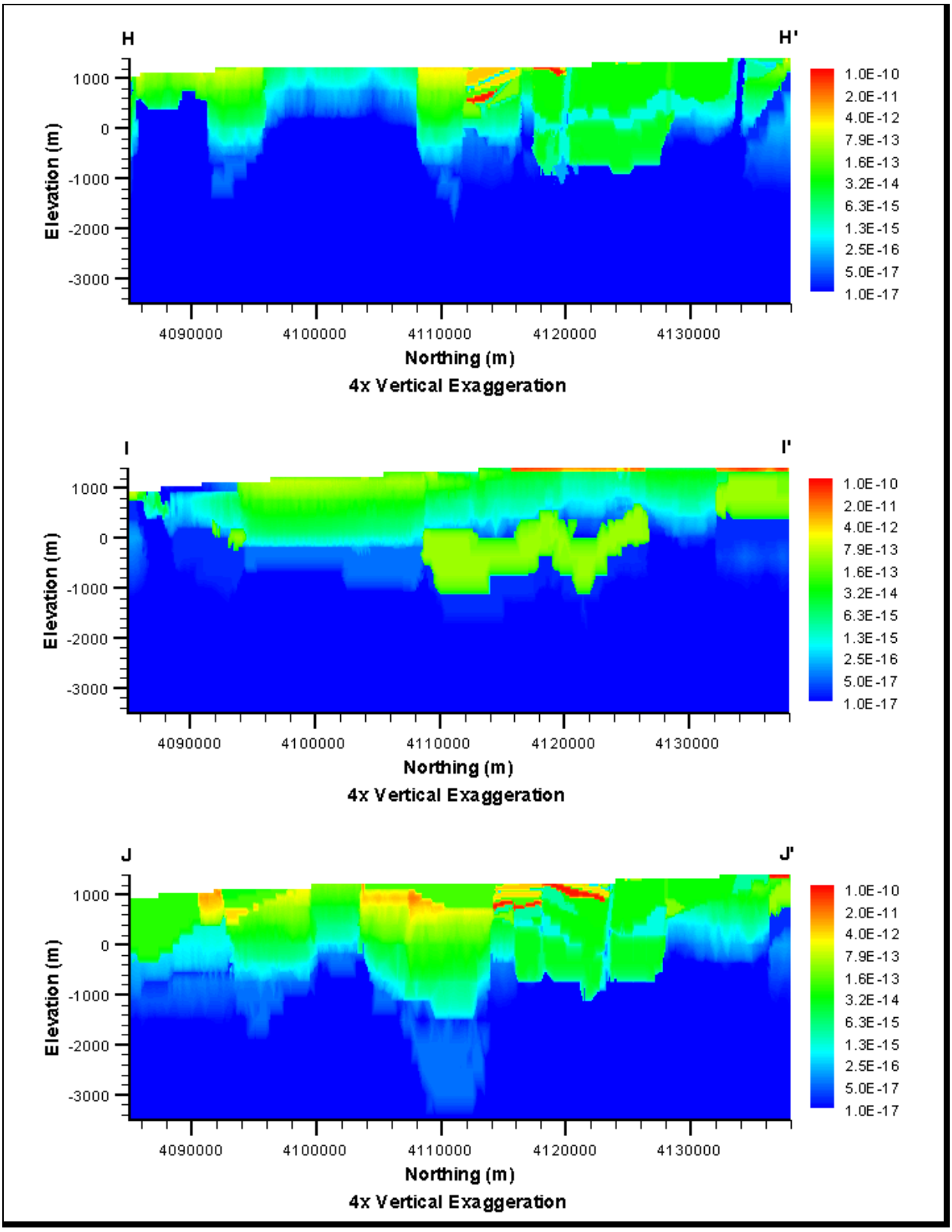
H
H'
1000
0
-1000
-2000
-3000
Elevation (m)
4090000
4100000
4110000
4120000
4130000
Northing (m)
4x Vertical Exaggeration
1.0E-10
2.0E-11
4.0E-12
7.9E-13
1.6E-13
3.2E-14
6.3E-15
1.3E-15
2.5E-16
5.0E-17
1.0E-17
I
I'
1000
0
-1000
-2000
-3000
Elevation (m)
4090000
4100000
4110000
4120000
4130000
Northing (m)
4x Vertical Exaggeration
1.0E-10
2.0E-11
4.0E-12
7.9E-13
1.6E-13
3.2E-14
6.3E-15
1.3E-15
2.5E-16
5.0E-17
1.0E-17
J
J'
1000
0
-1000
-2000
-3000
Elevation (m)
4090000
4100000
4110000
4120000
4130000
Northing (m)
4x Vertical Exaggeration
1.0E-10
2.0E-11
4.0E-12
7.9E-13
1.6E-13
3.2E-14
6.3E-15
1.3E-15
2.5E-16
5.0E-17
1.0E-17

Base HFM - All HSU Depth Decay and Anisotropy (BN-MME-ADA)

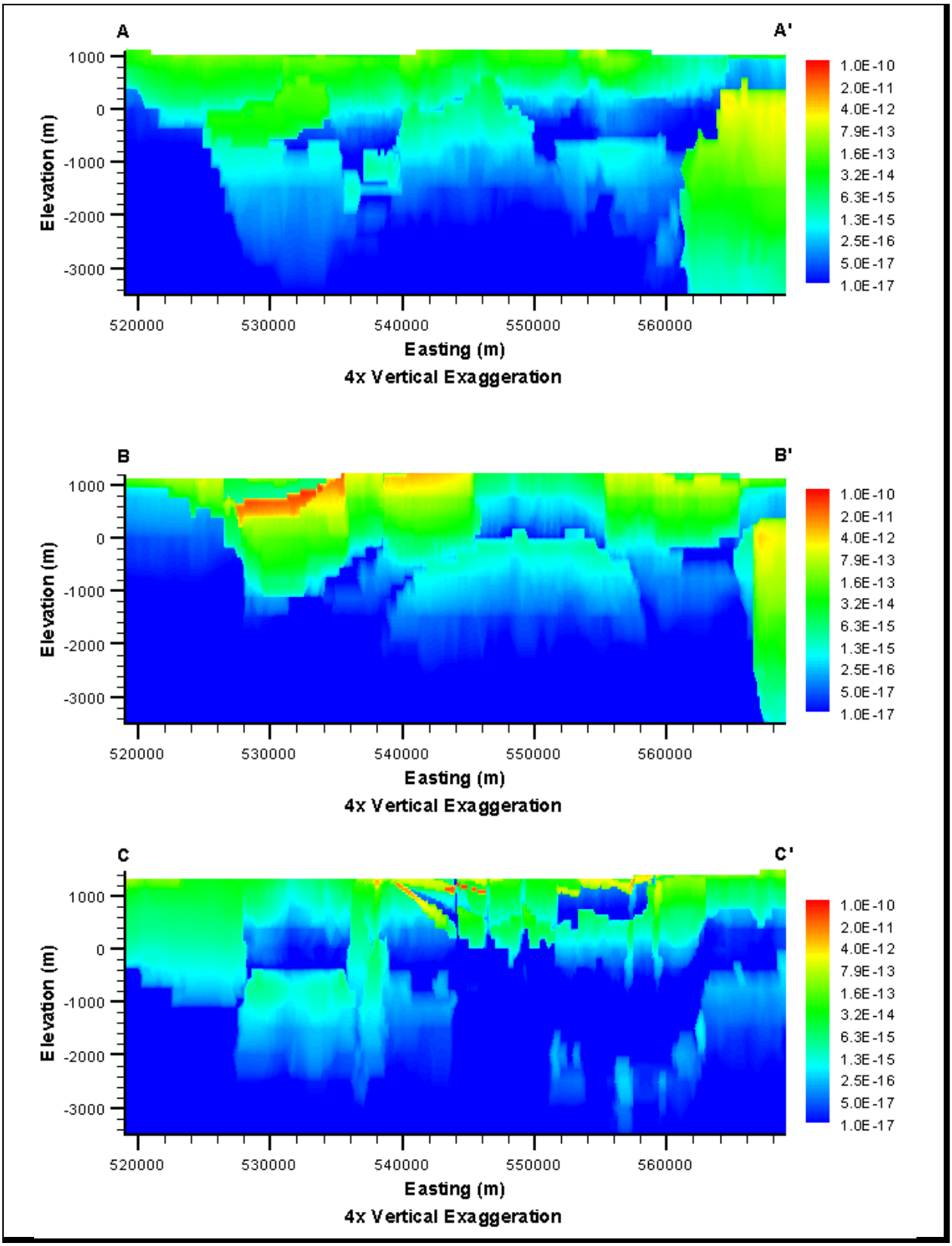
A
A'
1000
0
-1000
-2000
-3000
Elevation (m)
520000
530000
540000
550000
560000
Easting (m)
4x Vertical Exaggeration
1.0E-10
2.0E-11
4.0E-12
7.9E-13
1.6E-13
3.2E-14
6.3E-15
1.3E-15
2.5E-16
5.0E-17
1.0E-17
B
B'
1000
0
-1000
-2000
-3000
Elevation (m)
520000
530000
540000
550000
560000
Easting (m)
4x Vertical Exaggeration
1.0E-10
2.0E-11
4.0E-12
7.9E-13
1.6E-13
3.2E-14
6.3E-15
1.3E-15
2.5E-16
5.0E-17
1.0E-17
C
C'
1000
0
-1000
-2000
-3000
Elevation (m)
520000
530000
540000
550000
560000
Easting (m)
4x Vertical Exaggeration
1.0E-10
2.0E-11
4.0E-12
7.9E-13
1.6E-13
3.2E-14
6.3E-15
1.3E-15
2.5E-16
5.0E-17
1.0E-17

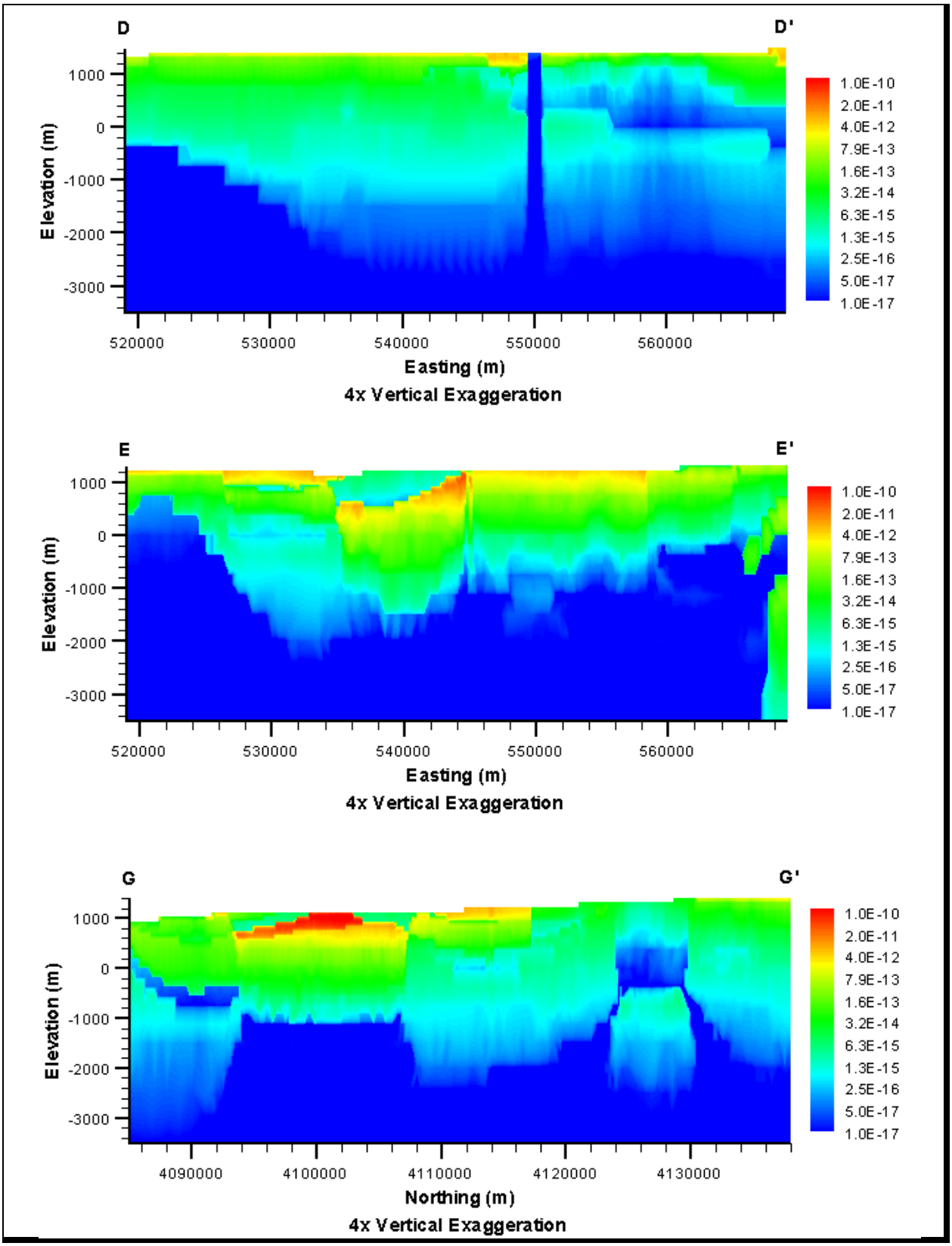
D
D'
1000
0
-1000
-2000
-3000
Elevation (m)
520000
530000
540000
550000
560000
Easting (m)
4x Vertical Exaggeration
1.0E-10
2.0E-11
4.0E-12
7.9E-13
1.6E-13
3.2E-14
6.3E-15
1.3E-15
2.5E-16
5.0E-17
1.0E-17
E
E'
1000
0
-1000
-2000
-3000
Elevation (m)
520000
530000
540000
550000
560000
Easting (m)
4x Vertical Exaggeration
1.0E-10
2.0E-11
4.0E-12
7.9E-13
1.6E-13
3.2E-14
6.3E-15
1.3E-15
2.5E-16
5.0E-17
1.0E-17
G
G'
1000
0
-1000
-2000
-3000
Elevation (m)
4090000
4100000
4110000
4120000
4130000
Northing (m)
4x Vertical Exaggeration
1.0E-10
2.0E-11
4.0E-12
7.9E-13
1.6E-13
3.2E-14
6.3E-15
1.3E-15
2.5E-16
5.0E-17
1.0E-17

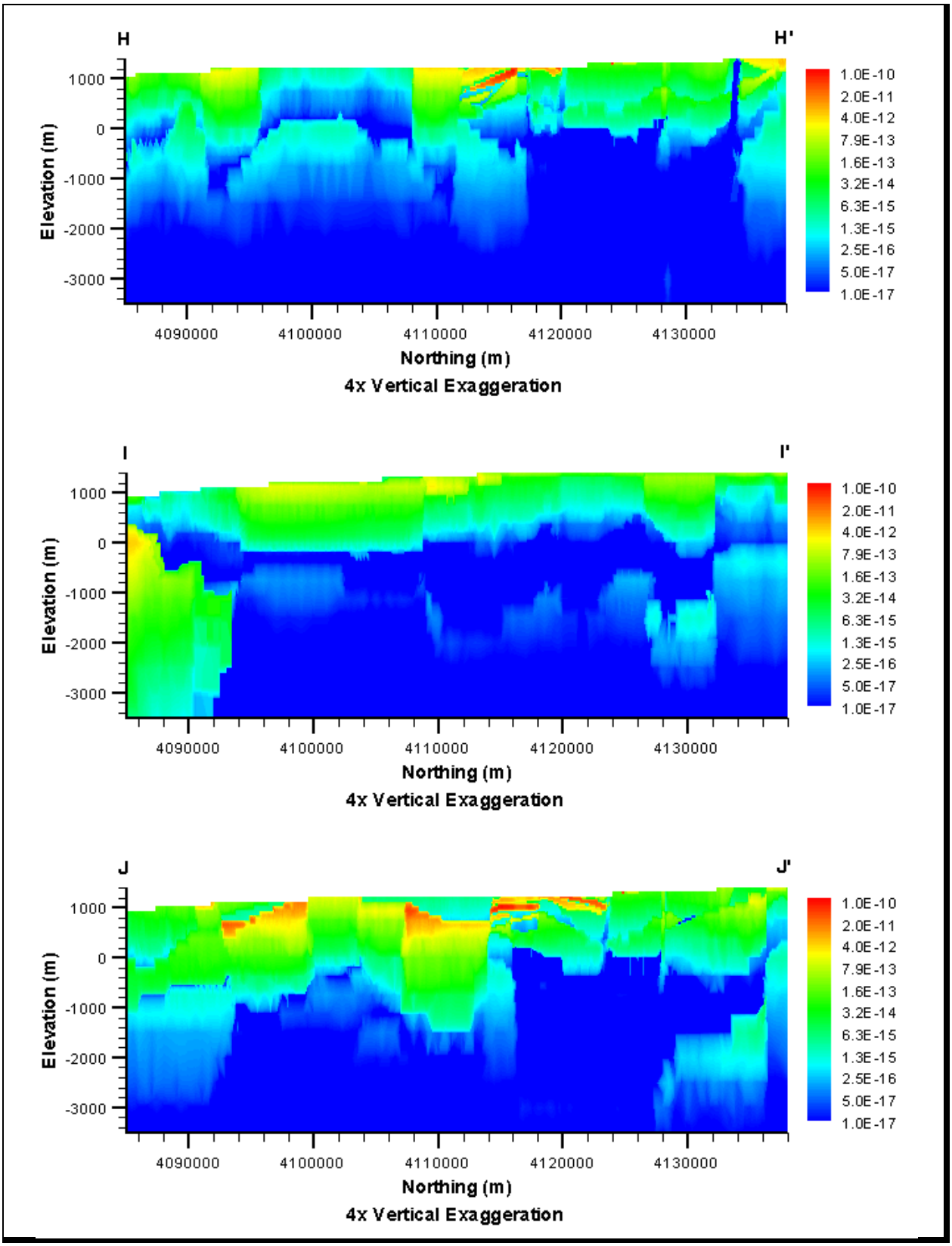
H
H'
1000
0
-1000
-2000
-3000
Elevation (m)
4090000
4100000
4110000
4120000
4130000
Northing (m)
4x Vertical Exaggeration
1.0E-10
2.0E-11
4.0E-12
7.9E-13
1.6E-13
3.2E-14
6.3E-15
1.3E-15
2.5E-16
5.0E-17
1.0E-17
I
I'
1000
0
-1000
-2000
-3000
Elevation (m)
4090000
4100000
4110000
4120000
4130000
Northing (m)
4x Vertical Exaggeration
1.0E-10
2.0E-11
4.0E-12
7.9E-13
1.6E-13
3.2E-14
6.3E-15
1.3E-15
2.5E-16
5.0E-17
1.0E-17
J
J'
1000
0
-1000
-2000
-3000
Elevation (m)
4090000
4100000
4110000
4120000
4130000
Northing (m)
4x Vertical Exaggeration
1.0E-10
2.0E-11
4.0E-12
7.9E-13
1.6E-13
3.2E-14
6.3E-15
1.3E-15
2.5E-16
5.0E-17
1.0E-17

SCCC HFM - Selected HSU Depth Decay and Anisotropy (SCCC-MME-SDA)

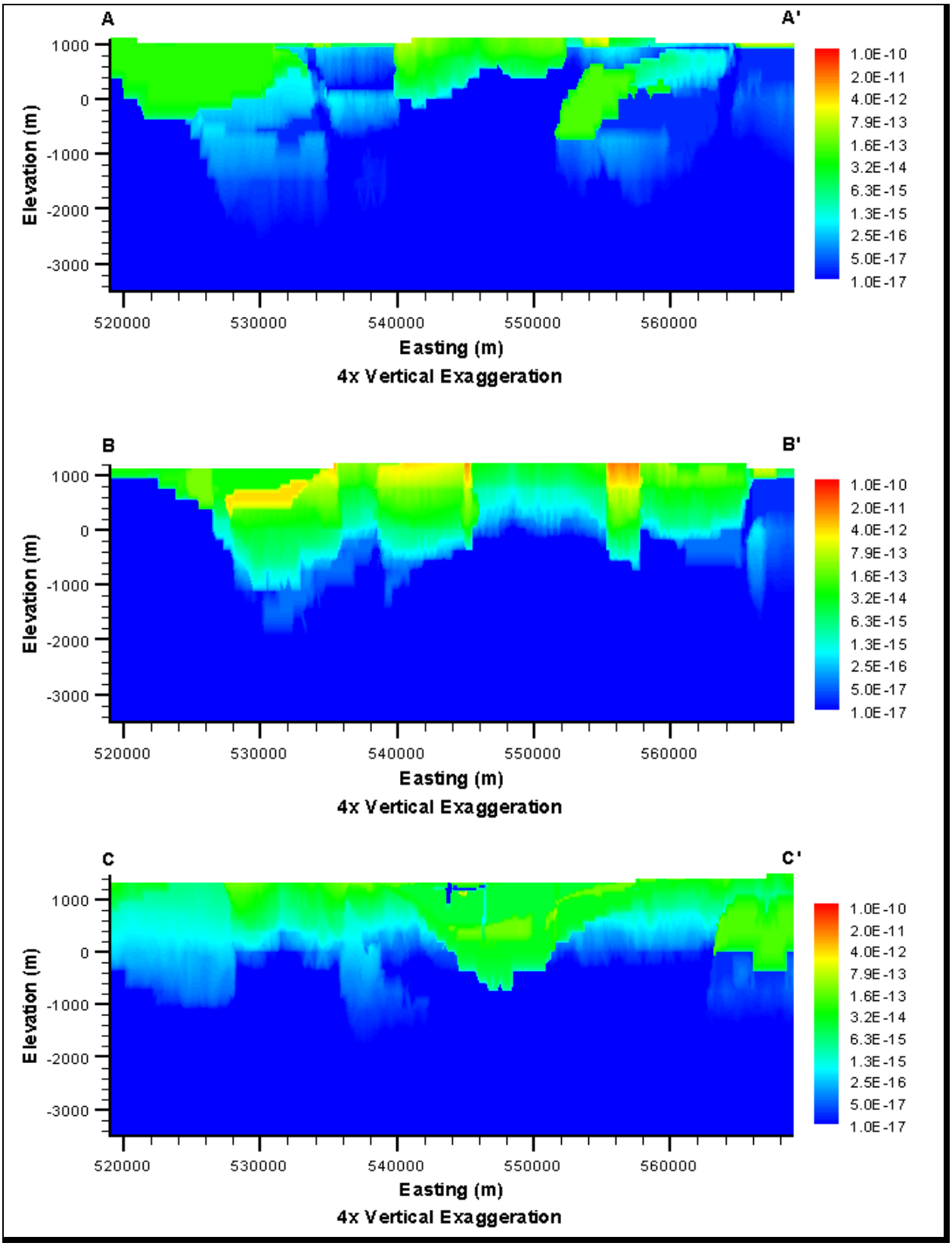
A
A'
1000
0
-1000
-2000
-3000
Elevation (m)
520000
530000
540000
550000
560000
Easting (m)
4x Vertical Exaggeration
1.0E-10
2.0E-11
4.0E-12
7.9E-13
1.6E-13
3.2E-14
6.3E-15
1.3E-15
2.5E-16
5.0E-17
1.0E-17
B
B'
1000
0
-1000
-2000
-3000
Elevation (m)
520000
530000
540000
550000
560000
Easting (m)
4x Vertical Exaggeration
1.0E-10
2.0E-11
4.0E-12
7.9E-13
1.6E-13
3.2E-14
6.3E-15
1.3E-15
2.5E-16
5.0E-17
1.0E-17
C
C'
1000
0
-1000
-2000
-3000
Elevation (m)
520000
530000
540000
550000
560000
Easting (m)
4x Vertical Exaggeration
1.0E-10
2.0E-11
4.0E-12
7.9E-13
1.6E-13
3.2E-14
6.3E-15
1.3E-15
2.5E-16
5.0E-17
1.0E-17

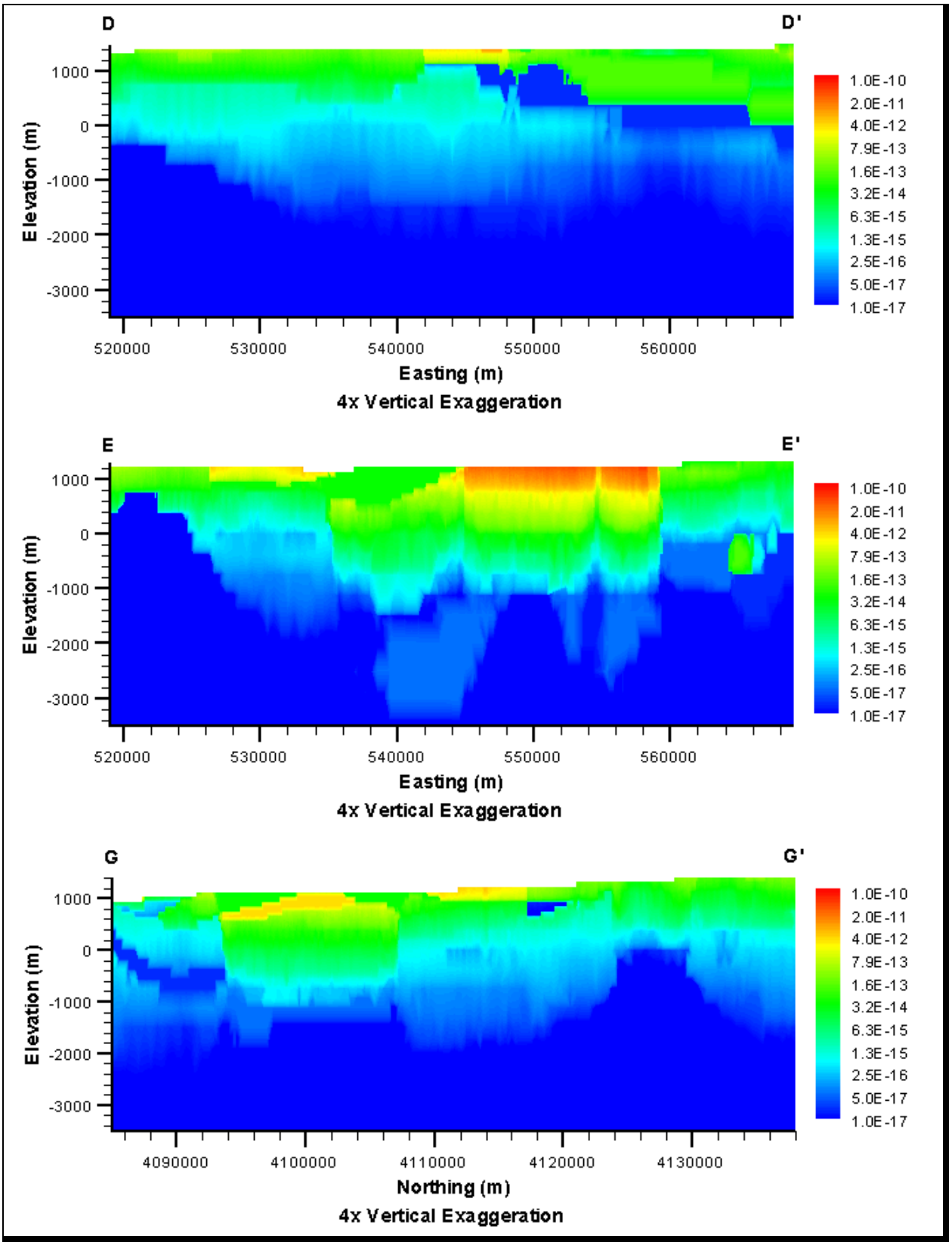
D
D'
1000
0
-1000
-2000
-3000
Elevation (m)
520000
530000
540000
550000
560000
Easting (m)
4x Vertical Exaggeration
1.0E-10
2.0E-11
4.0E-12
7.9E-13
1.6E-13
3.2E-14
6.3E-15
1.3E-15
2.5E-16
5.0E-17
1.0E-17
E
E'
1000
0
-1000
-2000
-3000
Elevation (m)
520000
530000
540000
550000
560000
Easting (m)
4x Vertical Exaggeration
1.0E-10
2.0E-11
4.0E-12
7.9E-13
1.6E-13
3.2E-14
6.3E-15
1.3E-15
2.5E-16
5.0E-17
1.0E-17
G
G'
1000
0
-1000
-2000
-3000
Elevation (m)
4090000
4100000
4110000
4120000
4130000
Northing (m)
4x Vertical Exaggeration
1.0E-10
2.0E-11
4.0E-12
7.9E-13
1.6E-13
3.2E-14
6.3E-15
1.3E-15
2.5E-16
5.0E-17
1.0E-17

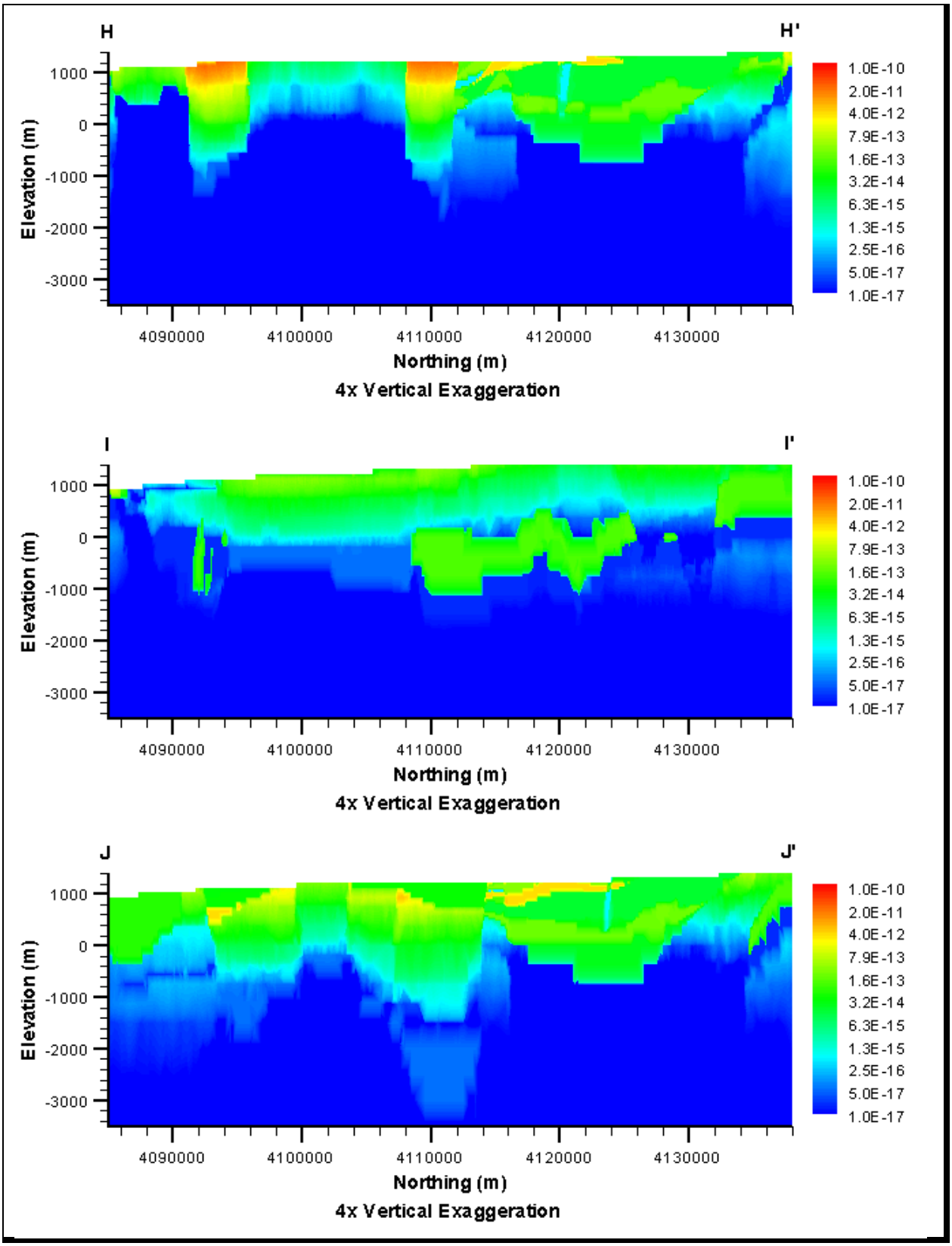
H
H'
Elevation (m)
1000
0
-1000
-2000
-3000
4090000
4100000
4110000
4120000
4130000
Northing (m)
4x Vertical Exaggeration
1.0E-10
2.0E-11
4.0E-12
7.9E-13
1.6E-13
3.2E-14
6.3E-15
1.3E-15
2.5E-16
5.0E-17
1.0E-17
I
I'
Elevation (m)
1000
0
-1000
-2000
-3000
4090000
4100000
4110000
4120000
4130000
Northing (m)
4x Vertical Exaggeration
1.0E-10
2.0E-11
4.0E-12
7.9E-13
1.6E-13
3.2E-14
6.3E-15
1.3E-15
2.5E-16
5.0E-17
1.0E-17
J
J'
Elevation (m)
1000
0
-1000
-2000
-3000
4090000
4100000
4110000
4120000
4130000
Northing (m)
4x Vertical Exaggeration
1.0E-10
2.0E-11
4.0E-12
7.9E-13
1.6E-13
3.2E-14
6.3E-15
1.3E-15
2.5E-16
5.0E-17
1.0E-17

Basement Ridge Model (RIDGE-MME-SDA)

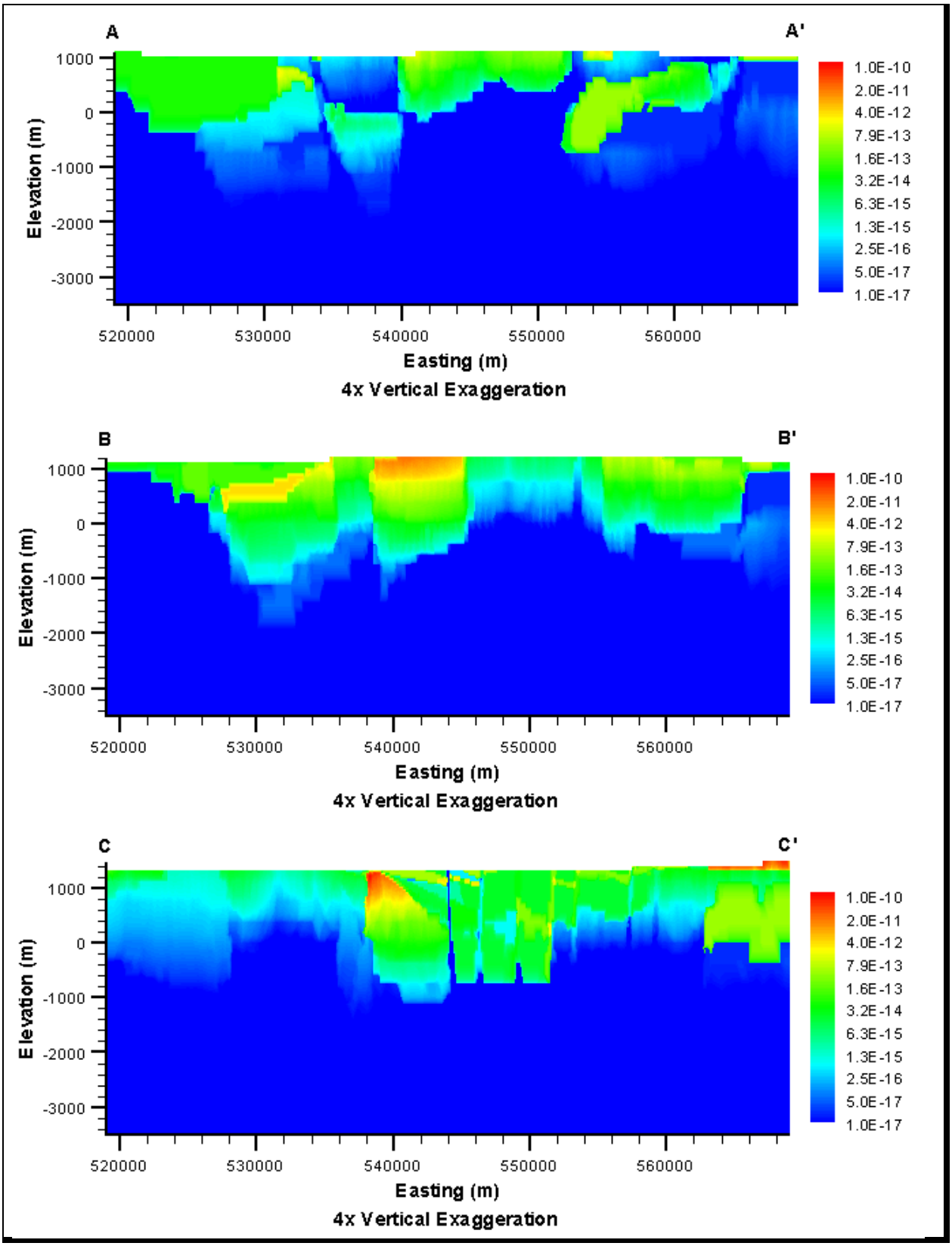
A
A'
1000
0
-1000
-2000
-3000
Elevation (m)
520000
530000
540000
550000
560000
Easting (m)
4x Vertical Exaggeration
1.0E-10
2.0E-11
4.0E-12
7.9E-13
1.6E-13
3.2E-14
6.3E-15
1.3E-15
2.5E-16
5.0E-17
1.0E-17
B
B'
1000
0
-1000
-2000
-3000
Elevation (m)
520000
530000
540000
550000
560000
Easting (m)
4x Vertical Exaggeration
1.0E-10
2.0E-11
4.0E-12
7.9E-13
1.6E-13
3.2E-14
6.3E-15
1.3E-15
2.5E-16
5.0E-17
1.0E-17
C
C'
1000
0
-1000
-2000
-3000
Elevation (m)
520000
530000
540000
550000
560000
Easting (m)
4x Vertical Exaggeration
1.0E-10
2.0E-11
4.0E-12
7.9E-13
1.6E-13
3.2E-14
6.3E-15
1.3E-15
2.5E-16
5.0E-17
1.0E-17

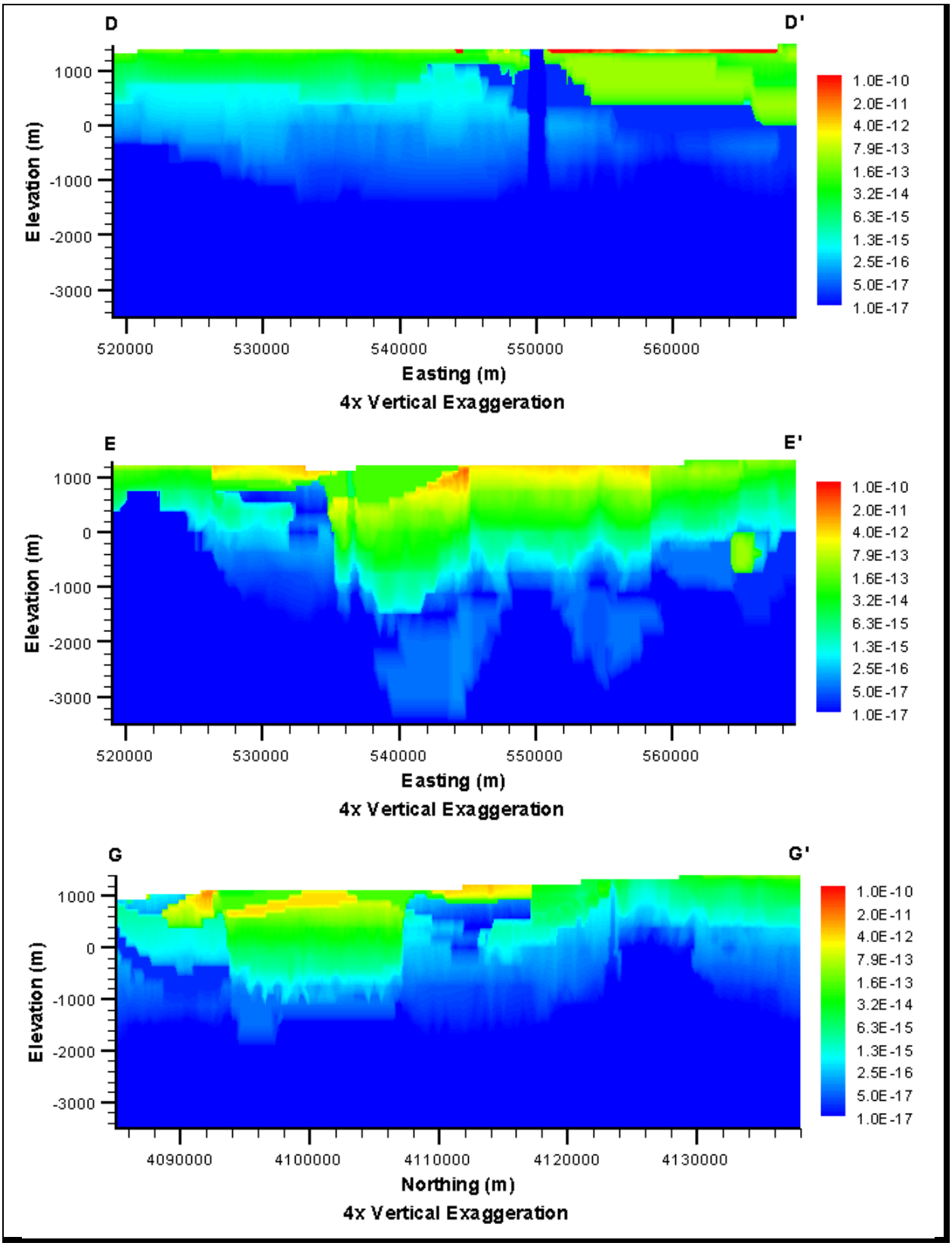
D
D'
1000
0
-1000
-2000
-3000
Elevation (m)
520000
530000
540000
550000
560000
Easting (m)
4x Vertical Exaggeration
1.0E-10
2.0E-11
4.0E-12
7.9E-13
1.6E-13
3.2E-14
6.3E-15
1.3E-15
2.5E-16
5.0E-17
1.0E-17
E
E'
1000
0
-1000
-2000
-3000
Elevation (m)
520000
530000
540000
550000
560000
Easting (m)
4x Vertical Exaggeration
1.0E-10
2.0E-11
4.0E-12
7.9E-13
1.6E-13
3.2E-14
6.3E-15
1.3E-15
2.5E-16
5.0E-17
1.0E-17
G
G'
1000
0
-1000
-2000
-3000
Elevation (m)
4090000
4100000
4110000
4120000
4130000
Northing (m)
4x Vertical Exaggeration
1.0E-10
2.0E-11
4.0E-12
7.9E-13
1.6E-13
3.2E-14
6.3E-15
1.3E-15
2.5E-16
5.0E-17
1.0E-17

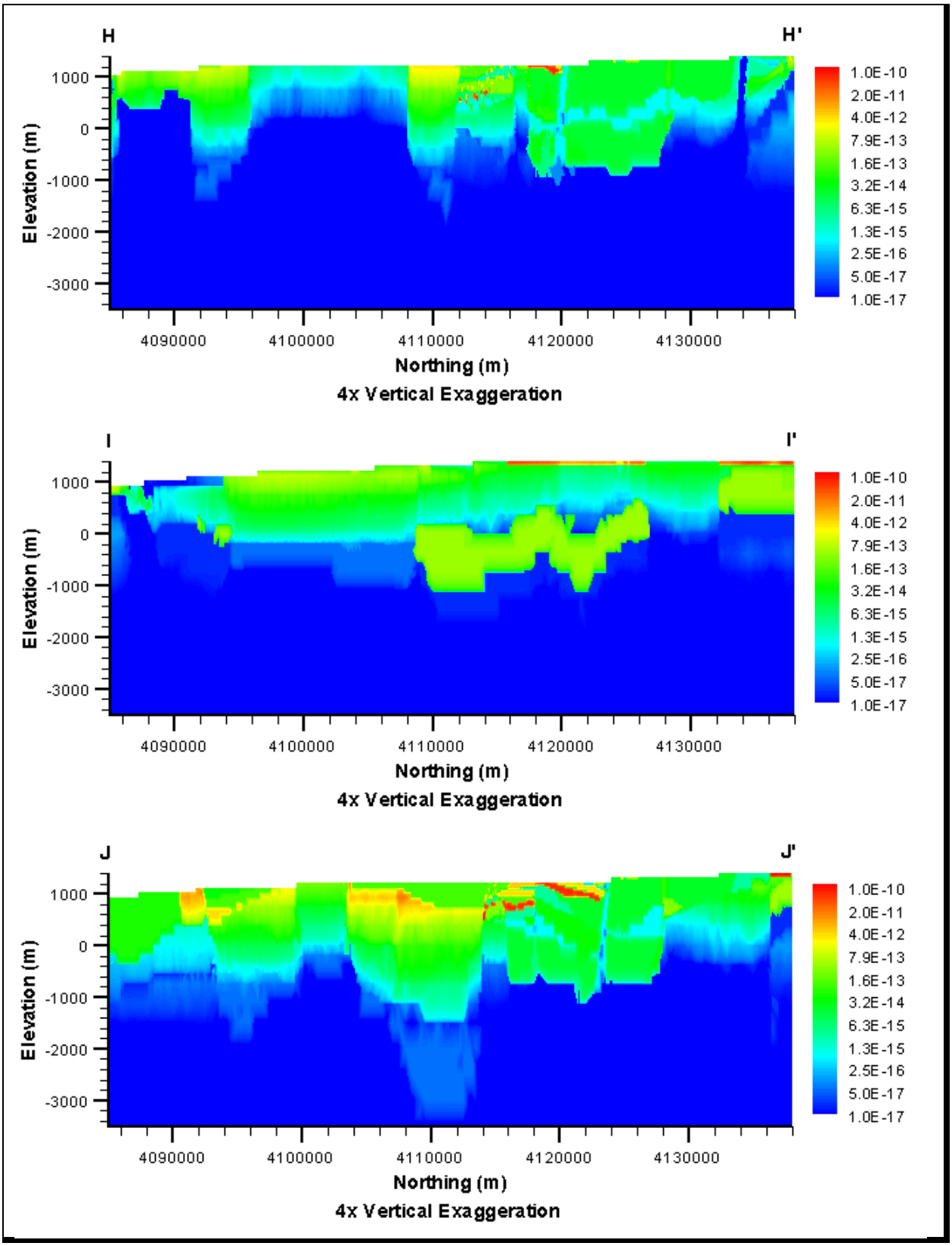
H
H'
1000
0
-1000
-2000
-3000
Elevation (m)
4090000
4100000
4110000
4120000
4130000
Northing (m)
4x Vertical Exaggeration
1.0E-10
2.0E-11
4.0E-12
7.9E-13
1.6E-13
3.2E-14
6.3E-15
1.3E-15
2.5E-16
5.0E-17
1.0E-17
I
I'
1000
0
-1000
-2000
-3000
Elevation (m)
4090000
4100000
4110000
4120000
4130000
Northing (m)
4x Vertical Exaggeration
1.0E-10
2.0E-11
4.0E-12
7.9E-13
1.6E-13
3.2E-14
6.3E-15
1.3E-15
2.5E-16
5.0E-17
1.0E-17
J
J'
1000
0
-1000
-2000
-3000
Elevation (m)
4090000
4100000
4110000
4120000
4130000
Northing (m)
4x Vertical Exaggeration
1.0E-10
2.0E-11
4.0E-12
7.9E-13
1.6E-13
3.2E-14
6.3E-15
1.3E-15
2.5E-16
5.0E-17
1.0E-17

Thirsty Canyon Lineament (TCL-MME-SDA)

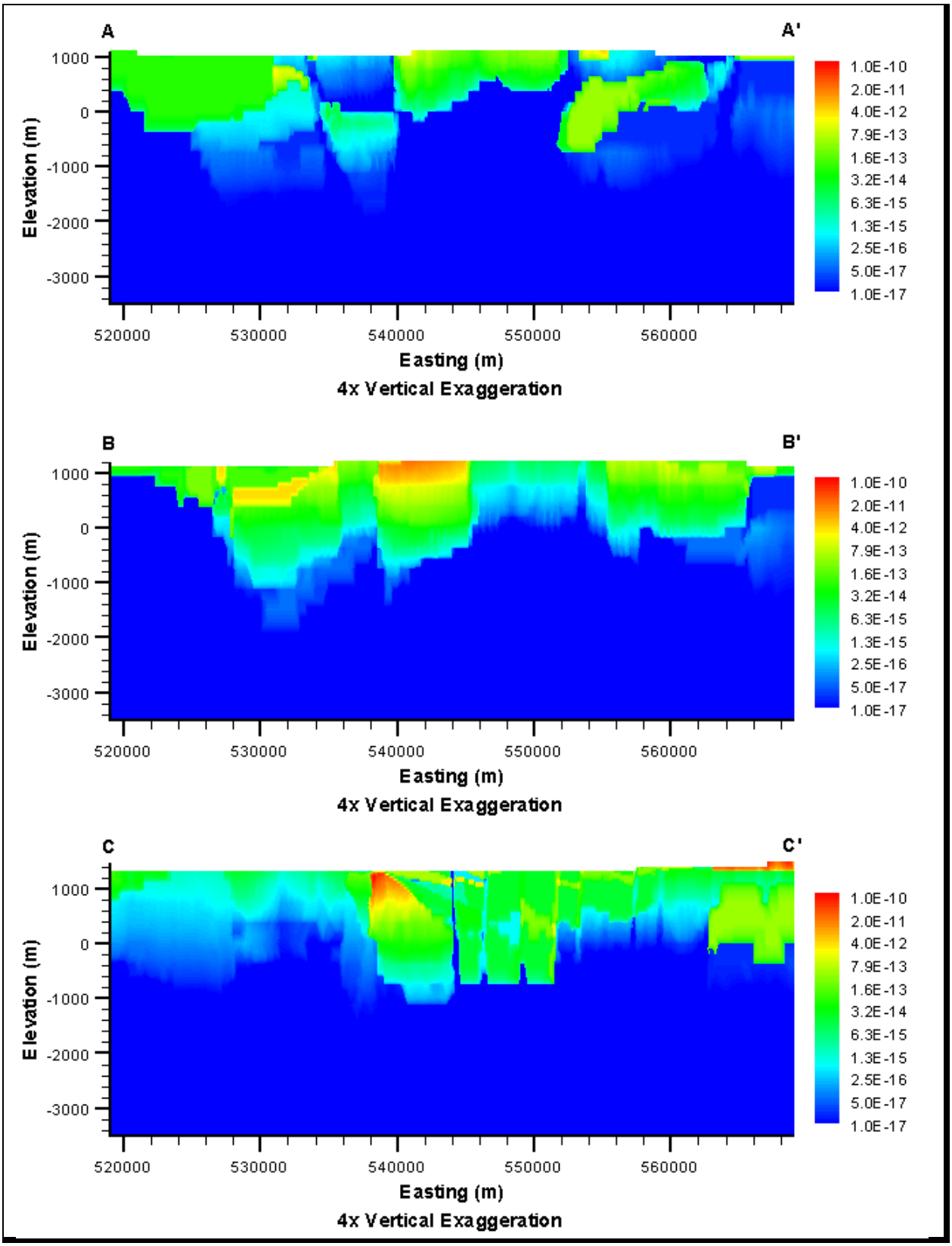
A
A'
1000
0
-1000
-2000
-3000
Elevation (m)
520000
530000
540000
550000
560000
Easting (m)
4x Vertical Exaggeration
1.0E-10
2.0E-11
4.0E-12
7.9E-13
1.6E-13
3.2E-14
6.3E-15
1.3E-15
2.5E-16
5.0E-17
1.0E-17
B
B'
1000
0
-1000
-2000
-3000
Elevation (m)
520000
530000
540000
550000
560000
Easting (m)
4x Vertical Exaggeration
1.0E-10
2.0E-11
4.0E-12
7.9E-13
1.6E-13
3.2E-14
6.3E-15
1.3E-15
2.5E-16
5.0E-17
1.0E-17
C
C'
1000
0
-1000
-2000
-3000
Elevation (m)
520000
530000
540000
550000
560000
Easting (m)
4x Vertical Exaggeration
1.0E-10
2.0E-11
4.0E-12
7.9E-13
1.6E-13
3.2E-14
6.3E-15
1.3E-15
2.5E-16
5.0E-17
1.0E-17

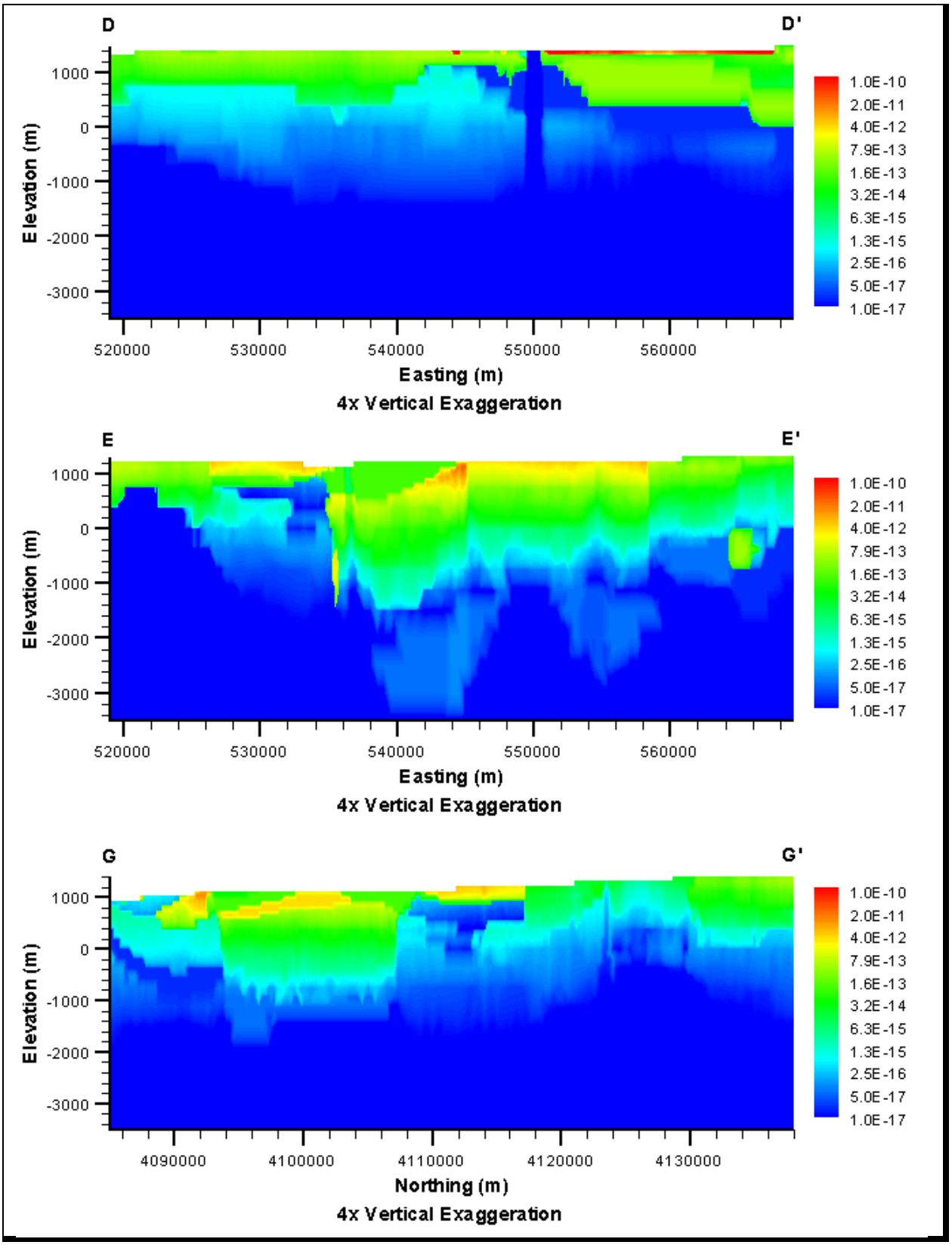
D
D'
1000
0
-1000
-2000
-3000
Elevation (m)
520000
530000
540000
550000
560000
Easting (m)
4x Vertical Exaggeration
1.0E-10
2.0E-11
4.0E-12
7.9E-13
1.6E-13
3.2E-14
6.3E-15
1.3E-15
2.5E-16
5.0E-17
1.0E-17
E
E'
1000
0
-1000
-2000
-3000
Elevation (m)
520000
530000
540000
550000
560000
Easting (m)
4x Vertical Exaggeration
1.0E-10
2.0E-11
4.0E-12
7.9E-13
1.6E-13
3.2E-14
6.3E-15
1.3E-15
2.5E-16
5.0E-17
1.0E-17
G
G'
1000
0
-1000
-2000
-3000
Elevation (m)
4090000
4100000
4110000
4120000
4130000
Northing (m)
4x Vertical Exaggeration
1.0E-10
2.0E-11
4.0E-12
7.9E-13
1.6E-13
3.2E-14
6.3E-15
1.3E-15
2.5E-16
5.0E-17
1.0E-17

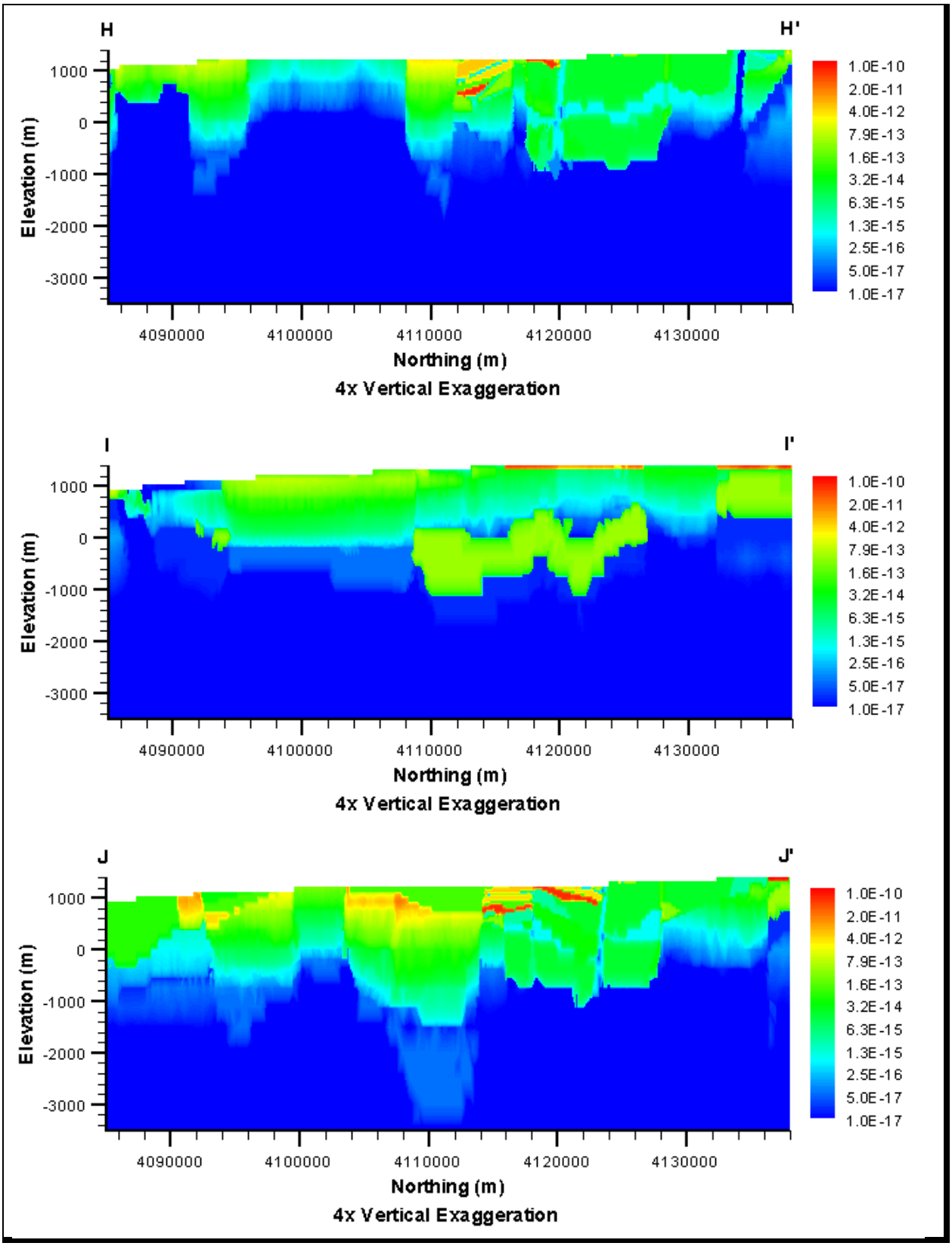
H
H'
1000
0
-1000
-2000
-3000
Elevation (m)
4090000
4100000
4110000
4120000
4130000
Northing (m)
4x Vertical Exaggeration
1.0E-10
2.0E-11
4.0E-12
7.9E-13
1.6E-13
3.2E-14
6.3E-15
1.3E-15
2.5E-16
5.0E-17
1.0E-17
I
I'
1000
0
-1000
-2000
-3000
Elevation (m)
4090000
4100000
4110000
4120000
4130000
Northing (m)
4x Vertical Exaggeration
1.0E-10
2.0E-11
4.0E-12
7.9E-13
1.6E-13
3.2E-14
6.3E-15
1.3E-15
2.5E-16
5.0E-17
1.0E-17
J
J'
1000
0
-1000
-2000
-3000
Elevation (m)
4090000
4100000
4110000
4120000
4130000
Northing (m)
4x Vertical Exaggeration
1.0E-10
2.0E-11
4.0E-12
7.9E-13
1.6E-13
3.2E-14
6.3E-15
1.3E-15
2.5E-16
5.0E-17
1.0E-17

Raised Pre-Tertiary Surface (PZUP-MME-SDA)

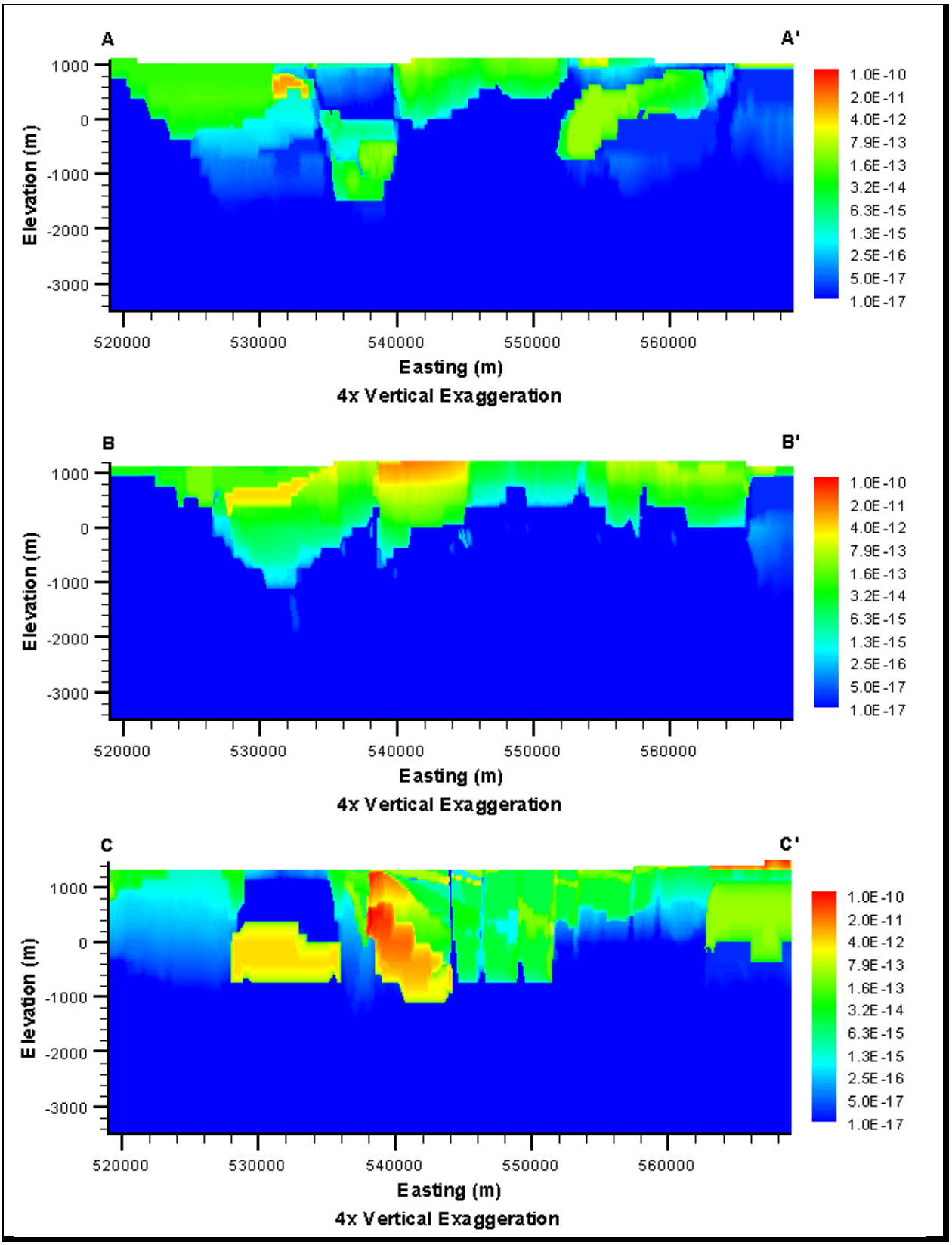
A
A'
1000
0
-1000
-2000
-3000
Elevation (m)
520000
530000
540000
550000
560000
Easting (m)
4x Vertical Exaggeration
1.0E-10
2.0E-11
4.0E-12
7.9E-13
1.6E-13
3.2E-14
6.3E-15
1.3E-15
2.5E-16
5.0E-17
1.0E-17
B
B'
1000
0
-1000
-2000
-3000
Elevation (m)
520000
530000
540000
550000
560000
Easting (m)
4x Vertical Exaggeration
1.0E-10
2.0E-11
4.0E-12
7.9E-13
1.6E-13
3.2E-14
6.3E-15
1.3E-15
2.5E-16
5.0E-17
1.0E-17
C
C'
1000
0
-1000
-2000
-3000
Elevation (m)
520000
530000
540000
550000
560000
Easting (m)
4x Vertical Exaggeration
1.0E-10
2.0E-11
4.0E-12
7.9E-13
1.6E-13
3.2E-14
6.3E-15
1.3E-15
2.5E-16
5.0E-17
1.0E-17

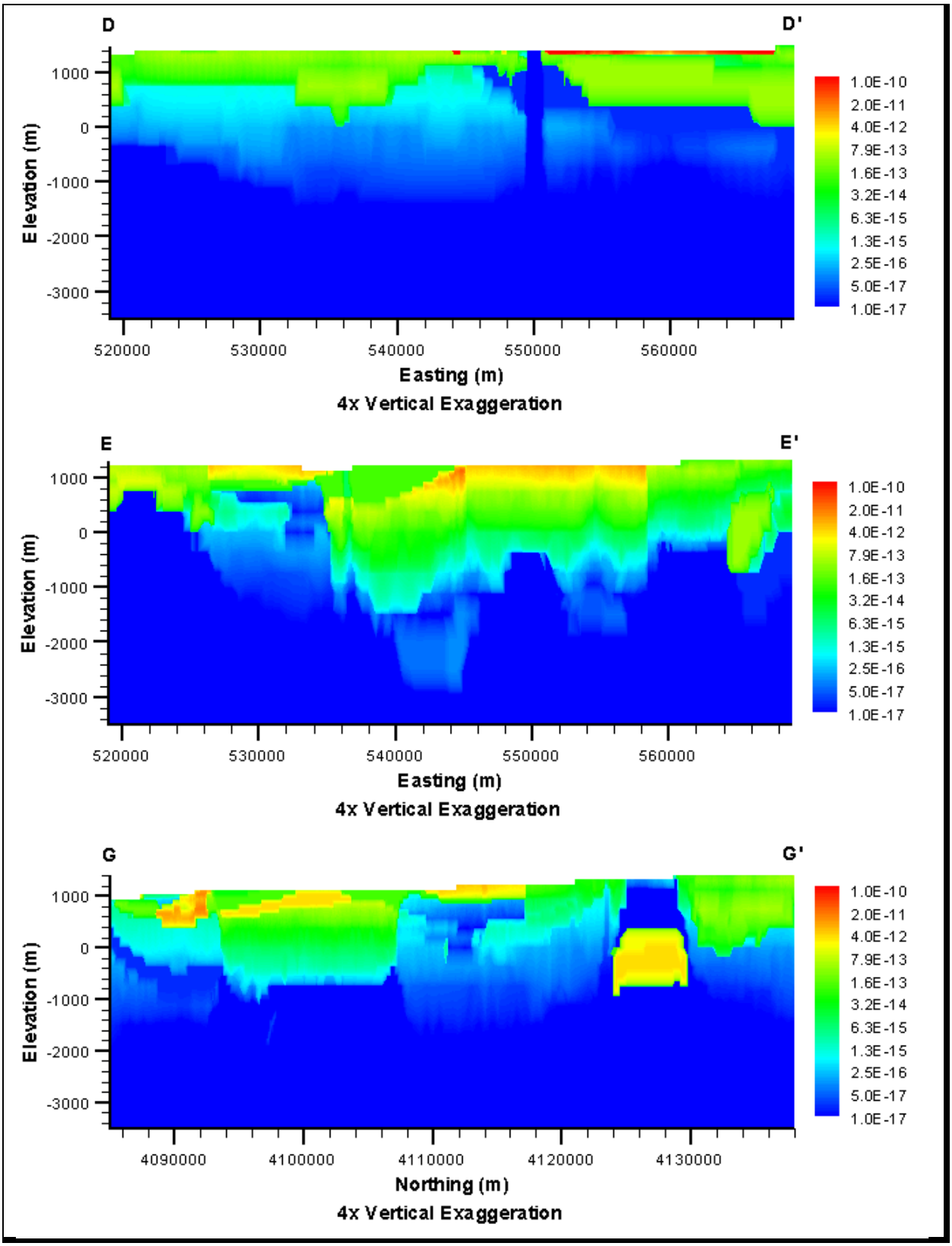
D
D'
1000
0
-1000
-2000
-3000
Elevation (m)
520000
530000
540000
550000
560000
Easting (m)
4x Vertical Exaggeration
1.0E-10
2.0E-11
4.0E-12
7.9E-13
1.6E-13
3.2E-14
6.3E-15
1.3E-15
2.5E-16
5.0E-17
1.0E-17
E
E'
1000
0
-1000
-2000
-3000
Elevation (m)
520000
530000
540000
550000
560000
Easting (m)
4x Vertical Exaggeration
1.0E-10
2.0E-11
4.0E-12
7.9E-13
1.6E-13
3.2E-14
6.3E-15
1.3E-15
2.5E-16
5.0E-17
1.0E-17
G
G'
1000
0
-1000
-2000
-3000
Elevation (m)
4090000
4100000
4110000
4120000
4130000
Northing (m)
4x Vertical Exaggeration
1.0E-10
2.0E-11
4.0E-12
7.9E-13
1.6E-13
3.2E-14
6.3E-15
1.3E-15
2.5E-16
5.0E-17
1.0E-17

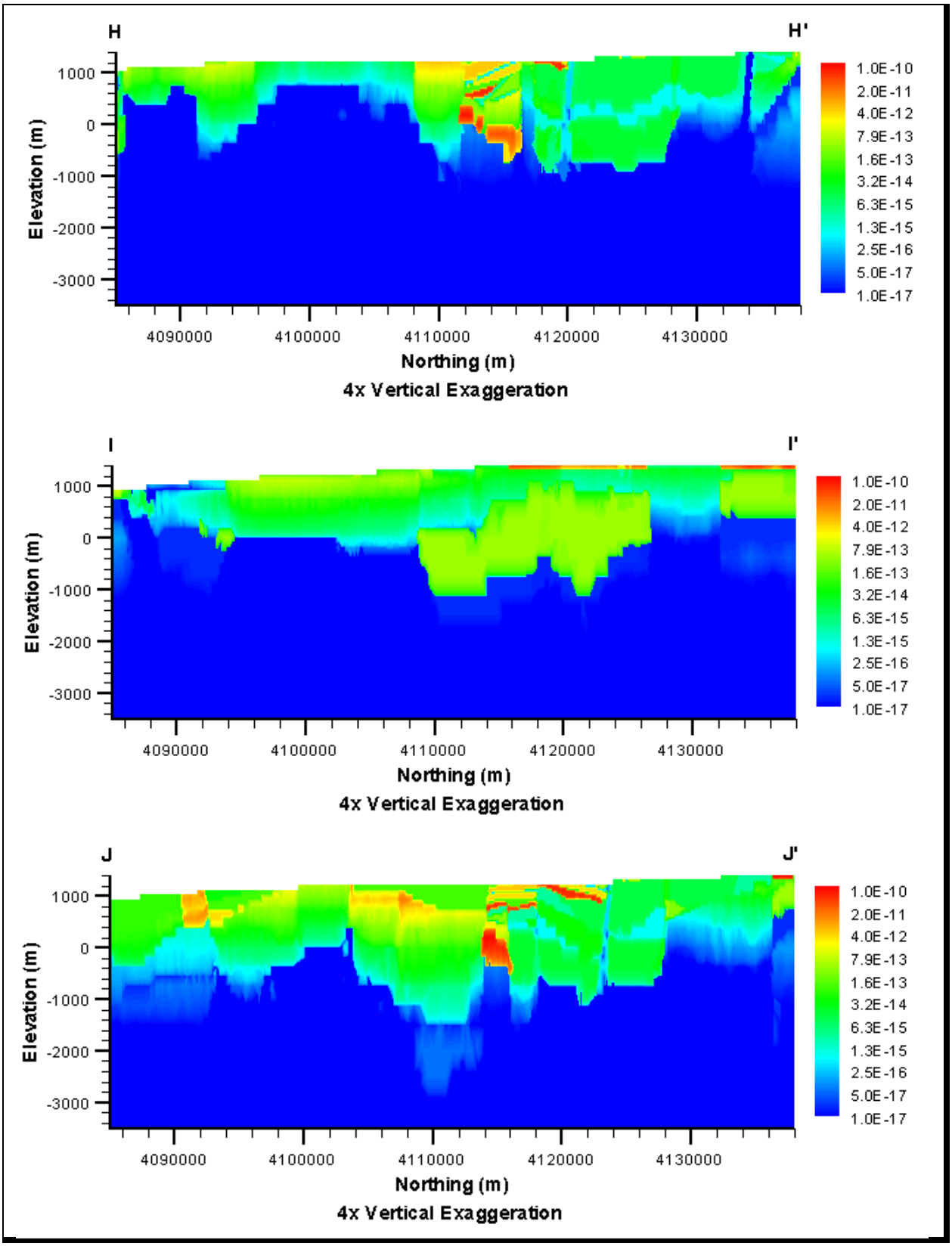
H
H'
1000
0
-1000
-2000
-3000
Elevation (m)
4090000
4100000
4110000
4120000
4130000
Northing (m)
4x Vertical Exaggeration
1.0E-10
2.0E-11
4.0E-12
7.9E-13
1.6E-13
3.2E-14
6.3E-15
1.3E-15
2.5E-16
5.0E-17
1.0E-17
I
I'
1000
0
-1000
-2000
-3000
Elevation (m)
4090000
4100000
4110000
4120000
4130000
Northing (m)
4x Vertical Exaggeration
1.0E-10
2.0E-11
4.0E-12
7.9E-13
1.6E-13
3.2E-14
6.3E-15
1.3E-15
2.5E-16
5.0E-17
1.0E-17
J
J'
1000
0
-1000
-2000
-3000
Elevation (m)
4090000
4100000
4110000
4120000
4130000
Northing (m)
4x Vertical Exaggeration
1.0E-10
2.0E-11
4.0E-12
7.9E-13
1.6E-13
3.2E-14
6.3E-15
1.3E-15
2.5E-16
5.0E-17
1.0E-17

Contiguous Imbricate Thrust Sheet (SEPZ-MME-SDA)

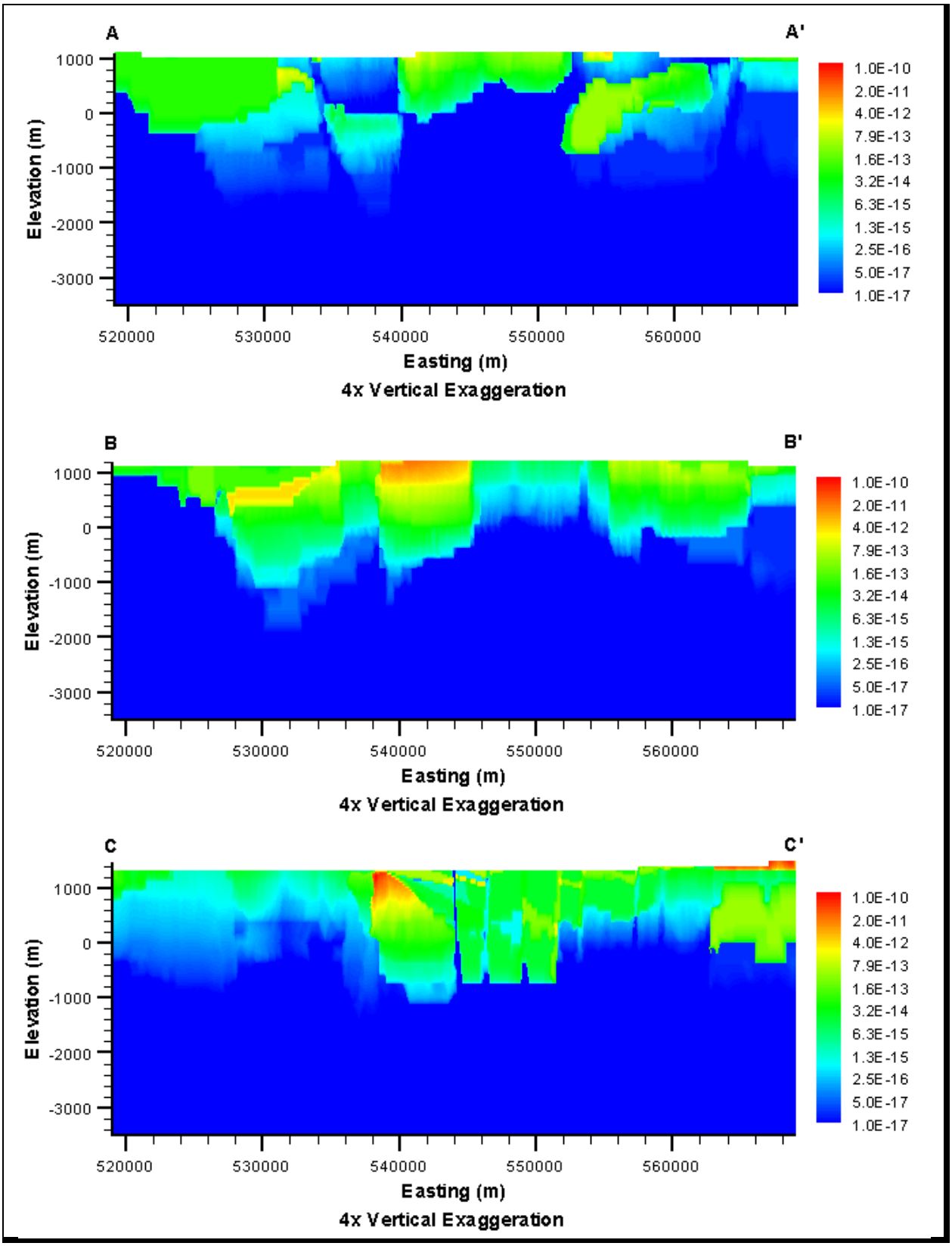
A
A'
1000
0
-1000
-2000
-3000
Elevation (m)
520000
530000
540000
550000
560000
Easting (m)
4x Vertical Exaggeration
1.0E-10
2.0E-11
4.0E-12
7.9E-13
1.6E-13
3.2E-14
6.3E-15
1.3E-15
2.5E-16
5.0E-17
1.0E-17
B
B'
1000
0
-1000
-2000
-3000
Elevation (m)
520000
530000
540000
550000
560000
Easting (m)
4x Vertical Exaggeration
1.0E-10
2.0E-11
4.0E-12
7.9E-13
1.6E-13
3.2E-14
6.3E-15
1.3E-15
2.5E-16
5.0E-17
1.0E-17
C
C'
1000
0
-1000
-2000
-3000
Elevation (m)
520000
530000
540000
550000
560000
Easting (m)
4x Vertical Exaggeration
1.0E-10
2.0E-11
4.0E-12
7.9E-13
1.6E-13
3.2E-14
6.3E-15
1.3E-15
2.5E-16
5.0E-17
1.0E-17

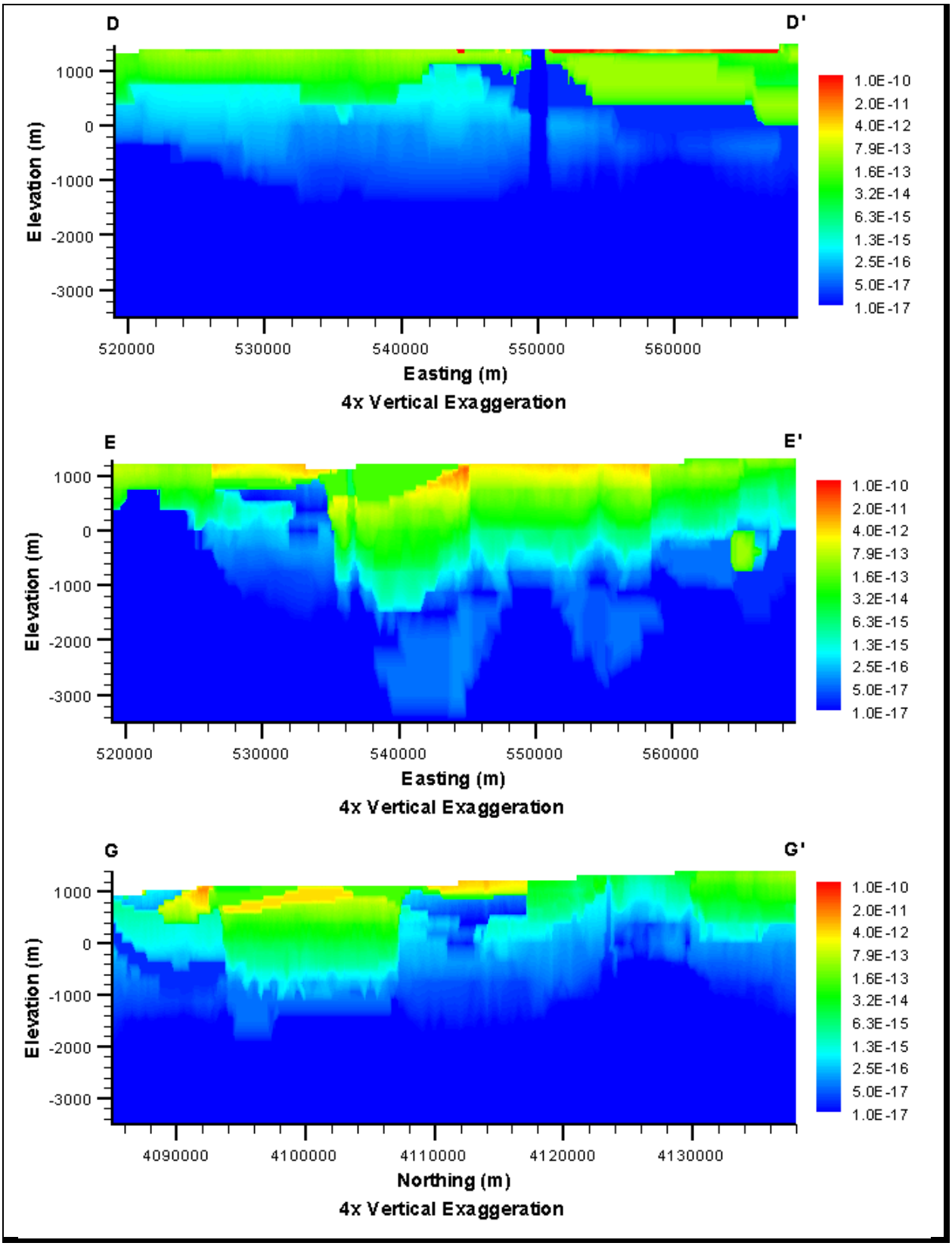
D
D'
1000
0
-1000
-2000
-3000
Elevation (m)
520000
530000
540000
550000
560000
Easting (m)
4x Vertical Exaggeration
1.0E-10
2.0E-11
4.0E-12
7.9E-13
1.6E-13
3.2E-14
6.3E-15
1.3E-15
2.5E-16
5.0E-17
1.0E-17
E
E'
1000
0
-1000
-2000
-3000
Elevation (m)
520000
530000
540000
550000
560000
Easting (m)
4x Vertical Exaggeration
1.0E-10
2.0E-11
4.0E-12
7.9E-13
1.6E-13
3.2E-14
6.3E-15
1.3E-15
2.5E-16
5.0E-17
1.0E-17
G
G'
1000
0
-1000
-2000
-3000
Elevation (m)
4090000
4100000
4110000
4120000
4130000
Northing (m)
4x Vertical Exaggeration
1.0E-10
2.0E-11
4.0E-12
7.9E-13
1.6E-13
3.2E-14
6.3E-15
1.3E-15
2.5E-16
5.0E-17
1.0E-17

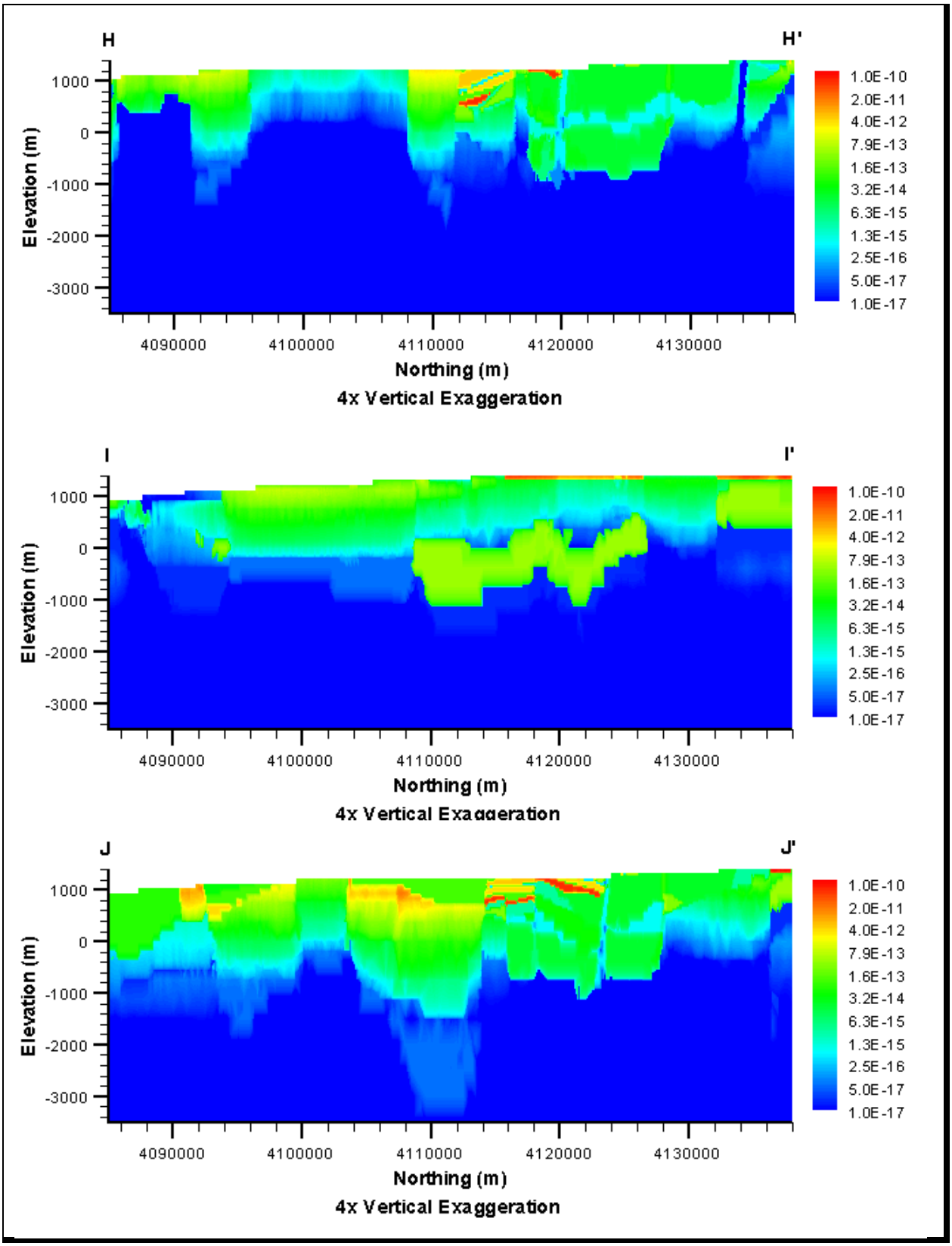
H
H'
1000
0
-1000
-2000
-3000
Elevation (m)
4090000
4100000
4110000
4120000
4130000
Northing (m)
4x Vertical Exaggeration
1.0E-10
2.0E-11
4.0E-12
7.9E-13
1.6E-13
3.2E-14
6.3E-15
1.3E-15
2.5E-16
5.0E-17
1.0E-17
I
I'
1000
0
-1000
-2000
-3000
Elevation (m)
4090000
4100000
4110000
4120000
4130000
Northing (m)
4x Vertical Exaggeration
1.0E-10
2.0E-11
4.0E-12
7.9E-13
1.6E-13
3.2E-14
6.3E-15
1.3E-15
2.5E-16
5.0E-17
1.0E-17
J
J'
1000
0
-1000
-2000
-3000
Elevation (m)
4090000
4100000
4110000
4120000
4130000
Northing (m)
4x Vertical Exaggeration
1.0E-10
2.0E-11
4.0E-12
7.9E-13
1.6E-13
3.2E-14
6.3E-15
1.3E-15
2.5E-16
5.0E-17
1.0E-17

Deeply Rooted Belted Range Fault Thrust (DRT-MME-SDA)

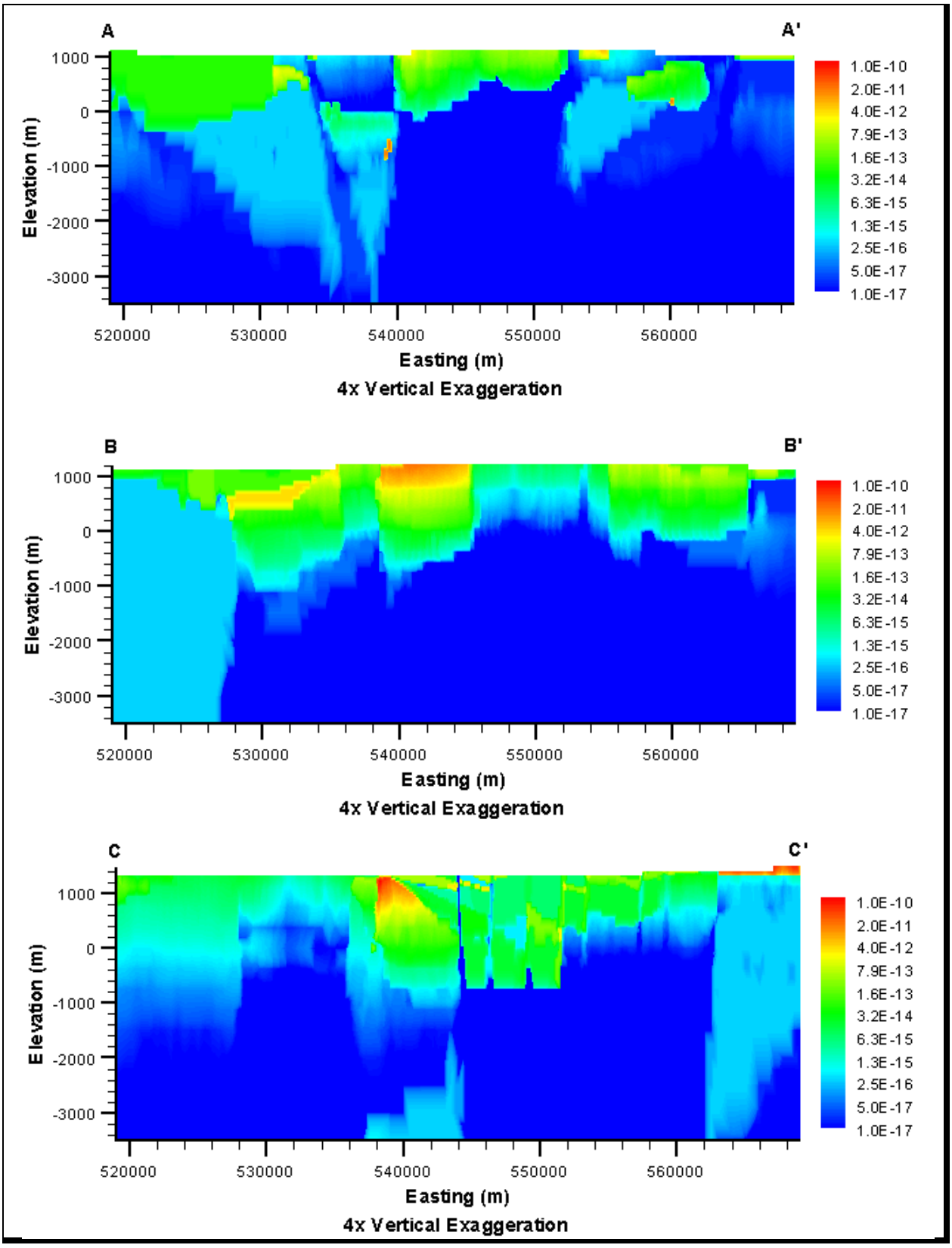
A
A'
1000
0
-1000
-2000
-3000
Elevation (m)
520000
530000
540000
550000
560000
Easting (m)
4x Vertical Exaggeration
1.0E-10
2.0E-11
4.0E-12
7.9E-13
1.6E-13
3.2E-14
6.3E-15
1.3E-15
2.5E-16
5.0E-17
1.0E-17
B
B'
1000
0
-1000
-2000
-3000
Elevation (m)
520000
530000
540000
550000
560000
Easting (m)
4x Vertical Exaggeration
1.0E-10
2.0E-11
4.0E-12
7.9E-13
1.6E-13
3.2E-14
6.3E-15
1.3E-15
2.5E-16
5.0E-17
1.0E-17
C
C'
1000
0
-1000
-2000
-3000
Elevation (m)
520000
530000
540000
550000
560000
Easting (m)
4x Vertical Exaggeration
1.0E-10
2.0E-11
4.0E-12
7.9E-13
1.6E-13
3.2E-14
6.3E-15
1.3E-15
2.5E-16
5.0E-17
1.0E-17

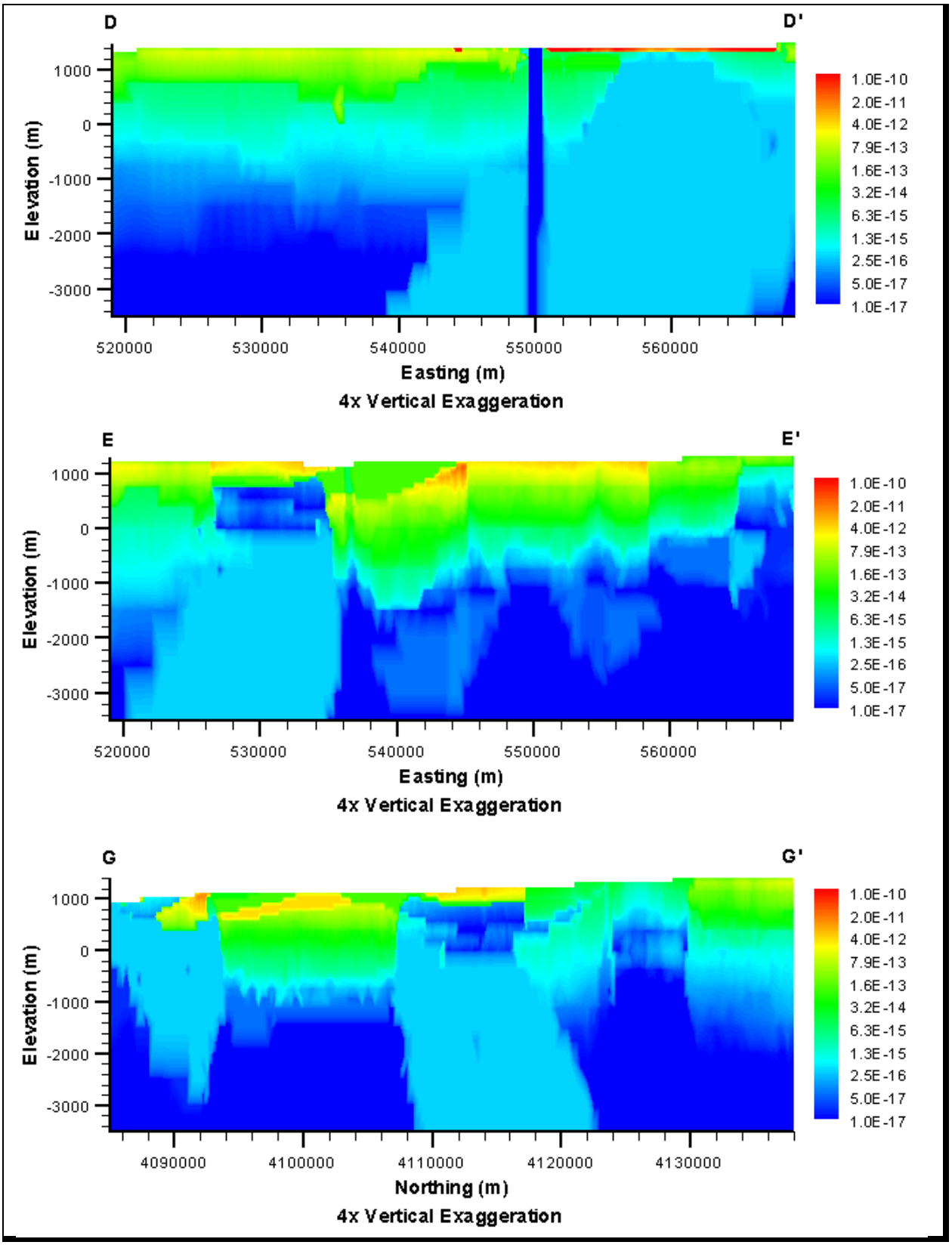
D
D'
1000
0
-1000
-2000
-3000
Elevation (m)
520000
530000
540000
550000
560000
Easting (m)
4x Vertical Exaggeration
1.0E-10
2.0E-11
4.0E-12
7.9E-13
1.6E-13
3.2E-14
6.3E-15
1.3E-15
2.5E-16
5.0E-17
1.0E-17
E
E'
1000
0
-1000
-2000
-3000
Elevation (m)
520000
530000
540000
550000
560000
Easting (m)
4x Vertical Exaggeration
1.0E-10
2.0E-11
4.0E-12
7.9E-13
1.6E-13
3.2E-14
6.3E-15
1.3E-15
2.5E-16
5.0E-17
1.0E-17
G
G'
1000
0
-1000
-2000
-3000
Elevation (m)
4090000
4100000
4110000
4120000
4130000
Northing (m)
4x Vertical Exaggeration
1.0E-10
2.0E-11
4.0E-12
7.9E-13
1.6E-13
3.2E-14
6.3E-15
1.3E-15
2.5E-16
5.0E-17
1.0E-17

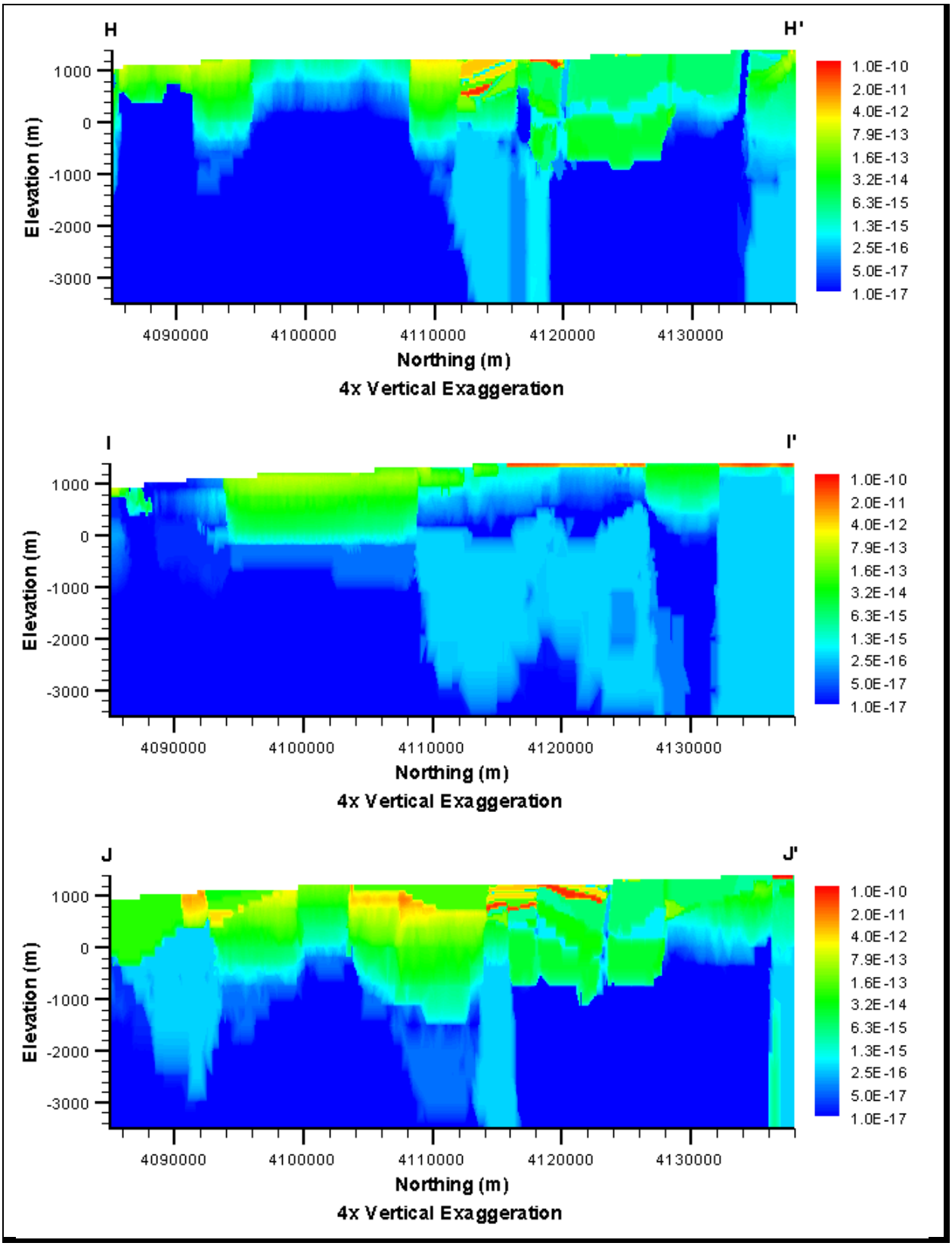
H
H'
1000
0
-1000
-2000
-3000
Elevation (m)
4090000
4100000
4110000
4120000
4130000
Northing (m)
4x Vertical Exaggeration
1.0E-10
2.0E-11
4.0E-12
7.9E-13
1.6E-13
3.2E-14
6.3E-15
1.3E-15
2.5E-16
5.0E-17
1.0E-17
I
I'
1000
0
-1000
-2000
-3000
Elevation (m)
4090000
4100000
4110000
4120000
4130000
Northing (m)
4x Vertical Exaggeration
1.0E-10
2.0E-11
4.0E-12
7.9E-13
1.6E-13
3.2E-14
6.3E-15
1.3E-15
2.5E-16
5.0E-17
1.0E-17
J
J'
1000
0
-1000
-2000
-3000
Elevation (m)
4090000
4100000
4110000
4120000
4130000
Northing (m)
4x Vertical Exaggeration
1.0E-10
2.0E-11
4.0E-12
7.9E-13
1.6E-13
3.2E-14
6.3E-15
1.3E-15
2.5E-16
5.0E-17
1.0E-17

Raised Pre-Tertiary Surface (PZUP-DRIA-SDA)

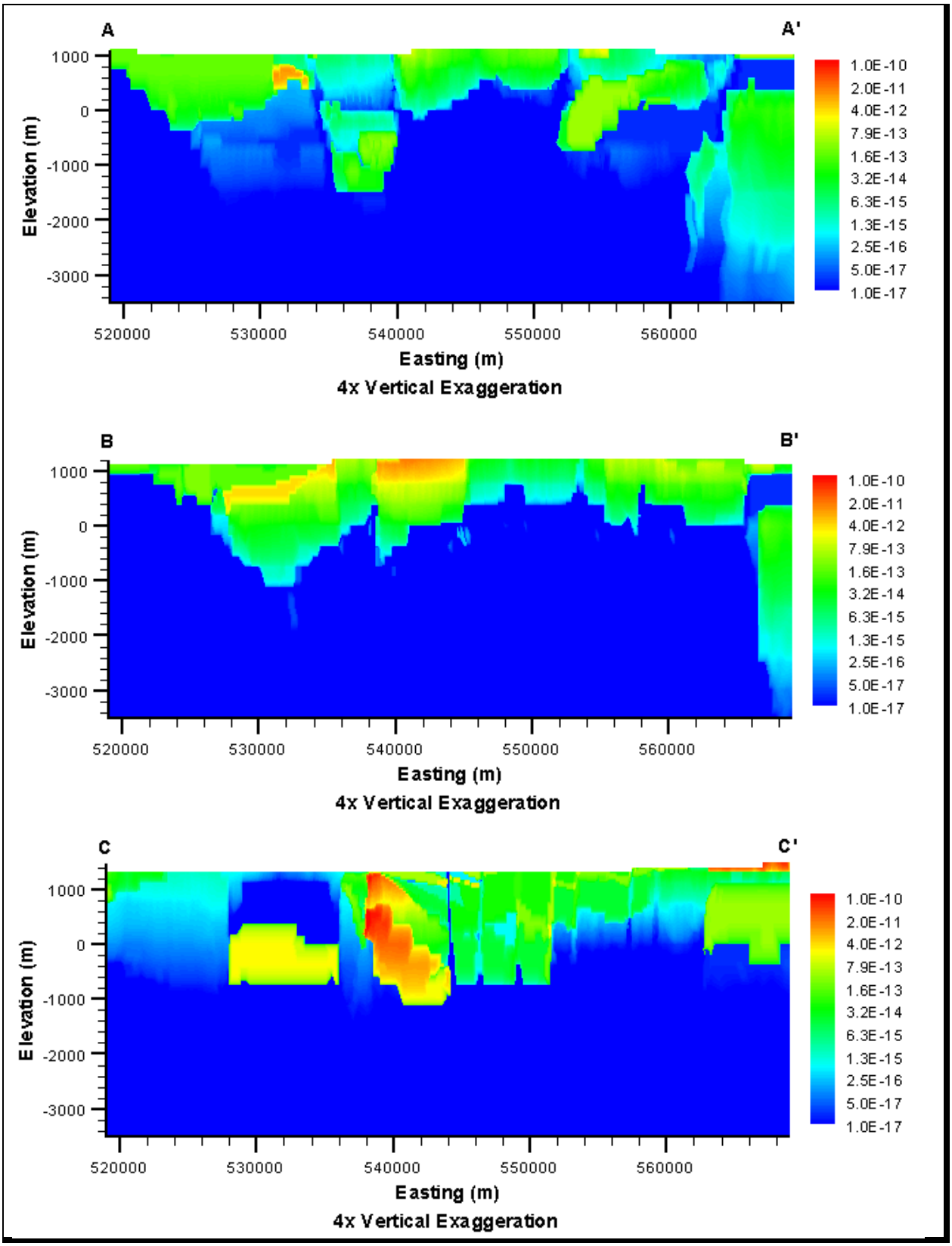
A
A'
1000
0
-1000
-2000
-3000
Elevation (m)
520000
530000
540000
550000
560000
Easting (m)
4x Vertical Exaggeration
1.0E-10
2.0E-11
4.0E-12
7.9E-13
1.6E-13
3.2E-14
6.3E-15
1.3E-15
2.5E-16
5.0E-17
1.0E-17
B
B'
1000
0
-1000
-2000
-3000
Elevation (m)
520000
530000
540000
550000
560000
Easting (m)
4x Vertical Exaggeration
1.0E-10
2.0E-11
4.0E-12
7.9E-13
1.6E-13
3.2E-14
6.3E-15
1.3E-15
2.5E-16
5.0E-17
1.0E-17
C
C'
1000
0
-1000
-2000
-3000
Elevation (m)
520000
530000
540000
550000
560000
Easting (m)
4x Vertical Exaggeration
1.0E-10
2.0E-11
4.0E-12
7.9E-13
1.6E-13
3.2E-14
6.3E-15
1.3E-15
2.5E-16
5.0E-17
1.0E-17

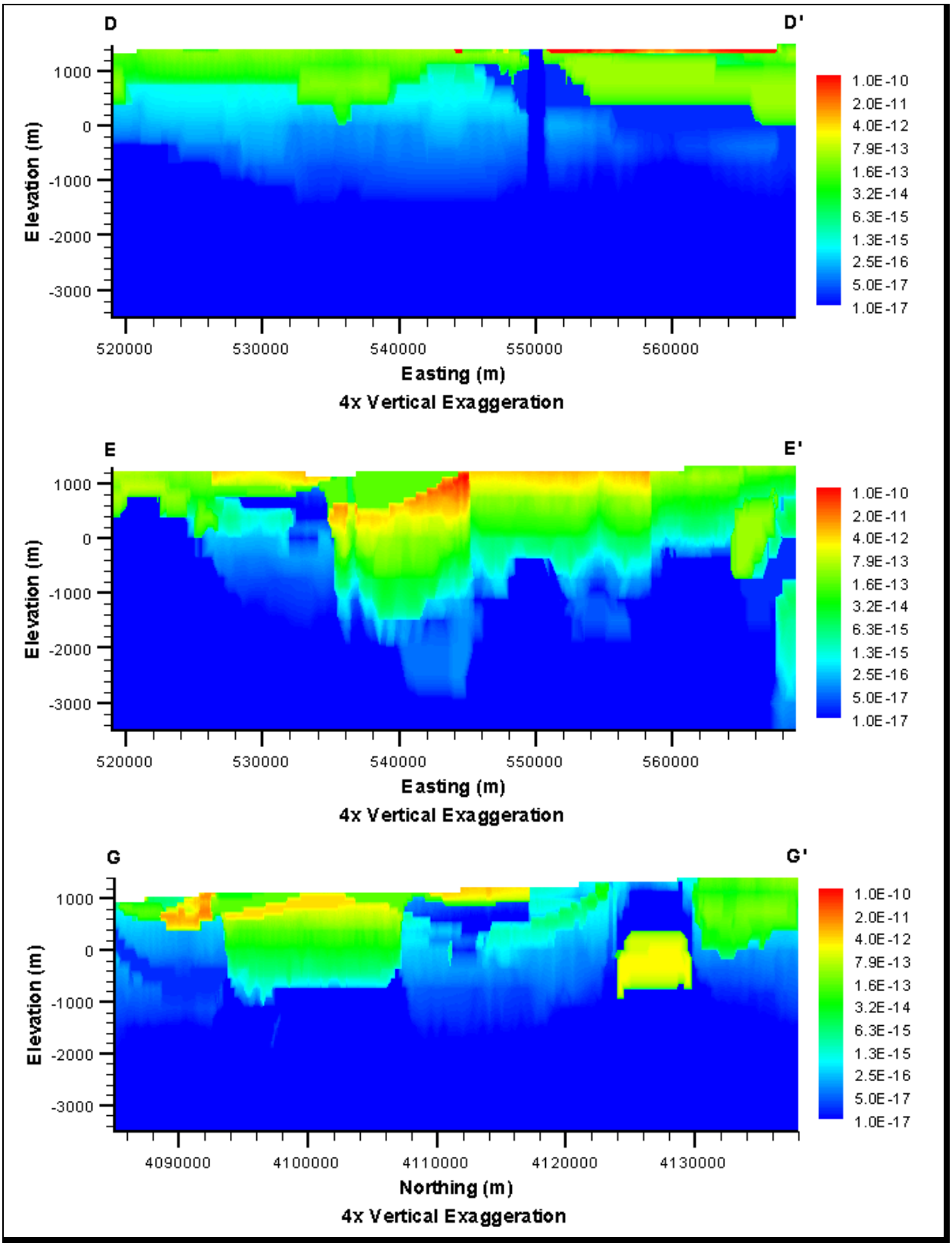
D
D'
1000
0
-1000
-2000
-3000
Elevation (m)
520000
530000
540000
550000
560000
Easting (m)
4x Vertical Exaggeration
1.0E-10
2.0E-11
4.0E-12
7.9E-13
1.6E-13
3.2E-14
6.3E-15
1.3E-15
2.5E-16
5.0E-17
1.0E-17
E
E'
1000
0
-1000
-2000
-3000
Elevation (m)
520000
530000
540000
550000
560000
Easting (m)
4x Vertical Exaggeration
1.0E-10
2.0E-11
4.0E-12
7.9E-13
1.6E-13
3.2E-14
6.3E-15
1.3E-15
2.5E-16
5.0E-17
1.0E-17
G
G'
1000
0
-1000
-2000
-3000
Elevation (m)
4090000
4100000
4110000
4120000
4130000
Northing (m)
4x Vertical Exaggeration
1.0E-10
2.0E-11
4.0E-12
7.9E-13
1.6E-13
3.2E-14
6.3E-15
1.3E-15
2.5E-16
5.0E-17
1.0E-17

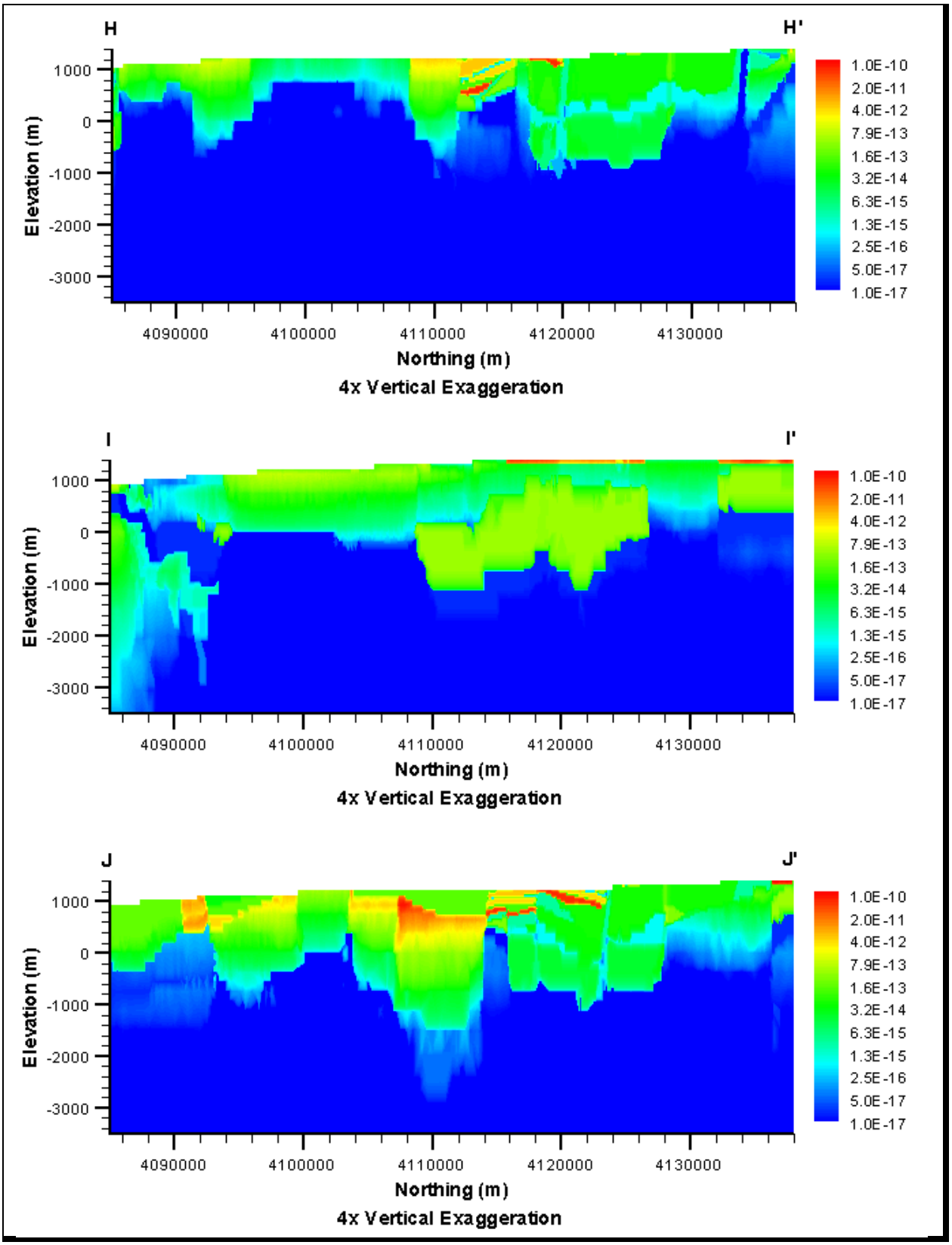
H
H'
1000
0
-1000
-2000
-3000
Elevation (m)
4090000
4100000
4110000
4120000
4130000
Northing (m)
4x Vertical Exaggeration
1.0E-10
2.0E-11
4.0E-12
7.9E-13
1.6E-13
3.2E-14
6.3E-15
1.3E-15
2.5E-16
5.0E-17
1.0E-17
I
I'
1000
0
-1000
-2000
-3000
Elevation (m)
4090000
4100000
4110000
4120000
4130000
Northing (m)
4x Vertical Exaggeration
1.0E-10
2.0E-11
4.0E-12
7.9E-13
1.6E-13
3.2E-14
6.3E-15
1.3E-15
2.5E-16
5.0E-17
1.0E-17
J
J'
1000
0
-1000
-2000
-3000
Elevation (m)
4090000
4100000
4110000
4120000
4130000
Northing (m)
4x Vertical Exaggeration
1.0E-10
2.0E-11
4.0E-12
7.9E-13
1.6E-13
3.2E-14
6.3E-15
1.3E-15
2.5E-16
5.0E-17
1.0E-17

Raised Pre-Tertiary Surface (PZUP-USGSD-SDA)

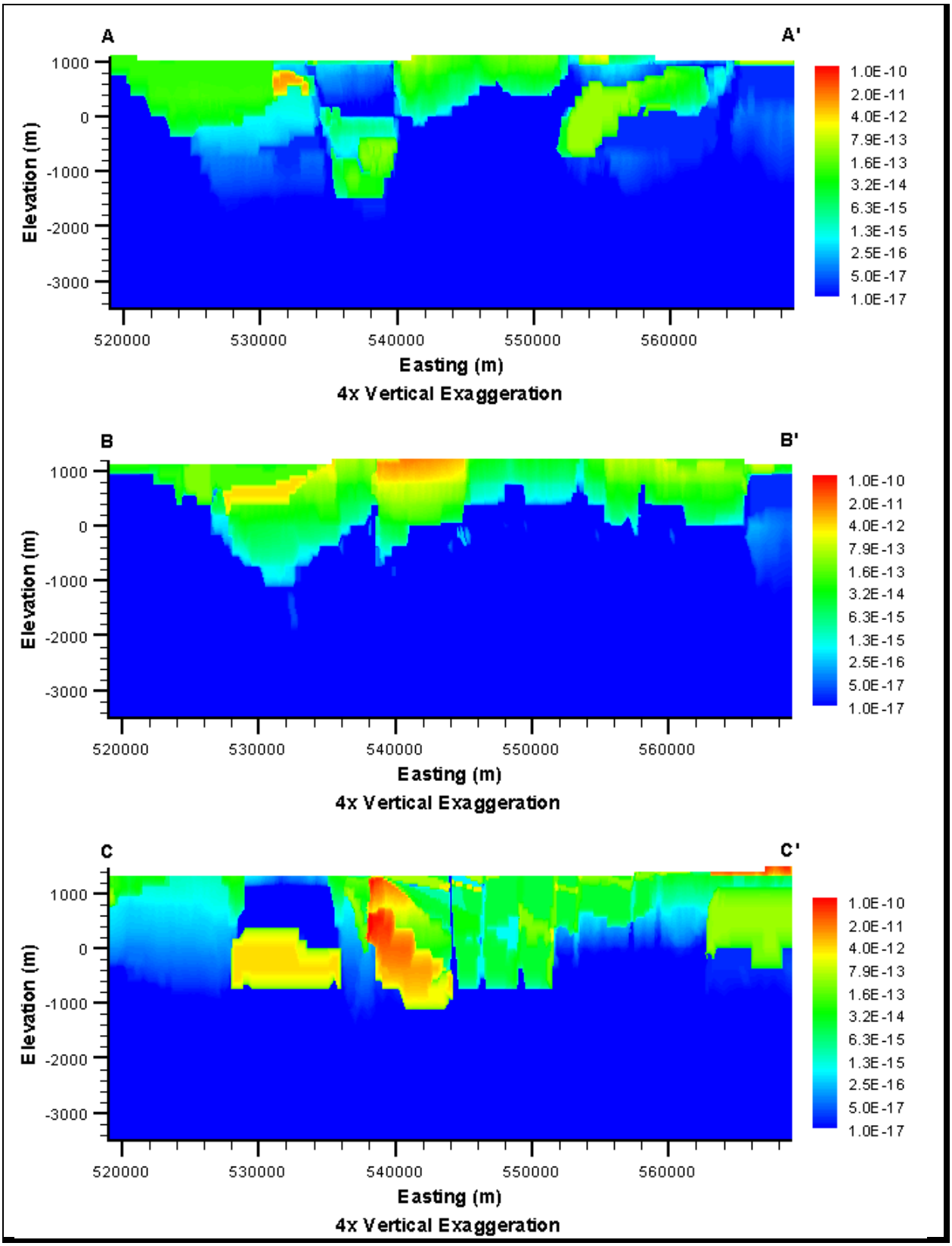
A
A'
1000
0
-1000
-2000
-3000
Elevation (m)
520000
530000
540000
550000
560000
Easting (m)
4x Vertical Exaggeration
1.0E-10
2.0E-11
4.0E-12
7.9E-13
1.6E-13
3.2E-14
6.3E-15
1.3E-15
2.5E-16
5.0E-17
1.0E-17
B
B'
1000
0
-1000
-2000
-3000
Elevation (m)
520000
530000
540000
550000
560000
Easting (m)
4x Vertical Exaggeration
1.0E-10
2.0E-11
4.0E-12
7.9E-13
1.6E-13
3.2E-14
6.3E-15
1.3E-15
2.5E-16
5.0E-17
1.0E-17
C
C'
1000
0
-1000
-2000
-3000
Elevation (m)
520000
530000
540000
550000
560000
Easting (m)
4x Vertical Exaggeration
1.0E-10
2.0E-11
4.0E-12
7.9E-13
1.6E-13
3.2E-14
6.3E-15
1.3E-15
2.5E-16
5.0E-17
1.0E-17

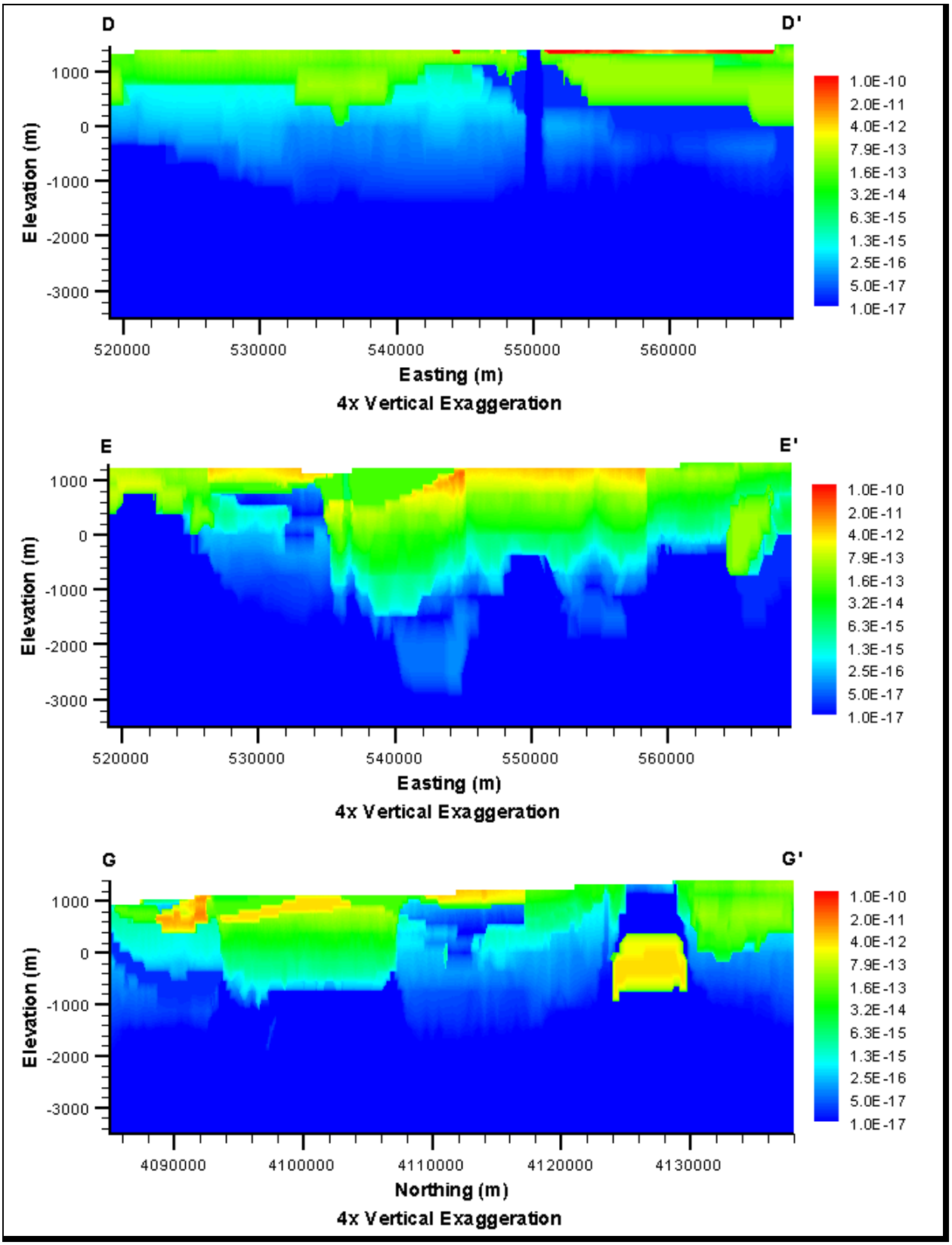
D
D'
1000
0
-1000
-2000
-3000
Elevation (m)
520000
530000
540000
550000
560000
Easting (m)
4x Vertical Exaggeration
1.0E-10
2.0E-11
4.0E-12
7.9E-13
1.6E-13
3.2E-14
6.3E-15
1.3E-15
2.5E-16
5.0E-17
1.0E-17
E
E'
1000
0
-1000
-2000
-3000
Elevation (m)
520000
530000
540000
550000
560000
Easting (m)
4x Vertical Exaggeration
1.0E-10
2.0E-11
4.0E-12
7.9E-13
1.6E-13
3.2E-14
6.3E-15
1.3E-15
2.5E-16
5.0E-17
1.0E-17
G
G'
1000
0
-1000
-2000
-3000
Elevation (m)
4090000
4100000
4110000
4120000
4130000
Northing (m)
4x Vertical Exaggeration
1.0E-10
2.0E-11
4.0E-12
7.9E-13
1.6E-13
3.2E-14
6.3E-15
1.3E-15
2.5E-16
5.0E-17
1.0E-17

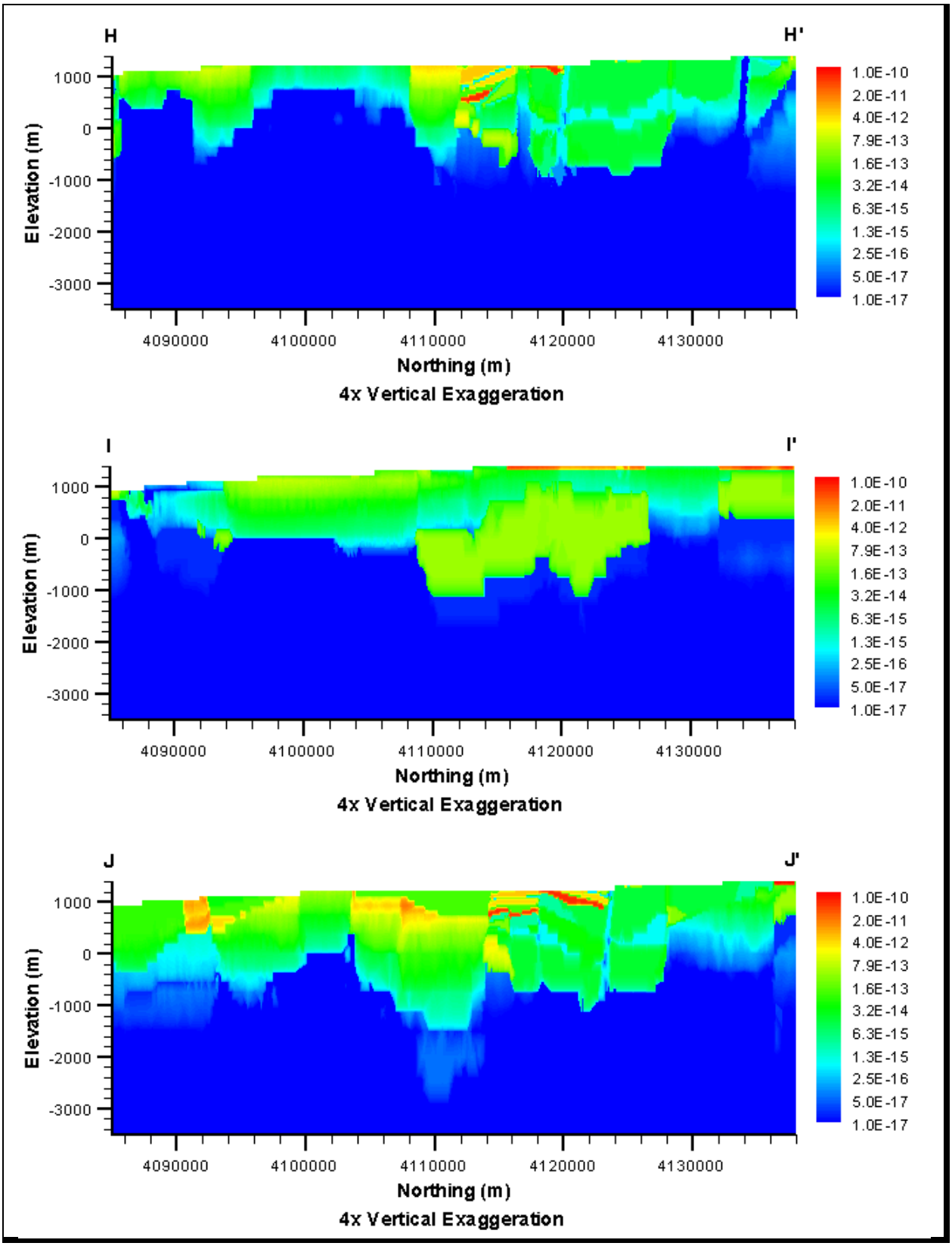
H
H'
1000
0
-1000
-2000
-3000
Elevation (m)
4090000
4100000
4110000
4120000
4130000
Northing (m)
4x Vertical Exaggeration
1.0E-10
2.0E-11
4.0E-12
7.9E-13
1.6E-13
3.2E-14
6.3E-15
1.3E-15
2.5E-16
5.0E-17
1.0E-17
I
I'
1000
0
-1000
-2000
-3000
Elevation (m)
4090000
4100000
4110000
4120000
4130000
Northing (m)
4x Vertical Exaggeration
1.0E-10
2.0E-11
4.0E-12
7.9E-13
1.6E-13
3.2E-14
6.3E-15
1.3E-15
2.5E-16
5.0E-17
1.0E-17
J
J'
1000
0
-1000
-2000
-3000
Elevation (m)
4090000
4100000
4110000
4120000
4130000
Northing (m)
4x Vertical Exaggeration
1.0E-10
2.0E-11
4.0E-12
7.9E-13
1.6E-13
3.2E-14
6.3E-15
1.3E-15
2.5E-16
5.0E-17
1.0E-17

Deeply Rooted Belted Range Fault Thrust (DRT-DRIA-SDA)

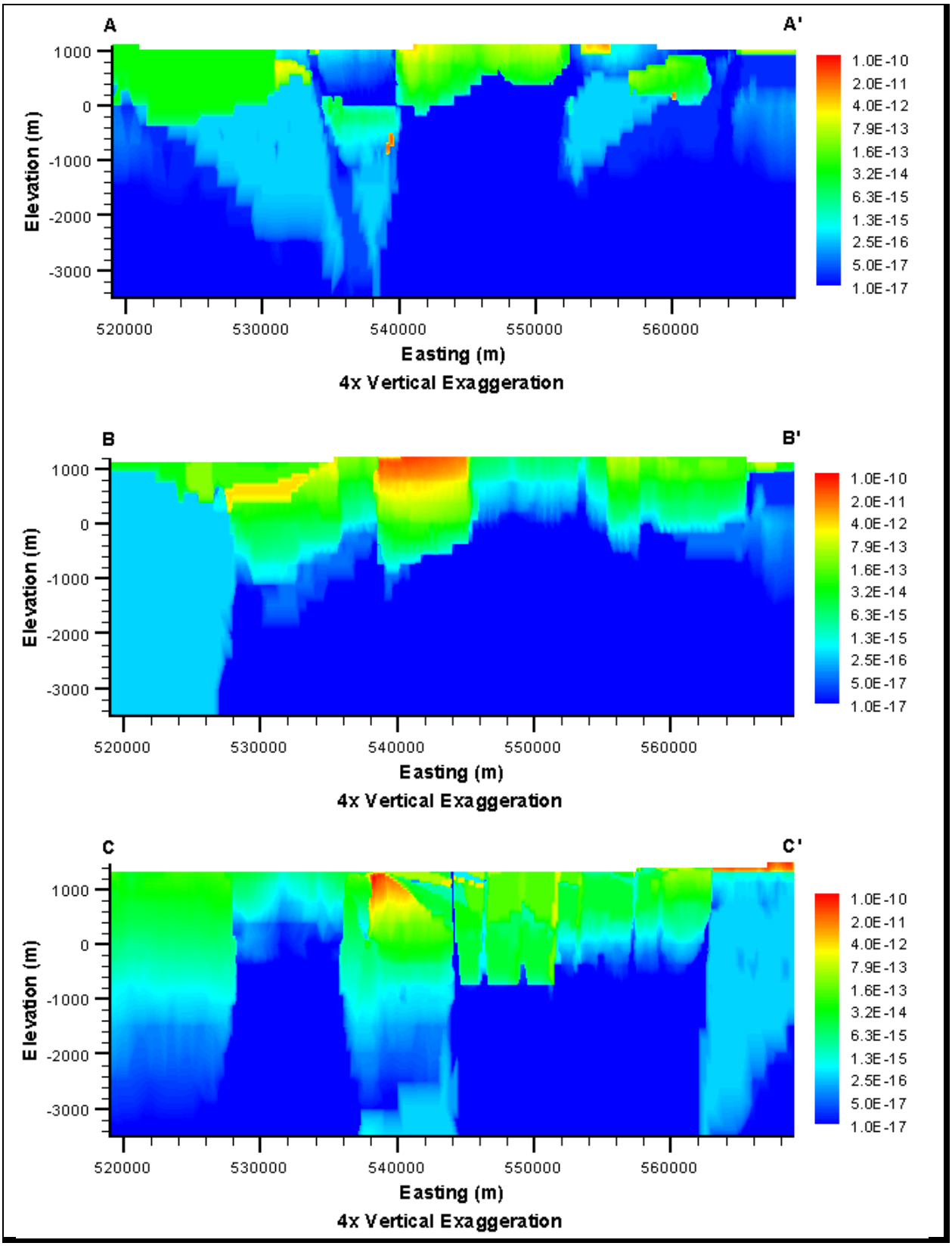
A
A'
1000
0
-1000
-2000
-3000
Elevation (m)
520000
530000
540000
550000
560000
Easting (m)
4x Vertical Exaggeration
1.0E-10
2.0E-11
4.0E-12
7.9E-13
1.6E-13
3.2E-14
6.3E-15
1.3E-15
2.5E-16
5.0E-17
1.0E-17
B
B'
1000
0
-1000
-2000
-3000
Elevation (m)
520000
530000
540000
550000
560000
Easting (m)
4x Vertical Exaggeration
1.0E-10
2.0E-11
4.0E-12
7.9E-13
1.6E-13
3.2E-14
6.3E-15
1.3E-15
2.5E-16
5.0E-17
1.0E-17
C
C'
1000
0
-1000
-2000
-3000
Elevation (m)
520000
530000
540000
550000
560000
Easting (m)
4x Vertical Exaggeration
1.0E-10
2.0E-11
4.0E-12
7.9E-13
1.6E-13
3.2E-14
6.3E-15
1.3E-15
2.5E-16
5.0E-17
1.0E-17

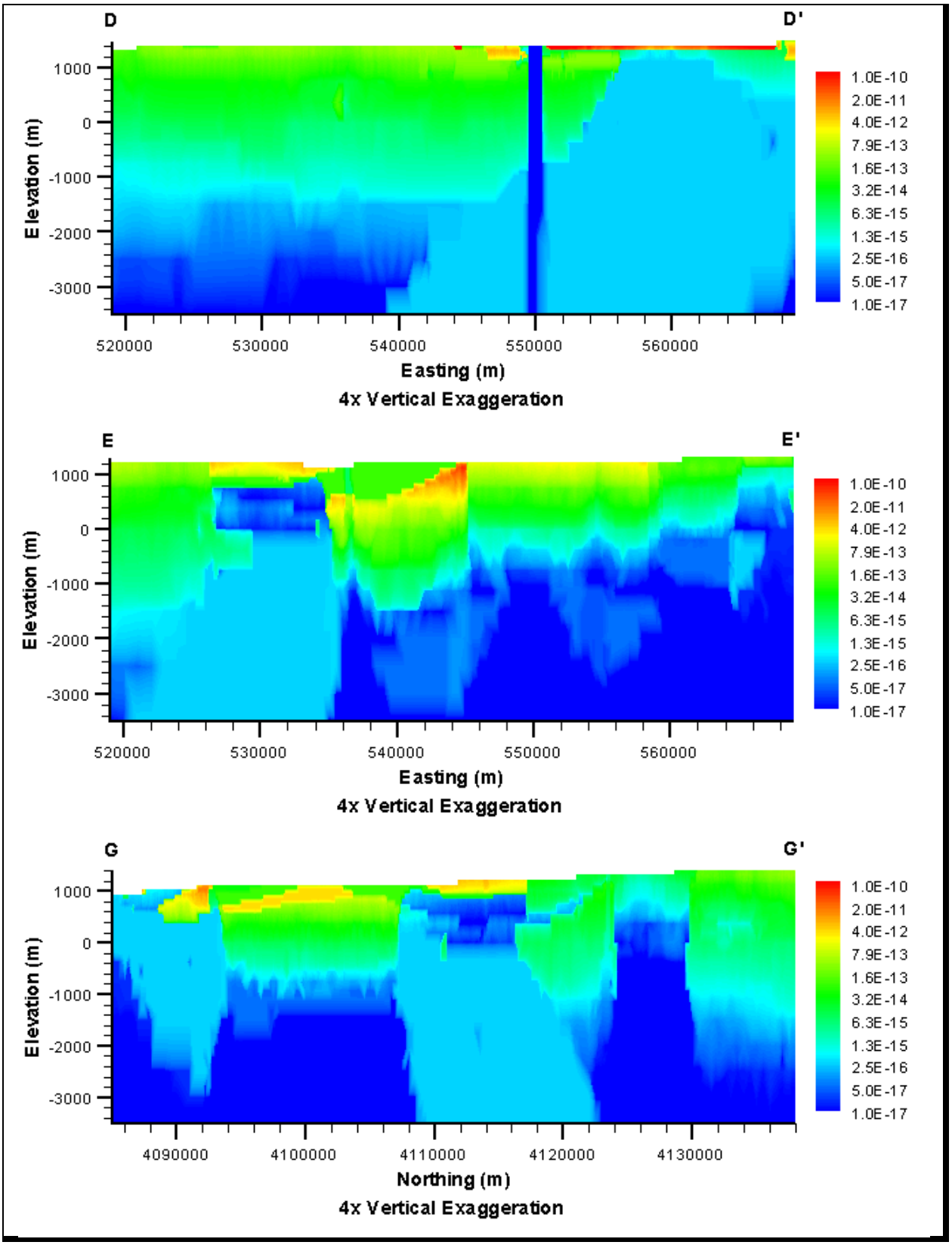
D
D'
1000
0
-1000
-2000
-3000
Elevation (m)
520000
530000
540000
550000
560000
Easting (m)
4x Vertical Exaggeration
1.0E-10
2.0E-11
4.0E-12
7.9E-13
1.6E-13
3.2E-14
6.3E-15
1.3E-15
2.5E-16
5.0E-17
1.0E-17
E
E'
1000
0
-1000
-2000
-3000
Elevation (m)
520000
530000
540000
550000
560000
Easting (m)
4x Vertical Exaggeration
1.0E-10
2.0E-11
4.0E-12
7.9E-13
1.6E-13
3.2E-14
6.3E-15
1.3E-15
2.5E-16
5.0E-17
1.0E-17
G
G'
1000
0
-1000
-2000
-3000
Elevation (m)
4090000
4100000
4110000
4120000
4130000
Northing (m)
4x Vertical Exaggeration
1.0E-10
2.0E-11
4.0E-12
7.9E-13
1.6E-13
3.2E-14
6.3E-15
1.3E-15
2.5E-16
5.0E-17
1.0E-17

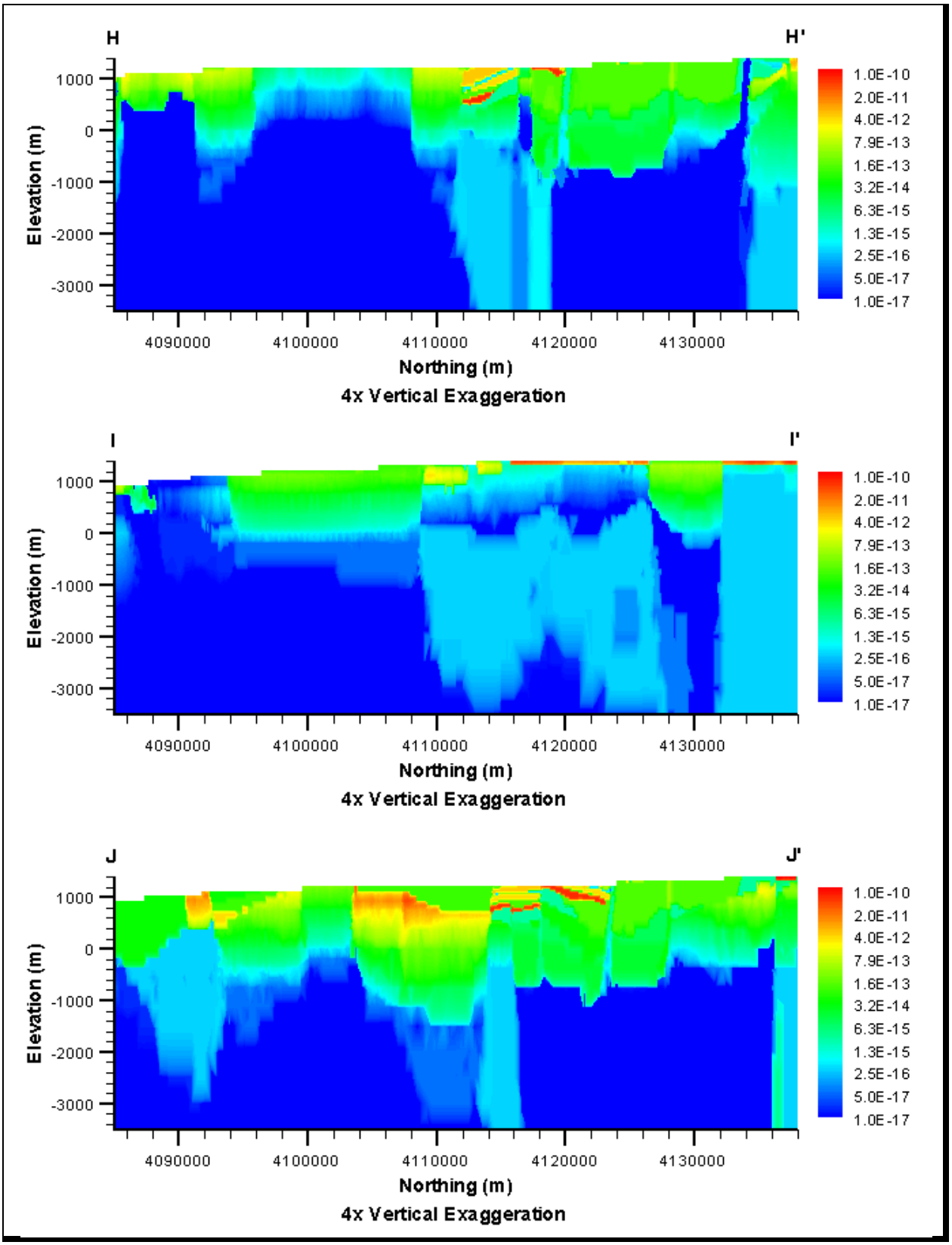
H
H'
1000
0
-1000
-2000
-3000
Elevation (m)
4090000
4100000
4110000
4120000
4130000
Northing (m)
4x Vertical Exaggeration
1.0E-10
2.0E-11
4.0E-12
7.9E-13
1.6E-13
3.2E-14
6.3E-15
1.3E-15
2.5E-16
5.0E-17
1.0E-17
I
I'
1000
0
-1000
-2000
-3000
Elevation (m)
4090000
4100000
4110000
4120000
4130000
Northing (m)
4x Vertical Exaggeration
1.0E-10
2.0E-11
4.0E-12
7.9E-13
1.6E-13
3.2E-14
6.3E-15
1.3E-15
2.5E-16
5.0E-17
1.0E-17
J
J'
1000
0
-1000
-2000
-3000
Elevation (m)
4090000
4100000
4110000
4120000
4130000
Northing (m)
4x Vertical Exaggeration
1.0E-10
2.0E-11
4.0E-12
7.9E-13
1.6E-13
3.2E-14
6.3E-15
1.3E-15
2.5E-16
5.0E-17
1.0E-17

Deeply Rooted Belted Range Fault Thrust (DRT-USGSD-SDA)

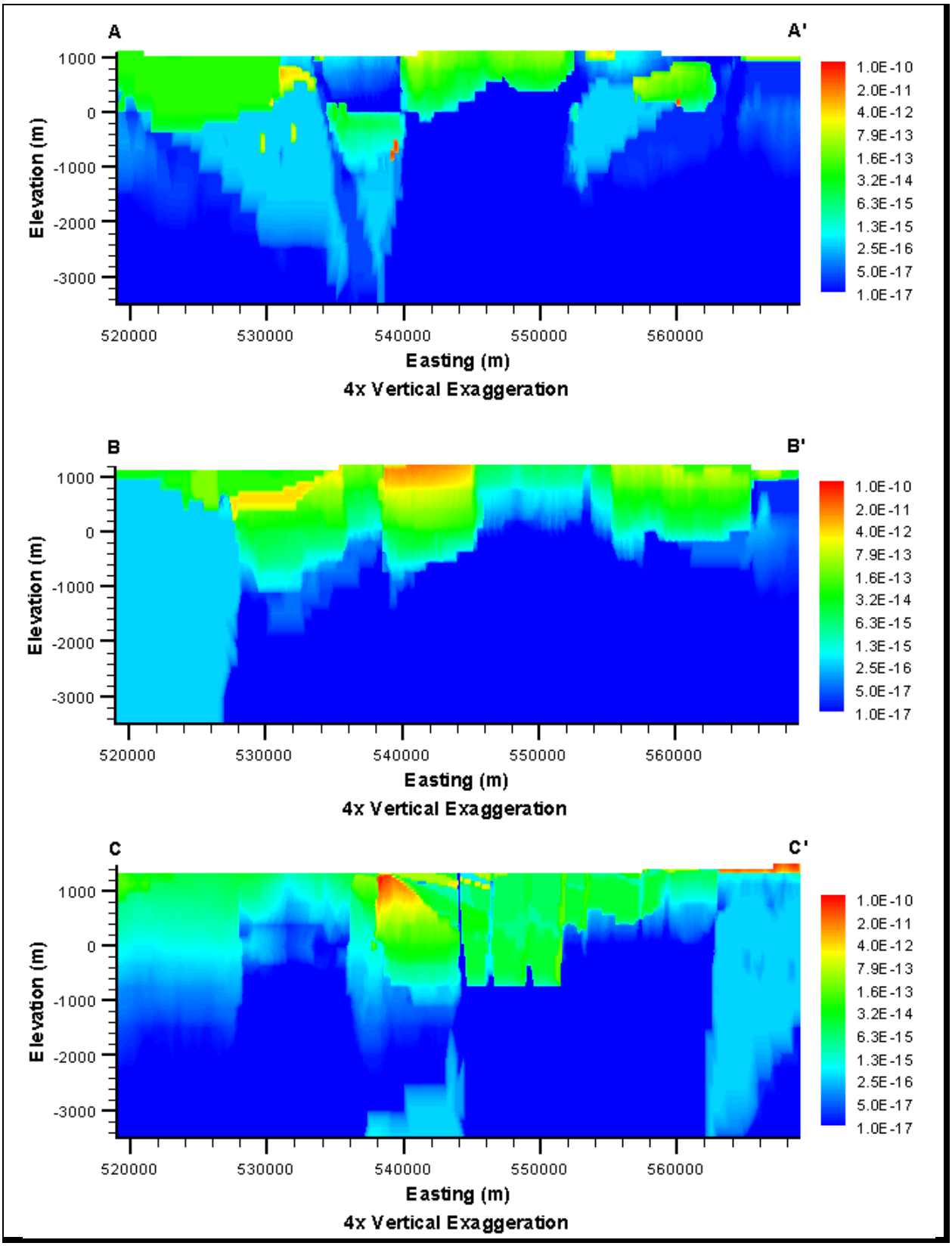
A
A'
1000
0
-1000
-2000
-3000
Elevation (m)
520000
530000
540000
550000
560000
Easting (m)
4x Vertical Exaggeration
1.0E-10
2.0E-11
4.0E-12
7.9E-13
1.6E-13
3.2E-14
6.3E-15
1.3E-15
2.5E-16
5.0E-17
1.0E-17
B
B'
1000
0
-1000
-2000
-3000
Elevation (m)
520000
530000
540000
550000
560000
Easting (m)
4x Vertical Exaggeration
1.0E-10
2.0E-11
4.0E-12
7.9E-13
1.6E-13
3.2E-14
6.3E-15
1.3E-15
2.5E-16
5.0E-17
1.0E-17
C
C'
1000
0
-1000
-2000
-3000
Elevation (m)
520000
530000
540000
550000
560000
Easting (m)
4x Vertical Exaggeration
1.0E-10
2.0E-11
4.0E-12
7.9E-13
1.6E-13
3.2E-14
6.3E-15
1.3E-15
2.5E-16
5.0E-17
1.0E-17

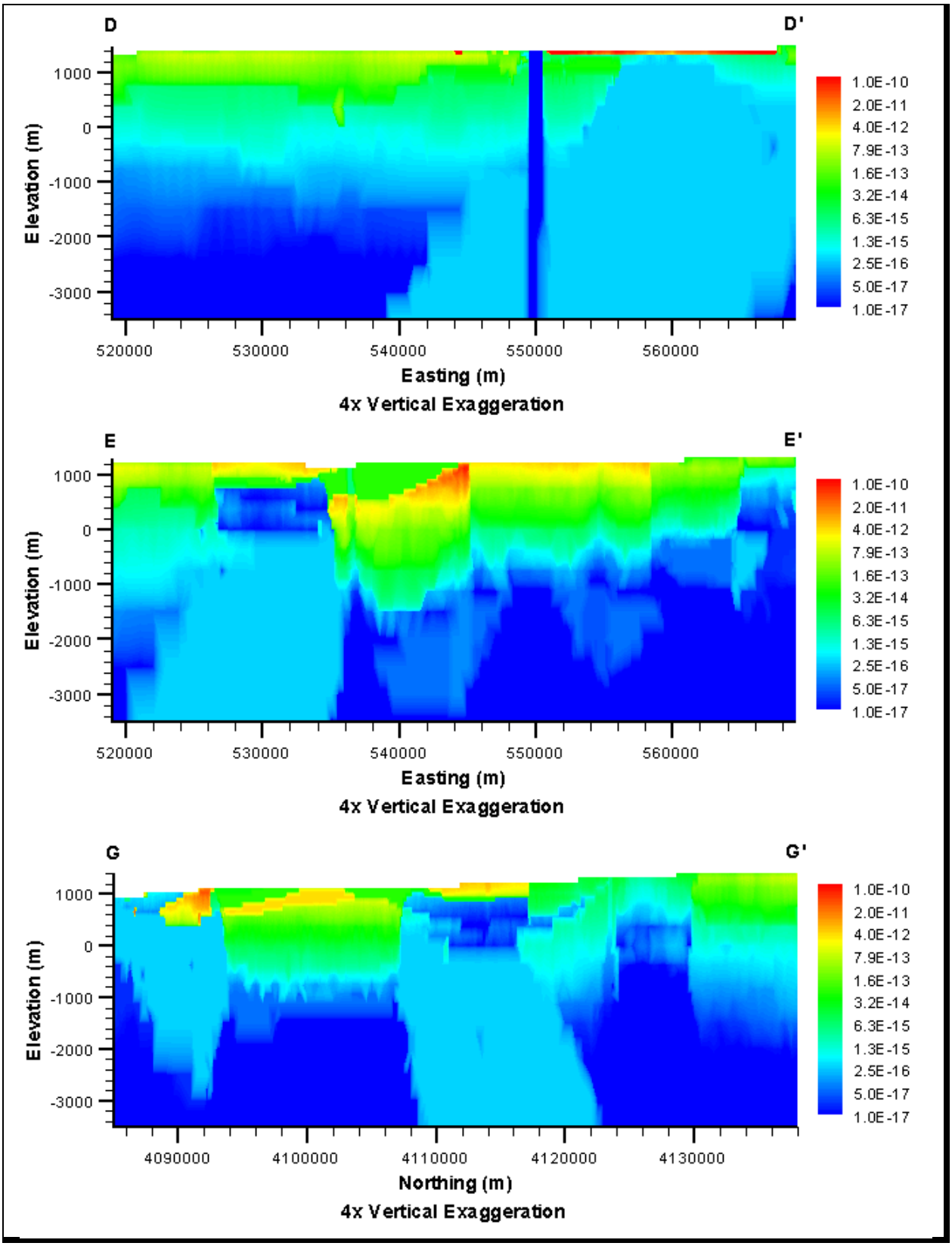
D
D'
1000
0
-1000
-2000
-3000
Elevation (m)
520000
530000
540000
550000
560000
Easting (m)
4x Vertical Exaggeration
1.0E-10
2.0E-11
4.0E-12
7.9E-13
1.6E-13
3.2E-14
6.3E-15
1.3E-15
2.5E-16
5.0E-17
1.0E-17
E
E'
1000
0
-1000
-2000
-3000
Elevation (m)
520000
530000
540000
550000
560000
Easting (m)
4x Vertical Exaggeration
1.0E-10
2.0E-11
4.0E-12
7.9E-13
1.6E-13
3.2E-14
6.3E-15
1.3E-15
2.5E-16
5.0E-17
1.0E-17
G
G'
1000
0
-1000
-2000
-3000
Elevation (m)
4090000
4100000
4110000
4120000
4130000
Northing (m)
4x Vertical Exaggeration
1.0E-10
2.0E-11
4.0E-12
7.9E-13
1.6E-13
3.2E-14
6.3E-15
1.3E-15
2.5E-16
5.0E-17
1.0E-17

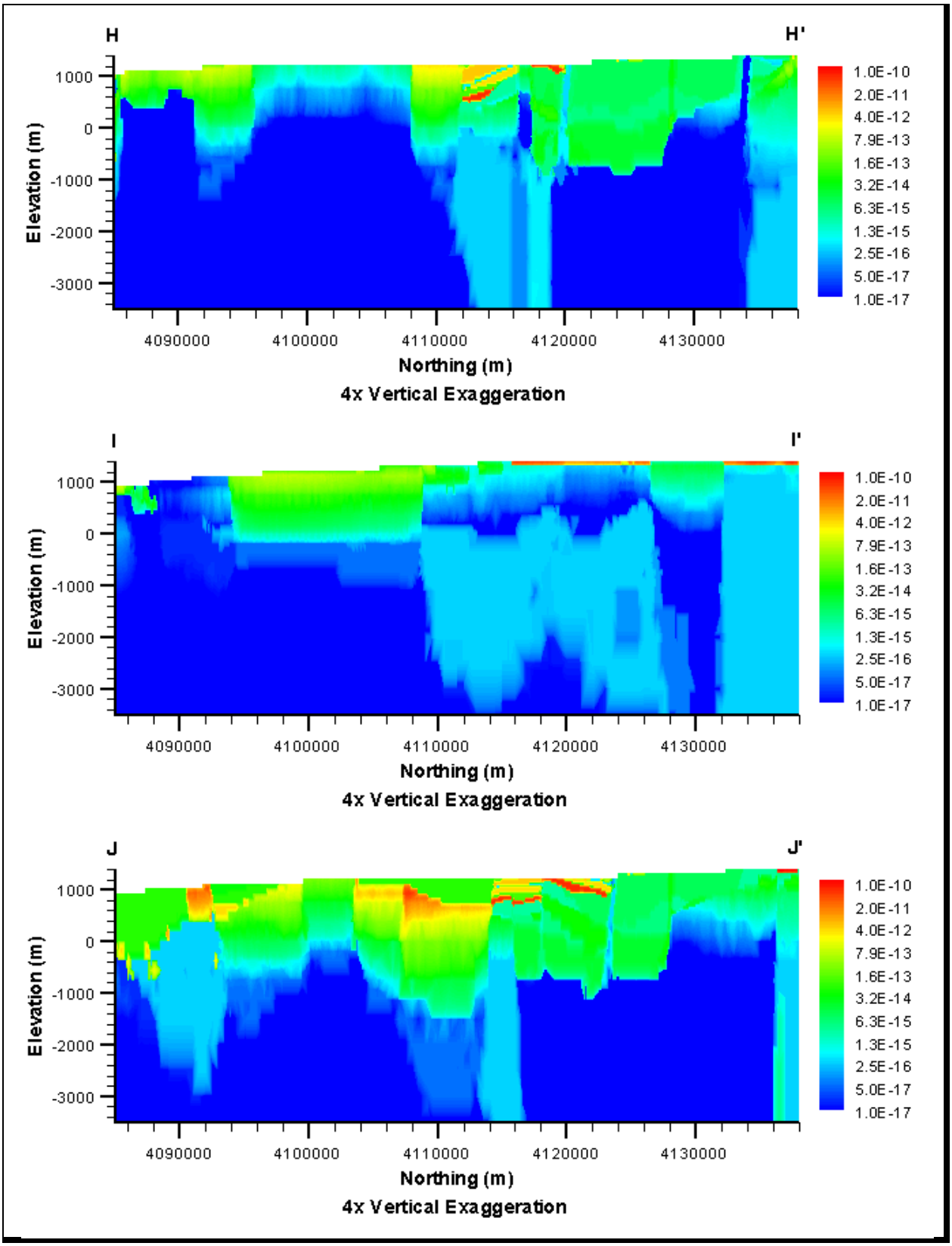
H
H'
1000
0
-1000
-2000
-3000
Elevation (m)
4090000
4100000
4110000
4120000
4130000
Northing (m)
4x Vertical Exaggeration
1.0E-10
2.0E-11
4.0E-12
7.9E-13
1.6E-13
3.2E-14
6.3E-15
1.3E-15
2.5E-16
5.0E-17
1.0E-17
I
I'
1000
0
-1000
-2000
-3000
Elevation (m)
4090000
4100000
4110000
4120000
4130000
Northing (m)
4x Vertical Exaggeration
1.0E-10
2.0E-11
4.0E-12
7.9E-13
1.6E-13
3.2E-14
6.3E-15
1.3E-15
2.5E-16
5.0E-17
1.0E-17
J
J'
1000
0
-1000
-2000
-3000
Elevation (m)
4090000
4100000
4110000
4120000
4130000
Northing (m)
4x Vertical Exaggeration
1.0E-10
2.0E-11
4.0E-12
7.9E-13
1.6E-13
3.2E-14
6.3E-15
1.3E-15
2.5E-16
5.0E-17
1.0E-17

Appendix F

Well and Spring Head Calibration Data

F.1.0 INTRODUCTION

This appendix contains summary information on the hydraulic heads, the complete water elevations dataset, and the hydrograph analysis documentation.

F.1.1 Hydraulic Head Summary Data

The hydraulic head summary data discussed in the main text of this document is shown in Table F.1-1. The mean water level elevations shown in Table F.1-1 are the suggested target heads for flow model calibration.

Table F.1-1
Summary of Hydraulic Heads at Selected Sites within the Pahute Mesa/Oasis Valley Area and Vicinity
(Page 1 of 11)

Site Name	Mean Hydraulic Head (m amsl)[a]	Minimum Hydraulic Head (m amsl)[b]	Maximum Hydraulic Head (m amsl)[b]	Standard Deviation[c]	Variance on the Mean[d]	Total Uncertainty[e]	Data Points Used	First Measurement[b]	Last Measurement[b]	Comments[f]
Beatty Wash Terrace Well	1,048.77	1,044.85	1,049.44	0.35	0.10	9.39	48	10/13/1984	09/27/2001	—
Beatty Well No 1	996.70	—	—	—	—	—	1	10/26/1962	—	—
Boiling Pot Road Well	1,102.77	1,102.39	1,103.25	0.28	0.09	9.38	42	05/08/1997	06/26/2001	—
Coffer Dune Well	1,181.47	1,181.26	1,181.69	0.12	0.04	2.36	37	04/13/1998	06/26/2001	—
Coffer Lower ET Well	1,175.36	1,174.96	1,176.02	0.31	0.11	2.43	31	08/03/1998	06/2620/01	—
Coffer Middle ET Well	1,174.46	1,173.92	1,175.03	0.36	0.14	2.46	26	01/07/1999	06/26/2001	—
Coffer Windmill Well	1,231.39	—	—	—	—	—	1	07/30/1970	—	—
ER-18-2	1,287.90	1,283.98	1,287.90	—	—	—	1	05/24/1999	06/06/2001	—
ER-19-1-1 (deep)	1,326.01	1,324.55	1,338.67	0.95	0.35	0.35	29	02/03/1994	09/25/2001	—
ER-19-1-2 (middle)	1,498.92	1,468.87	1,533.33	15.75	5.25	5.25	36	02/15/1994	09/25/2001	—
ER-19-1-3 (shallow)	1,564.44	1,564.06	1,566.70	0.2	0.10	0.10	17	02/03/1994	04/11/2001	—
ER-20-1	1,277.68	1,277.55	1,278.94	0.1	0.04	0.04	28	09/18/1992	09/24/2001	—
ER-20-2-1	1,341.04	1,340.42	1,350.20	0.34	0.13	9.42	29	08/03/1993	09/25/2001	—
ER-20-5-1 (3-in. string)	1,275.54	1,275.13	1,276.43	0.38	0.18	0.18	17	11/17/1995	05/14/1996	—
ER-20-6-1 (3-in. string)	1,356.61	1,354.78	1,359.25	0.07	0.04	0.04	10	03/21/1996	03/20/2001	—
ER-20-6-2 (3-in. string)	1,356.62	1,354.29	1,356.64	0.03	0.03	0.03	4	04/01/1996	03/20/2001	—
ER-20-6-3 (3-in. string)	1,356.50	1,355.25	1,356.58	0.08	0.05	0.05	11	04/16/1996	09/24/2001	—
ER-30-1	1,280.06	1,280.01	1,280.13	0.05	0.03	0.03	9	06/21/1994	06/24/1994	—

Table F.1-1
Summary of Hydraulic Heads at Selected Sites within the Pahute Mesa/Oasis Valley Area and Vicinity
(Page 2 of 11)

Site Name	Mean Hydraulic Head (m amsl)[a]	Minimum Hydraulic Head (m amsl)[b]	Maximum Hydraulic Head (m amsl)[b]	Standard Deviation[c]	Variance on the Mean[d]	Total Uncertainty[e]	Data Points Used	First Measurement[b]	Last Measurement[b]	Comments[f]
ER-EC-1	1,271.08	1,270.98	1,271.81	0.02	0.01	0.04	8	05/10/1999	09/24/2001	—
ER-EC-2A (498.3-681.5 m)	1,264.22	1,263.06	1,264.24	0.03	0.04	0.07	2	02/18/2000	03/26/2001	—
ER-EC-2A (498.35-1515.8 m)	1,266.26	1,260.14	1,266.36	0.10	0.12	0.14	3	02/18/2000	08/07/2000	—
ER-EC-4 (290.2-1062.8 m)	1,222.46	1,222.40	1,222.48	0.02	0.02	0.04	4	07/18/1999	08/24/2000	—
ER-EC-4 (290.2-699.5 m)	1,222.50	1,222.49	1,222.53	0.02	0.02	0.04	5	10/05/2000	10/03/2001	—
ER-EC-4 (Lower Interval)	1,220.17	—	—	—	—	—	1	02/16/2000	—	—
ER-EC-5	1,237.55	1,237.34	1,237.62	0.05	0.04	0.06	7	07/19/1999	03/26/2001	—
ER-EC-6 (481.9-1164.3 m)	1,273.53	1,273.50	1,273.55	0.02	0.02	0.04	6	06/06/2000	09/24/2001	—
ER-EC-6 (481.9-1524 m)	1,273.60	1,273.58	1,274.25	0.01	0.01	0.03	4	04/20/1999	03/13/2000	—
ER-EC-7	1,236.67	1,236.46	1,236.76	0.1	0.08	0.10	7	08/30/1999	03/26/2001	—
ER-EC-8	1,222.36	1,222.24	1,222.43	0.05	0.04	0.06	8	08/04/1999	10/03/2001	—
ER-OV-01	1,235.86	1,235.61	1,236.48	0.02	0.01	0.03	17	10/02/1997	09/13/2001	—
ER-OV-02	1,174.04	1,173.67	1,174.10	0.05	0.02	0.05	17	10/02/1997	09/13/2001	—
ER-OV-03a	1,154.35	1,154.13	1,154.54	0.13	0.07	0.09	16	10/02/1997	09/13/2001	—
ER-OV-03a2	1,122.86	1,122.48	1,123.01	0.09	0.04	0.07	17	10/02/1997	09/13/2001	—
ER-OV-03a3	1,154.24	1,154.08	1,154.44	0.13	0.06	0.09	17	10/02/1997	09/13/2001	—
ER-OV-03b	1,184.52	1,184.29	1,184.61	0.07	0.03	0.06	17	10/02/1997	09/13/2001	—
ER-OV-03c	1,212.28	1,211.97	1,212.33	0.04	0.02	0.04	17	10/02/1997	09/13/2001	—

Table F.1-1
Summary of Hydraulic Heads at Selected Sites within the Pahute Mesa/Oasis Valley Area and Vicinity
(Page 3 of 11)

Site Name	Mean Hydraulic Head (m amsl)[a]	Minimum Hydraulic Head (m amsl)[b]	Maximum Hydraulic Head (m amsl)[b]	Standard Deviation[c]	Variance on the Mean[d]	Total Uncertainty[e]	Data Points Used	First Measurement[b]	Last Measurement[b]	Comments[f]
ER-OV-03c2	1,212.31	1,211.98	1,212.41	0.04	0.02	0.04	23	10/02/1997	09/13/2001	—
ER-OV-04a	1,056.85	1,056.36	1,057.02	0.12	0.06	0.08	17	10/02/1997	09/13/2001	—
ER-OV-05	1,190.50	1,190.19	1,190.52	0.02	0.01	0.03	17	10/02/1997	09/13/2001	—
ER-OV-06a	1,236.82	1,236.76	1,236.99	0.03	0.01	0.03	27	10/02/1997	09/13/2001	—
ER-OV-06a2	1,235.64	1,235.41	1,235.67	0.03	0.01	0.04	17	10/02/1997	09/13/2001	—
Gexa Well 4	1,010.05	954.99	1,010.10	—	—	—	1	09/01/1989	03/14/1996	—
Hagestad 1	1,841.84	1,802.13	1,843.77	1.48	0.53	0.53	31	01/24/1958	12/05/1963	—
Matheny Well	1,039.12	1,037.54	1,039.12	—	—	—	1	04/12/1988	03/21/1997	—
MOV ET Well	1,123.26	1,122.76	1,124.04	0.37	0.11	2.43	46	05/08/1997	06/26/2001	—
Pioneer Road Seep Well	1,112.22	1,111.73	1,112.61	0.25	0.08	9.37	43	05/22/1997	06/26/2001	—
PM-1 (2356.408 m)	1,359.49	1,355.14	1,360.53	0.5	0.13	0.13	61	01/01/1969	06/06/2001	—
PM-2	1,442.76	1,439.27	1,447.37	0.13	0.04	0.04	54	01/01/1969	09/24/2001	—
PM-3 (Upper Borehole)	1,330.42	1,331.00	1,331.61	—	—	—	1	09/09/1988	09/13/1988	—
PM-3 (Lower Borehole)	1,330.35	1,329.57	1,331.00	0.41	0.18	0.18	21	09/21/88	09/30/91	—
PM-3-1 (Piez 1)	1,330.58	1,329.72	1,330.58	—	—	—	1	04/10/1992	06/05/2001	—
PM-3-2 (Piez 2)	1,331.18	1,330.42	1,331.18	—	—	—	1	04/10/1992	06/05/2001	—
Springdale ET Deep Well	1,131.67	1,131.18	1,132.12	0.28	0.07	2.39	60	06/20/1996	06/26/2001	—
Springdale ET Shallow Well	1,131.13	1,130.56	1,131.50	0.36	0.10	2.42	57	08/14/1996	06/26/2001	—

Table F.1-1
Summary of Hydraulic Heads at Selected Sites within the Pahute Mesa/Oasis Valley Area and Vicinity
(Page 4 of 11)

Site Name	Mean Hydraulic Head (m amsl)[a]	Minimum Hydraulic Head (m amsl)[b]	Maximum Hydraulic Head (m amsl)[b]	Standard Deviation[c]	Variance on the Mean[d]	Total Uncertainty[e]	Data Points Used	First Measurement[b]	Last Measurement[b]	Comments[f]
Springdale Lower Well	1,129.70	1,128.33	1,130.82	0.81	0.21	9.50	58	06/20/1996	06/26/2001	—
Springdale Upper Well	1,143.29	1,143.13	1,143.45	0.09	0.02	2.35	60	06/06/1996	09/27/2001	—
Springdale Windmill Well	1,175.24	1,174.39	1,175.43	0.09	0.03	2.35	44	04/01/1941	09/25/2000	—
TW-1 (1125 m)	1,430.40	1,428.93	1,430.49	0.02	0.02	0.02	5	04/07/1980	07/26/2001	—
TW-1 (1127-1137 m)	1,271.57	—	—	—	—	—	1	06/09/1961	—	—
TW-1 (170 m)	1,751.17	—	—	—	—	—	1	09/30/1960	—	—
TW-1 (492 m)	1,749.67	1,749.61	1,749.67	—	—	—	1	11/10/1960	11/18/1960	—
TW-1 (560 m)	1,564.20	1,564.20	1,564.36	—	—	—	1	02/17/1961	02/21/1961	—
TW-1 (826 m)	1,437.07	1,437.07	1,437.16	—	—	—	1	08/14/1962	08/16/1962	—
TW-1 (839 m)	1,437.31	1,437.01	1,437.71	0.26	0.17	0.17	9	09/25/1963	10/17/1963	—
TW-1 (839-1279 m)	1,277.25	1,276.41	1,277.33	0.06	0.05	0.05	6	09/25/1963	12/05/1963	—
U-12s (451.1 m)	1,784.75	1,778.87	1,791.00	1.92	0.51	0.51	57	08/06/1966	07/25/2001	—
U-19ab	1,494.97	1,494.74	1,495.35	0.29	0.29	0.29	4	07/17/1980	06/30/1985	—
U-19ab 2	1,497.89	1,497.48	1,498.11	0.36	0.42	0.42	3	12/03/1984	12/12/1984	—
U-19ad	1,372.21	—	—	—	—	—	1	06/16/1979	—	—
U-19ae	1,369.77	1,369.47	1,370.08	0.43	0.61	0.61	2	01/24/1982	02/23/1982	—
U-19ai	1,428.99	1,428.29	1,429.82	0.46	0.29	0.29	10	06/30/1980	10/11/1980	—
U-19aj	1,432.38	—	—	—	—	0.58	1	02/23/1981	—	—

Table F.1-1
Summary of Hydraulic Heads at Selected Sites within the Pahute Mesa/Oasis Valley Area and Vicinity
(Page 5 of 11)

Site Name	Mean Hydraulic Head (m amsl)[a]	Minimum Hydraulic Head (m amsl)[b]	Maximum Hydraulic Head (m amsl)[b]	Standard Deviation[c]	Variance on the Mean[d]	Total Uncertainty[e]	Data Points Used	First Measurement[b]	Last Measurement[b]	Comments[f]
U-19aq	1,428.95	1,428.45	1,429.36	0.47	0.54	0.54	3	01/10/1987	06/17/1987	—
U-19ar	1,398.93	1,398.12	1,399.64	0.77	0.89	—	3	11/05/1985	03/28/1986	—
U-19aS (857 m)	1,392.69	—	—	—	—	—	1	07/27/1964	—	—
U-19au	1,358.57	1,358.28	1,360.02	0.14	0.09	0.09	9	06/05/1987	06/30/1988	—
U-19au 1	1,358.78	1,358.62	1,359.10	0.28	0.32	0.35	3	02/22/1988	03/02/1988	—
U-19ay	1,396.93	1,396.87	1,399.15	0.05	0.06	0.06	3	12/22/1987	01/09/1989	—
U-19az	1,424.58	1,417.08	1,425.06	0.18	0.07	0.07	26	12/16/1988	07/02/1990	—
U-19ba	1,488.78	1,484.44	1,488.89	0.05	0.03	0.03	10	09/15/1989	12/11/1990	—
U-19bg 1	1,394.52	1,394.34	1,394.70	0.14	0.13	0.13	5	08/20/1991	11/18/1991	—
U-19bh	1,425.93	1,410.52	1,426.06	0.08	0.06	0.06	7	06/24/1991	06/12/2001	—
U-19bj	1,493.23	1,493.23	1,495.90	—	—	—	1	09/24/1992	06/12/2001	—
U-19bk	1,427.93	1,427.67	1,428.14	0.14	0.06	0.06	24	09/24/1992	06/11/2001	—
U-19d 2	1,427.59	1,417.59	1,428.45	—	—	—	1	06/23/1964	01/13/1965	—
U-19e	1,432.87	1,425.46	1,432.87	—	—	—	1	09/06/1966	01/01/1969	—
U-19g	1,424.23	1,422.81	1,425.25	0.98	0.80	0.80	6	09/27/1965	01/04/1976	—
U-19x	1,392.02	—	—	0	0	—	2	08/21/1976	06/30/1978	—
U-20 WW (Open)	1,351.54	1,351.48	1,351.61	0.09	0.13	0.13	2	07/01/1982	07/16/1985	—
U-20a	1,328.66	1,328.66	1,328.93	—	—	—	1	02/13/1964	01/01/1969	—

Table F.1-1
Summary of Hydraulic Heads at Selected Sites within the Pahute Mesa/Oasis Valley Area and Vicinity
(Page 6 of 11)

Site Name	Mean Hydraulic Head (m amsl)[a]	Minimum Hydraulic Head (m amsl)[b]	Maximum Hydraulic Head (m amsl)[b]	Standard Deviation[c]	Variance on the Mean[d]	Total Uncertainty[e]	Data Points Used	First Measurement[b]	Last Measurement[b]	Comments[f]
U-20a 2 WW	1,343.25	1,342.95	1,345.39	—	—	—	1	03/30/1964	10/23/1975	—
U-20ah	1,354.02	1,352.40	1,355.75	1.02	0.59	0.59	12	12/15/1980	04/01/1981	—
U-20ai	1,356.20	1,355.14	1,357.27	0.67	0.51	0.51	7	09/26/1981	10/30/1985	—
U-20ak	1,278.46	1,277.72	1,279.25	0.54	0.41	0.41	7	07/11/1982	11/30/1985	—
U-20am	1,356.97	1,356.67	1,357.27	0.43	0.61	0.61	2	10/13/1983	02/01/1984	—
U-20an	1,363.10	1,362.88	1,363.37	0.25	0.29	0.29	3	10/10/1984	03/12/1985	—
U-20ao	1,317.29	—	—	—	—	—	1	05/17/1985	—	—
U-20ar 1	1,364.42	1,363.50	1,366.17	0.49	0.35	0.37	8	02/09/1987	05/08/1987	—
U-20as	1,284.43	1,284.41	1,284.70	0.03	0.03	0.03	4	04/22/1986	06/06/1986	—
U-20at 1	1,284.41	1,284.03	1,284.64	0.29	0.29	0.29	4	12/09/1986	02/13/1987	—
U-20av	1,338.00	1,336.20	1,338.38	0.53	0.75	0.77	2	08/04/1986	12/08/1986	—
U-20aw	1,371.43	1,371.30	1,371.60	0.1	0.06	0.06	10	12/10/1986	11/04/1988	—
U-20ax	1,329.93	1,328.87	1,367.12	0.24	0.08	0.08	37	08/31/1987	05/26/1993	—
U-20ay	1,360.98	1,357.82	1,363.89	0.06	0.04	0.04	9	06/22/1987	01/11/1988	—
U-20az	1,345.05	1,334.48	1,345.05	—	—	—	1	12/12/1988	08/31/1989	+1 to 5 m
U-20bb (579.12 m)	1,367.70	1,341.03	1,367.70	—	—	—	1	07/15/1988	12/18/1989	+10 to 20 m
U-20bb (676.66 m)	1,272.94	1,272.94	1,298.11	—	—	—	1	02/13/1990	04/19/1990	-1 to 5 m
U-20bb 1	1,280.00	1,279.71	1,280.23	0.16	0.08	2.40	17	05/15/1990	07/09/1990	—

Table F.1-1
Summary of Hydraulic Heads at Selected Sites within the Pahute Mesa/Oasis Valley Area and Vicinity
(Page 7 of 11)

Site Name	Mean Hydraulic Head (m amsl)[a]	Minimum Hydraulic Head (m amsl)[b]	Maximum Hydraulic Head (m amsl)[b]	Standard Deviation[c]	Variance on the Mean[d]	Total Uncertainty[e]	Data Points Used	First Measurement[b]	Last Measurement[b]	Comments[f]
U-20bc	1,303.07	1,299.70	1,303.87	0.13	0.05	0.05	23	07/07/1988	08/02/1989	—
U-20bd (689.15 m)	1,355.79	1,355.72	1,355.87	0.05	0.04	0.04	7	04/28/1989	05/16/1989	—
U-20bd 1	1,355.50	1,355.35	1,355.68	0.14	0.13	0.13	5	01/09/1990	03/14/1990	—
U-20bd 2	1,355.86	1,355.58	1,356.21	0.24	0.21	0.24	5	01/09/1990	03/14/1990	—
U-20be	1,303.78	1,303.48	1,319.39	0.2	0.10	0.10	15	06/14/1989	06/05/1991	—
U-20bf	1,338.18	1,332.77	1,353.98	0.43	0.15	0.15	31	08/28/1989	01/30/1991	—
U-20bg	1,352.49	1,350.07	1,352.98	—	—	—	1	01/08/1991	09/25/2001	+5 m
U-20c	1,275.28	1,273.15	1,275.28	—	—	—	1	02/25/1965	11/13/2000	—
U-20e	1,360.32	—	—	—	—	—	1	02/07/1969	—	—
U-20g	1,357.27	—	—	—	—	—	1	10/30/1964	—	—
U-20i	1,361.24	—	—	—	—	—	1	08/30/1967	—	—
U-20m	1,412.14	—	—	—	—	—	1	10/04/1968	—	—
U-20n PS 1DD-H (922 m)	1,350.32	1,345.84	1,350.32	—	—	—	1	05/17/1985	07/09/1998	—
U-20y	1,276.94	1,275.28	1,278.03	0.76	0.51	0.51	9	12/18/1974	02/18/1975	—
UE-12n 15a	1,841.00	1,840.44	1,841.97	0.64	0.57	0.57	5	05/31/1988	06/20/1988	—
UE-18r	1,271.89	1,269.74	1,272.34	0.61	0.21	0.21	35	01/29/1968	06/06/2001	—
UE-18t	1,306.27	1,305.73	1,307.35	0.22	0.07	0.09	43	10/06/1978	06/06/2001	—
UE-19b 1 WW	1,427.93	1,427.90	1,427.96	0.04	0.06	0.08	2	06/19/1964	01/13/1965	—

Table F.1-1
Summary of Hydraulic Heads at Selected Sites within the Pahute Mesa/Oasis Valley Area and Vicinity
(Page 8 of 11)

Site Name	Mean Hydraulic Head (m amsl)[a]	Minimum Hydraulic Head (m amsl)[b]	Maximum Hydraulic Head (m amsl)[b]	Standard Deviation[c]	Variance on the Mean[d]	Total Uncertainty[e]	Data Points Used	First Measurement[b]	Last Measurement[b]	Comments[f]
UE-19c WW	1,430.50	1,428.32	1,438.38	0.47	0.18	0.18	26	04/30/1964	06/12/2001	—
UE-19e WW	1,432.03	1,429.70	1,433.02	1.56	1.56	1.56	4	09/03/1964	06/26/1975	—
UE-19fs	1,350.02	1,349.11	1,351.24	—	—	—	1	08/17/1965	—	—
UE-19gS	1,424.76	1,423.11	1,425.25	—	—	—	1	05/06/1965	—	—
UE-19gS WW	1,425.24	1,413.05	1,428.60	0	0	0.02	3	03/24/1965	01/13/1976	—
UE-19h	1,423.14	1,422.84	1,472.70	0.11	0.04	0.04	35	08/09/1965	06/11/2001	—
UE-19i	1,396.26	1,396.26	1,408.45	—	—	—	1	09/01/1965	01/01/1969	—
UE-19z	1,429.66	1,429.21	1,429.82	0.26	0.21	—	6	07/12/1977	09/24/1977	—
UE-20ab	1,357.88	1,355.75	1,357.88	—	—	—	1	06/02/1978	10/30/1978	—
UE-20av	1,319.66	1,319.32	1,319.66	—	—	—	1	12/15/1986	01/15/1987	—
UE-20bh 1	1,348.55	1,347.63	1,349.47	0.54	0.20	0.20	30	10/29/1991	09/25/2001	—
UE-20c	1,267.05	—	—	—	—	—	1	02/28/1964	11/13/2000	—
UE-20d	1,273.90	1,272.54	1292.35	0.67	0.95	0.97	2	08/19/1964	01/14/1965	—
UE-20e 1	1,365.47	1,359.49	1365.50	—	—	—	1	06/04/1964	04/05/1975	—
UE-20f (1384.7 m)	1,268.62	1,268.58	1,268.67	0.06	0.08	0.09	2	04/07/1964	11/13/2000	—
UE-20f (4171 m)	1,322.86	1,269.19	1,337.55	1.22	1.41	1.41	3	01/13/1965	11/24/1974	—
UE-20h WW	1,356.48	1,353.50	1,356.97	0.69	0.98	0.98	2	08/20/1964	01/01/1969	—
UE-20j WW	1,411.96	—	—	—	—	—	1	10/23/1964	—	—

Table F.1-1
Summary of Hydraulic Heads at Selected Sites within the Pahute Mesa/Oasis Valley Area and Vicinity
(Page 9 of 11)

Site Name	Mean Hydraulic Head (m amsl)[a]	Minimum Hydraulic Head (m amsl)[b]	Maximum Hydraulic Head (m amsl)[b]	Standard Deviation[c]	Variance on the Mean[d]	Total Uncertainty[e]	Data Points Used	First Measurement[b]	Last Measurement[b]	Comments[f]
UE-20n 1 (1005.84 m)	1,318.78	—	—	—	—	—	1	06/01/1987	—	—
UE-20n 1 (863.8 m)	1,349.75	1,346.16	1,349.75	0	0	—	2	06/12/1987	10/16/2000	—
UE-20p	1,423.11	1,412.29	1,423.11	—	—	—	1	10/01/1968	09/27/1970	—
UE-29a 1 HTH	1,189.97	1,188.12	1,194.45	1.42	0.19	0.19	219	06/21/1982	09/26/1997	—
UE-29a 2 HTH	1,187.62	1,186.24	1,191.31	1.1	0.15	0.15	219	06/21/1982	09/26/1997	—
USW UZ-N91	1,186.72	1,185.59	1,191.34	1.1	0.15	0.17	217	01/21/1986	09/26/1997	—
Ute Spr Drainage Well	1,066.02	1,065.00	1,066.82	0.63	0.19	9.48	43	05/22/1997	06/26/2001	—
WW-8	1,410.46	1,404.21	1,410.46	—	—	—	1	01/03/1963	09/13/2000	—
Spring	1,171.96	—	—	—	—	2.32	1	—	—	—
Crystal Springs Area	1,188.72	—	—	—	—	9.29	1	—	—	—
Revert Springs Channel	1,018.03	—	—	—	—	9.29	1	—	—	—
Revert Springs Area	1,027.18	—	—	—	—	14.52	1	—	—	—
Revert Springs Area	1,027.18	—	—	—	—	æ	1	—	—	—
Spring (Report R10)	1,127.76	—	—	—	—	9.29	1	—	—	—
Spring	1,057.66	—	—	—	—	9.29	1	—	—	—
Springdale Culvert	1,126.24	—	—	—	—	2.32	1	—	—	—
Torrance Spring	1,121.66	—	—	—	—	2.32	1	—	—	—
Ute Springs Area	1,083.56	—	—	—	—	0.58	1	—	—	—

Table F.1-1
Summary of Hydraulic Heads at Selected Sites within the Pahute Mesa/Oasis Valley Area and Vicinity
(Page 10 of 11)

Site Name	Mean Hydraulic Head (m amsl)[a]	Minimum Hydraulic Head (m amsl)[b]	Maximum Hydraulic Head (m amsl)[b]	Standard Deviation[c]	Variance on the Mean[d]	Total Uncertainty[e]	Data Points Used	First Measurement[b]	Last Measurement[b]	Comments[f]
Spring	1,097.28	—	—	—	—	—	1	—	—	—
OVU Culvert Spring	1,149.10	—	—	—	—	2.32	1	—	—	—
Hot Springs Area	1,097.28	—	—	—	—	9.29	1	—	—	—
Hot Springs Pump House	1,094.23	—	—	—	—	9.29	1	—	—	—
Hot Springs Bath House 1	1,094.23	—	—	—	—	9.29	1	—	—	—
Hot Springs Bath House 2	1,094.23	—	—	—	—	9.29	1	—	—	—
Hot Springs blw Culvert 1	1,094.23	—	—	—	—	9.29	1	—	—	—
Hot Springs Culvert 2	1,092.71	—	—	—	—	9.29	1	—	—	—
Hot Springs abv Culvert 2	1,092.71	—	—	—	—	9.29	1	—	—	—
Ute Springs Area	1,085.09	—	—	—	—	14.52	1	—	—	—
Spring	1,097.28	—	—	—	—	—	1	—	—	—
Ute Springs Culvert	1,051.56	—	—	—	—	9.29	1	—	—	—
Ute Springs	1,085.09	—	—	—	—	14.52	1	—	—	—
Oleo Road Spring	1,167.38	—	—	—	—	2.32	1	—	—	—
Goss Springs - North	1,139.34	—	—	—	—	9.29	1	—	—	—
Goss Springs	1,139.34	—	—	—	—	9.29	1	—	—	—
Spring id 179	1,139.35	—	—	—	—	—	—	—	—	—
Spring	1,158.24	—	—	—	—	—	1	—	—	—

Table F.1-1
Summary of Hydraulic Heads at Selected Sites within the Pahute Mesa/Oasis Valley Area and Vicinity
(Page 11 of 11)

Site Name	Mean Hydraulic Head (m amsl)[a]	Minimum Hydraulic Head (m amsl)[b]	Maximum Hydraulic Head (m amsl)[b]	Standard Deviation[c]	Variance on the Mean[d]	Total Uncertainty[e]	Data Points Used	First Measurement[b]	Last Measurement[b]	Comments[f]
Spring	1,211.58	—	—	—	—	2.32	1	—	—	—

Source: SNJV, 2004

[a]Meters above mean sea level
[b]Applies to all data available
[c]Applies only to data used
[d](2 x Standard Deviation)/Square Root (Number of Data Points Used)
[e]Total uncertainty is the variance on the mean plus variance associated with the land surface elevation
[f]Shows sites that should be used with caution with a positive or negative error associated with the hydraulic head
— Not Applicable or Not Available

F.2.0 REFERENCES

Stoller-Navarro Joint Venture. 2004. *Hydrologic Data for the Groundwater Flow and Contaminant Transport Model of Corrective Action Units 101 and 102: Central and Western Pahute Mesa, Nye County, Nevada*. Las Vegas, NV.

DISTRIBUTION

Tim Murphy — 2 HC/2CD
State of Nevada
Division of Environmental Protection
1771 E. Flamingo Road, Suite 121A
Las Vegas, NV 89119

Bill R. Wilborn — 2 HC/2CD
Environmental Restoration Project
U.S. Department of Energy
National Nuclear Security Administration
Nevada Site Office
P.O. Box 98518, MS/505
Las Vegas, NV 89193-8518

Alicia Tauber — 1 CD
Environmental Management Records
U.S. Department of Energy
National Nuclear Security Administration
Nevada Site Office
P.O. Box 98518, MS/505
Las Vegas, NV 89193-8518

U.S. Department of Energy — 1 HC
National Nuclear Security Administration
Nevada Site Office
Technical Library
P.O. Box 98518, M/S 505
Las Vegas, NV 89193-8518

U.S. Department of Energy — 1 CD
Office of Scientific and Technical Information
P.O. Box 62
Oak Ridge, TN 37831-0062

Southern Nevada Public Reading Facility — 1 HC
c/o Nuclear Testing Archive
P.O. Box 98521, M/S 400
Las Vegas, NV 89193-8521

Manager, Northern Nevada FFACO — 1 HC
Public Reading Facility
c/o Nevada State Library & Archives
100 N Stewart Street
Carson City, NV 89701-4285

Edward M. Kwicklis — 1 CD
Los Alamos National Laboratory
Hydrology, Geochemistry, and Geology Group, EES-6
Earth and Environmental Sciences Division
Bikini Atoll Rd., SM-30
Los Alamos, NM 87545

Andrew V. Wolfsberg — 1 CD
Los Alamos National Laboratory
Hydrology, Geochemistry, and Geology Group, EES-6
Earth and Environmental Sciences Division
Bikini Atoll Rd., SM-30
Los Alamos, NM 87545

Naomi Becker — 1 CD
Los Alamos National Laboratory, M/S F665
Bikini Atoll Rd., SM30
Los Alamos, NM 87545

Gayle Pawloski — 1 CD
Lawrence Livermore National Laboratory
7000 East Avenue, L-221
Livermore, CA 94550-9234

Mavrik Zavarin — 1 CD
Lawrence Livermore National Laboratory
7000 East Avenue, L-221
Livermore, CA 94550-9234

Bonnie Thompson — 1 CD
USGS WRD
160 North Stephanie Street
Henderson, NV 89074

Chuck E. Russell — 1 CD
Desert Research Institute
755 E. Flamingo
Las Vegas, NV 89119

Ken Ortego Bechtel Nevada P.O. Box 98521, M/S NLV 082 Las Vegas, NV 89193-8521	1 CD
John P. McCord Stoller-Navarro Joint Venture 7710 W. Cheyenne, Bldg. 3 Las Vegas, NV 89129	1 CD
Greg Ruskauff Stoller-Navarro Joint Venture 7710 W. Cheyenne, Bldg. 3 Las Vegas, NV 89129	1 CD
Stoller-Navarro Joint Venture FFACO Support Office 7710 W. Cheyenne Ave., Bldg. 3 Las Vegas, NV 89129	1 HC/1 CD
Stoller-Navarro Joint Venture Central Files 7710 W. Cheyenne, Bldg. 3 Las Vegas, NV 89129	1 HC/1 CD

Plate 1 - Pahute Mesa Model Area Showing Topography, Selected Geographic Features, and Wells and Springs Used in Calibration of the Flow Model

EXPLANATION

Calibration Data Points
- Spring
- Well
- City

- Pahute Mesa Model Area
- NTS Area Boundaries
- 29 NTS Area Numbers
- Faults in Numerical Model
- Nevada Highways

ET Unit

0 1 2 4 6 8 10
Miles

0 2 4 8 12 16 20
Kilometers

Projection and Grid: Universal Transverse Mercator Zone 11, 1927 North Amercian Datum Meters

P:\Ugsh\Ugta_common\Ugta_GIS\PM_Model_Area\PM Model Area_pete.mxd